

AD-A217 381

PROCEEDINGS  
OF THE  
38th ANNUAL  
FREQUENCY CONTROL SYMPOSIUM

1984

Co-Sponsored by the



U.S. ARMY ELECTRONICS RESEARCH  
AND DEVELOPMENT COMMAND  
ELECTRONICS TECHNOLOGY AND  
DEVICES LABORATORY

and



THE INSTITUTE OF ELECTRICAL AND  
ELECTRONICS ENGINEERS, INC.  
SONICS AND ULTRASONICS GROUP

IEEE Catalog No. 84CH2062-8

Library of Congress No. 58-60781

29 May -- 1 June 1984

Marriott Hotel  
Philadelphia, Pennsylvania

Accession For	
NTIS GRA&I	✓
DTIC TAB	✓
Unannounced	✓
Justification	
per lbr	
IEEE out of stock	
A-1	

90 01 23 180

Abstracting is permitted with credit to the source. Libraries are permitted to photocopy beyond the limits of US copyright law for private use of patrons those articles in this volume that carry a code at the bottom of the first page, provided the per-copy fee indicated in the code is paid through the Copyright Clearance Center, 21 Congress Street, Salem, MA 01970. Instructors are permitted to photocopy isolated articles for noncommercial classroom use without fee. For other copying, reprint or republication permission, write to Director, Publishing Services, IEEE, 345 East 47th Street, New York, NY 10017. All rights reserved. Copyright © 1984 by The Institute of Electrical and Electronics Engineers, Inc.

## THIRTY-EIGHTH ANNUAL FREQUENCY CONTROL SYMPOSIUM

Co-Sponsored by

U.S. ARMY ELECTRONICS RESEARCH AND DEVELOPMENT COMMAND  
ELECTRONICS TECHNOLOGY AND DEVICES LABORATORY

AND

THE INSTITUTE OF ELECTRICAL AND ELECTRONICS ENGINEERS, INC.  
SONICS AND ULTRASONICS GROUP

### SYMPOSIUM CHAIRMEN

General Chairman.....Dr. John R. Vig, U.S. Army ERADCOM  
Technical Program Chairman.....Dr. Samuel R. Stein, National Bureau of Standards

### TECHNICAL PROGRAM COMMITTEE

Dr. A. Ballato  
U.S. Army, ERADCOM

Mr. M. Bloch  
Frequency Electronics, Inc.

Dr. J. Brown  
Schlumberger-Doll Research

Dr. L. Cutler  
Hewlett-Packard Company

Dr. L. Dworsky  
Motorola, Inc.

Dr. E. EerNisse  
Quartex, Inc.

Mr. M. Frerking  
Rockwell International

Dr. H. Hellwig  
Frequency and Time Systems, Inc.

Dr. W. Horton  
Piezo Crystal Company

Mr. C. Jensik  
Piezo Crystal Company

Dr. R. Kagiwada  
TRW - DSSG

Mr. D. Kemper  
Quartztek, Inc.

Mr. D. Koehler  
Sandia National Laboratory

Mr. J. Kusters  
Hewlett-Packard Company

Mr. T. Lukaszek  
U.S. Army, ERADCOM

Dr. T. Meeker  
Bell Laboratories

Dr. T. Parker  
Raytheon Research Division

Mr. V. Rosati  
U.S. Army, ERADCOM

Mr. L. Rueger  
Johns Hopkins Applied Physics Laboratory

Mr. S. Schodowski  
U.S. Army, ERADCOM

Dr. S. Stein  
EFRATOM, Div. of Ball Corp.

Dr. J. Vig  
U.S. Army, ERADCOM

Dr. R. Wagers  
Texas Instruments

Mr. C. Wardrip  
NASA - GSFC

Mr. J. White  
Naval Research Laboratory

Dr. G. Winkler  
U.S. Naval Observatory

Dr. N. Yannoni  
U.S. Air Force/RADC

## TECHNICAL SESSION CHAIRMEN

### ACCELERATION EFFECTS IN QUARTZ CRYSTALS AND ATOMIC OSCILLATORS

E.P. EerNisse, Quartex, Inc.

### CRYSTAL RESONATOR THEORY

J.H. Staudte, Consultant

### DESIGN OF QUARTZ CRYSTAL OSCILLATORS

F.L. Walls, National Bureau of Standards

### GAS CELL FREQUENCY STANDARDS

H. Robinson, Duke University

### SYSTEMS FOR TIME AND FREQUENCY DISTRIBUTION AND CHARACTERIZATION

R. Smythe, Piezo Technology Inc.

### QUARTZ RESONATOR STUDIES I

C. Jensik, Piezo Crystal Company

### QUARTZ RESONATOR STUDIES II

T. Meeker, Bell Laboratories

### IMPURITIES IN QUARTZ CRYSTALS

J.C. Brice, Philips Research Laboratories

### PIEZOELECTRIC RESONATORS

R. Filler, U.S. Army ERADCOM

### HYDROGEN MASERS AND OTHER FREQUENCY STANDARDS

R. Vessot, Smithsonian Astrophysical Observatory

### FILTERS, TRANSDUCERS AND OTHER APPLICATIONS OF QUARTZ AND OTHER RESONATORS

A. Ballato, U.S. Army ERADCOM

### ATOMIC BEAM FREQUENCY STANDARDS

L. Cutler, Hewlett Packard Company

### PROPERTIES OF PIEZOELECTRIC MATERIALS

J. Martin, Oklahoma State University

### PERFORMANCE OF QUARTZ CRYSTAL OSCILLATORS

D.E. Newell, Northern Illinois University

### SAW DEVICES I

J. Brown, Schlumberger-Doll Research

### SAW DEVICES II

R. Rosenfeld, Sawtek, Inc.



## TABLE OF CONTENTS

<b>Awards Program</b> .....	1
<b>1984 Award Winners</b> .....	2
<b>PROPERTIES OF QUARTZ AND OTHER MATERIALS</b>	
The Growth of High Purity, Low Dislocation Quartz A.F. Armington, U.S. Air Force, Rome Air Development Center and J.F. Balascio, Motorola, Inc. ....	3
Cultured Quartz of Low Aluminum Content from Production Sized Autoclaves B. Sawyer and D.R. Kinloch, Sawyer Research Products, Inc. ....	8
Distribution of Aluminum and Hydroxide Defect Centers in Irradiated Quartz H.G. Lipson and A. Kahan, U.S. Air Force, Rome Air Development Center .....	10
Aluminum-Related Acoustic Loss in AT-Cut Quartz Crystals J.J. Martin, Oklahoma State University .....	16
The Constants of Alpha Quartz R.W. Ward, Quartztronics, Inc. ....	22
Effect of Irradiation and Annealing on the Electrical Conductivity of Quartz Crystals E.R. Green, J. Toulouse, J. Wacks and A.S. Nowick, Columbia University .....	32
Probable Ion Signature in Quartz Electrodiffusion Data W.P. Hanson, Piezo Crystal Company .....	38
Sweeping and Irradiation Studies in Quartz J.G. Gualtieri and J.R. Vig, U.S. Army ERADCOM .....	42
Computer Controlled Quartz Electrodiffusion (Sweeping) with Real Time Data Collection W. P. Hanson, Piezo Crystal Company .....	50
An X-Ray Irradiation System for Total-Dose Testing of Quartz Resonators L.J. Palkuti and Q.T. Truong, Advanced Research and Applications Corp. ....	55
Results from Gamma Ray and Proton Beam Radiation Testing of Quartz Resonators J.R. Norton, J.M. Cloeren and J.J. Suter, Johns Hopkins University .....	63
<b>CRYSTAL RESONATOR THEORY, DESIGN AND PROCESSING</b>	
The Vibration Sensitivity of VHF Quartz Crystals for Missile Applications R.D. Weglein, Hughes Aircraft Company .....	73
Acceleration Sensitivity Compensation and $\Gamma$ Symmetry in Quartz Oscillators D.A. Emmons, R.M. Garvey and B.T. Milliren, Frequency & Time Systems, Inc. ....	80
A Vibration Compensation Scheme for a Tactical Rubidium Oscillator W. Weidemann, EFRATOM .....	86
Vibration Effects on EHF System Performance Employing Low Noise Rubidium Standard and Crystal Filters E.M. Perdue, Raytheon Company .....	92
Reactive Ion Beam Etching for VHF Crystal Resonators J.S. Wang, S.K. Watson and K.F. Lau, TRW Electronic Systems Group .....	101
Etch Figures and Etch Rate in AT, BT, X and Y Cut Quartz Plates C.R. Tellier, Ecole Nationale Supérieure de Mécanique et des Microtechniques .....	105

## TABLE OF CONTENTS (Continued)

Chip Crystal Resonator with Load Capacitors Y. Kojima, Y. Fujiwara, S. Yamada and N. Wakatsuki, Fujitsu Ltd. ....	114
AT-Cut Strip Resonators Enclosed in Cylindrical Package M. Okazaki and N. Manabe, Nihon Dempa Kogyo Co., Ltd. ....	119
Electrode Stress Effects for Length-Extensional and Flexural Resonant Vibration of Quartz Bars E.P. EerNisse, Quartex, Inc. ....	126
An Analysis of Nonlinear Resonance in Electroded Contoured AT- and SC- Cut Quartz Crystal Resonators H.F. Tiersten, Rensselaer Polytechnic Institute. ....	132
Analysis and Design of Coupled Mode AT Rectangular Resonators J. Tomase and L. Dworsky, Motorola, Inc. ....	141
Harmonic and Anharmonic Modes of AK-Cut Crystal Resonators F. Euler and A. Kahan, U.S. Air Force, Rome Air Development Center ....	150
Frequency Shifts Arising from In-Plane Temperature Gradient Distribution in Quartz Resonators J.P. Valentin, Laboratoire de Chronométrie, Electronique et Piézoélectricité ENSMM and G. Théobald and J.J. Gagnepain, Université de Franche ....	157
Frequency-Temperature Behavior of Thickness Vibrations of Doubly-Rotated Quartz Plates Affected by Plate Dimensions and Orientations P.C.Y. Lee, Princeton University and Y.K. Yong, Rutgers University ....	164
On the Change in Orientation of the Zero-Temperature Contoured SC-Cut Quartz Resonator with the Radius of the Contour D.S. Stevens and H.F. Tiersten, Rensselaer Polytechnic Institute ....	176
Piezo Electric Ceramic Resonators and Filters S. Fujishima, J. Merlina and J. Miyazaki, Murata Erie North America, Inc. ....	184
Further Results on 5 MHz and 10 MHz Resonators with BVA and QAS Designs J.P. Aubry and A. Debaisieux, Compagnie d' Electronique et Piézoélectricité (CEPE) ....	190
Frequency Stability of Quartz Crystal at Very Low Temperatures: Preliminary Results G. Robichon, Compagnie d' Electronique et Piézoélectricité (CEPE) and J. Gros Lambert and J.J. Gagnepain, Université de Franche ....	201
Lateral-Field Excitation of Berlinite A. Ballato, M. Mizan, R. Tilton and T. Lukaszek, U.S. Army ERADCOM, E.R. Hatch, Georgia Institute of Technology and U.S. Army ERADCOM and B. Chai, Allied Corporation. ....	206
Aging Studies on Quartz Crystal Resonators and Oscillators R.L. Filler, J.A. Kosinski, V.J. Rosati and J.R. Vig, U.S. Army ERADCOM. ....	225
<b>FILTERS AND TRANSDUCERS</b>	
Force Sensing Using Quartz Crystal Flexure Resonators W.C. Albert, Singer-Kearfott. ....	233
Stress-Compensated Quartz Resonators Having Ultra-Linear Frequency-Temperature Responses M. Nakazawa, Shinshu University, H. Yamaguchi, Miyota Seimitsu Company and A. Ballato and T. Lukaszek, U.S. Army ERADCOM ....	240
Extended Pressure and Temperature Operation of BT-Cut Pressure Transducers G. Kaitz, Hewlett-Packard Company. ....	245

## TABLE OF CONTENTS (Continued)

Filter Applications of High Frequency Chemically Polished Fundamental Mode Bulk Wave Quartz Crystal Resonators P.J. Kavolis and W.P. Hanson, Piezo Crystal Company .....	251
A New Generation of UHF Filters from 300 MHz to Some GHz Using "Dielectric Resonators" B. D'Albaret, Compagnie d' Electronique et de Piézo Electricité—(CEPE) .....	254
<b>SAW DEVICES AND MICROWAVE RESONATORS</b>	
Temperature Stable Microwave Resonators Using ZnO Shear Mode Transducers S.V. Krishnaswamy and B.R. McAvoy, Westinghouse R&D Center and R.A. Moore, Westinghouse Defense and Electronics Center. ....	263
Performance of Fundamental-Mode UHF Oscillators Using Bulk-Acoustic-Wave Resonators S.G. Burns and R.S. Ketcham, Ames Laboratory—USDOE .....	266
A Review of Surface Acoustic Wave Devices and their Current Applications R.C. Rosenfeld and R.M. Hays, Jr., Sawtek, Inc. ....	271
The Effects of Temperature, RF Power, Radiation and Time on SAW Resonator Electrical Characteristics A. Vulcan and C. Gloeckl, Frequency Electronics, Inc. ....	273
Tuning SAW Oscillators Using Magnetic Bubble Garnet Films S.M. Hanna, Polytechnic Institute of New York and F.J. Friedlaender, Purdue University .....	279
SBAW Versus SAW Oscillator Aging R. B. Stokes, K.H. Yen and K.F. Lau, TRW Electronic Systems Group .....	282
Narrow Bandpass Filter Using Double-Mode SAW Resonators on Quartz M. Tanaka, T. Morita, K. Ono and Y. Nakazawa, Toyo Communication Equipment Co., Ltd. ....	286
Theoretical Analysis of Dynamic Thermal Effects in SAW Devices G. Theobald and D. Hauden, CNRS .....	294
Transient Thermal Response of Surface Acoustic Wave Resonators B. Sinha, Schlumberger-Doll Research. ....	300
Bias Controlled Frequency Trimming of SAW devices in a DC O <sub>2</sub> Plasma J. Day and T.E. Parker, Raytheon Research Division and G. Jackson, Massachusetts Institute of Technology. ....	310
<b>CRYSTAL OSCILLATORS, OSCILLATOR NOISE AND FREQUENCY CONTROL CIRCUITRY</b>	
Development of a Low "G" Sensitivity Missile Clock A. Vulcan, Frequency Electronics, Inc. ....	315
Simulation of Oscillator Noise J.A. Barnes, Austron, Inc. ....	319
Balanced Feedback Oscillators A. Benjaminson, S.T. Research Corporation .....	327
Analysis and Design of the Relaxation Quartz Crystal Oscillators D. Vasiljević, University of Belgrade .....	334
GPS User Receivers and Oscillators D. Hessick and W. Euier, Magnavox, Inc. ....	341

## TABLE OF CONTENTS (Continued)

A Time and Frequency Reference System for the Tacamo Aircraft T.C. Jewell and J.D. Geist, Frequency & Time Systems, Inc. ....	363
New Approach of Fast Warm Up for Crystal Resonators and Oscillators J.P. Valentin, M.D. Décailliot and R.J. Besson, Ecole Nationale Supérieure de Mécanique et des Microtechniques .....	366
Space Qualified High Performance Digitally Tuned Quartz Crystal Oscillators R.M. Garvey, D.A. Emmons and A.F. Beaubien, Frequency & Time Systems, Inc. ....	374
Manufacturing Methods and Technology for Tactical Miniature Crystal Oscillator D. Brown, E. Laszlo, R. McGill and P. Stoermer, Bendix Communications Division .....	380
<b>ATOMIC FREQUENCY STANDARDS, TIME TRANSFER AND DISSEMINATION</b>	
Lifetime and Reliability of Rubidium Discharge Lamps for Use in Atomic Frequency Standards C.H. Volk and R.P. Frueholz, The Aerospace Corporation, T.C. English, EFRATOM and T.J. Lynch and W.J. Riley, EG&G Inc. ....	387
Analysis of Dicke Narrowing in Wall Coated and Buffer Gas Filled Cells with Application to Gas Cell Atomic Clocks R.P. Frueholz and C.H. Volk, The Aerospace Corporation .....	401
Evaluation of the Performance of Passive Rubidium Frequency Standards Using Cavity Operated in Mode $TE_{011}$ , $TE_{111}$ and $TE_{101}$ P. Tremblay, N. Cyr and M. Tetu, Université Laval .....	408
A New Miniaturized Passive Hydrogen Maser F.L. Walls and K.B. Persson, National Bureau of Standards. ....	416
Design and Performance of New Hydrogen Masers Using Cavity Frequency Switching Servos H.E. Peters, Sigma Tau Standards Corporation .....	420
Operation and Performance of a Hydrogen Maser with a New State Selector S. Urabe, Y. Ohta, T. Morikawa and Y. Saburi, Radio Research Laboratories. ....	428
Experimental Determination of the Energy of Stored Ions from the Side-Bands in their Microwave Spectrum M. Jardino, F. Plumelle, M. Desaintfuscien and J.L. Duchene, Université Paris. ....	431
Development of the Superconducting Cavity Maser as a Stable Frequency Source G.J. Dick, California Institute of Technology and D.M. Strayer, Jet Propulsion Laboratory. ....	435
Accuracy Evaluation of the RRL Primary Cesium Beam Frequency Standard K. Nakagiri, M. Shibuki, S. Urabe, M. Ishizu, Y. Ohta, T. Morikawa and Y. Saburi, Radio Research Laboratories. ....	447
Results on a Laser Diode Optically Pumped Cesium Beam P. Cerez, G. Avila and M. de Labacherie, CNRS, M. Tetu, Université Laval and E. de Clercq, Laboratoire du Temps. ....	452
Cesium Clocks Deployed in the Global Positioning System: Design and Performance Data H. Hellwig and M. Levine, Frequency & Time Systems, Inc. ....	458
Modification of an O-1695A/U Cesium Beam Frequency Standard for Retrofit of Replacement Cesium Beam Tubes J.C. Robb, Frequency & Time Systems, Inc. ....	464

## TABLE OF CONTENTS (Continued)

O-1695A/U Retrofit or Replace? M. Meirs, I. Pascaru, D. Silvermetz, and D. Jones, Frequency Electronics, Inc . . . . .	471
A Brief Introduction to the Atomic Time and Frequency Standards at Shanghai Observatory Z. Zao-Cheng, A. Qi-Ziang, H. Hang-Xiang, K. Wen-Wei and D. Xiu-Feng, Shanghai Observatory . . . . .	476
<b>MEASUREMENTS AND SPECIFICATIONS</b>	
Software for Two Automated Time Measurement Systems S.R. Stein, EFRATOM and G.A. Gifford, Naval Research Laboratory . . . . .	483
The Specification of Quartz for Piezoelectric Devices J.C. Brice, Philips Research Laboratories. . . . .	487
X-Ray Handedness Determination on Finished Doubly Rotated Quartz Plates H. Merigoux and J.F. Darces, Laboratoire de Cristallographie et Synthese Minerales and J. Lamboley, Q.E. Alcatel. . . . .	496
Resistance-Measurements of Quartz Crystals at Very Low Drive Levels J.S. Yerna, Philips Quartz Crystal Devices. . . . .	499
Further Results of Temperature Compensated Crystal Oscillator Testing V. Rosati and P. Thompson, U.S. Army ERADCOM. . . . .	507
<b>AUTHOR INDEX</b> . . . . .	511
<b>SPECIFICATIONS AND STANDARDS GERMANE TO FREQUENCY CONTROL</b> . . . . .	513
<b>PROCEEDINGS AVAILABILITY INFORMATION</b> . . . . .	515

## AWARDS PROGRAM

### INTRODUCTION

For a number of years, sentiment has been expressed at Symposium program committee meetings for the creation of Symposium sponsored awards that recognize outstanding contributions in all fields covered by the Annual Frequency Control Symposium. Therefore, in early 1983, the program committee voted to create two such awards. One, the Cady Award, named after Walter Guyton Cady, is to recognize outstanding contributions related to piezoelectric frequency control devices. The other, the Rabi Award, named after Professor I. I. Rabi, is to recognize outstanding contributions related to fields such as atomic and molecular frequency standards, time transfer, and frequency and time metrology. Each award consists of \$500.00, and a limited edition original print and certificate in a leather binder. The awards are presented to the recipients at the Symposium. At the discretion of the Technical Program Committee, the recipients may be reimbursed for travel expenses to attend the ceremony during which the award is presented.

### ELIGIBILITY CRITERIA

Either award is open to any worker in any of the fields of endeavor traditionally associated with the Annual Frequency Control Symposium. The nominee for either award should be responsible for significant contributions of a technical nature to the field selected. No posthumous awards will be made. The time span over which the contributions have occurred is not limited, and nominations will be considered for totality and breadth of achievement as well as specificity and depth of contribution.

The significance of the contributions may be measured, in part by:

- The degree of initiative, ingenuity, and creativity displayed.
- The quality of the work and degree of success attained.
- The overall importance of the work and impact on the frequency control and associated communities.

### NOMINATIONS

Anyone may nominate another for either award. Each nomination should include the following:

1. Name of nominee.
2. Current address.
3. Name of award for which nominated.
4. *Description of accomplishments, including:*
  - a. Initiative, ingenuity, and creativity;
  - b. Quality and degree of success;
  - c. Importance of the work and impact on the frequency control and associated communities;
  - d. Proposed citation, one or two sentences (see examples on next page).
5. Name, address and phone number of nominator.

It is strongly suggested that the nomination not exceed two typewritten pages. Nominations for the award should be submitted to the Chairman of the Technical Program Committee by the date announced for the submission of summaries.

### SELECTION OF RECIPIENTS

The selection of the recipient for each award will be made by the Technical Program Committee during the spring meeting. The decision of the committee is final. If, in the opinion of the committee, no suitable nominee exists, no award will be given.

## 1984 AWARD WINNERS



*AWARD WINNERS: David W. Allan, Frank W. Neilson, (accepted by his son, David Neilson) William B. Benedick, Robert A. Graham and Arthur W. Warner*

### THE CADY AWARD

Arthur W. Warner was presented the Cady Award for his contributions to the development of high precision quartz crystal units.

### THE RABI AWARD

David W. Allan was presented the Rabi Award for his contributions to the statistics of atomic clocks, measurement techniques, time scale and time coordination and distribution.

### THE SAWYER AWARD

The Sawyer Award recipients were William B. Benedick, Robert A. Graham and Dr. Frank W. Neilson for their fundamental experimental studies of the physical properties of crystalline quartz under extreme pressures and rates of loading leading to applications including a high pressure quartz stress gauge with nanosecond time resolution.

## THE GROWTH OF HIGH PURITY, LOW DISLOCATION QUARTZ

Alton F. Armington  
 Rome Air Development Center  
 Solid State Science Division  
 Hanscom Air Force Base, MA 01731  
 and  
 Joseph F. Balascio  
 Motorola, Inc.  
 Components Division  
 Carlisle, PA 17013

Summary

Hydrothermal growth runs were conducted in research and production size autoclaves employing both sodium hydroxide and sodium carbonate as the mineralizers. Inert liners were used in some of the runs conducted in the research size autoclaves. The variables examined during the course of this investigation were the effects of lithium additions, nutrient and seed quality on the growth of alpha quartz.

Introduction

The availability of high purity, low dislocation alpha quartz is limited at the present time. This limitation is due to a lack of demand for this product, as well as, the inability to routinely produce it. The latter limitation is due, in part, to a lack of understanding of all the criteria necessary to produce a high purity, low dislocation material. Both the Air Force (RADC) and the Army (ERADCOM) are attempting to overcome this limitation. As part of the program to improve frequency and timing devices, a project has been initiated with Motorola to meet this need by attempting to use the information gathered in research autoclaves over the past few years as a basis for the production of high grade quartz in commercial autoclaves. It is believed that such a high quality material will improve the radiation resistance, aging and short time frequency offsets required for several precision applications of timing devices. This paper will discuss some of the preliminary results of this program.

Cation impurities that are believed to have an effect on performance are the group one elements (lithium, sodium and potassium), aluminum and iron. The role of aluminum in quartz appears to be well documented and this impurity seems to be the most damaging to quartz properties. The role that other impurities play in quartz is less understood. The group one impurities that join with aluminum to provide electrical neutrality are a cause of offset since they are easily disassociated from the aluminum by relative low energies. The use of sweeping (solid state electrolysis) to replace the group one impurities with hydrogen, which is more strongly bound, can essentially eliminate the active group one impurities. The other impurity present in quartz is iron. This impurity cation is usually less than the aluminum content. Work to the present time indicates that this impurity ion may not be a significant damaging impurity. The present aim of this work is to reduce impurities to a part per million with the exception of aluminum which we hope to reduce below a part per million. Since as yet there is no resonator evaluation of this material at the present time, this must be regarded as a tentative goal pending these evaluations.

The role of dislocations in quartz properties is less defined. It does appear that bundles of dis-

locations are responsible for etch pit formation during processing. The possibility that dislocations are sinks for impurities must also be considered. These impurities may be a cause of etch channeling and may also migrate during operation and affect resonator performance. If the dislocations can be eliminated, this should eliminate both of these possibilities.

Experimental

Hydrothermal growth runs were conducted in unlined production size autoclaves and both lined and unlined autoclaves with inside diameters from one to four inches. All vessels were instrumented in a similar fashion and were controlled and monitored by process control computers.

The characterization techniques employed for the evaluation of the alpha quartz crystals grown had been previously presented in these proceedings. (1,2)

Results and DiscussionsMineralizers

One of the goals of this program is to develop the ability to grow high purity, low dislocation alpha quartz from either the sodium hydroxide or the sodium carbonate mineralizer. Typically prepared reagent grade mineralizer solutions were analyzed for their starting purity with respect to some of the impurities of interest. Table 1 lists these data. The mineralizers were found to be of equivalent reagent grade quality with neither possessing an unexpected impurity level nor a significant difference in levels between them. The growth runs in which these particular solutions were used are in parenthesis. Lithium was not analyzed since all of these solutions intentionally contained this cation.

To follow the effect of the addition of lithium to the mineralizer, a series of runs was conducted without its addition in both lined and unlined autoclave runs. Impurity levels in those crystals were then compared with quartz crystals grown in runs with the lithium addition (Table 2). All other conditions remained the same for these runs. The nutrient supply used was fractured cultured quartz crystals with an average aluminum content of about 15 ppm. Data obtained so far indicate that there is a greater uptake of iron by the crystals grown in an unlined vessel when lithium is not present in the mineralizer. Also the aluminum content in crystals grown in runs conducted without a liner was significantly lower than that found in alpha quartz grown in lined autoclave runs. These results may be an indication that the walls of a steel autoclave serve as a nucleation site for various compounds containing trace amounts of aluminum and lithium. After this group of runs, all others were conducted with lithium additions to the mineralizer.



## Nutrient

During the conduction of these growth runs, a variety of nutrient supplies were employed. The preparation methods used to generate these alpha quartz nutrients are schematically illustrated in Table 3. Growth runs were completed utilizing the five different nutrient supplies shown in this table. Cultured Quartz I and Cultured Quartz II were produced by successive recrystallizations from natural quartz nutrient. Cultured Quartz III is pure Z Cultured Quartz II nutrient, obtained by removing all X regions before fracturing the material for nutrient. The synthetic alpha quartz was produced through the conversion of fused quartz in an inert liner with sodium hydroxide as the mineralizer. Table 4 compares the typical impurity levels found in each of the nutrient supplies. All ppm values reported in this paper were determined by atomic absorption unless otherwise indicated. The levels shown for Cultured Quartzes I and III were determined from pure Z sections. It is known that the X regions usually contain higher ppm levels and therefore, would increase the average ppm level for each cultured quartz nutrient supply (eg. Cultured Quartz II compared to Cultured Quartz III). The high sodium level detected in the converted nutrient supply may have been due to the occlusion of some mineralizer in the sample analyzed.

A number of quartz crystals were grown from each nutrient supply and some were analyzed for their uptake of impurities. Table 5 compares these impurity levels as a function of the nutrient supply employed. A substantial reduction of approximately 14 ppm of aluminum was achieved between crystals grown from the natural quartz nutrient and the pure Z recrystallized cultured nutrient. These data indicate that it is possible to produce high purity cultured quartz in unlined autoclave runs. In fact, the purity of the crystal grown from the Cultured Quartz III nutrient is almost equivalent with that grown from the converted optical quartz nutrient.

## Inert Liner Runs

In most of the research size runs liners have been used both to ease the cleaning procedure, as well as, possibly to increase the purity of the product crystals. Some results comparing inert liner runs are shown in Table 6. In these, only pure Z (Cultured Quartz III) material was used as nutrient. The results indicate that with the use of a high grade nutrient, very high purity can be obtained with or without an inert liner. Within the limits of our present analytical technique, the purity is essentially the same. It should be emphasized that in all the unlined runs, the autoclaves were **thoroughly cleaned between runs**, even chemically. Without this treatment we find higher impurity levels. The question as to whether or not silver liners can reduce the number of inclusions in the as-grown crystal is unanswered. However, we have generated enough samples to be able to determine if there is a significant difference and are in the process of analyzing these data.

## Scale Up Factors

Table 7 gives some results using autoclaves of different inside diameters. All data contained in this table are from unlined runs. Obviously, these values represent some of the highest purities obtained and thus are better than those usually reported for as-grown alpha quartz. Runs A, B and C were produced in research size autoclaves. Runs D and E represent data from two different quartz manufacturers. The nutrient supply used in all cases was of high quality, but not

the same material.

The inability to differentiate the impurity content among the crystals analyzed in Table 7 is related to the present limit of reliable detection for the analysis methods commonly employed. Table 8 shows a comparison of EPR and AA results at low impurity levels. Crystal X was grown from a 3" inside diameter autoclave; Y from a commercial autoclave and crystal Z from a lined autoclave run. It appears, that at these impurity levels, both techniques are marginal. We have recently gained access to an inductively coupled quadrupole mass spectrometer which is reported to be accurate to the part per billion range and have begun checking some of the material using this technique. We hope to be able to assess the accuracy of this technique in the next few months. Until that time, our analytical methods may not produce precise results at very low impurity levels.

## Seed Effects

In order to determine the effects of seed preparation procedures on the quality of the crystals grown from these seeds, for the most part, only high Q

( $2.4 \times 10^6$ ) and low etch channel density seeds ( $111 \text{ cm}^{-2}$ )

were employed. The seeds were  $0^\circ\text{X}$  and each seed possessed good x-ray orientation. All seeds were inspected with a polariscope in order to determine whether or not any strain was present. In the few instances when strain was detected in a seed, the location of the strained area was recorded and the seed mounted in the growth rack so that it could be properly identified and the as-grown crystal separated upon conclusion of the hydrothermal growth run. During these early growth runs, some seeds were also cut from the plus X region of an as-grown crystal and

these seeds were then oriented as a pure Z  $0^\circ\text{X}$  seed.

Table 9 lists the three major etching solutions employed for seed preparation techniques. All three etchants have been used primarily to etch seeds for five to ten minutes, respectively, at room temperature. The ammonium bifluoride etchant, however, has been employed to etch seeds up to 60 minutes in five minute intervals. The third etchant solution listed in this table was the only etchant used at elevated temperatures and extended etching times. The purpose for this was to produce chemically polished transparent seeds for growth.

Among these seed preparation techniques, little differentiation has been found with respect to the etch channel density measured on crystals grown upon seeds. What was discovered, however, was that strained seeds resulted in higher etch channel densities in the as-grown crystals than that found in crystals grown upon unstrained seeds. Table 10 compares these results. These data also indicated that the sodium content of the strained crystals was somewhat greater than that of crystals grown upon unstrained seeds in the same run. More data are being gathered with respect to this observation. The average growth rate, as presently determined, does not seem to correlate with the etch channel density differences between the two crystal groups.

Lower etch channel densities can be achieved by using Z seeds cut from the +X region. We are continuing this work and have had some success. Figure 1 shows topographs of two crystals grown in the same run. One of these crystals was grown on a Z seed cut from the +X growth area. The other was grown upon a

standard Z seed. It can be seen that the dislocations have been considerably reduced by use of the +X seed material. Preliminary etch channel densities for crystals grown on this type of seed are 2, 18, and

$22\text{cm}^{-2}$ , which are considerably lower than the results reported for unswept crystals. The use of a liner might give better results, but we do not have sufficient data to substantiate this. These studies are continuing.

### Conclusions

The initial results of this project have shown that high purity alpha quartz can be produced in unlined autoclaves of various sizes provided that the nutrient is of low impurity content. Whether there are real differences among the actual impurity levels in the crystals grown will depend upon the more sensitive method of analysis mentioned in this paper.

Strain in pure Z seeds tend to result in higher etch channel densities and incorporation of sodium. Crystals grown from Z seeds cut from the +X region possessed much lower etch channel densities than those crystals grown upon unstrained pure Z seeds.

Data with respect to resonator characteristics still needs to be determined on most of these crystals in order to correlate performance to crystal quality.

### Acknowledgements

The authors would like to acknowledge the contributions of the following individuals to this investigation: N. Yannoni (RADDC), John Vig and John Gualtieri (ERADCOM) for discussions on numerous aspects of this subject. We would also like to acknowledge John Larkin and Meckie Harris of RADDC and Thomas Walker, Motorola, Inc. for contributions in all aspects of the experimental work.

Portions of this work were performed under contract F19628-82-C-0067 with the U.S. Air Force.

### References

1. Armington, A. F.; Larkin, J. J.; O'Conner, J.; Cormier, J. E. and Horrigan, J. A., Proc. 37th Ann. Freq. Control Sympos., 177 (1983).
2. Balascio, J. F. and Lias, N. C., Proc. 37th Ann. Freq. Control Sympos., 157 (1983).

TABLE 1

TYPICAL IMPURITY LEVELS IN REAGENT GRADE MINERALIZERS  
(PPM BY WEIGHT)

MINERALIZER	K	AL	FE	TOTAL
Na <sub>2</sub> CO <sub>3</sub> (GC1)	0.7	0.5	0.5	1.7
NaOH (GC4)	1.6	0.5	0.5	2.6
NaOH (GC5)	0.7	0.5	0.5	1.7

TABLE 2

EFFECT OF LITHIUM ADDITION TO THE MINERALIZER

RUN NO.	Z GROWTH RATE (MILS/DAY)	LINER	Li	Na	K (PPMA)	AL	Fe
X-39	16.0	No	1.0	1.5	<0.5	3.6	2.7
QA-20	28.0	Yes	4.7	1.1	<0.5	16.0	0.8
QA-21	21.0	Yes	4.0	1.2	<0.5	15.0	<0.5
X-35*	30.0	No	1.5	0.8	<0.5	3.6	<0.5
QA-25*	25.0	Yes	4.4	2.7	<0.5	13.0	<0.5

\* LITHIUM ADDITIONS TO MINERALIZER

TABLE 3

PREPARATION OF NUTRIENT SUPPLIES

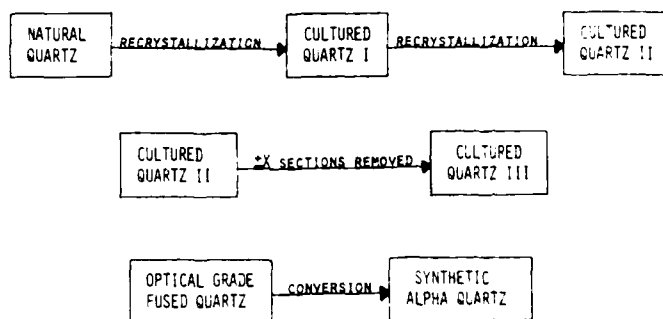


TABLE 4

COMPARISON OF TYPICAL IMPURITY LEVELS IN NUTRIENT SUPPLIES

NUTRIENT SUPPLY	Li	Na (PPM BY WEIGHT)	K	AL	Fe	TOTAL
SYN. QTZ	0.8	342.0	0.5	2.3	1.0	346.6
NAT. QTZ	2.5	10.0	3.4	21.0	2.7	39.6
CUL. QTZ I	1.3	8.3	<0.5	6.0	<0.5	16.6
CUL. QTZ III	0.8	2.5	0.7	2.4	0.8	7.2

TABLE 5

TYPICAL IMPURITY LEVELS FOUND IN CRYSTALS  
GROWN FROM DIFFERENT NUTRIENT SUPPLIES

NUTRIENT SUPPLY	Li	Na (PPM BY WEIGHT)	K	AL	Fe	TOTAL
SYN. QTZ	<0.5	<0.5	<0.5	0.6	<0.5	2.6
NAT. QTZ	3.0	8.8	1.3	14.5	0.7	28.3
CUL. QTZ I	1.1	3.3	0.8	3.9	0.8	9.9
CUL. QTZ II	0.7	2.5	<0.5	1.7	<0.5	5.9
CUL. QTZ III	<0.5	0.9	0.5	0.6	<0.5	3.0

TABLE 6

EFFECTS OF LINER ON CRYSTAL PURITY

RUN NO.	Z GROWTH RATE (MILS/DAY)	LINER	Li	Na	K (PPMA)	AL	Fe
X46A	16.0	NO	<0.5	2.3	<0.5	0.8	0.5
X56A	20.0	NO	1.9	<0.5	2.2	<0.5	0.8
X50B	25.0	NO	1.5	<0.5	<0.5	0.9	0.8
X52	16.0	NO	<0.5	1.5	<0.5	<0.5	0.5
9A33	22.0	YES	<0.5	0.6	<0.5	<0.5	0.8
9A36	28.0	YES	<0.5	1.8	<0.5	<0.5	<0.5
9A31	20.0	YES	<0.5	0.5	<0.5	<0.5	0.9

TABLE 7

IMPURITY LEVELS IN CRYSTALS GROWN FROM VARIOUS AUTOCLAVES

CRYSTAL	AUTOCLAVE I.D. (IN.)	Li	Na	K (PPMA)	AL	Fe
A	1	<0.5	1.5	<0.5	<0.5	0.5
B	3	<0.5	2.3	<0.5	0.8	0.5
C	4	<0.5	0.7	0.7	<0.5	<0.5
D	10	<0.5	1.5	<0.5	0.5	<0.5
E	13	<0.5	1.4	<0.5	0.9	<0.5

TABLE 8

COMPARISON OF ALUMINUM LEVELS BY AA AND EPR

SAMPLE	ATOMIC ABSORPTION	ELECTRON PAIR RESONANCE
X	< 0.5	0.12
Y	< 0.5	0.80
Z	< 0.5	1.20

TABLE 9

ETCHING CONDITIONS EMPLOYED ON PURE Z SEEDS

ETCHANT USED	ETCHING TIME (MIN.)	ETCHING TEMP. (°C)
7.0M NH <sub>4</sub> HF <sub>2</sub>	5 - 60	22
48% HF	5 - 15	22
40% NH <sub>4</sub> F + 48% HF (EQUIVOLUME)	5 - 90	22;75

TABLE 10

COMPARISON OF CRYSTALS GROWN UPON  
UNSTRAINED AND STRAINED PURE Z SEEDS

RUN NO.	UNSTRAINED SEEDS			STRAINED SEEDS		
	Z GROWTH RATE (MILS/DAY)	Na (PPM)	$\alpha$ (CM <sup>-2</sup> )	Z GROWTH RATE (MILS/DAY)	Na (PPM)	$\alpha$ (CM <sup>-2</sup> )
GC1	21.2	8.8	158	21.2	12.0	518
GC8	19.0	7.1	185	19.6	11.0	572
GC11	31.2	1.9	166	31.8	3.2	528
GC12	20.3	8.0	203	19.3	8.5	568
AVG.	22.9	6.5	178	23.0	8.7	547

# X-RAY TOPOGRAPHS OF CRYSTALS



Z SEED

X SEED

FIGURE 1

COMPARISON OF DISLOCATION DENSITIES IN CRYSTALS  
GROWN FROM Z AND +X SEEDS IN SAME RUN

CULTURED QUARTZ OF LOW ALUMINUM CONTENT  
FROM PRODUCTION SIZED AUTOCLAVES

Baldwin Sawyer and D. R. Kinloch

Sawyer Research Products, Inc.  
Eastlake, Ohio 44094

Background

Recent studies of cultured quartz radiation stability (or "hardness") have called for quartz whose Z-region aluminum content is 1 ppm or less<sup>1</sup>. A report of unusually high purity quartz grown in silver from devitrified, high purity, silica given at the 1982 Frequency Control Symposium<sup>2</sup> tends to confirm the predicted advantages.

Development

During '82 and '83 two low-aluminum runs were grown slowly in unlined production-sized autoclaves at the Sawyer Research Products cultured quartz plant, supported in part by the USAF, using previously grown crystals as nutrient. Three other low-aluminum runs were also slow-grown from selected high-purity nutrients.

Analytical

The EPR analytical results of these samples from five runs are shown in the table together with details of growth conditions, nutrient used, and IR indicated Q capability.

A number of use studies of this material both as grown and "sweet" (i.e. electrolytically treated in solid state) have been begun. Preliminary indications are that the quality looks high, but full evaluations were yet to be completed at the time of this paper.

Conclusions

Some general conclusions can be drawn at this time as follows:

1) Feasibility of Z growth containing less than 1.0 pp. Al in unlined production sized autoclaves has been shown. A combination of the two controls; slow growth, and low aluminum nutrient material (believed to be less than 10 ppm Al) was used.

2) It is to be hoped that Al content tolerances will be suggested by the end-use test results. These might take the form of two different requirements to achieve radiation hardened quartz behavior; for swept quartz, and for unswept quartz.

3) Aluminum content may become a useful means of characterizing cultured quartz for other uses than radiation hardened applications.

<sup>1</sup> Halliburton L.E., Martin J.J., Sibley W.A., "A Study of the Defects Produced by the Irradiation of Quartz" Rome Air Development Center, Tech. Report-80-120 (1980).

<sup>2</sup> Doherty S.P., Morris S.E., Andrews D.C., and Croxall D.F., "Radiation Effects in Synthetic and High Purity Synthetic Quartz: Some Recent Infrared Electron Spin Resonance and Acoustic Loss Results," Proceedings 36th Annual Symposium on Frequency Control, (1982).

LOW ALUMINUM RUN SUMMARY  
FROM PRODUCTION AUTOCLAVES

PARTICULARS: AUTOCLAVE'S ENCLOSED VOLUME - 261 LITERS  
GROWTH PROCESS: HYDROTHERMAL, 2 CHAMBER  
NORMAL OPERATING PRESSURE 82.7 MPa (12,000 psi)  
NORMAL OPERATING TEMPERATURE RANGE 340 - 360°C  
INITIAL SOLUTION: 0.8 M Na<sub>2</sub>CO<sub>3</sub>, 0.05 M LiNO<sub>2</sub>

RUN NUMBER	AVE. TOT. Z GROWTH RATE mm/DAY	NUTRIENT MATERIAL	ALUMINUM CONTENT OF Z GROWTH BY EPR ppm			IND Q CAPABILITY 10 <sup>6</sup>
			AVERAGE	MAXIMUM	MINIMUM	
H33-31 *	0.37	Cultured on Z plates	0.6			3.3
F12-46 *	0.29	Cultured on Y-bars	0.97	1.15	0.79	3.7
F36-43	0.23	Cultured on Y-bars	0.4			2.7
F27-43	0.28	Arkansas Quartzite	0.6			2.9
G23-37	0.28	Brazilian Lascas	0.8	1.0	0.6	3.3

\* Engineering cost supported in part by USAF

## DISTRIBUTION OF ALUMINUM AND HYDROXIDE DEFECT CENTERS IN IRRADIATED QUARTZ

Herbert G. Lipson and Alfred Kahan

Solid State Sciences Division  
Rome Air Development Center  
Hanscom Air Force Base, Bedford MA, 01731Summary

Irradiated quartz is characterized using low temperature infrared Fourier spectroscopy, and peaks associated with as-grown  $\text{OH}^-$  and  $\text{Al-OH}^-$  defect centers are measured. Defect center distributions are determined from scanning small crystal regions perpendicular to the growth axis. We find that even when  $\text{Co}$  irradiations produce a uniform  $\text{OH}^-$  decrease across the sample, the corresponding  $\text{Al-OH}^-$  profile may or may not be uniform. Initially the formation of  $\text{Al-OH}^-$  is governed by the concentration and distribution of as-grown  $\text{OH}^-$ , but with increasing dose as-grown  $\text{OH}^-$  can remain at a constant level or deplete. In some cases  $\text{Al-OH}^-$  forms even after all as-grown  $\text{OH}^-$  is depleted, indicating an additional hydrogen source in the crystal. When  $\text{Al-OH}^-$  saturates and as-grown  $\text{OH}^-$  remains at a constant level, the  $\text{Al-OH}^-$  distribution indicates the substitutional aluminum profile of the sample.

**Key Words:** Quartz, Defect Centers, Radiation Effects, Infrared Spectroscopy.

Introduction

Specific point defect models for synthetic high quality quartz are well established and are reviewed in several publications.<sup>1,2</sup> The major defects are substitutional aluminum impurities in silicon sites, compensated with interstitial alkali-metals to form  $\text{Al-M}^+$  ( $\text{M} = \text{Li}, \text{Na}, \text{or K}$ ), and water molecules adjacent to oxygen sites to form as-grown  $\text{OH}^-$  centers. The frequency of a resonator fabricated from quartz is determined by the elastic, piezoelectric, and dielectric constants of the crystal. The quality of the fabricated resonator is affected both by the amount and the distribution of  $\text{Al-M}^+$  and  $\text{OH}^-$  centers in the crystal. Room temperature ionizing radiation dissociates both  $\text{Al-M}^+$  and  $\text{OH}^-$ , and two new centers are formed,  $\text{Al-OH}^-$  and aluminum-holes,  $\text{Al-e}^-$ . In this process, the as-grown  $\text{OH}^-$  is the hydrogen ion source for  $\text{Al-OH}^-$ . It is believed that a major part of the observed transient and steady-state radiation induced frequency offsets can be attributed to radiation induced alkali-metal ion migration, and to changes in the material constants, caused by redistribution of defect centers. The point defect structure of quartz is also modified by sweeping (electrodifussion). Sweeping a crystal in an air atmosphere, at elevated temperatures, dissociates  $\text{Al-M}^+$ , saturates  $\text{OH}^-$  defects, and forms  $\text{Al-OH}^-$ . In this process, external water vapor is the hydrogen ion source for  $\text{Al-OH}^-$ , and, at the same time, most of the alkali-metal ions are physically "swept" out of the crystal. Sweeping a crystal in a vacuum atmosphere also dissociates  $\text{Al-M}^+$  and forms  $\text{Al-OH}^-$ , but similar to the radiation process, the hydrogen source is the as-grown  $\text{OH}^-$  which is reduced, or depleted, as the alkali metal ions are swept towards the cathode.

For synthetic quartz, the major growth direction is along the crystallographic z-axis. The quality and impurity content of the nutrient used for crystal growth

varies. In addition, during the growth period of several months, thermodynamic conditions change and introduce variations in quartz quality, aluminum impurity, and water molecule concentrations between the seed and the z-growth surfaces. Singly or doubly rotated crystal resonator disks, for example, AT- or SC-cuts, are fabricated from z-growth bars, and their cross sections incorporate material grown during the entire growth cycle. In order to insure high quality and uniform crystals for high precision resonator applications, it has become standard practice to measure the room temperature strength and uniformity of as-grown  $\text{OH}^-$  related infrared bands, and to select crystals with low and fairly uniform absorption strength. The as-grown  $\text{OH}^-$  absorption levels are also correlated with resonator Q-values. There are also indications that large variations in radiation sensitivity of crystals fabricated from quartz grown in the same autoclave run, or even from the same bar, may be associated with differences in impurity distributions along the growth axis. Consequently, sensitive non-destructive characterization techniques to determine localized impurity distributions in as-grown, swept, and irradiated crystals are of practical importance.

When room temperature irradiation dissociates  $\text{Al-M}^+$  and  $\text{OH}^-$  and forms  $\text{Al-OH}^-$ , the alkali-metals migrate to some unknown site and form a  $\text{M}^-$ -center. In all previous investigations it was implicitly assumed that the rate at which  $\text{OH}^-$  dissociates and  $\text{Al-OH}^-$  forms are the same, that is, the governing effect is the break-up of  $\text{Al-M}^+$ , and, as a consequence, as-grown  $\text{OH}^-$  dissociates to compensate the substitutional aluminum and forms  $\text{Al-OH}^-$ . This, however, may not be the case. The governing mechanism may as well be the dissociation of  $\text{OH}^-$ . Alternately, the governing mechanism may involve the precursor of the unknown  $\text{M}^-$ -center. In this sequence, radiation dissociates this center, which in turn dissociates  $\text{Al-M}^+$  and as-grown  $\text{OH}^-$  and forms  $\text{Al-OH}^-$ . Consistent with the defect models considered for quartz, the interpretation of radiation effects on crystals swept in an air atmosphere is straightforward. One does not expect any observable steady-state radiation effects. All  $\text{M}^-$ -ions have been swept from the crystal, and all defect sites are saturated with hydrogen ions. Radiation will not cause ionic migration, and the material constants and the resonator frequency remain unchanged. However, steady-state radiation effects do exist and these are then attributed to incomplete sweeping, caused by crystal non-uniformities and extended defects.

One of the difficulties in interpreting the defect structure of quartz in a consistent manner is the fact that the centers associated with the dissociated alkali-metal ion are not observed by any of the standard characterization techniques. In addition, the interpretation of radiation effects is complicated by the presence of  $\text{Al-e}^-$ . The relative ratio of  $\text{Al-OH}^-$  and  $\text{Al-e}^-$  defects formed for a given dose of radiation varies from sample to sample, and the sequence of forma-

tion is not established. There are several possibilities which must be considered: (1) Al-e<sup>-</sup> forms depending on the availability of electron traps, and is independent of hydrogen related centers. (2) Both defects, Al-OH<sup>-</sup> and Al-e<sup>-</sup>, form at the same time in the same crystal region, with undetermined factors governing the preference of forming one defect center over the other, and (3) Al-e<sup>-</sup> forms if, and only if, all as-grown OH<sup>-</sup> is exhausted and there is still excess Al-M<sup>+</sup> in the crystal.

In this paper, we wish to examine whether radiation effects in quartz are governed by as-grown OH<sup>-</sup> or by substitutional aluminum impurities, and whether radiation induced migration of alkali-metal and hydrogen ion is localized to several atomic distances, or can extend across the entire crystal. In order to investigate these effects, we need to evaluate the spatial impurity distribution of the crystal. Experimentally, OH<sup>-</sup> and Al-OH<sup>-</sup> are characterized by vibration spectra measured by low temperature infrared spectroscopy, Al-e<sup>-</sup> is determined from electron spin resonance, and Al-M<sup>+</sup> from a combination of low and high temperature dielectric and acoustic loss investigations. It is very difficult to utilize non-destructive methods such as ESR, or dielectric and acoustic loss measurements, to determine the spatial distribution of respective defect centers in a crystal large enough to fabricate standard size resonators. However, we previously reported the application of low temperature infrared Fourier spectroscopy to scan large crystals normal to the growth axis before and after sweeping to determine Al-OH<sup>-</sup> and as-grown OH<sup>-</sup> distribution from their relative band strengths.<sup>4,5</sup> We again utilize this technique to study different types of quartz samples exposed to successive <sup>60</sup>Co irradiation doses.

#### Experimental Procedures

The quartz samples used for this investigation were rectangular in shape, between 1 and 2 cm in size, with parallel x-, y-, and z-faces. The quartz type, aluminum concentrations, and 3581 cm<sup>-1</sup> band peak heights are listed in Table 1.

Table 1. Quartz samples

Sample Designation	Type	Aluminum Concentration ppm	3581 cm <sup>-1</sup> Band Peak Height (cm <sup>-1</sup> )
D14-45	Premium-Q	1	0.08 - 0.11
BH-A	Premium-Q	11	0.25 - 0.37
E42-21	High-Q	6-8	0.08 - 0.12
QA-32	RADC/ESM	4, 32	0.37 - 0.40

The High-Q and Premium-Q samples were grown by the same process at SARP, except that for Premium-Q lithium salt was added to the nutrient and the Na<sub>2</sub>CO<sub>3</sub> mineralizer. The RADC/ESM sample was grown with a NaOH mineralizer and lithium salt additive. The aluminum concentrations were determined from electron spin resonance (ESR) measurements. The 4 ppm value for QA-32 was measured by atomic absorption. The peak height of the 3581 cm<sup>-1</sup> infrared band at 85 K is related to the OH<sup>-</sup> concentration.

Infrared transmissions were measured between 3100 and 3700 cm<sup>-1</sup> with the focused beam of a Nicolet 170SX Fourier spectrometer. The normal beam size was 3 mm in diameter, but 1.5 mm beams were also used to scan more localized regions. The sample, mounted inside a dewar cooled to 85 K, was moved across the spectrometer beam axis. Measurements were made with the beam aligned

along the x- or y-axis of the crystal, that is, normal to the z-growth direction. Beam positions are designated by the distance of the center of the 3 mm beam from the +z-face of the sample, the section of the crystal furthest from the seed. For one sample, measurements were also made with the beam aligned along the z-axis, and positions are designated along the y-axis. The samples were irradiated with successive doses of 0.2, 0.2, and 0.4 Mrad at the RADC <sup>60</sup>Co source, and were measured after each irradiation.

Figure 1 shows typical absorption spectra measured normal to the z-growth axis, calculated from transmission. These spectra are for sample BH-A, before irradiation and after total doses of 0.2 and 0.8 Mrad. At 85 K, the four principal bands associated with as-grown OH<sup>-</sup> impurities in synthetic quartz have strong peaks at 3348, 3396, 3438, and 3581 cm<sup>-1</sup> before irradiation. Smaller peaks, probably associated with other sites, are also observed. The 3581 cm<sup>-1</sup> band has a strong narrow peak and easily determined background whereas the absorption of the other three bands are broad and superimposed on Si-O lattice bands. After the 0.2 Mrad irradiation the 3581 cm<sup>-1</sup>, as well as the other as-grown OH<sup>-</sup> bands, are reduced considerably, and two new peaks, a large one at 3366 cm<sup>-1</sup> and a smaller one at 3306 cm<sup>-1</sup> are observed. These bands are associated with Al-OH<sup>-</sup>. The 0.8 Mrad irradiation depletes the as-grown OH<sup>-</sup> bands and produces very small additional changes in the Al-OH<sup>-</sup> associated peak heights.

We are interested in evaluating only relative changes in as-grown OH<sup>-</sup> and Al-OH<sup>-</sup>, and for this purpose it is sufficient to compare absorption peak heights instead of integrated changes in band areas. For these reasons, we select the narrow 3581 cm<sup>-1</sup> band and the stronger 3366 cm<sup>-1</sup> band at 85 K to monitor changes in as-grown OH<sup>-</sup> and Al-OH<sup>-</sup> defect centers, respectively. Both the 3366 and 3581 cm<sup>-1</sup> bands have large dichroic ratios with maximum strengths when the electric vector is perpendicular to the optic, the c- or z-, axis. The comparative measurements for this investigation were made with unpolarized radiation, and maximum band strengths are obtained only when the beam is aligned along the z-axis. The values given in Table 1 are for the beam aligned either along the x- or y-direction, and are lower than would be obtained using a polarizer with the angle set for maximum band strength.

Based on ESR measurements, low concentration of <sup>3+</sup> substitutional aluminum is defined as <1 ppm of Al<sup>3+</sup>, medium concentration between 1-5 ppm, and high as >5 ppm. For comparison purposes we arbitrarily define low OH<sup>-</sup> or Al-OH<sup>-</sup> concentration as <0.1 cm<sup>-1</sup>, medium as 0.1 to 0.3 cm<sup>-1</sup>, and high as >0.3 cm<sup>-1</sup>. For this definition of Al-OH<sup>-</sup> concentration it is assumed that the 3366 cm<sup>-1</sup> peak has reached its saturation level.

#### Results

Figure 2 shows the peak absorption coefficients of the 3581 cm<sup>-1</sup> and 3366 cm<sup>-1</sup> bands measured along the y-axis for Premium-Q sample BH-A, with high substitutional aluminum concentration, as a function of radiation dose. The measurement at any point along the y-axis includes the absorption of material deposited during the entire growth process. The data indicates a high level and uniform distribution of as-grown OH<sup>-</sup> concentration, 0.6 cm<sup>-1</sup>. After 0.2 Mrad irradiation the absorption decreases by 0.4 cm<sup>-1</sup> and introduces an Al-OH<sup>-</sup> band of 1.0 cm<sup>-1</sup> absorption strength. The ratio of Al-OH<sup>-</sup> production to OH<sup>-</sup> reduction is 2.5, that is, for each 0.1 cm<sup>-1</sup> decrease in OH<sup>-</sup> absorption there is an Al-OH<sup>-</sup> increase of 0.25 cm<sup>-1</sup>. The decrease in OH<sup>-</sup> is in proportion to the available OH<sup>-</sup>, and it is not line-



ar with dose. With further dose, the as-grown  $\text{OH}^-$  decreases and approaches a constant absorption level of  $0.15 \text{ cm}^{-1}$ , and at the same time,  $\text{Al-OH}^-$  increases and approaches saturation. The growth process is along the z-axis, and measurements along the y-axis do not reveal defect non-uniformities that may be incorporated in the crystal.

Figure 3 shows the variations of the peak absorption coefficients of the  $3581 \text{ cm}^{-1}$  and  $3366 \text{ cm}^{-1}$  bands associated with  $\text{OH}^-$  and  $\text{Al-OH}^-$ , respectively, along the z-growth axis, for the same Premium-Q crystal BH-A. The as-grown  $\text{OH}^-$  absorption varies from  $0.25$  to  $0.37 \text{ cm}^{-1}$ . This extent of non-uniformity is common even in high quality quartz, with  $\text{OH}^-$  concentrations usually stronger near the seed. The  $0.2 \text{ Mrad}$  irradiation reduces the  $\text{OH}^-$  fairly uniformly,  $0.17$ – $0.20 \text{ cm}^{-1}$ , to a level of  $0.07$  to  $0.20 \text{ cm}^{-1}$ . The  $\text{Al-OH}^-$  distribution follows that of the initial  $\text{OH}^-$  only for one-half of the crystal, but for the second-half, between the center and the -z-face, the  $\text{Al-OH}^-$  is more uniform than either the initial or the radiation reduced  $\text{OH}^-$ . In the z-growth direction the ratio of  $\text{Al-OH}^-$  production to  $\text{OH}^-$  reduction varies between  $1.7$  to  $2.8$ . Also, for the same initial  $\text{OH}^-$  concentration, a larger  $\text{Al-OH}^-$  to  $\text{OH}^-$  ratio is observed towards the -z-face of the crystal. In some regions of the crystal, the defect distribution after the accumulated  $0.8 \text{ Mrad}$  irradiation shows approach to  $\text{OH}^-$  depletion and  $\text{Al-OH}^-$  saturation.

Figure 4 shows the variation in peak absorption coefficients for the  $3581 \text{ cm}^{-1}$  and  $3366 \text{ cm}^{-1}$  bands along the z-growth axis for Premium-Q crystal D14-45, as a function of radiation dose. Crystals grown in this autoclave run have low aluminum concentrations, as determined from ESR measurements, and this particular bar, 43A, also indicates low as-grown  $\text{OH}^-$  along the growth axis. The as-grown  $\text{OH}^-$  absorption is approximately  $0.07 \text{ cm}^{-1}$  over two-thirds of the thickness, rising to  $0.11 \text{ cm}^{-1}$  in the section closest to the seed. A  $0.2 \text{ Mrad}$  irradiation reduces  $\text{OH}^-$  relatively uniformly across the sample,  $0.04$  to  $0.05 \text{ cm}^{-1}$ , to an absorption level varying from  $0.025$  to  $0.055 \text{ cm}^{-1}$ . This decrease is about a factor of  $2$ – $2.5$ , with the largest reduction occurring in the crystal section containing the highest initial  $\text{OH}^-$  concentration. The  $\text{Al-OH}^-$  absorption distribution across the sample formed as a result of this initial dose varies from  $0.04$  to  $0.075 \text{ cm}^{-1}$ , and exhibits the same non-uniformity as the initial  $\text{OH}^-$  distribution. The ratio of  $\text{Al-OH}^-$  production to  $\text{OH}^-$  reduction is  $1.0$  to  $1.5$ , with the higher value associated with the crystal region with the higher initial  $\text{OH}^-$ .

Irradiating the crystal to a total dose of  $0.4 \text{ Mrad}$  continues the trends observed for the initial irradiation. The  $\text{Al-OH}^-$  absorption increase is approximately  $0.03 \text{ cm}^{-1}$  across the sample. Increasing the accumulated radiation dose to  $0.8 \text{ Mrad}$  shows very little additional decrease in as-grown  $\text{OH}^-$ . The  $\text{OH}^-$  is depleted at one end of the crystal, rises gradually across the crystal, and reaches an absorption strength of  $0.04 \text{ cm}^{-1}$  at the other end. The residual  $\text{OH}^-$  absorption profile reflects the as-grown non-uniformity, with a constant  $0.07 \text{ cm}^{-1}$  subtracted from the initial value. After the  $0.8 \text{ Mrad}$  dose,  $\text{Al-OH}^-$  absorption shows a fairly uniform distribution, with somewhat lower values in the center of the crystal.

Figure 5 shows the absorption coefficients of the  $\text{OH}^-$  and  $\text{Al-OH}^-$  associated bands along the z-growth axis, as a function of radiation dose, for a sodium compensated High-Q crystal, E42-21, containing a high concentration of substitutional aluminum and low as-grown  $\text{OH}^-$ . The as-grown  $\text{OH}^-$  absorption values vary

from  $0.08$  to  $0.12 \text{ cm}^{-1}$ , with the higher values near the seed. A  $0.2 \text{ Mrad}$  irradiation reduces the overall  $\text{OH}^-$  absorption to  $0.01$ – $0.02 \text{ cm}^{-1}$ , and the absorption values of  $\text{Al-OH}^-$  formed vary from  $0.12 \text{ cm}^{-1}$  at one end of the crystal to  $0.20 \text{ cm}^{-1}$  at the other end. The  $\text{Al-OH}^-$  distribution shows a slight resemblance to the initial  $\text{OH}^-$ . The initial as-grown  $\text{OH}^-$  absorption level of this crystal is similar to Premium-Q D14-45 depicted in Figure 4, but the two samples differ in their radiation response. For this case the ratio of  $\text{Al-OH}^-$  production to  $\text{OH}^-$  reduction varies from  $1.3$  to  $2.0$ .

Irradiating the crystal to  $0.4 \text{ Mrad}$  reduces  $\text{OH}^-$  absorption from  $0.005 \text{ cm}^{-1}$  to  $0.002 \text{ cm}^{-1}$ , increases  $\text{Al-OH}^-$  absorption by about  $0.1 \text{ cm}^{-1}$  over most of the crystal, and the  $\text{Al-OH}^-$  peak shows an almost linear gradient between the two ends of the sample. Irradiating the crystal to  $0.8 \text{ Mrad}$  depletes as-grown  $\text{OH}^-$  across the entire sample and increases  $\text{Al-OH}^-$  in a fairly uniform manner, maintaining the same  $\text{Al-OH}^-$  gradient. This sample shows a surprisingly large change in  $\text{Al-OH}^-$  for the  $0.002 \text{ cm}^{-1}$  reduction in  $\text{OH}^-$ . The same effect can be noted close to the +z-face of sample D14-45 of Figure 4. Local variations in  $\text{Al-OH}^-$  increase are also observed for the same magnitude of  $\text{OH}^-$  decrease.

Figure 6 shows the absorption coefficients along the z-growth axis, as a function of radiation dose, for the lithium doped crystal QA-32, grown at RADC. ESR impurity analysis indicates that this crystal has a very high substitutional aluminum impurity concentration,  $32 \text{ ppm}$ , while atomic absorption results for another section of this crystal shows  $4 \text{ ppm}$ . We find that as-grown  $\text{OH}^-$  absorption values are uniform across the sample, but are very high, an average of  $0.35 \text{ cm}^{-1}$ . The  $0.2 \text{ Mrad}$  irradiation reduces as-grown  $\text{OH}^-$  absorption to  $0.06$ – $0.12 \text{ cm}^{-1}$ . The as-grown  $\text{OH}^-$  of this sample, and the initial irradiation results, are similar to that of Premium-Q BH-A, but with a much sharper gradient in  $\text{Al-OH}^-$ .  $\text{Al-OH}^-$  absorption increases from  $0.08$  to  $0.36 \text{ cm}^{-1}$  over one-half of the sample and remains at the  $0.36 \text{ cm}^{-1}$  level over the second-half of the sample. The  $\text{Al-OH}^-$  to  $\text{OH}^-$  ratio varies from  $0.5$  to  $1.5$ . At this level of irradiation,  $\text{OH}^-$  has decreased relatively uniformly across the entire sample, has not depleted at any point, yet we obtain a  $4.5:1$  variation in  $\text{Al-OH}^-$  absorption.

Irradiating the crystal to  $0.4 \text{ Mrad}$  continues the trends observed for  $0.2 \text{ Mrad}$ . As-grown  $\text{OH}^-$  absorption is reduced to an average of  $0.03 \text{ cm}^{-1}$ , and the corresponding increase in  $\text{Al-OH}^-$  absorption is  $0.15$ – $0.20 \text{ cm}^{-1}$ . The sharp gradient in  $\text{Al-OH}^-$  absorption, a rise of  $0.3 \text{ cm}^{-1}$  across one-half of the sample, is retained. An additional  $0.4 \text{ Mrad}$  irradiation depletes  $\text{OH}^-$  and further increases  $\text{Al-OH}^-$ . This crystal also shows a very large increase in  $\text{Al-OH}^-$  for a small decrease in  $\text{OH}^-$ . Measurements taken closer to the +z-face after this irradiation indicate that the gradient in  $\text{Al-OH}^-$  is even more pronounced than that observed for the lower doses. After the accumulated  $0.8 \text{ Mrad}$  dose, visual darkening, usually associated with  $\text{Al}^{3+}$ , can be observed in the high  $\text{Al-OH}^-$  region of the crystal, but not close to the +z-face. This is further evidence for the large aluminum concentration gradient.

#### Discussion

We have observed previously that in synthetic quartz the concentration of as-grown  $\text{OH}^-$  and aluminum impurities are unrelated. For Premium-Q crystals one can obtain all possible combinations of high and low as-grown  $\text{OH}^-$  and substitutional  $\text{Al}^{3+}$  concentration levels, but empirically we find that all High-Q crystals have high  $\text{Al}^{3+}$  concentrations. The samples chosen for

this investigation include a variety of these combinations of  $\text{OH}^-$  and  $\text{Al}^{3+}$  concentrations.

All experimental results are consistent with the mechanisms that radiation dissociates  $\text{Al-M}^+$  and as-grown  $\text{OH}^-$ , and forms  $\text{Al-OH}^-$ . The sequence of mechanisms affecting the defect centers may include a precursor for  $\text{M}^-$ -centers, the dissociation of  $\text{Al-M}^+$ , and the dissociation of  $\text{OH}^-$  to compensate the liberated  $\text{Al}^{3+}$  sites. We also find that initially the formation of  $\text{Al-OH}^-$  is governed by the concentration and distribution of as-grown  $\text{OH}^-$ . With successive irradiations the as-grown  $\text{OH}^-$  centers can remain at a constant level or deplete, and  $\text{Al-OH}^-$  can continue to increase or saturate. When as-grown  $\text{OH}^-$  is depleted, the  $\text{Al-OH}^-$  distribution, even if saturated, does not necessarily reflect the substitutional aluminum profile, as the formation of  $\text{Al-OH}^-$  may be inhibited by lack of as-grown  $\text{OH}^-$ . Conversely, when as-grown  $\text{OH}^-$  remains at a constant level with additional dose,  $\text{Al-OH}^-$  distribution does reflect the substitutional aluminum profile.

It is difficult to draw conclusions regarding final levels, or distributions, of the defect centers. We encounter both depletion and saturation effects. It is expected that after as-grown  $\text{OH}^-$  is depleted, additional irradiation will not increase  $\text{Al-OH}^-$ . This however is not the case. The most puzzling feature observed in Fig. 5 is the additional increase in  $\text{Al-OH}^-$  with dose after  $\text{OH}^-$  is depleted. The basic issue raised by this data is what is the source of the additional hydrogen ions. Are we observing an additional stage of defect formation, with hydrogen ions being released from "hidden" traps, or is this increase due to migration of ions across the crystal, distances in the order of millimeters or centimeter?

It is always simple to interpret phenomena by assuming additional unknown defect centers. The object, however, is to interpret the data in a consistent manner by assuming the minimum number of known defects.

Martin shows evidence that even in a lithium compensated Premium-Q sample, there are sodium compensated non-aluminum sites which dissociate with radiation. When the irradiated crystal is annealed, the dissociated sodiums form  $\text{Al-Na}^+$ , rather than recombining into the original  $\text{Na}^+$ -centers. Consequently, Premium-Q samples, which initially did not show any 50 K anelastic loss peak, show  $\text{Al-Na}^+$  centers after irradiation and anneal. Similarly, Green, Toulouse, and Nowick discuss irradiation induced conductivity in terms of complex alkali-metal centers which anneal in the same temperature range as  $\text{Al-e}^-$ .

One possibility of interpreting the  $\text{Al-OH}^-$  increase with no apparent decrease in  $\text{OH}^-$  is a two-step process involving an interaction with the sodium compensated center,  $\text{Na}^+$ -center, identified by Martin. When the sample is irradiated, both  $\text{Al-M}^+$  and  $\text{Na}^+$ -centers dissociate and become compensated with hydrogen ions from dissociating  $\text{OH}^-$ . This process forms  $\text{Al-OH}^-$ ,  $\text{M}^-$ -centers, and an infrared inactive sodium-hydrogen complex. After further irradiation, as more  $\text{Al-M}^+$  dissociates and  $\text{OH}^-$  becomes depleted, the sodium-hydrogen complex starts to dissociate, hydrogen ions are released from their trapping sites, and become available to compensate  $\text{Al}^{3+}$  to form additional  $\text{Al-OH}^-$ . At the same time the liberated sodium ions add to other  $\text{M}^-$ -ions from the dissociating  $\text{Al-M}^+$ .

One difficulty with this proposed two-step process is the fact that it assumes that the hydrogen complex is both created and dissociated with irradiation, and its existence depends on the availability of as-grown  $\text{OH}^-$  to compensate  $\text{Al-M}^+$ . It is more reasonable to as-

sume that the initial irradiation also dissociates the sodium compensated center and immediately forms  $\text{M}^-$ -centers. Consequently, we would like to propose another model for interpreting our data. Martin's results shows evidence for "hidden" sodiums, and our results, the increase in  $\text{Al-OH}^-$  at no apparent decrease in  $\text{OH}^-$ , shows evidence for "hidden" hydrogens. We suggest that the two phenomena are related and that the additional source of hydrogen is  $\text{NaOH}$ . The molecular  $\text{NaOH}$  is incorporated in the crystal during crystal growth. In crystal growth using the  $\text{NaOH}$  mineralizer process, this molecule is provided directly from the mineralizer, and in crystal growth using the  $\text{Na}_2\text{CO}_3$  mineralizer process, the  $\text{NaOH}$  molecule is formed in solution. This is similar to the process of incorporating water molecules during crystal growth. At the present time we are unable to propose a specific configuration for this center, whether the molecule is incorporated at an oxygen vacancy or at some other site, for example, the configuration depicted on p. 64 of Ref. 1. The fact that  $\text{NaOH}$  dissociates after as-grown  $\text{OH}^-$  is depleted implies that the two processes are independent and one may become exhausted before the other is depleted. When the sample is annealed the  $\text{NaOH}$  molecule is not re-formed, as evidenced from the newly created  $\text{Al-Na}^+$  centers. Consequently, after annealing, or air sweeping, we may also observe an increase in  $\text{OH}^-$  related bands.

In the same crystal, for the same  $\text{OH}^-$  decrease we observe differences in the amount of  $\text{Al-OH}^-$  increase. One possible interpretation is that the aluminum concentration varies across the crystal and the radiation induced hydrogen ion mobility extends over large distances. We can also assume that the concentration of the "hidden"  $\text{Na}^+$ -centers is non-uniform, and the local decrease in  $\text{OH}^-$  in then the sum of the dissociating  $\text{Al-M}^+$  and  $\text{Na}^+$ -centers. If the  $\text{Na}^+$ -center is the proposed  $\text{NaOH}$  molecule, then the local decrease in as-grown  $\text{OH}^-$  is the difference between the magnitudes of  $\text{Al-OH}^-$  and the dissociating  $\text{NaOH}$ .

These considerations suggests some further experiments. The possibility of radiation induced mobility over large distances could be clarified by annealing a crystal which exhibits large non-uniformities in  $\text{Al-OH}^-$  to its original state, and physically slicing it into a number of sections. The radiation sequence is then repeated on each section, and infrared results are compared with those obtained for the whole crystal.

As discussed in the Introduction, another center that complicates the interpretation of infrared data is the aluminum-hole,  $\text{Al-e}^-$ . ESR measurements show that this center is created by irradiation, but we do not know its distribution along the z-growth axis or the sequence of its formation. Is  $\text{Al-e}^-$  created at (1) low doses of irradiation prior to any decrease in as-grown  $\text{OH}^-$ , (2) in proportion to  $\text{Al-OH}^-$ , or (3) does it form from residual  $\text{Al-M}^+$  centers, after as-grown  $\text{OH}^-$  and other hydrogen related defects are exhausted?

A non-destructive method could be employed to evaluate the contribution of  $\text{Al-e}^-$  without utilizing ESR measurements.  $\text{Al-e}^-$  anneals between 240 and 300 °C. It is suggested that two sets of experiments be performed. The first set is the sequence of irradiations and infrared evaluations outlined in this investigation. After saturation and depletion effects are complete, the sample is annealed between 500-500 °C to return it to its original state. The second set of experiments is the same sequence of irradiations and infrared evaluations, but the sample is annealed at 300 °C after each dose of irradiation to dissociate  $\text{Al-e}^-$ . We do not necessarily expect a large decrease in as-grown  $\text{OH}^-$  or increase in  $\text{Al-OH}^-$  after each anneal, as

an undetermined fraction of the dissociated aluminums may become compensated with  $M^+$  to re-form  $Al-M^+$ . However, after subsequent irradiations, additional  $Al-OH$  should form from the larger reservoir of  $Al-M^+$ . The difference between the two sets of irradiation experiments, one with and one without the  $300^\circ C$  anneal, can be attributed to  $Al-e^-$ .

The question whether the growth of  $Al-OH^-$  as a function of irradiation is inhibited by lack of as-grown  $OH^-$  can be clarified by sweeping the sample in an air atmosphere after irradiation effects are saturated. Radiation induced changes anneal below the usual sweeping temperatures, and air sweeping will provide the hydrogen to saturate  $Al-OH^-$ , as well as all other hydrogen related defect sites. In the swept sample, the  $Al-OH^-$  profile will reflect the substitutional aluminum distribution, and the difference in band strength for the two processes is a measure of how much  $OH^-$  was required to fully compensate the available  $Al^{3+}$  centers.

### Conclusions

Low temperature Fourier spectroscopy is a powerful tool for studying the defect structure of high quality quartz. The high throughput and small beam size associated with the Fourier spectrophotometer allows us to determine the spatial variations in defect concentrations across the sample. Using this technique we observe large variations in substitutional and interstitial impurity concentration and distribution, as well as differences in formation rates of various defects as a function of irradiation. These variations and differences make it is very difficult to predict the radiation response of quartz crystals. We have

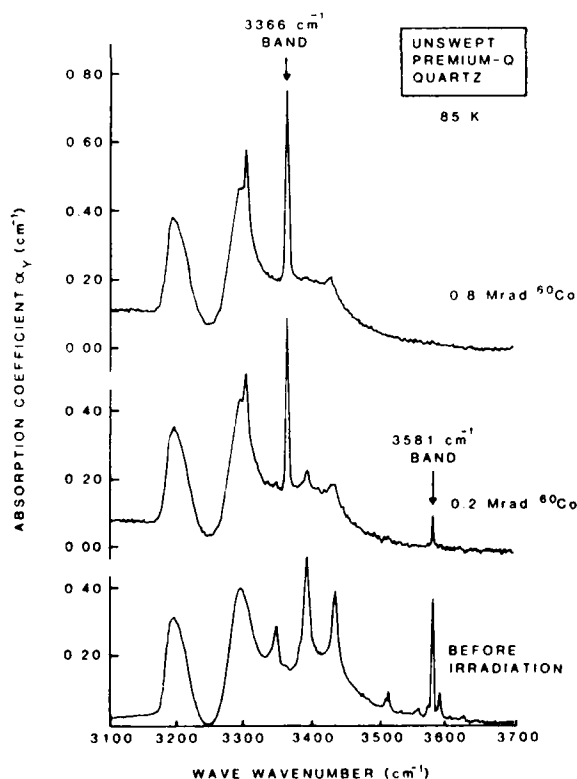


Figure 1. Absorption spectra for unswept Premium-Q quartz sample BH-A before irradiation and after 0.2 and 0.8 Mrad doses.

also shown that there exists an additional source of hydrogen in the crystal, not associated with the usual as-grown  $OH^-$  bands, which contributes to the formation of  $Al-OH^-$  defects. Possible models proposed for this additional source of hydrogen are the presence of a sodium-hydrogen complex or molecular  $NaOH$ . In crystal growth using the  $NaOH$  mineralizer process, this molecule is provided directly from the mineralizer, and in crystal growth using the  $Na_2CO_3$  mineralizer process, the  $NaOH$  molecule is formed in solution.

### References

1. D.B. Fraser, *Physical Acoustics*, Vol. 5, W.P. Mason, editor, Academic Press, New York, (1968), 59.
2. L.E. Haliburton, N. Koumvakalis, M.E. Markes, and J.J. Martin, *J. Appl. Phys.*, **52**, 3565(1981).
3. D.M. Dodd and D.B. Fraser, *J. Phys. Chem. Solids*, **26**, 673 (1965).
4. F. Euler, H.G. Lipson, A. Kahan, and A.F. Armington, *Proc. 36th Annual Frequency Control Symposium*, 115(1982).
5. H.G. Lipson, A. Kahan, and J. O'Connor, *Proc. 37th Annual Frequency Control Symposium*, 169(1983).
6. M.E. Markes and L.E. Halliburton, *J. Appl. Phys.*, **50**, 8172(1979).
7. J.J. Martin (these Proceedings).
8. E.R. Green, J. Toulouse, and A.S. Nowick (these Proceedings).

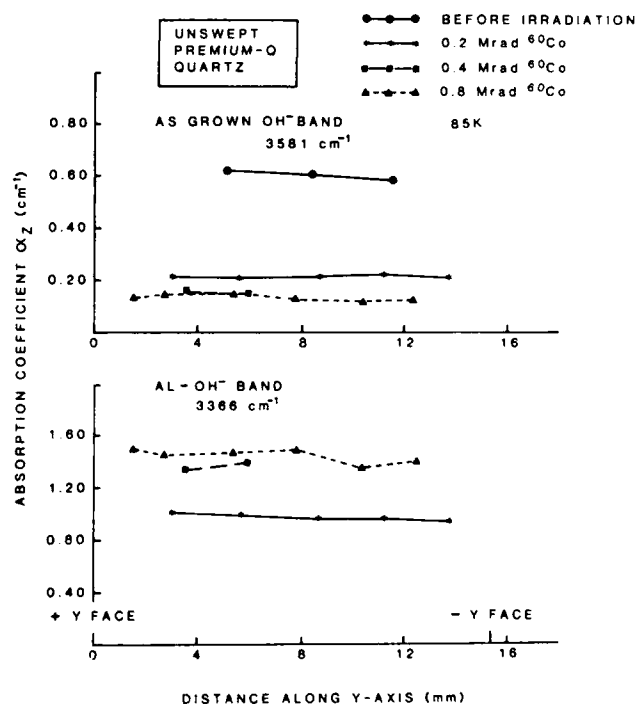


Figure 2. Peak strength absorption coefficients for  $3581\text{ cm}^{-1}$  and  $3366\text{ cm}^{-1}$  bands as a function of position along the y-axis for various total radiation doses. Premium-Q sample BH-A.

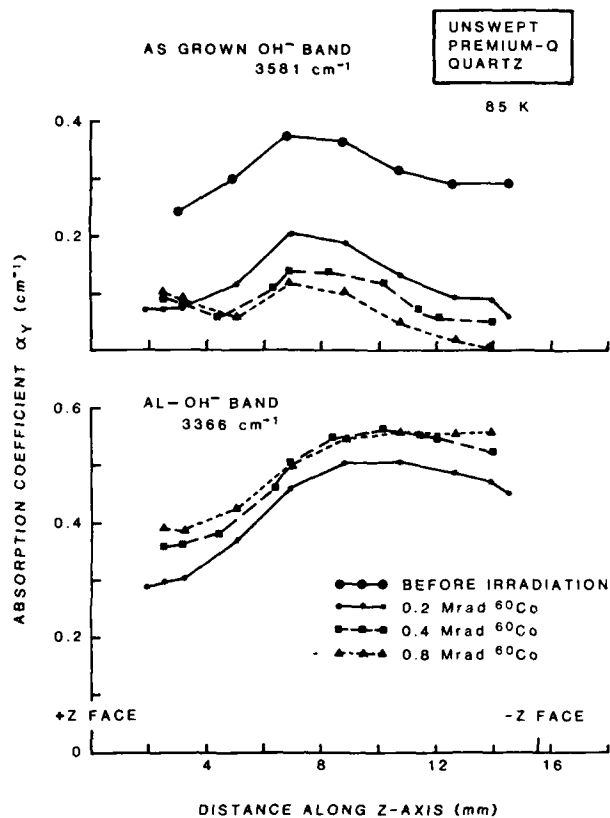


Figure 3. Peak strength absorption coefficients for 3581  $\text{cm}^{-1}$  and 3366  $\text{cm}^{-1}$  bands as a function of position along the z-growth axis for various total radiation doses. Premium-Q sample BH-A.

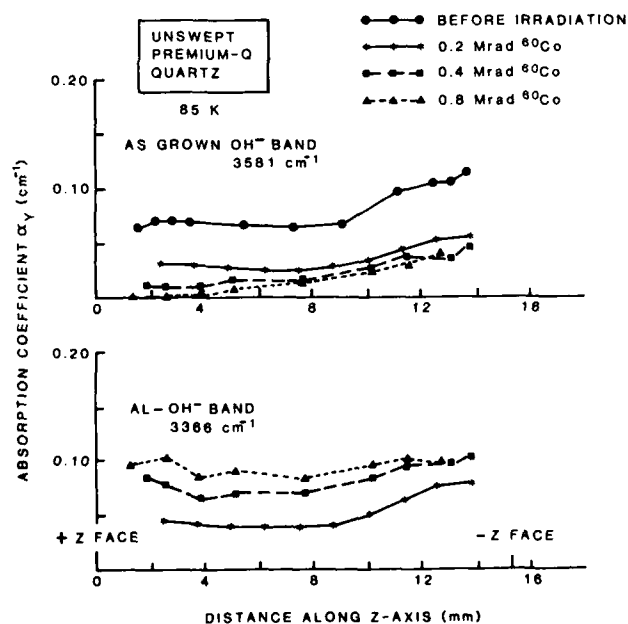


Figure 4. Peak strength absorption coefficients for 3581  $\text{cm}^{-1}$  and 3366  $\text{cm}^{-1}$  bands as a function of position along the z-growth axis for various total radiation doses. Premium-Q sample D14-45.

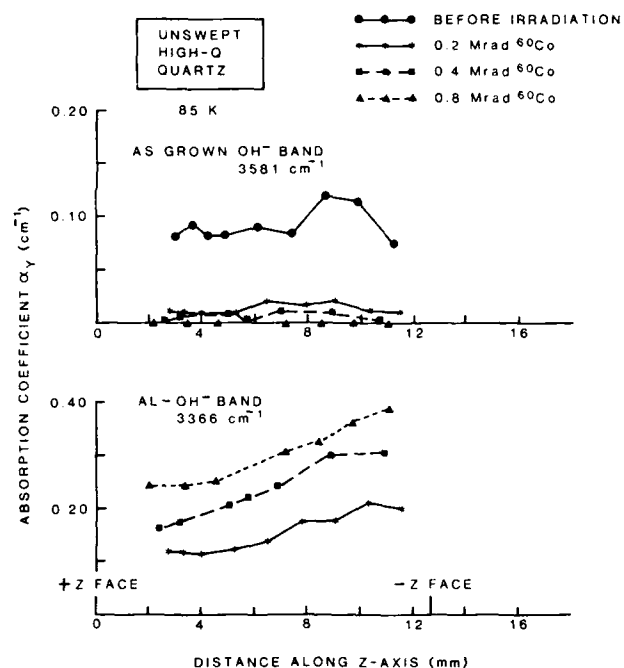


Figure 5. Peak strength absorption coefficients for 3581  $\text{cm}^{-1}$  and 3366  $\text{cm}^{-1}$  bands as a function of position along the z-growth axis for various total radiation doses. High-Q sample E42-21.

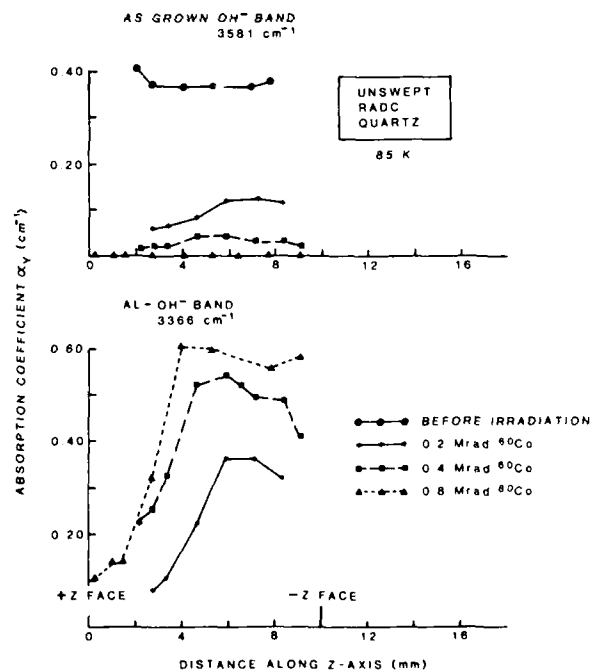


Figure 6. Peak strength absorption coefficients for 3581  $\text{cm}^{-1}$  and 3366  $\text{cm}^{-1}$  bands as a function of position along the z-growth axis for various total radiation doses. RADC/ESM sample QA-32.

## ALUMINUM-RELATED ACOUSTIC LOSS IN AT-CUT QUARTZ CRYSTALS

J. J. Martin

Department of Physics  
Oklahoma State University  
Stillwater, Oklahoma 74078

SUMMARY

The substitutional aluminum ions present in all quartz require charge compensation. In as-grown synthetic quartz, interstitial alkali ions serve as the charge compensators. Irradiation at temperatures above 200 K replaces the alkali with either a proton or a hole trapped on an adjacent oxygen. Electrodiffusion (sweeping) can be used to replace the alkali with either a proton or another specific alkali. A study of the acoustic loss spectra of a series of 5 MHz 5th overtone AT-cut resonator blanks as a function of sweeping and irradiation has been completed. No acoustic loss peaks were observed at temperatures less than 100°C which could be attributed to either the  $\text{Al-Li}^+$  or  $\text{Al-OH}^-$  centers. Na-swept samples showed the expected large loss peak at 53 K while unswept samples had only very small 53 K peaks. This shows that in as-grown synthetic quartz lithium is the primary charge compensating ion. Irradiation removed the 53 K peak and introduced new peaks at 23 K, 100 K and 135 K. Annealing studies show that these peaks can be attributed to the Al-hole center. The anneal study also shows that the decay of the Al-hole center is matched by the return of the alkali to the aluminum site.

Introduction

Alpha-quartz is used in a wide variety of precision electronic devices where aging and radiation-induced instabilities are undesirable. It is now well-known that quartz-controlled oscillators may exhibit transient and steady-state frequency and Q shifts when exposed to ionizing radiation.<sup>1-4</sup> Early results obtained by King<sup>5</sup> and other investigators<sup>6-9</sup> suggested that these effects were associated with the presence of impurities.

Substitutional  $\text{Al}^{3+}$  is present in all quartz<sup>10</sup> and requires charge compensation. Examples of such charge compensators are interstitial  $\text{Li}^+$  or  $\text{Na}^+$  ions, or holes or protons at an oxygen ion adjacent to the aluminum. The proton forms an  $\text{OH}^-$  molecule which is infrared active.<sup>10,11</sup> The  $\text{Al-Na}^+$  defect is responsible for the acoustic loss peak observed near 53 K in 5 MHz 5th overtone AT-cut crystals.<sup>12</sup> Irradiation at room temperature destroys the  $\text{Al-Na}^+$  centers;<sup>5,13</sup> this destruction being responsible for much of the steady state frequency offset. Recent work at Oklahoma State University has shown that the alkali ions become mobile under irradiation only if the temperature is greater than 200 K.<sup>13-15</sup> Following a room temperature irradiation, either a hole which can be observed by ESR techniques or a proton

is found trapped on an oxygen adjacent to the  $\text{Al}^{3+}$ . The interstitial alkali ions are usually in the relatively large c-axis channels and at high temperatures can move along the channel under an applied electric field. King,<sup>5</sup> and later Kats<sup>11</sup> and Fraser<sup>12</sup> used this technique to "sweep" hydrogen and specific alkalis into the sample. Sweeping hydrogen in to replace the alkalis has been shown to improve the radiation hardness of quartz oscillators.<sup>8</sup>

The identification of both growth- and radiation-induced defects which affect the performance of quartz resonators is an important part of our project. Recently, using sweeping, IR absorption, and acoustic loss measurements, Martin and Doherty<sup>16</sup> reported that the  $\text{Al-OH}^-$  center does not have an acoustic loss peak at temperatures below 370 K. They also reported that irradiation of both unswept and H-swept Premium Q quartz resonator blanks produced acoustic loss peaks at 23 K and 100 K and a broad loss peak between 125 K and 165 K. King and Sander<sup>1</sup> had earlier reported the two higher temperature peaks and had suggested that they were caused by the Al-hole center. The 23 K peak had also been observed earlier and was attributed to changes in the interaction between the resonant vibrations of the blank and the thermal phonons.<sup>17</sup> We report here a comparison of the acoustic loss spectra of as-received and  $\text{Li}^+$ ,  $\text{Na}^+$ , and  $\text{H}^+$  swept resonators fabricated from the same bar of Premium Q grade quartz. Results were also obtained for Supreme Q grade material and for a natural quartz crystal. We also report an isochronal anneal study of the three peaks induced by a room temperature irradiation which shows that they are associated with the Al-hole center. An isochronal anneal study was also made on an irradiated Na-swept resonator to directly compare the decay of the Al-hole and  $\text{Al-OH}^-$  centers with the recovery of the  $\text{Al-Na}^+$  centers.

Experimental Procedure

Samples for this study were cut from an unswept pure Z-growth Sawyer Premium Q bar of cultured quartz that has been given an in-house designation PQ-E. Samples from this bar have been intensively studied at Oklahoma State University using ESR,<sup>10,14</sup> IR, and acoustic loss techniques. All of these investigations show that the bar is of high quality but that it contains somewhat more aluminum (10-15 ppm) than the average Premium Q material (5-8 ppm). Consequently, aluminum related effects are more readily observed. Five MHz 5th overtone AT-cut plano convex resonator blanks of the Warner design<sup>18</sup> were

fabricated for this study by K&W Mfg. Confirming measurements were made on five MHz 3rd overtone AT-cut samples fabricated by Frequency Electronics from a Toyo Supreme Q bar labeled SQ-B. A 5.12 MHz natural quartz resonator was also measured. H-swept, Li-swept, and Na-swept blanks were prepared from both PQ-E and SQ-B quartz by the method reported earlier.<sup>13,16</sup> Infrared absorption scans show that Al-OH<sup>-</sup> centers are present in the H-swept sample but not in the alkali-swept samples.

The acoustic loss,  $Q^{-1}$ , of the resonator blanks was measured by the log decrement method from 5 to 370 K. The measurements were made in a variable temperature helium Dewar with the blank mounted in a gap holder. The blank was driven for 10 to 40 ms at its series resonant frequency and then allowed to freely decay. The decaying rf signal was detected with a superheterodyne detector and displayed on a variable persistence storage oscilloscope. The exponential decay times were measured by using a digital timer gated by a window detector.

### Results and Discussion

Figure 1 compares the acoustic loss spectra for the unswept Toyo, the unswept Sawyer and the natural quartz samples. Both the Sawyer blank and the natural quartz crystal show relatively small 53 K Al-Na<sup>+</sup> loss peaks. The SQ-B blank shows a Al-Na<sup>+</sup> peak height of  $dQ^{-1} = 5 \times 10^{-5}$ . Figure 2 compares the acoustic loss,  $Q^{-1}$ , spectra for unswept, Li-swept, and Na-swept PQ-E series resonator blanks. The unswept blank shows a small Al-Na<sup>+</sup> loss peak at 53 K with a height  $dQ^{-1}$  of approximately  $5 \times 10^{-7}$ . The Li sweep removed this peak and did not introduce any new peaks. The Na-swept blank showed a very large 53 K peak with  $dQ^{-1} = 2 \times 10^{-4}$  as shown in Figure 2. The Na-swept Toyo sample showed nearly the same 53 K Al-Na<sup>+</sup> peak as the Na-swept Sawyer sample. Since the material from which these blanks were fabricated contains 10 to 15 ppm aluminum, we conclude that the concentration, C, of Al-Na<sup>+</sup> centers is given by

$$C = [5(\pm 20\%) \times 10^4] dQ^{-1} \quad (1)$$

where C is in ppm and  $dQ^{-1}$  is the height of the 53 K Al-Na<sup>+</sup> loss peak. Thus, the unswept PQ-E blank probably contains about 0.3 ppm Al-Na<sup>+</sup> centers; the remaining 10 to 15 ppm of aluminum must be compensated by Li<sup>+</sup>. Since the mineralizer used in growing Premium Q quartz is predominantly Na<sub>2</sub>CO<sub>3</sub>, the essentially total exclusion of Na<sup>+</sup> from the aluminum sites by the addition of a small amount of Li<sub>2</sub>CO<sub>3</sub> to the solution is remarkable.<sup>19,20</sup> The as-grown Toyo Supreme Q blank contains substantial amounts of Na<sup>+</sup> but Li<sup>+</sup> must still be the majority charge compensator because the 53 K peak increased by a factor of four when the sample was Na-swept. The natural quartz resonator also contains only a small number of Al-Na<sup>+</sup> centers. An additional, much smaller, loss peak related to the Al-Na<sup>+</sup> center was observed at approximately 135 K in the Na-swept blanks. Park and Nowick<sup>21</sup> have also observed two Na-related peaks in their dielectric loss measurements.

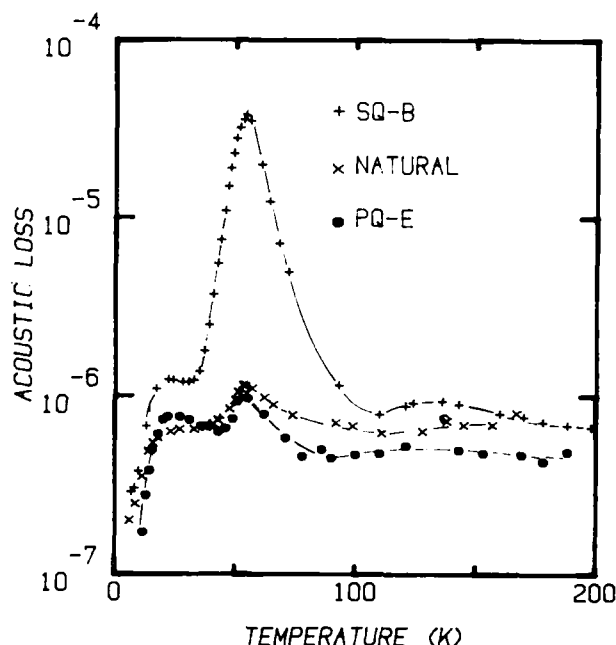


Fig. 1. The acoustic loss spectra of unswept Sawyer, unswept Toyo resonator blanks and a natural quartz crystal are compared. The Al-Na<sup>+</sup> center is responsible for the peak at 53 K.

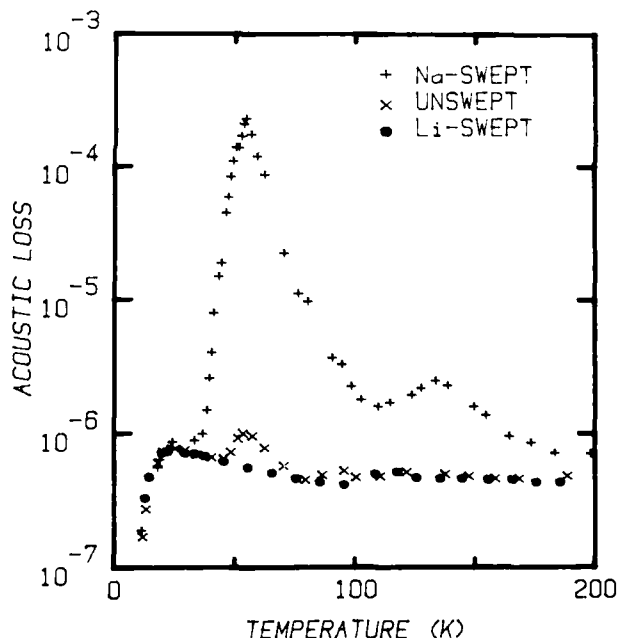


Fig. 2. The acoustic loss spectra of unswept, Na-swept and Li-swept resonator blanks all fabricated from the same bar of Sawyer Premium Q quartz are shown.

In contrast to earlier work<sup>12</sup> which reported a Li<sup>+</sup> related loss peak near 105 K, the results shown in Fig. 2 for the Premium Q blanks and similar results for the Toyo samples show no evidence of a Al-Li<sup>+</sup> acoustic loss at temperatures below 100°C. Toulouse, Green and Nowick<sup>22</sup> have recently reported the absence of Li<sup>+</sup> related dielectric loss peaks in both Sawyer Premium Q and Toyo Supreme Q samples. They suggest that because of the small size of the Li<sup>+</sup> ion the double well Na<sup>+</sup>

sites have collapsed into a single well for the  $\text{Li}^+$ . The resulting  $\text{Al-Li}^+$  pair then probably lies along the x-axis. Such a single well model would show neither acoustic nor dielectric loss peaks.

Figure 3 compares the acoustic loss spectra for the unswept, Li-swept, and H-swept blanks. The results for the Li and H-sweeps are essentially identical, as were the results for a D-sweep which have been omitted from Fig. 3 for clarity. Infrared absorption measurements made at liquid nitrogen temperature show that the H-swept blank contains 10-15 ppm  $\text{Al-OH}^-$  centers. Thus, it appears that neither the  $\text{Al-OH}^-$  nor the  $\text{Al-OD}^-$  centers show significant acoustic loss peaks at temperatures below about 370 K. It should be noted that at higher temperatures, the interstitial alkali ions become thermally liberated from the  $\text{Al}^{3+}$  trapping site and diffuse along the c-axis channels. This diffusion causes an acoustic loss which increases exponentially with temperature.<sup>17</sup> Lipson *et al.*<sup>23</sup> and Koehler<sup>24</sup> have shown that this high temperature loss is not present in H-swept quartz which contains no alkali ions and, therefore, must be caused by the alkali diffusion. Infrared absorption studies of the  $\text{Al-OH}^-$  center<sup>11,26</sup> show that it is strongly polarized with the electric dipole perpendicular to the c-axis. This orientation would probably not have a double well structure that would give rise to an acoustic loss.

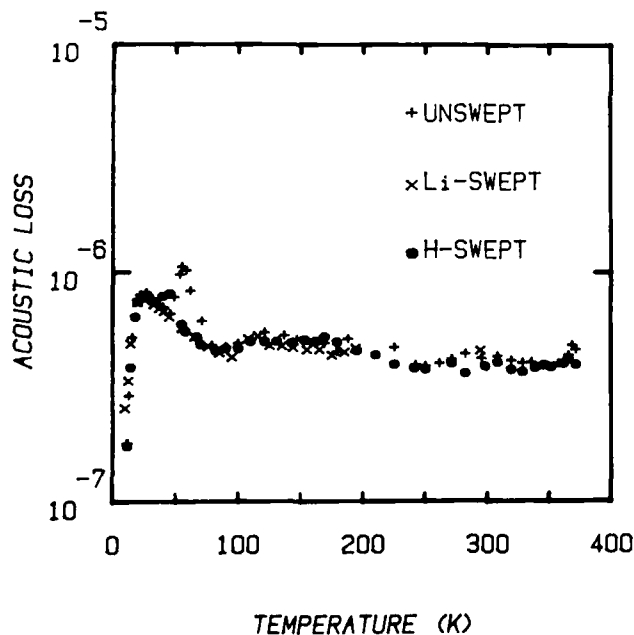


Fig. 3. The acoustic loss spectra of unswept, Li-swept and H-swept resonator blanks fabricated from a single bar of Premium Q quartz are shown. No loss peaks are observed that can be attributed to either the  $\text{Al-Li}^+$  or the  $\text{Al-OH}^-$  centers.

Figure 4 shows the effects of a high dose (10Mrad) on the acoustic loss spectrum of the unswept PQ-E sample. The irradiation has removed the 53 K  $\text{Al-Na}^+$  peak and introduced additional loss peaks at 23 K, 100 K, and 135 K. Martin and Doherty<sup>16</sup> and Martin *et al.*<sup>26</sup> have attributed these three peaks to the Al-hole center. Figure 5 shows the acoustic loss,  $Q^{-1}$ , versus temperature spectrum for the Na-swept blank in the as-swept condition and after a room temperature irradiation. The irradiation has removed the large 53 K

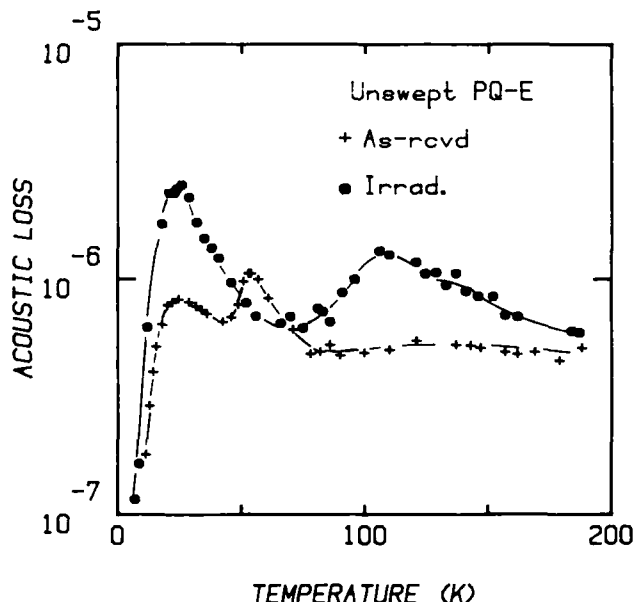


Fig. 4. The acoustic loss spectrum of the unswept blank is shown in the as-received condition and after a room temperature irradiation. The irradiation removed the 53 K peak due to the  $\text{Al-Na}^+$  center and introduced a peak at 23 K and overlapping peaks at 100 K and 135 K which are caused by the Al-hole center.

and 135 K  $\text{Al-Na}^+$  loss peaks while introducing the 23 K peak and the overlapping 100 K and 135 K peaks. The post-irradiation acoustic loss spectra for the unswept and Li-swept blanks are essentially the same as for the Na-swept sample. These three loss peaks are also observed in irradiated H-swept resonators fabricated from this same bar. However, their strength is reduced by approximately a factor of five. An inspection of the results reported by Doherty *et al.*<sup>13</sup> for the acoustic loss of their Na-swept resonator D14-45DC shows that the 23 K peak is small but present in their results. D14-45 series quartz is Premium Q grade material with an aluminum content less than 1 ppm, so we would expect aluminum-related loss peaks to be much smaller. Their Na loss peak is about 0.035 times that of our Na-swept PQ-E resonator blank. It should also be noted that their resonator was partially H-swept. Thus, it appears that these three peaks, and the Na peak as well, scale with the aluminum content.

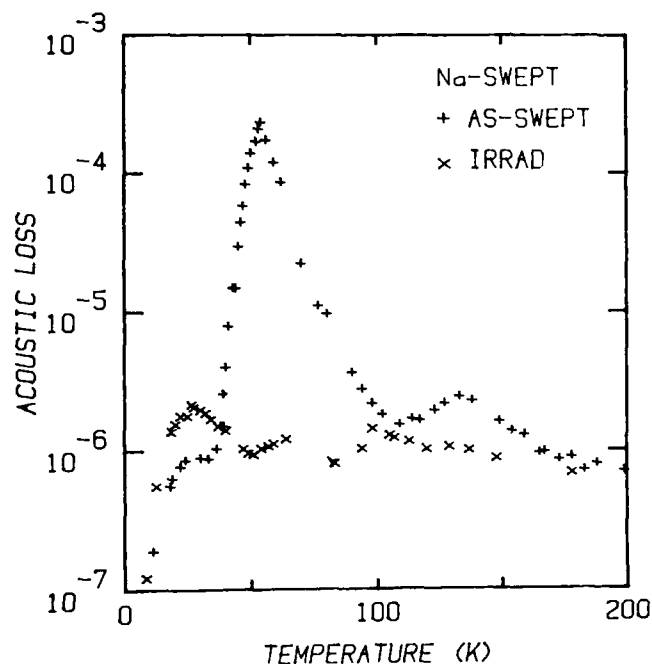


Fig. 5. The acoustic loss spectrum of the Na-swept blank is shown in the as-swept condition and after a room temperature irradiation. The irradiated spectrum is nearly identical to that of the irradiated unswept sample shown in Fig. 4.

The thermal anneal behavior of the Al-hole and Al-OH<sup>-</sup> centers in unswept quartz has been studied by Jani, Bossoli and Halliburton<sup>27</sup> and by Sibley *et al.*,<sup>15</sup> respectively. The Al-hole centers, as observed by ESR techniques, anneal out slightly below 550 K while the Al-OH<sup>-</sup> center anneals out between 620 K and 670 K. If the three radiation-induced loss peaks are due to the Al-hole center, they should show the same annealing pattern as the Al-hole center ESR spectrum. We have carried out an isochronal anneal study on the unswept blank and on the Li-swept blank. The results for the unswept blank show that the 23 K, 100 K, and 135 K loss peaks all anneal out between 500 and 550 K, as shown in Fig. 6. Since the three loss peaks occur in the same relative strength in unswept, Li-swept, Na-swept samples and follow the same annealing pattern as the Al-hole we conclude that all three loss peaks are most likely caused by the Al-hole center. When the anneal of the unswept blank is continued to higher temperatures, the Al-Na<sup>+</sup> center loss peak recovers between 600 and 650 K as shown in Fig. 6.

The isochronal anneal study also showed that after a room temperature irradiation and subsequent 670 K anneal, the 53 K Al-Na<sup>+</sup> peak in the unswept blank increased from an initial value of  $5 \times 10^{-7}$  to  $2.2 \times 10^{-6}$  after the anneal. The Al-Na<sup>+</sup> loss peak also appeared in the Li-swept sample as a result of the annealing although it was absent in the as-Li-swept sample. These latter results suggest that sodium is trapped at sites other than aluminum during growth. The irradiation and anneal treatment just described evidently rearranged the alkalis within the sample. It

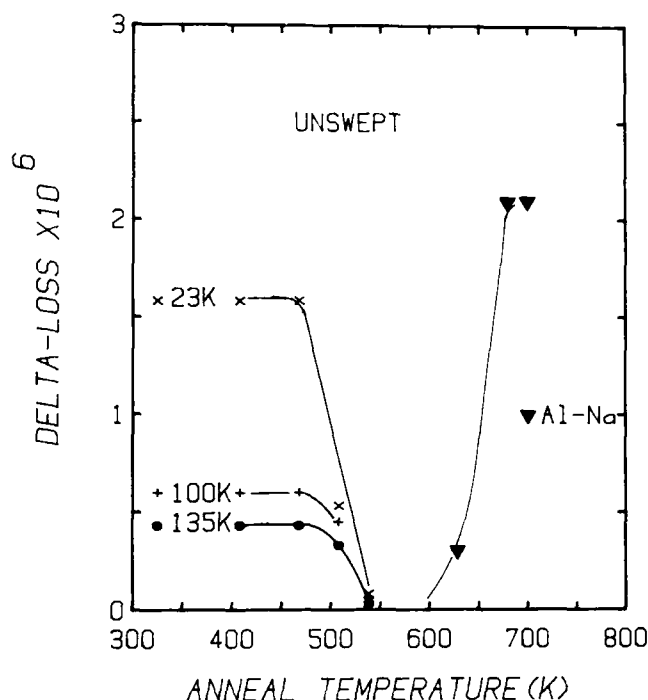


Fig. 6. The isochronal anneal behavior of the radiation induced peaks at 23 K, 100 K and 135 K shows that the three peaks go out together and at the same temperature as the Al-hole centers. These data were taken on the unswept blank. The Al-Na<sup>+</sup> center grows to four times its original concentration after the irradiation and subsequent anneal.

is conceivable that this process would take place at the 50 to 80°C operating temperature of a crystal oscillator (although very slowly) and contribute to the long term aging of the crystal.

The decay of the radiation induced Al-hole center should be matched by the corresponding growth of the Al-OH<sup>-</sup> and/or Al-M<sup>+</sup> centers. Sibley *et al.*<sup>15</sup> have measured the high temperature annealing behavior of the radiation-induced Al-OH<sup>-</sup> centers. Their results do not show any changes in the Al-OH<sup>-</sup> concentration for the 500-550 K temperature range where the Al-hole center decays. This result suggests that the anneal of the Al-hole center is matched by the return of an alkali ion to the Al site. Since our unswept samples contain mostly Li<sup>+</sup> ions and the Al-Li<sup>+</sup> center does not have an acoustic loss peak, Fig. 6 does not show the expected lower temperature return of the alkali ions to the aluminum site. We have repeated the isochronal anneal study using the Na-swept blank. In this case, acoustic loss measurements of the 23 K Al-hole peak and 53 K Al-Na<sup>+</sup> peak were used to track the behavior of the hole and the alkali centers. Polarized infrared absorption measurements of the 3367 cm<sup>-1</sup> band were also made on the Na-swept blank in order to track the Al-OH<sup>-</sup> center. Figure 7 shows the results of the anneal plotted in terms of the aluminum content. The decay of the 23 K Al-hole between 500 K and 550 K loss peak is matched by a 25% growth in the 53 K Al-Na<sup>+</sup> acoustic loss peak. The remaining growth of the 53 K peak closely matches the decay of



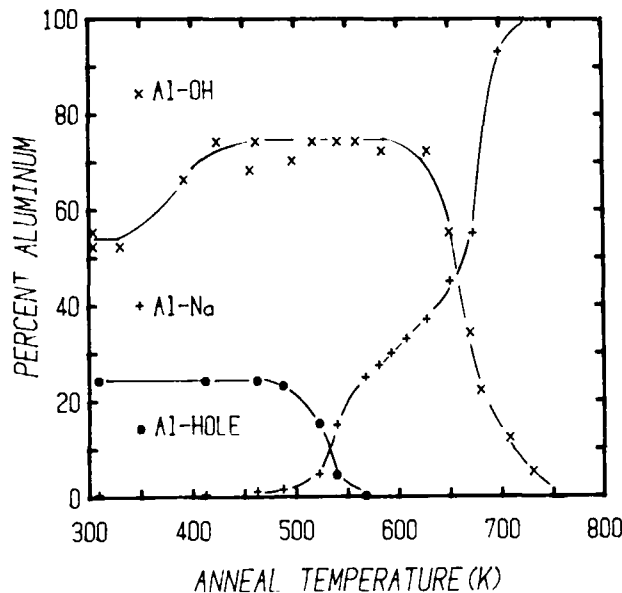


Fig. 7. The isochronal anneal of the 23 K Al-hole center peak and the Al-OH<sup>-</sup> infrared band which were produced by a room temperature irradiation of the Na-swept blank are shown. The decay of the Al-hole centers between 500 and 550 K is matched by a 25% recovery of the Al-Na<sup>+</sup> centers. The higher temperature decay of the Al-OH<sup>-</sup> centers is matched by the final recovery of the Al-Na<sup>+</sup> centers.

Al-OH<sup>-</sup> as measured by infrared absorption. The increase in the Al-OH<sup>-</sup> center observed near 350 K does not have a corresponding change in either the Al-hole centers or Al-Na<sup>+</sup> centers. Subramaniam, Halliburton and Martin<sup>28</sup> have also observed this lower temperature anneal step of the Al-OH<sup>-</sup> centers. The annealing results shown in Fig. 7 suggest that the room temperature irradiation converted approximately 25% of the Al sites into Al-hole centers with the remaining 75% becoming Al-OH<sup>-</sup> centers. In the irradiation process, the Na<sup>+</sup> leaves the Al site and is subsequently trapped at an as yet unknown site in the crystal. When the Al-hole centers anneal out the 500 K to 550 K temperature range the Na<sup>+</sup> ion returns to the Al site. In unswept material the decay of the Al-hole centers must be accompanied by the return of Li<sup>+</sup> ions since no corresponding increase in the Al-OH<sup>-</sup> centers is seen.

Often defect-related acoustic loss peaks can be described by

$$dQ^{-1} = D\omega\tau[1 + \omega^2\tau^2]^{-1} \quad (2)$$

where  $dQ^{-1}$  is the loss above the intrinsic background,  $D$  is the strength factor,  $\omega$  is the angular frequency, and  $\tau$  is the relaxation time for reorientation of the defect. The relaxation is usually thermally activated as the defect must go over an energy barrier to reach the other equivalent sites.<sup>16</sup> Thus,

$$\tau = \tau_0 \exp(E/kT) \quad (3)$$

where  $E$  is the barrier height and  $\tau_0$  contains the number of equivalent orientations and the attack rate. We have fit Eq. 2, with the relaxation time given by Eq. 3, to the 53 K and 135 K Al-Na<sup>+</sup> center loss peaks and to the three radiation-induced Al-hole loss peaks. The calculated parameters are given in Table I. Our activation energies and relaxation times for the Al-Na<sup>+</sup> center are in good agreement with Park and Nowick's dielectric loss results,<sup>21</sup> as well as those of Stevels and Volger.<sup>29</sup>

Stevels and Volger have also reported a radiation-induced dielectric loss peak with  $E = 7.5$  meV and  $\tau_0 = 5 \times 10^{-7}$  sec. This activation energy is in reasonable agreement with our 23 K peak, but the relaxation time is much longer. Taylor and Farnell<sup>30</sup> have also made dielectric loss measurements on irradiated quartz; they found a loss peak near  $E = 7.5$  meV in agreement with Stevels and Volger and an additional peak at temperature with  $E = 1.2$  meV and  $\tau_0 = 6.2 \times 10^{-5}$  s.

Table I. Acoustic-loss peak parameters

Defect	T(K)	E(meV)	$\tau_0$ (sec)
Al-Na <sup>+</sup>	53	57	$1.65 \times 10^{-13}$
Al-Na <sup>+</sup>	135	130	$4.44 \times 10^{-13}$
Al-hole	23	8	$8.3 \times 10^{-10}$
Al-hole	100	90	$1.0 \times 10^{-12}$
Al-hole	135	110	$2.7 \times 10^{-12}$

### Conclusions

Sweeping Li<sup>+</sup>, H<sup>+</sup>, or D<sup>+</sup> into high-aluminum-content Premium Q grade quartz AT-cut resonators removes the small Al-Na<sup>+</sup> loss peak at 53 K but does not introduce any new loss peaks at temperatures below 370 K. Therefore, we conclude that the Al-Li<sup>+</sup> and Al-OH<sup>-</sup> centers do not have anelastic loss peaks in this temperature region. Na-swept samples exhibit a very large 53 K loss peak. This shows that in as-grown quartz most of the Al sites are compensated by Li<sup>+</sup>. Irradiation at room temperature replaces the interstitial alkali at the Al sites with a mixture of Al-hole and Al-OH<sup>-</sup> centers. These radiation induced Al-hole centers are responsible for acoustic loss peaks at 23 K, 100 K and 135 K. The thermal decay of the Al-hole center is accompanied by a corresponding return of the alkali ions to the Al sites. The higher temperature decay of the Al-OH<sup>-</sup> center is also matched by the growth of the Al-M<sup>+</sup> centers.

### ACKNOWLEDGEMENTS

The author would like to thank J. C. King, D. R. Koehler, A. Kahan, H. G. Lipson, S. P. Doherty and L. E. Halliburton for a number of helpful discussions. This work was supported by the U. S. Air Force under contract with the Solid State Sciences Division, Rome Air Development Center and monitored by A. F. Armington, RADC/ESM, Hanscom AFB, MA, 01031.

# REFERENCES

1. J. C. King and H. H. Sander, IEEE Trans. Nucl. Sci. NS-19, 23 (1972).
2. P. Pelligrini, F. Euler, A. Kahan, T. M. Flanagan, and T. F. Wrobel, IEEE Trans. Nucl. Sci. NS-25, 1267 (1978).
3. T. J. Young, D. R. Koehler, and R. A. Adams, Proceedings of the 32nd Annual Symposium on Frequency Control, p.34 (1978). Copies available from the Electronic Industries Association, 2001 Eye Street, N.W., Washington, D.C. 20006.
4. D. R. Koehler and J. J. Martin, Proceedings of the 37th Annual Symposium on Frequency Control, pp.130-135 (1984).
5. J. C. King, Bell System Technical J. 38, 573 (1959).
6. R. A. Poll and S. L. Ridgway, IEEE Trans. Nucl. Sci. NS-13, 130 (December, 1966).
7. T. M. Flanagan and T. F. Wrobel, IEEE Trans. Nucl. Sci. NS-16, 130 (December, 1969).
8. B. R. Capone, A. Kahan, R. N. Brown, and J. R. Buckmelter, IEEE Trans. Nucl. Sci. NS-17, 217 (December, 1970).
9. T. M. Flanagan, IEEE Trans. Nucl. Sci. NS-21, 390 (December, 1974).
10. L. E. Halliburton, N. Koumvakalis, M. E. Markes, and J. J. Martin, J. Appl. Phys. 52, 3565 (1981).
11. A. Kats, Philips Res. Repts. 17, 133 (1962).
12. D. B. Fraser, J. Appl. Phys. 35, 2913 (1964).
13. S. P. Doherty, J. J. Martin, A. F. Armington and R. N. Brown, J. Appl. Phys. 51, 4164 (1980).
14. M. E. Markes and L. E. Halliburton, J. Appl. Phys. 50, 8172(1979).
15. W. A. Sibley, J. J. Martin, M. C. Wintersgill, and J. D. Brown, J. Appl. Phys. 50, 5449 (1979).
16. J. J. Martin and S. P. Doherty, Proceedings of the 34th Annual Symposium on Frequency Control, U.S. Army Electronics Command, Fort Monmouth, NJ, pp. 81-84 (1980).
17. D. B. Fraser, Physical Acoustics, (W. P. Mason, ed.) Vol. V, Chap. 2, Academic Press, New York (1968).
18. A. W. Warner, Bell System Technical J. 40, 1193 (1960).
19. J. C. King, A. A. Ballman and R. A. Laudise, J. Phys. Chem. Solids 23, 1019 (1962).
20. B. Capone, A. Kahan and B. Sawyer, Proceedings of the 25th Annual Symposium on Frequency Control, pp. 109-112 (1971).
21. D. S. Park and A. S. Nowick, Phys. Stat. Sol.(a) 26, 617 (1979).
22. J. Toulouse, E. R. Green and A. S. Nowick, Proceedings of the 37th Annual Symposium on Frequency Control, pp. 125-129 (1983).
23. H. G. Lipson, A. Kahan, R. N. Brown and F. Euler, Proceedings of the 35th Annual Symposium on Frequency Control pp.329-334 (1981).
24. D. R. Koehler, Proceedings of the 35th Annual Symposium on Frequency Control, pp. 327-328 (1981).
25. H. G. Lipson, F. Euler and A. F. Armington, Proceedings of the 32nd Annual Symposium on Frequency Control, pp.11-23 (1978).
26. J. J. Martin, L. E. Halliburton and R. B. Bossoli, Proceedings of the 35th Annual Symposium on Frequency Control, pp. 317-320 (1981).
27. M. G. Jani, R. B. Bossoli and L. E. Halliburton, Phys. Rev. B. 27, 2285 (1983).
28. B. Subramaniam, L. E. Halliburton and J. J. Martin, J. Phys. Chem. Solids, in press.
29. J. M. Stevels and J. Volger, Philips Res. Repts. 17, 284 (1962).
30. A. L. Taylor and G. W. Farnell, Can. J. Phys. 42, 595 (1964).

## THE CONSTANTS OF ALPHA QUARTZ

ROGER W. WARD

QUARTZTRONICS, INC.  
1020 ATHERTON DRIVE BLDG C  
SALT LAKE CITY, UTAH 84123  
801-266-6994

SUMMARY

Anyone performing calculations on quartz crystal devices requires numerical values for the physical constants used in his equations. However, as with any physical constant, there is no absolute value which may be assigned to a constant of quartz--only a "best" value based upon numerous observations performed under controlled laboratory conditions on a variety of documented samples.

With time, and much effort, the quartz engineer accumulates his own list of "best" values for the frequently used constants of quartz. Still, when a new calculation involves an obscure constant, a literature search is required to find that obscure value.

Such a literature search has been conducted, and a list of "good" constants for alpha quartz is presented.

NOMENCLATURE

The word "quartz" as used herein means electronic grade crystalline  $\text{SiO}_2$  at temperatures below  $573^\circ\text{C}$ , either natural or man-made (cultured).

Historically, the term rock crystal, low-quartz, alpha quartz, and crystalline quartz has been used for "quartz".

Modern usage in certain industries uses the term "quartz" to refer to fused quartz--quartz which has been heated to above its melting point. Fused quartz is non-piezoelectric and non-crystalline; hence, of no usefulness to the quartz engineer. Sosman [1], p. 43, says: "The use of the single word 'quartz' to refer to vitreous silica can not be too strongly condemned. It has arisen through carelessness or ignorance and is already causing troublesome confusion." Sosman suggests the use of "quartz-glass" or "fused quartz" for this material.

Some quartz engineers refer to cultured quartz as "synthetic" quartz. Synthetic gives the connotation of "not real", so is to be avoided in this context, since cultured quartz is "real" quartz.

HISTORY

Ever since man first held a piece of quartz in his hand, he has been aware of one of quartz' physical constants--its density. Since then, most physical constants of quartz have been studied and measured.

There are thousands of references in the literature on the subject. Many of the measurements are of little value today since details of the experiments were often neglected--i.e., temperature, source of the quartz, standards, etc.

Quartz obtained from most locations is not useful for electronic applications, due to excessive twinning, inclusions, and fracturing. Through World War II, all quartz used was natural quartz, mostly from Brazil. Since then, the art of culturing quartz has evolved to where cultured quartz is used almost exclusively for electronic applications.

The constants presented here may be applied to only the finest grades of cultured quartz--those that most nearly imitate natural quartz. Devices fabricated from lower quality cultured quartz have physical constants enough different from natural quartz to produce sizeable errors when compared to otherwise identical natural quartz devices.

ACTUAL DEVICES

Due to the assumptions used in any theory, and also due to the probability that the calculated device has a different geometry (diameter, contour, electrode size) than the units measured to produce a given physical constant, and due to manufacturing tolerances (especially angular orientation) it is usually impossible to theoretically predict quartz device behavior to better than an equivalent angular orientation of about  $\pm 1^\circ$  for double-rotated cuts.

To better refine a theory, it is necessary to make a matrix of actual devices--all of the same physical design, except for a well controlled slight variation in orientation.

For example, EerNisse [2] in 1975 predicted the SC-cut to occur at  $\phi = 22^\circ 30'$ . Kusters and Leach [3] experimentally showed that for their crystal design,  $\phi = 21^\circ 56'$ , a variation of  $34'$ . Kusters and Leach determined  $\phi$  by a carefully controlled experiment involving a matrix of orientations about EerNisse's predicted angle, careful measurements, and computer reduction of the data to define the orientation for the zero thermal transient effect (assuming that the in-plane stress of EerNisse is the same mechanism measured by Kusters and Leach in their thermal transient tests).

Similarly, Adams et al. [4] determined the temperature coefficients of the elastic

stiffnesses of quartz, using a matrix of precisely oriented, identically prepared resonators, as opposed to Bechmann's et al. [5] determination of the same coefficients using a varied assortment of crystal designs of moderate orientational precision. And yet, neither set of constants can predict temperature behavior of the SC-cut, as actually manufactured, to better than an equivalent angular orientation of  $\frac{1}{2}^\circ$ ; but both can be used to predict the existence of, and the shape of, the temperature curve for the SC-cut, and do so accurately enough to allow the experimental cuts to be selected with enough precision to "close the loop" with only one or two iterations of the actual devices! What more could one ask for?

Similar experimental tests will always be required to ultimately define a desired quartz device orientation. (Unless the theory can be expanded to include the now unsolvable effects of the boundary conditions; finite diameter, contoured surfaces; and film stress, mounting stress, etc.).

### THE CONSTANTS

In 1927, Sosman [1] published 800 pages devoted to the physical properties of silica in its many forms, with the major emphasis on quartz. Sosman studies in detail the many measurements of each property presented in the literature and studied in his own lab. He points out errors and omissions of each researcher, and attempts to arrive at a "best" value for that constant of quartz. Hence, Sosman was used as the primary resource for this presentation.

There are many interesting historical notes included in the references, too numerous to include here, but one observation made by Dr. Virgil Bottom emphasizes the historical contribution made by Pierre Curie, the "Father of Piezoelectricity": "It is remarkable, therefore, that the Curies were able to obtain a value for  $d_{11}$  in quartz which is only about 7% below the best value known today. Between 1880 and 1970, no fewer than thirty independent measurements of  $d_{11}$  in quartz have been reported and half of these values are further from the value commonly accepted today than that given by the Curies in 1880." Dr. Bottom goes on to conclude that, "... it may truthfully be said of Pierre Curie that he laid the cornerstone of modern electronic communication." [6]

The constants presented in Table I are not represented to be "The" constants, or "the best" constants, but only "good" constants--for the reasons outlined above. "The" constant only exists for a given piece of quartz of a given design. Change the design and some of the measurable constants will change. Use another piece of quartz from the same autoclave or the same vug (a cavity in which the crystals grow in nature) and the constants will change (at least to the precision allowed by modern "state-of-the-art" measurement techniques).

No attempts have been made to "improve" upon these constants by curvefitting several sets of data, or by re-calculation. The only modification has been to convert a few constants to the same units of measurement. Where this has been done, the conversion constant used is noted.

The temperature at which a measurement was made is indicated, if available. When no temperature is noted, the measurement can be assumed to have been made at room temperature.

No representation is made as to completeness, accuracy, or appropriateness of any constant. Indeed, only a few of the constants found in the literature noted the error band of the values given; hence, allowing for the small differences between different sources, no error bands are indicated in Table I.

The author would appreciate receiving suggestions for the inclusion of other constants, or new or better values for the ones presented, with the intent of publishing a new list from time to time as data warrants. Such suggestions may be sent to the author at the address above.

### REFERENCES

- [1] R.B. Sosman, The Properties of Silica. New York: Chemical Catalog Co., 1927. (Available from University Microfilm, 300 N. Zeeb Rd, Ann Arbor MI 48106 (313-761-4700).)
- [2] E.P. EerNisse, "Quartz Resonator Frequency Shifts Arising from Electrode Stress", Proceedings, 29th Annual Symp. on Freq. Control, US Army Electronics Command, Ft. Monmouth, NJ, pp 1-4 (1975). Copies available from Electronics Industries Association, 2001 Eye St, NW, Washington DC 20006.
- [3] J.A. Kusters and J. Leach, "Further Experimental Data on Stress and Thermal Gradient Compensated Crystals", Proc. IEEE, Vol. 65, pp 282-284, Feb 1977.
- [4] C.A. Adams, G.M. Enslow, J.A. Kusters, and R.W. Ward, "Selected Topics in Quartz Crystal Research", Proceedings, 24th Annual Symposium on Frequency Control, US Army Electronics Command, Ft. Monmouth NJ, pp 55-63 (1970). National Technical Information Service, Sills Bldg, 5285 Port Royal Road, Springfield VA 22161, Accession Nr. AD746210.
- [5] R. Bechmann, A. Ballato, and T.J. Lukaszek, "Higher Order Temperature Coefficients of the Elastic Stiffnesses and Compliances of Alpha-Quartz", Proc. IRE, Vol 50, pp 1812-1822, Aug 1962; p. 2451, Dec 1962.
- [6] V.E. Bottom, "The Centennial of Piezoelectricity", unpublished paper, 1980.

- [7] C. Frondel, **Dana's System of Mineralogy Volume III Silica Minerals**, New York: John Wiley and Sons, 1962.
- [8] R.A. Heising, **Quartz Crystals for Electrical Circuits**, New York: D. Van Nostrand, 1946. (Reprinted 1978, Electronic Industries Association, 2001 Eye St NW, Washington DC 20006.)
- [9] W.G. Cady, **Piezoelectricity**, New York: Dover, 1964.
- [10] V.E. Bottom, "Dielectric Constants of Quartz", *Journal of Applied Physics*, V.43, No. 4, Apr 1972, p. 1493.
- [11] R.N. Thurston, H.J. McSkimin, and P. Andreatch, Jr., "Third Order Elastic Coefficients of Quartz", *Journal of Applied Physics*, V. 37, No. 1, Jan 1966, p. 267.
- [12] V.E. Bottom, "Measurement of the Piezoelectric Coefficients of Quartz Using the Fabry-Perot Dilatometer", *Journal of Applied Physics*, V.41, No. 10, Sep 1970, p. 3941.
- [13] G.E. Graham and F.N.D.D. Pereira, "Temperature Variations of the Piezoelectric Effect in Quartz", *Journal of Applied Physics*, V. 42, No. 7, June 1971, p. 3011.
- [14] S.V. Kolodieva, A.A. Fotchenkov, and S.A. Linnik, "Change in the Anisotropy of Electrical Conductivity of Quartz Crystals", *Soviet Physics--Crystallography*, Vol. 17, No. 3, pp 509-511, Nov-Dec 1972.
- [15] C.H. Scholz, "Static Fatigue of Quartz", *J. of Geophysical Research*, Vol. 77, No. 11, pp 2104-2144, Apr 10, 1972.
- [16] A. Ballato and M. Mizan, "Simplified Expressions for the Stress-Frequency Coefficients of Quartz Plates", *IEEE Trans. Sonics and Ultrasonics*, Vol SU-31, No. 1, pp 11-17, Jan 1984.

TABLE I

"GOOD" FUNDAMENTAL MATERIAL CONSTANTS FOR CRYSTALLINE QUARTZ

CONSTANT NAME	VALUE	REFERENCE																					
AXIAL RATIO c/a	1.1015 @ -250°C 1.1014 -200 1.1009 -100 1.1003 0 1.0996 100 1.0988 200 1.0979 300 1.0960 400 1.0956 500 1.0946 550 1.0940 573  1.09997 ? 1.100 20  ***** -6.14X10 <sup>-6</sup> /°C @ 0°C	SOSMAN [1] P. 205, 368-370. SEE ALSO FRONDEL [7] P. 7, 20, 39       HEISING [8] P. 103 CADY [9] P. 27  FRONDEL P. 39 SOSMAN P. 377																					
TEMPERATURE COEFFICIENT																							
COMPOSITION	SILICON 46.72% OXYGEN 53.28% by weight	SOSMAN P. 22,27																					
COMPRESSIBILITY COEFFICIENT, VOLUME, (TRUE)	2.76X10 <sup>-6</sup> /kg/cm <sup>2</sup> @ 0 kg/cm <sup>2</sup> 2.65 2039 2.53 4079 2.42 6118 2.33 8157 2.25 10197 2.18 12236  NOTE: 1 megabarye = 10 <sup>6</sup> dyne/cm <sup>2</sup> = 1.0197 kg/cm <sup>2</sup>	SOSMAN P. 427. ALSO SEE P. 426-433																					
CONDUCTIVITY, THERMAL	<table> <thead> <tr> <th>PARALLEL</th><th>PERPENDICULAR</th><th>TEMP</th></tr> </thead> <tbody> <tr> <td>--</td><td>0.68</td><td>-252°C</td></tr> <tr> <td>0.117</td><td>0.0586</td><td>-190</td></tr> <tr> <td>0.0476</td><td>0.02409</td><td>-78</td></tr> <tr> <td>0.0325</td><td>0.01731</td><td>0</td></tr> <tr> <td>0.0215</td><td>0.01333</td><td>100</td></tr> <tr> <td>0.029</td><td>0.016</td><td>20</td></tr> </tbody> </table> cal/cm/s/°C	PARALLEL	PERPENDICULAR	TEMP	--	0.68	-252°C	0.117	0.0586	-190	0.0476	0.02409	-78	0.0325	0.01731	0	0.0215	0.01333	100	0.029	0.016	20	SOSMAN P. 419, 420      FRONDEL P.116
PARALLEL	PERPENDICULAR	TEMP																					
--	0.68	-252°C																					
0.117	0.0586	-190																					
0.0476	0.02409	-78																					
0.0325	0.01731	0																					
0.0215	0.01333	100																					
0.029	0.016	20																					
CURIE TEMPERATURE (LOW-HIGH INVERSION, ALPHA-BETA INVERSION)	573.3°C (ON HEATING)	SOSMAN P. 116-125 FRONDEL P. 3, 117 CADY P. 31																					

TABLE I, CONT.

DENSITY, ABSOLUTE	2.65067 g/cm <sup>3</sup> @ 0°C 2.64822 @ 25  2.665 g/cm <sup>3</sup> @ -250°C 2.664 -200 2.659 -100 2.651 0 2.641 100 2.630 200 2.616 300 2.601 400 2.581 500 2.554 573  *****	FRONDEL P. 114 CADY P. 412  SOSMAN P. 361 (ALSO P. 291-295)
TEMPERATURE COEFFICIENT, TRUE	12X10 <sup>-6</sup> /°C @ -200°C 25.2 -100 33.6 0 40.0 100 46.6 200 54.9 300 67.4 400 100 500 141 550  ***** $T^1 = -34.92 \times 10^{-6} / ^\circ\text{C}$ $T^2 = -15.9 \times 10^{-9} / ^\circ\text{C}^2$ $T^3 = 5.30 \times 10^{-12} / ^\circ\text{C}^3$  (APPARENTLY REFERENCED TO 25°C)	SOSMAN P. 291, 362, 366 SEE ALSO FRONDEL P. 114  BECHMANN [5] SEE ALSO CADY P. 412
DIELECTRIC CONSTANT	4.6 PARALLEL TO Z-AXIS 4.60  4.5 PERPENDICULAR TO Z-AXIS 4.51  ***** $e_{11}^T = e_{22}^T = 39.97 \times 10^{-12} \text{ F/m}$ $e_{11}^S - e_{11}^T = -0.76$ $e_{33}^T = 41.03$ $e_{33}^S - e_{33}^T = 0$ *****	SOSMAN P. 515 BOTTOM [10]  SOSMAN BOTTOM SEE ALSO CADY P. 414, FRONDEL 116  BECHMANN
TEMPERATURE COEFFICIENT	PARALLEL: $K = 4.926 [1 - 1.10 \times 10^{-3} (T-10) - 2.4 \times 10^{-5} (T-10)^2]$ PERPENDICULAR: $K = 4.766 [1 - 9.9 \times 10^{-4} (T-10)]$ FOR T=10 TO 31°C  *****	SOSMAN P. 523 AND GRAPH P. 524
FIELD STRENGTH COEFFICIENT	K=0 TO 2000 V/cm (PARALLEL) K=0 TO 12000 V/cm (PERPENDICULAR)	CADY P. 415

TABLE I, CONT.

ELASTIC COEFFICIENTS, THIRD ORDER	$C_{111} = -2.10 \times 10^{12} \text{ dyn/cm}^2$ $C_{112} = -3.45$ $C_{113} = +0.12$ $C_{114} = -1.63$ $C_{123} = -2.94$ $C_{124} = -0.15$ $C_{133} = -3.12$ $C_{134} = +0.02$ $C_{144} = -1.34$ $C_{155} = -2.00$ $C_{222} = -3.32$ $C_{333} = -8.15$ $C_{344} = -1.10$ $C_{444} = -2.76$	THURSTON [11]									
ELECTRIC STRENGTH	$4 \times 10^6 \text{ V/cm}$ @ $-80^\circ\text{C}$ 7 @ 60	CADY P. 413									
HARDNESS, PENETRATION (AUERBACH)	$30.8 \times 10^3 \text{ kg/cm}^2$ PARALLEL TO Z 22.9 PERPENDICULAR TO Z	SOSMAN P. 491									
MHO	7	SOSMAN P. 494									
SCRATCH	667 (CORUNDUM = 1000)	SOSMAN P. 494									
HEAT CAPACITY, TRUE	$5.4 \times 10^{-3} \text{ cal/g}$ @ $-250^\circ\text{C}$ 41.0 -200 111.2 -100 166.4 0 204.3 100 232.7 200 254.3 300 270.0 400 291.0 500 340(?) 573 (IN $20^\circ\text{C}$ grams)	SOSMAN P. 314, 331									
HEAT OF SOLUTION	30.29 kg-cal/formula wt in 34.6% HF	SOSMAN P. 318									
HEAT OF TRANSFORMATION LATENT (LOW --> HIGH QUARTZ)	2.5 cal/g 0.15 kg-cal/formula wt	SOSMAN P. 312									
LATTICE CONSTANT "a"	4.9035 Angstroms @ $18^\circ\text{C}$ 4.903 ? 4.91331 25 4.90288 25 4.91267 25	SOSMAN P. 226 HEISING P. 103 FRONDEL P. 25 CADY P. 735 CADY									
MAGNETIC SUSCEPTIBILITY (VACUUM)	<table> <tr> <th>PARALLEL</th> <th>PERPENDICULAR</th> <th>TYPE</th> </tr> <tr> <td><math>-1.21 \times 10^{-6}</math></td> <td><math>-1.20 \times 10^{-6}</math></td> <td>VOLUME</td> </tr> <tr> <td>-0.45</td> <td>-0.45</td> <td>MASS</td> </tr> </table>	PARALLEL	PERPENDICULAR	TYPE	$-1.21 \times 10^{-6}$	$-1.20 \times 10^{-6}$	VOLUME	-0.45	-0.45	MASS	SOSMAN P. 576
PARALLEL	PERPENDICULAR	TYPE									
$-1.21 \times 10^{-6}$	$-1.20 \times 10^{-6}$	VOLUME									
-0.45	-0.45	MASS									



TABLE I, CONT.

MAGNETO-OPTIC ROTATION (VERDET CONSTANT)	0.15866 min @ 2194.92 angstroms, 20°C 0.04617            3612.5 0.02750            4678.15 0.02257            5085.82 0.01664            5892.9 0.01368            6438.47  *****	SOSMAN P. 776																																														
TEMPERATURE COEFFICIENT	$w = w_{20} [1 + 0.00011(T - 20)]$ FOR T=20 TO 100°C	SOSMAN P. 777																																														
MELTING POINT	<1670°C	FRONDEL P. 3																																														
PENETRATION, MODULUS OF	<table><tr><td>PARALLEL</td><td>PERPENDICULAR</td></tr><tr><td>1062 kg/cm<sup>2</sup></td><td>859 kg/cm<sup>2</sup></td></tr></table>	PARALLEL	PERPENDICULAR	1062 kg/cm <sup>2</sup>	859 kg/cm <sup>2</sup>	SOSMAN P. 465																																										
PARALLEL	PERPENDICULAR																																															
1062 kg/cm <sup>2</sup>	859 kg/cm <sup>2</sup>																																															
PIEZOELECTRIC COEFFICIENTS	<table><tr><td colspan="2">STRAIN</td></tr><tr><td>d<sub>11</sub> = -2.30X10<sup>-12</sup>m/v</td><td></td></tr><tr><td>d<sub>11</sub> = -2.27</td><td></td></tr><tr><td>d<sub>11</sub> = -2.25</td><td></td></tr><tr><td>d<sub>11</sub> = -2.30</td><td></td></tr><tr><td colspan="2"> </td></tr><tr><td>d<sub>14</sub> = 0.57X10<sup>-12</sup>m/v</td><td></td></tr><tr><td>d<sub>14</sub> = 0.85</td><td></td></tr><tr><td>d<sub>14</sub> = 0.67</td><td></td></tr><tr><td colspan="2">NOTE: 1 esu/dyne = 3 X 10<sup>4</sup>m/v</td></tr><tr><td>d<sub>11</sub> = 2.32X10<sup>-12</sup>m/v @ 1.5°K</td><td></td></tr><tr><td>2.32</td><td>4.2</td></tr><tr><td>2.31</td><td>-196 °C</td></tr><tr><td>2.22</td><td>20</td></tr><tr><td>2.05</td><td>100</td></tr><tr><td colspan="2"> </td></tr><tr><td colspan="2">STRESS</td></tr><tr><td>e<sub>11</sub> = 0.171C/m<sup>2</sup></td><td></td></tr><tr><td>e<sub>11</sub> = 0.180</td><td></td></tr><tr><td colspan="2"> </td></tr><tr><td>e<sub>14</sub> = 0.0403</td><td></td></tr><tr><td>e<sub>14</sub> = 0.04</td><td></td></tr><tr><td colspan="2">*****</td></tr></table>	STRAIN		d <sub>11</sub> = -2.30X10 <sup>-12</sup> m/v		d <sub>11</sub> = -2.27		d <sub>11</sub> = -2.25		d <sub>11</sub> = -2.30				d <sub>14</sub> = 0.57X10 <sup>-12</sup> m/v		d <sub>14</sub> = 0.85		d <sub>14</sub> = 0.67		NOTE: 1 esu/dyne = 3 X 10 <sup>4</sup> m/v		d <sub>11</sub> = 2.32X10 <sup>-12</sup> m/v @ 1.5°K		2.32	4.2	2.31	-196 °C	2.22	20	2.05	100			STRESS		e <sub>11</sub> = 0.171C/m <sup>2</sup>		e <sub>11</sub> = 0.180				e <sub>14</sub> = 0.0403		e <sub>14</sub> = 0.04		*****		SOSMAN P. 559 BOTTOM [12] HEISING P. 20 CADY P. 219  SOSMAN HEISING CADY  GRAHAM [13]  BECHMANN CADY P. 219, 224  BECHMANN CADY
STRAIN																																																
d <sub>11</sub> = -2.30X10 <sup>-12</sup> m/v																																																
d <sub>11</sub> = -2.27																																																
d <sub>11</sub> = -2.25																																																
d <sub>11</sub> = -2.30																																																
d <sub>14</sub> = 0.57X10 <sup>-12</sup> m/v																																																
d <sub>14</sub> = 0.85																																																
d <sub>14</sub> = 0.67																																																
NOTE: 1 esu/dyne = 3 X 10 <sup>4</sup> m/v																																																
d <sub>11</sub> = 2.32X10 <sup>-12</sup> m/v @ 1.5°K																																																
2.32	4.2																																															
2.31	-196 °C																																															
2.22	20																																															
2.05	100																																															
STRESS																																																
e <sub>11</sub> = 0.171C/m <sup>2</sup>																																																
e <sub>11</sub> = 0.180																																																
e <sub>14</sub> = 0.0403																																																
e <sub>14</sub> = 0.04																																																
*****																																																
PRESSURE COEFFICIENT	d <sub>11</sub> varies by <0.1% to 3519 kg/cm <sup>2</sup>	SOSMAN P. 559																																														
RESISTIVITY	<table><tr><td>PARALLEL</td><td>PERPENDICULAR</td><td>TEMPERATURE</td></tr><tr><td>0.1X10<sup>15</sup></td><td>20X10<sup>15</sup></td><td>20°C</td></tr><tr><td>0.8X10<sup>12</sup></td><td></td><td>100</td></tr><tr><td>70X10<sup>9</sup></td><td></td><td>200</td></tr><tr><td>60X10<sup>6</sup></td><td>ohm/cm</td><td>300</td></tr></table>	PARALLEL	PERPENDICULAR	TEMPERATURE	0.1X10 <sup>15</sup>	20X10 <sup>15</sup>	20°C	0.8X10 <sup>12</sup>		100	70X10 <sup>9</sup>		200	60X10 <sup>6</sup>	ohm/cm	300	SOSMAN P. 528-537 ALSO SEE KOLODIEVA [14]																															
PARALLEL	PERPENDICULAR	TEMPERATURE																																														
0.1X10 <sup>15</sup>	20X10 <sup>15</sup>	20°C																																														
0.8X10 <sup>12</sup>		100																																														
70X10 <sup>9</sup>		200																																														
60X10 <sup>6</sup>	ohm/cm	300																																														

TABLE I, CONT.

REFRACTIVE INDEX	<p><u>ORDINARY RAY:</u>  <math>n_o^2 = 3.4269 + 1.0654 \times 10^{-2} / (L^2 - 0.010627)</math>  <math>+ 111.49 / (L^2 - 100.77)</math></p> <p><u>ORDINARY RAY:</u>  <math>n_o^2 = 3.53445 + 0.008067 / (L^2 - 0.0127493)</math>  <math>+ 0.002682 / (L^2 - 0.000974)</math>  <math>+ 27.2 / (L^2 - 108)</math></p> <p><u>EXTRAORDINARY RAY:</u>  <math>n_e^2 = 3.5612557 + 0.00844614 / (L^2 - 0.0127493)</math>  <math>+ 0.00276113 / (L^2 - 0.000974)</math>  <math>+ 127.2 / (L^2 - 108)</math></p> <p>where L=wavelength in mμ</p> <p><math>n_o = 1.54425</math> (Na @ 18°C)  <math>n_e = 1.55336</math>  *****</p>	<p>SOSMAN P. 588-625</p> <p>FRONDEL P. 129</p> <p>FRONDEL</p> <p>CADY P. 723</p>
TEMPERATURE COEFFICIENTS	<p>ORDINARY RAY: <math>-6.50 \times 10^{-6} / ^\circ\text{C}</math>  EXTRAORDINARY RAY: <math>-7.544</math>  *****</p>	<p>FRONDEL P. 129,  SOSMAN P. 637</p>
BIREFRINGENCE, TEMPERATURE COEFFICIENT	<p><math>B = B_o - (972T + 1.6T^2) 10^{-9}</math>  FOR T=4 TO 99°C</p>	<p>SOSMAN P. 684,  FRONDEL P. 131</p>
ROTARY POWER	<p>201.9°/mm @ 2265.03 angstroms  95.02            3034.12  21.724          5892.9  11.589          7947.63  0.972          25000</p> <p>ROTATION IS CW IN RIGHT HAND QUARTZ  AND CCW IN LEFT HAND QUARTZ.  *****</p>	<p>SOSMAN P. 648  FRONDEL P. 132</p>
TEMPERATURE COEFFICIENT	<p>about <math>+1.4 \times 10^{-4} / ^\circ\text{C}</math> at 20°C  (independent of wavelength)</p>	<p>SOSMAN P. 689</p>
SPECIFIC HEAT	<p>0.1412 cal/g/°C @ -50°C  0.1664            0  0.1870            50  0.2043            100</p>	<p>CADY P. 411</p>

TABLE I, CONT.

STIFFNESSES	<div><math>c^D</math></div> <div><math>c^{11} = 87.49</math> <math>c^{13} = 11.91</math> <math>c^{33} = 107.2</math> <math>c^{14} = -18.09</math> <math>c^{44} = 57.98</math> <math>c^{66} = 40.63</math></div> <div><math>c^E</math></div> <div><math>86.74 \times 10^9 \text{ N/m}^2</math> 11.91 107.2 -17.91 57.94 39.88</div> <div>*****</div>	BECHMANN SEE ALSO HEISING P. 40 ff, SOSMAN P. 463, CADY P. 137-155 (GRAPHS) ALSO CADY P. 757		
TEMPERATURE COEFFICIENTS	<div>FIRST</div> <div><math>i,j</math></div> <div><math>\times 10^{-6}/^\circ\text{C}</math></div> <div>SECOND</div> <div><math>\times 10^{-9}/^\circ\text{C}^2</math></div> <div>THIRD</div> <div><math>\times 10^{-12}/^\circ\text{C}^3</math></div> <div>11</div> <div>-48.5 -49.6</div> <div>-107 -107</div> <div>-70 -74</div> <div>13</div> <div>-550 -651</div> <div>-1150 -1021</div> <div>-750 -240</div> <div>33</div> <div>-160 -192</div> <div>-275 -162</div> <div>-250 67</div> <div>14</div> <div>101 89</div> <div>-48 -19</div> <div>-590 -521</div> <div>44</div> <div>-177 -172</div> <div>-216 -261</div> <div>-216 -194</div> <div>66</div> <div>178 167</div> <div>118 164</div> <div>21 29</div>	BECHMANN ADAMS [4] SEE ALSO HEISING P. 55, CADY P. 136-140		
STRENGTH COMPRESSIVE	STRENGTH 24,000 kg/cm <sup>2</sup> 150,000	CONFINING PRESS 1 atm 25000 atm	TEMP 20°C 400	FRONDEL P. 109
COMPRESSIVE	24500 kg/cm <sup>2</sup> 22400	PARALLEL PERPENDICULAR		SOSMAN P. 481 SEE ALSO SCHOLZ [15]
TENSILE	1120 850	PARALLEL PERPENDICULAR		
RUPTURE (BENDING)	1380 920	PARALLEL PERPENDICULAR		
SYMMETRY	TRIGONAL TRAPEZOHEDRAL or TRIGONAL ENANTIOMORPHOUS HEMIHEDRAL  TRIGONAL HOLOAXIAL or ENANTIOMORPHOUS HEMIHEDRAL  CLASS 18, SYMMETRY D <sub>3</sub> (SCHONFLIES) SYMMETRY 32 (HERMANN-MAUGUIN)			SOSMAN P. 183  CADY P. 19  CADY P. 19

TABLE I, CONT.

THERMAL EXPANSION COEFFICIENT, LINEAR (MEAN FROM 0°C)	PARALLEL	PERPENDICULAR	TEMPERATURE	SOSMAN P. 370	
	$4.10 \times 10^{-6}/^{\circ}\text{C}$	$8.60 \times 10^{-6}/^{\circ}\text{C}$	-250°C		
	5.50	9.90	-200		
	6.08	11.82	-100		
	7.10	13.24	0		
	7.97	14.45	100		
	8.75	15.61	200		
	9.60	16.89	300		
	10.65	18.50	400		
	12.22	20.91	500		
	15.00	25.15	573		
	*****				
FIRST SECOND THIRD			BECHMANN		
i j	$\times 10^{-6}/^{\circ}\text{C}$	$\times 10^{-9}/^{\circ}\text{C}^2$		$\times 10^{-12}/^{\circ}\text{C}^3$	
11	13.71	6.5		-1.9	
33	7.48	2.9		-1.5	
NOTE: $a_{11} = a_{22}$					
THERMOELASTIC COEFFICIENTS (HIGHER ORDER)	ORDER	$a_{11}^{(n)}$	$a_{33}^{(n)}$	UNIT	BALLATO [16]
	1	13.16	6.37	$10^{-6}/^{\circ}\text{C}$	
	2	15.68	8.18	$10^{-9}/^{\circ}\text{C}^2$	
	3	-7.86	6.88	$10^{-12}/^{\circ}\text{C}^3$	
	REFERENCED TO 0°C				
WAVELENGTH Cu K $\alpha_1$ , X-RAY	1.5374 angstroms 1.54051			HEISING P. 97 FRONDEL P. 25	
VOLUME, UNIT CELL	$37.40 \times 10^{-24} \text{ cm}^3$			SOSMAN P. 225	
YOUNG'S MODULUS	$1.03 \times 10^{12} \text{ dynes/cm}^2$			CADY P. 155	
	0.78				
	PERPENDICULAR			FRONDEL P. 122	
	PARALLEL				
$s'_{33} \times 10^{12} = 1269 - 841 \cos^2 \theta + 543 \cos^4 \theta - 862 \sin^3 \theta - 862 \sin^3 \theta \cos \theta \sin^3 \theta$ $\text{cm}^2/\text{dyne}$					
NOTE: $Y_m = 1/s'_{33}$					

NOTE: PARALLEL = PARALLEL TO Z-AXIS (OPTICAL AXIS)  
PERPENDICULAR = PERPENDICULAR TO Z-AXIS

# EFFECT OF IRRADIATION AND ANNEALING ON THE ELECTRICAL CONDUCTIVITY OF QUARTZ CRYSTALS

E.R. Green, J. Toulouse, J. Wacks and A.S. Nowick  
Krumb School of Mines, Columbia University  
New York, N.Y. 10027

## Summary

In order to better understand the defects produced in  $\alpha$ -quartz by irradiation, electrical conductivity measurements provide a valuable tool. A detailed study was made of the radiation-induced conductivity (RIC) of a variety of crystals, including both cultured and natural crystals that had been either Li- or Na-swept. X-ray irradiation was carried out at and below room temperature (from 150-300 K) and subsequent annealing up to  $\sim 450^\circ\text{C}$ . Immediately after low-temperature irradiation the RIC showed an activation energy,  $E$ , of  $0.28 \pm 0.02\text{ eV}$ . With annealing  $E$  increased and the RIC decreased. Irradiation at 150 K gave a larger RIC than irradiations above 200 K, where alkalis  $M^+$  are known to be released from  $\text{Al-M}^+$  pairs. Isochronal annealing to elevated temperatures showed an overshoot phenomenon, whereby the conductivity fell to values below those of the unirradiated crystal, after which it annealed upwards.

Consideration of the principal results of these experiments led to the conclusion that the RIC is most readily explained in terms of electronic rather than ionic defects, viz., polaron-like holes that have a hopping activation energy of 0.28 eV. There remain questions to be answered, however, before this mechanism can be regarded as definitely established.

## Introduction

The effects of radiation on the frequency of quartz-crystal resonators is well known.<sup>1-3</sup> Radiation induced changes in frequency are related to changes in defect structures induced by the radiation. Of central importance in this regard is the  $\text{Al-M}^+$  defect, where  $\text{Al}$  denotes an  $\text{Al}^{3+}$  ion substituting for  $\text{Si}^{4+}$ , and  $M^+$  an alkali (primarily  $\text{Li}^+$  or  $\text{Na}^+$ ) located in an adjacent interstitial position. The  $\text{Al-Na}^+$  center can be detected through a characteristic pair of anelastic loss peaks<sup>4</sup> as well as by a pair of dielectric loss peaks.<sup>5,6</sup> There are no comparable  $\text{Al-Li}^+$  peaks, however.<sup>7</sup> It has been shown<sup>8,9</sup> that irradiation at temperatures above 200 K liberates the alkali from the  $\text{Al-M}^+$  pair, replacing it either with a hole  $h^+$  or a proton  $\text{H}^+$  which binds to a nearby oxygen ion to form an  $\text{OH}^-$  ion. The corresponding  $\text{Al-h}^+$  defect is directly observable by means of electron spin resonance (ESR) measurements<sup>10</sup> while the  $\text{Al-OH}$  center is observable through characteristic infrared (IR) absorption bands.<sup>11,9</sup> Thus, techniques are available for the study of the formation and annealing of these two centers. On the other hand, our ability to follow the course of the alkalis subsequent to their liberation from  $\text{Al-M}^+$  centers by irradiation has been very limited. Radiation induced dielectric peaks at very low temperatures have been studied which appear to be due to alkali centers,<sup>12</sup> but the details concerning such peaks are not yet fully sorted out. Yet there is considerable evidence that radiation-induced frequency

changes are greatly influenced by defects involving the alkalis.

An opportunity to follow the alkalis subsequently to irradiation is offered by electrical conductivity measurements. It is well known that the conductivity of unirradiated  $\alpha$ -quartz crystals is ionic in origin and that the carriers are  $M^+$  ions liberated from  $\text{Al-M}^+$  pairs, which then migrate preferentially along the open c-axis channels of the crystal structure.<sup>13</sup> Radiation-induced conductivity (RIC) has also been studied. Here it was shown (using a pulse irradiation source) that there are two effects: one at very short times ( $\sim \text{msec}$ ) which has been attributed to electronic defects, and the second at longer times which has been attributed to  $M^+$  ions freed from  $\text{Al-M}^+$  centers.<sup>4</sup> A strong argument that the longer term RIC is due to  $M^+$  ions is the high anisotropy of the effect, viz. the fact that the conductivity parallel to the c-axis is much larger than that perpendicular to the c-axis, suggesting the migration of interstitial ions in the open channels.<sup>14,15</sup>

The present work is a further and more detailed study of the long-term RIC and of the effects of annealing after irradiation. Most of the crystals studied were electrodiffused ("swept") so that the alkali present was essentially either all  $\text{Li}^+$  or all  $\text{Na}^+$ . X-ray irradiation was carried out at and below room temperature, and the effects on conductivity immediately following the irradiation and after step annealing up to temperatures  $\sim 450^\circ\text{C}$  will be reported. The work leads to conclusions that were initially quite unexpected.

## Theory of the Conductivity

This section will review some of the basic equations that describe the conductivity and will be required for later reference.

If the conductivity,  $\sigma$ , is dominated by one carrier, e.g. the alkali ion,  $M^+$ , it can be expressed as

$$\sigma = x_c N_0 e \mu_c \quad (1)$$

where  $x_c$  is the mole fraction of the carriers,  $N_0$  the number of  $\text{SiO}_2$  molecules per unit volume,  $e$  the charge on the carrier and  $\mu_c$  its mobility. It is the quantity  $\mu_c$  that can be highly anisotropic in the crystal of  $\alpha$ -quartz. Except where otherwise stated, in this paper  $\mu_c$  and  $\sigma$  will both refer to the direction parallel to the c-axis. In general both  $x_c$  and  $\mu_c$  are temperature dependent. The mobility is given by

$$\mu_c = ed^2 w_c / kT \quad (2)$$

where  $d$  is the component of jump distance parallel to the  $c$ -axis,  $kT$  has the usual meaning, and  $w_c$  is the jump frequency of the carrier defect, given by

$$w_c = v_0' \exp(-E_m/kT) \quad (3)$$

Here  $v_0'$  (usually  $\sim 10^{13} \text{ sec}^{-1}$ ) includes both the attempt frequency and an entropy factor for the migrating defect, while  $E_m$  is the motional activation energy.

For the quantity  $x_c$  there are two important cases. Under equilibrium conditions, with most of the  $M^+$  carriers associated as  $Al-M^+$  pairs, the value of  $x_c$  is obtained from the mass action relation for the association equilibrium, and takes the form:

$$x_c \propto \exp(-mE_A/kT) \quad (4)$$

where  $E_A$  is the association energy of the pair and  $m = \frac{1}{2}$  or 1 depending on the detailed situation involving other defects.<sup>13</sup> Thus, combining eqs. (1)-(4), in the lower temperature range (where association is nearly complete),  $\sigma$  obeys the Arrhenius-type relation

$$\sigma T = A \exp(-E/kT) \quad (5)$$

in which the "conductivity activation energy"  $E$  is given by

$$E = E_m + mE_A \quad (6)$$

The preexponential factor  $A$  can also be explicitly evaluated.

The second relatively simple case for  $x_c$  is the nonequilibrium one, where, immediately after irradiation  $x_c$  is frozen in at a constant value, independent of temperature. This applies so long as the temperature is kept low enough to avoid annealing. In this case, we again obtain Eq. (5), but now

$$E = E_m \quad (7)$$

and

$$A = x_c N_0 d^2 e^2 v_0' / k \quad (8)$$

Since all other constants are reasonably well known, Eq. (8) may be used to calculate  $x_c$  from the experimental value of the preexponential factor  $A$ .

#### Methods

The principal cultured crystals studied were high quality crystals taken from the  $Z$ -growth region: Toyo Supreme Q (bar SQ-A), Sawyer Premium Q (bar PQ-E) and High aluminum grown in the Soviet Union (bar HA-A). The natural crystal (NQ) was a clear crystal from Arkansas.

Electrodiffusion experiments were carried out at Oklahoma State University by Dr. J. Martin.<sup>16</sup> These included  $Li^+$  sweeping,  $Na^+$  sweeping and, in one case,  $H^+$  sweeping.

X-ray irradiation was carried out for a period of 2 to 4 hours using a conventional tungsten-filament tube at 40 kV and 20 mA. The dose was  $\sim 3 \times 10^6$  R. The very soft X-rays were filtered out by the layer of sputtered silver used as electrodes.

For irradiation below room temperature a special cell was built to make it possible to carry out conductivity measurements without warm-up. The cell was cooled with a dry-ice/ethanol mixture and with liquid nitrogen for still lower temperatures. With the aid of a heating coil it was possible to achieve the

temperature range from 150 - 400 K in this apparatus. For the higher temperature measurements the sample was placed in a standard conductivity cell which could go up to 500° C.

Conductivity measurements were made with a General Radio type 1620A Capacitance Bridge assembly over the frequency range 20 Hz - 100 kHz. In most cases, complex impedance analysis was used to obtain the bulk conductance.<sup>13</sup> The samples were plates of surface area 1 cm<sup>2</sup> and thickness 1.0 - 1.5 mm coated with sputtered silver electrodes.

## Results

### Unirradiated Crystals

A listing of the samples studied and the best estimates of their Al contents is given in Table I. (In most cases the Al content was obtained from the peak height of the principal Al-Na dielectric loss peak in the Na swept material; in some cases the strength of the  $Al-h^+$  ESR signal after the irradiation sequences of Markes and Halliburton<sup>6</sup> was used). Arrhenius plots of the conductivity are given in Fig. 1. At the lower temperatures all of these plots give good straight lines. Table II lists the activation energies,  $E$ , and preexponentials,  $A$ , obtained from these straight line portions. The results show that differences in  $\sigma$  between Li-swept and Na-swept samples from the same stone are small, generally well within an order of magnitude. Except for the HA-A samples,  $\sigma_{Li} > \sigma_{Na}$ ; however  $E_{Li}$  is slightly greater than  $E_{Na}$  for all of the cultured crystals. It should be recalled that  $E$  is made up of terms related both to the motion and the association energy of the carrier [Eq. (6)]. The significance of these results and of the corresponding preexponentials,  $A$ , will be discussed elsewhere.<sup>17</sup>

The two lowest curves of Fig. 1 are especially interesting. The second lowest is the SQ-A H-swept

Table I. Crystals Studied.

Name	Type	Al(ppma)
NQ	Natural	69
SQ-A	Cultured (Toyo)	13
PQ-E	Cultured (Sawyer)	15
HA-A	Cultured (Russian)	355
GEC	Cultured (GEC Ltd)	<0.1

sample (i.e. air swept). It shows that substituting  $H^+$  for alkalis lowers  $\sigma$  by two orders of magnitude, yet keeps  $E$  unchanged. This strongly suggests that residual alkalis are still the carriers, and that  $H^+$  is far less mobile than alkali ions.

The lowest curve is that for the highest purity (GEC) sample<sup>18</sup> and indicates that here too,  $\sigma$  is suppressed because of the very low alkali content. The similarity between this curve and that of the H-swept SQ-A sample in Fig. 1 is quite striking.

### Irradiated Crystals: Low Temperatures

With the apparatus described earlier, it has been

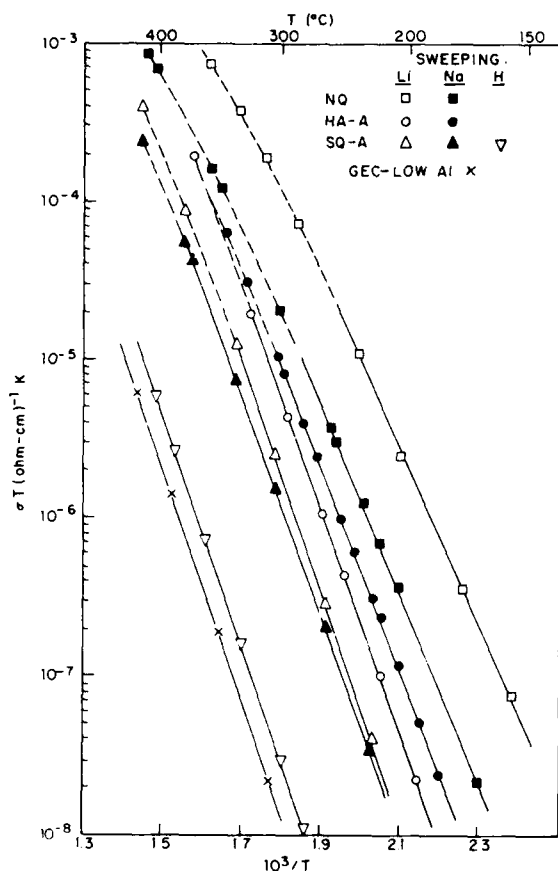


Fig. 1. Arrhenius plots of the conductivity ( $\log \sigma T$  vs.  $T^{-1}$ ) for various unirradiated samples.

possible to carry out irradiations below room temperature and then to begin measurements immediately *in situ*. Three different sets of samples were investigated in this manner: HA-A and NQ (both Li and Na-swept), and PQ-E (Li-swept only). Figure 2 shows results for NQ-Li after irradiation at 210 K. Curve (a) is the initial run (up to  $-29^{\circ}\text{C}$ ); then after several additional runs in this temperature range (not shown), curve (b) was

Table II. Summary of Results on Conductivity of Unirradiated Samples.

Sample	E (eV)	A ( $\Omega^{-1}\text{cm}^{-1}\text{K}$ )
NQ-Li	1.11	$1.4 \times 10^6$
NQ-Na	1.19	$1.2 \times 10^6$
HA-A-Li	1.38	$1.9 \times 10^7$
HA-A-Na	1.32	$1.6 \times 10^7$
SQ-A-Li	1.43	$1.5 \times 10^7$
SQ-A-Na	1.36	$2.2 \times 10^6$
SQ-A-H	1.42	$2.3 \times 10^5$
GEC-Low Al	1.42	$1.4 \times 10^5$

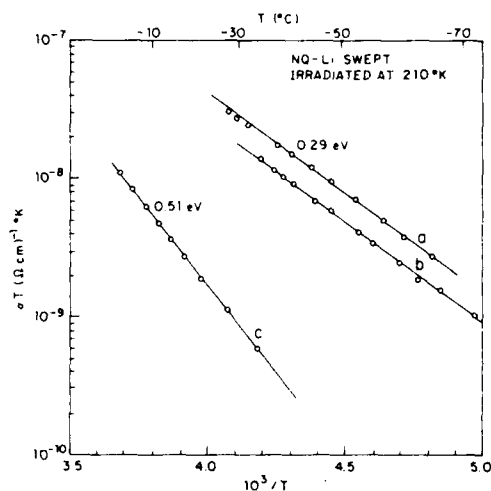


Fig. 2. Conductivity plots of an NQ-Li swept sample irradiated at 210 K: a) immediately after irradiation, b) after several runs below  $-29^{\circ}\text{C}$ , and c) after a  $\frac{1}{2}$  h anneal at  $40^{\circ}\text{C}$ .

obtained, showing that only a small amount of annealing and virtually no change in activation energy ( $E = 0.29\text{ eV}$ ) have occurred. After  $\frac{1}{2}$  h at  $40^{\circ}\text{C}$  curve (c) is obtained, showing considerable annealing and an appreciable increase in  $E$ .

It is noteworthy that  $\sigma$  in curve (a), say at 220 K, is  $10^{11}$  times higher than the value extrapolated from Fig. 1 for the same crystal. In this sense, then, the effect of irradiation is truly spectacular. For the same irradiation, high quality cultured crystals, such as SQ-A and PQ-E give initial conductivities almost an order of magnitude lower than that for the natural crystal, NQ, but of course still enormously greater than the equilibrium values.

Figure 3 shows the effect of irradiation temperature, showing initial runs on a PQ-E-Li swept sample after two different irradiations, one at 150 K and the other at 240 K. It is striking that the conductivity after 150 K irradiation is so high even though the irradiation temperature lies below the range in which alkalis are liberated from  $\text{Al-M}^+$  centers.<sup>8,9</sup> Table III summarizes the results for the various as-irradiated samples showing the values of  $E$  and  $A$  obtained as well as the conductivity at  $-51^{\circ}\text{C}$  ( $1000/T = 4.5$ ). It is interesting that the initial activation energies fall within a narrow range of  $0.28 \pm 0.02\text{ eV}$  except for the sample irradiated at the highest temperature (240 K). The final column of Table III is the value of  $x_c$  calculated from Eq. (8) and the measured value of  $A$ , under the assumption that  $E = E_m$  (i.e.  $x_c$  is a constant).

As annealing after irradiation is continued at higher and higher temperatures or for long time periods,  $\sigma$  continues to decrease and  $E$  to increase, in the manner already shown in Fig. 2. Further annealing studies were carried out in the range above room temperature.

#### Irradiated Crystals: Elevated Temperatures

For the study of behavior of irradiated samples well above room temperature, there seemed to be no need to irradiate below room temperature. Therefore, for convenience, room temperature irradiations were used. As already indicated, considerable annealing of the conductivity takes place as irradiated crystals are warmed up. Figure 4 shows a series of isothermal

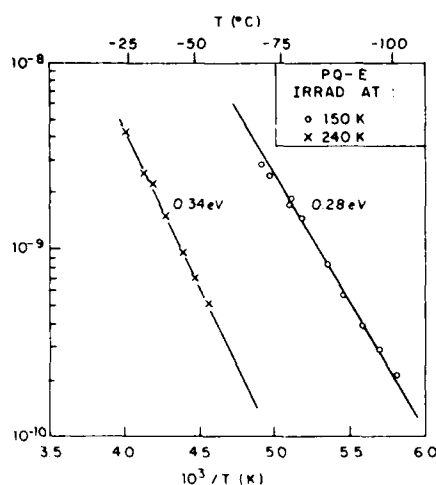


Fig. 3. Conductivity plots of a PQ-E-Li swept sample immediately after irradiation at two different temperatures: 150 K and 240 K.

annealing curves carried out at successively increasing temperatures. It shows a surprising reversal of the direction of annealing. Thus, while  $\sigma$  decreased with time at temperatures up to 219° C, it remained almost constant at 240° and 267° C, then started to increase isothermally at 331° and higher. It is helpful to plot the data isochronally, as in Fig. 5. Here we plot  $\log \sigma T$  versus  $1/T$  in the usual way, but comparing the equilibrium data of Fig. 1 with values obtained after 1h anneal at successively increasing temperatures. The SQ-A cultured and the natural NQ samples, both Li swept, are shown. The cross-over or "overshoot" effect demonstrated in Fig. 5 has been observed for all of the alkali swept samples studied after irradiation. Note that the conductivity finally returns to the equilibrium curve only after anneals at ~ 450° C.

It is illuminating to represent the annealing data as a plot of  $\Delta \ln \sigma$  versus temperature, where

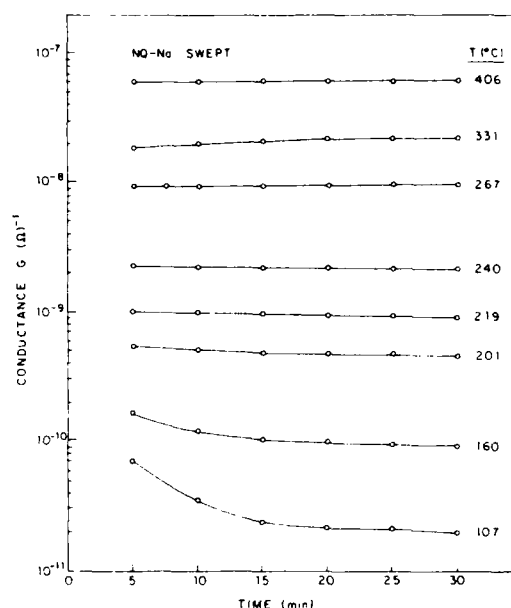


Fig. 4. Isothermal annealing curves carried out at successively increasing temperatures for NQ-Na swept sample after room temperature irradiation.

$$\Delta \ln \sigma \equiv \ln (\sigma_{\text{irr}} / \sigma_{\text{unirr}}) \quad (9)$$

Here  $\sigma_{\text{irr}}$  is the conductivity of the irradiated and isochronally annealed sample while  $\sigma_{\text{unirr}}$  is that of the unirradiated sample. Thus  $\Delta \ln \sigma$  is the difference in ordinates between the irradiated and unirradiated curves in Fig. 5.  $\Delta \ln \sigma = 0$  represents the cross-over of the two curves, while negative values represent the range in which the irradiated curve falls below the unirradiated. Figure 6 shows such a plot for the NQ-Na swept and the NQ-Li swept samples. It is interesting that the Li-swept case crosses over sooner than the Na-swept. A similar plot for the cultured SQ-A-Na crystal

Table III. Summary of Results on Conductivity of As-Irradiated Samples. [ $x_c$  is the mole fraction of carriers calculated from Eq. (8)].

Sample	Irrad. Temp. (°K)	$\sigma T$ at -51° C	E (eV)	$A(\text{ohm}^{-1}\text{cm}^{-1}\text{K})$	$x_c(\text{ppm})$
NQ-Na	210	$3 \times 10^{-9}$	0.27	$4.6 \times 10^{-3}$	$3 \times 10^{-2}$
NQ-Li	210	$8 \times 10^{-9}$	0.29	$2.9 \times 10^{-2}$	$1.8 \times 10^{-1}$
HA-A-Na	215	$7 \times 10^{-11}$	0.26	$4.3 \times 10^{-5}$	$3 \times 10^{-4}$
HA-A-Li	210	$3 \times 10^{-11}$	0.30	$2.1 \times 10^{-4}$	$1.4 \times 10^{-3}$
PQ-E-Li	150	$1.2 \times 10^{-8}$	0.28	$2.9 \times 10^{-2}$	$1.8 \times 10^{-1}$
PQ-E-Li	240	$6 \times 10^{-10}$	0.34	$3.2 \times 10^{-2}$	$2 \times 10^{-1}$



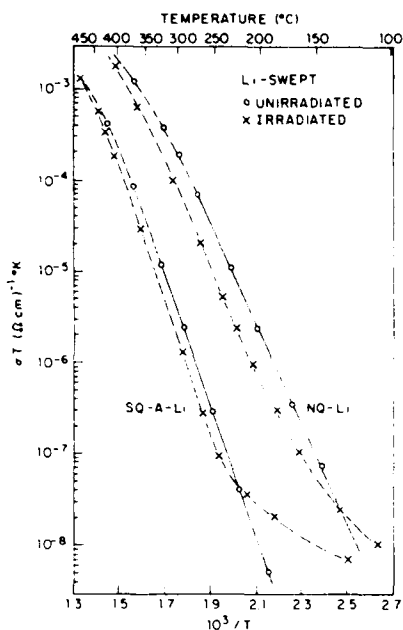


Fig. 5. Conductivity plots comparing unirradiated sample (circles) to isochronally (1h) annealed sample at successively increasing temperatures following room temperature irradiation (crosses). Data are for NQ and SQ-A samples, both Li-swept.

is shown in Fig. 7. In this case we have also marked the annealing stages observed by others on similar samples, using ESR, IR and anelastic relaxation methods.<sup>19</sup> Stage I is the region in which Al-OH centers increase, apparently without comparable changes in the other observable centers. Stage II is the well defined annealing stage in which the Al-h<sup>+</sup> center anneals out with a partial recovery of Al-Na<sup>+</sup>. Finally, in stage III the Al-OH centers disappear and are replaced by Al-Na, which now account for all of the Al centers, as before irradiation.

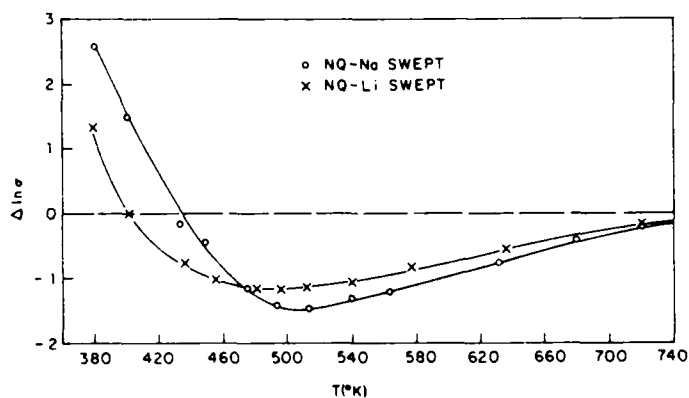


Fig. 6. Isochronal plot of  $\Delta \ln \sigma$  versus temperature for two samples: NQ-Na and NQ-Li swept.  $\Delta \ln \sigma$  is defined by Eq. (9).

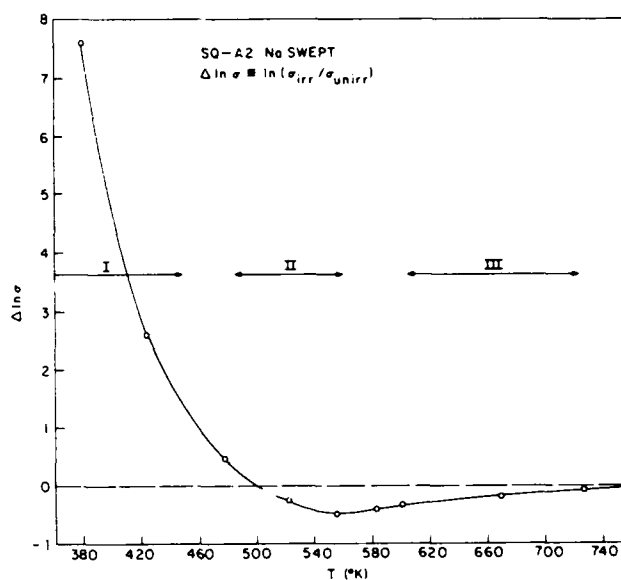


Fig. 7. Isochronal plot similar to Fig. 6 for SQ-A, Na swept sample. Also shown are the temperature ranges of three annealing stages previously reported.<sup>19</sup>

The comparison of these stages with the present annealing curve is somewhat inexact because of differences in the type of irradiation and the samples employed by ourselves and the other investigators. A more exact comparison has been made in this laboratory between the conductivity annealing of the NQ-Na and NQ-Li samples of Fig. 6 and the annealing out of the low temperature dielectric peak produced by irradiation.<sup>12</sup> While this dielectric peak has been attributed to alkali centers rather than to Al-h<sup>+</sup>, we have recently shown that it anneals almost precisely together with the Al-h<sup>+</sup> center, i.e. in Stage II.<sup>17</sup> Comparison of the annealing curves of the low temperature dielectric peak<sup>12</sup> with the data of Fig. 5 shows that it anneals precisely in the range in which  $\Delta \ln \sigma$  is close to its minimum value. In other words, the  $\Delta \ln \sigma$  curves are essentially quiescent when the important Stage II annealing process is taking place. This observation will be of special significance to the discussion of the next section.

### Discussion

It has been customary to regard the long-term radiation-induced conductivity (RIC) as due to ionic (alkali ion) carriers, that are considerably enhanced in their numbers by the irradiation. The principal argument for this viewpoint is the high anisotropy of the long-time RIC, favoring the direction parallel to the crystal c-axis.<sup>14,15</sup> This anisotropy is more consistent with freed alkali ions running along c-axis channels than with electrons and/or holes in energy bands of the crystal. The present work, however, has yielded a number of key facts that are difficult to explain by the ionic mechanism. These facts may be summarized as follows:

- 1) The magnitude of the RIC immediately after irradiation is not diminished, but is in fact increased, when irradiation is carried out below 200 K (where other experiments have demonstrated that alkali ions are not liberated from Al-M<sup>+</sup> centers).<sup>8,9</sup> See Fig. 3.

2) The magnitude of the RIC is smallest for the cultured crystal (HA-A) that has the highest Al content. See Table III.

3) Immediately after low temperature irradiation an activation energy  $E = 0.28 \pm 0.02$  eV is found for both Li- and Na-swept samples (although the value for Na is perhaps consistently slightly lower than that for Li). See Table III.

4) Upon annealing, the conductivity shows the overshoot phenomenon, falling to values below that of the unirradiated crystal. See Fig. 5.

5) The important annealing Stage II (where  $Al-h^+$  centers, as well as the low-temperature dielectric peak attributed to alkali centers, disappear) takes place in a range in which  $\ln \sigma$  is not changing. See Fig. 6.

As already mentioned, these facts do not absolutely rule out an ionic mechanism, but one must invoke complexities that strain the model, e.g. the existence of a variety of ill-defined deep traps of different depths for the alkalis. We will not attempt to develop such a model in this paper.

On the other hand, if we were to postulate an electronic model, specifically claiming that low-mobility electron holes dominate the long-term conductivity after irradiation, then most of the above mentioned facts can be readily explained. It is then reasonable to suppose that the minimum in the  $\ln \sigma$  curves (Figs. 6 and 7) represents the point in which the dominance of hole conductivity ceases and ionic conductivity begins to take over. The minimum is not then a point of zero change, where the concentration of carriers remains constant, but merely the sum of a sharply decreasing curve for the conductivity contributed by holes and an increasing curve for that contributed by alkalis. Item 5 above is then no longer a problem. As for items 1 and 2, for hole dominated RIC, the largest conductivities should indeed arise when the fewest  $Al-h^+$  centers are produced, viz., when T is below 200 K or when the Al content is relatively low.

In terms of this interpretation, the holes must be self trapped by the lattice relaxations and therefore move as polarons. The initial activation energy of 0.28 eV would then represent the activation energy for migration of these holes and, of course, the same value should then be obtained for Li- as for Na-swept crystals (item 3). The values of  $x_c$  in the last column of Table III then represent the concentration of such holes. Note the extremely small value for these freely migrating defects ( $10^{-4}$  to  $10^{-1}$  ppm).

Two questions then arise. First, is there any other evidence for such defects in quartz? A possible "yes" answer comes from work on ultraviolet photoelectron spectroscopy in amorphous  $SiO_2$ , which makes it possible to probe the structure of the valence band.<sup>20</sup> A narrow nonbonding orbital subband is found near the valence-band edge indicating low hole mobility with possible lattice trapping of these holes. It is also indicated that the valence-band structure of crystalline  $\alpha$ -quartz should be similar. The second question is whether such polaron-like holes could migrate preferentially along the c-axis, in order to account for the large anisotropy. This question is unanswered at present.

Further experiments to demonstrate more directly whether the RIC is electronic in origin are desirable. Nevertheless, at this stage, the explanation of the present experiments in terms of electronic defects seems to provide the most reasonable interpretation for the observations reported herein, and a new viewpoint

concerning radiation-induced conductivity.

### Acknowledgements

The authors are grateful to Prof. Joel Martin for carrying out electrodiffusion on the various samples studied here. This work was supported by the U.S. Air Force under contract F 19628-82-K-0013 and monitored by H.G. Lipson, KADC Hanscom AFB.

### References

1. J.C. King and H.H. Sander, *Rad. Effects* **26**, 203 (1975).
2. B.R. Capone, A. Kahan, R.N. Brown and J.R. Buckmelter, *IEE Trans. on Nucl. Sci.* **NS-13**, 130 (1966).
3. H.G. Lipson, F. Euler and P.A. Ligor, *Proc. 33rd Ann. Freq. Control Symp.*, USAERADCOM, Ft. Monmouth, N.J., p. 122 (1979).
4. D.B. Fraser, in *Physical Acoustics*, Vol. V, W.P. Mason, editor, Academic Press, N.Y., 1968, Chapter 2.
5. J.M. Stevels and J. Volger, *Philips Res. Rep.* **17**, 283 (1962).
6. D.S. Park and A.S. Nowick, *Phys. Stat. Sol. (a)* **26**, 617 (1974).
7. J. Toulouse, E.R. Green and A.S. Nowick, *Proc. 37th Ann. Freq. Control Symp.*, USAERADCOM, p. 125, (1983).
8. S.P. Dougherty, J.J. Martin, A.F. Armington and R.N. Brown, *J. Appl. Phys.* **51**, 4164 (1980).
9. L.E. Halliburton, N. Koumvakalis, M.E. Markes and J.J. Martin, *J. Appl. Phys.* **52**, 3565 (1981).
10. M.E. Markes and L.E. Halliburton, *J. Appl. Phys.* **50**, 8172 (1979).
11. H.G. Lipson, F. Euler and A.F. Armington, *Proc. 32nd Ann. Freq. Control Symp.*, USAERADCOM, p. 11 (1978).
12. J. Toulouse and A.S. Nowick, *Proc. Symp. on Defect Properties and Processing of High-Technology Nonmetallic Materials*. In press, 1984.
13. H. Jain and A.S. Nowick, *J. Appl. Phys.* **53**, 477 (1982).
14. R.C. Hughes, *Rad. Effects* **26**, 225 (1975).
15. H. Jain and A.S. Nowick, *J. Appl. Phys.* **53**, 485 (1982).
16. J.J. Martin, R.B. Bossoli and L.E. Halliburton, *Proc. 37th Ann. Freq. Control Symp.*, USAERADCOM, p. 164 (1983).
17. J. Toulouse and A.S. Nowick, to be published.
18. S.P. Dougherty, S.E. Morris, D.C. Andrews and D.F. Croxall, *Proc. 36th Ann. Freq. Control Symp.*, USAERADCOM, p. 66 (1982).
19. J.J. Martin, this Symposium.
20. T.H. DiStefano and D.E. Eastman, *Phys. Rev. Lett.* **27**, 1560 (1971).

## Probable Ion Signature in Quartz Electrodiffusion Data

William P. Hanson

Piezo Crystal Company, Carlisle, PA 17013

### Summary

Quartz electrodiffusion data indicate that specific ions are being transported over clearly defined temperature ranges during the first phase of sweeping. Data from over 160 bars show seven current density peaks occurring between 25 C and 525 C. Peaks up to  $.6 \mu\text{A}/\text{cm}^2$  have been recorded. Typical intensities are around  $.05 \mu\text{A}/\text{cm}^2$ .

A relationship between the peaks and annealing temperatures of alkali defect centers seems probable. Most of the peaks occur over the same temperature range that Al-defect centers anneal, as reported by Martin (1). Other defect centers may account for some of the unknown peaks. The relationship between annealing temperatures and current density peaks indicates the peaks may be single ion signatures, possibly providing a measure of the total number of defect centers in a particular bar.

### Introduction

Quartz electrodiffusion is a thermally controlled "purification" process. Unwanted alkali-ions are pulled along the optic axis of quartz by an electric field. Current produced by the transportation of alkali ions increases exponentially as temperature increases and linearly as the electric field increases.

Electrodiffusion run parameters vary throughout the industry. A typical Piezo Crystal Company electrodiffusion run has three phases: 1. a heating up phase, 2. a pure sweep phase and 3. a cool down phase. The point where phase one changes to phase two is the point where the temperature reaches a maximum. This point is referred to as the "phase 1-phase 2 transition point". The transition point is the point where the current density usually reaches a maximum and must be separated from the "current density peaks" which occur during the temperature rise of phase one. During phase two (the pure sweep phase) the electric field and temperature are constant. The third phase (the cool down phase) is signified by the exponential drop in current density at the end of an electrodiffusion run. Of the 160 bars swept, none showed any current density peaks during phase three. The complete run typically takes seven days: two days to warm up, three days of pure sweep time, and two days of cooling. The electric field is initially applied at room temperature and held constant throughout the run. The maximum temperature reached is typically 525 C. Temperatures up to 550 C have been tried successfully.

### Electrodiffusion Data

Electrodiffusion data plotted as current density vs. time provide an easy way to compare one bar to another. Variations in current density, peak intensities, and peak locations are easily seen. Figure one is a current density vs. time plot of a typical electrodiffusion run. The first 48 hours of the data show an exponential increase in the current density; this is referred to as phase one (increasing temperature and constant electric field). The current density reaches a maximum value when the temperature reaches a maximum, in this case 525 degrees C. It is during this first phase where the current density peaks are seen. There are no noticeable peaks in this particular bar. The second phase occurs from hour 48 to 120. This is the pure sweep phase (constant temperature and electric field), showing an exponential decrease in the current density. The third phase is the cool down phase (decreasing temperature and

constant electric field), from hour 120 to 168, showing the exponential decrease in current density as a function of temperature.

### Threshold Current Density

Figure two is the same data plotted as current density vs. temperature. Any anomalies that are a function of temperature can be seen easily. This bar did not have any current density peaks during phase one. One interesting point can be seen by comparing the minimum detectable current level of phase one (temperature rise) to phase three (temperature decrease) as a function of temperature. The threshold current level as a function of temperature changed from 160 C in phase one to over 400 C in phase three. This change is typical for bars with or without current density peaks.

### Current Density Peaks

Current density peaks occur during the heating up of the bars. Figure three is a current density vs. time graph showing some typical peaks. Two peaks can be seen; one peak occurs between the 24 and 30 hour marks. Another peak, displayed as a plateau, can be seen at hour 42. Figure four is the same data graphed as current density vs. temperature. The current density scale has been expanded so the peaks can be seen more clearly. The temperature at which the peaks occur can be pinpointed at 300 C and 450 C. The 300 C peak is very common, occurring in over 40% of the bars. The 450 C peak occurred in only 6% of the bars.

Electric fields of 1900 to 2000 volts/cm are typical. The electric field is applied at room temperature and held constant throughout the electrodiffusion run. Figure five is an example of an extreme case of current density peaks. There are three peaks occurring at 285 C, 350 C, and 425 C. One peak is nearly as intense as the phase 1-phase 2 transition peak (maximum temperature reached), a very unusual case.

Comparing figures one, three, and five, a pattern can be seen in the final current density before the cool down of the oven (phase three). Figure one (bar S155) has no peaks. The current density dropped 74.2% from its maximum value at the 48 hour mark. Figure three (bar S170) has two peaks. The current density dropped 57.0% from its maximum value. Figure five (bar S161) has three peaks, dropping only 31.4%. All of these bars were swept during the same run, all bars were premium Q pure Z "SC" bars from the same supplier. The final current density seems to be related to the number and intensity of the current density peaks. The fewer the peaks and the less intense the peaks, the greater the percent drop in current density.

### Swept Bar Database

The bars included in the database were all swept between September 1983 and May 1984. Bars were usually swept in lots of 5. Of the 169 bars, 55% had one, two, or three peaks. None of the bars had more than three peaks. 45% had no detectable peaks with a resolution of 5 nano-amperes/cm<sup>2</sup>. Considering the data from all bars there are seven current density peaks. The current density peaks range in temperature from 130 C to 505 C. The following table categorizes the peak data as a function of the number of peaks per bar.

### Swept Bar Database

169	Bars
55.0%	Had peaks
31.4%	Had one peak
20.1%	Had two Peaks
3.6%	Had three Peaks

The swept bar database shows seven distinct current density peaks over the tested temperature range. The temperature ranges and percent of bars are listed in the table below. Figure six is a histogram of the peaks as a function of temperature.

Peak #	Temperature Range	Percent
1	130 C	1.5%
2	200 C to 230 C	17.6%
3	260 C to 310 C	42.0%
4	330 C to 370 C	14.5%
5	400 C to 430 C	12.2%
6	450 C to 470 C	6.1%
7	490 C to 500 C	6.1%

### Comparison of Al-alkali Defect Centers to Current Density Peaks

Martin (1), measured the temperature ranges at which Al-OH, Al-Na<sup>+</sup>, and Al-hole defect centers anneal. Al-hole defect centers are known to exist after radiation but probably do not exist prior to radiation exposure. For comparison purposes only, the five regions Martin defines as annealing regions are compared to current density peaks in the following table.

Annealing Regions of Al-Defect Centers		Sweeping Peak Regions
Al-OH	50 - 150 C	130C
	350 - 400 C	330 - 370 C
Al-Na <sup>+</sup>	175 - 450 C	260 - 310 C
	350 - 450 C	400 - 430 C
Al-hole	200 - 280 C	200 - 230 C
No Data		450 - 470 C
No Data		490 - 500 C

Al-OH and Al-Na<sup>+</sup> defect centers anneal over two separate temperature ranges. All of the sweeping peaks occur within a range where an Al-defect center anneals except the two that are above 450 C. Another defect center, not necessarily Al related, may be associated with the two peaks about 450 C. There are no definite data to indicate the sweeping peaks are caused by the annealing of the Al-defect center, only that the sweeping peaks occur within a temperature range where an Al-defect center anneals. A model of the process could be described as follows: during phase one (increasing temperature and constant electric field) defect centers, not necessarily just Al-defect centers, anneal. The annealing of the centers releases the associated alkali ion. The ion, captured by the electric field, migrates along the optic axis of the quartz bar, producing current. This model is not completely satisfactory, but provides a hypothesis to test.

### Identification of "The Ion" Causing a Current Density Peak in an Electrodiffusion Run

An experiment was conducted to try to identify the ion associated with the first current density peak. Electronic grade "AT" bars were used, making it easier to measure impurity levels. The oven temperature was increased by 30 C past the point where the first peak occurred, held constant for 1 hour and then decreased at the same rate. Two bars (AT0027 and

AT0028) were cut in half and labeled AT0027A, AT0027B, AT0028A, and AT0028B. The "A" halves of the bars were partially swept. Figure seven is a current density vs. time graph of bar AT0028A. A definite peak at the 24 hour mark can be identified. Figure eight is the same data plotted as current density vs. temperature. The peak occurs at 270 C. The threshold current density increased from 175 C during phase one to just less than 250 C during phase three. The bars were analyzed for Aluminum and Sodium content. The following table summarizes the data.

Bar ID	Unswept Al in ppm	Swept Al in ppm	Unswept Na in ppm	Swept Na in ppm
AT0027	5.6	4.5	.005	.005
AT0028	5.6	3.7	.005	.005

(Data measured at Oklahoma State University)

The change in aluminum content is probably not significant. Aluminum concentration, from one end to another, in a bar can vary more than the measured differences between swept and unswept bars. The sodium content is a little confusing because of the extremely small value. The data from this experiment are inconclusive. Further experiments need to be conducted if the ions are to be identified.

### Conclusions and Discussions

1. There are at least seven different current density peaks which occur during phase one (increasing temperature and constant electric field) of electrodiffusion runs.

2. The current density peaks are probably related to the annealing of defect centers. Aluminum related defect centers may account for several of the peaks.

Many more experiments need to be done before the current density peaks are related to one ion or perhaps several ions. If the current density peaks are uniquely related to an ion then the electrodiffusion data may indicate the total number of defect centers in a bar.

Forty five percent of the bars swept had no measurable current density peaks. Perhaps the bars least sensitive to radiation are the bars without current density peaks, making the sweeping process a sorting process. The real question is whether or not the electrodiffusion data can be useful in determining the radiation hardness of finished resonators; although there is some interest in determining the relationship between etch channels in resonators and electrodiffusion data.

### Acknowledgements

The author wishes to thank Dr. Martin and Dr. Halliburton from Oklahoma State University for helpful conversations and analyzing the bars. Dr. Kahan and Dr. Euler at Hanscom have provided helpful suggestions. Thanks to Wally Samuelson at Piezo for the enlightening conversations and helpful suggestions.

### References

1. J. J. Martin Aluminum-Related Acoustic Loss in AT-Cut Quartz Crystals, 1984 Frequency Control Symposium
2. R. N. Brown, J. J. O'Connor, A. F. Armington, Sweeping and Q Measurements at Elevated Temperatures In Quartz, Rome Air Development Center, In-House Report RADC-TR-79-175, May 1979
3. D. R. Koehler, Radiation-Induced Conductivity and High Temperature Q Changes In Quartz Resonators, Proc. 35th Ann. Freq. Control Symposium, pp. 322-328, 1981
4. J. J. Martin, L. E. Halliburton, R. B. Bossoli, The Influence of Crystal Growth Rate and Electrodiffusion (Sweeping) on Point Defects in a-Quartz, Proc. 37th Ann. Freq. Control Symposium, pp. 77-81, 1982

5. F. Euler, H. G. Lipson, A. Kahan, A. F. Armington, Characterization of Alkali Impurities in Quartz, Proc. 36th Ann. Freq. Control Symposium, pp. 115-123, 1982
6. L. E. Halliburton, N. Koumvakalis, M. E. Markes, and J. J. Martin, Radiation Effects in Crystalline SiO<sub>2</sub>: The Role of

Figure 1.

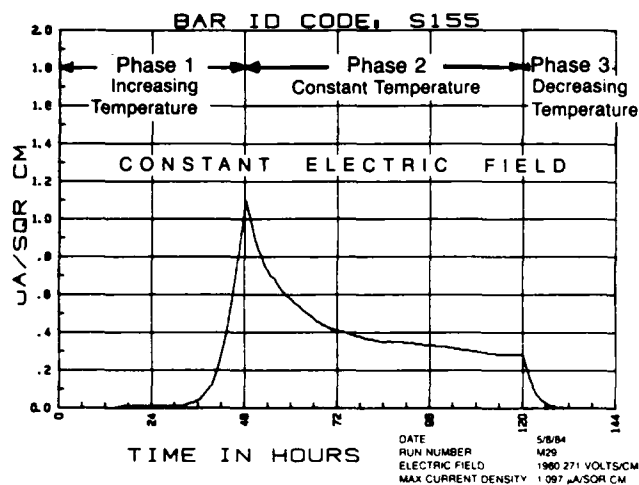


Figure 2.

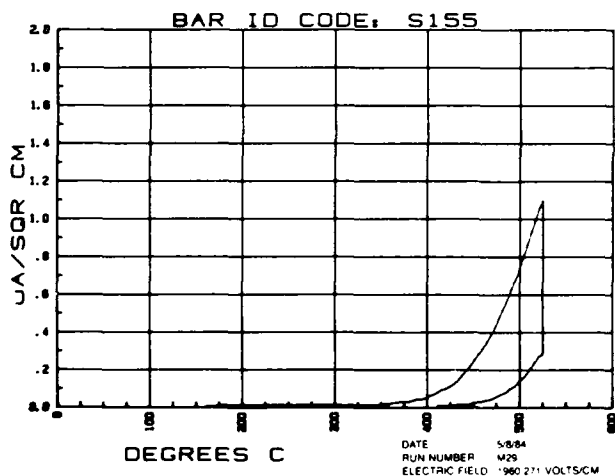
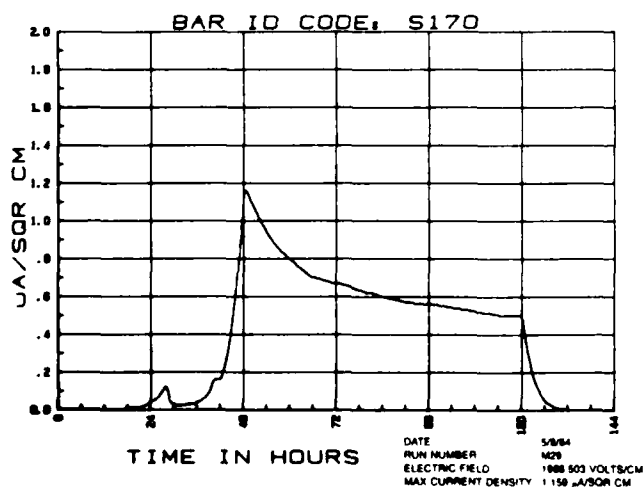


Figure 3.



- Aluminum, vol. 52 May 1981 J. Applied Physics
7. W. Hanson, Computer Controlled Quartz Electrodiffusion (Sweeping) with Real Time Data Collection, Given at the 1983 Freq. Control Symposium and printed in the Proc. 37th Ann. Freq. Control Symposium

Figure 4.

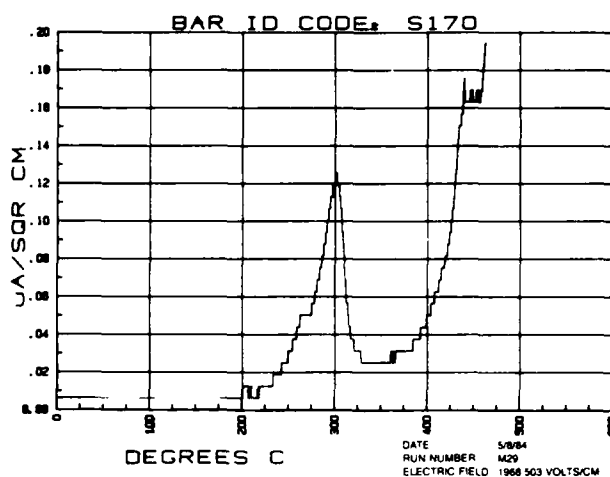


Figure 5.

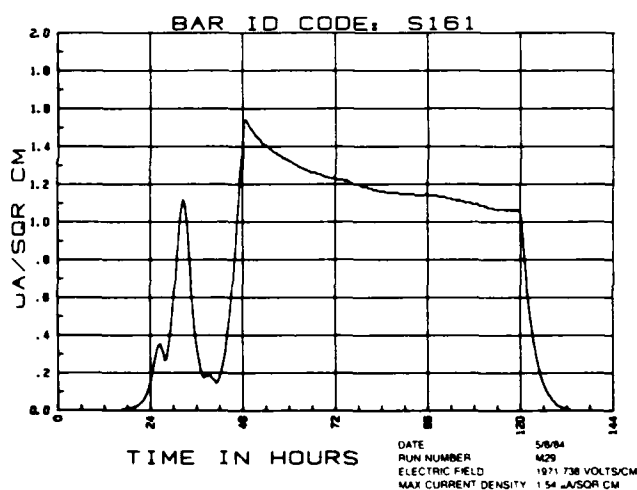


Figure 6.

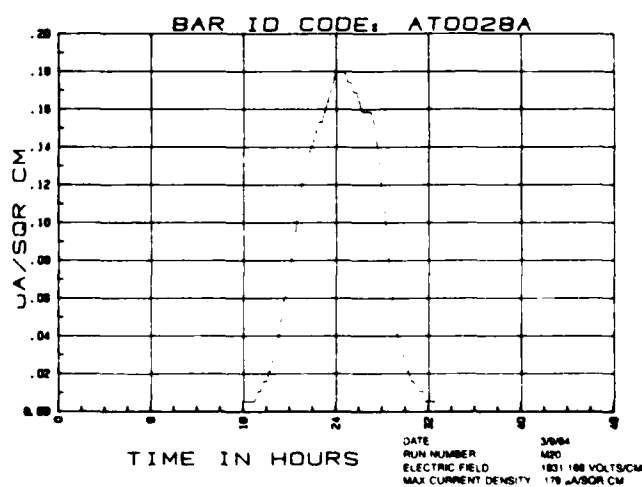


Figure 7.

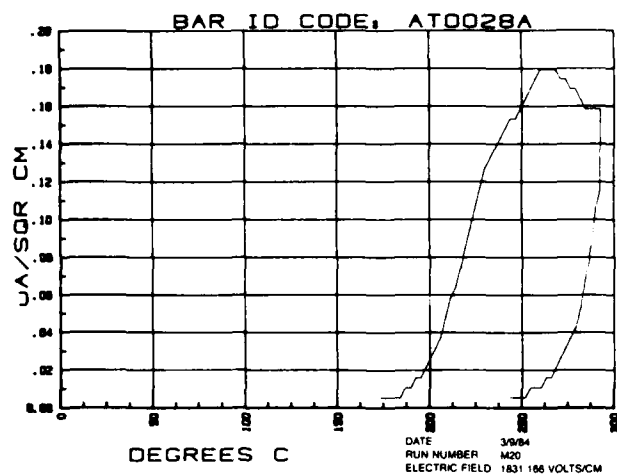
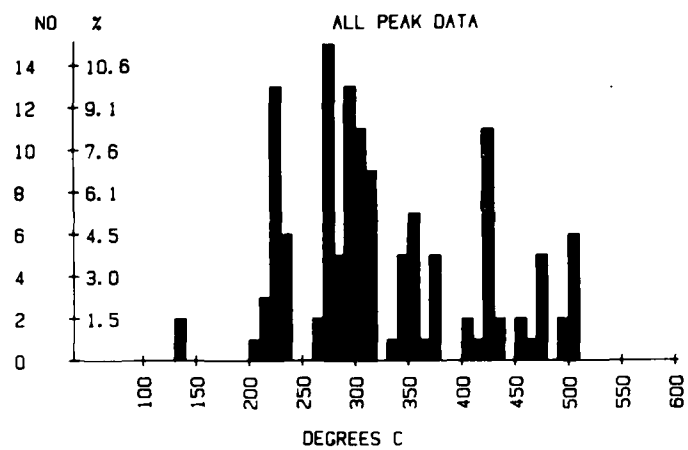


Figure 8.



## SWEEPING AND IRRADIATION STUDIES IN QUARTZ\*

John G. Gaultieri and John R. Vig

US Army Electronics Technology and Devices Laboratory (ERADCOM)  
Fort Monmouth, New Jersey 07703Abstract

Sweeping (in air) and irradiation effects in quartz were examined in a program aimed at the improvement of quartz material for high-stability radiation-resistant resonators. Resistivity changes as a function of transported charge were recorded and depth-profiled secondary ion mass spectrometry (SIMS) results were used to analyze for impurities before and after  $\gamma$ -irradiation. Both swept and unswept samples of high purity cultured quartz were studied. Fully swept samples were found to be nearly free of etch channels.

Color-center striae in irradiated unswept samples were analyzed using spatially scanned absorption spectrometry. The scanned absorption at 460 nm was then correlated with SIMS analyses at selected regions within the sample.

Radiation induced steady state frequency shifts were measured using swept resonator samples from two different suppliers of high purity quartz. No significant steady state frequency shift differences were found between the two groups of resonators when irradiated to 0.76 Mrad and 7.6 Mrad levels.

Introduction

Sensitive experimental techniques are required to monitor electrolysis (sweeping) and irradiation effects on high quality quartz. Specifically, characterizations of impurity/defect concentrations and diffusion resulting from these treatments are indispensable. The ability to correlate the results of these characterizations with device performance is a long-range goal. Another objective is to develop techniques which will be useful for quality assurance in the manufacture of high quality resonators made of swept quartz. Before we can achieve these goals, reliable techniques for sweeping and impurity analysis will have to be developed and certified.

It is known that sweeping cultured quartz leads to improvement in quartz resonator radiation sensitivity<sup>1,2</sup>. However, considerable variation in the radiation response of resonators cut from different bars has been reported<sup>1</sup>. During the sweeping experiments that are reported in this paper, variability in the current density vs time response of individual quartz bars was noted. However, we found uniformity in the radiation induced frequency deviations of resonators fabricated from the swept quartz material, when irradiated with up to 7.6 Mrad of  $\gamma$ -radiation.

Experimental Procedures

Samples to be swept were cut from lumbered Y bars supplied by different vendors. In Fig. 1 the location and dimensions of the sample bars are shown.

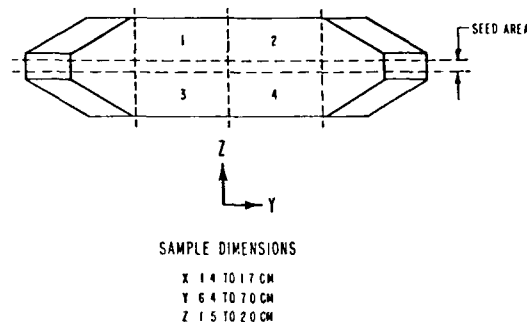


Fig 1. Y-Bar Location (Regions 1-4) and Typical Dimensions of Sample Bars Used in Sweeping

The bars were placed in a 6 cm diameter X 90 cm long quartz tube which was inserted into a temperature controlled programmable furnace with tube ends extending outside the furnace. A thermocouple contained in an ungrounded sheath was placed in contact with the quartz to monitor the sample temperature. The tube was fitted with a ground joint containing 3 ports for thermocouple, lead-in wires and gas input. A gas output port was located on the opposite end of the tube. A diagram of the apparatus is given in Fig. 2.

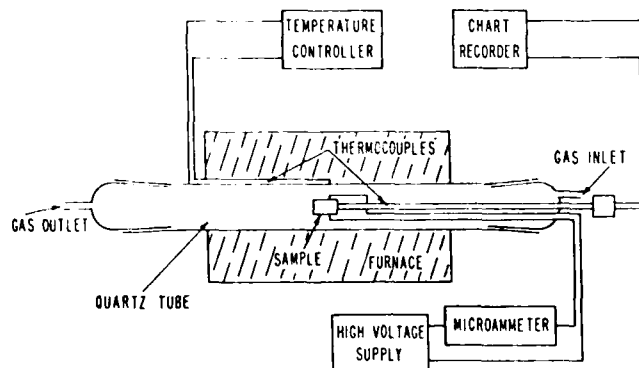


Fig 2. Diagram of Sweeping Apparatus

\* This paper was presented at the 37th Annual Frequency Control Symposium (AFCS). The paper was not published in the Proceedings of the 37th AFCS because a security classification question was unresolved at the time the Proceedings went to print.

Initially, platinum foil lined electrodes were pressed onto the sample to accomplish electrical contact. More efficient electrical contact could be achieved by vapor depositing a thickness of 200 angstroms chrome followed by 60 angstroms chrome-gold mixture and finally 700 angstroms gold onto the sawn Z-surfaces. The vapor deposition was performed in a cryopumped ultrahigh vacuum system. Gold ribbon lead-in wires were thermocompression bonded to a small area on the electrodes which had received an additional 10 $\mu$ m thick gold electroplating. The furnace was programmed to raise the sample temperature to 500 deg C at a rate of 20 deg/hr. Once the sweeping temperature was reached, an electric field was applied parallel to the Z-axis. The field was applied either fully or in steps, but was kept constant at some final value throughout the run. Once the current density levelled off, the furnace was programmed to lower the temperature, at a rate of 20 deg/hr, to 25 deg C. The field was maintained during the cooldown period.

Both treated and untreated samples were analyzed using secondary ion mass spectrometry (SIMS).<sup>\*</sup> Although SIMS is a surface sputter-erosion process, the material removal rate can be increased enabling analysis at depths below the surface, i.e., depth profiles are recorded. Analysis can be performed on square areas with sides of only 400  $\mu$ m. SIMS analysis is very useful for the evaluation of high purity quartz because it offers: 1) very high sensitivities (ppb range), 2) depth profiling, 3) 0.5 mm spatial resolution, and 4) detection of all elements.

$\gamma$ -ray irradiations were carried out using the <sup>60</sup>Co source at Fort Monmouth. Color-center absorption measurements were made with a Cary-14 spectrophotometer. A special arrangement for linear translation of samples was incorporated using a stepper motor driven stage.

## Results and Discussion

### Sweeping Data

Using samples cut from the same quartz bars, it was found that initial resistivities<sup>+</sup> were higher for platinum foil lined pressure electrodes than for the vapor deposited chrome-gold electrodes. Further, the resistivity increased by only a factor of 5 over a 120 hour sweeping period. By contrast, samples with chrome-gold vapor deposited electrodes had lower initial resistivities but the resistivity sometimes increased by a factor of 10<sup>4</sup> in only 48 hours of sweeping.

<sup>\*</sup>SIMS analysis was performed by ATOMIKA, Inc., Inglewood, CA.

<sup>+</sup>The bulk resistivity of quartz, obtained by dividing the field by the current density.

The final stabilized current density has been attributed to the sweeping of protons (H<sup>+</sup>) through the lattice, whereas the large initial current density, which decreases very rapidly, is most likely due to the sweeping of high mobility alkali ions. The much less rapid mid-range current density decrease is probably the sweeping action of low mobility interstitial ions such as Ca<sup>2+</sup>. It is proposed that sweeping can be considered complete for a particular field-temperature setting when a long-term stabilized current density is reached or, as discussed later, when the resistivity levels off. In Figs 3,4,5 and 6 plots of current density as a function of time are shown for sweeping runs on quartz from 3 different suppliers (the suppliers are coded A,B and C).

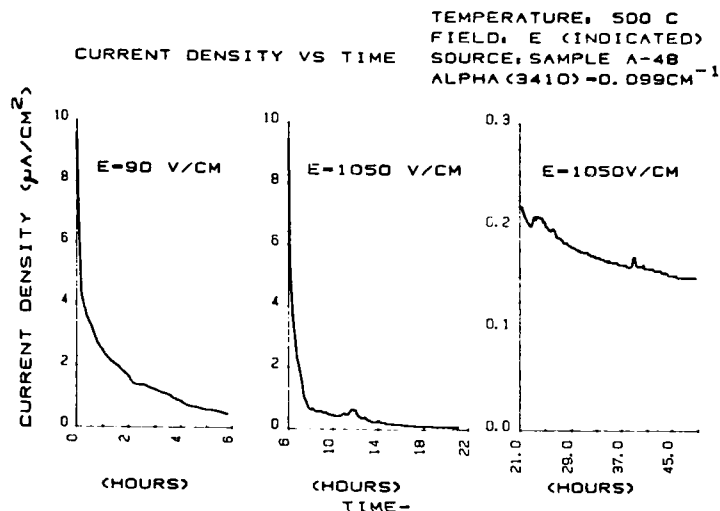


Fig 3. Sweeping Current Density vs Time. The Individual Plots are in Time Sequence and Represent a Change in Field Followed by a Change in Current Scale.

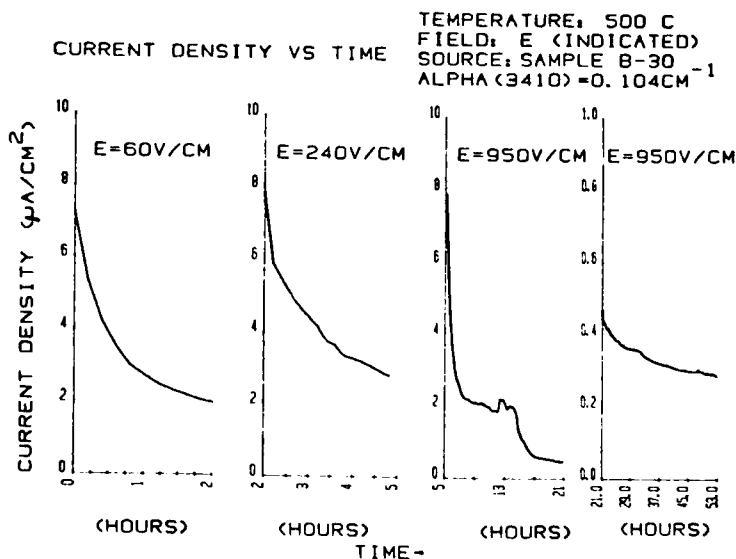


Fig 4. Sweeping Current Density vs Time. The Individual Plots are in Time Sequence and Represent Two Changes in Field Followed by a Change in Current Scale.



## CURRENT DENSITY VS TIME

TEMPERATURE: 500 C  
FIELD: 1000 V/CM  
SOURCE: SAMPLE C-21  
 $\text{ALPHA (3410)} = 0.153\text{CM}^{-1}$

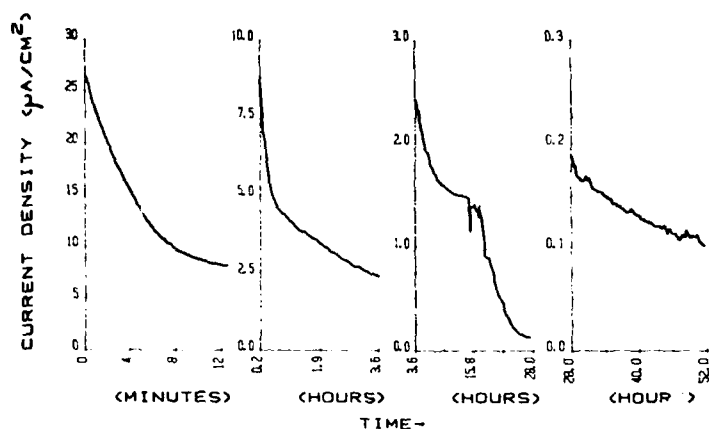


Fig 5. Sweeping Current Density vs Time. The Individual Plots are in Time Sequence and Represent Three Changes in Current Scale.

## CURRENT DENSITY VS TIME

TEMPERATURE: 500 C  
FIELD: 1000 V/CM  
SOURCE: SAMPLE C-28  
 $\text{ALPHA (3410)} = 0.087\text{CM}^{-1}$

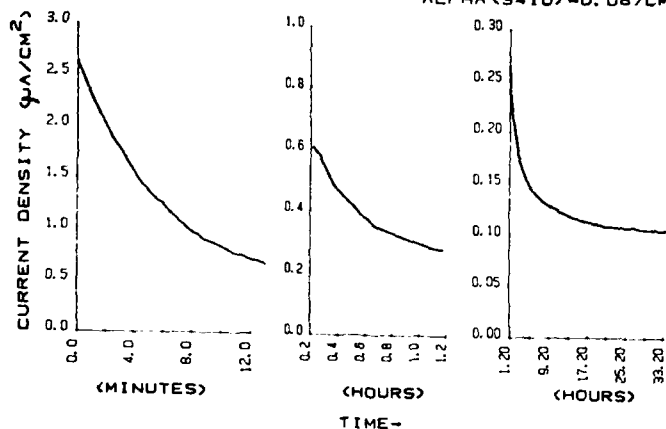


Fig 6. Sweeping Current Density vs Time. The Individual Plots are in Time Sequence and Represent Two Changes in Current Scale.

In each figure the sequential plots are indicative of either a change in scale or a step-up in applied field. The sweeping run depicted in Fig 3 shows that the field was stepped up once after 6 hours and the current density scale was changed after 21 hours. Final current stabilization occurred after 48 hours. In Fig 4, the field was stepped up twice, at 2 hours and again at 5 hours. There was a change in scale at 21 hours and the current stabilized after approximately 53 hours. In Figs 5 and 6, the field was turned on fully from the start but there were changes in scale throughout the runs. In these runs the samples were cut from different bars from the same supplier. Note in Fig 5, the initial current density is higher than in Fig 6 by an order of magnitude and the time to current stabilization is longer. Note also the differences in absorption coefficient at  $3410\text{ cm}^{-1}$ .

In Figs 7,8,9 and 10 resistivity vs. transported charge are plotted in order to determine the number density of swept ions when the resistivity stabilized<sup>3</sup>.

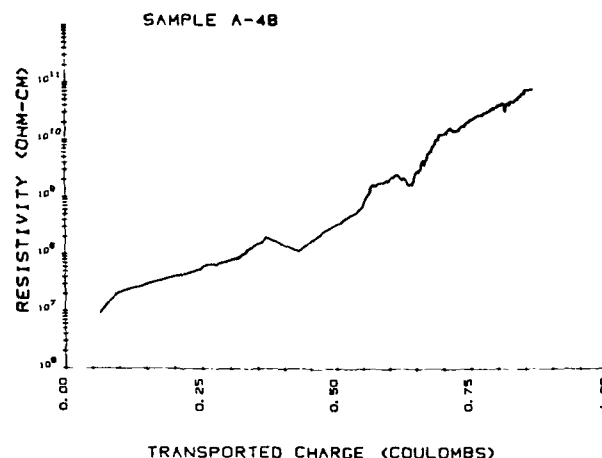


Fig 7. Resistivity vs. Transported Charge. The Ratio of Final Resistivity to Initial Resistivity was  $\sim 10^4$ .

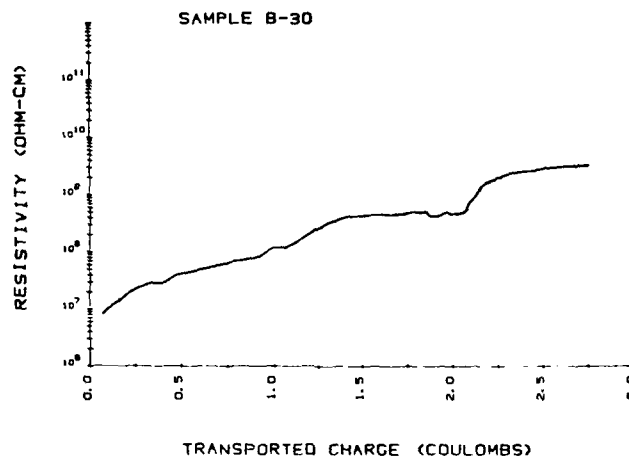


Fig 8. Resistivity vs. Transported Charge. The Ratio of Final Resistivity to Initial Resistivity was  $\sim 500$ .

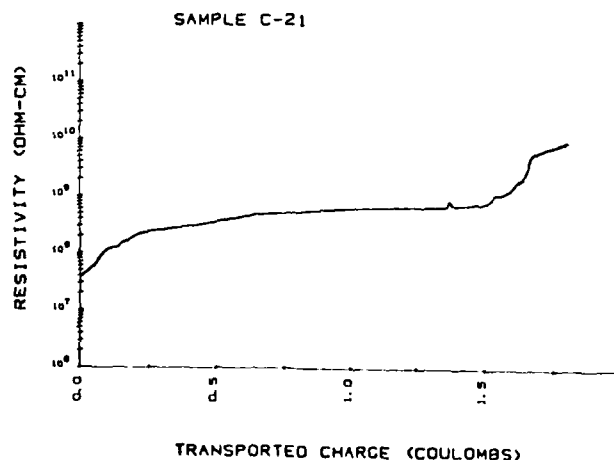


Fig 9. Resistivity vs. Transported Charge. The Ratio of Final Resistivity to Initial Resistivity was  $\sim 250$ .

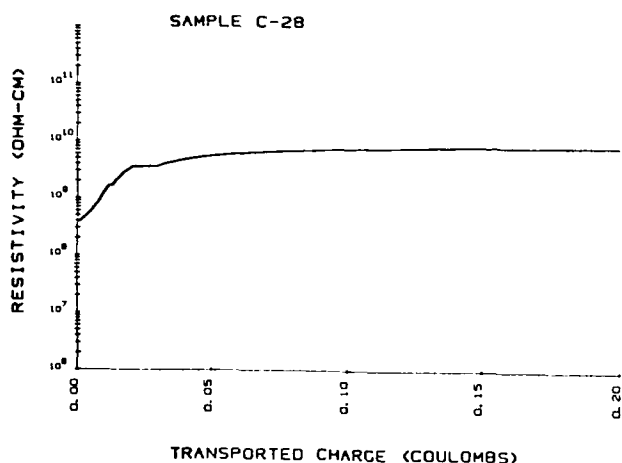


Fig 10. Resistivity vs. Transported Charge. The Ratio of Final Resistivity to Initial Resistivity was  $\sim 20$ .

Table I summarizes the data obtained from Figs 3-10, and shows that there is variability in starting material resistivity which is inversely related to the time required to sweep to a stabilized resistivity in the  $10^{10}$ - $10^{11}$  ohm-cm region. The number density of "singly charged" ions swept shows variability among supplier and even a greater difference between the C-21 and C-28 bars.

TABLE I SWEEPING DATA

Supplier-Sample	Resistivity			$N/cm^3$
	Initial (ohm-cm)	Final (ohm-cm)	Stabilization Time (hours)	
A-48	$9 \times 10^6$	$9 \times 10^{10}$	48	$4 \times 10^{17}$
B-32	$8 \times 10^6$	$4 \times 10^9$	52.5	$8 \times 10^{17}$
C-21	$4 \times 10^7$	$1 \times 10^{10}$	28	$7 \times 10^{17}$
C-28	$4 \times 10^8$	$9 \times 10^9$	9	$1 \times 10^{17}$

\*From resistivity data,  $N = q/\epsilon v$  (assuming only singly charged ions).  
 $q$  = transported charge,  $\epsilon$  = electronic charge,  $v$  = sample volume

Small areas of coloration were evident in the C material after sweeping and before irradiation. No coloration could be detected in either A or B bars after sweeping or after irradiation with up to 7.6 Mrad  $^{60}\text{Co}(\gamma)$ . AT-cut wafers were removed from the bars and etched in ammonium bifluoride for 2 hours at 75°C. No etch channels could be found in any of the wafers. Prolonged etching for 17 hours also produced no etch channels. AT-cut wafers from unswept control bars always contained at least 100 channels/cm<sup>2</sup>. After fabrication of AT-cut resonators, etching of the polished blanks made of swept quartz revealed extremely small diameter channels with a density of  $\leq 5 \text{ cm}^{-2}$ . The channel diameters appeared to be much smaller than the channels typically observed in unswept blanks etched the same amount.

## SIMS RESULTS (electrode areas)

Both treated and untreated samples from an "A" bar swept using platinum foil pressure electrodes, were analyzed by the SIMS method. Elements analyzed included Na, Li, Al, Fe, Cr, Cu and Ca. Depth profiling of each element on both anode and cathode side was also recorded. The data for each impurity is plotted in Figs 11-17 showing the depth profiling under both electrodes. Each figure contains four depth profiles in order to compare concentrations of swept and unswept samples before and after irradiation (with  $3.7 \times 10^6 \text{ Rad (Si)}$ ).

In comparing the concentrations of swept and unswept samples on the cathode sides, which were the sides adjacent to the seed, steeper increases and higher levels of concentration were recorded for all impurities, with the possible exception of the low mobility  $\text{Ca}^{2+}$  ion. This suggests that sweeping is responsible for the movement of the principal quartz impurities Al and Fe, which were probably interstitial, as well as the alkali metals. The sweeping of Al is not as clear cut as the sweeping of Fe when comparing concentrations on anode and cathode sides. The sweeping of Fe may be related to the reduction in etch channels since quartz grown in silver lined autoclaves having low Fe content shows low etch channel densities<sup>4</sup>.

## SODIUM IMPURITY DEPTH PROFILE

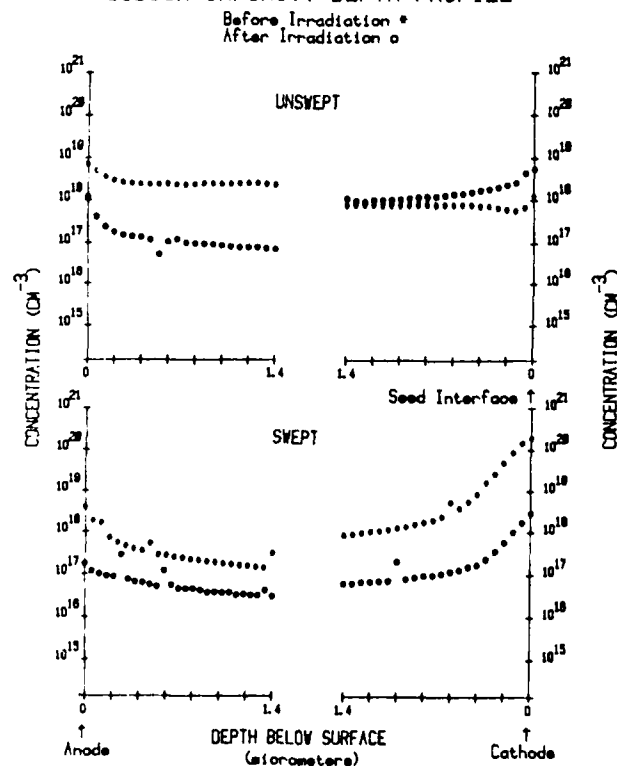


Fig 11. SIMS Depth Profile for Sodium Comparing Unswept to Swept Before and After Irradiation Under Each Electrode.

# LITHIUM IMPURITY DEPTH PROFILE

Before Irradiation \*  
After Irradiation o

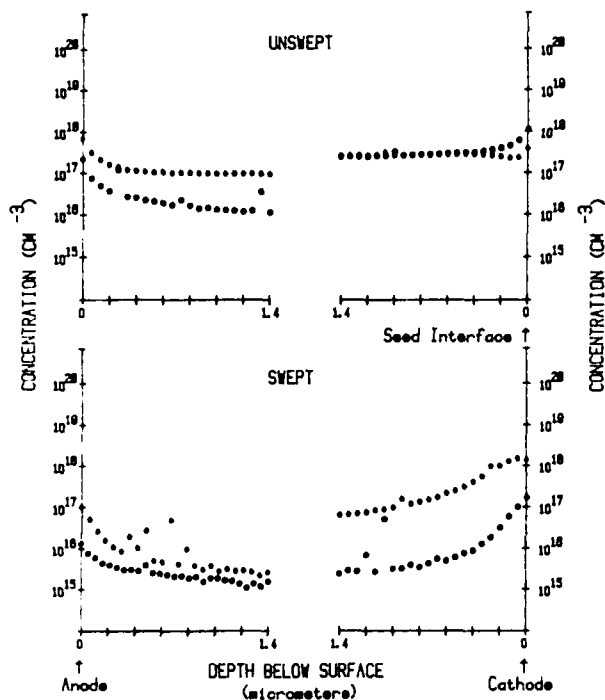


Fig 12. SIMS Depth Profile for Lithium

# IRON IMPURITY DEPTH PROFILE

Before Irradiation \*  
After Irradiation o

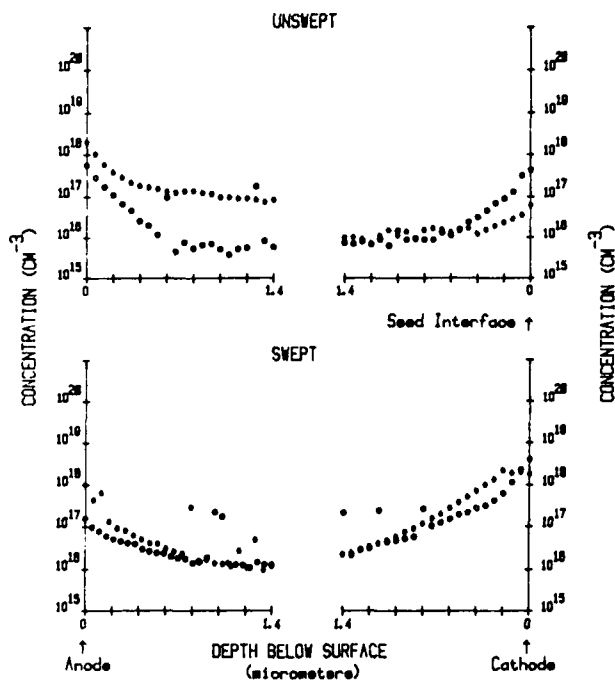


Fig 14. SIMS Depth Profile for Iron

# ALUMINUM IMPURITY DEPTH PROFILE

Before Irradiation \*  
After Irradiation o

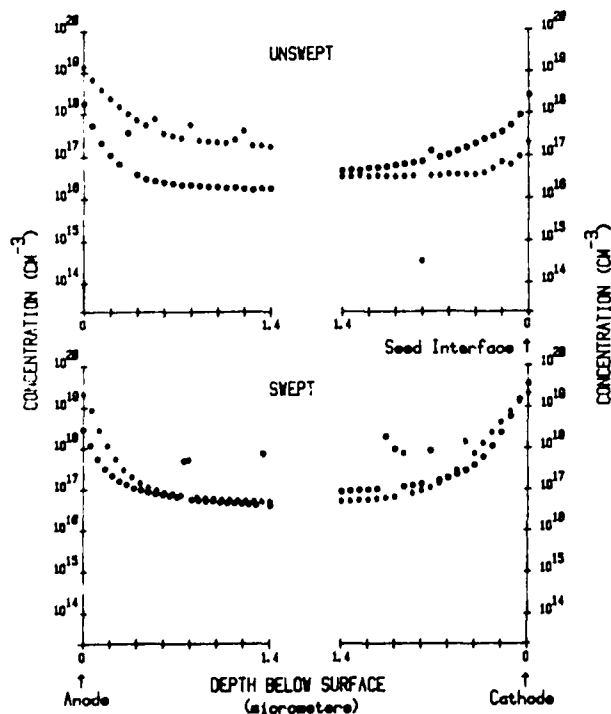


Fig 13. SIMS Depth Profile for Aluminum

# CHROMIUM IMPURITY DEPTH PROFILE

Before Irradiation \*  
After Irradiation o

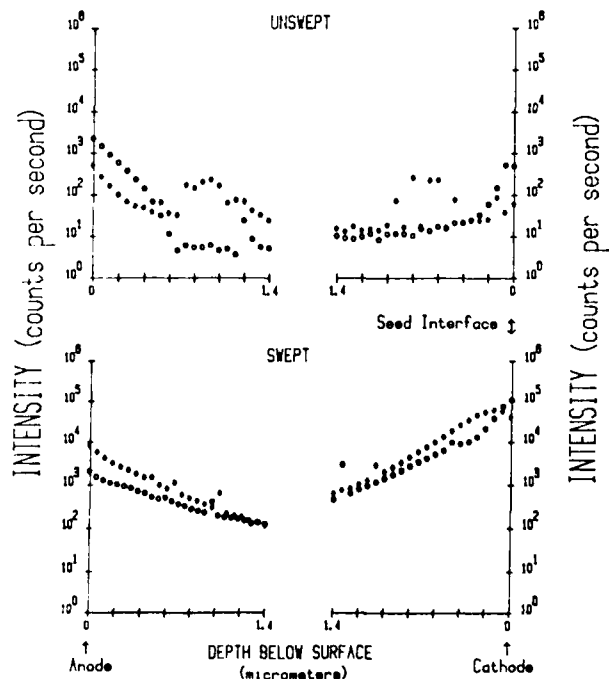


Fig 15. SIMS Depth Profile for Chromium Without Concentration Calibration.

## COPPER IMPURITY DEPTH PROFILE

Before Irradiation \*  
After Irradiation o

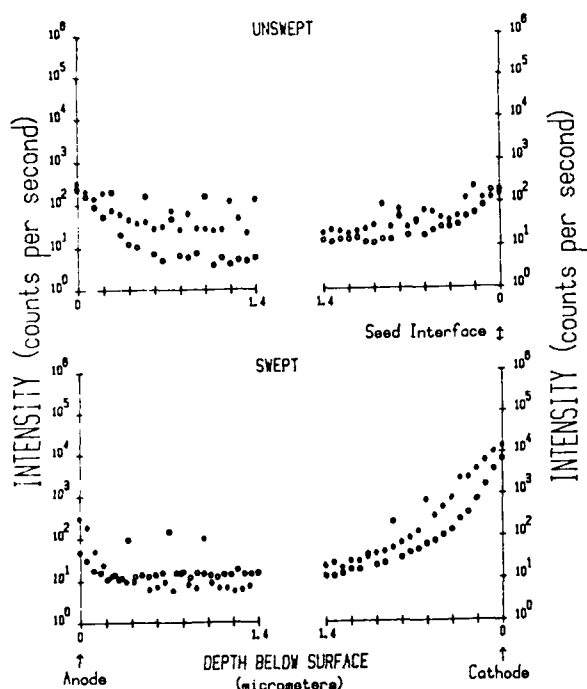


Fig 16. SIMS Depth Profile for Copper Without Concentration Calibration.

## CALCIUM IMPURITY DEPTH PROFILE

Before Irradiation \*  
After Irradiation o

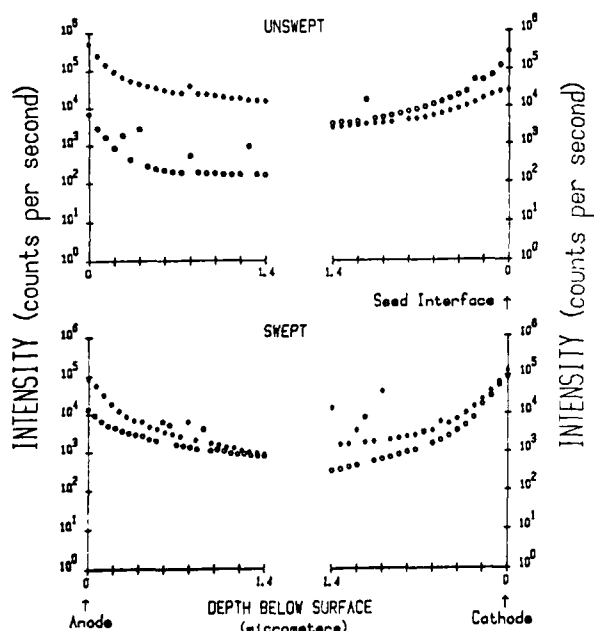


Fig 17. SIMS Depth Profile for Calcium Without Concentration Calibration.

There is a small increase in concentration at the side closest to the seed after irradiation for the impurities Na, Li, Al and Ca in the unswept samples. Also, large decreases at the side away from the seed are evident for these impurities. These concentration decreases are not found for Fe, Cr and Cu (Fig 14, 15 and 16), nor are large decreases evident for any impurity in the swept sample. The increase in impurity level near the seed interface and decrease on the side away from the seed for the irradiated unswept sample could be the result of a higher density of defects near the seed, which act as trapping centers for diffusing ions. The concentration levels of Fe, Cr and Cu are considerably below that of the other ions, and if the fewer trapping centers on the side away from the seed were not filled, there would be little directional preference observed. After sweeping, the picture changes markedly, probably through modification or reduction in the number of defect sites. The reduction of etch channels in swept quartz reinforces this assumption. High mobility of interstitial sodium was found by Halliburton<sup>5</sup> even at temperatures as low as 77 deg K under a radiation field. Our samples were irradiated for 28 hours at 37 rad/sec at 25 deg C. Also, Chentsova<sup>6</sup> found that an increase in activation energy for conduction in quartz similar to that found during sweeping in air is achieved by  $\gamma$ -irradiation of quartz. He explained the increase in activation energy as the result of formation of hole centers during irradiation accompanied by radiation stimulated diffusion of alkali ions to trapping centers due to electrons ejected by the radiation.

## SIMS and Color Center Absorption (along Z)

Z-growth cultured quartz usually has a variable growth irregularity described as "breathing of crystal growth". This growth fluctuation is associated with periodic changes in crystal temperature and solute deposition which are mutually interacting. After irradiation, these areas are decorated by room temperature stable color-centers forming visible striae oriented parallel to the growth (Z) surface. The presence of color-centers has been related to resonator frequency offsets in quartz<sup>1,2</sup>. Color-center absorption variations (striae) are easily recorded by translating a sample, dimensioned as described in the experimental section, in the Z-direction with the striae oriented parallel to the spectrometer slit, the probe beam in the X-direction with polarization parallel to Z and wavelength fixed at 460 nm. The solid curves in Fig 18 refer to the transmission at 460 nm for both swept and unswept samples. The striae appear in unswept material but are not usually visible in swept bars of high purity quartz. SIMS analysis was carried out for all impurities mentioned above at specific points along the Z-axis as indicated in Fig 18.

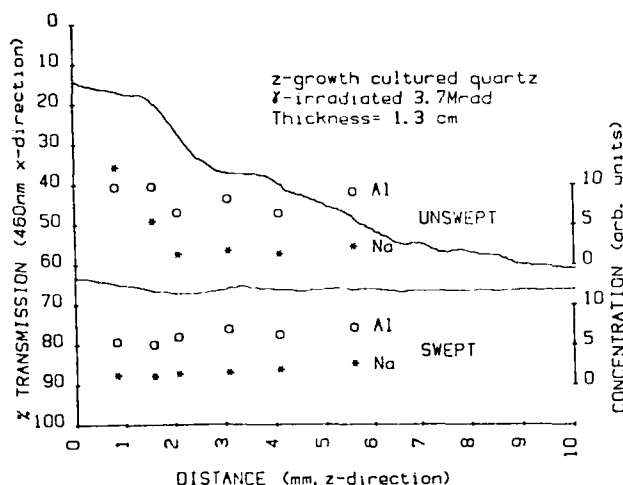


Fig 18. Spatially Scanned Transmission (left vertical scale) and SIMS Analysis (right vertical scale) of Aluminum and Sodium. Distance is Measured from the Seed Interface.

Only the sodium concentration showed strong correlation with the density of color-center absorption. Aluminium levels are also plotted for comparison. It was suggested that cations in shallow traps, not compensating  $Al^{3+}$  defects, contribute to steady state frequency offset and should be proportional to room temperature stable color-centers<sup>2</sup>. The SIMS data suggests that the presence of sodium is somehow related to the coloration in agreement with Kats<sup>3</sup>, Leitz<sup>7</sup> and Lell<sup>8</sup>. The lithium content showed much weaker correlation with this coloration.

#### Radiation Induced Steady State Frequency Shifts

Twenty resonators were fabricated from two swept bars, ten from the A-48 sample and ten from the B-30 sample. The resonators were 5 MHz, 3rd overtone, AT-cuts with 14 mm blank diameters, bonded with silver filled polyimide and cold-weld sealed in HC-36 enclosures.

For each resonator, the frequency at a reference temperature was determined by performing a frequency vs. temperature measurement in a transmission type ( $\pi$ -network) system. The reproducibility of measurements was determined by disconnecting each resonator from its  $\pi$ -network, then reconnecting and remeasuring the reference frequencies without any irradiation between measurements. The average reproducibility was  $5.6 \times 10^{-8}$ ; the standard deviation was  $5.8 \times 10^{-8}$ , and the maximum frequency deviation (for the 20 resonators) was  $18.5 \times 10^{-8}$ . As an additional check on the reproducibility, one resonator from each group was not irradiated but kept as a control sample and was measured each time with the irradiated samples. The elapsed time between successive measurements of each resonator ranged from 1 to 2 days.

The reference frequencies were remeasured by the same method after a radiation dose of 0.76 Mrad, then again after an additional dose of 6.84 Mrad. (The frequency resolution of the measurement technique did not permit the evaluation of radiation hardness at low dose levels). The irradiation was performed with a  $^{60}Co$  source, at a rate of 540 rad/sec.

Although the two bars that were used in this experiment were obtained from two different suppliers, no significant differences in radiation hardness were noticeable between the two groups of resonators. For both groups, the magnitudes of the radiation induced frequency shifts were comparable to the reproducibility of measurements. The group A resonators did have a significantly higher average resonator Q. The average Q was  $1.5 \times 10^6$  for group A and  $1.1 \times 10^6$  for group B.

#### Conclusions

1. Vapor-deposited electrodes allow shorter sweeping times to achieve high resistivity levels.
2. The stabilized resistivity as a function of transported charge is one candidate to determine when sweeping is complete for particular (fixed) electric field/temperature levels.
3. Initial resistivity and/or total transported charge to a stabilized resistivity are probably convenient measures of the purity of an unswept sample. The final resistivity is an indicator of the purity of the swept sample.
4. SIMS analysis showed that: A) several different species of interstitial cations are swept. B) color-center absorption can be related to an increase in Na content in the sample, and C) radiation stimulated diffusion of interstitial cations and the trapping of these ions at areas of high defect density was likely.
5. Air sweeping, when properly done, is capable of producing near etch-channel-free quartz. (Previously, only vacuum swept quartz has been reported to be free of etch channels<sup>9</sup>.) Etch channel density is another candidate for a completeness of sweeping measure.

#### Acknowledgement

The authors appreciate the contributions of Raymond L. Filler, John A. Kosinski and Ron Brandmayr for frequency measurements, computational assistance and etching experiments, respectively. The authors would also like to thank Piezo Crystal Co. for fabricating the AT-cut resonators used in the radiation hardness studies.

### References

1. T.M. Flanagan and T.F. Wrobel, "Radiation Effects in Swept - Synthetic Quartz", IEEE Trans. Nucl. Sci. NS-16 (Aug-Dec), 130 (1969).
2. J.C. King and H.H. Sander, "Transient Change in Q and Frequency of AT-cut Quartz Resonators Following Exposure to X-rays", IEEE Trans. Nucl. Sci. NS-20, No. 6, 117 (1973).
3. A. Kats, "Hydrogen in Alpha-Quartz", Philips Research Reports, 17, 133 (1962).
4. R.L. Barnes, P.E. Freeland, E.D. Kolb, R.A. Laudise and J.R. Patel, "Dislocation-Free and Low-dislocation Quartz Prepared by Hydrothermal Crystallization", Jour. Cryst. Growth 43, 676 (1978).
5. L.E. Halliburton, M. Markes, J.J. Martin, S.P. Doherty, N. Koumvakalis and W.A. Sibley, "Radiation Effects in Synthetic Quartz the Role of Electrodiffusion and Radiation Induced Mobility of Interstitial Ions", IEEE Trans. Nucl. Sci. NS-26, No. 6, 4851 (1979).
6. L.G. Chentsova, L.I. Tsinober, M.I. Samoilovich and S.V. Kolodieva "Some Features of the Electrolysis of Quartz Crystals in Air and in Vacuum", Soviet Physics - Crystallography 17, No. 2, Sept-Oct, 317 (1972).
7. J. Leitz and M.R. Hanisch, "Über Die Bildung Von Farbzentren Um Quarz Durch Elektrolyse", Naturwiss., 46, 67 (1959).
8. E. Leil, "Radiation Effects in Doped Fused Silica", Phys. and Chem. Glass, 3 84 (1962).
9. J.R. Vig, J.W. LeBus and R.L. Filler, "Chemically Polished Quartz", Proc. 31st Annual Symposium on Frequency Control, pp. 131-143, 1977.

# COMPUTER CONTROLLED QUARTZ ELECTRODIFFUSION (SWEEPING) WITH REAL TIME DATA COLLECTION \*

by William P. Hanson  
Piezo Crystal Company  
Carlisle, PA 17013

## INTRODUCTION

Quartz electrodiffusion (sweeping) is a process designed to minimize the frequency shift of a resonator which is subjected to radiation. The electrodiffusion process generally lasts 7 to 15 days, making data collection difficult. Computerizing the sweeping process provides a method to monitor the electrodiffusion process on a twenty four hour basis and analyze data in real time. The electric field, oven temperature and data collection are controlled by computer. Real time data analysis provides the current density, conductance, and Coulomb transfer rates. Natural quartz, premium Q pure Z quartz, and electronic grade quartz have been swept in air. Resonators fabricated from premium Q pure Z cultured quartz swept by Piezo have been tested for frequency shifts due to irradiation.

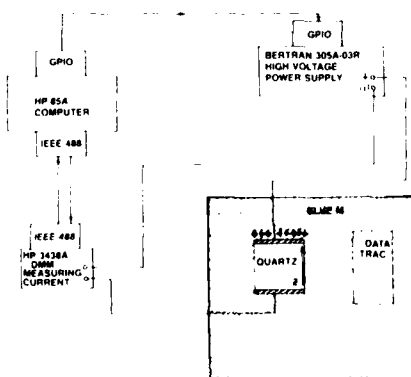
The electrodiffusion process is dependent upon many parameters. Two of these parameters are the intensity of the electric field across the bar and the temperature of the bar. Two classes of experiments were conducted to examine these parameters. Each class isolated one parameter from the other. The first held the electric field constant while the temperature was increased linearly. This experiment examined current density as a function of temperature. The second class held the temperature constant while the electric field was increased linearly. This experiment examined current density as a function of electric field intensity.

## ELECTRODIFFUSION SETUP

The electrodiffusion setup is portrayed in figure one. An HP-85A computer controls the Bertan high voltage power

FIGURE 1

ELECTRODIFFUSION SETUP



supply and HP DMM. The HP-85A computer utilizes two different types of computer interfaces. The GPIB interface controls the Bertan high voltage power supply. The GPIB interface is a 16 bit binary interface, allowing 50mV increments in the electric field. The IEEE-488 (HB-IB) interface controls the HP-3438A DMM, which is set up to measure the current passing through the quartz bar on the ground side. The u-DATA TRAC controls the BLUE-M oven.

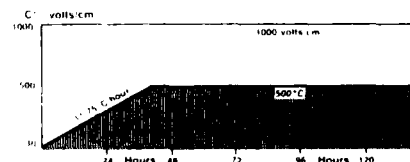
The Z-faces of the quartz bars were optically polished to aid in the inspection for inclusions, microscopic cracks, and other physical imperfections. Physical imperfections could inhibit the electrodiffusion process by blocking the Z-channels in the quartz bar. Inclusions and cracks could also be places where impurities are concentrated. Electrical contact to both Z-faces was made with 2 mil thick platinum foil. The platinum foil was attached to stainless steel blocks by pressure contacts. Electrical connections to the stainless steel blocks were made with platinum wires insulated with Vycor™ glass tubing.

The computer program running on the HP-85A is interrupt driven. Real time data analysis routines run continuously. The interrupt routines control data collection and the intensity of the electric field. Data analysis includes calculations of current density, conductance/cm, and the Coulomb transfer rate. Some program variables can be changed during the sweeping run. The intensity of the electric field can be adjusted up or down to within the limits of the power supply. The electric field ramp time can also be adjusted. The ramp time determines the incremental changes in the electric field. The time between data points can be adjusted with one minute being typical. Intervals down to .3 seconds are possible.

## DATA ANALYSIS

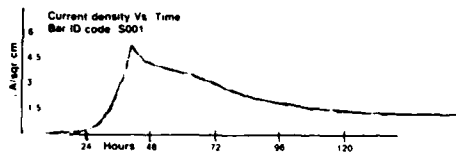
Two fundamental classes of experiments were conducted. The first class examined the effect of temperature on the electrodiffusion process. Bar S001, a cultured premium Q pure Z 'SC' bar, is a member of the first class of experiments. Figure 2 is a profile of the temperature and electric field intensity during the sweeping run of bar S001.

FIGURE 2



\* This paper was presented at the 37th Annual Frequency Control Symposium (AFCS). The paper was not published in the Proceedings of the 37th AFCS because a security classification question was unresolved at the time the Proceedings went to print.

FIGURE 3



Figures 2 and 3 have the same time axis. During the period when the temperature increased linearly the current density increased exponentially, as expected. Electrodiffusion occurred during this period; however, the process was masked by current density increase due to temperature rise. The temperature stopped increasing at the 40 hour mark, stabilizing at 500 degrees C. At this point the electrodiffusion process becomes clearly evident. The current density begins to decrease exponentially, mostly because the density of migrating ions in the bar is decreasing. In addition, some Z-channels become blocked, halting the migration of ions down that channel thereby further reducing the current density.

#### OHMICITY TEST

After 172 hours of sweeping the electric field was decreased to 0 volts/cm to begin an ohmicity test. An ohmicity test examines the relationship between the current density and the electric field. If the electrodiffusion process has stopped the current density will vary linearly with the electric field. Figure 4 is a profile of the electric field intensity and temperature throughout the sweeping run of bar S001. Figure 5 shows the data collected during the ohmicity test.

FIGURE 4

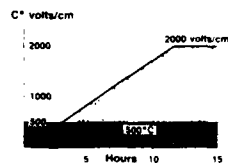
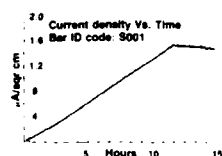


FIGURE 5

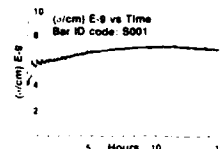


The ohmicity test for bar S001 shows a nearly linear relationship between the current density and the electric field; however, it is slightly exponential. The conductance of the bar is also important. In order to compare data from different size bars the volume is included in the calculation giving us units of conductance/cm instead of conductance.

$$\text{conductance/cm} = \frac{\text{Amps}}{\text{volume (cm}^3\text{)}} / \text{electric field}$$

Figure 6 is a graph of the conductance/cm for bar S001. The data was taken during the ohmicity test. The time axis is the same as figures 4 and 5. Like the ohmicity test, the conductance/cm shows the electrodiffusion process is continuing. If the electrodiffusion process was completed it is predicted the conductance/cm would be constant over a varying electric field.

FIGURE 6



#### THE SECOND CLASS OF EXPERIMENTS

Bar A005 is a member of the second class of experiments. The second class of experiments examined the effect of an electric field on the electrodiffusion process. The temperature was held constant while the electric field was increased linearly. Figure 7 is a profile of the electric field and temperature throughout the sweeping run of bar A005. Bar A005 is an electronic grade 'AT' bar. Figure 8 is a graph of the current density data collected during the sweeping run.

FIGURE 7

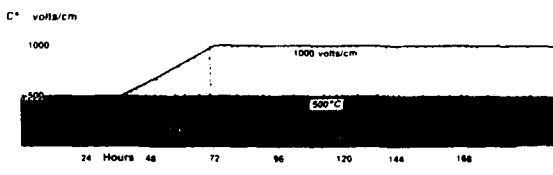
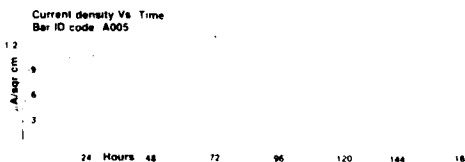


FIGURE 8



Interestingly, the current density data from the second class of experiments does not look like the data from the first class. The current density increases rapidly during the first few hours, and then decreases for nearly 12 hours. The current density does not always reach a maximum when the electric field reaches a maximum. All bars tested so far from the second class of experiments reached at least 90% of the maximum current density during the first few hours. The current density decreased after the electric field reached a maximum. The decrease, however, looks less exponential than the first class of experiments. The reasons for this difference between the two classes are unclear.



### OHMICITY TEST

The electrodiffusion process continued for 100 hours after the electric field peaked at 1000 volts/cm. An ohmicity test was conducted at this point. The electric field was reduced to 0 volts/cm and then raised over a 12 hour period to 2000 volts/cm. Figure 9 is a graph of the electric field intensity and temperature during the time of the ohmicity test. Figure 10 is a graph of the current density data collected during the ohmicity test of bar A005.

FIGURE 9

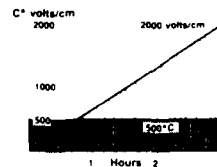
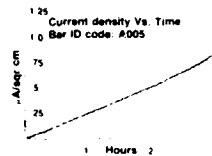
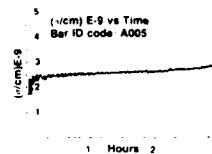


FIGURE 10



The current density is again nearly linear; however, the electrodiffusion process is continuing. The electric field was held constant for three hours after the ohmicity test. Figure 10 shows a slight decrease in the current density after the electric field stabilized at 2000 volts/cm. Figure 11 is a graph of the conductance/cm during the ohmicity test. The conductance is nearly a constant over the electric field range tested; however, the electrodiffusion process is still continuing after 100 hours.

FIGURE 11



### LOWER TEMPERATURE ELECTRODIFFUSION

Bar A001 is a cultured premium Q pure Z 'AT' bar. This bar was swept like the first class of experiments except

FIGURE 12

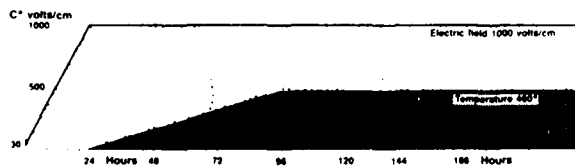
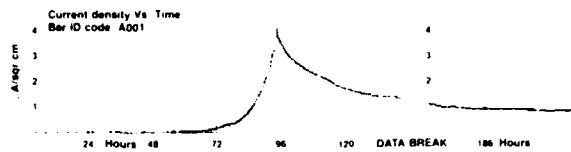


FIGURE 13



the temperature was set at 460 degrees C instead of 500 degrees C to study the effect of temperature on the completeness of the electrodiffusion process. Figure 12 is a graph of the electric field and temperature during the sweeping run. There was no current detected during the first 24 hour period. Figure 13 is a graph of the current density during the sweeping run.

Like the other class one experiments the current density peaked at the same time the temperature reached a maximum. The current density dropped off exponentially after the temperature stabilized at 460 degrees C, and after 224 hours the current density stabilized at .09  $\mu$ A/sq. cm.

### OHMICITY TEST FOR LOWER TEMPERATURE BAR

The ohmicity test for bar A001 was conducted after 224 hours of sweeping. Figure 14 is a graph of the temperature and electric field during the ohmicity test. Figure 15 is a graph of the current density during the ohmicity test. The current density increased exponentially during the ohmicity test. In comparison, both of the previous ohmicity tests showed nearly a linear relationship between the current density and electric field. The increase in temperature from 460 degrees C to 500 degrees C improved the linear relationship between current density and electric field.

FIGURE 14

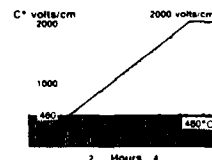


FIGURE 15

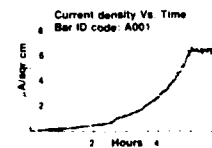
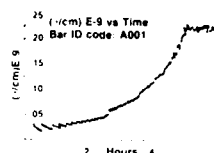


Figure 16 is a graph of the conductance/cm during the ohmicity test of bar A001. Like the current density graph the conductance/cm increases exponentially with increasing electric field intensity showing the incompleteness of sweeping.

FIGURE 16



## NATURAL QUARTZ ELECTRODIFFUSION

Bar S004 is a 'SC' natural quartz bar. This bar was swept as part of the second class of experiments and is presented as an example of natural quartz electrodiffusion. Figure 17 is a graph of the electric field and temperature during the sweeping of bar S004. Figure 18 is a graph of the current density data collected during the sweeping run. Part of the cooling down of the oven has been included in this data. The current density decreases exponentially during the cooling cycle of the oven. The current density data is presented in figure 18. The current density increased rapidly during the first few hours similar to the class two experiments. The current density decreased some after the 72 hour mark; however, the decrease is not significant.

FIGURE 17

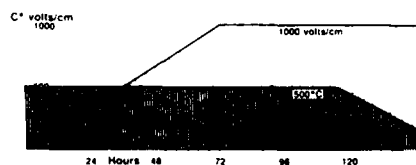
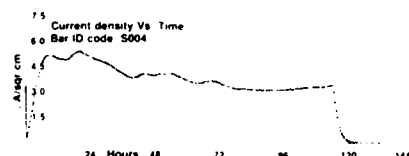


FIGURE 18



The conductance/cm data is compared to current density data for each class of experiments in Figures 19 through 22. The first two Figures show the data for bar S001. Both graphs look very similar. This data is from the first class of experiments which raised the temperature while the electric field was held constant. Figures 21 and 22 show a very different situation. This set of data is from bar A005 a member of the second class of experiments, showing a very smooth exponential decrease in conductance/cm.

FIGURE 19

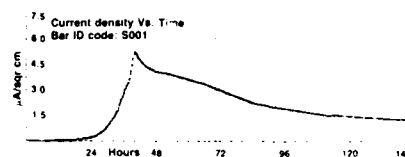


FIGURE 20

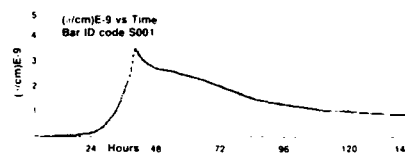


FIGURE 21

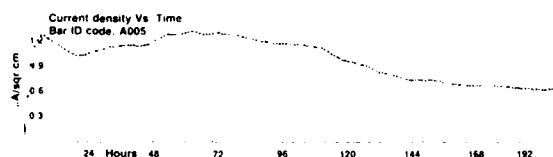
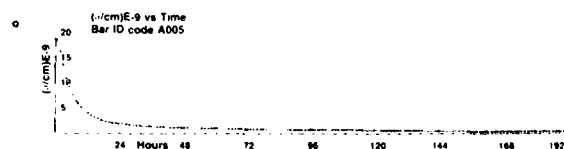


FIGURE 22



## IRRADIATION OF RESONATORS BUILT FROM PIEZO SWEPT QUARTZ

Resonators fabricated from Piezo swept quartz were irradiated two different times. Cobolt 60 was used as a source of gamma radiation. The first irradiation was 1 megarad. The data is summarized below.

PIEZO CRYSTAL COMPANY  
ELECTRODIFFUSION DATA—BAR A003

## BAR DATA

Quartz: RIGHT-HANDED PREMIUM Q PURE Z  
Volume: 33.49 CUBIC CM  
Z-Area: 21.75 CM

ELECTRODIFFUSION CONTROL PARAMETERS  
Temp: 500 DEGREES C  
Time: 102 HOURS  
Electric Field: 1000 VOLTS/CM

ELECTRODIFFUSION DATA  
Current Density at 102 Hours: .11  $\mu$ A/Square cm

#### RADIATION HARDNESS DATA

##### RADIATED WITH 1 MILLION RADS

CRYSTAL: 10 MHZ 3RD OVERTONE AT				
S/N	TURNOVER	INITIAL FREQUENCY	FREQUENCY AFTER 1 MRAD	DELTA F/RAD
1	71 C	9,999,989.0 Hz	9,999,989.3 Hz	+ 3.0E-14
3	70 C	9,999,960.7 Hz	9,999,959.8 Hz	- 9.0E-14
4	65 C	9,999,991.0 Hz	9,999,992.5 Hz	+ 1.5E-13
5	65 C	10,000,006.3 Hz	10,000,007.2 Hz	+ 9.0E-13
6	68 C	9,999,979.1 Hz	9,999,979.1 Hz	+ 0.0E-99
7	68 C	9,999,971.9 Hz	9,999,973.8 Hz	+ 1.9E-13
9	68 C	9,999,977.8 Hz	9,999,980.2 Hz	+ 2.4E-13
10	70 C	9,999,928.9 Hz	9,999,931.9 Hz	+ 3.0E-13
11	68 C	9,999,942.7 Hz	BROKEN	N/A

MEAN OF ABSOLUTE VALUES + 1.4E-13/RAD

##### CONTROL GROUP—UNIRRADIATED

2	67 C	9,999,964.4 Hz	9,999,965.1 Hz	+ 7.0E-14
8	69 C	9,999,960.7 Hz	9,999,960.8 Hz	+ 1.0E-14

MEAN OF ABSOLUTE VALUES + 4.0E-14

A linear model for the change in frequency due to irradiation has been assumed. The frequency change at low levels of irradiation may be significant. A more complete set of data needs to be taken in order to define the changes in frequency during irradiation. The same crystals were irradiated again with 9 more megarads. The change in frequency due to the last nine megarads of gamma radiation was undetectable. The control group and the irradiated group changed frequency  $2.5 \times 10^{-14}$ /Rad and  $2.1 \times 10^{-14}$ /Rad respectively. The resolution of the measurements is only  $2 \times 10^{-14}$ .

#### CONCLUSIONS

The current density increases exponentially with temperature. The first class of experiments shows this rise effectively. The converse is also true. The current density decreases exponentially with decreasing temperature, as was shown in the cooling down of bar S004.

The current flow as a function of electric field approaches an ohmic condition with time. The ohmicity test indicated the linear relationship between electric field and current density at the end of the sweeping runs. Both classes of experiments reached nearly the same degree of linearity after approximately 170 hours, with the exception of the bar which was swept at 460 degrees C.

The higher the temperature the more quickly the relationship between electric field intensity and temperature approaches a linear relationship. The limiting temperature is the alpha-beta turning point around 573 degrees C.

#### PROPOSALS

1. Define an acceptable test for radiation hardness in order to compare different processing techniques.
2. Identify the electrical conditions which signal the point when the electrodiffusion process has reached an acceptable level of radiation hardness.
3. Measure the ohmicity of the quartz during the sweeping process and use it as one of the identifying conditions for radiation hardness.

#### REFERENCES

1. R. N. Brown, J. J. O'Conner, A. F. Arminston, "SWEEPING AND Q MEASUREMENTS AT ELEVATED TEMPERATURES IN QUARTZ," Rome Air Development Center, In-House Report RADC-TR-79-175, May 1979
2. D. R. Koehler, "RADIATION-INDUCED CONDUCTIVITY AND HIGH TEMPERATURE Q CHANGES IN QUARTZ RESONATORS," Proc. 35th Ann. Freq. Control Symposium, pp. 322-328, 1981
3. J. J. Martin, L. E. Halliburton, and R. B. Bossoli, "THE INFLUENCE OF CRYSTAL GROWTH RATE AND ELECTRODIFFUSION (SWEEPING) ON POINT DEFECTS IN  $\alpha$ -QUARTZ," Proc. 36th Ann. Freq. Control Symposium, pp. 77-81, 1982
4. F. Euler, H. G. Lipson, A. F. Arminston, "CHARACTERIZATION OF ALKALI IMPURITIES IN QUARTZ," Proc. 36th Ann. Freq. Control Symposium, pp. 115-123, 1982

I wish to thank Wallace Samuelson for his generous guidance. His expertise in resonator technology, and his considerable patience has been a strong motivating force to me personally and professionally.

# AN X-RAY IRRADIATION SYSTEM FOR TOTAL-DOSE TESTING OF QUARTZ RESONATORS

Leslie J. Palkuti and Quang T. Truong

Advanced Research and Applications Corporation  
Sunnyvale, CA 94086

## Abstract

An x-ray irradiation system has been developed for the evaluation of the total-dose sensitivity of quartz resonators. The x-ray radiation response of premium-Q, swept (PQS), resonators in ceramic flat-packs was compared with in-situ cobalt-60 irradiations. A multi-frequency reflectometer measurement system incorporating a crystal oven with an x-ray window was used simultaneously to measure the radiation response of the crystal c-mode frequency and a temperature-sensitive frequency. Excellent correlation between x-ray and cobalt-60 irradiations was obtained in both the deposited dose as determined by calorimetry and in the radiation-induced frequency shifts of the resonator c-mode.

These correlation studies indicate that the ARACOR Model 4100 X-ray Irradiation System produces the same radiation response in crystal resonators that are obtained with in-situ cobalt-60 irradiations. Combined with reflectometer measurements, this x-ray irradiation method provides a unique capability for quick turnaround radiation characterization at the resonator stage of fabrication. Additional advantages of the method include the wide range of dose rates (0.01 to 300 rad/sec) available in an instrument that can be utilized in a production-testing area.

## Key Words:

Quartz crystal, quartz resonator, SC-cut, radiation sensitivity, x rays, cobalt-60, total-dose sensitivity, reflectometer.

## Introduction

The total-dose radiation-induced frequency offsets of precision quartz oscillators are important in modern communication, navigation and radar systems for both terrestrial and space applications. These total-dose radiation effects produced primarily in the quartz resonator are dependent on the growth and processing of the quartz blank as well as the processing used to package the crystal. At the present time, no demonstrated electrical measurement technique has been developed to evaluate these total-dose effects in quartz resonators. Therefore, extensive effort and cost must be expended for radiation exposures for screening purposes and qualification tests of resonators intended for precision timing applications in space and other military applications. In addition, military applications require the development of resonators that exhibit reduced radiation-induced frequency shifts. These development programs also require extensive resonator radiation characterization with quick turnaround for timely feedback for process modifications. The standard methods for radiation characterization require extensive lead time and are costly because oscillators must be fabricated and tested at remote radiation locations such as cobalt-60, Van de Graaff, flash x-ray or linear accelerator

facilities. In addition, extensive equipment must be transported to remote locations, since the oscillators must be instrumented during radiation exposure.

To overcome the disadvantage of remote total-dose radiation testing and provide quick-turnaround radiation characterization, an x-ray irradiation system was developed to provide a uniform, intense and characterized x-ray beam.<sup>1</sup> This x-ray system was successfully demonstrated by correlation tests with cobalt-60 exposures for total-dose testing of semiconductor integrated circuits directly at the wafer stage of fabrication.<sup>2</sup> Preliminary analysis indicated that similar x-ray irradiation can be implemented for in-situ characterization of quartz resonators provided a suitable instrumentation system was developed. To provide the frequency measurements at the resonator stage of fabrication a multichannel reflectometer<sup>3</sup> measurement system was utilized with a specifically designed temperature chamber adapted with an x-ray window. In this paper, we describe the x-ray irradiation system as utilized for quartz resonator irradiations including the temperature control and frequency measurement instrumentation. In addition, x-ray deposition calculations for various quartz blank geometries are compared with measurements and the results of correlation tests comparing x-ray irradiations with cobalt-60 exposures are reported.

## Experimental Procedure

The schematic of the x-ray irradiation system, the PIN diode dosimeter, temperature chamber and frequency measurement instrumentation are shown in Figure 1. A detailed description of ARACOR Model 4100 Semiconductor Irradiation System, including details on the dosimetry calibration, is given in reference 1. For quartz resonator irradiations, the semiconductor wafer probe station in the Model 4100 was replaced with a quartz resonator temperature chamber (Brightline Model 2707). This temperature chamber is a double crystal oven specifically fabricated with a low-Z, x-ray window (2.5-cm polyurethane foam and 1-mm Al) and includes a remote temperature controller. With the x-ray window, the oven had a thermal gain of about 2000.

To measure the average x-ray dose deposited in the crystal blank, the PIN diode dosimeter described in reference 1 was utilized. Suitable filters, consisting of samples of the materials used in the oven, resonator enclosure, and crystal blank were interposed between the x-ray source and the dosimeter to simulate the actual setup that was irradiated.

The resonator frequencies were measured utilizing a multichannel reflectometer (Brightline 2107) and an HP 5335A precision counter utilizing a reference frequency provided by a rubidium atomic frequency standard (Efratom). The Model 2107 Reflectometer is an improved version of the instrument described in reference 3. An HP 9816 controller was used to operate the irradiation system as well as the measurement system via an IEEE-488 interface.

To obtain a direct measurement of the crystal blank temperature during irradiation, a temperature-

\* This work was supported by the U.S. Army Electronics Technology and Devices Laboratory under Contract DAAB08-83-C-J006.

sensitive mode in addition to the normal c-mode of the resonators was also monitored by the multichannel reflectometer. The direct temperature measurement of the crystal during irradiation provided (1) a direct measure of the radiation dose rate absorbed by the crystal via calorimetry and (2) direct assurance that the radiation-induced frequency shifts in the c-mode were not the result of radiation-induced heating. In these experiments the maximum radiation dose rates were limited so that the radiation-induced temperature increases in the c-mode frequency were negligible.

A plot showing the fractional frequency of the c-mode,  $f_C$ , and the temperature sensitive mode,  $f_T$ , for a typical 12-hour measurement sequence is shown in Figure 2. The measured Allan variance,  $\sigma(\tau)$ , for  $f_C$  of about  $1.5 \times 10^{-10}$  for 10-sec averaging times was typical for the reflectometer. For the cobalt-60 irradiations, sixty-foot cables were required between the resonator and the reflectometer, resulting in a five times increase in the instrument noise. To improve the sensitivity of the reflectometer measurements, digital signal processing was sometimes applied to extract the radiation-induced frequency shifts. With this digital filtering, the sensitivity of the measurement system was improved to about  $3 \times 10^{-11}$ . The temperature fluctuations measured by  $f_T$  in Figure 2 are the result of temperature excursions of the crystal blank due to temperature fluctuations in the laboratory. The sensitivity of the temperature measurement was significantly better than  $1 \text{ m}^\circ\text{C}$ .

The temperature coefficient of the reflectometer was characterized by subjecting the measurement system to thermal cycling. These measurements indicated a negligible temperature coefficient (less than  $1 \times 10^{-11}$  per  $\text{m}^\circ\text{C}$ ) for the two channels used in these experiments. Note in Figure 2 that the laboratory temperature fluctuations ( $f_T$ ) are not reproduced in the c-mode frequency data.

The samples used in these experiments were SC-cut resonators enclosed in ceramic ( $\text{Al}_2\text{O}_3$ ) flatpacks. The details of the fabrication of such resonators are outlined in reference 4 and the references therein. The crystal blanks were fabricated from premium-Q cultured quartz material that had been electrodiffused (swept) in air. Resonators were tested from two groups with a c-mode frequency of 10.23 (3d harmonic) and 5.115 (fundamental) MHz. Seven resonators were studied.

The x-ray radiation response of each resonator was characterized over the dose range from 3 rad( $\text{SiO}_2$ ) to  $10^6$  rad( $\text{SiO}_2$ ) covering both the low-dose and high-dose regimes. Some crystals were irradiated to  $10^7$  rad( $\text{SiO}_2$ ). The following x-ray irradiation procedure was utilized. The resonator was mounted into the oven and the oven temperature set to the lower turning point (approximately  $70^\circ\text{C}$ ). After a two-day stabilization period, the initial low-dose response was determined by irradiating to  $10^4$  rad( $\text{SiO}_2$ ) with a dose rate from 10-150 rad per min. A two-day annealing period was followed by irradiation to  $10^6$  rad( $\text{SiO}_2$ ) with a dose rate ranging from 250-7500 rad per min. Another two-day annealing period was followed by additional low-dose irradiations. Between each low-dose test the resonator was allowed to anneal for at least 24 hours. Low-dose irradiations were also performed after a 30-day annealing period.

Cobalt-60 irradiations were conducted on selected resonators in a dry-room cobalt source (International Neutronics, Inc., Palo Alto, CA). Dosimetry was performed using Far West fiber optic dosimeters that are

traceable to NBS. The same in-situ measurement setup shown in Figure 1 was used with the addition of longer cables. The cobalt-60 irradiations were conducted at dose rates of 250 and 1.5 Krad per min. The cobalt-60 irradiations had to be limited to about  $10^5$  rad( $\text{SiO}_2$ ) so that radiation-induced degradation to the resonator-oven heater elements was small. Note that the heater elements were shielded during the x-ray irradiations.

#### Dose Deposition in Crystal Blanks

The tungsten characteristic radiation and the bremsstrahlung produced by the x-ray tube are attenuated as they pass through the resonator oven and the resonator package before being deposited in the quartz blank. The beam is also attenuated as it passes through the crystal blank. To obtain a reasonably uniform dose distribution in quartz blanks of the various thicknesses, prefiltering of the x-ray beam was optimized. In addition, the x-ray power supply was operated near its maximum voltage (50 to 60 kV) to provide the most uniform deposition profile in the quartz blanks.

The material configuration used in these experiments is shown in Figure 3. The resonator package was thermally insulated from the inner oven by polyurethane foam. The inner oven wall of 20-mils Al provided adequate thermal isolation. Additional foam isolated the inner and outer ovens. A  $1.5\text{-cm}^2$  window was cut into the outer oven to reduce x-ray attenuation. Al filtering was added outside the oven to improve the dose uniformity in the crystal blank.

The highest average dose rates that were achieved with the x-ray irradiation system for the ceramic and Kovar packages are shown in Figure 4. The additional attenuation by the Kovar package is evident in the figure. In glass-enclosed resonators, dose rates similar to ceramic packages are obtained. Maximum dose rates of 3.5 and 20 Krad per min could be achieved for the Kovar and ceramic packages, respectively. Thus, a  $10^6$ -rad( $\text{SiO}_2$ ) irradiation can be performed in 50 minutes.

Depth-dose calculations were performed to determine the dose uniformity in the quartz blanks. Utilizing the x-ray spectrum measured by Brown, et al.,<sup>5</sup> and x-ray cross sections tabulated by McMaster, et al.,<sup>6</sup> the x-ray dose deposition was determined for the material stack shown in Figure 4. From these data, the dose uniformity in various quartz blanks could be determined. The front-to-back dose ratios are plotted in Figure 5 along with experimental data measured with the PIN diode. The tradeoff between dose rate and dose uniformity is evident. Note that for dose rates less than 1 Krad/min, a  $\pm 5$  percent dose uniformity is obtained. The data shown in Figure 5 can be used to estimate the dose uniformity for both the ceramic and Kovar packages. For example, at the maximum irradiation rate, the dose variation in a 40 mil crystal blank is  $\pm 15$  and  $\pm 10$  percent for a ceramic and a Kovar package, respectively.

#### Dose Measurement by Calorimetry

The deposited dose in the crystal blank could be measured directly by monitoring the crystal temperature during irradiation. Since the crystal was enclosed in a temperature chamber, these measurements could be made without influence of external effects. The temperature rise,  $\Delta T$ , of a crystal blank subjected to irradiation by a steady dose rate of ( $\dot{Q}/m$ ) rad per min that is turned on at  $t=0$  can be expressed by:

$$\Delta T = \frac{K}{C} \left( \frac{\dot{Q}}{m} \right) \left[ 1 - \exp(-t/K) \right] \quad (1)$$

where K is the inner oven time constant and C is the specific heat of  $\alpha$ -quartz. Thus, the steady-rate temperature rise is

$$\Delta T_{ss} = \frac{K}{C} \left( \frac{\dot{Q}}{m} \right) \quad (2)$$

and is a function of the ratio of the time constant and the specific heat. From the initial temperature rise, viz.:

$$\frac{\Delta T}{\Delta t} = \frac{1}{C} \left( \frac{\dot{Q}}{m} \right) \quad (3)$$

the specific heat can be directly determined.

Monitoring the crystal temperature as a function of time verified the form of equation (1) and a value for K of 280 sec was determined. Equation (2) was experimentally confirmed by irradiations performed at a number of dose rates for both x rays and cobalt 60. The x-ray and cobalt-60 irradiations were characterized by a K/C of 47 m°C per Krad, as shown in Figure 6. The experimental verification of equation (3) is shown in Figure 7 for both cobalt 60 and x rays. The same value of C=0.252 cal/g°C was determined for the x rays and cobalt 60. This value of C is within 20 percent of handbook values<sup>7</sup> and is within the limit of the accuracy of both x-ray<sup>1</sup> and cobalt-60<sup>8</sup> dosimetry. These results demonstrate that the measured and calculated deposition in the quartz blanks can be accurately determined.

#### Resonator Irradiation Results

Figure 8 is a plot of the radiation measurements of a 10.23-MHz(3rd overtone) resonator that was irradiated with both x rays and by cobalt-60 gamma rays. The features of the responses shown are typical for all the resonators irradiated. The similarity between the cobalt-60 and x-ray irradiations are evident in these data.

Initial irradiations for both x rays and cobalt 60 resulted in large negative frequency shifts followed by a smaller positive shift at low doses as shown in Figures 9 and 10 for x rays and cobalt 60, respectively. Although the initial radiation responses for all the resonator studies were negative, the magnitude of these frequency shifts was highly variable, ranging between 0.1 and 40 ppb for the 10.23-MHz(3d overtone) and between 1 and 10 ppb for the 5.115-MHz(fundamental) resonators.

The detailed cobalt-60 and x-ray responses for a 10.23-MHz(3d overtone) resonator are shown on a linear scale in Figures 11, 12 and 13. The preirradiation doses for each irradiation exposure are indicated. For each exposure the crystal temperature during irradiation is also indicated. The similarity in the frequency shifts produced by cobalt 60 and x rays is evident. In Figure 14 a typical high-dose radiation response is given illustrating the high-dose rate capability of the irradiation system. This measurement system allows the characterization of resonators with a wide range of frequencies in the same setup. As an example, both the low- and high-dose responses (after preirradiation) are shown in Figures 15 and 16 for a 5.115-MHz(fundamental) resonator.

#### Annealing Behavior

In addition to the frequency changes that occur during irradiation, quartz resonators will typically exhibit frequency shifts that are significantly larger than the normal aging response for about 1 to 3 days

after radiation exposure. Often these frequency shifts are in a direction to return the crystal frequency to its preirradiation value (see, for example, the response in Figure 11) and, hence, the term annealing applies. However, in a number of instances the resonator frequency shift continues after irradiation in the same direction as the frequency was shifting during irradiation (see, for example, the response in Figure 9) and, therefore, exhibits reverse annealing behavior. For simplicity, we use the term annealing for frequency shifts following irradiation exposure, irrespective of the sign of the responses.

The x-ray irradiation procedure described here is particularly suited to the characterization of the annealing responses because the resonator can be monitored continuously without interrupting either the thermal or the electrical environment of the resonator. Examples of the annealing responses of some resonators are given below.

For the resonators measured, the annealing response (both in magnitude and duration) varied depending on the irradiation history of the resonator. Usually, longer annealing responses were observed when the resonators were irradiated to high doses. In Figure 17 the annealing behavior of a 10-MHz (3d overtone) resonator is shown after an initial 25-Krad(SiO<sub>2</sub>) exposure. The negative frequency shift of 3 ppb over a 24-hour period continued in the same direction as the frequency was shifting near the end of the radiation exposure. In Figure 18 the annealing behavior after 10 Krad(SiO<sub>2</sub>) is shown. The radiation response of this crystal had been stabilized by preirradiation to a dose in excess of 10<sup>6</sup> rad(SiO<sub>2</sub>). Annealing periods of about 8-48 hours were observed.

#### Conclusions

An x-ray irradiation procedure has been developed for the characterization of radiation-induced frequency shifts in quartz blanks at the resonator stage of fabrication. Utilizing the ARACOR Model 4100 Irradiation System, radiation exposures over a dose-rate range of 0.01 and 300 rad(SiO<sub>2</sub>) can be performed in a production facility without requiring off-site testing. Maximum dose rates of 2 and 18 Krad(SiO<sub>2</sub>) per min are obtained for ceramic and Kovar packaged resonators, respectively, with a dose uniformity of better than  $\pm 15$  percent. A frequency measurement system employing a multichannel reflectometer and remote oven allowed resonator-response measurements without the influences of oscillator component degradation. In addition, the multichannel measurements provided a means to directly monitor the crystal temperature and, therefore, the crystal could be used as its own radiation dosimeter.

Excellent correlation was obtained between cobalt 60 and x rays for the energy deposited (absorbed dose) as measured by calorimetry and also for the radiation-induced frequency shifts (radiation response). No significant differences between cobalt-60 and x-ray radiation responses were observed in both the low-dose and high-dose regimes. The instrument was also shown to be highly suitable for measurements of annealing effects in quartz resonators.

Finally, the results reported here suggest that the x-ray irradiations, combined with reflectometer frequency measurements, can provide an accurate and detailed characterization of quartz resonator radiation response without the need for oscillator fabrication.

tion or off-site testing. The procedures outlined are convenient and cost-effective and after an investment in the required instrumentation can be performed as a minor modifications of a resonator testing sequence directly on the production floor.

#### Acknowledgments

We thank J. R. Vig of the U. S. Army Electronics Technology and Devices Laboratory for suggesting the use of and kindly supplying a reflectometer in the dual mode configuration. Also, we thank J. Gualtieri of the same organization for providing the test resonators and some of the instrumentation employed in these measurements. We are grateful to C. Stone of Brightline Corporation for fabricating the resonator ovens and providing us with assistance in the operation of the Brightline Reflectometer.

#### References

1. L. J. Palkuti and J. J. LePage, "X-Ray Wafer Probe for Total-Dose Testing," IEEE Trans. on Nuclear Science, Vol. NS-29:6, December 1982.
2. L. J. Palkuti, "Automated Radiation Testing of IC's at the Wafer Stage," SEMICON/84, San Mateo, CA, May 1984.
3. C. S. Stone and O. J. Baltzer, "A Frequency Domain Reflectometer for Quartz Resonator Investigations," Proc. of the 36th Annual Symposium on Frequency Control, pp 321-326, 1982.
4. R. L. Filler, J. M. Frank, R. D. Peters and J. R. Vig, "Polyimide Bonded Resonators," Proc. of the 32nd Annual Symposium on Frequency Control, pp 181-186, 1978.
5. D. B. Brown, J. V. Gilfrick and M. Peckarar, "Measurement and Calculation of Absolute Intensities of X-Ray Spectra," J. Appl. Phys., 46, 4537, 1975.
6. W. H. McMaster, N. K. Del Grande, I. H. Mallett, J. H. Hubbell, "Compilation of X-Ray Cross Sections," University of California Research Library, UCRL-50174, 1969.
7. "Thermodynamic Properties of Elements and Oxides," Handbook of Chemistry and Physics, pp D-51, 1982-83.
8. T. Rentzell, International Neutronics, private communications.
9. L. J. Palkuti, cobalt-60 radiation response of AT-cut resonators, unpublished data.

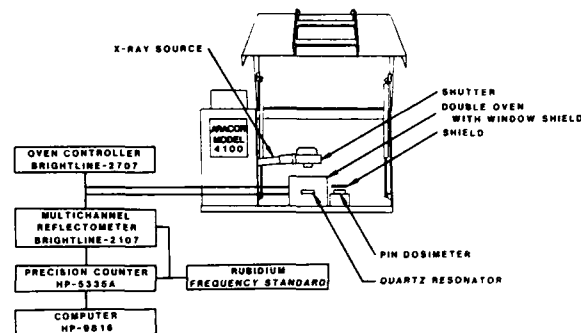


Figure 1. Schematic of x-ray irradiation setup.

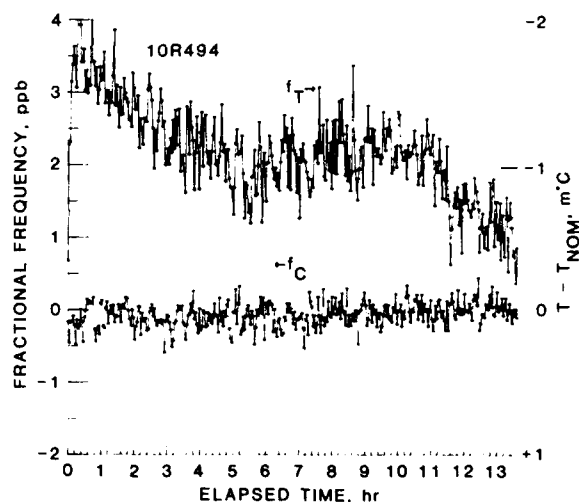


Figure 2. Frequency stability of the c-mode,  $f_C$ , and the temperature-sensitive mode,  $f_T$ , for measurements conducted overnight. Frequency measurements were made with a 10 second averaging period.

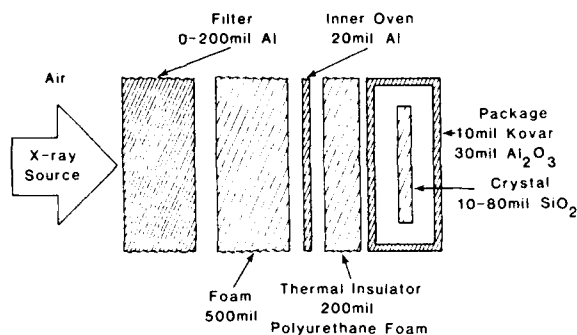


Figure 3. Schematic showing the materials between the x-ray beam and the quartz blank. Al prefiltering was used to improve the dose distribution in the quartz blank at the expense of irradiation dose rate.

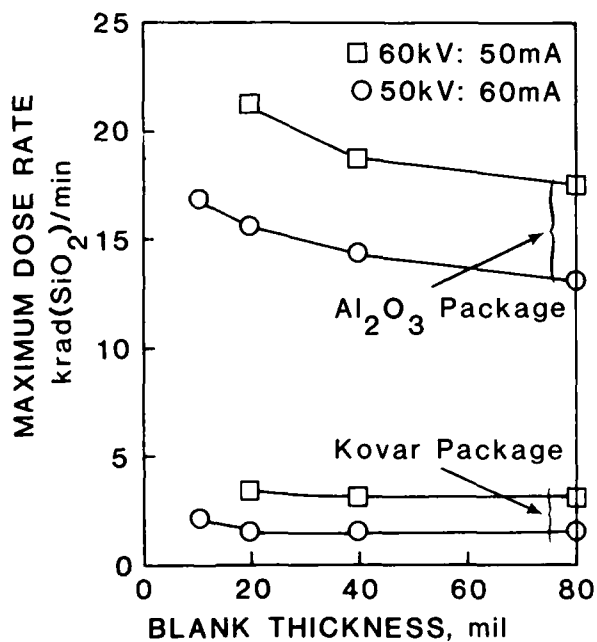


Figure 4. The highest average dose rate absorbed in the quartz resonators operated in the B-2707 oven. The quartz blank was positioned at 7.5 cm from the x-ray tube. The lid thickness for the ceramic and metal packages were 30 mils and 10 mils, respectively.

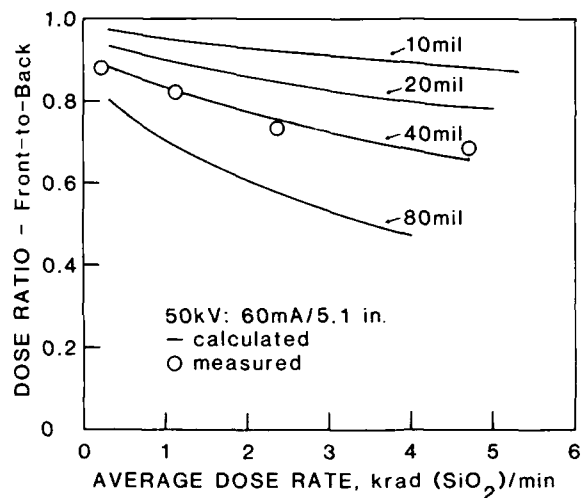


Figure 5. Comparison of calculated and experimental x-ray dose deposition for quartz blank thicknesses ranging from 10 to 80 mils. The dose rate is reduced by additional prefiltering with Al sheets. The distance between the blank and the x-ray tube was 7.5 cm.

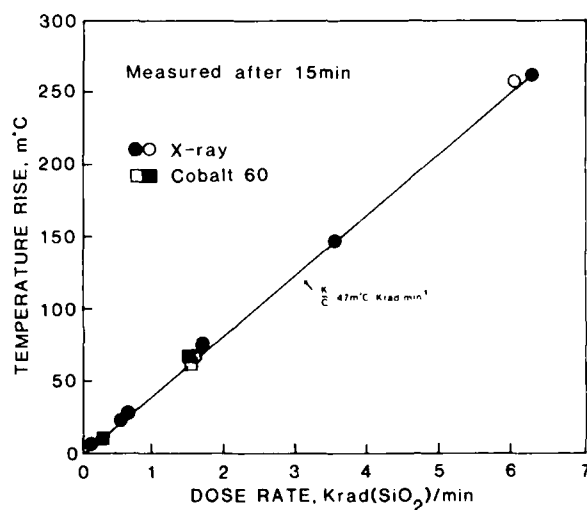


Figure 6. The steady-state temperature rise during x-ray and cobalt-60 irradiation.



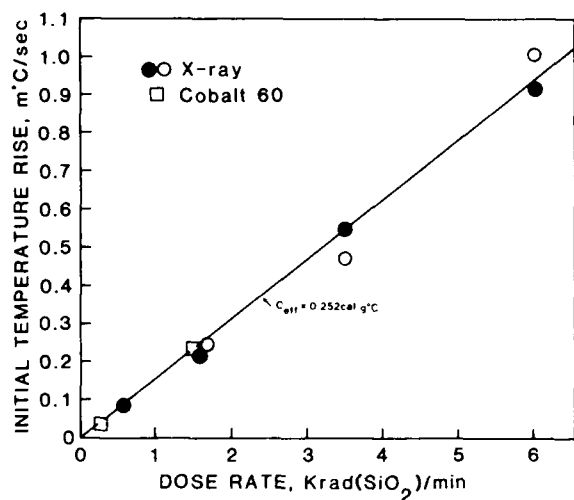


Figure 7. Direct measurement of the specific heat of  $\alpha$  quartz during x-ray and cobalt-60 irradiations.

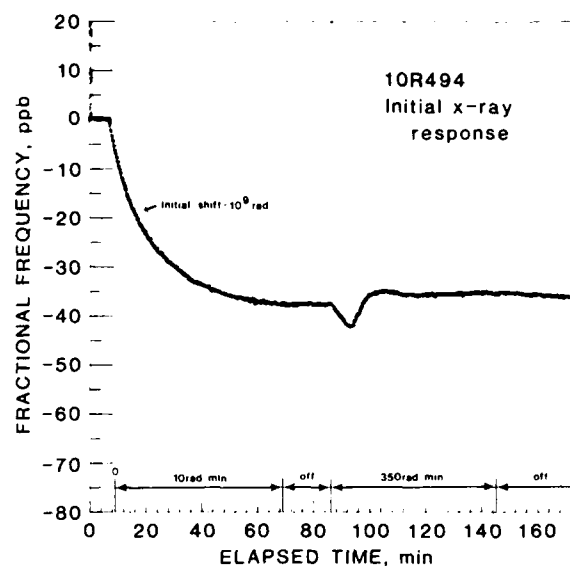


Figure 9. Initial x-ray radiation response for a 10.23 MHz (3d overtone) resonator.

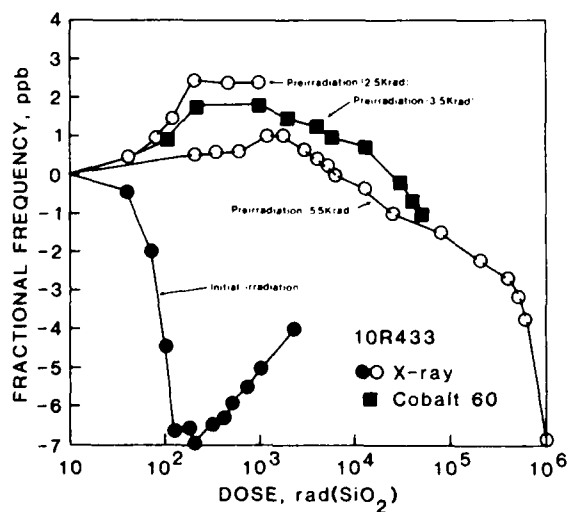


Figure 8. Summary of the radiation response of 10.23 MHz (3d overtone) resonator to both x-ray and cobalt-60 irradiation.

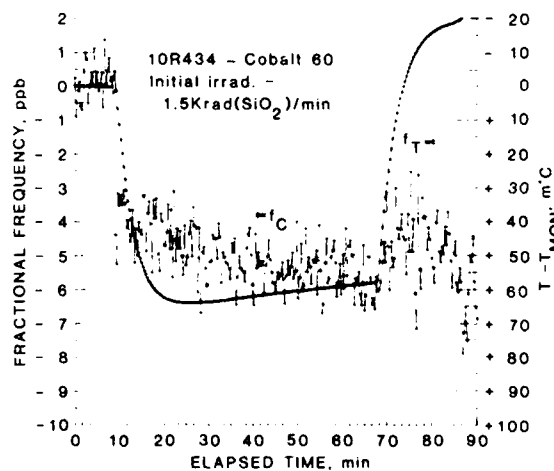


Figure 10. Initial cobalt-60 radiation response of a 10.23 MHz (3d overtone) resonator. The temperature response during radiation exposure is also shown.

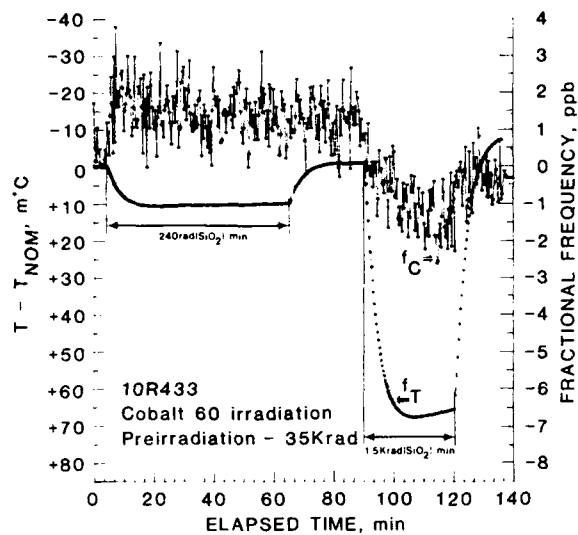


Figure 11. Cobalt-60 radiation response of a 10.23 MHz (3d overtone) resonator for 240 and 1500 rad per minute.

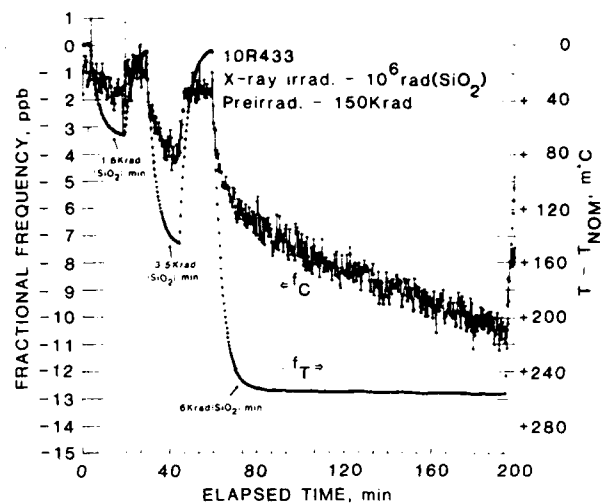


Figure 13. X-ray radiation response of a 10.23 MHz (3d overtone) resonator to a dose of  $10^6$  rad(SiO<sub>2</sub>).

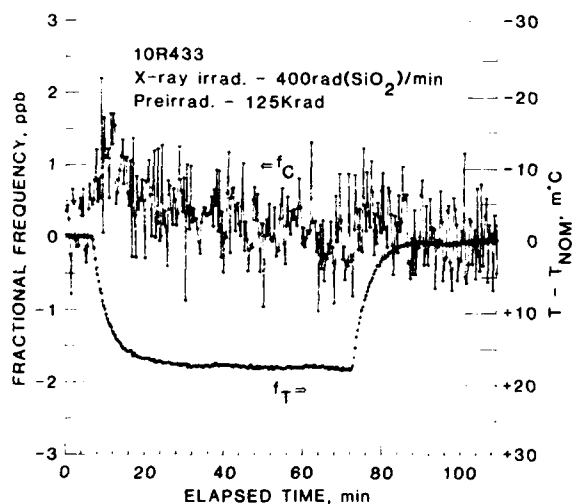


Figure 12. X-ray response of a 10.23 MHz (3d overtone) resonator at 400 rad per minute.

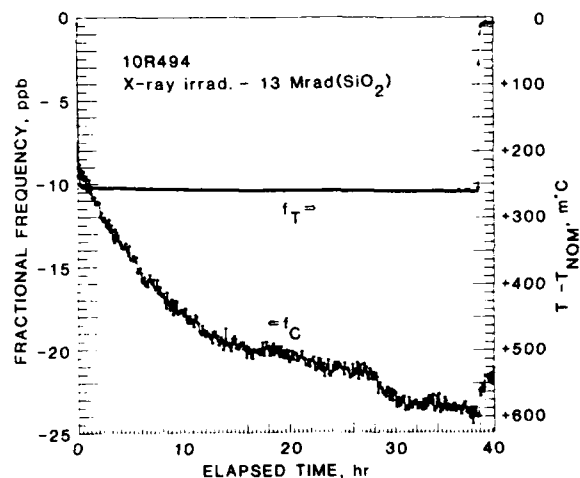


Figure 14. X-ray response of a 10.23 MHz (3d overtone) resonator to a dose of  $1.3 \times 10^7$  rad(SiO<sub>2</sub>).

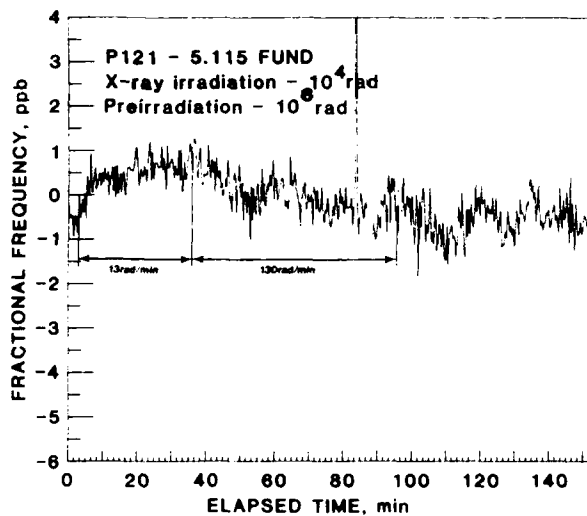


Figure 15. Low-dose x-ray radiation response for 5.115 MHz (fundamental) resonator.

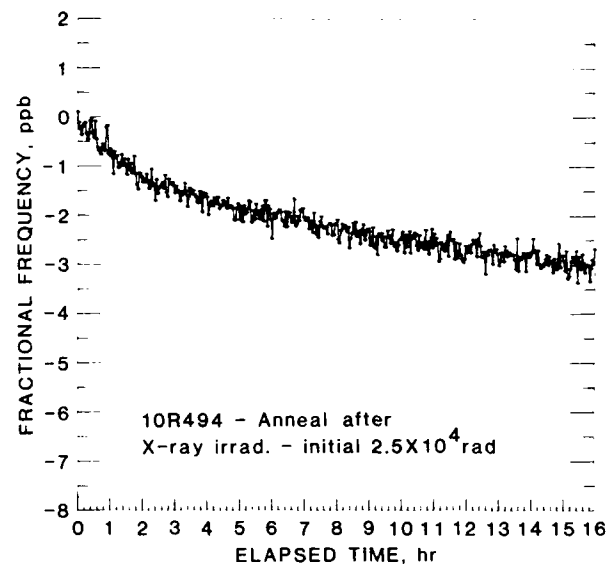


Figure 17. Annealing behavior of a 10.23 MHz (3d overtone) resonator after the first irradiation exposure.

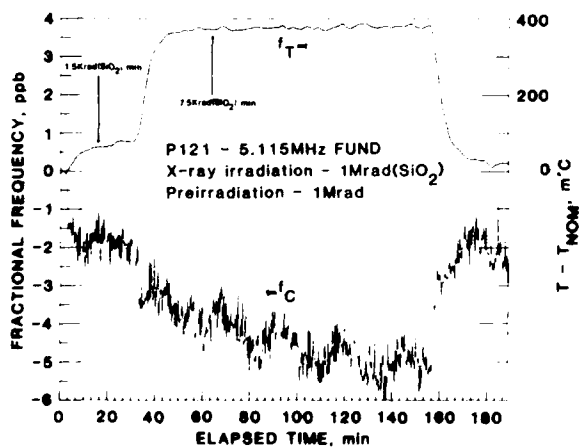


Figure 16. High-dose x-ray radiation response of 5.115 MHz (fundamental) resonator.

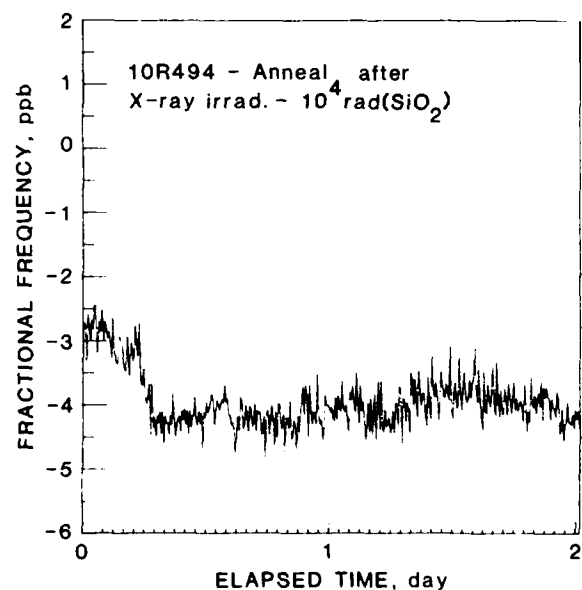


Figure 18. Annealing behavior of a 10.23 MHz (3d overtone) resonator following a 10 Krad(SiO<sub>2</sub>) exposure. The resonator was preirradiated to a dose in excess of 10<sup>6</sup> rad(SiO<sub>2</sub>) about 30 days prior to this measurement.

# RESULTS FROM GAMMA RAY AND PROTON BEAM RADIATION TESTING OF QUARTZ RESONATORS

J. R. Norton, J. M. Cloeren,

J. J. Suter

The Johns Hopkins University  
Applied Physics Laboratory  
Laurel, Maryland 20707

## SUMMARY

This paper summarizes the results of radiation tests on cultured quartz resonators. The tests were conducted to determine the frequency shifts ( $\Delta f/f$ ) of the resonators as a result of high and low levels of proton and gamma irradiation. All resonators tested were 5 MHz, 5th overtone, AT cut units manufactured in different lots by Bliley Electric Company from nine bars of Premium-Q, swept, cultured quartz produced by Sawyer Research Products. Generally, the results were as follows:

Resonators manufactured from the same bar of cultured quartz showed consistent frequency changes ( $\Delta f/f$ ) when subjected to high level gamma radiation. However, this consistency did not exist when the resonators were exposed to low level gamma radiation.

For low level radiation no apparent correlation exists between the aluminum content of a resonator and its radiation induced frequency shift ( $\Delta f/f$ ).

A correlation exists between the low level radiation induced frequency shift ( $\Delta f/f$ ) of a resonator and the manufacturing lot in which the resonator was produced.

The low level radiation sensitivity of a resonator cannot be extrapolated from high level radiation data.

The radiation sensitivities of resonators subjected to low level radiation may be grouped into one of four distinctive signatures.

The signatures and the frequency shifts ( $\Delta f/f$ ) of resonators subjected to low level proton and gamma radiation are very similar.

Radiative preconditioning of resonators reduces the radiation induced frequency shifts ( $\Delta f/f$ ) at both high and low levels of gamma and proton radiation.

## INTRODUCTION

The radiation susceptibility of quartz resonators is a significant parameter contributing to the performance of spacecraft oscillators. To meet various sponsor and mission requirements, The Johns Hopkins University Applied Physics Labora-

tory (JHU/APL) initiated a study of the effects of high and low dose and dose rates of gamma and proton radiation on quartz resonators. In each of the radiation experiments, the resonators were installed in test oscillators with the flat surface of the resonator perpendicular to the radiation source. All measurements were made with the test oscillators operating at the resonator turn-over temperature. The tests showed that the measured frequency shifts ( $\Delta f/f$ ) were dominated by proton and gamma radiation effects on the resonator and not by proton and gamma radiation effects on the test oscillator electronics.

## GAMMA RADIATION TESTS

### High Level Gamma Radiation Tests

Principally, the high level radiation testing of quartz resonators and oscillators was conducted to determine if a quartz oscillator would continue to function when exposed to an ionizing radiation environment between 10 and 50 krads. The direction and magnitude of any resulting frequency shifts were also of great interest.

Initially, quartz resonators, which had not been previously exposed to radiation, were installed in test oscillators, which were then exposed to a Cobalt-60 radiation source. The source delivered a dose rate of 67 rads per second to the outside surfaces of the test oscillator, and approximately 34 rads per second to the resonator (due to shielding of the test oscillator structure). The test oscillators were exposed to incremental radiation doses of 1, 2, 7, and 10 krads. A sufficient time interval was allowed between the incremental radiation exposures for frequency stabilization. This procedure produced an accurate measurement of the steady-state frequency shifts ( $\Delta f/f$ ) resulting from the radiation exposure. In all instances the oscillators continued to function throughout the range of radiation exposures.

### High Level Gamma Radiation Test Results

Test data for nine of the resonators are shown in Fig. 1. Note the frequency shifts, after an initial exposure to 10 to 20 krads, became much smaller when the resonators were subsequently exposed to additional radiation. This effect was observed in the majority of resonators. Data analysis after testing the first six resonators

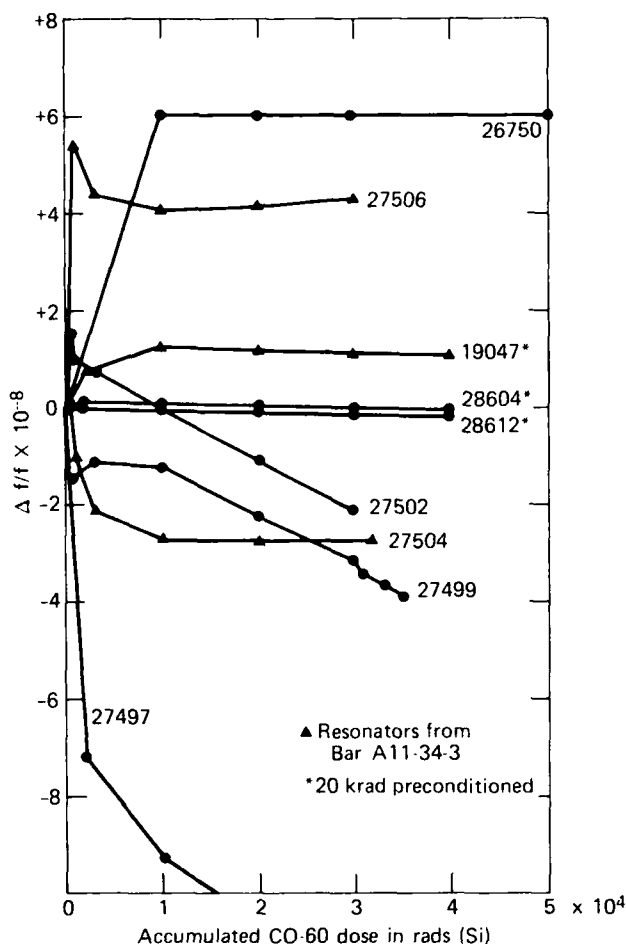


Fig. 1 Quartz oscillator steady state frequency changes induced by high level gamma radiation.

resulted in a decision to precondition subsequent test resonators by exposure to 20 krad before installation in the test oscillators. Data for all resonators tested in the high level radiation

experiment are tabulated in Table 1. It is interesting to observe, for the high level gamma radiation test, that 67 percent of the resonators had negative frequency shifts. Additionally, as indicated in Table 1 and Fig. 1, resonators manufactured from the same quartz bar produced consistent radiation coefficients. Resonators manufactured from bar A13-1-1 had high radiation coefficients which persisted even after exposure to 30 krad. However, for resonators manufactured from quartz bar A11-34-3, K5F and K18F had relatively low radiation coefficients which became smaller at the higher accumulated radiation doses.

#### Low Level Gamma Radiation Tests

Low level gamma radiation testing of quartz resonators and oscillators was initiated in order to estimate oscillator performance in a low level background radiation environment. Based on data collected from the high level radiation tests, a radiation sensitivity specification of  $1 \times 10^{-10}$  per rad for a 4 rad exposure appeared easy to meet and was therefore adopted as a basis for screening resonators. Low level gamma radiation experiments were conducted using a Cobalt-60 radiation source which produced a dose rate of 0.1 rad per minute at the resonator surface. Each resonator was incrementally exposed to 0.1, 1, and 3 rads. An examination of the initial low level gamma radiation experiment results indicated that the radiation induced frequency shifts were much larger than expected from the extrapolation of the high level radiation test data. This confirmed the findings previously reported in the literature<sup>1</sup> namely, that the radiation induced frequency shifts of a resonator cannot accurately be predicted over a large range of exposures using only data for a particular range of exposure. Since no radiation data existed in our range of interest (total exposures up to 4 rads with a dose rate of 0.1 rad per minutes), a systematic plan for low level radiation testing of quartz resonators was developed. This plan would yield the required frequency shift versus radiation data, and hopefully lend insight into the

TABLE 1

#### Quartz Resonator Test Results For High Level Gamma Radiation

RESONATOR SERIAL NUMBER	BAR NUMBER	AUTO- CLAVE NUMBER	ALUMINUM CONTENT OF BAR (ppm)	RADIATION SENSITIVITY + ( $\times 10^{-11}$ )
19047*	A11-34-3	NA	12.00	0.0140
26750	NA	NA	NA	0.0018
27497	A13-1-1	NA	NA	-0.1200
27499	A13-1-1	NA	NA	-0.0850
27502	A11-39-4	NA	NA	-0.0980
27504	A11-34-3	NA	12.00	-0.0116
27506	A11-34-3	NA	12.00	0.0100
28602	K5F	D14-45	0.64	0.0010
28604*	K5F	D14-45	0.64	-0.0028
28605H*	K13F	A6-26	0.79	-0.0013
28611H*	K18F	D14-45	0.92	-0.0118
28612*	K18F	D14-45	0.92	-0.0020

\* Resonators with 20 krad gamma preconditioning.

NA Data not available.

+ Frequency shift ( $\Delta f/f$ ) for the last 10 krad exposure divided by 10 krad.

radiation sensitivity mechanisms of resonators. Generally, the test plan was as follows:

1. Resonators used in the experiment would be manufactured by Bliley Electric Company using six bars of Premium-Q, cultured, Z-growth quartz produced by Sawyer Research Products.

2. Each quartz-bar used for resonator fabrication would be divided into sections as shown in Fig. 2. During resonator fabrication, traceability to the parent bar and section would be maintained.

3. A sample from each bar would be analyzed for aluminum content by Oklahoma State University, since it had been reported that there was a correlation between aluminum content of the bar and radiation sensitivity of a resonator made from the bar.<sup>2</sup>

4. Each test resonator would be exposed to low level gamma radiation from a Cobalt-60 source. The dose rate would be 0.1 rad per minute and the total accumulated dose would be 4 rads received at incremental exposures of 0.1, 1 and 3 rads.

5. Each tested resonator which displayed a steady-state low level radiation coefficient of less than  $1 \times 10^{-10}$  per rad for a 4 rad exposure would be considered spaceflight qualified and reserved for use in JHU/APL space qualified oscillators.

The first resonators, identified by the serial number series 318XX, were fabricated from quartz bars K15K and K17K (see Table 2). The aluminum content of these bars was measured at 5.4 and 5.7 ppm, respectively. Fifty-six percent of these resonators were found to have radiation coefficients of less than  $1 \times 10^{-10}$  per rad. The next lot of resonators, series S/N 324XX, which was fabricated from the same bars (K15K and K17K), all had radiation coefficients greater than  $1 \times 10^{-10}$  per rad. The third manufacturing lot of resonators, series S/N 324XX, was fabricated from quartz bars K13F and K18F. These bars had a low aluminum content of 0.79 and 0.92 ppm, respectively. When five of six resonators (an 83% yield) were found to have radiation coefficients less than  $1 \times 10^{-10}$  per rad, a correlation between low aluminum

content and radiation coefficient seemed to confirm the findings reported in the literature. The fourth manufacturing lot of resonators, series S/N 340XX, was also fabricated from quartz bars K13F and K18F. Two of the three resonators (67%) exhibited radiation coefficients less than  $1 \times 10^{-10}$  per rad. This seemed to reaffirm a correlation between low level radiation coefficients and the aluminum content of the parent quartz. The fifth manufacturing lot of resonators, series S/N 346XX, was fabricated from quartz bar K11K. This bar had the highest aluminum content of all bars tested, 8.3 ppm. Based on the test results of manufacturing lot 1 through 4, we expected only a small number of resonators would have a radiation coefficient of less than  $1 \times 10^{-10}$  per rad. Surprisingly, all ten resonators in this lot exhibited coefficients less than  $1 \times 10^{-10}$  per rad. The remarkable performance and consistency of this lot of resonators, manufactured from a parent quartz bar with very high aluminum content, cast doubt on the relationship between the aluminum content of the parent quartz bar and the radiation coefficient of the resonator made from that quartz. This ambiguity was decisive in initiating additional testing which would not only continue to seek a correlation between the aluminum content of the parent quartz bar and the radiation coefficient of the resonators, but also study the possible correlation of other mechanisms to the variations in the radiation coefficient of resonators manufactured from the same parent quartz. It was conjectured that one possible mechanism could be related to lot-to-lot variation in the resonator manufacturing process. The sixth and seventh manufacturing lots of resonators, series S/N 347XX and S/N 352XX, were fabricated from bars K13F and K18F. The sixth manufacturing lot produced two resonators out of a total of five, a 40% yield, which had radiation coefficients less than  $1 \times 10^{-10}$  per rad. As shown in Table 2, bars K13F and K18F had very low aluminum content. The seventh manufacturing lot produced only one acceptable resonator from a total of five resonators, a 20% yield. Again, the results showed that low aluminum content of the parent quartz bar does not necessarily produce resonators with low radiation coefficients. The eighth and final manufacturing lot of resonators tested, series S/N 257XX, was fabricated from quartz bar K5F, which had the lowest aluminum content of 0.64 ppm. As shown in Table 2, quartz bar K5F produced only two acceptable resonators out of 11, an 18% yield, with a radiation coefficient of less than  $1 \times 10^{-10}$  per rad. Once again we see a poor yield of acceptable resonators manufactured from a parent quartz bar of low aluminum content. In our opinion, this is a further indication that no correlation exists between the aluminum content of the parent quartz and the low level frequency versus radiation coefficient of the associated resonators.

Two of the resonators tested (S/N 33817 and S/N 33822) had excellent radiation sensitivities but abnormally high aging rates. Since we felt that these high aging rates were caused by contamination during manufacturing, Bliley was asked to reprocess them. The resonators were later retested for radiation sensitivity without further preconditioning. The retest results for S/N 33822 are shown in Fig. 3-A; the original test results are shown in Fig. 3-B. Note the slight improvement in aging rate after the reprocessing, but a very different radiation sensitivity (signature). This was explained, after consultation with Bliley, by the fact that during reprocessing the resonators were subject to a temperature of 355°C

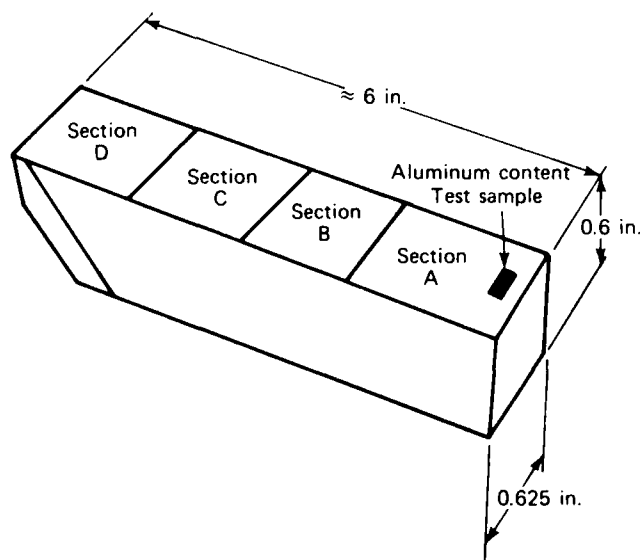


Fig. 2 Cultured z-growth quartz bar.

TABLE 2

## Quartz Resonator Yields for Low Level Gamma Radiation Tests

TEST SERIES	MANUFACTURING LOT	BAR NO.	ALUMINUM CONTENT OF BAR (ppm)	TOTAL RESONATORS FROM BAR	ACCEPTABLE RESONATORS*	ACCEPTABLE RESONATOR YIELD (%)
1	318XX	K15K K17K	5.40 5.70	9	5	56
2	324XX	K15K K17K	5.40 5.70	3	0	0
3	338XX	K13F K18F	0.79 0.92	6	5	83
4	340XX	K13F K18F	0.79 0.92	3	2	67
5	346XX	K11K	8.30	10	10	100
6	347XX	K13F K18F	0.79 0.92	5	2	40
7	352XX	K13F K18F	0.79 0.92	5	1	20
8	257XX	K5F	0.64	11	2	18

\* Resonators with a total frequency sensitivity of  $< 1 \times 10^{-10}$  per rad from a 4 rad exposure.

which removed the effects of the original radiation preconditioning. The reprocessed resonator (S/N 33822) was then removed from the test oscillator and re-preconditioned with 20 krad of gamma radiation, and retested. The results of this retest are shown in Fig. 3-C. The test results for the reprocessed resonator S/N 33822 are comparable to that of S/N 33817. Note that reprocessing of these resonators caused a significant change in their radiation sensitivity. From these data, one may conclude that the radiation sensitivity of the resonators was related to the manufacturing process since the same quartz blank was used for the original and reworked resonators.

#### Low level Gamma Radiation Data Analysis

After reducing the test data from the low level gamma radiation tests to graphic form, four distinctive signatures of radiation sensitivity were readily identifiable. These signatures are shown in Fig. 4. The signature which occurred most frequently is characterized by a large positive frequency shift during irradiation, followed by a gradual recovery to the pre-test aging rate. Figure 4-A shows an example of this signature. Thirty-four percent of the resonators tested produced this signature. We found no correlation between the signature and the aluminum content of the parent quartz or manufacturing lot of the resonators.

In an effort to correlate resonator performance, the data were reduced to a series of bar charts showing resonator performance as a function of quartz bar, bar section, and manufacturing lot. Figure 5 shows no clear correlation between resonator yield and the parent quartz bar. However, Fig. 6 shows a strong correlation between resonator yield and manufacturing lot. Bar K13F

was used by Bliley to fabricate resonators in four different manufacturing lots: series 338XX, 340XX, 347XX and 352XX. Figure 7 presents the test data for all resonators manufactured from bar K13F, and identifies the bar section from which each resonator was made. Clearly, the percentage yield of resonators is much better correlated to specific manufacturing lots than to the parent quartz bar or bar section.

In conclusion, the low level gamma radiation test data show that:

1. The low level radiation coefficient of a resonator is not correlated to the aluminum content of the parent quartz bar.

2. The low level radiation coefficient of the resonator is not related to the section of the parent quartz bar from which it was manufactured.

3. There exists a strong correlation between the low level radiation coefficient of a resonator and the manufacturing lot in which the resonator was produced. This suggests that the low level radiation coefficient of a resonator is dependent on small variations in the manufacturing process which is generally thought to be consistent.

4. Four distinctive signatures of radiation sensitivity are identifiable, possibly indicating that there are several radiation sensitive mechanisms which may exist singularly or in combination in each quartz resonator. These mechanisms may be activated by different radiation levels.

5. The majority of the resonators showed a positive frequency shift (refer to Table 3).

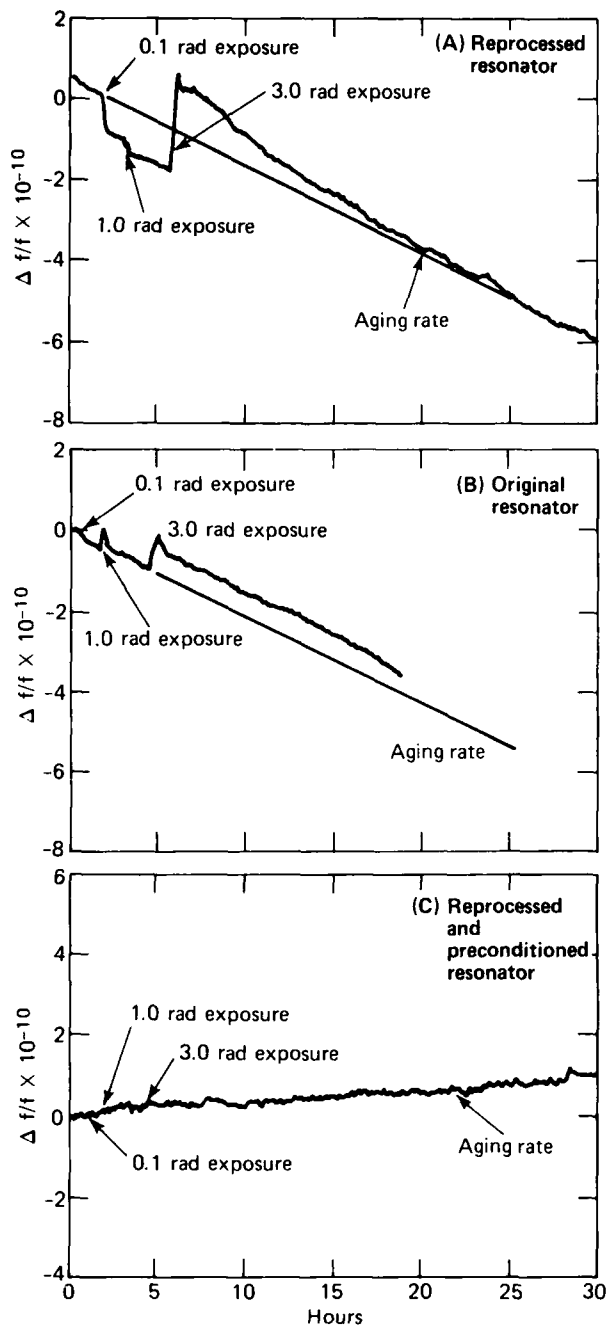


Fig. 3 Quartz resonator S/N 33822 radiation test results.

#### PROTON RADIATION TESTS

In order to investigate the frequency shifts of resonators in a simulated space environment, the resonators were exposed to protons generated by the cyclotron at Harvard University. Technical specifications for the Harvard University Proton Cyclotron are listed in Table 4. The test oscillators used in the proton beam tests were the same units used previously in the gamma radiation tests.

#### Test Procedures and Objectives

The oscillators were mounted on a fixed table in front of the proton beam. Two lasers, mounted in the same horizontal plane as the oscillators, were used to locate the resonators symmetrically around the isocenter of the proton beam. This configuration is shown in Fig. 8. The Bragg curve

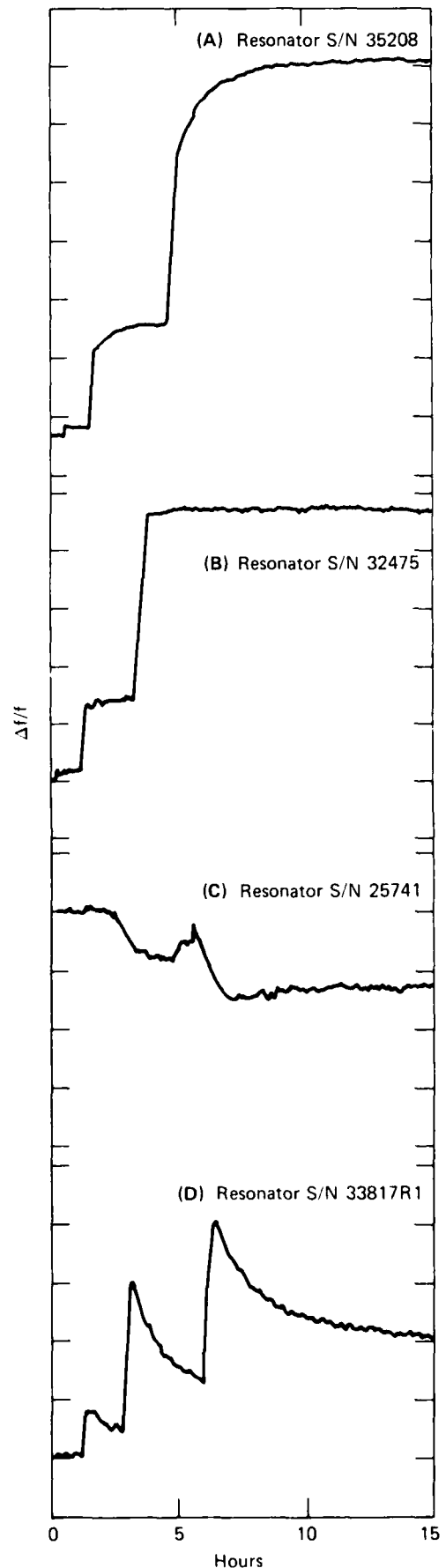


Fig. 4 Four distinctive signatures of radiation sensitivity.



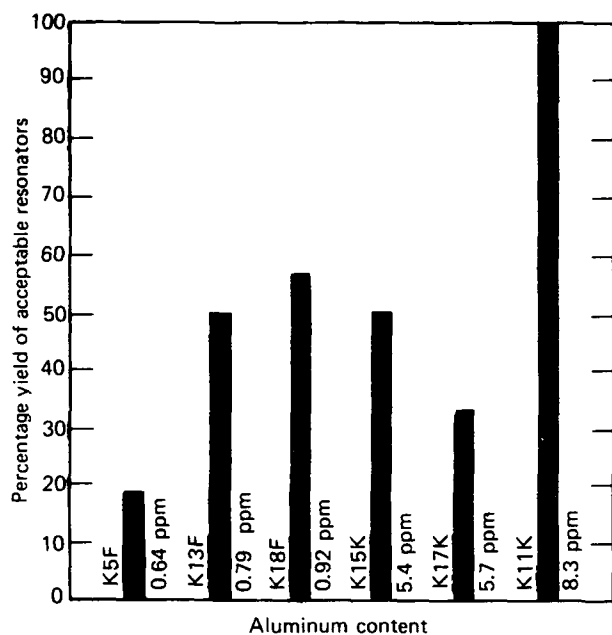


Fig. 5 Yield of acceptable resonators as a function of aluminum content and bar.

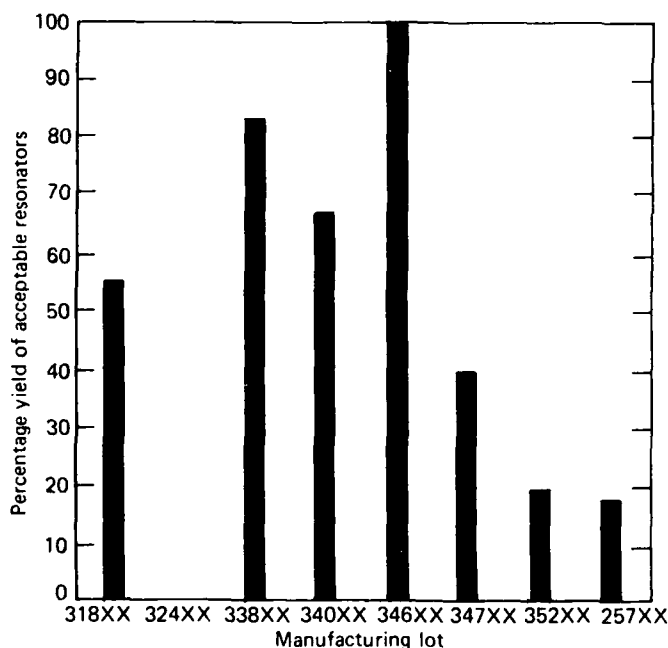


Fig. 6 Yield of acceptable resonators as a function of manufacturing lot.

(percent of radiation dose as a function of proton beam penetration depth) was calculated before the radiation experiments to confirm that the resonators received a uniform radiation dose (refer to Fig. 8). Before each proton radiation test, the proton beam was carefully calibrated. This calibration resulted in a proton beam dose rate uncertainty of 3%. The proton beam energy uncertainty was 5%. Before each radiation experiment, the resonator frequency was allowed to stabilize so that the radiation sensitivity of the resonators could be correlated to the proton beam dose. The proton beam irradiation of the resonators included the following test measurements:

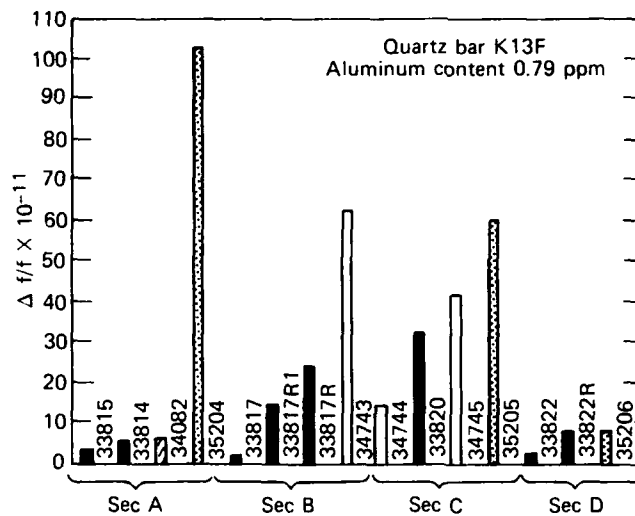


Fig. 7 Quartz resonator radiation sensitivity as function of bar section.

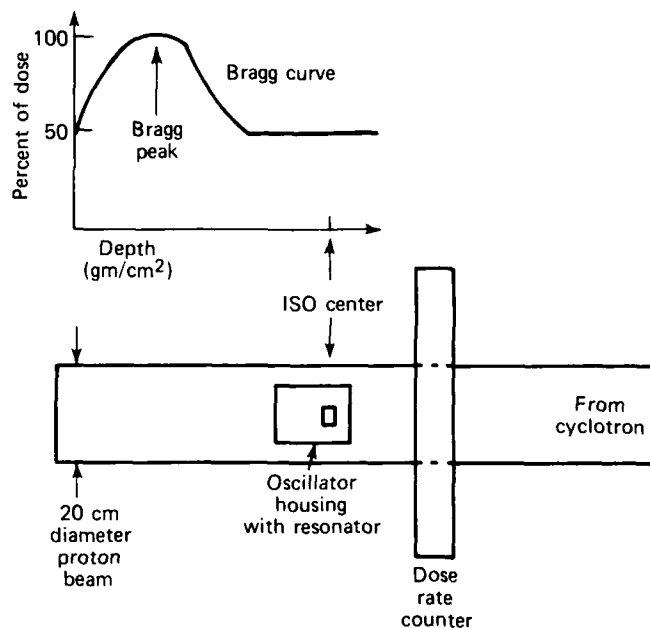


Fig. 8 Harvard cyclotron test setup and proton beam geometry.

1. Resonator frequency shift ( $\Delta f/f$ ) as a function of proton beam dose rates and total accumulated dose for fixed values of the proton beam energy, 153 MeV.

2. Resonator frequency shift ( $\Delta f/f$ ) as a function of the proton beam energy for fixed dose rate and accumulated dose.

In the first test, the oscillators were subjected to a 153 MeV proton beam with a dose rate equal to 0.1 rad per minute and total accumulated doses of 0.1, 1.0, and 3.0 rads. The results of this test are presented in Figs. 9 and 10, together with the data from similar gamma ray tests (dose rates equal to 0.1 rad per minute and total accumulated doses of 0.1, 1.0, and 3.0 rads). Figures 9 and 10 show that frequency shift as a function of time due to proton and gamma irradiation of the resonators are very similar.

TABLE 3

## Quartz Resonator Test Results for Low Level Gamma Radiation

SERIAL NUMBER	BAR NUMBER	AUTO- CLAVE NUMBER	SECTION NUMBER	ALUMINUM CONTENT OF BAR (ppm)	RADIATION SENSITIVITY* ( $\times 10^{-11}$ )
25734	K5F	D14-45	A	0.64	54
25735	K5F	D14-45	A	0.64	25
25737	K5F	D14-45	A	0.64	67
25738	K5F	D14-45	A	0.64	-6.5
25739	K5F	D14-45	A	0.64	34
25740	K5F	D14-45	B	0.64	20
25741	K5F	D14-45	B	0.64	-5
25742	K5F	D14-45	B	0.64	42
25743	K5F	D14-45	B	0.64	22
25745	K5F	D14-45	B	0.64	40
25746	K5F	D14-45	B	0.64	17
28605	K13F	A6-26	A	0.79	.1
28611	K18F	D14-45	A	0.92	-.3
31816	K15K	H39-24	NA	5.4	4
31817	K15K	H39-24	NA	5.4	18
31818	K15K	H39-24	NA	5.4	8
31819	K15K	H39-24	NA	5.4	5
31821	K17K	H39-24	NA	5.7	15
31822	K17K	H39-24	NA	5.7	2
31823	K17K	H39-24	NA	5.7	34
31823R <sup>o</sup>	K17K	H39-24	NA	5.7	3
31823R1	K17K	H39-24	NA	5.7	2.2
31823R2	K17K	H39-24	NA	5.7	1.9
31824	K17K	H39-24	NA	5.7	6
31825	K17K	H39-24	NA	5.7	20
31825R	K17K	H39-24	NA	5.7	9
32472	K15K	H39-24	NA	5.4	19
32473	K15K	H39-24	NA	5.4	13
32475	K17K	H39-24	NA	5.7	11
32606	K17K	H39-24	NA	5.7	32
33814	K13F	A6-26	A	0.79	5
33815	K13F	A6-26	A	0.79	3
33817	K13F	A6-26	B	0.79	1
33817R	K13F	A6-26	B	0.79	24
33817R1	K13F	A6-26	B	0.79	14
33820	K13F	A6-26	C	0.79	32
33820R	K13F	A6-26	C	0.79	31
33822	K13F	A6-26	D	0.79	2
33822R	K13F	A6-26	D	0.79	8
33822R1	K13F	A6-26	D	0.79	1
33823	K18F	D14-45	B	0.92	5
34079	K18F	D14-45	A	0.92	16
34080	K18F	D14-45	C	0.92	.8
34082	K13F	A6-26	A	0.79	6.3
34627	K11K	H39-24	A	8.3	2
34628	K11K	H39-24	A	8.3	6
34629	K11K	H39-24	A	8.3	1.5
34630	K11K	H39-24	B	8.3	9
34631	K11K	H39-24	B	8.3	6
34632	K11K	H39-24	B	8.3	8
34632R	K11K	H39-24	B	8.3	6
34633	K11K	H39-24	C	8.3	10
34636	K11K	H39-24	D	8.3	4.5
34637	K11K	H39-24	D	8.3	-6
34638	K11K	H39-24	D	8.3	9
34743	K13F	A6-26	B	0.79	62
34744	K13F	A6-26	C	0.79	-14
34744R	K13F	A6-26	C	0.79	-8.9
34745	K13F	A6-26	C	0.79	41
34746	K18F	D14-45	D	0.92	1.5
34747	K18F	D14-45	D	0.92	1
35204	K13F	A6-26	A	0.79	102
35205	K13F	A6-26	C	0.79	60
35206	K13F	A6-26	D	0.79	8
35207	K18F	D14-45	B	0.92	70
35208	K18F	D14-45	B	0.92	60

\* Frequency Shift ( $\Delta f/f$ ) per rad for a 4 rad exposure.

NA - Data not available.

<sup>o</sup> - Retested Resonator.

TABLE 4

Technical Specifications of the Harvard Cyclotron<sup>3</sup>

PARAMETER	VALUE
Proton Energy Range	10-153 MeV
Proton Beam Pulse Length	400 $\mu$ s
Proton Beam Pulse Repetition	10 ms
Standard Beam Diameter	20 cm
Proton Dose Rate Range	0.1-150 rads/min
Proton Beam Power	160 Watts

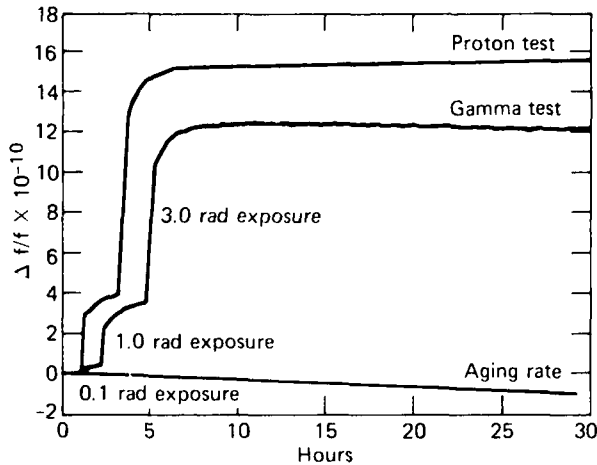


Fig. 9 Low level gamma and proton radiation test data for resonator 33820.

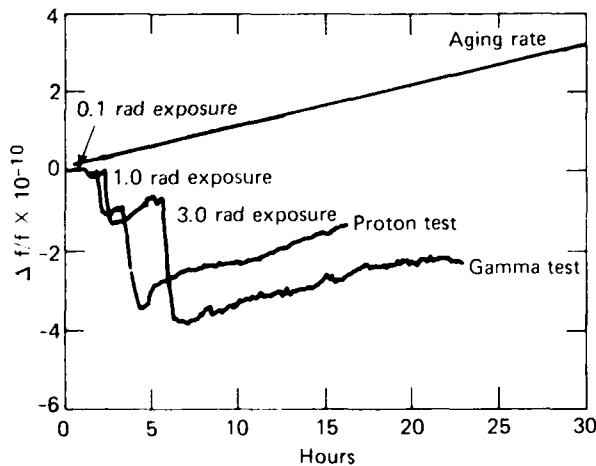


Fig. 10 Low level gamma and proton radiation test data for resonator 34744.

This similarity indicates that the mechanisms which caused the frequency shifts in the resonators are due to ionization effects rather than nuclear interactions. This is apparent because the only common interactions of proton and gamma radiation with matter is ionization. Hence, it is concluded from these data that the protons only interact with the quartz resonators by means of ionization processes. Therefore, it seems logical that one may use gamma radiation in the low level

radiation testing of resonators to predict the resonator response to proton radiation.

In the second test, resonators were subjected to a proton beam with energies of 70, 110, and 130 MeV. The proton dose rate in these tests was 0.1 rad per minute, and the total accumulated dose was 1.0 rad. Figure 11 shows the frequency shift ( $\Delta f/f$ ) as a function of time for three different values of proton beam energy. The quartz resonators subjected to the proton beam were shielded by multiple layers of aluminum, copper, glass, and foam enclosures. The total equivalent aluminum shielding thickness was calculated to be 6.3 gm/cm<sup>2</sup>. The minimum proton energy needed to penetrate this shielding material was calculated to be approximately 77 MeV<sup>4</sup>. As shown in Fig. 11, the resonator frequency shift ( $\Delta f/f$ ) is negligible for 70 MeV protons. This confirms the pretest prediction that protons need an energy level greater than 77 MeV in order to penetrate the resonator shielding. The test results also confirm that the frequency shift was not caused by effects in the oscillator electronics, since the oscillator electronics were not shielded against the proton beam.

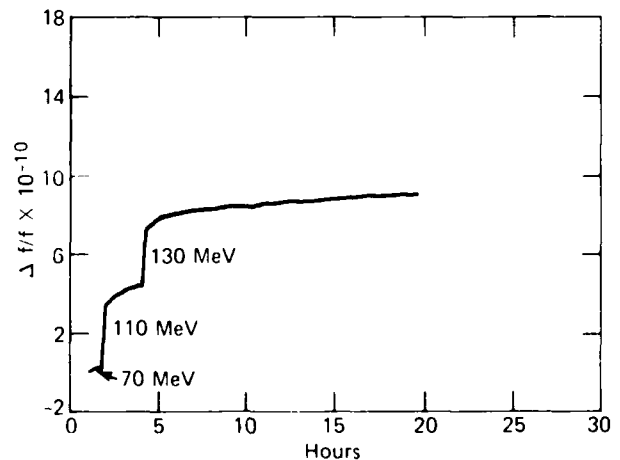


Fig. 11 Frequency shift of resonator 33820 as a function of proton energy.

## Proton Radiation Test Data Analysis

In conclusion, the data from the proton radiation tests showed:

1. An excellent correlation exists between low level proton and gamma radiation sensitivities of a given resonator.

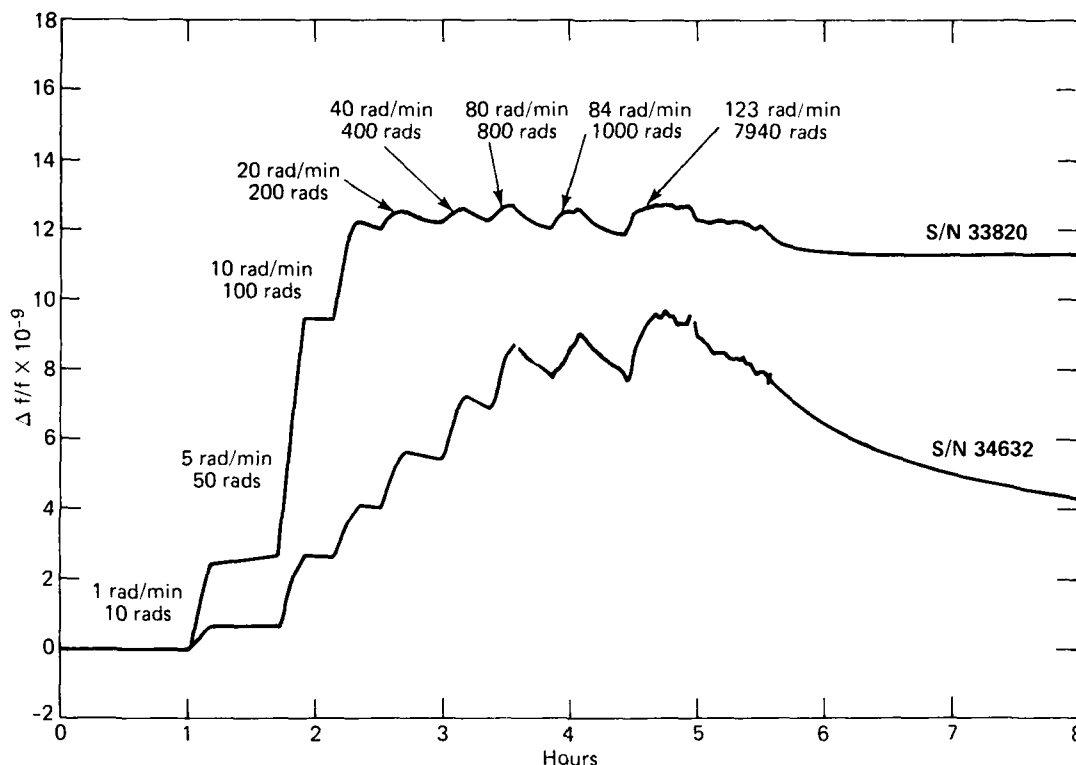


Fig. 12 Frequency shift of quartz resonators during proton radiation tests.

2. At a given high accumulated dose for each resonator there is a significant decrease in radiation sensitivity to both proton and gamma radiation (refer to Figs. 1 and 12).

3. The response of a given resonator to proton radiation is both accumulated dose and dose rate dependent (refer to Fig. 12).

#### CONCLUSIONS

The primary effect of high level gamma radiation ( $\leq 50$  krad) on the operation of a quartz resonators is a change in its operating frequency. The direction of this frequency coefficient is normally negative. However, positive frequency coefficients are not uncommon. The magnitude of the frequency offsets ( $\Delta f/f$ ) vary for each resonator and may be as great as  $1 \times 10^{-7}$  for a 30 krad exposure. The radiation sensitivity, ( $\Delta f/f$ ) per unit of radiation, for a given resonator normally becomes much less as the radiation dose accumulates. This effect indicates that preconditioning ( $\approx 20$ -50 krad) of a resonator reduces radiation sensitivity.

The data from the high level gamma radiation tests indicate there is a correlation between the radiation sensitivity of a particular resonator and the parent quartz bar from which it was manufactured. Resonators made from a given bar of parent quartz all show radiation sensitivities which are consistent in magnitude when subject to exposure of 20 to 30 krad.

The primary effect of low level gamma and proton radiation on the operation of a quartz resonator is a change in its operating frequency. The direction, magnitude, and character of these radiation induced frequency shifts are not comparable to the frequency shifts produced by high level radiation exposure and therefore cannot

be predicted from the review or extrapolation of high level radiation data. Each resonator has a radiation character of its own, which we refer to as a signature. All of the resonators which we tested could be grouped into one of four recognizable signatures. The radiation induced frequency changes resulting from a 4 rad exposure ranged from  $1 \times 10^{-12}$  to  $1 \times 10^{-9}$  ( $\Delta f/f$  per rad). The majority of resonators showed a net positive frequency change as a result of a 4 rad exposure.

The low level radiation test results strongly support a correlation between the radiation sensitivity ( $\Delta f/f$  per rad) of a particular resonator and the manufacturing lot in which it was made. This fact requires further investigation into the effect of resonator processing on the resonator radiation sensitivity. No correlation could be found with any other resonator variable. These include parent quartz bar, bar section, aluminum content, Q, turning point temperature, resistance, and aging.

The signature, magnitude, and direction of frequency changes resulting from low level gamma and proton radiation are nearly identical for a given quartz resonator. This indicates that the radiation induced frequency changes are primarily ionization effects, and that gamma radiation data for low level radiation exposures can be accurately used to predict the performance of a resonator when subjected to proton radiation.

#### Acknowledgements

The authors acknowledge Messrs. P. E. Partridge, R. H. Maurer, and E. C. Martin of the Applied Physics Laboratory and A. Koehler and B. Gottschalk of Harvard University for their many helpful technical discussions and use of their respective radiation facilities.

### References

1. T. M. Flanagan, "Hardness Assurance in Quartz Crystal Resonators," IEEE, Transactions on Nuclear Science, NS-21, p. 390 (1974).
2. J. J. Martin, et al., "Radiation - Induced Mobility of Interstitial Ions in Synthetic Quartz," Proceedings of the 33rd Annual Symposium on Frequency Control, p. 134 (1979).
3. A. M. Koehler, "The Harvard Cyclotron Laboratory," IEEE, Transactions on Nuclear Science, NS-28, p. 2642 (1979).
4. H. Bichsel, "Passage of Charged Particles through Matter," The American Institute of Physics Handbook, D. E. Gray, Editor, McGraw Hill, New York, Chapter 8, pp. 20-47 (1972).

# THE VIBRATION SENSITIVITY OF VHF QUARTZ CRYSTALS FOR MISSILE APPLICATIONS

R. D. Weglein

Hughes Aircraft Company, Canoga Park, CA 91304

## Abstract

This paper relates to the phase-noise degradation of VHF crystal oscillators when subjected to vibration. Increased phase noise reduces the performance of the pulse doppler radar in current missile seekers.

A performance summary is presented for a large number of commercially available SC-cut crystal and some internally-fabricated AT-cut crystals when subjected to sinusoidal vibration. Four groups of crystals on 3- and 4-post supports with 0° and 45° orientation between crystal and support post axes were examined. Following vibration tests, all crystal units were disassembled, optically inspected, stripped, and their crystallographic axes were precisely determined. The SC-cut crystals were procured in two groups, separated by a nine months period to examine the reproducibility of the detailed performance.

The vibration-induced phase noise of these crystals may be summarized as follows. Crystal resonators supported on four posts showed lower vibration sensitivity coefficient  $\Gamma$ , than those mounted on three posts. The average for each 4-post group ranged from 3.25 to 4.37 in units of 10<sup>-10</sup>/g, while the 3-post group varied between 4.65 to 10.86. The  $\Gamma$  variations within each group were much wider. The maximum  $\Gamma$  axis (worst case) observed earlier was not reproduced in the later crystal procurement group. The AT-cut crystals on Hughes-developed soft 4-post supports showed an average of 2.61 x 10<sup>-10</sup>/g, and varied between 1.2 and 3.7 for seven tested crystal units.

Theoretical predictions were compared with these results for in-plane acceleration on idealized supports and for stress coefficient. A theoretical comparison of the practically-imposed and idealized support boundary conditions sheds new light on the disparity between the measured results and theory that predicts a  $\Gamma = 3 \times 10^{-11}$ /g for the 4-post supported crystal plate.

## Introduction and Summary

VHF crystals and crystal oscillators for tactical missiles fall into a special class of components that require substantial improvement if their performance is to keep pace with new systems requirements. The stability of crystal oscillators in the 100 MHz range when subjected to vibration should not significantly degrade the signal sensitivity of the coherent radar receiver relative to its quiescent performance. To the extent that this is not the case, the receiver sensitivity and the doppler range are proportionately degraded. Although crystal resonator technology spans over at least three decades, relatively little attention has been focused in this area.

When an otherwise stable crystal oscillator is subjected to steady acceleration, its instantaneous frequency  $f_0$ , changes in accordance with the acceleration sensitivity coefficient  $\Gamma(1)$ . In general,  $\Gamma$  is a vector that depends in a complicated manner on the orientation of the anisotropic crystal platelet as well as on the platelet's orientation and fastening to the support structure.(2) The literature contains ample information on the measured performance of crystal oscillators, subjected to the static 2g tip-over test.(4,5,6) These studies are for the most part confined to the measurement of the small signal  $\Gamma$  in low frequency crystal resonators below 10 MHz via this static test. Some vibration performance of VHF crystal oscillators has also been reported recently.(7)(8)

Vibration frequencies to which VHF oscillators may be subjected in a missile environment extend from DC (constant acceleration represented by the 2g tip-over test) through the radar doppler range up to, say 50 KHz. The instantaneous frequency,  $f_0$ , is then modulated at the vibration frequency, yielding an FM spectrum of magnitude that tends to degrade the phase noise performance of the oscillator in accordance with  $\Gamma$ . Experimentally the vibration sensitivity coefficient is usually determined from spectrum analyzer measurements, as in equation 1,

$$\Gamma = [2f_m / (f_0 G)] 10^{P_{SS}/20}, \quad (1)$$

where  $f_m$  = the sinusoidal vibration frequency,  
 $f_0$  = the oscillator frequency ( $\approx 100$  MHz)  
 $G$  = the peak vibration amplitude in units of g (9.8 m/sec<sup>2</sup>),  
 $P_{SS}$  = the single-sideband phase noise power observed on the spectrum analyzer, relative to the oscillator power.

The noise output from the oscillator with and without vibrational excitation may be separated into two general groups, characterized by the frequency dependence of that noise, as is schematically shown in Figure 1. Noise close to the coherent oscillator frequency (phase noise) usually exhibits  $f_m^{-n}$

dependence, up to a "cross over" frequency  $f_c = f_0/Q$ , where  $f_m$  is the modulation or vibrational frequency and  $Q$  is the resonator quality factor. The range of  $n$  is such that  $3 > n > 1$ .(9) This frequency dependent noise(9) is due to flicker ( $n=1$ ) and white ( $n=2$ ) noise generation within both crystal and circuit.

Beyond  $f_c$ , the "noise floor" is for the most part electronic noise, generated by a combination of shot and white noise sources in the amplifying portion of the circuit.

The vibration-induced noise in this otherwise frequency-independent noise floor range consists in

part of discrete spurious peaks, as indicated schematically in Figure 1, that are usually the result of crystal and support resonances. The subject of these resonances (plate modes) is treated separately elsewhere(10).

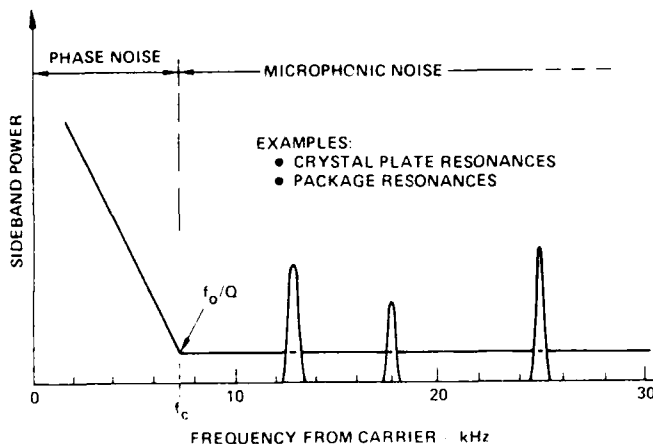


Figure 1. Oscillator Noise; Definition of Distinct Regions.

This paper summarizes the performance of, for the most part, commercially available SC-cut crystals when subjected to vibration. The motivation for the study was the hope of discovering trends that might lead to an improved understanding of the large discrepancy that persists between predicted(11) and observed(6) performance. The results of an 18-month effort on 45 crystals (38 SC-cut, 7 AT-cut) are reported, discussed and compared with available theoretical predictions.

Three groups of SC-cut crystal resonators, each unique in its relative support structure to crystal orientation, on three- and four-post supports were examined. One group of AT-cut crystals on a Hughes-developed four-post support configuration was also studied under vibration. All crystals were close to 100 MHz in frequency, utilized the 5th overtone thickness-shear mode of vibration and were encapsulated in a T05 enclosure. The SC-cut crystals were procured and tested in two groups with a nine month separation between groups to examine the reproducibility of the detailed performance. All crystals were tested under vibration in the same oscillator package, that had been modified and adapted to replace crystals easily and without the possibility of microphonic effects that might degrade the performance.

All crystals were examined under sinusoidal vibration at discrete frequencies between 80 and 2000 Hz, in the same phase noise test set, developed for this purpose, using the phase locking technique. Subsequent to the vibration testing sequence, all SC-cut crystals were removed from the T05 enclosure, inspected for assembly, mounting and adhesive uniformity as well as for lithography control.

Finally, the crystal orientation angles of the doubly-rotated quartz plates were determined with the aid of the laser-assisted precision x-ray niometer developed with ERADCOM support.(12)

The detailed results of this study in its several aspects, and a comparison with predictions as well as conclusions constitute the major topics of this report. The results suggest that if the idealized resonator support conditions, assumed in

the theoretical prediction, could be reduced to practice, substantial immunity from vibration might result in the phase noise performance of these quartz resonators.

## Experimental Results

The crystal plates were evaluated sequentially a) to ascertain their phase noise sensitivity to vibration  $\Gamma$ , b) to obtain optical views of the crystal fabrication and assembly processes inside the T05 enclosure, particularly with respect to the electrode metallization and epoxy adhesive distribution and, c) to determine the precise crystallographic orientation of the two rotation angles of the SC-cut. The motivation of the three-fold evaluation was to seek correlation between the elastic as well as mechanical constraints of the crystal platlets and their respective  $\Gamma$ 's. The parameters represented by these three groups are listed in Table 1.

TABLE 1. CRYSTAL GROUP PARAMETERS

GROUP	YEAR	CUT	NO SAMPLES	NO POSTS	$\Gamma$ , °
1	1982	SC	7	4	0
	1983	SC	9	4	0
2	1982	SC	6	3	0
	1983	SC	6	3	0
3	1983	SC	3	4	45
	1983	SC	6	4	45
HUGHES	1982	AT	7	4	45

HUGHES

## Vibration-Induced Phase Noise

Subsequent to an operational check and preliminary phase noise measurements in the quiescent state, all crystals were subjected to vibration in three mutually-perpendicular axes. The z-axis, normal to the package plane is also normal to the crystal platelet plane in all units. The results of these extensive tests are presented in Table 2-5, inclusive.

TABLE 2. SC-CUT CRYSTAL GROUP 1  
(96.56 MHz, 5TH O.T.)

YEAR	NO	X*	Y*	Z*	$\Gamma$ *	$\sigma$ *
1982	1	4.0	0.6	0.5	4.1	0.62
	2	2.5	0	3.2	4.1	
	5	5	0	0.8	5.1	
	7	3.2	0.5	2	3.8	
	11	5.0	1.0	0.7	5.2	
	12	5.0	2.0	0.1	5.4	
	14	5.0	1.5	0.6	5.2	
1983	1	2.30	1.33	2.40	3.48	1.46
	2	1.24	0.87	3.35	3.73	
	4	1.13	0.46	2.78	3.05	
	5	2.20	1.35	1.64	3.25	
	6	2.88	0.81	4.50	5.46	
	7	1.30	1.87	2.83	3.57	
	8	2.73	2.20	2.37	4.36	
	9	1.57	0.37	2.32	2.93	
	11	3.97	0.46	4.77	6.41	
	12	2.17	0.73	3.70	4.38	
1982	% MAX	86	0	14	-	-
1983	% MAX	20	0	80	-	-

\* 4 POST SUPPORT,  $\alpha = 0^\circ$       \*  $\times 10^{-10} g$

In each table, X, Y, Z are the vibration sensitivity coefficients pertinent to these three vibration axes and  $\Gamma$  is their geometric mean, expressed in units of  $10^{-10}g$ . The algebraic mean  $\Gamma$ , and the RMS deviation  $\sigma$ , are also calculated for each group. (% MAX) denotes the fraction of resonators (in percent) for which the largest  $\Gamma$  was observed along a particular axis. Thus, in Table 2, for example,  $\Gamma$  is quite constant for the two

procurement periods. However, while  $\sigma$  is somewhat greater for the later period, the trend (% MAX) is completely reversed between the 1982 and 1983 crystals of Group 1.

TABLE 3. SC-CUT CRYSTAL GROUP 2  
(96.56 MHz, 5TH O.T.)

YEAR	NO	X*	Y*	Z*	I*	I*	$\sigma$
1982	5	0	0.7	5.7			
	6	0	4.0	0.6	4.0		
	7	2.3	3.1	1.0	4.0	5.15	0.96
	9	2.0	6.4	1.1	6.8		
	10	0.8	1.1	5.6	5.8		
1983	3	1.30	6.75	1.83	7.12		
	4	2.06	2.23	4.78	3.52		
	5	3.11	3.01	8.90	9.90		
	10	6.20	5.36	3.11	8.77	10.91	2.36
	11	2.08	15.59	9.15	18.20		
1982	15	4.26	6.97	2.51	8.55		
	16	7.37	14.80	11.76	20.29		
	MAX	0	50	50			
1983	MAX	14.25	71.5	14.25			

3 POST SUPPORT  $\alpha = 0^\circ$

$\times 10^{-10} g$

TABLE 4. SC-CUT CRYSTAL GROUP 3  
(96.56 MHz, 5TH O.T.)

YEAR	NO	X*	Y*	Z*	I*	I*	$\sigma$
1982	1	1.26	0.64	1.27	1.89		
	2	2.73	0.70	3.07	4.17		
	3	1.00	0.52	1.70	2.04	3.04	1.17
	4	1.33	3.30	0.97	3.69		
	6	0.43	1.37	1.08	1.80		
1983	7	0.80	3.40	3.07	4.65		
	1	2.03	2.57	1.67	3.68		
	2	0.75	0.60	4.03	4.15	4.06	0.28
	3	1.73	3.80	1.20	4.34		
	MAX	0	56	44			

4 POST SUPPORT  $\alpha = 45^\circ$

$\times 10^{-10} g$

Similar observations may be obtained on examination of Tables 3 and 4. The 3-post supported plates of both periods in Group 2 showed consistently inferior performance. The axis of worst case  $\Gamma$  was not consistent from one procurement period to the next, as shown by comparing the relevant crystal groups in Tables 2 and 3. No comparison of this type was possible for Group 3 crystals. The lowest values of  $\Gamma$  and  $\sigma$  were obtained with the AT-cut crystal group listed in Table 5. Aside from the different crystal orientation, crystals in this group are cemented in place with a resilient silicone-rubber adhesive on each of the four posts. In excess of 80 percent of the crystal units in this group exhibited a worst-case axis of  $\Gamma$  normal to the platelet, in agreement with prior results.(5)

TABLE 5. AT-CUT-CRYSTAL GROUP  
(106.3 MHz, 5th O.T.)

YEAR	NO	X*	Y*	Z*	I*	I*	$\sigma$
1982	2	1.6	1.0	3.2	3.7		
	3	0.4	0.6	0.9	1.2		
	7	0.4	2.5	0	2.5	2.67	0.75
	8	0	0.9	2.8	2.9		
	9	1.4	1.4	1.8	2.7		
1982	11	1.6	1.3	2.2	3.0		
	MAX	0	16.7	83.3			

14 POST SOFT SUPPORT  $\alpha = 45^\circ$

$\times 10^{-10} g$

## Resonator Inspection

Subsequent to the completion of operational tests on all crystal units (phase noise with - and without vibration), the T05 enclosures were opened, the crystals extracted from the support-post structure and chemically etched to remove all metallization and remnant epoxy adhesive. In this disassembly sequence, optical inspection took place at every step and a number of features were recorded which might contribute to a correlation between assembly variations and performance. The observable features are listed below:

- relative orientation between support post axis and crystallographic axes (angle  $\alpha$ ).
- electrode metallization geometry and alignment with crystallographic axis and  $\alpha$ .
- electrode registration between top and bottom of platelet.
- amount and distribution of epoxy adhesive at all posts.
- general defects and flaws.

The general observations on each of these features follow.

a) Angle  $\alpha$  was observed by noting the deviation from the ground peripheral flat on each platelet and prior information obtained from the procurement sources. In general, deviation from the mean (see Tables 2-4) were found to be well within  $\pm 11^\circ$  for most assemblies of groups 1 and 3 (4 posts). Somewhat larger deviations were noted for group 2 (3 posts). b) The geometry of electrode metallization (Au or Al) appeared to be quite uniform on all platelets and alignment of the electrode axes with the post location was quite symmetrical. c) The electrode registration of top and bottom circular metallization that forms the high electric-field region of the resonator showed substantial deviation in the earlier crystal set of group 1, but improved substantially in the later set of that group, after registration masking was introduced to the metallization process. d) In all assemblies the extent of the conductive epoxy adhesive areas distributed over a nominally  $\pm 25$  mil peripheral area at each support post, with deviations in some units extending to  $\pm 35$  mils ( $\pm 12^\circ$ ). Considerable variation in total amount and spatial distribution of the epoxy adhesive areas generally observed. e) All units appeared to be free from particulate matter and defects.

All crystal platelets were identified individually so that their particular history could be traced with subsequent precision orientation measurements.

## Precision X-Ray Orientation

All SC-cut crystal plates described in this report were evaluated as to the precise crystallographic orientation of angles  $\phi$  and  $\theta$  that determine the doubly-rotated plane. Precision measurements were performed with the laser-assisted double X-ray goniometric technique, developed particularly for this function through USA ERA/COM sponsorship. The results for both procurements are summarized in Tables 6 and 7 where the Turn-Over-Temperature (T.O.T.) has been included for



completeness. This additional information, though not relevant to the present emphasis, may be of use to evaluate T.O.T. reproducibility. Each measurement represents the average value and RMS deviation  $\sigma$  of ten individual readings, so that the expected error in each measurement is  $\sigma/\sqrt{10}$ , or approximately  $10^{-4}$ . The averaging technique was used to minimize probable errors that arose from manipulating the inordinately small crystal platelets for which the crystal holder of the instrumentation was not optimally designed. In the 1983 procurement, this error was reduced two times by a more compatible crystal holder, though this fact cannot be deduced from a comparison of the two tables.

TABLE 6. PRECISION X-RAY ORIENTATION RESULTS (1982)

GROUP	SN	$\phi$ (°)	$\theta$ (°)	$\alpha$ (°)	TOT. (°C)
1 4 POSTS $\alpha = 0^\circ$	1	22.2050	0.0059	34.2020	0.0086
	2	0.1829	0.0133	0.2142	0.0074
	3	0.2171	0.0017	0.1707	0.0033
	11	0.1046	0.0092	0.1745	0.0048
	12	0.0985	0.0086	0.1709	0.0077
	14	0.1049	0.0031	0.1844	0.0028
2 3 POSTS $\alpha = 0^\circ$	5	23.6025	0.0066	34.1196	0.0067
	6	0.7011	0.0036	0.0684	0.0074
	7	0.7064	0.0031	0.1096	0.0019
	8	0.6520	0.0017	0.1701	0.0026
	9	0.7155	0.0085	0.0981	0.0028
	10	0.5688	0.0045	0.0277	0.0046
3 4 POSTS $\alpha = 45^\circ$	11	0.6568	0.0083	0.0786	0.0092
	13	0.6918	0.0172	0.0475	0.0088
	27				

NOTES  
 (1) EACH  $\theta$  REPRESENTS 10 SEPARATE MEASUREMENTS  
 (2) EXPECTED ERROR IS  $\sigma/\sqrt{10} = 3.16$   
 (3) AVERAGE OF 9 MEASUREMENTS  
 (4) FEWER MEASUREMENTS  
 (5) TURN OVER TEMPERATURE

TABLE 7. PRECISION X-RAY ORIENTATION RESULTS (1983)

GROUP	SN	$\phi$ REF. (°)	$\theta$ REF. (°)	REF. $\phi$ (°)	REF. $\theta$ (°)	TOT. (°C)
1 4 POSTS $\alpha = 0^\circ$	1	0.1222	-0.2378			43.4
	2	0.1150	-0.2426	22*	33*	42.4
	4	0.0994	-0.2344	0.3006	0.9869	42.8
	5	0.0957	-0.2316			43.7
	7	0.1257	-0.2188			44.9
	8	0.1261	-0.2261			42.5
2 3 POSTS $\alpha = 0^\circ$	9	0.1200	-0.2380			42.0
	11	0.1130	-0.2375			43.0
	12	0.1108	-0.2244			23.0
	16	0.1036	-0.6322	23*	34*	23.0
3 4 POSTS $\alpha = 45^\circ$	3	0.0543	-0.6265	0.6574	0.1223	21.0
	4	0.0946	-0.6470			23.28
	11	0.0976	-0.6349			21.27
	15	0.0265	-0.6505			26.30
	16	0.0811	-0.6187			36.2
	21	0.0137	0.0254	21*	34*	39.8
4 4 POSTS $\alpha = 45^\circ$	2	0.0495	0.0142	0.7852	0.2897	38.2
	3	0.0215	0.0061			36.0
	4	0.0552	-0.0120			33.2
	6	0.0027	-0.0142			31.0
	7	-0.1850	-0.0372			47.8
	1	-0.080	0.0711			52.0
5 4 POSTS $\alpha = 45^\circ$	2	-0.0635	0.0845			52.1
	3	-0.1131	0.0528			

\* NOMINAL SC-CUT ANGLES  $\phi = 22.4^\circ$   $\theta = 34.3^\circ$

\* TURN OVER TEMPERATURE

A cursory examination of both tables shows the surprisingly small angular spread in all cases, approximately 20 millidegrees for the 1983 units and slightly larger for the earlier set. All crystals, with the exceptions of those in group 2 (2 posts) are quite close to the angles of the stress compensated condition, for which the stress coefficient K (10<sup>-11</sup> cm<sup>2</sup>/dyne) is zero. (13) To date a direct relationship between K and  $\Gamma$  has not been established. For group 2 crystals, K = -0.02, while for all others K  $\leq$  +0.011 and these values persisted throughout the two procurement periods. In light of the inconsistent results for the vibration sensitivity for the two periods (nearly complete reversal of maximum  $\Gamma$  direction in some cases from 1982 to 1983) it would seem that one must look to

other than crystallographic orientation variations for an explanation of the demonstrated behavior.

### Comparison with Theoretical Results

Recent theoretical results (11) for in-plane acceleration in doubly-rotated cuts of quartz predict substantially improved performance under acceleration (vibration) that was demonstrated above. A summary of the theoretical results are shown in Figure 2, where the two important cases of three- and four-post supported SC-cut quartz plates are combined. The theory is based on idealized point supports at each post, where the exact location of each support is applied in the median plane of the thin quartz plate. (14) For a given support orientation angle  $\alpha$  with respect to the crystallographic axes of the quartz plate,  $\Gamma$  varies sinusoidally with a 180° period, as the acceleration vector rotates through one complete revolution. The maximum  $\Gamma$  varies for each particular  $\alpha$  and this functional behavior is plotted in Figure 2 for both 3- and 4-post support post cases and for crystal parameters appropriate to the experimental plates. The theoretical predictions clearly present the 4-post support structure as the preferred case, because of a) lower minimum and overall  $\Gamma_{\max}$  and b) the broad valley of low  $\Gamma_{\max}$  centered at  $\alpha = 45^\circ$ .

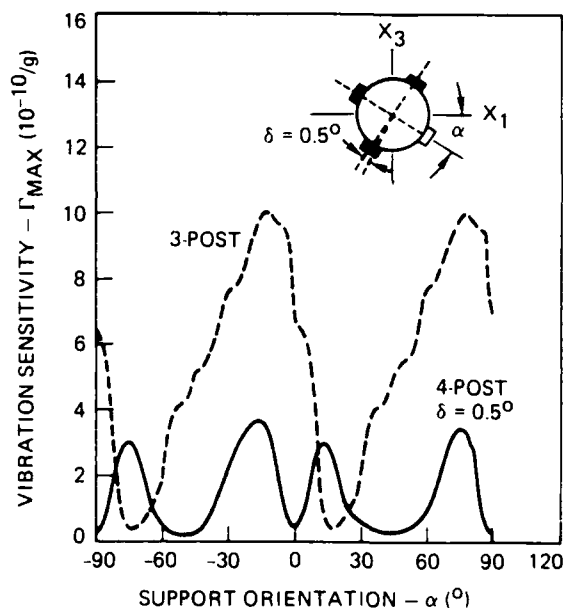


Figure 2. Theoretical Worst Case Vibration Sensitivity,  $\Gamma$ , of SC-Cut Crystal Plates for Idealized Support Structure Versus Support Orientation Angle  $\alpha$ ; (---) 3 POSTS, (---) 4 POSTS

The angle  $\alpha$  is referenced to the  $x_1$  crystal axis, synonymous with the projected x-axis in quartz that is often identified by a small flat ground edge, normal to x on the quartz plate perimeter. As an example, for the case,  $\alpha = 0$  (groups 1 and 2 of the experimental samples) the worst case ( $\Gamma_{\max}$  in units of 10<sup>-10</sup>/g) is predicted to be approximately 7.0 and 0.5 for the three- and four-post cases, respectively, for in plane acceleration along  $x_1$ . Similarly a  $\Gamma_{\max} = 0.25$  is estimated for the case  $\alpha = 45^\circ$  (group 3, 1983) and the acceleration vector along  $x_1$ . Out-of-plane acceleration has not been

computed to date.(14) Therefore, it is not known whether the computed cases represent, in fact, the worst case situation. The computation in Figure 2 assume that one of the four posts is placed in error by 0.5°. This is believed to cause the observed asymmetry in the relevant curve, in addition to some degradation in  $\Gamma$  near the two minima at 0° and 45°.(14)

The theoretical results are compared with our experimental performance of SC-cut crystals in Figures 3-5, and the AT-cut crystal cases are added in Figure 3 for completeness. The individual crystal  $\Gamma$ 's are shown there (1982 results), identified by the letter (x, for example) that denotes the direction along which the oscillator was vibrated in that case. The group 1 samples show qualitative agreement with theory for the worst case axis (x), but varies widely while the mean value  $\Gamma_e$  (4.06) is ten times the predicted value of 0.5. From a quantitative point of view, the 1983 results for the 4-post supported plates show similar behavior as is seen from Figure 4. The group 1 results ( $\alpha=0$ ) show again large distribution in  $\Gamma$ . The important difference lies in the nearly complete reversal of worst case  $\Gamma$  that is now normal (out-of-plane) to the crystal plate and, therefore, at variance, with the computed results. The group 3 behavior is quite similar both in the observed spread in  $\Gamma$  as well as in the deviations from the predicted worst case axis.

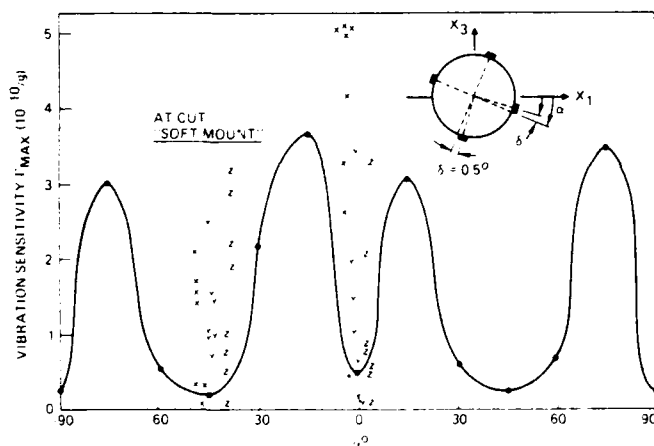


Figure 3. Vibration Sensitivity Results - Group 1, 1982;  $\Gamma = f_0$  (d/m)  $K_a = 2.2 \times 10^4 K_a$ ,  $f_0 = 100$  MHz;  $d = 0.250$ ",  $m = 5$ ; Ref (11)

The experimental results for the 3-post case (Figure 5) appear to be in reasonable agreement with predictions. Comparable agreement has been reported previously for large, low-frequency (5 MHz) SC-cut resonators(11) as is indicated on the figure. However, no experimental results are available for the case of  $\alpha \approx -15^\circ$  where a minimum  $\Gamma_{\max} \approx 0.5 \times 10^{-10}/g$  is predicted.

### Discussion

A summary of all relevant experimental results is presented in Table 8. It is observed that on the average, the AT-cut crystal group attained the lowest vibration sensitivity. The distinguishing feature of that group is the adhesive, a soft silicone-rubber like substance that remains resilient after the curing cycle. The possible bearing of this fact on the results will be discussed below.

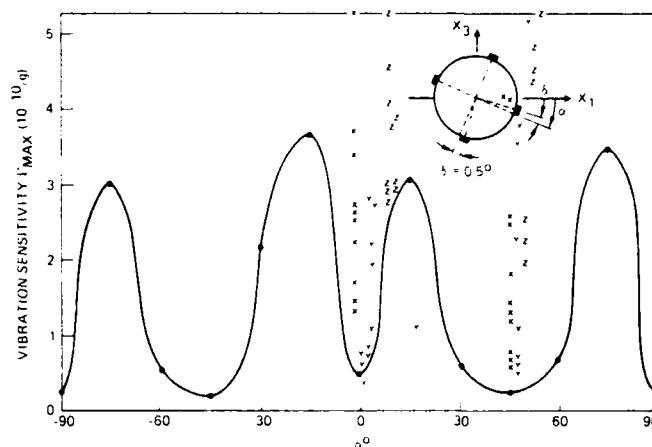


Figure 4. Vibration Sensitivity Results - Groups 1 and 3, 1983;  $\Gamma = f_0$  (d/m)  $K_a = 2.2 \times 10^4 K_a$ ,  $f_0 = 100$  MHz,  $d = 0.250$ ",  $m = 5$ ; Ref (11)

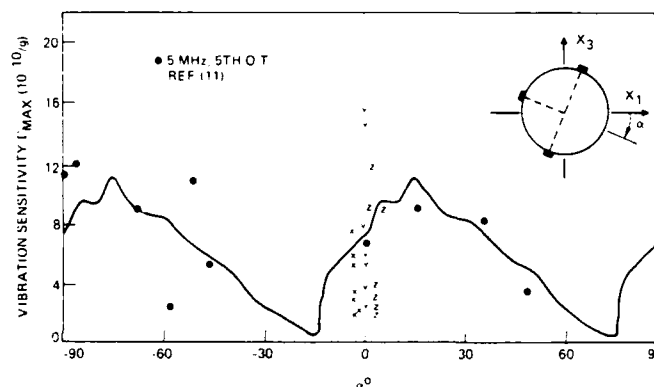


Figure 5. Vibration Sensitivity Results - Group 2, 1982/3;  $\Gamma = f_0$  (d/m)  $K_a = 2.5 \times 10^4 K_a$ ,  $f_0 = 100$  MHz,  $d = 0.250$ " 5; Ref (11)

TABLE 8. SUMMARY OF EXPERIMENTAL RESULTS(1)

YEAR	GROUP	SAMPLE SIZE	N	POSTS	$\Gamma_e$	$\Gamma_{\max}$	$\Gamma_{\min}$	$\Gamma_{\text{avg}}$	$\Gamma_{\text{std}}$	$\Gamma_{\text{max}}$
						$10^{-11} \frac{\text{CM}^2}{\text{DYNE}}$	$10^{-10} g$			
1982	1	7	0	4	22.1522	34.1361	0.005	4.10	86.1	14
1982	2	6	0	3	23.6507	34.7848	0.020	5.15	0.150	50
1982	AT	7	45	4	0	35.25	0.022	2.67	0.17	63
1983	1	9	0	4	22.1864	34.2192	0.005	4.06	20	80
1983	2	5	0	3	23.5751	34.7539	0.020	5.31	4	12.14
1983	3	3	45	4	21.8714	34.2202	0.01	4.16	0.17	44
1983	3	6	45	4	21.8510	34.3057	0.011	4.4	0.17	44

<sup>1</sup> SC CUT EXCEPT AS STATED

A cursory examination of the experimental results shows little evidence of a recognizable trend from which promising directions toward improvement in the vibration sensitivity might be elicited. The experimentally derived  $\Gamma_e$  in Table 8, shows little dependence on any recognizable parameter. What is most graphically shown, however, is the apparent superiority of the 4-post support structure vis-a-vis three posts. In some respects the present study on small VHF crystals is consistent with earlier more extensive work on large, low-frequency SC-cut crystal units (6). Both studies shows that thinner crystals with correspondingly higher frequencies yield lower  $\Gamma$ . The notion that the

stress coefficient  $K$ , which depends on crystallographic orientation might bear some relation to  $\Gamma$  is not supported in the present work. Indeed, for the same angles of the doubly-rotated cut, quite different directional  $\Gamma$  results were obtained from the two procurement lots that were produced nearly twelve months apart.

Comparison, insofar it is possible, between the SC-cut and the locally-produced AT-cut group shows that the latter group is superior in a statistically significant way. The most obvious difference between that group and the SC-cut groups lies in the manner by which the quartz plates are secured to the individual support posts. Whereas the externally procured crystal units feature a captured plate cemented with somewhat rigid conductive epoxy, the AT-cut plates are secured by a soft silicone rubber-like cement to the top of four platforms. The precise manner in which this relatively benign support affects the vibration sensitivity is not known. Theoretical computations, for the AT-cut, similar to those described earlier for the SC-cut have not been carried. Thus there are no guide lines from which to gain a sense of direction.

If the described analytical formalism is taken at face value, it might prove profitable to examine the idealized boundary conditions and compare these with what is implemented in practice. Figure 6 attempts to illustrate this comparison. Top and side views of the plate perimeter are shown in schematic

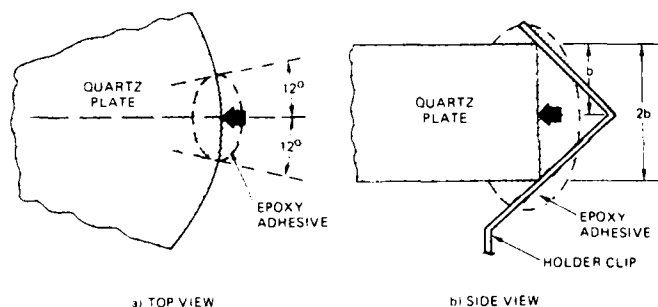


Figure 6. Ideal and Practiced Support Conditions; the Arrow Represents the Idealized Support Assumed in the Theoretical Computations

form. The idealized support boundary conditions, represented by the solid arrow, apply a point constraint in the central plane and along a diameter of the plate. The practically implemented support represented by the epoxy is shown distributed laterally over a  $\pm 12^\circ$  angular range and covering the entire vertical cross section of the plate thickness. Even this schematic representation is largely idealized, because the final extent of the manually-applied epoxy adhesive is not well controlled in practice permitting some spatially dependent stress to be applied over a  $\pm 12^\circ$  sector, subsequent to the curing procedure. Finally, the uniformity of the encapsulating cement region and stress condition at each of the four posts is only approximate, subject to variation. An examination of, for example, Figure 4, shows the large variation of the theoretical  $\Gamma$  that results from a change in  $\alpha$  near the minimum point at  $\alpha=0$ . A  $\pm 12^\circ$  variation raises the theoretical  $\Gamma_{\max}$  by nearly 10 fold. Intuitively, one might suspect that the variation in boundary conditions spatially within each post region as postulated above and coupled with

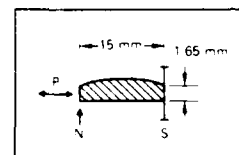
comparable variations between posts, might well tend to cancel the "stress-compensation" feature that is required to produce the promising theoretical vibration performance predicted for the SC-cut. The effect of the distribution and extent of the epoxy adhesive on the mode frequency of plate modes excited in such quartz resonator and supported in this manner has recently been demonstrated.(10) In this referenced study, the resonant frequency of the fundamental plate mode is raised by in excess of 30 percent if a distributed epoxy support is assumed rather than a point support.

Figure 6 reveals a second significant characteristic of the idealized support that is not met in practice. The ideal support is attached in the median plane of the quartz plate, representing a symmetrical boundary condition. Present practice in crystal assemblies features exclusively an asymmetrical support (from one side only). The precise effect of symmetrical support is not clear at this juncture. Pertinent computations have not been carried out to date that show the lack of symmetry effect on the vibration sensitivity  $\Gamma$  versus  $\alpha$ , comparable to Figures 3 and 4. However, symmetry in a variety of elastic and electromagnetic system leads to the reduction of permissible modes.(15) In turn, the excitation of modes is reduced and possibly reduces vibration-induced phase noise in the symmetrical crystal support configuration. Unpublished, related work suggests that a symmetrical support substantially reduces  $\Gamma$  relative to the normal asymmetrical support structure.(16) Table 9 summarizes relevant experimental results, where  $\Gamma_{\text{RMS}}$  is tabulated for plano-convex 5 MHz, 5th overtone (mostly) AT-cut resonators in various configurations.

TABLE 9. EFFECT OF CRYSTAL CUT & SUPPORT ON  $\Gamma(1)$

GROUP	CUT	NO OF POSTS	POST LOCATION	POST AXIS	$\Gamma_{\text{RMS}}$ 10 10 q
1	AT	2	Z	P(2)	108
2	AT	4	45°	N	105
3	AT	2	Z	N	55
3	AT	2	Z	N	52
3	AT	2	Z	N	57
4	AT	3 3 <sup>1</sup>	Z	N	48
4	AT	3	Z	N	65
5	SC	2	Z	N	20
6	AT	2	Z	S <sup>1</sup>	68
	AT	2	Z	S <sup>1</sup>	57

NOTES: 1) REF. (16)  
2) POST AXIS: P PARALLEL TO PLATE  
N NORMAL TO PLATE  
S SYMMETRICAL SUPPORT  
3) AT 90° LOCATION



A comparison of Group three (three samples) with Group six (two samples) in Table 9 shows that under the same constraints, the symmetrical (S) plate support, normal (N) to the resonator plane results in a ten times lower  $\Gamma$  as compared to asymmetrical support. Further support for this premise is offered by Group one result. The parallel (to the resonator) support may be considered symmetrical as well because its effective support occurs in the resonator median plane. The  $\Gamma_{\text{RMS}}$  of that group is also considerably reduced as compared to Group three (five times).

One further inference may be drawn from Table 9, with respect to a comparison between AT- and SC-cut resonators of otherwise identical designs. The  $\Gamma_{\text{RMS}}$  of the SC-cut plate is substantially lower than of the AT-cut plate in the same configuration and of the same frequency (2.5 times).

#### Conclusions

The phase-noise sensitivity to vibration,  $\Gamma$  of present state-of-the-art VHF quartz crystal resonators with SC-Cut Orientation is at least ten times (20 db) greater than the theoretical model of the four-post support plate predicts. The present support structure of the resonator, rather than the crystal plate itself, may be responsible for the discrepancy. It is suggested that, if the idealized support structure were at least in part, reduced to practice, substantial reduction in phase-noise sensitivity to vibration might result in VHF quartz crystal resonators.

#### Acknowledgement

The author gratefully acknowledges helpful technical discussions with Professor P. C. Y. Lee regarding his theoretical model of in-plane acceleration effects in doubly-rotated cuts of quartz.

#### References

- 1) R. L. Filler "The Effect of Vibration on Frequency Standards and Clocks" Proc. 35th A.F.C.S., Ft. Monmouth New Jersey, pp. 37-39, May 1981.
- 2) P.C. Y. Lee, C. Zee and C. A. Brebbia "Thickness Shear, Thickness Twist, and Flexural Vibration of Rectangular AT-Cut Quartz Plates with Patch Electrodes", J.A.S.A., Vol 72, No. 6, pp. 1855-1862, December 1982.
- 3) P. C. Y. Lee and Kuang-Ming Wu "Nonlinear Effect of Initial Stresses in Doubly-Rotated Crystal Resonator Plates" Proc. 34th A.F.C.S., pp. 403-410 May 1980.
- 4) A. Warner, B. Goldfrank, M. Meir and M. Rosenfield "Low 'g' Sensitivity Crystal Units and Their Testing" Proc. 33rd A.F.C.S., pp. 306-310, May 1979.
- 5) R. Filler and J. R. Vig "The Acceleration and Warmup Characteristics of Four-Point SC- and AT-Cut Resonator" Proc. 35th A.F.C.S., pp. 110-116, May 1981.
- 6) R. L. Filler, J. A. Kosinski and J. R. Vig "Further Studies on the Acceleration Sensitivity of Quartz Resonators" Proc. 37th A.F.C.S., pp. 265-271, Cat. No. 83CH1957-0, June 1983.
- 7) D. J. Healey, III and E. Y. Kwan "SC-Cut Quartz Crystal Units in Low-Noise Oscillator Applications at VHF" Proc. 35th A.F.C.S., pp. 440-453, May 1981.
- 8) D. J. Healey III, H. Hahn and S. Powell "A Measurement Technique for Determination of Frequency vs. Acceleration Characteristics of Quartz Crystal Units" Proc. 37th A.F.C.S., pp. 284-289, June 1983.
- 9) D. B. Leeson "Short Term Stable Microwave Sources" The Microwave Journal, pp. 59-69, June 1970.
- 10) R. D. Weglein, W. C. Hu and A. F. Margagliano "Microphonics in VHF Quartz Resonators and Oscillators", to be published.
- 11) P. C. Y. Lee and K. M. Wu "In-Plane Accelerations and Forces on Frequency Changes in Doubly-Rotated Quartz Plates" U.S. Army Research Office, Contract No. DAAG29-79-C-0019, Final Report, April 1983. (A part of this work is contained in Proc. 34th A.F.C.S., pp 403-411, May 1981.)
- 12) J. L. Chambers, "An Instrument for Automated Measurements of the Angles of Cuts of Doubly-Rotated Quartz Crystals" Proc. 36th A.F.C.S., pp. 302-313, 1982 E.I.A. 2001 Eye Street, N.W. Washington, D.C. 20006.
- 13) E. P. Eernisse, "Calculations on the Stress Compensated (SC-Cut) Quartz Resonator," 1976 Proc. A.F.C.S., pp. 8-11, June, 1976.
- 14) Private Communication from P. C. Y. Lee.
- 15) B. A. Auld, "Acoustic Fields and Waves," (book) Vol. I, Chapter 6; Vol. II, Chapter 13; John Wiley & Sons, N.Y., 1973.
- 16) D. Janiaud "Modelisation De L'Influence D'une Acceleration Sur La Frequence Des Resonateurs a Quartz," PhD Thesis O.N.E.R.A., Chatillon, 1978 (unpublished).

ACCELERATION SENSITIVITY COMPENSATION  
AND  $\Gamma$  SYMMETRY IN QUARTZ OSCILLATORSD.A. Emmons, R.M. Garvey and B.T. Milliren  
Frequency and Time Systems, Inc.  
Beverly, MASummary

Systems for precise navigation, secure communications, identification, synchronization, and many other applications require frequency sources of high stability and very good spectral purity. It has become increasingly important for such systems to maintain high performance under both dynamic and static conditions. A crystal oscillator which serves as the stable frequency source in a dynamic tactical environment is required to have extremely low sensitivity to acceleration forces in order to keep vibration-induced sidebands at the level of  $\mathcal{L}(f) = 10^{-10} \times f^{-2}$ , for 1 g input.

To achieve this, an acceleration sensitivity of no more than  $4 \times 10^{-12}$  per g, for vibration frequencies up to 2 kHz, is required. A number of active and passive compensation techniques show promise of reducing the overall oscillator sensitivity to the desired low level. Active compensation is achieved by means of a voltage feedback signal (proportional to input g) generated externally and applied to the oscillator circuit to counteract acceleration-induced frequency shifts. Passive methods encompass those which achieve direct compensation (via a second resonator, or other element) within the oscillating loop.

The success of any compensation method depends on the degree to which the intrinsic resonator sensitivity,  $\Gamma$ , is a single, symmetric vector quantity and thus amenable to complete cancellation.

Test methods must yield a fiduciary marking system to allow subsequent alignment exactly parallel to the axis of the compensating element. A very sensitive test for this symmetry is to plot g-response in the plane perpendicular to  $\Gamma$ . Results of dynamic measurements are presented.

Introduction

Precision systems for navigation, communications, network synchronization and many other applications require frequency sources of high stability and good spectral purity. High performance must also be maintained in an adverse dynamic environment.<sup>1,2</sup>

However, the frequency of a crystal reference oscillator is perturbed by acceleration forces. The response is described by a factor,  $\Gamma$  (fractional frequency shift per g), and manifests itself as vibration-induced phase noise near the carrier frequency. This is especially troublesome when frequency multiplication to high order,  $n$ , is involved. In that case noise sidebands scale as  $20 \log n$ . In many systems, degradation beyond -100 dBc at 1 Hz (referred to 5 MHz, and assuming 1 g peak vibration level) can not be tolerated. (See Figure 1).

Starting with the best available low  $\Gamma$  resonators, a general approach to further improvement is to

compensate for these effects in the oscillator. For the purpose of this discussion, the desired phase noise level (for 1 g input over a frequency range to 2 kHz) is  $\mathcal{L}(f) = 10^{-10} f^{-2}$  or better. To achieve this requires an effective compensated of  $4 \times 10^{-12}$  or better. This in turn will require a sensitivity reduction factor of 100 or more for most presently obtainable resonators.

The problem is made tractable by the vector nature of  $\Gamma$ , which permits single-axis compensation. Essential to the solution is the degree to which resonator and compensation element can be aligned exactly anti-parallel, and the degree to which the achieved compensation holds for all angles and frequencies. Special measurement techniques and considerations involving the finished oscillator system are required.

Presently Available Resonators

At present the best resonators available with some certainty show  $\Gamma$  values of a few  $\times 10^{-10}$ . SC-cut blanks can potentially be better than AT-cut, but AT-cut BVA resonators have also shown very low  $\Gamma$ .<sup>3</sup> Mounting of the blank, azimuth angles and support structure are important. Blank contour is important, but also observed is a large scatter in  $\Gamma$  magnitude and direction for what should be identical resonators<sup>4</sup>. Debaisieux<sup>5</sup> has recently reported  $< 2 \times 10^{-10}$  with moderately good yield in new resonator types.

To further improve performance, by compensation, we need knowledge of the symmetry and directional properties of  $\Gamma(\theta)$ , in general and in specific cases.

Orientation

We must address the general problem of finding  $\Gamma$  for a particular case, verifying its behavior, and mechanically attaching the resonator into an oscillator structure so that it needs no further orientation adjustment.

Figure 2 shows a resonator blank placed at a specific orientation in a coordinate system so that  $\Gamma$  (max) lies along the Z axis. Imagine this to be the end result of a process of alignment to be described below. The dotted line enclosure emphasizes that we do not know - a priori - in which direction  $\Gamma$  is pointing. Furthermore, the tolerance of mounting the blank in the enclosure is not relevant; all we have to work with is the enclosure.

A model of acceleration sensitivity which appears to fit nearly all cases is that  $\Gamma$  is a vector quantity. In the coordinate system shown, an acceleration input at a polar angle  $\theta$  produces a response proportional to  $|\Gamma| \cos \theta$ ; that is, the projection of  $\Gamma$  on the acceleration vector. In any plane through the Z axis, a circle drawn through the tip of  $\Gamma$ ,  $\Gamma \cos \theta$ , and the origin, describes the vector response. This kind of polar plot is in fact the most convenient way to compare data with the model.

A detailed discussion of the mechanical fixture and measurement process will follow later. We have found that a dynamic measurement system can give rapid convergence to the desired result, an important feature being that vibrations in the X-Y plane should produce zero response. The precision with which this zero response can be found makes it a more powerful technique than looking directly for the direction which maximizes response. For the latter case, note that the derivative of  $\cos \theta$  at  $\theta = 0$  is zero, while at approaching  $90^\circ$  it is large. Thus the  $1/2$  degree mechanical tolerance needed for ensuring a 100-fold reduction in effective  $\Gamma$  is more easily investigated in the X-Y plane.

The vector sensitivity  $\Gamma$  can in principle be cancelled by an equal and opposite compensation. This cancellation will not be exact if the resonator has asymmetric or non- $\cos \theta$  response for some angles. The relative magnitude of residual differences will set limits on the attainable compensation. If residuals exist at some azimuth angle, we might expect to see them projected onto the X-Y plane.

The single vector model has been discussed by numerous authors. Valdois<sup>6</sup> showed linearity of response to 50 g as well as the vector nature of  $\Gamma$ . Przyjenski<sup>7</sup> mapped the  $\cos \theta$  surface for a specific oscillator and also demonstrated a successful systems approach to single axis compensation.

#### Production Model Compensated Oscillator

For several years, Frequency and Time Systems already has been manufacturing high stability compensated oscillators as part of a cesium beam frequency standard; this oscillator is used for the AN/WSC-6 communications terminal (See Figure 3). This shipboard application requires that phase noise sidebands at 15 Hz from the carrier be less than -98 dBc, with approximately 1 g vibration input. To meet this requirement, standard high-Q resonators with  $\Gamma$  ranging from  $1$  to  $2 \times 10^{-9}$  are compensated to better than  $10^{-10}$ . The orientation precision required here is such that the static methods of measurement are adequate to verify that the required degree of compensation has been met for the individual oscillator.

This oscillator meets the need for low g-sensitivity over a specific range of low frequency vibration to 34 Hz. The requirement for high performance in a tactical environment with vibration to 2 kHz, requires new techniques.

#### Compensation

A number of active and passive compensation techniques show promise of reducing oscillator sensitivities. Active compensation is achieved by means of a voltage feedback signal (proportional to input g) generated by an external accelerometer and applied to the oscillator circuit to counteract acceleration-induced frequency shifts. Passive methods encompass those which achieve direct compensation (via

a second resonator or other element as sensor) within the oscillating loop.

The generalized scheme of  $\Gamma$  compensation is shown in Figure 4. The resonator is oriented for  $\Gamma$  in a known direction (up) so that the acceleration sensor may be fixed with its g-sensitivity vector,  $\vec{k}$ , in the opposite direction. A signal from the sensor proportional to the component of  $\vec{a}$  along the vertical is used to tune the oscillator frequency via the voltage control input to exactly cancel the intrinsic frequency shift  $\vec{\Gamma} \cdot \vec{a}$ .

Some important considerations are:

- Alignment - find  $\Gamma$  and orient to  $1/2$  degree for factor of 100 reduction.
- $\cos \theta$  behavior - must hold for both resonator and sensor.
- f response - either flat for both, or must track each other.
- Lack of Proximity - the unavoidable radial distance between sensor and resonator.
- Linearity - response linear with acceleration magnitude.

Proximity is important because angular velocity and acceleration inputs to the oscillator system give rise to centripetal forces whose effects are not cancelled, but are additive. A rotational rate of 0.1 revolution per second, for example, begins to show effects at the  $10^{-12}$  level.

For the external servo loop compensation, there is specific dependence on linearity and f response of the sensor, the linearity of voltage tuning, and the requirement that  $\Gamma$  be a constant, independent of tuning.

Figure 4 is easily generalized to include internal, or passive, compensation. The sensor may be any element having g-sensitive properties which serve to frequency tune the resonator in a way to cancel its intrinsic response. For example, a second resonator has been suggested for this purpose<sup>8,9,10</sup>. The second resonator must track the first in all respects, and must be aligned with the same exacting finesse. The g sensitivity of the pair must cancel either by selection or by equivalent circuit adjustments.

Perhaps the simplest sensor is a g-sensitive reactive element, such as a flexure plate capacitor as described by Valdois<sup>11</sup>. A very small change in capacitance with g is made to be part of the series frequency-determining load of the resonator. The element can be made small, placed close to the resonator, and mounted rigidly to it.<sup>12</sup>

In all of the methods, success depends on proper orientation of the resonator and alignment with the compensating element.

## Measurement System

Although static measurements in which an oscillator is reoriented in the earth's field to determine  $g$  sensitivity can give useful results, they do not lead quickly to the properly oriented resonator fixture that is required. Rapid convergence to a correct orientation is needed, and that requires real-time data from a resonator which is vibrating in an easily manipulated fixture.

This is accomplished by having the resonator available for mechanical alignment outside of the normal ovenized environment. Without thermal control, frequency drift would normally be a problem. And, for the sensitivity levels of interest, the high resolution of a reference oscillator-mixer system of measurement is needed.

We use a low-noise phase-locked-loop frequency discriminator as shown in Figure 5. The resonator under test is phase-locked to a wide tuning range tracking oscillator, and the loop time constant is short. Thus the amplified mixer output is proportional to the amplitude of frequency sidebands generated by vibration. The system bandwidth is much larger than the vibration frequencies, and the loop transfer function has a gain slope of -6 dB/octave over 10 to 20000 Hz. The natural frequency of the loop is greater than five times the bandwidth.

The noise floor of the system is such that acceleration-induced sidebands at the -50 dB level relative to maximum response can be observed.

For orientation testing we typically use a constant frequency at about 30 Hz. Off axis motion must be held to a minimum. The resonator is held in a rotatable clamp fixture, to which is attached the oscillator circuit board in close proximity. Flexible coax takes the buffered signal to an additional buffer amplifier and then to the mixer.

The basic requirement of the fixture is that it permit gimbal adjustment on two orthogonal axes, and that it have a reference plane to which the resonator  $F$  will be referred. The purpose is to find  $F$  and fix it with known orientation to a compact, rigid subassembly which ultimately becomes the compensated oscillator. In the process the subassembly response, with and without compensation element, is measured as the resonator angles are adjusted.

Referring again to Figure 2, the resonator can be oriented in this coordinate system by means of two mutually orthogonal axes, one of them parallel to  $X$ .

The fixture is vibrated along the  $X$  direction and the resonator is rotated for zero response. Then the fixture is vibrated along  $Y$  and the resonator is rotated about the  $X$  axis for zero response. The fixture can then be rotated about the  $Z$  axis to verify that the response is small or zero for all azimuth angles.

## Experimental Data

The fixture described above may also be mounted for vibration along the  $Z$  axis. If it is rotated on the vibration plate, along a polar angle, we can plot the  $\cos \theta$  response.

Typical data are shown in Figure 6. This is the response of a 4-point mount SC-cut 5 MHz resonator. Maximum response represents  $10^{-9}$  for this case. The theoretical  $\cos$  model is shown by the circle, and data points fall within about 5% of this at all points. Note that a 360 degree rotation gives 2-fold redundant data because of the bidirectional vibration. Thus a complete plot should display bilateral symmetry. In this case we have shown two sets of data. In the left half-plane are data points for rotation in the  $X$ - $Z$  plane, and on the right, rotation in the  $Y$ - $Z$  plane.

These are two arbitrarily chosen slices through the symmetric surface of  $F$  sensitivity. One limitation of such an examination, and to ultimate device performance as well, is the presence of residual mechanical modulation of circuit stray capacitances. Other sources of spurious response which limit the comparison with the theoretical model are: electromagnetic pickup from the vibrator driver; and residual off-axis motion of the vibrator.

Figure 7 shows data taken on the same resonator, for rotations in the  $X$ - $Y$  plane, with direction of vibration in the  $Z$  direction. The residual sensitivity for all directions is less than 1% of  $F(\max)$ , and additional alignment finesse can bring most data points within the  $1/2$  % circle. Again, the measurement limitations discussed above may limit the degree of certainty as to limits on the actual minimum response.

Similar plots can be shown for 3-point mount AT cut resonators. A 2-point mount fundamental AT-cut 5 MHz unit also shows a 5% fit to  $\cos \theta$  behavior. 10 MHz SC-cut units (4-point), some having  $F$  equal to  $8 \times 10^{-10}$  or less, also show the same behavior. In the  $X$ - $Y$  plane, all resonators examined thus far appear to show residual sensitivity below 1%, so that 100 fold reduction of sensitivity by compensation is seen to be feasible.

Using the capacitive type of  $g$ -sensitive variable reactance element for passive (local) compensation, a preliminary investigation has given the data of Figure 8. The vertical axis represents the resonator response (relative to the uncompensated case) in terms of power, or equivalent phase noise. The anomaly at 50 Hz was traced to a vibration table resonance giving off-axis motion. Ultimate measured performance was limited by imperfect fixturing and vibration modulation of stray capacitance, but a sideband reduction factor of 30 dB is seen over the frequency range to 110 Hz. Vibration direction was along the compensation axis.

## Oscillator System Considerations

At some frequency the intrinsic mechanical response of various elements in a compensated oscillator will limit the capabilities of the system. In Figure 9 some of these considerations are shown. The upper curve shows  $\Gamma$  of the resonator, assumed to be  $8 \times 10^{-10}$  as a worst case. It is expected to show flat response with frequency to above 2 kHz. Compensation at DC and low frequencies, by a factor of 150, gives the curve labeled  $\Gamma'$ . Depending on the frequency of the fundamental mechanical resonance of the compensating element, the compensator shows loss of correct action above some frequency in the hundreds of Hz range. As this frequency is approached, phase shift in the mechanical response leads to loss of compensation which is approximately represented by the curve of  $\Gamma''$ . This makes it necessary to consider a soft mounting for the resonator-compensator-oscillator which will attenuate the acceleration input above some frequency. That is, the input acceleration spectrum at the oscillator is attenuated to accommodate the loss of compensator effectivity at high frequencies. A modest amount of soft mounting, well damped, with a moderately low frequency natural resonance is feasible for this application.

## Conclusion

Summarizing the observed behavior of 3- and 4-point mount resonators, we see good agreement with a single vector model for the intrinsic acceleration sensitivity,  $\Gamma$ . The methods for investigation of the symmetry properties, and orientation for measurement, lead directly to methods for constructing compensated oscillator/sensor pairs for use in an oscillator which exhibits very low sensitivity to acceleration in a dynamic environment.

## Acknowledgement

This work was supported in part by the U.S. Army Electronics Technology and Devices Laboratory, Ft. Monmouth, NJ, under contract No. DAAK20-83-C-0393.

## References

1. R.L. Filler, "The Effect of Vibration on Frequency Standards and Clocks", Proc. 35th Annual Frequency Control Symposium, pp. 31-39 (1981).
2. V.J. Rosati and R.L. Filler, "Reduction of the Effects of Vibration On SC-Cut Crystal Oscillators", Proc. 35th ASFC, pp. 117-121 (1981).
3. R. Besson, J. Gros Lambert and F.L. Walls, "Quartz Crystal Resonators and Oscillators, Recent Developments and Future Trends". Ferroelectronics 43, pp. 57-65 (1982).
4. R.L. Filler, J.A. Kosinski and J.R. Vig, "The Effects of Blank Geometry on the Acceleration Sensitivity of AT and SC-Cut Quartz Resonators", Proc. 36th ASFC, pp. 215-219 (1982) and "Further Studies on the Acceleration Sensitivity of Quartz Resonators", Proc 37th ASFC, pp. 265-271 (1983).
5. A. Debaisieux, J.P. Aubry and J. Gros Lambert, "Design of SC Cut 10 MHz H.Q. Crystals with G Sensitivity Better than  $2 \times 10^{-10}/G$ ", Proc. 15th Annual PTTI Meeting (1983).
6. M. Valdois, J. Besson and J.J. Gagnepain, "Influence of Environmental Conditions on a Quartz Resonator", Proc. 28th ASFC, pp. 19-32 (1974).
7. J.M. Przyjemski, "Improvement in System Performance Using a Crystal Oscillator Compensated for Acceleration", Proc 32nd ASFC, pp. 426-431 (1978).
8. J.J. Gagnepain and F.L. Walls, "Quartz Crystal Oscillators with Low Acceleration Sensitivity", Technical Report NBSIR 71-855, National Bureau of Standards, Washington, DC 20234, March 1977.
9. R.J. Besson, French Patent 7829728 (1978).
10. A. Ballato, "Resonators Compensated for Acceleration Fields", Proc. 33rd ASFC pp. 322-336 (1979).
11. M. Valdois and B. Dupuy, U.S. Pat. No. 4,100,512 (1978).
12. D.A. Emmons, "Acceleration Sensitivity Compensation in High Performance Crystal Oscillators", Proc. 10th Annual PTTI Meeting, pp. 55-83 (November 1978).



# QUARTZ OSCILLATOR ACCELERATION COMPENSATION

- TACTICAL ENVIRONMENT
- STABILITY AND SPECTRAL PURITY
  - NAVIGATION
  - COMMUNICATIONS
  - FREQUENCY MULTIPLICATION
  - SYNCHRONIZATION
- ACCELERATION SENSITIVITY UNDER VIBRATION
  - $4 \times 10^{-10}$  per g +  $\chi = 10^{-6}$   $\epsilon^{-2}$
  - $4 \times 10^{-12}$  per g +  $\chi = 10^{-10}$   $\epsilon^{-2}$
- SENSITIVITY  $\epsilon$  REDUCTION
  - FACTOR OF >100 SOUGHT

FIGURE 1. QUARTZ OSCILLATOR ACCELERATION COMPENSATION

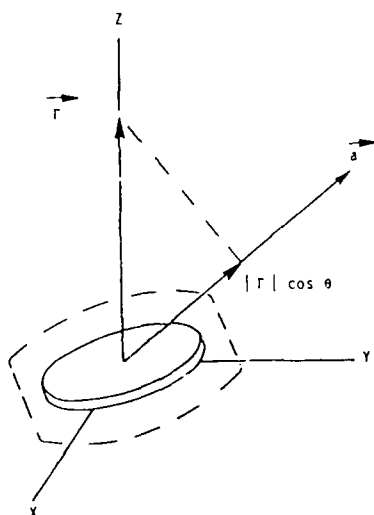


FIGURE 2. ACCELERATION SENSITIVITY OF QUARTZ RESONATOR

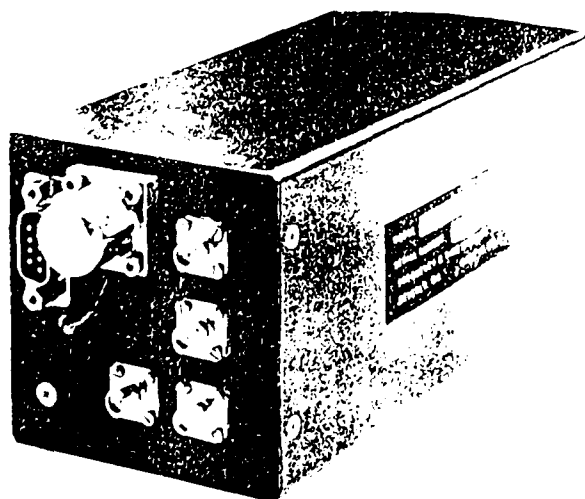


FIGURE 3. Model FTS 9110/120 with externally mounted acceleration sensor. Frontface dimensions are 2" x 2".

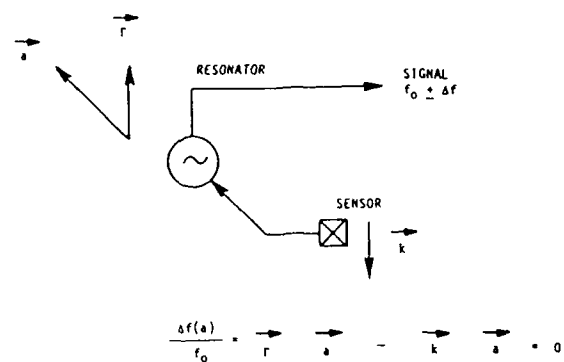


FIGURE 4. ACCELERATION COMPENSATION

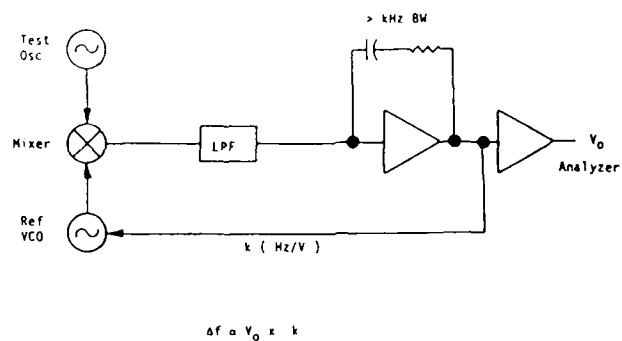


FIGURE 5. DYNAMIC MEASUREMENT

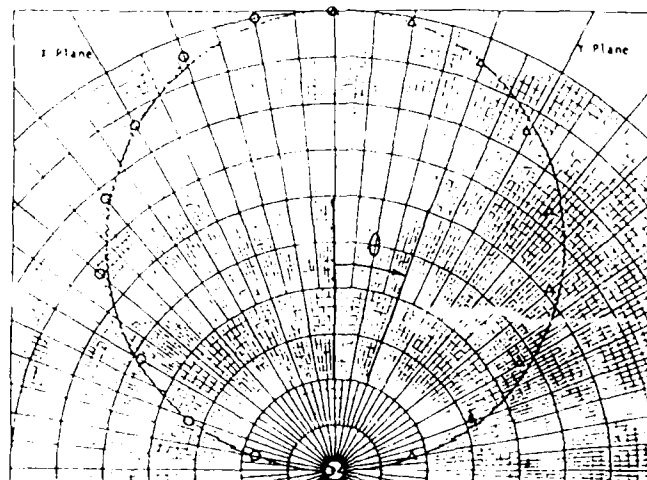


FIGURE 6. POLAR ANGLE  $\epsilon$  SENSITIVITY

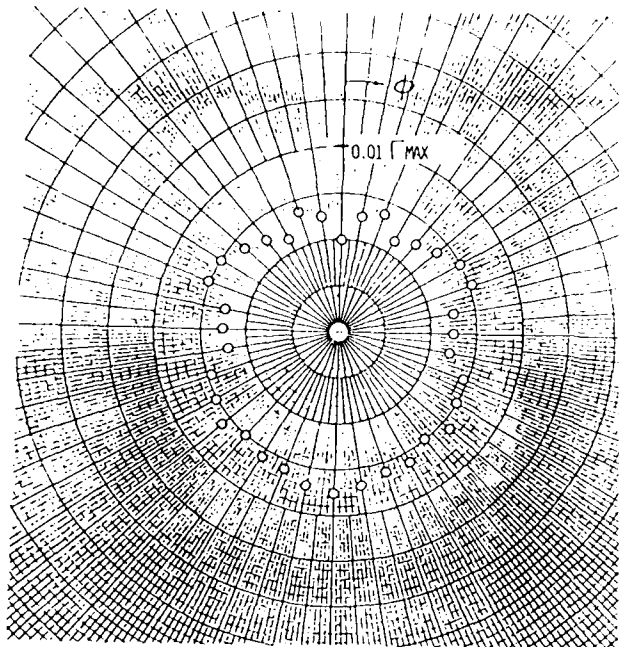


FIGURE 7. RELATIVE SENSITIVITY IN AZIMUTH

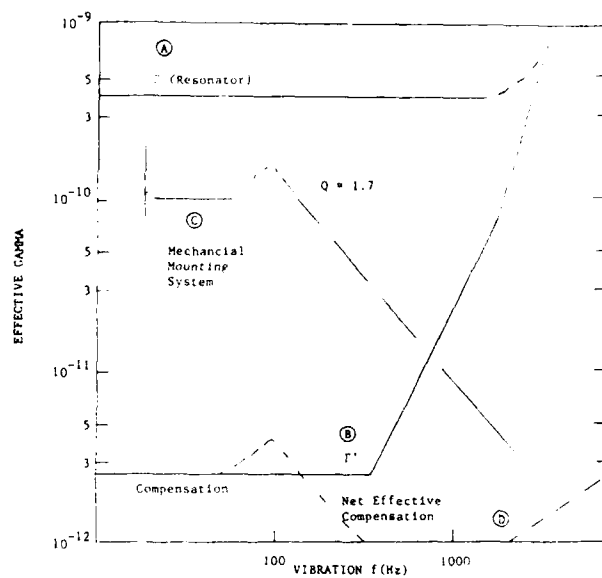


FIGURE 9. SYSTEM MODEL

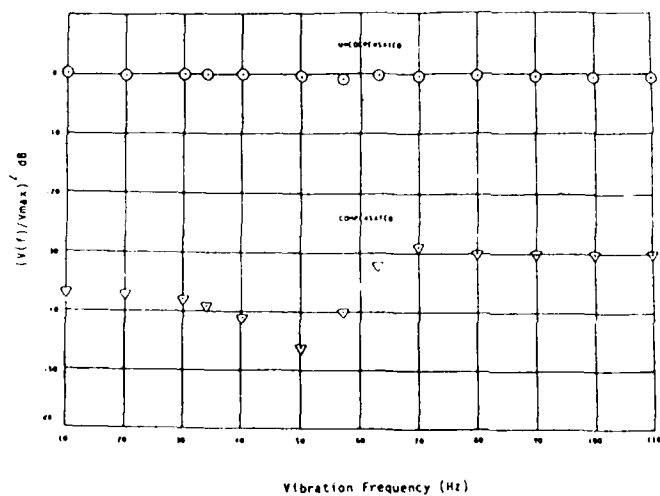


FIGURE 8. RELATIVE COMPENSATION VS. VIBRATION FREQUENCY

## A VIBRATION COMPENSATION SCHEME FOR A TACTICAL RUBIDIUM OSCILLATOR

Werner Weidemann

Efratom Division of Ball Corporation  
18851 Bardeen Avenue, Irvine, CA 92715

## ABSTRACT

Quartz crystals perform a very significant role in the Time and Frequency field of technology. Since the quartz crystal is used in stand-alone crystal oscillators as well as all Atomic Frequency Standards (AFS), the performance of the crystal is of paramount importance. Several adverse factors can degrade the crystal's performance in a stand-alone oscillator, producing unwanted offsets in the output frequency. Some of the factors, such as crystal aging, the crystal's temperature coefficient, and variations in the input line voltage/output load impedance, can be compensated for in an AFS. The biggest problem for both the stand-alone crystal oscillators and the present generation of AFS is vibration.

Under vibration, the AFS can provide improved performance over the stand-alone crystal oscillator if the vibrational response of the AFS's physics package is better than the vibrational response of the crystal. This of course is true only if the vibration frequencies are within the bandwidth of the atomic loop. For vibration frequencies outside the bandwidth of the atomic loop, the AFS is only as good as its internal crystal oscillator.

In order to improve the performance of an AFS under vibration, one can consider the following: (a) Design the internal AFS quartz crystal to be less sensitive to vibration. (b) Improve the AFS physics package. (c) Work to reduce the atomic servo loop time constant (i.e. Broadening the servo bandwidth). (d) A combination of the above.

Of the above, reducing the quartz crystal g-sensitivity yields by far the biggest gain in performance. This paper describes a method which falls into category (a), and specifically, it deals with vibration compensating a quartz crystal to make it less sensitive to g-forces.

## CRYSTAL VIBRATION PERFORMANCE CHARACTERISTICS

The frequency of the quartz crystal shifts as a function of gravity and acceleration. When the crystal is placed in a vibration environment, the crystal frequency is modulated by the vibration frequency.

In the case of sinusoidal vibration, the resulting sideband amplitude can be calculated as:  $L(f) = \frac{\Gamma \cdot g \cdot f_0}{2 \cdot f_v}$

Where:  $L(f)$  = Single sideband phase noise  
 $\Gamma$  = g-sensitivity of the crystal  
 $g$  = Vibration amplitude  
 $f_0$  = Oscillator frequency  
 $f_v$  = Vibration frequency

The vibration environment manifests itself as a degrader of oscillator performance primarily in the following areas: (a) Phase noise, (b) Short-term stability, and (c) Frequency offsets. Figure 1 illustrates the effects of sinusoidal and random vibration environments on phase noise performance.

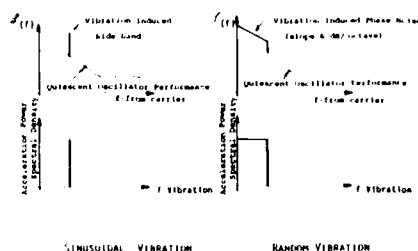


Figure 1. Phase Noise Under Vibration

Figure 2 illustrates the effects on an oscillator's phase noise for various "g-sensitive class" crystals when subjected to random vibrations. As illustrated, phase noise degrades to -92 dB, 100 Hz from the carrier (for a "parts in  $10^8/g$ " class crystals) when operating in a random vibration spectrum of 20 Hz to 2 KHz at a spectral density of  $0.01g^2/Hz$ . This is approximately 60 dB worse than the Efratom low noise (LN) Rb oscillator operating in a quiescent state. In the same figure, note that a "parts in  $10^9/g$ " class crystal performs 20 dB better than the "parts in  $10^8/g$ " class crystals.

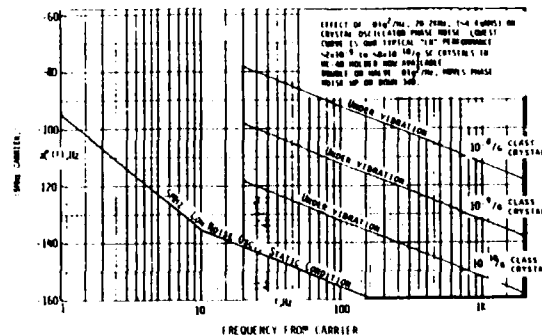


Figure 2. Crystal Oscillator Random Vibration vs. Phase Noise

Figure 1 is a log-log plot showing Acceleration (g) versus Time (Sec) for Performance Controlled. The y-axis ranges from  $10^{-1}$  to  $10^1$  g, and the x-axis ranges from 0.01 to 100 Sec. The plot displays five curves representing different performance levels:

- PERFORMANCE OF PARTS IN  $10^6$
- ACTUAL OPERATING IN M-100
- EXPECTED PERFORMANCE WITH AVAILABLE
- PERFORMANCE OF M-100 NO VIBRATION
- 100% DATA

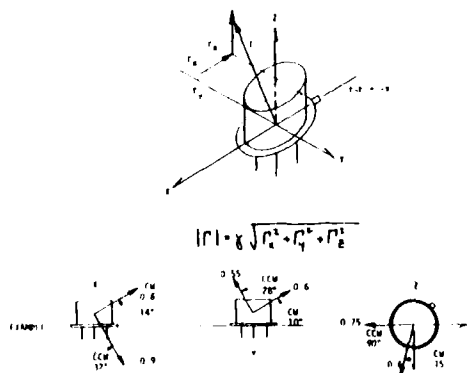
A legend at the bottom indicates the data source for each curve:

- ITAL (represented by a triangle)
- 8Y (represented by a circle)
- AD (represented by a square)

The crystal manufacturers have worked to reduce crystal g-sensitivity and, generally speaking, it is now possible to obtain crystals with a g-sensitivity better than  $2 \times 10^{-9}/\text{g}$  on a mass production basis. At the present level of technology, more than improved manufacturing techniques must be used to further reduce g-sensitivity.

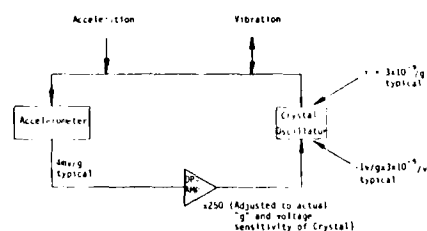
There are several approaches to this problem. After reviewing the various methods, active compensation of the crystal appears to hold the greatest promise and practicality. The Efratom concept is based on a paper presented at the 35th Annual Frequency Control Symposium in May 1981 by Vincent R. Rosati and Raymond L. Filler on "Reduction of the Effects of Vibration on the SC-Cut Quartz Crystal Oscillator."

Before attempting to describe an "active" compensation scheme, a review of parameters affecting the g-sensitivity of the quartz crystal is helpful at this point. The manufacturer's g-spec is generally defined as a vector whose components are as shown in Figure 4.



To simplify the effort, some idealistic parameters are defined as follows: The vibration input applied to the crystal causes the crystal to respond in such a way that the frequency vs. acceleration curve is linear up to 20 g's. The magnitude of the response is expected to be between a few tenths and several parts per billion per g. The response of a properly mounted crystal can be described by a constant  $\gamma$  vector.

GENEAL ACCELERATION WITH AN ACCELEROMETER, WHOSE SENSITIVE AXIS IS IN PARALLEL 1 AND DIFFERS THE AXIS OF CRYSTAL SENSITIVITY.



(2) Concepts taken from 1981 U.S. presentation by IRACOM, Geneva.

IN CONTRAST TO THE AT-CUT, THE SC CUT, DUE TO A DOUBLE ROTATION, IS AFFECTED BY DC ELECTRICAL STRESS. THIS EFFECT IS USED TO COMPENSATE THE CRYSTAL DURING VIBRATION.

PRODUCTION CRYSTALS USED BY ETHERAM ARE IN THE 10  $\mu$ W CLASS, FOR 2 TO 10  $\mu$ W.

SC-CUT CRYSTALS' DC VOLTAGE SENSITIVITY VS. ACCELERATION IS 2 TO 5  $\mu$ V/VOLT FOR 10G. COMPENSATION, A 20 VDC SWING IS NEEDED

SC CUT DC VOLTAGE TIPPING IS DESIRABLE OVER VARIATION TIPPING DUE TO ITS LINEARITY AND LACK OF HARMONICS

1 rotate crystal until  $r$  vertical

2 rotate accelerometer so sensitive axis is parallel to and opposite direction of  $r$

THE VECTOR CAN BE LOCATED AND ALIGNED AS SHOWN

THE ACCELEROMETER IS ROTATED TO PICK-UP THE OFF PLANE ANGLE

Figure 7. Accelerometer Mounting Scheme

The mechanical and electrical adjustments are precise but not of a magnitude to pose mass production problems. For example, when dealing with the electrical adjustments, to obtain a 20 dB compensation along the most sensitive axis, magnitudes must be within 10% including all non-linearities, frequency response limits, etc., and allowing no error in the mechanical alignment of the accelerometer. For the mechanical adjustments, in order to insure the cross axis response remains below -20 dB (i.e. no worse than the on-axis response), the alignment must be within  $\pm 6^\circ$ , allowing no error in magnitude of the analog, including all non-linearities, frequency response, etc.. To further illustrate this point, if the alignment were within  $\pm 3^\circ$ , the magnitudes must be within 5%.

The analog voltage of acceleration-induced frequency change is applied to a linear "voltage to frequency" modulating device, but in opposing phase. Since the acceleration-induced frequency change is instantaneously cancelled through the accelerometer, amplifier, and frequency modulator path, an active compensation scheme has been constructed.

The most convenient means by which the frequency of an SC-cut crystal can be modulated is to apply the DC voltage directly to the crystal terminals. Generally, the range of voltages can be 10 volts peak, covering accelerations up to 10 g's peak.

#### INVESTIGATION

The investigation was divided into three areas of concern: (a) Locating a suitable accelerometer, (b) Designing the supporting circuitry, and (c) Locating a suitable crystal.

(a) The subminiature piezoresistive accelerometer is very attractive for its size, weight, and dc response. Unfortunately, the wideband (several kilohertz) units are very delicate and easily damaged in an undamped configuration.

There are two solutions available. The first, to damp the moving parts with a silicone oil; the second, to use a precise set of stops to limit the motion at resonance.

The latter is a patented technique exclusive with a particular supplier. In evaluating oil damped accelerometers, they were found to have excessive temperature coefficients of damping, unstable dc responses, and overly optimistic manufacturer specifications. The final evaluation of such devices was that of an undamped 6 KHz unit which was found to be entirely satisfactory for this application. See Figure 8.

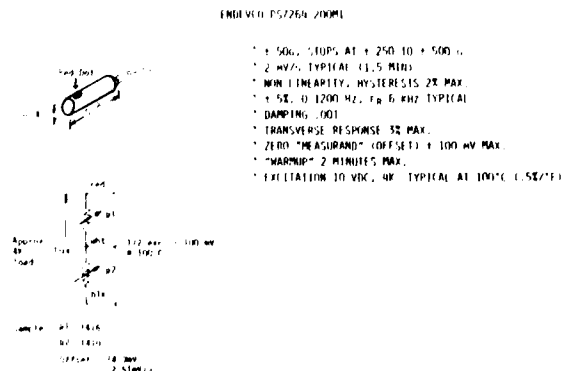


Figure 8. Accelerometer for Compensation Scheme

(b) The electronic portion is straightforward but exacting. The bridge compensation network must be adjustable to about 1 mV offset and the amplifier must have  $\sim 10$  MHz gain-bandwidth to keep phase shifts to less than  $6^\circ$  up to 2 KHz. In addition, the amplifier must be able to deliver large signal outputs up to about 2 KHz without significant phase shift. The 0 to 2 KHz high-level (tens of volts) compensation signal must not modulate the electronic circuitry of the oscillator, but only the crystal.

(c) The crystals tested initially were 5 and 10 MHz, third over-tone units in HC-40 holders with 3 point mounting. None of these exhibited the constant vector needed for all-axes (spherical) compensation. Figure 9 illustrates a polar graph of an unacceptable crystal g-vector. Note the requirements of Figure 10 as a comparison.

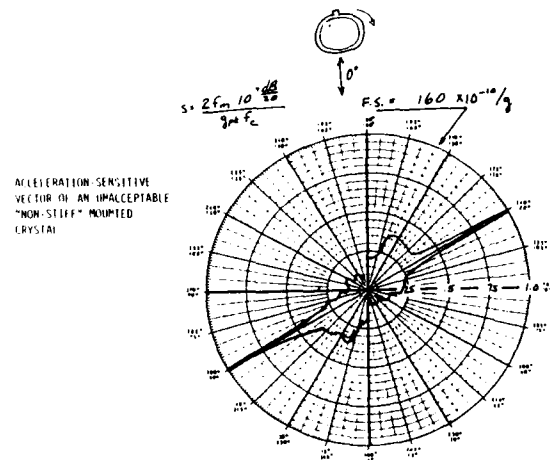


Figure 9. Acceleration-Sensitive Vector of an Unacceptable "Non-Stiff" Mounted Crystal

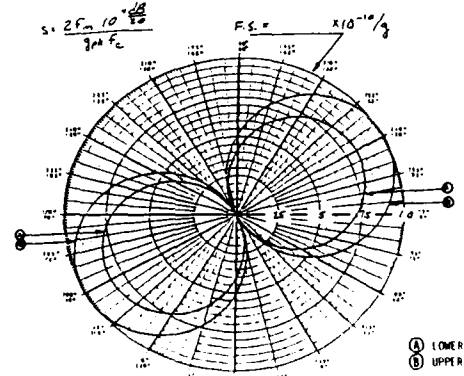


Figure 10. The Crystal's Acceleration-Sensitive Vector Requirements

The basic requirements for the active components to make the compensation scheme work are as follows:

- The magnitude of the vector should be stable to within 10%. It is desirable, however, to assign some of the 10% tolerance to the accelerometer, amplifier, etc.. Figure 10 illustrates the upper and lower tolerance limits for the crystal's acceleration-sensitive vector.

- The direction of the vector should be stable within  $6^\circ$  spherical, but again some of the tolerance should be assigned to the mechanical adjustments and electronic phase shifts.
- Figure 11 simulates the required stable acceleration-sensitive vector needed by a crystal for the proposed scheme to be functional. The crystal must not be sensitive to angular acceleration.

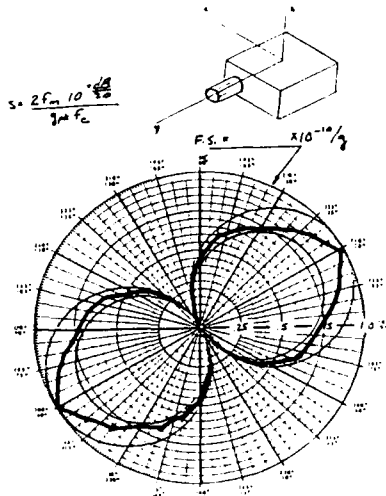


Figure 11. Simulation of an Acceptable Crystal Acceleration-Sensitive Vector

#### New Crystal Mounting Technique

During this investigation period, a separate project was being worked involving the testing of a new "flat-pack" crystal from Dr. John Vig of USA-ERADCOM. The flat-pack crystals appeared to have more stable vectors than previous crystals tested. After obtaining permission to copy the flat-pack mounting technique, both Peizo Crystal Corp., and Colorado Crystal Corp. participated in the fabrication of specially mounted crystals which provided the required stable vectors in all axes, to within  $\pm 6^\circ$ . In addition, the crystals with special internal mountings proved to have a better g-sensitivity than any of the previously tested crystals. Figure 12 illustrates the "old" mounting technique, and the new "stiffer" flat-pack mounting style.

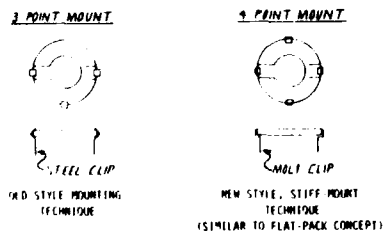


Figure 12. Improved Crystal Mounting

Polar charts for these crystals indicated that the vector had the required stability to advance to the actual testing of the Accelerometer Compensation Scheme. Figures 13 and 14 are examples of typical Polar charts demonstrated by the newly acquired crystals without any form of compensation provided. In addition, the new crystals exhibited a g-sensitivity of  $\sim 1 \times 10^{-9}/g$ .

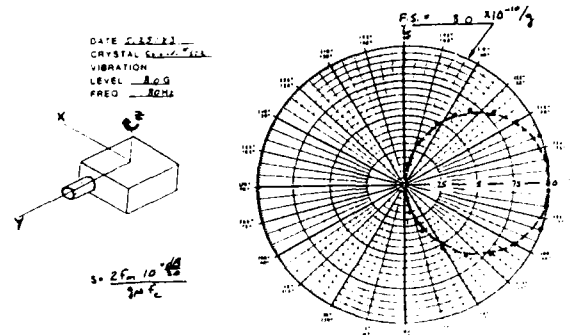


Figure 13. Polar Chart of "Stiff Mounted" Crystal, XY Plane Uncompensated

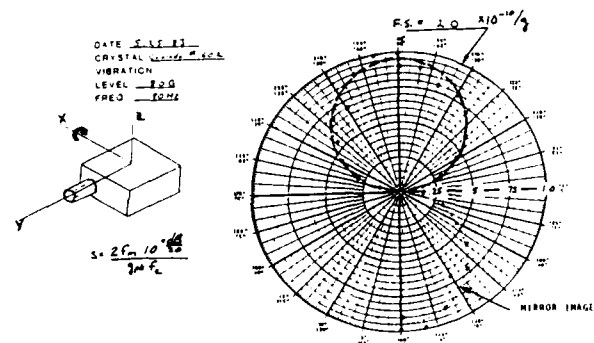


Figure 14. Polar Chart of "Stiff Mounted" Crystal, ZY Plane Uncompensated

#### COMPENSATION SCHEME TESTING

The compensation technique was tested by measuring the crystal sidebands during vibration, with and without the accelerometer compensation loop closed. These tests were conducted by mounting the crystal and accelerometer in an aluminum block on a specially designed crystal oscillator PC board, with both mounted directly to the equipment. After observing the expected 20 dB improvement for the most sensitive axis, the assembly was integrated into a Model M-100 Rubidium Frequency Standard.

Figures 15, 16, and 17 are phase noise plot test results with the special assembly integrated into the functional M-100. The three figures represent the X, Y, and Z axes respectively, presenting the sideband levels for both compensated and uncompensated operation. The less sensitive axes of the crystals are at least 5 times better, therefore only a few dB improvement will make these axes as good as the goal of 20 dB improvement for the most sensitive axes.

# INTEGRATION OF COMPENSATION SCHEME INTO M-100

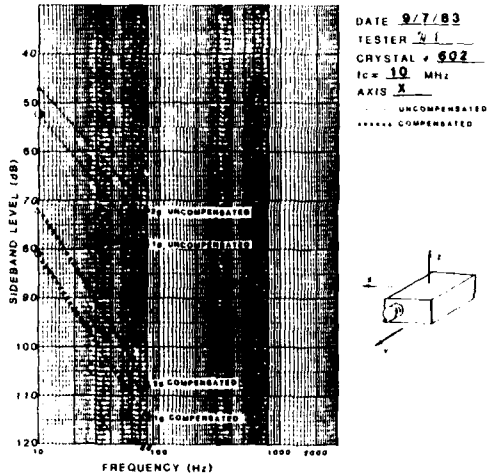


Figure 15. X Axis Phase Noise Plot With and Without Compensation

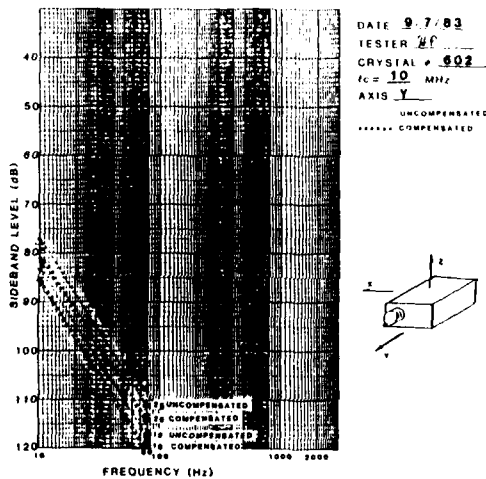


Figure 16. Y Axis Phase Noise Plot With and Without Compensation

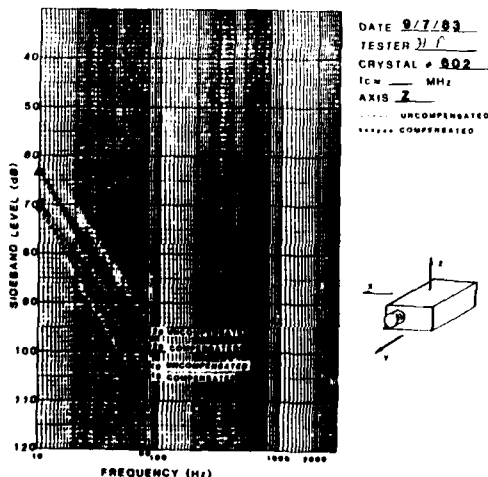


Figure 17. Z Axis Phase Noise Plot With and Without Compensation

Preliminary tests with the special assembly integrated into the M-100 indicated that the approximate 20 dB improvement obtained with the test setup was possible, but the test results were not consistently repeatable, varying with changes in frequency. The problems were identified as extraneous pickups by the wires connecting the accelerometer to the preamplifier. After resolving this issue, the approximate 20 dB improvement was consistent/repeatable up to a vibration frequency of about 100 Hz. When above 100 Hz, there was less improvement. In sensitive applications, shock mounts are more than adequate to provide acceptable attenuation after about 60 Hz. The primary goal of the compensation scheme is to provide attenuation in the frequency range in which shock mounts are not effective. For the Rb AFS, this frequency is approximately 1 to 60 Hz.

It was first thought that the g-sensitivity in the uncompensated mode is independent of the existing vibration frequency. The non-uniformity may be related to package resonance and measurement tolerances. The up-turn of the g-sensitivity of the compensated crystal is mainly related to a phasing problem. (The signal of the accelerometer does not remain in phase with the pickup of the crystal. This problem is caused by the mechanical resonance of the accelerometer [6 KHz] and extraneous pickup, e.g. by the connecting wires.) Figure 18 illustrates the typical improvement assuming an 8 g vibration level, a 20 dB improvement to 100 Hz, tapering off to 0 dB at 1 KHz. Figure 19 illustrates the magnitude of the g-sensitive vector of an average crystal both with and without compensation, as a function of the vibration frequency.

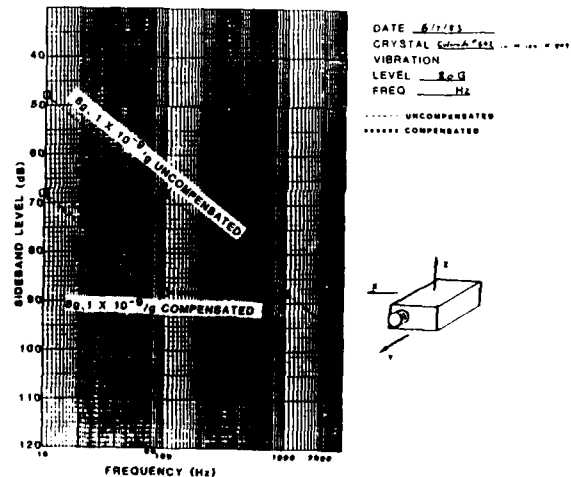


Figure 18. Typical Improvement of Sidebands With and Without Compensation at 8g Vibration Level

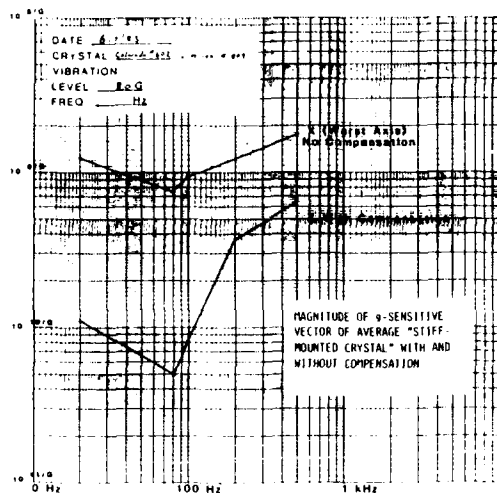


Figure 19. Magnitude of g-Sensitive Vector of Average "Stiff Mounted" Crystal With and Without Compensation

### CONCLUSIONS

The improvement of the g-sensitivity to  $1 \times 10^{-9}/g$  for the new stiff-mount crystals has eliminated the previously observed offsets in the output frequency during low frequency high level vibration. This would eliminate the need for a vibration compensation scheme if the user is only interested in timing functions. However, if the user requires a clean output spectrum the proposed vibration compensation scheme offers a significant improvement close to the carrier, an area where an improvement using any other method is very difficult to achieve. Figures 20 and 21 are the Polar charts illustrating the improvement obtained by using the Accelerometer Compensation Scheme. Note the Full Scale (FS) of Figures 13 and 14 ( $FS = 8.0 \times 10^{-10}/g$  and  $FS = 2.0 \times 10^{-10}/g$  respectively) as compared to the FS in Figures 20 and 21 ( $FS = 0.63 \times 10^{-10}/g$  and  $FS = 1.4 \times 10^{-10}/g$  respectively). Whereas no further improvement can be expected in the XY plane (Figure 20) due to the almost unidirectional plot, further improvement in the ZY plane (Figure 21) could have been accomplished by better alignment of vector of the accelerometer with that of the crystal; this being

illustrated by the difference in sensitivity at  $90^\circ/270^\circ$  compared to  $180^\circ/360^\circ$  (Figure 21).

In conclusion, the Active Compensation Scheme described works and is ready to support low phase noise applications in hostile vibration environments for Stand-Alone Crystal Oscillators and Atomic Frequency Standards.

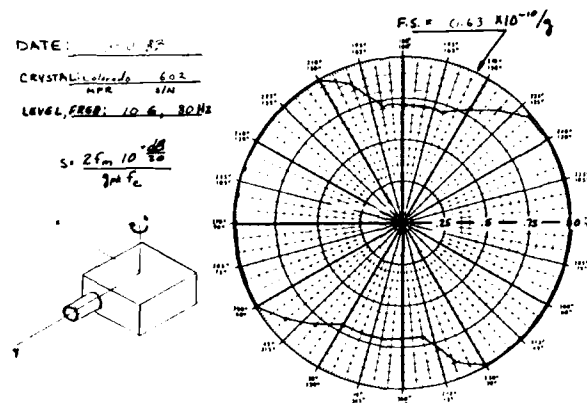


Figure 20. Improvement Obtained by Using the Accelerometer Compensation Scheme for XY Plane

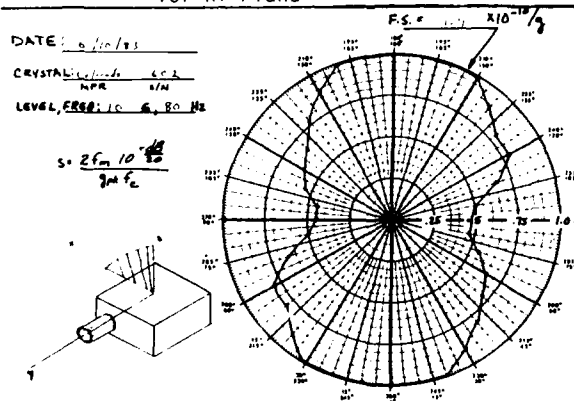


Figure 21. Improvement Obtained by Using the Accelerometer Compensation Scheme for ZY Plane



# VIBRATION EFFECTS ON EHF SYSTEM PERFORMANCE EMPLOYING LOW NOISE RUBIDIUM STANDARD AND CRYSTAL FILTERS

Edward M. Perdue

Raytheon Company  
Communication Systems Laboratory  
Marlborough, Massachusetts 01752

## ABSTRACT

Every system has its particular vibrational input specifications as well as on-board vibration. It is the vibration induced sidebands that push the RMS integrated phase noise and spurious above the system specification.

When communication systems were designed for HF to UHF, vibrational induced sidebands were not a concern. Now with modern SHF and EHF systems, vibrational induced sidebands become very important.

This paper will present test data characterizing the rubidium standard and monolithic crystal filter with 1 Grms vibration inputs from 20 to 5000 Hz. The paper presents applications for the monolithic crystal filter in EHF systems that improve phase noise and spurious. It will show their limitations as they exist now and suggest better methods for specifying filters to insure low vibration induce sidebands.

## KEY WORDS

Acceleration sensitivity, acceleration desensitizing, acceleration effects, atomic standards, BER, carrier drop-out, EHF systems, monolithic crystal filters, phase noise, phase noise clean-up, quartz oscillator, spurious, systems application, vibration induce sidebands.

## 1. APPLICATION VERSUS NOISE/SPURIOUS ENHANCEMENT

Many different types of systems are being developed for future applications. The technologies of these systems are demanding higher operating frequencies, fast pseudo random hopping for anti-jamming, and stable time base and low phase noise/spurious. With this also comes the demand for smaller, lower weight, and lower dissipation equipment.

Each development phase of a system reintroduces side effects associated with thermal and vibration as a result of repackaging, new concepts, and size reduction. Various articles discuss effects of vibration 1-6 and means to reduce the effects 2,3 on quartz oscillator. Likewise, methods 7,8 have been discussed to reduce vibration effects on atomic standards (quartz oscillator).

With the complexity of the systems, atomic standards are being utilized to provide both frequency/time accuracy and low phase noise. Typical phase noise data of various atomic standards are shown in Figure 1 purely as examples showing only specification data from data sheets (not typical). Consideration for generation of higher frequencies includes the enhancement of any phase noise (whether it be discrete spurious or oscillator phase noise) by the factor.

20 Log (N) (1)

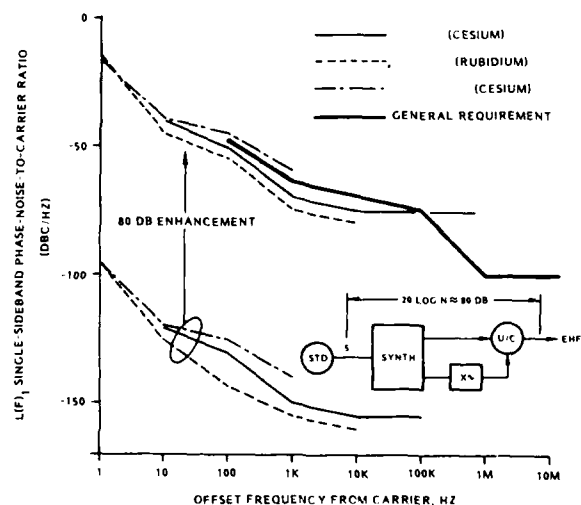


Figure 1. Typical Standard Phase-Noise at 5 MHz Enhanced to EHF Versus Requirements

Figure 2 illustrates this concept as applied to all kinds of systems presently deployed should they utilize a standard as their base frequency. For the typical EHF system, the noise enhancement is approximately 80 dB. Enhancing the phase noise of those shown in Figure 1 by 80 dB illustrates the effect against the general system transmit requirements. This leaves little or no margin for system vibration induced sidebands.

Figure 1 also suggests the necessity for spectral clean-up at the 5 MHz level, and several higher frequency points in the synthesis chain. Monolithic crystal filters from 5 up to 150 MHz are available.

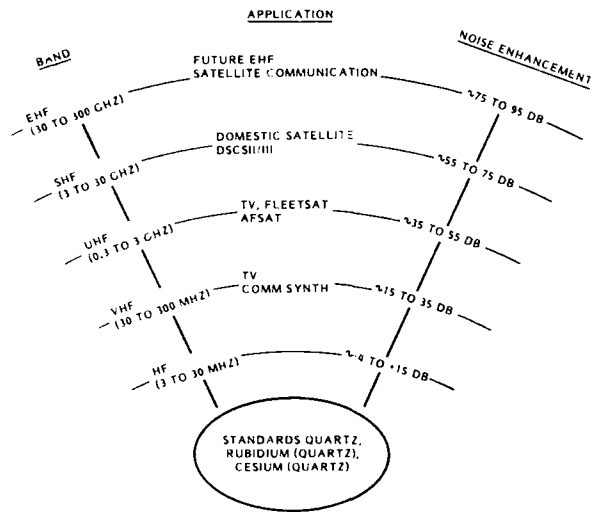


Figure 2. Noise Enhancement of Standards Utilized in Various Systems

## II. TYPICAL PSK BER PERFORMANCE OF COMMUNICATION SYSTEMS

One could choose a multitude of different modulation schemes to discuss system degradation due to interference or unwanted sidebands. Simple PSK (phase shift key) is used as an example to illustrate importance of a spectrally pure carrier since present systems use digital signal processing, modulation, etc.

A PSK modulated system is represented by a RF vector of  $0^\circ$  or  $180^\circ$  for BPSK (binary phase shift keying). The performance of such a system depends on how well the signal is demodulated into "0"s and "1"s at the receiving end. The performance of such a system is described by an error probability function:

$$P_e = \frac{\exp(-E_b/N_0)}{2\sqrt{\pi(E_b/N_0)}} \quad (2)$$

This function is for an ideal system; i.e., no interference, no LO sidebands, only white receiver thermal noise.

The equation (1) has been expanded <sup>9</sup> to include RMS jitter or integrated phase noise and sidebands offset from the carrier (LO) over the data bandwidth. Equation (1) is thus:

$$P_{e^*} = \frac{\pi}{4} \exp\left\{-\frac{\pi}{8\sigma_{\phi T}^2}\right\} + \frac{\exp(-E_b/N_0)}{2\sqrt{\pi(E_b/N_0)}} \quad (3)$$

This equation is plotted in Figure 3 along with various values of  $\sigma_{\phi T}$ .

$\sigma_{\phi T}$  for discrete components is represented by:

$$\sigma_{\phi T}^2 = \phi_1^2 + \phi_2^2 + \phi_3^2 + \dots + \phi_N^2 \quad (4)$$

and for a continuation phase noise,

$$\sigma_{\phi P}^2 = \int_{f_a}^{f_b} L(f) df \quad (5)$$

and the total RMS noise,

$$\sigma_{\phi T} = \sqrt{\sigma_{\phi D}^2 + \sigma_{\phi P}^2} \quad (6)$$

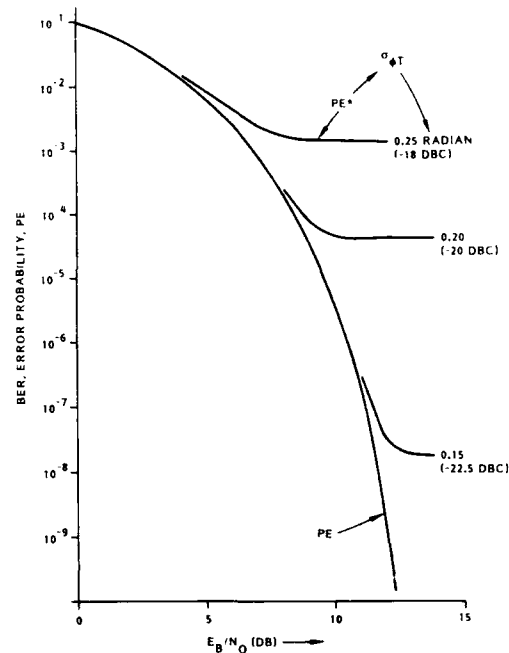


Figure 3. BER Performance for PSK Modulation

Figure 4 is representative of a SHF carrier phase noise.

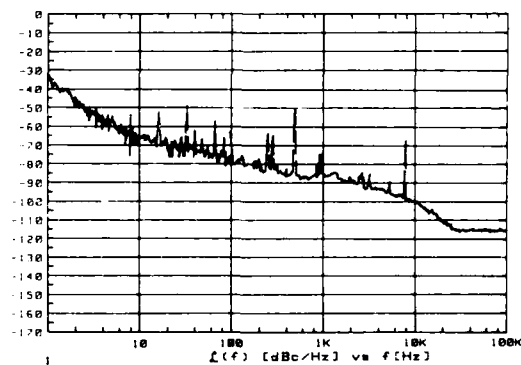


Figure 4. Typical Phase Noise Plot for an SHF Carrier

Normally a system optimally powered will operate at  $E_b/N_0$  at 10 dB for a  $10^{-5}$  BER. It is reasonable that for an interfering signal, the system could increase its signal above the interfering signal to improve performance. However, for a LO sideband, the system performance can not be im-

proved by an increase in signal power; as the sideband remain at a constant relationship to the carrier power. Thus, any degradation on the carrier will produce a floor in the BER performance; i.e., further increasing power has no effect of improving system performance.

Therefore, most systems have specified that the integrated noise about the carrier over the data bandwidth must be less than 0.1 radian. This is equivalent to a discrete sideband of -26 dBc as follows:

$$0.1 \text{ radian} \approx -26 \text{ dBc}$$

### III. TYPICAL LOCAL OSCILLATOR GENERATION

The literature contains many basic concepts for frequency synthesis. Modern synthesis includes low to high frequency operation, tuneability, slow to fast speed switching and settling, low spurious, integrated phase noise lower than 0.1 radian, etc. Coupled with these requirements are small size and weight, low power dissipation, simplification, maintainability, and reliability. These latter requirements introduce additional requirements. Power supplies become switcher supplies to reduce weight but introduce ripple problems (readily reducible by regulators). Choices between filtering circuits must be made (i.e. VCO-PLL versus crystal filter versus a different frequency scheme. Smaller size normally leads to higher concentration of parts thus a higher heat concentration requiring cooling. This introduces vibration effects for circuits utilizing quartz crystals or anything that may change the phase of the RF signal. Normally the above requirements fit platforms that in turn have specific vibration inputs to the equipment. Thus the jurisdiction design of a modern synthesizer must deal with size, power, ripple, vibration, etc.

Figure 5 illustrates the typical approach to the modern synthesizer. The figure is also representative of the various filter technologies. Note

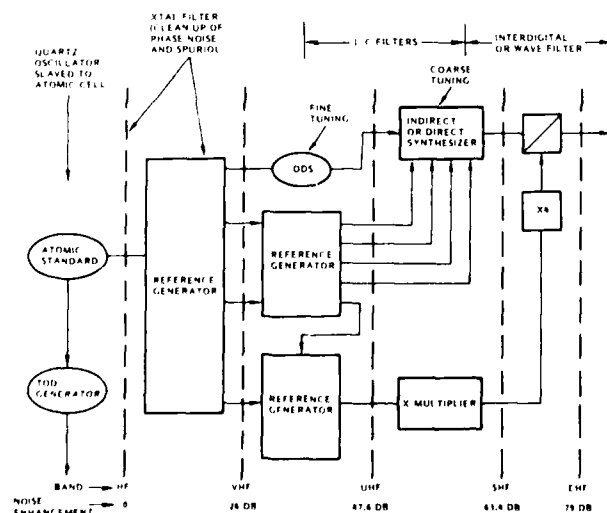


Figure 5. Typical Modern Synthesizer

that the xtal filter is placed at a point in the synthesizer that has the most enhancement of sidebands by multiplication. Having illustrated the effective multiplicative factor, the importance of exploring vibrational effects of xtal filters becomes clear.

Figure 6 is representative of one piece of hardware containing a reference frequency generation and the monolithic crystal filter. Size is of importance as the module shown contains components on both sides. This type of module is very rigid and will transfer any vibrations with an estimated gain of one into the xtal filter.

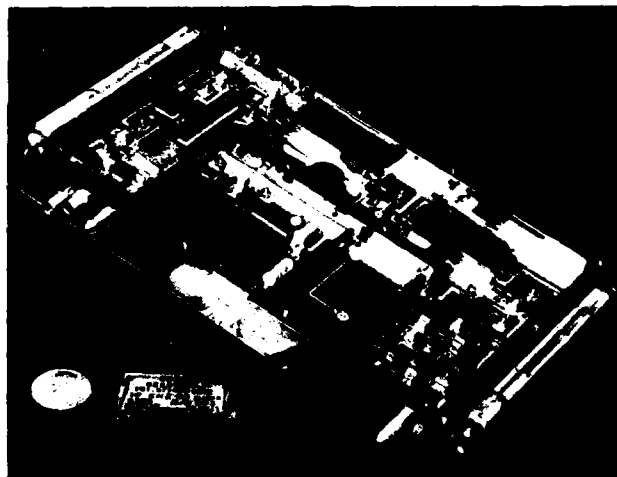


Figure 6. Typical Reference Generator Utilizing XTAL Filters, (0.23H x 0.675W x 1.175L)

### IV. TYPICAL VIBRATION INPUTS FOR VARIOUS PLATFORMS

Most people have a general impression about what vibration means. Only those closely related to system testing can appreciate the problems associated with vibration. Even then it may not be fully understood or the characteristic of the requirements appreciated.

The understanding of vibration takes on different meanings for different disciplines. A vibration specification may mean to one group, that if it (equipment) survives with no damage there is no need to be concerned. This statement may be safe for all commercial television, radio, and maybe up into the UHF communication. Others understand vibration as a problem area to avoid. However, if vibration problems do come up, as it does, the immediate response is "quick fixes". Laboratories are becoming better equipped to characterize vibration; not only the vibration, but the effects of vibration on the equipment can be better characterized.

The type of vibration inputs this author is familiar with are the typical ship and airborne platforms. Figure 7 illustrates several platforms; some requiring discrete inputs, some requiring random inputs. An overview suggest a device such as a quartz oscillator or monolithic crystal filter should be provided with a data sheet characterizing

the device for one Grms discrete 10 Hz to 10,000 Hz. Along with the characterization, resonant points should be noted and their sideband level. As will be shown later, this type of characterization allows for extrapolation to any level of vibration, any frequency, and the sideband level.

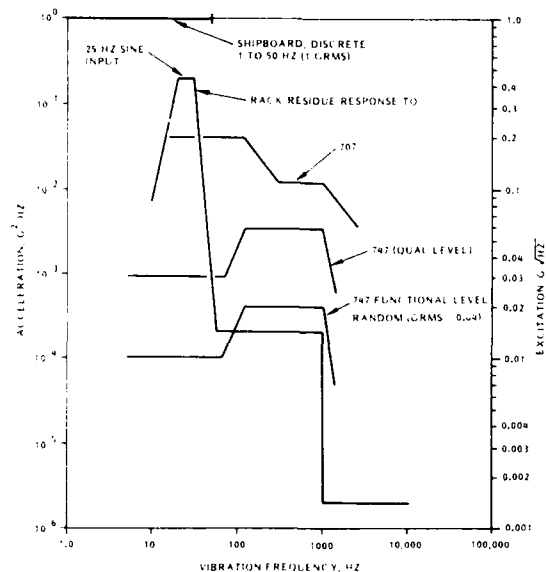


Figure 7. Vibrational Input Requirements for Various Programs

#### V. VIBRATION EFFECTS ON THE STANDARD AND SYSTEM IMPLICATION

The characterization of the rubidium standards has been reported before<sup>7, 8</sup>. The sidebands generated while being vibrated are governed by the relationship<sup>6</sup>:

$$L(f_v) = 20 \text{ Log} \left\{ \frac{\tau a f_0}{2 f_v} \right\} \quad (7)$$

Figure 8 shows the actual measured sideband envelope of an M-100/LN being vibrated at one Grms discrete tones from 10 Hz to 2000 Hz. The measurement was at 100 MHz (X20). The calculation for an acceleration of  $10^{-9}$ g fall right on the measured result.

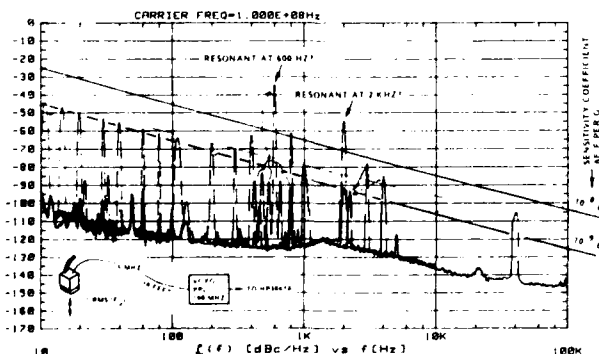


Figure 8. Rb STD-S/N-1211, Vibrated at 1 Grms Discrete Frequencies

The measurement also shown the mechanical resonant structure.

The first step in reducing the vibration effects is via mechanical isolation mounts. Per figure 9, isolation mounts act as low pass structures filtering out frequencies greater than 80 Hz.

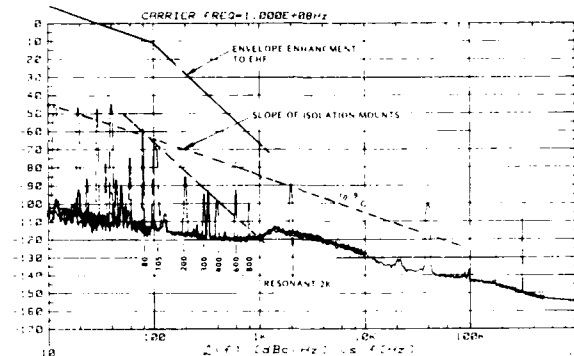


Figure 9. Rb STD at 1 Grms on Isolation Mounts (WB1-030) (WR1-030)

The second step would consist of employing acceleration feedback methods as discussed by C. Colson.

The sidebands illustrated in Figures 8 and 9 are enhanced by 53 dB for an EHF system. Utilizing mechanical isolation mounts, the vibration induced sidebands are contained in the region of dc to 50 to 80 Hz. However, as the enhanced sideband envelope shows in Figure 9, the sidebands are sufficiently high to cause carrier "drop out" for sidebands close to the carrier.

The proper choice of modulation schemes can operate under these large sideband levels induced by vibration at the standard. For example, a PSK system using differential demodulation and a data rate 50 times the sideband frequency will see less than  $10^\circ$  shift from bit-to-bit. Figure 10 simply illustrates the effect. Should the data rate (such as 75 bits/second) be comparable to the sideband frequency, the sideband levels projected for EHF would be disastrous on system performance. From this example, it becomes readily apparent that the standard must be improved; i.e., its vibration sensitivity should approach  $10^{-11}$ g. Newer standards will need to include acceleration feedback<sup>7</sup>, or/

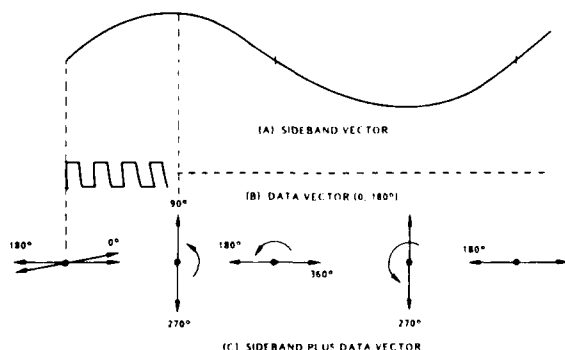


Figure 10. Sideband Effects on Differentially Decoded PSK

and SC-cut crystals, and a match of the orientation of the crystal with vibrational axis.

#### VI. VIBRATION EFFECTS OF MONOLITHIC CRYSTAL FILTERS

In the EHF communication systems, phase noise and spurious from a 5 MHz reference standard is enhanced by approximately 80 dB. The available reference standards may or may not meet the system phase-noise/spurious after multiplication. This necessitates exploring methods of cleaning up the spectrum. As Figure 5 indicates, a monolithic crystal filter can be employed after the atomic standard and in the reference generator. In addition it can be used for various frequencies through 160 MHz.

The environmental effects are of great importance for monolithic crystal filters placed at such a low point in the multiplication chain. First, for cleanup purposes the filter must track over temperature without the aid of ovens (power dissipation and size also importance parameter) and minimize insertion variation. Secondly, the filter must operate with minimal effects from vibration (as unwanted sidebands). To meet the temperature range requirements, filters (5 MHz) with 325 Hz bandwidth have been manufactured with less than 1 dB insertion loss variation. However, the vibration aspect of the monolithic crystal filter has been the more difficult parameter to improve. The following sections discusses work at 5 MHz and 100 MHz.

##### A. 5 MHz Crystal Filter

The utilization of a crystal filter at 5 MHz could expect any vibrational generated sidebands to be enhanced by 80 dB (to EHF). To gather information about the sensitivity of crystal filters to vibrational inputs, measuring capabilities in excess of -130 dBc is required.

Figure 11 illustrates the test setup utilized

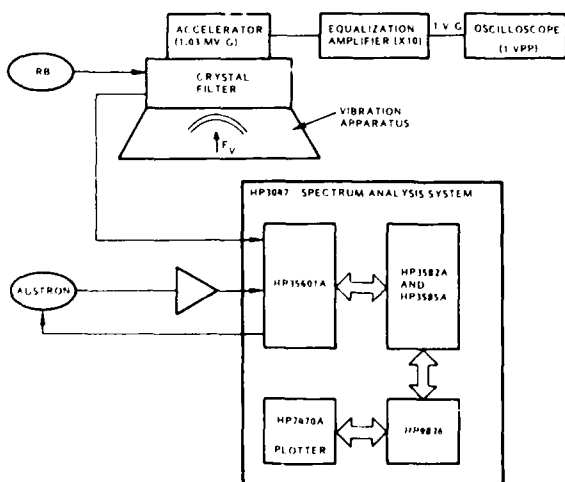


Figure 11. Test Set-Up to Evaluate a Crystal Filter Under Vibration

to evaluate crystal filters at 5 MHz. The vibrational sidebands are characterized by applying one Grms vibrational discrete frequencies from 20 Hz to as high as 10,000 Hz to the filter. The measurement leads to a characteristic envelope of the sideband level for a 5 MHz crystal filter.

Figure 12 is a typical plot illustrating the sidebands generated at discrete points and the envelope. From this envelope, the resonant point (325 Hz) is readily apparent. A quick addition of 80 dB (for EHF enhancement) to the -40 dBc resonant point leads to an unuseable system.

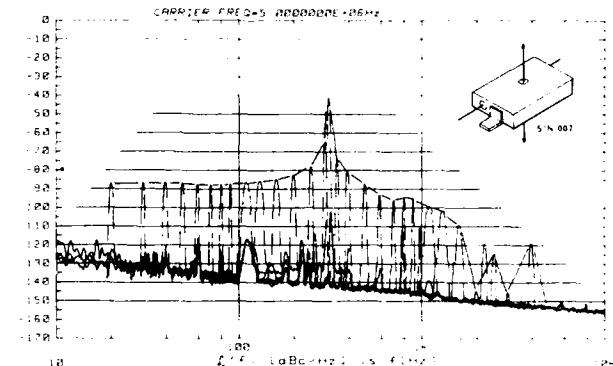


Figure 12. Characterization of 5 MHz Filter for Vibration-Versus-Sideband Level

Table 1 is a listing of eleven 5 MHz crystal filters evaluated under vibration inputs. Crystal filters with serial numbers 001 to 007 have no

Table 1. 5 MHz Crystal Filter(s) Vibration Characterization

Serial Number	3 dB Bandwidth (Hz)	Phase Slope (Degree/Hz)	Sideband Level at 100 Hz (dBc)	Resonant Frequency (Hz)	Point Level (dBc)	t
001	350 Hz	0.775	-73	250	-46 dBc	$5.9 \times 10^{-10}$
002	425	0.48	-65	250	-37	$1.3 \times 10^{-8}$
003	350 Hz	0.73	-66	275	-45	$7.9 \times 10^{-9}$
004	325	0.72	-84	275	-58	$1 \times 10^{-9}$
005	2175	0.069	-94	325	-62	$11 \times 10^{-9}$
006	2200	0.075	-105	325	-60	$8.6 \times 10^{-10}$
007	2150	0.074	-85	315	-42	$8.7 \times 10^{-9}$
008	2200	0.069	-87	325	-52	$7.42 \times 10^{-9}$
009	2300	0.075	-88	325	-52	$6.1 \times 10^{-9}$
010B	2200	0.077	-115	?	<-110	$7.7 \times 10^{-10}$
011B	2200	0.069	-115	2650	<-110	$13.0 \times 10^{-10}$

compensation for vibration. Serial numbers 008 and 009 have the mounting post stiffened with epoxy with no resultant lowering of the sensitivity to vibration. A dramatic lowering of sidebands result with 010B and 011B. The mount was changed from the standard wire clip to a mount designed to survive 50G shock. You have to ask "What about sideband envelope characteristic?" None exist.

Figure 13 is a composite plot of all the vibration envelopes (1 Grms discrete, 10-10,000 Hz) of the crystal filters listed in Table 1. Visually it becomes very apparent that for high frequency systems, the mount plays an important role in reducing the vibration sensitivity. Between 30 to 80 dB improvement can be realized at various vibration frequencies as one goes from simple two point

mounts to more rigid mounts. In no way does this example show the best obtainable results; only what can be obtained as a first exploration.

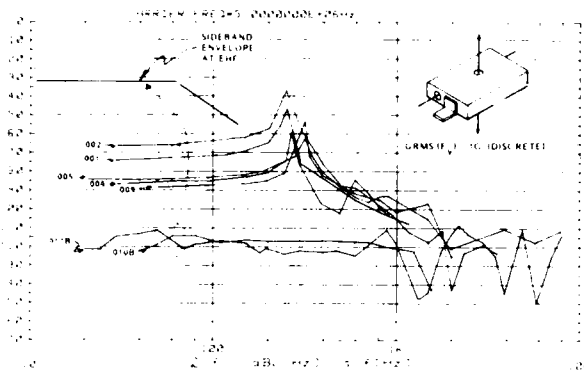


Figure 13. Vibrational Sideband Envelope for 1G Drive Level on 5 MHz XTAL Filter

Note that 80 dB of enhancement of the 5 MHz filter sideband discrete envelope plus isolation mounts keeps the discrete sidebands below -32 dBc at frequencies below 80 Hz.

#### B. Orientation of 5 MHz Crystal Filter

The orientation of any crystal should be a large factor in one's mounting in a system (if practical). For the system discussed here the crystal filter is mounted as should in Figure 14. The

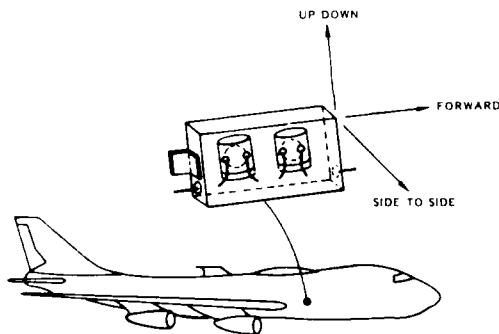


Figure 14. Orientation of Filter in Platform

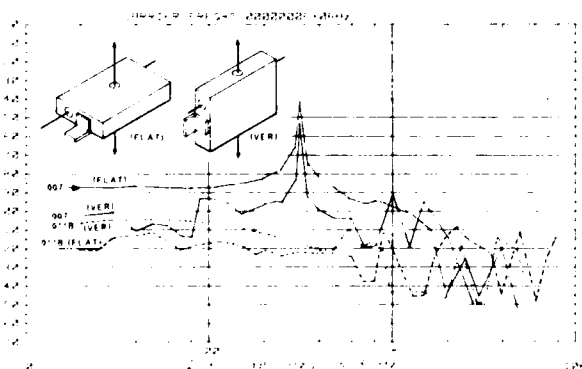


Figure 15. Vibration Sensitivity Related Orientation of Filter

worst case for the crystal filter S(S/N-007) is the side-to-side motion. The platform has the least vibration inputs in this axis (this does not include engine noise).

An evaluation of the 5 MHz crystal filter was made in two axis. Figure 15 illustrates the results of the S/N-007 and S/N-011B crystal filter.

#### C. 100 MHz Monolithic Crystal Filter

The next level at which one may use monolithic crystal filters is at 100 MHz. From this point any vibration induced sidebands are enhanced by 53 dB. There are four types of 100 MHz monolithic crystal filters that have been evaluated to date. Figure 16 illustrates the vibration induced sideband envelopes of the various types. The ruggedization of the mounts leads up to 25 to 50 dB improvement and shifting the resonant point out beyond known vibration inputs.

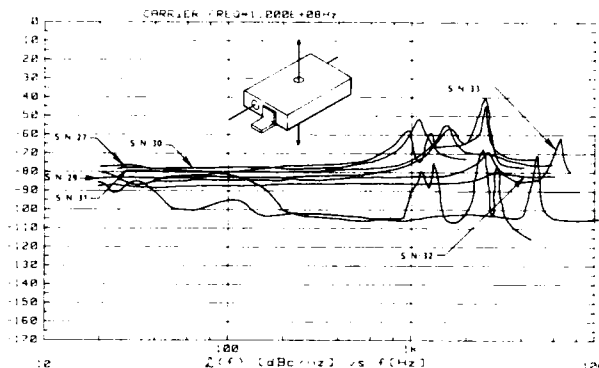


Figure 16. Vibration Induced Sideband Envelope for 1 Grms Drive Level for 100 MHz Monolithic Crystal Filter

#### VII. VIBRATION EFFECTS ON L-C AND INTERDIGITAL FILTERS

Any element that experiences an electrical phase shift due to vibration will produce PM sidebands on the carrier. The element does not necessarily have to be a quartz filter or oscillator as discussed in preceding sections.

With the test method described, two other classes of filters were evaluated; i.e., a 1200 MHz interdigital filter and a 1200 MHz L-C filter. The following table shows the two types of filters to be very similar in electrical characteristics but entirely different with respect to mechanical characteristics.

Parameter	Filter Type	
	L - C	Interdigital
3 dB BW	44 MHz	9.5 MHz
+64 MHz	-41 dB	-63 dB
-64 MHz	-63 dB	-66 dB
H x W x L	.023 x 0.5 x 1.0	0.5 x 2.0 x 2.0
Elements	Inductors - Capacitors	Rods, Cavity

Both filters were characterized for discrete vibration frequencies of 1 Grms. The sideband envelope is illustrated in Figure 17. For EHF applications (and 30 dB enhancement of these vibration sidebands), the interdigital filter characterized exhibits vibration sidebands too high for satisfactory operation.

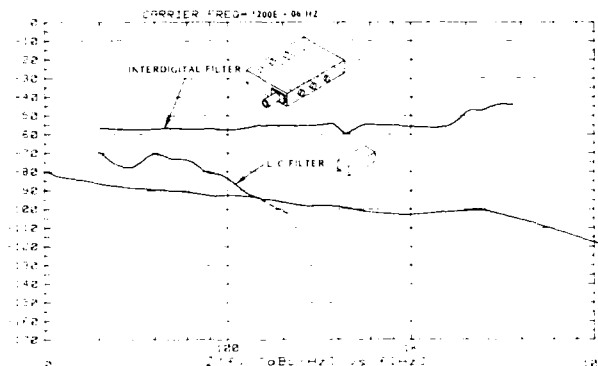


Figure 17. Vibration Induced Sideband Envelope for Two Types of 1200 MHz Filter with 1 Grms Drive Level

#### VII. IMPORTANCE OF VIBRATION INDUCED SIDEBAND ENVELOPES OF VIBRATION SENSITIVE ELEMENTS

Throughout the preceding discussion, a relationship between system performance and vibration induced sidebands have been established. There is a relationship for oscillators that defines the vibration induced sideband (with respect to frequency of vibration) as long as the sensitivity is known and is given by equation 7. The sidebands have a  $1/f_v$  characteristic.

On the other hand, filters have a flat sideband characteristic as the phase slope is constant at the center frequency of the filter. A relationship relating phase slope and sideband level has been attempted. However, the filters have a strong component connected to the mechanical structure as viewed in Figure 13 for the 5 MHz crystal filter. It is possible that the sideband relationship for filters may be defined as:

$$L(f_v) = 20 \text{ Log} \left[ \tau a \phi_s f_0 R(f_v) \right] \quad (8)$$

where:  $a$  is acceleration level in g's  
 $\tau$  is acceleration sensitivity, parts/g  
 $\phi_s$  is filter phase slope, radian/Hz  
 $f_0$  is filter center frequency, Hz  
 $L$  is sideband/carrier ratio, dBc  
 $R(f_v)$  is 1 except around the mechanical resonant point of the mounting structure.

The phase slope of a filter may be approximated by:

$$\phi_s = \frac{n \cdot 2 \text{ Tan}^{-1} \left( \frac{\Delta f}{BW_3 \text{ dB}} \right)}{BW_3 \text{ dB}} \text{ Deg/Hz} \quad (9)$$

$$2 \text{ Tan}^{-1} \left( \frac{\Delta f}{BW_3 \text{ dB}} \right) = \frac{\pi}{2} \text{ Radians for } \Delta f = BW_3 \text{ dB}$$

Therefore:

$$\phi_s = \frac{\pi}{2} \frac{n}{BW_3 \text{ dB}}$$

Then:

$$L(f_v) = 20 \text{ Log} \left[ \tau a \frac{\pi}{2} \frac{n \cdot f_0}{BW_3 \text{ dB}} \right] \quad (10)$$

Equation (10) is plotted in Figure 18. From Figure 18, increasing the filter bandwidth at a specific center frequency decreases vibration induced sidebands for a specific acceleration sensitivity,  $\tau$ . In the same sense, if acceleration sensitivity,  $\tau$ , can be lowered, vibration induced sidebands decrease.

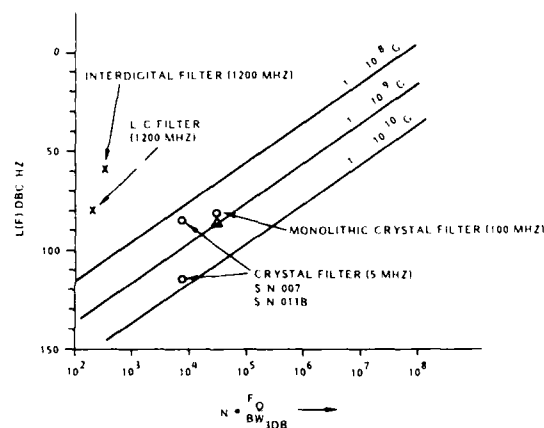


Figure 18. Vibration Induced Sideband Level as a Function of Filter Bandwidth, Center Frequency, Number of Elements, and Acceleration Sensitivity

From the above discussion, it is apparent that filters should be supplied with an acceleration sensitivity factor or the level of the vibration induced sideband for a 1 Grms drive level (100 Hz).

Figures 19 and 20 illustrate that from a 1 Grms envelope, one can immediately correct for system vibration input and for system multiplicative factor. Then a determination can be made to the possibility the system will function properly with the data rate being transmitted.

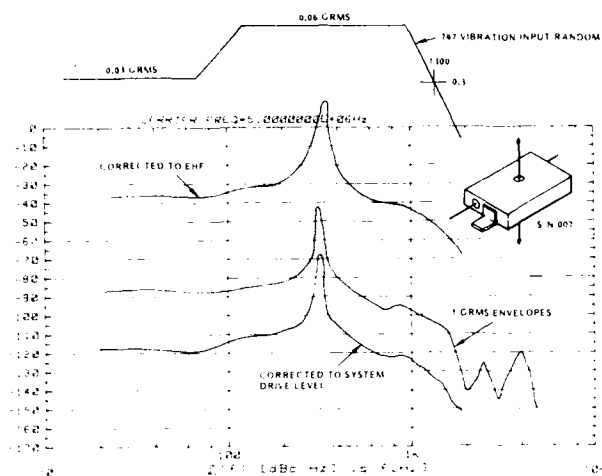


Figure 19. Vibration Envelope Extrapolation of Standard 5 MHz Crystal Filter Mount to EHF

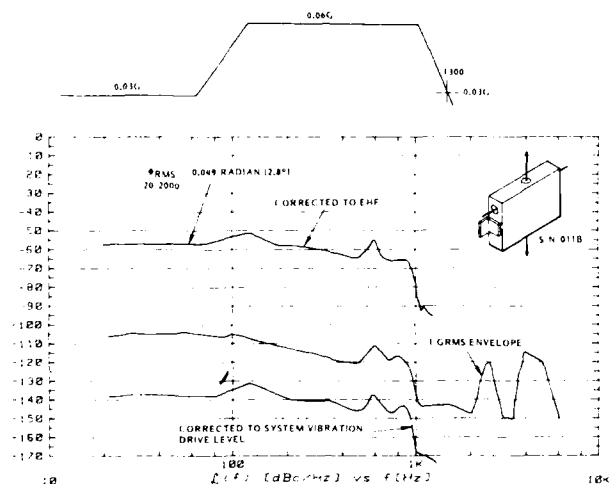


Figure 20. Vibration Envelope Extrapolation of Improved 5 MHz Crystal Filter Mount to EHF

## IX. CONCLUSION

Elements that may produce unwanted sidebands due to vibration have not been an important consideration for UHF systems. However, as systems have developed, one can follow its history right up the frequency spectrum. With the higher frequency, spectral purity becomes more important. Types of filtering at lower reference frequencies dictates narrow band.

Measurements discussed in this article show the EHF performance to be marginal or severely degraded under tactical vibration requirements utilizing standard crystal filters, atomic standards, and other elements.

Additional measurements show the situation to be manageable via:

1. proper mount design
2. choose of orientation
3. and mechanical isolation

A relationship was developed to characterize the filter similar to that utilized with atomic standards. In addition a method of testing was presented for obtaining a vibration induced sideband envelope. From the characterization it is apparent that any component that:

1. Has a sensitivity to vibration and,
2. Is to be used in high frequency systems which are to transmit low data rate; should be provided with acceleration sensitivity and/or vibration induced sideband level for 1 Grms at 100 Hz.

The results presented here are by no means the best obtainable.



#### REFERENCES

1. A. Balats, T.J. Lukaszeki, and G.J. Iafrate, "Subtle Effects in High Stability Vibrators", Proc. 34th Annual Frequency Control Symposium (1980).
2. V.R. Rosati and R.L. Filler, "Reduction of the Effects of Vibration on SC-Cut Quartz Crystal Oscillators", Proc. 35th Annual Frequency Control Symposium (1981).
3. R.L. Filler and J.R. Vig, "The Acceleration and Warm-Up Characteristics of Four-Point-Mounted SC and AT-Cut Resonators", Proc. 35th Annual Frequency Control Symposium (1981).
4. R.L. Filler, "The Effect of vibration on Frequency Standards and Clocks", Proc. 35th Annual Frequency Control Symposium (1981).
5. R.L. Filler, J.A. Kosinski, and J.R. Vig, "The Effect of Blank Geometry on the Acceleration Sensitivity of AT-and SC-cut Quartz Resonators", Proc. 36th Annual Frequency Control Symposium (1982).
6. R.L. Filler, J.A. Kosinski, and J.R. Vig, "Further Studies on the Acceleration Sensitivity of Quartz Resonators", Proc. 37th Annual Frequency Control Symposium (1983).
7. C. Colson, "Vibration Compensation of the Seek Talk Rubidium Oscillator", Proc. 36th Annual Frequency Control Symposium, (1982).
8. T.M. Kwon, and T. Hahn, "Improved Vibration Performance in Passive Atomic Frequency Standards by Servo-Loop Control", Proc. 37th Annual Frequency Control Symposium, (1983).
9. C.J. Walejsza, Jr., "Effects of Oscillator Phase Noise on PSK Demodulation", Compat Technical Review, Volume Number 1, Spring 1976.
10. W.P. Robins, Phase Noise in Signal Sources, Peter Peregrinus, Ltd., London, U.K., 1982.
11. U.L. Rohde, Digital PPL Frequency Synthesizers, Prentice-Hall, Inc., Englewood Cliffs, N.J. 1983.

# REACTIVE ION BEAM ETCHING FOR VHF CRYSTAL RESONATORS

J.S.Wang, S.K.Watson, and K.F.Lau

TRW Electronic Systems Group  
One Space Park, Redondo Beach, California 90278

## ABSTRACT

Both conventional ion beam etching and the newly developed reactive ion beam etching (RIBE) are being examined as potential techniques in fabricating VHF crystal resonator devices. The quality of a crystal resonator is critically dependent upon surface finish and parallelism. A technique to obtain a smooth etched surface is, therefore, very desirable. This paper is a report on our research efforts and the results of our experiments using conventional ion beam etching and reactive ion beam etching for VHF crystal resonators.

In Ar ion beam milling, undesirable trenching and redeposition were usually observed near the edge of the etched wall. These problems could be reduced with reactive ion beam etching because the compounds resulting from the reaction between the substrate and the reactive gases are volatile and can be pumped out. However, a fluorocarbon accumulation was found on the etched surface, preventing the reactive ion etching from proceeding. By using the combination of ion milling and RIBE, an etch rate as high as 30  $\mu\text{m/hr}$  has been achieved with a gas mixture of Ar and  $\text{C}_2\text{F}_6$ . The etched surface was clear and smooth. This improvement in technique was found to be very successful for the long etching times necessary for VHF resonator fabrication.

An AT-quartz resonator with an 8  $\mu\text{m}$  membrane thickness has been fabricated. The resonator has a loaded Q of 25000 as determined by transmission measurements at the fundamental frequency of 200 MHz. Our innovative RIBE techniques and VHF resonator work will be reported.

## I. Introduction

Crystal resonators fabricated by mechanical polishing have a physical limitation on thickness and size. The industrial thickness limitation, for AT cut quartz corresponding to 50 MHz fundamental thickness mode resonance, is about 33  $\mu\text{m}$ . For many years, researchers<sup>(1,2)</sup> have been trying to reduce the thickness of quartz plates in order to obtain higher frequency resonators. Chemical polishing<sup>(1)</sup> and ion milling<sup>(2)</sup> were the two main techniques used in these efforts. By using wet chemical polishing, resonators having fundamental frequencies of 400 MHz have been made. However, the quality of the etched surface is affected by many parameters such as chemical strength, etching environments, and crystal orientation. Other difficulties with chemical polishing have also been reported.<sup>(3)</sup> Recently, ion milling, a dry etching process, has been

applied in fabricating thin crystal membrane resonators<sup>(4)</sup>. The ion milling rate, however, is low (about 5  $\mu\text{m/hr}$ ), and several problems have been associated with this technique. Quartz masks used in ion milling are difficult to fabricate, and the side wall angle of the mask is hard to control. Redeposition from sputtered materials - substrates or masks - onto the edge of the membrane cannot be prevented. Consequently, the aluminum electrode on the top of the redeposited layer breaks down when this layer peels off the substrate. The fabrication cost in using this technique is still high. This paper will report on a new approach to fabricate thin membrane crystal resonators. Using a combination of chemical reaction and ion bombardment, reactive ion beam etching,<sup>(5)</sup> has proven superior in this process. An etching rate as high as 30  $\mu\text{m/hr}$  has been achieved and a smooth and finished surface has been obtained. An anisotropic chemically etched Si mask<sup>(6)</sup> with a window array has been used, enabling the production of many membranes from a single substrate. This technique will be of importance in the crystal resonator industry.

## II REACTIVE ION BEAM ETCHING

The experimental set-up is shown in Figure 1. The system is a slightly modified version of a conventional ion-beam machine (Millatron II, Commonwealth Scientific Co.); alterations were made to permit the use of reactive gases. A gas such as freon is used to create a plasma in the volume contained between the cathode, the cylindrical anode, and the inner grid. By means of a grid held at a negative potential, a well-collimated ion beam is extracted from the plasma and impinges on a rotating, water-cooled substrate holder at ground potential. A shutter with an attached probe for current density measurements is provided to protect the substrate during initial beam tuning. Typical system conditions are outlined in the figure.

Previous researchers<sup>(7)</sup> have found that the etch rate and surface profile of an etched wafer are dependent upon the angle of the substrate holder with respect to the incident ion beam. This dependence was investigated by etching quartz crystals in an Ar ion beam while varying the angle of the substrate holder. All other parameters were maintained constant. A Si mask with an array of square openings having 35° sidewalls was used to define the membrane pattern in the substrate. An angle of approximately 35° was found to provide the highest etch rate (12  $\mu\text{m/hr}$ ) while simultaneously creating a flat surface. At angles greater than 35°, the centers of the membranes are etched at a faster rate than the surrounding edge areas, resulting in roughly 'V' shaped surfaces: the 35° sidewalls of the Si mask shadow the edges during a

portion of the substrate holder rotation cycle, reducing the etch rate in those areas. At angles less than  $35^\circ$ , the membrane centers are etched only by the incident ions while the membrane edges are etched by two processes: incident ion bombardment and bombardment by ions reflected from the side walls. The higher etch rate near the side walls produces an undesirable convex shaped surface, commonly known as 'trenching' (8). All subsequent experiments were conducted at a  $35^\circ$  angle of incidence unless otherwise noted.

In order to investigate and characterize the reactive ion beam etching technique, the inert Ar plasma was replaced by a reactive gas. Both  $CF_4$  and  $C_2F_6$  were initially tested, but due to the consistently higher etch rates for  $C_2F_6$  (1.7:1 for pure  $C_2F_6$  vs. pure  $CF_4$ ) all further tests were conducted with the latter. Unlike Ar etching where surface removal is purely due to physical sputtering, the  $C_2F_6$  chemically interacts with Si to form volatile  $SiF_4$  (10-12) which can be pumped from the system. Using  $C_2F_6$  at  $2 \times 10^{-4}$  Torr, an accelerating voltage of 1250 V, and a current density of  $3 \text{ mA/cm}^2$  at a  $35^\circ$  angle of incidence, etch rates as high as  $23 \mu\text{m/hr}$  were achieved. Under the same conditions, Ar etched at a rate of  $12 \mu\text{m/hr}$ . However, the quality of the etched surfaces using  $C_2F_6$  was very poor. Surface profiles (Sloan Dektak IIA) of the  $C_2F_6$  etched surfaces revealed irregularities on the order of  $1 \mu\text{m}$ - $2 \mu\text{m}$  (See Figure 2). As shown in Figure 3, the etch rate for  $C_2F_6$  was not constant over the etch time. From an initial etch rate of  $21 \mu\text{m/hr}$  the etch rate declined to about  $13 \mu\text{m/hr}$  after 30 min. Conducting detailed studies of the chemical etching mechanism, several investigators (9-13) have concluded that in a system using  $C_2F_6$  carbon is absorbed on the substrate surface. This carbon accumulation accounts for the declining etch rate and poor surface quality.

To overcome the surface quality problems associated with 100%  $C_2F_6$ , mixtures of Ar and  $C_2F_6$  were used with very encouraging results. We believe that the Ar serves the purpose of physically sputtering the adsorbed carbon layer, thus removing the main rate limiting factor on the chemical  $C_2F_6$  etching process. The variation of etch rate with percentage of Ar is plotted in Figure 4. As the percentage of Ar to  $C_2F_6$  increases, a maximum etch rate is obtained at roughly 40% Ar. Etch rates as high as  $30 \mu\text{m/hr}$  were achieved with the 40%Ar+60%  $C_2F_6$  mixture. In addition, the surfaces etched in the 40%Ar+60%  $C_2F_6$  mixture were extremely smooth and flat. Dektak profiles show etched surfaces which are slightly convex, varying by less than 1000 Å in a  $200 \mu\text{m}$  scan range (See Figure 5). In Figure 6, SEM photographs of a membrane with  $45 \mu\text{m}$  sidewalls etched at  $22.5 \mu\text{m/hr}$  reveal the superior surface quality attainable with 40%Ar-60%  $C_2F_6$  mixtures.

### III. VHF Quartz Crystal Resonator

Reactive Ion Beam etching has been used to fabricate a thin quartz membrane for VHF resonators. A double-sided polished quartz plate,  $50 \mu\text{m}$  thick, was used as a substrate. The substrate was first mounted on a water cooled stage and covered with a Si mask having  $400 \mu\text{m}$  square open windows. The plate was etched through the Si mask, and the thickness of the membrane was varied by controlling the etch rate ( $20 \mu\text{m/hr}$ ) and etch time. In most cases, a low ion accelerating voltage and a high current density were used in order to obtain the fine, finished surfaces. Several membranes have been fabricated on the same plate by using a Si window-array mask. Electrodes were then deposited on the two sides of the membrane through a predesigned Si

mask. The overlapping electrodes fell only on the center portion of the membrane. The etched plate, with the membrane array, was finally diced in a chip form, and mounted in a To-5 package.

The main features of these miniature devices, using reactive ion beam etching versus other techniques, are small volume, light weight, and planar mounting. This technique could be of importance for hybridizing a frequency source on a substrate and mounting it in a package.

An AT-quartz membrane resonator with an  $8 \mu\text{m}$  membrane thickness has been fabricated. The resonator has a loaded Q of 25,000 as determined by transmission measurements at the fundamental resonant frequency of 200 MHz. Figure 7 shows the insertion loss amplitude of a resonator at the fundamental resonant frequency of 141 MHz. Spurious responses at frequencies higher than resonance were also detected. No studies of temperature effects and aging have yet been made.

### IV. Summary

We have developed a special Reactive Ion Beam Etching technique to fabricate thin quartz membrane resonators. Etch rates as high as  $30 \mu\text{m/hr}$  have been obtained, and mirror-like surface finishes have been achieved. With the high etch rates attainable with this technique, process times and fabrication costs can be reduced. Also, as is done with IC chips, many resonators can be fabricated and cut from a single wafer. Resonators in this form can be used in a hybridized circuit. A resonator with a loaded Q of 25,000 at the fundamental resonant frequency of 200 MHz, has been made.

Accurate thickness control is very important in using the reactive ion beam etching technique for VHF crystal fabrication. However, a method of end point detection has not yet been worked out. So far, the resonators fabricated using this technique, have had Q factors lower than the expected Q for quartz material. Both of these problems will be dealt with in future studies.

### V. Acknowledgements

The authors wish to thank Dr. K.H. Yen for his generous guidance in the course of this work, P. Ng for electrode aligner design and P. Scarola for graphic presentations. This work is supported by the TRW IR&D project.

### References

1. J.R. Vig, J.W. Lebus and R.W. Filler, Proc. 31st Annual Symp. on Freq. Control, p. 131, 1977.
2. M. Berte, Elec. Lett., Vol. 13, P.248 1977
3. W.P. Hanson, Proc. 31st Annual Symp. on Freq. Control, p. 131, 1977.
4. B. d'Albarel and P. Siffert, 36th Annual Symp. on Freq. Control, 1982. p. 405
5. D.F. Downey, W.R. Bottoms, and P.R. HANLEY, Solid State Tech, 121, Feb. 1981
6. K.E. Bean, IEEE Trans. on Electron Devices. Vol. ED-25, Oct. 1978, p.1186
7. R.N. Castellano, J.L. Hokanson, Proc. 29th Annual Symp. on Freq. Control, p.128, 1975.
8. D. Bollinger and R. Fink, Solid State Tech., p.97, Dec. 1980.
9. B. Heath, J. Electrochem. Soc: p.396, Feb. 1982.
10. H.F. Winters, J. Appl. Phys. 49 (10), p. 5165, October 1978
11. J.W. Coburn, H.F. Winters and T.J. Chuang, J. Applied Phys. 48(8), p.3532, Aug 1977,

12. T.M. Mayer and R.A. Barker, J. Electrochem Soc., p.585, March 1982,  
 13. Y.M. Horike, M. Shibagaki, K. Kadoro, JPN. J. Appl. Phys. 18(12), p.2309, 1979.

## REACTIVE ION BEAM ETCHING APPARATUS

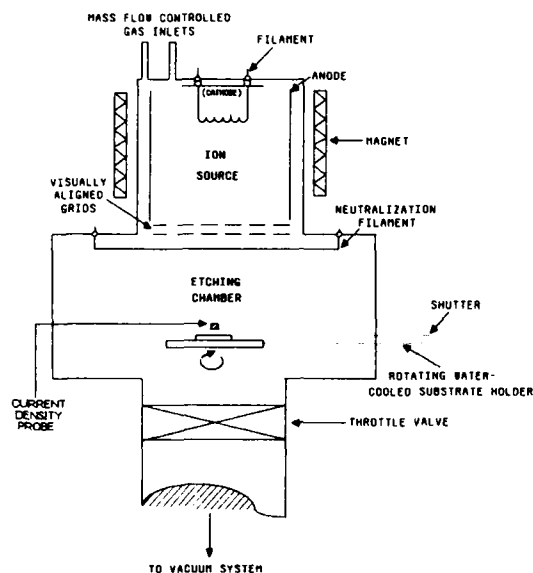


FIG.1 Experimental set-up for Reactive Ion Beam Etching. Typical conditions: Substrate: Quartz. Accelerating voltage: 1250V. Beam current density:  $3\text{mA/cm}^2$ . Base pressure:  $2 \times 10^{-6}$  Torr. Pressure during etching:  $2 \times 10^{-4}$  Torr. Gases used: Ar,  $\text{CF}_4$ ,  $\text{C}_2\text{F}_6$ .

ETCHED  
SURFACE  
VARIATION  
A

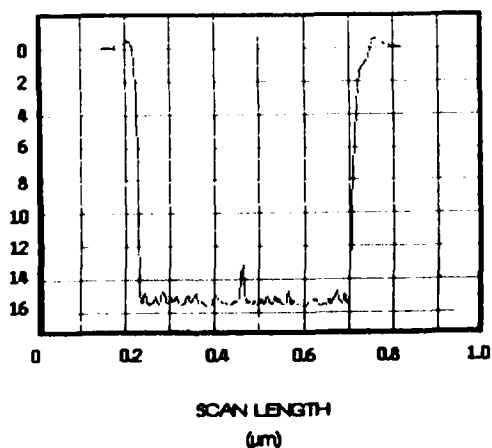


FIG.2 Dektak profile of surface etched in 100%  $\text{C}_2\text{F}_6$ . Etch depth:  $15\mu\text{m}$

ETCH RATE  
(μm/hr)

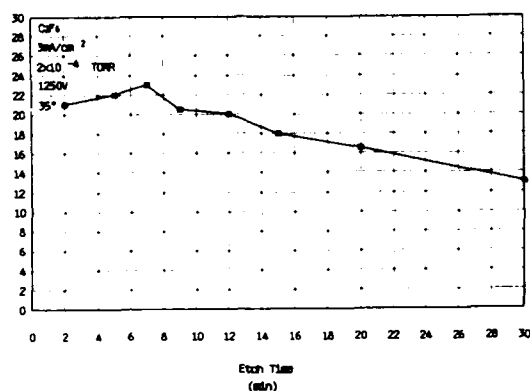


FIG.3 Graph of etch rate as a function of time for surfaces etched in 100%  $\text{C}_2\text{F}_6$ .

ETCH RATE  
(μm/hr)

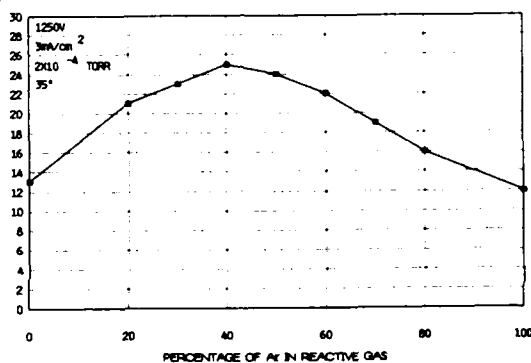


FIG.4 Graph of etch rate vs. percentage of Ar in  $\text{C}_2\text{F}_6$ . Etch time: 30 min.

ETCH DEPTH  
(μm)

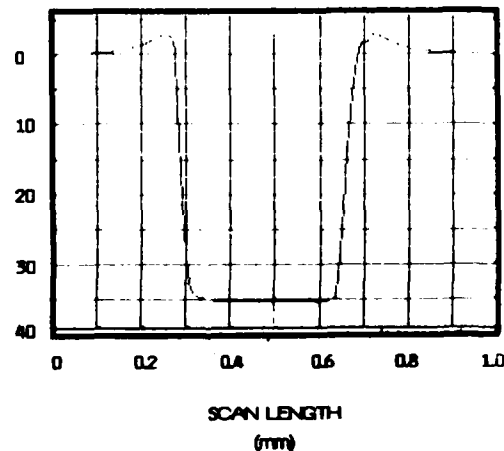


FIG.5a Dektak profile of surface etched in 40% Ar - 60%  $\text{C}_2\text{F}_6$ . Etch depth:  $35\mu\text{m}$ .

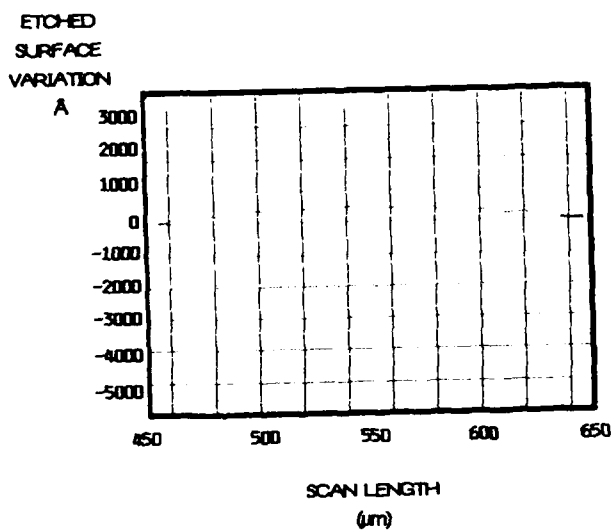


FIG.5b Enlarged view of surface variation in figure (5a). Scan range = 200 $\mu$ m.

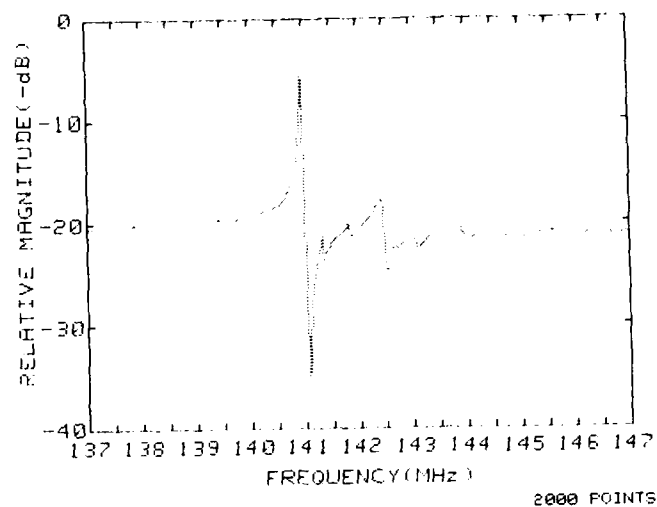


FIG.7 Insertion loss as a function of frequency. Fundamental resonant frequency: 141 MHz.

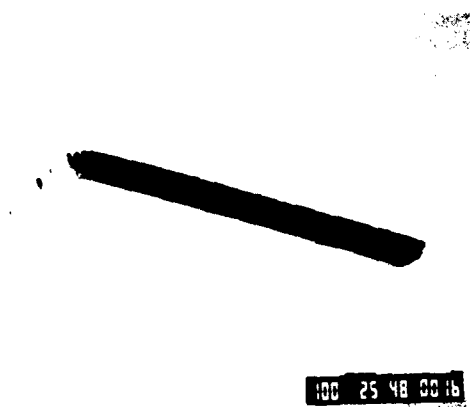


FIG.6a SEM photograph of surface etched in 40% Ar - 60% C<sub>2</sub>F<sub>6</sub>. Etch depth: 45 $\mu$ m. Magnification: 150X.



FIG.6b Cross section of etched surface. Etch depth: 45 $\mu$ m. Magnification: 150X.

## ETCH FIGURES AND ETCH RATES IN AT, BT, X AND Y CUT QUARTZ PLATES

C.R. Tellier

Laboratoire de Chronométrie, Electronique et Piézoélectricité  
E.N.S.M.M., Route de Gray, 25030 Besançon Cédex, France.Summary

The kinetics of etching of AT, BT, X and Y-cut quartz plates are studied and the etch rate data are plotted in the well known Arrhenius form. The specific behavior in the low temperature region can be understood in terms of surface texture dependent etch rate but the high temperature region allows us to determine an apparent activation energy which is found to be almost independent of the cut.

The variation in the roughness parameters with the depth of etch depends on the orientation of the quartz plate. Moreover, for a given cut, the changes in the roughness parameters during dissolution depend on the direction of measurement of the roughness parameters. The scanning electron micrographs agree well with the profilometry traces. The shape of the etch figures for a given cut shows directional effects attributed to asymmetrical etch rate distributions. These results can be understood in terms of correlated symmetries of the crystal plane and the etch patterns.

By comparison of the observed patterns with some theoretical predictions made by Irving some indications are also given on the possibility of determining the approximate shape of the etch rate surface from a rectangular combination of etch rate distributions.

Introduction

The construction of high frequency quartz resonators requires very thin quartz plates<sup>1-3</sup>. As it is well known surface imperfections can markedly disturb the vibrations of resonators and consequently can degrade the performance of high precision quartz resonators<sup>4-9</sup>. Quartz resonator plates are commonly processed by mechanical polishing which creates a damaged surface layer<sup>4-8</sup>. As suggested by some authors<sup>4-6</sup> an alternative and simple method to achieve clean and smooth surfaces consists of chemically etching quartz resonators down to suitable thicknesses. Some experiments on AT-cut<sup>6-10</sup> and SC-cut<sup>11</sup> quartz resonators have been carried out satisfactorily, quartz surfaces become smoother and smoother whereas chemical polishing produces no significant Q degradation. A recent work<sup>12</sup> on X, Y and Z-cut platelets has revealed that the morphology of the etch figures depends on the orientation of the crystal plate.

The purpose of this study is to investigate the kinetics of etching of AT, BT, X and Y-cut quartz resonators and to give valuable informations on the changes of surface topography with prolonged etching.

Experimental Procedure

The resonators used were synthetic plano-convex quartz plates. Prior to etching these plates

were lapped with a 5  $\mu\text{m}$  abrasive. The etching phenomena described in this work were produced entirely by a concentrated solution of ammonium bifluoride (typical concentration 10.5 mol  $\text{l}^{-1}$ ) maintained at a constant temperature, T, in the range 290 - 360 K for various periods of time.

The surface textures were examined after any isothermal etching with a scanning electron microscope (SEM). The SEM micrographs were taken along an observation angle of 0°. In addition to SEM studies the surface textures were characterized using a microprocessor-based surface profilometer. The profilometry traces were made along two specified directions of the various crystal plates. The directions of traces for the various crystal plates are successively

1. for X-cut plates : the crystallographic Y and Z directions.
2. for Y-cut plates : the crystallographic X and Z directions.
3. for AT-cut plates : the X direction and the  $\beta_{\text{AT}}$  direction lying at 90° to the X direction.
4. for BT-cut plates : the X direction and the  $\beta_{\text{BT}}$  direction lying at 90° to the X direction.

These profilometry traces were used to derive values for two widely used statistical and vertical roughness parameters, the centre line average roughness,  $R_a$ , and the r.m.s. roughness,  $R_q$ , respectively defined as<sup>13</sup>.

$$R_a = L^{-1} \int_0^L |z| dx$$

$$R_q = \left[ L^{-1} \int_0^L z^2 dx \right]^{1/2}$$

where z is measured from the centre line and L is the profile length in the x-direction.

Dissolution Rates of Quartz Plates

Even if a chemical reaction is too complex to be formulated in terms of the mass action law, an apparent activation energy,  $E_a$ , can be still obtained from a plot of the  $\log$  of the reaction rate, R, versus the reciprocal of the absolute temperature,  $T^{-1}$ , according to the well-known Arrhenius equation<sup>14</sup>

$$R = A \exp \left\{ -\frac{E_a}{k_B T} \right\}$$

where  $k_B$  is the Boltzmann constant. The pre-exponential term A includes general concentration terms.

For thin quartz plates the dissolution rate, R, can be, for various isothermal etchings, reasona-

bly evaluated from the slope of the linear changes in the decrement,  $\Delta d$ , in thickness with time,  $t$ . Moreover the decrement,  $\Delta d$ , in thickness of a resonator which oscillates in a thickness mode is conveniently expressed in terms of the change,  $\Delta f$ , in frequency as

$$\Delta d = -K \frac{\Delta f}{f_i f_f}$$

where  $f_i$  and  $f_f$  are the initial and the final frequency. The constant of proportionality  $K$  depends on the orientation of the quartz plate and on the overtone of the vibration.

The data obtained for various cuts are plotted in Figs. 1 and 2. It is seen that the situation is complex but one can roughly distinguish two different behaviors which correspond to an high temperature region (curves BC) and to a low temperature region (curves AB). Plots in the high temperature region consist of straight lines whose slope corresponds to an activation energy of about  $0.44 \pm 0.04$  eV (table 1). Hence as shown in table 1 the orientation has only a slight effect on the etch rate.

In the low temperature region the rate data corresponding to the X-cut and the Y-cut plates are particularly incongruous. But it must be remarked that this situation is only associated with freshly lapped plates. Effectively if the same chemically etched quartz plate is further etched in a fresh  $\text{NH}_4\text{F}$  HF solution the data obtained lie on a straight line (curve DE) which runs parallel with the curve BC.

### Surface Texture

#### Surface Profilometry

Changes in roughness parameters,  $R_a$  and  $R_z$ , with the depth of etch,  $\Delta d_s = \Delta d/2$ , of the planar surface of various resonators are represented in Figs 3 to 5. These show that the influence of the depth of etch on roughness parameters is different for each direction of a given cut and, for a given direction, also varies with the orientation of the crystal plane. Except for AT-cut plates etching causes effectively a marked decrease in both roughness parameters measured along a specified direction and in contrast an increase, followed in some cases by a slight decrease, in roughness parameters related to the perpendicular direction. The effect of crystal orientation is conveniently illustrated by the behaviors of AT-cut and Y-cut resonators. For quartz C-3 (inset of Fig. 3) measurements along the X-axis reveal that the  $R_a$  and  $R_z$  parameters decrease and approach equilibrium values smaller than initial values whereas chemical etching on Y-2 and Y-3 plates produces an increase of both  $R_a$  and  $R_z$  parameters (Figs 3 and 4). Moreover it must be remarked that it exists a qualitative similarity between behaviors of Z traces for X-cut and Y-cut plates and the  $\beta$  trace for BT-cut plates and between behaviors of X traces for Y-cut and BT-cut plates and the Y trace for X-cut plates.

Such markedly oriented changes are also typified by the relevant surface profilometry traces shown in Figs 6 to 9. The surface profiles in Figs 6b, 7a, 8a and 9a exhibit a relatively stable shape when the depth of etch reaches typical values summarized in table 2. The surface profiles in Figs 6a, 8b and 9b resulting from prolonged etching

are respectively elongated parallel to the crystallographic X and Z directions. The enlargement of surface profiles produced by repeated etchings is common in all the figures examined. A clear correspondence between the evolution of surface profiles during etching and the changes in roughness parameters with the depth of etch is thus established.

### Scanning Electron Microscopy

SEM micrographs made after different isothermal etchings provide further information (Figs 10 to 12). Etch figures with distinctive shapes differing with crystal plate orientation are revealed in agreement with experimental results on surface profilometry. For a given cut the shape and the orientation of the etch figures are uniform at any stage of etching. For X-cut and specially for Y-cut plates when the depth of etch reaches a particular value the etch figures become stable in shape but vary only in size with subsequent etching, moreover on the X and Y planes the etch figures are elongated parallel to the Z axis. The BT-cut plate etched by the  $\text{NH}_4\text{F}$  HF etchant reveals etch figures of shape varying with the depth of etch, repeated etchings result in a ridged background extended along the X axis (Fig. 12c). As previously observed by several workers<sup>6,10</sup> only the AT-cut plate presents a smoothly etched surface with uniformly shaped etch figures slightly elongated along a direction close to the X axis.

### Discussion

Without attempting to describe the details of the etching process some typical results will be discussed in relation to the surface texture of quartz plates. Let us focus attention on curves AB in Figs 1 and 2. The etch rates in the low temperature region are very rapid and are partly concerned with freshly lapped quartz plates. These physically uncertain Arrhenius plots are best understood if one compares the typical depths of etch of table 2 corresponding to the formation of stable etch figures with the depths of etch related to points B (Table 3). Moreover one can remark that for some curves representing the variation in the roughness parameters with the depth of etch there actually exists a point of inflexion I (Figs 3 to 5). This point I corresponds for various quartz plates to a particular value of the depth of etch also indicated in table 3.

Comparison of tables 2 and 3 clearly shows that the break B in any rate-temperature curve is tied in with the formation of relatively stable etch figures on the crystal surface. The conclusion that the etch rate in the low temperature region depends on the surface texture is corroborated by the Arrhenius curve DE related to the chemically etched quartz plate which gives a single straight line of slope comparable with that obtained in the high temperature region. Moreover for mechanically lapped quartz plates the etch rate is susceptible of enhancement due to the formation of a disturbed surface layer.

SEM micrographs agree well with the profilometry traces made along two perpendicular directions and reveal that for different orientations distinct types of etch figures occur. From Figs 10, 11 and 12, there is some evidence that

1. For X and Y- cut plates typical etch figures elongated along the Z axis develop on crystal surfaces. The etch figures on the X- cut plate show a diagonal symmetry compatible with the symmetry of the basal X plane.

2. Prolonged etching of BT- cut plates is accompanied by a progressive extension of etch pits along the X direction.

3. Subsequent etching of AT- cut plate gives rise to a concave background with pits slightly elongated along the X axis.

Thus the morphology of the etch figures reflects the crystallography and the orientation of the surface on which they are formed.

Moreover Figs 1 and 2 reveal that the etch rate varies with the crystal orientation. For example it is evident that the Y plane etches differently from the BT- cut plane by a factor of about 0.2 at 353 K. But the surface orientation affects only slightly the activation energy with deviation less than 12 % from the average value of 0.44 eV. A consequence of a diffusion controlled reaction is that different crystallographically oriented surfaces should etch at the same rate<sup>15,16</sup>, therefore it is reasonable to assume that the etching mechanism is primarily determined by the surface orientation and properties. The fact that etch rates are approximately insensitive to stirring is also in contradiction with numerous experiments on diffusion controlled reactions<sup>15</sup>. Moreover some authors<sup>17,18</sup> have stated that the symmetry elements of an etch pit or of an etch hillock in general correspond to the symmetry of the crystal plane on which the etch figure is produced. The morphology of the triangular pits which develop on Z- cut quartz platelets<sup>12</sup> provides an additional argument in favor of a surface orientation-governed reaction.

The surface profilometry traces which exhibit after prolonged etching an approximately stable shape are also interesting because they suggest a convenient way to use<sup>15</sup> the reciprocity condition and stability criterion<sup>15</sup> to explain the final shape of dissolution figures. In terms of the stability criterion presented by Irving<sup>15</sup> a concave intersection is stable provided there is no plane of lower rate lying between the two planes forming the intersection and reciprocally a convex intersection is stable provided there is no plane between them with higher etch rate. In other words let  $R_h$  and  $R_o$  be the etch rate normal to a plane h and to the reference plane and  $\theta_h$  the angle between them. If  $R_h < R_o \cos \theta_h$  hillocks will propagate and if  $R_h > R_o \cos \theta_h$  etch pits will form<sup>15,19</sup>.

The traces shown in Figs 6, 7, 8 and 9 clearly indicate that the etch rate variation depends on the direction of measurement of  $\theta_h$ . This assumption is consistent with the observed background of pits elongated along some specified direction. Thus some attempts can be made to describe the observed etch figure phenomena by a rectangular combination of etch rate distributions. For example, Irving<sup>15</sup> stated that a concave background with pits elongated along the X axis results from the rectangular combination shown in Fig. 13a. Such a concave background develops on AT-cut plates. Thus since the X axis is common to AT, BT, Z and Y-cut plates we can try to verify if the etch rate orientation dependence for the  $\beta$  axis agrees approximately with the theoretical predictions.

The expected variation is plotted in Fig. 13b. As usual<sup>20</sup>, the etch rate of the Z plane is assumed to be a hundredfold greater than the etch rate related to the Y plane and for convenience we have made use of some primarily data on an almost "AT-cut" plate lying about 31° of the Z axis. Since only orientations neighbouring the reference AT-cut plane need to be considered in applying the statement on reciprocity, the conditions for the formation of a concave background structure are satisfied by the expected variation of surface rate with orientation. It seems also that on the basis of this treatment we can partially explain the striations observed on deeply etched BT-cut plates<sup>21</sup>. However it must be noticed that a complete comparison of theoretical predictions with etch rate data requires a detailed knowledge of the etch rate versus orientation data. In particular the etching of planes lying in the vicinity of the AT-cut and BT-cut planes must be systematically studied.

### Conclusion

The etch rate of quartz plates of various orientations in a solution of  $\text{NH}_4\text{F}$  HF has been investigated in the temperature range 290 - 360K. The Arrhenius plots are found to be linear in a high temperature region which corresponds to the formation of stable etch figures. The measured activation energies are only slightly affected by the surface orientation. In contrast the variation of the etch rate with the surface orientation is pronounced.

A clear correspondence between the shape of dissolution figures and the surface orientation is established. Moreover the shape of profilometry traces depends on the direction of the trace. The SEM micrographs and the profilometry traces provide some evidence for asymmetrical etch rate distributions. A rectangular combination of etch rate distributions as presented by Irving<sup>15</sup> allows us to explain to a first approximation the formation of distinctive dissolution figures on some crystal planes.

### Acknowledgements

The author would like to thank Mr Buron (Cetehor, Besançon, France) for providing the SEM micrographs.

### References

1. W.G. Cady, "Piezoelectricity", Vol. 2, Dover Publications, New York, Chapter 13 (1964).
2. P. Vigoureux and C.F. Booth, "Quartz Vibrators and their Applications", His Majesty's Stationery Office, London, Chapter 7, (1950).
3. J.P. Valentin, J. Ph. Michel and R.J. Besson, C.R. Acad. Sci., Sér. B, 289, 155 (1979).
4. Y. Sekiguchi and H. Funakubo, J. Mater. Sci. 15, 3066 (1960).
5. H. Fukuyo and N. Oura, Proc. 30th Annual Symposium on Frequency Control, Fort Monmouth, N.J. 1976, Electronic Industries Association, Washington, DC, p. 254 (1976).
6. J.R. Vig, J.W. Lebus and R. Filler, Rep. ECOM-4548, (1977), (US Army Electronics Command, Fort Monmouth, N.J.)



7. J.R. Vig, H. Wasshausen, C. Cook, M. Katz and E. Hafner, Proc. 27th Annu. Symp. on Frequency Control, Fort Monmouth, N.J., 1973, Electronic Industries Association, Washington, DC, p. 98, (1973).
8. J.R. Vig, C.F. Cook, K. Schwidtal, J.W. Lebus and E. Hafner, Proc. 28th Annu. Symp. on Frequency Control, Fort Monmouth, N.J., 1974, Electronic Industries Association, Washington, DC, p. 96 (1974).
9. H. Fukuyo, N. Oura, N. Kitajima and H. Kono, J. Appl. Phys. 50, 3653 (1979).
10. C.R. Tellier, Surf. Technol. 21, 83 (1984)
11. J.R. Vig, R.J. Brandmayr, R.L. Filler, Report No DELET-TR-80-5 (U.S. Army Electronic Research and Development Command, Fort Monmouth, N.J., 1980).
12. C.R. Tellier and F. Jouffroy, J. Mater. Sci., 18, 3621 (1983).
13. T.R. Thomas "Rough Surfaces", Longman, London, Chapter 4, (1981).
14. H. Eyring and E.M. Eyring "Modern Chemical Kinetics", Reinhold, New York (1965).
15. B.A. Irving in P.J. Holmes (Ed.) "The Electrochemistry of Semiconductors", Academic Press, London, pp. 256-289 (1962).
16. B. Schwartz and H. Robbins, J. Electrochem. Soc. 123, 1903 (1976).
17. R.B. Heimann in J. Grabmaier (Ed.) "Silicon Chemical Etching", Springer, Berlin, 197 (1982).
18. M.W. Wegner and J.M. Christie, Phys. Chem. Minerals, 9, 67 (1983).
19. B.W. Batterman, J. Appl. Phys., 28-1236 (1957).
20. F.M. Ernsberger, J. Phys. Chem. Solids, 13-347 (1960).
21. C.R. Tellier and C. Buron, Surf. Technol., (1984) to be published.

Quartz Plates		$E_a$ (eV)	
X-cut	quartz X-R2	curve BC 0.438	curve DE
	quartz X-R3	0.438	0.436
Y-cut	quartz Y-R2	0.484	0.494
	quartz Y-R3	0.475	
BT-cut : quartz BT-7		0.432	
AT-Cut : quartz C-3		0.390	

Table 1 : The activation energy,  $E_a$ , as determined from curves BC and DE for various quartz plates.

Quartz Plate	Direction of trace	$\Delta d_s (\mu m)$	type of background structure
BT-7	$\beta$ - direction	$> 2$	convex
C-3	X - direction	$\geq 2.5$	concave
X-R2	Y - direction	$> 1.6$	approximately convex
Y-R2	X - direction	$\geq 1.2$	approximately convex

Table 2 : The formation of approximately stable etch profiles.

Quartz	$\Delta d_s (\mu m)$ point B in Figs 1,2	$\Delta d_s (\mu m)$ point I in Figs 3,4	$\Delta d_s (\mu m)$ point I in Fig. 5
C-3	2.45	X-trace : 2	
X-R2	1.6	Y-trace : 1.7 Z-trace : 1.67	Y-trace : 1.7 Z-trace : 1.62
X-R3	1.5	Z-trace : 1.4	
Y-R2	1.2	Z-trace : 1.25	Z-trace : 1.3
Y-R3	0.84	Z-trace : 0.9	Z-trace : 0.95
BT-7	2.5	X-trace : 2.5	

Table 3 : Typical values of the depth of etch.

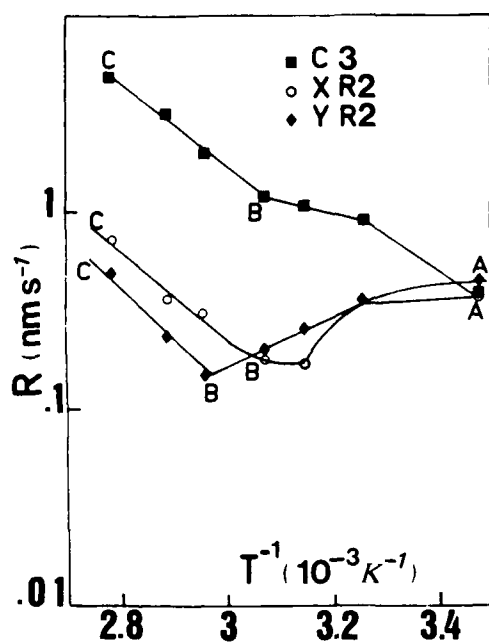


Figure 1 : Plot of  $\ln R$  vs  $T^{-1}$  for various quartz plates.

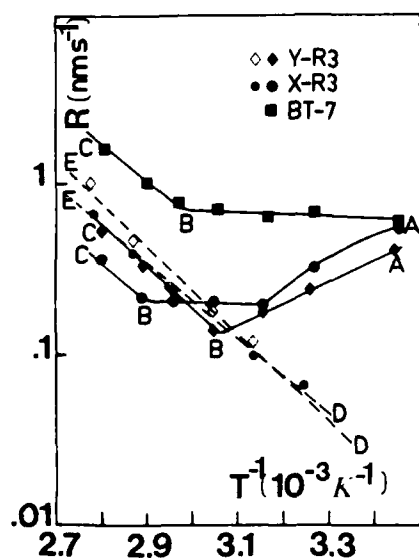


Figure 2 : Plot of  $\ln R$  vs  $T^{-1}$  for various quartz plates.  
Dotted curves are for chemically etched plates.

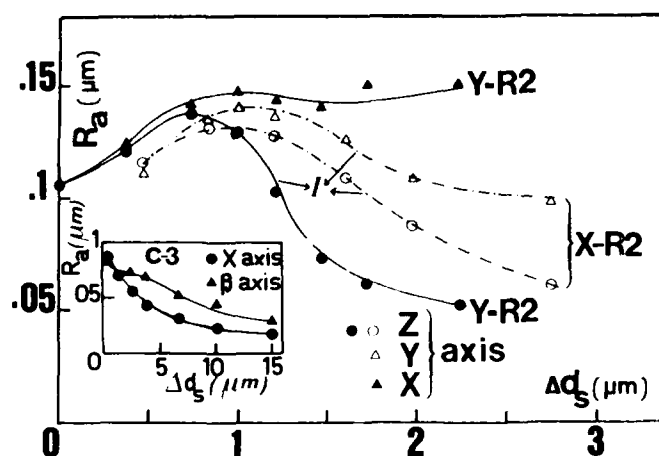


Figure 3: The roughness parameter,  $R_a$ , as a function of the depth,  $\Delta d_s$ , of etch for various quartz plates and for various profilometry traces.

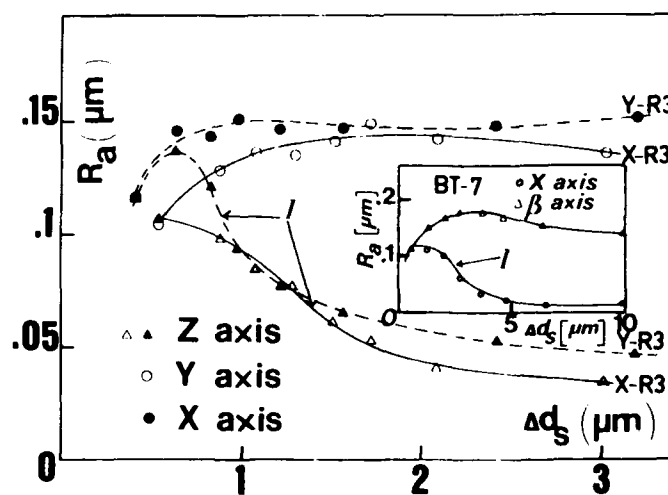


Figure 4: The roughness parameter,  $R_a$ , as a function of the depth,  $\Delta d_s$ , of etch for various quartz plates and for various profilometry traces.

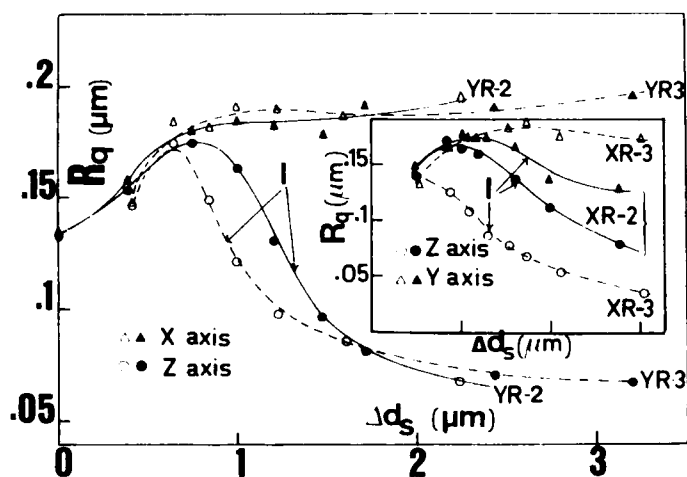


Figure 5: The roughness parameter,  $R_q$ , as a function of the depth,  $\Delta d_s$ , of etch for various quartz plates and for various profilometry traces.

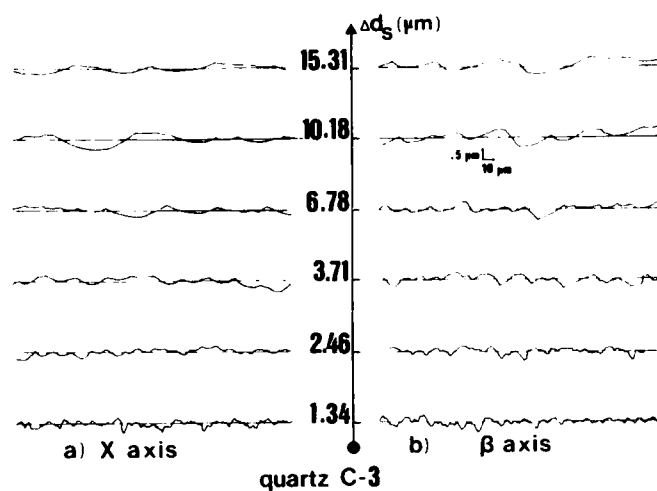


Figure 7: Changes in the surface profilometry traces with the depth of etch for an AT-cut quartz plate.

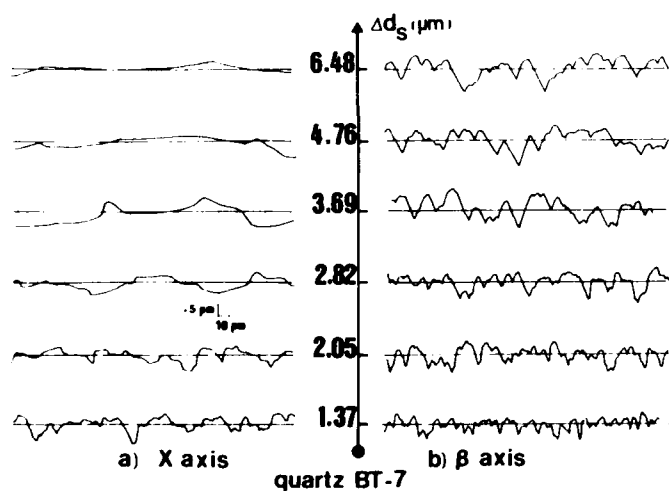


Figure 6: Changes in the surface profilometry traces with the depth of etch for a BT-cut quartz plate.

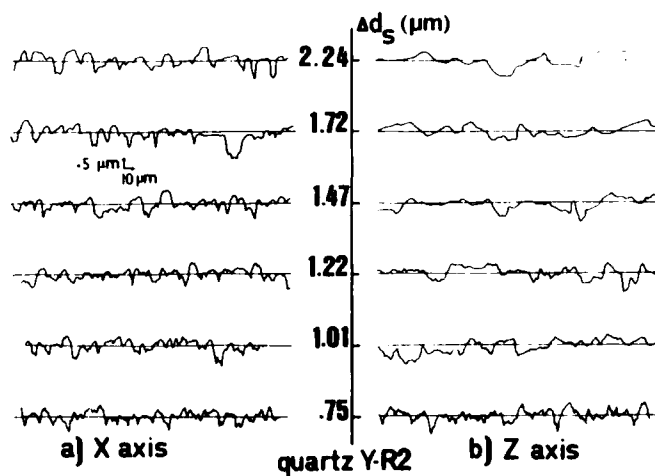


Figure 8: Changes in the surface profilometry traces with the depth of etch for an Y-cut quartz plate.

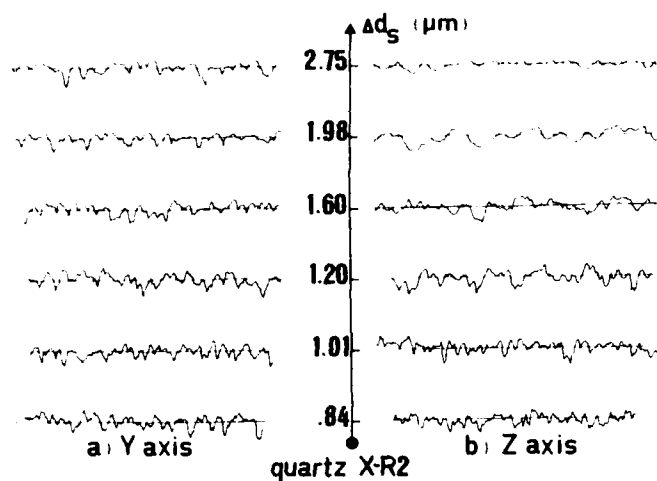


Figure 9: Changes in the surface profilometry traces with the depth of etch for an X-cut quartz plate.

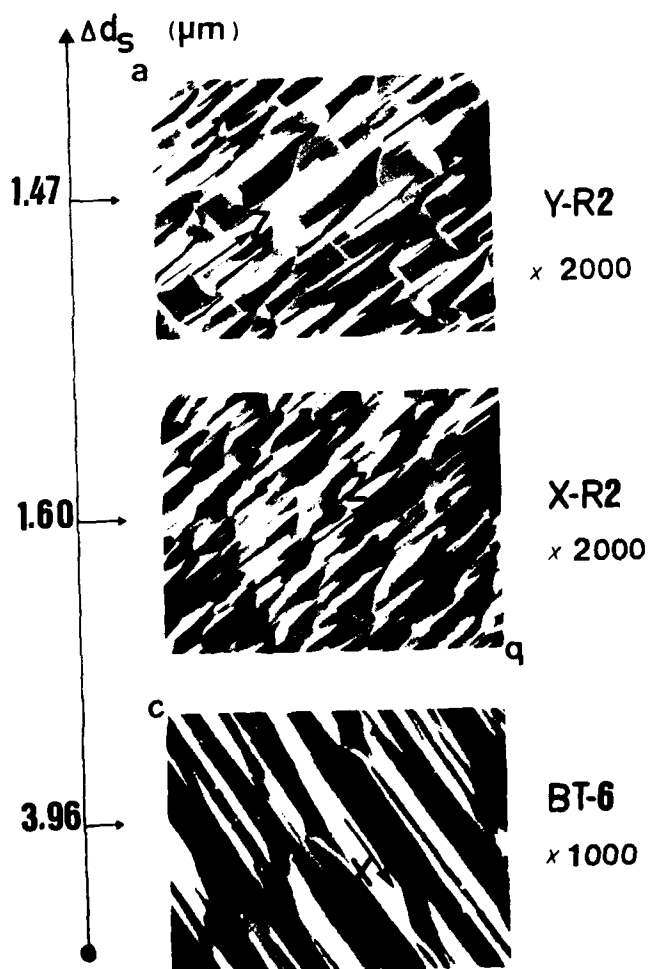


Figure 10 : SEM micrographs for various quartz plates

- a) Quartz Y-R2 ( $\Delta d_s = 1.01 \mu\text{m}$ )
- b) Quartz X-R2 ( $\Delta d_s = 1.01 \mu\text{m}$ )
- c) Quartz BT-6 ( $\Delta d_s = 1.95 \mu\text{m}$ )

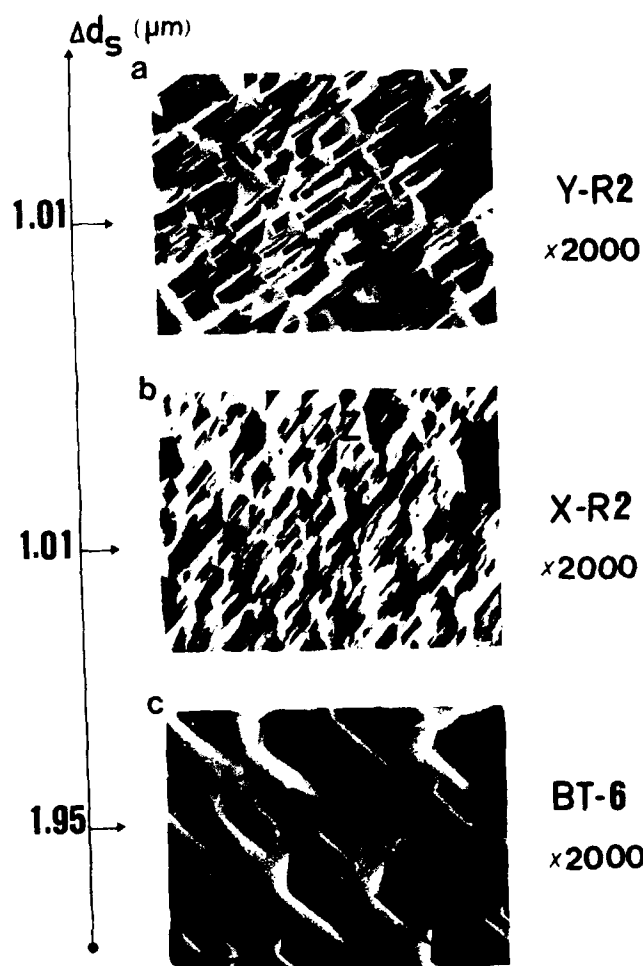


Figure 11 : SEM micrographs for various quartz plates

- a) Quartz Y-R2 ( $\Delta d_s = 1.47 \mu\text{m}$ )
- b) Quartz X-R2 ( $\Delta d_s = 1.60 \mu\text{m}$ )
- c) Quartz BT-6 ( $\Delta d_s = 3.96 \mu\text{m}$ )

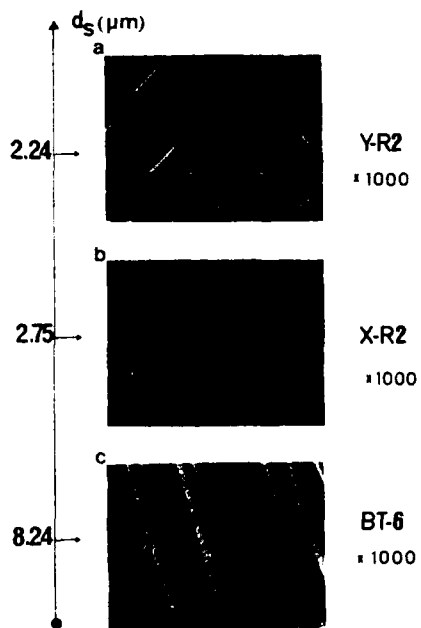


Figure 12 : SEM micrographs for various quartz plates

- a) Quartz Y-R2 ( $\Delta d_s = 2.24 \mu\text{m}$ )
- b) Quartz X-R2 ( $\Delta d_s = 2.75 \mu\text{m}$ )
- c) Quartz BT-6 ( $\Delta d_s = 8.24 \mu\text{m}$ )

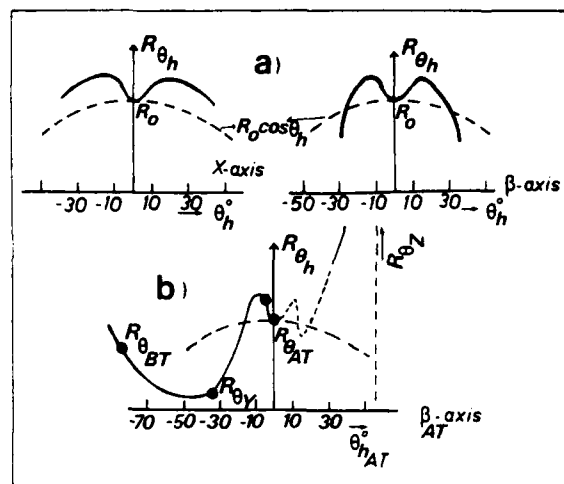


Figure 13: Etch rate vs orientation

- A rectangular combination of etch rate distributions leading to the formation of a concave background.
- b) Expected plot of etch rate vs orientation: some experimental data are indicated in the figure.

## CHIP CRYSTAL RESONATOR WITH LOAD CAPACITORS

Yuji Kojima, Yoshiro Fujiwara, Seiichi Yamada, and Noboru Wakatsuki

FUJITSU LIMITED

1015, Kamikodanaka Nakahara-ku Kawasaki, 211, JAPAN

**ABSTRACT**

This paper reports on the miniaturization of a chip resonator using  $\text{LiNbO}_3$  and the integration of this resonator and two capacitors for a 4 or 8 bit one chip microprocessor clock generator, which has an amplifier to form a Colpitts oscillator.

The strip type crystal resonator using  $\text{LiNbO}_3$  was developed with a suitable crystal orientation and suitable outline dimensions. The size of a 4 MHz  $\text{LiNbO}_3$  crystal strip is  $4.5 \times 0.6 \times 0.5$  mm. This is almost 20 times smaller than that of a AT-cut quartz.

Two capacitors were integrated into the same package with the resonator strip chip. As the mechanical energy is strongly concentrated around the center of the strip on the driving electrodes, the strip can be mounted directly on a ceramic substrate without reducing the Q factor. This film dielectric for capacitors is pre-printed on the substrate. The resonator and two capacitors are encapsulated under a ceramic cap. The resonator is  $8.0 \times 3.2 \times 2.5$  mm when used as a chip component.

The capacitors' values and resonant resistance of the resonator are optimally defined by examination of oscillation rise time, which is chosen as less than 50  $\mu\text{s}$ . The capacitor value of  $20 \pm 8$  pF and resonant resistance value of less than 150  $\Omega$  gives stable oscillation for typical Fujitsu N-Mos or C-Mos 4 bit microprocessors.

**1. Introduction**

Electronic devices are becoming digitized more and more, greatly increasing the demand for stable clock signal oscillators used in fundamental operational processors. Therefore, mechanical resonators using piezo-electric material are attracting attention due to their high Q, high stability, and miniaturization. Especially, for one chip microprocessors which have been used recently in many electronic devices, the frequency range required for resonators extends from several MHz to several tens of MHz, and thickness shear mode resonators of quartz, ceramic, or  $\text{LiTaO}_3$  are used. The  $\text{LiTaO}_3$  chip resonator is small and is most suitable for miniaturization [1][2], thin structure, light weight, and automatic assembly. However, to satisfy a demand for smaller size, we investigated a  $\text{LiNbO}_3$  piezo-electric single crystal. Since mechanical resonator characteristics strongly depend on the material, we noticed that  $\text{LiNbO}_3$  has a high electro-mechanical coupling factor, and investigated the crystal axis orientation and element shape to obtain a smaller size chip component. This resonator, when used in microprocessors, features not only small size but also a faster (1/100 of quartz) rise time and stable oscillation. To promote higher density assembly and to decrease the number of components, two load capacitors conventionally mounted externally in an oscillator circuit were mounted in the same package, of resonator as thick film capacitors, to realize a three terminal chip resonator with built-in load capacitor.

The paper first describes features of the  $\text{LiNbO}_3$  chip resonator comparing it with  $\text{LiTaO}_3$ , and describes an application example and optimum using conditions for the widely used 4-bit microprocessor, noting the oscillator rise time and temperature characteristics. Then the thick film process production of external capacitors is described. At the end, the resonator characteristics are explained.

**2.  $\text{LiNbO}_3$  and  $\text{LiTaO}_3$  chip resonators**

If a piezo-electric shear mode resonator is made in a strip type and the strip longitudinal direction agrees with that of the displacement direction, there is no mode transformation at the strip side terminal face and spurious response is suppressed [3]. As a result, the resonator can be miniaturized. Figure 1 shows the strip type resonator structure, where  $2W$  is the strip width,  $2H$  is the strip longitudinal length, and  $2l$  is the driving electrode length.

$\text{LiTaO}_3$  and  $\text{LiNbO}_3$  have a high coupling factor for shear waves, and the energy concentrates around the driving electrodes. The crystal axis orientation and element shape of  $\text{LiTaO}_3$  have already been investigated from viewpoints of temperature and spurious characteristics [2]. Similarly investigating  $\text{LiNbO}_3$  by an vibration analysis, the optimum crystal orientation and element shape are obtained. Table 1 shows the calculated crystal orientation, compared with that of  $\text{LiTaO}_3$ . The velocity is almost equal, but the coupling factor of  $\text{LiNbO}_3$  is 1.3 times higher than that of  $\text{LiTaO}_3$  and a smaller size chip can be expected. To determine the element shape, for the strip width, a condition that never generates unwanted spurious response must be obtained first. Figure 2 shows a conditions generating no spurious response for  $\text{LiNbO}_3$  and  $\text{LiTaO}_3$ , that is, there is a no-spurious condition in a narrower strip of  $\text{LiNbO}_3$ . For the strip length, resonant resistance of resonator has an important factor. Since  $\text{LiNbO}_3$  has a higher coupling factor, it is found that the resonant resistance does not degrade even if the strip length is less than that of  $\text{LiTaO}_3$  as shown in Fig. 3.

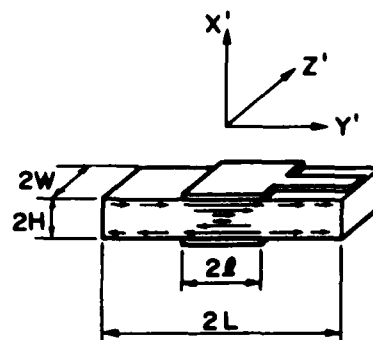
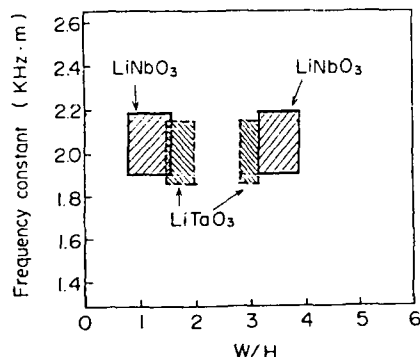
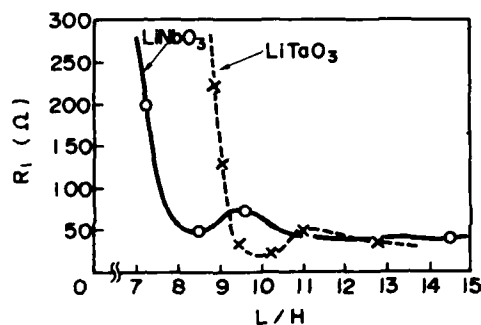


Fig. 1. Piezoelectric strip construction

Table 1. Crystal orientation

	Crystal orientation			Velocity (m/s)	Coupling factor
	$\alpha$	$\theta$	$\phi$		
LiTaO <sub>3</sub>	0°	-48°	0°	4340	0.47
LiNbO <sub>3</sub>	-90°	90°	-15°	4580	0.61

(Eulerian coordinates)

Fig. 2. Conditions generating no spurious response of resonator for LiNbO<sub>3</sub> and LiTaO<sub>3</sub>Fig. 3. Relationship between the ratio L/H and R<sub>1</sub>

Consequently, when LiNbO<sub>3</sub> is used, the strip is smaller than that of LiTaO<sub>3</sub> and batch processing using a wafer unit increases the effect. Figure 4 shows the case when 4 MHz chips are produced from a two inch wafer. One wafer can produce about 500 chips at the same time. Furthermore, powdered LiNbO<sub>3</sub> material is cheap and a large 3-inch or 4-inch crystal can be grown. Thus the LiNbO<sub>3</sub> chip resonator is much more economical than the LiTaO<sub>3</sub> chip resonator.

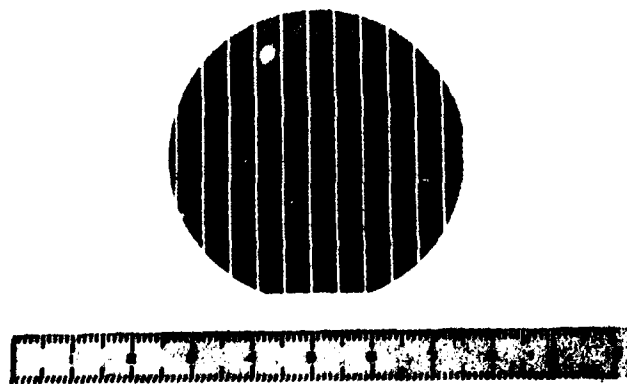
Fig. 4. One LiNbO<sub>3</sub> wafer forms about strips

Figure 5 shows admittance characteristics of LiNbO<sub>3</sub> and LiTaO<sub>3</sub> resonators using these crystal orientations, compared with those of quartz. Because of the coupling factor of the piezo-electric material, both resonators have a capacitance ratio less than 1/30 than that of quartz. Therefore, the difference between the resonant and anti-resonant frequencies is considerable and the inductive frequency range, that is, the range where oscillation is possible in a Colpitts circuit, can be twenty times as wide as that of quartz. Moreover, since spurious response points near the main frequency are few and of low level compared to those of quartz resonators, oscillation frequency jumps and stoppage failures can be expected to become fewer. The temperature characteristic of a thickness shear mode resonant frequency of the LiTaO<sub>3</sub> X-cut is known to be a secondary curve [4]. On the other hand, the LiNbO<sub>3</sub> resonator temperature characteristic is approximately linear with a -70 ppm/°C slope. This is a little high, but is acceptable for conventional use of a microprocessor, Figure 6 compares the temperature characteristics of the LiNbO<sub>3</sub> with those of the LiTaO<sub>3</sub> resonator.

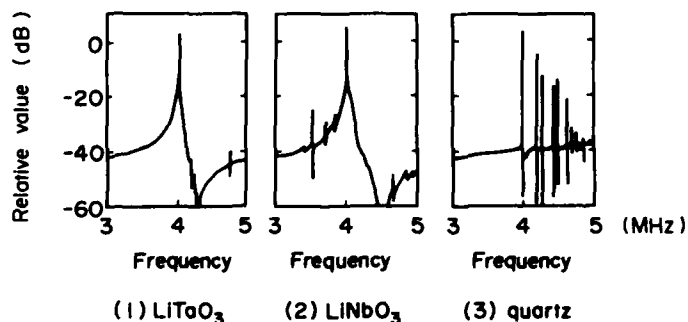
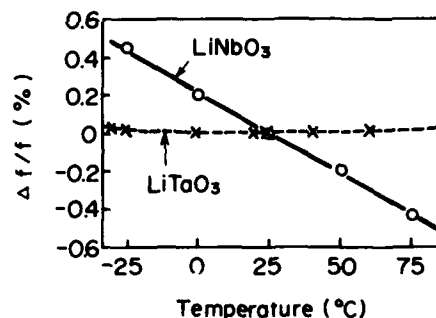


Fig. 5. Frequency response for 4 MHz resonator

Fig. 6. Temperature characteristics of LiNbO<sub>3</sub> and LiTaO<sub>3</sub> resonator

### 3. Load Capacitor

#### 3.1 Optimum capacitor

The oscillator circuit in ordinary microprocessors is regarded as a modified the Colpitts circuit. As shown in Fig. 7, it consists of an amplifier, a resonator, and two capacitors. Depending on value of the two capacitors for the resonator, there are cases where stable oscillation is not obtained. The proper values of load capacitors for stable oscillation are determined from measurement results of the rise time in the operating temperature range and output voltages of clock signal high level and low level. N-MOS and C-MOS 4-bit microprocessor widely used for public and industrial objectives were investigated here. The time until the circuit oscillates stably when a 5 V pulse voltage is applied as the power voltage V<sub>cc</sub> is called rise time. This depends on the load capacitor, temperature, etc. This rise time is required to be stable and high speed.



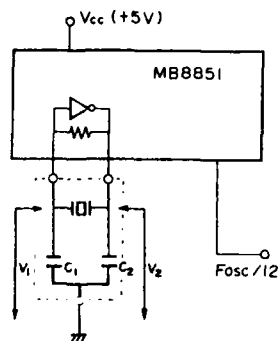


Fig. 7. 1 chip microprocessor and clock oscillator

For a typical Fujitsu 4-bit microprocessor, the MB8851 (C-MOS), Figure 8 shows the results of  $\text{LiNbO}_3$  4MHz resonator investigated in the temperature range from  $-40^\circ\text{C}$  to  $85^\circ\text{C}$ . When the temperature rises, the oscillation-possible range becomes narrow. Figure 9 shows the no-oscillation region and oscillation rise time for room temperature. The smaller the load capacitor, the faster the rise time, and the rise time is 50  $\mu\text{s}$  or less near  $C_1$  and  $C_2$  values near 20 pF. Figure 10 shows the relationship between the high level and low level oscillation output and the load capacitor. If the load capacitor is small (10 pF or less), the high level is 4.0 V or less and discrimination becomes difficult. The investigation using the N-MOS 4 bit microcomputer MB8841 found that stable oscillation and 100  $\mu\text{s}$  or less rise time was obtained similarly with a capacitor of about 20 pF.

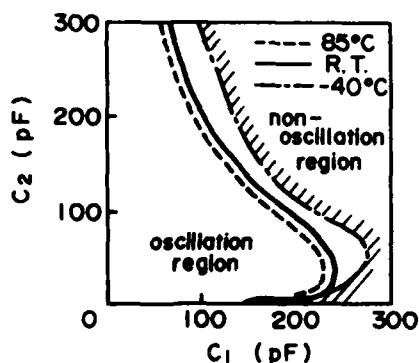


Fig. 8. Relationship between  $C_1$ ,  $C_2$  and oscillation region

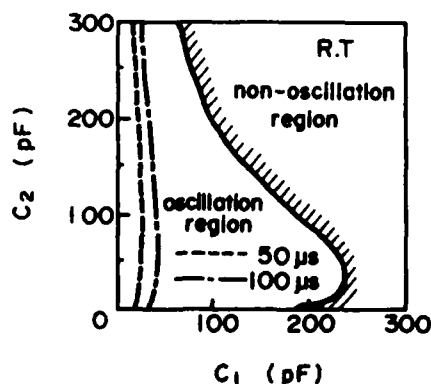


Fig. 9. Relationship between  $C_1$ ,  $C_2$  and oscillation rise time

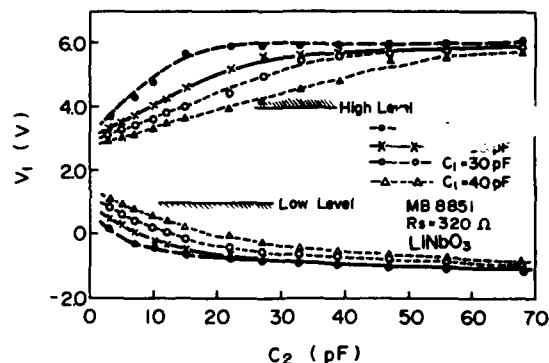


Fig. 10. Relationship between  $C_2$  and oscillation voltage  $V_1$  (MB8851)

### 3.2 Thick film capacitor characteristics

From the previous investigation, it was found that the optimum load capacitor was about 20 pF for 1-chip microprocessor oscillator circuits. This is a value which can be realized with about 0.7  $\text{mm}^2$  thick film capacitor if its specific dielectric constant  $K$  is about 100, and stable oscillation can be expected even when the capacitance change is  $\pm 20\%$ . The production accuracy of this thick film capacitor can be easily realized. We made about 30  $\mu\text{m}$  thick and 0.7  $\text{mm}^2$  area capacitors on an alumina substrate using  $\text{BaTiO}_3$  thick film paste ( $K=100$ ). The dielectric layer was a three layer structure where print, dry, and fire were repeated three times. Characteristics of this thick film capacitor are described below. Figure 11 shows temperature characteristics of only the capacitor. The capacitance change is  $\pm 200$  ppm/ $^\circ\text{C}$  over the temperature range from  $-35^\circ\text{C}$  to  $85^\circ\text{C}$  and approximately 0.3 pF in the range included in the stable oscillation region. Table 2 summarizes other electrical characteristics. The  $\tan\delta$  is small, 0.1% or less, the insulation resistance is  $1 \times 10^{10}$  or more ohms, and the breakdown voltage is more than 500 V, equivalent to ceramic capacitors.

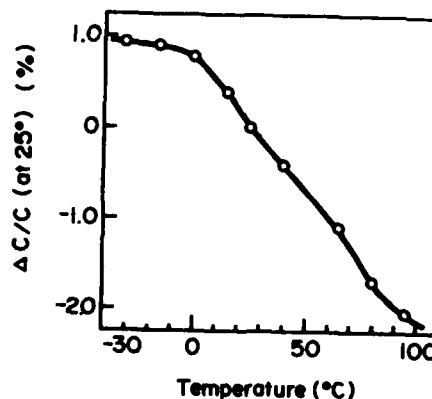


Fig. 11. Temperature characteristics of thick film capacitor

Table 2. Characteristic of thick film capacitors

$\tan\delta$	Insulation resistance	breakdown voltage
<0.1%	$>1 \times 10^{10} \Omega$ (at 100 V)	>500 V

#### 4. Resonator with Built-in Capacitors

Construction of a resonator with built-in capacitors by mounting a chip resonator element on a substrate where the thick film capacitors are formed, is described. Figure 12 shows the resonator structure. Three external terminal electrodes are formed at three locations on the substrate, left and right and center, via through holes connecting the surface and the rear face, opposite to the capacitor face. All these processes use the thick film process and are formed by one time printing on a large-size substrate. This is suitable for mass production. The 96% alumina substrates are also much used as in hybrid ICs and a large substrate can be obtained cheaply. Figure 13 shows an example on a large substrate (114.3 x 95.5 mm<sup>2</sup>). 338 chips can be made at the same time from this substrate. Since this is a energy trapping resonator where resonator energy concentrates around the driving electrode, the resonator is directly mounted on the capacitor upper electrode formed on the alumina substrate, with conductive paste. [5]

In the final process, giving space in the vibration portion of the resonator element on the base substrate and sealing the entire protection cap, the capacitor built-in chip type resonator is completed. Table 3 shows dimensions of chip type and SIP type resonators. The SIP type resonator can be produced by adding a lead frame to the chip type and by transfer-molding. Both types share the same process.

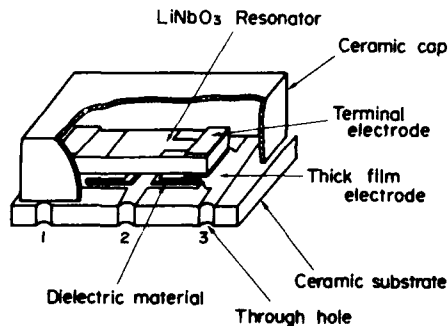


Fig. 12. Structure of LiNbO<sub>3</sub> resonator

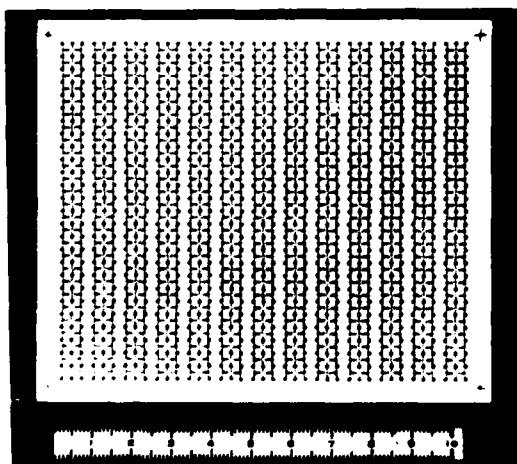
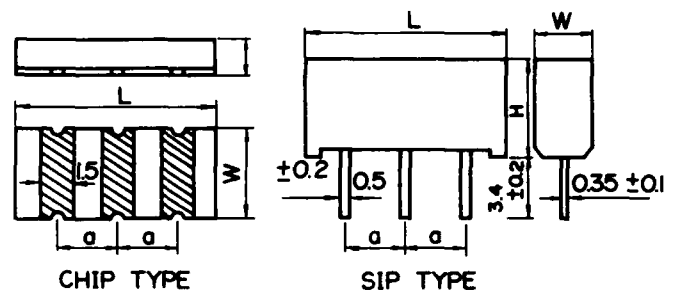


Fig. 13. One large substrate (114.3 x 95.5 mm<sup>2</sup>)

Table 3. Outline and dimension



( Unit = mm )

Dimension		L	W	H	a
Configuration					
Chip type	A type	10.0±0.5	4.5±0.5	2.5±0.3	2.54±0.2
	B type	8.0±0.5	3.2±0.5	2.5±0.3	
SIP type	A type	11.0±0.2	4.3±0.2	6.3±0.2	
	B type	9.0±0.2	4.3±0.2	5.3±0.2	

#### 5. Overall Characteristics

Overall Characteristics of the LiNbO<sub>3</sub> chip resonator including 20 ± 8 pF capacitor, in a 4-bit C-MOS microprocessor application, are same as the circuit consists of the resonator and the two discrete capacitors. The oscillation rise time was 200 μs or less over the -50°C to 100°C temperature range. Figure 14 compares rise times of the LiNbO<sub>3</sub> chip resonator and a quartz. It shows that the former is about 100 times faster than the latter. On the other hand, frequency temperature characteristics over the temperature range, as shown in Fig. 15, agree with LiNbO<sub>3</sub> resonant frequency temperature characteristics depending on material characteristics shown in Fig. 6.

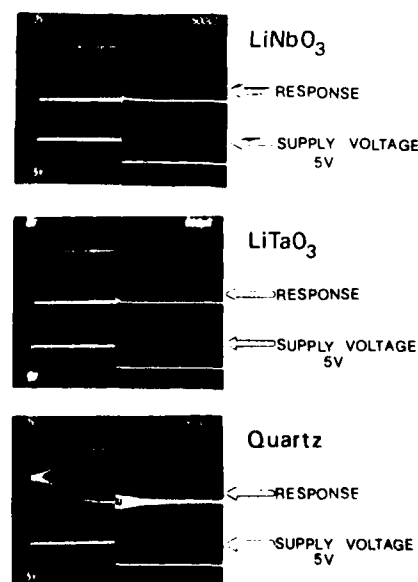


Fig. 14. Oscillation rise time

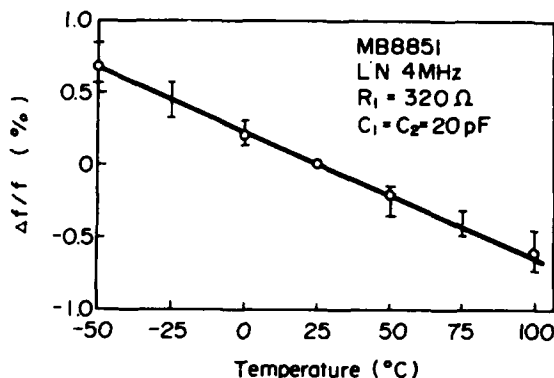


Fig. 15. Relation between temperature and oscillation frequency (Temperature characteristics of LiNbO<sub>3</sub> chip resonator)

Fig. 16 shows temperature characteristic for the oscillation voltage. It shows stable oscillation over the temperature range. Figure 17 shows the oscillation voltage for power supply voltage change. The clock signal assures  $\pm 0.8$  V margin for wide range variations of about 20% at the 5 V power voltage. This can be said to be a stable clock signal oscillation. Thus we could obtain stable oscillation without adjustment even in the built-in type by using  $20 \text{ pF} \pm 8 \text{ pF}$  for the two load capacitors.

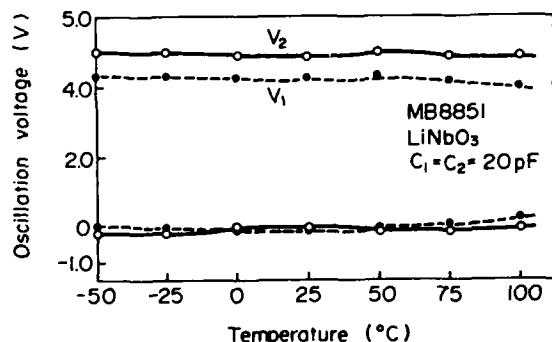


Fig. 16. Relationship between temperature and oscillation voltage

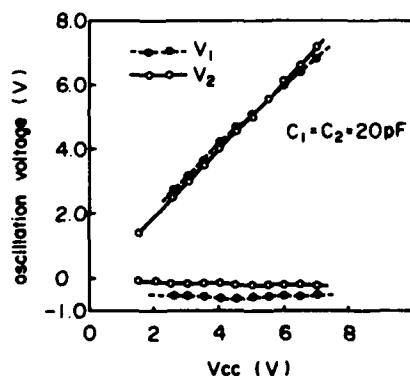


Fig. 17. Relationship between supply voltage  $V_{cc}$  and oscillation voltage  $V_1, V_2$

## 6. Conclusion

We developed a strip type resonator generating no spurious response and having a low resonant resistance by using LiNbO<sub>3</sub> single crystal having a large electro-mechanical coupling factor and by investigating optimum crystal orientations corresponding to the vibration mode. Compared to the LiTaO<sub>3</sub> chip resonator, this type resonator is smaller and more economical, and is suitable for clock oscillators in 4-bit one chip micro-processors. When the element is used in an oscillator, two external capacitors are needed. The optimum value was determined by the time to reach stable oscillation from power-on time. For our company's C-MOS (MB8851) and N-MOS (MB8841), the optimum value is  $20 \pm 8 \text{ pF}$ , and with this value, stable oscillation is obtained without adjustment. The rise time is 50  $\mu\text{s}$  or less in the  $-35^\circ\text{C}$  to  $+85^\circ\text{C}$  temperature range (approximately 1/20 of quartz). Since the strip type resonator is a energy trapping resonator where the oscillation energy concentrates around the electrode, the resonator element can be directly mounted on the substrate. Consequently, by directly mounting the resonator on the upper electrode of the thick film capacitor formed on the alumina substrate, the resonator and capacitors could be integrated. Thus we could reduce the number of components of 1/3 of the conventional number and realize a three terminal chip element with 1/3 mounting area. When it is used in combination with a micro-computer, its stable oscillation against changes in temperature and power voltage was confirmed.

## Acknowledgements

The authors wish to thank Dr. T. Hara and Mr. H. Tominaga for their guidance and suggestions during this study

## Reference

- [1] Y. Fujiwara, S. Yamada, and N. Wakatsuki, "Strip type LiTaO<sub>3</sub> chip resonator with zero temperature coefficient", Paper of technical group US, IECE Japan 82-46, November 1982
- [2] Y. Fujiwara, S. Yamada, and N. Wakatsuki, "Miniaturized LiTaO<sub>3</sub> strip resonator", Proc. 37th Annu. Symp. Freq. Cont., p.343 June 1983
- [3] K. Nakamura, H. Shimizu, "On the equivalent circuits for thickness twist mode and thickness shear mode in piezoelectric plates", Paper of technical group US, IECE Japan 69-21, October 1969
- [4] M. Onoe and T. Ashiba, "Zero temperature coefficient of resonant frequency in an X-cut Lithiumtantalate at room temperature", Proc. IEEE (Letters), vol. 57, No.8, p.1446, August 1969
- [5] Y. Kojima, Y. Fujiwara, S. Yamada, and N. Wakatsuki, "Design of strip type LiTaO<sub>3</sub> chip resonator", Paper of technical group US, IECE Japan 83-1, May 1983

## AT-CUT STRIP RESONATORS ENCLOSED IN CYLINDRICAL PACKAGE

Masanobu OKAZAKI and Naoki MANABE

NDK (Nihon Dempa Kogyo Co., Ltd.)  
1-21-2 Nishihara Shibuya-ku  
Tokyo, JAPAN

Summary

Miniaturization of the electronic components leads miniaturization of the electronic equipment, such as clocks, video tape recorders and their cameras. This is the recent tendency. To meet such demands from the market, chip type resistors and capacitors or high integrated IC have been developed. Among these chip type components, sometimes, crystal requires the biggest area on the print circuit board. Therefore, strong demands for miniaturization of the crystal have been increasing.

One candidate to meet this requirement is an AT-Cut strip resonator elongated to the X axis which authors have been studied. As a result of our investigation, the development of a new miniature AT-Cut resonator enclosed in a cylindrical package as  $\phi 3.0 \text{ mm} \times 28.8 \text{ mm}$ , which is well known as the standard package for wrist watch crystal, is succeeded. The resonator named "MS-309" was achieved the same electrical characteristics as the conventional HC-49/U holder crystal. Therefore, the MS-309 helps more miniaturization of the equipments not only in the consumer field but also in the professional communication field.

Introduction

An AT-Cut resonator vibrates in a thickness twist mode in which the direction of the displacement is parallel to the diagonal, X, axis. There are many advantages to use AT-Cut strip shaped resonator elongated to the X axis for miniaturization of crystal blanks. It was reported that a miniature AT-Cut strip resonator, which had good electric characteristics, was realized by tilting the edges along the X axis. (1)(2) Fig. 1 shows the tilting way under the coordinate system. The theoretical tilting angle  $\alpha$  is given by the following equation.(3)

$$\alpha = \tan^{-1} \frac{C_{56}}{C_{66}}$$

where  $C_{56}$  and  $C_{66}$  are stiffness constants referred to the rotated coordinates. According to the experimental results, the effective range of  $\alpha$  is from 4 degrees to 6 degrees.

A type of resonator applying this technique, named "AT-35", was reported at the 31st F.C.S. In this case, a strip resonator was mounted at both ends along the X axis in the flat package as the AT-35. However, there were difficulties in reducing the size more than the AT-35 because the AT-35 wafer dimension is the smallest size for both end mounting without worsening the electrical characteristics. To overcome such difficulties, it was considered that mounting of one of the short edges might give better characteristics. In fact, crystal impedance did not increase in spite of decreasing the length of crystal wafer.

On the other side, a tuning-fork crystal resonator for wrist watch enclosed in a cylindrical package have been available at the mass production level. So it was tried to apply this cylindrical package for an AT-Cut strip resonator. Finally, the miniature AT-Cut strip resonator, named "MS-309", has been developed. This MS-309 has the good electric characteristics and the high environmental performance. And the frequency range developed is very wide from 4.19 MHz for clock application to 17.7 MHz for V.T.R one.

Miniaturization

Almost all performance of resonators rely on the design of the wafer. Therefore, care must be taken for the design of the wafer. Crystal impedance of an AT-Cut resonator is fairly sensitive to the length along the X axis which is the displacement direction of the thickness shear mode, while it is not so sensitive to the length along the Z' axis. However, if the length along the Z' axis is shortened unnecessarily, the frequency temperature curve shifts from the original cubic to the parabolic. And, this must be avoided.

The length along the Z' axis should be selected so that the coupling between the thickness shear vibration of the desired frequency and the face shear mode of the wafer must not be originated. Frequency of the face shear mode is given by the following formula.

$$f = \frac{n}{8c} \left( \frac{C_{55} - C_{56}^2/C_{66}}{\rho} \right)^{1/2}$$

where  $n$  is the degree of overtone,  $2c$  is the length along the Z' axis,  $C_{55}$  and  $C_{66}$  are stiffness constants,  $\rho$  is the density. This face shear is the strongest vibration of the undesired modes, so that care must be taken. Fig. 2 shows the comparison of crystal impedance at room temperature with two different wafer design. The design A is considered to avoid the coupling of each mode, while the design B is intentionally selected for the ratio of  $c$  to  $h$  to make the coupling.

The length along the X axis should also be selected not to couple with other undesired modes than the discussed above. Fig. 3 shows the frequency spectrum for the resonators changing the length along the X axis and keeping the length along the Z' axis constant. When the length along the X axis is shortened in order to miniaturize the wafer, edges of wafer must be beveled or curved so that the vibration energy should be concentrated around the center of wafer. In this case, theoretical result may not be fit to the practical result. Therefore, it was required to investigate the practical frequency spectrum chart as shown in Fig. 3.

The degree of beveling and curving also gives the influence to crystal impedance of the resonator. Fig. 4 shows the relation between crystal impedance and operation time of curving by pipe method. As shown in the this figure, there is optimum operation condition. In the range of higher frequency like 17.7 MHz, a good result is achieved without curving process because the length along the X axis against thickness can maintain enough.

#### Mounting

The rectangular AT-Cut resonator has the length along the X axis. Although the direction of the X axis is very sensitive to stress, it is necessary to support the short edges along the X axis. There are two ways of mounting method considered such as one end mounting and both end mounting. Fig. 5 shows an example of one end mounting. In this case, another end is free. So, the vibration of the resonator never receive any influence created by mechanical shock and by thermal shock. Fig. 6 shows a comparison of resistance against mechanical shock in each case of mounting methods. As shown in this figure, the frequency drift of 4.19 MHz resonator with one end mounting is less than both end mounting after tested under the condition of three natural drops from 75 cm height.

As discussed above, the one end mounting method can offer to keep low crystal impedance. Fig. 7 shows the wafer size and its typical equivalent constants of 4.19 MHz for both end mounting and one end mounting. In spite of decreasing the wafer length by 30%, the Q value of one end mounting type achieved twice that of both end mounting.

#### Electrode

The electrode is an essential part for vibrating the piezoelectric resonator. Especially, the shape and the material of electrode are important factors. This resonator is mounted on a base by soldering. So it is necessary to solve the problem such as the migration of the material to solder and spreading of solder to the electrode. The dispersion of equivalent resistance is affected significantly of the soldering area. So, the electrode shape is determined as shown in Fig. 8 to keep the soldering area as narrow as possible.

The construction of the electrode is decided as a multi-layer structure of Cr and Ag in order to prevent electrode migration. This selection brought the excellent aging characteristics.

In the range of high frequency like 17.7 MHz, it is more effective to choose plating back than beveling in order to lower crystal impedance. This way also leads to the effective energy trap. Fig. 9 shows the change of crystal impedance of 17.7 MHz crystal resonator as a function of the plating back.

#### Production Process

The manufacturing process of this resonator is very simple. Especially, the fabrication technique after etching process is the same as mass production technique of the tuning fork resonator for wrist watch. From this point of view, the resonator has the high possibility of mass production.

As shown in Fig. 10, production process are as follows. At the first cutting process, crystal wafers are cut to certain angles and length. Then, wafers are ground to specified thickness and they are lapped to specified frequency using the abrasive powder. At the second cutting process, these crystal wafers are broken into strips. Then, the strips are processed to convex shape by pipe method. But in the range of higher frequency than 10 MHz, any curving is not required. The strips are etched chemically to remove mechanical damages received by beveling so that the surface becomes smooth. After that, the strips are cleaned with water and chemicals. The electrode of Cr and Ag is attached to the strips by the vacuum evaporation. Next step is the supporting of the strip on a base by soldering. A small quantity of silver is additionally evaporated on the electrode so that the frequency is adjusted within a desired range. Finally, the can containing the resonator is evacuated and sealed, so that the sealed resonator will vibrate stably over a long time. Fig. 11 shows the final "MS-309".

#### Characteristics

The wafer size of this miniature resonator, called "MS-309", is reduced very much. So, the electrical equivalent constants of this resonator are slightly different from conventional AT-Cut's. Table 1 shows typical equivalent constants of conventional resonator and "MS-309" at 4.19 MHz. Table 2 shows their typical equivalent constants at 17.7 MHz. These differences have no influence on practical use for oscillators. Besides, "MS-309" has very high Q value. Then, the oscillator applied "MS-309" can maintain the stable frequency. This resonator has a good cubic curve of frequency vs temperature characteristics which is the inherent characteristics of an AT-Cut resonator. Therefore, it is stable against temperature variation. Fig. 12 shows a typical frequency temperature curve of 4.19 MHz "MS-309". Although inflection point of T-C curve is slightly risen from the original AT-Cut, T-C curve is broad around the room temperature. So, this resonator is useful for the high accurate and miniature clock oscillator.

"MS-309" is very stable for changing of environmental conditions due to one end mounting, especially it shows the high resistance against thermal shock and the good aging rate. Fig. 13 shows the result of thermal shock test on 4.19 MHz resonator. During the test, resonators are exposed 10 cycles of thermal changes at -40°C and at +85°C. The frequency and crystal impedance drift little. Fig. 14 shows the result of accelerated aging at +85°C for 4.19 MHz resonator. This condition is equivalent to a period of more than 10 years at room temperature.

#### Conclusions

The miniature AT-Cut strip resonator enclosed in a cylindrical package as  $\phi 3 \text{ mm} \times 18.8 \text{ mm}$  has developed. The shape of wafer is the strip type with tilted edges which is given superior temperature characteristics of the original AT-Cut cubic curve offered by the conventional HC-49/U. "MS-309" has excellent electric characteristics and environmental performances so that there are a lot of potential applications which authors are expected.

# References

- (1) M. Onoe and M. Okazaki  
"Miniature AT-Cut Strip Resonator with Tilted Edges".  
Proc. 29th F.C.S. pp42-48 1975
- (2) M. Onoe and M. Okazaki et al.  
"4 MHz AT-Cut Strip Resonator for Wrist Watch".  
Proc. 31st F.C.S. pp48-54 1977
- (3) R. D. Mindlin  
"Thickness-Twist Vibration of a Quartz Strip".  
Proc. 24th F.C.S. ppl7-20 1970

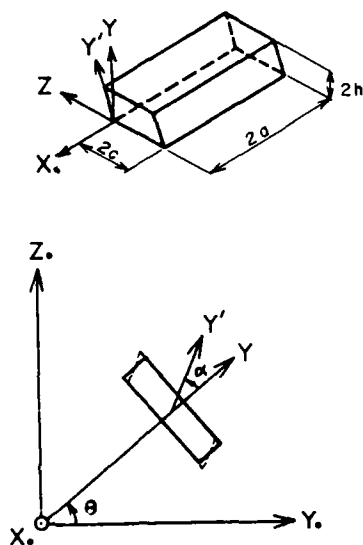


Fig. 1. A strip resonator with tilted edges under the coordinate system.

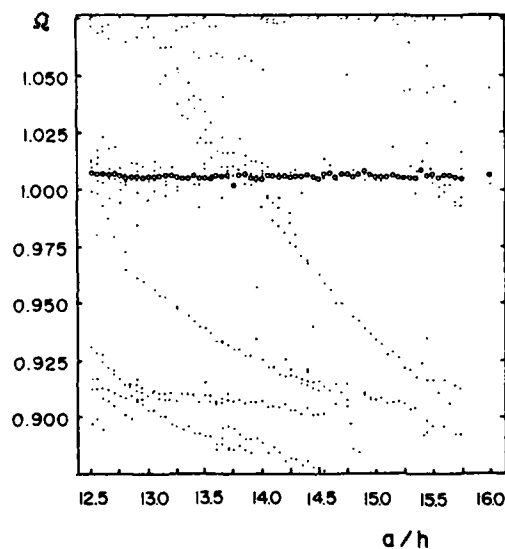


Fig. 3. The frequency spectrum for the resonators.  
( $c/h = \text{const.}$ )

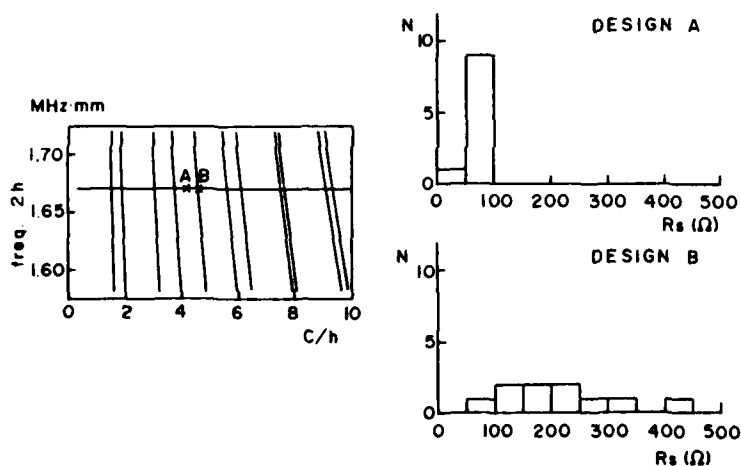


Fig. 2. The comparison of crystal impedance at room temperature with two different length along the  $Z'$  axis.

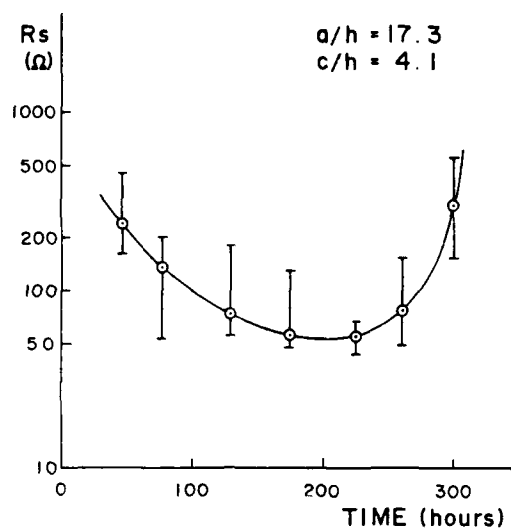


Fig. 4. The relation between crystal impedance and operation time of curving by pipe method.

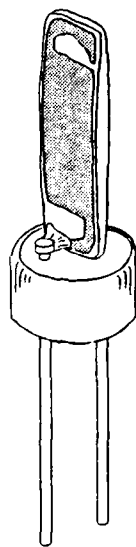


Fig. 5. One end mounting structure.

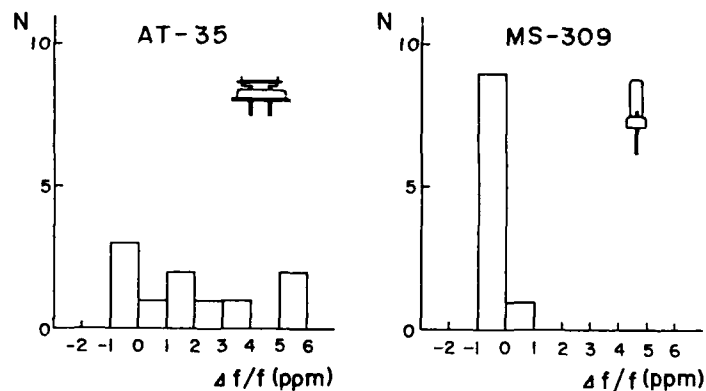


Fig. 6. The comparison of resistance against mechanical shock between both end mounting (AT-35) and one end mounting (MS-309).

	AT-35	MS-309
freq. (MHz)	4 . 1 9 4 3 0 4	
2 a (mm)	9 . 9	6 . 9
2 c (mm)	1 . 5	1 . 6
$R_s$ ( $\Omega$ )	3 0	2 9
Q	$20 \times 10^4$	$40 \times 10^4$

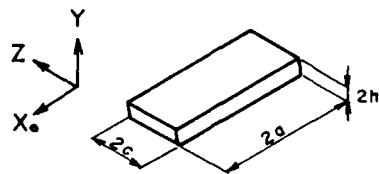


Fig. 7. The wafer size and its typical equivalent constants for both end mounting (AT-35) and one end mounting (MS-309).

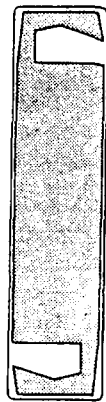


Fig. 8. The electrode shape to prevent the spreading of soldering area.

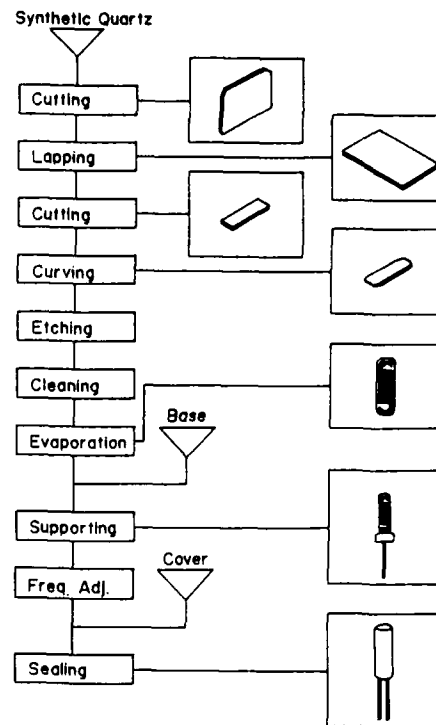


Fig. 10. Production process

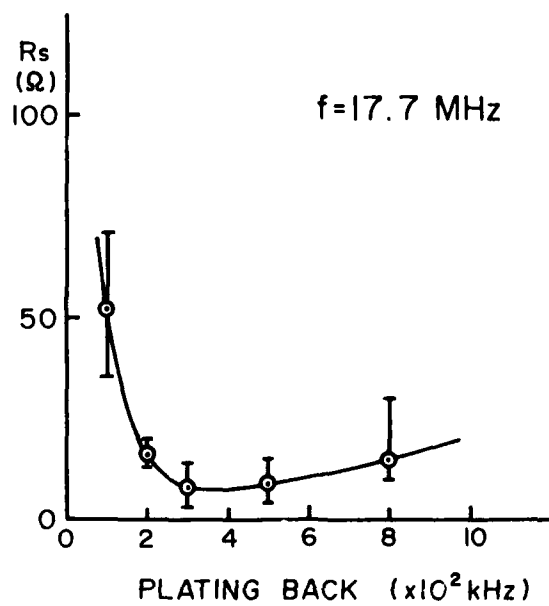


Fig. 9. Change of crystal impedance as a function of plating back.

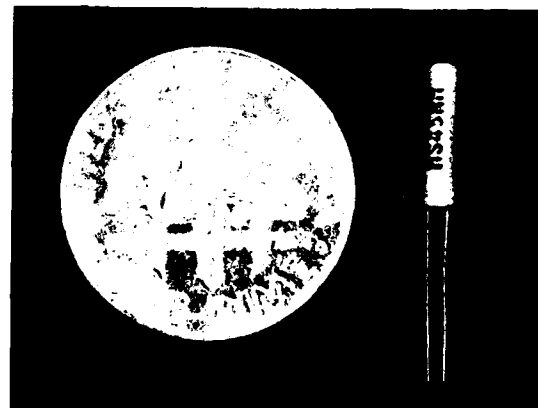


Fig. 11. A new resonator of "MS-309"



	HC-49/U	MS-309
freq. (MHz)	4.194304	
$R_s$ ( $\Omega$ )	25	29
$C_o$ (pF)	2.7	1.6
$C_i$ (fF)	7.0	3.4
$C_o/C_i$	390	460
$L_i$ (mH)	140	420
Q	$15 \times 10^4$	$40 \times 10^4$

Table 1. Typical equivalent constants of the conventional resonator and "MS-309" at 4.19 MHz.

	HC-43/U	MS-309
freq. (MHz)	17.73447	
$R_s$ ( $\Omega$ )	8	10
$C_o$ (pF)	5.7	2.9
$C_i$ (fF)	24	13
$C_o/C_i$	240	230
$L_i$ (mH)	3.4	6.4
Q	$4.7 \times 10^4$	$6.8 \times 10^4$

Table 2. Typical equivalent constants of the conventional resonator and "MS-309" at 17.7 MHz.

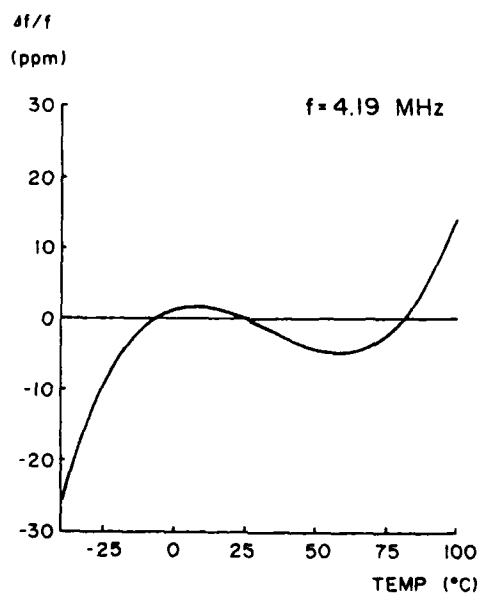


Fig. 12. Typical frequency temperature characteristics of "MS-309".

ELECTRODE STRESS EFFECTS FOR LENGTH-EXTENSIONAL  
AND FLEXURAL RESONANT VIBRATIONS OF QUARTZ BARS

Errol P. EerNisse  
Quartex, Inc.  
Salt Lake City, UT

SUMMARY

The frequency shifts caused in length-extensional and flexural modes of long, thin bars of quartz are calculated approximately. A stress coefficient  $K$  is defined for the modes and calculated for all possible crystallographic orientations of the bar. A stress-compensated cut with temperature compensation is found for the length-extensional mode. No stress compensated orientation was found in the calculations for the flexure mode for any of the commonly used electrode patterns.

INTRODUCTION

Electrode stress was identified in earlier work as a potential source of frequency drift in thickness-shear mode quartz resonators.<sup>1</sup> Calculations of the frequency shifts in resonant frequency due to stresses from electrode metallization through nonlinear elastic effects showed that there was an orientation whereby the nonlinear elastic effects on resonant frequency are zero, thus

leading to the SC-cut.<sup>2-3</sup> Recent demands for small size and large numbers of resonator devices have led to photolithographic manufacturing processes. These devices tend to be very small and since they are made using chrome/gold electrode metallization with high internal stresses, the initial stress levels in the quartz can be large. Thus it is logical to assume that if the nonlinear elastic effects in these devices are typical, the stored frequency shifts in the devices are large, leading one to conclude that long-term drift problems can arise.

Two types of devices that have been used for photolithographic manufacturing are the

length-extensional bar<sup>4</sup> and the flexure mode

tuning fork.<sup>5-7</sup> The resonant frequency of both of these devices is controlled by the elastic compliance along the length direction, so analysis for both is similar. This work reports on the theoretical development of a theory to handle nonlinear elastic effects in such devices and presents calculated results that demonstrate the size of the effects in existing device designs as well as the options, when available, to reduce the effects by proper choice of crystallographic orientation.

GENERAL THEORY

The previous analytical model for electrode stress effects was based on the work of Thurston and Brugger.<sup>1,8</sup> This theoretical development was sufficient for resonators where the initial stress is homogeneous and

the resonant mode can be adequately described by a one-dimensional model. However, for cases where the initial stress is not uniform and/or where the resonator is of a shape where a one-dimensional model for the resonant mode is inadequate, Tiersten has developed a perturbation technique of general application. The reader is referred to several good references on the fundamentals of the

theory.<sup>9-10</sup>

The perturbation technique is derived using rigorous expressions for the interaction between an initial stress (biasing stress) and small amplitude acoustic waves at a point and integrating an energy-related stationary function over the volume of the resonator to obtain the frequency perturbation. In this way, one can obtain a useful approximation to the frequency change due to a biasing stress even if one has only a reasonable approximation to the resonant mode shape being perturbed. The present work uses only a selected portion of the overall theory. The frequency shift  $\Delta f/f_0$  is given by

$$\Delta f/f_0 = (f - f_0)/f_0 \quad (1)$$

where  $f$  is the perturbed frequency, and  $f_0$  is the unperturbed resonant frequency. We restrict ourselves here to perturbations of the resonant modes of a traction-free body caused by an initial stress in the bulk and wherein only the elastic effects play a predominant role (neglect piezoelectric stiffening and electric boundary conditions). The resulting expression can be put into a form which has some similarity to that of Thurston and Brugger:

$$\begin{aligned} \Delta f/f_0 = & \int_V \{ (T_{LM} \delta_{IJ} + C_{LIMJAB} s_{ABKN} T_{KN}) \tilde{g}_{J,M} \tilde{g}_{I,L} \\ & + 2 \rho_0 4 \pi^2 f_0^2 s_{JIKN} T_{KN} \tilde{g}_J \tilde{g}_I \} dV / (4 \pi f_0) \end{aligned} \quad (2)$$

Here,  $T_{LM}$  is the initial stress,  $\delta_{IJ}$  is the delta operator,  $C_{LIMJAB}$  is the third-order elastic constant,  $s_{ABKN}$  is the elastic compliance,  $\rho_0$  is the unstressed mass density, and  $\tilde{g}_J$  is the normalized displacement for the unperturbed resonant frequency  $f_0$ . Summation of repeated indices and differentiation

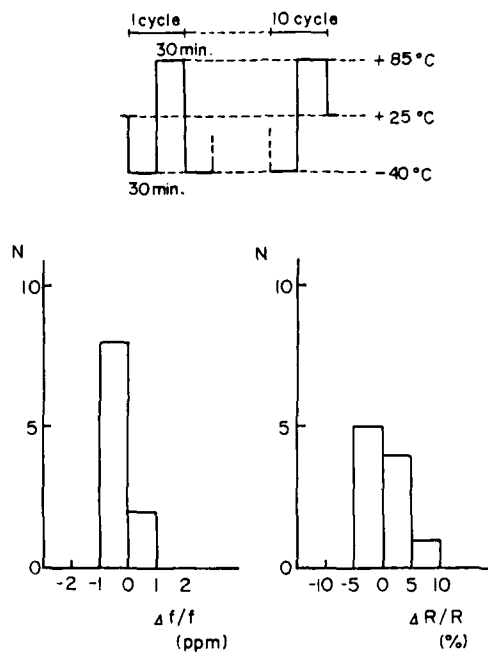


Fig. 13. The result of thermal shock test.

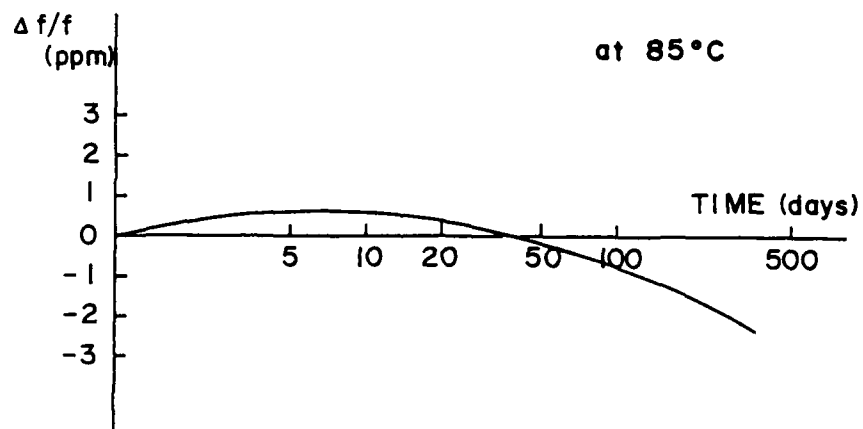


Fig. 14. The result of accelerated aging for 4.19 MHz resonator.

denoted by commas are assumed. In deriving Eq. 2, we have invoked the traction-free boundary conditions, the divergence theorem, uniform biasing stresses, and the relation

$$4 \pi^2 f_0^2 = \int_V c_{LKMR} \tilde{g}_{L,K} \tilde{g}_{M,R} dV \quad (3)$$

where  $c_{LKMR}$  is the elastic stiffness (the inverse of  $s_{LKMR}$ ). Also, it is assumed in deriving Eq. 2 that the initial (biasing) stresses are small enough to ignore terms of order higher than one and rotations in the initial (biasing) displacement gradients.

Normalization of  $\tilde{g}_J$  is by  $N$ , where

$$N^2 = \int_V \rho_0 \tilde{u}_J \tilde{u}_J dV \quad (4)$$

and

$$\tilde{g}_J = \tilde{u}_J / N \quad (5)$$

with  $\tilde{u}_J$  the displacement for the unperturbed resonant mode.

#### LENGTH-EXTENSIONAL MODE THEORY

Consider a bar resonator of IEEE standard orientation notation<sup>11</sup> (Zxtwt)  $\phi, \theta, \psi$  with length  $l$ , width  $w$ , and thickness  $t$  as in Fig. 1. When vibrating in a length-extensional mode, all the stresses  $\tilde{T}_{IJ}$  (in the plate axes system) associated with the resonant mode are zero except for  $\tilde{T}_{11}$ , which is given to good approximation for long bars (using engineering matrix notation)

$$\tilde{T}_1 = {}_0\tilde{T}_1 \sin(\pi x_1/l). \quad (6)$$

The displacements  $\tilde{u}_I$  are given by

$$\tilde{u}_I = \int s_{I1} \tilde{T}_1 dx_1 \quad I=1,2,3. \quad (7)$$

Thus, by integration over  $x_1$ ,

$$\tilde{u}_1 = -1 s_{11} {}_0\tilde{T}_1 \cos(\pi x_1/l) / \pi. \quad (8)$$

We find from Eq. 3 and Eqs. 7 and 8 that

$$4 \pi^2 f_0^2 = \pi^2 / (l^2 \rho_0 s_{11}) \quad (9)$$

and  $N^2$  is

$$N^2 = s_{11}^2 l^2 {}_0\tilde{T}_1^2 \rho_0 t w l / (2 \pi^2) \quad (10)$$

if terms like  $(w/l)^2$  and  $(t/l)^2$  are neglected.

Equations 7, 8, and 10 can be used to form the  $\tilde{g}_K$ . Substitution of  $\tilde{g}_K$  into Eq. 2 and integration over  $V$  leads to an expression that can be evaluated with known values of the constants for quartz to obtain actual numerical answers for  $\Delta f/f_0$ . The reader is

spared the details, which are involved because one must decide which axes system to use in performing the contraction of the tensor expressions in Eq. 2 to the scalar form of the answer. In the application of Eq. 2, terms of

$(t/l)^2$  and  $(w/l)^2$  turn up after carrying out the integrations. These are ignored here for long bars. It has been found that in this one-dimensional case, use of the crystal axes system was most practical.

#### THEORETICAL RESULTS: LENGTH-EXTENSIONAL MODE

The electrode pattern used for the length-extensional mode is shown in Fig. 1. The initial (biasing) stress is  $T_{11}=T_{33}=T$ ,

where  $T$  is given by  $-t_f T_f/w$  with  $T_f$  the electrode stress and  $t_f$  the total electrode thickness on the two opposing surfaces. The scalar  $T$  was set equal to one for the calculations. All other  $T_{IJ}$  are zero. The frequency shift can be represented by the relation

$$\Delta f / f_0 = K T \quad (11)$$

where the stress coefficient  $K$  is the numerical answer from solving Eq. 2 with  $T=1$ . Here,  $K$  has the flavor of the  $K$  stress coefficient used in the past works on

thickness-shear mode resonators.<sup>2,3</sup>

Calculations for  $K$  have been carried out for all values of  $\phi, \theta, \psi$  using the published

third-order coefficients.<sup>12</sup> As a check, our calculations for the Eq. 2 term containing  $C_{LMKJAB}$  were compared to Tiersten and

Ballato,<sup>13</sup> who calculated nonlinear modulation effects in length-extensional resonators. Our results for that term compare directly with their results except that we interpret their Figs. 2-4 as actually being their  $\beta_1$

parameter, not their  $\beta$  parameter as stated in their text.

There is not enough space here to show all the results. Figures 2-6 show results for  $K$  plotted in the  $\phi, \theta$  plane with  $\psi$  held

constant. From a practical standpoint,

$\psi=0^\circ$  and  $\psi=90^\circ$  can be reasonably accomplished in the photolithographic process. Also, no particular advantage was found at other values

of  $\psi$  over what was found for  $\psi=0^\circ$ . For these reasons, only results for  $\psi=0^\circ$  and  $\psi=90^\circ$  are discussed in any detail here, i.e., Figs. 2 and 6. It is apparent in Figs. 2 and 6 that there are loci for  $K=0$  in both cases.

The orientation commonly used for temperature compensation is  $30^\circ, 2^\circ, 0^\circ$ . As seen in Fig. 2,  $K=-0.127 \times 10^{-11} \text{ cm}^2/\text{dyn}$  at this orientation. A typical stress level in the Cr/Au films used in photolithography is  $2 \times 10^9 \text{ dyn/cm}^2$  tension in the film (compression in the quartz). If the device has a width  $w$  of 0.0085 cm and film

thicknesses totalling 2000 Å, the frequency shift stored in the device after fabrication

is  $-0.127 \times 10^{-11} \times (-2 \times 10^9) \times 2000 \times 10^{-8} / 0.0085$ , or +6.0 ppm. As the stress relieves, the 6 ppm will diminish, causing a downward drift in frequency.

There are loci for  $K=0$  in both Figs. 2 and 6. The piezoelectric coupling is not appreciable in Fig. 6 near the  $K=0$  loci. There is appreciable coupling for  $\phi > 0$  in Fig. 2 along the  $K=0$  loci represented by the dashed-line. Figure 7 shows the calculated piezoelectric coupling and temperature coefficient (slope of the frequency vs. temperature curve) along the dashed-line  $K=0$  loci of Fig. 2. There is reasonable temperature compensation all along the loci

for  $\phi > 10^\circ$ , with two orientations where the calculated temperature slope  $\approx 0$ , at

$(12^\circ, 2^\circ)$  and  $(27^\circ, 10^\circ)$ . The exact values for these two orientations will be slightly different because of small inaccuracies in the values of the constants used in the calculations for both the stress-caused and temperature-caused frequency shifts and because of the approximate nature of the solution in Eq. 6 used for the displacement.

The contours of zero temperature slope lie nearly along constant  $K$  lines in Fig. 2, i.e., along constant  $\phi$ , which makes it difficult to adjust the temperature behavior and stress behavior independently. In the case of the SC-cut, the temperature slope zero loci and the stress zero loci are orthogonal in the  $\phi, \theta$  plane, thus allowing independent adjustment of the resonator response to temperature and stress effects.

#### FLEXURE MODE THEORY

If the bar in Fig. 1 vibrates in lateral deflection in the  $y$  direction, i.e., flexure in the  $xy$  plane, the analysis is similar to that of an extensional bar in that the same extension compliance  $s_{11}$  comes into the

calculation. The deflections are different, however, and are difficult to write down analytically in rigorous form wherein all the traction-free boundary conditions on all surfaces are satisfied. Beam theory is normally used, which satisfies relations between moments and bending curvatures along the length of the bar. We use the results of beam theory here, admitting in the beginning that point-wise satisfaction of the continuity equation, boundary conditions, and the divergence theorem used in deriving Eq. 2 is not rigorous. However, the integrals over the volume of the bar lead to the proper frequency relation and to physically sensible results for the predominant term in Eq. 2, the one containing  $C_{LIMJAB}$ .

Let  $G(kx/l)$  be the commonly used<sup>14</sup> normalized beam function which describes the lateral deflection in the  $y$  direction, with  $k$  being a constant determined by the end conditions of the bar. This deflection is the predominant one, so if one ignores contributions to Eq. 4 from  $u_2$  and  $u_3$ , we find that

$$N^2 = \rho_0 t w \int_0^1 G(kx/l)^2 dx \quad (12)$$

where we know that

$$\int_0^1 G(kx/l)^2 dx = 1. \quad (13)$$

The predominant strain is along the  $x$  direction with odd symmetry about the neutral plane of bending at  $y=0$ . It is given by

$$\bar{g}_{1,1} = y (\partial^2 G / \partial x^2) / N^2 \quad (14)$$

with the other strains associated with the bending given approximately by

$$\bar{g}_{I,J} = s_{IJ11} \bar{g}_{1,1} / s_{1111}. \quad (15)$$

Note here that if one integrates Eq. 15 over  $x_2(y)$  to obtain  $\bar{u}_2$  that there is a constant of integration of  $G(kx/l)$  equal to the deflection at  $y=0$ .

Substitution of Eq. 15 into Eq. 3 leads to

$$4 \pi^2 f_0^2 = \int_V s_{IJ11} c_{IJKL} s_{KL11} \bar{g}_{1,1}^2 dv / s_{11}^2. \quad (16)$$

Since  $s_{IJKL}$  is the inverse of  $c_{IJKL}$ , Eq. 16 reduces to

$$4 \pi^2 f_0^2 = t w^3 \int_0^1 (\partial^2 G / \partial x^2)^2 dx / (12 s_{11} N^2). \quad (17)$$

or, from the properties of  $G(kx/l)$ ,<sup>14</sup>

$$4 \pi^2 f_0^2 = k^4 w^2 / (12 \rho_0 s_{11} l^4) \quad (18)$$

which is the usual result for the resonant frequency of a long, thin bar vibrating laterally in the xy plane.

The  $\tilde{g}_{I,J}$  used in Eq. 2 are found in Eq. 15. The predominant  $\tilde{g}_I$  used in the third term of Eq. 2 was taken as  $G(kx/l)/N$  since we ignore here terms containing  $(w/l)^2$  and  $(t/l)^2$ .

#### THEORETICAL RESULTS FOR THE FLEXURE MODE

The expressions to be evaluated in Eq. 2 for the flexure mode turn out, as one might expect, to be almost identical to the results for the length extensional mode. The first and second terms in the integral of Eq. 2 are identical to their counterparts for the length-extensional mode, the third term being slightly different because the predominant deflection is different. The electrode patterns differ as seen in Fig. 1, so the biasing stresses are different. The most common electrode patterns are as seen in Fig. 1, or minor variations such as the side electrodes passing over the edge to cover a small portion of the top and bottom surfaces near the edge. In either case, the biasing stress can be approximated as follows if  $w_e$  is

the net width of the electrode material on the top or bottom surface and  $t_f$  is the total

electrode thickness from opposing sides and  $T_f$  is electrode stress:

$$T_1 = -t_f T_f (w_e/t + 1/w) \quad (19)$$

$$T_2 = -w_e t_f T_f / t w \quad (20)$$

$$T_3 = -t_f T_f / w \quad (21)$$

or, if  $T = -t_f T_f / t$

$$T_1 = T (w_e/w + t/w) \quad (22)$$

$$T_2 = T w_e/w \quad (23)$$

$$T_3 = T t/w. \quad (24)$$

It is impractical to carry out calculations for all  $t/w$  and  $w_e/w$ , so representative values were used of 0.5 for

both ratios. Again, Eq. 11 is used to present the results. Figure 8 shows the results for  $\psi=0$ . Note that  $K$  has about the same general behavior with  $\theta$  as the length-extensional mode except for the vertical offset caused by the third term in the integral of Eq. 2 being different for the flexure mode because the predominant deflection is in the y direction instead of the x direction. Based on the theory presented here, the  $K$  for the flexure mode does not become zero anywhere in Fig. 5. In fact, a survey of all orientations shows that  $K \neq 0$  anywhere.

Alternate electrode patterns have been used. For instance, the first watch crystals used only electrodes on the top and bottom surfaces with the orientation tilted out of the xy crystal plane to obtain piezoelectric

excitation.<sup>5,6</sup> Another electrode pattern used early on in the watch industry left out the side electrode of Fig. 1 and used only thin strips along the edges of the top and bottom

surfaces.<sup>7</sup> In either case, Eqs. 22-24 can be used for the biasing stress by letting  $t/w$  approach 0. Figure 9 shows some results for this case. Again,  $K \neq 0$ . Also, a survey of all orientations showed that  $K \neq 0$  anywhere.

#### REFERENCES

1. E. P. EerNisse, Proc. 29th Ann. Sym. on Freq. Control, 1 (1975).
2. E. P. EerNisse, Proc. 30th Ann. Sym. on Freq. Control, 8 (1976).
3. A. Ballato, E. P. EerNisse, and T. J. Lukaszek, Proc. 1978 Ultrasonics Symposium, IEEE Cat. #78CH 1344-ISU.
4. R. J. Dinger, Proc. 35th Ann. Sym. on Freq. Control, 144 (1981).
5. J. H. Staudte, Proc. 27th Ann. Sym. on Freq. Control, 50 (1973).
6. J. A. Kusters, C. A. Adams, H. E. Karrer and R. W. Ward, Proc. 30th Ann. Sym. on Freq. Control, 175 (1976).
7. K. Oguchi, E. Momosaki, Proc. 32nd Ann. Sym. on Freq. Control, 277 (1978).
8. R. N. Thurston and K. Brugger, Phys. Rev. 133, A1604 (1964).
9. H. F. Tiersten, J. Acoust. Soc. Am. 64, 832 (1978).
10. H. F. Tiersten, J. Acoust. Soc. Am. 70, 1567 (1981).
11. IEEE Standard on Piezoelectricity, IEEE Std. 176-1978.
12. R. N. Thurston, H. J. McSkimin, and P. Andreatch, Jr., J. Appl. Phys. 37, 267 (1965).
13. H. F. Tiersten and A. Ballato, J. Acoust. Soc. Am. 73, 2022 (1983).
14. D. Young, J. Appl. Mech. 17, Trans. ASME 72, 448 (1950).

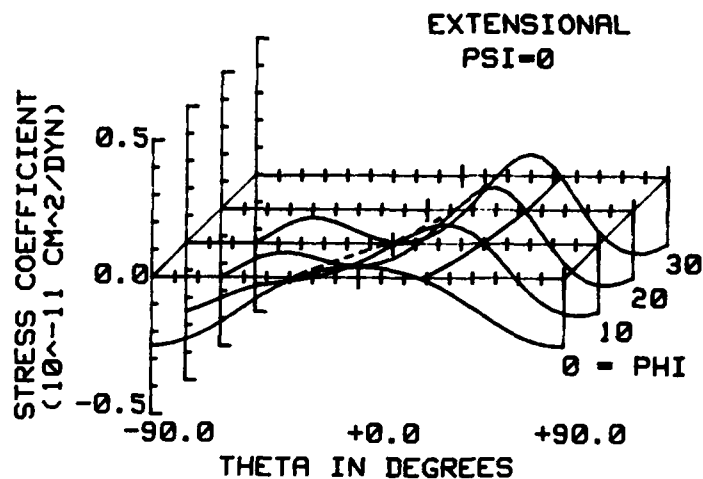
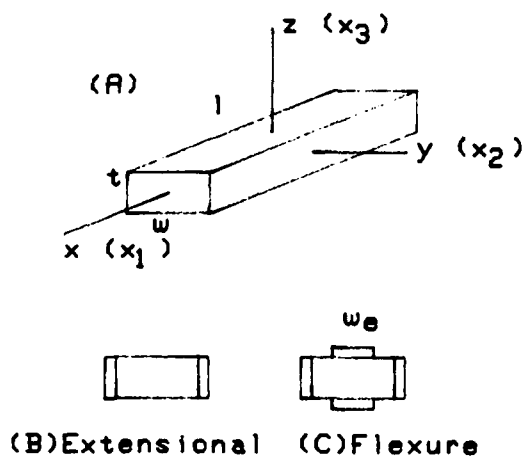


Figure 1. a) Long, thin bar showing the plate axes and dimensions. b) Electrode pattern for the extensional mode. c) Electrode pattern for the flexure mode.

Figure 2. Extensional mode stress coefficient  $K$  vs.  $\phi$  and  $\theta$  for  $\psi = 0^\circ$ .

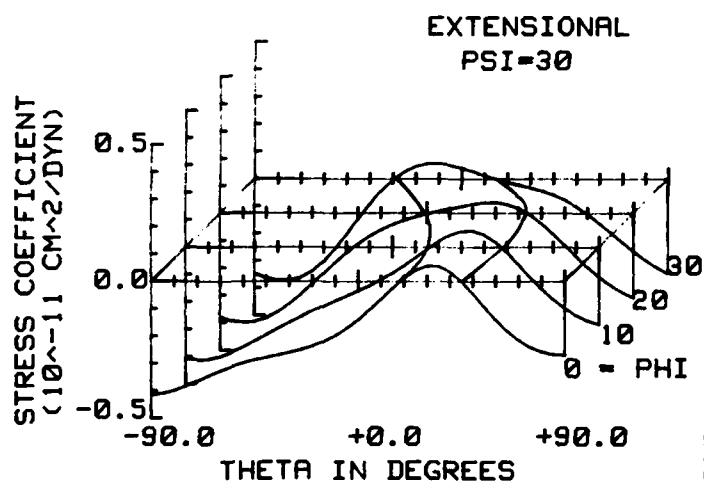


Figure 3. Extensional mode stress coefficient for  $\psi = 30^\circ$ .

Figure 4. Extensional mode stress coefficient for  $\psi = 45^\circ$ .

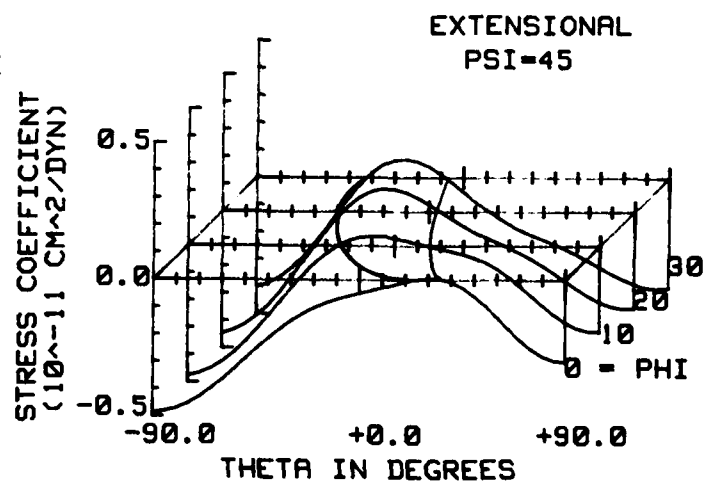
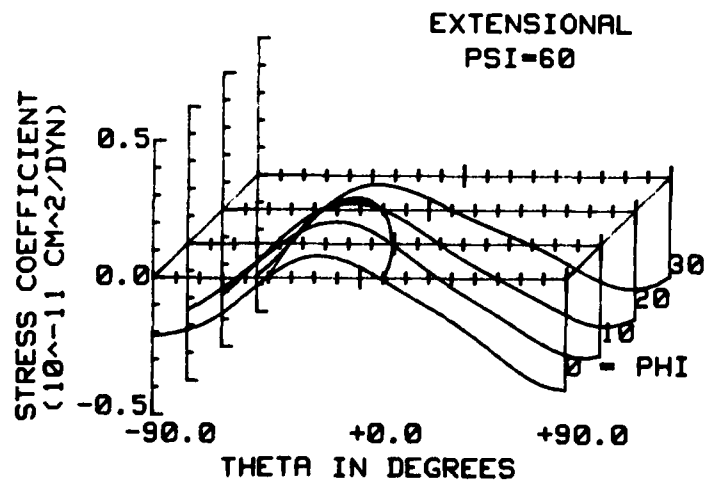


Figure 5. Extensional mode stress coefficient for  $\psi = 60^\circ$ .



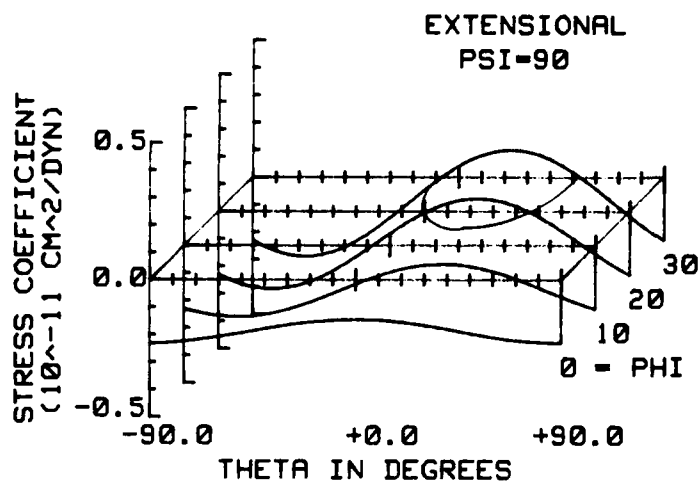


Figure 6. Extensional mode stress coefficient for  $\psi=90^\circ$ .

Figure 7. Piezoelectric coupling in arbitrary units and slope of frequency shift vs. temperature in ppm/C<sup>0</sup> for the dashed-line  $K=0$  loci of Fig. 2.

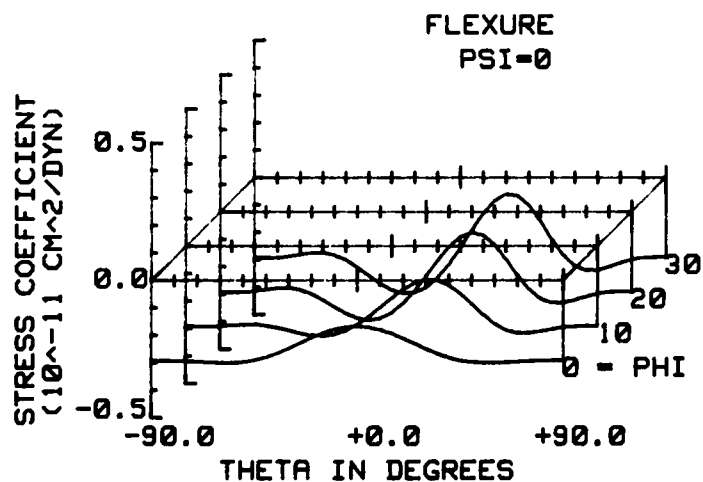
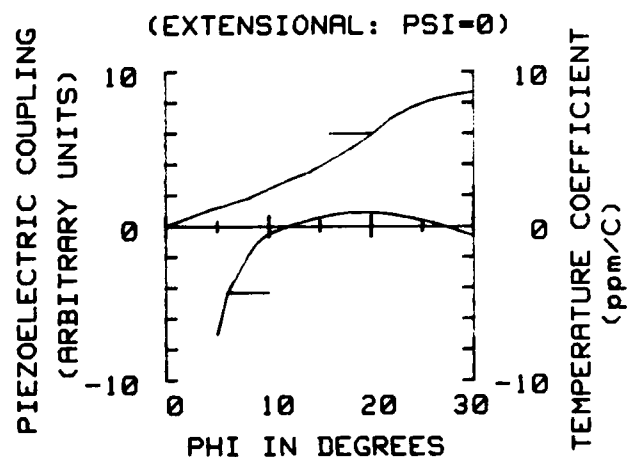


Figure 8. Flexure mode stress coefficient for  $\psi=0^\circ$

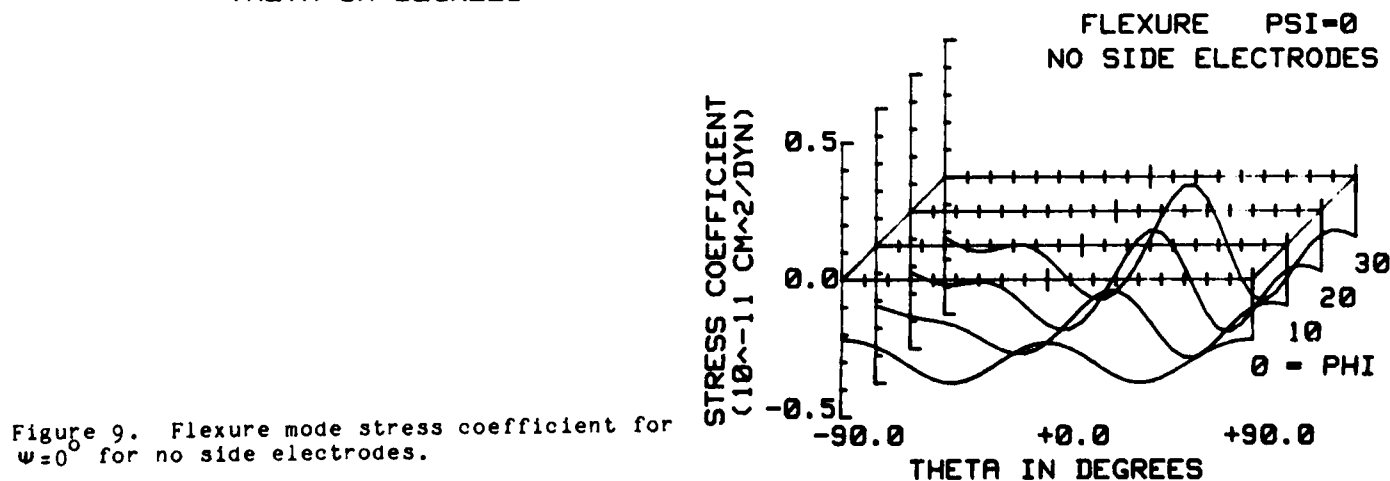


Figure 9. Flexure mode stress coefficient for  $\psi=0^\circ$  for no side electrodes.



AN ANALYSIS OF NONLINEAR RESONANCE IN ELECTRODED CONTOURED  
AT- AND SC-CUT QUARTZ CRYSTAL RESONATORS

H.F. Tiersten  
Department of Mechanical Engineering,  
Aeronautical Engineering & Mechanics  
Rensselaer Polytechnic Institute  
Troy, New York 12180-3590

### Abstract

Since the modes of motion in contoured quartz resonators are essentially thickness-modes varying slowly along the plate, only the thickness dependence of the elastic nonlinearities are retained in the equations. The nonlinearities contain terms up to cubic in the small mechanical displacement field, and all terms present in the general anisotropic case are included. The linear portions of the equations are respectively the same as the equations that have been used heretofore in the analyses of contoured AT- and SC-cut quartz resonators, with a change in the thickness differentiated term that arises from a nonlinearity in the boundary conditions on the major surfaces. The steady-state solutions are obtained by means of an asymptotic iterative procedure and an expansion in the linear eigensolutions while retaining the nonlinear correction to the eigensolution that has a resonant frequency in the vicinity of the driving frequency. The slow variations in the mode along the plate are included in the nonlinear correction by averaging over the plate. Lumped parameter representations of the solutions, which are valid in the vicinity of a resonance and relate the amplitude of the mode nonlinearly to the voltage across the electrodes, are obtained. The expression for the current through the crystal is determined, the external circuitry is incorporated in the description and an equation relating the mode amplitude nonlinearly to the driving voltage and other circuit parameters is obtained. The analysis holds for the fundamental and odd harmonic overtones. Nonlinear resonance curves are calculated for AT-cut quartz using the known nonlinear coefficients. Such calculations cannot be performed for SC-cut quartz because the coefficient of the cubic nonlinearity is not known. An equation relating the change in resonant frequency resulting from the nonlinearity to the current through the crystal, independent of the external circuitry, is derived.

### 1. Introduction

Since an accurate description of the modes of motion in contoured AT- and SC-cut quartz crystal resonators exists<sup>1,2</sup> and an understanding of the nonlinear behavior of these devices is of interest, an analysis of nonlinear resonance in contoured quartz resonators is performed. Inasmuch as the modes in the contoured resonator are essentially thickness-modes with slow transverse variation along the plate, only the thickness dependence of the elastic nonlinearities are retained in the treatment, but with the full anisotropy of doubly-rotated cuts included. First the case of pure thickness-resonance is considered and then the treatment is extended to include the transverse shape of the harmonic modes in the contoured resonator. The analysis of nonlinear thickness-resonance is presented in detail because couplings that were ignored in earlier work<sup>3</sup> are included here.

In fact one of the couplings that was ignored in the earlier work<sup>3</sup> arises not from the inclusion of the full anisotropy of the nonlinear interaction in this work, but from a term that exists even in the isotropic case and was improperly ignored in the earlier analysis<sup>3</sup>. Furthermore, although that work<sup>3</sup> treats a

trapped energy resonator, it was for the case of strip electrodes only and did not consider the transverse behavior of the modes in both directions in the plane of the plate, as is done in this work. The type of nonlinearity that was ignored in Ref.3 was properly included in recent work<sup>4</sup> on the nonlinear vibrations of quartz rods, in which it was shown that this type of nonlinearity causes a change in the resonant frequency through its influence on the wavelength.

The linear portions of the equation in the dominant thickness eigendisplacement of interest, which is used in the description of the transverse behavior of the modes in the contoured resonator, are the same as those that have been used<sup>2,5</sup> in the analyses of contoured SC-cut quartz resonators, but with a change in the thickness-wavenumber caused by the quadratic nonlinearities considered here. Since the analysis is to be applicable to the doubly-rotated SC-cut, in the case of both the pure thickness resonator and that of the contoured resonator the mechanical displacement field is decomposed along the eigenvector triad of the pure thickness solution, exactly as in the existing work<sup>2</sup> on the linear case. Of course, all conditions imposed on that work are applicable here and since the nonlinearity is small also, only the thickness dependence of all electrical variables is included in the treatment, as in all the other work in this area<sup>1-3</sup>. Naturally, the nonlinear portions of the equation in the dominant thickness eigendisplacement are the same as those that occur in the pure thickness case, but with a slow transverse variation, since it has been shown<sup>2</sup> that this equation reduces to the pure thickness equation when the transverse variation is suppressed.

The steady-state solutions to the nonlinear forced vibration problems are obtained by means of an asymptotic iterative procedure and an expansion in the eigensolutions while retaining the nonlinear correction to the eigensolution that has a resonant frequency in the vicinity of the driving frequency. The slow transverse variation in the mode is included in the nonlinear correction by appropriately averaging over the plate. Lumped parameter representations of the solutions, which are valid in the vicinity of a resonance and relate the amplitude of the mode nonlinearly to the voltage across the electrodes, are obtained. The expression for the current is determined, the external circuitry is incorporated in the description and an equation relating the mode amplitude nonlinearly to the driving voltage is obtained. Nonlinear resonance curves are calculated for AT-cut quartz showing the influence of driving voltage, quality factor, load resistance and harmonic overtone on the resonant frequency. Finally, an equation relating the change in resonant frequency resulting from the nonlinearity to the current through the crystal, independent of the external circuitry, is obtained. Both this latter equation and the calculations indicate a significant dependence of the change in resonant frequency resulting from the nonlinearity on the order of the harmonic overtone of the contoured resonator.

## 2. Thickness Equations

A schematic diagram of a plano-convex quartz crystal resonator is shown in Fig.1 along with the associated coordinate system. Since the modes of interest in contoured crystal resonators are essentially thickness-modes varying slowly along the plate and the amplitude of the motion itself is small, it is appropriate to consider only the thickness ( $X_2$ ) dependence of the elastic nonlinearities, by virtue of the small piezoelectric coupling of quartz. Accordingly, we write the pure thickness equations for the general anisotropic case in the form

$$\bar{c}^{(1)} u_{1,22} - \rho \ddot{u}_1 + \rho \omega^2 K X_2 = -\gamma[(u_{1,2})^3]_{,2} - \beta_1 [(u_{1,2})^2]_{,2} - 2\beta_2 [u_{1,2} u_{2,2}]_{,2} - 2\beta_3 [u_{1,2} u_{3,2}]_{,2}, \quad (2.1)$$

$$\bar{c}^{(2)} u_{2,22} - \rho \ddot{u}_2 = -\beta_2 [(u_{1,2})^2]_{,2}, \quad (2.2)$$

$$\bar{c}^{(3)} u_{3,22} - \rho \ddot{u}_3 = -\beta_3 [(u_{1,2})^2]_{,2}, \quad (2.3)$$

where

$$\gamma = \frac{1}{2} c_{222} + c_{3266} + \frac{1}{6} c_{46666}, \quad \beta_1 = \frac{1}{2} (3c_{226} + c_{3666}),$$

$$\beta_2 = \frac{1}{2} (c_{222} + c_{3266}), \quad \beta_3 = \frac{1}{2} (c_{224} + c_{3466}), \quad (2.4)$$

since  $u_1$  is taken to be the "large" thickness-driven eigendisplacement in this work. We note that the mechanical displacement field  $u_i$  is referred to the eigenvector triad of the linear piezoelectric thickness solution, in accordance with Sec.2 of Ref.2, and the  $\bar{c}^{(n)}$  denote the piezoelectrically stiffened eigenvalues. As a result of decomposing  $u$  in the diagonal system, the linear portions of Eqs.(2.1) - (2.3) are uncoupled in this general anisotropic case. The elastic constants on the right-hand side of (2.4) are obtained by transforming the mechanical displacement components  $\tilde{u}_i$  in the original coordinate system to the eigenvector components  $u_i$  in the nonlinear thickness ( $X_2$ )-dependent terms<sup>7</sup>.

Also referred to the eigenvector triad, the corresponding components of the Piola-Kirchhoff double vector take the form

$$K_{21} = \bar{c}^{(1)} u_{1,2} + \left( e_{26} C + c^{(1)} K + e_{26} \frac{V}{2h} \right) e^{i\omega t} + \gamma (u_{1,2})^3 + \beta_1 (u_{1,2})^2 + 2\beta_2 u_{1,2} u_{2,2} + 2\beta_3 u_{1,2} u_{3,2}, \quad (2.5)$$

$$K_{22} = \bar{c}^{(2)} u_{2,2} + \beta_2 (u_{1,2})^2,$$

$$K_{23} = \bar{c}^{(3)} u_{3,2} + \beta_3 (u_{1,2})^2, \quad (2.6)$$

where, since  $u_1$  is the "large" driven eigendisplacement, we have included<sup>2</sup> the linear (in  $X_2$ ) eigenpotential, which causes the term  $e_{26} C$  and the inhomogeneous forcing term  $c^{(1)} K + e_{26} V/2h$  in (2.5) where

$$c^{(1)} = \bar{c}^{(1)} (1 - k_{26}^2), \quad k_{26}^2 = e_{26}^2 / \epsilon_{22} \bar{c}^{(1)}, \quad (2.7)$$

and  $\omega$  is the driving frequency. Note that the first index 2 in  $K_{2j}$  refers to the normal to the plate and the second index  $j$  refers to the respective coordinates of the eigenvector triad. Note further that we have omitted the linear (in  $X_2$ ) eigenpotential from  $K_{22}$  and  $K_{23}$  in (2.6) which would have caused terms  $e_{22j} C$  ( $j=2, 3$ ) in  $K_{22}$  and  $K_{23}$ , respectively, that couple the  $\bar{c}^{(j)}$  eigensolutions for shorted electrodes<sup>8-10</sup>. Since the piezoelectric coupling is small in quartz and the  $\bar{c}^{(j)}$

are sufficiently widely separated in cut of interest, the resulting coupled transcendental frequency equation<sup>8-10</sup> very accurately uncouples and we effectively have three independent transcendental frequency equations<sup>9</sup>, one for each thickness eigendisplacement  $u_i$ . By virtue of the forms taken for  $K_{2j}$  in (2.5) and (2.6), which indicate that the  $u_1$  eigendisplacement is driven linearly by the voltage while the  $u_2$  and  $u_3$  eigendisplacements are not, the aforementioned uncoupling is already built into the description. Since both the thickness of the electrodes  $2h'$  and the amplitude of the dominant eigendisplacement  $u_1$  are small, the boundary conditions take the form

$$K_{21} = \mp 2\rho h' \dot{u}_1, \quad \bar{\varphi} = \frac{V}{2} e^{i\omega t}, \quad \text{at } X_2 = \pm h, \quad (2.8)$$

$$K_{22} = 0, \quad K_{23} = 0, \quad \text{at } X_2 = \pm h. \quad (2.9)$$

The expression for the  $X_2$  component of the electric displacement vector, which determines the current, takes the form<sup>2</sup>

$$D_2 = e_{221} u_{1,2} - \epsilon_{22} \bar{\varphi}_{,2}. \quad (2.10)$$

As already alluded to verbally, the components of  $e_{22j}$ ,  $K_{2j}$  and  $u_i$  occurring in this work are respectively related to the  $\hat{e}_{22r}$ ,  $\hat{K}_{2r}$  and  $\hat{u}_i$ , which are referred to the conventional plate axes by the transformations<sup>2</sup>

$$e_{22j} = Q_{jr} \hat{e}_{22r}, \quad K_{2j} = Q_{jr} \hat{K}_{2r}, \quad u_j = Q_{jr} \hat{u}_r, \quad (2.11)$$

in which  $Q_{jr}$  denotes the orthogonal matrix obtained from the thickness eigenvalue problem<sup>2</sup>.

## 3. Nonlinear Thickness Vibrations

As noted in the Introduction, although this problem was treated in Ref.3, coupling caused by an existing quadratic nonlinearity was improperly ignored. Furthermore, the treatment in Ref.3 was for the AT-cut only and not for the general anisotropic case considered here, in which the equations are referred to the eigenvector triad of the linear thickness solution. In addition, solution of the nonlinear pure thickness vibration problem serves as a convenient, if not essential, model for the solution of the nonlinear resonance problem for the contoured resonator, since the mode in the contoured resonator is very nearly a thickness mode. Consequently, the relevant part of the solution of the nonlinear pure thickness vibration problem, namely the nonlinear eigensolution, is presented here.

Since the linear solution forms the essential starting point for the nonlinear resonance solution, it is briefly reproduced<sup>11</sup> here with the slightly changed notation. In order to satisfy the inhomogeneous boundary condition (2.8)<sub>2</sub>, we have taken  $\bar{u}_1$  and  $\bar{\varphi}$  in the form

$$\bar{u}_1 = u_1 + K X_2, \quad \bar{\varphi} = \frac{V X_2}{2h} + \varphi, \quad (3.1)$$

in which  $e^{i\omega t}$  has been suppressed, and we note that  $K$  and  $V/2h$  already appear in the equations in Sec.2 since they are on the  $u_1$  and  $\varphi$  variables. Since  $2h'$  is small, from (2.5) and (2.8)<sub>1</sub>, we have

$$K = - \frac{e_{26}}{2h c^{(1)}}, \quad (3.2)$$

and we note that the linear portion of (2.1) takes the form

$$\bar{c}^{(1)} u_{1,22} + \rho \omega^2 u_1 = - \rho \omega^2 K X_2, \quad (3.3)$$

and

$$\varphi = \frac{e_{26}}{\epsilon_{22}} u_1 + C X_2, \quad \varphi = 0 \text{ at } X_2 = \pm h, \quad (3.4)$$

and we note that  $C$  already appears in (2.5). The linear eigensolution ( $V=0$ ) takes the form

$$u_{1n} = A_n \sin \eta_n X_2, \quad \varphi_n = \frac{e_{26}}{\epsilon_{22}} u_{1n} + C_n X_2, \quad (3.5)$$

$$\omega_n = \sqrt{\frac{\epsilon(1)}{\rho}} \eta_n, \quad C_n = -\frac{e_{26} A_n}{\epsilon_{22} h} \sin \eta_n h, \quad (3.6)$$

$$\tan \eta_n h = \frac{\eta_n h}{k_{26}^2 + \hat{R} \eta_n^2}, \quad \hat{R} = \frac{2\rho' h'}{\rho h}, \quad (3.7)$$

and since  $k_{26}^2 \ll 1$  and  $\hat{R} \ll 1$ , from (3.7)<sub>1</sub>, we obtain

$$\eta_n h = \frac{n\pi}{2} \left( 1 - \frac{4k_{26}^2}{n^2 \pi^2} - \hat{R} \right). \quad (3.8)$$

In the vicinity of a resonance, say the  $N$ th, one term dominates the series solution of the forced vibration problem, and we are interested in finding the influence of the nonlinearities on the  $N$ th eigensolution at the driving frequency  $\omega$ , which is near  $\omega_N$ . To this end we systematically obtain the solution to the nonlinear pure thickness vibration problem by systematically iterating from the linear solution to successive orders in the dominant but small amplitude  $A_N$ . Since we are ultimately interested in considering a driving voltage and damping, we use complex notation. From (3.5)<sub>1</sub> we see that the zeroth iterate, which is the linear solution, for the  $N$ th eigensolution may be written in the form

$$u_{1N} = \sin \eta_N X_2 \frac{1}{2} [A_N e^{i\omega t} + A_N^* e^{-i\omega t}], \quad (3.9)$$

the substitution of which in (2.2) yields

$$\bar{c}^{(2)} u_{2,22} - \rho_1 \ddot{u}_2 = \frac{\beta_2}{2} \eta_N^3 \sin 2\eta_N X_2 [A_N A_N^* + A_N^2 e^{i2\omega t}], \quad (3.10)$$

where the real part of the complex bracket is understood in the usual way. Since the piezoelectric coupling and amplitude  $A_N$  of the dominant displacement are both small, the influence of the external circuitry on the nonlinear eigensolution can be shown<sup>4,5</sup> to be negligible and can be ignored. In order to satisfy the boundary condition (2.9)<sub>1</sub>, with (2.6)<sub>1</sub>, the solution of (3.10) is taken in the form

$$u_2 = \sum_m B_m \sin \eta_m X_2 e^{i2\omega t} + \sum_m C_m \sin \eta_m X_2, \quad (3.11)$$

where the  $B_m$  and  $C_m$  are obtained from the orthogonality of the  $\sin \eta_m X_2$ . We now suppose that at most only one term in the series need be retained for our purposes<sup>1,2</sup> and write

$$u_2 = C_M \sin \eta_M X_2 + B_M \sin \eta_M X_2 e^{i2\omega t}, \quad (3.12)$$

where from orthogonality, we find

$$B_M = \frac{\beta_2}{2} \frac{A_N^2 \eta_N^3}{h\rho(4\omega^2 - \hat{\omega}_M^2)}, \quad C_M = \frac{\beta_2}{2} \frac{A_N A_N^* \eta_N^3}{h\rho(-\hat{\omega}_M^2)}, \quad (3.13)$$

and

$$\hat{\omega}_M^2 = \bar{c}^{(2)} \eta_M^2 / \rho, \quad p_{NM} = \frac{2h}{\pi} \left[ \frac{\sin(2N-M)\pi/2}{2N-M} - \frac{\sin(2N+M)\pi/2}{2N+M} \right]. \quad (3.14)$$

Clearly, similar first iterate equations and solutions can be found for  $u_3$  and  $u_1$ . Since the procedure for finding their influence is essentially the same as for  $u_2$ , in the interest of brevity we will omit them in the derivation and then simply include them in the final results. Furthermore, for  $u_2$  the only case of interest is  $M=N$  because  $c^{(2)} \approx 4c^{(1)}$ .

Substituting from (3.9) and (3.12) in both the quadratic and cubic terms in (2.1) and (2.8)<sub>1</sub>, with (2.5) in the absence of  $\beta_1$  and  $\beta_3$ , while retaining all terms of order  $A_N^2 A_N^*$  and containing the time dependence  $e^{i\omega t}$  only and employing some trigonometric identities, for  $M=N$  we obtain the inhomogeneous differential equation

$$\bar{c}^{(1)} u_{1,22} - \rho_2 \ddot{u}_1 = -\rho \omega^2 K X_2 e^{i\omega t} + \frac{9}{16} \gamma A_N^2 A_N^* \eta_N^4 (\sin \eta_N X_2 + \sin 3\eta_N X_2) e^{i\omega t} + \beta_2 (A_N^* B_N + A_N C_N) \eta_N^3 \sin 2\eta_N X_2 e^{i\omega t}, \quad (3.15)$$

and homogeneous boundary conditions

$$\bar{c}^{(1)} u_{1,2} + e_{26} C \pm 2\rho' h' \ddot{u}_1 = \left[ -\frac{3}{16} \gamma A_N^2 A_N^* \eta_N^3 (3 \cos \eta_N h + \cos 3\eta_N h) - \beta_2 (A_N^* B_N + A_N C_N) \eta_N^2 \frac{1}{2} (1 + \cos 2\eta_N h) \right] e^{i\omega t} \text{ at } X_2 = \pm h, \quad (3.16)$$

for the second iterate  $u_1$  of the nonlinear thickness problem. It should be noted that the right-hand side of (3.16) is negligible because  $A_N$  is small and  $\eta_N h \approx N\pi/2$ . Since we regard  $A_N$  and  $\eta_N$  on the right-hand side of (3.15) and (3.16) as presently unknown and the  $\sin \eta_N X_2$  term will arise as a solution of the linear differential operator on the left-hand side, the  $\sin \eta_N X_2$  term is regarded as homogeneous and we say the iterate is corrected<sup>1,3</sup>. As the  $N$ th eigensolution of the linear differential equation (3.15), we take

$$u_1 = u_N e^{i\omega t}, \quad u_N = A_N \sin \eta_N X_2 + G_N \sin 2\eta_N X_2 + L_N \sin 3\eta_N X_2, \quad (3.17)$$

the substitution of which in (3.15) yields

$$\rho \hat{\omega}_N^2 = \bar{c}^{(1)} \eta_N^2 (1 + \mu), \quad (3.18)$$

$$G_N = -\frac{16}{27} \frac{\beta_2}{\bar{c}^{(1)} \gamma} \frac{f_N}{\eta_N} r_{c2} \mu A_N, \quad L_N = -\frac{\mu A_N}{8}, \quad (3.19)$$

where

$$\mu = \frac{9}{16} \frac{\gamma}{\bar{c}^{(1)}} \eta_N^2 A_N A_N^*, \quad f_N = \left[ (-1)^{\frac{N-1}{2}} - \frac{(-1)^{\frac{N+1}{2}}}{3} \right], \quad r_{c2} = \frac{2\bar{c}^{(1)}}{\bar{c}^{(2)}} \left( \frac{\bar{c}^{(2)} - 2\bar{c}^{(1)}}{4\bar{c}^{(1)} - \bar{c}^{(2)}} \right). \quad (3.20)$$

Substituting from (3.17), (3.19), (3.20)<sub>1</sub> and (3.6)<sub>2</sub> into (3.16), we obtain

$$\tan \eta_N h = \eta_N h [1 + \mu p_N] / [(k_{26}^2 + \hat{R} \eta_N^2) (1 - \mu q_N) + \mu \hat{R} \eta_N^2], \quad (3.21)$$

where

$$p_N = 1 - \frac{1}{24} \frac{\cos 3\gamma_N h}{\cos \gamma_N h} - \frac{32}{27} \frac{\kappa_2 f_N r_{c2}}{N\pi} \frac{\cos 2\gamma_N h}{\cos \gamma_N h} + \frac{8}{9} \frac{\kappa_2 f_N r_{c2}}{N\pi \cos \gamma_N h} (\cos 2\gamma_N h + 1), \quad q_N = \frac{1}{8} \frac{\sin 3\gamma_N h}{\sin \gamma_N h} + \frac{16}{27} \frac{\kappa_2 f_N r_{c2}}{N\pi} \frac{\sin 2\gamma_N h}{\sin \gamma_N h}, \quad \kappa_2 = \frac{\beta_2^2}{\gamma_N^2(1)}. \quad (3.22)$$

Since  $k_{26}^2 \ll 1$ ,  $\hat{R} \ll 1$  and  $\mu \ll 1$ , the roots  $\gamma_N h$  of (3.21) must differ from  $N\pi/2$  by small quantities, say  $\tilde{\Delta}_N$ , and we write

$$\gamma_N h = (N\pi/2) - \tilde{\Delta}_N, \quad N \text{ odd}. \quad (3.23)$$

Substituting from (3.23) into (3.21) with (3.22), expanding and retaining terms linear in  $\tilde{\Delta}_N$ , we obtain

$$\tilde{\Delta}_N = \frac{2}{N\pi} k_{26}^2 + \frac{N\pi \hat{R}}{2} - \left(\frac{4}{3}\right) \frac{32}{27} \frac{\kappa_2 f_N r_{c2} \mu}{N\pi}, \quad (3.24)$$

the substitution of which in (3.18), along with (3.20)<sub>1-2</sub> and (3.23), yields the nonlinear eigenfrequency  $\omega_N$  for pure thickness vibrations in the form

$$\tilde{\omega}_N = \sqrt{\frac{\tilde{c}(1)}{\rho}} \frac{N\pi}{2h} \left[ 1 - \frac{4k_{26}^2}{N^2 \pi^2} - \hat{R} + \frac{9}{16} \frac{\gamma}{\tilde{c}(1)} \frac{1}{4h^2} \left( \frac{N^2 \pi^2}{2} + \frac{4}{3} \left( \frac{64}{27} \right) r_{c2} \kappa_2 \right) A_N A_N^* \right], \quad (3.25)$$

and we recall that the influence of the nonlinear coefficients  $\beta_1$  and  $\beta_3$  is not contained in (3.25) because they were omitted in the treatment. Since we are interested in the driven nonlinear solution for the contoured resonator, we carry the nonlinear solution for pure thickness vibrations no further, i.e., we do not obtain the driven solution for pure thickness vibrations or present the dependence on  $\beta_1$  and  $\beta_3$ . As we shall see, the amount of the solution to the nonlinear pure thickness vibration problem presented in this section is crucial for obtaining the solution to the problem of the nonlinear vibrations of the contoured resonator, which is presented in the next section.

#### 4. Nonlinear Vibrations of Contoured Resonators

In the linear case it has been shown that the inhomogeneous differential equation for the forced vibrations of contoured SC-cut quartz resonators driven by the application of a voltage across the surface electrodes may be written in a form given in Eq.(3.23) of Ref.2. In view of that equation and the reasoning leading to it and the solution to the nonlinear pure thickness problem presented in the last section, it can be shown<sup>14,15</sup> that, for a driving frequency  $\omega$  in the vicinity of the linear resonant frequency  $\omega_{Nmp}$  of one of the families of modes associated with the Nth harmonic, the inhomogeneous differential equation for the nonlinear forced vibrations of a contoured SC-cut quartz resonator driven by a voltage across the surface electrodes, i.e., the equation for the second iterate, may be written in the form

$$\sum_{n \neq N} \left[ M_n \frac{\partial^2 u_1^n}{\partial x_1^2} + P_n \frac{\partial^2 u_1^n}{\partial x_3^2} - \frac{n^2 \pi^2 \tilde{c}(1)}{4h^2} u_1^n - \rho u_1^n \right] + M_N \frac{\partial^2 u_1^N}{\partial x_1^2} + P_N \frac{\partial^2 u_1^N}{\partial x_3^2} + \rho \omega^2 u_1^N \tilde{u}_N e^{i\omega t}$$

$$- \gamma_N^2 \tilde{c}(1) u_1^N (\hat{A}_N \sin \gamma_N X_2 + 4\hat{G}_N \sin \gamma_N X_2 + 9\hat{L}_N \sin 3\gamma_N X_2) e^{i\omega t} = \frac{\rho \omega^2 e^{i\omega t}}{c(1) 2h} + \frac{9}{16} \gamma_N^2 \tilde{c}(1) u_1^N (\sin \gamma_N X_2 + \sin 3\gamma_N X_2) e^{i\omega t} + \beta_2^2 u_1^N \frac{\gamma_N^2 f_N r_{c2}}{N\pi} \sin 2\gamma_N X_2 e^{i\omega t}, \quad (4.1)$$

where  $M_n$  and  $P_n$  are given in Eqs.(3.16) and (3.17) of Ref.2,  $\tilde{u}_N$  is given by (3.17) with  $A_N$ ,  $G_N$  and  $L_N$  and

$$\tilde{u}_1^N = \tilde{u}_1^N(X_1, X_3), \quad \hat{c}_n^{(1)} = \tilde{c}(1) \left( 1 - \frac{8k_{26}^2}{n^2 \pi^2} - 2\hat{R} \right),$$

$$2h = 2h_0 \left[ 1 - \frac{X_1^2 + X_3^2}{4Rh_0} \right], \quad (4.2)$$

and we note that  $\tilde{u}_1^N$  is a slowly varying function of  $X_1$  and  $X_3$ .

It has been shown that the linear eigensolutions of the associated homogeneous problem, i.e., of (4.1) without the nonlinear terms and with  $V=0$ , can be written in the form<sup>15,1</sup>

$$u_{1nmp} = e^{-\alpha_n \frac{X_1^2}{2}} H_m(\sqrt{\alpha_n} X_1) e^{-\beta_n \frac{X_3^2}{2}} \cdot H_p(\sqrt{\beta_n} X_3) \sin \frac{n\pi X_2}{2h_0} e^{i\omega_{nmp} t}, \quad (4.3)$$

where  $H_m$  and  $H_p$  are Hermite polynomials and

$$\alpha_n^2 = n^2 \pi^2 \tilde{c}(1) / 8Rh_0^3 M_n, \quad \beta_n^2 = n^2 \pi^2 \tilde{c}(1) / 8Rh_0^3 P_n. \quad (4.4)$$

The linear eigenfrequencies  $\omega_{nmp}$  may be found from the relation

$$\rho \omega_{nmp}^2 = (\hat{c}_n^{(1)} n^2 \pi^2 / 4h_0^2) + M_n \gamma_{mn}^2 + P_n \mu_{pn}^2, \quad (4.5)$$

where

$$\gamma_{mn}^2 = \alpha_n (1 + 2m), \quad \mu_{pn}^2 = \beta_n (1 + 2p), \quad m, p = 0, 2, 4, \dots, \quad (4.6)$$

which are determined from the condition that the series for  $H_m$  and  $H_p$  terminate and they be polynomials. Since only the harmonics are of interest in this work, we have

$$\tilde{u}_1^N = e^{-\alpha_N \frac{X_1^2}{2}} e^{-\beta_N \frac{X_3^2}{2}}, \quad m = p = 0, \quad \omega = \tilde{\omega}_{N00}. \quad (4.7)$$

Consider the Nth homogeneous equation, i.e., the nonlinear one consisting of all terms not included in the sum in (4.1) but with  $V=0$ , multiply by  $\tilde{u}_1^N$  and integrate over the entire surface to obtain the weighted average with respect to  $X_1$  and  $X_3$  since the solution function in (4.3) is essentially the slowly varying thickness solution. The weighted average turns out to be most convenient because of the use of orthogonality in the forced vibration analysis. Then from the resulting  $X_2$ -dependent problem, by following the procedure used in the pure thickness problem treated in Sec.3, we obtain

$$\hat{G}_N = -\frac{16}{27} \kappa_2 \tilde{c}(1) \frac{f_N r_{c2}}{N\pi} \hat{A}_N, \quad \hat{L}_N = -\frac{\hat{A}_N}{8}, \quad (4.8)$$

$$-M_N \alpha_N - P_N \beta_N - \frac{N^2 \pi^2}{4h_0^2} \left( 1 - \frac{8k_{26}^2}{N^2 \pi^2} - 2\hat{R} + \left( \frac{4}{3} \right) \frac{128}{27} \frac{\kappa_{26}^2 r_{c2}}{N^2 \pi^2} \hat{\mu} \right) \bar{c}^{(1)} + \omega_{NOO}^2 = \frac{\bar{c}^{(1)} N^2 \pi^2}{4h_0^2} \hat{\mu}, \quad (4.9)$$

where

$$\hat{\mu} = \frac{9}{32} \frac{\gamma}{\bar{c}^{(1)}} \frac{\tau_{NN}^2 \hat{A}^*}{N^2 \pi^2}. \quad (4.10)$$

In obtaining (4.9) we have used the condition

$$\tau_{NN}^h = N\pi/2 - \hat{\Delta}_N, \quad (4.11)$$

which is analogous to (3.23), and from which we obtain

$$\hat{\Delta}_N = \frac{2}{N\pi} k_{26}^2 + \frac{N\pi\hat{R}}{2} - \left( \frac{4}{3} \right) \frac{32}{27} \frac{\kappa_{26}^2 r_{c2}}{N\pi} \hat{\mu}, \quad (4.12)$$

in the same way that (3.24) was found. Substituting from (4.5) and (4.2)<sub>2</sub> in (4.9), we may write

$$\omega_{NOO}^2 = \omega_{NOO}^2 + \frac{N^2 \pi^2 \bar{c}^{(1)}}{4h_0^2} \hat{\mu} \left[ 1 + \left( \frac{4}{3} \right) \frac{128}{27} \frac{\kappa_{26}^2 r_{c2}}{N^2 \pi^2} \right], \quad (4.13)$$

where

$$\omega_{NOO}^2 = \frac{N^2 \pi^2}{4h_0^2} \frac{\bar{c}^{(1)}}{\rho} \left[ 1 + \frac{1}{N\pi} \sqrt{\frac{2h_0}{R}} \left( \sqrt{\frac{M_N}{\bar{c}_N^{(1)}}} + \sqrt{\frac{P_N}{\bar{c}_N^{(1)}}} \right) \right], \quad (4.14)$$

and we have employed (4.4) in writing (4.14).

We now write the steady-state solution of the inhomogeneous equation (4.1) in the form

$$u_1 = \tilde{u}_{NOO} (\hat{A}_N \sin \tau_{NN} X_2 + \hat{G}_N \sin 2\tau_{NN} X_2 + \hat{L}_N \sin 3\tau_{NN} X_2) e^{i\omega t} + \sum_{n \neq N} \sum_{m \neq 0} \sum_{p \neq 0} H_{nmp}^{nmp} \tilde{u}_{nmp} \sin \tau_{nn} X_2 e^{i\omega t}, \quad (4.15)$$

together

and we note that we are interested only in the vicinity of nonlinear resonance, i.e., when the term containing  $\tilde{u}_{NOO}$  is dominant. Substituting from (4.15) into (4.1), using the orthogonality of the eigensolutions in the plane, then substituting from (4.5) for the linear terms and (4.9) for the nonlinear terms and then using the orthogonality in the thickness direction and, as usual, replacing the circular electrode by the circumscribed square, we obtain

$$(\omega^2 - \omega_{NOO}^2) \hat{A}_N = (-1)^{\frac{N-1}{2}} \frac{4e_{26} \omega_{NOO}^2 V}{c^{(1)} N^2 \pi^2 L_{NOO}}, \quad (4.16)$$

and we do not bother to write any of the  $H^{nmp}$  because, as already noted, we are interested in the solution only when  $\omega$  is in the vicinity of  $\omega_{NOO}$  and the NOOth eigenmode is dominant and all other eigenmodes are negligible and where

$$\omega_{NOO} = \frac{2\pi}{\sqrt{\alpha_N} \sqrt{\beta_N}} \operatorname{erf} \sqrt{\frac{\alpha_N}{2}} \ell \operatorname{erf} \sqrt{\frac{\beta_N}{2}} \ell, L_{NOO} = \frac{\pi}{\sqrt{\alpha_N} \sqrt{\beta_N}}. \quad (4.17)$$

From Eqs. (4.10), (4.11) and (4.13), we may write

$$\omega_{NOO}^2 = \omega_{NOO}^2 + \omega_N^2 \hat{A}_N \hat{A}_N^*, \quad \omega_N^2 = (\bar{c}^{(1)}/\rho) (N^2 \pi^2 / 4h_0^2), \quad (4.18)$$

where

$$\alpha = \frac{9}{32} \frac{\gamma}{\bar{c}^{(1)}} \frac{N^2 \pi^2}{4h_0^2} + \frac{4}{9\bar{c}^{(1)} 2h_0^2} \left[ \beta_2^2 r_{c2} + \beta_3^2 r_{c3} - \frac{\beta_1^2}{3} \right], \quad (4.19)$$

and we have included the influence of the nonlinear coefficients  $\beta_1$  and  $\beta_3$ , which have been omitted from the derivation<sup>6</sup>, as we said we would, and where

$$r_{c3} = (2\bar{c}^{(1)}/\bar{c}^{(3)}) [(\bar{c}^{(3)} - 2\bar{c}^{(1)})/4\bar{c}^{(1)} - \bar{c}^{(3)}], \quad r_{c1} = -2/3. \quad (4.20)$$

Thus, for an  $\omega$  in the vicinity of  $\omega_{NOO}$ , the solution can very accurately be written

$$\tilde{u}_1 = \hat{A}_N \sin \frac{N\pi X_2}{2h_0} \tilde{u}_{NOO} e^{i\omega t} - \frac{e_{26} V X_2}{c^{(1)} 2h} e^{i\omega t},$$

$$\omega = \frac{V X_2}{2h} e^{i\omega t} + \frac{e_{26}}{\epsilon_{22}} \hat{A}_N \tilde{u}_{NOO} \left( \sin \frac{N\pi X_2}{2h} - (-1)^{\frac{N-1}{2}} \frac{X_2}{h} \right) e^{i\omega t}, \quad (4.21)$$

where  $\hat{A}_N$  must satisfy (4.16) with (4.18).

In order to find the nonlinear relation between the amplitude  $\hat{A}_N$  and the driving voltage  $V$  of a typical reduced test circuit, we substitute from (4.21) into (2.10), which is then substituted into

$$I_c = - \int_{A_e} \vec{D}_2 \cdot d\vec{X}_1 d\vec{X}_3, \quad (4.22)$$

where  $A_e$  is the area of the electrode and  $I_c$  is the current, to obtain

$$I_c = \frac{i\omega e_{22}}{2h} (1 + \hat{k}_{26}^2) \hat{A}_N V - i\omega e_{26} \frac{\hat{A}_N}{h} \omega_{NOO}, \quad (4.23)$$

in which, for convenience, we have again replaced the circular electrode by the circumscribed square and

$$\hat{A}_e = A_e \left( 1 + \frac{\ell^2}{8Rh_0} \right), \quad \tilde{A}_N = (-1)^{\frac{N-1}{2}} \hat{A}_N,$$

$$\hat{k}_{26}^2 = \frac{k_{26}^2}{1 - k_{26}^2}. \quad (4.24)$$

The equation for the reduced test circuit takes the form

$$V_g + I_c (R_g + R_L) + V = 0, \quad (4.25)$$

where  $R_g$  and  $R_L$  are the generator and load resistance, respectively. Substituting from (4.23) and (4.25) into (4.16), we obtain

$$\frac{N^2 \pi^2 \tilde{A}_N}{4\omega^2} [\omega^2 - \omega_{NOO}^2 (1 + \alpha \tilde{A}_N \tilde{A}_N^*)] \cdot \left[ 1 + i\omega \frac{(R_g + R_L) e_{22}}{2h} (1 + \hat{k}_{26}^2) \hat{A}_e \right] = i\omega (R_g + R_L)$$

$$\cdot \epsilon_{22} \hat{k}_{26}^2 \frac{\omega_{NOO}^2 \tilde{A}_N}{h L_{NOO}} - \frac{e_{26}}{c^{(1)}} \frac{\omega_{NOO}}{L_{NOO}} V_g, \quad (4.26)$$

and, as usual, we have replaced  $\omega_{NOO}$  by  $\hat{\omega}_{NOO}$ , where

$$\hat{\omega}_{NOO} = \omega_{NOO} + i\omega_{NOO}/2Q_N, \quad (4.27)$$

in which  $Q_N$  is the unloaded quality factor of the resonator in the  $N$ th harmonic family of modes. Equation (4.26) is the nonlinear equation relating the amplitude of the mechanical displacement to the generator voltage. Since (4.26) contains  $\tilde{A}_N^*$  as well as  $\tilde{A}_N$ , we multiply (4.26) by its complex conjugate and after some algebraic manipulation obtain

$$\sigma[d^2 + c^2 - 2(d+ca)\omega_{NOO}^2 + (1+a^2)\omega_{NOO}^4\alpha^2\sigma^2] = e^2\gamma_g, \quad (4.28)$$

where

$$\begin{aligned} \sigma &= \tilde{A}_N \tilde{A}_N^*, \quad \gamma_g = V_g V_g^*, \quad a = \omega(R_g + R_L) \frac{e_{22}}{2h} (1 + k_{26}^2) \hat{A}_e, \\ b &= \omega(R_g - R_L) \frac{e_{22}}{h L_{NOO}^2} \frac{k_{26}^2 \omega_{NOO}^2}{4\omega^2}, \quad v = \frac{N^2 \pi^2}{4\omega^2}, \quad e = \frac{e_{26} \omega_{NOO}}{c(1) L_{NOO} v}, \\ c &= -\frac{\omega_{NOO}^2}{Q_N} + a(\omega^2 - \omega_{NOO}^2) - b, \quad d = \omega^2 - \omega_{NOO}^2 + \frac{\omega_{NOO}^2 a}{Q_N}. \end{aligned} \quad (4.29)$$

A very interesting and valuable relation giving the change  $\Delta_N$  from the linear resonant frequency at maximum current due to the nonlinearity can be obtained from (4.18)<sub>1</sub> and (4.23), independent of the external circuitry, by noting that at resonance,  $V$  can be neglected in (4.23) to obtain

$$I_c \approx -i\omega e_{26} \frac{\tilde{A}_N}{h} L_{NOO}. \quad (4.30)$$

Then substituting  $\tilde{A}_{NOO} = \omega_{NOO} + \Delta_N$  in (4.18)<sub>1</sub> and employing (4.30), we obtain

$$\Delta_N = \frac{\omega h^2 I_c I_c^*}{2\omega_{NOO} e_{26}^2 \omega_{NOO}^2}, \quad (4.31)$$

which is the complete equation relating the change in resonant frequency to the square of current. If the coefficients of the quadratic nonlinearities  $\beta_1$ ,  $\beta_2$  and  $\beta_3$ , which turn out to have a very small influence on the total nonlinear behavior, are neglected and the electrodes are assumed to be sufficiently large that the error functions in (4.17) can be taken to be unity, which is approximately true in almost all practical cases, Eq.(4.31) can be put in a very illuminating form. When the foregoing approximations are made and we substitute from (4.17)<sub>1</sub> and (4.19) with (4.4) into (4.31), we obtain

$$\Delta_N \approx \frac{9}{8(32)^2} \frac{\gamma_N \pi^2 I_c I_c^*}{\sqrt{M_N P_N} \omega_{NOO}^2 R h_o^3}, \quad (4.32)$$

which clearly shows that  $\Delta_N$  for the contoured resonator depends much more strongly on the order of the overtone, than for the thickness vibrator or even the trapped energy resonator<sup>3</sup>. In hindsight this seems obvious because in the contoured resonator the confinement of the mode increases rapidly with the order of the overtone, which results in an increase in the amplitude of the mechanical displacement for a given current level. Equation (4.32) also reveals an explicit dependence of  $\Delta_N$  on the effective planar elastic constants  $M_N$  and  $P_N$  as well as a dependence on the radius of the contour  $R$  and the center thickness  $2h_o$ .

## 5. Results

Calculations can now readily be performed for AT-cut quartz since the fourth order nonlinear elastic constant  $c_{6666}$ , which appears in the expression for  $\gamma$  given in (2.4)<sub>1</sub>, is known<sup>11</sup> for the AT-cut. However,

since  $c_{6666}$  is not known for any other cut, including the SC-cut, such calculations cannot be performed for the SC-cut. Calculations have been performed using the known values of the second order elastic, piezoelectric and dielectric constants of quartz<sup>16</sup>, the third order elastic constants of quartz<sup>17</sup> and the above-mentioned value of  $c_{6666}$  for the AT-cut<sup>11</sup>. The results of the calculations are presented in Figs.2-7 and Table I. All the results appearing in the figures are for a nominal 5 MHz (actual 5.2 MHz) fundamental plano-convex resonator with a center thickness  $2h_o = .3282$  mm, a radius of curvature  $R = 5$  cm and an electrode diameter  $2l = 3$  mm for a few driving voltages  $V_g$ , load resistances  $R_L$  and unloaded quality factors  $Q_N$ . Figure 2 shows the amplitude of the current as a function of the driving frequency for the conditions shown in the figure. The response curve shown in Fig.2 is exactly the same as the one that would have been obtained from a linear analysis. This is a result of the fact that the frequency scale used in Fig.2 is too large to show the nonlinear effect. Figure 3 shows current response curves as a function of driving frequency for a few driving voltages  $V_g$  to a small enough frequency scale to exhibit the influence of the nonlinearity. The middle curve is for the same conditions as Fig.2 and indicates a clear nonlinear effect in the vicinity of resonance. The dotted curve shown in Fig.3 was obtained from Eq.(4.31) and, as can be seen from the figure, it goes through the maximum current points of all the solid response curves shown in the figure. Figure 4 shows current response curves for a fixed driving voltage  $V_g$  and load resistance  $R_L$  for a few quality factors  $Q_N$ . Figure 5 shows current response curves for a fixed driving voltage  $V_g$  and quality factor  $Q_N$  for two values of load resistance  $R_L$ . Figures 6 and 7 show current response curves for the same values of  $R_L$  and  $Q_N$  and two different driving voltages for the first, third and fifth harmonics. It is clear from both figures that the order of overtone, i.e., value of  $N$ , has a significant influence on the shift in resonant frequency resulting from the elastic nonlinearity, as already indicated by Eq.(4.32). In fact, the figures indicate, as does Eq.(4.32), that the value of  $N$  has a stronger influence on the shift in frequency  $\Delta_N$  than the current  $I_c$ .

A comparison of the coefficient of nonlinear dependence of frequency on current obtained from the complete relation (4.31) with that obtained from the approximate formula (4.32) is given in Table I for two different plano-convex resonators for a number of radii of curvature of the contour for the first, third and fifth harmonics. Both resonators have an electrode diameter of 3 mm. It can be seen from the table that the agreement is much better for the thinner resonator than for the thicker one. This is a result of the fact that the confinement is considerably sharper in the thinner resonator than in the thicker one, as shown by Eqs.(4.3) and (4.4), and both have the same small electrode diameter of 3 mm. This means that the electrode diameter of 3 mm is much too small to be practical in the case of the thicker resonator but that it is fine for the thinner resonator. The table also shows that for the fundamental mode ( $N=1$ ) of the thinner resonator the agreement decreases with increasing radius of curvature of the contour. This is also a result of the fact that for  $N=1$  the larger values of  $R$  do not result in sufficient confinement to get nearly all of the mode under the 3 mm diameter electrode. However, the table shows that for  $N=3$  or  $N=5$ , the entire mode is essentially completely under the 3 mm diameter electrode.

### Acknowledgements

The author wishes to thank J. Vig of the U.S. Army Electronics Technology and Devices Laboratory for motivating this investigation, R.C. Smythe of Piezo Technology, Inc. for many valuable discussions and D.S. Stevens of Rensselaer Polytechnic Institute for performing the calculations and plotting the curves.

This work was supported in part by the Army Research Office under Contract No. DAAG 29-82-K-0130 and the National Science Foundation under Grant No. MEA-8115340.

### References

1. H.F. Tiersten and R.C. Smythe, "An Analysis of Contoured Crystal Resonators Operating in Overtones of Coupled Thickness Shear and Thickness Twist," *J. Acoust. Soc. Am.*, **65**, 1455 (1979).
2. H.F. Tiersten and D.S. Stevens, "An Analysis of Contoured SC-Cut Quartz Crystal Resonators," *Proceedings of the 36th Annual Symposium on Frequency Control*, U.S. Army Electronics Research and Development Command, Fort Monmouth, New Jersey, **37** (1982).
3. H.F. Tiersten, "Analysis of Nonlinear Resonance in Thickness-Shear and Trapped Energy Resonators," *J. Acoust. Soc. Am.*, **59**, 866 (1976).
4. H.F. Tiersten and A. Ballato, "Nonlinear Extensional Vibrations of Quartz Rods," *J. Acoust. Soc. Am.*, **73**, 2022 (1983).
5. D.S. Stevens, H.F. Tiersten, *Proceedings of the 36th Annual Symposium on Frequency Control*, U.S. Army Electronics Research and Development Command, Fort Monmouth, New Jersey, **46** (1982).
6. For more detail see H.F. Tiersten, "An Analysis of Nonlinear Resonance in Electroded Contoured Quartz Crystal Resonators," to be issued as a technical report, Rensselaer Polytechnic Institute, Troy, New York.
7. The relation between the nonlinear constants in (2.4), which in the general anisotropic case are referred to the eigenvector triad of the thickness solution, and the constants referred to the original coordinate system in the plate will be given in Ref.6. Since calculations are not performed here for the doubly-rotated SC-cut because the most important nonlinear constant is not known and no transformation is required in the case of the AT-cut, for which calculations are performed, the relations are not actually needed in this work.
8. H.F. Tiersten, *Linear Piezoelectric Plate Vibrations* (Plenum, New York, 1969), Chap.9, Sec.2.
9. H.F. Tiersten, "Electromechanical Coupling Factors and Fundamental Material Constants of Thickness Vibrating Piezoelectric Plates," *Ultrasonics*, **8**, 19 (1970).
10. A. Ballato, "Doubly-Rotated Thickness Mode Plate Vibrators," in *Physical Acoustics*, edited by W.P. Mason and R.N. Thurston (Academic, New York, 1977), Vol.XIII, Sec.III.
11. H.F. Tiersten, "Analysis of Intermodulation in Thickness-Shear and Trapped Energy Resonators," *J. Acoust. Soc. Am.*, **57**, 667 (1975).
12. Only one term is retained because only the largest term is considered to be of any potential importance. If more are thought to be required, they may be included without difficulty. In actuality it turns out that all  $\beta_i$  are negligible, including  $\beta_2$  for  $M=N$ , which has the largest influence. It is perhaps worth noting that a form of solution consisting of a small number of terms rather than a series has been obtained. However, the analysis for this form is lengthy and differs for different  $\beta_i$  and is considered to be too cumbersome to include here since the actual influence of all  $\beta_i$  is small anyway. This procedure will be included in Ref.6.
13. The procedure is a straightforward iterative procedure except when the functional form resulting from the nonlinear terms is identical with that satisfying the basic linear differential equation, at which point the coefficients associated with the functional form due to the nonlinearity are treated as unknown and identical with the coefficients of the linear solution. This is the reason the  $\sin \eta_i X_2$  term in (3.15) is homogeneous whereas (3.10) is an inhomogeneous equation. This procedure is appropriate because the term on the right-hand side of (3.15) actually is a homogeneous term and appears to be inhomogeneous (known) only because of the nature of the formal procedure employed which tends to be misleading whenever this type of coincidence of functions occurs.
14. Equation (4.1) has been obtained by expansion in the plate waves for the contoured resonator. The terms for  $n \neq N$  are just the usual linear terms and only one of the terms with subscript  $N$  is actually nonlinear, i.e., the one for  $m=M$  and  $p=P$ . The terms containing  $M_N$  and  $P_N$  are linear terms because of the slow variation of  $\tilde{u}_1^N$  and the fact that  $\hat{A}_N$  is small. The remaining terms containing  $N$  are due to either thickness ( $X_2$ ) or time derivatives and simply contain  $\tilde{u}_1^N(X_1, X_2)$ . These latter terms are the same as those occurring in the nonlinear pure thickness problem treated in Sec.3, but now contain  $\tilde{u}_1^N$ , which is never differentiated in the nonlinear terms. This occurs essentially because the linear and nonlinear behavior remain separate in the equations since  $\tilde{u}_1^N$  varies slowly and  $\hat{A}_N$  is small, and, as a consequence, the linear terms that do not appear in a pure thickness problem result in exactly the same solution functions at the second iterate stage as at the zeroth iterate stage.
15. C.J. Wilson, "Vibration Modes of AT-Cut Convex Quartz Resonators," *J. Phys.*, **D7**, 2449 (1974).
16. R. Bechmann, "Elastic and Piezoelectric Constants of Alpha-Quartz," *Phys. Rev.*, **110**, 1060 (1958).
17. R.N. Thurston, H.J. McSkimin and P. Andreatch, Jr., "Third Order Elastic Constants of Quartz," *J. Appl. Phys.*, **37**, 267 (1966).

TABLE I  
COEFFICIENT OF NONLINEAR DEPENDENCE  
OF FREQUENCY ON CURRENT

	$\Delta_N / I_c^2$		
	N = 1	N = 3	N = 5
$2h_o = .3282 \text{ mm}^*$			
R = 5 cm	$2.73 \times 10^6$ 2.63	$83.6 \times 10^6$ 87.8	$361 \times 10^6$ 374
10 cm	1.83 1.33	43.1 44.1	182 188
20 cm	1.33 .67	23.2 22.1	92.4 94.0
$2h_o = .9846 \text{ mm}^{**}$			
R = 5 cm	2.19 .28	18.8 9.6	55.8 41.0
10 cm	2.01 .14	14.0 4.8	36.7 20.6
20 cm	1.88 .07	11.2 2.4	26.4 10.3

\* Nominal 5 MHz fundamental

\*\* Nominal 5 MHz 3rd overtone  $2l = 3 \text{ mm}$

Upper number from complete relation  
Lower number from approximate formula

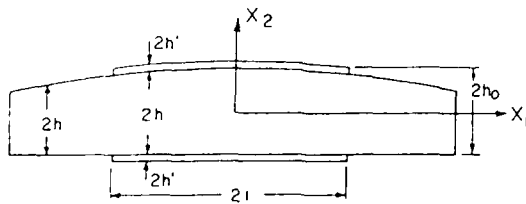


Figure 1  
Cross-Section of Plano-Convex Resonator

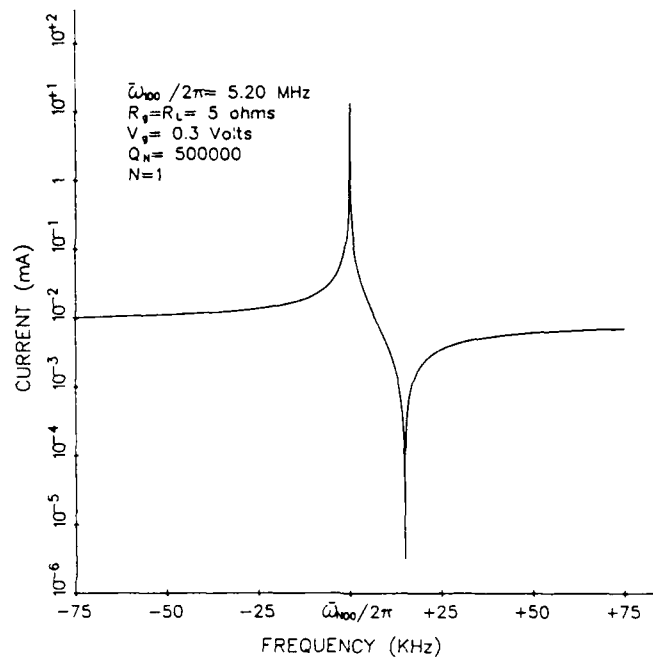


Figure 2  
Current-vs-Frequency Response Curve for Large  
Frequency Range

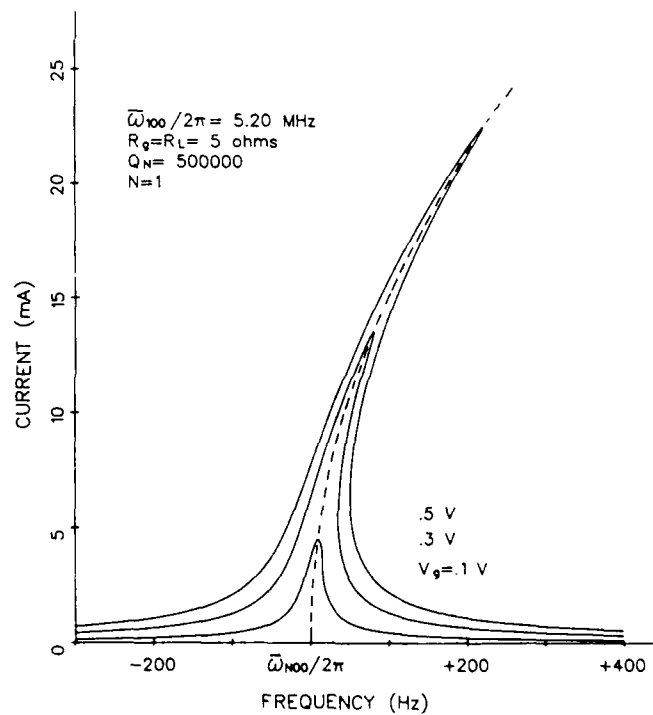


Figure 3  
Current-vs-Frequency Response Curves for Different  
Generator Voltages for Small Frequency Range



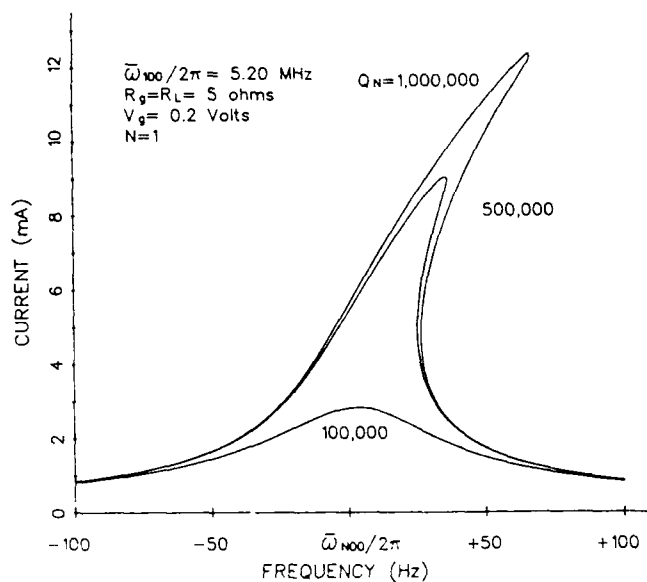


Figure 4

Current-vs-Frequency Response Curves for Different Quality Factors

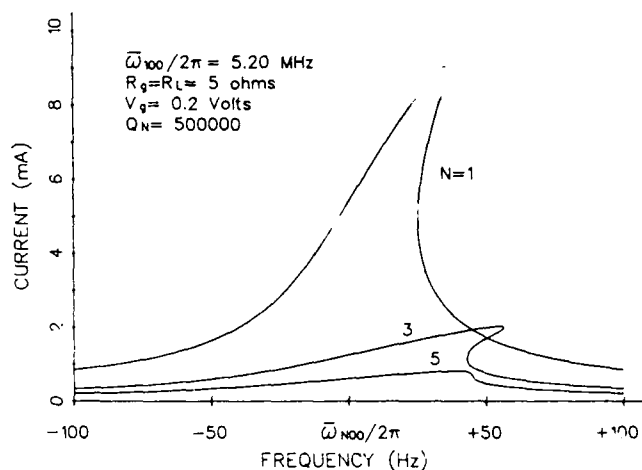


Figure 6

Current-vs-Frequency Response Curves for the First, Third and Fifth Harmonics

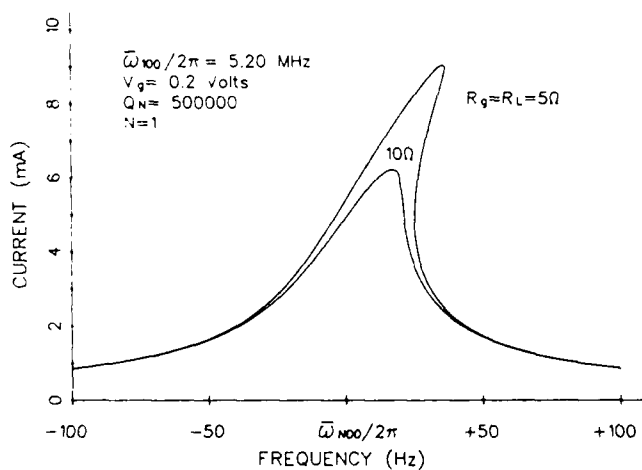


Figure 5

Current-vs-Frequency Response Curves for Different Load Resistances

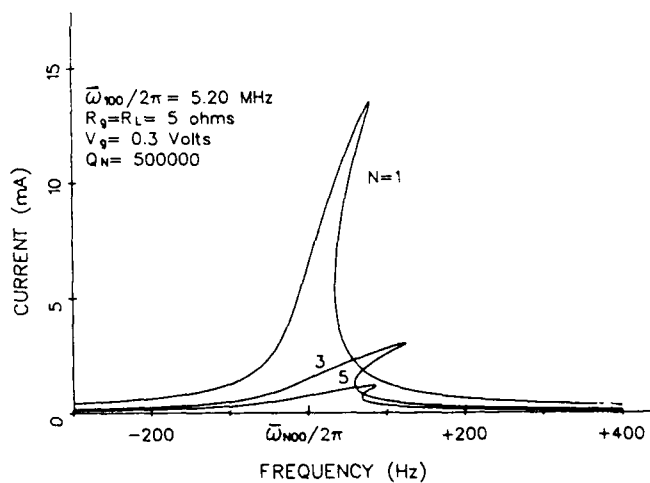


Figure 7

Current-vs-Frequency Response Curves for the First, Third and Fifth Harmonics

ANALYSIS AND DESIGN OF COUPLED MODE  
AT RECTANGULAR RESONATORS

Joseph P. Tomase and Lawrence N. Dworsky

Motorola, Inc.  
Schaumburg, Ill.ABSTRACT

A review of the predominant vibration modes of rectangular AT quartz resonators ("strip resonators") is presented, including the implications of coupled mode interplay to device design.

A three dimensional mode-matching theory for AT strip resonators was presented by Milsom et al. in 1981.<sup>1</sup> Milsom expressed the acoustic displacements as the linear sum of partial modes, each mode having a wave number whose components in all three directions were in general complex. This paper develops a simplified version of Milsom's model which, by scaling the equations as shown by Mindlin in 1982, contains all real equations.<sup>2</sup> Since free-edge boundary conditions cannot be satisfied using a finite number of modes, a Galerkin form approximation is used at the (X) edges.

A computer program has been written, based upon this model, to be used for the design of AT strip resonators. The model's predictions are shown to be in good agreement with experimental data.

INTRODUCTION

The ever increasing demand on the crystal industry today is for devices with reduced size, improved electrical and frequency-temperature performance capabilities, the ability to withstand shock levels in excess of ten thousand g's, and last but not least, low cost. As a result, much interest is being directed towards the miniature AT rectangular resonator. The operation of these devices however, involves an interplay between the desired fundamental X-thickness shear mode and other vibration modes.

It has been demonstrated by Mindlin and more recently by Milsom et al., that the flexural and face shear modes are never cut off.<sup>3,1</sup> Therefore for fundamental mode AT rectangular resonators, coupling to these two modes must be avoided. When one of these undesired modes is excited, considerable energy transfer can occur. This will result in a decrease in the resonator's motional capacitance with a corresponding increase in its motional resistance, and will also cause a change in the frequency of resonance. This coupling can be avoided however, by modeling the coupled mode system of the AT rectangular resonator, thus enabling the determination of the proper design parameters, (the proper resonator width to thickness ratio).

Mindlin extended the theory of flexural motions to AT quartz plates and determined that, "the resonances in a bounded plate commonly designated as thickness-shear, or thickness-shear overtones, are simply local regions in the spectrum of flexural resonances over which the frequency does not change as rapidly as elsewhere, with change of plate dimensions."<sup>3</sup> He also stated that face shear vibrations are strongest when flexural vibrations are excited, therefore the avoidance of X-thickness shear to flexural mode coupling will also result in the avoidance of coupling to the face shear mode. With this point in mind, the following formulation will model X-thickness shear to flexural mode coupling only.

This analysis is a simplified form of the analysis presented by Milsom, assuming a fully electroded plate which is clamped at one end.

COUPLED MODE EQUATIONS OF MOTION

For the rectangular cross section of a bar of AT-cut quartz, as shown in figure 1, Newton's Law and Gauss' Law may be written in the following form, assuming that  $u_z = 0$ .

$$\frac{\partial T_{11}}{\partial x} + \frac{\partial T_{21}}{\partial y} = \rho \ddot{u}_x \quad (1)$$

$$\frac{\partial T_{12}}{\partial x} + \frac{\partial T_{22}}{\partial y} = \rho \ddot{u}_y \quad (2)$$

$$\frac{\partial D_x}{\partial x} + \frac{\partial D_y}{\partial y} = 0 \quad (3)$$

T,  $\rho$ , u and D are respectively stress, density, particle displacement and electric flux density. The constitutive equations may be written as,

$$T_{11} = c_{11} \frac{\partial u_x}{\partial x} + c_{12} \frac{\partial u_y}{\partial y} + c_{14} \frac{\partial u_y}{\partial z} + e_{11} \frac{\partial \phi}{\partial x} \quad (4)$$

$$T_{12} = T_{21} = c_{56} \frac{\partial u_x}{\partial z} + \left( \frac{\partial u_x}{\partial y} + \frac{\partial u_y}{\partial x} \right) c_{66} + e_{26} \frac{\partial \phi}{\partial y} + e_{36} \frac{\partial \phi}{\partial z} \quad (5)$$

$$T_{22} = c_{12} \frac{\partial u_x}{\partial x} + c_{22} \frac{\partial u_y}{\partial y} + c_{24} \frac{\partial u_y}{\partial z} + e_{12} \frac{\partial \phi}{\partial x} \quad (6)$$

$$D_x = e_{11} \frac{\partial u_x}{\partial x} + e_{12} \frac{\partial u_y}{\partial y} + e_{14} \frac{\partial u_y}{\partial z} - \xi_{11} \frac{\partial \phi}{\partial x} \quad (7)$$

$$D_y = e_{25} \frac{\partial u_x}{\partial z} + e_{26} \left( \frac{\partial u_x}{\partial y} + \frac{\partial u_y}{\partial x} \right) - \xi_{22} \frac{\partial \phi}{\partial y} - \xi_{23} \frac{\partial \phi}{\partial z} \quad (8)$$

where c, e,  $\xi$  and  $\phi$  are respectively the elastic constants, piezoelectric constants, dielectric constants and electric potential, and  $u_x$  and  $u_y$  are each functions of x, y and z.

The homogeneous boundary conditions for an unclamped and unelectroded piezoelectric resonator are as follows:

$$\begin{array}{ll} \text{At } x = \left( \pm \frac{L_1}{2} \right) & \text{At } y = \left( \pm \frac{L_2}{2} \right) \\ T_{11} = 0 & T_{12} = 0 \\ T_{21} = 0 & T_{22} = 0 \\ D_x = 0 & \phi = 0 \end{array}$$

Since electrodes on the X-Z surfaces produce a y-directed electric field, then as shown by Tiersten, all potential and electrical variations with respect to x and z may be ignored.<sup>4</sup> Therefore equations (1) and (2) may be written as,

$$\begin{aligned} & c_{11} \frac{\partial^2 u_x}{\partial x^2} - (c_{12} + c_{66}) \frac{\partial^2 u_y}{\partial x \partial y} + (c_{14} + c_{56}) \frac{\partial^2 u_y}{\partial x \partial z} \\ & + 2c_{56} \frac{\partial^2 u_x}{\partial y \partial z} - c_{66} \frac{\partial^2 u_x}{\partial y^2} + c_{55} \frac{\partial^2 u_x}{\partial z^2} + e_{26} \frac{\partial^2 \phi}{\partial y^2} \\ & - \rho \omega^2 u_x = 0 \end{aligned} \quad (9)$$

and,

$$\begin{aligned} & (c_{56} + c_{14}) \frac{\partial^2 u_x}{\partial x \partial y} - (c_{66} + c_{12}) \frac{\partial^2 u_x}{\partial x \partial z} + c_{66} \frac{\partial^2 u_y}{\partial x^2} \\ & + c_{22} \frac{\partial^2 u_y}{\partial y^2} + 2c_{24} \frac{\partial^2 u_y}{\partial y \partial z} + c_{44} \frac{\partial^2 u_y}{\partial z^2} \\ & - (e_{26} + e_{12}) \frac{\partial^2 \phi}{\partial x \partial y} - \rho \omega^2 u_y = 0 \end{aligned} \quad (10)$$

where,

$$\frac{\partial^2 \phi}{\partial y^2} = \frac{e_{26}}{\epsilon_{22}} \frac{\partial^2 u_x}{\partial y^2} \quad (11)$$

Using the values for the elastic constants as presented by Fenlon et al., for right-handed, 35.25 degree, AT-cut quartz, the coefficients of the terms of equations (9) and (10) which are differentiated with respect to z, normalized to  $c_{66}$  become as follows.<sup>5</sup>

$$\frac{(c_{14} + c_{56})}{c_{66}} = -0.04 \quad (12)$$

$$\frac{2c_{56}}{c_{66}} = 0.17 \quad (13)$$

$$\frac{c_{55}}{c_{66}} = 2.37 \quad (14)$$

$$\frac{2c_{24}}{c_{66}} = 0.39 \quad (15)$$

$$\frac{c_{44}}{c_{66}} = 1.33 \quad (16)$$

Since  $L_z$  is much longer than  $L_x$  and  $L_y$ , it may be assumed that  $u_x$  and  $u_y$  are slowly changing with respect to z, and therefore in equations (9) and (10), the

$(c_{14} + c_{56})$ ,  $2c_{56}$  and  $2c_{24}$  coefficients (of terms differentiated with respect to z) will be assumed equal to zero.

Since the rectangular resonators which are being modeled utilize a cantilevered mount, the boundary conditions on  $u_x$  and  $u_y$  will be approximated by,

$$\frac{\partial u_y}{\partial z} = \frac{\partial u_x}{\partial z} = 0 \quad \text{at } z = L_z \quad (17)$$

and,

$$u_x = u_y = 0 \quad \text{at } z = 0 \quad (18)$$

Therefore it will be assumed that,

$$u_x = u_x(x, y) \sin\left(\frac{n\pi z}{2L_z}\right) \quad (19)$$

and

$$u_y = u_y(x, y) \sin\left(\frac{n\pi z}{2L_z}\right) \quad (20)$$

where,  $n = 1, 3, 5, \dots$

Therefore equations (9) and (10) may be rewritten as,

$$\begin{aligned} & c_{11} \frac{\partial^2 u_x}{\partial x^2} + (c_{12} + c_{66}) \frac{\partial^2 u_y}{\partial x \partial y} + \overline{c_{66}} \frac{\partial^2 u_x}{\partial y^2} \\ & + \left( \frac{-c_{55} n^2 \pi^2}{4L_z^2} + \rho \omega^2 \right) u_x = 0 \end{aligned} \quad (21)$$

where  $\overline{c_{66}} = \left( c_{66} + \frac{e_{26}^2}{\epsilon_{22}} \right)$ , and

$$\begin{aligned} & (c_{66} + c_{12}) \frac{\partial^2 u_x}{\partial x \partial y} + c_{66} \frac{\partial^2 u_y}{\partial x^2} + c_{22} \frac{\partial^2 u_y}{\partial y^2} \\ & + \left( \frac{-c_{44} n^2 \pi^2}{4L_z^2} + \rho \omega^2 \right) u_y = 0 \end{aligned} \quad (22)$$

where (21) is the equation of motion for the X-thickness shear modes, and (22) is the equation of motion for the flexural modes. For these two equations, the  $\sin\left(\frac{n\pi z}{2L_z}\right)$  term has dropped out and thus,

$$u_x = u_x(x, y) \quad \text{and} \quad u_y = u_y(x, y) \quad (23)$$

Therefore the z-dependency of these equations resides in the

$$\frac{-c_{55}n^2\pi^2}{4L_z^2} \text{ and } \frac{-c_{44}n^2\pi^2}{4L_z^2} \text{ coefficients.}$$

Equations (21) and (22) are a pair of linear, coupled second order partial differential equations, which must be solved.

The y-directed electric field results in a predominantly X-thickness shear solution  $u_x$ , which is odd in y. For  $D_y$  to be non-zero,  $u_x$  must be even in x. Therefore,

$$u_x = A_x \cos(k_0 \beta_1 x) \sin(k_0 \beta_2 y) \quad (24)$$

$$\text{where, } k_0 = \left( \frac{\pi}{L_2} \right) \quad (25)$$

Therefore  $u_y$ , a predominantly flexural mode solution, will be even in y and odd in x. Therefore,

$$u_y = A_y \sin(k_0 \beta_1 x) \cos(k_0 \beta_2 y) \quad (26)$$

Substituting equations (24) and (26) into equations (21) and (22) results in,

$$\left( -c_{11}\beta_1^2 - \overline{c_{66}}\beta_2^2 + \frac{\rho\omega^2}{k_0^2} - \frac{c_{55}n^2\pi^2}{4k_0^2L_z^2} \right) A_x - (c_{12} + c_{66})\beta_1\beta_2 A_y = 0 \quad (27)$$

and

$$-\beta_1\beta_2(c_{66} + c_{12}) A_x + \left( \frac{\rho\omega^2}{k_0^2} - \frac{c_{44}n^2\pi^2}{4k_0^2L_z^2} - c_{22}\beta_2^2 - c_{66}\beta_1^2 \right) A_y = 0 \quad (28)$$

Multiplying the  $A_y$  term in equation (27) by  $\frac{\beta_1\beta_2}{\beta_1\beta_2}$  results in,

$$\left( -c_{11}\beta_1^2 - \overline{c_{66}}\beta_2^2 + \frac{\rho\omega^2}{k_0^2} - \frac{c_{55}n^2\pi^2}{4L_z^2k_0^2} \right) A_x - (c_{12} + c_{66})\beta_1^2\beta_2^2 \left( \frac{A_y}{\beta_1\beta_2} \right) = 0 \quad (29)$$

Multiplying the  $A_y$  term in equation (28) by  $\frac{\beta_1\beta_2}{\beta_1\beta_2}$

and both sides of equation (28) by  $\beta_1\beta_2$  gives,

$$-\beta_1^2\beta_2^2(c_{66} + c_{12}) A_x$$

$$\left( \frac{\rho\omega^2}{k_0^2} - \frac{c_{44}n^2\pi^2}{4k_0^2L_z^2} - c_{22}\beta_2^2 - c_{66}\beta_1^2 \right)$$

$$\frac{\beta_1^2\beta_2^2}{\beta_1\beta_2} \cdot \frac{A_y}{\beta_1\beta_2} = 0 \quad (30)$$

Expressing equations (29) and (30) in matrix form gives,

$$\begin{vmatrix} \Omega & \Psi \\ \lambda & \Theta \end{vmatrix} \begin{vmatrix} A_x \\ \frac{A_y}{\beta_1\beta_2} \end{vmatrix} = 0 \quad (31)$$

where,

$$\Omega = \frac{\rho\omega^2}{k_0^2} - \frac{c_{55}n^2\pi^2}{4k_0^2L_z^2} - c_{11}\beta_1^2 - \overline{c_{66}}\beta_2^2 \quad (32)$$

$$\Psi = -(c_{12} + c_{66})\beta_1^2\beta_2^2 \quad (33)$$

$$\lambda = -(c_{12} + c_{66})\beta_1^2\beta_2^2 \quad (34)$$

$$\Theta = \left( \frac{\rho\omega^2}{k_0^2} - \frac{c_{44}n^2\pi^2}{4k_0^2L_z^2} - c_{66}\beta_1^2 - c_{22}\beta_2^2 \right) \beta_1^2\beta_2^2 \quad (35)$$

Let,

$$A_N = \frac{A_x}{\left( \frac{A_y}{\beta_1\beta_2} \right)} \quad (36)$$

Therefore all coefficients in the matrix as well as  $A_N$  are real. Nontrivial solutions are obtained when the determinant of the above matrix is zero.  $u_x$  and  $u_y$  can now be written as the linear sum of two terms. In order to satisfy the boundary conditions, coefficients  $B_N$  are required.

$$u_x = \sum_{N=1}^2 \frac{B_N A_N A_{YN}}{\beta_1 \beta_{2N}} \cos(k_0 \beta_1 x) \sin(k_0 \beta_{2N} y) \quad (37)$$

$$u_y = \sum_{N=1}^2 B_N A_{YN} \sin(k_0 \beta_1 x) \cos(k_0 \beta_{2N} y) \quad (38)$$

Multiplying both sides of equations (37) and (38) by  $\frac{\beta_1}{A_{YN}}$  gives,

$$\frac{u_x \beta_1}{A_{YN}} = \sum_{N=1}^2 \frac{B_N A_N \cos(k_0 \beta_1 x) \sin(k_0 \beta_{2N} y)}{\beta_{2N}} \quad (39)$$

$$\frac{u_y \beta_1}{A_{YN}} = \sum_{N=1}^2 B_N \beta_1 \sin(k_0 \beta_1 x) \cos(k_0 \beta_{2N} y) \quad (40)$$

From the boundary conditions at  $y = \pm \frac{L_2}{2}$ ,

$$T_{12} = \overline{c_{66}} \frac{\partial u_x}{\partial y} + c_{66} \frac{\partial u_y}{\partial x} = 0 \quad (41)$$

and

$$T_{22} = c_{12} \frac{\partial u_x}{\partial x} + c_{22} \frac{\partial u_y}{\partial y} = 0 \quad (42)$$

Substituting equations (39) and (40) into equations (41) and (42) gives,

$$\begin{aligned} & \overline{c_{66}} \frac{\partial}{\partial y} \left( B_1 A_1 \cos(k_0 \beta_1 x) \frac{\sin(k_0 \beta_{21} y)}{\beta_{21}} \right. \\ & \quad \left. + B_2 A_2 \cos(k_0 \beta_1 x) \frac{\sin(k_0 \beta_{22} y)}{\beta_{22}} \right) \\ & - c_{66} \frac{\partial}{\partial x} \left( B_1 \beta_1 \sin(k_0 \beta_1 x) \cos(k_0 \beta_{21} y) \right. \\ & \quad \left. + B_2 \beta_1 \sin(k_0 \beta_1 x) \cos(k_0 \beta_{22} y) \right) = 0 \end{aligned} \quad (43)$$

and

$$\begin{aligned} & c_{12} \frac{\partial}{\partial x} \left( B_1 A_1 \cos(k_0 \beta_1 x) \frac{\sin(k_0 \beta_{21} y)}{\beta_{21}} \right. \\ & \quad \left. + B_2 A_2 \cos(k_0 \beta_1 x) \frac{\sin(k_0 \beta_{22} y)}{\beta_{22}} \right) \\ & - c_{22} \frac{\partial}{\partial y} \left( B_1 \beta_1 \sin(k_0 \beta_1 x) \cos(k_0 \beta_{21} y) \right. \\ & \quad \left. + B_2 \beta_1 \sin(k_0 \beta_1 x) \cos(k_0 \beta_{22} y) \right) = 0 \end{aligned} \quad (44)$$

Differentiating, equations (43) and (44) become, in matrix form,

$$\begin{vmatrix} \Omega & \Psi \\ \lambda & \Theta \end{vmatrix} \begin{vmatrix} B_1 \\ B_2 \end{vmatrix} = 0 \quad (45)$$

where,

$$\Omega = (A_1 \overline{c_{66}} + \beta_1^2 c_{66}) \cos \left[ \frac{\pi \beta_{21}}{2} \right] \quad (46)$$

$$\Psi = (A_2 \overline{c_{66}} + \beta_1^2 c_{66}) \cos \left[ \frac{\pi \beta_{22}}{2} \right] \quad (47)$$

$$\lambda = (A_1 c_{12} + \beta_{21}^2 c_{22}) \sin \left[ \frac{\pi \beta_{21}}{2} \right] \quad (48)$$

$$\Theta = (A_2 c_{12} + \beta_{22}^2 c_{22}) \sin \left[ \frac{\pi \beta_{22}}{2} \right] \quad (49)$$

Therefore all coefficients in the above matrix as well as  $\left( \frac{B_1}{B_2} \right)$  are real.

In order to match the boundary conditions on  $x$ , another set of arbitrary constants,  $C_M$ , are needed.

$$u_x = \sum_M C_M \cos(k_0 \beta_{1M} x) \sum_{N=1}^2 \frac{B_{MN} A_{MN} \sin(k_0 \beta_{2MN} y)}{\beta_{2MN}} \quad (50)$$

$$u_y = \sum_M C_M \beta_{1M} \sin(k_0 \beta_{1M} x) \sum_{N=1}^2 \frac{B_{MN} \cos(k_0 \beta_{2MN} y)}{\beta_{2MN}} \quad (51)$$

At  $x = \pm \frac{L_1}{2}$

$$T_{11} = c_{11} \frac{\partial u_x}{\partial x} + c_{12} \frac{\partial u_y}{\partial y} = 0 \quad (52)$$

$$T_{21} = T_{12} = \overline{c_{66}} \frac{\partial u_x}{\partial y} + c_{66} \frac{\partial u_y}{\partial x} = 0 \quad (53)$$

Substituting equations (50) and (51) into (52) and (53) gives,

$$\begin{aligned} T_{11} = \sum_M \frac{C_M \sin(k_0 \beta_{1M} \frac{L_1}{2})}{\beta_{1M}} \sum_{N=1}^2 B_{MN} (c_{11} \beta_{1M}^2 A_{MN} \\ + c_{12} \beta_{1M}^2 \beta_{2MN}^2) \frac{\sin(k_0 \beta_{2MN} y)}{\beta_{2MN}} = 0 \end{aligned} \quad (54)$$

and

$$\begin{aligned} T_{12} = \sum_M C_M \cos \left( \frac{k_0 \beta_{1M} L_1}{2} \right) \sum_{N=1}^2 B_{MN} (\overline{c_{66}} A_{MN} \\ + c_{66} \beta_{1M}^2) \cos(k_0 \beta_{2MN} y) = 0 \end{aligned} \quad (55)$$

Because  $T_{11}$  and  $T_{12}$  cannot be satisfied exactly for all  $y$  using only a finite number of modes, a Galerkin form approximation will be utilized. Since  $T_{11}$  is odd in  $y$ , and  $T_{12}$  is even in  $y$ , then

$$\int_{-\frac{L_2}{2}}^{\frac{L_2}{2}} T_{11} \sin(k_0 y) dy = 0 \quad (56)$$

$$\int_{-\frac{L_2}{2}}^{\frac{L_2}{2}} T_{12} \cos(k_0 y) dy = 0 \quad (57)$$

Integrating equations (56) and (57) results in,

$$\begin{bmatrix} G_{IM} \end{bmatrix} \begin{bmatrix} C_M \end{bmatrix} = 0 \quad (58)$$

where,

$$G_{IM} = \frac{\sin\left(\frac{k_0 \beta_{1M} L_1}{2}\right)}{\beta_{1M}} \sum \frac{B_{MN}(c_{11} \beta_{1M}^2 A_{MN} + c_{12} \beta_{1M}^2 \beta_{2MN}^2) \sin\left(\frac{\pi \beta_{2MN} - 1}{2}\right) - \sin\left(\frac{\pi \beta_{2MN} + 1}{2}\right)}{\beta_{2MN} - 1} \quad (59)$$

and

$$G_{2M} = \cos \frac{k_0 \beta_{1M} L_1}{2} \sum B_{MN} (c_{66} A_{MN} + c_{66} \beta_{1M}^2) \cdot \frac{\sin\left[\frac{\pi}{2} \beta_{2MN} - 1\right]}{\beta_{2MN} - 1} + \frac{\sin\left[\frac{\pi}{2} \beta_{2MN} + 1\right]}{\beta_{2MN} + 1} \quad (60)$$

Nontrivial solutions result when,

$$\det \begin{bmatrix} G_{IM} \end{bmatrix} = 0 \quad (61)$$

Choices of  $\omega$  which satisfy equation (61) are resonances of the crystal.

#### MOTIONAL CAPACITANCE AND ENERGY

The capacitance between two isolated conductors is defined as,

$$C = \frac{Q}{V} \quad (62)$$

where  $Q$  is the charge on one of its conductors and  $V$  is the potential difference between them. For the electroded rectangular piezoelectric resonator,

$$Q = \iint_S D_y ds \quad (63)$$

From equation (8), and once again neglecting all potential and electrical term variations with respect to  $x$  and  $z$ , then

$$D_y = e_{26} \frac{\partial u_x}{\partial y} - \xi_{22} \frac{\partial \phi}{\partial y} \quad (64)$$

Now,

$$\nabla \cdot D = \rho_{free} \quad (65)$$

but since  $\rho_{free} = 0$  for quartz,

$$\nabla \cdot D = 0 \quad (66)$$

therefore,

$$\nabla \cdot D_y = e_{26} \frac{\partial^2 u_x}{\partial y^2} - \xi_{22} \frac{\partial^2 \phi}{\partial y^2} = 0 \quad (67)$$

where  $\phi = 0$  at  $y = \pm \frac{L_2}{2}$ . Solving equation (67)

for  $\frac{\partial^2 \phi}{\partial y^2}$  and integrating twice with respect to  $y$ ,

$$\phi = \frac{e_{26}}{\xi_{22}} \left( u_x \right) + y A(x, z) \quad (68)$$

At  $y = \frac{L_2}{2}$ ,

$$\phi = \frac{e_{26}}{\xi_{22}} u_x \left( x, \frac{L_2}{2} \right) \sin \left( \frac{n \pi z}{2L_z} \right) + \frac{L_2}{2} A(x, z) \quad (69)$$

and thus,

$$A(x, z) = \frac{-2e_{26}}{L_2 \xi_{22}} u_x \left( x, \frac{L_2}{2} \right) \sin \left( \frac{n \pi z}{2L_z} \right) \quad (70)$$

Differentiating equation (68) with respect to  $y$ , then

$$\frac{\partial \phi}{\partial y} = \frac{e_{26}}{\xi_{22}} \frac{\partial \left[ u_x(x, y) \sin \left\{ \frac{n \pi z}{2L_z} \right\} \right]}{\partial y} + A(x, z) \quad (71)$$

which may be rewritten as,

$$- \xi_{22} A(x, z) = e_{26} \frac{\partial \left[ u_x(x, y) \sin \left\{ \frac{n \pi z}{2L_z} \right\} \right]}{\partial y} - \xi_{22} \frac{\partial \phi}{\partial y} \quad (72)$$

Comparing equation (72) to equation (64) gives,

$$D_y = - \xi_{22} A(x, z) \quad (73)$$

and thus,

$$D_y = \left( \frac{2e_{26}}{L_2} \right) \cdot \left( u_x \left( x, \frac{L_2}{2} \right) \sin \left[ \frac{n \pi z}{2L_z} \right] \right) \quad (74)$$

Substitution of equation (74) into equation (63) gives,

$$Q = \frac{2e_{26}}{L_2} \int_0^{L_z} \int_{-L_1/2}^{L_1/2} u_x \left( x, \frac{L_2}{2} \right) \sin \left[ \frac{n \pi z}{2L_z} \right] dx dz \quad (75)$$

The energy stored in a capacitor is given by,

$$W = \frac{1}{2} CV^2 \quad (76)$$

which may be written as,

$$W = \frac{1}{2} QV \quad (77)$$

Now since equation (62) may be written as,

$$C = \frac{Q^2}{QV} \quad (78)$$

the denominator of equation (78) is just equal to twice the stored energy in the capacitor.

The motional capacitance of a piezoelectric resonator is that portion of the total device capacitance which arises from the mechanical vibration of the quartz itself. Now since the total stored energy in the system,  $W$ , equals the maximum kinetic energy,  $T$ , of the system, then,

$$W = T = \frac{1}{2}mv^2 = \frac{1}{2} \iiint \rho(\dot{u}_x^2 + \dot{u}_y^2) dv \quad (79)$$

Therefore upon substitution, and since  $QV = 2W$ ,

$$QV = \rho \omega^2 \int_0^{L_z} \int_{-\frac{L_x}{2}}^{\frac{L_x}{2}} \int_{-\frac{L_y}{2}}^{\frac{L_y}{2}} (u_x^2 + u_y^2) \sin^2 \left[ \frac{n\pi z}{2L_z} \right] dx dy dz \quad (80)$$

Now since,

$$C_{\text{mot}} = \frac{Q^2}{QV} \quad (81)$$

then,

$$C_{\text{mot}} = \frac{4e_{26}^2 \left\{ \int_0^{L_z} \int_{-\frac{L_x}{2}}^{\frac{L_x}{2}} \int_{-\frac{L_y}{2}}^{\frac{L_y}{2}} u_x(x, \frac{L_z}{2}) \sin \left( \frac{n\pi z}{2L_z} \right) dx dz \right\}^2}{\rho \omega^2 \int_0^{L_z} \int_{-\frac{L_x}{2}}^{\frac{L_x}{2}} \int_{-\frac{L_y}{2}}^{\frac{L_y}{2}} (u_x^2 + u_y^2) \sin^2 \left( \frac{n\pi z}{2L_z} \right) dx dy dz} \quad (82)$$

which may be written as,

$$C_{\text{mot}} = \frac{4e_{26}^2 \left[ \frac{8L_z}{\pi^2} \right] T_1}{\rho \omega^2 L_z^2 (T_2 + T_3)} \quad (83)$$

where,

$$T_1 = \int_{-\frac{L_x}{2}}^{\frac{L_x}{2}} u_x(x, \frac{L_z}{2}) dx \quad (84)$$

$$T_2 = \int_{-\frac{L_x}{2}}^{\frac{L_x}{2}} \int_{-\frac{L_y}{2}}^{\frac{L_y}{2}} u_x^2(x, y) dx dy = \text{Energy in X-TS mode} \quad (85)$$

$$T_3 = \int_{-\frac{L_x}{2}}^{\frac{L_x}{2}} \int_{-\frac{L_y}{2}}^{\frac{L_y}{2}} u_y^2(x, y) dx dy = \text{Energy in Flexure mode} \quad (86)$$

Values of  $L_x$  and  $L_y$  for which  $\left[ \frac{T_2}{T_3} \right]$  are large correspond to resonator widths which result in minimized coupling between the X-TS mode and the flexure mode.

#### COMPUTER DESIGN

A computer program has been written based upon this model, to be used for the design of fundamental mode AT rectangular resonators. The program predicts resonator width to thickness ratios which result in minimized coupling between the X-thickness shear mode and the flexure mode, thereby resulting in activity dip free temperature performance. The computer program's output is graphically represented in figures 2 and 3. From figure 2 it can be

seen that values of  $x$  for which the  $\left[ \frac{T_2}{T_3} \right]$  ratios are

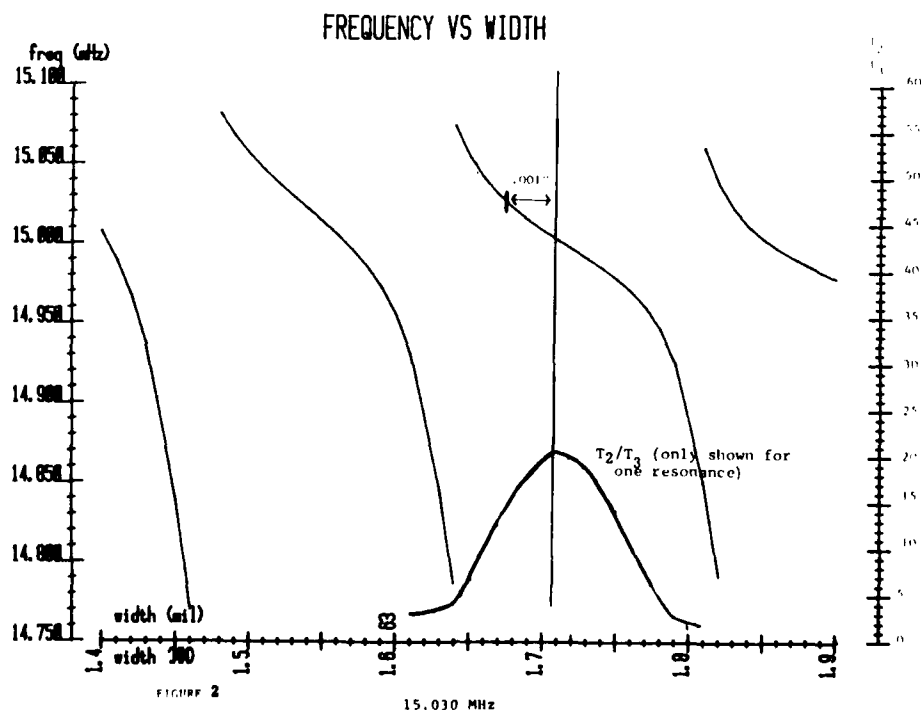
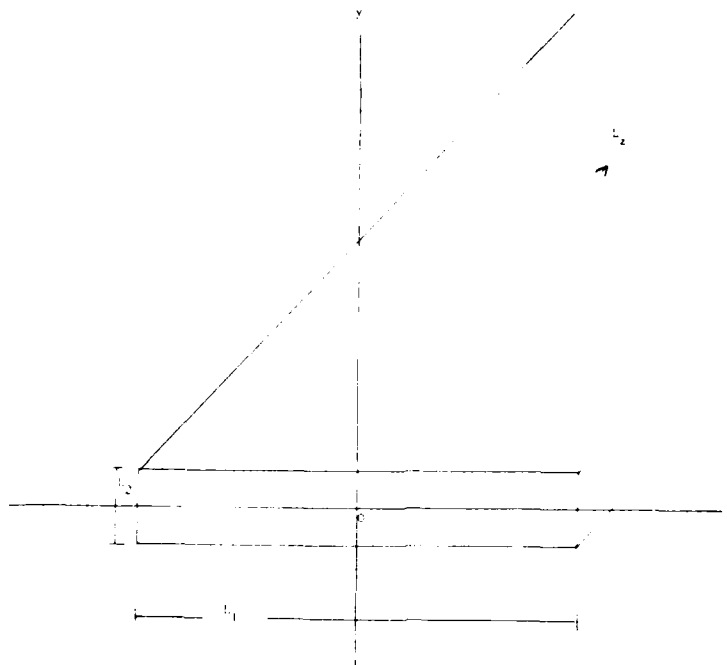
large, (where again  $T_2$  is the energy in the X-thickness shear mode and  $T_3$  is the energy in the flexure mode), correspond to resonator width to thickness ratios which result in minimized coupling. Examples of the impact of this mode coupling on resonator temperature performance can be seen from figures 4 and 5. The experimentally determined frequency-width pairs are typically .0005" to .001" less than the computer program's indicated optimum frequency-width pair.

#### CONCLUSION

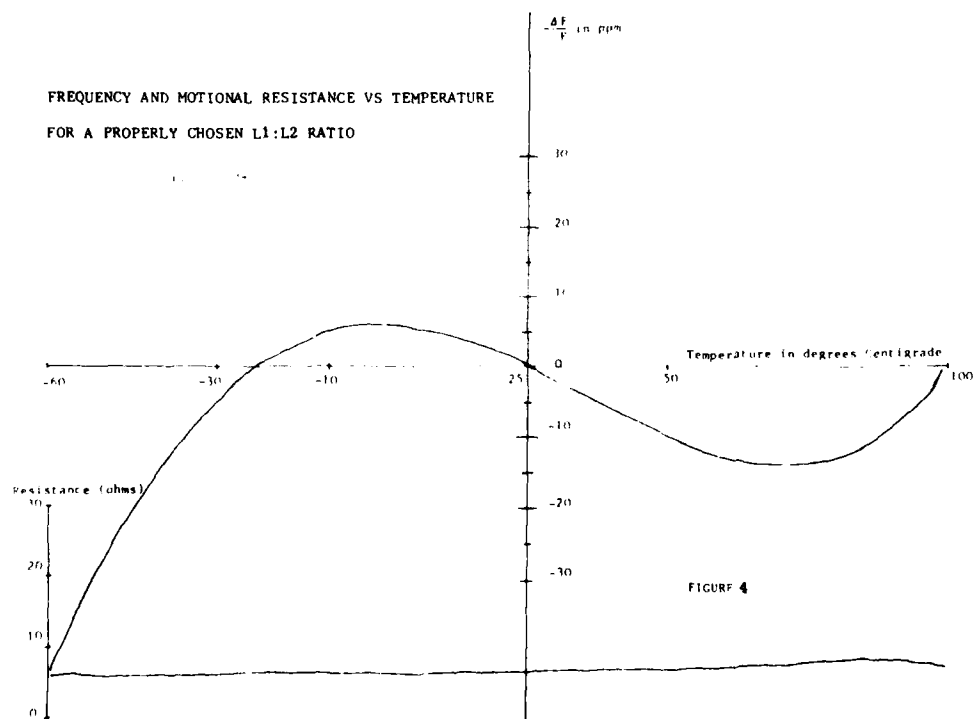
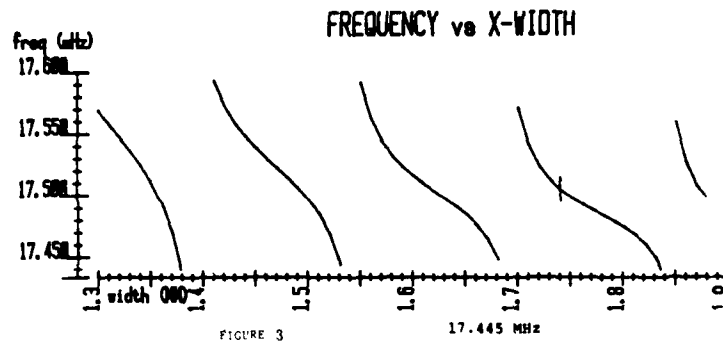
A simplified version of the Milsom model has been developed which, by scaling the equations as shown by Mindlin, contains all real equations. The formulation models X-thickness shear to flexural mode coupling only, and assumes a fully electroded plate which is clamped at one end. Since free edge boundary conditions cannot be satisfied using a finite number of modes, a Galerkin form approximation was used at the (X) edges. Expressions were developed which relate the  $L_x$ ,  $L_y$  and  $L_z$  dimensions of the rectangular resonator to the motional capacitance, and the resultant energies in the X-thickness shear and flexure modes. A computer program has been written based upon this model, and its predictions were shown to be in good agreement with experimental data.

#### REFERENCES

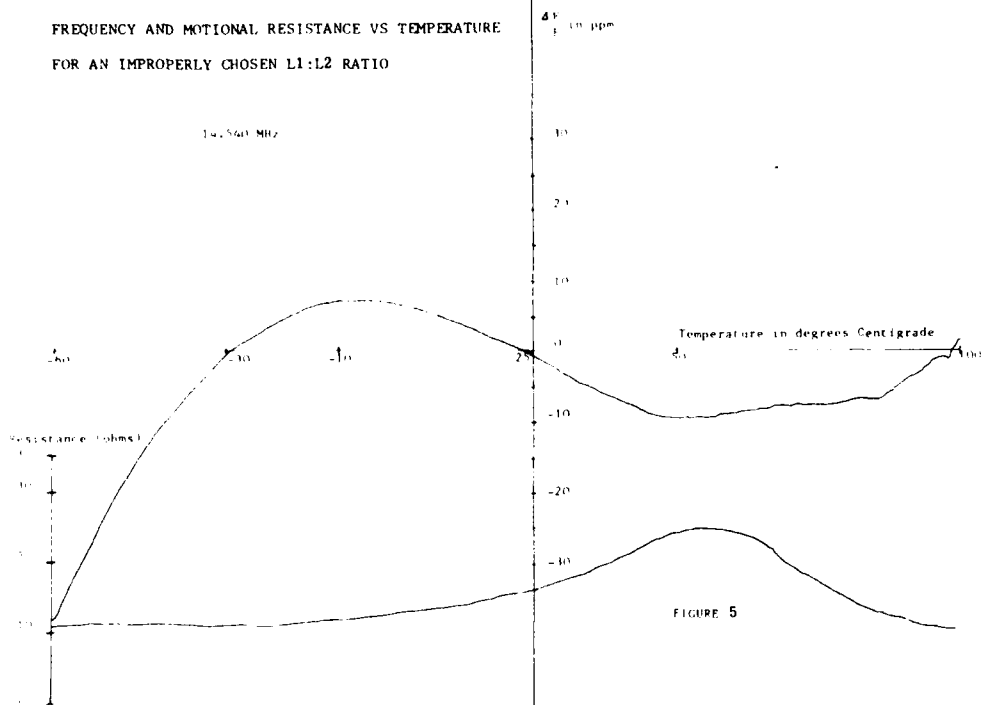
1. R.F. Milsom, D.T. Elliott, and M. Redwood, "Three-dimensional Mode-Matching Theory of Rectangular Bar Resonators using Complex Wavenumbers," Proceedings of the 35th Annual Symposium on Frequency Control, pp. 174-186, 1981.
2. R.D. Mindlin, "Third Overtone Quartz Resonator," Proceedings of the 36th Annual Symposium on Frequency Control, pp. 3-21, 1982.
3. R.D. Mindlin, "Thickness-Shear and Flexural Vibrations of Crystal Plates," Journal of Applied Physics, 22(3), pp. 316-323, 1951.
4. H.F. Tiersten, "Analysis of Trapped Energy Resonators Operating in Overtones of Coupled Thickness-Shear and Thickness-Twist," J. Acoust. Soc. Am., Vol 59, p 879, 1976.
5. P. Fenlon, L. Dworsky, J. Lawrence, and D. Ryback, "The Physical Constants of Quartz," 5th Quartz Crystal Conference Proceedings, pp. 176-187, 1983.
6. L. Dworsky and G. Kennedy, "Air-Gap Probe Evaluation of Thin Quartz Plates," Proceedings of the 35th Annual Symposium on Frequency Control, pp. 237-243, 1981.







FREQUENCY AND MOTIONAL RESISTANCE VS TEMPERATURE  
FOR AN IMPROPERLY CHOSEN L1:L2 RATIO



## HARMONIC AND ANHARMONIC MODES OF AK-CUT CRYSTAL RESONATORS

Ferdinand Euler and Alfred Kahan

Solid State Sciences Division  
Rome Air Development Center  
Hanscom Air Force Base, MA 01731

Summary

We report static frequency-temperature characteristics,  $f(T)$ , for doubly rotated quartz vibrating in thickness shear c-mode with angular combinations  $30^\circ \leq \phi \leq 46.1^\circ$  and  $21^\circ \leq \theta \leq 28.44^\circ$ . The  $f(T)$  of these orientations are similar to AT- and BT-cuts and, in good agreement with theoretical predictions, have turnover temperatures between 80 and 115  $^\circ\text{C}$ . These turnover temperature values are relatively insensitive to crystallographic misalignments. Compared to the fundamental mode of vibrations, the 3rd overtone shows a larger number of modes and the resonances are weaker. There are also indications of activity dips and coupling with spurious resonances. The frequencies of the harmonic and anharmonic modes are in fairly good agreement with calculations based on a trapped-energy resonator model, including effects of coupled thickness shear and thickness twist vibrations. Computations indicate that for several orientations the 3rd harmonic is seriously affected by interaction between the a- and c-modes. This leads to exponentially decaying vibrations and impaired energy trapping.

**Key Words:** Quartz, Crystal Resonators, Frequency Standards, Vibration Spectra

Introduction

In previous publications<sup>1,2</sup> we described the existence of a set of doubly rotated quartz orientations for thickness shear mode of vibrations. These crystals have turnover temperatures,  $T_{to}$ , in the range of practical interest for ovenized oscillators, and possess static frequency-temperature,  $f(T)$ , characteristics similar to AT- or BT-cuts. At the same time, the  $T_{to}$  values of these crystals are relatively insensitive to crystallographic misalignments. We designated these quartz orientations as the AK-cut. Figure 1 shows the crystallographic positions of these cuts relative to the Y-, X-, AT-, SC-, and BT-cut orientations. For  $T_{to}$  of practical interest, the AK-cut occupies the crystallographic region of  $30^\circ \leq \phi \leq 45^\circ$  and  $20^\circ \leq \theta \leq 29^\circ$ . We show three calculated  $T_{to}$  isotherms, 80, 100, and 120  $^\circ\text{C}$ , respectively. With the AK-cut, a  $T_{to}$  tolerance of 5  $^\circ\text{C}$  requires an angular precision of a few degrees, rather than the minutes or seconds of arc necessary for the AT- or SC-cuts. The AT-, SC-, and AK-cuts are applied in the slow shear vibration mode, the c-mode, and the BT-cut is utilized in the fast shear vibration mode, the b-mode.

We reported<sup>2</sup> experimental  $f(T)$  of seven orientations, measured on 10 MHz 3rd overtone quartz resonators, vibrating in the lowest fundamental or 3rd harmonic,  $f_{100}$  or  $f_{300}$ , respectively. The measured  $f(T)$  and  $T_{to}$  values agree well with theoretical predictions. In this publication we show data of seven additional orientations. Based on the experimental confirmation of calculated  $T_{to}$  for 14 orientations, one can now define angular combinations for specified  $T_{to}$  values with a

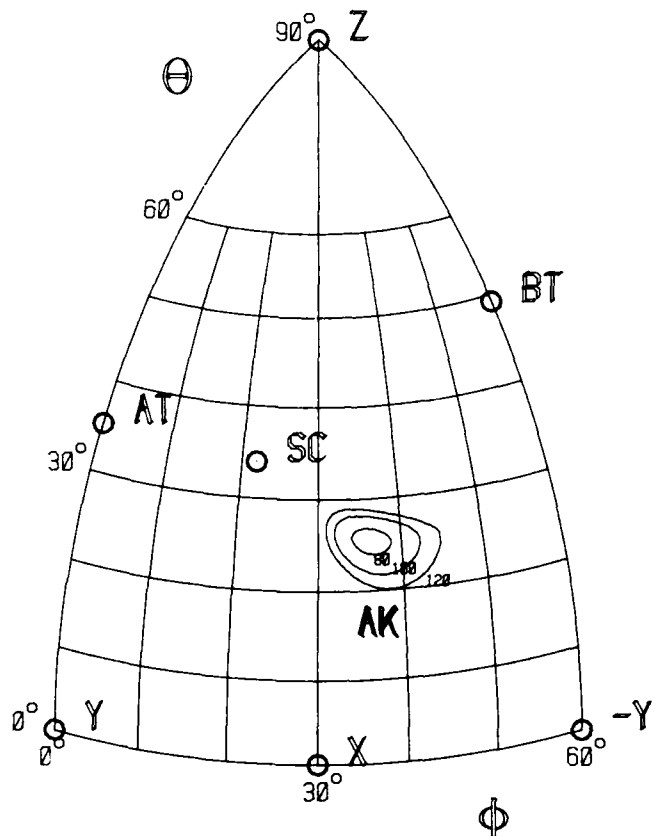


Figure 1. Synopsis of singly and doubly rotated quartz orientations utilized for precision resonators. The AK-cuts are depicted by turnover temperature isotherms, demonstrating low sensitivity to crystallographic misalignment.

high degree of confidence. We developed an automatic frequency scanning technique which enables us to track the mode spectra over a large temperature range. We recorded anharmonic  $f_{1mp}$  and  $f_{3mp}$  frequency spectra and find that, compared to the fundamental, the 3rd overtone modes exhibit an abundance of anharmonics, spurious resonances, activity dips, and in some cases, no clearly dominant resonance which can be designated as the main 300 mode. The interfering spurious modes have fast moving  $f(T)$  characteristics and strongly couple when they cross major resonances.

The analysis developed by Tiersten and Stevens<sup>3</sup> for contoured SC-cut trapped energy resonators, which includes the effects of coupled thickness shear and thickness twist vibrations, has been applied

to calculate  $f_{\text{mp}}$  values for AK-cut orientations. For most orientations the analysis predicts harmonic and anharmonic mode patterns, and these agree well with measured values. For other orientations, calculations yield complex  $f_{\text{mp}}$  values, indicating that these vibrations decay and fail to trap the energy. This lack of energy trapping agrees with measured weaknesses of the 3rd overtone modes.

#### Experimental Procedures

The quartz resonators utilized for this study were fabricated at Frequency Electronics, Inc., as 10 MHz 3rd overtone plano-convex units having a blank diameter of 13.8 mm (0.550 in), radius of curvature of 30.285 cm (1.75 diopters), mass loading of 0.0029, and maximum crystal thicknesses between 0.55 and 0.64 mm. In Refs. 1 and 2 we presented  $f(T)$  and  $T_{\text{co}}$  results on seven combinations of rotation angles ( $\Phi, \Theta$ ). For this study we selected an additional seven orientations with the aim to cover the crystallographic region predicting  $T_{\text{co}}$  values of practical interest. The Miller indices of the lattice planes used to fabricate the resonators included [111], [322], [323], [211], [212], and [312]. For each orientation 6 resonators were fabricated in one batch and under the same conditions.

The resonators are placed in a heater and connected through a  $\Pi$ -network to a network analyzer with a dynamic range exceeding 100 dB. A programmable synthesizer, with the upper limit at 13 MHz, provides a step-wise variable frequency. Temperature is measured with a thermocouple attached to the resonator enclosure and connected to a digital thermometer. A programmable temperature controller provides linear ramps with adjustable rates, e.g. 0.2 or 0.4 °C/minute. A data bus connects these components to a desktop computer and printer for automatic data recording.

Resonators from each orientation were frequency scanned first at room temperature and near 150 °C for resonance modes between 3.3 and 13 MHz. This scanning range includes all the fundamental and the 3rd overtone c-, and b-modes, as well as the fundamental a-modes. The scanning is performed typically in steps of 5 Hz and is set to detect resonances exceeding 2 dB above the parallel capacitance background. The major resonance modes of interest are then individually tracked between room temperature and 150 °C, with temperature intervals of 0.5 to 1 °C, and the resonance frequency, resistance and motional inductance are determined. In this case, the controlling program calls for repetitive frequency sweeping through the series resonance in small frequency steps. Selected 5th overtone frequency scans and temperature tracks were also made with a high-frequency network analyzer.

Figure 2 shows the frequency and resonance resistance data obtained from this type of measurement. For this particular resonator, in the temperature range between 50 and 100 °C, the b-mode contains three mild frequency jumps but strong and narrow resistance loss peaks. Figure 3 shows on an enlarged scale the 55 °C loss peak strength in 0.5 °C intervals. We note a fast moving spurious mode through the major resonance and a corresponding decrease in peak height.

In order to determine more accurately the influence of activity dips, coupling of spurious modes and major resonances, and interaction of major modes, we automated the frequency scan as a function of temperature measurements. The frequency is swept in 1500 steps to cover frequency ranges of up to 100 kHz,

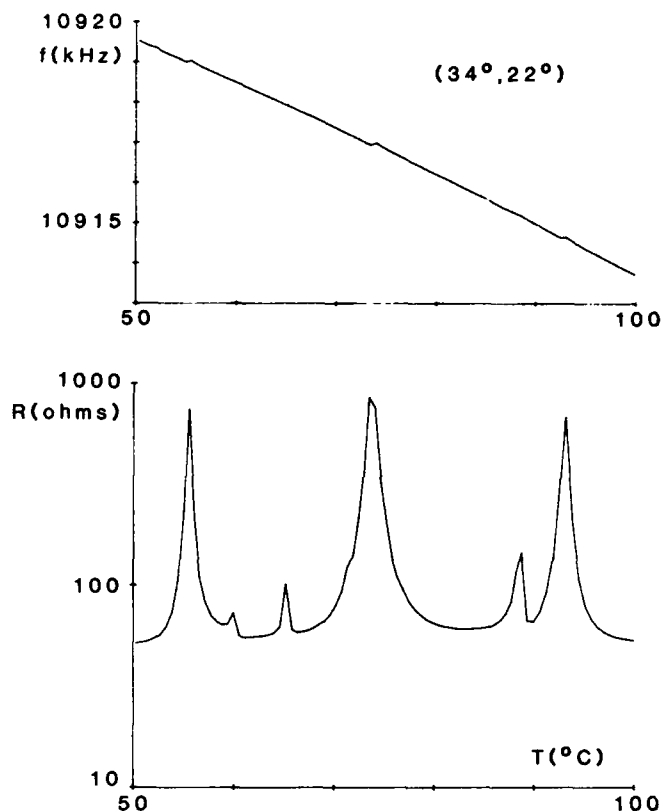


Figure 2. Frequency and resonance resistance as a function of temperature for b-mode, showing frequency jumps and resistance peaks.

taking about 45 seconds for each sweep. As the temperature is ramped with 0.4 °C/min, the sweep is repeated at predetermined intervals, for example, every 5 °C. The resulting mode spectra are automatically plotted after each measurement and recorded on tape for later data processing. Figure 4 shows an example of such a plot for orientation (40.9, 23.55), frequencies between 9.97 and 10.03 MHz, and temperatures between 30 and 150 °C. This is the frequency region where one would expect the strong  $f_{300}$  resonance. Instead, we find the region infested with spurious modes, resonance strengths transferred between adjacent modes and rising and falling as a function of temperature, and this results in a complete obliteration of the major mode. This type of a graphic display is of great assistance in tracking several mode amplitudes and frequency positions simultaneously as a function of temperature.

#### Results and Discussion

Figure 5 shows calculated  $T_{\text{co}}$  isotherms between 75 and 160 °C for c-mode vibrations as a function of rotation angles ( $\Phi, \Theta$ ). The  $T_{\text{co}}$  calculations for the AK-cut are described in Refs. 1 and 2, and are based on the temperature coefficients of elastic constants derived in Ref. 4. These calculations do not distinguish between fundamental and overtone modes. Figure 5 also shows the experimental  $T_{\text{co}}$  values of the 100 modes for all 14 orientations. The agreement between prediction and measurement is reasonable, considering the fact that the temperature coefficients of elastic constants utilized for these computations are

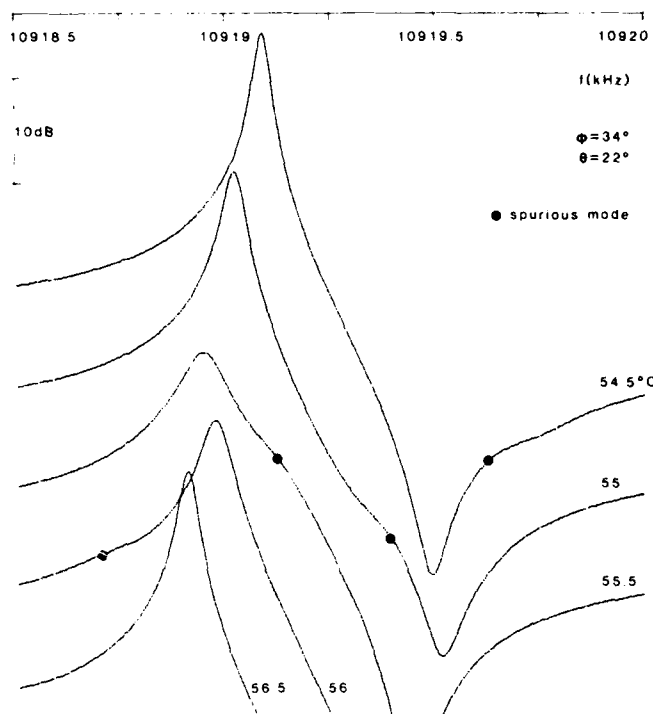


Figure 3. Interaction between b-mode and fast moving spurious mode for the 55 °C resistance peak shown in Fig. 2.

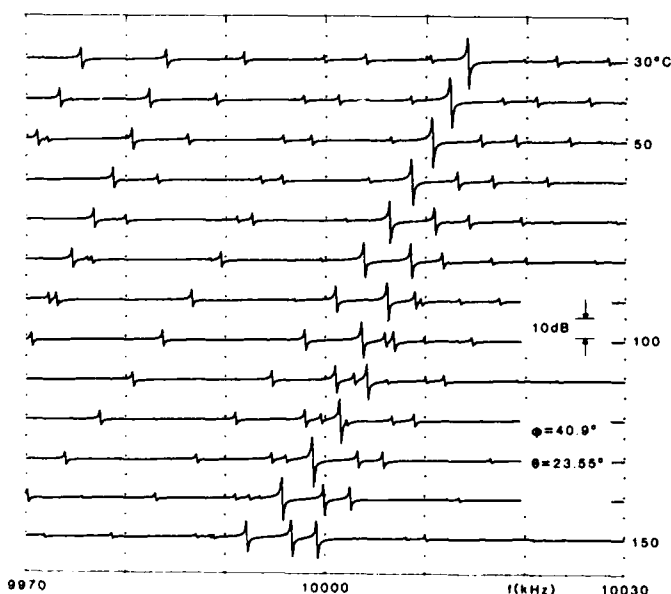


Figure 4. Temperature track of 3rd overtone mode spectra for (40.9, 23.55) orientation.

derived from temperature coefficients of frequencies of crystals with vastly different angular orientations than the AK-cut. Also, there is good correlation between calculated and measured frequency-thickness

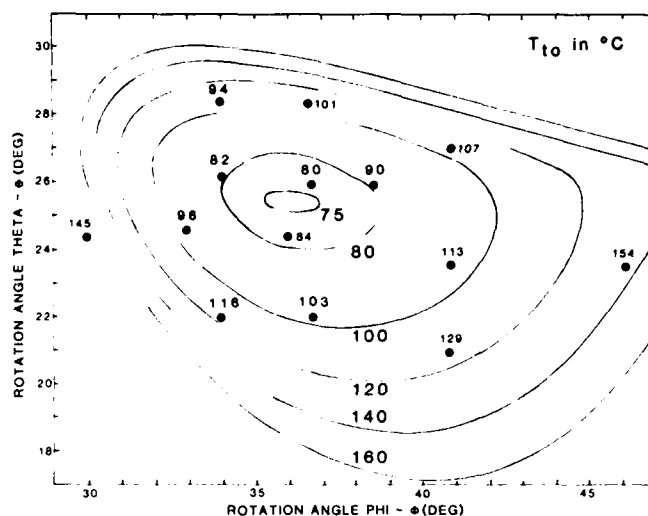


Figure 5. Calculated turnover temperature isotherms for AK-cut. Measured values in degrees centigrade are indicated next to the experimental points.

constants, as well as the frequency separation of the b- and c-modes. Based on these results, we feel confident that the major claim for the AK-cut crystal, angular insensitivity of  $T_{10}$  in the temperature range of interest to ovenized oscillators, is substantiated.

For the AK-cut, similar to other doubly rotated cuts, we expect intricate anharmonic mode spectra, especially for the overtone modes. The practical development and utilization of the AK-cut will depend on the frequency separation and strength of the b-mode and nearby anharmonic c-modes. The experimental 3rd overtone 10 MHz AK-cut resonators were fabricated with diameter, contour, and electrode dimensions and thicknesses developed for the SC-cut. Best results for an AT-cut are obtained for the 5th overtone 5 MHz resonator. The ideal geometry and configuration for the AK-cut resonator has not yet been determined. In order to obtain some insight for these parameters, we measured all resonators in the fundamental, 3rd overtone, and for two specific cases in the 5th overtone.

Tiersten and Stevens<sup>3</sup> developed a formalism for the SC-cut contoured trapped-energy resonator, which includes effects of coupled thickness shear and thickness twist vibrations. This analysis predicts very well the harmonic and anharmonic modes of the singly rotated AT-cut and the doubly rotated SC-cut. In principle, it is also applicable to other cuts. We applied this formalism to calculate the harmonic and anharmonic  $f_{nmp}$  for the AK-cut orientations, and find that for all AK-cut angles the lowest frequency,  $f_{100}$ , is consistent with the value calculated from the frequency-thickness constant. Table I shows the calculated frequency separations of the lowest anharmonic modes from  $f_{100}$  for one selected orientation, (36.58, 26.0). For symmetric crystal configurations, m and p values are restricted to even numbers. The 102 mode is situated approximately 80 kHz from the 100 mode, and the higher inharmonic modes appear in two doublets, followed by one triplet. The frequencies, for the range of AK-cut angles, vary within a few kHz of the values shown.

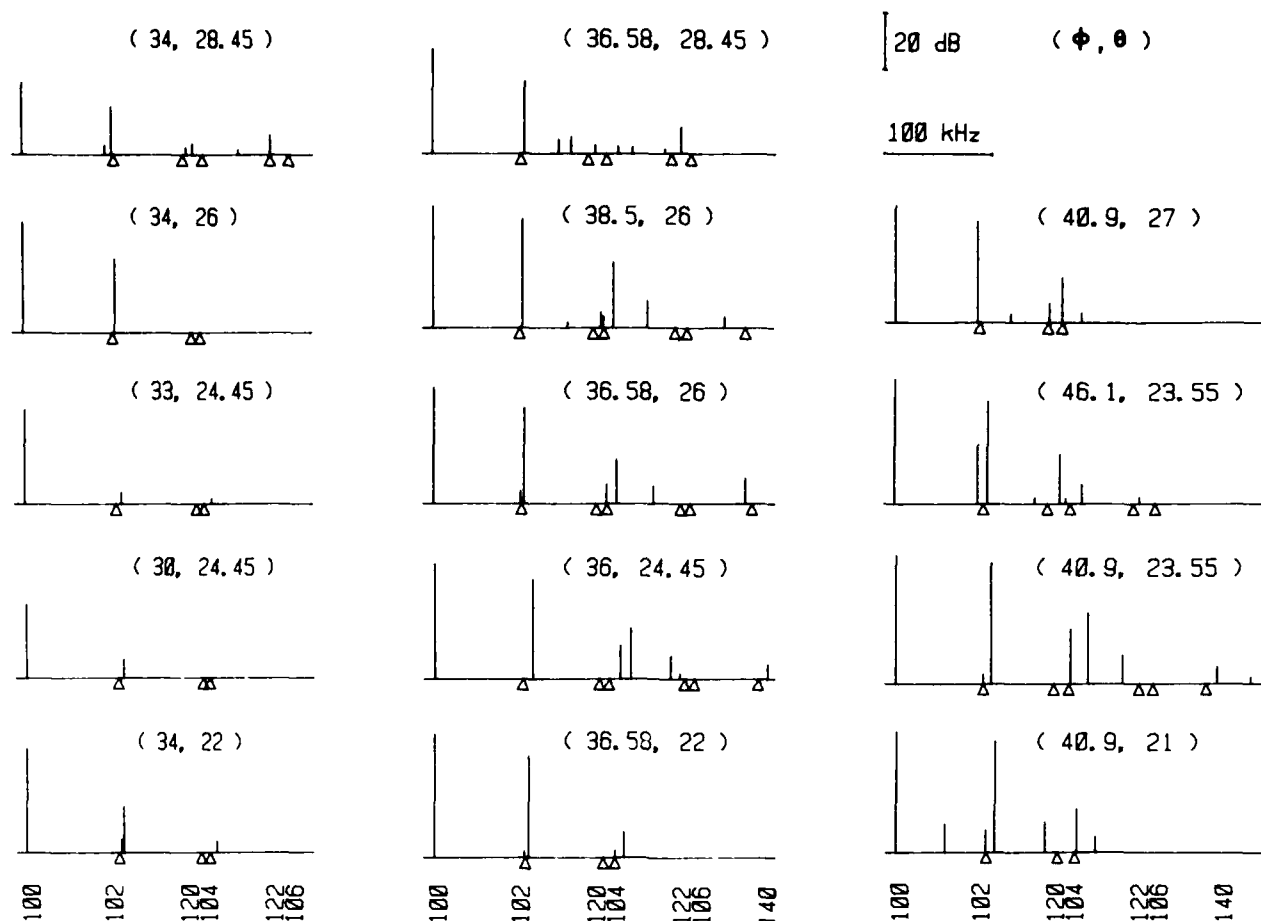


Figure 6. Fundamental c-mode spectra for 14 AK-cut crystal  $(\Phi, \Theta)$  orientations. Triangles indicate calculated mode frequencies.

Table 1. Calculated  $f_{\text{imp}} - f_{100}$ , in kHz, for AK-cut crystal orientation  $(36.58, 26.0)$ , 1.75 diopters, and mass loading 0.0029.

nmp:	102	120	104	122	106	140	124	108
Separation:	81	150	160	228	237	294	303	313

Figure 6 shows the fundamental mode frequency spectra for the 14 orientations under investigation. The vertical bars indicate the measured amplitudes, and their horizontal spacing shows the measured frequency separations relative to  $f_{100}$ . The triangles represent the calculated  $f_{\text{imp}}$  values. For all orientations, the 102 mode assignment is reasonably accurate, within 5 kHz, and the 100 and 102 are always the strongest and second strongest modes. The higher inharmonics have weak measured counterparts, and specific assignments are rather uncertain. For orientations with the lowest  $T_{10}$ , 80-85 °C range, the resonance resistance values of the 102 mode are 3.7 to 12 times as high as for the corresponding 100 mode. It is then anticipated that an oscillator can be operated in the 100 mode without specialized circuitry to suppress the 102 mode. Similarly, for these orientations, the frequency separation and relative strength of the b-mode do not seem to be a problem.

Several orientations show measured modes in frequency regions not predicted by computations. Most noticeable of these are two weak, but not negligible, "in-between" resonances, located 40 kHz above the 100 and 102 modes, respectively. For the  $(33.0, 24.44)$  orientation we measured the mode spectra of all available resonators, with a 2 dB floor, and find that the two extra resonances occur only in two of the six units, while the other four resonators show only the 100, 102, and a very weak 104 mode. Subsequently, we measured the mode spectra of the 6 resonators for other orientations as well, and find similar statistics, that is, some do and some do not show the additional modes. For  $(40.9, 21.0)$ , they occur in 5 of 6 units. We conclude, that the extra modes are not intrinsic to the AK-cut orientations, but are related to fabrication processes affecting crystal symmetry.

We also carried out  $f_{3\text{mp}}$  calculations and encountered the following peculiarity. The coefficient  $\sqrt{M_n}$ , defined in Eq. 3.16 of Ref. 3, contains the expression  $C = \cot(Kn\pi/2)$  in one of its terms, with

$K = \sqrt{c_c/c_a}$ , where  $c_c$  and  $c_a$  are the wave velocities of the fundamental c- and a-modes, respectively. Values for K range from 0.58 to 0.73. For  $K = 2/3$  and  $n = 3$ ,  $C = \pm\infty$ . Below this pole, C is strongly negative, makes  $\sqrt{M_n}$  imaginary and  $f_{3\text{mp}}$  complex, and it indicates that the vibrations decay exponentially and the energy

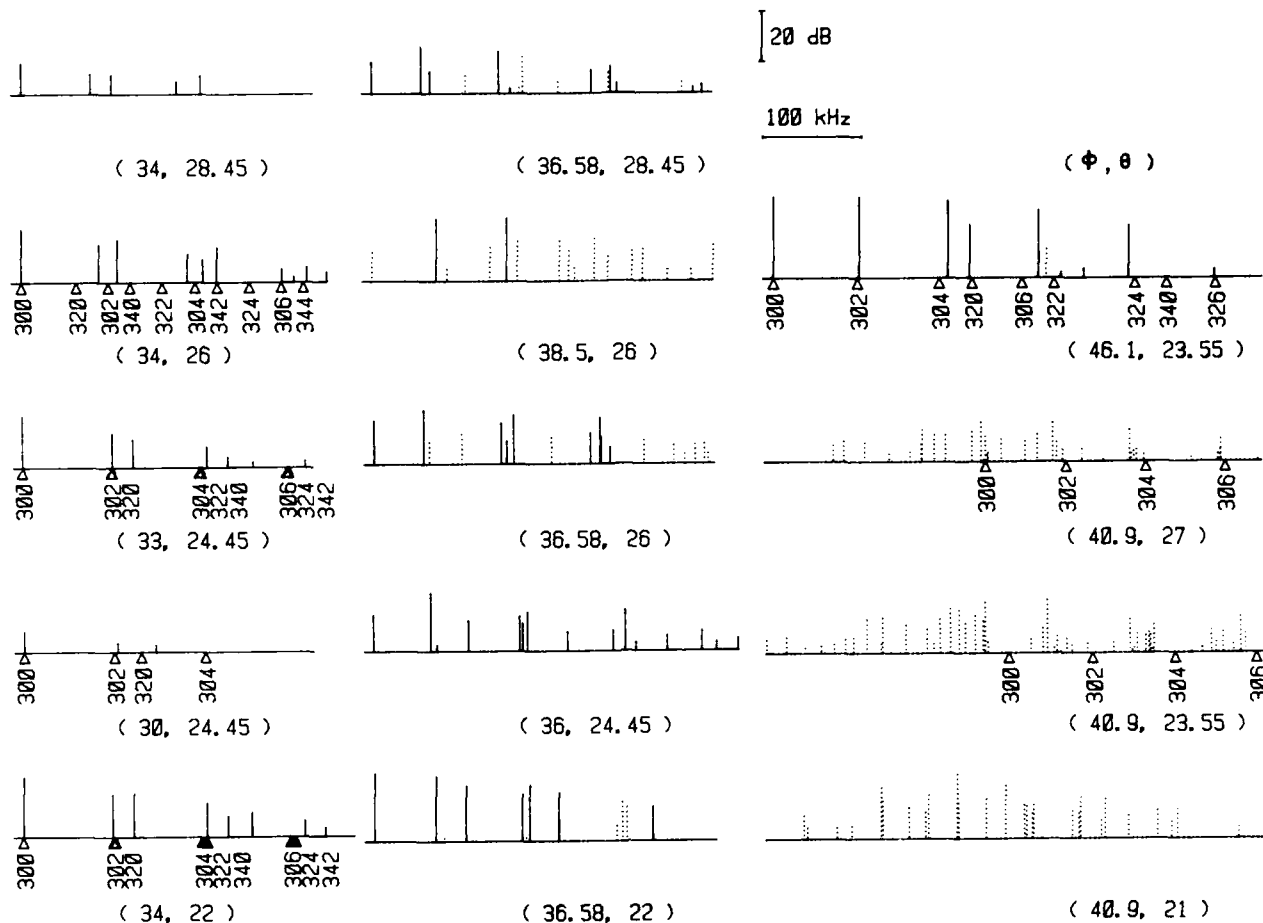


Figure 7. 3rd overtone mode spectra for 14 AK-cut crystal ( $\Phi, \theta$ ) orientations. Solid bars are the c-modes, dotted bars are spurious modes, and the triangles show the calculated mode frequencies.

is not trapped. This is the case for all orientations with  $36^\circ \leq \Phi \leq 38.5^\circ$  and (34, 28.45). For (40.9, 21), we calculate  $K = 0.667$ , that is, C is very close to the pole on the positive side, and it yields very high values for  $M_n$  and  $f_{3mp}$ . With higher angles, K increases, C moves away from the pole and the frequency spectra return to more normal patterns. This peculiar interaction between the c- and a-modes indicates that the 3rd harmonic may be undesirable for operating many of the AK-cut orientations.

Figure 7 shows the room temperature 3rd overtone mode spectra for the 14 orientations and indicates the position of calculated  $f_{3mp}$ . The mode sequence, and their relative separation, are more angle dependent than their  $f_{1mp}$  counterparts and are influenced by proximity to the pole in C. There is fairly good agreement between calculated and measured 300 modes, but there are substantial deviations for the anharmonic modes. Most of the spectra are for resonators that did not exhibit the two additional fundamental modes, and in this respect we expect that they also be the "cleanest" in the 3rd overtone. Compared to the fundamental, the number of observed modes are more numerous and harder to assign. The nature of the modes was investigated by measuring all resonators at  $150^\circ\text{C}$ , and also tracking selected modes as a function of tempera-

ture. This enabled us to distinguish two kinds of modes. The solid lines denote "c-type" vibrations, that is, they have  $T_0$ . The dotted lines indicate fast moving modes which do not appear to have turnovers, but exhibit reasonably well defined  $f(T)$  curves. However, they are not the higher frequency b-modes.

For  $\Phi = 40.9^\circ$  we do not observe turnovers for any 3rd overtone mode. In addition, all resonances are also seriously affected by strong coupling with spurious modes. Figure 4 showed an example of this behavior. At  $30^\circ\text{C}$  there is a series of weak modes, and one fairly strong resonance near 10014 kHz. As the temperature rises, however, this mode becomes weaker, couples to several spurious modes, and its identity becomes confused. The  $f_{3mp}$  mode spectra shown in Fig. 7 for  $\Phi = 40.9^\circ$  are similarly affected by spurious modes. This obliteration of c-modes can be understood as a physical manifestation of highly negative  $M_n$  and supports the theoretical results of Tiersten and Stevens.

The difficulties encountered in calculating the 3rd overtone do not extend to the 5th overtone. We calculate real 5th overtone spectra for all angular orientations, except for (46.1, 23.55), where we approach another pole of C expected for  $K = 4/5$ . Figure 8 shows observed and calculated mode spectra comparisons

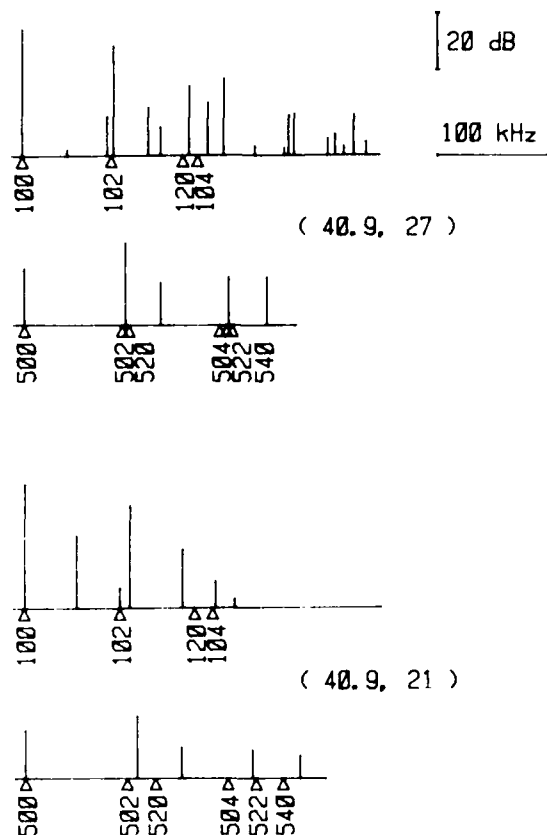


Figure 8. Fundamental and 5th overtone c-mode spectra for two selected orientations.

of the fundamental and 5th overtone for two  $\phi = 40.9^\circ$  orientations,  $\theta = 21^\circ$  and  $27^\circ$ . No spurious mode problems are encountered. This indicates that from a practical point of view a 5th overtone crystal is preferable.

Table 2 presents a synopsis of observed  $T_{to}$  values for the 14 orientations, both for fundamental and for overtone modes. We also indicate possible mode assignments. The 100 mode  $T_{to}$  data were plotted in Fig. 5, and these agree well with theoretical predictions. The 102 mode  $T_{to}$  values are lower, and the differences range from about 70 to 6  $^\circ\text{C}$ . We did not compute the temperature dependences of the anharmonic modes, and we are uncertain why we observe these large  $T_{to}$  differences. For some orientations we measured the temperature dependence of the two "in-between" modes and find regular  $f(T)$  characteristics with reasonable turnover temperatures. These values are also listed in Table 2, and they support the hypothesis that these modes are "c-type" vibrations.

Table 2 also shows  $T_{to}$  data for  $f_{3mp}$ . We do not observe any  $f_{3mp}$  turnovers for  $\phi = 40.9^\circ$ , due to the severe coupling with spurious modes. For lower  $\phi$ -angles the 100 mode has a lower  $T_{to}$  than the 300, and the reverse is true for the higher  $\phi$ -angles. We observe differences as high as  $40^\circ\text{C}$  at  $\phi = 30^\circ$  and at  $\phi = 46.1^\circ$ . In contrast to 100 and 102 modes, the 302 mode  $T_{to}$  can be either above or below the corresponding 300 mode. For (40.9, 27) we also measured the 500 mode, showing  $T_{to}$  identical with the 100 resonance.

Table 2. Turnover temperatures  $T_{to}$  and resonant frequencies  $f_{to}$  of major modes for fourteen AK-cut crystal orientations.

phi	theta	nmp	fundamental $f_{to}$ kHz	$T_{to}$ $^\circ\text{C}$	nmp	3rd overtone $f_{to}$ kHz	$T_{to}$ $^\circ\text{C}$
30	24.45	100	3405	144	300	10073	172
		102	3494	102	302	10166	160
					320	10206	193
33	24.45	100	3381	95	300	10003	108
			3425	85	302	10094	125
		102	3462	70	320	10114	115
			3514	<30	304	10189	113
					322	10207	107
34	22	100	3381	116	300	10002	127
			3425	110	302	10093	149
		102	3470	98	320	10113	127
			3516	90	304	10186	145
		104	3557	80	322	10206	125
34	26	100	3382	82	300	10008	98
		102	3466	45	320	10088	145
					302	10102	38
					340	10178	>145
					322	10189	83
34	28.45	100	3380	94	300	10005	111
		102	3461	29		10073	>145
						10097	58
						10159	>145
						10173	98
36	24.45	100	3368	84	300	9946	84
		102	3456	62		10009	107
						10038	1
36.58	22	100	3385	103	300	10004	104
		102	3472	91		10067	120
36.58	26	100	3394	80	300	10015	68
			3436	66		10066	88
		102	3478	49			
36.58	28.45	100	3394	102	300	10006	75
		102	3479	<35		10055	81
						10064	41
38.5	26	100	3405	90	300?	10015	-16
		102	3487	62		10078	+17
			3571	23		10148	+19
40.9	21	100	3359	129	300	-	-
			3405	127			
		102	3451	119			
40.9	23.55	100	3357	113	300	-	-
			3402	110			
		102	3446	100			
40.9	27		3490	87			
		100	3358	109	300	-	-
		102	3437	75			
			3505	103	500	16556	109
			3520	<28			
46.1	23.55		3534	61			
		100	3365	154	300	10003	115
		102	3451	148	302	10088	118
					304	10175	113
					320	10192	< 30
					306	10264	90

Table 2 shows that for (38.5, 26.0) the three major resonances have very low turnovers, -16, 17, and  $19^\circ\text{C}$ , respectively. Figure 9 shows the original  $f(T)$  plot for the  $T_{to} = -16^\circ\text{C}$  mode. We note a jump in fre-



quency, or possible activity dip, at 68 °C. This gave an indication that the resonance may not be the 300 mode, but may be associated with a spurious mode. We further investigated the origin of this anomaly by multiple mode tracking over an extended temperature range. Figure 10 shows the results, and indeed we are observing the interaction of two resonances, one decreasing and one increasing in strength with increasing temperature. The two resonances are of equal strength around 70 °C, and at this temperature we observe the frequency jump to the stronger resonance.

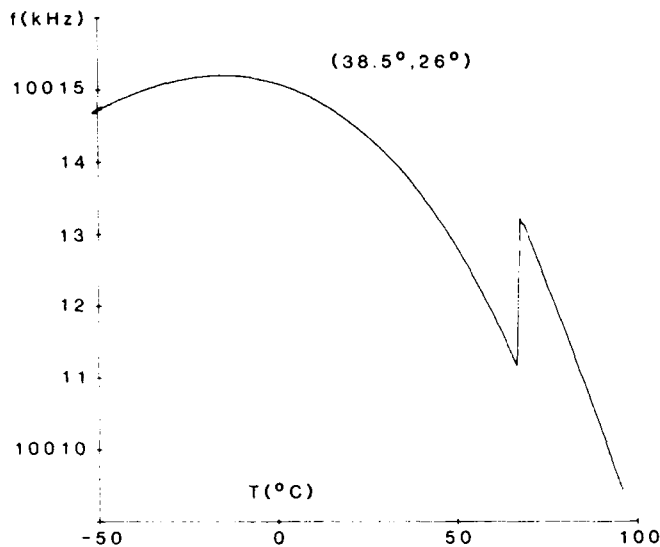


Figure 9. Frequency as a function of temperature for (38.5, 26) orientation showing a turnover at -16 °C and a frequency jump at 68 °C.

#### Conclusions

The data shown in this paper confirm our contention that the AK-cut offers practical turnover temperatures that are relatively insensitive to crystallographic misorientations. The measured  $T_0$  values agree well with the calculated predictions. Fourteen orientations have been experimentally studied and all crystals show a number of inharmonic modes both in the fundamental and 3rd overtone. The design goal of having the main n00 mode exceed in strength all other modes by at least 6 dB is achievable. For the 3rd overtone the major resonances of several orientations are seriously affected by interaction between the c- and a-modes. This leads to exponentially decaying vibrations and impaired energy trapping. Preliminary measurements show that these orientations do possess regular c-modes in the 5th overtone. Work is currently in progress to optimize the mode structure by judicious choices of resonator disk size, curvature, electrode diameter and other geometrical and operational parameters.

#### Acknowledgments

The authors wish to thank Professor H.F. Tiersten and D.S. Stevens for stimulating discussions. They also wish to acknowledge the capable technical assistance of Robert J. Andrews.

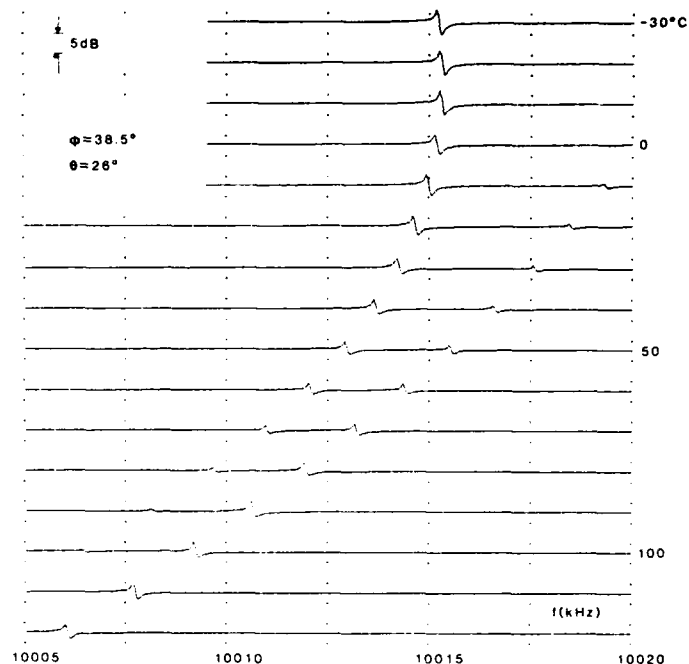


Figure 10. Multimode frequency track between -30 and 140 °C for resonator shown in Fig. 9. Data indicate that the frequency jump occurs when the two resonances are approximately of equal strength.

#### References

1. A. Kahan, Proc. 36th Annual Frequency Control Symposium (AFCS), 170(1982).
2. A. Kahan and F.K. Euler, Proc. 14th Precise Time and Time Interval (PTTI), 577(1982).
3. H.F. Tiersten and D.S. Stevens, Proc. 36th AFCS, 37(1982).
4. A. Kahan, Proc. 36th AFCS, 159(1982).
5. B. Goldfrank (private communication).

## FREQUENCY SHIFTS ARISING FROM IN-PLANE TEMPERATURE GRADIENT DISTRIBUTION IN QUARTZ RESONATORS

J.P. Valentin\*, G. Théobald\*\*, J.J. Gagnepain\*\*

\*Laboratoire de Chronométrie, Electronique et Piézoélectricité  
ENSM, route de Gray - 25030 Besançon - France\*\*Laboratoire de Physique et Métrologie des Oscillateurs du CNRS  
associé à l'Université de Franche Comté Besançon  
32, avenue de l'Observatoire - 25000 Besançon - France

## SUMMARY

A new model of temperature distribution in a quartz crystal resonator is presented. The relative importances of thermal exchanges between the crystal and the surrounding medium by heat conduction through the supports and by radiation with the enclosure are evaluated. Thermal diffusion in the crystal itself and in the electrodes also are compared. The conclusions lead to a temperature gradient distribution which is in the main plane of the crystal, and which does not present a functional dependence (at least at the first order) along the plate thickness as it was the case in previous models.

Also is included the influence of the internal heat source due to the energy dissipated by the internal friction.

The corresponding in-plane thermal stresses are calculated in the isotropic approximation, and anisotropy is introduced by means of the stress-strain relations. Then, by using a perturbation method, the frequency shifts are obtained, for both static and dynamic thermal behaviors.

## INTRODUCTION

The quartz resonator, under static thermal conditions, i.e. thermal equilibrium and uniform temperature distribution, has been exhaustively studied. When the temperature distribution is nonuniform, stresses and strains appear and the resonance frequency of the resonator is modified. The first calculation of the influence of a non-uniform temperature distribution was made by Holland<sup>(1)(2)</sup>, using the infinite plane plate model schematized figure 1.

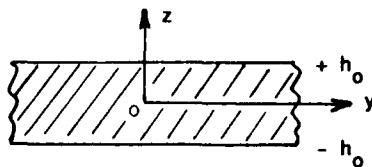


Figure 1

This model presents three difficulties

- the actual boundary conditions are not taken into account,
- the energy trapping does not appear,
- only thermal gradient  $\partial T / \partial z$  can occur, without any radial component.

Next, theoretical results were given by Théobald<sup>(3)</sup> and Sinha<sup>(4)</sup>, still based upon the infinite plate model. Recently, Valentin<sup>(5)</sup> pointed out that the heat transfers through the quartz itself and not through the electrodes. Consequently, the thermal gradients mainly are radial rather than perpendicular to the plate. On this statement, a new thermal model for trapped energy quartz resonator was proposed<sup>(6)</sup>.

In order to determine the effects of temperature perturbations on the resonance frequency, it needs to introduce such in plane gradient distribution. Therefore, in the present study, a brief review of the results concerning the thermal exchanges from the quartz crystal to surroundings, is presented. Then, the crystal temperature distribution is determined in the two following cases: the temperature of the surrounding medium is either time independent or time dependent. The thermal stresses are derived from the equilibrium equation for a thin crystal plate, in the static and dynamic cases. Finally, neglecting the mechanical effects from the holders, frequency shifts arising from the thermal stresses in a plate free to expand, is calculated.

## THERMAL MODEL OF THE QUARTZ RESONATOR

In a quartz resonator, as shown in Fig. 2, thermal exchanges with the surrounding medium can take place by conduction inside the crystal and the electrodes, and by radiation between the resonator surfaces and the enclosure. Inside the enclosure the residual pressure does not exceed  $10^{-5}$  millibar. Therefore, exchanges by gaseous conduction and convection can be neglected.

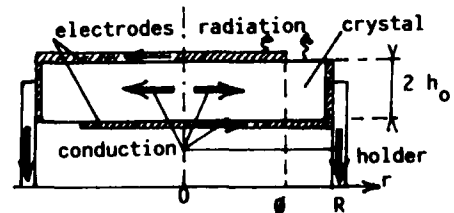


Figure 2

Considering a plano-convex crystal plate, the energy trapping imposes a thermal power distribution  $q(r)$  inside the resonator central part which obeys a quasi-gaussian law. Therefore  $q(r)$

can be written

$$q(r) = \mu e^{-r^2/r_0^2}$$

When the curvature radius of the convex surface is optimized, that is the case for all metrological resonators, generally  $r_0 = R/3$ . Then, the crystal bulk radial conductance  $Y_{\text{quartz}}$  is approximated by the following expression

$$Y_{\text{quartz}} = 2 \lambda h_0 \frac{2\pi}{\log R/r_0}$$

where  $\lambda$  is the average thermal conductivity of the  $\alpha$ -quartz.

Electrodes can be considered like foils of chromium and gold. Their conductance  $Y_{\text{elect}}$  is given by

$$Y_{\text{elect}} = (\lambda e_{\text{Au}} + \lambda e_{\text{Cr}}) \frac{2\pi}{\log \emptyset/r_0}$$

where  $\lambda e_{\text{Au}}$  is the product of the gold thermal conductivity by its thickness and likewise for chromium.

Considering a quartz plate, 1.6 mm thick, with  $R$  and  $\emptyset$  respectively equal to 7.5 mm and 5 mm, and coated with 2000 Å of chromium and gold, the conductance ratio  $Y_{\text{quartz}}/Y_{\text{elect}}$  is 60. This shows that radial conduction inside the electrodes is negligible.

The electrodes are electrically connected to the holders by a gold plated strip on each surface (Fig. 3). Thermal transfers take place inside these strips and inside the crystal underneath. Comparison of thermal conductances indicates a ratio of the order of 100 to 500. Again thermal transfer inside the plating is negligible.

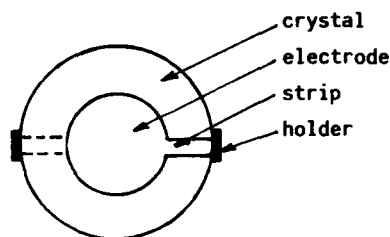


Figure 3

The thermal conductance due to radiation between the resonator and the enclosure is expressed by (5)

$$Y_r = \frac{\epsilon_e \epsilon_q \sigma S_q (T_q + T_e) (T_q^2 + T_e^2)}{1 - (1 - \epsilon_q) (1 - \epsilon_e) \frac{S_q}{S_e}}$$

where  $\epsilon_e$  and  $\epsilon_q$  are the energetical emission factors of enclosure and quartz materials,  $\sigma$  is the Stefan's constant,  $S_q$  and  $S_e$  are the emissive surfaces of the quartz crystal and the enclosure.  $T_q$  and  $T_e$  are the respective temperatures.

Considering enclosures made of glass or ceramic, the  $\epsilon_e$  factor is of the order of 0.92 to 0.98. In the case of quartz crystal, the  $\epsilon_q$  factor of free surfaces is 0.95 and 0.04 for gold plated surfaces. Under these conditions, for temperatures around 350 K and  $S_q/S_e = 1/3$ , the previous equation gives

$$Y_r(\text{electrodes}) = 6 \cdot 10^{-5} \text{ W/K}$$

$$Y_r(\text{crystal}) = 2 \cdot 10^{-3} \text{ W/K}$$

main faces

$$Y_r(\text{crystal edge}) = 5 \cdot 10^{-4} \text{ W/K}$$

These various results are summarized figure 4 and the proposed thermal model is schematized in figure 5.

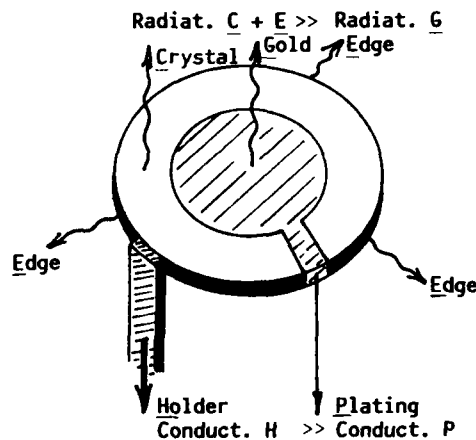


Figure 4

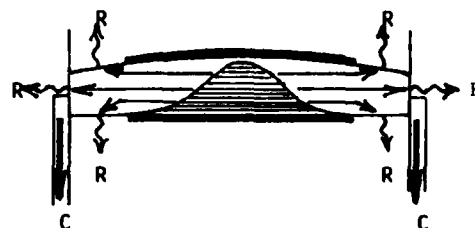


Figure 5

If the enclosure is made of bright metal, all previous computed conductances by radiation must be divided by 10. For this study, we consider this last case, since quartz resonators enclosures are usually made with gold plated copper.

Thermal conductance of holders rules the relative importance of the transfers by conduction in comparison to the radiative transfers. For holders, an average value of the thermal conductance can be chosen about  $2 \cdot 10^{-3} \text{ W/K}$ . Then, it can be shown that most of the thermal exchanges are due to radial heat conduction in the crystal. The transfers inside the electrodes and by radiation are negligible. Therefore the induced thermal gradients will be located in the main plane of the crystal without any functional dependence along the thickness. A comparison between the

regular model of the infinite plane plate and the new model is presented in figure 6. In the first case, the thermal flux transfers only through the thickness of the crystal ; in the second case the thermal flux transfers only through the main plane of the crystal.

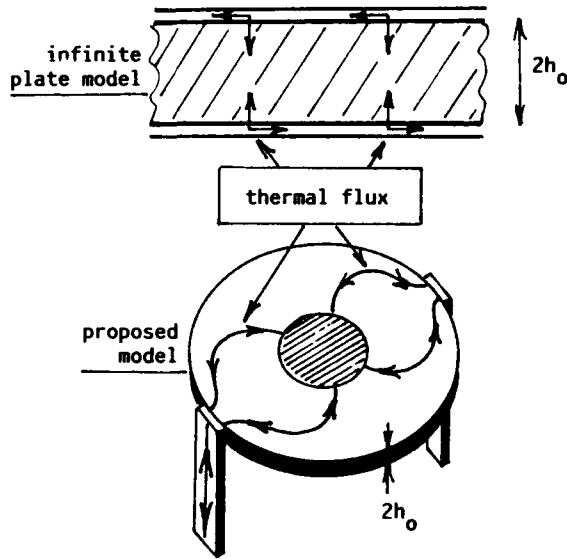


Figure 6

Two practical cases will be considered.  
1) The steady state of a resonator with internal heat dissipation and linear thermal transfer from resonator edge to surrounding medium with constant external temperature.  
2) The transient rate of a resonator with linear thermal transfer as previously and time dependent external temperature ; this last case leading to the dynamic temperature behavior.

#### STEADY STATE

##### Temperature distribution

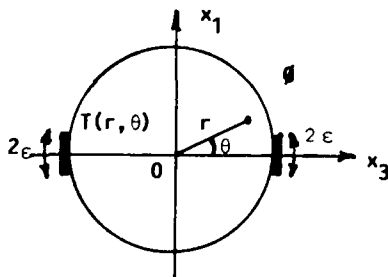


Figure 7

The circular quartz plate of radius R is represented in Fig. 7.  $T(r, \theta)$  is the temperature of the crystal, which is mounted by two holders having an angular width  $= 2\epsilon$ . The external temperature is called  $\emptyset$ . Using polar coordinates  $(r, \theta)$  in

the  $x_1x_3$  plane, the temperature diffusion equation is given by

$$\nabla^2 T = \frac{\partial^2 T}{\partial r^2} + \frac{1}{r} \frac{\partial T}{\partial r} + \frac{\partial^2 T}{\partial \theta^2} = - \frac{q(r)}{\lambda} \quad (1)$$

when the thermal power distribution  $q(r)$  is referred to the unit volume and obeys a Gaussian law, as previously pointed out. The isotropic approximation is assumed. Symmetry considerations allow one to choose a solution with the form

$$T = U_0(r) + U_1(r, \theta) \quad (2)$$

where

$$U_1(r, \theta) = \sum_{k=1}^{\infty} U_{2k}(r) \cos 2k\theta \quad (3)$$

$$U_0(r) \text{ is solution of } \nabla^2 U_0(r) = - \frac{q(r)}{\lambda} \quad (4)$$

and

$$U_1(r, \theta) \text{ is solution of } \nabla^2 U_1(r, \theta) = 0 \quad (5)$$

The linear thermal transfer at the boundary is written

$$\lambda \frac{\partial T}{\partial r} + HT = H\emptyset \quad \text{for } r = R \quad (6)$$

where H is the transfer coefficient.

Let  $H_1$  be the value of H at the fixation points, i.e. for  $-\epsilon < \theta < \epsilon$  and  $\pi - \epsilon < \theta < \pi + \epsilon$ , and  $H_2$  the value for  $\epsilon < \theta < \pi - \epsilon$  and  $\pi + \epsilon < \theta < 2\pi - \epsilon$ . According to the fact that thermal radiation between the resonator edge and the gold plated enclosure is very small, then  $H_2$  will be made zero.

Using the notation  $h = H/\lambda$ , the transfer coefficient can be expanded into a Fourier's series

$$h = h_0 + \sum_{k=1}^{\infty} h_{2k} \cos 2k\theta \quad (7)$$

with

$$h_0 = \frac{2}{\pi} (h_1 - h_2) \epsilon + h_2 \quad (8)$$

and

$$h_{2k} = \frac{4}{\pi} (h_1 - h_2) \frac{\sin 2k\epsilon}{2k} \quad (9)$$

Considering the condition  $\epsilon \ll \pi$ , the previous equations can be solved by using a method of successive approximations. After calculation, the following expression is obtained

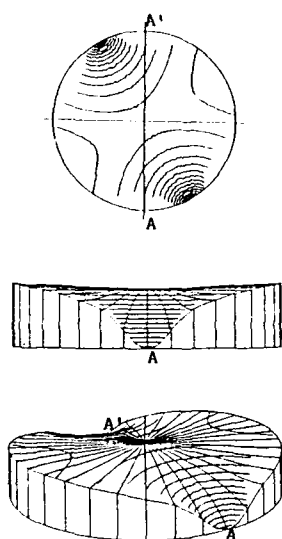
$$T = \emptyset + \frac{\mu r^2}{4\lambda} \left\{ \frac{\pi}{R h_1 \epsilon} + f(R) - f(r) + 2 \sum_{k=1}^{\infty} \frac{1}{k} \left[ 1 - \left( \frac{r}{R} \right)^{2k} \cos 2k\theta \right] \right\} \quad (10)$$

with

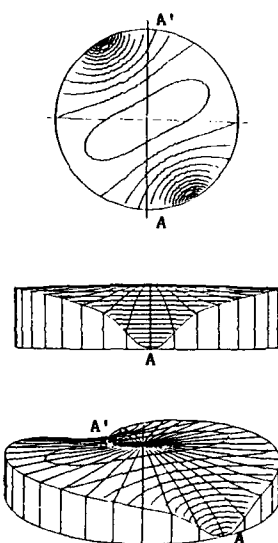
$$f(r) = \sum_{n=1}^{\infty} \frac{(-1)^{n+1}}{n n!} \left(\frac{r}{r_0}\right)^{2n} \quad (11)$$

From this last result, various families of isotherms have been obtained by computer. The first series of the following figures shows how the temperature repartition depends on energy trapping for a resonator maintained by two opposite holders. The curves are the isotherms. In the perspective-views, the temperature of each point of the resonator refers to the external temperature.

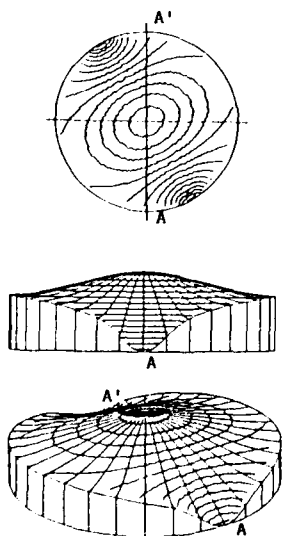
The topography of the resonator is evolutive. Without energy trapping ( $r_0 = R$ ) the top appears as a "pass". For weak energy trapping ( $r_0 = 2R/3$ ) the top becomes a "mesa", next a smoothed hill ( $r_0 = R/3$ ) and finally a hill for strong energy trapping ( $r_0 = R/5$ ). The second series of figures shows how the temperature repartition depends on holders thermal conductance. For this last series, the trapping is normal in all cases.



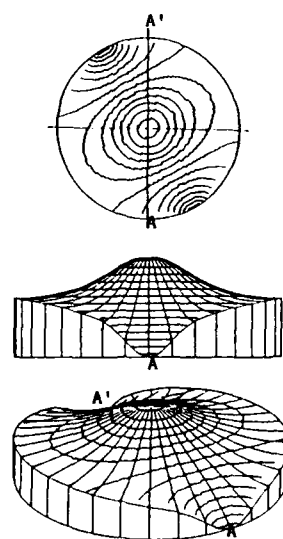
Without energy trapping  
 $r_0 = R$



Weak energy trapping  
 $r_0 = 2 R/3$

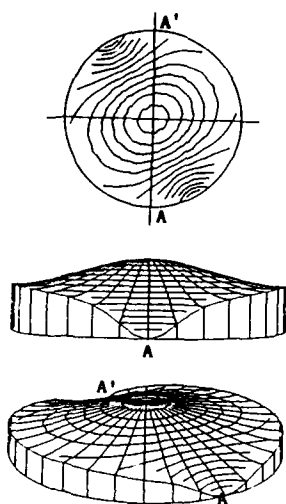


Normal energy trapping  
 $r_0 = R/3$

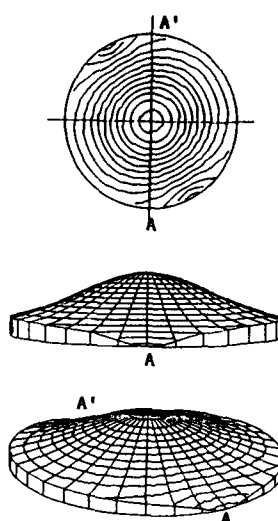


Strong energy trapping  
 $r_0 = R/5$

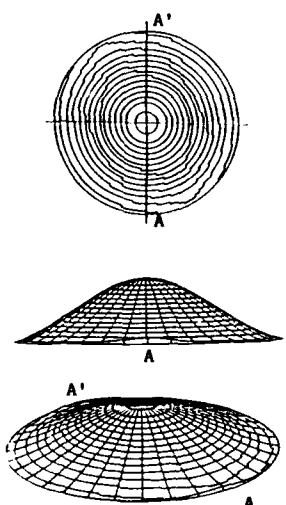
#### TEMPERATURE REPARTITION DEPENDS ON ENERGY TRAPPING



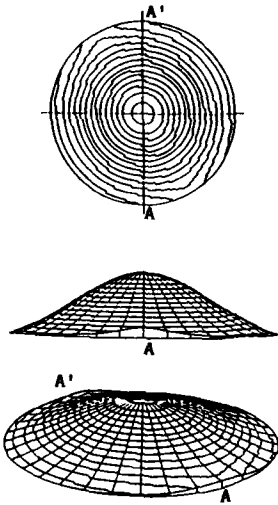
Large conductance  $h_1 = 1000 \text{ m}^{-1}$



Medium conductance  $h_1 = 100 \text{ m}^{-1}$



Weak conductance  $h_1 = 10 \text{ m}^{-1}$



No conductance  $h_1 = 1 \text{ m}^{-1}$

### TEMPERATURE REPARTITION DEPENDS ON HOLDERS THERMAL CONDUCTANCE

#### Thermal stress:s

Referred to the rectangular coordinates, the state of stress is specified by the three in-plane stress components  $T_1$ ,  $T_3$  and  $T_5$ , without any functional dependence along the thickness. The figure 8 indicates the chosen notations.

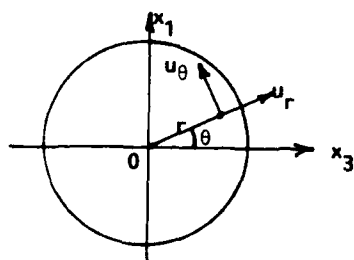


Figure 8

Let be  $u_r$  and  $u_\theta$  the mechanical displacements and  $\sigma_r$ ,  $\sigma_\theta$  and  $\tau_{r\theta}$  the stress components in polar coordinates. Calculation of the stress distribution is made in the case of the isotropic approximation. The anisotropy of quartz crystal is introduced later by means of the strain-stress constitutive equations.

Introducing the thermoelastic displacement potential  $\Psi$ , the thermomechanical equilibrium is written as

$$\nabla^2 \Psi = \frac{\partial^2 \Psi}{\partial r^2} + \frac{1}{r} \frac{\partial \Psi}{\partial r} + \frac{1}{r^2} \frac{\partial^2 \Psi}{\partial \theta^2} = \alpha \frac{s_{11} - s_{13}}{s_{11}} T + C_1 \quad (12)$$

where  $\alpha$  is the thermal expansion coefficient in the isotropic approximation,  $T$  the temperature,

$C_1$  a constant to be calculated, and the  $s_{ij}$ 's are the elastic compliances.

According to the general form of the temperature (eq. 2 and 3), a similar form is chosen for the potential

$$\Psi = \sum_{k=0}^{\infty} \Psi_{2k}(r) \cos 2k\theta \quad (13)$$

The  $U_1(r, \theta)$  component being a solution of  $\nabla^2 U_1(r, \theta) = 0$  does not induce any thermal stress<sup>(7)</sup>.

Then, the stress distribution depends only on the  $r$  coordinate, and the displacement takes the form

$$u_r = \alpha \frac{s_{11} - s_{13}}{s_{11}} \frac{1}{r} \int_0^r r U_0(r) dr + \frac{r}{2} C_1 \quad (14)$$

$$u_\theta = 0$$

Using Hooke's law the stress expressions at the center of the resonator are given by

$$\sigma_r = \sigma_\theta = \frac{\alpha}{s_{11}} \left\{ -\frac{T_c}{2} + \frac{1}{R^2} \int_0^R r U_0(r) dr \right\} \quad (15)$$

$$\tau_{r\theta} = 0$$

where  $T_c$  is the temperature of the center. Since  $\sigma_r = \sigma_\theta$  and  $\tau_{r\theta} = 0$ , thus  $T_1 = T_3 = \sigma_r = \sigma_\theta$  and  $T_5 = 0$ . As a consequence of such a stress distribution, it appears that SC-cut<sup>(8)</sup> will minimize the effect of the above mentioned static thermal distribution.

#### TRANSIENT RATE

The problem which is now examined corresponds to a time dependent external temperature and leads to the theoretical determination of the phenomenological coefficient  $\tilde{\alpha}$  introduced by Ballato<sup>(9)</sup>, for characterizing dynamic behavior of quartz resonators.

The internal energy dissipation is neglected and the initial temperature in the crystal is taken equal to zero. The boundary condition will be simplified by imposing at the boundary a temperature distribution  $\theta(\theta, t)$ , as shown in figure 9, rather than the previous distribution of equations 7, 8 and 9. Then, the thermal exchanges at the edge will be very small except at the fixation points.

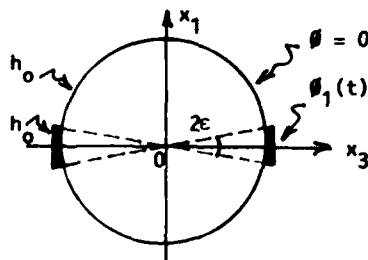


Figure 9

The external temperature can be expanded into a Fourier's series

$$\phi(\theta, t) = \phi_0(t) + \sum_{k=1}^{\infty} \phi_{2k}(t) \cos 2k\theta \quad (16)$$

with

$$\phi_0(t) = \frac{2\epsilon}{\pi} \phi_1(t) \quad (17)$$

$$\phi_{2k}(t) = \frac{4}{\pi} \frac{\sin 2k\epsilon}{2k} \phi_1(t) \quad (18)$$

The diffusion equation, the heat transfer equation at the edge and the initial condition are

$$\nabla^2 T = \frac{1}{\chi} \frac{\partial T}{\partial t} \quad (19)$$

$$\frac{\partial T}{\partial r} + h_0 T = h_0 \phi(\theta, t) \quad \text{for } r = R \quad (20)$$

$$T = 0 \quad t = 0 \quad (21)$$

$\chi$  being the thermal diffusivity constant.

Using the Duhamel's theorem and after calculation, the solution of the previous equations is given by the following expression

$$T = \sum_{k=0}^{\infty} \sum_s \frac{B_{2k,s}}{\chi \alpha_{2k,s}^2} J_{2k}(\alpha_{2k,s} r) \cos 2k\theta \phi_1(t) \quad (22)$$

$$- \sum_{k=0}^{\infty} \sum_s \frac{B_{2k,s}}{\chi^2 \alpha_{2k,s}^4} J_{2k}(\alpha_{2k,s} r) \cos 2k\theta \dot{\phi}_1(t)$$

$$- \sum_{k=0}^{\infty} \sum_s \frac{B_{2k,s}}{\chi \alpha_{2k,s}^2} J_{2k}(\alpha_{2k,s} r) \cos 2k\theta e^{-\chi \alpha_{2k,s}^2 t} \times \left\{ \phi_1(0) - \frac{\dot{\phi}_1(0)}{\chi \alpha_{2k,s}^2} \right\}$$

with

$$B_{0,s} = \frac{4R \chi \alpha_{0,s}^3}{R^2 \alpha_{0,s}^2 + R^2 h_0^2} \frac{\epsilon}{\pi} \frac{J_1(\alpha_{0,s} R)}{J_0^2(\alpha_{0,s} R)} \quad (23)$$

$$B_{2k,s} = \frac{8R^2 \chi \alpha_{2k,s}^3}{(R^2 \alpha_{2k,s}^2 + R^2 h_0^2 - 4k^2)} \times \frac{h_0 \sin 2k\epsilon}{2\pi k(2k + h_0 R)} \times \frac{J_{2k+1}(\alpha_{2k,s} R)}{J_{2k}^2(\alpha_{2k,s} R)} \quad (24)$$

where  $J_{2k}$  are the Bessel's function of  $2k$  order and  $\alpha_{2k,s}$  are the roots of the following set of  $k$  transcendental equations when  $r = R$

$$\frac{d J_{2k}}{dr} (\alpha_{2k,s} r) + h_0 J_{2k}(\alpha_{2k,s} r) = 0 \quad (25)$$

In the equation (22) the first term is proportional to  $\phi_1(t)$  and so represents the static

thermal behavior of the resonator. The second term is proportional to the time derivative of the external temperature and corresponds to the dynamic temperature effect. The third term introduces the transient rate.

As previously, thermal stresses can be obtained using the thermoelastic displacement potential  $\Psi$  and the Hooke's law. After calculation, they may be written at the center of the resonator in the form

$$T_1 = \frac{\alpha}{s_{11}} \sum_s \left\{ \frac{B_{0,s}}{X^2 \alpha_{0,s}} \left( \frac{1}{2} - \frac{J_1}{\alpha_{0,s} R} \right) + \frac{B_{2,s}}{X^2 \alpha_{2,s}} \left( \frac{2J_2}{\alpha_{2,s}^2 R^2} + \frac{J_3}{\alpha_{2,s} R} - \frac{1}{4} \right) \right\} \dot{\phi}_1(t) \quad (26)$$

$$T_2 = \frac{\alpha}{s_{11}} \sum_s \left\{ \frac{B_{0,s}}{X^2 \alpha_{0,s}} \left( \frac{1}{2} - \frac{J_1}{\alpha_{0,s} R} \right) - \frac{B_{2,s}}{X^2 \alpha_{2,s}} \left( \frac{2J_2}{\alpha_{2,s}^2 R^2} + \frac{J_3}{\alpha_{2,s} R} - \frac{1}{4} \right) \right\} \dot{\phi}_1(t) \quad (27)$$

$$T_3 = 0 \quad (28)$$

The stress components being known, the perturbation method proposed by Tiersten<sup>(10)</sup> enables to obtain the relative frequency changes due to the dynamic temperature effect.

The following table presents the typical results obtained after computation for the regular quartz cuts and for medium ( $h_1 = 100$ ) and large ( $h_1 = 1000$ ) conductances.

It can be pointed out that the  $\tilde{a}$  coefficient does not vary so much with the holders conductance in the case of the AT cut, but is divided by six when the conductance varies from medium to large in the case of the SC cut. It can be also pointed out that the  $\tilde{a}$  coefficient is very sensitive to a slight variation of the angles  $\theta$  or  $\phi$  for doubly rotated cuts.

#### References

- (1) R. Holland, IEEE Trans., SU.21, n°3, p. 171 (1974).
- (2) R. Holland, Proc. IEEE Ultrasonics Symp., IEEE Cat. # 74 CHO 896-15U, p. 592 (1974).
- (3) G. Theobald et al., 33<sup>rd</sup> Ann. Freq. Cont. Symp., Philadelphia, p. 239 (1979).
- (4) B.K. Sinha and H.F. Tiersten, 34<sup>th</sup> Ann. Freq. Cont. Symp., Philadelphia, p. 393 (1980).
- (5) J.P. Valentin, D<sup>al</sup> Thesis, n°178, University of Besançon, France (1983).
- (6) J.P. Valentin, "Thermal gradient distributions in trapped energy quartz resonators", (to be published J. Appl. Phys.).
- (7) B.A. Boley, J.H. Weiner, Theory of thermal stresses, John Wiley and Sons Inc. (1960).
- (8) E.P. Eer Nisse, 29<sup>th</sup> Ann. Freq. Cont. Symp., Atlantic-City, p. 1 (1975).
- (9) A. Ballato and J. Vig, 32<sup>nd</sup> Ann. Freq. Cont. Symp., Philadelphia, p. 180 (1978).
- (10) H.F. Tiersten, J. Acoust. Soc. Am., 64 (3), p. 832 (1978).

#### Acknowledgment

The authors would like to thank Dr J. Gros Lambert for his providing assistance in computer programming.

TEMPERATURE DYNAMIC COEFFICIENTS  $\tilde{a}$  ( $s K^{-1}$ )

cut	Y	AT	BT	$\theta = 34.2$ $\phi = 22.6$	$\theta = 34.4$ $\phi = 22.6$	$\theta = 34.4$ $\phi = 21.8$
$h_1 = 100$	$-130 \cdot 10^{-5}$	$-0.35 \cdot 10^{-5}$	$1.35 \cdot 10^{-5}$	$9 \cdot 10^{-7}$	$90 \cdot 10^{-7}$	$77 \cdot 10^{-7}$
$h_1 = 1000$	$-17 \cdot 10^{-5}$	$-0.30 \cdot 10^{-5}$	$0.40 \cdot 10^{-5}$	$1.5 \cdot 10^{-7}$	$12 \cdot 10^{-7}$	$9 \cdot 10^{-7}$



## FREQUENCY-TEMPERATURE BEHAVIOR OF THICKNESS VIBRATIONS OF DOUBLY-ROTATED QUARTZ PLATES

## AFFECTED BY PLATE DIMENSIONS AND ORIENTATIONS

P.C.Y. Lee

Department of Civil Engineering  
Princeton University  
Princeton, N.J. 08544

and

Y.K. Yong

Department of Civil Engineering  
Rutgers University  
Piscataway, N.J. 08854

## SUMMARY

In a previous paper, three-dimensional linear field equations for small vibrations superposed on thermally induced deformations by steady and uniform temperature changes are derived from the nonlinear field equations of thermoelasticity in Lagrangian formulation. From the solutions of these equations for the simple-thickness vibrations and measurements by Bechmann, Ballato, and Lukaszek for various doubly-rotated quartz plates, values of the first temperature derivatives  $C_{pq}^{(1)}$  and effective second temperature derivatives  $\tilde{C}_{pq}^{(2)}$  of quartz were calculated.

The first temperature derivatives are needed for predicting the changes of wave speed in a crystal as a function of temperature, and the second temperature derivatives are essential for calculating the turn-over-point temperature when the frequency-temperature behavior exhibits a parabolic characteristic as in the cases of flexural or extensional vibrations of a quartz beam. When the frequency-temperature behavior has a cubic expression as in the case of thickness-shear vibrations of AT- or SC-cuts, the third temperature derivatives are needed for computation.

In the present paper, the previous work is extended to include the third-order perturbations so that values of the effective third temperature derivatives  $\tilde{C}_{pq}^{(3)}$  are obtained for quartz.

In order to study the effect of a free edge, a system of two-dimensional equations of crystal plates subject to uniform and steady temperature changes is derived from the three-dimensional variational stress equations of incremental motion by expanding the incremental displacement in a power series of the thickness coordinate according to Mindlin's procedure. Then a system of four coupled equations governing the thickness-shear, thickness-twist, thickness-stretch, and flexural modes are employed to study the vibrations of a doubly-rotated crystal strip with a pair of free edges.

From the analytical solutions, dispersion relations and frequency spectrum for an SC-cut quartz strip with a pair of free edges are computed. Then changes in the thickness-shear resonance frequencies as a function of temperature are predicted for various values of length-to-thickness ratio of the plate  $a/b$ , orientation angles  $\phi$  and  $\theta$ .

## INTRODUCTION

In a previous paper<sup>1</sup>, three-dimensional linear field equations for small vibrations superposed on thermally induced deformations by steady and uniform temperature changes are derived from the nonlinear field

equations of thermoelasticity in Lagrangian formulation. From the solutions of these equations for the simple-thickness vibrations and measurements by Bechmann, Ballato and Lukaszek<sup>2</sup> for various

doubly-rotated quartz plates, values of  $C_{pq}^{(1)}$  and  $\tilde{C}_{pq}^{(2)}$  of quartz were calculated.

The first temperature derivatives are needed for predicting the changes of wave speed in a crystal as a function of temperature, and the second temperature derivatives are essential for calculating the turn-over-point temperature when the frequency-temperature behavior exhibits a parabolic characteristic as in the cases of flexural or extensional vibrations of a quartz beam. When the frequency-temperature behavior has a cubic expression as in the case of thickness-shear vibrations of AT- or SC-cuts, the third temperature derivatives are needed for computation.

In the present paper, the previous work<sup>1</sup> is extended to include the third order perturbations so that values of the effective third temperature derivatives  $\tilde{C}_{pq}^{(3)}$  are obtained for quartz. By regrouping the terms in the incremental stress-strain-temperature relations, certain expressions in terms of the elastic stiffnesses, temperature derivatives and thermal expansion coefficients can be identified as having similar significance as the temperature coefficients of  $C_{pq}$  defined by Bechmann. Therefore values of these expressions are calculated and are listed with values of the temperature coefficients of  $C_{pq}$  obtained by Mason<sup>3</sup>, Koga et al<sup>4</sup>, Bechmann, Ballato and Lukaszek<sup>2</sup>, Adams, Enslow, Kusters and Ward<sup>5</sup>, and Kahan<sup>6</sup>. Based on the values of  $C_{pq}^{(1)}$ ,  $\tilde{C}_{pq}^{(2)}$  and  $\tilde{C}_{pq}^{(3)}$ , the first, second and third temperature coefficients of frequency for the thickness vibrations of various doubly rotated cuts are computed and compared with the observed values of Bechmann, Ballato and Lukaszek<sup>2</sup>. The inflection temperature, lower and upper turn-over temperature of the thickness-shear vibrations of various angles of the AT-cut are calculated and compared with experimental values.

In order to study the effect of a free edge, a system of two-dimensional equations of crystal plates subject to uniform and steady temperature changes is derived from the three-dimensional variational stress equations of incremental motion by expanding the incremental displacement in a power series of the thickness coordinate according to Mindlin's procedure. Then a system of four coupled equations governing the thickness-shear, thickness-twist, thickness stretch, and flexural modes are employed to study the vibration of a doubly-rotated crystal strip with a pair of free edges.

From the analytical solutions, dispersion relations and frequency spectrum for an SC-cut quartz strip with a

pair of free edges are computed. Then changes in the thickness-shear resonance frequencies as a function of temperature are predicted for various values of length to thickness ratio of the plate  $a/b$ , orientation angles  $\phi$  and  $\Theta$ .

#### EQUATIONS OF INCREMENTAL MOTION SUPERPOSED ON HOMOGENEOUS THERMAL STRAINS

The variation of resonant frequencies of quartz resonators due a steady and uniform ambient temperature change is considered. Since the small amplitude vibrations of the crystal resonators generate negligible heat, the equations of motion are assumed to be uncoupled from the heat equation. The small amplitude vibrations of the crystal subject to steady and uniform temperature is described by three consecutive states through which the crystal undergoes. The first state is the natural state at which the crystal body is free of stress and strain, at rest and at a uniform reference temperature,  $T_0$ . Next, the body expands or contracts freely under the steady and uniform temperature change of  $\Theta = T - T_0$ . This is the initial state: the crystal is still statically at rest and free of stress and strain. At the third and final state, small amplitude waves are superposed on the initial state. Since the waves generate negligible heat, there is no temperature change when the crystal body goes from the initial state to the final state. The material properties, displacements, stresses and strains are all referred to a common rectangular Cartesian frame of reference at the natural state. Fig. 1 shows the reference frame and the three states through which the crystal undergoes. If  $x_i$ ,  $y_i$  and  $z_i$  ( $i = 1, 2, 3$ ) are the generic material points at the natural, initial and final state, respectively, then the initial, final and incremental displacements are respectively:  $U_i = y_i - x_i$ ;  $\bar{U}_i = z_i - x_i$ ;  $u_i = \bar{U}_i - U_i = z_i - y_i$ . The incremental quantities, such as the incremental stress, strain and surface traction are defined as the difference between the respective quantities in the final and initial state given in the table below:

	Final	Initial	Incremental
Stress	$\bar{T}_{ij}$	$T_{ij}$	$t_{ij} = \bar{T}_{ij} - T_{ij}$
Strain	$\bar{E}_{ij}$	$E_{ij}$	$e_{ij} = \bar{E}_{ij} - E_{ij}$
Surface Traction	$\bar{P}_i$	$P_i$	$p_i = \bar{P}_i - P_i$

TABLE 1

The nonlinear governing equations in Lagrangian formulation for the initial state are:

$$\begin{aligned} E_{ij} &= 1/2 (U_{j,i} + U_{i,j} + U_{k,i} U_{k,j}) \\ T_{ij} &= C_{ijkl}^0 E_{kl} + 1/2 C_{ijklmn}^0 E_{kl} E_{mn} \\ &\quad + 1/6 C_{ijklmnpq}^0 E_{kl} E_{mn} E_{pq} \\ &\quad + 1/24 C_{ijklmnpqrs}^0 E_{kl} E_{mn} E_{pq} E_{rs} - \lambda_{ij}^0 \\ (T_{ij} + T_{jk} U_{i,k}),_{,j} &= \rho \ddot{U}_i \text{ in } V \\ P_i &= n_j (T_{ij} + T_{jk} U_{i,k}) \text{ on } S. \end{aligned} \quad (1)$$

Where  $V$  and  $S$  are the volume and surface of the crystal body at the natural state.

The equations for the final state should necessarily have the same form as (1), namely:

$$\begin{aligned} \bar{E}_{ij} &= 1/2 (\bar{U}_{j,i} + \bar{U}_{i,j} + \bar{U}_{k,i} \bar{U}_{k,j}) \\ \bar{T}_{ij} &= C_{ijkl}^0 \bar{E}_{kl} + 1/2 C_{ijklmn}^0 \bar{E}_{kl} \bar{E}_{mn} \\ &\quad + 1/6 C_{ijklmnpq}^0 \bar{E}_{kl} \bar{E}_{mn} \bar{E}_{pq} \\ &\quad + 1/24 C_{ijklmnpqrs}^0 \bar{E}_{kl} \bar{E}_{mn} \bar{E}_{pq} \bar{E}_{rs} - \lambda_{ij}^0 \\ (\bar{T}_{ij} + \bar{T}_{jk} \bar{U}_{i,k}),_{,j} &= \rho \ddot{\bar{U}}_i \text{ in } V \\ \bar{P}_i &= n_j (\bar{T}_{ij} + \bar{T}_{jk} \bar{U}_{i,k}) \text{ on } S. \end{aligned} \quad (2)$$

$n_j$  are the components of the unit outward normal to the bounding surface  $S$  of the crystal.  $C_{ijkl}^0$ ,  $C_{ijklmn}^0$ ,  $C_{ijklmnpq}^0$  and  $C_{ijklmnpqrs}^0$  are the temperature dependent elastic constants which have the following relations:

$$\begin{aligned} C_{ijkl}^0 &= C_{ijkl} + C_{ijkl}^{(1)} \cdot \Theta + 1/2 C_{ijkl}^{(2)} \cdot \Theta^2 + 1/6 C_{ijkl}^{(3)} \cdot \Theta^3 \\ C_{ijklmn}^0 &= C_{ijklmn} + C_{ijklmn}^{(1)} \cdot \Theta + 1/2 C_{ijklmn}^{(2)} \cdot \Theta^2 \\ C_{ijklmnpq}^0 &= C_{ijklmnpq} + C_{ijklmnpq}^{(1)} \cdot \Theta \\ C_{ijklmnpqrs}^0 &= C_{ijklmnpqrs} \end{aligned} \quad (3)$$

$$\text{where } C_{ijkl}^{(n)} = \frac{\partial^{(n)} C_{ijkl}}{\partial T^n}, \quad n = 1, 2, 3$$

$$C_{ijklmn}^{(n)} = \frac{\partial^{(n)} C_{ijklmn}}{\partial T^n}, \quad n = 1, 2$$

$$\text{and } C_{ijklmnpq}^{(n)} = \frac{\partial^{(n)} C_{ijklmnpq}}{\partial T^n}, \quad n = 1$$

are the  $n^{\text{th}}$  temperature derivatives of the second-, third- and fourth-order elastic stiffnesses, respectively. The stress coefficients of temperature,  $\lambda_{ij}^0$ , has the relation:

$$\lambda_{ij}^0 = \lambda_{ij}^{(1)} \cdot \Theta + 1/2 \lambda_{ij}^{(2)} \cdot \Theta^2 + 1/6 \lambda_{ij}^{(3)} \cdot \Theta^3 + 1/24 \lambda_{ij}^{(4)} \cdot \Theta^4$$

where  $\lambda_{ij}^{(n)}$  are the  $n^{\text{th}}$  order stress coefficients of temperature.

When the difference is taken between the respective equations of (2) and (1) and following the definitions of Table 1, we obtain the incremental field equations:

$$\begin{aligned} e_{ij} &= 1/2 (u_{j,i} + u_{i,j} + U_{k,j} u_{k,i} + U_{k,i} u_{k,j}) \\ t_{ij} &= (C_{ijkl}^0 + C_{ijklmn}^0 E_{mn} + 1/2 C_{ijklmnpq}^0 E_{mn} E_{pq} \\ &\quad + 1/6 C_{ijklmnpqrs}^0 E_{mn} E_{pq} E_{rs}) e_{kl} \\ (t_{ij} + t_{jk} U_{i,k} + T_{jk} U_{i,k}),_{,j} &= \rho u_i \text{ in } V \\ P_i &= n_j (t_{ij} + t_{jk} U_{i,k} + T_{jk} U_{i,k}) \text{ on } S \end{aligned} \quad (5)$$

In the above equations, quadratic terms of incremental quantities are dropped, since small amplitude waves are considered.

At the initial state, the crystal expands freely, that is, the initial stress is zero. When values of the linear thermal expansion coefficients:

$$\alpha_{ij}^{\theta} = \alpha_{ij}^{(1)} \cdot \theta + \alpha_{ij}^{(2)} \cdot \theta^2 + \alpha_{ij}^{(3)} \cdot \theta^3 \quad (6)$$

are measured instead of those of  $\lambda_{ij}^{\theta}$ , we have by its definition and symmetry,

$$1/2(U_{j,i} + U_{i,j}) = \alpha_{ij}^{\theta} = \alpha_{ji}^{\theta} \quad (7)$$

Therefore, the initial strain is

$$E_{ij} = \alpha_{ij}^{\theta} + 1/2 \alpha_{ki}^{\theta} \alpha_{kj}^{\theta} \quad (8)$$

The magnitude of the quadratic term of (8), estimated from Bechmann's values<sup>(2)</sup> of  $\alpha_{ij}^{(1)}$ ,  $\alpha_{ij}^{(2)}$  and  $\alpha_{ij}^{(3)}$  for quartz, are of the order of  $10^{-3}$  smaller than the first term and hence are neglected. Hence, to summarize, the initial state is reduced to a simple state of stress-free, homogenous thermal strain:

$$U_{j,i} = U_{i,j} = E_{ij} = \alpha_{ij}^{\theta},$$

$$T_{ij} = 0,$$

$$\text{and } \ddot{U}_i = 0 \quad (9)$$

When the first two equations of (9) are substituted into (5), we get the incremental field equations for small amplitude waves superposed on homogenous thermal strain,

$$e_{ij} = 1/2(u_{j,i} + u_{i,j} + \alpha_{kj}^{\theta} u_{k,i} + \alpha_{ki}^{\theta} u_{k,j}) \quad (10a)$$

$$t_{ij} = (C_{ijkl} + D_{ijkl}^{(1)} \cdot \theta + D_{ijkl}^{(2)} \cdot \theta^2 + D_{ijkl}^{(3)} \cdot \theta^3) e_{kl} \quad (10b)$$

$$(t_{ij} + \alpha_{ik}^{\theta} t_{jk}),_j = \rho u_i \text{ in } V \quad (10c)$$

$$p_i = n_j (t_{ij} + \alpha_{ik}^{\theta} t_{jk}) \text{ on } S \quad (10d)$$

$$\text{where } D_{ijkl}^{(1)} = C_{ijkl}^{(1)} + C_{ijklmn} \alpha_{mn}^{(1)}$$

$$D_{ijkl}^{(2)} = 1/2 \hat{C}_{ijkl}^{(2)} + C_{ijklmn} \alpha_{mn}^{(2)}$$

$$D_{ijkl}^{(3)} = 1/6 \hat{C}_{ijkl}^{(3)} + C_{ijklmn} \alpha_{mn}^{(3)} \quad (11)$$

$$\text{and } \hat{C}_{ijkl}^{(2)} = C_{ijkl}^{(2)} + 2C_{ijklmn} \alpha_{mn}^{(1)} + C_{ijklmnpq} \alpha_{mn}^{(1)} \alpha_{pq}^{(1)}$$

$$\begin{aligned} \hat{C}_{ijkl}^{(3)} = & C_{ijkl}^{(3)} + 3C_{ijklmn} \alpha_{mn}^{(2)} + 6C_{ijklmn} \alpha_{mn}^{(1)} \\ & + 6C_{ijklmnpq} \alpha_{mn}^{(1)} \alpha_{pq}^{(1)} + 3C_{ijklmnpq} \alpha_{mn}^{(1)} \alpha_{pq}^{(1)} \\ & + C_{ijklmnpqrs} \alpha_{mn}^{(1)} \alpha_{pq}^{(1)} \alpha_{rs}^{(1)} \end{aligned} \quad (12)$$

Equations (10) are similar to those of classical elasticity except for the extra terms associated with temperature change,  $\theta$ . In equation (10b), terms  $\theta^4$  or higher powers are dropped. Examination of relations in (11) reveals that  $D_{ijkl}^{(n)}$  has the same symmetry as  $C_{ijkl}$ . Furthermore, the only temperature derivatives of elastic stiffnesses that appear explicitly are  $C_{ijkl}^{(1)}$ ,  $\hat{C}_{ijkl}^{(2)}$  and  $\hat{C}_{ijkl}^{(3)}$ .  $C_{ijkl}^{(1)}$  is the first temperature derivative of

$C_{ijkl}$ , while  $\hat{C}_{ijkl}^{(2)}$  and  $\hat{C}_{ijkl}^{(3)}$  are respectively called the

effective second and third temperature derivatives of  $C_{ijkl}$ . These are the temperature derivatives which values are to be determined from the experimental data on the frequency-temperature behavior of thickness vibrations of various doubly rotated quartz crystal plates. For problems of small vibrations superposed on

homogenous thermal strains, values of  $C_{ijkl}^{(2)}$ ,  $C_{ijkl}^{(3)}$ ,  $C_{ijklmn}^{(1)}$ ,  $C_{ijklmn}^{(2)}$ ,  $C_{ijklmnpq}^{(1)}$ ,  $C_{ijklmnpq}^{(2)}$  and  $C_{ijklmnpqrs}$  need not be known.

#### Thickness Vibrations Subject to Homogenous Thermal Strains

The incremental displacement equations of motion are obtained by substituting (10a) into (10b) and the result into (10c) and (10d):

$$G_{ijkluk,jl} = \rho u_i \text{ in } V \quad (13a)$$

$$P_i = n_j G_{ijkluk,jl} \text{ on } S \quad (13b)$$

where:

$$\begin{aligned} G_{ijkl} = & C_{ijkl} + G_{ijkl}^{(1)} \cdot \theta + G_{ijkl}^{(2)} \cdot \theta^2 + G_{ijkl}^{(3)} \cdot \theta^3 \\ G_{ijkl}^{(1)} = & C_{ijkl}^{(1)} + C_{ijklmn} \alpha_{mn}^{(1)} + C_{ijksl} \alpha_{ks}^{(1)} + C_{sjkl} \alpha_{is}^{(1)} \\ G_{ijkl}^{(2)} = & 1/2 \hat{C}_{ijkl}^{(2)} + C_{ijklmn} \alpha_{mn}^{(2)} + C_{ijksl} \alpha_{ks}^{(2)} + C_{sjkl} \alpha_{is}^{(2)} \\ & + C_{ijksl} \alpha_{ks}^{(1)} + C_{sjkl} \alpha_{is}^{(1)} + C_{ijslmn} \alpha_{mn}^{(1)} \alpha_{ks}^{(1)} \\ & + C_{sjklmn} \alpha_{mn}^{(1)} \alpha_{is}^{(1)} + C_{sjtl} \alpha_{is}^{(1)} \alpha_{kt}^{(1)} \\ G_{ijkl}^{(3)} = & 1/6 \hat{C}_{ijkl}^{(3)} + C_{ijklmn} \alpha_{mn}^{(3)} + C_{ijksl} \alpha_{ks}^{(3)} + C_{sjkl} \alpha_{is}^{(3)} \\ & + C_{ijksl} \alpha_{ks}^{(2)} + C_{sjkl} \alpha_{is}^{(2)} + C_{ijslmn} \alpha_{mn}^{(1)} \alpha_{ks}^{(2)} \\ & + C_{sjklmn} \alpha_{mn}^{(1)} \alpha_{is}^{(2)} + 1/2 \hat{C}_{ijsl}^{(2)} \alpha_{ks}^{(1)} + 1/2 \hat{C}_{sjkl}^{(2)} \alpha_{is}^{(1)} \\ & + C_{ijslmn} \alpha_{mn}^{(2)} \alpha_{ks}^{(1)} + C_{sjklmn} \alpha_{mn}^{(2)} \alpha_{is}^{(1)} \\ & + C_{sjtl} \alpha_{is}^{(1)} \alpha_{kt}^{(2)} + C_{sjtl} \alpha_{is}^{(2)} \alpha_{kt}^{(1)} \\ & + C_{sjtl} \alpha_{is}^{(1)} \alpha_{kt}^{(1)} + C_{sjtlmn} \alpha_{mn}^{(1)} \alpha_{is}^{(1)} \alpha_{kt}^{(1)} \end{aligned} \quad (13c)$$

Terms containing  $\theta^4$  or higher powers are dropped.  $G_{ijkl}^{(n)}$  has the major symmetry,

$$G_{ijkl}^{(n)} = G_{klij}^{(n)}$$

but not the minor symmetry

$$G_{ijkl}^{(n)} \neq G_{jikl}^{(n)} \neq G_{ijlk}^{(n)}$$

For thickness vibrations of infinite plates, the boundary conditions are at the traction free major surfaces are:

$$P_i = n_j G_{ijkluk,jl} = 0 \text{ at } n_j x_j = \pm b \quad (14)$$

where  $x_j$  refers to the crystallographical axes of quartz and  $n_j$  is the unit outward normal to the faces of the plate. A doubly rotated quartz plate defined by  $(y, x, w, l)$   $\phi$ ,  $\theta$  would have the following components for  $n_j$ :

$$n_1 = -\cos\theta \sin\phi, \quad n_2 = \cos\theta \cos\phi, \quad n_3 = \sin\theta \quad (15)$$

Fig. 2 shows the orientation of a doubly rotated plate and the normal,  $n_j$ .

The assumed harmonic solution for antisymmetric thickness-vibrations:

$$u_k = A_k \sin \xi n_p x_p e^{i\omega t} \quad (16)$$

will satisfy (13a) and (14) if and only if

$$(Q_{ik} - \lambda \delta_{ik}) A_k = 0$$

$$\text{where } Q_{ik} = Q_{ki} = G_{ijkl} n_j n_l$$

$$\lambda = \rho \frac{w^2}{\xi^2} = \rho \left( \frac{2bw}{n\pi} \right)^2 \quad n = 1, 2, 3, \dots \quad (17c)$$

In order to obtain analytical relations from which  $C_{ijkl}^{(1)}$ ,  $\tilde{C}_{ijkl}^{(2)}$  and  $\tilde{C}_{ijkl}^{(3)}$  can be calculated from known

material properties, the Rayleigh-Schrodinger perturbation method is employed<sup>8</sup>. The amplitude and eigenvalue are assumed to be polynomial functions of temperature change,  $\Theta$ :

$$A_k = A_k^{(0)} + A_k^{(1)} \cdot \Theta + A_k^{(2)} \cdot \Theta^2 + A_k^{(3)} \cdot \Theta^3 \quad (18a)$$

$$\lambda = \lambda^{(0)} + \lambda^{(1)} \cdot \Theta + \lambda^{(2)} \cdot \Theta^2 + \lambda^{(3)} \cdot \Theta^3 \quad (18b)$$

By inserting (18) into (17a) and equating coefficients of like powers of  $\Theta$ , yields:

$$\Theta^0: (Q_{ik}^{(0)} - \lambda^{(0)} \delta_{ik}) A_k^{(0)} = 0 \quad (19a)$$

$$\Theta^1: (Q_{ik}^{(0)} - \lambda^{(0)} \delta_{ik}) A_k^{(1)} + (Q_{ik}^{(1)} - \lambda^{(1)} \delta_{ik}) A_k^{(0)} = 0 \quad (19b)$$

$$\Theta^2: (Q_{ik}^{(0)} - \lambda^{(0)} \delta_{ik}) A_k^{(2)} + (Q_{ik}^{(1)} - \lambda^{(1)} \delta_{ik}) A_k^{(1)} + (Q_{ik}^{(2)} - \lambda^{(2)} \delta_{ik}) A_k^{(0)} = 0 \quad (19c)$$

$$\Theta^3: (Q_{ik}^{(0)} - \lambda^{(0)} \delta_{ik}) A_k^{(3)} + (Q_{ik}^{(1)} - \lambda^{(1)} \delta_{ik}) A_k^{(2)} + (Q_{ik}^{(2)} - \lambda^{(2)} \delta_{ik}) A_k^{(1)} + (Q_{ik}^{(3)} - \lambda^{(3)} \delta_{ik}) A_k^{(0)} = 0 \quad (19d)$$

$$\text{where } Q_{ik}^{(0)} = C_{ijkl} n_j n_l$$

$$\text{and } Q_{ik}^{(n)} = G_{ijkl}^{(n)} n_j n_l \quad n = 1, 2, 3 \quad (19e)$$

The zeroth order equation (19a) can be used to solve for  $\lambda^{(0)}$  and  $A_k^{(0)}$  uniquely by requiring normalization

$$A_k^{(0)} A_k^{(0)} = 1 \quad (20a)$$

From the dot product of (18a),

$$A_k A_k = A_k^{(0)} A_k^{(0)} + 2A_k^{(1)} A_k^{(0)} \cdot \Theta + (A_k^{(1)} A_k^{(1)} + 2A_k^{(2)} A_k^{(0)}) \cdot \Theta^2$$

where terms containing  $\Theta^3$  or higher powers are dropped, we see that the extra conditions for normalization of  $A_k$  are:

$$A_k^{(1)} A_k^{(0)} = 0 \quad (20b)$$

$$\text{and } A_k^{(2)} A_k^{(0)} = -1/2 A_k^{(1)} A_k^{(1)} \quad (20c)$$

The constraint (20b) is used along with any two independent relations of (19b) to determine  $A_k^{(1)}$  uniquely. Similarly  $A_k^{(2)}$  is uniquely determined from two independent relations of (19c) and constraint (20c).

Multiplication of (19b) to (19d) by  $A_i^{(0)}$ , respectively, and using (19a), (20a), (20b) and (20c) leads to

$$\lambda^{(1)} = A_i^{(0)} Q_{ik}^{(1)} A_k^{(0)} \quad (21a)$$

$$(17a) \quad \lambda^{(2)} = A_i^{(0)} Q_{ik}^{(2)} A_k^{(0)} + A_i^{(0)} Q_{ik}^{(1)} A_k^{(1)} \quad (21b)$$

$$(17b) \quad \lambda^{(3)} = A_i^{(0)} Q_{ik}^{(3)} A_k^{(0)} + A_i^{(0)} (Q_{ik}^{(1)} - \lambda^{(1)} \delta_{ik}) A_k^{(2)} + A_i^{(0)} Q_{ik}^{(2)} A_k^{(1)} \quad (21c)$$

In equations (21),  $\lambda^{(n)}$  are considered as measured or known quantities, since they can be related to Bechmann's definition of temperature coefficient of temperature:

$$\lambda^{(1)} = 2\lambda^{(0)} T_f^{(1)} \quad (22a)$$

$$\lambda^{(2)} = 2\lambda^{(0)} T_f^{(2)} + \lambda^{(0)} (T_f^{(1)})^2 \quad (22b)$$

$$\lambda^{(3)} = 2\lambda^{(0)} T_f^{(3)} + 2\lambda^{(0)} T_f^{(1)} T_f^{(2)} \quad (22c)$$

$T_f^{(n)}$  are the temperature coefficients measured from the frequency-temperature behavior of thickness vibrations of doubly rotated quartz crystal plates.

#### Temperature Derivatives of Elastic Stiffnesses of Quartz

The quantities of  $Q_{ik}^{(n)}$  in equations (21) can be expanded using definitions (19e) and (13c). Doing so, equations (21) are rearranged so as to have the unknown temperature derivatives on the left hand side:

$$C_{ijkl}^{(1)} n_j n_l A_i^{(0)} A_k^{(0)} = 2\lambda^{(0)} T_f^{(1)} - [C_{ijklmn}^{(1)} \alpha_{mn}^{(1)} + 2C_{ijsl}^{(1)} \alpha_{ks}^{(1)}] n_j n_l A_i^{(0)} A_k^{(0)} \quad (23a)$$

$$\tilde{C}_{ijkl}^{(2)} n_j n_l A_i^{(0)} A_k^{(0)} = 4\lambda^{(0)} T_f^{(2)} + 2\lambda^{(0)} (T_f^{(1)})^2 - 2A_i^{(0)} Q_{ik}^{(1)} A_k^{(1)} - 2[C_{ijklmn}^{(2)} \alpha_{mn}^{(2)} + 2C_{ijsl}^{(2)} \alpha_{ks}^{(2)} + 2(C_{ijsl}^{(1)} + C_{ijslmn}^{(1)} \alpha_{mn}^{(1)}) \alpha_{ks}^{(1)} + C_{sjtl}^{(1)} \alpha_{is}^{(1)} \alpha_{kt}^{(1)}] n_j n_l A_i^{(0)} A_k^{(0)} \quad (23b)$$

$$\tilde{C}_{ijkl}^{(3)} n_j n_l A_i^{(0)} A_k^{(0)} = 12\lambda^{(0)} T_f^{(3)} + 2\lambda^{(0)} T_f^{(1)} - 6(A_i^{(0)} Q_{ik}^{(1)} A_k^{(2)} + A_i^{(0)} Q_{ik}^{(2)} A_k^{(1)} - \lambda^{(1)} A_k^{(0)} A_k^{(2)}) - 6[C_{ijklmn}^{(3)} \alpha_{mn}^{(3)} + 2C_{ijsl}^{(3)} \alpha_{ks}^{(3)} + 2(C_{ijsl}^{(1)} + C_{ijslmn}^{(1)} \alpha_{mn}^{(1)}) \alpha_{ks}^{(2)} + 2(1/2 C_{ijsl}^{(2)} + C_{ijslmn}^{(2)} \alpha_{mn}^{(2)}) \alpha_{ks}^{(1)} + 2C_{sjtl}^{(1)} \alpha_{is}^{(1)} \alpha_{kt}^{(2)} + (C_{sjtl}^{(1)} + C_{sjtlmn}^{(1)} \alpha_{mn}^{(1)}) \alpha_{is}^{(1)} \alpha_{kt}^{(1)}] n_j n_l A_i^{(0)} A_k^{(0)} \quad (23c)$$

The left hand side of (23) can be further expanded in terms of the six independent components referred to the crystallographic axis, since quartz is a trigonal crystal:

$$C_{66}^{(1)} x_1 + C_{22}^{(1)} x_2 + C_{44}^{(1)} x_3 + C_{14}^{(1)} x_4 + C_{13}^{(1)} x_5 + C_{33}^{(1)} x_6 = Y^{(1)} \quad (24a)$$

$$\tilde{C}_{66}^{(2)} x_1 + \tilde{C}_{22}^{(2)} x_2 + \tilde{C}_{44}^{(2)} x_3 + \tilde{C}_{14}^{(2)} x_4 + \tilde{C}_{13}^{(2)} x_5 + \tilde{C}_{33}^{(2)} x_6 = Y^{(2)} \quad (24b)$$

$$\tilde{C}_{66}^{(3)} x_1 + \tilde{C}_{22}^{(3)} x_2 + \tilde{C}_{44}^{(3)} x_3 + \tilde{C}_{14}^{(3)} x_4 + \tilde{C}_{13}^{(3)} x_5$$

+  $C_{33}^{(3)} x_6 = y^{(3)}$  (24c)  
 where  $y^{(1)}$ ,  $y^{(2)}$  and  $y^{(3)}$  are the respective right hand expressions of equations (23) and,

$$\begin{aligned} x_1 &= A_1^{(0)2} n_2^2 - 2A_1^{(0)} A_2^{(0)} n_1 n_2 + A_2^{(0)2} n_1^2 \\ x_2 &= A_1^{(0)2} n_1^2 - 2A_1^{(0)} A_2^{(0)} n_1 n_2 + 2A_2^{(0)2} n_2^2 \\ x_3 &= 2(A_1^{(0)2} n_2 n_3 + 2A_1^{(0)} A_2^{(0)} n_1 n_3 + 2A_1^{(0)} A_3^{(0)} n_1 n_2 \\ &\quad - A_2^{(0)2} n_2 n_3 + A_2^{(0)} A_3^{(0)} n_1^2 - A_2^{(0)} A_3^{(0)} n_2^2) \\ x_4 &= A_1^{(0)2} n_3^2 + 2A_1^{(0)} n_1 n_3 + A_2^{(0)2} n_3^2 + 2A_2^{(0)} A_3^{(0)} n_2 n_3 \\ &\quad + A_3^{(0)2} n_1^2 + A_3^{(0)2} n_2^2 \\ x_5 &= 2(A_1^{(0)} A_3^{(0)} n_1 n_3 + A_2^{(0)} A_3^{(0)} n_2 n_3) \\ x_6 &= A_3^{(0)2} n_3^2 \end{aligned} \quad (25)$$

Measured values of temperature coefficients of frequency  $Tf^{(n)}$  for various doubly rotated cuts by Bechmann, Ballato and Lukaszek<sup>2</sup>, thermal expansion coefficients  $\alpha_{ij}^{(n)}$  and second order elastic stiffnesses  $C_{ijkl}$  of Bechmann, Ballato and Lukaszek<sup>2</sup>, and third order elastic stiffnesses  $C_{ijk'mn}$  of Thurston, McSkimin and Andreatch<sup>9</sup> are used to compute values of  $y^{(1)}$ ,  $y^{(2)}$  and  $y^{(3)}$ .  $x_i$  are calculated according to (25).

We employ the following algorithm to find a reduced dataset from which we calculate temperature derivatives:

- 1) Obtain the least squares estimate of  $C_{pq}^{(1)}$  and their standard errors from a given data set.
- 2) Construct a 99.9% confidence interval.
- 3) Reject data outside the interval.
- 4) Obtain a subset of data.
- 5) Go back to step 1.

We begin the calculation with 117 data points given in Table V of Ref. 2, and after five repeated calculations, the number of data points is reduced to 28. These 28 data points are listed in Table 2. In the last column of the table, a value of 1.0 is assigned as the weight for observations from the well know cuts like the AT, X, Y and IT, and a value of 0.5 for the rest of the observations. Least squares estimated values of

$C_{ijkl}^{(1)}$  (or  $C_{pq}^{(1)}$ ),  $\bar{C}_{ijkl}^{(2)}$  (or  $\bar{C}_{pq}^{(2)}$ ) and  $\bar{C}_{ijkl}^{(3)}$  (or  $\bar{C}_{pq}^{(3)}$ ) are tabulated in Table 3 along with their standard error.

In the incremental stress-strain-temperature relations (10b), we observe that  $D_{ijkl}^{(n)}/C_{ijkl}$  ( $n=1,2,3$ ) have similar significance to the temperature coefficients of elastic stiffnesses,  $TC_{ijkl}^{(n)}$ , used in Ref. 2. These coefficients are not equivalent, for they are defined in two different formulations, but for

purposes of comparison, we report the values of

$D_{ijkl}^{(n)}/C_{ijkl}$  in Tables 4, 5, and 6. Based on our values of  $C_{pq}^{(1)}$ ,  $\bar{C}_{pq}^{(2)}$  and  $\bar{C}_{pq}^{(3)}$ , the first, second and third

temperature coefficients of frequency for the thickness vibrations of various doubly rotated cuts are predicted and compared with observed values<sup>2</sup> in Table 7. Fig. 3 gives the frequency-temperature curves for various angles of AT-cut. The dotted line is given by Bechmann<sup>10</sup>. Fig. 4 shows the presently calculated  $T_{max}$  and  $T_{min}$ , and the observed values versus the orientation angle  $\theta$  for the AT-cut in the range  $\theta = 35^\circ$  to  $40^\circ$ . Also exhibited is the calculated inflection temperature  $T_i$  defined by

$$T_i = T_0 - Tf(2)/3Tf(3).$$

It may be seen from Table 7 and figs. 3 and 4 that the results of our present calculation are either comparable or slightly better than those in Ref. 2.

#### Incremental Two-Dimensional Equations of Motion for Small Amplitude Waves Superposed on Homogenous Thermal Strain

Given in Fig. 5 is a crystal plate with its coordinates and dimensions which will be used in the subsequent discussions. The variational incremental potential and kinetic energy of a crystal at the final state are:

$$\delta V = \int_V \tau_{ij} \delta e_{ij} dv \quad (26a)$$

$$\delta K = \int_V \frac{1}{2} \rho \delta(\dot{u}_i \dot{u}_i) dv \quad (26b)$$

where  $dv$  is the differential volume referred to the natural frame of reference. By Hamilton's principle:

$$\delta \int_{t_0}^{t_1} (K - V) dt + \int_{t_0}^{t_1} \delta W dt = 0 \quad (27)$$

where  $\delta W = \int_S p_i \delta u_i dS$  is the variational incremental work done. Substitution of (26b) into the kinetic energy term of (27) and integration by parts, yields:

$$\begin{aligned} \delta \int_{t_0}^{t_1} K dt &= \int_V \rho \dot{u}_i \delta u_i \Big|_{t_0}^{t_1} dv - \int_{t_0}^{t_1} dt \int_V \rho \ddot{u}_i \delta u_i dv \\ &= - \int_{t_0}^{t_1} dt \int_V \rho \ddot{u}_i \delta u_i dv \end{aligned} \quad (28)$$

since  $\delta u_i$  vanishes at  $t_0$  and  $t_1$ . The strain-displacement relation (10a) is put into (26a) and the result into the potential energy term of (27) which gives, after some rearrangement,

$$\delta \int_{t_0}^{t_1} V dt = \int_{t_0}^{t_1} dt \int_V (\tau_{ij} + \alpha_{ik}^0 \tau_{kj}) \delta u_{i,j} dv$$

which is equivalent to

$$\begin{aligned} \delta \int_{t_0}^{t_1} V dt &= \int_{t_0}^{t_1} dt \int_V \{ (\tau_{ij} + \alpha_{ik}^0 \tau_{kj}) \delta u_{i,j} \\ &\quad - (\tau_{ij} + \alpha_{ik}^0 \tau_{kj})_{,j} \delta u_i \} dv \end{aligned}$$

By applying the divergence theorem on the first term in the integrand of the right hand side to transform it into a surface integral, we obtain the desired expression for the potential energy,

$$\delta \int_{t_0}^{t_1} V dt = \int_{t_0}^{t_1} dt \left\{ \int_S n_j (\tau_{ij} + \alpha_{ik}^0 \tau_{kj}) \delta u_i ds \right.$$

$$- \int_V (\tau_{ij} + \alpha_{ik} \tau_{kj})_{,j} \delta u_i dv \quad (29)$$

A useful variational equation is obtained when (28) and (29) are substituted into (27):

$$\int_{t_0}^t dt \left\{ \int_V [(\tau_{ij} + \alpha_{ik} \tau_{kj})_{,j} - \rho \ddot{u}_i] \delta u_i dv + \int_S [p_i - n_j (\tau_{ij} + \alpha_{ik} \tau_{kj})] \delta u_i dS \right\} = 0 \quad (30)$$

For ease and clarity of writing, we introduce the definition,

$$\beta_{ik} = \delta_{ik} + \alpha_{ik}^{\ominus} \quad (31)$$

where  $\delta_{ik}$  is a Kronecker delta. Then, (30) can be rewritten as

$$\int_{t_0}^t dt \left\{ \int_V (\beta_{ik} \tau_{kj,j} - \rho \ddot{u}_i) \delta u_i dv + \int_S (p_i - n_j \beta_{ik} \tau_{kj}) \delta u_i dS \right\} = 0 \quad (32)$$

This is the variational incremental stress-temperature equation of motion, which closely resembles the variational stress equations of motion for classical elasticity, except for expansion coefficients  $\alpha_{ik}^{\ominus}$ .

Following Mindlin's<sup>11</sup> procedure, we convert the incremental three-dimensional equations to an infinite series of two-dimensional equations by expanding the displacement in an infinite series of powers of the thickness coordinate of the plate and integrating through the thickness. Thus, we let

$$u_i(x_1, x_2, x_3, t) = \sum_{n=0}^{\infty} x_2^n u_i^{(n)}(x_1, x_3, t) \quad (33)$$

Inserting (33) into the first integrand of (32) and integrating through the thickness yields

$$\int_A \left[ \sum_{n=0}^{\infty} (\beta_{ik} \tau_{kj,j}^{(n)} - n \beta_{ik} \tau_{k2}^{(n-1)} + \beta_{ik} F_k^{(n)} - \rho \sum_{m=0}^{\infty} A_{mn} \ddot{u}_i^{(m)}) \delta u_i^{(n)} \right] dA = 0 \quad (34)$$

$$\text{where } \tau_{kj}^{(n)} = \int_{-b}^b \tau_{kj} x_2^n dx_2 \quad \text{is the } n\text{th order incremental stress,} \quad (35a)$$

$$F_k^{(n)} = \left[ x_2^n \tau_{k2} \right]_{-b}^b \quad \text{is the } n\text{th order incremental face traction} \quad (35b)$$

$$\text{and } A_{mn} = \frac{2b^{m+n+1}}{m+n+1} \quad \text{when } (m+n) \text{ is even} \\ = 0 \quad \text{when } (m+n) \text{ is odd} \quad (35c)$$

The differential area of the major surface of the plate is  $dA$ . Since the coefficients of  $\delta u_i^{(n)}$  must vanish separately, we have the incremental stress-temperature equations of motion of order  $n$  given by

$$\beta_{ik} \tau_{kj,j}^{(n)} - n \beta_{ik} \tau_{k2}^{(n-1)} + \beta_{ik} F_k^{(n)} = \rho \sum_{m=0}^{\infty} A_{mn} \ddot{u}_i^{(m)} \quad (36)$$

Substitution of (33) into (10a), and rearranging and using definition (31), yields:

$$e_{ij} = \sum_{n=0}^{\infty} x_2^n e_{ij}^{(n)} \quad (37a)$$

$$\text{where } e_{ij}^{(n)} = 1/2 [\beta_{kj} u_{k,i}^{(n)} + \beta_{ki} u_{k,j}^{(n)}]$$

$$+ (n+1)(\delta_{2i} \beta_{kj} u_k^{(n+1)} + \delta_{2j} \beta_{ki} u_k^{(n+1)}) \quad (37b)$$

is the  $n$ th order incremental strain-displacement-temperature relation. The  $n$ th order incremental stress-strain-temperature relation is derived by substituting (37a) into (10b) and employing the results into (35a) to give

$$\tau_{ij}^{(n)} = \sum_{m=0}^{\infty} D_{ijkl} A_{mn} e_{kl}^{(m)} \quad (38a)$$

$$\text{where } D_{ijkl} = C_{ijkl} + D_{ijkl}^{(1)} \cdot \theta + D_{ijkl}^{(2)} \cdot \theta^2 + D_{ijkl}^{(3)} \cdot \theta^3 \quad (38b)$$

The second integrand of (32) will yield the necessary boundary conditions for the two dimensional equations. If the  $n$ th order incremental surface traction is defined as

$$p_i^{(n)}(x_1, x_3, t) = \int_{-b}^b p_i(x_1, x_2, x_3, t) x_2^n dx_2 \quad (39)$$

then employing (39), (35a) and (33) in the second integrand of (32) will yield the necessary boundary conditions, namely,

$$\text{specify } p_i^{(n)} = n_j \beta_{ik} \tau_{kj}^{(n)} \text{ or } u_i^{(n)} \text{ on } C \quad (40)$$

where  $C$  is the edge of the plate. Equations (36), (37a), (37b) and (38a) are respectively very similar to equations 3.0211, 3.036, 3.035 and 3.043 of Ref. 11. The dissimilarity arises from the temperature effects.

#### Thickness Vibration of SC-Cut Plates With One Pair of Free Edges

The SC-cut has triclinic symmetry and as such the three components of thickness vibrations, namely the slow shear, fast shear and thickness stretch, are coupled. The thickness shear modes are always coupled to flexure through the same elastic stiffness.

Consequently, four displacement components,  $u_2^{(0)}$ ,  $u_1^{(1)}$ ,  $u_2^{(1)}$  and  $u_3^{(1)}$ , are needed to capture its frequency-temperature characteristics in a finite plate. Fig. 6 shows the motion of each of the four components.

The infinite series of two-dimensional plate equations are truncated by retaining terms of order zero and one only, that is, setting

$$u_i^{(n)} = 0 \quad \text{for } n > 1$$

$$\text{and } \tau_{ij}^{(n)} = 0 \quad \text{for } n > 1$$

The resulting equations of motion from (36) are

$$\beta_{ik} \tau_{kj}^{(0)} = 2b \rho u_i^{(0)} \quad (41a)$$

$$\beta_{ik} \tau_{kj}^{(1)} - \beta_{ik} \tau_{k2}^{(0)} = \frac{2b^3}{3} \rho u_i^{(1)} \quad (41b)$$

where the incremental face tractions,  $F_k^{(n)}$ , are zero since the major surfaces of the plate are free. From the definition (31) we observe that  $\beta_{ik}$  is a predominantly

diagonal tensor because the magnitude of  $\alpha_{ik}^{\ominus}$  for quartz is  $10^{-6}$ . Therefore, the off-diagonal terms can be neglected without loss of accuracy:

$$\beta_{ij} = 0 \quad \text{for } i \neq j$$

$$\text{and } \beta_{ii} = \beta_i = 1 + \alpha_{ii}^{\ominus} \quad i = 1, 2, 3 \quad (42)$$

Components  $u_1^{(0)}$  and  $u_3^{(0)}$  are neglected, and we are left with four branches  $u_2^{(0)}$ ,  $u_1^{(1)}$ ,  $u_2^{(1)}$  and  $u_3^{(1)}$ . The plate is assumed to vibrate as a strip and, consequently, we set  $\frac{\partial(\cdot)}{\partial x_3} = 0$ . With these simplifications, the equations of motion, (41a) and (41b), becomes:

$$\begin{aligned} \beta_2 \tau_{12,1}^{(0)} &= 2b\rho u_2^{(0)} \\ \beta_1 \tau_{11,1}^{(1)} - \beta_1 \tau_{12}^{(0)} &= \frac{2b^3}{3} \rho u_1^{(1)} \\ \beta_2 \tau_{12,1}^{(1)} - \beta_2 \tau_{22}^{(0)} &= \frac{2b^3}{3} \rho u_2^{(1)} \\ \beta_3 \tau_{13,1}^{(1)} - \beta_3 \tau_{23}^{(0)} &= \frac{2b^3}{3} \rho u_3^{(1)} \end{aligned} \quad (43)$$

Only the zeroth and first order strains remain which can be written as follows:

$$\begin{aligned} e_{11}^{(0)} &= e_{33}^{(0)} = e_{13}^{(0)} = 0 \\ e_{22}^{(0)} &= \beta_2 u_2^{(0)} \\ e_{23}^{(0)} &= 1/2 \beta_3 u_3^{(0)} \\ e_{12}^{(0)} &= 1/2 (\beta_2 u_{2,1}^{(0)} + \beta_1 u_1^{(1)}) \\ e_{22}^{(1)} &= e_{33}^{(1)} = e_{23}^{(1)} = 0 \\ e_{11}^{(1)} &= \beta_1 u_{1,1}^{(1)} \\ e_{13}^{(1)} &= 1/2 \beta_3 u_{3,1}^{(1)} \\ e_{12}^{(1)} &= 1/2 \beta_2 u_{2,1}^{(1)} \end{aligned} \quad (44)$$

Equations (44) are put into the zeroth and first order stress-strain-temperature relations of (38) to yield the stress-displacement-temperature relations,

$$\begin{aligned} \tau_{12}^{(0)} &= 2bk^2 (\beta_2 D_{66} u_{2,1}^{(0)} + \beta_1 D_{66} u_1^{(1)} + \beta_2 D_{26} u_2^{(1)} + \beta_3 D_{46} u_3^{(1)}) \\ \tau_{22}^{(0)} &= 2bk^2 (\beta_2 D_{26} u_{2,1}^{(0)} + \beta_1 D_{26} u_1^{(1)} + \beta_2 D_{22} u_2^{(1)} + \beta_3 D_{24} u_3^{(1)}) \\ \tau_{23}^{(0)} &= 2bk^2 (\beta_2 D_{46} u_{2,1}^{(0)} + \beta_1 D_{46} u_1^{(1)} + \beta_2 D_{24} u_2^{(1)} + \beta_3 D_{44} u_3^{(1)}) \\ \tau_{11}^{(1)} &= \frac{2b^3}{3} (\beta_1 D_{11} u_{1,1}^{(1)} + \beta_2 D_{16} u_{2,1}^{(1)} + \beta_3 D_{15} u_{3,1}^{(1)}) \\ \tau_{12}^{(1)} &= \frac{2b^3}{3} (\beta_1 D_{16} u_{1,1}^{(1)} + \beta_2 D_{66} u_{2,1}^{(1)} + \beta_3 D_{56} u_{3,1}^{(1)}) \\ \text{and } \tau_{13}^{(1)} &= \frac{2b^3}{3} (\beta_1 D_{15} u_{1,1}^{(1)} + \beta_2 D_{56} u_{2,1}^{(1)} + \beta_3 D_{55} u_{3,1}^{(1)}) \end{aligned} \quad (45)$$

where  $k^2 = \pi^2/12$  is the usual shear correction factor for thickness vibrations<sup>11</sup>. Substitution of (45) into (43) gives the displacement-temperature equations of motion,

$$\begin{aligned} k^2 (\beta_2 D_{66} u_{2,1}^{(0)} + \beta_1 \beta_2 D_{66} u_{1,1}^{(1)} + \beta_2^2 D_{26} u_{2,1}^{(1)} + \beta_2 \beta_3 D_{46} u_{3,1}^{(1)}) \\ = \rho u_2^{(0)} \end{aligned}$$

$$\begin{aligned} \beta_1^2 D_{11} u_{1,1}^{(1)} + \beta_1 \beta_2 D_{16} u_{2,1}^{(1)} + \beta_1 \beta_3 D_{15} u_{3,1}^{(1)} \\ - \frac{3k^2}{b^2} (\beta_1 \beta_2 D_{66} u_{2,1}^{(0)} + \beta_1^2 D_{66} u_1^{(1)} + \beta_1 \beta_2 D_{26} u_2^{(1)} \\ + \beta_1 \beta_3 D_{46} u_3^{(1)}) = \rho u_1^{(1)} \\ \beta_1 \beta_2 D_{16} u_{1,1}^{(1)} + \beta_2^2 D_{66} u_{2,1}^{(1)} + \beta_2 \beta_3 D_{56} u_{3,1}^{(1)} \\ - \frac{3k^2}{b^2} (\beta_2^2 D_{26} u_{2,1}^{(0)} + \beta_1 \beta_2 D_{26} u_1^{(1)} + \beta_2^2 D_{22} u_2^{(1)} \\ + \beta_2 \beta_3 D_{24} u_3^{(1)}) = \rho u_2^{(1)} \\ \beta_1 \beta_3 D_{15} u_{1,1}^{(1)} + \beta_2 \beta_3 D_{56} u_{2,1}^{(1)} + \beta_3^2 D_{55} u_{3,1}^{(1)} \\ - \frac{3k^2}{b^2} (\beta_2 \beta_3 D_{46} u_{2,1}^{(0)} + \beta_1 \beta_3 D_{46} u_1^{(1)} + \beta_2 \beta_3 D_{24} u_2^{(1)} \\ + \beta_3^2 D_{44} u_3^{(1)}) = \rho u_3^{(1)} \end{aligned} \quad (46)$$

In order to have even shear across the surface of the plate, we let  $u_1^{(1)}$  be symmetric and  $u_2^{(0)}$  antisymmetric by setting:

$$\begin{aligned} u_2^{(0)} &= A_1 b \sin \xi x_1 e^{i\omega t} \\ u_1^{(1)} &= A_2 \cos \xi x_1 e^{i\omega t} \\ u_2^{(1)} &= A_3 \cos \xi x_1 e^{i\omega t} \\ u_3^{(1)} &= A_4 \cos \xi x_1 e^{i\omega t} \end{aligned} \quad (47)$$

Equations (47) are employed in (46) to yield the dispersion matrix (48) given in Table 8.

Four wave numbers  $\bar{\xi}_1$  are obtained by solving the the polynomial from the determinant of the dispersion matrix. Fig. 7 shows the dispersion relation for an SC cut plate. The rank of (48) is three, hence three amplitude ratios can be determined for each wave number, namely,

$$\begin{aligned} \alpha_{1q} &= A_{2q}/A_{1q} \\ \alpha_{2q} &= A_{3q}/A_{1q} \\ \alpha_{3q} &= A_{4q}/A_{1q} \quad \text{for } q = 1, 2, 3, 4 \end{aligned} \quad (49)$$

The boundary conditions at the free edges, according to (40), are

$$\beta_2 \tau_{12}^{(0)} = \beta_1 \tau_{11}^{(1)} = \beta_2 \tau_{12}^{(1)} = \beta_3 \tau_{13}^{(1)} = 0 \quad (50)$$

where the stress-displacement-temperature relations for the above stresses are given in (45). Substitution of (47) and (49) into (50) gives the frequency matrix:

$$\begin{aligned}
& \sum_q (\beta_2^2 D_{66} \bar{\epsilon}_q + \beta_1 \beta_2 D_{66} \alpha_{1q} + \beta_2^2 D_{26} \alpha_{2q} + \beta_2 \beta_3 D_{46} \alpha_{3q}) \cos \bar{\epsilon}_q r A_{1q} = 0 \\
& \sum_q (\beta_1^2 D_{11} \bar{\epsilon}_q \alpha_{1q} + \beta_1 \beta_2 D_{16} \bar{\epsilon}_q \alpha_{2q} + \beta_1 \beta_3 D_{15} \bar{\epsilon}_q \alpha_{3q}) \sin \bar{\epsilon}_q r A_{1q} = 0 \\
& \sum_q (\beta_1 \beta_2 D_{16} \bar{\epsilon}_q \alpha_{1q} + \beta_2^2 D_{66} \bar{\epsilon}_q \alpha_{2q} + \beta_2 \beta_3 D_{56} \bar{\epsilon}_q \alpha_{3q}) \sin \bar{\epsilon}_q r A_{1q} = 0 \\
& \sum_q (\beta_1 \beta_3 D_{15} \bar{\epsilon}_q \alpha_{1q} + \beta_2 \beta_3 D_{56} \bar{\epsilon}_q \alpha_{2q} + \beta_3^2 D_{55} \bar{\epsilon}_q \alpha_{3q}) \sin \bar{\epsilon}_q r A_{1q} = 0 \quad (51)
\end{aligned}$$

where  $r$  is the ratio  $a/b$ . The resonant frequency of a finite free-free plate is the frequency that satisfies both the frequency matrix and dispersion matrix. A simple algorithm for finding the resonant frequency at a certain temperature  $T$  would be as follows:

- a) Calculate the temperature dependent material properties,  $D_{pq}$  and  $\beta_i$ ,

$$\begin{aligned}
D_{pq} &= C_{pq} + D_{pq}^{(1)} \cdot \Theta + D_{pq}^{(2)} \cdot \Theta^2 + D_{pq}^{(3)} \cdot \Theta^3 \quad p, q = 1, 2, \dots, 6 \\
\beta_i &= 1 + \alpha_{ii}^{(1)} \cdot \Theta + \alpha_{ii}^{(2)} \cdot \Theta^2 + \alpha_{ii}^{(3)} \cdot \Theta^3 \quad i = 1, 2, 3 \quad (52)
\end{aligned}$$

where  $\Theta = T - T_0$

- b) Pick a frequency  $\Omega$  and find the wave numbers and amplitude ratios from the dispersion matrix (48)
- c) Check if the wave numbers and amplitude ratios from part (b) satisfy the frequency matrix (51)
- d) Iterate to part (b) until the frequency  $\omega$  satisfies the dispersion matrix (48) and frequency matrix (51) within a predefined error limit.

The rank of the frequency matrix is three, hence three ratios of the amplitudes can be uniquely determined,

$$\begin{aligned}
\bar{\alpha}_2 &= A_{12}/A_{11} \\
\bar{\alpha}_3 &= A_{13}/A_{11} \\
\bar{\alpha}_4 &= A_{14}/A_{11} \quad (53)
\end{aligned}$$

There remains only one unknown  $A_{11}$ . If we define  $\bar{\alpha}_1 = A_{11}/A_{11} = 1$ , the assumed displacement functions (47) now becomes

$$\begin{aligned}
u_2^{(0)} &= \sum_q \bar{\alpha}_q b \sin \bar{\epsilon}_q x_1 e^{i\omega t} \\
u_1^{(1)} &= \sum_q \bar{\alpha}_q \alpha_{1q} \cos \bar{\epsilon}_q x_1 e^{i\omega t} \\
u_2^{(1)} &= \sum_q \bar{\alpha}_q \alpha_{2q} \cos \bar{\epsilon}_q x_1 e^{i\omega t} \\
u_3^{(1)} &= \sum_q \bar{\alpha}_q \alpha_{3q} \cos \bar{\epsilon}_q x_1 e^{i\omega t} \quad (54)
\end{aligned}$$

Equations (54) are used to calculate the mode shapes of a particular resonant frequency. Fig. 8 shows the frequency spectrum of an SC cut plate for  $a/b = 17$  to 23 and  $\lambda = 0.91$  to 1.09. The symbols in the figure, TT-n, TS-n and F-n, denote thickness-twist, thickness shear and flexure with  $n$  number of half waves. At  $a/b = 19.8$  and  $\lambda = 0.94333$ , the frequency spectrum gives TS-1 which is the fundamental thickness shear mode. Fig. 9 shows the mode shapes of the four displacement components at TS-1. The four components are seen to be coupled.

The algorithm given in (52) can be used to calculate the frequency  $\Omega$  of a mode of vibration at any temperature. We consider the frequency-temperature of the fundamental thickness shear mode (TS-1) of the SC-cut plate. If the reference frequency is taken at 25°C, we can define the frequency-temperature curve with reference to this frequency as:

$$\frac{f(T) - f(T_0 = 25^\circ\text{C})}{f(T_0 = 25^\circ\text{C})} = \frac{\Delta f}{f_0} \quad (55)$$

The thickness shear mode exhibits different frequency-temperature curve when the  $a/b$  ratio is varied. As observed from Fig. 10, the curves for increasing  $a/b$  ratios move towards the infinite plate curve, though not quite approaching it. The infinite plate curve was calculated using equations (17). The same curve would be obtained if we let  $\bar{\epsilon}_1 = 0$  in the dispersion relations matrix (48) and calculate the frequency-temperature behavior of the cut-off frequency of the thickness shear mode. This would represent the behavior of an infinite strip which is the same as an infinite plate. For plate vibrations with  $a/b$  less than 50, the finite plate theory would give a better prediction than the infinite plate solution.

When the ratio  $a/b$  is fixed, the frequency-temperature characteristics are dependent on the angles of cut:  $\phi$  and  $\Theta$ . Fig. 11 investigates the changes in the frequency-temperature curves at  $a/b = 19.8$ ,  $\phi = 21.9^\circ$  and various  $\Theta$ . The infinite plate solution for  $\phi = 21.9^\circ$  and  $\Theta = 33.9^\circ$  is also shown in the figure. Fig. 12 gives similar curves for  $a/b = 19.8$ ,  $\Theta = 33.9^\circ$  and various  $\phi$  angles. The optimum curve from Fig. 11 is  $\phi = 21.9^\circ$  and  $\Theta = 33.8^\circ$ ; from Fig. 12,  $\phi = 10.8^\circ$  and  $\Theta = 33.9^\circ$ .

#### References

1. P.C.Y. Lee and Y.K. Yong, "Temperature Derivatives of Elastic Stiffnesses Derived from the Frequency-Temperature Behavior of Quartz Plates," J. Appl. Physics (Accepted for publication).
2. R. Bechmann, A.D. Ballato and T.J. Lukaszek, "Higher-Order Temperature Coefficients of the Elastic Stiffnesses and Compliances of the Alpha-Quartz," USAELRDL Tech. Report 2261, Sept. 1963.
3. W.P. Mason, "Zero Temperature Coefficient Quartz Crystals for Very High Temperatures," Bell System Tech. J., Vol. 30, April 1951, pp. 366-380.
4. I. Koga, M. Aruga and Y. Yoshimaka, "Theory of Plane Elastic Waves in a Piezoelectric Crystalline Medium and Determination of Elastic and Piezoelectric Constants of Quartz," Phys. Rev., Vol. 109, March 1958, pp. 1467-1473.
5. C.A. Adams, G.M. Enslow, J.A. Kusters and R.W. Ward, "Selected Topics in Quartz Crystal Research," Proc. 24th Ann. Freq. Control Symp., 1970, pp. 55-63.
6. Alfred Kahan, "Elastic Constants of Quartz and Their Temperature Coefficients," Proc. 36th Ann. Freq. Control Symp., 1982, pp. 159-167.
7. "Standards on Piezoelectric Crystals, 1949," Proc. IRE, 37, 1949, p. 1378.
8. A. Nayfeh, Perturbation Methods, John Wiley & Sons, New York, 1973.
9. R.N. Thurston, H.J. McSkimin and P. Andreatch, Jr., "Third Order Elastic Constants of Quartz," J. Appl. Phys., 37, 1966, p. 267.



10. R. Bechmann, "Thickness-Shear Mode Quartz Cut with Small Second- and Third-Order Temperature Coefficients of Frequency (RT-Cut)," Proc. IRE, Vol. 48, August 1960, pp. 1494.

11. R.D. Mindlin, "An Introduction to the Mathematical Theory of Vibrations of Elastic Plates," U.S. Army Signal Corps Engineering Lab., Fort Monmouth, N.J., 1955.

TABLE 2  
Selected Data for Least Squares Regression.

ANGLES OF CUT IN DEGREES		MODE	OBSERVED VALUES			WEIGHTS IN
PHI	THETA		$T_f^{(1)}$	$T_f^{(2)}$	$T_f^{(3)}$	LEAST
			$10^{-6}/^{\circ}\text{C}$	$10^{-9}/^{\circ}\text{C}^2$	$10^{-12}/^{\circ}\text{C}^3$	SQUARES FIT
10.0	-38.00	A	-94.70	***	***	0.5
30.0	0.0	A	-20.50	-53.20	-36.60	1.0
0.0	-49.22	B	0.0	-40.00	-128.00	0.5
0.0	-55.00	B	-13.70	-71.70	-171.90	0.5
0.0	-60.00	B	-24.50	-75.00	-134.80	0.5
5.0	-48.00	B	-1.50	-43.10	-122.60	0.5
30.0	20.00	B	-9.30	-21.80	-34.40	0.5
30.0	40.00	B	-22.20	-39.30	-46.50	0.5
30.0	50.00	B	-28.00	-43.90	-33.10	0.5
0.0	35.25	C	0.0	-0.45	108.60	1.0
0.0	0.0	C	92.50	***	***	1.0
5.0	-24.00	C	33.10	-58.50	-334.00	0.5
5.0	-28.00	C	-1.70	-16.40	-51.60	0.5
10.0	-30.00	C	0.80	-11.50	-30.00	0.5
10.0	-31.00	C	0.61	-10.70	-34.20	0.5
10.0	-32.00	C	0.26	-9.80	-32.40	0.5
10.0	-38.00	C	-5.50	-5.90	1.70	0.5
10.0	-40.00	C	-8.80	-6.50	13.50	0.5
10.0	-48.00	C	-27.40	-19.60	40.00	0.5
12.5	-33.50	C	-0.40	-7.40	-14.00	0.5
20.0	34.33	C	-0.06	-10.10	68.40	1.0
30.0	10.00	C	13.30	-7.90	34.40	0.5
30.0	20.00	C	7.00	-16.90	-0.40	0.5
30.0	30.00	C	5.00	-20.50	-12.40	0.5
30.0	32.00	C	4.30	-14.90	11.60	0.5
30.0	34.00	C	0.75	-12.96	17.40	0.5
30.0	36.00	C	-4.55	-14.30	20.60	0.5
30.0	60.00	C	-72.80	-101.70	***	0.5

TABLE 3

TEMPERATURE DERIVATIVES OF THE ELASTIC STIFFNESSES FOR ALPHA-QUARTZ AT 25°C

pq	First Temperature Derivatives		Effective Second Temperature Derivatives		Effective Third Temperature Derivatives	
	$C_{pq}^{(1)}, 10^6 \text{ N/m}^2/^{\circ}\text{C}$		$\bar{C}_{pq}^{(2)}, 10^3 \text{ N/m}^2/^{\circ}\text{C}^2$		$\bar{C}_{pq}^{(3)}, \text{ N/m}^2/^{\circ}\text{C}^3$	
	Estimate	Std. Error	Estimate	Std. Error	Estimate	Std. Error
66	5.0747	0.029	11.066	1.68	-55.824	19.1
22	1.5976	0.035	-12.989	1.19	-38.145	11.1
44	-5.3780	0.045	-26.505	2.04	-20.468	24.8
14	0.91675	0.018	4.2849	0.715	85.773	8.3
13	-2.1983	0.061	-18.806	3.5	-8.9302	32.8
33	-6.5255	0.190	-20.835	10.2	46.255	95.3

TABLE 4

First Temperature Coefficients of the Elastic Stiffnesses for  
Alpha-Quartz  $10^{-6}/^{\circ}\text{C}$

	Present	Mason <sup>3</sup>	Koga <sup>4</sup>	Bechmann <sup>2</sup>	Adams <sup>5</sup>	Kahan <sup>6</sup>
	$D_{pq}^{(1)}/C_{pq}$	$TC_{pq}^{(1)}$	$TC_{pq}^{(1)}$	$TC_{pq}^{(1)}$	$TC_{pq}^{(1)}$	$TC_{pq}^{(1)}$
$pq$	at 25°C	at 50°C	at 20°C	at 25°C	at 25°C	at 25°C
11	-68.2	-53.5	-44.3	-48.5	-49.6	-35.6
13	-705	-510	-492	-550	-651	-612
14	84.2	90.0	98.0	101	89.0	93.2
23	-197	-165	-188	-160	-192	-205
44	-186	-171	-172	-177	-172	-184
66	158	168	180	178	167	180

TABLE 5  
Second Temperature Coefficients of the Elastic Stiffnesses for  
Alpha-Quartz  $10^{-9}/^{\circ}\text{C}^2$

Present	Mason <sup>3</sup>	Koga <sup>4</sup>	Bechmann <sup>2</sup>	Adams <sup>5</sup>	Kahan <sup>6</sup>
$D_{pq}^{(2)}/C_{pq}$	$TC_{pq}^{(2)}$	$TC_{pq}^{(2)}$	$TC_{pq}^{(2)}$	$TC_{pq}^{(2)}$	$TC_{pq}^{(2)}$
pq at 25°C	at 50°C	at 20°C	at 25°C	at 25°C	at 25°C
<hr/>					
11	-117	-75.0	-407	-107	-117
13	-1022	-2000	-596	-1150	-900
14	-54.4	-270	-13.0	-48.0	-46.6
33	-158	-187	-1412	-275	-100
44	-272	-212	-225	-216	-273
66	152	-5.0	201	118	172

TABLE 6

Third Temperature Coefficients of the Elastic Stiffnesses for  
Alpha-Quartz  $10^{-12}/^{\circ}\text{C}^3$

Present	Mason <sup>3</sup>	Koga <sup>4</sup>	Bechmann <sup>2</sup>	Adams <sup>5</sup>	Kahan <sup>6</sup>	
$D_{pq}^{(3)}/C_{pq}$	$TC_{pq}^{(3)}$	$TC_{pq}^{(3)}$	$TC_{pq}^{(3)}$	$TC_{pq}^{(3)}$	$TC_{pq}^{(3)}$	
pq at 25°C	at 50°C	at 20°C	at 25°C	at 25°C	at 25°C	
-----						
11	-61.9	-15.0	-371	-70	-74	-100
13	-43.4	600	-5559	-750	-240	45.4
14	-816	-630	-625	-590	-521	-612
33	93.7	-410	-243	-250	67	254
44	-45.6	-65.0	-190	-216	-194	-247
66	-239	-167	-777	21	29	25.4

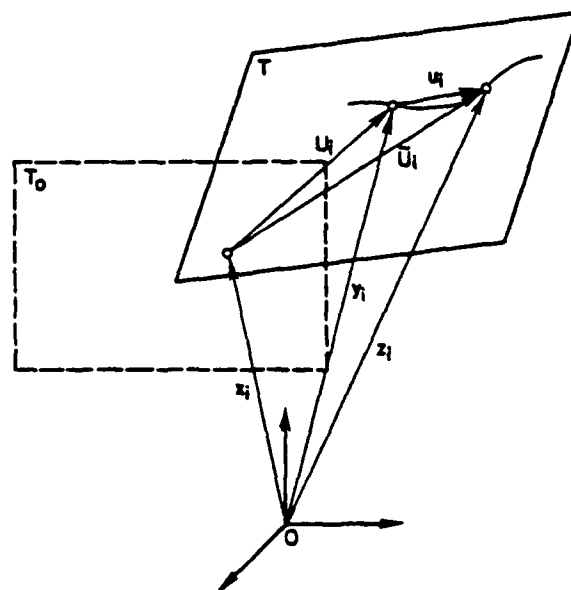


Figure 1: Reference Frame of Crystal.

TABLE 7

Measured and Calculated  $T_f^{(n)}$  for the Thickness Modes A, B, and C  
of Some Selected Quartz Plates.

ANGLES OF CUT IN DEGREES PHI INETA	MODE	OBSERVED CALCULATED		OBSERVED CALCULATED		OBSERVED CALCULATED	
		$T_f^{(1)}$ $10^{-6}/^{\circ}\text{C}$	$10^{-6}/^{\circ}\text{C}$	$T_f^{(2)}$ $10^{-9}/^{\circ}\text{C}^2$	$10^{-9}/^{\circ}\text{C}^2$	$T_f^{(3)}$ $10^{-12}/^{\circ}\text{C}^3$	$10^{-12}/^{\circ}\text{C}^3$
10.0	-28.00	A	-76.50	-85.01			
10.0	-38.00	A	-94.70	-94.80			
12.5	-34.00	A	-81.00	-85.41	-129.00	-118.85	-58.90
15.0	-33.00	A	-75.00	-78.98	-110.00	-113.53	82.50
15.0	-35.00	A	-72.00	-81.20	-88.30	-115.75	90.30
20.0	-36.00	A	-70.00	-74.19	-91.20	-111.42	266.00
30.0	0.0	A	-20.50	-20.42	-51.20	-52.87	-36.60
30.0	10.00	A	-29.30	-31.48	-67.00	-68.79	-58.30
30.0	20.00	A	-42.00	-44.96	-86.00	-86.36	-92.70
30.0	30.00	A	-54.80	-57.31	-105.00	-99.96	-119.00
0.0	-40.00	B	20.70	19.35	-15.20	-23.77	-112.60
0.0	-45.00	B	10.70	8.27	-32.00	-37.36	-128.00
0.0	-49.22	B	0.0	-0.98	-40.00	-48.54	-128.00
0.0	-50.00	B	-1.30	-2.69	-44.40	-50.59	-130.00
0.0	-55.00	B	-13.70	-13.46	-71.70	-63.40	-118.00
0.0	-60.00	B	-24.50	-24.02	-75.00	-75.76	-134.80
5.0	-43.00	B	35.70	8.33	-9.50	-37.32	195.80
5.0	-45.00	B	3.20	4.52	-44.60	-41.63	-169.60
5.0	-47.00	B	0.90	0.68	-41.10	-46.03	-169.60
5.0	-48.00	B	-1.50	-1.26	-43.10	-48.26	-172.60
5.0	-49.00	B	-5.10	-3.20	-53.50	-50.51	-156.00
10.0	-24.00	B	18.20	-0.54	-34.00	-12.66	-124.00
10.0	-26.00	B	16.60	2.91	-43.80	-12.89	-108.00
10.0	-30.00	B	10.00	15.34	-27.00	-29.41	-103.00
10.0	-32.00	B	9.80	12.97	-33.80	-32.64	-197.30
10.0	-33.00	B	7.50	11.79	-39.90	-33.92	-168.50
10.0	-34.00	B	5.70	10.61	-41.50	-35.12	-141.70
10.0	-35.00	B	5.40	9.41	-42.90	-36.27	-50.80
10.0	-38.00	B	1.10	5.74	-39.00	-39.73	-91.30
10.0	-40.00	B	-2.40	3.19	-41.90	-42.14	-115.40
10.0	-42.00	B	-5.90	0.56	-47.50	-44.70	-81.20
12.5	-30.00	B	2.22	7.16	-27.20	-34.37	-74.95
12.5	-31.00	B	2.50	6.59	-32.30	-36.32	-69.20
12.5	-32.00	B	2.10	5.83	-33.80	-37.71	-68.10
12.5	-33.00	B	1.80	4.97	-34.90	-38.66	-90.50
12.5	-33.50	B	-1.30	4.51	-43.40	-39.39	-118.50
12.5	-34.00	B	-1.10	4.07	-44.70	-39.90	-156.60
15.0	-31.00	B	-11.20	-0.73	-39.10	-39.19	-26.40
15.0	-32.00	B	-8.80	-0.74	-39.10	-40.55	-88.00
15.0	-33.00	B	-7.50	-1.13	-33.20	-41.63	-64.80
15.0	-34.00	B	-7.30	-1.72	-37.40	-42.59	-60.30
15.0	-35.00	B	-3.40	-2.40	-28.10	-43.08	-39.10
15.0	-35.00	B	-7.45	-2.42	-33.50	-43.49	-58.00
15.0	-35.50	B	-8.50	-2.79	-39.30	-43.93	-75.10
20.0	-36.00	B	-19.90	-11.67	-40.50	-44.59	20.30
30.0	10.00	B	19.00	-15.73	-42.50	-43.49	-60.00
30.0	20.00	B	-9.30	-9.22	-21.80	-24.19	-34.00
30.0	30.00	B	-19.10	-17.87	-24.50	-19.97	-28.90
30.0	40.00	B	-22.20	-21.99	-39.10	-37.14	-46.50
30.0	50.00	B	-28.00	-27.75	-43.70	-48.80	-33.10
0.0	50.00	C	-82.50	-82.54	-86.68	-86.68	-86.68
0.0	40.00	C	-17.50	-23.96	-16.00	-29.35	
0.0	35.25	C	0.0	-0.18	-0.45	0.15	108.60
0.0	30.00	C	96.30	90.64			110.43
0.0	25.00	C	92.50	92.80			
0.0	20.00	C	89.70	81.48			
5.0	-24.00	C	65.80	63.04			
5.0	-25.00	C	33.10	32.88	-58.50	-44.13	-334.00
5.0	-26.00	C	-0.57	2.41	-82.20	-92.29	-60.00
5.0	-27.00	C	-6.00	-5.25	-28.30	-27.09	-66.20
5.0	-28.00	C	-1.70	-1.69	-16.40	-18.03	-51.60
10.0	-28.00	C	3.30	-0.16	-40.00	-21.28	-48.00
10.0	-30.00	C	0.80	0.56	-11.50	-12.30	-30.00
10.0	-31.00	C	0.61	0.43	-10.10	-10.14	-34.20
10.0	-32.00	C	0.26	0.10	-9.80	-9.54	-32.40
10.0	-33.00	C	-0.87	-0.41	-7.81	-7.33	-21.50
10.0	-34.00	C	-1.70	-1.10	-6.30	-6.45	-10.50
10.0	-35.00	C	-0.20	-1.95	-5.80	-5.84	-7.20
10.0	-36.00	C	-1.40	-2.98	-6.00	-5.51	-5.41
10.0	-38.00	C	-5.50	-5.54	-5.90	-5.61	1.70
10.0	-40.00	C	-8.80	-8.76	-6.50	-6.76	13.50
10.0	-48.00	C	-27.40	-27.52	-19.60	-21.93	40.00
12.5	-25.00	C	12.10	14.49	-35.00	-38.59	-34.70
12.5	-26.00	C	12.30	14.38	-37.90	-40.94	-115.00
12.5	-27.00	C	12.50	16.72	-38.60	-43.66	-98.00
12.5	-28.00	C	14.60	7.80	-39.70	-42.68	-132.00
12.5	-31.00	C	2.00	1.41	-10.50	-10.00	-28.00
12.5	-31.50	C	1.50	1.07	-9.10	-9.16	-10.00
12.5	-32.00	C	1.90	0.73	-8.80	-8.46	-23.10
12.5	-32.50	C	1.40	0.36	-8.70	-7.86	-24.90
12.5	-33.00	C	0.80	-0.03	-7.60	-7.16	-19.60
12.5	-33.50	C	-0.40	-0.46	-7.40	-6.93	-14.00
12.5	-34.00	C	-0.04	-0.91	-7.50	-6.59	-14.39
25.0	-28.00	C	3.70	4.05	-23.15	-29.75	-13.70
25.0	-30.00	C	3.50	6.14	-24.20	-24.74	-12.80
25.0	-34.00	C	4.90	1.26	-18.00	-12.10	-5.60
30.0	10.00	C	13.30	13.64	-7.90	-12.80	34.40
30.0	30.00	C	5.00	4.74	-20.80	-20.89	-12.40
30.0	32.00	C	4.30	4.20	-14.90	-17.58	11.60
30.0	34.00	C	0.75	0.72	-12.96	-15.58	19.40
30.0	36.00	C	-4.55	-4.50	-14.30	-15.77	20.60
30.0	40.00	C	-14.90	-15.49	-20.56	-20.56	27.00
30.0	50.00	C	-46.40	-44.95	-50.10	-49.24	44.50
30.0	60.00	C	-72.80	-72.41	-101.70	-89.39	
15.0	-30.00	C	11.30	5.48	-21.10	-12.16	-47.80
15.0	-31.00	C	6.60	3.21	-13.70	-9.90	-19.20
15.0	-32.00	C	6.60	1.78	-9.70	-8.47	-19.20
15.0	-33.00	C	4.70	0.58	-7.20	-7.51	-17.50
15.0	-34.00	C	1.80	-0.60	-7.16	-6.88	-10.10
15.0	-34.50	C	1.30	-1.20	-7.30	-6.66	-6.60
15.0	-35.00	C	-0.20	-1.83	-7.02	-6.52	-2.60
15.0	-35.50	C	-0.60	-2.47	-7.30	-6.43	-4.70
17.5	-34.50	C	2.49	-0.91	-8.74	-7.79	-4.41
17.5	-35.00	C	0.20	-1.67	-8.10	-7.20	-0.61
17.5	-35.50	C	1.34	-2.45	-8.40	-7.18	-2.78
17.5	-36.00	C	-1.02	-1.28	-8.90	-7.22	2.90
20.0	-34.33	C	-0.06	-0.06	-10.00	-10.00	50.94
20.0	-34.00	C	4.00	4.00	-12.60	-13.70	-28.10
20.0	-30.00	C	4.60	10.88	-30.30	-17.40	-29.40
20.0	-32.00	C	7.10	5.22	-24.90	-9.81	-19.40
20.0	-34.00	C	7.00	0.45	-11.80	-8.43	0.60
20.0	-36.00	C	2.70	2.70	-10.30	-15.10	9.78
20.0	-37.00	C	-0.70	-5.17	-7.20	-8.73	13.20
20.0	-38.00	C	-4.10	-7.08	-11.45	-9.34	12.80
20.0	-39.00	C	-6.20	-9.07	-11.32	-10.20	19.90
25.0	-26.00	C	4.30	3.38	-23.20	-30.26	-11.80

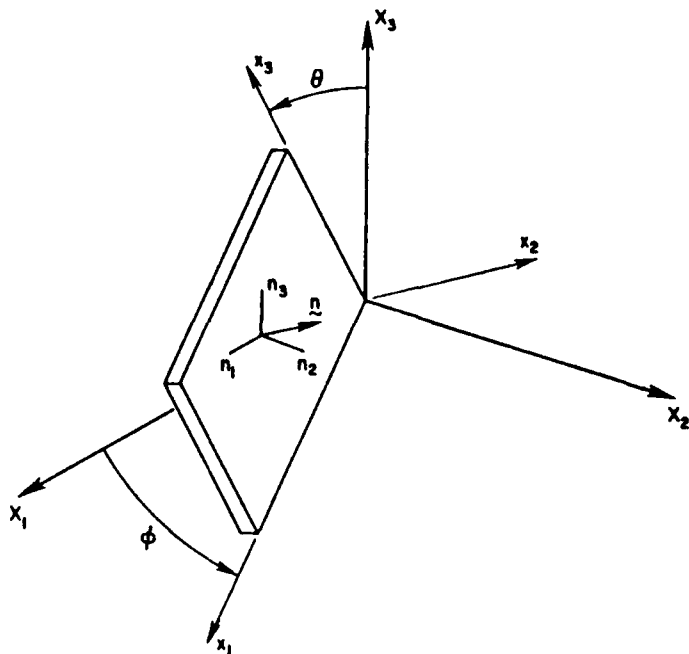


Figure 2: Crystal Plate Normal and Orientation with respect to Crystallographic Axes.

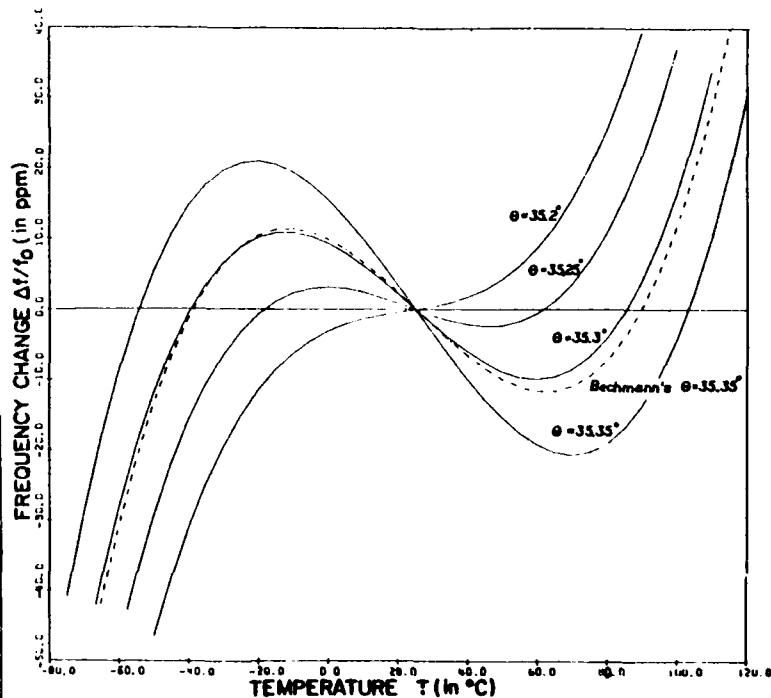


Figure 3: Frequency-Temperature Curves of Thickness Vibrations (Mode C) of AT-cut Resonators.

TABLE 8  
DISPERSION RELATION MATRIX

$$\begin{bmatrix} 3(\beta_2^2 \bar{D}_{66} \bar{\xi}^2 - 3\alpha^2) & 3\beta_1 \beta_2 \bar{D}_{66} \bar{\xi} & 3\beta_2^2 \bar{D}_{26} \bar{\xi} & 3\beta_2 \beta_3 \bar{D}_{46} \bar{\xi} \\ 3\beta_1 \beta_2 \bar{D}_{66} \bar{\xi} & (\beta_1^2 \bar{D}_{11} \bar{\xi}^2 + 3\beta_1^2 \bar{D}_{66} - 3\alpha^2) & (\beta_1 \beta_2 \bar{D}_{16} \bar{\xi}^2 + 3\beta_1 \beta_2 \bar{D}_{26}) & (\beta_1 \beta_3 \bar{D}_{15} \bar{\xi}^2 + 3\beta_1 \beta_3 \bar{D}_{46}) \\ 3\beta_2^2 \bar{D}_{26} \bar{\xi} & (\beta_1 \beta_2 \bar{D}_{16} \bar{\xi}^2 + 3\beta_1 \beta_2 \bar{D}_{26}) & (\beta_2^2 \bar{D}_{66} + 3\beta_2^2 \bar{D}_{22} - 3\alpha^2) & (\beta_2 \beta_3 \bar{D}_{56} \bar{\xi}^2 + 3\beta_2 \beta_3 \bar{D}_{24}) \\ 3\beta_2 \beta_3 \bar{D}_{46} \bar{\xi} & (\beta_1 \beta_3 \bar{D}_{15} \bar{\xi}^2 + 3\beta_1 \beta_3 \bar{D}_{46}) & (\beta_2 \beta_3 \bar{D}_{56} \bar{\xi}^2 + 3\beta_2 \beta_3 \bar{D}_{24}) & (\beta_3^2 \bar{D}_{55} \bar{\xi}^2 + 3\beta_3^2 \bar{D}_{44} - 3\alpha^2) \end{bmatrix} \begin{bmatrix} A_1 \\ A_2 \\ A_3 \\ A_4 \end{bmatrix} = 0$$

where  $\bar{\xi} = \xi b$ ,  $\alpha^2 = \omega^2 / \omega_1^2$ ,  $\omega_1^2 = \frac{3k^2 C_{66}}{\rho b^2}$ ,  $\bar{D}_{pq} = D_{pq} / C_{66}$  and  $\bar{D} = D_{pq} / k^2 C_{66}$  (46)

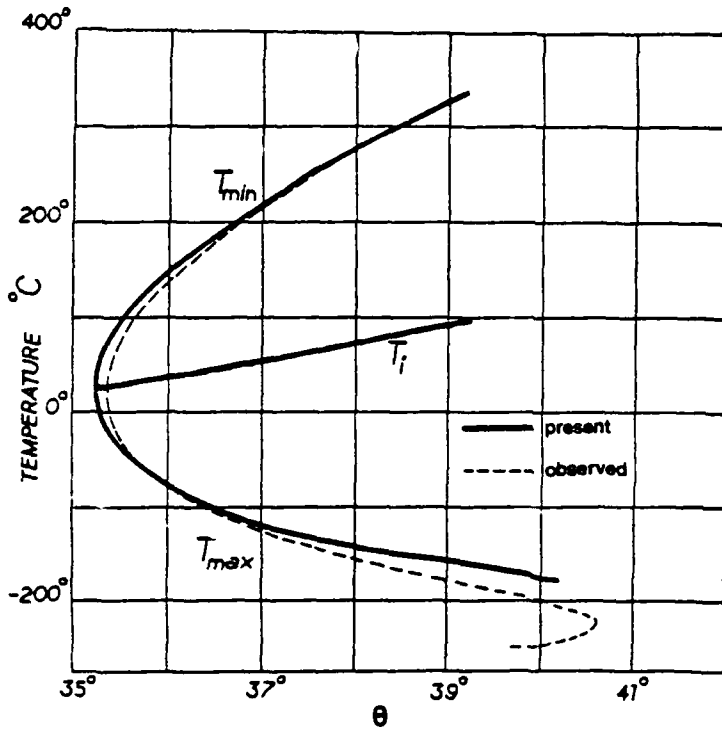


Figure 4: Observed and Calculated Temperature of Zero Temperature Coefficient of Frequency vs Orientation Angle for the AT-cut

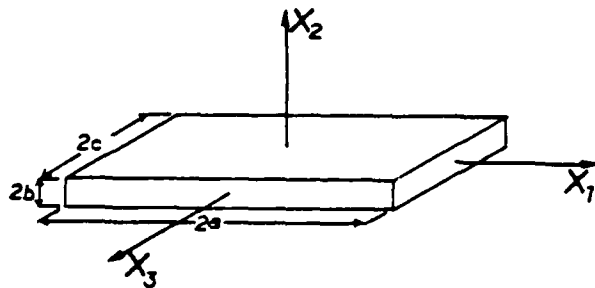


Figure 5: Crystal Plate Coordinates and Dimensions.

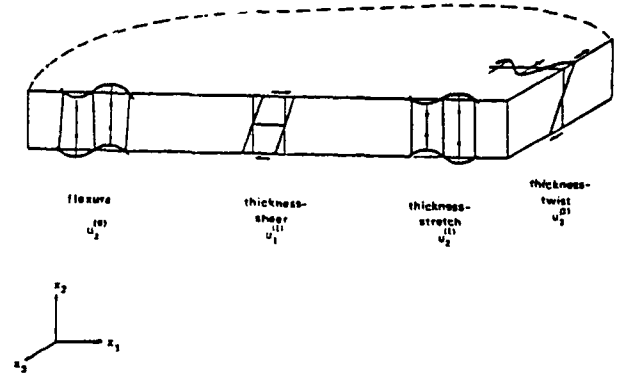


Figure 6: Displacement components of an SC-cut Plate.

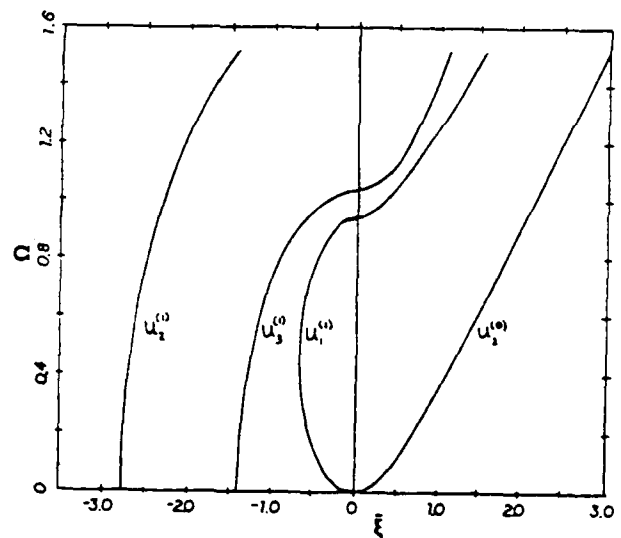


Figure 7: Dispersion Relation for an SC-cut Plate.

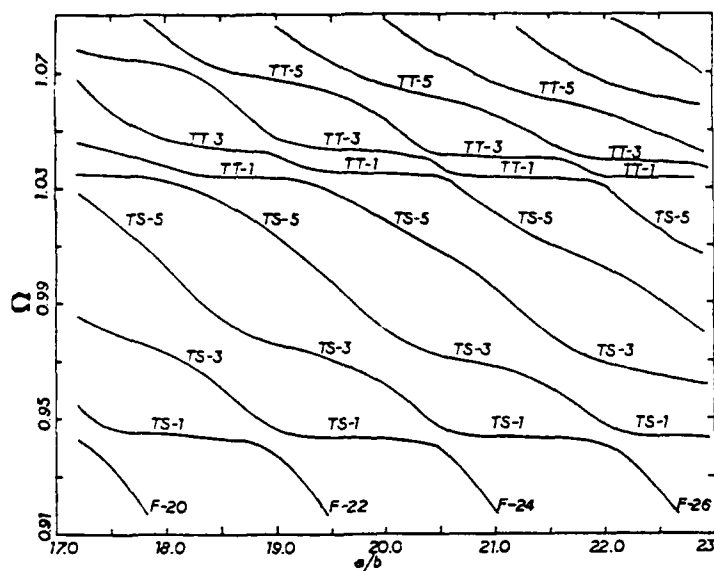


Figure 8: Frequency Spectrum of an SC-cut Plate: TT=Thickness  
Twist, TS=Thickness Shear, F=Flexure, and n=# of phase  
reversals.

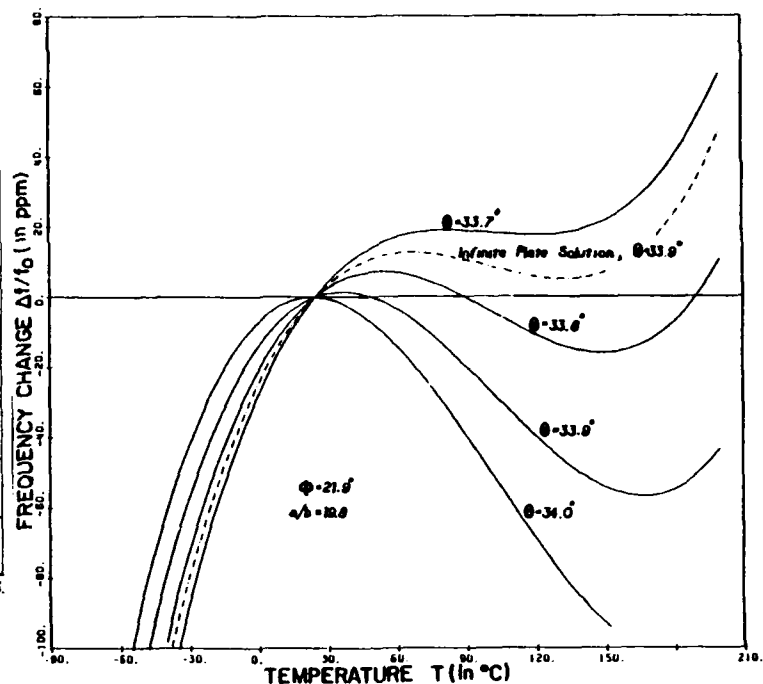


Figure 11: Thickness-Shear Frequency-Temperature Curves of SC-cut Plates for various angle theta.

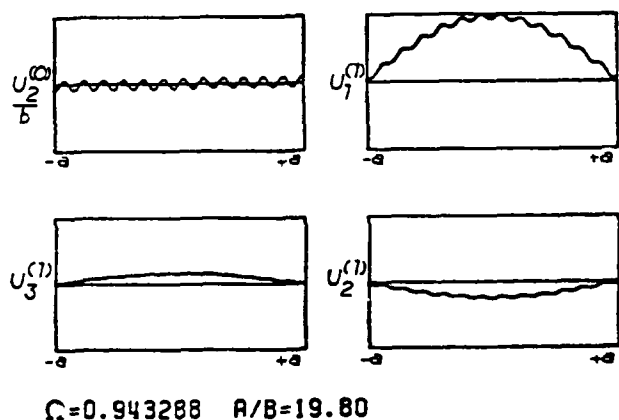


Figure 9: Displacement Mode Shapes of an SC-cut Plate at the Fundamental Thickness-Shear Frequency

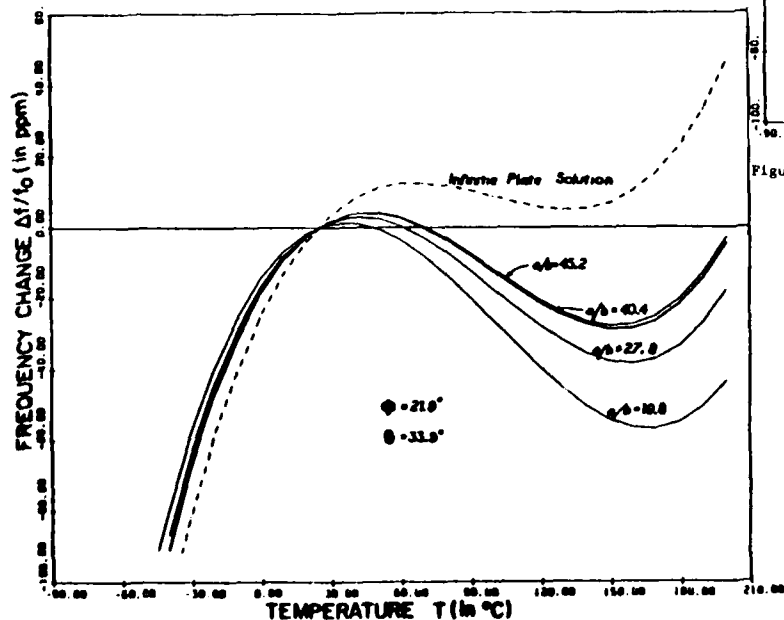


Figure 10: Thickness-Shear Frequency-Temperature Curves of SC-cut Plates for various a/b ratios.

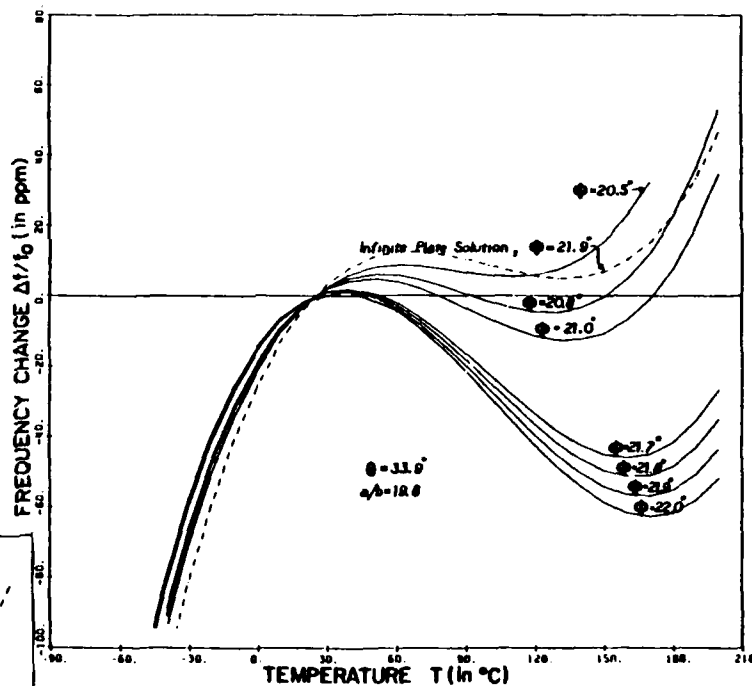


Figure 12: Thickness-Shear Frequency-Temperature Curves of SC-cut Plates for various angle  $\phi$ .

ON THE CHANGE IN ORIENTATION OF THE ZERO-TEMPERATURE CONTOURED  
SC-CUT QUARTZ RESONATOR WITH THE RADIUS OF THE CONTOUR

D.S. Stevens and H.F. Tiersten  
Department of Mechanical Engineering,  
Aeronautical Engineering & Mechanics  
Rensselaer Polytechnic Institute  
Troy, New York 12180-3590

### Abstract

In order to calculate the dependence of the actual orientation of the zero-temperature electroded, contoured SC-cut quartz resonator on the radius of the contour, the actual orientation of the zero-temperature unelectroded flat SC-cut quartz plate vibrating in the pure thickness-mode of interest must be known. However, on account of small inaccuracies in the measured temperature derivatives of the elastic constants of quartz, only the nominal  $\phi$  and  $\theta$  angles of zero-temperature cuts of the unelectroded flat quartz plates vibrating in pure thickness-modes can be calculated. In recent work on contoured AT-cut quartz resonators a 6' correction to the nominal  $\theta$  angle was obtained. Since the  $\theta$  angle of the SC-cut is very near the  $\theta$  angle of the AT-cut, the 6' correction can be taken to hold for the SC-cut also. In this work the corresponding correction to the nominal  $\phi$  angle is obtained from measurements on zero-temperature electroded, contoured SC-cut quartz resonators at 25°C. With this correction to the nominal  $\phi$  angle, the dependence of the actual orientation of the zero-temperature electroded, contoured SC-cut quartz resonator on the radius of the contour at 25°C is calculated for the fundamental and third and fifth harmonics.

### 1. Introduction

As a result of small inaccuracies in the measured temperature derivatives of the elastic constants of quartz<sup>1</sup>, only the nominal  $\phi$  and  $\theta$  angles of zero-temperature cut quartz resonators can be calculated. In recent work<sup>2</sup> on contoured AT-cut quartz resonators a 6' correction to the nominal  $\theta$  angle was obtained using some old data of Bechmann<sup>3</sup> and recent data of Lukaszek<sup>4</sup>. Furthermore, the change in angle of the zero-temperature contoured AT-cut quartz resonator was calculated as a function of the radius of the contour and shown<sup>2</sup> to be in exceptionally fine agreement with Tyler's known measured design curve<sup>5</sup> when the 6' correction is employed. Since the  $\theta$  angle of the SC-cut is very near the  $\theta$  angle of the AT-cut, the 6' correction can be taken to hold for the SC-cut also.

In this work the corresponding correction to the nominal  $\phi$  angle is obtained from measurements by Warner<sup>6</sup> on the third overtone of a contoured SC-cut quartz resonator at 25°C. The correction to the  $\phi$ -angle turns out to be 48.3'. With these corrections to the nominal  $\phi$  and  $\theta$  angles, the actual orientation of the zero-temperature contoured SC-cut quartz resonator is calculated as a function of the radius of the contour at 25°C for the first, third and fifth harmonics.

The formalism used in earlier calculations of this nature<sup>2,7</sup> is, of course, used here also. The formalism consists of finding the equivalent trapped energy mode<sup>2,7</sup> for the harmonics of the contoured SC-cut quartz resonator<sup>8</sup>, which is then substituted in the equation for the perturbation in eigenfrequency due to a bias<sup>9</sup>, along with the temperature induced biasing deformation field, the first temperature derivatives of the fundamental elastic constants of quartz<sup>10</sup> and the temperature derivative of the effective piezoelectric constant for the thickness mode of interest in

SC-cut quartz<sup>7</sup>, to obtain the change in frequency with temperature for a given orientation of a given contoured resonator. A numerical search is then made to find those orientations for which the calculated change in frequency vanishes as a function of the radius of the contour. Results have been obtained for the fundamental and third and fifth harmonic, which we believe to be quite accurate in view of the accuracy of the earlier work<sup>2</sup>.

### 2. Perturbation Equations

The equation for the perturbation in eigenfrequency<sup>2</sup> mentioned in the Introduction may be written in the form

$$\Delta_{\mu} = H_{\mu} / 2\omega_{\mu}, \quad \omega = \omega_{\mu} - \Delta_{\mu}, \quad (2.1)$$

where  $\omega_{\mu}$  and  $\omega$  are the unperturbed and perturbed eigenfrequencies, respectively, and

$$H_{\mu} = - \int_V [\tilde{K}_{LY}^{\mu} g_{Y,L}^{\mu} + \tilde{K}_{L,L}^{\mu} f^{\mu}] dV, \quad (2.2)$$

and  $V$  is the undeformed volume of the piezoelectric plate at the reference temperature  $T_0$ . In (2.2)  $g_Y^{\mu}$  and  $f^{\mu}$  denote the normalized mechanical displacement vector and electric potential, respectively, of the  $\mu$ th eigensolution, and are defined by

$$g_Y^{\mu} = \frac{u_Y^{\mu}}{N_{\mu}}, \quad f^{\mu} = \frac{\phi^{\mu}}{N_{\mu}}, \quad N_{\mu}^2 = \int_V \rho u_Y^{\mu} u_Y^{\mu} dV, \quad (2.3)$$

where  $u_Y^{\mu}$  and  $\phi^{\mu}$  are the mechanical displacement and electric potential, respectively, which satisfy the equations of linear piezoelectricity

$$\begin{aligned} \tilde{K}_{LY}^{\mu} &= \tilde{K}_{LY}^{\mu} \alpha_{\alpha,M}^{\mu} + e_{MLY}^{\mu} \tilde{\phi}_{,M}^{\mu}, \\ \tilde{K}_L^{\mu} &= e_{LMY}^{\mu} u_{Y,M}^{\mu} - \epsilon_{LM}^{\mu} \tilde{\phi}_{,M}^{\mu}, \end{aligned} \quad (2.4)$$

$$\tilde{K}_{LY,L}^{\mu} = \rho \ddot{u}_Y^{\mu}, \quad \tilde{K}_{L,L}^{\mu} = 0, \quad (2.5)$$

subject to the appropriate boundary conditions. The quantities  $\tilde{K}_{LY}^{\mu}$ ,  $e_{MLY}^{\mu}$  and  $\epsilon_{LM}^{\mu}$  denote the second-order elastic, piezoelectric and dielectric constants, respectively, and  $\rho$  denotes the mass density. Equations (2.4) are the linear piezoelectric constitutive relations and (2.5) are the stress equations of motion and charge equation of electrostatics, respectively. The upper cycle notation for many dynamic variables and the capital Latin and lower case Greek index notation is being employed for consistency with Ref. 9 as is the remainder of the notation in this section. The variables  $\tilde{K}_{LY}^{\mu}$  and  $\tilde{K}_L^{\mu}$  in (2.2) denote the portion of the Piola-Kirchhoff stress tensor and reference electric displacement vector, respectively, resulting from the biasing state and a change in the fundamental material constants in the presence of the  $g_Y^{\mu}$  and  $f^{\mu}$ , and are given by

$$\begin{aligned}\hat{K}_{LY}^n &= (\hat{c}_{LYM\alpha} + \Delta c_{LYM\alpha}) g_{\alpha,M}^{\mu} + (\hat{e}_{MLY} + \Delta e_{MLY}) \hat{f}_M^{\mu}, \\ \hat{E}_L^n &= (\hat{e}_{LMY} + \Delta e_{LMY}) g_{Y,M}^{\mu} - (\hat{e}_{LM} + \Delta e_{LM}) \hat{f}_M^{\mu},\end{aligned}\quad (2.6)$$

where  $\hat{c}_{LYM\alpha}$ ,  $\hat{e}_{MLY}$ , and  $\hat{e}_{LM}$  are effective constants that depend on the biasing state<sup>9</sup> and  $\Delta c_{LYM\alpha}$ ,  $\Delta e_{LMY}$  and  $\Delta e_{LM}$  denote small changes in the fundamental elastic, piezoelectric and dielectric constants, respectively, due to a change in temperature.

When nonlinearities due to biasing deformation only are included, we have

$$\begin{aligned}\hat{e}_{LM} &= b_{LMCD} E_{CD}^1 - 2e_o E_{LM}^1, \\ \hat{e}_{LMY} &= -k_{LMYBC} E_{BC}^1 + e_{LMK} w_{Y,K}, \\ \hat{c}_{LYM\alpha} &= T_{LM}^1 \delta_{\alpha} + c_{LYM\alpha AB} E_{AB}^1 + c_{LYKM} w_{\alpha,K} \\ &\quad + c_{LKM\alpha} w_{Y,K},\end{aligned}\quad (2.7)$$

where for a thermoelastic biasing state and relatively small changes in temperature  $T$  from the reference temperature  $T_0$ ,

$$\begin{aligned}T_{LM}^1 &= c_{LMKN} E_{KN}^1 - v_{LM} (T - T_0), \\ E_{KN}^1 &= \frac{1}{2} (w_{K,N} + w_{N,K}),\end{aligned}\quad (2.8)$$

$c_{LYM\alpha AB}$ ,  $b_{LMCD}$  and  $k_{LMYBC}$  denote the third-order elastic constants, the electrostrictive constants and the first-order electroelastic constants, respectively,  $e_o$  denotes the permeability of free-space,  $w_K$  denotes the static biasing displacement field, and  $v_{LM}$  denotes the thermoelastic coupling coefficients. Thus, in this description the present position  $\chi$  is related to the reference position  $\bar{\chi}$  by

$$\chi(X_L, t) = \bar{\chi} + w(X_L) + u(X_L, t). \quad (2.9)$$

### 3. Temperature Induced Biasing State

A cross-section of the contoured plate along with the associated coordinate system is shown in Fig.1. Since it has been shown<sup>2</sup> that the change in frequency resulting from the thermal stresses caused by the presence of the electrodes is two or three orders of magnitude smaller than the total change, the presence of the electrodes is ignored in the determination of the biasing deformation state. Consequently, we have the ordinary stress equations of equilibrium

$$T_{ML,M}^1 = 0, \quad (3.1)$$

along with the constitutive equations (2.8)<sub>1</sub>. Since the outside edges of the plate are traction free and we have ignored the electrodes on the major surfaces, we have

$$\hat{N}_M T_{ML}^1 = 0, \quad (3.2)$$

on all surfaces, where  $\hat{N}_M$  denotes the unit normal to the surfaces of the plate at  $T = T_0$ . From (3.1) and (3.2) we have

$$T_{ML}^1 = 0, \quad (3.3)$$

throughout the plate. Since the thermoelastic coupling constants  $v_{LM}$  are related to the coefficients  $\alpha_{JK}$  by the usual relation

$$v_{ML} = c_{MLJK} \alpha_{JK}, \quad (3.4)$$

from (2.8)<sub>1</sub>, (3.3) and (3.4), we have

$$E_{JK}^1 = \alpha_{JK} (T - T_0), \quad (3.5)$$

throughout the plate.

Now, the homogeneous strain state is given by (3.5) and the static homogeneous (global) infinitesimal rigid rotation is arbitrary<sup>11</sup>. In fact, the change in frequency due to a homogeneous infinitesimal rigid rotation has been shown to vanish<sup>12</sup>. Consequently, we may select the homogeneous infinitesimal rigid rotation to take any value that is convenient and in particular to vanish, and we have

$$\Omega_{KL}^1 = \frac{1}{2} (w_{L,K} - w_{K,L}) = 0, \quad (3.6)$$

which with (2.8)<sub>2</sub> and (3.5) yields

$$w_{J,K} = \alpha_{JK} (T - T_0). \quad (3.7)$$

The substitution of (3.5), (3.7) and (3.3) in (2.7)<sub>3</sub> yields  $\hat{c}_{LYM\alpha}$  as a known linear function of  $(T - T_0)$  throughout the plate.

### 4. Eigenmodes in Contoured Resonators and the Equivalent Trapped Energy Mode

It has been shown<sup>6</sup> that the eigensolutions for contoured SC-cut quartz resonators, referred to coordinate axes obtained from the eigenvector triad of the pure thickness solution for the SC-cut, can be written in the form

$$u_{lnmp} = \sin \frac{n\pi X_2}{2h} u_{nmp} e^{i\omega_{nmp} t}, \quad (4.1)$$

where the  $X_2$ -axis is shown in Fig.1 and  $u_1$  is in the direction of the thickness eigendisplacement of interest<sup>8</sup> and

$$u_{nmp} = A e^{-\alpha_n \frac{X_1^2}{2}} H_m(\sqrt{\alpha_n} X_1) e^{-\beta_n \frac{X_3^2}{2}} H_p(\sqrt{\beta_n} X_3), \quad (4.2)$$

and along with  $u_1$  we have

$$\varphi = \frac{e_{26}}{e_{22}} u_{nmp} \left( \sin \frac{n\pi X_2}{2h} - (-1)^{\frac{n-1}{2}} \frac{X_2}{h} \right) e^{i\omega_{nmp} t}, \quad (4.3)$$

where for the modes of interest<sup>13</sup>

$$n = 1, 3, 5, \dots; m, p = 0, 2, 4, \dots \quad (4.4)$$

In (4.2)  $H_m$  and  $H_p$  are Hermite polynomials and

$$\alpha_n^2 = \frac{n^2 \pi^2 \hat{c}^{(1)}}{8Rh_o^3 M_n}, \quad \beta_n^2 = \frac{n^2 \pi^2 \hat{c}^{(1)}}{8Rh_o^3 P_n}, \quad (4.5)$$

where

$$\begin{aligned}M_n &= c_{11} - \frac{c_{16}^2}{c^{(1)}} + r_2 (c_{12} + c_{66}) + \\ &\quad \frac{4(r_2 \bar{c}^{(2)} + c_{12})(r_2 \bar{c}^{(1)} - c_{66})}{n\pi \bar{c}^{(2)} \kappa_2} \cot \kappa_2 \frac{n\pi}{2},\end{aligned}$$

$$P_n = c_{58} + r_3(c_{36} + c_{57}) + \frac{4(r_3 \bar{c}^{(3)} + c_{45})(r_3 \bar{c}^{(1)} - c_{36})}{n\pi \bar{c}^{(3)} \kappa_3} \cot \kappa_3 \frac{n\pi}{2}, \quad (4.6)$$

and

$$\kappa_2 = \sqrt{\frac{\bar{c}^{(1)}}{\bar{c}^{(2)}}}, \quad \kappa_3 = \sqrt{\frac{\bar{c}^{(1)}}{\bar{c}^{(3)}}}, \quad r_2 = \frac{c_{12} + c_{66}}{\bar{c}^{(1)} - \bar{c}^{(2)}}, \quad r_3 = \frac{c_{36} + c_{57}}{\bar{c}^{(1)} - \bar{c}^{(3)}}. \quad (4.7)$$

In Eqs. (4.3) - (4.9) the material constants are the transformed constants discussed in Ref. 8 and the  $\bar{c}^{(i)}$  ( $i=1,2,3$ ) are the eigenvalues for the piezoelectrically stiffened plane waves for the thickness direction of the SC-cut<sup>8</sup>. The eigenfrequencies for this eigensolution are given by<sup>8</sup>

$$\omega_{nmp}^2 = \frac{n^2 \pi^2 \bar{c}^{(1)}}{4h_0^2} \left[ 1 + \frac{1}{n\pi} \sqrt{\frac{2h_0}{\bar{R}}} \left( \sqrt{\frac{M_n}{\bar{c}^{(1)}}} (2m+1) + \sqrt{\frac{P_n}{\bar{c}^{(1)}}} (2p+1) \right) \right], \quad (4.8)$$

where

$$\bar{c}^{(1)} = \bar{c}^{(1)} \left( 1 - \frac{8k_{26}^2}{n^2 \pi^2} - 2\hat{R} \right), \quad k_{26}^2 = \frac{\epsilon_{26}^2}{\bar{c}^{(1)} \epsilon_{22}}, \quad \hat{R} = \frac{2\rho'h'}{oh}, \quad (4.9)$$

and  $\rho$  and  $\rho'$  are the mass densities of the quartz and electrodes, respectively.

In addition to  $u_{1nmp}$  given in (4.1) there are both  $u_{2nmp}$  and  $u_{3nmp}$ , which are an order of magnitude smaller than  $u_{1nmp}$ , but are required in this work because the SC-cut is thermally compensated for the pure thickness mode of interest. However, since the  $u_2$ - and  $u_3$ -displacement fields accompanying the larger  $u_1$ -displacement field are known only for the electroded and unelectroded flat plate<sup>8,13</sup>, we fit the Gaussian mode shape given in (4.1) and (4.2) for the contoured resonator to a trapped energy mode<sup>13</sup> in a flat plate in accordance with the diagram shown in Fig. 2. Since the Gaussian mode shape is sharply confined to the vicinity of the center of the contoured resonator, we replace the circular electrode by the circumscribed square for convenience in performing the perturbation integrals (2.2). Furthermore, for the same reasons we take the flat plate to have the thickness  $2h_0$  in the central region and the thicknesses  $2h_1$  and  $2h_3$  of the contoured resonator at the lines of inflection of the Gaussian mode shape in the  $X_1$ - and  $X_3$ -directions, respectively, which are given by

$$2h_1 = 2h_0 (1 - a_1^2/4Rh_0), \quad 2h_3 = 2h_0 (1 - a_3^2/4Rh_0). \quad (4.10)$$

The equivalent trapped energy mode is fitted to the Gaussian by matching the Gaussian at the center of the plate and requiring the volumes under the Gaussian mode shape and the equivalent trapped energy mode to be separately the same under the inner rectangular region defined by the lines of inflection of the Gaussian mode shape in the two directions and the outer regions. This is a reasonable procedure for our purposes because such a function can match the Gaussian quite well, we integrate over the mode shape in the perturbation

integral (2.2) and the analysis in Sec. 3 shows that the thermally induced biasing state is very accurately a homogeneous one.

Since the equivalent trapped energy mode is to be determined by matching to the known Gaussian mode shape in accordance with the foregoing procedure, the dispersion relations are not needed and only the continuity of the mechanical displacement  $u_1$  need be imposed at the line of inflection in each direction. The solution functions for the trapped energy eigenmodes have been shown<sup>13</sup> to be of the form

$$\begin{aligned} \bar{u}_1 &= \bar{B} \sin \frac{n\pi X_2}{2h} \cos \bar{\xi} X_1 \cos \bar{\nu} X_3, \\ u_1^S &= B^S \sin \frac{n\pi X_2}{2h} e^{-\bar{\xi}^S(X_1-a_1)} \cos \bar{\nu} X_3, \\ u_1^T &= B^T \sin \frac{n\pi X_2}{2h} \cos \bar{\xi} X_1 e^{-\bar{\nu}^T(X_3-a_3)}, \\ u_1^C &= B^C \sin \frac{n\pi X_2}{2h} e^{-\bar{\xi}^S(X_1-a_1)} e^{-\bar{\nu}^T(X_3-a_3)}. \end{aligned} \quad (4.11)$$

In accordance with the matching procedure outlined, we take

$$\bar{B} = A_{nmp}, \quad (4.12)$$

and obtain  $\bar{\xi}$  and  $\bar{\nu}$  from the relation

$$\begin{aligned} \int_0^{a_1} e^{-\alpha \frac{X_1^2}{2}} H_m(\sqrt{\alpha} X_1) dX_1 \int_0^{a_3} e^{-\beta \frac{X_3^2}{2}} H_p(\sqrt{\beta} X_3) dX_3 \\ = \int_0^{a_1} \cos \bar{\xi} X_1 dX_1 \int_0^{a_3} \cos \bar{\nu} X_3 dX_3, \end{aligned} \quad (4.13)$$

from which, by separately equating the product integrals, we obtain the transcendental equations

$$\begin{aligned} \frac{\sin \bar{\xi} a_1}{\bar{\xi} a_1} &= \sqrt{\frac{\pi}{2\alpha n a_1^2}} \operatorname{erf}\left(\sqrt{\frac{\alpha n a_1^2}{2}}\right), \\ \frac{\sin \bar{\nu} a_3}{\bar{\nu} a_3} &= \sqrt{\frac{\pi}{2\beta n a_3^2}} \operatorname{erf}\left(\sqrt{\frac{\beta n a_3^2}{2}}\right), \end{aligned} \quad (4.14)$$

for the fundamental and harmonic overtones. The one root of each of (4.14) determines the values of  $\bar{\xi}$  and  $\bar{\nu}$  for the equivalent trapped mode. Equation (4.13), and, of course, (4.14) are for the harmonic modes only, for which  $H_n = H_p = 1$ .

Since the equivalent trapped energy mode is continuous at the junctions, the relations between the amplitudes in the different regions are

$$\begin{aligned} B^S &= \bar{B} \cos \bar{\xi} a_1, \quad B^T = \bar{B} \cos \bar{\nu} a_3, \\ B^C &= \bar{B} \cos \bar{\xi} a_1 \cos \bar{\nu} a_3, \end{aligned} \quad (4.15)$$

which with (4.12) gives all amplitudes of the equivalent trapped energy mode in terms of the amplitude of the Gaussian mode shape. By following a procedure similar to the one employed in the treatment of the central region, for  $H_n = H_p = 1$ , we obtain<sup>4,2</sup>

$$\bar{v}^S = \frac{\cos \bar{\xi} a_1}{\sqrt{\frac{\pi}{2\alpha_n}} \operatorname{erfc}\left(\sqrt{\frac{\alpha_n}{2}} a_1\right)}, \quad \bar{v}^T = \frac{\cos \bar{v} a_3}{\sqrt{\frac{\pi}{2\beta_n}} \operatorname{erfc}\left(\sqrt{\frac{\beta_n}{2}} a_3\right)}. \quad (4.16)$$

We now have the  $u_1$ -displacement field for the equivalent trapped energy mode.

As noted earlier in addition to the  $u_1(\bar{u}_1)$  displacement field there are accompanying  $u_2(\bar{u}_2)$  and  $u_3(\bar{u}_3)$  displacement fields, and to the same order in  $\xi(\bar{\xi})$  there are accompanying corrections to the  $u_1(\bar{u}_1)$  displacement fields, which are given by<sup>8</sup>

$$\begin{aligned} \bar{u}_1 &= \bar{B} \left( 1 + \frac{c_{16}}{\bar{c}(1)} \bar{\xi} X_2 \right) \sin \frac{n\pi X_2}{2h} \cos \bar{\xi} X_1 \cos \bar{v} X_3, \\ \bar{u}_2 &= \left[ \frac{r_2 \bar{\xi} 2h}{n\pi} \bar{B} \cos \frac{n\pi X_2}{2h} + \bar{C} \cos \frac{\kappa_2 n\pi X_2}{2h} \right] \sin \bar{\xi} X_1 \cos \bar{v} X_3, \\ \bar{u}_3 &= \left[ \frac{r_3 \bar{v} 2h}{n\pi} \bar{B} \cos \frac{n\pi X_2}{2h} + \bar{E} \cos \frac{\kappa_3 n\pi X_2}{2h} \right] \cos \bar{\xi} X_1 \sin \bar{v} X_3, \end{aligned} \quad (4.17)$$

where

$$\begin{aligned} \bar{C} &= (-1)^{\frac{n+1}{2}} \frac{(r_2 \bar{c}^{(2)} + c_{12}) \bar{\xi} 2h \bar{B}}{\bar{c}^{(2)} \kappa_2 n\pi \sin \kappa_2 n\pi/2}, \\ \bar{E} &= (-1)^{\frac{n+1}{2}} \frac{(r_3 \bar{c}^{(3)} + c_{57}) \bar{v} 2h \bar{B}}{\bar{c}^{(3)} \kappa_3 n\pi \sin \kappa_3 n\pi/2}, \end{aligned} \quad (4.18)$$

and

$$\begin{aligned} u_1^S &= B^S \left( 1 + \frac{c_{16}}{\bar{c}(1)} \bar{\xi} X_2 \right) \sin \frac{n\pi X_2}{2h} e^{-\bar{\xi}^S (X_1 - a_1)} \cos \bar{v} X_3, \\ u_2^S &= \left[ \frac{r_2 \bar{\xi}^S 2h}{n\pi} B^S \cos \frac{n\pi X_2}{2h} + C^S \cos \frac{\kappa_2 n\pi X_2}{2h} \right] \\ &\quad \cdot e^{-\bar{\xi}^S (X_1 - a_1)} \cos \bar{v} X_3, \\ u_3^S &= \left[ \frac{r_3 \bar{v} 2h}{n\pi} B^S \cos \frac{n\pi X_2}{2h} + E^S \cos \frac{\kappa_3 n\pi X_2}{2h} \right] \\ &\quad \cdot e^{-\bar{\xi}^S (X_1 - a_1)} \sin \bar{v} X_3, \end{aligned} \quad (4.19)$$

where

$$\begin{aligned} C^S &= (-1)^{\frac{n+1}{2}} \frac{(r_2 \bar{c}^{(2)} + c_{12}) \bar{\xi}^S 2h B^S}{\bar{c}^{(2)} \kappa_2 n\pi \sin \kappa_2 n\pi/2}, \\ E^S &= (-1)^{\frac{n+1}{2}} \frac{(r_3 \bar{c}^{(3)} + c_{57}) \bar{v} 2h B^S}{\bar{c}^{(3)} \kappa_3 n\pi \sin \kappa_3 n\pi/2}, \end{aligned} \quad (4.20)$$

with similar expressions<sup>14</sup> for  $u_1^T$  and  $u_2^T$ . As noted earlier in this section this solution is referred to the eigenvector triad of the pure thickness solution for the SC-cut<sup>8</sup>. For purposes of calculation of the temperature dependence of the resonant frequency it is advisable<sup>14</sup> to transform back to the original conventional coordinate axes for the SC-cut, thus

$$\tilde{u}_\alpha = Q_{\alpha\beta} u_\beta, \quad (4.21)$$

where  $\tilde{u}_\alpha$  denotes the components of the mechanical displacement in the original coordinate system for the

SC-cut and  $Q_{\alpha\beta}$  denotes the transformation from that system to the eigenvector triad<sup>8</sup>.

### 5. Orientation of the Zero-Temperature Cut

The change in the resonant frequency with temperature of any electroded contoured SC-cut quartz plate resulting from the thermally induced biasing may now be determined from (2.1) and (2.2) with (2.6) and (2.7). However, Eq.(2.2) cannot be used for calculation as it appears because the temperature derivatives of the complete piezoelectric and dielectric tensors are not presently known, nor are all the fundamental coefficients appearing in (2.7) known. Nevertheless, since the piezoelectric coupling and wavenumbers along the plate are both small, the temperature dependence of only the transformed<sup>8</sup> thickness piezoelectric and dielectric constants  $e_{26}$  and  $\epsilon_{22}$  need be retained in  $H_\mu$ . Moreover, since  $(1/e_{26})de_{26}/dT \gg (1/\epsilon_{22})d\epsilon_{22}/dT$ , we ignore  $(1/\epsilon_{22})d\epsilon_{22}/dT$ . Furthermore,  $(1/e_{26})de_{26}/dT$  can and should be excluded from wave terms in  $H_\mu$  because the existing temperature derivatives of the fundamental elastic constants of quartz effectively contain the small influence of the temperature dependence of the piezoelectric and dielectric constants, which results from the piezoelectric stiffening of the waves. In addition, we ignore the  $\hat{e}_{\mu LY}$  since they are not known. Then the  $(1/e_{26})de_{26}/dT$  that we retain is not fundamental but effective. In view of the foregoing, the general electroelastic perturbation integral in (2.2) with (2.6) and (2.7) may be written in the reduced form<sup>14</sup>

$$\begin{aligned} H_\mu &= - \int_V \left[ (\hat{c}_{LYM\alpha} + \Delta c_{LYM\alpha}) \tilde{g}_{\alpha, M}^{\mu} \tilde{g}_{Y, L}^{\mu} \right. \\ &\quad \left. - \frac{2e_{26}^2}{\epsilon_{22}} \frac{\Delta e_{26}}{e_{26}} g_{1,2}^{(\mu)} \frac{g_1^{(\mu)}(h)}{h} \right] dV, \end{aligned} \quad (5.1)$$

where

$$\Delta \equiv (T - T_0) d/dT \quad (5.2)$$

In (5.1) the first term under the integral sign is decomposed in the original conventional coordinate system for the SC-cut because the  $\hat{c}_{LYM\alpha}$  and  $\Delta c_{LYM\alpha}$  are known in that coordinate system, while the second term is decomposed along the eigenvector triad<sup>8</sup> of the pure thickness solution<sup>14</sup>. From (5.1) for the geometry shown in Fig.2, we obtain

$$\begin{aligned} H_\mu &= -4 \int_{-h}^h dX_2 \left[ \int_0^\ell dX_1 \left( \int_0^\ell (\bar{\varphi} + \bar{C}) dX_3 + \int_{\frac{1}{2}}^\infty \varphi^T dX_3 \right) \right. \\ &\quad \left. + \int_\ell^\infty dX_1 \left( \int_0^\ell \varphi^S dX_3 + \int_\ell^\infty \varphi^C dX_3 \right) \right], \end{aligned} \quad (5.3)$$

where

$$\begin{aligned} \varphi &= (\hat{c}_{LYM\alpha} + \Delta c_{LYM\alpha}) \tilde{g}_{\alpha, M}^{\mu} \tilde{g}_{Y, L}^{\mu}, \\ \bar{C} &= -2 \frac{e_{26}^2}{\epsilon_{22}} \frac{\Delta e_{26}}{e_{26}} g_{1,2}^{\mu} \frac{g_1^{\mu}(h)}{h}. \end{aligned} \quad (5.4)$$

The  $\hat{c}_{LYM\alpha}$  in (5.4) are known as linear expressions in  $(T - T_0)$  from the analysis in Sec.3 and the change in the elastic constants with temperature  $\Delta c_{LYM\alpha}$  are given by

$$\Delta c_{LYM\alpha} = (dc_{LYM\alpha}/dT) (T - T_0), \quad (5.5)$$

where the  $dc_{LYM\alpha}/dT$  are obtained from the first temperature derivatives of the fundamental elastic constants



of quartz<sup>10</sup>  $d\tilde{c}_{\text{eff}}/dT$  referred to the principal axes by the tensor transformation relation

$$\frac{d}{dT} c_{2LYM\alpha} = a_{LD} a_{YE} a_{MF} a_{\alpha G} \frac{d}{dT} \tilde{c}_{2DEFG}, \quad (5.6)$$

where the  $a_{YE}$  are the matrix of direction cosines for the transformation from the principal axes to the coordinate system containing the axes referred to the electroded plate. When the conventional IEEE notation<sup>15</sup> for doubly-rotated plates is written in the form  $(Y, X, w, \ell)\phi, \theta$ , where  $\psi = 0$ , the rotation angles  $\phi$  and  $\theta$  are the first two Euler angles, and for the SC-cut the nominal angles are  $\theta = -34.184^\circ$ ,  $\phi = 21.93^\circ$ , from which the  $a_{YE}$  can be determined<sup>16</sup>. Clearly, the transformation relations for the second and third order elastic, piezoelectric and dielectric constants, and coefficients of linear expansion may be written in the respective forms

$$\begin{aligned} \tilde{c}_{2KLMN} &= a_{KD} a_{LE} a_{MF} a_{NG} \tilde{c}_{2DEFG}, \\ \tilde{c}_{KLMNAB} &= a_{KD} a_{LE} a_{MF} a_{NG} a_{AH} a_{BI} \tilde{c}_{DEFGHI}, \\ \tilde{e}_{KLM} &= a_{KD} a_{LE} a_{MF} \tilde{e}_{DEF}, \\ \tilde{\alpha}_{KL} &= a_{KM} a_{LN} \tilde{\alpha}_{MN}, \quad \tilde{\alpha}_{KL} = a_{KM} a_{LN} \tilde{\alpha}_{KN}, \end{aligned} \quad (5.7)$$

where the tensor quantities with the upper cycle are referred to the principal axes of the crystal.

In order for the temperature dependence of the resonant frequency of a contoured SC-cut quartz resonator to be calculated, the temperature dependence of  $e_{26}$  must be known. An estimate has been made using data<sup>17</sup> on the temperature dependence of the resonant frequencies of both the fundamental and fifth harmonic overtone trapped energy modes in SC-cut quartz plates with rectangular electrodes. From the data provided by Lukaszek<sup>17</sup> and the analysis we obtain the estimate<sup>14,7</sup>

$$(1/e_{26})de_{26}/dT = -4.8 \times 10^{-4}/^\circ K. \quad (5.8)$$

Calculations have been performed using the known values of the second order elastic, piezoelectric and dielectric constants of quartz<sup>18</sup>, the third order elastic<sup>19</sup> and thermoelastic<sup>20</sup> constants of quartz and the first temperature derivatives of the fundamental elastic constants of quartz<sup>10</sup> along with the estimate in (5.8). The results of the calculations are presented in Figs. 4-7. However, before we present the results of the calculations for the SC-cut, in Fig. 3, which is Fig. 7 of Ref. 2, we show a comparison of log-log plots of the calculated shift in rotation angle for the zero-temperature AT-cut for the fundamental mode with Taylor's known measured design curve<sup>5</sup> for the fundamental mode of the plano-convex AT-cut resonator in order to demonstrate the accuracy that can be achieved with such calculations. It can be seen from the figure that the calculated results are not straight lines, but curves and, in fact, a different curve for each different center thickness and each electrode size. Although all the calculated curves tend to follow the general trend of the single measured design line very closely for decreasing radius of curvature of the contour, they deviate differently with increasing  $R$ , the greater the deviation, the greater the center thickness. At this point it should be noted that as a result of (4.5), the calculations become invalid for large  $R$  and  $h_0$  and the larger  $h_0$ , the smaller the value of  $R$  at which the calculations become invalid. Nevertheless, it can be seen from the figure that for practical cases the agreement is exceptionally fine. It should also be noted that the  $6'$  correction to the nominal angle  $\theta = -35^\circ 15'$  for the zero-temperature AT-cut unelectroded flat plate, which was obtained<sup>2</sup> using

data of Bechmann<sup>3</sup> and Lukaszek<sup>4</sup> and made the actual angle  $\theta = -35^\circ 21'$ , was employed in plotting the calculated results in Fig. 3. Thus it is clear that the  $6'$  correction to the nominal  $\theta$  angle is of crucial importance for the calculation of the actual orientation of zero-temperature AT-cuts.

As noted in the Introduction, since the  $\theta$  angle of the SC-cut is very near the  $\theta$  angle of the AT-cut, the  $6'$  correction can be taken to hold for the SC-cut also. The corresponding correction to the nominal  $\phi$  angle, which is required for the calculation of the actual orientation of zero-temperature SC-cuts, has been obtained from measurements by Warner<sup>5</sup> on the third overtone of a contoured SC-cut quartz resonator at  $25^\circ C$ . The resonator had a center thickness  $2h_0 = .5486$  mm, a radius of curvature  $R = 25$  cm, an electrode diameter  $2\ell = 6.48$  mm and electrode thickness  $2h' = 900$  Å, and the actual orientation given by Warner<sup>5</sup> was  $\phi = 21.930^\circ$ ,  $\theta = -34.34^\circ$ . Using the above-mentioned  $6'$  correction to the  $\theta$  angle, we find that the nominal  $\theta$  angle is  $\theta = -34.24^\circ$ . Applying the formalism presented in this work to the resonator used by Warner, we calculate the nominal  $\phi$  angle to be  $\phi = 21.125^\circ$ , which means that the correction to the nominal  $\phi$  angle is  $.805^\circ$  or  $48.3'$ .

Figure 4 shows semilog plots of the actual rotation angle  $\theta$  for an actual fixed angle  $\phi = 21.93^\circ$  for the zero-temperature cut as a function of the radius of curvature  $R$  for the first, third and fifth harmonics for the two center thicknesses shown in the figure. The experimental point noted on the third harmonic is that of Warner<sup>5</sup>. The figure clearly shows that the actual angle  $\theta$  of the zero-temperature SC-cut is a significant function of  $R$  for the third and fifth harmonic, as well, of course, as for the fundamental. This dependence of the third and fifth harmonic on  $R$  constitutes a well-known significant difference between the behavior of the SC- and AT-cuts. Figure 5 shows semilog plots of the actual rotation angle  $\phi$  for an actual fixed angle  $\theta = -34.60^\circ$  for the zero temperature cut as a function of  $R$  for the same harmonics and center thicknesses as Fig. 4. It is clear from Figs. 4 and 5 that the change in  $\phi$  with  $R$  for a fixed  $\theta$  is about 10 times as great as the corresponding change in  $\theta$  for a fixed  $\phi$ . Figure 6 shows log-log plots of the change in rotation angle  $\Delta\theta$  referred to an actual reference angle  $\theta = -34^\circ 36'$  for an actual fixed angle  $\phi = 21.93^\circ$  as a function of  $2h_0/R$  for the same harmonics and center thicknesses. Figure 7 shows log-log plots of the change in rotation angle  $\Delta\phi$  referred to an actual reference angle  $\phi = 22^\circ 40'$  for an actual fixed angle  $\theta = -34.60^\circ$  as a function of  $2h_0/R$  for the same harmonics and center thicknesses. The dotted curve in both Figs. 6 and 7 is for  $N=1$  for the thicker resonator. The equivalent curves for  $N=3$  and  $N=5$  for the thicker resonator are indistinguishable from the respective ones for the thinner resonator. At this point it should be noted that although the calculations for  $N=1$  become invalid for some large value of  $R$ , the smaller that value of  $R$ , the larger  $h_0$ , as a result of (4.5), the calculation for  $N=3$  and  $N=5$  remains valid over the entire range shown in Figs. 6 and 7, as a result of the  $n^2$  in the numerators of (4.5). The electrode diameter used in all calculations was  $2\ell = 6.48$  mm.

#### Acknowledgements

We wish to thank A.W. Warner of Frequency Electronics, Inc., for providing the data that enabled us to obtain the correction to the nominal  $\phi$  angle. We also wish to thank A. Ballato and T.J. Lukaszek of the U.S. Army Electronics Technology and Devices Laboratory for kindly providing the data used in the estimation of  $(1/e_{26})de_{26}/dT$ .

This work was supported in part by the Army Research Office under Contract No. DAAG 29-82-K-0130 and the National Science Foundation under Grant No. MEA 8115340.

# References

1. R. Bechmann, A.D. Ballato and T.J. Lukaszek, "Higher Order Temperature Coefficients of the Elastic Stiffnesses and Compliances of Alpha-Quartz," *Proc. IRE*, **50**, 1812 (1962).
2. D.S. Stevens, H.F. Tiersten and B.K. Sinha, "Temperature Dependence of the Resonant Frequency of Electroded Contoured AT-Cut Quartz Crystal Resonators," *J. Appl. Phys.*, **54**, 1704 (1983).
3. R. Bechmann, "Influence of the Order of Overtone on the Temperature Coefficient of AT-Type Quartz Resonators," *Proc. IRE*, **43**, 1667 (1955).
4. T.J. Lukaszek, private communication.
5. L.A. Tyler, "The Design of Fundamental Mode Thickness-Shear Quartz Resonators," prepared for the Department of the Army under Contract No. DA-039-SC-7106 by Union Thermoelectric Division of Comptometer Corporation, Niles, Illinois, 1961, AD274031, Fig.16.
6. A.W. Warner, private communication.
7. D.S. Stevens and H.F. Tiersten, "Temperature Induced Frequency Changes in Electroded Contoured SC-Cut Quartz Crystal Resonators," *Proceedings of the 36th Annual Symposium on Frequency Control*, U.S. Army Electronics Research and Development Command, Fort Monmouth, New Jersey, **46** (1982).
8. H.F. Tiersten and D.S. Stevens, "An Analysis of Contoured SC-Cut Quartz Crystal Resonators," *Proceedings of the 36th Annual Symposium on Frequency Control*, U.S. Army Electronics Research and Development Command, Fort Monmouth, New Jersey, **37** (1982).
9. H.F. Tiersten, "Perturbation Theory for Linear Electroelastic Equations for Small Fields Superposed on a Bias," *J. Acoust. Soc. Am.*, **64**, 832 (1978).
10. B.K. Sinha and H.F. Tiersten, "First Temperature Derivatives of the Fundamental Elastic Constants of Quartz," *J. Appl. Phys.*, **50**, 2732 (1979).
11. A.E.H. Love, *A Treatise on the Mathematical Theory of Elasticity*, 4th ed. (Cambridge University Press, Cambridge, 1927) also (Dover, New York, 1944) Secs.18 and 118.
12. H.F. Tiersten and B.K. Sinha, "Temperature Dependence of the Resonant Frequency of Electroded Doubly-Rotated Quartz Thickness-Mode Resonators," *J. Appl. Phys.*, **50**, 8038 (1979).
13. H.F. Tiersten, "Analysis of Trapped Energy Resonators Operating in Overtones of Coupled Thickness-Shear and Thickness-Twist," *J. Acoust. Soc. Am.*, **59**, 879 (1976).
14. For more detail see D.S. Stevens and H.F. Tiersten, "On the Dependence of the Orientation of the Zero-Temperature Contoured SC-Cut Quartz Resonator on the Radius of the Contour," to be issued as a technical report, Rensselaer Polytechnic Institute, Troy, New York.
15. IEEE Standard on Piezoelectricity - IEEE Std. 176 - 1978.
16. This transformation determines what we have referred to as the original conventional coordinate system for the SC-cut.
17. T.J. Lukaszek, private communication.
18. R. Bechmann, "Elastic and Piezoelectric Constants of Alpha-Quartz," *Phys. Rev.*, **110**, 1060 (1958).
19. R.N. Thurston, H.J. McSkimin and P. Andreatch, Jr., "Third-Order Elastic Constants of Quartz," *J. Appl. Phys.*, **37**, 267 (1966).
20. F. Kohlrausch, *Lehrbuch der prakt. Physik*, **16**, Aufl. 5. 158 (1930). Constants employed in Ref.21.

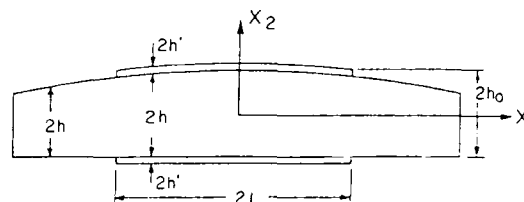


Figure 1

Cross-Section of the Plano-Convex Resonator

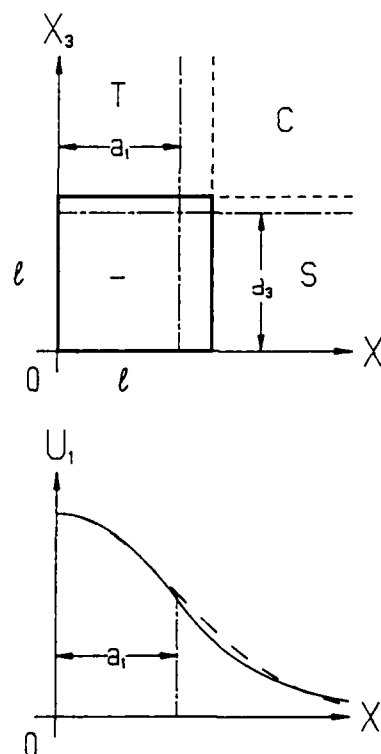


Figure 2

Diagram of One Quadrant of the Equivalent Trapped Energy Resonator Showing the Gaussian Mode Shape for the Contoured Resonator and the Equivalent Trapped Energy Mode Shape

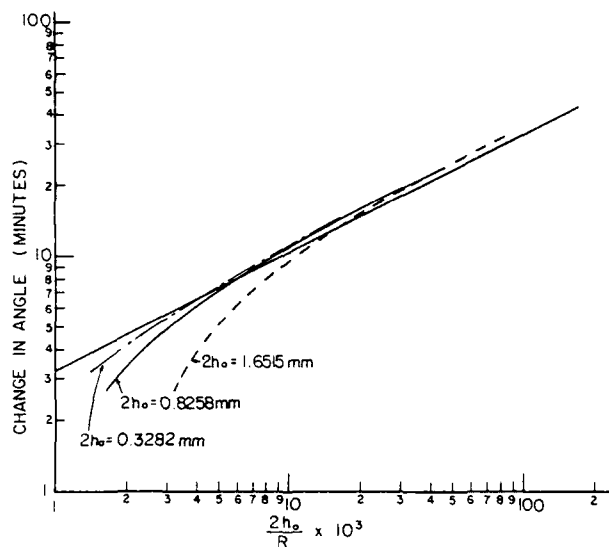


Figure 3

Comparison of the Calculated Change in Rotation Angle  $\Delta\theta$  from  $\theta = -35^\circ 8.5'$  for the Zero Temperature Coefficient of Frequency for the Fundamental Mode of the Contoured AT-cut Resonator with Tyler's Known Measured Design Curve. The calculated curves are for center thicknesses  $2h_0$  of 0.8258, 1.6515 and 0.3282 mm, with electrode diameters  $2\ell$  of 8, 10 and 4 mm, respectively.

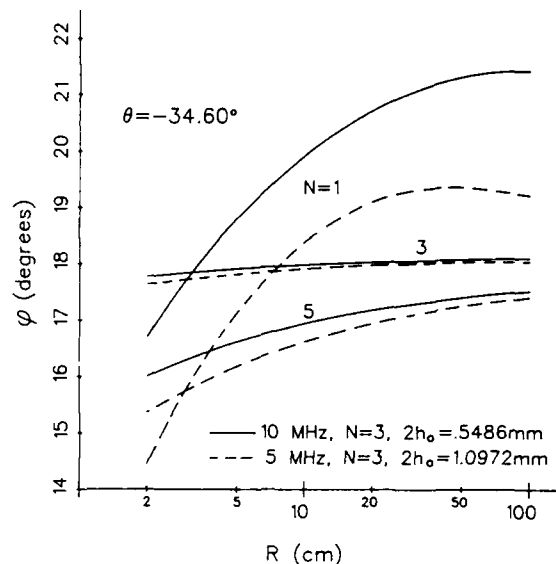


Figure 5

Actual Rotation Angle  $\phi$  for the Zero Temperature Coefficient of Frequency SC-Cut at  $25^\circ\text{C}$  for an Actual Fixed Value of  $\theta = -34.60^\circ$  as a Function of the Radius of Contour  $R$  for the First, Third, and Fifth Harmonics for Resonators with the Nominal Resonant Frequencies and Center Thicknesses Shown. The electrode diameter is  $2\ell = 6.48$  mm.

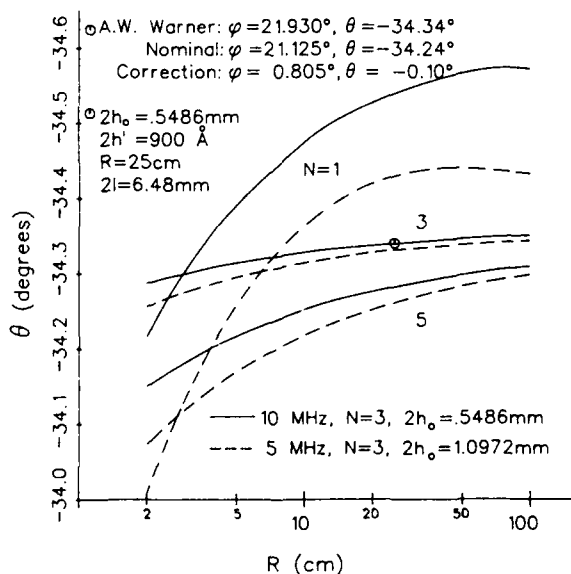


Figure 4

Actual Rotation Angle  $\theta$  for the Zero Temperature Coefficient of Frequency SC-Cut at  $25^\circ\text{C}$  for an Actual Fixed Value of  $\phi = 21.93^\circ$  as a Function of the Radius of Contour  $R$  for the First, Third and Fifth Harmonics for Resonators with the Nominal Resonant Frequencies and Center Thicknesses Shown. The electrode diameter is  $2\ell = 6.48$  mm.

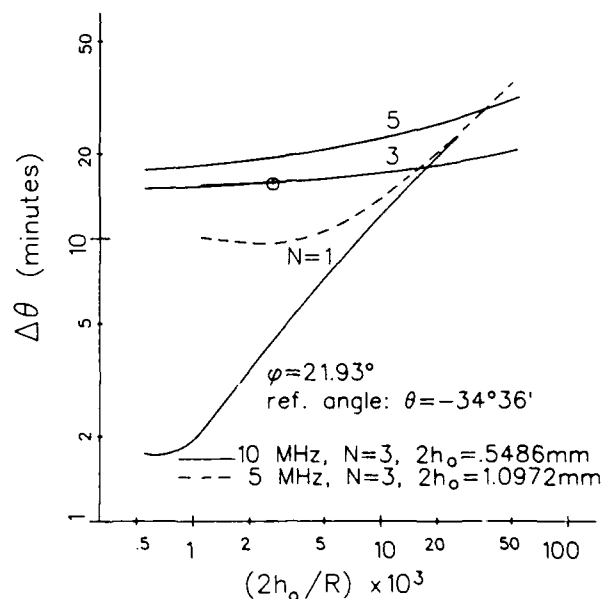


Figure 6

Change in Rotation Angle  $\Delta\theta$  from  $\theta = -34^\circ 36'$  for the Zero Temperature Coefficient of Frequency SC-Cut at  $25^\circ\text{C}$  for an Actual Fixed Value of  $\phi = 21.93^\circ$  as a Function of the Ratio of the Center Thickness-to-Radius of Contour for the First, Third and Fifth Harmonics for Resonators with the Nominal Resonant Frequencies and Center Thicknesses Shown. The electrode diameter is  $2\ell = 6.48$  mm.

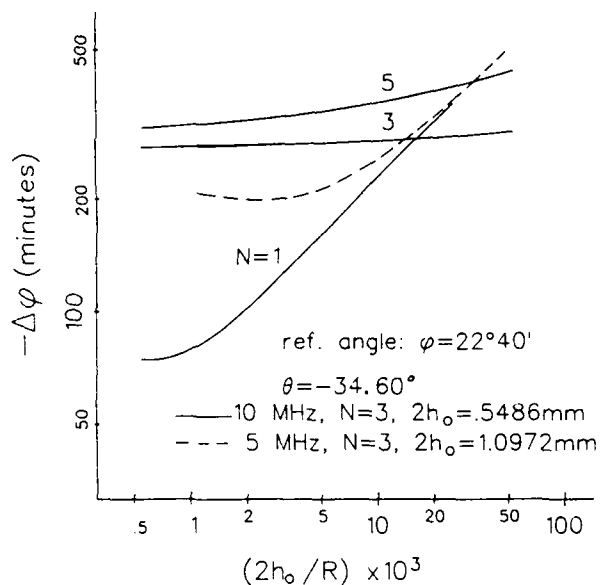


Figure 7

Change in Rotation Angle  $\Delta\varphi$  from  $\varphi = 22^\circ 40'$  for the Zero Temperature Coefficient of Frequency SC-Cut at  $25^\circ\text{C}$  for an Actual Fixed Value of  $\theta = -34.60^\circ$  as a Function of the Ratio of the Center Thickness-to-Radius of Contour for the First, Third and Fifth Harmonics for Resonators with the Nominal Resonant Frequencies and Center Thicknesses Shown. The electrode diameter is  $2\ell = 6.48\text{ mm}$ .

## PIEZO ELECTRIC CERAMIC RESONATORS AND FILTERS

S. FUJISHIMA, J. MERLINA, AND J. MIYAZAKI

MURATA ERIE NORTH AMERICA, INC.

1148 Franklin Road  
Marietta, GA 30067  
(404) 952-9777Summary

The manufacturing process of piezoelectric ceramic resonators and filters, and their characteristics are reviewed, placing special emphasis on high productivity and application to semi-conductor circuits.

The advantages of ceramic resonators are a short start up time for clock oscillators in microprocessors, and a wide frequency shift in VCO circuits. The merits of ceramic filters are stability and a wide bandpass in communication use.

Finally, the unique packages for ceramic resonators and filters, which adapts to high productivity and use with automatic insertion or placing machines, are described.

Introduction

Piezoelectric ceramics have played a major role in the development of solid state electronics as a material of choice for component manufacture.

While ceramic dielectric capacitors have been widely used for more than a decade, piezoelectric ceramic resonators and filters have only recently become commonly used for frequency control and selection in communications and microprocessor controlled equipment.

In the future, even greater expectations are held for this unique material in the area of new applications and more stringent performance criteria for current products.

In this paper we will describe the manufacture, operation and typical specifications which can be obtained from currently available ceramic resonators as compared to quartz technology.

Also, we will describe the unique package for ceramic resonators and filters which allows use with automatic insertion or automatic placing machines now using ceramic capacitors.

Manufacturing Process and Material Characteristics

The manufacturing process for ceramic resonators differs significantly from quartz resonators, especially in the formation of the raw materials. Instead of high temperature autoclaves forming large crystals from which wafers are cut with great precision, piezoelectric ceramic resonator

fabrication begins with powders.

In the old days, we made wafers by the manufacturing process of pressing, firing, cutting, and grinding. However, we have succeeded in recently developing a new manufacturing process called the green sheets method. Fig. 1 shows this new manufacturing process compared to the old process. In Fig. 1 the sheeting process is most important and we are using a rolling or extruding machine for this.

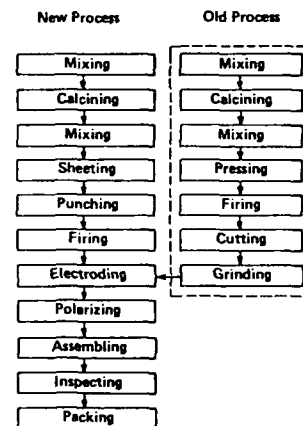


FIG. 1  
New Manufacturing Process by Green Sheet  
Method Comparing to Old Process

The old method of electroding used a printing machine with silver paint. However, silver material is very expensive and is subject to the migration phenomena, especially in thinner wafers. So, we have developed a new electroding process which is based on the sputtering technique, using a Ni alloy. This new process is very suitable to mass production and cost savings, as well as avoiding silver migration troubles.

There are many material requirements for making quality frequency control devices like resonators and filters. We must consider the following:

- (1) Good temperature and aging characteristics of the resonant frequency for each vibration mode.
- (2) High mechanical Q and small dielectric constant for higher frequency use.

- (3) Pore free ceramic structure and a uniform piezoelectric characteristic to allow fine electrode patterns.
- (4) Small package size for solid state circuits.

We have studied many kind of impurities which improve mechanical Q values, and combinations of Ti and Zr in PZT materials which improve temperature characteristics to meet today's requirements.<sup>(1)</sup>

For example, Fig. 2 shows the temperature coefficient of the resonant frequency in an expansion mode, shear mode, and thickness mode related to the combination of Ti and Zr.<sup>(2)</sup> This is quite similar to the phenomena found in the cut angle of zero-temperature coefficient quartz crystals. In addition to the material, we can see that the vibration mode in ceramic resonators also affects the temperature characteristic. Fig. 3 shows typical temperature characteristics of the resonant frequency in each vibration mode compared to the AT cut quartz crystals.

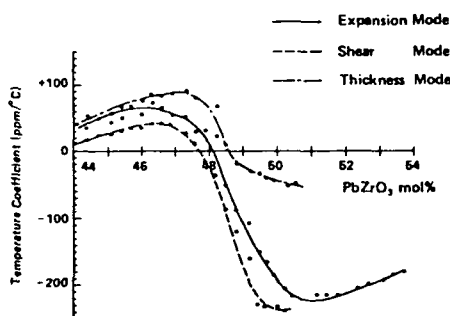


FIG. 2  
Temperature Coefficient Characteristics of Resonant Frequency By  $\text{PbZrO}_3$  Ratio to  $\text{PbTiO}_3$

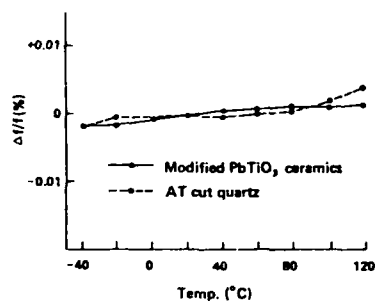


FIG. 3  
Temperature Characteristics of Resonant Frequency for  $\text{PbTiO}_3$  Ceramics and AT cut Quartz Crystals

To make ceramic resonators higher than 10MHz,  $\text{PbTiO}_3$  materials are better than PZT material because the mechanical Q is larger and the dielectric constant is smaller. Also,  $\text{PbTiO}_3$  materials are more suitable for making 3rd overtone rather than fundamental resonators because it is theoretically impossible to

make fundamental frequencies using a trapped mode. It is possible to make 3rd overtone because the Poisson's ratio  $\sigma$  of  $\text{PbTiO}_3$  is less than 0.3. Fig. 4 shows this relationship, and we could improve the temperature coefficient of the resonant frequency by adding Lanthanum impurities.<sup>(3)</sup> The mechanical Q value of this material is more than 4,000, and the temperature coefficient of the resonant frequency is less than 0.2 ppm/°C from -40°C to +120°C temperature range.

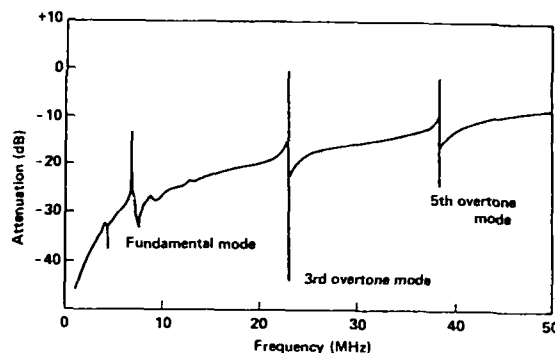


FIG. 4  
Frequency Characteristic of Resonant Frequency for  $\text{PbTiO}_3$  Ceramics

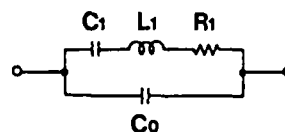
We are using the EMAS<sup>(4)</sup> (Electronic Material Association Standard) in Japan to measure all piezoelectric constants of our piezoelectric ceramic materials.

We are also using MIL-STD-202E to make the environmental tests for our materials.

Table 1 shows all items for this test and each condition is decided by each requirement.

#### Design and Characteristics of Ceramic Resonators

Fig. 5 shows the equivalent circuit of piezoelectric ceramic resonators, CERALOCK<sup>®</sup>, which is quite similar to quartz crystals. (<sup>®</sup> is registered by Murata in USA, UK, W. Germany, Japan and etc.)



**C<sub>1</sub> : Equivalent Compliance**  
**L<sub>1</sub> : Equivalent Mass**  
**R<sub>1</sub> : Equivalent Resistance**  
**C<sub>0</sub> : Parallel Equivalent Capacity**

FIG. 5  
2-Terminal Type Equivalent Circuit

In Fig. 5 we can obtain next expression:

$$f_r = \frac{1}{2\pi} \sqrt{\frac{1}{L_1 C_1}} \quad f_r : \text{resonant frequency}$$

$$f_a = \frac{1}{2\pi} \sqrt{1 + \frac{C_1}{C_0}} \quad f_a : \text{anti-resonant frequency}$$

$$k^2 = \frac{C_1}{C_0} = 2.41 \sqrt{\frac{f_a - f_r}{f_r}} \quad k : \text{coupling coefficient}$$

$$Q_m = \frac{1}{2\pi f_r C_1 R_1} \quad Q_m : \text{mechanical Q}$$

We can make the piezoelectric ceramic resonators in a wide frequency range from 100KHz to 100MHz utilizing the "expansion mode", "thickness shear mode" or "trapped energy mode" of vibration, however, present usage is concentrated in and around 450KHz, 2MHz, 4.5MHz, and 10.7MHz. (5)

Table 2 shows equivalent constants of typical piezoelectric ceramic resonators compared to quartz crystals.

Fig. 6 shows an example of frequency and impedance characteristics, and also phase angles for a 450KHz ceramic resonator. We can understand from Fig. 6 that the impedance of the resonator is inductive between  $f_r$  and  $f_a$ , and that a Colpitts circuit is most useful for the oscillator.

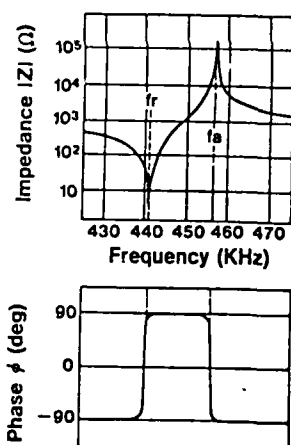


FIG. 6  
Impedance and Phase Characteristics  
for Ceralock (CSB455E)

Fig. 7 shows an example of an oscillation circuit using a C-MOS IC. In Fig. 7,  $R_f$  is a resistor for bias and  $R_d$  is a damping resistor for higher harmonics.

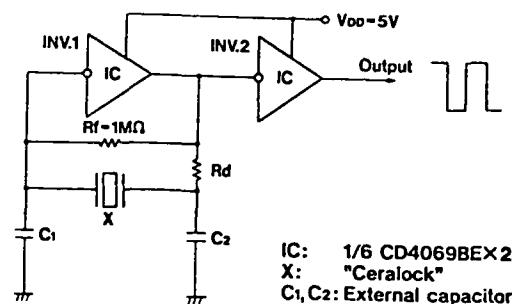


FIG. 7.

Basic Oscillation Circuit of "Ceralock"

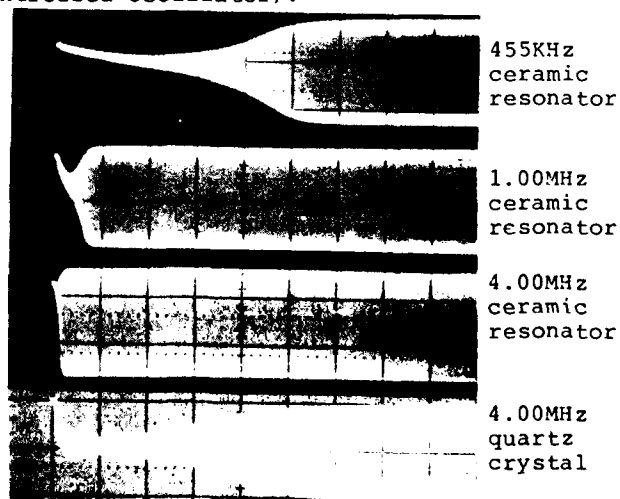
This oscillating frequency is shown in next expression in which the value is shown in Table 2.

$$f_{osc} = \frac{1}{2\pi} \sqrt{\frac{1}{L \frac{C_1 C_2}{C_1 + C_2}}}$$

The advantage of ceramic resonator is the short start up time of the oscillator because of the small mechanical Q value. This is suitable for switching the oscillator.

The start up time of the oscillator circuit is proportional to the mechanical Q value of the resonator and inversely proportional to the frequency. Fig. 8 shows an example of this relation. We can understand that the start up time of ceramic resonators is one decade shorter than quartz crystals.

Another benefit of ceramic resonators is the possibility of a wide frequency shift because of the large frequency difference between  $f_r$  and  $f_a$ . This is suitable to VCO's (Voltage Controlled Oscillator).



Photograph of start up time for clock oscillator  
using ceramic resonator and quartz crystal  
(Horizontal line is 0.2 μs/div.)

FIG. 8

Fig. 9 shows an example of a synchronized horizontal signal generator circuit for color TV, and Fig. 10 shows the relation of the oscillating frequency to the control voltage.

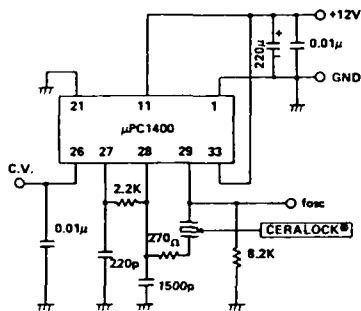


FIG. 9

One example of VCO Circuit for color TV

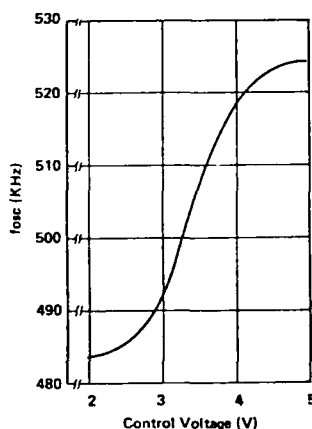
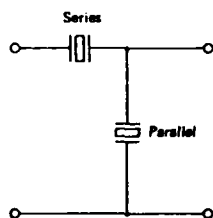


FIG. 10

Oscillated Frequency by Control Voltage

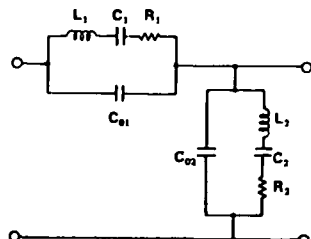
### Design and Characteristics of Ceramic Filters

There are many kinds of ceramic filters, so called CERAFIL<sup>®</sup> (® is registered by Murata in USA, UK, W. Germany, Japan and etc). Fig. 11 shows the structure of ladder type ceramic filters and Fig. 12 shows the equivalent circuits. When we adjust the resonant frequency and anti-resonant frequency of both series and parallel resonators to satisfy the next expression, we can obtain the frequency characteristics shown in Fig. 13. (6)



Structure of Ladder Type Ceramic Filter (One Section)

FIG. 11



Equivalent Circuit for Ladder Type Ceramic Filter (One Section)

FIG. 12

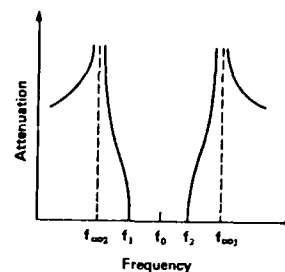


FIG. 13

Frequency Characteristic for Ladder Type Ceramic Filter

$$m_1^2 = \frac{f_{\infty 1}^2 - f_2^2}{f_{\infty 1}^2 - f_1^2}$$

$$m_2^2 = \frac{f_2^2 - f_{\infty 2}^2}{f_1^2 - f_{\infty 2}^2}$$

$$C = \frac{1}{2\pi f_0 \sqrt{(Z_{\pi} Z_T)}} \left[ \frac{1+m_1^2}{1+m_2^2} \right]^{\frac{1}{2}}$$

$$C_{01} = \frac{1-m_1^2}{2} C$$

$$C_{02} = \frac{2}{m_2^2 - 1} C$$

$$C_1 = \frac{f_{\infty 1}^2 - f_0^2}{f_0^2} C_{01}$$

$$C_2 = \frac{f_0^2 - f_{\infty 2}^2}{f_{\infty 2}^2} C_{02}$$

$$L_1 = \frac{1}{4\pi^2 f_0^2 C_1}$$

$$L_2 = \frac{1}{4\pi^2 f_{\infty 2}^2 C_2}$$

The selectivity and bottom level is proportional to the number of ladder sections.

For higher than frequencies of 4MHz, we use the thickness or thickness shear trapped vibration mode. In this case, if we make a split partial electrode shown in Fig. 14, we can obtain four terminal ceramic filters without using a coil. This is accomplished by the coupling of two vibration modes which are symmetrical and anti-symmetrical as shown in Fig. 15. (7)

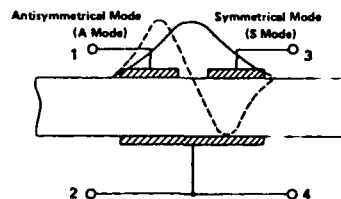
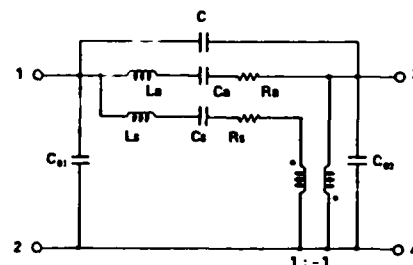


FIG. 14

Multicoupling Energy Trapped Mode Filter





## Packaging

Piezoelectric ceramic resonators and filters are very important frequency control devices for electronic circuits. However, in order to use these devices, we must make practical packages. Wire mounts and hermetic seals are typical packages for quartz crystals, but it is difficult to make small configurations and mass production with these packages. It is not necessary to use metal sealed cases for ceramic resonators and filters because they do not pick up electro-magnetic noise because of their low impedance. Also, mechanical damping of the ceramic elements does not have much effect on the electrical performance due to the low mechanical Q value. For these reasons, we can use quite different packaging from the ordinary for ceramic resonators and filters. (8)

Fig. 16 shows an example of the package for lower frequency ceramic resonators. We are using spring metal terminals and plastic cases which are welded together by an automatic ultrasonic welding machine.

Fig. 17 shows an example of the package for higher frequency ceramic filters. Here we are using a special wax on the partial electrodes, and a phenol resin on the whole ceramic element. The wax is absorbed into the resin, making a cavity around the electrodes during the curing process. (9)

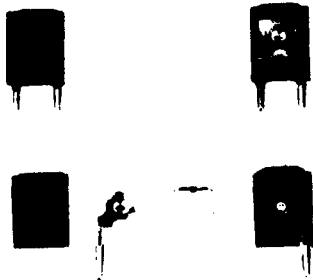


FIG. 16

Photograph of Structure for Ceramic Resonator Package

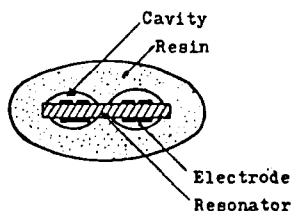


FIG. 17

Cross Section of Package for Ceramic Filter

This package is very useful because of its simplicity and small configuration. It is also very strong and resistant to shock.

Fig. 18 shows an example of the package for chip type ceramic resonators and filters. We can use reflow soldering process to mount these devices on the chassis.

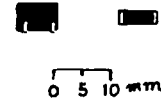


FIG. 18

Photograph of CHIP type Ceramic Resonator  
Left is 455KHz, Right is 4.00MHz

Recently, we began supplying ceramic filters radially taped and reeled for automatic insertion equipment. We are now introducing chips which are suitable for automatic surface mounting by standard automatic placement machines.

Configurations of these ceramic resonators and filters are the same as the IEC (International Electrotechnical Commission) standards (10) which are commonly used around the world.

## Conclusion

The new technology using the green sheets method for making ceramic wafers is very useful for the mass production of piezoelectric ceramic resonators and filters.

The compensation to make zero temperature coefficients at resonant frequency for each vibration mode, in each frequency range is also possible by adjusting the ratio of mole % of Ti and Zr in PZT materials. This is very similar to adjusting the cut angle for quartz crystals.

It is easy to change the mechanical Q value of ceramic resonators widely from the 500 to 5,000 range by the proper choice of impurities for the raw materials. The moderate mechanical Q value of ceramic resonators is advantageous for switching clock oscillators used in microprocessors.

The high coupling coefficient of piezoelectric ceramic materials is suitable for resonators in VCO use or wide bandwidth filters.

The unique packaging using metal spring contacts or phenol resin coatings makes small sizes and stable configurations including surface mountable products.

We look forward to the rapid spread of these piezoelectric ceramic resonators and filters in many semiconductor circuits.

Test	Test Conditions
Shock Resistance	Dropped freely, 3 times, on a concrete floor from a height of 30 cm, except CSB resonators at frequencies lower than 299 KHz, which are dropped from a height of 10 cm.
Vibration Resistance	Vibrations of 10~55 Hz frequency and 1.52 mm total amplitude are applied for 1 hour each along X, Y and Z directions.
Terminal Strength	0.5 kg weight is reciprocated along the terminal's axial direction, while 0.25 kg weight is reciprocated along a direction 90° to the axial direction.
Solderability	The terminal is immersed up to a point 2 mm from its bottom, into 230° ± 5° C soldering oven for a period of 5 sec.
Soldering	The terminal is immersed up to a point 2 mm from its bottom, into 350° ± 10° C soldering oven for a period of 3 sec.
Humidity Resistance	Ceramic resonator is held for 100 hours inside a constant temperature and constant humidity oven held at 40° ± 2° C and 90~95% RH.
Storage at High Temperature	Held in 85 ± 2° C constant temperature oven for 1000 hours.
Storage at Low Temperature	Held in - 25 ± 2° C constant temperature oven for 100 hours.
Temp. Cycle	Subject to 5 cycles of 30 min. at - 25° C, 30 min. at + 20° C, 30 min. at 85° C.
Thermal Shock	Subject to 5 cycles of 30 min. at - 55° C, 30 min. at + 85° C.

#### Enviromental Test Conditions

TABLE 1

Device	Ceramic Resonator					X'tal		
	CSB456J	CSA1000MK	CSA400MS11	CSA400MG	CSA2000MX11	453.5KHz	2.457MHz	4.00MHz
Frequency	455KHz	1.00MHz	4.00MHz	4.00MHz	20MHz			
L (μH)	6.1×10 <sup>3</sup>	8.7×10 <sup>3</sup>	170	450	470	8.63×10 <sup>3</sup>	7.1×10 <sup>3</sup>	1.4×10 <sup>3</sup>
C (pF)	21.5	3.1	10.2	3.7	0.13	0.015	0.006	0.012
C <sub>0</sub> (pF)	268.5	31.9	70.0	35.7	15.67	5.15	2.49	3.09
R (Ω)	5.5	56.0	6.8	10.1	16.3	1.06×10 <sup>3</sup>	76.0	14.9
Qm	3100	1000	600	1100	3600	2.3×10 <sup>3</sup>	1.4×10 <sup>3</sup>	2.3×10 <sup>3</sup>
Fa - F <sub>0</sub> (KHz)	17	38	270	190	85	0.6	2.9	7.5

#### Equivalent Constants of Typical Ceramic Resonators and Quartz Crystals

TABLE 2

#### Reference

- 1) T. Ogawa, H. Adachi, K. Minai, Pat. No. 1028188 (1980) Japanese.
- 2) S. Fujishima, S. Kakei, T. Ogawa, S. Arai, K. Togawa, "High grade piezoelectric ceramics and its applications" Proc. of Electro Mechanical Symposium (1982), p. 65 Japanese.
- 3) T. Ogawa, T. Kittaka, Pat. No. 129869 (1982) Japanese
- 4) EMAS 6001-6005 (1982) Japanese
- 5) K. Togawa, T. Ishiguro, "New Application Techniques for Electronic Components" The Transistor Techniques, June 1983, p. 358, Japanese.
- 6) S. Fujishima, S. Nosaka, "New Development of Ceramic Filters" The Electronics, May 1965, p. 566, Japanese
- 7) S. Fujishima, "Piezoelectric Ceramics and their applications" Proc. of the Symposium in the Electrical and Electronic Society, 1982, p. 4 - 57, Japanese
- 8) S. Fujishima, "Research and Development of Piezoelectric Devices in Japan" Ultrasonics Symposium Proc. p. 128, Sept. 1979
- 9) I. Toyoshima, Pat. No. 595152 (1971) Japanese
- 10) IEC Pub. 642

## FURTHER RESULTS ON 5 MHZ AND 10 MHZ RESONATORS WITH BVA AND QAS DESIGNS

Jean Pierre AUBRY and André DEBAISIEUX

Compagnie d'Electronique et de Piézo Electricité - C E P E  
95 100 - ARGENTEUIL FRANCESUMMARY

BVA design has been extensively described in the past few years. Most of the results were given at 5 MHz.

Last year, we have introduced a QAS design 10 MHz SC cut 3rd OT, which gives, in HC 40 can, very low G sensitivity : 16 % of crystals manufactured in a batch were founded better than  $2.10^{-10}$  / G.

We have followed up our work on highly stable 10 MHz crystal resonators and this paper describes recent results obtained with :

- 10 MHz SC Cut 3rd OT ( HC 40 can ) QAS design
- 10 MHz SC Cut 5Th OT ( T 3516 can ) QAS design
- 10 MHz SC Cut 5Th OT ( T 3516 can ) BVA design

compared to 5 MHz SC Cut 3rd OT BVA design resonators.

In the smaller can ( HC 40 ), we have developed a new mounting configuration for the 10 MHz 3rd OT QAS resonator. The ratio of resonators with a G sensitivity better than  $2.10^{-10}$  / G is now observed up to 80 % per batches.

Others improvements are also observed ( short term stability  $< 5.10^{-13}$ , retrace  $< 2.10^{-10}$  ... ) which make these resonators very usefull regarding recent high level oscillator specifications.

On the other hand, we have developped 10 MHz 5Th OT SC Cut resonators, with BVA or QAS design mounted in a larger can, called T 3516 ( diameter 35 mm, height 16 mm ).

These resonators do have the improvements due to the quartz bridge mounting technique in addition to the classical advantages of the SC Cut and of the fifth

overtone.

Results obtained with these resonators and measured either with passive reference system or with oscillators (  $Q > 1.4.10^6$ ,  $\sigma_y(\tau) < 4.10^{-13}$  from 1 to 100 s, typical ageing  $< 1.10^{-11}$  / day ... ) are described and discussed.

INTRODUCTION

The actual specifications of oscillators requested by modern system in numerous fields ( positionning, communications, aerospace applications ... ) do require improvements of crystal resonators parameters.

Long term ageing is now requested in terms of  $10^{-11}$  per day, short term stability in  $10^{-13}$  and G sensitivity in  $10^{-10}$  / G.

Among the studies devoted to quartz crystal resonators a large number of papers deal with G sensitivity.

Various contributions to this effect were investigated and some models have been proposed to reach low G sensitivity resonators. However, there are not yet many crystals which have been shown, till recently, to have a low G sensitivity in all directions of space ( 10 ).

The 5 MHz BVA design was an interesting solution to solve this problem. Nevertheless, for specifications in which the G sensitivity is the single difficult parameter, BVA is a good but luxurious solution.

Last year we have presented a QAS design which makes use of the quartz bridge mounting of the BVA design.

In this paper, we present the actual performances on low G sensitivity distribution obtained with an improved QAS design. The improvement observed is due to some change in the configuration of the mounting ribbons.

To meet low ageing requirements, we have developed new oscillators working with 5 MHz ( SC Cut 3rd overtone ) and 10 MHz ( SC Cut 5th overtone ) BVA resonators. The main goal of these studies is an ageing rate around  $5.10^{-12}$  per day and around  $1.10^{-10}$  per month.

The further objective is  $1.10^{-9}$  per year. We describe the low ageing results we have obtained with these 10 MHz BVA design resonators.

#### RECENT DEVELOPMENTS ON RESONATORS AND OSCILLATORS

In recent years, the G sensitivity was one of the most intensively studied parameter, both theoretically and experimentally, by many workers ( 3 - 12 ).

It is now well established that G sensitivity is caused by stresses, of various origin, which can apply on the vibrating area.

The first theoretical approach dealing with force-frequency effect and in plane acceleration frequency effect was given by Professor PCY Lee and co-workers ( 3 - 4 ).

These studies lead to the definition of  $\Psi$  angles for which one of these effects becomes negligible (  $K_f(\Psi) = 0$  ).

The force-frequency model was applied to doubly rotated cuts, including anisotropy of quartz, by Ballato ( 5 ).

These models do not give a full explanation of G sensitivity of crystal resonators, and all the attempts to correlate deviations from " ideal " geometry of mounting and poor experimental results were in failure.

A more detailed explanation on G sensitivity, not yet completed, was given by Janiaud and others ( 6 - 8 ).

This model involves all forces ( surface and body

forces, static, dynamic or initial stresses, torques ... ) applied by the mounting support or acceleration induced.

The conclusions of this work are that most of the G sensitivity is due to :

- . torques or mechanical couples at the crystal boundary ( initials or induced )
- . induced compressive forces.

That means that one has to find a mounting design which keeps as good as possible the initial symmetry of mounting free from induced stresses or torques.

An experimental verification was given by Goldfrank and Warner ( 12 ) who correlates thermocompression, bounding mis - alignment, mechanical couples and G sensitivity of 5 MHz SC 5th overtone resonators.

An experimental demonstration of the main influence of mounting symmetry on G sensitivity was given by Professor Besson and its BVA design ( 13 ).

The QAS design, which allows a G sensitivity better than  $2.10^{-10}$  / G, involves the quartz bridge technique of the BVA and confirms the influence of the symmetry of mechanical configuration on G sensitivity.

Long term ageing has been also intensively studied. The most influent parameters are the mechanical ( initial ) stress release from plated metallization or mounting springs, the chemistry of the surface and the residual contamination after encapsulation.

Additional cleaving using U.V. ozone reactions with surface contamination was recently introduced ( 14 ).

Many technological parameters including ultra vacuum gold plating, ultra clean processing, high vacuum sealing, are involved in long term ageing. Others main requirements such as frequency retrace, warm up time, short term stability ... which involve both the resonator and the oscillator, are mostly experimental parameters.

The actual knowledge leads to the conclusion that these performances are strongly affected by the cut and the applied technology ( mounting, processing

oven, mechanical assembly ... ).

The actual needs expressed for modern oscillators have lead C E P E to use all the theoretical and technological resonator improvements and all the possibilities of low noise design electronic in highly miniaturized ovens, to reach new crystals and new oscillator performances ( 2 ).

### BVA AND QAS RESONATORS

#### - 1 - BVA and QAS design

BVA design resonators, working with AT Cut fifth overtone or SC Cut third overtone at 5 MHz, have already been described ( 13 ), and the experimental results have confirmed the interest of this design.

BVA crystal resonator involves non-sticky electrodes and monolithic mounting.

The vibrating area is supported by small quartz bridges which are attached to a quartz ring. This ring can be taken as a stress-free mounting support. It works as a mechanical filter between the base and the vibrating area.( Figure 1 ).

In addition, the quartz bridges give a good symmetry of stresses along the thickness of the resonator. The thickness of the bridges can be reduced to apply the induced stresses close to the nodal plane of vibrations.

The quartz bridges are manufactured by ultrasonic machining, which removes quartz material between central part and ring in order to leave only the quartz bridges.

Two disks made of quartz ( same cut and same orientation than the resonator ) are put on both sides of the resonator. One is flat and parallel, the other one is piano-concave. Quartz bridges and rings are also manufactured by ultrasonic machining on these two disks.

In front of the vibrating area of the resonator, a " gap " is done in the disks, by mechanical means or chemical etching, in order to leave a distance of 5

or 10<sup>-3</sup> mm between the vibrating area surface and the disk.

Gold metallization is plated in the bottom of these 5 or 10 mm depth " holes ".

The only surfaces in contact between the three pieces are then on the rings.

The three parts are maintained by clips ( 2, 3 or 4 ) of given rigidity and shape. This assembly is supported by springs ( Figure 2 ).

The design parameters usable to adjust electrical coefficients are the radius of curvature, gap thickness and diameter of metallization.

In the course of this study one have fabricated both 5 MHz 3rd OT and 10 MHz 5th OT SC cut resonators.

The vibrating area is 15 mm in diameter and the overall one 24 mm.

Radius of curvature from 100 mm up to 3000 mm have been tried.

Classical lapping, contouring and surface finishing are used. The final frequency adjustment is obtained by light and successive polishing of the surface.

The parameters which are used to improve mechanical properties ( endurance or performance ) are :

- dimensions ( length, width, thickness ) of bridges
- location, number and orientation of bridges
- clips supporting the three quartz pieces
- springs supporting the overall assembly

The vibrating plate of a BVA resonator can also be directly plated. This leads to the QAS design ( 5 Mhz 3rd OT or 10 MHz 5th OT ) SC cut resonators. These four types of resonators are encapsulated in a special metal can, called T 3516 ( 35 mm in diameter, 16 mm height ) ( Figure 3 ).

After a high temperature and low pressure baking out, crystals are sealed by " cold-weld " under high vacuum.

An other QAS design is shown on figure 2 and 3. This is the 10 MHz SC Cut 3rd OT resonator, encapsulated in HC 40 can, introduced last year ( 1 ).

The vibrating area is 10 mm in diameter and the ring is 15 mm in diameter. Metallization is plated on the vibrating area.

The dimensions, number and location of the quartz bridges are the adjustable mechanical parameters of this design.

The way the ring is supported by the mounting ribbons is also of great importance in electrical performances under vibrations, even if the ring is not a part of the vibrating area.

## - 2 ) ENVIRONMENTAL ENDURANCE

Most of the oscillators for which these resonators are designed must be able to operate safely after environmental shocks and vibrations ( generally up to 2000 or 3000 Hz ).

The elasticity of the mounting spring and the mass supported by this spring lead to mechanical resonances under vibrations, at given frequencies.

When these mechanical resonant frequencies fall into the vibration spectrum applied, the induced deformation can wear and even brake the resonator.

One of the goal of a crystal designer is to raise the mechanical resonances of crystal resonators at frequencies higher than 2000 or 3000 Hz.

A classical equipment used to locate the resonant frequencies of the mounting support is shown on figure 4. The resonator itself is used as a sensor, because its own deformations induce, through the piezoelectric effect, electrical charges on the electrodes which can be measured.

Low frequency spectral density analysis of the electrical signal recorded under vibrations gives the frequency response spectrum of the device. Main peaks of amplitude are interpreted as mechanical resonances of the overall assembly of the resonator.

Figure 5 gives the response of a classical 5 MHz BVA resonator. Resonances appear at frequencies around 1200 Hz making this resonator not suitable for space applications.

Figure 6 gives the response of a 10 MHz BVA resonator, specially designed by C E P E for space application. Up to 2000 Hz ( which is the upper limit of applied vibrations during the launching for this mission ), the frequency spectrum is free for any resonances.

The difference between both responses is only due to a modification of the springs supporting the three quartz pieces. It shows the flexibility of the BVA design.

Figure 7 gives the frequency response under vibrations of a QAS 10 MHz SC 3rd OT ( HC 40 ) resonator.

Figure 8 gives the response of a QAS 10 MHz SC 5th OT ( T 3516 ) resonator.

With these two resonators, one can observe that the worst ( lowest ) mechanical resonance appears at frequencies far higher than 2000 Hz. Out of plane and in plane acceleration give different resonant frequencies but we are concerned by the lowest one.

Some of these resonators have been submitted to 30 G eff, between 10 and 2000 Hz. Neither frequency drift nor failure were observed.

In conclusion of this study about environmental endurance, we can say that, by an accurate choice of the mounting design, BVA and QAS resonators can be strongly vibration resistant and suitable for space application.

## ELECTRICAL PERFORMANCES

### - 1 ) MOTIONAL PARAMETERS

Among the designs we have just described, Table I gives typical motional parameters measured on  $\pi$  network.

Frequency / Overtone / Type	R ( $\Omega$ )	L ( H )	Q ( $10^6$ )
5 MHz SC 3rd OT BVA	95	7,5	2,5
	QAS	80	6
10 MHz SC 5th OT BVA	80	1,8	1,4
	QAS	75	1,6
10 MHz SC 3rd OT QAS	60	1,2	1,3

TABLE 1

The turn over temperature dispersion is not much larger with a BVA or QAS design than with classical resonators.

For each type, motional parameters can be largely adjusted ( for example BVA 5 MHz : L can range from 4 H to 10 H ) by manufacturing parameters ( radius of curvature, gap thickness ... ).

#### - 2 ) G sensitivity

Although BVA design allows G sensitivity down to  $3 \cdot 10^{-10}$  / G, this parameter was not the main one taken into account to choose the actual BVA design described in this work.

We do prefer to improve G sensitivity performances of small size crystals ( HC 40 ) to meet actual requirements ( ageing  $< 5 \cdot 10^{-10}$  / day, G sensitivity  $< 5 \cdot 10^{-10}$  / G ).

The mechanical equipment used to perform a 2 G tip over test and the system used to follow the frequency drift of the resonator alone ( Passive Reference System ) are described elsewhere ( 1 ).

By turning around two axis of rotation of the ovenized resonator, one comes to find experimentally the direction of the worst frequency deviation. This gives the amplitude and orientation versus resonator coordinates of the G sensitivity vector  $\vec{r}$ .

The parameters we have been able to study are :

- cut angles
- bridges location and shape
- mounting configuration

This work performed on 10 MHz 3rd OT resonators in HC 40, leads to the following exclusions : low G sensitivity resonators, although achievable with AT cut is more easily obtained with SC cut.

The relation between G sensitivity and exact crystal cut (  $\varphi$  angle around SC ) is largely smaller than the influence of resonator design. Low G sensitivity resonators have been manufactured with plates from 21,95 up to 22,75°, at frequencies 10 or 10,230 MHz.

Figure 9a gives the G sensitivity distribution of the previous QAS design.

Figure 9b gives the G sensitivity distribution of the new QAS design.

One can see that the mean value has been lightly reduced, but the sigma of the distribution has been largely reduced.

This low sigma value means that this design is quite free from light deviations of mounting configuration and is very interesting for industrial purpose.

#### - 3 ) SHORT TERM STABILITY

The passive reference system which has been used to follow small frequency drift during G sensitivity tests, allows to measure short term stability of the ovenized resonator.

Short term stability characterization of a resonator can then be done either with the passive reference system or in classical oscillators. Classical methods ( LF beating frequency counting, frequency difference multiplication ... ) are used ( 15, 16 ).

Table 2 gives typical short term stabilities ( 2 samples Allan variance ) measured at 5 and 10 MHz with BVA or QAS resonators on the passive reference system (  $\tau = 10$  s ).

Frequency / Cut / Overtone / Design	$\sigma_y (\tau = 10 \text{ s})$
5 MHz SC 3rd OT BVA ( Figure 10 )	$4,2 \cdot 10^{-13}$
10 MHz SC 5th OT BVA QAS ( Figures 11 - 12 )	$4,5 \cdot 10^{-13}$ $5,8 \cdot 10^{-13}$
10 MHz SC 3rd OT QAS ( Figure 13 )	$3,1 \cdot 10^{-13}$

TABLE 2

Table 3 gives the short term stability of some typical resonators, measured either with passive reference system or with oscillators.

To perform the measurements shown on tables 2 and 3, the same short term reference was used ( BVA 5 MHz ).

	Passive reference	Oscillator
BVA 5 MHz 3rd OT	$4,2 \cdot 10^{-13}$	$3,1 \cdot 10^{-13}$
BVA 10 MHz 5th OT	$4,5 \cdot 10^{-13}$	$3,7 \cdot 10^{-13}$
QAS 10 MHz 3rd OT	$3,1 \cdot 10^{-13}$	$2,5 \cdot 10^{-13}$

TABLE 3

Table 3 shows clearly that the values observed with an oscillator are lower than those observed with the passive reference system.

The oscillators used in these measurements were specially designed for short term performance. They involve low noise electronic design, highly miniaturised ovens with PID control ( 2 ).

Figure 13 gives, for example, the short term stability measured with the passive reference system ( solid line ) and the complete oscillator ( dashed line ).

One can see that between 10 and 100 s the oscillator offers better performance than the passive system.

We do believe that we have not yet reached the proper limits of the crystal resonators.

In order to overcome the problem of the stability of the reference used, we have performed a measurement of three oscillators, in the same time, by the cross variance method ( 15 ). The three oscillators under test were measured through their LF beating frequencies. For  $\tau = 10 \text{ s}$ , the experimental data were :

$$\sigma_{AB} = 3,6 \cdot 10^{-13} \quad \sigma_{BC} = 2,5 \cdot 10^{-13} \quad \sigma_{AC} = 4 \cdot 10^{-13}$$

In the conditions of simultaneous measurements, J. Gros Lambert have shown that we can solve directly this system by the relations.

$$\sigma_{AB} = \sqrt{\sigma_A^2 + \sigma_B^2} \quad \sigma_{BC} = \sqrt{\sigma_B^2 + \sigma_C^2} \quad \sigma_{AC} = \sqrt{\sigma_A^2 + \sigma_C^2}$$

This simple calculation leads to :

$$\sigma_A = 3,4 \cdot 10^{-13} \quad \sigma_B = 1,1 \cdot 10^{-13} \quad \sigma_C = 2,3 \cdot 10^{-13}$$

indicating that values close to  $1 \cdot 10^{-13}$  are achievable by these oscillators. The resonators were QAS 3rd OT in oscillators A and B and BVA in oscillator C.

On alternative method usable to identify the short term stability is to use a 3 samples method instead of 2 samples in the Allan variance.

The stability calculated by this method is given by

$$\sigma = \sqrt{\frac{\sum_{i=1}^{N-2} \left( f_{i+1} - \frac{f_i + f_{i+2}}{2} \right)^2}{2(N-1)}}$$

This way of calculation forgets the mean slope of frequency drift and gives the frequency distribution around this mean slope.

With this method, the 3 previous oscillators were founded , for  $\tau = 10 \text{ s}$  :

$$\sigma_{AB} = 2,4 \cdot 10^{-13} \quad \sigma_{BC} = 1,7 \cdot 10^{-13} \quad \sigma_{AC} = 2,8 \cdot 10^{-13}$$

The same calculation leads to



$$\zeta_A = 2,3 \cdot 10^{-13} \quad \zeta_B = 6,9 \cdot 10^{-14} \quad \zeta_C = 1,6 \cdot 10^{-13}$$

These results show that, disregarding the initial slope of frequency drift, short term stability in terms of parts in  $10^{-14}$  are achievable with QAS resonators.

An other mean to overcome the limitation due to the short term stability of the reference oscillator is to compare the oscillator to an H2 Maser which has a lowest contribution than  $1 \cdot 10^{-13}$  for  $\tau = 10$  s.

Such experiments are actually on course at the " Laboratoire de l'Horloge Atomique " of Professor Audoin in the Faculté des Sciences of Orsay.

#### - 4 ) FREQUENCY RETRACE AND WARM-UP TIME

In equipment submitted to intermittent operation, for mobile communications for example, frequency retrace and warm-up time are required as small as possible.

For definition of performances, we generally perform a frequency retrace measurement 24 H after the power supply turned off. In these conditions, up to date requirements can be a frequency error less than  $\pm 1 \cdot 10^{-9}$  after 10 minutes.

Such specification is difficult to meet with classical resonators.

Figure 14 gives a typical example of frequency retrace of a new oscillator using both a PID oven and a QAS 3rd OT SC Cut resonator. Frequency error as low as  $2 \cdot 10^{-10}$  after 100 min. is observed and the  $1 \cdot 10^{-9}$  window is reached within 10 minutes after turn-on ( power consumption less than 5 W ).

#### - 5 ) AGEING

If most of the low G sensitivity, low retrace specifications are related to classical ageing requirements one observe actually a strong interest for very low ageing rate resonators for continuous operation.

Ageing less than  $\pm 1 \cdot 10^{-11}$  / day is now requested and this is an area for which well designed BVA resonators could be the key-word of the solution.

Figure 15 gives the frequency drift during the pre-ageing period ( 1 month ) of an oscillator using a BVA resonator. After a step of  $1 \cdot 10^{-9}$  during the first 2 days, the frequency of the oscillator decreases with a mean slope of  $2 \cdot 10^{-10}$  / month.

Figure 16 gives the frequency drift observed during the 10 following days. Mean slope is approximately  $4 \cdot 10^{-11}$  in 10 days (  $1,2 \cdot 10^{-10}$  / month or  $4 \cdot 10^{-12}$  per day ).

On figures 15 and 16, the dashed lines indicate a slope of  $2 \cdot 10^{-9}$  / month. The C E P E experiments on ageing indicate that :

- . 10 MHz QAS 3rd OT resonators exhibit typical ageing around  $5 \cdot 10^{-9}$  / month
- . 10 MHz QAS 5th OT resonators ( or 5 MHz QAS 3rd OT ) can provide intermediate slopes, less than  $1 \cdot 10^{-9}$  per month.
- . 10 MHz BVA 5th OT resonators ( or 5 Mhz BVA 3rd OT ) offer the best ageing rate available today : one or two parts in  $10^{-10}$  per month can be achieved.

We are still on work to find the mean slope and the total frequency drift of oscillators after a longer period of time ( 6 months - 1 year ) of continuous operation.

### CONCLUSION

The introduction of BVA and QAS design resonators have opened new ways to meet the requirements of oscillators for use in modern equipments ( communications, local positionning ).

To reach the full benefit of these resonators, we have built up new oscillators which use miniaturised ovens with PID control and appropriate electronic design.

Typical values on ageing, short term stability or G sensitivity are now achievable with an improvement of 10 compared to today's best commercial oscillators.

The ageing drift shown by a BVA type oscillator can range around  $5 \cdot 10^{-12}$  per day after a short pre-ageing

period of time.

If proper resonator processing is applied, short term stability ( Allan variance ) can be measured less than  $5 \cdot 10^{-13}$  from 1 to 100 s ( typical  $2 \cdot 10^{-13}$  at 10 s ).

G sensitivity of resonators ( 10 MHz or 10,230 MHz in HC 40, 5 MHz or 5,115 MHz in T 3516 ) can be as low as  $2 \cdot 10^{-10}$  / G on industrial basis if appropriate mounting configuration is used.

Frequency retrace and warm-up time can be very low and these resonators were shown to be strongly shock and vibration resistant which allows their use in military or space applications.

Future developments will deal with long term ageing ( less than  $1 \cdot 10^{-9}$  per year ) and with highest frequencies ( 20 MHz .... ).

#### BIBLIOGRAPHY

- 1 ) A. DEBAISIEUX, JP. AUBRY and J. GROSLAMBERT  
Design of SC Cut 10 MHz H.Q. crystals with G sensitivity better than  $2 \cdot 10^{-10}$  / G  
Proc. 15th PITI 1983
- 2 ) C. BEAUVY, G. MAROTEL and P. RENOULT  
High performances from a new design of crystal oscillator  
Proc. 15th PITI 1983
- 3 ) P.C.Y. LEE and K.M. WU  
Non linear effect of initial stresses in doubly rotated crystal resonator  
Proc. 34th AFCS 1980
- 4 ) P.C.Y. LEE and K.M. WU  
The influence of support configuration on the acceleration sensitivity of quartz resonator plates.  
Proc. 31st AFCS 1977
- 5 ) A. BALLATO, E.P. LERNISSE and I. LUKASZEK  
The force frequency effect on doubly rotated quartz resonator  
Proc. 31st AFCS 1977
- 6 ) D. JANIAUD, L. NISSIUR and JJ. GAGNEPAIN  
Analytical calculation of initial stress effects on anisotropic crystals : application to quartz resonators  
Proc. 32nd AFCS 1978
- 7 ) D. JANIAUD  
Influence du support sur la sensibilité aux accélérations d'un résonateur à quartz  
C.R. Acad. SC Paris t 285 B 1977
- 8 ) M. VALDOIS, R. BESSON and JJ. GAGNEPAIN  
Influence of support configuration on the acceleration sensitivity of quartz resonator plates  
Proc. 31st AFCS 1977
- 9 ) R.L. FILLER and J.R. VIG  
The acceleration and warm-up characteristics of four point mounted SC and AT cut resonators.  
Proc. 35th AFCS 1981
- 10 ) R.L. FILLER, J.A. KOSINSKI and J.R. VIG  
Further studies on the acceleration sensitivity of quartz resonators  
Proc. 37th AFCS 1983
- 11 ) D.A. EMMONS  
Acceleration sensitivity compensation in high performance crystal oscillators.  
Proc. 10th PITI 1978
- 12 ) B. GOLDFRANK and A. WARNER  
Further developments on SC cut crystals  
Proc. 34th AFCS 1980
- 13 ) R.J. BESSON  
A new piezoelectric resonator design  
Proc. 30th AFCS 1976
- 14 ) J.R. VIG  
Private communication
- 15 ) J. GROSLAMBERT, D. FESI, M. OLIVIER and JJ. GAGNEPAIN  
Characterization of frequency fluctuations by crosscorrelations and by using three or more oscillators  
Proc. 35th AFCS 1981

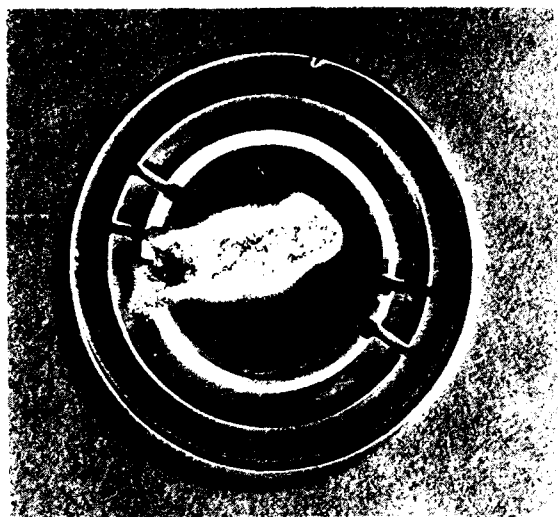


Figure 1 : Vibrating part of QAS or BVA resonators



Figure 2a : QAS resonator

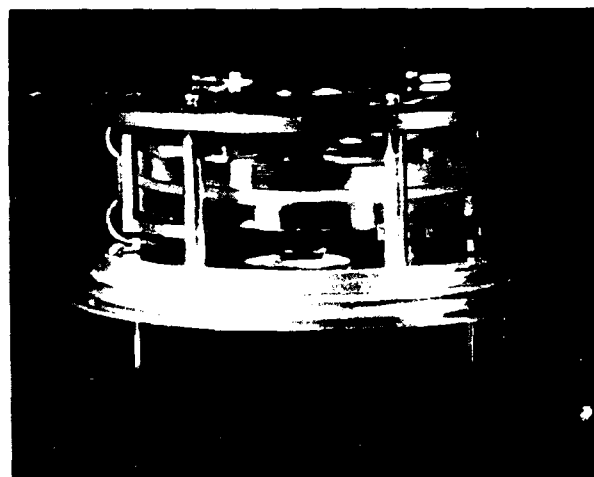
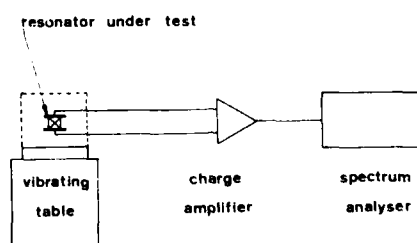


Figure 2b : BVA resonator

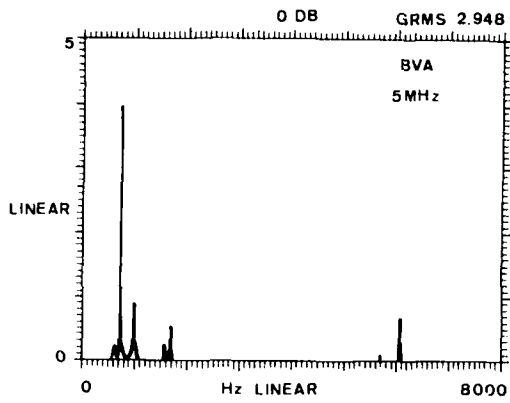


Figure 3 : I 3516 and I 2111 cans for  
 BVA and QAS resonators



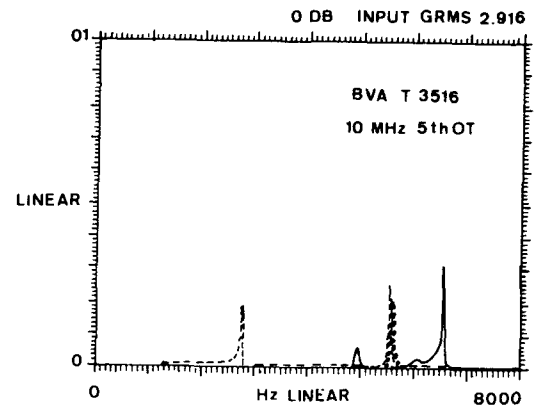
RESONANT FREQUENCY OF MONTING STRUCTURE TEST EQUIPMENT

Figure 4



FREQ. SUSPENSION QUARTZ BVA

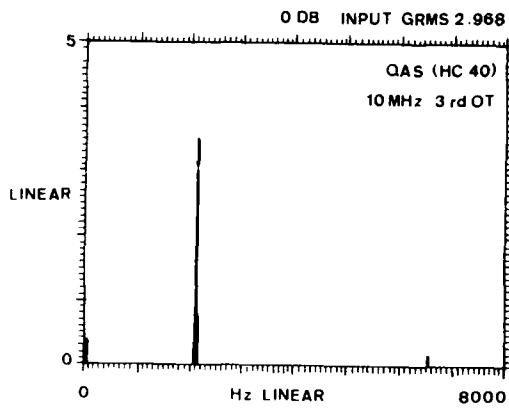
Figure 5



FREQ. SUSPENSION QUARTZ

Figure 6

— x axis  
... y axis  
--- z axis



FREQ. SUSPENSION QUARTZ QAS 2111

Figure 7

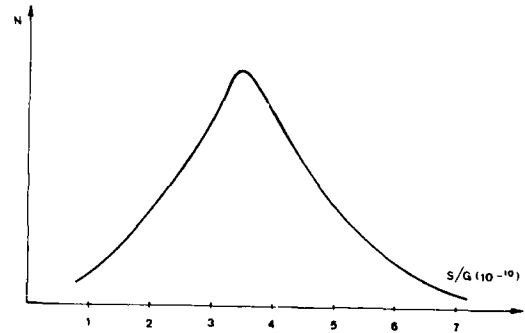
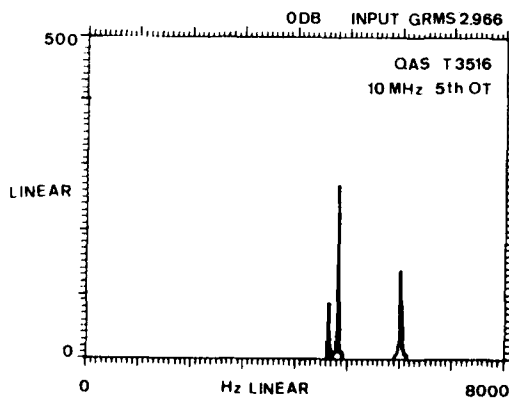


Figure 9a : Previous QAS design  
G sensitivity distribution



FREQ. SUSPENSION QUARTZ

Figure 8

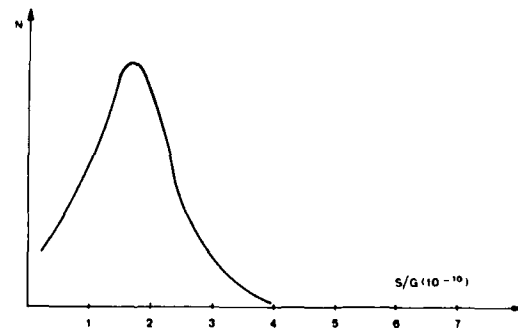
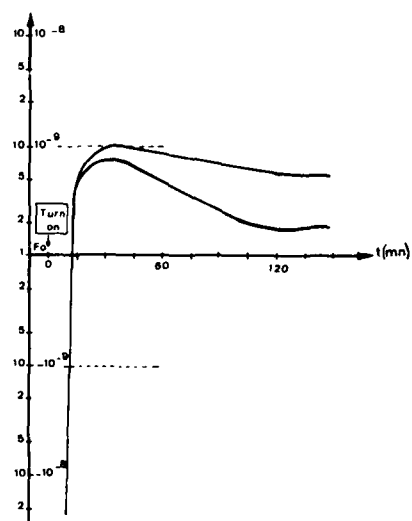
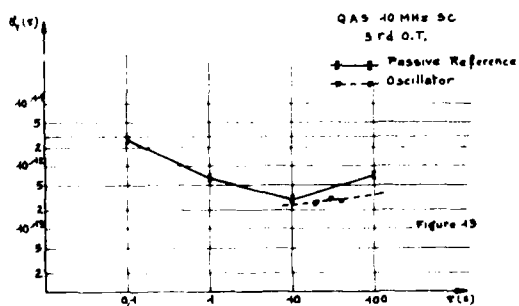
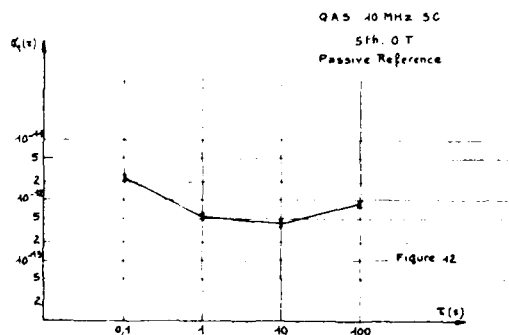
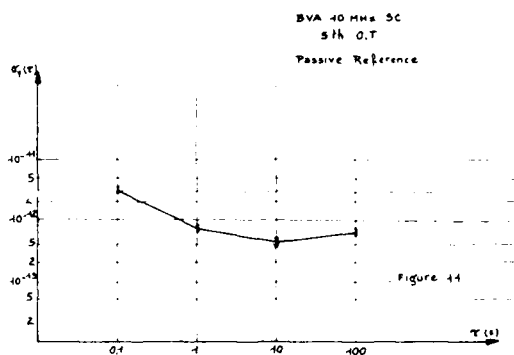
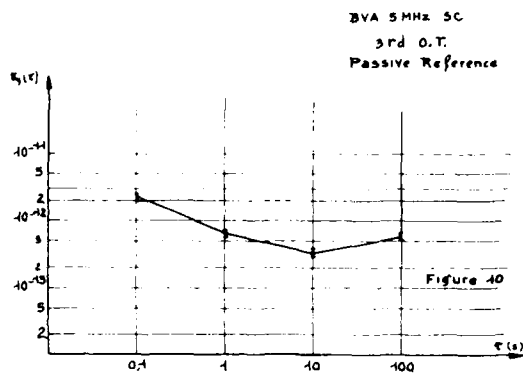
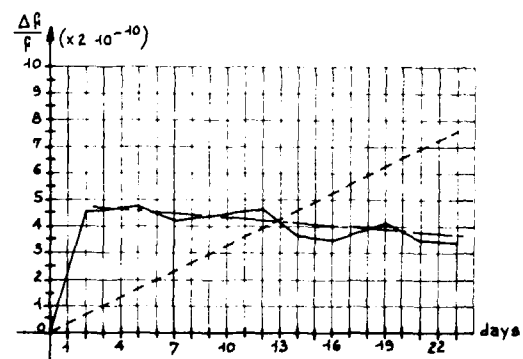


Figure 9b : Actual QAS design G sensitivity  
distribution



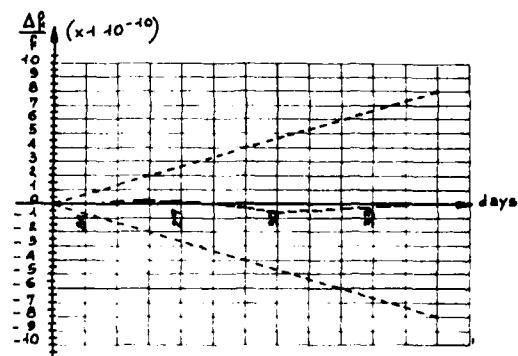
RETRACE OF QAS 10 MHz 3rd O.T. OSCILLATOR

Figure 14



BVA initial ageing

Figure 15



BVA ageing

Figure 16

# FREQUENCY STABILITY OF QUARTZ CRYSTAL AT VERY LOW TEMPERATURES : PRELIMINARY RESULTS

G. Robichon\*, J. Gros Lambert, J.J. Gagnepain

Laboratoire de Physique et Métrologie des Oscillateurs du C.N.R.S.  
associé à l'Université de Franche-Comté - Besançon  
32 avenue de l'Observatoire - 25000 Besançon - France

## Summary

Improvements of both short and long term stabilities of quartz crystal resonators can be obtained by cooling to very low temperatures. According to larger Q-factors and to the reduction of the noise levels of the crystal and the electronics, the short term stability must be increased. The diffusion mechanisms of the impurities being frozen, lower ageing is expected. Measurements are performed with the only crystal resonator in liquid helium ; the electronics composed of a frequency source and a phase lock loop is at room temperature. The static and dynamic temperature coefficients are first evaluated. As expected from the theory the a coefficient is found to be much smaller than at room temperature. A medium quality AT-cut, 5 MHz, 5th overtone crystal is studied. Over 10 sec its stability at 1.5 K is  $2 \times 10^{-13}$ , and the ageing over a day is of the order of  $10^{-11}$ . These results correspond to an improvement by a factor 10 of the stabilities of this crystal from room temperature to low temperature.

## Introduction

The frequency stability of quartz crystal oscillators is limited at short term by the noise of the electronics of the sustaining and the output amplifiers and the noise of the crystal itself. In addition perturbations can be due to the influence of temperature fluctuations and drift. At long term, the frequency ageing comes from impurity diffusion, stress relaxation, etc. The improvements, which have been achieved during the past years, are due to a better quality of the resonators, the utilization of electronic components with lower noise, the choice of crystals with better purity. More precise temperature compensation was made by using new crystal cuts, and/or more stable temperature controlled ovens. Such improvements are obtained step by step and take a long while.

One possibility of reducing the instabilities consists in cooling the quartz resonator, and eventually the electronics, down to liquid helium temperature. At very low temperature higher Q-factors are obtained according to the decrease of the acoustic attenuation. The white noise is reduced as the square root of temperature (Nyquist's law). The  $1/f$  frequency fluctuations of the resonator are also reduced following the increase in Q-factor. As it becomes more difficult for impurities to escape from their potential wells and therefore to diffuse, better long term stability can be expected. Finally the temperature of the liquid helium bath can be controlled with accuracy and this enables to minimize the influence of thermal perturbation. All these parameters change in such a way that improvement of the frequency stabilities seems feasible.

The application to frequency standards would be of course limited to a laboratory environment on account of the heavy cryogenic technology. However these experiments lead to some evaluation of the ultimate stability of quartz crystal and understanding of its fundamental properties.

## Quartz crystal properties at low temperatures

### Acoustic attenuation and Q-factor

The acoustic attenuation is mainly due to phonon interactions which involve one sound wave phonon and two thermal phonons in three-phonon processes<sup>1</sup>. The modelization of the processes can be made in the approximations of high or low temperatures.

At high temperature the Q-factor (or the acoustic attenuation  $\alpha$ , both being related by  $2Qs_0\alpha = Q_0$ ) is given by

$$\frac{1}{Q} = \frac{CT\langle\gamma^2\rangle}{E_0} \frac{Q_0\tau}{1+Q_0^2\tau^2} \quad (1)$$

where  $T$  is the absolute temperature,  $C$  the specific heat,  $\gamma$  an effective Grüneisen constant,  $E_0$  the low frequency Young modulus,  $Q_0$  the sound wave angular frequency and  $\tau$  the mean thermal phonon relaxation time.  $s_0$  is the mean sound wave velocity.

At low temperature it can be considered that the thermal phonons always are in thermal equilibrium. A simpler calculation leads to

$$\frac{1}{Q} \propto \langle\gamma^2\rangle h Q_0 \left(\frac{k_B T}{h}\right)^4 \frac{1}{Q_0\tau} \quad (2)$$

which indicates a  $T^4$  dependance law versus temperature ( $h$  and  $k_B$  are the Planck's and Boltzmann's constants). The junction between the two models is not easy to do. Experimentally it corresponds to a peak of maximum interaction for  $T = 20K$ , as shown in Fig. 1. Eventually a large absorption can appear around  $T = 50K$ . It corresponds to the relaxation of  $Na^+$  interstitial impurities. This curve shows that to obtain a net gain in Q-factor it is necessary to cool the crystal below 10K. In principle lower the temperature higher the Q-factor. Therefore the crystals were operated between 1K and 1.5K. These temperatures correspond to superfluid helium, which has the advantage to be more stable.

On table I are given the values of the unloaded Q-factor of different resonators at 1.5K or 4.2K. The dispersion of these values can be interpreted by the presence of a floor due to the influence of the mounting or of the wave scattering by point defects.

\* G. Robichon is from the Compagnie d'Electronique et Piézoélectricité (CEPE), Argenteuil, France, and presently detached at LPMO where the study was performed.

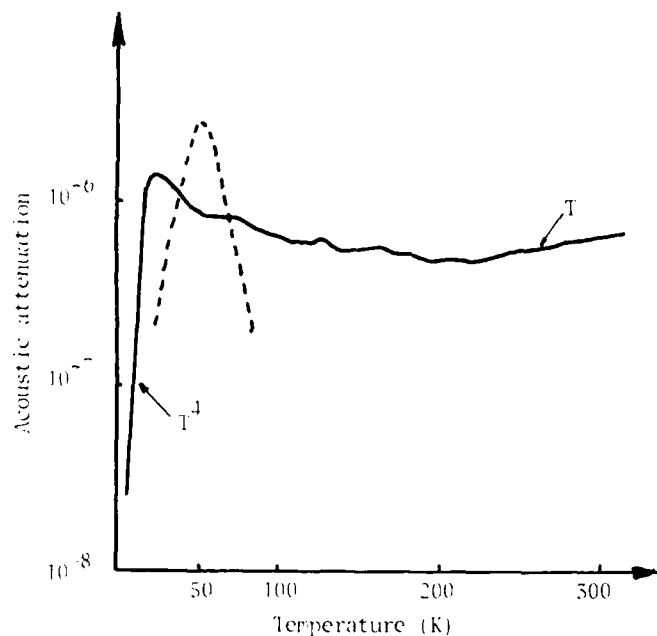


Fig. 1 : Acoustic attenuation versus temperature of a 5 MHz 5th overtone AT cut crystal (The dotted peak corresponds eventually to  $\text{Na}^+$  impurity relaxation)

Resonators	$Q_0 \times 10^6$ at 4.2K	$Q_0 \times 10^6$ at 1.5K
AT # F6	29	
AT E1	34	
AT T 1102	12	
AT BC 81	28	
AT G4	91	150
AT B4	18	
AT BD 87	25	
AT 11	5	9
FC 246	6	
FC 247	4.4	4.4
SC 206	11	

Table I

Q-factors at low temperature of different 5 MHz crystals

#### Thermal behavior

The static frequency-temperature characteristics are represented in Fig. 2 for AT and FC cut crystals. As expected from the theory the temperature coefficient of the frequency of the AT crystal decreases and is of the order of a few  $10^{-9}/\text{K}$  near  $T = 1.5\text{K}$ . More surprising is the behavior of the FC crystal, which exhibits a turn-over point. This is not interpreted yet, but remembers some similar behaviors observed in amorphous solids with the relaxation of two-level systems.

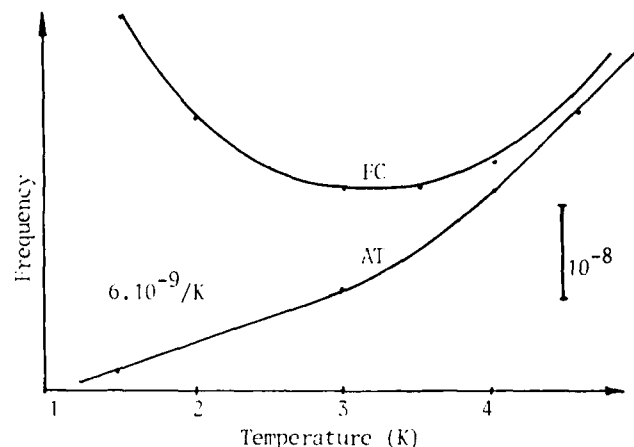


Fig. 2 : Static frequency-temperature characteristics

The total frequency excursion on the all temperature scale is important. Measurements performed on a large number of units gave in average :  $F(300\text{K}) - F(4.2\text{K}) = 5\ 700\ \text{Hz}$ .

The dynamic temperature coefficient was evaluated at 1.5K by modulating at .1 Hz the temperature of the oven within the helium bath and recording the corresponding frequency change. The a coefficient can be deduced from the phase difference between frequency and temperature. As shown in Fig. 3 this phase difference is small. Thus a cannot be measured precisely, but its upper limit can be evaluated. This yields a  $< 6 \times 10^{-10}\ \text{s/K}$ .

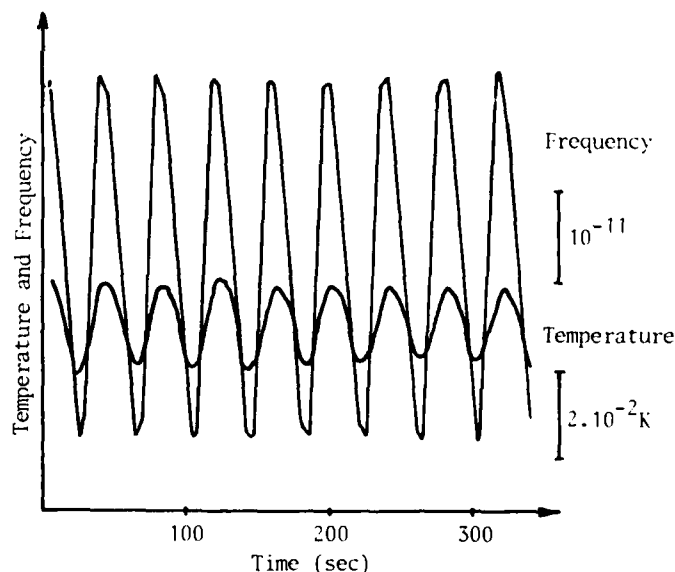


Fig. 3 : Frequency variation induced by a temperature modulation

The  $\tilde{a}$  coefficient is inversely proportional to the thermal diffusivity constant  $\kappa^2$ , as

$$\kappa = \frac{\lambda}{\rho C} \quad (3)$$

$\tilde{a}$  depends on the thermal conductivity  $\lambda$  and the specific heat  $C$  ( $\rho$  is the specific mass which slightly varies with temperature). Their dependance versus temperature is given in Fig. 4.  $\lambda$  is almost the same at 1.5K and at room temperature, even if it experiences a

strong variation around 10K. But the specific heat  $C$  tremendously decreases and at low temperature can be several orders of magnitude lower ; this explains the very small value of  $\alpha$  which has been observed.

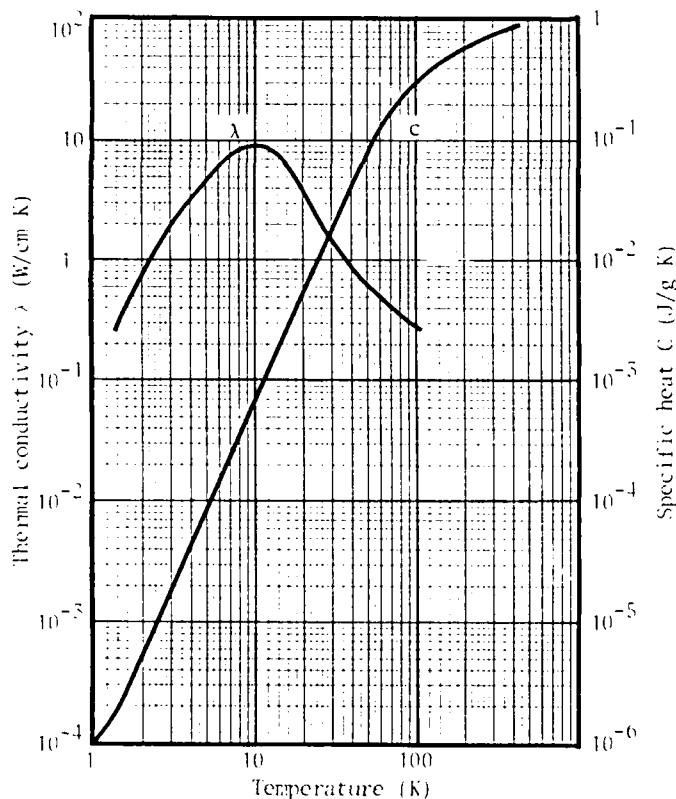


Fig. 4 : Thermal conductivity and specific heat of quartz as a function of temperature

#### Noise

Thermal white noise is represented by Nyquist's law, i.e.  $\overline{e^2} = 4k_B T R \Delta f$  where  $R$  is the equivalent noise resistance and  $\Delta f$  the bandwidth of the system. The corresponding phase and frequency fluctuation will be

proportional to  $[\overline{e^2}]^{1/2}$  therefore to  $T^{1/2}$ . This will correspond at low temperature to a reduction by approximately one order of magnitude.

$1/f$  noise is present in quartz crystals, and it has been shown that its level is related to the unloaded Q-factor of the resonator. The power spectral density of the  $1/f$  frequency fluctuations  $S_y(f)$  of an AT-cut crystal was measured at room temperature and then at 4.2K and at 1K<sup>3</sup>. The results (Table II) indicate a large decrease of the noise level with temperature, which follows the increase of the Q-factor.

Temperature	300 K	4.2 K	1 K
$Q_0$	$2.4 \cdot 10^6$	$5 \cdot 10^6$	$9 \cdot 10^6$
$S_y(1 \text{ Hz})$	$1.6 \cdot 10^{-24}$	$1.4 \cdot 10^{-25}$	$3.5 \cdot 10^{-26}$

Table II

Power spectral density of the  $1/f$  frequency fluctuations of a 5 MHz quartz crystal versus temperature

#### Low temperature dual crystal passive system

The concept of dual crystal passive system<sup>4</sup> seemed to be well adapted for operating a crystal in liquid helium<sup>5</sup>. The schematic diagram of the system, which has been used, is shown in Fig. 5. It consists in locking a room temperature crystal oscillator to the passive resonator, which is at low temperature. The driving signal is phase modulated and interrogates the crystal in reflection by means of a directional coupler. Therefore the link between the passive resonator in the dewar and the electronics outside the dewar is made by a single coaxial cable which carries the incident or reference signal and the reflected one. This allows one a maximum of cable-effect compensation and is compatible with the cable length (1 m to 1.5 m) due to the size of the cryogenic equipment. After interrogation and detection by a lock-in amplifier the signal

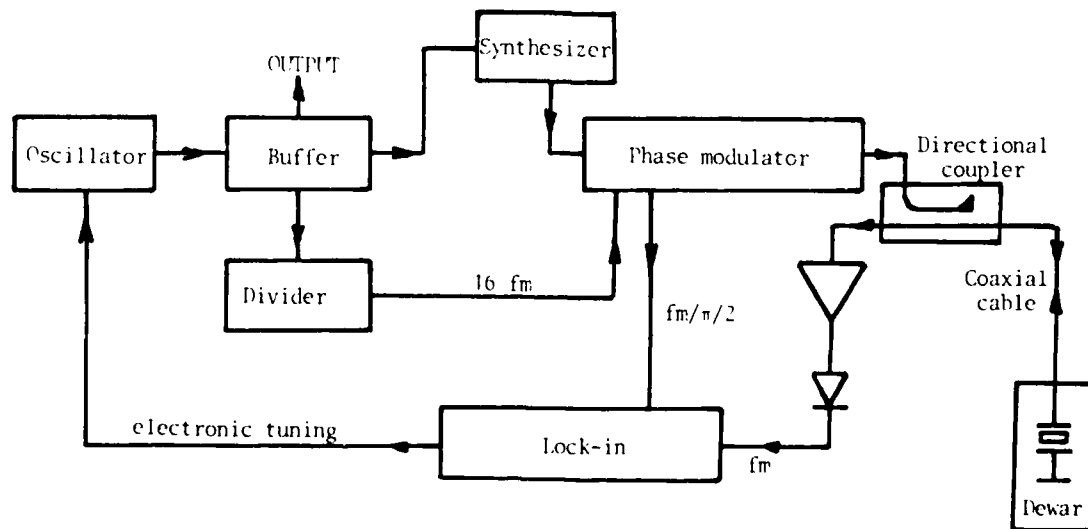


Fig. 5 : Dual crystal passive system



is applied to the frequency tuning input of the oscillator. This system is equivalent to a phase-lock-loop, which acts as a frequency discriminator. The main problem is in the adaptation of the coaxial cable impedance to the crystal impedance ; at low temperature the motional resistance of the resonator can become as small as a few ohms, therefore a transformer is necessary to realize this impedance matching and this has to be adapted to each individual resonator, because of the dispersion of the values of the motional resistances. In case of mismatching and a too important standing wave ratio the response of the system, i.e. the control voltage as a function of the driving source frequency is perturbed by spurious effects. The response is shown in Fig. 6. The slope of this characteristic is proportional to  $Q/P$ , where  $Q$  is the loaded  $Q$ -factor of the resonator and  $P$  the power it receives. Increasing the power will improve the accuracy of the loop, but this has a limitation due to the nonlinearities of the crystal and particularly to the amplitude-frequency effect. On account of the high value of  $Q$  the applied power cannot exceed a few  $\mu W$ .

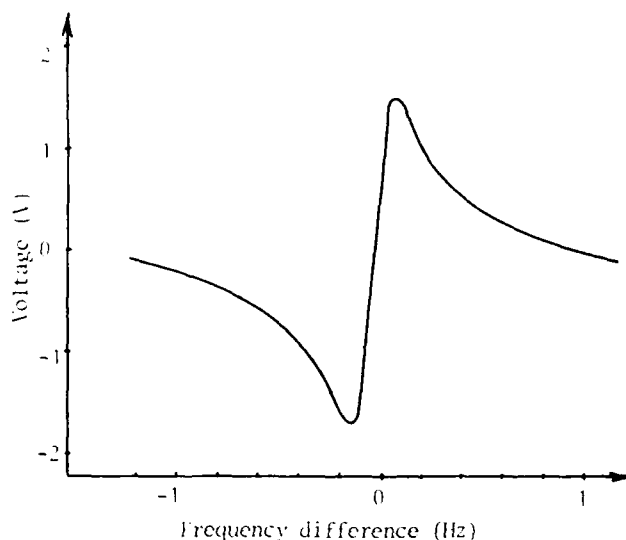


Fig. 6 : Open Phase Lock Loop Response

#### Experimental results

Before proceeding to frequency measurements the stability of the temperature of the crystal was tested. This was achieved by using an SC-cut crystal, the temperature fluctuations being measured by means of the B-mode. The resonator during the operations was placed in a copper can, under vacuum and in contact with a copper cylinder, inside the can, regulated in temperature. The temperature regulation is made with an AC wheatstone bridge, at 1 kHz, using a germanium resistor as temperature sensor and a lock-in amplifier for detection. The heater was made with a heating resistor in contact with the copper cylinder. The temperature stability of the crystal is given, in Fig. 7, for operating temperatures at 4.2K and 1.5K. The stability at 1.5K is equal to  $2 \times 10^{-5} K$  over 10 sec. Considering the frequency-temperature characteristic of Fig. 2, which presents a slope of  $6 \times 10^{-7} / K$  at that temperature, the corresponding frequency fluctuations would be of the order of  $1 \times 10^{-13}$ . At this level, temperature fluctuations still can be a limitation in the performances.

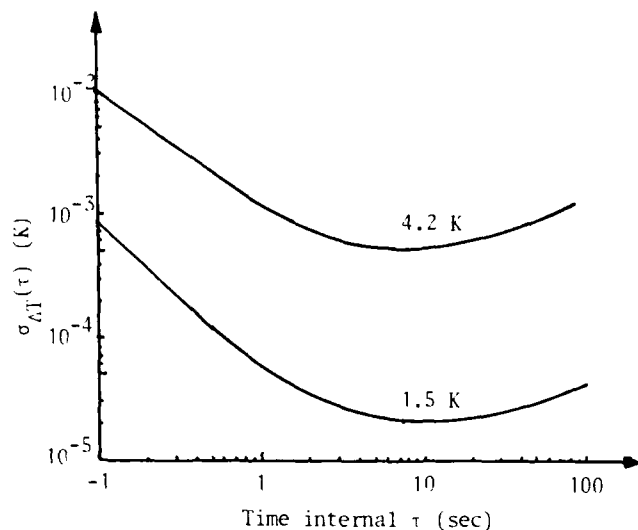


Fig. 7 : Temperature stability at 1.5K and 4.2K

The frequency stability was measured on a 5 MHz 5th overtone, AT-cut, resonator of regular type. This resonator can be considered to be of medium quality since at room temperature its stability (over a few sec) is of the order of  $10^{-12}$ . In Fig. 8 comparison is made with the stability obtained when operating the same crystal at low temperature. An improvement by at least one order of magnitude is obtained. These residual fluctuations come rather from the dual crystal passive system than from the crystal itself ; the driving power being low on account of the strong nonlinearities of the resonator. Therefore a compromise must be chosen.

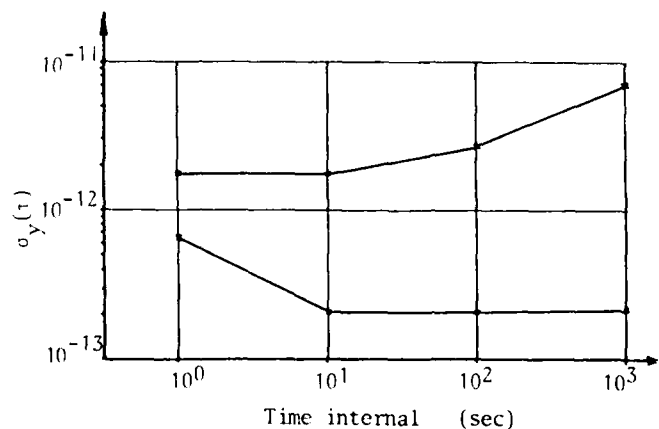


Fig. 8 : Short term stability of a 5 Miz, 5th overtone, AT-cut quartz resonator at room temperature and at 1.5 K

On Fig. 9 is given the frequency ageing of the same resonator again at room temperature and at 1.5K. It is important to notice that the frequency ageing at low temperature was recorded immediately after the crystal was cooled down and the power turned on. No ageing appears, at the opposite of what is always observed at room temperature, and the residual ageing which is lower than  $10^{-11}/\text{day}$  is rather due to long term instabilities of the phase lock loop which was not controlled in temperature.

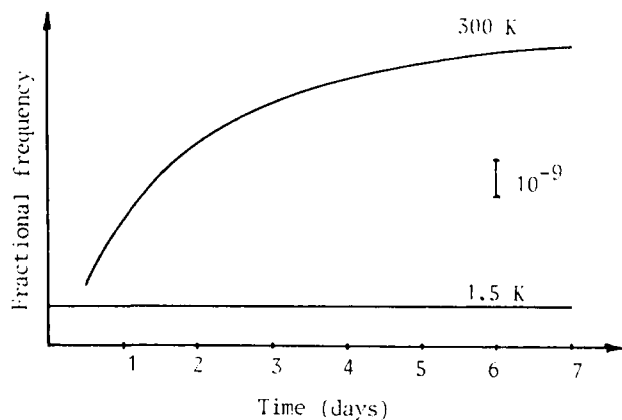


Fig. 9 : Frequency ageing at 300 K and at 1.5 K

### Conclusion

These results show that operating a crystal at very low temperature can improve its stabilities by at least one order of magnitude. The dual crystal passive system was the easiest way to perform these preliminary experiments. However some limitations come from the signal over-noise ratio and from the crystal nonlinearities. It would be most interesting now to repeat this measurement by using a conventional oscillator and cooling at the same time crystal and electronics. The actual results let expect for the future performances in the  $10^{-14}$  range at short term and the  $10^{-12}$ /day range at long term.

### Acknowledgement

This work was supported by the Air Force Office of Scientific Research under grant AFOSR-82-0318.

### References

- (1) H.J. Maris, Interaction of sound waves with thermal phonons in dielectric crystals. Physical Acoustics, vol. VIII, Academic Press (1971).
- (2) J.P. Valentin, G. Théobald, J.J. Gagnepain, Frequency shifts arising from in-plane temperature gradient distribution in quartz resonators. This symposium.
- (3) J.J. Gagnepain, J. Uebersfeld, G. Goujon, P. Handel Relation between  $1/f$  noise and Q-factor in quartz resonators at room and low temperatures. 35th AFCS (1981).
- (4) S.R. Stein, C.M. Manney, F.L. Walls, J.E. Gray, R. Besson, A systems approach to high performance oscillators. 32nd AFCS (1978).
- (5) B. Komiyama, Quartz crystal oscillator at cryogenic temperature. 35th AFCS (1981).

## LATERAL-FIELD EXCITATION OF BERLINITE

Arthur Ballato,+ Elizabeth R. Hatch,\*\* Muhammad Mizan,+  
Bruce H.T. Chai,\* Richard S. Tilton,+ & Theodore J. Lukaszek+

+U.S. Army Electronics Technology & Devices Laboratory, Fort Monmouth, New Jersey 07703

\*Georgia Institute of Technology, Atlanta, Georgia 30332

°Allied Corporation, Corporate Headquarters, Morristown, New Jersey 07960

## ABSTRACT

Simple thickness modes in crystal plates are considered. The formalism for obtaining the piezoelectric coupling coefficients for thickness- and lateral-directed exciting electric fields is applied to berlinite ( $\text{AlPO}_4$ ). The laterally excited plate resonator is represented by transmission line equivalent networks. Thickness excitation is used to explore experimentally the coupling strength with harmonic. Lateral excitation experiments are used to confirm the coupling versus azimuth dependence of the modes. Calculations of temperature coefficient, thickness and lateral coupling coefficients are extended to doubly rotated orientations, and network applications to SAW excitation are given.

Key Words: aluminum phosphate, berlinite, crystals, piezoelectricity, plate vibrations, equivalent networks, acoustic loss, bulk acoustic waves, surface acoustic waves, temperature coefficient.

## INTRODUCTION

Excitation of piezoelectric plates in thickness modes is usually accomplished by directing the driving electric field in the plate thickness direction; this is known as thickness excitation (TE). Much less common is excitation by a field in the plane of the plate; this has received some attention over the years /1-34/, and is referred to as lateral excitation (LE). The older phrase, "parallel-field excitation" is ambiguous, and is now deprecated. Lateral excitation has a number of potential advantages over TE for certain applications. We call attention to some of these in our use of LE in conjunction with calculations of, and experiments on, plates of alpha aluminum phosphate (berlinite).

Berlinite is a more highly piezoelectric analog of quartz, possessing numerous surface and bulk wave cuts with quite good frequency - temperature behavior. Although the substance has been known for more than thirty years, it is only in the past eight years that serious interest has focused on it, particularly for SAW applications /32-59/. Work on this promising crystal has been hindered until recently by lack of adequate specimens for research purposes and by uncertainty regarding the ultimate availability of material of quality and size sufficient for commercial application at reasonable cost. These crystal synthesis obstacles have now largely been surmounted, and assessment of berlinite's technological viability can now proceed on the straightforward basis of its material properties.

## LATERAL EXCITATION

Lateral excitation was applied to quartz plates by Atanasoff and Hart /1/ to measure the elastic constants; their work was reviewed by Cady /2/. Bechmann /3,4/ did some early theoretical

work; this was followed by experimental work by Bechmann /6,7,9,10/, Ianouchevsky /8,11-13/, and Warner /14/. One of Bechmann's 1 MHz units is shown in Fig. 1. It is a standard biconvex Bliley design with the new LE electrode pattern. Figure 2 shows a design of Ianouchevsky at 2 MHz with the top portion of the glass envelope removed. The combination of lens shape and special mounting jaws yielded an exceedingly high Q. A patent, awarded to Bechmann /15/, is seen in Fig. 3. This shows some possible electroding arrangements for LE, including removal of some of the central electrode material from the plate to reduce its damping and aging effects on the resonator active region. Composite excitation, a mixture of TE and LE, is also featured. In this patent, crystal contour is not mentioned, and the drawings show flat plates. If the plates are not contoured, as shown in Figs. 1 and 2, the electrode configuration tends to "untrap" the vibratory energy and produce degraded performance. Methods of obtaining "energy trapping" and efficient use of the applied lateral field by the use of special geometries has recently been proposed /71/.

Some of the reasons advanced for the study and use of LE are:

- lessened thermal transients /14/.
- reduced aging, since the electrode is absent from the region of greatest motion.
- higher Q values, since electrode damping is reduced.
- ability to eliminate undesired modes, e.g., the b mode in SC-cut quartz /30/.
- increased stability at a given harmonic, since motional inductances are larger.
- means of experimentally driving certain plate modes for measurement.
- availability of certain filter configurations /29/.
- similarity to the predominant excitation arising from SAW IDTs /70/.

## EQUIVALENT NETWORKS

Input immittances for TE and LE of the three thickness modes of traction-free, laterally unbounded, piezoelectric plates are given in Fig. 4. One recognizes a duality between the two canonical forms of excitation. The modes (including harmonics) are driven via the piezoelectric coupling coefficients  $k$  and  $k_s$ , the calculation of which will be outlined subsequently. Static capacitance values  $C_0$  and  $C_0$  are determined by the electrode systems:  $C_0$ , for the TE case, is usually adequately approximated by the formula for a parallel plate capacitor; the  $C_0$  value (LE) requires a more difficult calculation, and depends upon gap width and length, as well as thickness of plate, etc.

The LE admittance in Fig. 4 is exactly realized by the network of Fig. 5. The negative  $C_0$ , appearing in the TE version, is absent. Bisection of Fig. 5 yields Fig. 6. Figure 5 is redrawn in Fig. 7 for

the case of a single mode excited; the position of  $C_0$  is also reoriented to correspond to the direction of the applied field which is obtained from voltage between terminals A and B. Inductances  $L_1$  and  $L_2$  model the presence of electrode mass; they appear in the formulas to be given below for the vibrator critical frequencies for the important case of  $L_1 = L_2 = L$ . These should not be confused with motional inductance appearing in the traditional Butterworth-Van Dyke equivalent circuit consisting of  $C_0$ ,  $C_1$ ,  $L_1$ , and  $R_1$ , to which the more comprehensive transmission line networks of Figs. 5, 6, and 7 may be reduced in the immediate vicinity of resonance for materials such as quartz where the piezoelectric effect is not large. For substances where the piezo coupling is substantial, and/or where a broadband network representation is required, the transmission line network must be used. In Figs. 5, 6, and 7, the transformer turns ratios  $n$  are related to the piezo-electric coupling factors  $k$  by

$$\begin{aligned} n^2 &= \frac{C_0}{k^2} \frac{A}{2h} = \frac{C_0}{k^2} f_0^2 (4M) \\ &= \frac{C_0}{k^2} f_0 (2Z), \end{aligned} \quad (1)$$

where  $C_0$  is the lateral static capacitance;  $\bar{c}$  is the effective elastic stiffness;  $A$  is a patch of area, normal to the thickness direction, represented by the transmission lines;  $M$  is the total mass of that portion of the plate ( $\rho A 2h$ );  $Z$  is the acoustic impedance of the transmission line ( $A \rho v$ );  $\rho$  is the mass density;  $v$  is the acoustic velocity ( $v^2 = \bar{c}/\rho$ );  $2h$  is the plate thickness;  $f_0$  is the nominal plate fundamental frequency for that mode ( $v/4h$ );  $\omega$  is the acoustic wavenumber ( $\omega/v$ ).

Electrode mass loading is represented by the normalized quantity

$$\mu = m/(\rho h), \quad (2)$$

where  $m$  is the mass-loading per unit area. The inductance  $L$  in the equivalent network that represents mass loading is equal to

$$L = \mu A = \mu \rho h A. \quad (3)$$

Frequency variables, used below, are defined as follows:

$$X = \omega h, \text{ and} \quad (4)$$

$$\Omega = 2X/\pi = f/f_0. \quad (5)$$

Input reactances, obtained from Fig. 4, are plotted for LE and TE in Fig. 8. The differences between the excitation types are most apparent in the vicinity of the resonances. For TE, the reactance poles are harmonic, and the zeros are anharmonic; for LE the situation is reversed. The LE critical frequency equations are found as described in Figs. 9 and 10; transverse-resonance is a procedure very like the negative impedance concept /73/. When  $\mu = 0$ , the resonance frequencies of the various harmonics are integer multiples. For this case, the graphical construction for obtaining the anti-resonances is given in Fig. 11. Here it is seen that the pole-zero separation diminishes rapidly with harmonic. Figure 12 plots the frequency displacement  $\delta_A$  versus  $k$  for various harmonic numbers  $M = 1, 3, 5, \dots$ . The displacement is defined as

$$\delta_A^{(M)} = M - \Omega_A^{(M)} = M - f_A^{(M)} / f_0; \quad (6)$$

from the figure the pole-zero separations may be found for any value of  $k$  and  $M$ .

## COUPLING FACTORS

We consider plane wave propagation to take place along the thickness ( $X_2$ ) axis of an arbitrarily oriented quartz plate, and the impressed electric field to be along the  $X_1$  axis. The plate orientation /28/ is specified with respect to the crystallographic axes by the rotations  $(YXW\ell)\phi/\theta$ , and the  $X_1$  axis of the electric field is further specified by a ccw rotation about the plate thickness ( $X_2$ ) by angle  $\psi$ , as seen in Fig. 13.

The formalism for determining the coupling factors  $k_m$  and  $\underline{k}_m$ , driving mode  $m$  is given in Figure 14 in schematic form. The quantities  $c$ ,  $e$ , and  $\epsilon$  are the material elastic stiffnesses, piezo-electric constants, and dielectric permittivities, respectively. These calculations will be carried out for berlinite in the sequel, as they have been for quartz /63-66/.

## BERLINITE

Alpha aluminum phosphate,  $AlPO_4$ , also known as berlinite, is of crystal class 32, and is an isomorph of quartz. Quartz, shown in Fig. 15 in ideal form, has the enantiomorphic molecular forms given in Figs. 16a and b. The transition to berlinite may be thought of by considering two molecules of quartz

$(SiO_2)_2 = Si_2O_4$ , and then replacing the

two silicon atoms (Column IV of the Periodic Table): one by aluminum (Column III), and one by phosphorous (Column V). The result is berlinite, having twice the unit cell of quartz. The chemical bonding in quartz is nearly all covalent; with berlinite, the bonding has a greater ionic component. The piezoelectric coupling is greater than in quartz. The above-mentioned replacement of  $Si_2$  by  $AlP$  is also shown in Fig. 16a,b.

Growth of cultured quartz has been commercially viable for more than thirty years; Fig. 17 contains a number of samples. Berlinite presents a number of challenges to growth, one of which being its retrograde solubility. However, recent advances in its growth /72/ have permitted this material to be synthesized in sizes that are suitable for commerce. Figure 18 gives representative samples of early berlinite growth, along with an early piece of cultured quartz. It also shows some plate specimens used for LE. Figure 19 shows more recent bars of berlinite grown by Allied Corporation. The sample plates were fashioned from bars of these types whose lengths well exceed 100 mm, yielding plates upwards of 25 mm on a side. The size and quality of the growth specimens ought to be considered with the corresponding quartz growth history in mind. The growth of berlinite has, by comparison, come very far in a very short time.

Figure 20 compares frequency constants ( $v/2$ ) for the TE mode of rotated-Y-cuts of quartz and berlinite as function of angle theta. Bechmann's constants /62/ for quartz and the berlinite constants of Chang and Barsch /34/ have been used. It is seen that  $AlPO_4$  is slightly slower than quartz, but that the curve shapes are very similar. The angles marked as AT' and BT' are the points of zero first-order temperature coefficient in analogy with the quartz case. For the values of /34/ these occur at +28.6° and -37.3°; using the newer values of Bailey, et al. /59/, the angles are +31° and -46°.

An alternative scheme to that in Fig. 14 for obtaining the excitation coefficients for TE and LE of the thickness modes of plates was given by Bechmann /3,4/. One can use this procedure to obtain, in a rapid, though approximate manner, information about which modes are driven for plates of various generic orientations and electric field directions. Tables 1 and 2 list, respectively, the excitation coefficients for TE and LE of crystals in class 32, i.e., berlinite and quartz. The  $m_j$  and  $f_j$  are direction cosines of the plate and field, respectively, and the  $\Xi_j$  are the coefficients driving the modes /23/.

Table 3 is a brief comparison of piezocoupling and temperature coefficient for five materials; it is seen that berlinite falls in the gap between lithium tantalate and quartz, and has a zero temperature coefficient as do the other two. It is unknown at present, and of considerable interest, whether or not  $AlPO_4$  possesses a locus of stress compensation as does quartz; nor is it known the sizes of the temperature coefficients of the coupling factors. These temperature coefficients can drastically affect the temperature behavior of a resonator when operated in the region between resonance and antiresonance, as is the case with certain cuts of lithium tantalate /36/.

#### PLATE SAMPLES

Plates used for these investigations were grown and prepared by Allied Corporation, and are of five orientations: X, Y, AND Z cuts, and  $(YX\ell) \pm 45^\circ$  plates. All are roughly rectangular in outline and between 15 and 20 mm on a side; final thicknesses are approximately 0.560 to 0.570 mm. These had been first lapped with 3 micrometer alumina powder from 0.69 to 0.57 mm, and then polished with Nalco 1060 amorphous silica solution. Parallelism of the major surfaces is about one wavelength. All crystals are left-handed; they were measured optically, with confirmation from squeeze tests and surface morphology.

#### MEASUREMENT EQUIPMENT

The measurements reported here are of two kinds: (1) LE measurements of the three thickness modes a, b, and c, versus azimuth angle  $\psi$ , for the purpose of verifying the calculated azimuthal dependence of  $k_m$  and the relative mode strengths and maxima with respect to the crystallographic axes; (2) TE measurements on various harmonics, for the purpose of exploring the coupling factor dependence on harmonic. The apparatus is shown in Figure 21. It consists of a Generator/Sweeper HP 8601A, Network Analyzer HP 8407A, Phase-Magnitude Display HP 8412A, Frequency Counter HP 5245L, Wayne-Kerr B801 Bridge, Anzac H-1 hybrid, variable air capacitor GR 874-VC, and special air gap fixtures for TE excitation /74/, and LE excitation (Fig. 24). With these items swept-frequency /67-69/, balanced and unbalanced bridge /68,69/ measurements could be made.

#### TE HARMONICS

Table 4 lists measured and calculated approximate frequencies at maximum admittance; in some cases the admittance-frequency curve had two adjacent peaks leading to a loss of accuracy. The plate in this instance is a  $45^\circ$ -rotated-Y-cut on the AT' side. Similar results were obtained with other samples. Harmonics from 1 to 41 were observed, along with resonance amplitude in dB. Figure 22 shows four of the spectrographs for harmonics  $M = 1, 3, 5$ , and 21. The unusual feature of the data for

measurements on berlinite as function of harmonic is that the mode strength decreases much less rapidly than is to be expected, even taking into account the mode shape for overtones of finite plates. Thus the effective Q value at a given harmonic is better than one would infer from measurements made at the fundamental. This may be related to a limiting Q value occurring at low frequencies rather than  $(Q \cdot f)$  being a constant for all frequencies. For quartz,  $(Q \cdot f)$  equals a constant, at room temperature, excluding losses other than due to bulk viscosity, had been inferred from measurements on BAW plates /60,61a/. As seen in Fig. 23 /61b/, a more probable internal friction curve for quartz calls for Q to approach a constant at low frequencies. The same may be true for  $AlPO_4$ , and this may explain both the results in Table 4 and the generally observed fact that, on a prorated basis, berlinite appears to have better loss behavior in higher frequency SAW devices than in lower frequency BAW configurations.

#### UNROTATED CUTS

Figure 24 is a picture of the LE apparatus. A crystal sample is placed on the plastic turntable that is mounted on the 12:1 reduction gearbox housing. Thin paper shims support the specimen on the turntable at its edge regions. Translation tables are used to position the slightly canted razor blades over the sample. The height of the blade edges from the crystal are adjustable, as is the blade gap. In general, the crystal-to-blade height was kept as small as possible, so that the blade edges nearly touched the sample; the gap was adjusted for maximum response. This arrangement does not produce optimum excitation /71/, but is adequate for exploring the azimuthal dependence of coupling ( $k$ ).

In Fig. 25 is indicated the expected output of a hybrid bridge or Wayne-Kerr bridge with  $C_0$  balanced out; the output is proportional to  $k^2$ , and the dependence on azimuth  $\psi$  goes approximately as the cosine squared.

Computations made in this paper are from Bailey, et al., /59/, with some comparisons with the data of Chang and Barsch /34/. Table 5 lists values of frequency constant  $N_m$ , TE coupling factor  $k_m$ , and LE coupling factors  $k_m$  ( $\psi = 0^\circ$ ) and  $k_m$  ( $\psi = 90^\circ$ ) for X-, Y-, and Z-cut berlinite;  $m$  is the mode index:  $m = a, b$ , or  $c$ . It is seen that the modes not driven by TE in X and Y cuts are driven by LE, and vice versa. The Z cut can be LE-driven /2, page 442/; the b and c modes are degenerate, and the  $\psi$  angle is of no consequence. The coupling factors and associated capacitance ratios for X-cut berlinite are given in Figs 26 and 27, respectively. Figure 28 is an example of the results obtained. With the field applied on-axis, the response was maximum, as expected; as  $\psi$  was continuously varied by rotating the turntable, via the gear reduction box, the coupling strength diminished continuously, closely following the  $\cos^2 \psi$  law. The figure shows the spectrograph at  $\psi$  equals  $45^\circ$  where the strength is reduced to one-half.

Coupling factor and capacitance ratio plots are given in Figs. 29 and 30 for the Y cut, and in Fig. 31 is shown the shear mode coupling for the Z cut.

## SINGLY ROTATED CUTS

Table 6 lists  $N_m$ ,  $k_m$ , and  $\underline{k}_m$  values for three rotated-Y-cut orientations. Here, again, an X-directed field drives those modes that can't be driven by TE, and vice versa, whereas the LE field at  $\psi$  equals  $90^\circ$  drives the TE modes. Coupling values for LE are generally comparable to those for TE. Figure 32 plots the TE coupling versus  $\theta$  angle; corresponding plots for LE at  $\psi$  equals  $0^\circ$  and  $90^\circ$  are given in Figs. 33 and 34. Coupling and capacitance ratio versus azimuth are plotted in Figs. 35 and 36 for a (YXL)- $45^\circ$  plate (BT' side). The spectrographs corresponding to Fig. 28 are given in Fig. 37 for this cut. Coupling factors and capacitance ratios versus  $\psi$  for (YXL)+ $30^\circ$  and + $45^\circ$  plates are shown in Figs. 38-41.

## TEMPERATURE COEFFICIENTS

The first-order temperature coefficients (TCs) of rotated-Y-cut berlinite are graphed in Figs. 42-44 for the a, b, and c modes, respectively. The complete loci of zeros of the first-order TCs for modes b and c are shown in Fig. 45; the corresponding values according to /34/ are given in Fig. 46.

First-order TCs for doubly rotated cuts (YXwL)  $12^\circ/\theta$  are given, for modes a, b, and c, in Figs. 47-49; the corresponding values from /34/ are seen in Fig. 50, and do not show much difference.

## DOUBLY ROTATED CUTS

The TE and LE coupling factors are plotted versus  $\theta$  for doubly rotated plates having  $\phi$  equals  $12^\circ$  in Figs. 51-53. In Table 7 are listed several cuts having zero TC for mode b, including the BT' cut. Figure 54 gives the LE coupling squared values versus  $\psi$  for the BT' cut, and Fig. 55 plots the LE coupling squared values for the plate having  $\phi = 12^\circ$  and  $\theta = -29^\circ$ .

Table 8 contains values for cuts on the c mode, zero TC locus, including the AT' cut. The AT' plot is given in Fig. 56 as coupling factor squared. Figure 57 gives the same information for the cut with  $\phi = 12^\circ$  and  $\theta = +58^\circ$ .

## SAW EXCITATION

Surface acoustic wave excitation may be modeled by the network schematic shown in Fig. 58. The quasi-Rayleigh wave motion may be considered as an appropriate superposition of plane waves, driven by LE via the transmission line transformers in analogy with the figures for networks describing plate thickness modes. The "crossed-field," i.e., LE, model is the more accurate for representing SAW excitation /70/.

# REFERENCES\*

1. J.V. Atanasoff and P.J. Hart, "Dynamical Determination of the Elastic Constants and Their Temperature Coefficients for Quartz," *Phys. Rev.*, Vol. 59, January 1941, pp. 85-96.
2. W.G. Cady, *Piezoelectricity*, McGraw-Hill, New York, 1946; Dover, New York, 1964.
3. R. Bechmann, "Über Dickenschwingungen piezoelektrischer Kristallplatten," *Archiv der Elektrischen Übertragung*, Vol. 6, September 1952, pp. 361-368.
4. R. Bechmann, "Über Dickenschwingungen piezoelektrischer Kristallplatten," *Nachtrag, Archiv der Elektrischen Übertragung*, Vol. 7, July 1953, pp. 354-356.
5. R. Bechmann, "Filter crystals," *Proc. 12th AFCS*, May 1958, pp. 437-474.
6. R. Bechmann, "Improved High-Precision Quartz Oscillators Using Parallel Field Excitation," *Proc. IRE*, Vol. 48, March 1960, pp. 367-368.
7. R. Bechmann, "Parallel Field Excitation of Thickness Modes of Quartz Plates," *Proc. 14th AFCS*, May-June 1960, pp. 68-88.
8. V. Ianouchevsky, "Parallel Field Excitation," *Proc. IRE*, Vol. 48, June 1960, p. 1165.
9. R. Bechmann, "Excitation of Piezoelectric Plates by Use of a Parallel Field with Particular Reference to Thickness Modes of Quartz," *Proc. IRE*, Vol. 48, July 1960, pp. 1278-1280.
10. R. Bechmann, "Piezoelektrische Erregung von dickenschwingenden Quarzoszillatoren mittels eines Parallelfeldes," *Archiv der Elektrischen Übertragung*, Vol. 14, August 1960, pp. 361-365.
11. W. Ianouchewsky, "Quartz Étalons Lenticulaires Excités par le Champ Parallèle," *Annales Françaises de Chronométrie*, 31 ème année, 2 ème série, tome xv, 1961, pp. 41-51.
12. W. Ianouchevsky, "The Stability and Q-Factor of Quartz-Crystals Excited by the Parallel Field Technique," (*Observatoire de Paris, Paris, April 1963*), Final Report to U.S. Dept. of Army, Contract No. DA-91-591-EUC-1752, May 1961 to April 1963. Available from NTIS as document No. AD 410296.
13. W. Ianouchevsky, "High Q Crystal Units," *Proc. 17th AFCS*, May 1963, pp. 233-247.
14. A.W. Warner, "Use of Parallel-Field Excitation in the Design of Quartz Crystal Units," *Proc. 17th AFCS*, May 1963, pp. 248-266.
15. R. H. Bechmann, "Piezoelectric crystal apparatus," U.S. Patent 3,165,651, issued 12 January 1965.
16. A.D. Ballato and R. Bechmann, "Piezoelectric Crystal Element," U.S. Patent No. 3,202,846, issued 24 August 1965; U.K. Patent No. 1,028,102, issued 4 May 1966.
17. H. Schweppe, "Excitation of Two Adjacent Resonances with a Chosen Frequency Separation in a Ceramic Piezoelectric Resonator," *IEEE Trans. Sonics Ultrason.*, Vol. SU-17, January 1970, pp. 12-17.
18. T. Yamada and N. Niizeki, "Formulation of admittance for parallel field excitation of piezoelectric plates," *J. Appl. Phys.*, Vol. 41, August 1970, pp. 3604-3609.
19. T. Yamada and N. Niizeki, "A new formulation of piezoelectric plate thickness vibration," *Rev. Electrical Communication Labs., NTT*, Vol. 19, May-June 1971, pp. 705-713.
20. A. Ballato, H.L. Berton, and T. Tamir, "Transmission-Line Analogs for Stacked Crystals with Piezoelectric Excitation," Presented at 83rd meeting of the Acoustical Society of America, Buffalo, New York, 18-21 April 1972, paper NN3. Abstract: *J. Acoust. Soc. Am.*, Vol. 52, No. 1 (Part 1), July 1972, p. 178, paper NN3.
21. M. Onoe, "General equivalent circuit of a piezoelectric transducer vibrating in thickness modes," *Trans. Inst. Electronics and Comm. Engrs. Japan*, Vol. 55A, May 1972, pp. 239-244. In Japanese.
22. A. Ballato, "Transmission-Line Analogs for Stacked Piezoelectric Crystal Devices," *Proc. 26th AFCS*, June 1972, pp. 86-91.
23. A. Ballato, "Transmission-Line Analogs for Piezoelectric Layered Structures. Ph.D. Dissertation, Polytechnic Institute of Brooklyn, June 1972. University Microfilms, 313 N. First Street, Ann Arbor, MI 48106, Order No. 72-28,207; 264 pp.
24. A. Ballato, H.L. Berton, and T. Tamir, "Systematic Network Approach for Piezoelectrically Driven Crystal Plates and Stacks," Presented at 1972 IEEE Ultrasonics Symposium, Boston, Massachusetts, 4-7 October 1972, paper B-2. Abstract: *IEEE Transactions Sonics Ultrason.*, Vol. SU-20, No. 1, January 1973, p. 43, paper B-2.
25. A. Ballato, "Transmission-Line Analogs for Stacked Piezoelectric Crystal Devices," Technical Report ECOM-4041, U.S. Army Electronics Command, Fort Monmouth, NJ, October 1972, 21 pp., AD 754 545.
26. A. Ballato, "Networks for crossed-field and in-line excitation of bulk and surface acoustic waves," *Proc. Symp. Optical and Acoustical Micro-Electronics*, Polytechnic Institute of New York, April 1974, pp. 599-615.
27. A. Ballato, "Bulk and Surface Acoustic Wave Excitation and Network Representation," *Proc. 28th AFCS*, U.S. Army Electronics Command, Fort Monmouth, NJ, May 1974, pp. 270-279.

\* AFCS: Annual Frequency Control Symposium, U.S. Army Electronics R&D Command, Fort Monmouth, NJ 07703.

28. IEEE Standard on Piezoelectricity. Standard 176-1978, The Institute of Electrical and Electronics Engineers, Inc., 345 East 47th Street, New York, NY 10017.
29. T. Uno, "A LiTaO<sub>3</sub> Monolithic Crystal Filter by Parallel Field Excitation," *Trans. Inst. Electronics and Comm. Engrs. Japan*, Vol. E61, November 1978, pp. 915-916.
30. E. R. Hatch and A. Ballato, "Lateral-Field Excitation of Quartz Plates," *Proc. IEEE Ultrasonics Symposium*, October-November 1983, pp. 512-515.
31. Frequency Electronics, Incorporated, "Lateral Field, SC-Cut, Resonator Development," Contract DAAK20-83-C-0418 with ET&D Laboratory, ERADCOM, Ft. Monmouth, NJ 07703. November 1983 ff. FEI, Mitchel Field, NY 11553.
32. R. Taylor, R. Bechmann, and A. C. Lynch, "Crystals for Electrical Filters," *Research*, Vol. 2, No. 9, 1949, pp. 414-417.
33. J. M. Stanley, "Hydrothermal Synthesis of Large Aluminum Phosphate Crystals," *Ind. & Eng. Chem.*, Vol. 46, 1954, pp. 1684-1689.
34. Z.-P. Chang and G. R. Barsch, "Elastic Constants and Thermal Expansion of Berlinite," *IEEE Trans. Sonics Ultrason.*, Vol. SU-23, March 1976, pp. 127-135.
35. A. Ballato and G. J. Iafrate, "The Angular Dependence of Piezoelectric Plate Frequencies and Their Temperature Coefficients," *Proc. 30th AFCS*, June 1976, pp. 141-156.
36. A. Ballato, "Doubly Rotated Thickness Mode Plate Vibrators," in *Physical Acoustics*, Volume 13 (W. P. Mason and R. N. Thurston, eds.), Academic Press, New York, 1977, pp. 115-181.
37. W. R. McBride and M. E. Hills, "The Hydrothermal Growth of Aluminum Orthophosphate Crystals," *Fifth Intl. Conf. Cryst. Growth*, Boston, MA, July 1977, Abs. 65.
38. R.M. O'Connell and P.H. Carr, "High Piezoelectric Coupling Temperature-Compensated Cuts of Berlinite (AlPO<sub>4</sub>) for SAW Applications," *IEEE Trans. Sonics Ultrason.*, Vol. SU-24, No. 6, November 1977, pp. 376-384.
39. E.D. Kolb and R.A. Laudise, "Hydrothermal Synthesis of Aluminum Orthophosphate," *J. Cryst. Growth*, Vol. 43, 1978, pp. 313-319.
40. R.M. O'Connell and P.H. Carr, "Progress in Closing the Lithium Niobate - ST Cut Quartz Piezoelectric Coupling Gap," *Proc. 32nd AFCS*, May-June 1978, pp. 189-195.
41. D.G. Morency, W. Soluch, J.F. Vetelino, S.D. Mittleman, D. Harmon, S. Surek, and J.C. Field, "Experimental Measurement of the SAW Properties of Berlinite," *Proc. 32nd AFCS*, May-June 1978, pp. 196-201.
42. D.G. Morency, W. Soluch, J.F. Vetelino, S.D. Mittleman, D. Harmon, S. Surek, and J.C. Field, "Experimental Measurement of the SAW Properties of Berlinite," *Appl. Phys. Lett.*, Vol. 33, No. 2, 15 July 1978, pp. 117-119.
43. D.F. Croxall, I.R.A. Christie, B.J. Isherwood, A.G. Todd, and J. Birch, "Growth and Assessment of Berlinite Single Crystals," *Second Eur. Conf. Cryst. Growth*, Lancaster, U.K., 1979.
44. L.E. Halliburton, L.A. Kappers, A.F. Armington, and J. Larkin, "Radiation Effects in Berlinite," *Proc. 33rd AFCS*, May-June 1979, pp. 62-69.
45. J. D taint, M. Feldmann, J. Henaff, H. Poignant, and Y. Toudic, "Bulk and Surface Acoustic Wave Propagation in Berlinite," *Proc. 33rd AFCS*, May-June 1979, pp. 70-79.
46. E.J. Ozimek and B.H.T. Chai, "Piezoelectric Properties of Single Crystal Berlinite," *Proc. 33rd AFCS*, May-June 1979, pp. 80-87.
47. E.D. Kolb, R.L. Barnes, J.C. Grenier, and R.A. Laudise, "Solubility, Crystal Growth, and Perfection of Aluminum Orthophosphate," *Proc. 33rd AFCS*, May-June 1979, pp. 88-97.
48. B.H.T. Chai, M.L. Shand, E. Buckler, and M.A. Gilleo, "Experimental Data on the Piezoelectric Properties of Berlinite," *Proc. 1979 IEEE Ultrasonics Symp.*, September 1979, pp. 577-583.
49. M.L. Shand and B.H.T. Chai, "H<sub>2</sub>O in Berlinite Detected by Raman Scattering," *J. Appl. Phys.*, Vol. 51, 1980, pp. 1489-1490.
50. T.R. AuCoin, R.O. Savage, M.J. Wade, J.G. Gualtieri, and A. Schwartz, "Large High Quality Single Crystal Aluminum Phosphate for Acoustic Wave Devices," *Proc. 1980 Army Sci. Conf.*, June 1980, West Point, NY, Vol. 1, pp. 121-133.
51. J.F. Vetelino, "Methods of Temperature Compensation in SAW Devices," *Proc. Nat. Elec. Conference*, Vol. 35, 1981, pp. 340-346. See also references cited herein.
52. P.H. Carr, J.H. Silva, and B.H.T. Chai, "Second-Order Temperature Coefficients of Singly and Doubly Rotated Cuts of Berlinite," *IEEE Ultrasonics Symposium Proc.*, October 1981, pp. 328-331.
53. E.D. Kolb, A.M. Glass, R.L. Rosenberg, J.C. Grenier, and R.A. Laudise, "Dielectric and Piezoelectric Properties of Aluminum Phosphate," *IEEE Ultrasonics Symposium Proc.*, October 1981, pp. 332-336.
54. D.S. Bailey, F. Josse, D.L. Lee, J. Andle, W. Soluch, J.F. Vetelino, and B.H.T. Chai, "An Experimental Study of the SAW Properties of Several Berlinite Samples," *IEEE Ultrasonics Symposium Proc.*, October 1981, pp. 341-345.
55. J. Gualtieri and A. Ballato, "Evaluation of Alpha AlPO<sub>4</sub> for Advanced Acoustic Wave Devices," Technical Report DELET-TR-81-15, U.S. Army Electronics R&D Command, Fort Monmouth, NJ 07703, August 1981, 46 pp.
56. K. Nagai, T. Ogawa, J. Okuda, J. Asahara, and S. Taki, "Hydrothermal Synthesis of Aluminum Phosphate (Berlinite) for Piezoelectric Devices," *Proc. First Intl. Symp. on Hydrothermal Reactions*, March 1982, Tokyo, pp. 496-508.



57. D.S. Bailey, W. Soluch, D.L. Lee, J.F. Vetelino, J. Andle, and B.H.T. Chai, "The Elastic, Dielectric, and Piezoelectric Constants of Berlinite," Proc. 36th AFCS, June 1982, pp. 124-132.
58. J. Henaff, M. Feldmann, and M.A. Kirov, "Piezoelectric Crystals for Surface Acoustic Waves (Quartz,  $\text{LiNbO}_3$ ,  $\text{LiTaO}_3$ ,  $\text{Tl}_2\text{V}_2\text{S}_4$ ,  $\text{Tl}_2\text{Ta}_2\text{Se}_4$ ,  $\text{AlPO}_4$ , GaAs)," *Ferroelectrics*, Vol. 42, 1982, pp. 161-185.
59. D.S. Bailey, J.C. Andle, D.L. Lee, W. Soluch, J.F. Vetelino, and B.H.T. Chai, "Temperature Dependence of the Material and Acoustic Wave Parameters of Berlinite," *IEEE Ultrasonics Symposium Proc.*, October-November 1983, pp. 335-340.
60. H.E. Bömmel, W.P. Mason, and A.W. Warner, "Experimental Evidence for Dislocations in Crystalline Quartz," *Phys. Rev.*, Vol. 99, 1955, pp. 1894-1896.
- 61a. A.W. Warner, "Design and Performance of Ultraprecise 2.5-mc Quartz Crystal Units," *Bell Syst. Tech. J.*, Vol. 39, September 1960, pp. 1193-1217.
- 61b. W.P. Mason, "Use of Internal Friction Measurements in Determining the Causes of Frequency Instabilities in Mechanically Vibrating Frequency Standards," *IRE Trans. on Instrumentation*, Vol. I-7, December 1958, pp. 189-200.
62. R. Bechmann, "Elastic and Piezoelectric Constants of Alpha-Quartz," *Phys. Rev.*, Vol. 110, June 1958, pp. 1060-1061.
63. R. Bechmann, A. Ballato, and T.J. Lukaszek, "Frequency-Temperature Behavior of Thickness Modes of Double-Rotated Quartz Plates, Proc. 15th AFCS, May-June 1961, pp. 22-48.
64. R. Bechmann, A. Ballato, and T.J. Lukaszek, "Frequency-Temperature Characteristics of Quartz Resonators Derived from the Temperature Behavior of the Elastic Constants," Proc. 16th AFCS, April 1962, pp. 77-109.
65. R. Bechmann, A. Ballato, and T.J. Lukaszek, "Higher Order Temperature Coefficients of the Elastic Stiffnesses and Compliances of Alpha-Quartz," Proc. IRE, Vol. 50, August 1962, pp. 1812-1822; December 1962, p. 2451.
66. R. Bechmann, A. Ballato, and T.J. Lukaszek, "Higher Order Temperature Coefficients of the Elastic Stiffnesses and Compliances of Alpha-Quartz," Technical Report 2261, U.S. Army Electronics R&D Laboratories, Fort Monmouth, NJ, September 1963, 79 pp.; available from NTIS as Document AD 426 194.
67. J. Marique, "The Response of RLC Resonant Circuits to EMF of Sawtooth Varying Frequency," Proc. IRE, Vol. 40, No. 8, August 1952, pp. 945-950.
68. F.K. Priebe and A. Ballato, "Measurement of Mode Parameters by Sweep Frequency Methods in the Frequency Range from 20 to 250 MHz," Proc. 20th AFCS, April 1966, pp. 465-499.
69. F.K. Priebe, "Filter Crystal Parameter Measurements with Frequency-Modulated Signals: Frequency Range 1 MHz to 350 MHz," R&D Technical Report ECOM-2845, U.S. Army Electronics Command, Fort Monmouth, NJ, June 1967, 98 pp.
70. R.S. Wagers, "Surface Acoustic Wave Filters," *Precision Frequency Control*, (E. ... and A. Ballato, eds.), Academic Press, New York, Chapter 5, in press.
71. A. Ballato, "Microwave Resonator Using Lateral Excitation," Invention Disclosure CECOM-3231, 1983.
72. B.H. Chai, E. Buehler, and J.J. Flynn, "Hydrothermal Growing Process and Apparatus," U.S. Patent 4,382,840, issued May 10, 1983.
73. B. Parzen, Design of Crystal and Other Harmonic Oscillators. Wiley, New York, 1983.
74. G.K. Guttwein, T.J. Lukaszek, and A. Ballato, "Practical Consequences of Modal Parameter Control in Crystal Resonators," Proc. 21st AFCS, April 1967, pp. 115-137. Technical Report ECOM-2847, U.S. Army Electronics Command, Fort Monmouth, NJ, June 1967, 21 pp.

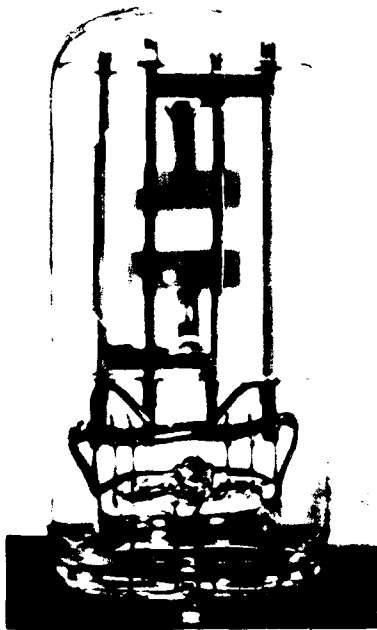


Figure 1. Bliley 1 MHz LE resonator /6/.

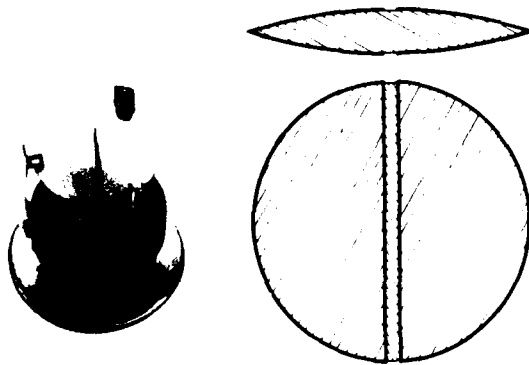


Figure 2. Ianouchevsky LE 2 MHz resonator /11/.

$$Z_{in}(TETM) = (y_{77}^o)^{-1} = \frac{1}{j\omega C_0} \left\{ 1 - \sum_{p=1}^3 (k^{(p)})^2 \frac{\tan \kappa^{(p)} h}{\kappa^{(p)} h} \right\}.$$

$$Y_{in}(LETM) = y_{77}^o = j\omega C_0 \left\{ 1 + \sum_{p=1}^3 (k^{(p)})^2 \frac{\tan \kappa^{(p)} h}{\kappa^{(p)} h} \right\}.$$

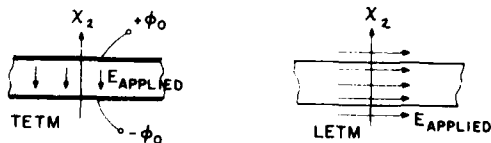


Figure 4. TE and LE input immittances.

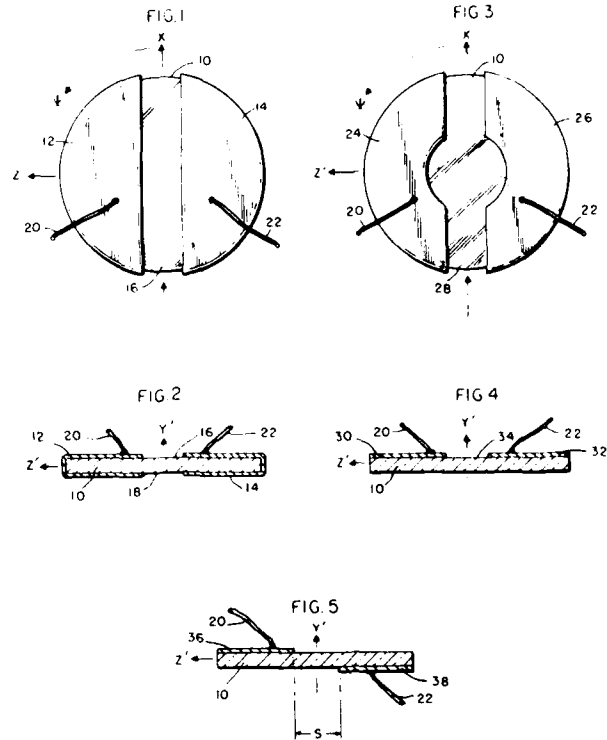


Figure 3. Bechmann lateral field patent /15/.

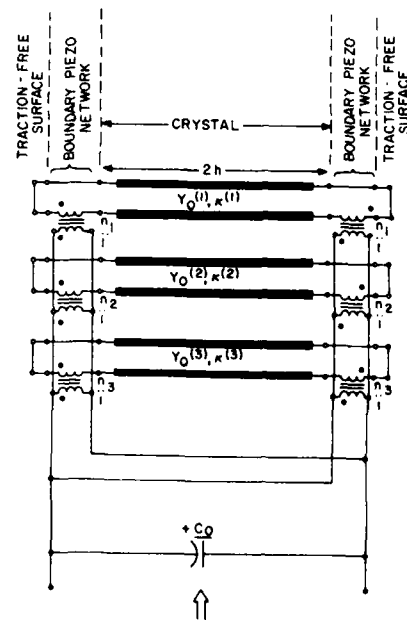


Figure 5. Thickness mode, lateral field exact equivalent network.

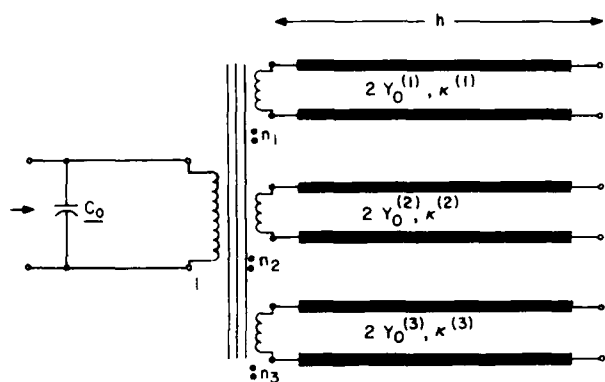


Figure 6. Bisected version of Figure 5.

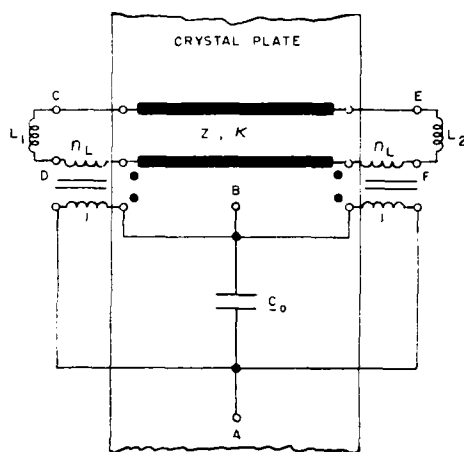


Figure 7. Single mode equivalent LE network.

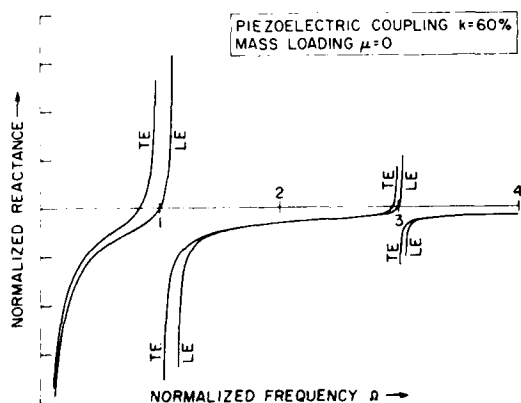
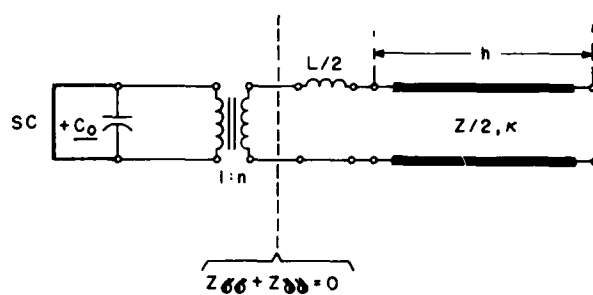


Figure 8. Reactance versus frequency comparison of TE (harmonic antiresonances) and LE (harmonic resonances).

## SHORT-CIRCUITED RESONANCES: $f_R^{(M)}$ (LE)

1. SHORT ELECTRICAL PORT.
2. APPLY TRANSVERSE-RESONANCE CONDITION



$$Z_{\text{SC}} + Z_{\text{SC}} = 0$$

$$Z_{\text{SC}} = 0$$

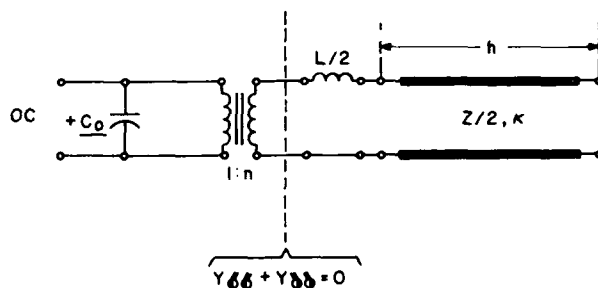
$$Z_{\text{SC}} = j\omega L/2 + Z/(j2 \tan \kappa h)$$

$$\frac{\tan X}{X} = [\mu X^2]^{-1}$$

Figure 9. Determination of resonance frequency equation from bisected version of Figure 7.

## OPEN-CIRCUITED RESONANCES: $f_A^{(M)}$ (LE)

1. OPEN ELECTRICAL PORT.
2. APPLY TRANSVERSE-RESONANCE CONDITION.



$$Y_{\text{OC}} = j\omega C_0/n^2$$

$$Y_{\text{OC}} = [j\omega L/2 + Z/(j2 \tan \kappa h)]^{-1}$$

$$\frac{\tan X}{X} = [-k^2 + \mu X^2]^{-1}$$

Figure 10. Determination of antiresonance frequency equation from bisected version of Figure 7.

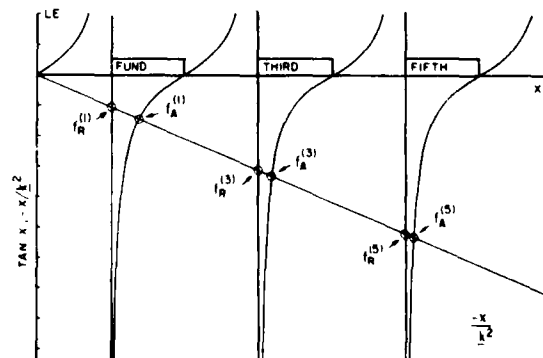


Figure 11. Graphical construction for the frequencies of an LE plate.

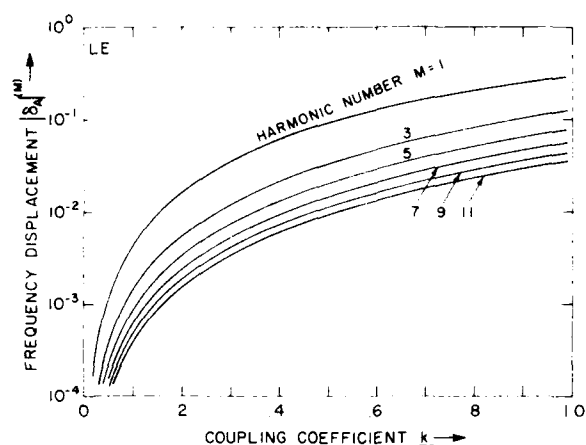


Figure 12. Frequency displacement versus lateral coupling as function of harmonic.

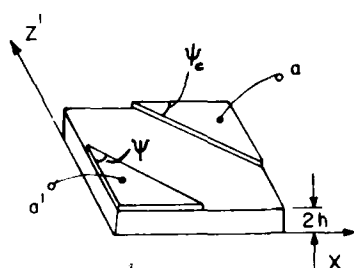


Figure 13. Definition of plate azimuth angle  $\psi_i$ .

- Rotation of coordinates:  $(\phi, \theta, \psi)$ . Refer  $\epsilon_{\alpha\beta\gamma}^E$ ,  $e_{\alpha k}$ , and  $\epsilon_{jk}^S$  to plate coordinates.
- Stiffen elastic constants:  

$$\bar{\epsilon}_{2j k 2} = \epsilon_{2j k 2} + e_{2j} e_{2k 2} / \epsilon_{22}^S$$
- Solve eigenvalue problem:  

$$[\bar{\epsilon}_{2j k 2} - \bar{\epsilon} \delta_{jk}] / \beta_k = 0; \bar{\epsilon}^{(m)} \text{ and } \beta_j^{(m)}$$
- Order roots and eigenvectors:  $m = \text{mode}$   
 $m=1; \bar{\epsilon}^{(1)}$  smallest root,  $\beta^{(1)}$  largest component along  $X_1$ : c mode  
 $2 \bar{\epsilon}^{(2)}$  largest root,  $\beta^{(2)}$  " " " "  $X_2$ : a mode  
 $3 \bar{\epsilon}^{(3)}$  intermediate root,  $\beta^{(3)}$  " " " "  $X_3$ : b mode
- $a = \text{quasiextensional mode}$ ;  $b = \text{fast quasishear mode}$ ;  $c = \text{slow quasishear mode}$
- Transform  $e_{22j}$  and  $e_{12j}$  to normal coordinates:  

$$e_{022p}^{(p)} = \beta_j^{(p)} e_{22j}; e_{012q} = \beta_k^{(q)} e_{12k}$$
- Modify the lateral  $e^0$  values:  

$$\bar{e}_{12q}^0 = e_{12q}^0 - (e_{11}^S / \epsilon_{11}^S) \epsilon_{12q}^0$$
- Modify the lateral permittivity:  

$$\bar{\epsilon}_{11} = \epsilon_{11}^S - (e_{11}^S)^2 / \epsilon_{11}^S$$
- Determine Piezoelectric Coupling Factors:  

$$TE: k_{21}^m = (e_{22m}^0)^2 / (\epsilon_{11}^S \bar{\epsilon}^{(m)})$$

$$LE: k_{12}^m = (e_{12m}^0)^2 / (\epsilon_{11}^S \bar{\epsilon}^{(m)})$$

Figure 14. Formalism for computing the TE ( $k_m$ ) and lateral ( $k_m$ ) coupling factors.

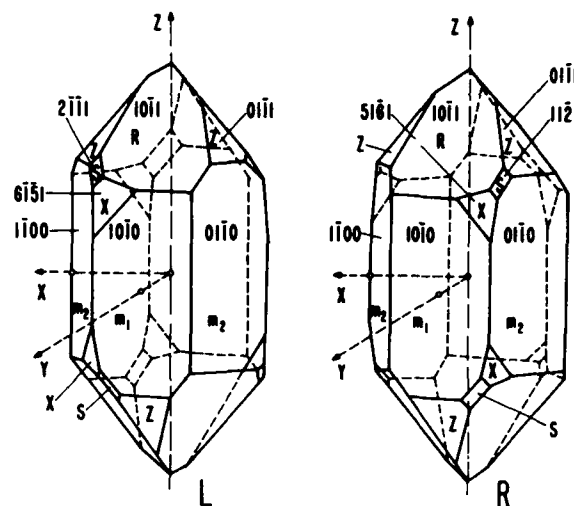


Figure 15. Enantiomorphs of quartz.

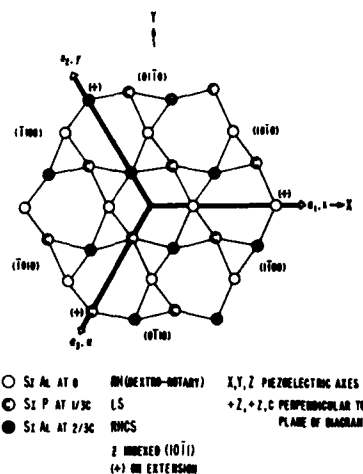


Figure 16a. Molecular construction of right-handed quartz and berlinite.

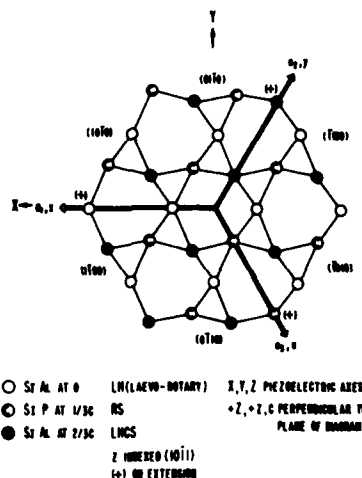


Figure 16b. Molecular construction of left-handed quartz and berlinite.

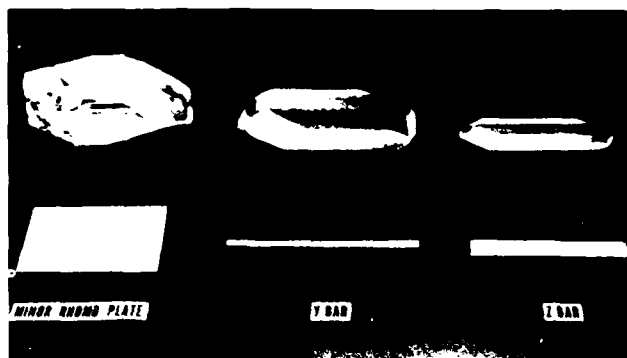


Figure 17. Cultured quartz bars. Lengths typically are 200 mm.

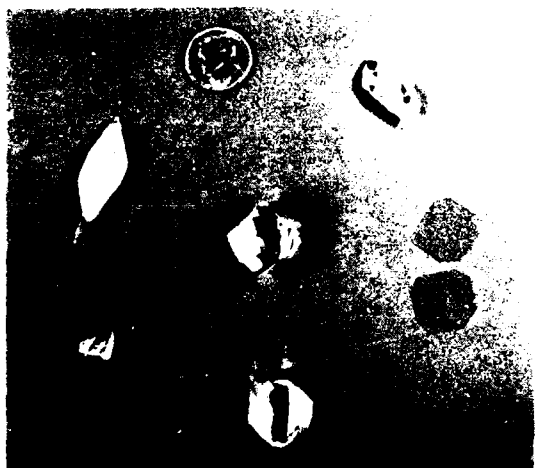


Figure 18. 1940s vintage cultured quartz (bottom); 1980s vintage berlinite (center); 1970s vintage berlinite (8, 10, & 1 o'clock); sample berlinite plates for measurements reported in this paper, cut from larger crystals of the type shown in Figure 19.



Figure 19. Allied Corporation berlinite. The larger samples are well in excess of 100 mm in length.

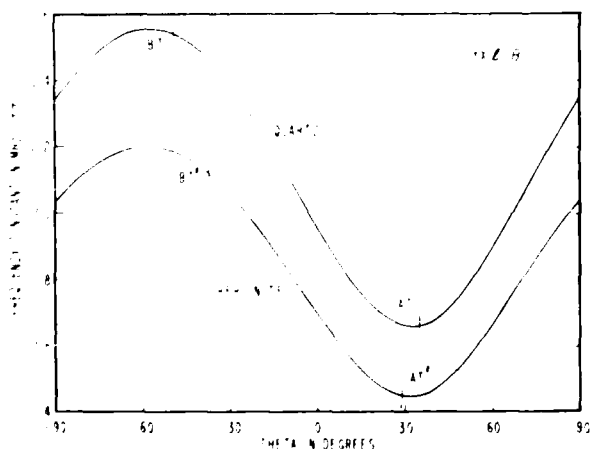


Figure 20. Rotated-y-cut frequency constants of quartz and berlinite compared.

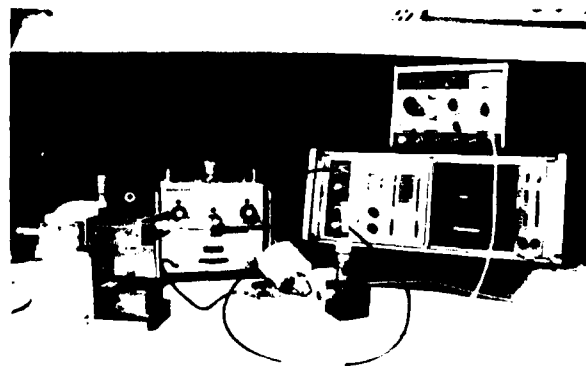


Figure 21. Measurement apparatus for TE and LE of thin plates.

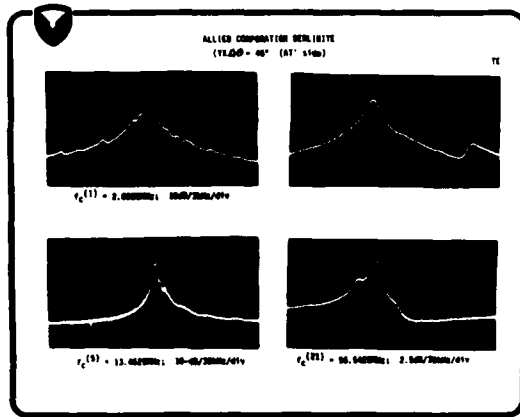


Figure 22. Mode spectrographs of (yxℓ)45° berlinite at harmonics 1, 3, 5, and 21.

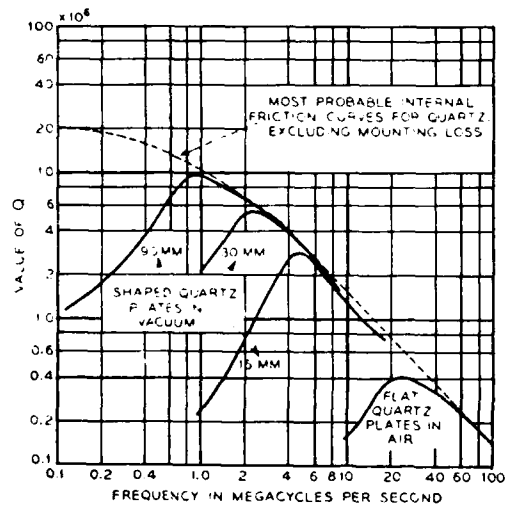


Figure 23. Q versus frequency for quartz plates /61 b/.



Figure 24. Turntable apparatus for LE experiments.

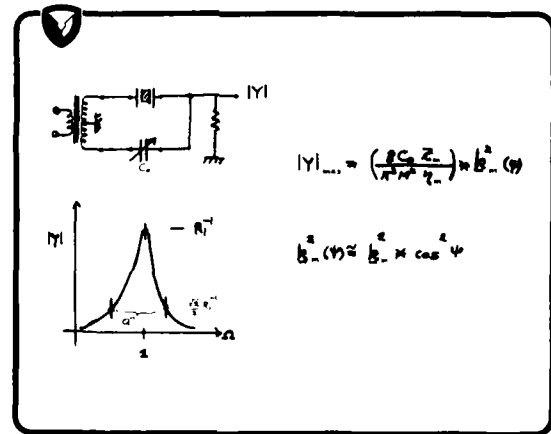


Figure 25. Lateral field circuit considerations.

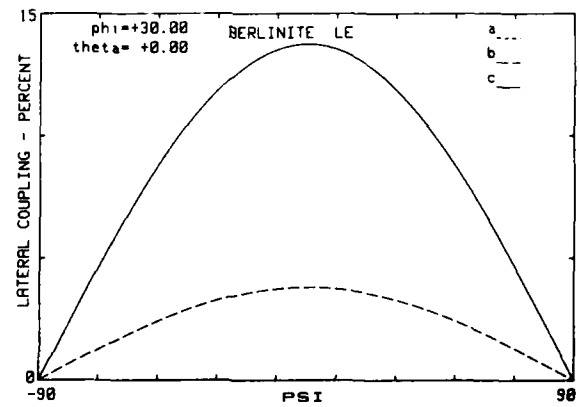


Figure 26. Lateral coupling factors versus psi for x-cut berlinite.

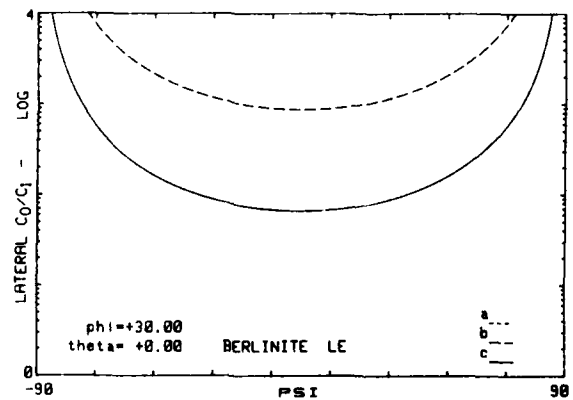


Figure 27. Lateral capacitance ratios versus psi for x-cut berlinite.

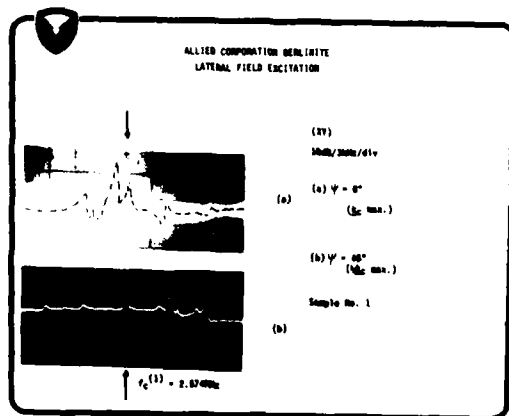


Figure 28. Mode spectrographs of x-cut berlinite with  $\psi = 0^\circ$  and  $45^\circ$ .

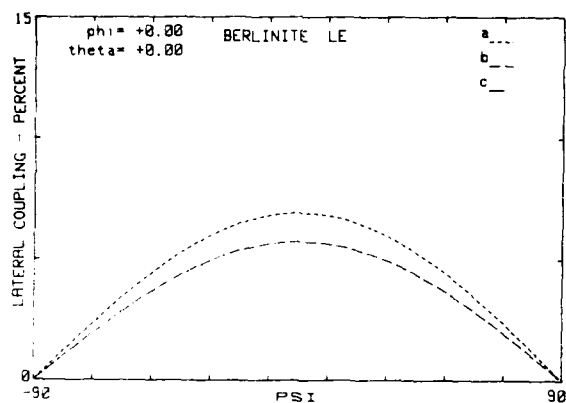


Figure 29. Lateral coupling factors versus  $\psi$  for y-cut berlinite.

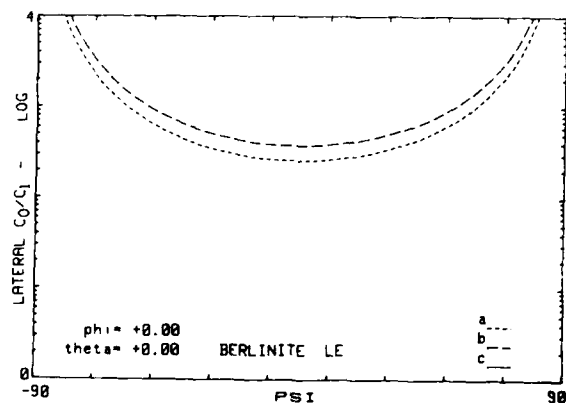


Figure 30. Lateral capacitance ratios versus  $\psi$  for y-cut berlinite.

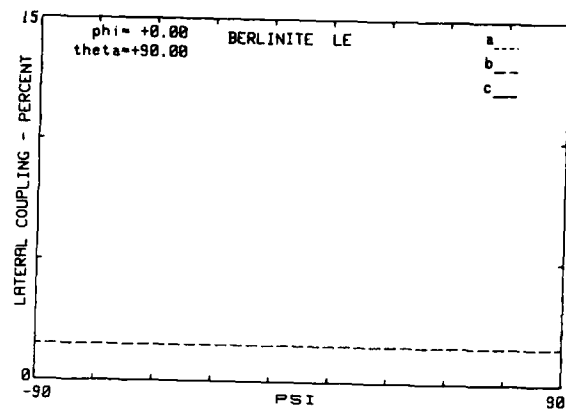


Figure 31. Lateral coupling factor versus  $\psi$  for z-cut berlinite.

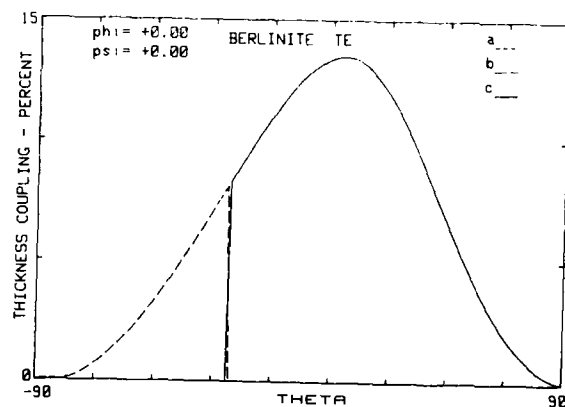


Figure 32. TE coupling versus  $\theta$  for rotated-y-cut berlinite.

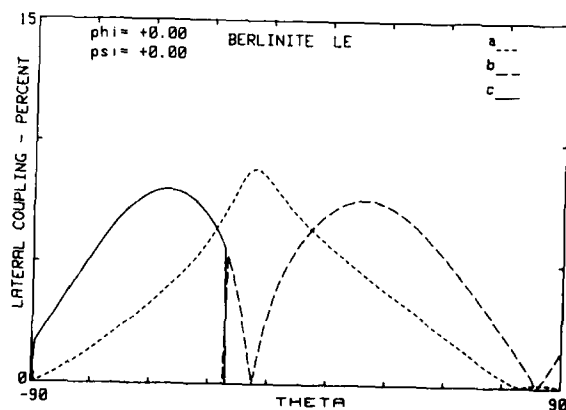


Figure 33. LE coupling versus  $\theta$  for rotated-y-cut berlinite with  $\psi = 0^\circ$ . (Field along X axis).

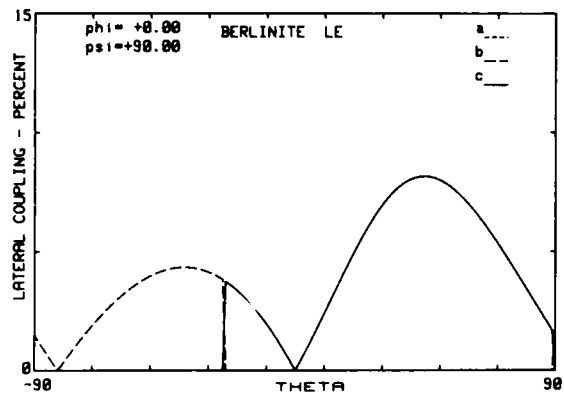


Figure 34. LE coupling versus theta for rotated-y-cut berlinite with  $\psi = 90^\circ$ . (Field along  $Z'$  axis).

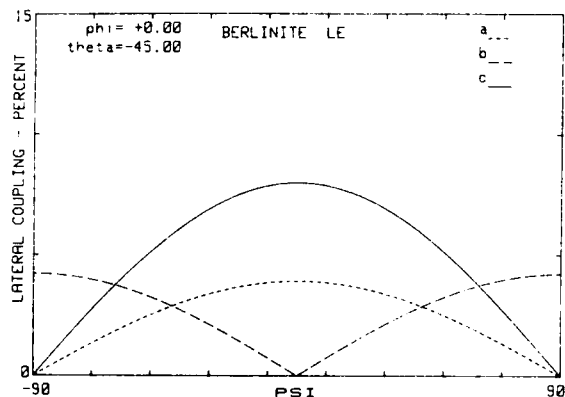


Figure 35. Lateral coupling factors versus  $\psi$  for  $(yx)\ell - 45^\circ$  berlinite.

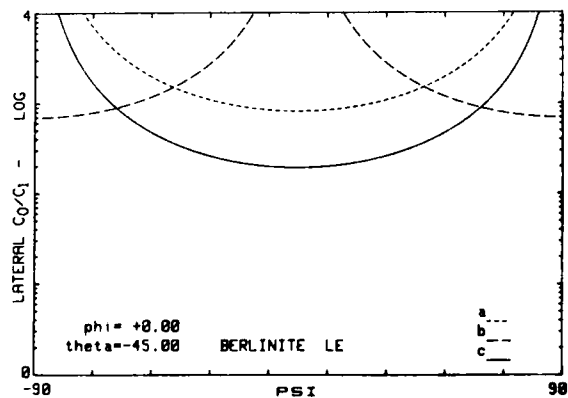


Figure 36. Lateral capacitance ratios versus  $\psi$  for  $(yx)\ell - 45^\circ$  berlinite.

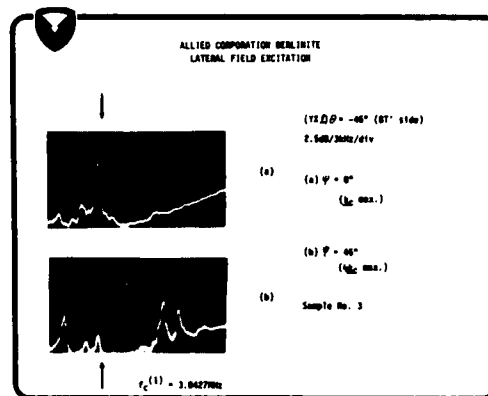


Figure 37. Mode spectrographs of  $(yx)\ell - 45^\circ$  berlinite with  $\psi = 0^\circ$  and  $45^\circ$ .

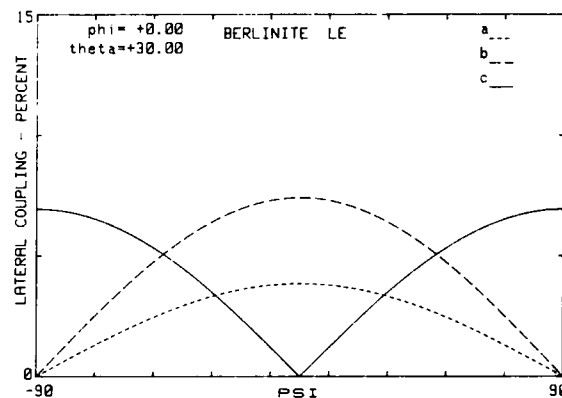


Figure 38. Lateral coupling factors versus  $\psi$  for  $(yx)\ell 30^\circ$  berlinite.

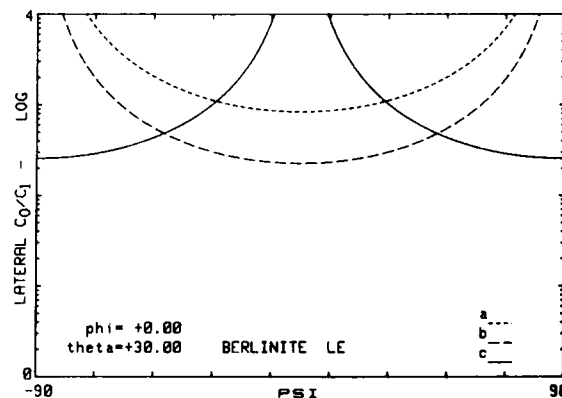


Figure 39. Lateral capacitance ratios versus  $\psi$  for  $(yx)\ell 30^\circ$  berlinite.



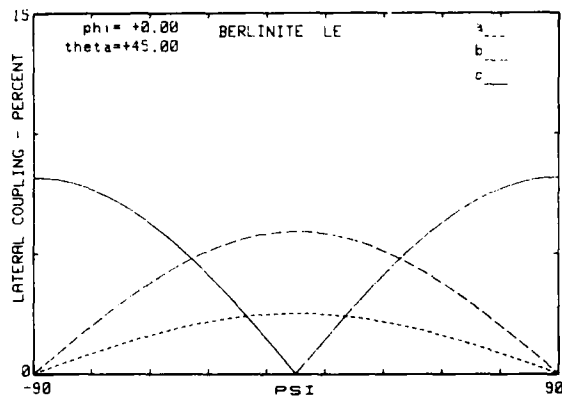


Figure 40. Lateral coupling factors versus psi for (yx) 45° berlinite.

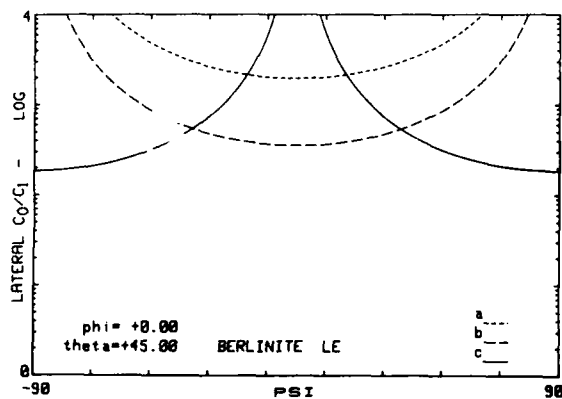


Figure 41. Lateral capacitance ratios versus psi for (yx) 45° berlinite.

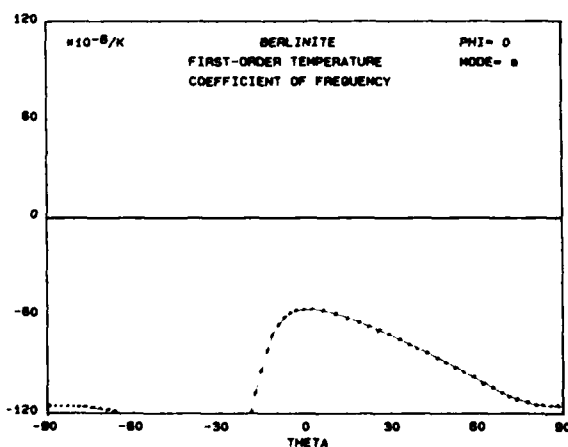


Figure 42. Temperature coefficient of mode a for rotated-y-cut berlinite as function of theta.

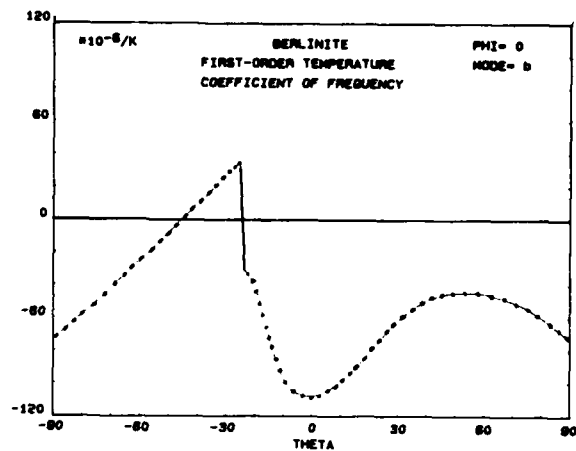


Figure 43. Temperature coefficient of mode b for rotated-y-cut berlinite as function of theta.

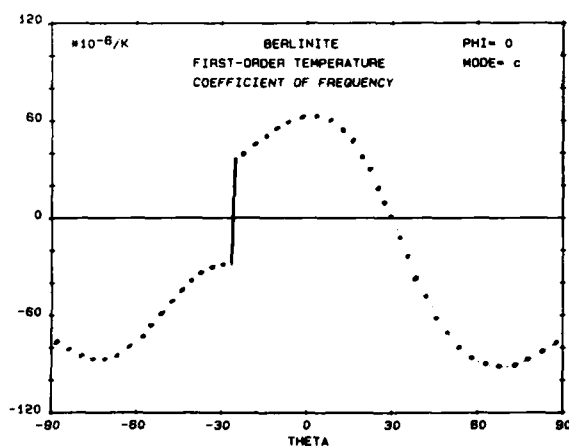


Figure 44. Temperature coefficient of mode c for rotated-y-cut berlinite as function of theta.

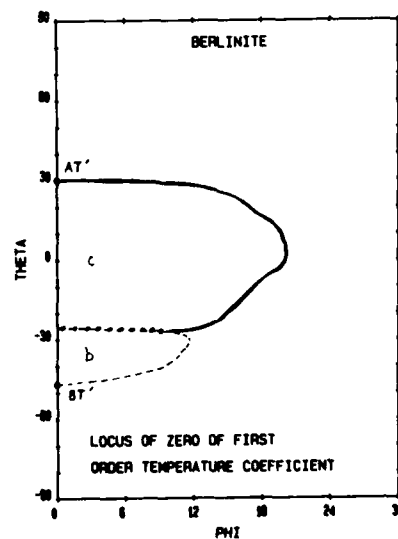


Figure 45. Loci of zero temperature coefficient for berlinite b and c modes; /59/.

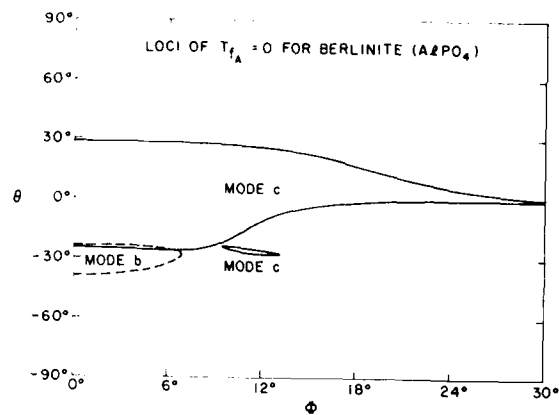


Figure 46. Loci of zero temperature coefficient for berlinite b and c modes; /34/.

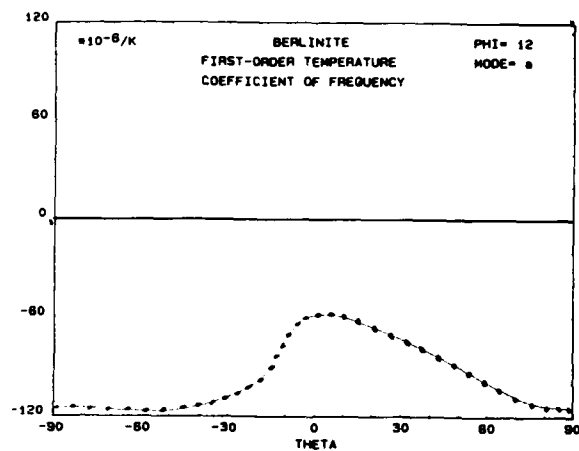


Figure 47. Temperature coefficient of mode a for (yxw)  $12^\circ/\theta$  berlinite.

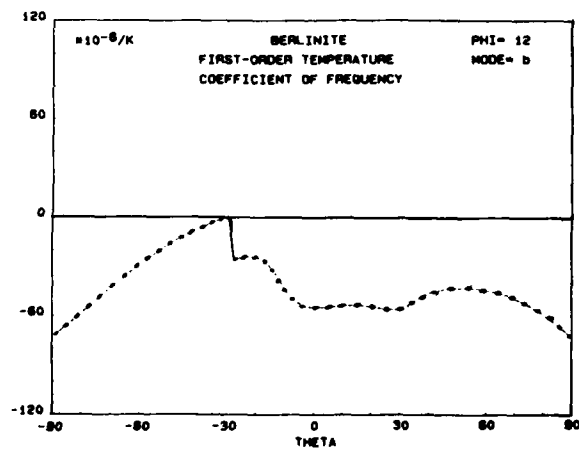


Figure 48. Temperature coefficient of mode b for (yxw)  $12^\circ/\theta$  berlinite.

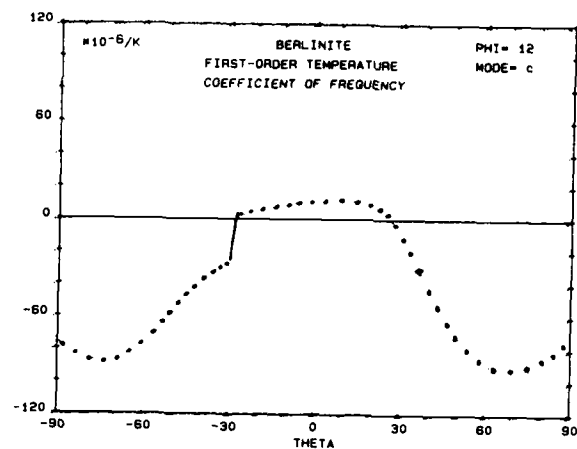


Figure 49. Temperature coefficient of mode c for (yxw)  $12^\circ/\theta$  berlinite.

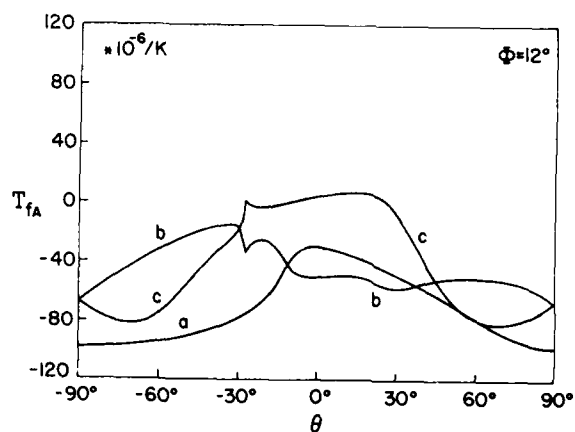


Figure 50. Temperature coefficients of modes a, b, and c for (yxw)  $12^\circ/\theta$  berlinite; /34/.

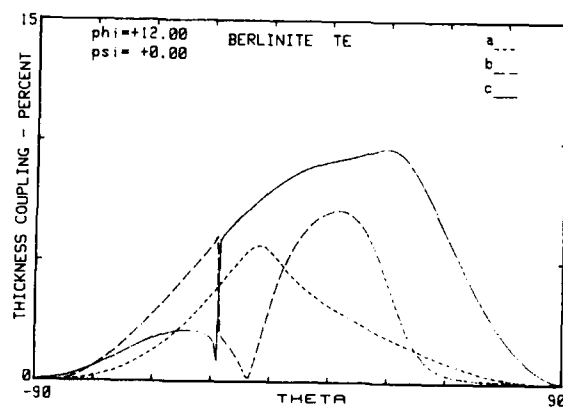


Figure 51. Thickness coupling factors versus theta for (yxw)  $12^\circ/\theta$  berlinite.

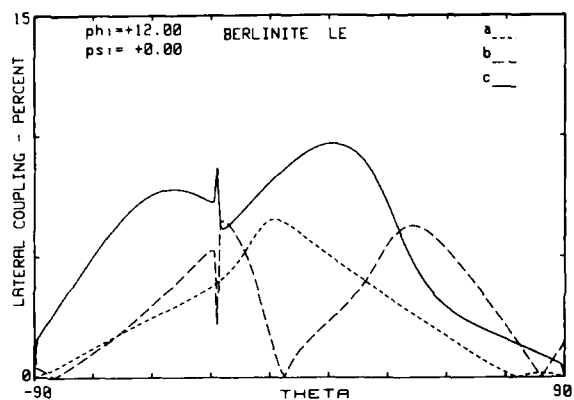


Figure 52. Lateral coupling factors, with  $\psi = 0^\circ$ , for  $(yxw\ell) 12^\circ/\theta$  berlinite.

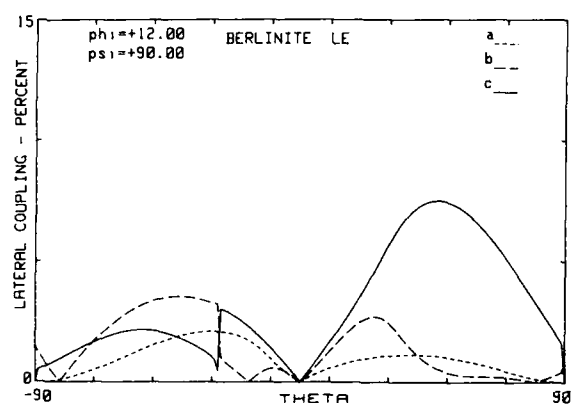


Figure 53. Lateral coupling factors, with  $\psi = 90^\circ$ , for  $(yxw\ell) 12^\circ/\theta$  berlinite.

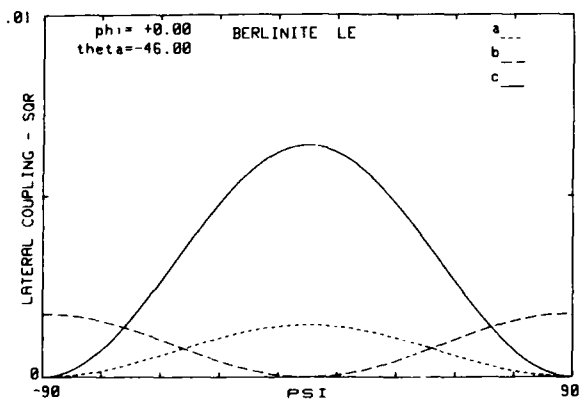


Figure 54. Lateral coupling factors versus  $\psi$  for BT' cut berlinite.

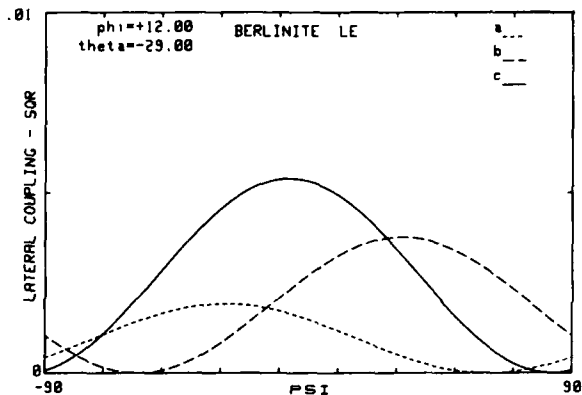


Figure 55. Lateral coupling factors versus  $\psi$  for  $(yxw\ell) 12^\circ/-29^\circ$  berlinite.

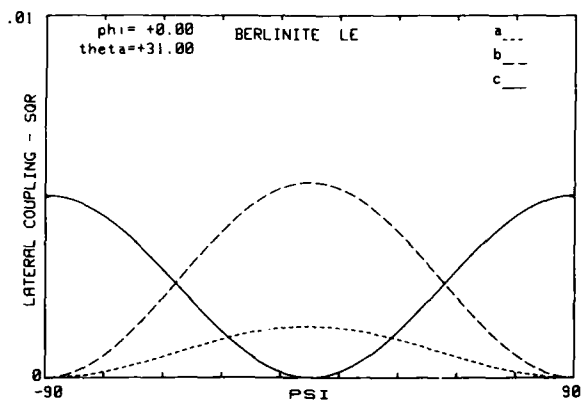


Figure 56. Lateral coupling factors versus  $\psi$  for AT' cut berlinite.

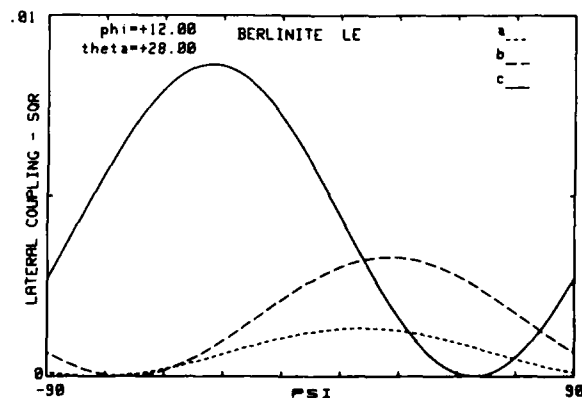


Figure 57. Lateral coupling factors versus  $\psi$  for  $(yxw\ell) 12^\circ/28^\circ$  berlinite.

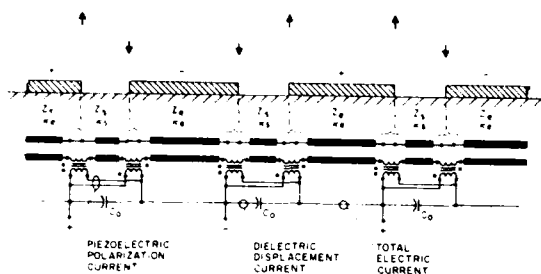


Figure 58. LE network applied to SAW IDT characterization.

TABLE 1. THICKNESS EXCITATION COEFFICIENTS FOR GENERIC PLATES IN CLASS 23.

CUT	X	Y	Z	$(YXL)\theta$	$(XYL)\theta$	$(YXW)\phi$	$(YXL)\phi\theta$
TETM							
1	✓	✓	0	✓	✓	✓	✓
2	0	0	0	0	✓	✓	✓
3	0	0	0	0	0	0	0

TABLE 2. LATERAL EXCITATION COEFFICIENTS FOR GENERIC PLATES IN CLASS 23.

CUT	X	Y	Z	$(YXL)\theta$	$(XYL)\theta$	$(YXW)\phi$	$(YXL)\phi\theta$
LETM							
1	0	0	0	0	✓	✓	✓
2	✓	✓	0	✓	✓	✓	✓
3	✓	✓	0	✓	✓	✓	✓
$f_i$	2 3 2 <sub>3</sub>	1 3 1 <sub>3</sub>	1 2 1 <sub>2</sub>	1 2 <sub>3</sub> 1 <sub>2</sub>	2 1 <sub>3</sub> 2 <sub>3</sub>	3 1 <sub>2</sub> 1 <sub>3</sub>	1 2 1 <sub>2</sub>
$m_i$	m1	m2	m3	m2,m3	m3,m1	m1,m2	m1,m2,m3

TABLE 3. PIEZOELECTRIC COUPLING AND TEMPERATURE COEFFICIENTS.

DATA	AXIS	ORIENTATION	NOTE	PIEZOELECTRIC COEFFICIENT, $d_{ij}$	TEMPERATURE COEFFICIENT, $10^{-5}/^\circ\text{C}$
$d_{31}$	$x_1$	$(111)$	SHEAR EXTENSION	4	50
$d_{32}$	$x_2$	$(111)$	SHEAR EXTENSION	4	72
$d_{33}$	$x_3$	$(111)$	SHEAR EXTENSION	12	40
$d_{11}$	$x_1$	$(111)$	SHEAR EXTENSION	12	40
$d_{12}$	$x_2$	$(111)$	SHEAR EXTENSION	12	40
$d_{13}$	$x_3$	$(111)$	SHEAR EXTENSION	12	40

TABLE 4.

SLOW-SHEAR RESONANCES OF BERLINITE  $(YXL)\theta = 45^\circ$  PLATE  
THICKNESS EXCITATION

n	$f(n)$ MHz		n	$f(n)$ MHz		n	$f(n)$ MHz	
	MEAS	CALC		MEAS	CALC		MEAS	CALC
1	2.6974	2.6936	22	40.790	40.404	6	78.114	78.114
3	8.0805	8.0807	17	—	45.791	4	83.507	83.501
5	13.466	13.468	19	—	51.178	3	88.890	88.886
7	18.850	18.855	18	21	56.543	7	94.277	94.275
9	24.235	24.242	14	23	61.955	8	99.668	99.662
11	29.620	29.629	10	25	67.343	8	105.054	105.049
13	instruct	35.016	27	72.728	72.727	6	110.445	110.437

TABLE 5.

UNROTATED BERLINITE CUTS  
 $(YXL)\phi/\theta$

$\phi$	$\theta$	m	$N_m$	$k_m$	$k_m$ (%)		
degrees			MHz-mm	%	$\psi = 0^\circ$	$\psi = 90^\circ$	
30	0	a	2.580	8.2	—	—	X cut
		b	2.203	—	3.8	—	
		c	1.434	—	13.7	—	
0	0	a	2.669	—	6.9	—	Y cut
		b	1.896	—	5.7	—	
		c	1.688	12.6	—	—	
0	-90	a	2.908	—	—	—	Z cut
		b	2.026	—	1.5	—	
		c	2.026	—	—	1.5	

TABLE 6.

SINGLY ROTATED BERLINITE CUTS  $(YXL)\theta$

$\phi$	$\theta$	m	$N_m$	$k_m$	$k_m$ (%)	
degrees			MHz-mm	%	$\psi = 0^\circ$	$\psi = 90^\circ$
0	-45	a	2.746	—	3.9	—
		b	2.169	4.2	—	4.2
		c	1.691	—	8.0	—
0	30	a	3.086	—	3.8	—
		b	1.653	—	7.4	—
		c	1.444	11.9	—	6.9
0	45	a	3.124	—	2.5	—
		b	1.766	—	5.9	—
		c	1.493	8.1	—	8.2

TABLE 7.

DOUBLY ROTATED, ZERO TC (MODE b) BERLINITE CUTS  
 $(YXL)\phi/\theta$

$\phi$	$\theta$	m	$N_m$	$k_m$	$k_m$ (%)	
degrees			MHz-mm	%	$\psi = 0^\circ$	$\psi = 90^\circ$
0	-46	a	2.757	—	3.8	—
		b	2.174	4.0	—	4.2
		c	1.682	—	8.0	—
6	-43	a	4.0	1.1	3.8	1.1
		b	2.38	4.3	2.1	4.1
		c	1.707	1.0	7.9	1.0
12	-29	a	2.630	3.7	3.9	2.1
		b	1.937	5.8	5.2	3.2
		c	1.903	1.6	7.3	0.9

TABLE 8.

DOUBLY ROTATED, ZERO TC (MODE c) BERLINITE CUTS  
( $YXWZ$ )  $\phi/\theta$ 

$\theta$	$\phi$	m	$N_m$	$k_m$	$k_m$ (%)	
degrees			MHz-mm	%	$\psi = 0^\circ$	$\psi = 90^\circ$
0	31	a	3.092	—	3.8	—
		b	1.656	—	7.3	—
		c	1.444	11.7	—	7.1
6	30	a	3.078	1.0	3.7	0.6
		b	1.661	2.3	6.9	1.3
		c	1.452	11.3	3.9	6.6
12	28	a	3.038	2.0	3.5	1.1
		b	1.687	4.8	5.1	2.6
		c	1.473	9.7	7.7	5.2
18	16	a	2.546	6.9	4.6	0.7
		b	2.172	2.9	2.6	0.3
		c	1.549	6.0	11.1	0.6
18	-6	a	2.864	4.0	3.7	1.2
		b	1.865	7.3	0.4	2.1
		c	1.457	6.4	11.7	1.8

AT<sup>I</sup> cut

## AGING STUDIES ON QUARTZ CRYSTAL RESONATORS AND OSCILLATORS

R.L. Filler, J.A. Kosinski, V.J. Rosati and J.R. Vig

US Army Electronics Technology and Devices Laboratory (ERADCOM)  
Fort Monmouth, New Jersey 07703Summary

Progress on improving the aging of high precision quartz crystal oscillators has been sparse over the past 25 years. In this paper, the causes of aging are reviewed and a progress report is presented on a program aimed at determining the mechanisms that limit the attainable aging. Aging rates have been measured as functions of aging temperature, blank frequency, and DC voltage on the resonator. When the aging of the same resonators were measured at different temperatures, no drastic or systematic variations of aging rates were observed. The aging rates of similarly fabricated resonators were found to vary inversely with blank thickness, independent of overtone. A DC voltage on the resonator can be a significant contributor to aging.

**Key words:** Quartz oscillator, crystal oscillator, aging, quartz, quartz crystal, quartz resonator, SC-cut, AT-cut, frequency stability.

Introduction

Progress on improving the aging attainable with high precision quartz crystal oscillators has been sparse over the past 25 years. Warner<sup>1</sup> had achieved  $1 \text{ pp}10^{10}$  per month ( $3 \text{ pp}10^{12}$  per day) in 1958 with 2.5 MHz 5th overtone AT-cut resonators, after several months of continuous operation. Subsequent reports<sup>2-7</sup> confirmed that the aging of this type of resonator was typically parts in  $10^{11}$  per day after the first 30 days and parts in  $10^{12}$  per day after a few months. Figure 1 shows the aging of two of these resonators measured at Ft. Monmouth<sup>7</sup>, between 1961 and 1965.

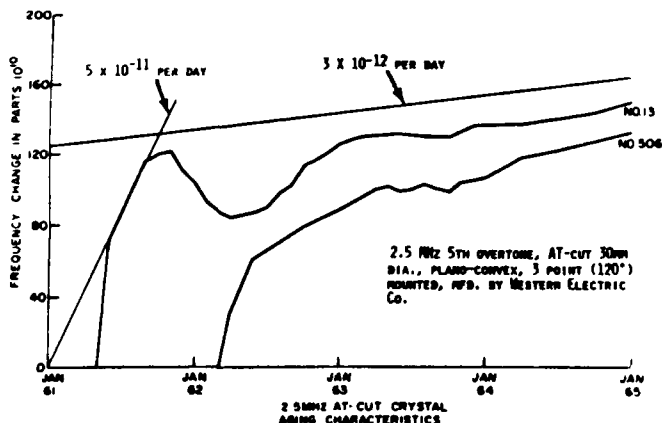


Figure 1. Aging of a precision resonator

Today, although aging rates of parts in  $10^{12}$  per day are occasionally observed, no manufacturer will guarantee parts in  $10^{12}$  per day aging. The lack of progress in the attainable aging is particularly puzzling because during the past 25 years many advancements have taken place which should have contributed to progress in making low aging resonators. These advancements include the availability of better ultrahigh vacuum systems, better cleaning techniques, better understanding of stress effects, the discovery of the SC-cut, etc.

Another puzzling fact is that there are at least ten organizations, worldwide, which can make resonators that are capable of aging rates of parts in  $10^{11}$  per day after 30 days of continuous operation. Although the processes used to make these resonators vary widely, the end results with respect to aging do not. The range of processes used to make parts in  $10^{11}$  per day resonators is shown in Table I. Parts in  $10^{11}$  per day aging has been achieved with AT, BT, and SC-cut resonators. SC-cut and AT-cut resonators processed the same way have been found to age at about the same rate.

PROCESS	RANGE OF PRACTICES
QUARTZ	NATURAL, CULTURED, SHEET CULTURED
CLEAN ROOM	CLASS 100 TO NO CLEAN ROOM
CLEANING PROCESS	NET CLEANING ONLY, NET CLEANING + H-FIRING, NET CLEANING + UV/OZONE, PLASMA CLEANING
ETCHING	LIGHT ETCH TO DEEP ETCH
MOUNTING	SOFT NI, SPRINGY MO, PT-M, QUARTZ
MOUNTING POINTS	2-POINT, 3-POINT, 4-POINT
BONDING	AU-GE, AG-FILLED POLYIMIDE, AU-AU THERMOCOMPRESSION, AG FILLED PYROCERAM, SOLDER
ELECTRODES	AU, NONE (BVA, PARALLEL FIELD)
DEPOSITION T	ROOM TEMPERATURE TO 250° C
BAKEOUT T	290° C TO 350° C (FOR UP TO 14 HRS)
SEALING T	160° C TO 300° C
BACKFILL GAS	NONE, HE, N <sub>2</sub>
PACKAGE	GLASS, METAL WITH GLASS TO METAL FEEDTHROUGHS, METAL WITH CERAMIC TO METAL FEEDTHROUGHS, CERAMIC FLATPACK
VACUUM SYSTEMS	VITON SEALED, METAL SEALED; ION PUMPED, CRYOPUMPED

Table I Range of processes for low aging resonators.

The mechanisms that can cause aging are as follows<sup>8</sup>:

1. Mass transfer due to contamination inside the resonator enclosure,
2. Stress relief in the resonator's:
  - a. mounts, b. bonds, c. electrodes, and d. quartz, and
3. Other effects: a. oscillator circuit aging (load reactance and drive level changes), b. oven control circuitry aging, c. radiation, d. quartz outgassing, e. diffusion effects (thermal

and DC voltage driven), f. pressure changes in the resonator enclosure due to leaks and outgassing, g. electric field change (doubly rotated resonators only).

Aging can be positive or negative. Occasionally, a reversal of aging direction is observed. Figure 2 illustrates the three types of aging behavior (computer generated). The curve showing the reversal is the sum of the other two curves.

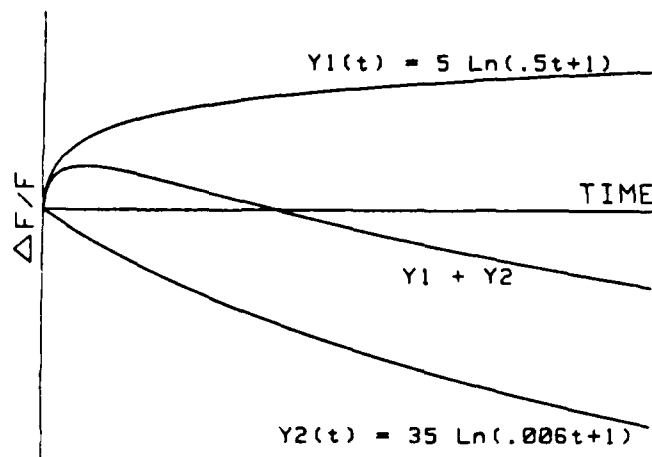


Figure 2. Typical aging behaviors.

No mechanism is known that would inherently limit the attainable aging to parts in  $10^{12}$  per day. This paper is a progress report on a research program aimed at identifying the dominant mechanism(s) that limit the aging attainable in currently available resonators. It is hoped that once the mechanisms are identified, it will be possible to produce resonators that age less than parts in  $10^{12}$  per day. The initial experiments were aimed at defining the dependence of aging on temperature, overtone and DC-voltage on the resonator.

#### Experimental Methods

The aging experiments were performed on three types of oven controlled oscillators: 1) commercially available high precision oscillators, 2) test oscillators designed specifically for measuring the aging of precision resonators, and 3) test oscillators designed for operation below room temperature. A schematic representation of the experimental setup is shown in Figure 3. The measurements were controlled by an HP9825 computer, the frequencies were measured by an HP5345 counter that was locked to an HP5601 cesium standard and the switch was a Racal Series 1200 rf switch. The test oscillators have external adjustments of drive level and oven temperatures. The low temperature oscillators were contained in a Kelvinox Series 100 freezer. The oscillator drive level and oven temperature controls were outside the freezer.

Since oven temperature drift due to thermistor aging<sup>10</sup> is one of the many possible aging mechanisms, the test ovens were tested by comparing the stabilities of the thermistors with the stabilities of Y-cut crystals. Since the slopes of the frequency vs. temperature characteristics

of such crystals are on the order of 100 ppm per deg C, any significant frequency changes can be attributed to the aging of the thermistor. The thermistors did age when new, as shown in Figure 4, however, after about the first 60 hours, the thermistors were stable, and remained stable upon subsequent warmups of the test ovens.

At the beginning of each aging test in the test oscillators, the oven temperatures were carefully adjusted to the resonators' turnover temperatures. At the conclusion of the aging tests, the ovens were readjusted to the resonators' turnover temperatures in order to determine the contribution of the ovens' temperature drifts to the total aging. Typical results are shown in Table II. In general, the contributions of the ovens' temperature drifts were negligible.

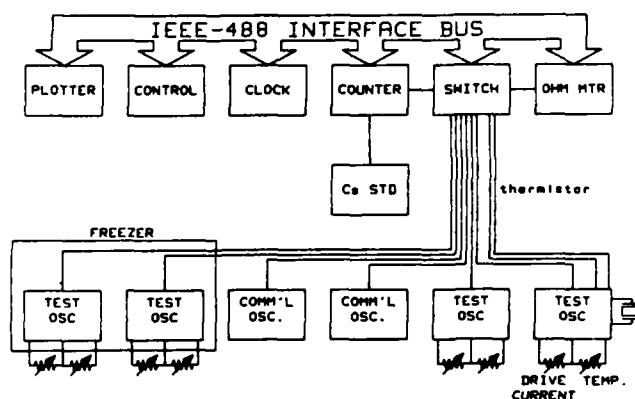


Figure 3. Aging test configuration

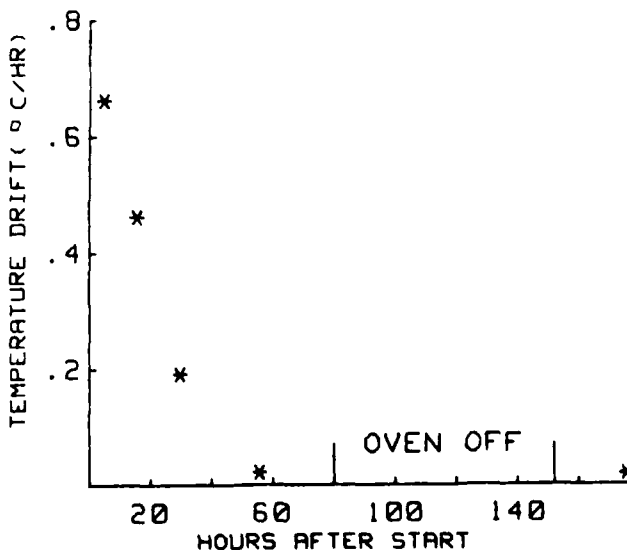


Figure 4. Thermistor drift

TEST OSC.	TOTAL F/F FOR 30 DAYS	F/F DUE TO TEMP. DRIFT	AGING RATE AT DAY 30	AGING RATE DUE TO TEMP. DRIFT	ERROR DUE TO TEMP. DRIFT
1	$3.3 \times 10^{-9}$	$8.8 \times 10^{-13}$	$8.7 \times 10^{-11}$ /DAY	$2.9 \times 10^{-14}$ /DAY	.03 %
2	$1.1 \times 10^{-9}$	$2.1 \times 10^{-13}$	$5.8 \times 10^{-12}$ /DAY	$7.0 \times 10^{-15}$ /DAY	.12 %
3	$7.0 \times 10^{-10}$	$7.8 \times 10^{-12}$	$1.8 \times 10^{-11}$ /DAY	$2.6 \times 10^{-13}$ /DAY	1.4 %
"	"	"	"	"	"
"	"	"	"	"	"
"	"	"	"	"	"

Table II. Effect of temperature drift in test oscillators.

#### Temperature Dependence of Aging

If there were a dominant aging mechanism that was thermally activated, e.g., the adsorption or desorption of a single contaminant, then the aging rate would vary drastically with aging temperature. To illustrate,<sup>11</sup> the average residence time on a surface of an adsorbing/desorbing molecule is given by  $\tau$ , where

$$\tau = \tau_0 e^{E_D/RT}$$

$\tau_0 \sim 10^{-13}$  sec,  $E_D$  is the desorption energy,  $T$  is temperature and  $R$  is the gas constant. Table III shows the variation of  $\tau$  with  $E_D$  and  $T$ . At an oven temperature of 100°C, molecules with  $E_D$  between 30 Kcal/mol and 40 Kcal/mol can have a significant contribution to aging. (For molecules with  $E_D < 30$  Kcal/mol, the adsorption/desorption process reaches completion in a short time so that at 100°C these molecules do not contribute to aging; for molecules with  $E_D > 40$  Kcal/mol, the adsorption/desorption process is so slow that these molecules do not contribute significantly to the aging either.) When the resonator is cooled from 100°C to below 0°C, the lifetime of the molecules that contributed significantly to the aging at 100°C increases by several orders of magnitude so that these molecules no longer contribute significantly to the aging.

$E_D$ KCAL/MOL	-50°C	25°C	100°C	300°C	350°C
10	$6 \times 10^{-6}$ SEC	$2 \times 10^{-6}$ SEC	$7 \times 10^{-6}$ SEC	$6 \times 10^{-10}$ SEC	$3 \times 10^{-10}$ SEC
20	50 DAYS	50 SEC	$5 \times 10^{-2}$ SEC	$4 \times 10^{-6}$ SEC	$10^{-6}$ SEC
30	$10^5$ YRS	30 YRS	10 HRS*	$3 \times 10^{-2}$ SEC	$3 \times 10^{-3}$ SEC
40	$10^{10}$ YRS	$6 \times 10^5$ YRS	900 YRS**	3 MIN	10 SEC
45	$10^{13}$ YRS	$3 \times 10^{12}$ YRS	$6 \times 10^5$ YRS	4 HRS	10 HRS

\*Turnover per 10 HRS  $\rightarrow$   $\sim$  1 PPM PER DAY  
 \*\*Turnover per 900 YRS  $\rightarrow$   $\sim$   $10^{-5}$  PER YEAR

DESORBS RAPIDLY (DOES NOT CONTRIBUTE TO AGING)

Table III. Average residence time of a molecule on a surface vs. temperature and desorption energy.

The aging of a group of six ceramic flatpack enclosed SC-cut resonators was measured at both the lower and upper turnover temperatures. Three of the resonators were 5 MHz fundamental mode and three were 10 MHz 3rd overtone. The aging was measured for four 30 day periods alternating between the two turnover temperatures. At the end of each 30 day period, the aging rate at day 30 was determined from the best fit to the data. The results are shown in Figures 5 and 6, in which the aging rates are the rates at day 30 of each period, LTP and UTP indicate the lower and upper turnover points, respectively, and the two numbers in parentheses to the right of each curve are the values of the two turnover temperatures for the resonator represented by each curve. As can be seen, the temperature differences between the UTP and LTP ranged from 19°C to 40°C.

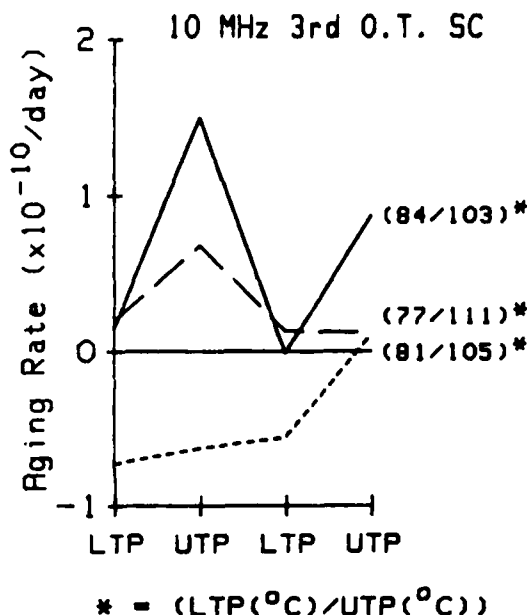


Figure 5. Aging rate vs. temperature for third overtone SC-cut resonators.

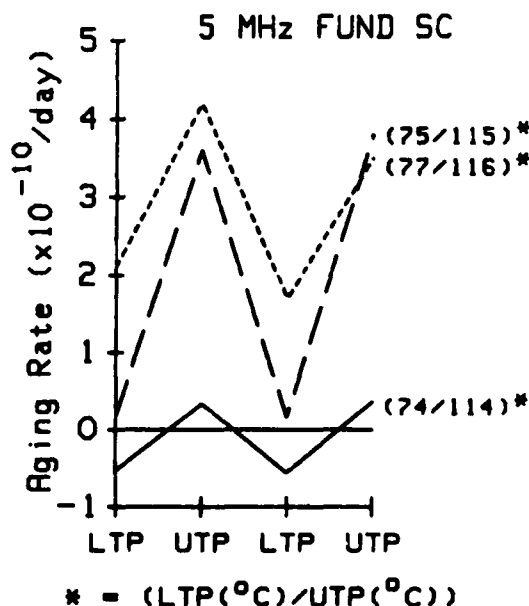


Figure 6. Aging rate vs. temperature for fundamental SC-cut resonators.



In all six cases, the aging became more positive at the UTP; i.e., the aging of the four resonators that exhibited positive aging at the end of the initial aging period at the LTP became more positive, and the aging of the two that exhibited negative aging rates at the end of the initial period at the LTP changed to positive aging rates at the UTP. The patterns repeated for the third and fourth periods.

In order to investigate the effects of a larger aging temperature difference, a group of "low temperature" ceramic flatpack enclosed resonators, with LTP's between  $-10^{\circ}\text{C}$  and  $0^{\circ}\text{C}$ , were fabricated. The fabrication of these resonators was identical to that of the "normal" ceramic flatpack resonators, except that the electrode depositions were performed in one step, at the upper turnover temperatures (about  $190^{\circ}\text{C}$ ).

The aging rates at day 30 of the "low temperature" resonators are compared in Figure 7 with the aging of a group of "normal" ceramic flatpack SC-cut resonators which had turnover temperatures between  $80^{\circ}\text{C}$  and  $100^{\circ}\text{C}$ . Figure 7 shows a histogram of number of units vs. the absolute values of the aging rates at day 30. Although the average aging temperature of the "low temperature" units was nearly  $100^{\circ}\text{C}$  lower, no drastic differences or obvious trends in aging rates can be observed.

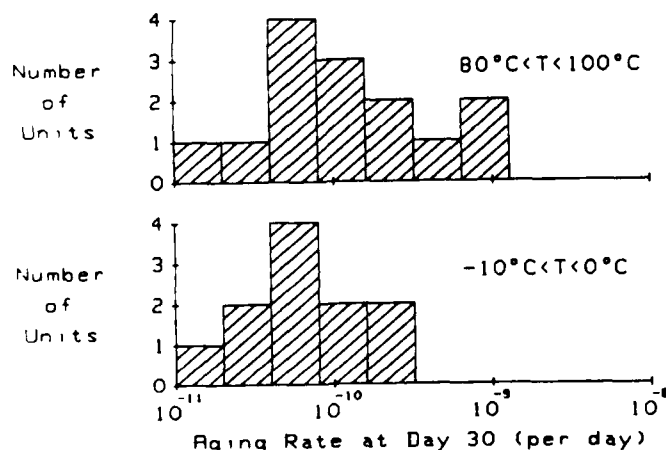


Figure 7. Aging rates of 5 MHz third overtone SC-cut resonators at  $-5^{\circ}\text{C}$  and at  $90^{\circ}\text{C}$ .

The aging rates of two Bliley BG61AH-5S AT-cut glass enclosed 5 MHz 5th overtone resonators were also measured at both the UTP ( $76^{\circ}\text{C}$  and  $79^{\circ}\text{C}$ ) and the LTP ( $-24^{\circ}\text{C}$  and  $-27^{\circ}\text{C}$ ). The aging was measured for 30 days at the UTP, then for 30 days at the LTP, then again for 30 days at the UTP. The results, shown in Figure 8, are inconclusive. The aging at the UTP of one of the resonators was significantly degraded subsequent to operation for 30 days at the LTP.

Low temperature storage can significantly affect the aging of oscillators. Figure 9 shows the aging of a commercial 10 MHz 3rd overtone SC-cut oscillator. After 45 days of continuous operation, the aging rate reached  $-6 \times 10^{-11}$  per day. The

oscillator was then turned off, stored at  $-40^{\circ}\text{C}$  for three days, and at the end of the three days was warmed up to room temperature and turned on. As can be seen from Figure 9, the aging rate reversed direction and increased significantly subsequent to the low temperature storage. After about 20 days of continuous operation, the aging levelled off to a rate of about  $1 \times 10^{-11}$  per day.

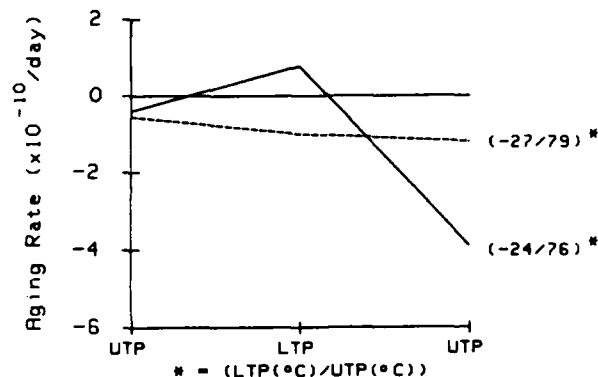


Figure 8. Aging rate vs. operating temperature for 5 MHz 5th overtone AT-cut resonators.

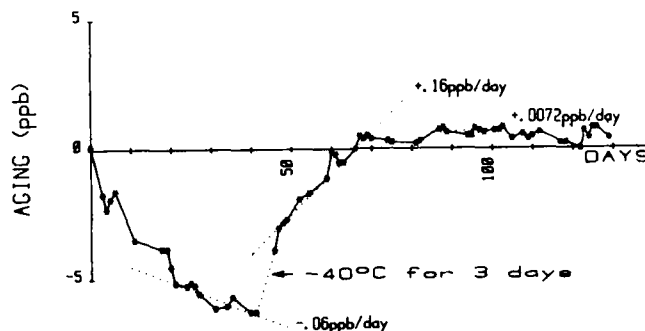


Figure 9. The effect of cold storage on aging rate.

#### Blank Thickness Dependence of Aging

The average aging rates of ceramic flatpack enclosed SC-cut 5 MHz fundamental, 10MHz 3rd overtone and 5 MHz 3rd overtone resonators are compared in Table IV. The blanks were 14 mm in diameter and the mounting structures, electrodes, and fabrication steps were the same for all three groups. The average aging rates vary approximately inversely with blank thickness, independent of overtone.

#### DC Bias Dependence of Aging

That a DC voltage across a quartz crystal produces changes in the crystal has been known for nearly 100 years.<sup>12</sup> Jacques Curie measured the direct current resistivity of quartz as a function of temperature, electric field intensity and direction, and time as part of a thesis on the electrical properties of crystals. The results were reported in 1886, 1888, and 1889. Curie, as well as numerous later workers<sup>12</sup>, recognized the dependence of resistivity on the length of time the field is applied.

In order to answer the question of whether or not a DC voltage across a quartz resonator affects the long term aging rate, a group of high precision SC-cut oscillators was tested with and without externally applied DC-voltage across the resonators. The results varied greatly from resonator to resonator. The results for one of the resonators that showed a dramatic response to the DC voltage is shown in Figure 10. The blank of this resonator was made of Sawyer Premium Q unswept quartz. The lower two curves show enlargements of the two regions enclosed in rectangles, which are the periods just before and just after the applications of the DC-voltages.

RESONATOR TYPES	AGING RATE RATIO	BLANK THICKNESS RATIO
10MHZ 3RD 5MHZ FUND	$\frac{1}{1.7}$	1.5
5MHZ 3RD 5MHZ FUND	$\frac{1}{2.6}$	3.0

Table IV. Comparison of aging rate to blank thickness for SC-cut resonators.

The initial aging rate was positive. After three weeks of continuous operation with no externally applied voltage, 12V was applied to the resonator. As expected, the frequency shifted by  $+5 \times 10^{-8}$  due to the polarization effect. (This instantaneous frequency change is not shown in Figure 10.) The instantaneous shift was followed by a rapid, approximately exponential decrease in frequency. After 24 hours, the rapid negative aging had completely offset the  $+5 \times 10^{-8}$  shift due to the polarization effect and the rapid negative aging was continuing. After about an additional two weeks, the aging rate levelled off to a rate of  $3 \times 10^{-11}$  per day. The total DC-voltage induced frequency change during the two weeks subsequent to the application of the voltage, after the polarization effect, was  $-6.3 \times 10^{-8}$ .

Thirty days after the voltage was applied, the voltage was removed. After an up and down frequency excursion, the aging resumed at about the pre-DC-voltage rate.

The aging rate continued at a nearly constant  $3 \times 10^{-11}$  per day for the next year. At day 412, a 20 V DC voltage of sign opposite to the originally applied 12V DC voltage was applied. After a down and up frequency excursion, the aging rate increased significantly. A month after the application of the 20 V voltage, the aging rate ( $2 \times 10^{-10}$  per day) was still several times higher than the rate prior to the application of the 20V. It took about seven weeks for the aging to decrease to the rate prior to the application of the 20V.

The aging of a second oscillator, with and without DC voltage on the resonator, is shown in the top half of Figure 11. The up/down and down/up frequency excursions are more visible in Figure 11.

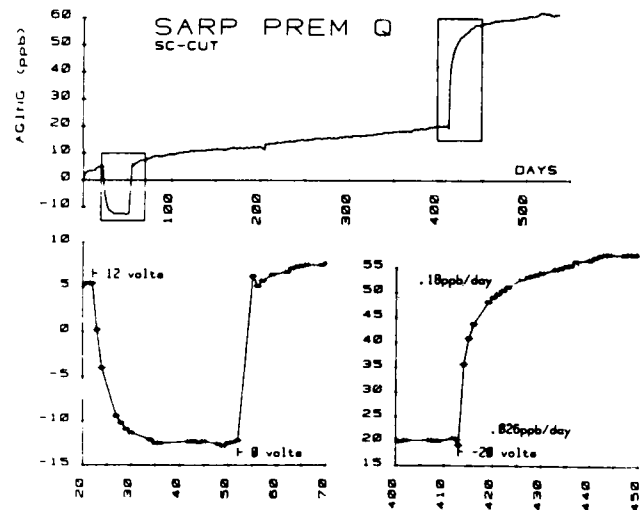
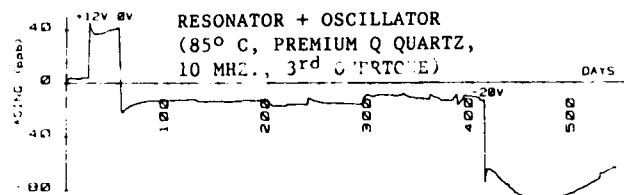


Figure 10. DC voltage-induced aging of a 10 MHz third overtone SC-cut resonator at 85°C.

### DC BIAS-INDUCED AGING



### "SWEEPING" CURRENT

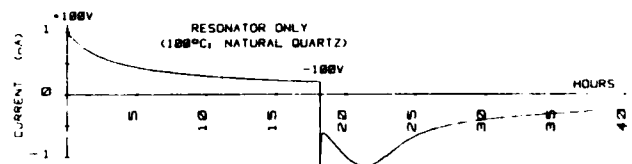


Figure 11. Similarity between the frequency change of an oscillator with a DC voltage on the resonator, and the "sweeping" current in a different resonator.

The lower part of Figure 11 shows the DC current measured through a resonator upon the application of a DC voltage. After 18 hours, the voltage was reversed. Although the resonator in the oscillator of the upper curve was made of Premium Q quartz whereas the resonator of the lower curve was made of natural quartz, and the other parameters and scales were also different, the similarity between the frequency vs. time and current vs. time subsequent to a reversal in voltage across the resonator is remarkable.

The current through the resonator was measured by means of a Keithley 619 electrometer while the blanks were mounted and bonded in an HC-6 type base. An HP611A high stability DC power supply was used for applying the DC voltages. The current varied greatly depending on the type of quartz material used. Typical currents at 100°C and 100V were  $1 \times 10^{-9}$ A for natural quartz,  $4 \times$

$10^{-11}$  A for Premium Q quartz, and less than  $2 \times 10^{-12}$  A for Premium Q swept quartz. The current between the pins of the base (after the blanks were removed) was  $4 \times 10^{-11}$  A at the same temperature and voltage. This current was subtracted from the total current to give the values quoted above.

The effect of 12V DC voltage on the aging of a 5 MHz 3rd overtone SC-cut resonator made of Premium Q swept quartz was also measured. Surprisingly, the results were nearly as dramatic as for the unswept quartz. The aging rate at the end of the initial 30 day period, with no externally applied DC voltage, was  $+2 \times 10^{-10}$  per day. The DC voltage reversed the aging rate so that even two weeks following the application of the DC voltage, the aging rate was still  $-2 \times 10^{-10}$  per day.

#### Discussion and Conclusion

Aging of the thermistor used to control oven temperature is a potential mechanism for apparent resonator aging. Properly selected, properly mounted and preconditioned thermistors have been found not to contribute significantly to the aging.

The results of investigations on the temperature dependence of aging are inconclusive. No "rule of thumb" exists for the temperature dependence. The sometimes heard folklore, that the aging rate doubles with every  $10^\circ\text{C}$  increase in temperature, and even the more general one, that the higher the temperature the higher the aging rate, are not correct. This study, as well as the one reported by Grata<sup>13</sup>, cast serious doubts on the value of accelerated aging tests for anything other than process control.

All of the resonators used in the temperature dependence investigations were mounted along the  $XX'$  and  $ZZ'$  ( $\phi = 0^\circ, 90^\circ, 180^\circ$  and  $270^\circ$ ) directions, i.e., none were mounted along the zero in-plane stress sensitivity directions<sup>14</sup>. It is therefore likely that stress relief in the mounting structure was a contributor to the aging results observed. At each aging temperature, some of the mounting stress relieved during the aging period. Since the mounting structure's thermal expansion coefficients are different from those of the quartz blanks, each time the aging temperature was changed, new mounting stresses were introduced. The experiment needs to be repeated with resonators that are mounted along the optimum mounting locations<sup>14</sup> and which experience minimal bending forces<sup>15</sup> as the temperature is changed.

The average aging of groups of similarly fabricated resonators have been found to vary approximately inversely with blank thickness, independent of overtone. Since the effects of contamination transfer, stress relief and some of the other known aging mechanisms also vary inversely with blank thickness, this result is not surprising.

A DC Voltage on the resonator can be a significant contributor to at least the initial aging of resonators. In the future, designers of high stability oscillators will need to design oscillator circuits so as to minimize the DC voltage on the resonator. That this has not generally been done in the past is evidenced by the fact that when high stability TCXO's from several different manufacturers were examined<sup>16</sup>, DC

voltages ranging from a fraction of a volt to about 4 V were found. (The circuit of the highest quality TXCO in the evaluation applied a DC voltage in excess of 2 V to the resonator and only one oscillator in the group applied less than 0.5V.). In principle, one can minimize the DC voltage without significantly lowering the effective Q of the resonator by placing a capacitor in series and a few megohm resistor in parallel with the resonator, or by coupling to the resonator inductively.

#### Acknowledgements

The authors thank Donald Boyce for his assistance with constructing parts of the aging test bed and with collecting some of the aging data, Maryann Nelson for her assistance with measuring some of the effects of DC voltages, and personnel of the General Electric Neutron Devices Department for their assistance with fabricating the ceramic flatpack enclosed resonators used in these experiments.

#### References

1. A. Warner, "Ultra-Precise Quartz Crystal Frequency Standards," IRE Trans. on Instrumentation, Vol 1-7, pp. 185-188, Dec. 1958
2. A. Warner, "Design and Performance of Ultraprecise 2.5 MHz Quartz Crystal Units," Bell System Technical Journal, Vol. 39, pp. 1193-1217, 1960
3. W.L. Smith, "An Ultra-Precise Standard of Frequency," US Army Contract No. DA-36-039 sc. - 73078, Final Report. Dec. 1960, AD 253034.
4. W.J. Spencer and R. L. Reynolds, "Characteristics of Frequency Control Devices for Satellite Environments," Symposium on Cleaning and Materials Processing for Electronics and Space Apparatus, ASTM Special Publication No. 342, American Society for Testing and Materials, pp. 155-163, 1962.
5. R. Sykes, W. L. Smith and W. J. Spencer, "Performance of Precision Quartz Crystal Controlled Frequency Generators," IRE Trans. on Instrumentation, Vol. 1-11, pp. 243-247, Dec. 1962
6. W. L. Smith and W. J. Spencer, "Quartz Crystal Controlled Oscillators," US Army Electronics Research and Developmental Laboratory Contract No. DA-36-039 sc. - 85373, Final Report, March 1963, AD 419717
7. E. Simon, "Long-Term Frequency Stability of Crystal Oscillators," Technical Report ECOM 2787, Dec. 1966, AD 647742
8. J. R. Vig, "Quartz Crystal Oscillator Stability," Proc. 4th Ann. Quartz Crystal Conf., Elect. Ind. Assoc., 2001 Eye St., N.W. Washington, DC 20006, pp. 125-173, 1982
9. H. W. Jackson, "Update on the Tactical Miniature Crystal Oscillator Program," Proc 36th Annual Symposium on Frequency Control, pp. 492-498, 1982.
10. S. D. Wood et al., "An Investigation of the Stability of Thermistors," Journal of Research of the National Bureau of Standards, Vol. 83, No. 3, May-June 1978

11. J. R. Vig, "Cleaning Quartz Crystal Resonators," Proc. 4th Annual Quartz Crystal Conference, Electronic Industries Assoc., 2001 Eve St., N. W. Washington, DC 20006, pp. 192-239, 1982
12. As reported by H. E. Wenden, "Ionic Diffusion and the Properties of Quartz-I. The Direct Current Resistivity," The American Mineralogist, Vol. 42, pp. 859-888, 1957
13. K. E. Grata, "Long Term Crystal Stability Study," Proc. 5th Quartz Crystal Conference, Electronic Industries Assoc., pp. 214-221, 1983
14. T. J. Lukaszek and A. Ballato, "Resonators for Severe Environments," Proc 33rd Annual Symposium on Frequency Control, pp. 311-321, 1979
15. E. D. Fletcher and A. J. Douglas, "A Comparison of the Effects of Bending Moments on the Vibration of AT and SC Cuts of Quartz," Proc. 33rd Annual Symposium on Frequency Control, pp. 346-350, 1979
16. V. Rosati and P. Thompson, "Further Results of Temperature Compensated Crystal Oscillator Testing," elsewhere in this Proceedings volume.

FORCE SENSING  
USING  
QUARTZ CRYSTAL FLEXURE RESONATORS

William C. Albert  
The Singer Company - Kearfott Division  
Fairfield, NJ 07006

### SUMMARY

The application of force sensitive quartz crystal resonators in the instrumentation field is gaining more acceptance year by year. Examples of such applications presently include accelerometers, pressure sensors and load cells. The advantages to be gained using this technology in instrumentation include: an inherent high resolution digital output, high dynamic range, low thermal sensitivity and low power. The unique properties of quartz crystal such as high Q, excellent mechanical and chemical stability, low thermal sensitivity and piezoelectric behavior are characteristics that have long been recognized and utilized by the frequency control industry. It is these very same unique properties that also make quartz crystal such an attractive material for instrumentation applications. It has been demonstrated that vibrating quartz crystal flexure beams exhibit a usable + or - 10 percent full-scale frequency change in response to tension and compression forces, respectively, due to "string-like" behavior.

The Appendix of this paper presents a modified Rayleigh method derivation of a vibrating beam resonant frequency along with the frequency/force coefficients. This derivation is then used in the paper to explain the force sensitive effect and how it is strongly influenced by length-to-thickness ratio of the beam geometry. The derivation is also used to demonstrate that the vibrating beam force sensing approach is about twenty-five times more sensitive than an edge-loaded shear mode force sensing crystal. The thermal sensitivities of both the bias frequency and the frequency/force scale factor are also presented along with a discussion of how these characteristics are related to the temperature coefficient of the quartz crystal elastic modulus. As an example, an accelerometer application is used to demonstrate how a dual beam push-pull mechanization can greatly reduce bias frequency thermal sensitivity as well as non-linear effects. The analysis also demonstrates that the frequency/force effect varies the motional capacitance of the classical crystal resonator equivalent circuit by up to + or - 20 percent.

### INTRODUCTION

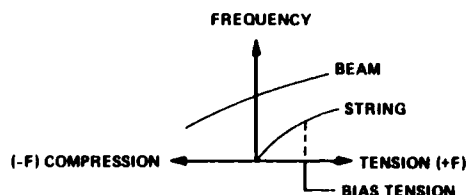


FIGURE 1  
FREQUENCY/FORCE EFFECTS

Like a taut string, the frequency of a vibrating flexure beam will increase with increasing tension (Figure 1). Unlike a string, a beam will also respond to compression by decreasing its frequency. In addition, a beam does not require a bias tension, the instability of which is a major error source of vibrating string instruments. There are two fundamental approaches to force sensing flexure crystals: the double ended tuning fork (double beam) approach, and the single beam approach. The advantages and disadvantages of each approach are discussed next.

### TUNING FORK (DOUBLE BEAM APPROACH)

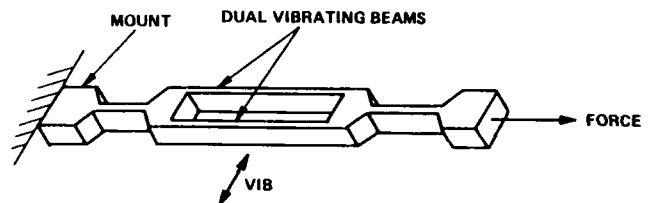


FIGURE 2  
DOUBLE BEAM APPROACH

An early double beam tuning fork configuration is illustrated in Figure 2.<sup>(1) (2)</sup> The tuning fork depends on the two beams vibrating 180° out of phase so that the moment and shear reactions at the beam roots cancel each other to maintain high Q. The advantage of this approach is that it is very simple and producible. The disadvantages are as follows:

- The two beams vibrate in a lock-in mode. Lock-in of two vibrating systems is a rather complicated non-linear behavior and to achieve proper operation the two beam geometries must be well matched.
- Another problem is uneven loading.<sup>(3)</sup> In order to maintain proper operation over the full-scale force measuring range, the force application mechanism is called upon to keep the two forces equal. Unequal loading or bending moments can cause irregularities in the force/frequency relationship. As data presented in a later section will illustrate, force sensing flexure crystals are capable of force sensing measurement thresholds on the order of  $10^{-7}$  to  $10^{-8}$  of full scale. Maintaining geometry matches and force application matches to this order is extremely difficult if not impossible.
- Because the applied force is shared by two beams, the frequency/force sensitivity is half that of the single beam approach for a given beam geometry.

## SINGLE BEAM APPROACH

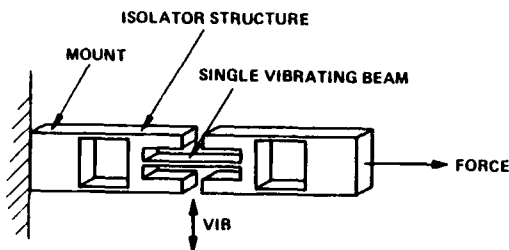


FIGURE 3  
SINGLE BEAM APPROACH

The problems associated with the dual beam tuning fork approach were overcome with the invention of the isolator structure illustrated in Figure 3.(4)(5) This single beam approach depends on the isolator structure to isolate the moment and shear reactions from the mount and, therefore, maintain high Q. Typical mounted Q's on the order of 50,000 are regularly obtained. The obvious advantages of this approach are the elimination of geometry matching and uneven loading problems. The disadvantages are that it is somewhat less producible than the dual beam approach and also requires a higher degree of design capability to achieve a structural design which is free of spurious resonances in the portion of the frequency spectrum which contains the beam resonant frequency. This paper is directed at the single beam approach.

## FREQUENCY/STRESS EFFECTS $(\Delta f/f)/\Delta s$

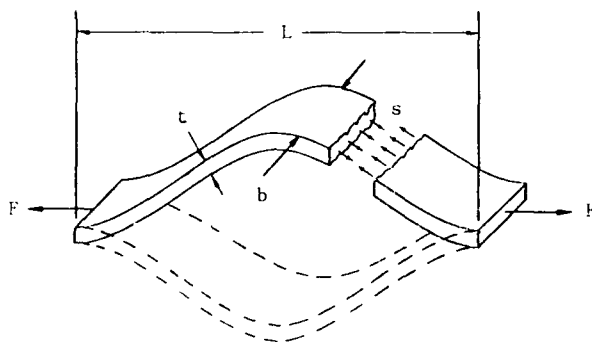


FIGURE 4  
FREQUENCY/STRESS EFFECT

Equation (1) is a rearrangement of just the first order frequency/force sensitivity term of Equation (17A) of the Appendix.

$$\frac{\Delta f}{f_0} = a_1 \frac{L^2}{Ebt^3} \Delta F = \frac{a_1}{E} \left( \frac{L}{t} \right)^2 \underbrace{\frac{\Delta F}{bt}}_{\text{STRESS } \Delta s} \quad (1)$$

Equation (1) can be further reduced to obtain the first order frequency/stress sensitivity.

$$\frac{\Delta f/f_0}{\Delta s} = \frac{a_1}{E} \left( \frac{L}{t} \right)^2 \quad (2)$$

Equation (2) indicates how this sensitivity is strongly influenced by the square of the length-to-thickness ratio and also indicates that highest sensitivity is obtained with a ribbon-like beam geometry where the plane of the ribbon is normal to the plane of the vibration. (Note that some current force sensitive flexure resonators that are fabricated using photo-etch techniques have ribbon-like beams but the ribbon plane is parallel to the plane of vibration. This results in a less favorable length-to-thickness ratio.) Typical t, L and b dimensions are 0.013, 0.44 and 0.10 cm, respectively, for a  $(L/t)^2$  of approximately 1100. It is this large magnification effect that results in the high frequency/stress sensitivity. A typical bias frequency of the example beam is 40 kHz and a full-scale frequency change is + or - 4 kHz in response to a + or - 9N axial force. Full-scale non-linearity is on the order of 6 percent.

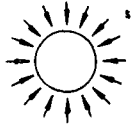

FORCE SENSING CRYSTAL APPROACH	FREQUENCY - STRESS SENSITIVITY $\frac{\Delta f/f_0}{\Delta s}$
 EDGE LOADED AT CUT	TYPICALLY $6 (10^{-7})/\text{psi}$
 VIBRATING BEAM	$a_1 \frac{1}{E} \left( \frac{L}{t} \right)^2$ TYPICALLY $150 (10^{-7})/\text{psi}$

FIGURE 5  
FREQUENCY/STRESS SENSITIVITY COMPARISON

In Figure 5 the vibrating beam approach is compared to a similar sensitivity of the edge-loaded AT cut approach(6)(7) and indicates that the beam approach is the more sensitive by a factor of up to twenty-five.

## TEMPERATURE SENSITIVITY

An instrument user is always concerned with the temperature sensitivity of bias and scale factor (Figure 6). For example purposes, a bias frequency of 40 kHz and a full-scale (FS) frequency change of + or - 4 kHz will be used. The bias frequency temperature sensitivity follows the classical flexure beam parabola where the temperature sensitivity is essentially zero at turnover and increases to about + or - 0.004 percent of FS/°C at 50°C away from turnover. The scale factor temperature sensitivity is an upward facing parabola where the temperature sensitivity is essentially zero at turnover and increases to about 4 ppm/°C at 50°C off turnover. These are very low temperature coefficients compared to other force sensing approaches based on strain sensing or magnetic principles.

# FORCE EFFECTS ON EQUIVALENT CIRCUIT

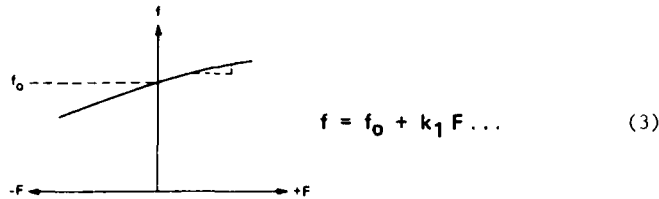
The derivation of the beam resonant frequency equations which include the force-frequency effects appears in the Appendix. The derivation presented in the Appendix is based on the vibrating beams acting as an exchange of kinetic and potential energy.

$$\Delta \text{KINETIC ENERGY} = \Delta \text{POTENTIAL ENERGY}$$

After a rearrangement and evaluation of the integrals of Equation (12A) of the Appendix, it can be shown that Equation (9) will result.

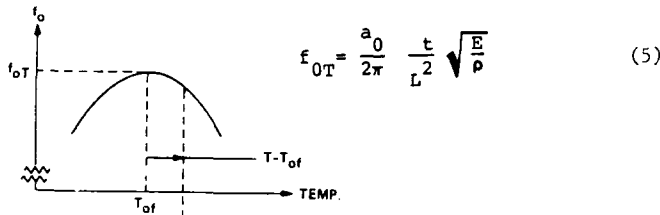
$$0.254 C_4^2 \omega^2 \rho b t L = 127 C_4^2 \frac{EI}{L^3} + 3.11 C_4^2 \frac{F}{L} \quad (9)$$

The C terms cancel to indicate that the effects being discussed are independent of vibration amplitude. The only variables remaining in Equation (8) are the resonant frequency ( $\omega$ ) and the axial force (F). The left is the inertial side of the equation, which is associated with the inductor of the classical crystal equivalent circuit and, after extracting  $\omega$ , is constant and, therefore, implies a constant inductor  $L_1$ . To the right are the two potential energy terms, one of which is variable and can even change sign because of compressive forces. Potential energy or energy storage effects are associated with the motional capacitance of the classical circuit; therefore,  $C_1$  varies with force (Figure 7). As previously stated, a force sensitive flexure crystal is capable of changing its frequency by a usable + or - 10 percent. Using the expression  $\omega = \sqrt{1/(L_1 C_1)}$  indicates that the motional capacitance changes approximately + or - 20 percent.



BIAS

$$f_0 = f_{0T} (1 + k_{Tf} (T - T_{0f})^2) \quad (4)$$



SCALE FACTOR

$$k_1 = k_{10T} (1 + k_{Tk} (T - T_{ok})^2) \quad (6)$$

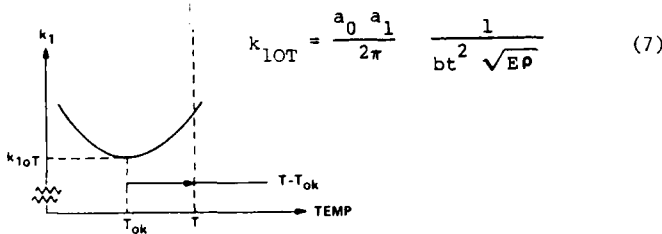


FIGURE 6  
TEMPERATURE SENSITIVITY

Typical turnover temperatures are anywhere from zero to 20°C depending on crystal cut, beam geometry and linear thermal sensitivity effects of material expansion and mounting and force application mechanisms. However, the shape of both the bias and scale factor temperature sensitivity curves is largely due to the second order temperature sensitivity of the elastic modulus. Equations (5) and (7) show that the elastic modulus is in the numerator of the bias ( $f_{0T}$ ) term and the denominator of the scale factor ( $k_{10T}$ ) term, both to the one-half power. This is the reason one curve faces down and the other faces up. The elastic modulus (E) is taken as the reciprocal of the compliance term ( $1/S_{11}$ ), and therefore, the temperature sensitivities,  $k_{Tf}$  and  $k_{Tk}$  [Equations (4) and (6)], of bias and scale factor are approximately equal to - or + 1/2 the second-order temperature sensitivity of the  $s_{11}$  coefficient<sup>(8)</sup> [Equation (8)] which agrees fairly well with observed results.

$$-k_{Tf} \approx k_{Tk} \approx 1/2 T s_{11}^{(2)} = 1/2 85.3 (10^{-9}) / (^\circ C)^2 \quad (8)$$

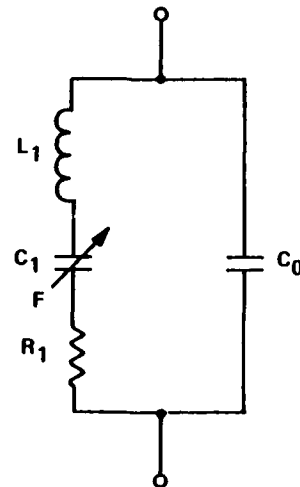


FIGURE 7  
FORCE EFFECT ON CLASSICAL  
CRYSTAL EQUIVALENT CIRCUIT

## VIBRATING BEAM ACCELEROMETER (VBA) APPLICATION

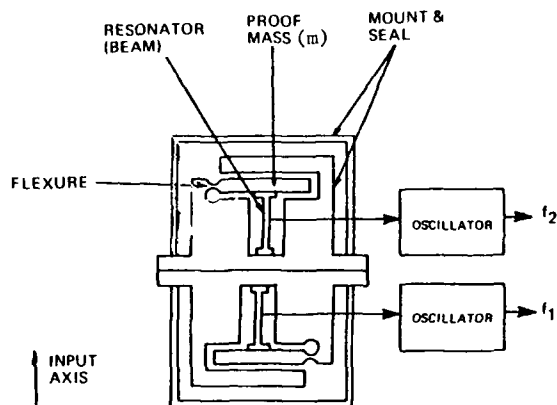


FIGURE 8  
VIBRATING BEAM ACCELEROMETER (VBA) SCHEMATIC

Figure 8 is an example of an accelerometer application (9) (10) which uses two back-to-back identical assemblies arranged so that an input acceleration places one beam in tension and one beam in compression (push-pull). The output signal is then taken as the difference frequency. Using an equation of the form of Equation (18A) of the Appendix, in which  $mg$  is substituted for  $F$ , the frequencies of the beam in tension, the beam in compression and the difference frequency are expressed as follows.

$$f_1 = f_{01} + k_{11} m_1 g + k_{21} (m_1 g)^2 + k_{31} (m_1 g)^3 \dots (10)$$

$$f_2 = f_{02} - k_{12} m_2 g + k_{22} (m_2 g)^2 - k_{31} (m_2 g)^3 \dots (11)$$

$$\begin{aligned} f_1 - f_2 = & f_{01} - f_{02} + (k_{11} m_1 + k_{12} m_2) g \\ & + (k_{21} m_1^2 - k_{22} m_2^2) g^2 \\ & + (k_{31} m_1^3 + k_{32} m_2^3) g^3 \dots (12) \end{aligned}$$

As Equation (12) indicates, working with the difference frequency achieves the following.

- The bias becomes nominally zero (actually, the  $f_{01}$  mismatch), and because of frequency differencing, the very important feature of common mode rejection of bias thermal effects, aging effects, and certain dynamic error sources is obtained.
- The scale factor becomes double since one frequency is increasing and the other is decreasing because of acceleration.
- Because of the squaring of a -1, we get a cancelling of the most troublesome non-linear  $g^2$  term.

### DIFFERENCE FREQUENCY EXAMPLE

The advantage of the dual beam approach is nicely illustrated in Figure 9, which is a 20-hour bias drift run where the upper curve shows the drifting of the two individual resonator frequencies from their nominal 40 kHz caused by cycling of the

laboratory temperature. Notice how nicely the two frequencies track with time. The bottom plot is the difference frequency over the same period of time. Notice that the amplitude has been reduced by a factor of about five. This factor of five, combined with the doubling of the scale factor, gives us an overall bias stability improvement of ten. In effect, doubling the size and complexity of the complete assembly has resulted in an order of magnitude performance improvement. One major division of Figure 9B is 0.2 mHz. Using this as a measuring threshold along with the 8 kHz (two beam) full-scale signal indicates a dynamic measuring range on the order of  $10^7$  to  $10^8$ . This is an example of the force measuring capability of the single beam approach.

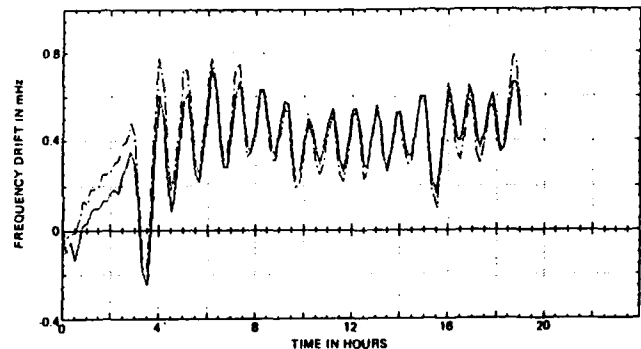


FIGURE 9A  
FREQUENCY DRIFT OF  
INDIVIDUAL BEAMS

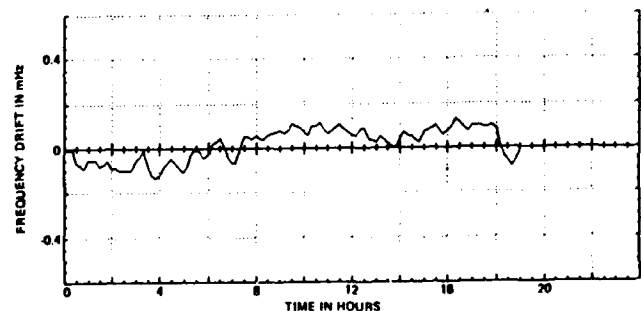


FIGURE 9B  
FREQUENCY DRIFT OF  
DIFFERENCE FREQUENCY

### CONCLUSIONS

The characteristics and capabilities of force sensing flexure crystals have been described. It is maturing technology which will have a performance-to-price ratio more favorable than most, if not all, other force sensing technologies. In addition, there is the advantage of an inherent high resolution digital output. Current applications of force flexure crystals include accelerometers (1) (9) (10), pressure transducers (3A) (5) and force sensors (load cells). (3) (11) (12)



# APPENDIX

## DERIVATION OF BEAM EQUATIONS

Figure 1A is an illustration of a fixed-fixed vibrating beam experiencing an axial force. Also illustrated are the linear displacement effect, the bending moment effect and the axial force effect on a typical  $\Delta x$  beam element. To determine the frequency-force effect a modified Rayleigh method will be used which follows these basic steps.

- 1 - Select a beam deflection shape.
- 2 - Assume harmonic motion.
- 3 - Determine the kinetic and potential energy changes.
- 4 - Assume conservation of energy and solve for the vibration frequency.

The following is an abbreviation of a more complete treatment(1A).

### BEAM DEFLECTION SHAPE

The deflection shape is determined from Equation (1A) and is the classical vibrating beam displacement equation found in the literature(2A).

$$y = C_1 \text{sh } qx + C_2 \text{ch } qx + C_3 \sin qx + C_4 \cos qx \quad (1A)$$

From the conditions of even symmetry ( $C_1 = C_3 = 0$ ) and the deflection and slope boundary conditions at the root ( $y = y' = 0$ ), Equation (1A) can be solved. The equations for the displacement, the slope and the curvature (also the bending moment distribution) along with the coefficients of the fundamental flexure vibration mode are presented in Table 1A for later use.

TABLE 1A  
DISPLACEMENT, SLOPE  
AND MOMENT DISTRIBUTIONS

$y = f(x)$ DISPLACEMENT	$y = C_4 \left[ \frac{C_2}{C_4} \text{ch } qx + \cos qx \right]$ (2A)
$y' = f'(x)$ SLOPE	$y' = C_4 q \left[ \frac{C_2}{C_4} \text{sh } qx \cdot \sin qx \right]$ (3A)
$y'' = f''(x)$ MOMENT DISTRIBUTION $M = EI y''$	$y'' = C_4 q^2 \left[ \frac{C_2}{C_4} \text{ch } qx \cdot \cos qx \right]$ (4A)

$$q = 4.73/L \quad C_2/C_4 = 0.133$$

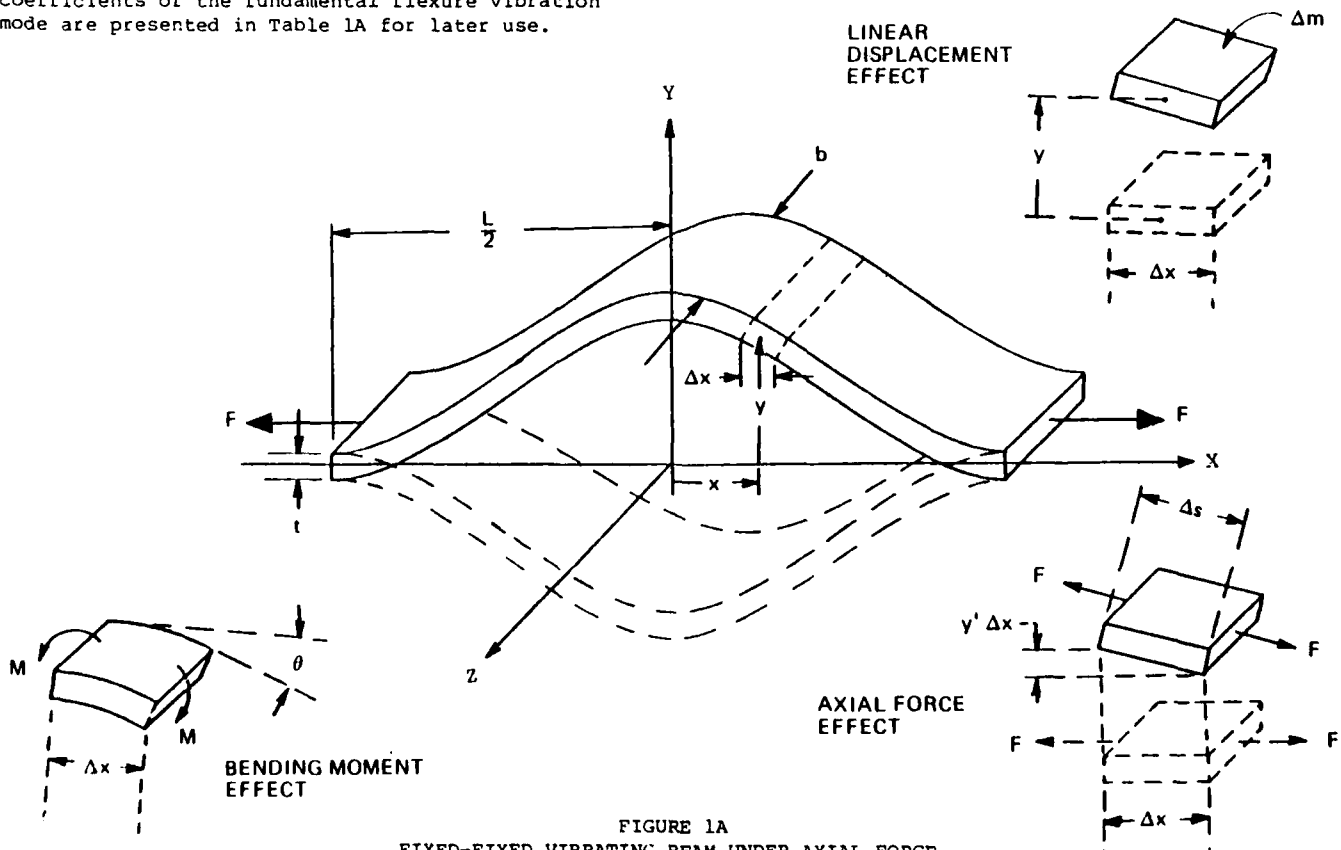


FIGURE 1A  
FIXED-FIXED VIBRATING BEAM UNDER AXIAL FORCE

### LINEAR KINETIC ENERGY ( $J_{KL}$ )

The linear kinetic energy is determined using the  $1/2$  mass  $\times$  velocity<sup>2</sup> relationship assuming the linear displacement of the  $\Delta x$  beam element experiences harmonic motion.

$$\Delta J_{KL} = 1/2 \quad m(\dot{y})^2 \quad (5A)$$

From Figure 1A,  $\Delta m = \rho b t \Delta x$  and for harmonic motion  $\dot{y} = y\omega$ . Making these substitutions into Equation (5A) results in the following equation for the total maximum linear kinetic energy of the beam.

$$J_{KL} = \omega^2 b t \rho \int_{x=0}^{L/2} y^2 dx \quad (6A)$$

### FLEXURE POTENTIAL ENERGY ( $J_{PM}$ )

The flexure potential energy is determined using the one-half the angular spring rate times the angular deflection<sup>2</sup> expression.

$$\Delta J_{PM} = 1/2 (\Delta M / \Delta \theta) \theta^2 \quad (7A)$$

From flexure theory,  $\theta = (M/EI) \Delta x$  and  $M = EI y''$ . Making these substitutions into Equation (7A) results in the following equation for the total flexure potential energy of the beam.

$$J_{PM} = EI \int_{x=0}^{L/2} (y'')^2 dx \quad (8A)$$

### AXIAL FORCE POTENTIAL ENERGY ( $J_{PF}$ )

Including the axial force effects is a second source of potential energy which modifies the standard Rayleigh method. The axial force potential energy is accounted for, using the force through distance relationship. The force is the axial tension (+F) or compression (-F), and the distance is the stretch of the beam element as it displaces. (It is assumed that the beam roots terminate in relatively massive structures that do not move.)

$$\Delta J_{PF} = F(\Delta s - \Delta x) \quad (9A)$$

Using some geometry and the binomial expansion, it can be shown that  $\Delta s = \Delta x [1 + 1/2 (y')^2 + \dots]$ . Making this substitution into Equation (9A) results in the following expression for the total axial force potential energy change in the beam caused by axial force effects. Note that this energy can be plus or minus.

$$J_{PF} = F \int_{x=0}^{L/2} (y')^2 dx \quad (10A)$$

### BEAM RESONANT FREQUENCY ( $\omega$ )

The beam resonant frequency as a function of axial force can now be solved for assuming conservation of energy.

$$J_{KL} = J_{PM} + J_{PF} \quad (11A)$$

Making the indicated substitutions results in Equation (12A).

$$\omega = \left[ \frac{EI \int (y'')^2 dx + F \int (y')^2 dx}{\rho b t \int y^2 dx} \right]^{1/2} \quad (12A)$$

When the integrals are evaluated<sup>(1A)</sup>, the following basic frequency-force relationship is obtained where  $\omega_0$  is the bias frequency determined for  $F = 0$  and  $S$  is a sensitivity term described by Equations (14A) and (15A).

$$\omega = \omega_0 (1 + SF)^{1/2} \quad (13A)$$

$$\omega_0 = a_0 \frac{t}{L^2} \sqrt{\frac{E}{\rho}} \quad (14A)$$

$$S = a_s \left( \frac{L^2}{E b t^3} \right) \quad (15A)$$

For the fundamental flexure mode,  $a_0 = 6.45$  and  $a_s = 0.294$ .<sup>(1A)</sup>

Equation (13A) indicates that to the extent of the assumptions made,  $\omega^2$  is linear with applied force.

Using the binomial expansion, Equation (13A) can also be expressed in the following convenient form.

$$\omega = \omega_0 \left( 1 + 1/2 SF - 1/8 S^2 F^2 + 1/16 S^3 F^3 \dots \right) \quad (16A)$$

After some substitution and rearrangement, Equation (16A) can also be expressed in another convenient form for direct comparison with alternate published solutions.<sup>(3A)</sup>

$$\omega = a_0 \frac{t}{L^2} \sqrt{\frac{E}{\rho}} \left[ 1 + a_1 \left( \frac{L^2}{E b t^3} \right) F + a_2 \left( \frac{L^2}{E b t^3} \right) F^2 + a_3 \left( \frac{L^2}{E b t^3} \right) F^3 \dots \right] \quad (17A)$$

For comparison purposes, coefficients  $a_0$  through  $a_3$  were evaluated for the fundamental mode<sup>(1A)</sup> and found to be 6.45, 0.147,  $-1.1(10^{-2})$  and  $1.6(10^{-3})$ , respectively. These values compare well with differential equation solution<sup>(3A)</sup> coefficients of 6.44, 0.148,  $-1.3(10^{-2})$  and  $1.9(10^{-3})$ .

Equation (14A) can also be expressed in terms of frequency ( $f$ ) and a power series of force ( $F$ ).

$$f = f_0 + k_1 F + k_2 F^2 + k_3 F^3 \dots \quad (18A)$$

The behavior of higher flexure modes as well as the influences of rotational inertia and shear effects are considered in Reference (1A).

TABLE 2A

## NOMENCLATURE

$a_0, a_1, a_2$  and  $a_3$  = Beam Power Series Coefficients

E	=	Elastic Modulus $7.8 (10^{11})$ dyne/cm <sup>2</sup> for quartz
F	=	Beam Axial Force (dynes)
f	=	Beam Vibrational Frequency in Hz ( $\omega/2\pi$ )
g	=	Acceleration in Earth Gravity multiples $\times 980\text{cm/s}^2$
I	=	Beam Cross Section Moment of Inertia (cm <sup>4</sup> )
$J_K$	=	Kinetic Energy (dyne cm)
$J_P$	=	Potential Energy (dyne cm)
(L,t,b)	=	Length, thickness, and width of beam (cm)
M	=	Bending Moment (dyne cm)
m	=	Mass (gm)
Q	=	Ratio of Maximum Energy to Energy Lost per Cycle $\times 2\pi$
sh, ch	=	Hyperbolic Sine and Cosine
T	=	Temperature (°C)
x	=	Location along Beam Length (cm)
y	=	Beam Displacement (cm)
$y'$	=	$dy/dx$ (beam slope)
$y''$	=	$d^2y/dx^2$ (beam curvature)
$\dot{y}$	=	Time Derivative of y
$\rho$	=	Density ( $2.65\text{ gm/cm}^3$ for quartz)
$\omega$	=	Beam Circular Frequency in rad/sec ( $2\pi f$ )

Other symbols as defined in various illustrations and text.

## REFERENCES

- (1) Serra, Norman R., "Technical Report on the Quartz Resonator Digital Accelerometer," Inertial Navigation: Systems and Components Proceedings, AGARD Conference, May 1968, (AGARD CP), pp. 487-516.
- (2) Erdley, H. F., U.S. Patent No. 3,238,789, Vibrating Bar Transducer, March 8, 1966.
- (3) Eer Nisse, E. P., and Paros, J. M., "Practical Consideration for Miniature Quartz Resonator Force Transducer," 37th Annual Symposium on Frequency Control, June 1-3, 1983, pp. 255-260.
- (4) Weisbord, Leon, U.S. Patent No. 3,470,400, Single Beam Force Transducer with Integral Mounting Isolation, September 30, 1969.

- (5) Paros, Jerome M., "Precision Digital Pressure Transducer," ISA Transactions, Vol. 12, No. 2, 1973, pp. 173-179.
- (6) Karrer, H. E. and Leach, J., "A Quartz Resonator Pressure Transducer," IEEE Transactions on Industrial Electronics and Control Instrumentation, Vol. IECI-16, No. 1, July 1969, pp. 44-50.
- (7) Michels and Perez, Physica, Vol. 17, May 1951, pp. 563-564.
- (8) Bechmann, R., Ballato, A. D., and Lukaszek, T. J., "Higher-Order Temperature Coefficients of the Elastic Stiffnesses and Compliances of the  $\alpha$ -Quartz," Proc. IRE, Vol. 50, 1962, 1812.
- (9) Albert, William C., "Vibrating Quartz Crystal Beam Accelerometer," ISA 28th International Instrumentation Symposium, Vol. 28, No. 1, 1982, pp. 33-44.
- (10) Albert, William C., and Weber, Raymond E., "Vibrating Beam Accelerometer for Strapdown Applications," IEEE 1982 Position Location and Navigation Symposium, pp. 319-322.
- (11) Hamilton, Brian J., "Magnetic Suspension: The Next Generation in Precision Pointing," Annual Rock Mountain Guidance and Control Conference, American Astronautical Society, January 30 to February 3, 1982.
- (12) Chuang, S. S., "Force Sensor Using Double-Ended Tuning Fork Quartz Crystals," 37th Annual Frequency Control Symposium, Philadelphia, June 1-3, 1983.

## APPENDIX REFERENCES

- (1A) Albert, William C., "Vibrating Quartz Crystal Beam Accelerometer," ISA 28th International Instrumentation Symposium, Vol. 28, No. 1, 1982, pp. 33-44.
- (2A) Curch, Austin A., Mechanical Vibration. John Wiley, New York, 1957, p. 202.
- (3A) Paros, Jerome M., "Precision Digital Pressure Transducer," ISA Transactions, Vol. 12, No. 2, 1973, pp. 173-179.

## STRESS-COMPENSATED QUARTZ RESONATORS HAVING ULTRA-LINEAR FREQUENCY-TEMPERATURE RESPONSES

Mitsuo Nakazawa,<sup>+</sup> Hideki Yamaguchi,<sup>\*</sup>  
Arthur Ballato,<sup>°</sup> and Theodore Lukaszek<sup>°</sup>

<sup>+</sup>Shinshu University, 500 Wakasato, Nagano-shi 380, Japan.

<sup>\*</sup>Miyota Seimitsu Co., 4107-5 Miyota, Nagano-ken 389-02, Japan.

<sup>°</sup>Electronics Technology and Devices Laboratory, USAERADCOM, Fort Monmouth, NJ 07703, USA.

### Abstract

The authors have conducted theoretical and experimental research on new quartz temperature sensors characterized by ultra-linear frequency-temperature responses and insensitivity to stresses. On the basis of the results of this research we can design stress-compensated quartz resonators with frequency-temperature responses superior to those of resonators employing older type quartz crystal cuts.

**Key Words:** quartz, resonators, frequency control, metrology, frequency vs. temperature, NLSC quartz cut, thermal transients, doubly rotated quartz cuts.

### Introduction

Precise and accurate temperature sensing is an important part of modern metrology. When temperature sensing was linked to frequency counting by Hammond, et al., in the mid-1960s, this aspect of metrology was advanced considerably. Within a decade came the introduction of stress- and temperature-transient-compensated quartz resonators. The virtues of each advance are considerable, but hitherto have not been consolidated. By searching for quartz orientations where stress compensation occurs simultaneously with linear temperature behavior, one is led to a family of cuts with enhanced temperature metrology potential.

The purpose of our research is to improve temperature sensitive quartz resonators which provide a frequency output extremely linear with respect to changes in temperature, and a further aim is to provide a temperature sensitive resonator compensated against the effects of stresses as well as against thermal transients and thermal hysteresis effects. We shall denote this sensor as the NLSC (NL stress compensated) cut. The NLSC cut makes the manufacture of sensors considerably easier, and has greater frequency-stability under stresses than the LC cut.

In this paper the NLSC cut sensor is discussed with reference to theoretical and experimental results, [1-8], and the optimum cut will be predicted.

### Theory

Suppose a thin quartz crystal plate whose electrical, mechanical and optical axes are defined in the directions of the  $X_1$ ,  $X_2$  and  $X_3$  axes, respectively, as shown in Fig. 1. We denote the direction normal to the main plane by polar coordinates  $(\phi, \theta)$ . Eigenfrequencies  $f$  of the quartz crystal plate are, in general, functions of temperature  $T$ . A Taylor expansion around reference temperature  $T_0$  is as follows:

$$f(T) \cong f(T_0) \left[ 1 + \alpha \Delta T + \beta/2 \Delta T^2 + \gamma/6 \Delta T^3 \right], \quad (1)$$

where  $\alpha$ ,  $\beta$ , and  $\gamma$  are first-, second- and third-order temperature coefficients of frequency, respectively, and  $\Delta T = T - T_0$ .

In the thin quartz crystal plate, the frequency equation for the thickness-vibration mode is solved as

$$f = \frac{y_0}{2y_0} (\bar{\kappa}/\rho)^{1/2}, \quad (q=1,3, \dots), \quad (2)$$

where  $\rho$  and  $y_0$  are the mass density and the thickness of the crystal plate, respectively, and  $\bar{\kappa}$  represents eigenvalues and solutions of the following equation:

$$\left| C_{ijkl} - \bar{\kappa} \delta_{ij} \delta_{kl} \right| = 0, \quad (3)$$

and

$$C_{ijkl} = C_{ijkl}^E + (m_j e_{sqj}^S m_l)^{-1} * (e_{hij} m_h) * (m_h e_{hkl}), \quad (4)$$

$C_{ijkl}^E$  = the elastic stiffness constants in a constant electric field,

$e_{hij}$  = the piezoelectric constants,

$\epsilon_{sqj}^S$  = the dielectric constants at constant strain,

$\delta_{ij}$  = Kronecker's delta,

$m_j, m_l$  = the  $j$ th or  $l$ th component of unit normal vector perpendicular to the plate plane.

$y_0$ ,  $\rho$  and  $\bar{\kappa}$  of the quartz crystal plate are in general functions of temperature  $T$ , and these temperature coefficients for  $y_0$  and  $\bar{\kappa}$  depend on the azimuth  $\phi$  and colatitude  $\theta$  in Fig. 1.

With a suitable choice of the angles  $\phi$  and  $\theta$  in equations (1) to (4), it is found that the following relationships may be obtained:

$$\alpha \neq 0; \quad \beta = 0; \quad \gamma \cong 0. \quad (5)$$

From equations (1) and (5) it can easily be seen that the frequency-temperature characteristics show a linear relationship. We solve the simultaneous equations given above by substituting the elastic stiffness constants, piezoelectric constants, dielectric constants, mass density and their temperature coefficients etc., into equations (4), (3) and (2) sequentially [9,10]. Fig. 2 shows the loci of  $\alpha = 0$ ,  $\beta = 0$ , and also the zero frequency-stress coefficients for the thickness  $c$  mode of the quartz crystal plates as functions of the polar angles  $\phi$  and  $\theta$  in Fig. 1. In this figure it is seen that

the AT, FC, IT and SC cut resonators invented in the past as having zero frequency-temperature coefficients fall on the locus curve of  $\alpha = 0$ , and that the LC cut, which has been developed as a thermometric quartz resonator, falls in the vicinity of the locus curve of  $\beta = 0$  [11].

As is well known, the LC cut comprises a cut located at an orientation where the second- and the third- order frequency-temperature coefficients are substantially equal to zero or at least negligibly small, while the first-order frequency-temperature coefficient is not zero. The doubly rotated LC cut, however, is difficult to manufacture because the two orientation angles  $\phi$  and  $\theta$  are such that the cut is not located near X-ray planes of any reasonable strength, and is uncompensated either against any in-plane stresses, such as electrode stresses, leading to a component of aging, or against thermal transients and thermal hysteresis, etc. [12].

Accordingly, it is highly desirable to develop a new quartz temperature sensor with the following features: (1) Improved temperature sensitivity, providing a frequency output extremely linear with respect to changes in temperature, and (2) Compensation against the effects of stresses as well as against thermal transients and thermal hysteresis effects.

In order to satisfy these requirements, the following cuts in the NLSC family have been developed: Doubly rotated cuts whose orientations are defined in terms of the polar angles  $\phi$  and  $\theta$ , which angles lie on the locus where the second-order frequency-temperature coefficients are zero between the angles  $\phi = 10^\circ \pm 2^\circ$  and  $\theta = 110^\circ \pm 5^\circ$ . These cuts fall close to, or on, the locus of zero coefficients of stress, as shown in Fig. 3. In Fig. 3 it can be seen that Sinha's locus [3] of zero stress coefficient of frequency and our locus of zero temperature coefficient of frequency, i.e.,  $\beta = 0$ , are expressed, in the range of the angles  $\phi = 10^\circ \pm 2^\circ$  and

$$\theta = 110^\circ \pm 5^\circ, \text{ as } \phi = a\theta + b, \quad (6)$$

$$\text{where } a = -1.5200 \text{ and } b = 1.8126 \times 10^2 \text{ degrees, and } \phi = c\theta + d, \quad (7)$$

$$\text{where } c = -5.7140 \times 10^{-2} \text{ and } d = 1.6395 \times 10^1 \text{ degrees.}$$

These equations are solved as

$$\left. \begin{aligned} \phi_0 &= (a d - b c) / (a - c) \cong 9.96^\circ, \\ \text{and } \theta_0 &= (d - b) / (a - c) \cong 112.70^\circ. \end{aligned} \right\} \quad (8)$$

Table 1 shows the calculated physical features of the NLSC family cuts operating on the thickness-shear c mode in the vicinity of the angles  $\phi_0$  and  $\theta_0$ . In Fig. 3 the region enclosed by two curves shows the cut angles exhibiting the linear frequency-temperature responses. From these results we can predict the stress-compensated quartz cuts with ultra-linear frequency-temperature responses in the vicinity of the angles  $\phi_0$  and  $\theta_0$ .

### Experiments

1) Resonance frequency vs. temperature characteristics.

The circular NLSC cut resonator plate used in these experiments is cut at the angles  $\phi = 9.2^\circ$  and  $\theta = 113.2^\circ$ , as defined in Fig. 1 and to 0.165 mm thickness and 7.40 mm diameter. The electrodes

are of silver evaporation applied to a chrome adhesion film in the ordinary way. The resonator is kept in  $N_2$  gas in the 8U- type holder. In this resonator the resonance frequency responses for the a, b and c modes are measured as shown in Fig. 4. As can be seen in the figure, the piezoelectric coupling coefficient of the c mode is smaller than that of the b mode. Values of piezoelectric coupling for thickness excitation (TE) and lateral excitation (LE) for the three thickness modes of the nominal NLSC cut at  $\phi_0/\theta_0$  are given in Table 2. The NLSC cut resonator is at first kept for about 4 hours in an oven filled with liquid  $N_2$ . After confirming the steady state, we begin to measure the resonance frequency vs. temperature characteristics by controlling heater temperature using a copper-constantin thermocouple in the oven. Fig. 5 shows the calculated resonance frequency vs. temperature characteristics for the NLSC cut, while Fig. 6 shows the measured resonance frequency vs. temperature characteristics for the same cut operating on the fundamental c mode in the  $-190^\circ\text{C}$  to  $290^\circ\text{C}$  temperature range. The resonance frequency is about 10.447578 MHz at  $25^\circ\text{C}$ . These characteristics in Figs. 5 and 6 coincide well with each other. From Fig. 6 it is seen that the first-order frequency-temperature coefficient  $\alpha$  is found to be about 13.7 ppm/ $^\circ\text{C}$  by using the least-squares method. The theoretical value is about 14.4 ppm/ $^\circ\text{C}$ , as given in Table 1 for bi-plano plates.

2) Oscillation frequency vs. temperature characteristics.

Fig. 7 shows the oscillation circuits used. The NLSC crystal used in this oscillator experiment is cut at the same angles described before, to 0.28 mm thickness and 7.40 mm diameter. This particular NLSC cut is made into a bi-convex-lens shape of 120 mm radii of curvature. Fig. 8 shows the oscillation frequency vs. temperature characteristics for this NLSC cut. The oscillation frequency is 6.195098 MHz at  $25^\circ\text{C}$ . From the figure the first-order frequency-temperature coefficient  $\alpha$  is found to be about 15.10 ppm/ $^\circ\text{C}$  by using the least-squares method. There is a small difference between the resonance and oscillation frequency responses vs. temperature with respect to  $\alpha$ . It is felt that this difference comes from the difference in shapes of the NLSC cuts used in the experiments, and possibly at least partially from the differences between the conditions between the experiments; the resonance experiment is open-loop, at, or near the zero reactance point  $f_R$ , whereas the oscillation frequency is closed-loop at a load reactance point  $f_L$ . The temperature coefficient difference between the two points involves the temperature coefficient of the piezoelectric constant  $k_m$  for the mode.

3) Thermal time constants.

It is of interest to know the thermal time constant of the NLSC cut sensor [13]. Fig. 9 shows an experimental circuit arrangement with respect to measurements of thermal transients. Fig. 10 shows the thermal shock responses for an NLSC cut sensor operating on the fundamental c mode. The oscillation frequency is about 6.195 MHz at  $25^\circ\text{C}$ . The responses are observed for  $0^\circ\text{C} \rightleftharpoons 30^\circ\text{C}$  rapid temperature changes. The NLSC cut sensor is at first immersed in ice water, then in  $30^\circ\text{C}$  water, and vice versa. In the figure we see that the thermal time constant of the NLSC cut in the  $0^\circ$  to  $30^\circ\text{C}$  thermal shock tests is given as  $\tau_c = 11$  s. Similarly, Fig. 11 shows other thermal shock responses for the same NLSC cut temperature sensor. It is seen that the thermal time constant measurements

are given as  $\tau_c = 7.5$  s and 8 s for the  $70^\circ\text{C} \rightleftharpoons 100^\circ\text{C}$  and  $100^\circ\text{C} \rightleftharpoons 70^\circ\text{C}$  thermal shock tests, respectively, as shown in Fig. 11.

In general, the thermal time constant is found to be

$$\tau = \rho C y_0^2 / K, \quad (9)$$

where  $\rho$ ,  $C$ ,  $K$  and  $y_0$  are the mass density, specific heat, thermal conductivity and thickness for the crystal, respectively. Hence, from equation (9) we see that the thermal time constants of the NLSC cut temperature sensors can be further improved by changes in dimensioning and packaging.

### Conclusions

It is found that from our theoretical and experimental research that materialization of the stress-compensated quartz temperature sensors with ultralinear frequency-temperature responses can be precisely predicted, thus helping to pave the way for the design of temperature sensing systems.

### Acknowledgments

This work was supported by a donation from the Miyota Seimitsu Co. The authors wish to thank Messrs. Tadashi Takemae, Akira Miyahara, Naonori Izuka, Shigekazu Kobayashi, and Hideaki Ito; and Professor Kiyoshi Matsuyama of Shinshu University, for their help and encouragement. The authors also wish to thank Professors Makoto Ichikawa and Hiroshi Takahashi of Shinshu University, and Dr. Hitohiro Fukuyo of Chiba University for their support and suggestions.

### References

- 1) V.E. Bottom: Note on the anomalous thermal effect in quartz oscillator plates, *Amer. Mineralogist*, Vol. 32, 1947, pp. 590-591.
- 2) E. P. EerNisse: Calculations on the stress compensated (SC-cut) quartz resonator, *Proc. 30th Annual Freq. Control Symp.*, 1976, pp. 8-11.
- 3) B. Sinha: Stress compensated orientation for thickness-shear quartz resonators, *Proc. 35th Annual Freq. Control Symp.*, 1981, pp. 213-221.
- 4) M. Nakazawa, H. Ito, A. Usui, A. Ballato, and T. Lukaszek: New quartz resonators with precision frequency linearity over a wide temperature range, *Proc. 36th Annual Freq. Control Symp.*, 1982, pp. 290-296.
- 5) M. Nakazawa, N. Izuka, A. Ballato, and T. Lukaszek: A study of quartz crystal temperature sensors, 12th Special Committee on the Application Technology Investigation for the Precision Frequency, *IEEEJ*, No. 12-3, 1983, pp. 1-6.
- 6) A. Ballato and M. Mizan: Simplified expressions for the stress-frequency coefficients of quartz plates, *IEEE Trans. Sonics Ultrason.*, Vol. SU-31, No. 1, 1984, pp. 11-18.
- 7) W. L. Smith and W. J. Spencer: Quartz crystal thermometer for measuring temperature deviations in the  $10^{-3}$  to  $10^{-6}$  °C range, *Rev. Sci. Instrum.*, Vol. 34, 1963, pp. 268-270.
- 8) D. C. Hammond, C. A. Adams, and P. Schmidt: A linear, quartz-crystal, temperature-sensing element, *ISA Trans.*, Vol. 4, 1965, pp. 349-354.
- 9) I. Koga, M. Aruga, and Y. Yoshinaka: Theory of plane elastic waves in a piezoelectric crystalline medium and determination of elastic and piezoelectric constants of quartz, *Phys. Rev.*, Vol. 109, 1958, pp. 1467-1473.
- 10) R. Bechmann, A. Ballato, and T. Lukaszek: Frequency-temperature characteristics of quartz resonators derived from the temperature behavior of the elastic constants, 16th Annual Freq. Control Symp., 1962, pp. 77-109.
- 11) A. Ballato: *Physical Acoustics*, (W. P. Mason and R. N. Thurston, editors), Academic Press, Inc., N.Y., London, Vol. 13, chapter 5, 1977, pp. 115-181.
- 12) T. J. Lukaszek and A. Ballato: Resonators for severe environments, *Proc. 32nd Annual Freq. Control Symp.*, 1978, pp. 311-321.
- 13) J. R. Vig, R. L. Filler, and J. A. Kosinski: SC-cut resonators for temperature compensated oscillators, *Proc. 36th Annual Freq. Control Symp.* 1982, pp. 181-186.

TABLE 1  
CALCULATED PHYSICAL FEATURES OF THE NLSC FAMILY CUTS  
OPERATING ON THE THICKNESS-SHEAR c MODE.

No.	$\phi/\theta$ (deg.)	$f \cdot y_0$ (MHz-mm)	$v$ ( $10^3$ m/s)	$\alpha$ ( $10^{-5}/^\circ\text{C}$ )	$\theta/2$ ( $10^{-10}/(^\circ\text{C})^2$ )	$\gamma/6$ ( $10^{-11}/(^\circ\text{C})^3$ )
1	10/110	1.6932	3.3864	1.7453	-2.8086	4.4257
2	10/111	1.6993	3.3986	1.6869	-1.4006	4.2048
3	10/112	1.7058	3.4116	1.6274	-0.1776	3.9473
4	10/113	1.7127	3.4253	1.5672	0.9203	3.6514
5	9.2/113.2	1.7198	3.4396	1.4397	-11.0074	3.3085
6	9.96/112.7	1.7108	3.4217	1.5794	0.0142	3.7309
7	10/112.5	1.7092	3.4184	1.5974	0.3835	3.8041
8	10.25/112.5	1.7076	3.4153	1.6350	3.9972	3.8859

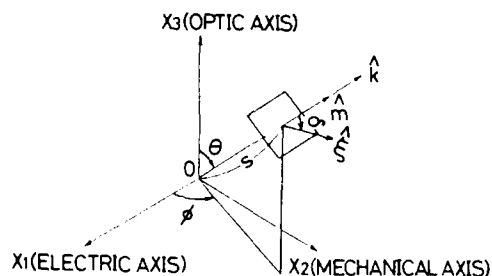


Fig.1 A thin quartz crystal plate.

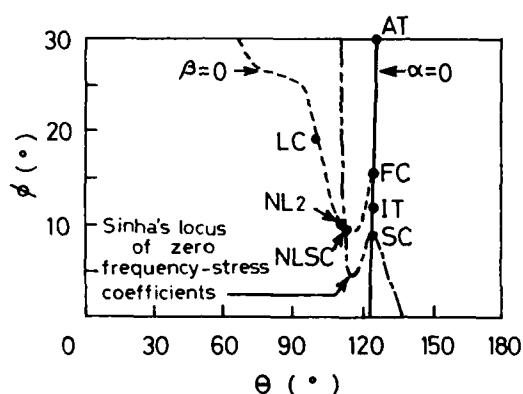


Fig.2 Loci of  $\alpha=0$  and  $\beta=0$  for the thickness c mode of quartz crystal plates as functions of the polar angles  $\phi$  and  $\theta$  in Fig.1. Sinha's locus of zero stress coefficient is also shown.

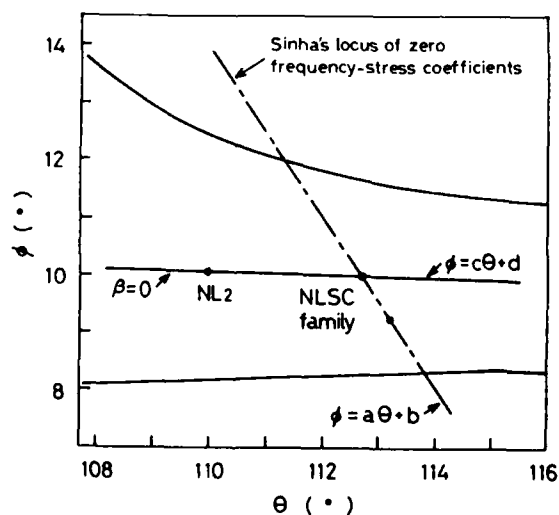


Fig.3 Our temperature compensated orientations ( $\phi=c\theta + d$  for  $\beta=0$ ) and Sinha's stress compensated orientations ( $\phi=a\theta + b$ ) in the vicinity of the angles  $\phi=10^\circ \pm 2^\circ$  and  $\theta=110^\circ \pm 5^\circ$ .

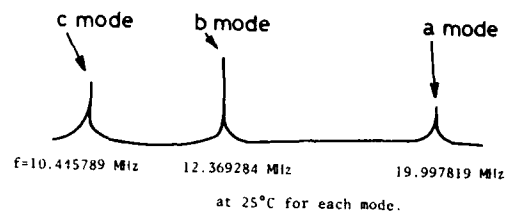


Fig.4 Resonance frequency responses for the NLSC cut operating on the thickness vibration modes.

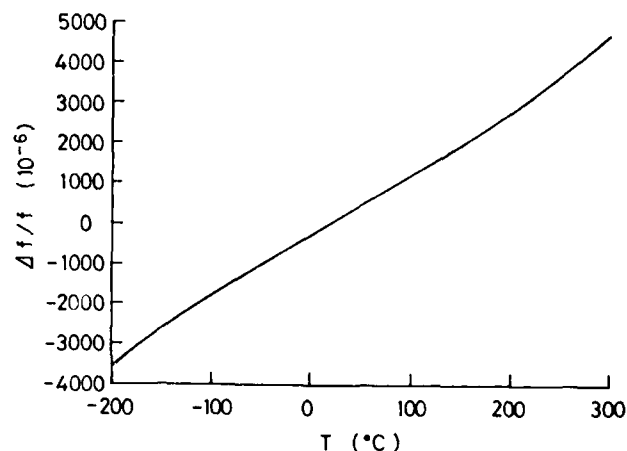


Fig.5 Calculated resonance frequency vs. temperature characteristics for the NLSC cut operating on the fundamental c mode.

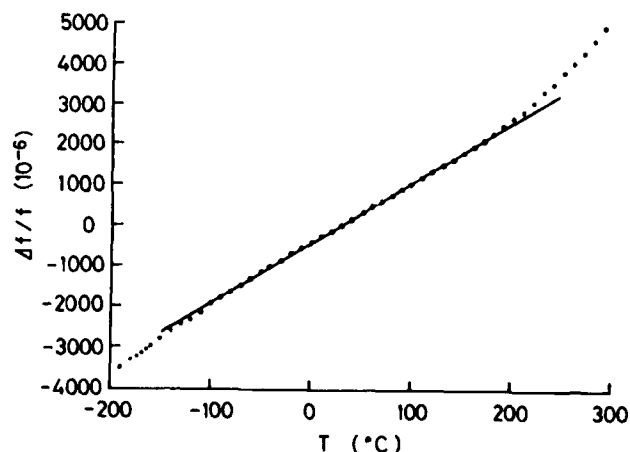


Fig.6 Measured resonance frequency vs. temperature characteristics for the NLSC cut operating on the fundamental c mode.

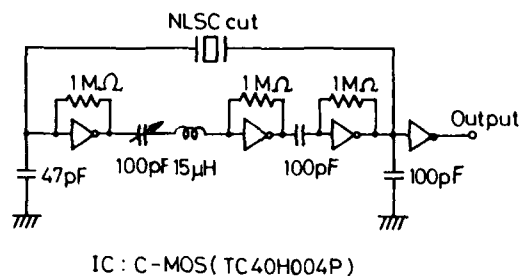


Fig.7 NLSC cut quartz oscillator circuits.

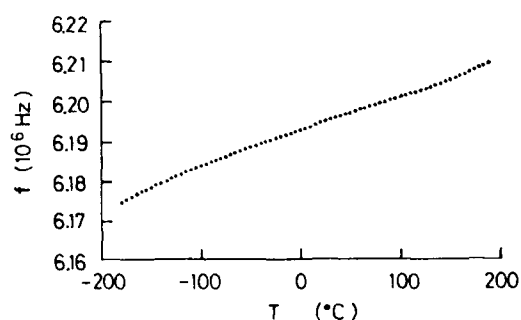


Fig.8 Oscillation frequency vs. temperature characteristics for the NLSC cut unit.

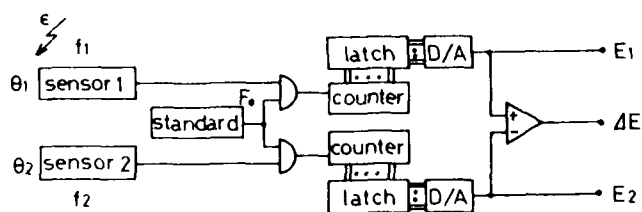


Fig.9 An experimental circuit arrangement for the measurements of the thermal time constants.

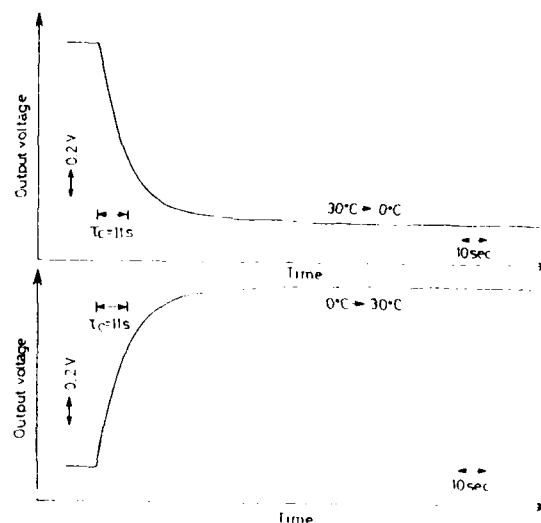


Fig.10 Thermal shock responses for an NLSC cut quartz temperature sensor operating on the fundamental c mode in the 0°C ⇌ 30°C temperature transients ( $f \approx 6.195$  MHz at 25°C).

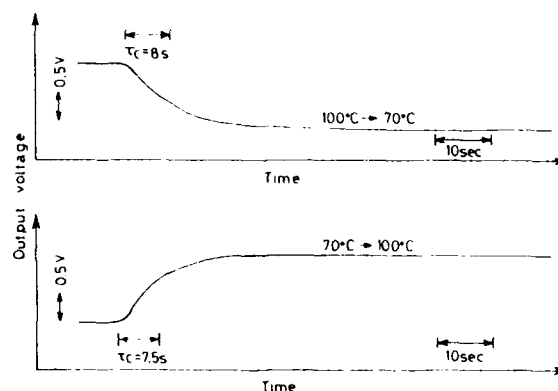


Fig.11 Thermal shock responses for an NLSC cut quartz temperature sensor operating on the fundamental c mode in the 70°C ⇌ 100°C temperature transients ( $f \approx 6.195$  MHz at 25°C).

Table 2

THERMOMETRIC QUARTZ CUTS							
$\hat{\phi} = 30^{\circ} - \phi$ ; $\hat{\theta} = \theta - 90^{\circ}$ .							
$\hat{\phi}$	$\hat{\theta}$	m	$N_m$	$k_m$	$k_m$ (%)		
degrees			MHz-mm	%	$\psi = 0^{\circ}$	$\psi = 90^{\circ}$	
20.	20.	a	3.264	4.4	6.0	1.6	} NLSC
		b	2.090	7.5	2.0	2.8	
		c	1.695	4.2	10.5	1.6	
11.17	9.39	a	3.165	3.2	7.7	0.5	} LC
		b	2.140	7.6	0.1	1.3	
		c	1.727	9.2	7.8	1.6	



# EXTENDED PRESSURE AND TEMPERATURE OPERATION OF BT-CUT PRESSURE TRANSDUCERS

Gwen Kaitz  
Hewlett Packard Co.  
5301 Stevens Creek Blvd.  
Santa Clara, California 95050

## ABSTRACT

Improved performance of the BT cut quartz pressure transducer at extended pressures and temperatures has been achieved through sweeping. Previously, high impurity concentrations within the quartz resonator resulted in exponential resistance increases at temperatures beyond 150°C, thus rendering it inoperable above this temperature. By sweeping natural quartz, the impurity ions are driven out and replaced by hydrogen ions which bond with the oxygen atoms to form stable hydroxide molecules. The resistance vs. temperature slope of the transducer is markedly decreased and stays well below 200 ohms up to and including 225°C. The resistance vs. pressure slope is also flatter as the temperature is increased, staying below 20 ohms at all temperatures and pressures.

Hysteresis test results have shown that the homogeneity of the unit is important from the standpoint of impurity levels. Differences in natural quartz due to different levels of impurities result in higher hysteresis at the high ends.

## INTRODUCTION

Hewlett Packard has fabricated 5 MHz BT cut pressure transducers from quartz crystal since 1972. The pressure vs. frequency characteristic which this crystal exhibits when a hydrostatic pressure is applied radially to the resonator body makes it a very useful and accurate pressure measuring device. These transducers are built into pressure probes (figure 1) which are widely used in the petroleum industry for the logging of oil wells and to evaluate reservoir performance. They also have application in making pressure measurements in gas wells. Presently this probe has a maximum operating range of 150°C and 11K psi.

In light of market demands, the need for a pressure probe which is operational at higher temperatures and pressures has become increasingly important. The current probe is inoperable at extended temperatures because the quartz pressure transducer exhibits exponential increases in resistance above 150°C. We have developed an extended range pressure transducer which is operational to 200°C and 15K psi. This transducer utilizes the same design and configuration as the present transducer but it is processed from swept natural quartz, whereas, the current units are fabricated from unswept natural quartz. Unswept natural quartz contains high levels of impurities, mostly alkali ions, which are abundant in the environment. Such ions are found interstitially in the lattice structure

since they typically don't bond to the other ions, but instead provide a charge balance for alumina centers within the quartz. Above 150°C, these ions, given thermal energy, are mobilized in the lattice. As a result of this ionic mobility, the series resistance of the unit increases dramatically, thus rendering the unit inoperable at temperatures greater than 150°C.

By sweeping the quartz before processing it, the impurity ions are driven from the lattice along channels parallel to the z-axis (figure 2). In turn, the series resistance of the unit is lowered significantly at the higher temperatures.

## SWEEPING PROCESS

Natural quartz crystals are first cut into rectangular sections whose faces are at 45 degrees relative to the z-axis. These units are inspected for inclusions, fractures, and defects which may inhibit the transport of ions along the channels in the z direction.

Units are then irradiated with gamma radiation. This radiation of the quartz leaves it in varying shades of darkness. The degree of darkness depends upon the concentration and type of impurity ions within each section. There appear to be two distinguishable colors after irradiation, one being yellow in nature, similar to citrine quartz, and the other deep grey, similar to a smokey quartz.

Three unswept units which were relatively light in color compared to the other units after irradiation were chosen for direct processing without sweeping in an attempt to establish a correlation between the degree of darkening and the resistance of the completed unit. After processing, resistances were found to be greater than 500 ohms at 200°C for all three units. This is typical of the unswept units; hence, it appears that no such correlation exists, and any darkening of the resonator results in high resistance units. Therefore, no further selection process was used after the initial inspection for defects and all the irradiated units were suitable for sweeping. The saw cut surfaces were plated with chrome/gold electrodes in a right angle configuration in order to establish an electric field in the z direction (figure 3).

Electrical contact with the electrodes was then made through spring loaded steel plates on two of the surfaces (figure 3). The chrome beneath the plating prohibited

diffusion into the quartz; whereas, gold plating alone diffused badly.

The sweeping was done in air in a forced convection furnace (figure 4). The temperature was increased over an eight hour period to 450°C, where it was maintained for approximately five days. Heating too rapidly resulted in thermal shock and fracturing of the units. An electric field of 1000 V/cm was established along the z axis. The current was continuously monitored as a function of time. The current decreased rapidly over the first day or so, then reached a near steady state condition. The voltage was then increased another 1000 V to determine if sweeping was indeed complete. If the current again reached a steady state, sweeping was assumed to be complete (figure 7). The temperature was then decreased over another eight hour period while the electric field remained to insure that no diffusion of the removed impurities back into the quartz occurred.

Upon completion of sweeping, the units were re-irradiated with gamma radiation to determine the degree to which they had been swept. If thoroughly swept, the units appeared completely clear. If not, darkening remained in part of the unit (figure 6).

The units were then processed into transducers for testing.

#### RESISTANCE vs. TEMPERATURE TESTS

Resistance vs. temperature tests were run on several fabricated swept transducers and unswept transducers up to and including 200°C. For the swept transducers, results showed that resistances stay well below 200 ohms over the entire temperature range.

In fig. 8, the dashed line represents a typical swept extended range unit's resistance vs. temperature curve. The solid line is representative of the resistance vs. temperature characteristics of the present unswept transducer. It is readily apparent that the resistance of the unswept unit is well above 200 ohms before reaching 200°C; whereas, the resistance of the swept unit remains well below 200 ohms and is relatively flat over the entire temperature range. 100% of the completely swept units tested exhibited low resistance at the higher temperatures.

#### RESISTANCE vs. PRESSURE TESTS

Resistance vs. pressure tests were also conducted on several transducers to determine if pressure induced activity dips existed at the higher pressures. Pressures were varied from atmospheric to 22.5K psi at constant temperatures ranging from room temperature to 200°C. Resistances stayed well below 200 ohms over the entire pressure range at all temperatures (figure 9). The resistance vs. pressure slope decreases as the temperature increases. This behavior is consistent with the fact that an activity dip has been found around 0°C.

#### HYSTERESIS TESTING

Results from calibration testing of the assembled probe indicate that the hysteresis increases considerably with extended temperature and pressure range (figure 11). Hysteresis above 150°C and 11K psi is much larger than below these limits. This hysteresis manifests itself as a frequency offset as pressure is increased and then decreased at constant temperatures.

Figure 10 illustrates a typical hysteresis curve for a processed swept transducer at temperatures up to and including 200°C. The maximum hysteresis was approximately 4 psi, four times greater than at 11K psi and 150°C.

Improvements in hysteresis have been made by extensively cycling the finished transducer before calibration. In almost all instances, hysteresis improved up to 50%. The cycling relaxes the residual stresses incurred during processing of the unit. It is also important that the units be completely swept to insure homogeneity throughout the unit. Impurities in the lattice structure can cause stresses and strains, both shear and direct. They also result in different temperature expansion properties within the unit.

#### CONCLUSION

Sweeping of natural quartz has succeeded in lowering the resistance of BT cut crystals at extended pressures and temperatures. Fabricated pressure transducers are now operational up to and including 200°C and 15K psi. Resistance of these units stays well below 200 ohms and is relatively constant throughout the entire temperature range. No activity dips exist over the pressure range up to and including 22.5K psi. Hysteresis, however, increases considerably as temperature and pressure are increased. Work to improve the hysteresis further is presently underway.

#### REFERENCES

1. Leach, J., "5 MHZ BT CUT RESONATORS," Proc. 24th AFCS, pp. 117-125, 1970.

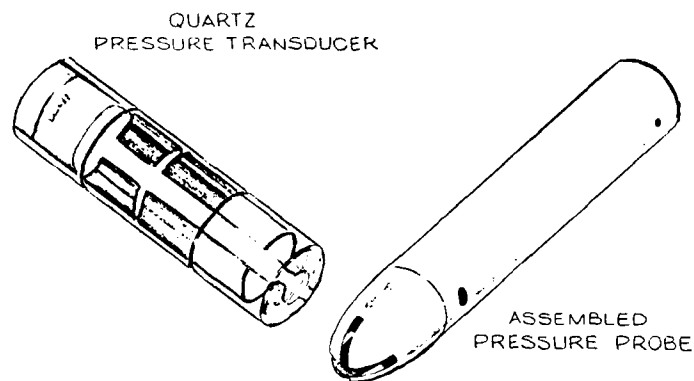


FIGURE 1

## SWEEPING

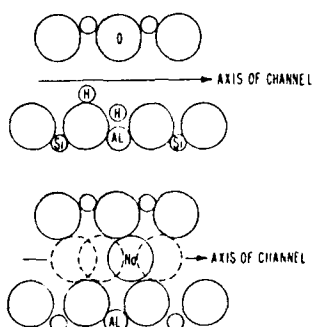
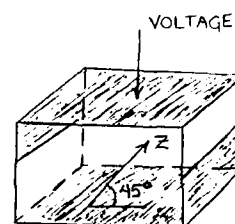


FIGURE 2

## ELECTRODE CONFIGURATION



UNSWEPT RECTANGULAR SECTION

FIGURE 3

## SWEEPING SET-UP

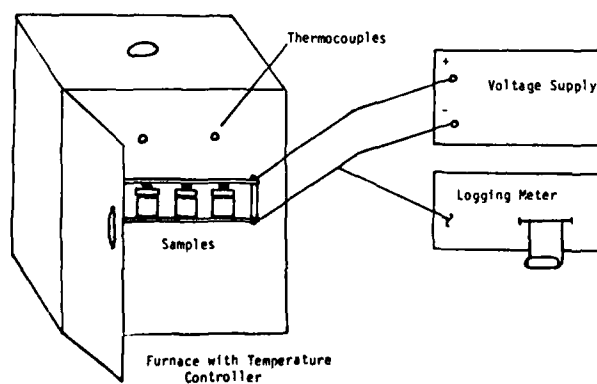


FIGURE 4

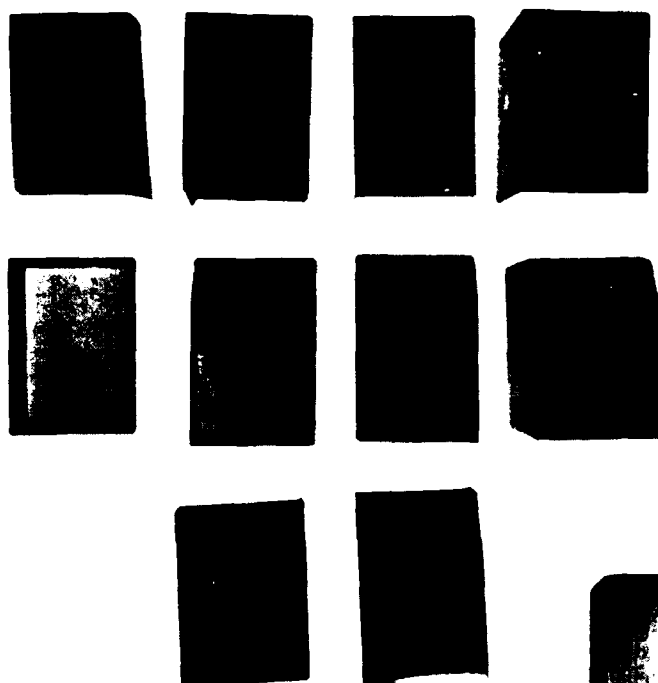


FIGURE 5. Unswept samples after irradiation.

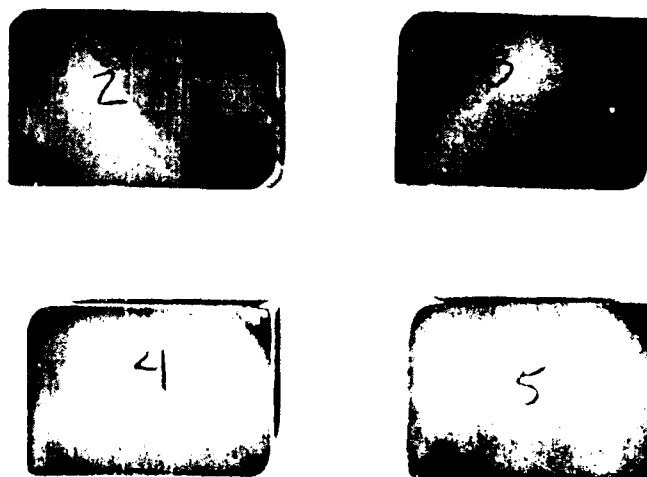


FIGURE 6. Completely and partially swept samples after irradiation.

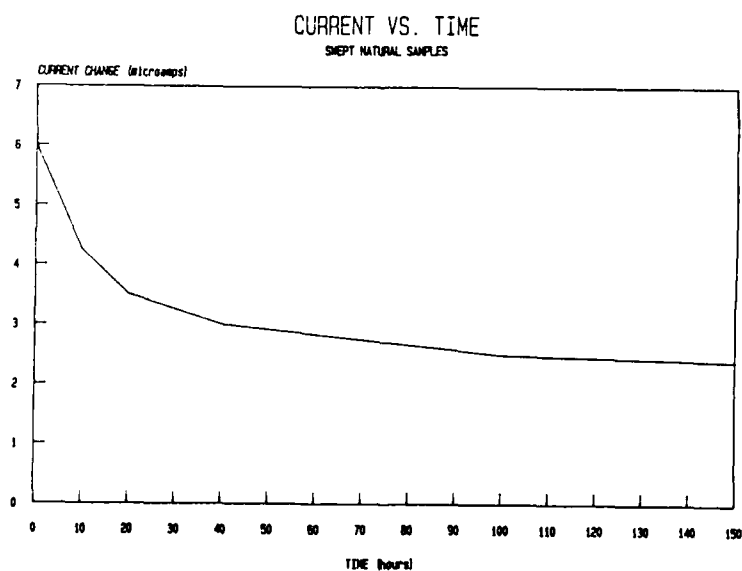


FIGURE 7

# RESISTANCE VS. TEMPERATURE

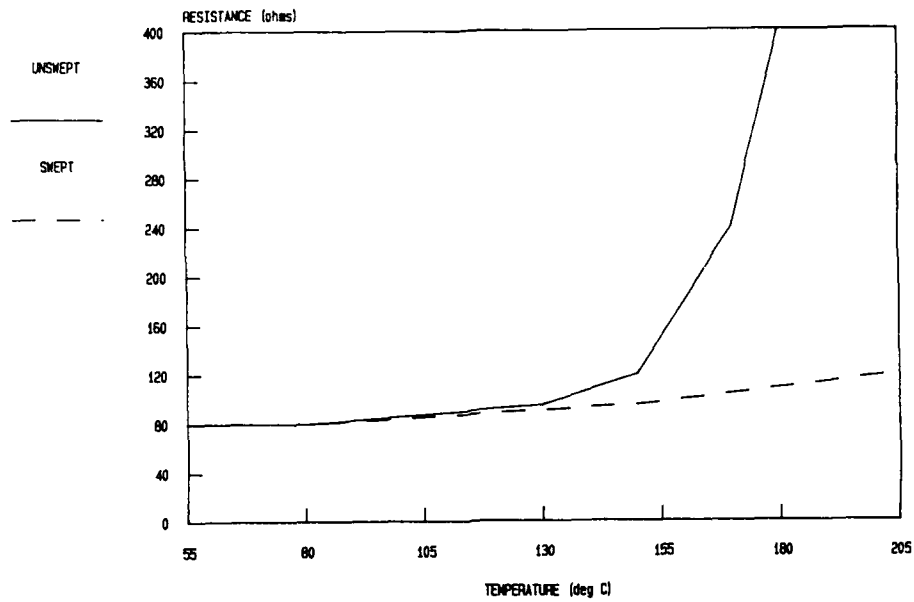


FIGURE 8

# RESISTANCE VS. PRESSURE

SWEPT NATURAL TRANSDUCER

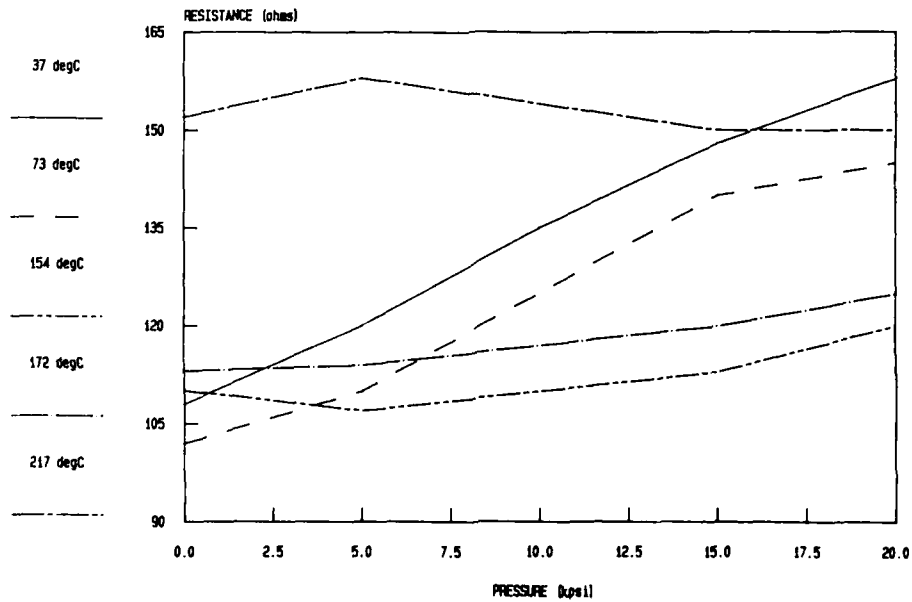


FIGURE 9

# HYSTERESIS

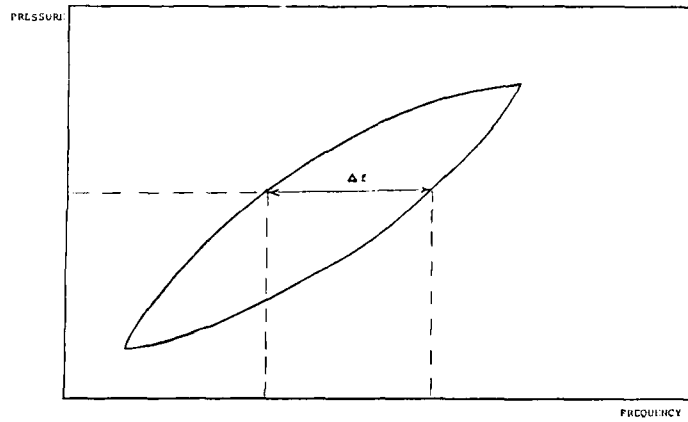


FIGURE 10. Typical hysteresis loop.

## 15KPSI CALIBRATION RUN SHEPT NATURAL TRANSDUCERS AT 200 DEG C.

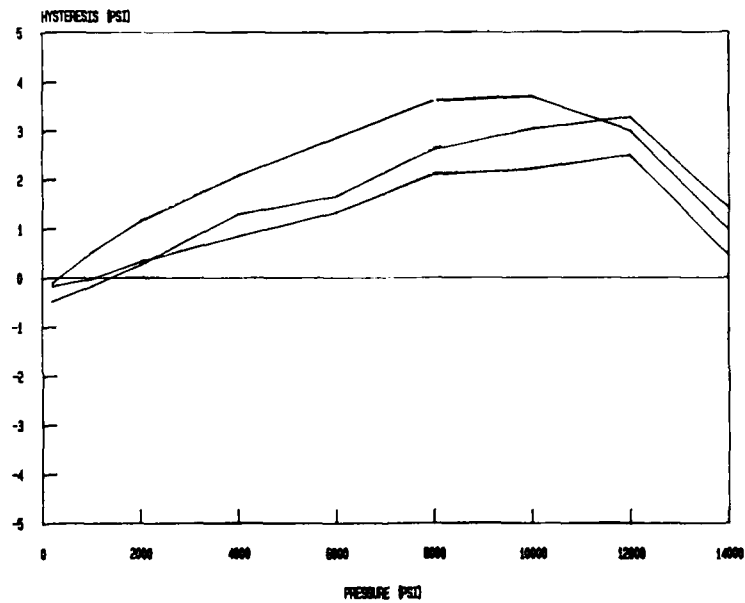


FIGURE 11

## Filter Applications of High Frequency Chemically Polished Fundamental Mode Bulk Wave Quartz Crystal Resonators

Perkunas J. Kavolis and William P. Hanson

Piezo Crystal Company, Carlisle, PA 17013

### Summary

A number of resonator techniques have been used to manufacture high frequency narrowband filters. Presented here are results of several filter designs manufactured using deep etched chemically polished quartz crystals. Crystal filters using chemically polished resonators between 40 and 150 MHz compare favorably with filters using SAW and ion milling technology. Furthermore, quartz resonators at these frequencies can be produced in quantity, with acceptable yield and cost using chemical etching techniques. The resulting filters have classical crystal filter characteristics, with few spurious responses, moderate insertion loss, and bandwidths from .07% to .6%.

### Introduction

At the 37th Annual Frequency Control Symposium, Hanson [1] presented results of some chemical polishing experiments. These experiments were based, in part, on two papers by Vig [2] [3]. The resonators resulting from these experiments were promising, but very expensive. In the year since that report considerable progress has been made in both design and manufacturing techniques of chemically polished quartz resonators. The practical frequency limit for AT-cut crystals has been extended to about 80 MHz on the fundamental mode, the frequency and electrical parameters can be well controlled, and spurious-free regions have been extended.

To demonstrate the usefulness of this new technology, we chose to design and build several crystal filters between 40 and 100 MHz. Designs up to .3% bandwidth were made. The narrowest feasible bandwidth was about .07% because of the limited crystal Q. Several crystal designs with differing electrodes and cuts were tried. We limited ourselves to below 150 MHz because of difficulties measuring and fabricating components above that frequency.

### Chemical Polishing

Chemical polishing is based on the use of an acid solution, such as Hydrofluoric Acid or Ammonium Fluoride, to etch mechanically polished quartz blanks. It is a complicated process, requiring the correct solution, high quality quartz, and great care and cleanliness for good results. Once an acceptable technique is developed, however, it becomes a straightforward task to repeat it to fabricate many chemically polished resonators. Such a technique has been developed for resonators below 200 MHz on the fundamental mode. Most of the resonators fabricated to date have been SC-cut quartz, but recently AT-cut resonators have been used up to 75 MHz.

Two of the primary advantages of the fundamental mode chemically polished resonators are the relatively low C0/C1 ratio, typically 500 to 1000, and the large spur-free region, generally over 500 KHz. Major shortcomings of this process are moderate to low Q, typically less than 40,000 and less accurate frequency setting than with overtone crystals. These characteristics make chemically polished crystals unattractive for very narrow bandwidth crystal filters and for some oscillators, but do not impair their usefulness in intermediate and wideband crystal filters.

Measured parameters of several recently manufactured crystals are shown in TABLE I. These crystals are typical of the results which can be obtained with chemical polishing.

All crystals were operated on the fundamental mode, and were packaged in coldweld TO-5 type holders. As can be seen

from the data, AT-cut crystals have a lower Q than the doubly-rotated SC and IT-cut crystals, as well as a lower C0/C1 ratio. Even the SC-cut crystals, however, have a lower C0/C1 ratio than ion milled resonators as reported earlier by Bidart and Chauvin [4].

### Filter Design and Performance

Several filters were constructed to demonstrate the performance of the chemically polished resonators. The designs were chosen as a demonstration only, and not to meet any specific requirement. Classical 2, 4 and 6 pole Butterworth and Chebyshev designs were used and were synthesized using effective parameter theory. Ordinary crystal filter assembly techniques and components were used. All filters had 50 ohm input and output impedances and were in a sealed enclosure with SMA connectors or solder-terminals. A number of different resonator designs were used; the effects are clearly visible in the filter performance table.

#### Filter 1

This filter is a 70 MHz 6-pole filter with a design bandwidth of 50 KHz. Filter test data and typical crystal parameters were:

Filter	Crystals
Center Frequency : 70.00 MHz	C0: 1.8 pF
3 dB Bandwidth : 51.23 KHz	C1: 3.0 fF
60 dB Bandwidth : 140.0 KHz	ratio C0/C1: 600
Insertion Loss : 4.3 dB	R: 40 ohms
Ripple : 0 dB	Spur-free: 90 KHz
Spurious Suppression: 17 dB	

Note the relatively small spur-free region of the crystals, and the poor spur suppression of the filter. This was due to the large C1, which did, however, yield a filter design of only 350 ohms characteristic impedance.

#### Filter 2

This is a 64 MHz, 4-pole filter with a design bandwidth of 100 KHz. The crystals used were SC-cut. The measured filter and crystal parameters were:

Filter	Crystals
Center Frequency : 64.005 MHz	C0: 0.5 pF
3 dB Bandwidth : 102 KHz	C1: 0.33 fF
60 dB Bandwidth : 950 KHz	ratio C0/C1: 1500
Insertion Loss : 7.2 dB	R: 400 ohms
Ripple : 0.8 dB	Spur-free : 800 KHz
Spurious Suppression: 50 dB	
Group Delay Ripple : 1.6 $\mu$ S	

The response of this filter is illustrated in Figures 1 and 2. The reduced C1 gave a substantial improvement in both the spur-free region and spurious suppression. The B-mode crystal response was suppressed by 26 dB. The characteristic impedance of this filter was about 3000 ohms. As with most crystal filters, the crystals were not all alike. There was one crystal which had a spur at approximately 300 KHz above the center frequency. This spur can be seen in Figure 1.

### Filter 3

This is a 100 MHz, 4-pole filter with a design bandwidth of 300 KHz. Because the bandwidth is .3%, an intermediate band design was used. The crystals used were SC-cut. The following parameters were measured:

Filter	Crystals
Center Frequency : 100.005 MHz	C0: 0.6pF
3 dB Bandwidth : 300 KHz	C1: 0.48 fF
60 dB Bandwidth : 750 KHz	ratio C0/C1: 1250
Insertion Loss : 7.0 dB	R: 150 ohms
Ripple : 0.8 dB	Spur-free: 700 KHz
Spurious Suppression: 30 dB	
Group Delay Ripple : 3.5 $\mu$ S	

The response of this filter is illustrated in Figures 3 and 4. Again, the low C1 resulted in a large spur-free region and good spurious suppression. The B-mode response of the SC-cut crystals was also suppressed by about 30 dB.

In order to reduce the characteristic impedance we paralleled two crystals at all locations where a crystal was called for. This allowed us to reduce the characteristic impedance of this filter to a realizable value, but also raised the spur level.

### Filter 4

Filter 4 was fairly low in frequency, only 38 MHz, with a bandwidth of 29 KHz. It was a two pole design. The crystals used were AT-cut, unlike the other three filters discussed here, which all used SC-cut crystals.

Filter	Crystals
Center Frequency : 38.436 MHz	C0: 0.75 pF
3 dB Bandwidth : 29.1 KHz	C1: 2.0 fF
30 dB Bandwidth : 192 KHz	ratio C0/C1: 375
Insertion Loss : 2.5 dB	R: 170 ohms
Ripple : 0.0 dB	Spur-free: 300 KHz
Spurious Suppression: 29 dB	

Figure 5 shows the passband and stopband of filter 4. The spurious performance of the AT-cut crystals was comparable to that of the SC cut crystals, especially when the relatively large C1 is taken into account. The large C1 of the crystals lowered the characteristic impedance of the filter to about 500 ohms, making it quite easy to build.

At the time this filter was constructed, AT-cut crystals could not be successfully chemically polished above about 50 MHz. Since that time, we have improved our techniques to the point where we can now reliably fabricate AT-cut crystals up to 80 MHz.

### Future Outlook

We foresee continued use of chemically polished fundamental mode quartz resonators in filters. By using AT-cut crystals, spurious suppression and insertion loss can be improved, and cost can be reduced. Center frequencies up to 200 MHz should be attainable in the near future. Currently, AT-cut crystals are useable only up to 80 MHz, but we hope to be able to extend this range. Immediate goals include further improvements and automation of production techniques for chemically polished resonators and investigation of the overtone modes of these resonators.

### Conclusion

Chemically polished fundamental mode resonators provide a viable alternative for filter design above 40 MHz. SC-cut resonators can currently be manufactured up to 200 MHz, AT-cut resonators up to 80 MHz, and experimental overtone designs to 1.2 GHz.

Filters up to nearly 200 MHz can be manufactured using conventional crystal filter design procedures. For filters beyond 200 MHz, special design techniques are necessary. We have not determined the useful limit of the resonators themselves, but other filter components, especially coils, require careful attention. At higher frequencies, stripline techniques must be used.

Some advantages offered by chemically polished quartz resonators are:

- large spur-free region
- low C0/C1 ratio
- excellent temperature stability
- acceptable cost
- high volume production is possible

Major drawbacks are:

- low to moderate resonator Q makes them unsuitable for very narrow band applications
- extremely tight tolerances on electrical parameters are not currently practical

Filters using this crystal technology offer several benefits:

- low loss
- wide bandwidths
- high stopband attenuation
- good selectivity
- classical crystal filter designs are possible
- reduced tooling costs

Piezo Crystal Company is currently producing commercial filters using AT-cut chemically polished resonators. As the manufacturing process is refined and new equipment is developed, we expect the performance of these crystals and the circuits using them to improve considerably beyond the results presented here.

Table I

SERIAL NO.	525	515-1	577	510	605
Fs (MHz)	70.005	63.953	99.998	38.445	73.189
CO (pF)	1.75	0.05	0.6	0.7	0.6
C1 (fF)	3.0	0.33	0.55	2.1	1.0
C0/C1	583	1500	1090	340	600
R (ohms)	20	330	100	255	120
Q	38,000	23,000	29,000	7,700	18,000
SPUR-FREE	87 KHz	800 KHz	500 KHz	300 KHz	700 KHz
CUT TYPE	SC	SC	IT	AT	AT

### References

1. W. P. Hanson, *Chemically Polished High Frequency Resonators*, Proc. 37th Ann. Freq. Cont. Symp., p. 261 (1983).
2. J. R. Vig, J. W. LeBus, and R. L. Filler, *Chemically Polished Quartz*, Proc. 31st Ann. Freq. Cont. Symp., p. 131 (1977).
3. J.R. Vig, R. J. Brandmayr and R. L. Filler, *Etching Studies on Singly and Double Rotated Quartz Plates*, Proc. 33rd Ann. Freq. Cont. Symp., p. 351 (1979).
4. L. Bidart and J. Chauvin, *Direct Frequency Crystal Oscillators*, Proc. 35th Ann. Freq. Cont. Symp., p. 365 (1981).



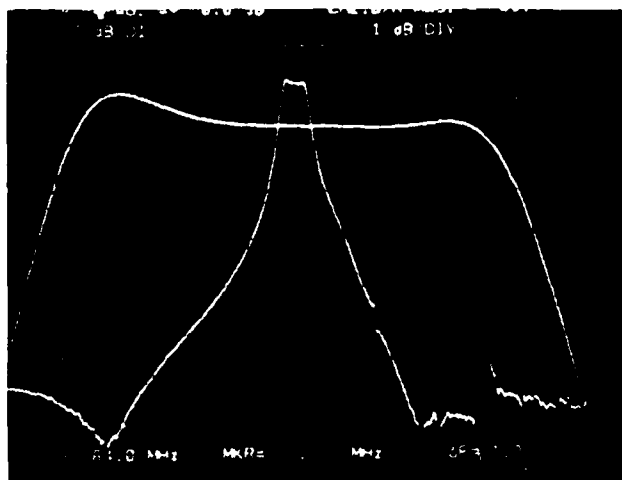


**Figure 1:** Filter 2 passband and stopband characteristics.  
Trace 1 - Vert: 10 dB/div., Horiz: 200 KHz/div.  
Trace 2 - Vert: 1 dB/div., Horiz: 10 KHz/div.

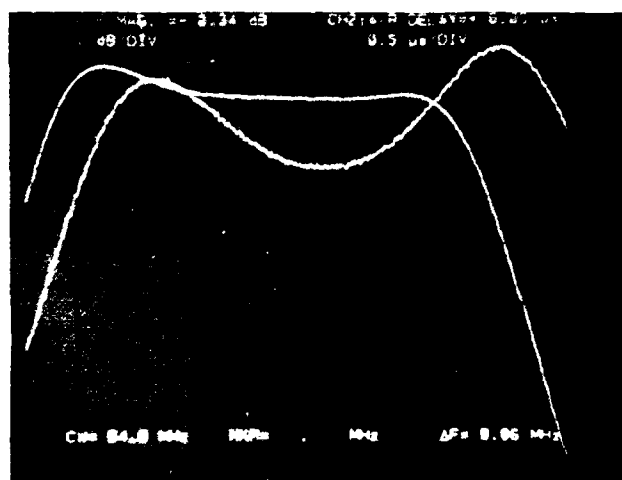


**Figure 2:** Filter 2 passband and group delay characteristics.  
Trace 1 - Vert: 1 dB/div., Horiz: 10 KHz/div.  
Trace 2 - Vert: 0.5  $\mu$ S/div., Horiz: 10 KHz/div.

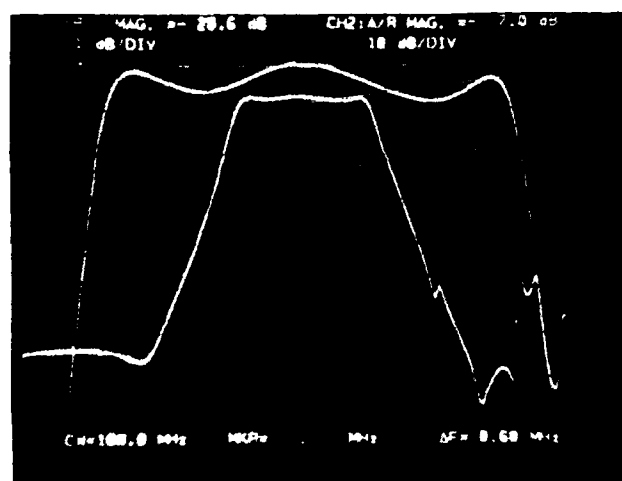


**Figure 3:** Filter 3 passband and stopband characteristics.  
Trace 1 - Vert: 1 dB/div., Horiz: 30 KHz/div.  
Trace 2 - Vert: 10 dB/Div., Horiz: 100 KHz/div.

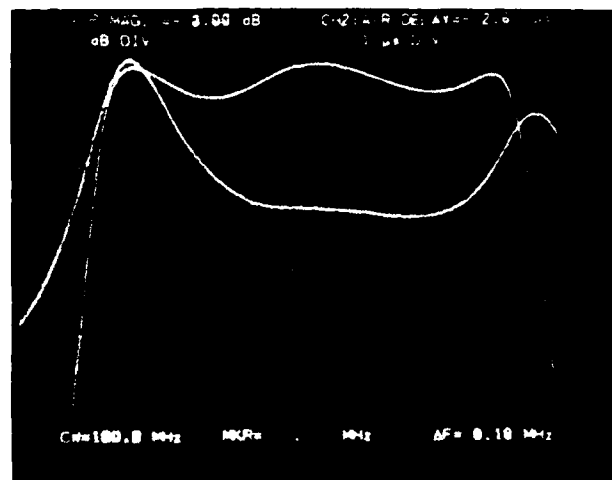


**Figure 4:** Filter 3 passband and group delay characteristics.  
Trace 1 - Vert: 1 dB/div., Horiz: 30 KHz/div.  
Trace 2 - Vert: 1  $\mu$ S/div., Horiz: 30 KHz/div.

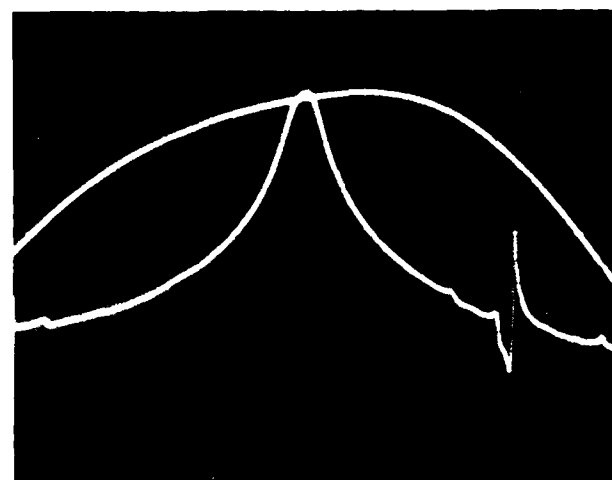


**Figure 5:** Filter 4 passband and stopband characteristics.  
Trace 1 - Vert: 1 dB/div., Horiz: 4 KHz/div.  
Trace 2 - Vert: 10 dB/div., Horiz: 100 KHz/div  
Center: - 38.436 MHz

# A NEW GENERATION OF UHF FILTERS FROM 300 MHz TO SOME GHz USING " DIELECTRIC RESONATORS "

Bertrand D'ALBARET

Compagnie d'Electronique et de Piézo Electricité - C E P E  
44 Avenue de la Glacière 95 100-ARGENTEUIL FRANCE

## SUMMARY

C E P E has succeeded in designing filters at frequencies much higher than those concerned by means of piezoelectric resonators.

By the use of dielectric ceramic resonators, metallized and positionned correctly, C E P E has designed filters operating at frequencies from a few hundred MHz to some GHz and having relative bandwidths of 0,5 to 10 %.

The results obtained by C E P E laboratories from several applications, already used in the new generation of radio-telephone, prove that " Dielectric filters " have a similar performance to those designed with air metallical cavities but they are much less cumbersome and cost less.

## INTRODUCTION

The extension to higher and higher frequencies of filters for the radio-telephone, the numerical telephone with elevated speed, and generally of aerial filters lead us to find performant filters less cumbersome, which would support high power.

Thanks to the Argon ion beam technique introduced by M. BERTÉ in 1977 ( 31st Symposium on Frequency Control ) and the use of the Lithium Tantalate, C E P E now provides piezoelectric filters up to 300 MHz in fundamental mode, reaching 5 % bandwidths and up to 700 MHz in third overtone ( see my paper dated 1982 at the 36th Symposium on Frequency Control Recent advances in UHF Crystal Filters ).

In this paper, we present new products concerning filters composed of dielectrical resonators and operating for the moment from 700 MHz to 2 GHz.

## STATE OF THE ART

It has been known for a long time that dielectrical samples exhibit electromagnetic resonances as soon as the wave-length gets shorter than the sample size. If the resonance frequency is stable, depending on the time, temperature.... etc, such devices, known as dielectrical resonators, are very useful for making microwave filters and oscillators allowing size reduction and easier manufacturing.

The composition used ( Zr, Sn )  $TiO_4$ , developed by THOMSON CSF Corbeville Laboratories, offers a concurrently low temperature coefficient of resonance frequency adjustable within 1 ppm/°C between - 20 and + 20 ppm/°C, low microwave loss : this is quite linear versus frequency, so that the resonators can be characterized by the product  $Q \times \text{frequency}$  which is about 40000 GHz ( from 2 GHz to 100 GHz ), and gives a good reproductibility of the dielectric constant  $\epsilon_r$  ( typically :  $37 \pm 0,5$  ).

The discontinuity between two media of different constants generates standing waves. So it is obvious for some interface geometries and for certain values of incident frequency that standing fields can be created similar to those existing inside metallic cavities.

## OFFERED POSSIBILITIES

In the range of very high frequencies called UHF ( practically from 300 MHz to 3 GHz ), resonators and filters designed with these elements are often constituted by pieces of lines.

The technique of coaxial lines loaded with dielectric imposes a particular form : resonators are identical to hollow tubes internally and externally metallized

( Fig. 1 ). A resonator of 10 mm diameter with silver metallization has typically a quality factor of 900 at 1 GHz. Furthermore the design of the coaxial structure is rather complicated due to the various work processes and metallization of elements with circular section.

The technique of microstriped lines ( Fig 2 ) facilitate the design of resonators from a rather wide dielectric substratum of which one face is metallized and the other receives a metallic conductor similar to a slim strip. But the quality factors are always low ( < 500 ) and furthermore it is practically impossible to adjust the resonance frequencies of the resonators and their mutual coupling.

### THE BISTRIPED RESONATOR

In order to offset these disadvantages, resonators have been designed from a parallelepiped constituted of dielectric material with a rectangular section of sides : a and b ( Fig 3 ). Anyway we design a line by metallizing two opposed faces of the parallelepiped and we have a resonator  $\lambda/4$  or  $\lambda/2$  according to length and termination of line.

Metallizations 1 and 2 cover two opposed sides of the dielectric. This line propagates electromagnetic and transverse waves with an efficient index  $n_e = \frac{\lambda_0}{\lambda_g}$

(  $\lambda_0$  = wave length in vacuum  
 $\lambda_g$  = wave length in the bistriped guid ).

and can present proper resonant frequencies depending on whether the length value L is an odd or even multiple of  $\lambda/4$  and according to conditions at the limits.

Half wave resonators can be obtained as shown in picture 3, that is to say in opened network with  $L = \frac{\lambda_g}{2}$  ; the resonator is metallized on two of its sides <sup>2</sup> 1 and 2 only.

A half wave resonator can also be obtained by metallizing extremity faces 3 and 4 further to faces 1 and 2 ( drawing 4 ). These conditions at limits make it a resonator  $\lambda_g/2$  for  $L = \lambda_g/2$ .

We can also get a quarter wave resonator ( drawing 5 ) by metallizing only extremity 3, as well as faces 1 and 2. Then, we obtain a resonator  $\lambda/4$  with length  $\lambda_g/4$ .

Table 6 gives quality factor and resonance frequency values according to section and length, and this, for a material with dielectric constant 37 and silver metallizations done with a silk-screen process.

We observed that quality factor Q is proportional to edge : a, and that with constant section, quality factor varies with the frequency squareroot.

We can write  $Q = K a \sqrt{f}$   
 K is a proportionality coefficient.

### METALLIZATION STUDY

As necessary metallization thickness must be superior to that of the skin effect, some measurements have permitted to draw on picture 7 the quality factor curve according to metallization thickness for silk-screen process with silver lake.

### FREQUENCY STUDY

Resonators can be adjusted in frequency : this one grows by grinding the non metallized extremity and decreases by grinding edges towards resonator center.

Frequency can also be adjusted by stricking on the resonator either dielectric or metal.

Picture 8 shows frequency difference  $\Delta f$  got either by displacement of a dielectric disc, or by displacement of an aluminium disc.

In order to characterize resonators in an electrical and a reproducible way, it has been necessary to define a test set. Measurement of quality factor and frequency of resonators highly depend on their environment. Consequently, all measurements have been carried out with the same test set ( Picture 9 ).

Resonators impedance being close to 50  $\Omega$ , quality

factor measurement is used ( fig 10 ).

Maximum coupling, that is to say, maximum attenuation is researched by making distance between captor and resonator vary : then we can get resonance frequency  $f_0$  and quality factor  $Q$  through formula :

$$Q = \frac{f_0}{0,5 \times B_w} \quad B_w = \text{bandwidth at 3 dB ( see picture 11 )}$$

### COUPLING COEFFICIENT MEASUREMENT

Coupling coefficient between two resonators with resonance frequency  $f_0$  depends on distance between them and on their mechanical environment. A metal test case has been defined with its captors for a choosen resonator section ( Picture 12 ), and so it has been possible to draw coupling coefficient curves according to the distance separating the resonators. Picture 13 presents this graph for resonators with section  $7 \times 7 \text{ mm}$  at frequency 900 MHz.

### FILTER REALIZATION

Consequently a passband filter can be made by disposing several resonators one beside the others inside a case ( fig 14 ). We have preferred resonators  $\lambda/4$  because of their lower length.

Resonators metallizations are respectively parallel between them and perpendicular to isolating substratum. Coupling between resonators is made through mutual inductance. Conductors 1 and 2 form coupling rings and are used as excitator and collector.

Filter putting into operation is made through previous adjustment of proper resonators frequencies and then through obtaining coupling coefficients requested by filter synthesis, and this by adjusting distances between resonators carefully.

It is also possible to make stopband filters as shown picture 15. A conductor which can be the core of a coaxial line ( 1 ) is placed perpendicularly to resonators on their short-circuit side and allows transmission and collection signal.

We now present a few examples of dielectrical filters which we have made using this principle.

### PASSBAND FILTERS

#### - e g 1 - 2 poles filter.

This concerns the local oscillator filter of the future 900 MHz radiotelephone. This filter is designed with resonators of section  $6 \times 6 \text{ mm}$ .

Central frequency  $f_0 = 1\,037,5 \text{ MHz}$

Insertion loss  $IL \leq 1 \text{ dB}$

1 dB Passbandwidth  $Pbw \geq 25 \text{ MHz}$

20 dB Attenuationbandwidth  $\leq 155 \text{ MHz}$

See response curve in Fig. 16.

#### - e g 2 - 3 poles filter.

An antenna filter at 900 MHz designed with resonators of section  $8 \times 8 \text{ mm}$ .

$f_0 = 900 \text{ MHz}$

$IL \leq 2 \text{ dB}$

3 dB  $Pbw \geq \pm 10 \text{ MHz}$

60 dB  $Abw \leq \pm 70 \text{ MHz}$

See response curve in Fig. 17.

#### - e g 3 - 4 poles filter.

This filter at 1,5 GHz designed with 4 resonators of section  $7 \times 7 \text{ mm}$  is used for a radar application. We can see the prototype on the photo Fig. 18.

$f_0 = 1,519 \text{ GHz}$

$PI \leq 2,5 \text{ dB}$

3 dB  $Pbw \geq \pm 12 \text{ MHz}$

40 dB  $Abw \leq \pm 60 \text{ MHz}$

60 dB  $Abw \leq \pm 100 \text{ MHz}$

See response curve in Fig. 19.

#### - e g 4 - 5 poles filter

This 1,3 GHz filter is used for the recuperation of the rhythm frequency in the future generation of numerical transmission system with very high speed on optical fiber. This filter is designed with resonators of section  $10 \times 10 \text{ mm}$  ( see photo Fig. 20 ).

$f_0 = 1,3 \text{ GHz}$

$IL \leq 6 \text{ dB}$

3 dB  $Pbw \geq \pm 1,5 \text{ MHz}$

20 dB  $Abw \leq \pm 6,9 \text{ MHz}$

30 dB  $Abw \leq \pm 20 \text{ MHz}$

See response curve in Fig. 21.

In addition, in order to preserve the phase coherence of all the repeaters, all the filters phases at the central frequency must be trimmed with a precision of  $\pm 20^\circ$  and a maximum drift of  $\pm 10^\circ$  is tolerated in the bandwidth  $\pm 20$  KHz and  $\pm 40^\circ$  in the bandwidth  $\pm 130$  KHz, in the temperature range  $+ 10^\circ\text{C}$ ,  $+ 50^\circ\text{C}$ .

### STOPBAND FILTER

See photo Fig. 22.

#### - e g 5 - 4 poles stopband filter

A 4 poles rejector designed with resonators of section  $6 \times 6$  mm.

$F_0 = 939$  MHz

$IL \leq 1$  dB

30 dB Abw  $\geq \pm 2,5$  MHz

3 dB Pbw  $\leq \pm 10$  MHz

See response curve in Fig. 23.

### DOUBLE FILTER

#### - e g 6 - 900 MHz Diplexer for the future european radio-telephone ( see photo Fig. 24 ).

This is made up of two 6 poles filters in the same case with a common input, which involve an excellent return loss (  $\geq 15$  dB ). We present hereunder results of first prototype ( see curves Fig. 25 ).

	<u>Transmitter</u>	<u>Receiver</u>
Insertion loss	2,5 dB	3 dB
0,5 dB Passbandwidth	890 - 915 MHz	935 - 960 MHz
60 dB Attenuationbandwidth	855 - 948 MHz	913 - 987 MHz

These first results will be ameliorated, especially for the insertion loss.

The temperature range is of  $- 35^\circ\text{C}$  to  $80^\circ\text{C}$ . Some trials at high level have demonstrated that these filters endure a power of approximately 25 W with the section of resonator choosen here :  $7 \times 7$  mm.

### SHIFTABLE FILTER

#### - e g 7 - Shiftable frequency filter by varactor

It is possible by an additionnal circuit including a varactor, to shift the frequency of each resonator by a variable tension, of a same margin  $\Delta F$  and so to change the central frequency preserving the same bandwidth. We can observe the phenomenon on the curves Fig. 26.

### CONCLUSION

The frequency limit for the fundamental mode is approximatively 2 GHz with this technology, but with the 3rd or 5th overtone, it seems that it is possible to design filters up to 5 or 10 GHz.

Filters manufactured according to this technology present a certain number of advantages. The main ones being :

- . the bulk is reduced because of the high dielectric constant of the material (  $\epsilon_r = 37$  )
- . realization possibilities from 300 MHz up to 5 or 10 GHz
- . high quality factor allowing a low insertion loss of 1 to 6 dB according to the bandwidth
- . relative bandwidth from 0,5 % to 10 %
- . remarkable out of band attenuation  $> 120$  dB
- . a low temperature coefficient : a few ppm /  $^\circ\text{C}$
- . faculty of supporting power  $> 20$  W
- . possibility of sweeping in frequency by a variable tension.

This technology has furthermore a great advantage : a very low cost.

C E P E is now ready to design a trial series in laboratory for frequency lower than 2,6 GHz and starting of definite series will take place from 1985.

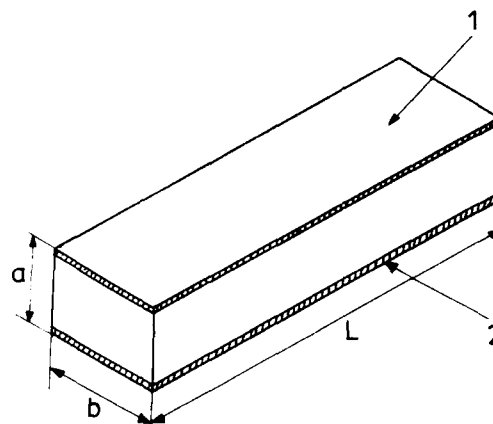
### BIBLIOGRAPHY

#### - 1 ) M. BERTÉ

" Acoustic-bulk-wave resonators and filters operating in the fundamental mode at frequencies greater than 100 MHz "

ELECTRONIC LETTERS , Vol 13, 1977 pp. 248

- 2 ) B. D'ALBARET and P. SIFFERT  
 " Recent advances in UHF Crystal Filters "  
 36th Annual Frequency Control Symposium  
 May 1982 pp.405.
- 3 ) MM. MAGE - SIMONET  
 " Matériaux diélectriques stables en température "  
 THOMSON CSF Mai 1982
- 4 ) BREVET THOMSON CSF Of Mr MAGE No 82 18236 of  
 the 23.10.82.



$\lambda / 2$  RESONATOR OPEN CIRCUIT  
 RESONATEUR  $\lambda / 2$  CIRCUIT OUVERT

Fig. 3

$\lambda / 2$  RESONATOR SHORT CIRCUIT  
 RESONATEUR  $\lambda / 2$  CIRCUIT COURT CHERT

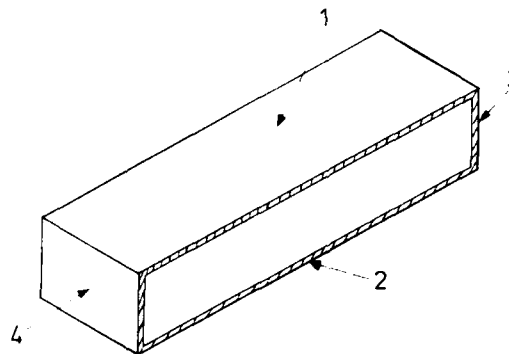


Fig. 4

MICROSTRIP LINE  
 LIGNE MICROSTRIP

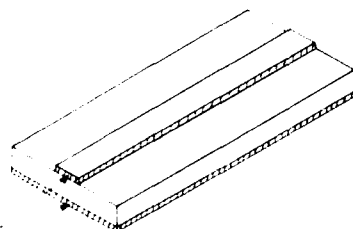
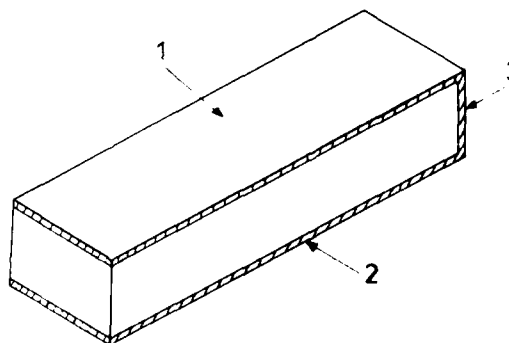


Fig. 2



$\lambda / 4$  RESONATOR  
 RESONATEUR  $\lambda / 4$

Fig. 5

No	Section a-b mm	Length longueur mm	Type Type	Frequency fréquence Hz	Quality factor facteur de Q	Volume volume mm <sup>3</sup>
1	5	15	$\lambda/4$	1.060	350	0.18
2	5	30	$\lambda/4$	1.030	500	0.25
3	5	45	$\lambda/4$	1.060	500	0.25
4	10	30	$\lambda/4$	1.040	700	0.30
5	10	45	$\lambda/4$	1.060	700	0.30
6	10	60	$\lambda/4$	1.050	1000	0.30
7	15	45	$\lambda/4$	1.060	1000	0.30

Fig. 6

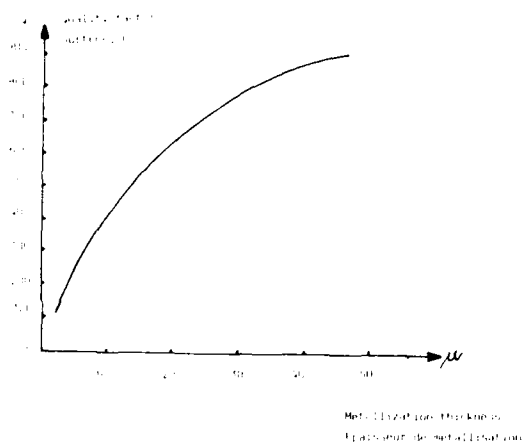


Fig. 7

#### FREQUENCY ADJUSTMENT BY MATERIAL ADDITION

Adjustment of the frequency of a resonator by the addition of material.



Section	Frequency (Hz)	Quality factor (Q)
1	1.060	350
2	1.030	500
3	1.060	500

Fig. 8

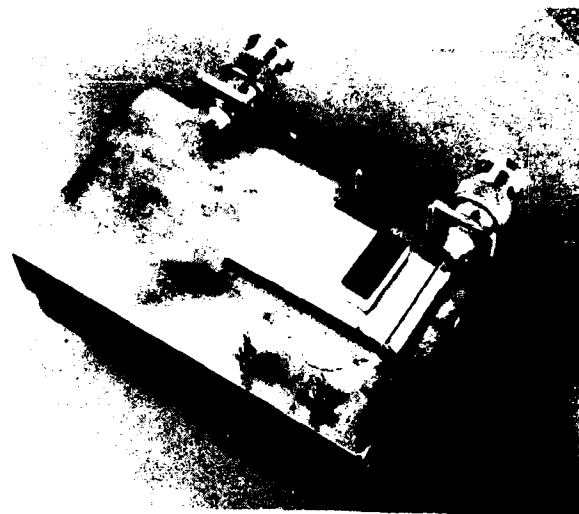


Fig. 9

#### FREQUENCY AND QUALITY FACTOR MEASUREMENT

Measurement of the frequency and quality factor of a resonator.

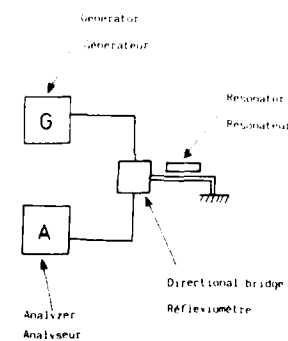


Fig. 10

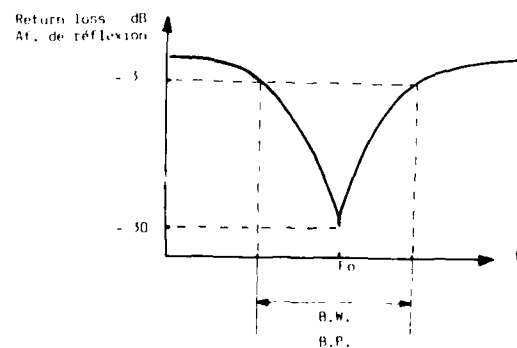


Fig. 11

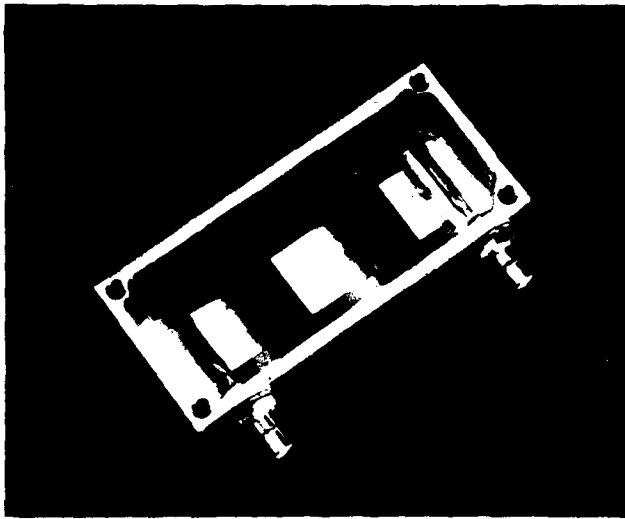


Fig. 12

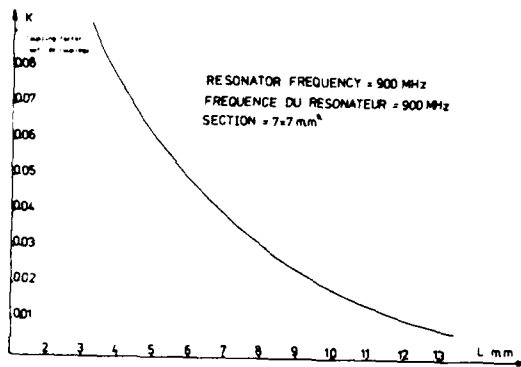


Fig. 13

PASSBAND FILTER SCHEME  
CORRECTION OF THE SCHEME BASED

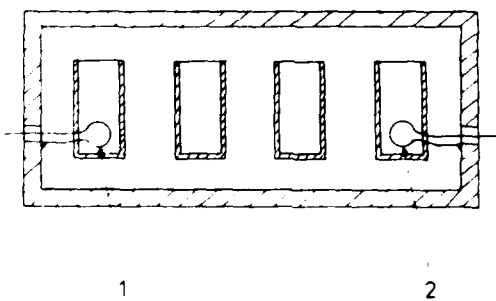
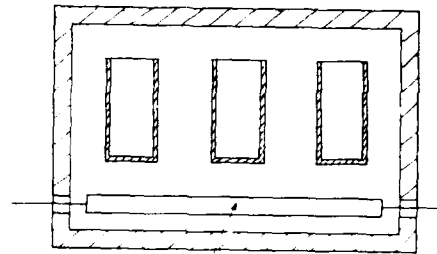


Fig. 14

STOPBAND FILTER SCHEME  
CORRECTION OF THE SCHEME BASED



1

Fig. 15

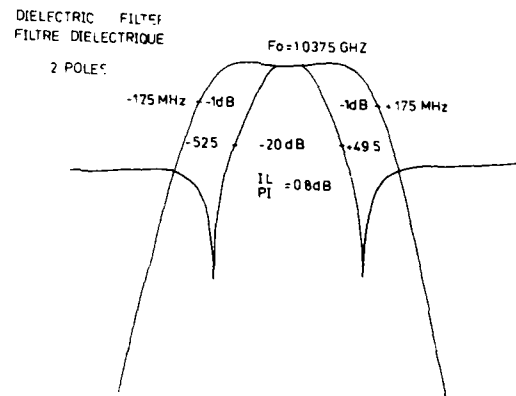


Fig. 16

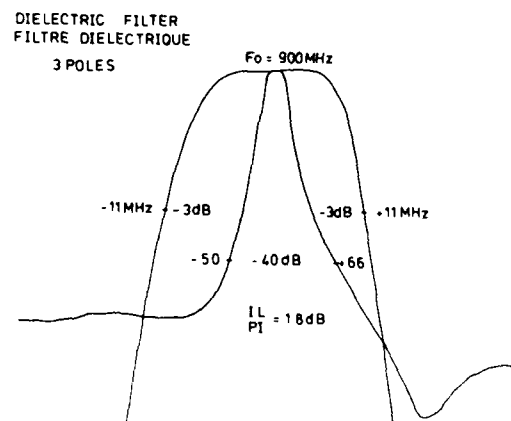


Fig. 17



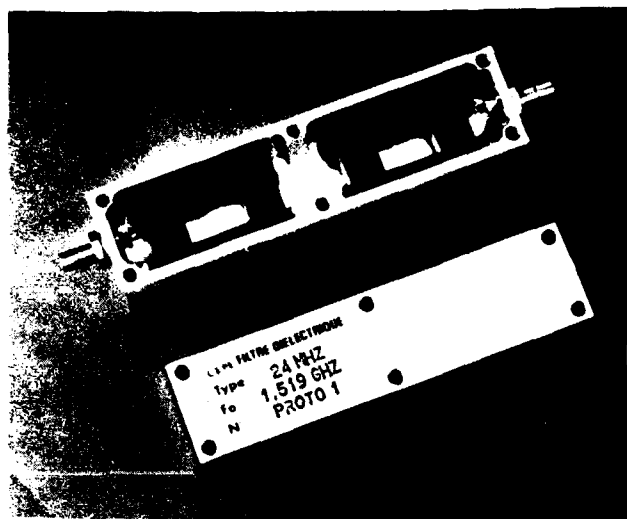


Fig. 18

DIELECTRIC FILTER  
FILTRE DIELECTRIQUE  
5 POLES

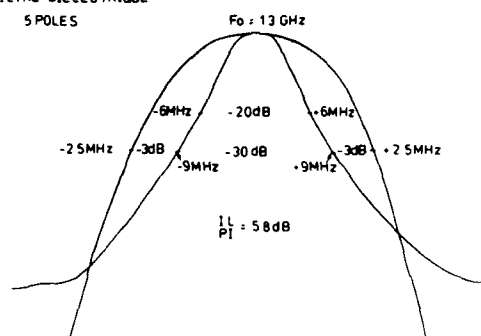


Fig. 21

DIELECTRIC FILTER  
FILTRE DIELECTRIQUE  
4 POLES

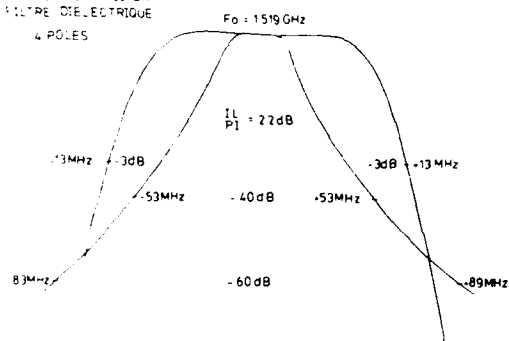


Fig. 19

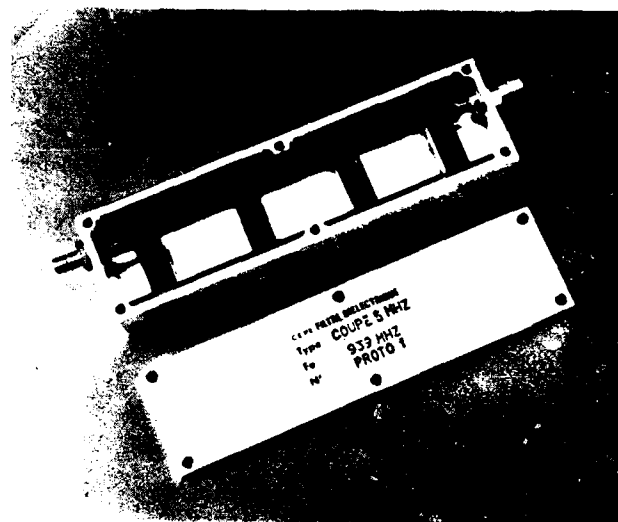


Fig. 22

DIELECTRIC FILTER  
FILTRE DIELECTRIQUE  
4 POLES

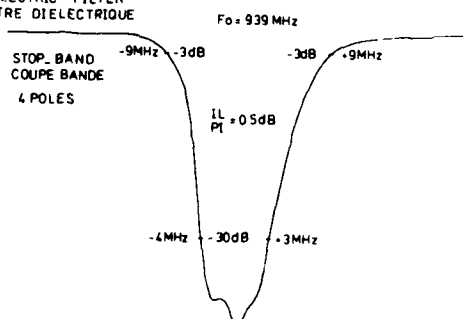


Fig. 23

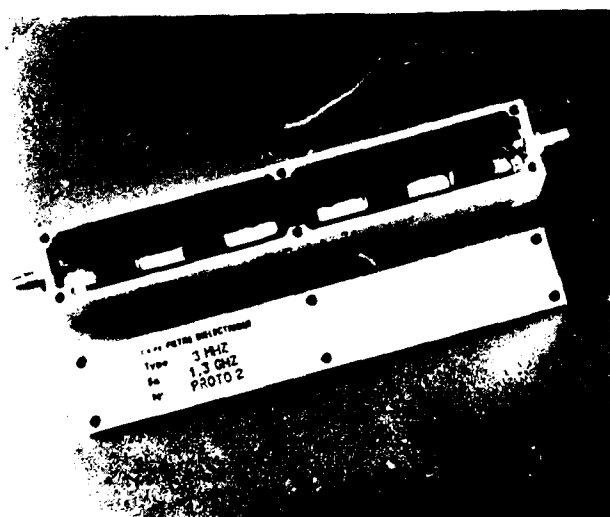


Fig. 20

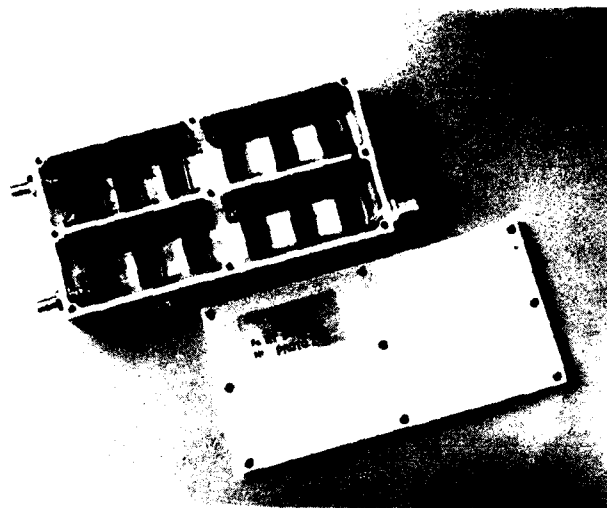


Fig. 24

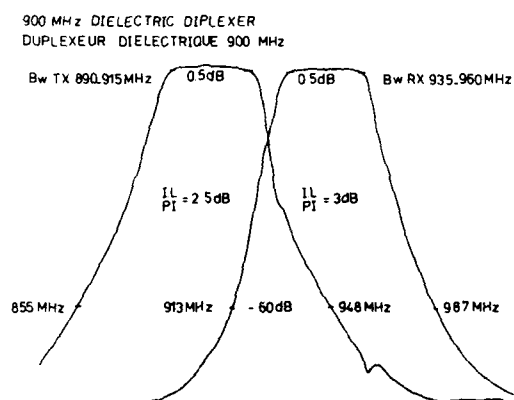


Fig. 25

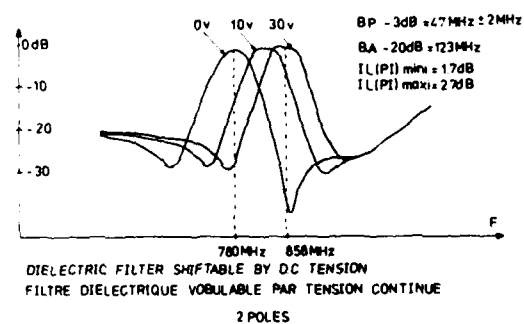


Fig. 26

## TEMPERATURE STABLE MICROWAVE RESONATORS USING ZnO SHEAR MODE TRANSDUCERS

S. V. Krishnaswamy and B. R. McAvoy  
Research and Development Laboratories  
Westinghouse Electric Corporation  
Pittsburgh, Pennsylvania 15235

R. A. Moore  
Systems Development Division  
Westinghouse Defense and Electronics Center  
Baltimore, Maryland 21203

### Abstract

Lithium tantalate is known to have temperature stable propagation directions for the bulk shear mode. Shear wave excitation requires that c-axis orientation of ZnO crystallites be either  $40^\circ$  or  $90^\circ$  from the substrate surface normal and applied RF field direction. We chose to deposit obliquely oriented film (c-axis tilted w.r.t. substrate normal).

We describe the performance of lithium tantalate transmission resonators fabricated with two ZnO shear mode transducers aligned on opposing faces of the substrate. The substrates have been fabricated using singly rotated cuts of LiTaO<sub>3</sub>. The plate of the cut is  $-19$  degrees away from the z axis along x. The complete results for a number of resonators tested so far will be described. The insertion loss for these resonators varies from  $-42$  dB to  $-22$  dB at resonance in S band. Loaded Q values in excess of  $10^4$  at 1.6 GHz have been observed. Temperature stability data of an overtone resonance near 1.6 GHz has been taken over a temperature range of  $-40^\circ\text{C}$  to  $+80^\circ\text{C}$ . A parabolic frequency dependence on temperature has been observed.

### Introduction

As a result of growing interest in developing a frequency standard that responds at microwave frequencies (1-3 GHz range) for low noise oscillator applications the high overtone bulk acoustic resonator (HBAR) has been under investigation during the last few years.<sup>1,2</sup> Earlier HBAR investigations have utilized high overtone longitudinal modes generated by ZnO transducers aligned on opposing faces of a nonpiezoelectric substrate. This configuration provides a transmission cavity resonator which takes advantage of the high Q, low propagation loss characteristics in materials such as YAG and MgAl<sub>2</sub>O<sub>4</sub>. In YAG substrates cut with  $\langle 111 \rangle$  normal, for example, loaded Q values in excess of 50,000 have been observed at 1.8 GHz. A vibration sensitivity of  $1 \times 10^{-11}/g$  has been measured for these resonators which is approximately two orders of magnitude lower than for a typical three-point mounted AT-cut quartz crystal.<sup>3</sup> This has led to compact, robust oscillators exhibiting low noise and vibration immunity at S-band. The temperature coefficient of these resonators is about 40 ppm/ $^\circ\text{C}$  and for a number of systems applications this is unsatisfactory.

Lithium tantalate is known to have temperature stable propagation directions for the bulk shear mode. Previous work<sup>4,5</sup> has mapped these directions. Plate shear lithium tantalate resonators have been demonstrated.<sup>6</sup> For our current work we have employed the first order temperature coefficient map represented in Figure 1. In this figure the dark areas are regions of positive temperature coefficient and the white area covers the region of negative coefficients. The borders between the regions define rotational angles of the substrate plate for which the first order temperature coefficient of frequency is zero. The inset in Figure 1 shows the convention for the rotational angles used. The shear mode propagation direction is normal to the rotated plate. In this initial work we have elected to concentrate on single rotated plates with  $\phi = 0$  and  $\theta$  near  $-19^\circ$ . This rotation as shown in the figure is  $19^\circ$  counterclockwise away from z about x. This cut allows for simple angular adjustments at the bottom boundary of the small positive "island" between  $\theta = 0$  and  $\theta = -30^\circ$ . The cut plates are polished to a thickness of about 940 microns which results in a shear mode overtone separation near 2 MHz. For the cut described, the fast and slow shear modes are not degenerate but are separated by about 0.2 MHz. Our observations to date have shown that the frequency change with temperature of the fast shear mode can be tracked without difficulty. The longitudinal mode resonances, if they exist, are readily identified because they have a 3.3 MHz separation.

Recently plate shear lithium tantalate resonators have been demonstrated.<sup>6</sup> For this purpose thin LiTaO<sub>3</sub> plates were obtained by direct ion milling of single crystal wafers. In this paper we describe the performance of lithium tantalate transmission resonators fabricated with two shear mode transducers aligned on opposing faces of the substrates.

### Experimental

The generation of shear modes using a plane parallel transducer geometry requires that the ZnO c-axis crystallite orientation be tilted with respect to the plane of the transducer contacts.<sup>7,8</sup> This inclination insures that the RF field excites the ZnO to produce shear waves while fully suppressing production of compressional waves. There are two angles of tilt for which this holds true:  $40^\circ$  and  $90^\circ$ . While different techniques have been proposed for depositing C-axis in-plane ( $90^\circ$  tilt) ZnO films, none of them appears satisfactory and reproducible. We have chosen

to deposit films with C-axis tilted with respect to substrate normal (oblique orientation). Recently, Wang, Lakin, and Landin<sup>9,10</sup> have taken a similar approach. They have successfully sputtered, using the magnetron technique, up to 10  $\mu\text{m}$  thick, ZnO films having C-axis tilt up to 45°. Using these films on silicon membrane, they have fabricated shear mode resonators operating in the 200-400 MHz range.

In an earlier paper,<sup>7</sup> we demonstrated the generation of shear mode bulk waves at microwave frequencies, with RF diode sputtered ZnO films. We obtained the obliquely oriented films by placing the substrate  $\sim 3$  cm radially away from the center and taking advantage of geometrical nature of vapor species incident on the growing film. Recently, we have demonstrated shear mode excitation in a ZnO film that was subjected to low energy ion bombardment during growth.<sup>8</sup> In this work we have restricted ourselves only to the latter technique.

Zinc oxide films used in this work were deposited by RF diode sputtering. Details of the system and the deposition parameters have been reported elsewhere.<sup>7</sup> ZnO films were deposited onto metallized LiTaO<sub>3</sub> substrates in a RF diode sputtering system which is routinely pumped down to  $5 \times 10^{-8}$  torr before sputtering. The 3 inch diameter  $\times$  1/4 inch thick hot pressed ZnO target (MRC Mars Grade) was sputtered in Ar + O<sub>2</sub> (5:2) mixture using sputtered-up configuration. The total pressure was 9 mTorr. An RF bias of  $\sim 100\text{V}$  is applied to the substrate during deposition.

The shear mode transducers are formed using an aluminum bottom contact in a coplanar RF line configuration.<sup>1</sup> The 1200Å thick film of chromium-aluminum provides a non-oriented bed for the ZnO sputtered layer as well as the RF ground plane. The ZnO deposition is made on this bottom contact through an appropriate mask. The top contact is made with a chrome aluminum deposition (1200Å) through a metal mask forming a finger over the ZnO film on the bottom contact. The extension of this finger provides a second RF contact pad. The area of the transducer thus formed is typically 125  $\mu\text{m}$   $\times$  125  $\mu\text{m}$ . The resonator substrates are mounted in a holder which provides compressional RF contacts to the transducer pads which connect to a 3 millimeter coaxial fitting.

Several transmission resonators were fabricated with two ZnO shear mode transducers aligned on opposing faces of the substrate. The resonator response is then measured using a HP 8410C network analyzer with a HP 8340A synthesized sweeper. This sweeper has a resolution of 1 Hz at 2 GHz.

#### Results and Discussion

All evaluations to date have been performed on resonators open to the atmosphere. The range of loaded Q values obtained in YAG using an open package is shown in Figure 2. The results for two orientations of YAG; cube edge and body diagonal are shown for longitudinal mode resonance. The effect of acoustic aperture size on insertion loss and loaded Q at room temperature for frequencies near 1.5 GHz are shown in the figure.

For the series of runs which measure the frequency-temperature characteristics of the lithium tantalate shear mode resonators an environmental oven has been modified to accommodate the open resonator package. The resonators are mounted in an enclosure within the oven. Dry nitrogen at a slight positive

pressure is let into the enclosure through a heat exchanger inside the oven. A Tenney, Jr. environmental chamber with a controlled temperature range of -80°C to +177°C is used together with a Doric 410A-P7 temperature monitor with a RTD detector attached to the resonator package. Overall temperature accuracy is  $\pm 0.2^\circ\text{C}$ .

Figure 3 shows the results for a shear mode transmission resonance near 1.1 GHz in lithium tantalate for a cut near  $\theta = -19^\circ$ ,  $\phi = 0$ . The shear mode propagation direction is along the plate normal as defined by the angles in Figure 1. A parabolic temperature-frequency characteristic is observed in the measured values as is shown in Figure 3. The square points in the figure are results obtained in a run made at a different time than that for the cross points. A second resonator was measured over an increased temperature range at a frequency near 1.6 GHz. The results are shown in Figure 4. The measurements made to date on the single rotated cut show a consistent turnover region near -40°C as shown in Figures 3 and 4. Other cuts currently are under investigation with the goal of providing a turnover near room temperature. Presently loaded Q values range between 10 and 30 thousand and higher values may be anticipated with improved resonator design.

We are pleased to acknowledge G. A. Ferguson and D. H. Watt for their assistance in film preparation and resonator fabrication. We would like to thank G. B. Draper for his help in device measurement. Many helpful discussions with R. W. Weinert, W. J. Takei and H. A. Salvo are gratefully acknowledged.

#### References

1. R. A. Moore, J. T. Haynes and B. R. McAvoy in 1981 Ultrasonics Symp. Proc., Chicago (IEEE, New York, 1981), p. 414.
2. J. T. Haynes, H. Salvo, R. A. Moore, and B. R. McAvoy in Proc. 37th Annual Symp. on Frequency Control, Philadelphia (IEEE, New York, 1983), p. 87.
3. H. Rossman and J. T. Haynes in Proc. 37th Annual Symp. on Frequency Control, Philadelphia (IEEE, New York, 1983), p. 272.
4. J. Murphy and M. M. Gad in 1978 IEEE Ultrasonics Symp. Proc., Cherry Hill, NJ (IEEE, New York, 1978), p. 172.
5. J. DeTaint and R. Lancon in Proc. 30th Annual Symp. on Frequency Control, Atlantic City (NTIS, Springfield, VA, 1976), p. 132.
6. J. P. Aubry in 1983 IEEE Ultrasonics Symp. Proc., Atlanta (IEEE, New York, 1983), p. 487.
7. S. V. Krishnaswamy, B. R. McAvoy, W. J. Takei, and R. A. Moore in 1982 IEEE Ultrasonics Symp. Proc., San Diego (IEEE, New York, 1982), p. 476.
8. S. V. Krishnaswamy, B. R. McAvoy and R. A. Moore in 1983 IEEE Ultrasonics Symp. Proc., Atlanta (IEEE, New York, 1983), p. 531.
9. J. S. Wang, Y. Y. Chen and K. M. Lakin, 1982 IEEE Ultrasonics Symp. Proc., p. 346.
10. J. S. Wang, K. M. Lakin and A. R. Landin, 1983 Frequency Control Symp. Proc., 1.

### FIRST ORDER TEMPERATURE COEFFICIENT OF FREQUENCY

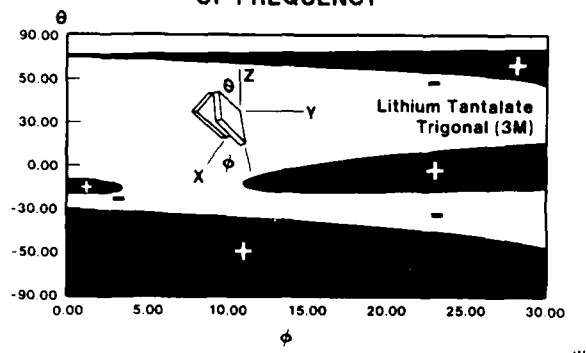


Figure 1. The zero temperature cuts are on the loci between the positive and negative temperature coefficients.

### TEMPERATURE COEFFICIENT OF FREQUENCY LT 19 Y2

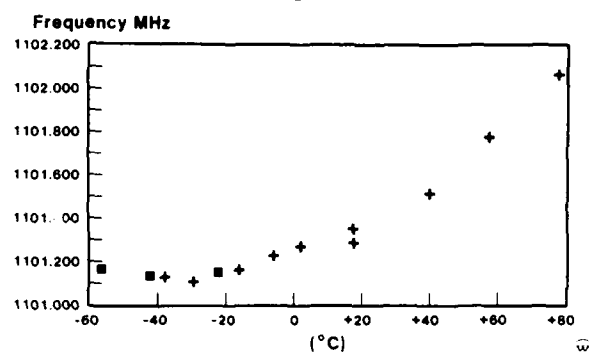


Figure 3. Temperature-frequency measurements on  $\theta = -19^\circ$ ,  $\phi = 0$  cut of lithium tantalate.

### INSERTION LOSS AND $Q_L$ vs APERTURE FOR TWO CUTS OF YAG

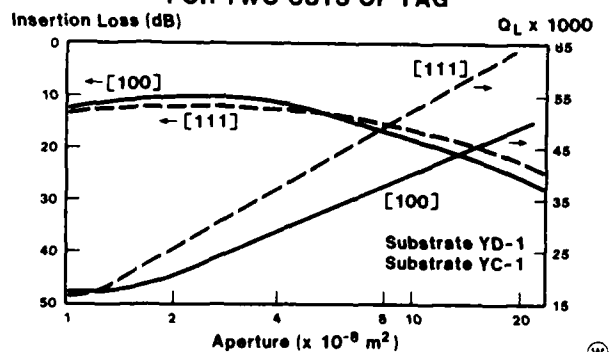


Figure 2. Insertion loss and loaded  $Q$  as a function of resonator acoustic aperture for the longitudinal mode in YAG.

### TEMPERATURE COEFFICIENT OF FREQUENCY

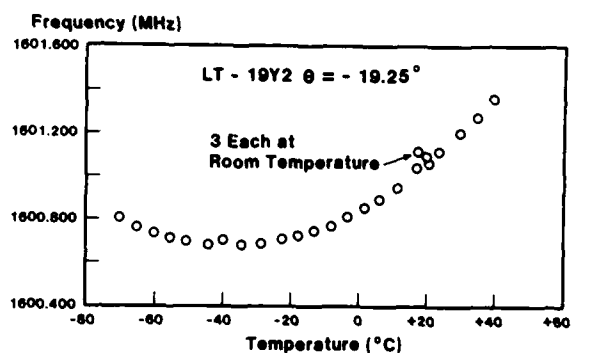


Figure 4. Extended range measurements on  $\theta = -19.25^\circ$ ,  $\phi = 0$  cut of lithium tantalate.

# PERFORMANCE OF FUNDAMENTAL-MODE UHF OSCILLATORS USING BULK-ACOUSTIC-WAVE RESONATORS

Stanley G. Burns      Richard S. Ketcham

Microelectronics Research Center  
Ames Laboratory - USDOE  
Iowa State University  
Ames, Iowa 50011

## Abstract

Fundamental-mode Pierce Oscillators in the 250 to 710 MHz range have been realized utilizing thin-film bulk-acoustic-wave (BAW) resonators. Initial oscillators have demonstrated a phase noise of 100 dBc/Hz (1 KHz offset) and power levels of +6 dBm. A linear-model design approach was used. The circuit topology used and resonator fabrication technique shows great promise for the creation of MMIC circuits in the 200 MHz to 2 GHz range.

## Introduction

The maximum frequency of operation of fundamental-mode crystal-controlled oscillators is restricted to the relatively low resonant frequencies of the crystal. Typically those fundamental modes are several 10's of MHz, though ion-beam milling techniques have been used to fabricate quartz resonators operating to 525 MHz<sup>1</sup>.

This paper describes the performance of Pierce Oscillator whose resonant element is a unique form of thin-film bulk-acoustic-wave (BAW) resonator. These resonators, illustrated in Fig. 1, have been fabricated with fundamental resonances from 200 MHz to over 800 MHz with Q's in excess of 9000. Oscillators in the 250 to 300 MHz range have been realized using composite resonators composed of a thin film of ZnO sputtered onto a thin Si supporting membrane<sup>2</sup>. Oscillators in the 580 to 710 MHz range have been realized using edge supported resonators composed of a thin film of AlN without the supporting Si membrane<sup>3</sup>.

## Oscillator Design

The Pierce Oscillator, Fig. 2, can be modeled as two interconnected networks, Fig. 3, where network A is a composite active device whose y-parameters are known measurable quantities and network B contains the tuning susceptances. The y-parameter matrix of the Pierce Oscillator is obtained by adding the y-parameter matrices of the individual networks and is given by:

$$Y_T = Y_A + Y_B$$

$$= \begin{bmatrix} (g_{1A} + jb_{1A}) & (g_{rA} + jb_{rA}) \\ (g_{fA} + jb_{fA}) & (g_{oA} + jb_{oA}) \end{bmatrix} + \begin{bmatrix} jb_{1B} & 0 \\ 0 & jb_{oB} \end{bmatrix} \quad (1)$$

$$= \begin{bmatrix} y_{11} & y_{12} \\ y_{21} & y_{22} \end{bmatrix}$$

Circuit oscillation implies a non-trivial solution of the network represented by (1) which requires that:

$$y_{11}y_{22} - y_{12}y_{21} = 0$$

or

$$[g_{1A} + j(b_{1A} + b_{1B})][g_{oA} + j(b_{oA} + b_{oB})] - (g_{rA} + jb_{rA})(g_{fA} + jb_{fA}) = 0. \quad (2)$$

Expanding Eq. (2) and collecting real and imaginary results in two equations that must be satisfied:

$$(b_{1B} + b_{1A})(b_{oB} + b_{oA}) = g_{1A}g_{oA} + b_{rA}b_{fA} - g_{fA}g_{rA} \quad (3a)$$

$$b_{1B}g_{oA} + b_{oB}g_{1A} = g_{rA}b_{fA} + b_{rA}g_{fA} - g_{1A}b_{oA} - b_{1A}g_{oA}. \quad (3b)$$

When the y-parameters of the composite active device, network A, are known, Eq. (3a) represents a hyperbola and Eq. (3b) represents a straight line in terms of the tuning susceptances,  $b_{1B}$  and  $b_{oB}$ . Equations (3a) and (3b) are solved simultaneously for either  $b_{1B}$  or  $b_{oB}$  by substitution and only those solutions where  $b_{1B}$  and  $b_{oB}$  represent capacitive susceptances are utilized.

Due to the nature of Eq. (3), three possible solution situations exist and are determined by

$$\psi = (g_{rA}b_{fA} + b_{rA}g_{fA})^2 - (2g_{1A}g_{oA})^2 + 4g_{1A}g_{oA}(g_{rA}g_{fA} - b_{rA}b_{fA}). \quad (4)$$

If this quantity is negative,  $b_{1B}$  and  $b_{oB}$  are complex quantities. Because  $b_{1B}$  and  $b_{oB}$  are inversely related, the onset of oscillation condition cannot be achieved using the passive susceptance tuning configuration of Fig. 3. If  $\psi$  is zero or positive, the onset of oscillation condition can be satisfied with one or two combinations of  $b_{1B}$  and  $b_{oB}$ , respectively. This quantity is used in establishing the values of the oscillator circuit components.

Because this analysis is based on linear small-signal y-parameters, not all solutions arrived at will result in stable oscillations. Some of the solutions, which predict initial instability, do not result in stable limit-cycles. A rigorous solution would have to incorporate a non-linear model.

## Experimental Results

A series of oscillators, one of which is shown in Fig. 4, were built according to this design procedure.

The oscillator pictured shows the thin-film resonator, top TO-18 header, the active device, bottom TO-18 header, and the input and output RF chip capacitors. Oscillator bias and output matching components, not shown in Fig. 4, are contained within the bias-test stand. Discrete devices were used to facilitate the collection of y-parameter data. In all the oscillators, MRFC904 bipolar chip transistors were used for the active device.

Y-parameter data from candidate resonators and active devices were obtained using an HP8505 network analyzer. Resonator data were obtained from just below series resonances to just above parallel resonance and active device data were obtained near the resonator's series resonance. An equivalent model of a 259 MHz ZnO composite resonator, based on y-parameter data, is shown in Fig. 5. Capacitors  $C_{m1}$  and  $C_{m2}$  represent mounting parasitics and typically are not equal due to asymmetries in the resonator mounting.

At each frequency point, Eq. (4) is evaluated. If it is zero or positive, Eq. (3) is solved for  $b_{1B}$  and  $b_{0B}$ . Only those solution points, where  $b_{1B}$  and  $b_{0B}$  represent capacitive susceptances, are utilized. A sample output, shown in Fig. 6 for the resonator modeled in Fig. 5, shows the two possible solutions for the required capacitor values.

Figure 7 shows the SSB phase noise characteristics of two oscillators using ZnO composite resonators. For the 259 MHz oscillator, the computed Q of the resonator is 2200 and the value of  $C_0$  is 3 pF. The output power level is -24 dbm. At a frequency offset of 100 Hz, the measured phase noise is -66 dbc/Hz. For the 262 MHz oscillator, the computed Q of the resonator is 2400 and the value of  $C_0$  is 15 pF. The output power level is -22 dbm. At a frequency offset of 100 Hz, the measured phase noise is -77 dbc/Hz. Both phase noise curves tend to flatten out at higher offset frequencies and is due to dynamic range limitations of the HP8566A and the test fixture. Based upon a linear extrapolation, the computed phase noise at a 1 KHz offset is 104 dbc/Hz for the 259 MHz oscillator and a -112 dbc/Hz for the 262 MHz oscillator. Broadband characteristics, Fig. 8, of two oscillators utilizing the AlN edge supported resonators point to harmonic operation to 2 GHz. To date, this property has not been utilized in our circuit design.

Figure 9 shows the oscillator frequency deviation characteristics as a function of temperature for the ZnO composite resonator based oscillators. All exhibited a sensitivity of approximately -7.5 kHz/°C, a figure which corresponds to the temperature characteristics of the resonators themselves. The resonator temperature coefficient can be changed; Wang et al.<sup>4</sup> have recently described a similar composite material resonator structure with high temperature stability. Figure 10 shows the frequency deviation characteristics for AlN edge supported resonator based oscillators. Both exhibited a temperature sensitivity of approximately -16 kHz/°C.

These data should be considered "worst case" because the circuits contain no thermal bias stabilization and the noise measurements did not rigorously correct for test equipment induced noise.

#### Conclusion and Future Work

This paper has described fundamental-mode oscillators whose operating frequency exceeds that achievable using quartz technology. Additional work is currently underway in the areas of non-linear modeling, noise modeling, and temperature stabilization of hybrid and monolithic UHF oscillators utilizing composite resonators. Since thin-film resonators using GaAs have been demonstrated at frequencies above 1 GHz<sup>5</sup>, work is now proceeding on fundamental-mode hybrid circuits at these frequencies. The thin-film resonator offers a significant size reduction so that the size of active and passive elements for an oscillator (or filter) are about the same. It is expected that integrated circuit fabrication techniques will permit direct integration of the resonator with active devices on the same substrate resulting in a new class of RF/LSI circuits.

#### Acknowledgment

The authors wish to thank Dr. K. Lakin and Mr. A. Landin of Ames Laboratory for their technical assistance in building the oscillator and the Metrology Standards Laboratory of Rockwell International, Cedar Rapids, Iowa, for the noise measurements.

This research was supported by the Air Force Office of Scientific Research and in part by the Iowa State University Engineering Research Institute.

#### References

1. M. Berte, Electron Letters, Vol. 13, p. 248, 1977.
2. K. M. Lakin and J. S. Wang, "Acoustic Bulk Wave Composite Resonators", Applied Physics Letters, Vol. 38(3), February 1, 1981.
3. K. M. Lakin, J. S. Wang and A. R. Landin, "Aluminum Nitride Thin Film and Composite Bulk Wave Resonators", 36th Annual Frequency Control Symposium, 1982.
4. J. S. Wang, A. R. Landin and K. M. Lakin, "Low Temperature Coefficient Shear Wave Thin Films for Composite Resonators and Filters", IEEE 1983 Ultrasonics Symposium Proceedings.
5. G. R. Kline and K. M. Lakin, "1.0 GHz Thin Film Bulk Acoustic Wave Resonators on GaAs", Applied Physics Letters, Vol. 43(8), October 15, 1983.

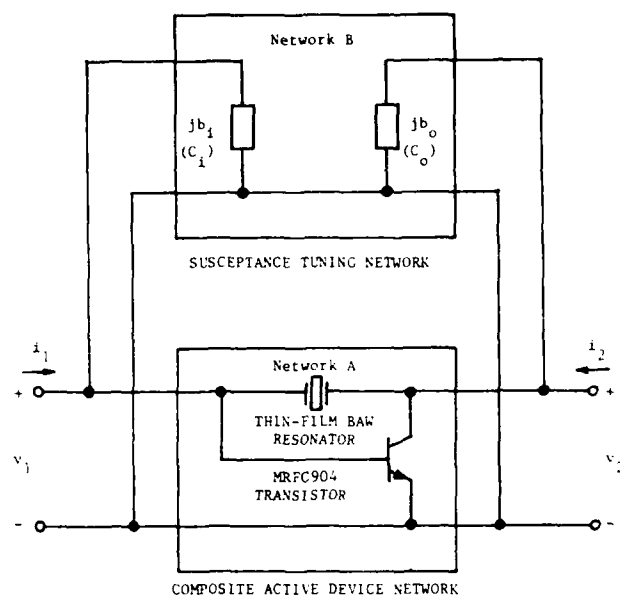
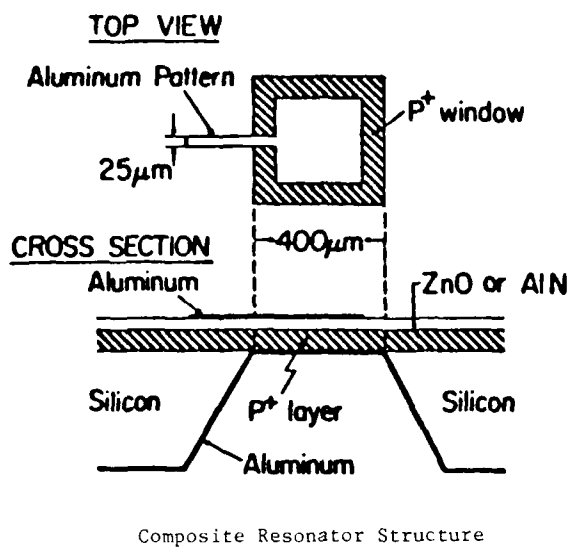


Fig. 3. Y-parameter Model of Transistor Based Pierce Oscillator

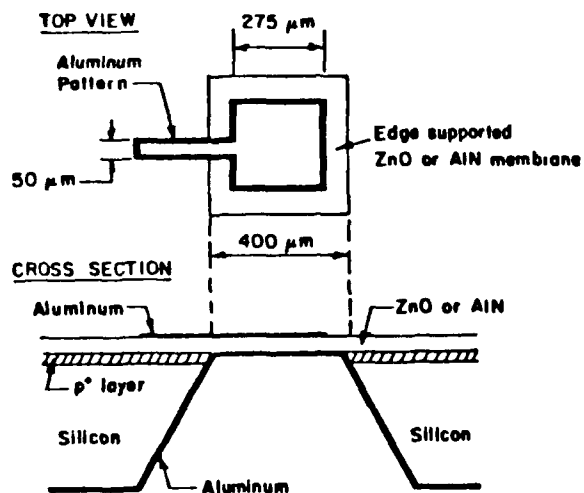


Fig. 1. Thin Film Resonators

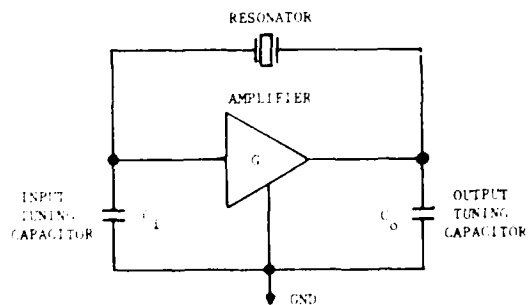


Fig. 2. Generalized Pierce Oscillator



Fig. 4. Photograph of 259 MHz Pierce Oscillator



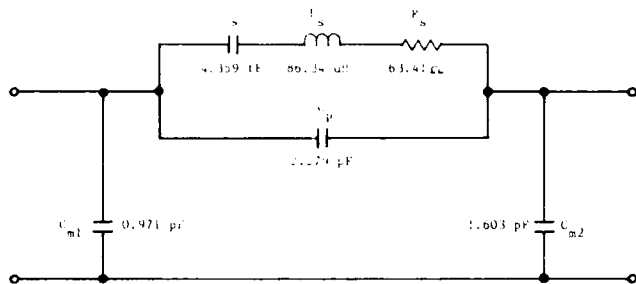


Fig. 5. Model of 259 MHz TO-18 Mounted ZnO Composite Resonator

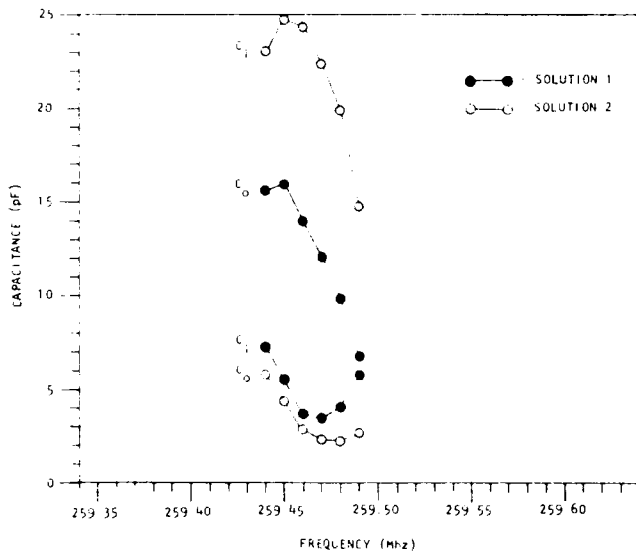


Fig. 6. Solution curves for  $C_0$  and  $C_1$

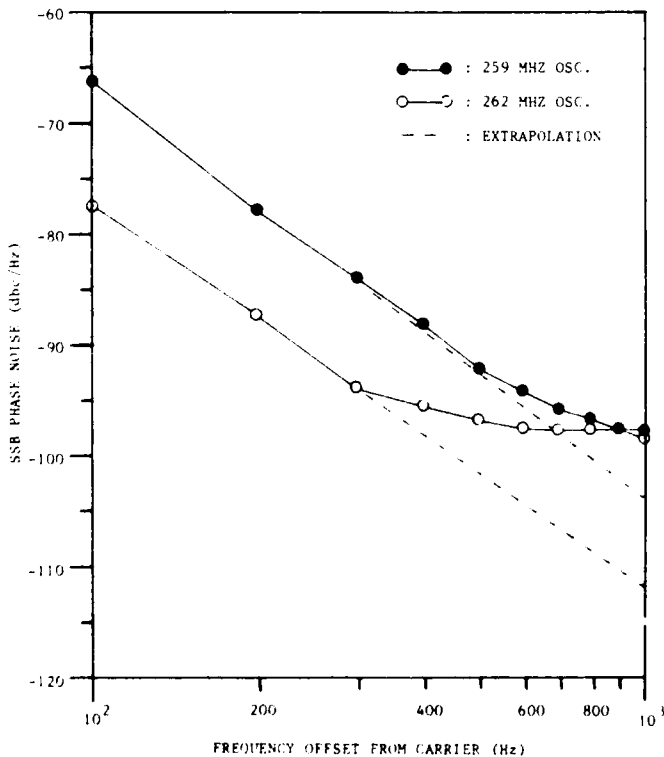
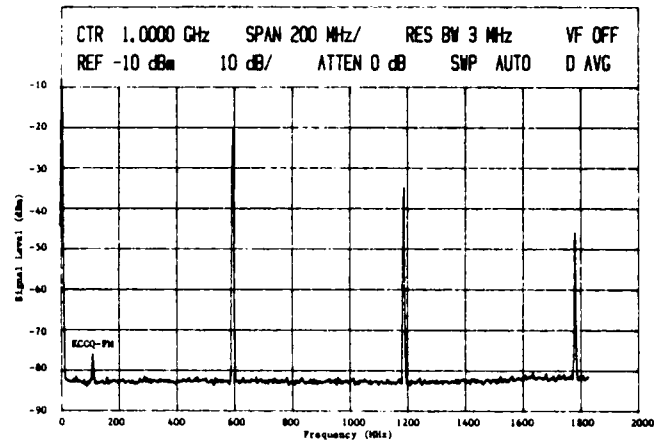
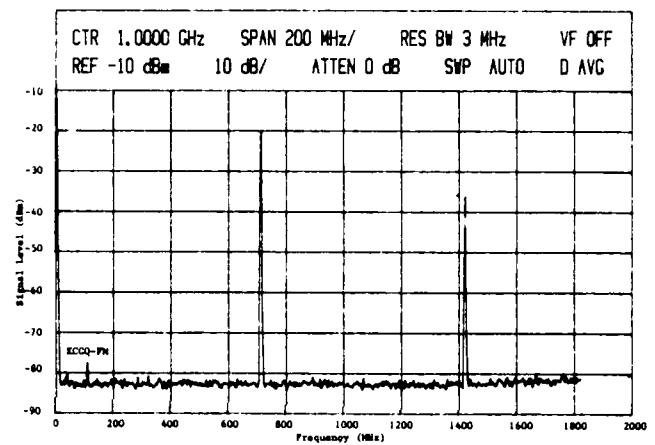


Fig. 7. Phase Noise Characteristics of ZnO Composite Resonator Based Pierce Oscillators



589 MHz Oscillator



706 MHz Oscillator

Fig. 8. Broadband Spectral Characteristics of AlN Edge Supported Resonator Based Oscillators

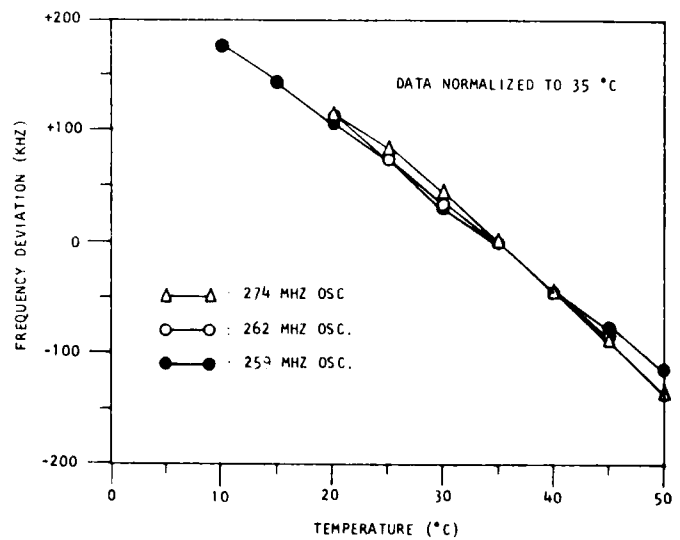


Fig. 9. Frequency Deviation vs. Temperature for ZnO Composite Resonator Based Oscillators

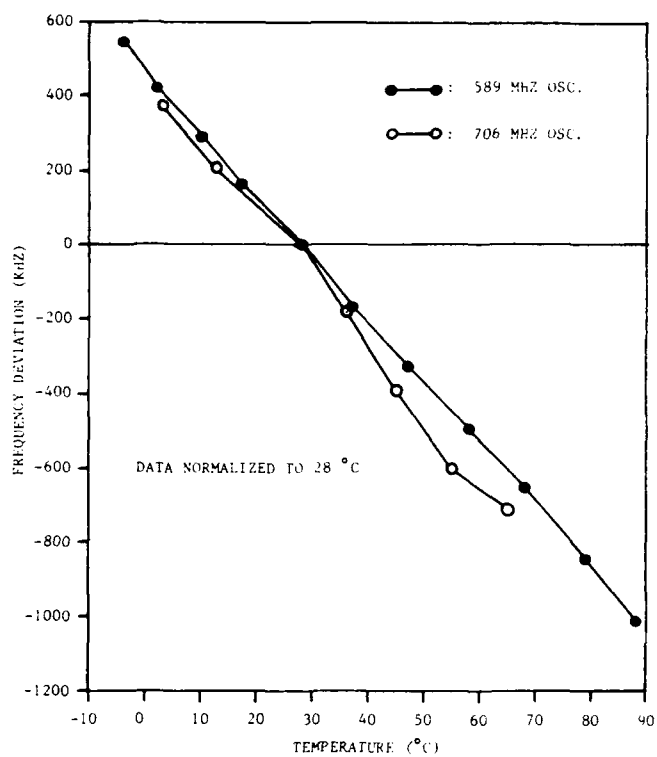


Fig. 10. Frequency Deviation vs. Temperature for AlN Edge Supported Resonator Based Oscillators

## A REVIEW OF SURFACE ACOUSTIC WAVE DEVICES AND THEIR CURRENT APPLICATIONS

Ronald C. Rosenfeld and Ronald M. Hays, Jr.

Sawtek Incorporated  
Post Office Box 18000  
Orlando, Florida 32860

State-of-the-art Surface Acoustic Wave (SAW) components including resonator products, low-loss SAW filters, and reflective array compressor (RAC) devices are readily available today for military, commercial, and consumer applications. SAW performance advantages are supported with high volume production capability and multiple-sourcing of most SAW device types. For example, CATV resonators are currently produced at rates exceeding million-a-year quantities while competition grows steadily for the military SAW requirements. This paper reviews SAW devices that are currently in production at U.S. SAW companies in which SAW components are a principal product and are primarily produced for sale. These companies are Andersen Labs, Crystal Technology, Phonon, RF Monolithics, and Sawtek. Conventional and low-loss band-pass filters, filter banks, dispersive and non-dispersive delay lines, reflective array compressors (RAC's), resonators, multipole resonator filters, and oscillators will be covered. Examples of SAW products from each of the SAW companies follow.

Figure 1 shows an Andersen Laboratories 9-channel filter bank for multi-channel signal processing applications. In this bank, the SAW filters are centered at 70 MHz and have bandwidths from 100 KHz to 12 MHz. The 6.5 x 8.6 x 0.9 inch package includes electronic RF channel switching, filters, amplifiers, and matching networks.

Crystal Technology produces SAW bandpass filters as well as lithium niobate wafers as shown in Figure 2. Lithium niobate and quartz are the most common substrates used in SAW devices.

Figure 3 shows the spectrum and samples of a 70 MHz, 11.4 MHz bandwidth filter from Phonon. A common military IF is at 70 MHz, and wideband 70 MHz filters are used in CATV satellite receivers.

RF Monolithics produces large numbers of SAW resonators at around 680 MHz for local oscillators in CATV set-top converters. Figure 4 shows a wafer of resonators and resonators in TO-5 packages.

A low-loss 3-phase bandpass filter produced at Sawtek is shown in Figure 5. Spiral inductor matching and phasing circuits are used to achieve 5 dB insertion loss in space-qualified filters.

These are just a few examples of the many SAW products that are commercially available today from U.S. SAW suppliers. The authors thank the companies that contributed slides and photographs to this paper and the oral presentation.

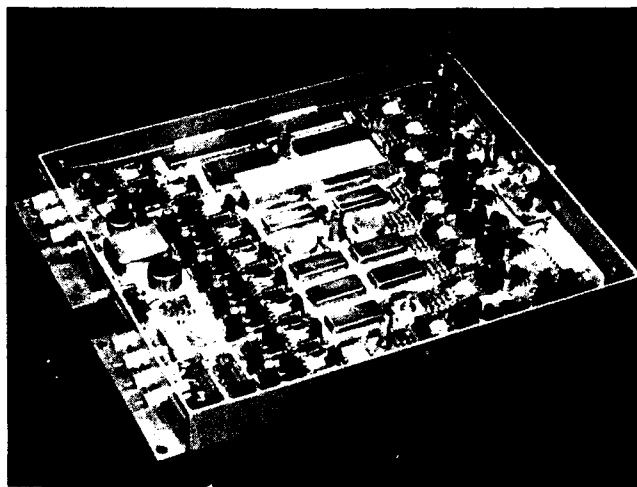


Figure 1 Andersen Laboratories Filter Bank

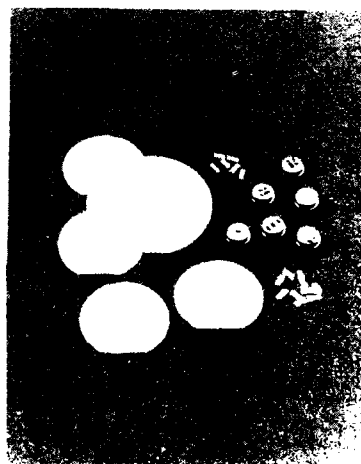


Figure 2 Crystal Technology Filters and Lithium Niobate Wafers

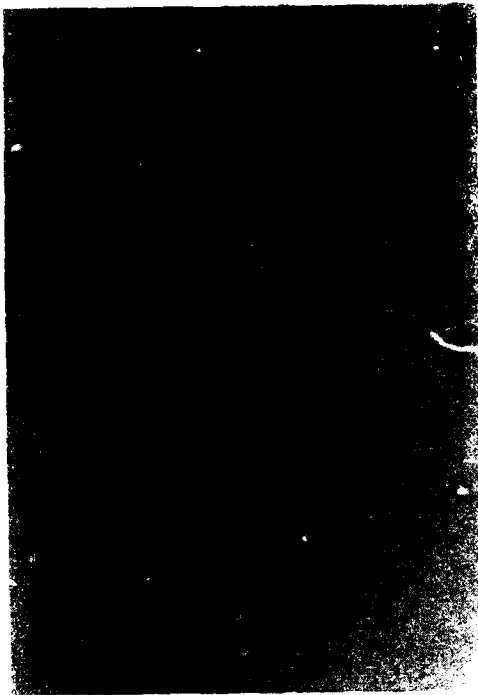


Figure 3 Phonon 70 MHz Bandpass Filter

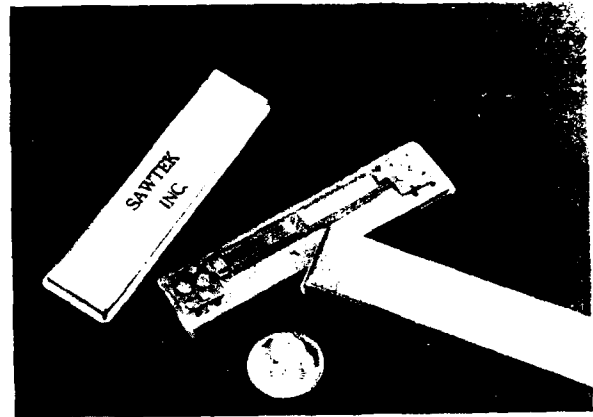


Figure 5 Sawtek Low-Loss Bandpass Filter

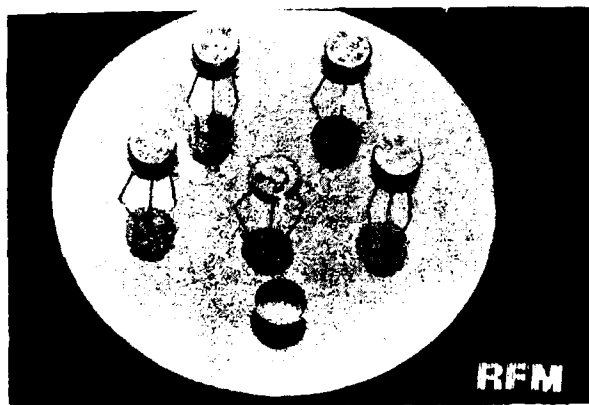


Figure 4 RF Monolithics CATV Resonators

## THE EFFECTS OF TEMPERATURE, RF POWER, RADIATION AND TIME ON SAW RESONATOR ELECTRICAL CHARACTERISTICS

Alfred Vulcan and Charles Gloeckl

Frequency Electronics, Inc.  
Mitchel Field, New York 11553Abstract

The development of SAW Resonators for use in a satellite UHF subsystem required a study of the effect of various environmental parameters on the SAW characteristics. Data was taken over a two-year period on thirty SAW resonators operating at 500 MHz. Since little data was available regarding the effects of the orbital environment on SAWs, the test program was used to qualify the devices for space applications. The results show that not only are the devices suitable for high reliability applications but they can operate at power levels and temperatures beyond those anticipated. The SAW resonators were subjected to temperatures as high as 110°C, 1 MRAD of accumulated radiation and +25 dBm of RF power.

All of the SAW resonators with the exception of six test units were operated continuously during the two-year period. The devices were subjected to the environmental stresses while operating in an oscillator specially designed to minimize the effects of component variations on performance. The oscillators were aged for several months prior to their use and were shown to have negligible influence on the test data. The parameters that were tested as representative of resonator quality were insertion loss and frequency.

Of the thirty resonators tested, three failures occurred. These failures, which were due to a metal migration mechanism, occurred at high RF power levels. The balance of the resonators which operated below +75°C and within the +13 to +18 dBm power range showed negligible parameter variation over the stress period. Subsequent to the life test the devices were delidded and microscopically examined. It was seen that migration in the high electric field areas was the primary contributor to parameter changes, and due to the unique physical construction of the resonators, damage was minimized and parameter degradation reduced. This study shows that SAW resonators can be used in space environments for seven to ten-year missions at reasonably high power levels and temperatures.

Introduction

In order to meet phase noise requirements of -165 dBc/Hz and -173 dBc/Hz at 1 MHz and 6.25 MHz, respective offsets, from a 500 MHz carrier, a 2-port 1-pole SAW resonator is used at the output of a satellite frequency synthesizer. The frequency response of a typical matched resonator is shown in Figures 1 and 2. The basic electrical characteristics of the SAW resonator, whose design is described in Reference 1 are listed in Table 1.

TABLE 1

Center Frequency	500 + .030 MHz
Loaded Q	2500 minimum
Insertion Loss	2.0 dB maximum
Bandwidth (3 dB down)	250 kHz average
Rejection at +3 MHz offset	22 dB minimum

Since no information was available regarding performance of SAW resonators during a seven-year orbital life with radiation, RF power, and temperature stresses, a two-year accelerated life-test program was undertaken to quantify possible life limiting effects.

Test Circuit

Since a group of 30 SAW devices was to be tested and the center frequency of each device in the matched condition was slightly different, use of transmission jigs would require the utilization of several frequency sources, multi-port power splitters, and several medium power 500 MHz amplifiers to simultaneously drive all of the devices. In addition, a method of controlling the RF power at the input to each SAW device would be required. In lieu of this complex and costly approach, an oscillator circuit was developed using a single transistor stage and active biasing. A schematic diagram of the oscillator is shown in Figure 3. A single stage grounded emitter power transistor, Q2, with active bias supplied by Q1 feeds resonant phase shifting network L1 and C4. The SAW resonator is matched with C10, C15, L5 and L8. Two resistive attenuators consisting of R7 through R12 isolate the SAW from the active circuits. The input and output power levels at the SAW matching networks are monitored at J2 and J1, respectively. A diode detector, CR2, and its associated circuitry provides a continuous analogue output corresponding to the SAW RF power level. This output is fed to a strip chart recorder so that a continuous record is kept of power level variations. The RF power circulating in the loop is determined by the transistor biasing and the value of resistors R1 through R3. The oscillator circuit is calibrated with a high frequency sampling scope which measures the voltage waveform at the SAW input and output ports.

To ensure measurement accuracy, SAWs undergoing the accelerated life test were periodically removed from the oscillator circuit and placed in unmatched and matched transmission jigs to measure the resonator frequency and insertion loss, respectively. The unmatched jig provided a sharp transmission peak at the SAW center frequency relative to the matched condition and hence provided more accurate frequency data. It was found that the frequency determined by this method closely matched the oscillator frequency of the SAW when measured at the same temperature. It is important to minimize the contribution of circuit components to oscillator frequency and loop power level so that any measured parameter changes can be attributed to the SAW resonator. Hence the oscillator circuits were temperature cycled between -55° and +100°C for 10 cycles and stabilization baked at +85°C for 30 days. Following this preconditioning, the oscillators were run with 100-ohm resistors replacing the SAW resonators for a period of ten days and the frequency change measured. It was seen that the overall stability of the oscillators run in this mode in a temperature stabilized chamber was at least five times better than the anticipated change in SAW resonant characteristics. Furthermore, a control group of six SAW oscillators was to be kept continuously running at +25°C so that a measured baseline would be established for the lot.

Test Program

Table 2 summarizes the test program for the 30 resonators. The first group of six devices is the control sample which was maintained at normal laboratory ambient temperature which typically varied between +29°C and +22°C and a continuous input RF power level of +13 dBm. The second group was at +25°C but had +18 dBm of incident RF power. A separate group of

TABLE 2

## SAW STRESS FACTORS

QUANTITY	RF POWER dBm	TEMPERATURE °C	TOTAL DOSE MRAD
6	+13	+25	--
6	+18	+25	--
6	+15 to +25	+25	--
6	+13	+25 to +110	--
6	--	+25	1.0

four SAWs remained unstressed for the length of the test but was periodically tested in transmission jigs to see if changes occurred in characteristics which might be attributable to the manufacturing or sealing processes. The third group was initially run at an RF level of +13 dBm with the RF power increased at approximately two-month intervals remaining at +25 dBm after 12-1/2 months. Another group of six resonators was run at an RF power level of +13 dBm but the temperature, which was initially at +25°C, was stepped to +110°C over a period of five months. The final set of SAW's was subjected to 1 MRAD of Cobalt 60 radiation with pre and post-radiation characteristics recorded.

The life test stress levels and dwell time periods were chosen to cover an extreme range of conditions, starting at generally benign levels and progressing to extremes which would damage the SAW devices. By microscopically analyzing the delidded devices at the completion of the program, the failure mechanisms could be identified.

The RF power stress levels were based upon considerations discussed in Reference 1 which show that at a power level of +24 dBm, device degradation occurs. This effect is shown in Figure 4, taken from Tanski. Since little information was available regarding the operation of SAW devices at high temperatures, it was felt that +110°C represented a reasonably high figure which exceeds that normally encountered in most device applications.

#### Resonator Description

The SAW resonators which underwent the accelerated life test were single pole devices which were optimized for minimum insertion loss and low VSWR at 500 MHz. The design incorporates segmented and withdrawal weighted lines to ensure maximum out-of-band rejection with minimum reentrant ripple. The quartz wafer had a ground plane on one side which was epoxied to two mounting bellows. The resonator was mounted in a TO-8 header and was hydrogen fired and coldweld sealed in a high vacuum. Due to this unique mounting mechanism, heat flow from the resonator was maximized by conduction through the quartz and bellows structure directly to the base of the header. Both the resonator deposited aluminum and active bond wires contained a small percentage of copper which has been shown to minimize stress induced migration effects under high power and high temperature conditions. Figure 5 shows the internal structure of the SAW resonator with the metallic bond wires and supporting bellows. The bellows structure was designed to ensure that the self-resonant frequency of the supported SAW filter was above 3,000 Hz. This was outside the limit of acoustical and mechanical stresses introduced by launch and stage separation. A sample of four devices were subjected to a high level random vibration spectrum of 22 G RMS for 5 minutes with no damage.

#### Test Results

All 30 of the resonators subjected to the life test were manufactured from a single lot of quartz and were processed as a single group. Figure 6 shows the frequency shift for the unstressed control group over the two-year period. It is seen that the maximum peak-to-peak frequency excursion is less than 2 kHz. This frequency change is well below the limit which was selected as 50 kHz for device failure. Insertion loss change of greater than 0.5 dB was also considered a failure. The control group variations are due to differences in ambient temperature when the particular devices were tested.

Figure 7 illustrates the resonant frequency changes of the SAWs operating at a fixed power level of +13 dBm. These devices were tested in the oscillator configurations described previously and it is seen that a maximum frequency excursion of 10 kHz occurred. Figure 8 plots the frequency changes of the test group which had an incident RF power level of +18 dBm. The large negative frequency excursion at this increased power level is predictable but well within the established guidelines for reliable operation.

Figure 9 shows that increasing the RF power level above +19 dBm begins to permanently affect the resonant frequency of the SAW devices. The power level is increased about every two months starting at +13 dBm until +25 dBm is reached after 12 months. Significant frequency changes occurred at +19 dBm in resonator 55-24 and a failure occurred in resonator 58-1 at the power level of +22 dBm. At +24 dBm all of the resonators except for 55-24 and 56-4 experienced excessive frequency offset which exceeded the 50 kHz limit.

The effect of high temperature on SAW reliability was originally hypothesized to be equivalent to RF power heating effects. Deterioration of the SAW devices would occur at a combination of RF power and temperature such that localized heating of the resonator elements would be equivalent to that accounted from RF heating alone.

Figure 10 shows the test results of the resonators which were subjected to a stepped temperature stress test while operating at a constant RF power level of +13 dBm. The case temperature of the resonators under test was increased from +25°C to +110°C over a five month period. As shown in the figure, no significant changes in resonant frequency occurred. Five of the six resonators which remained at +110°C for 18 months exhibited a frequency change of less than 20 kHz. The failure of 58-12 was due to a faulty bond at a header active post and is not related to the life test. It is seen from Figure 10 that two resonators were added to the test samples at +110°C after 12 months. These resonators shifted less than 5 kHz over the second year of testing.

All of the testing performed on the resonators consisted of an oscillator frequency and transmission jig insertion loss measurement. Without exception, the insertion loss remained below 3.0 dB (except for the devices which catastrophically failed). The data taken from the oscillator tests correlated very closely to that obtained from the transmission jig when the signal source feeding the SAW was set to the recorded oscillator frequency. Hence it can be concluded that the major failure mechanism is due to a change in resonant frequency. Of course, in the practical situation where the SAW device is used as a narrow band filter and the carrier frequency remains unchanged,

prohibitive attenuation of the signal would occur since the operating frequency now lies on the skirt of the device rather than at the center of the passband.

Figures 11 through 13 are Scanning Electron Photomicrographs of two of the resonators which were operated at +24 dBm and exhibited excessive frequency shifts. It is seen that stress induced metal migration occurred with the damage pattern following the RF electric field distribution at the resonator fingers. This corresponds to increased electric field intensity at the points of maximum damage. It is also seen that actual metal bridges have formed between resonator fingers which results in the rapid performance deterioration.

#### Radiation Effects

Six SAW devices were measured in the laboratory environment and subjected to a 1 MRAD dose of Cobalt 60 radiation at a rate of 150 RADS per second. The devices were then retested and no measurable change in insertion loss or resonant frequency was noted. It was concluded that the effect of total accumulation in normal applications would not effect the resonators. This was an expected result since the surface wave

dynamics of the quartz resonator is unaffected by the radiation, although the bulk characteristics of the quartz is altered. The radiation effect is noticeable in bulk mode crystal resonators used in satellite applications where typically a radiation coefficient of  $1 \times 10^{-12}/\text{RAD}$  is observed for high quality quartz resonators.

#### Summary

A number of high performance SAW resonators were exposed to RF power, temperature, and radiation stresses as well as shock and vibration inputs to determine their suitability for use in a high reliability satellite application. The accelerated stress program shows conclusively that at the levels normally encountered in satellite missions there are no life degrading effects or permanent damage to the resonators which would effect their intended function.

#### References

1. W. J. Tanski, Martin Bloch, and Alfred Vulcan, "High Performance SAW Resonator Filters For Satellite Use," Ultrasonics Symposium Proceedings, November, 1980, pp. 148-152.

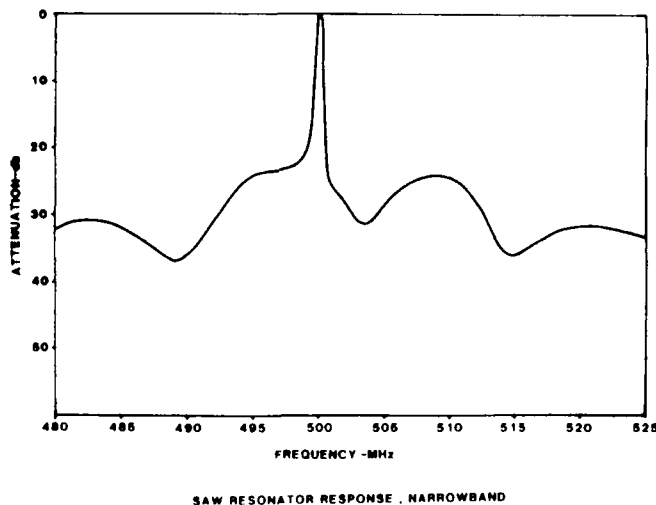


FIGURE 1

SAW RESONATOR RESPONSE, NARROWBAND

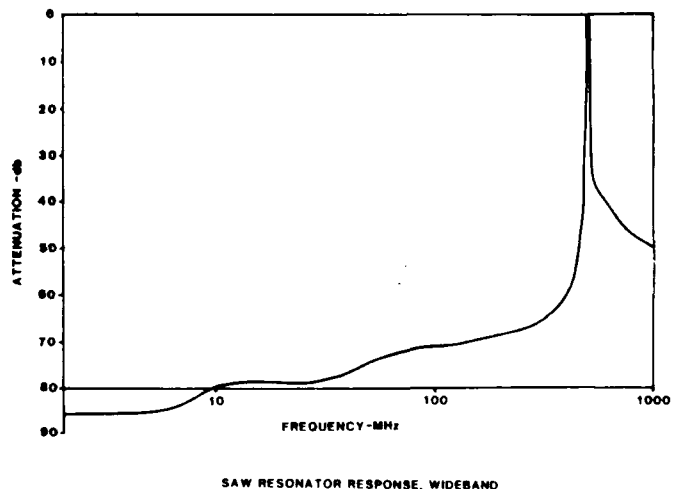


FIGURE 2

SAW RESONATOR RESPONSE, WIDEBAND

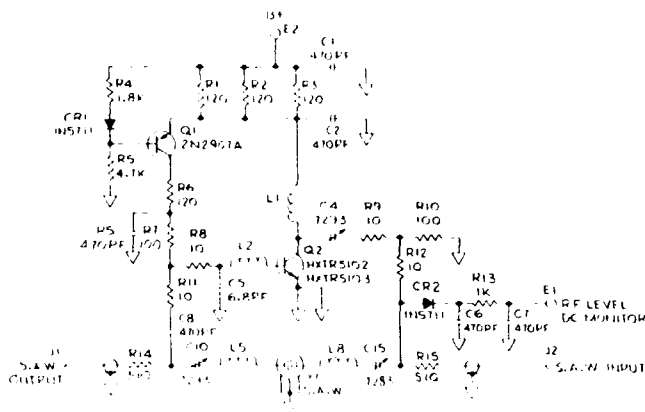


FIGURE 3

500 MHZ SAW OSCILLATOR, SCHEMATIC DIAGRAM

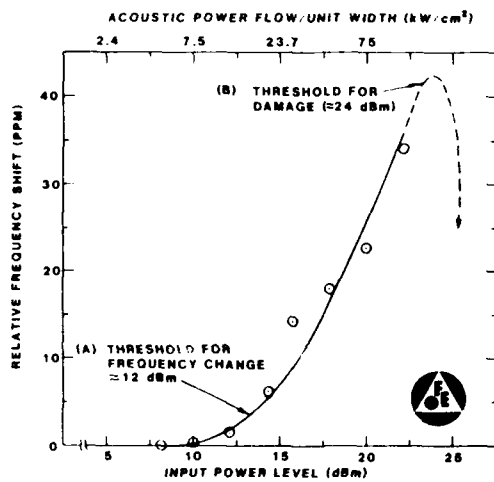


FIGURE 4

SAW STRESS CURVE



FIGURE 5

PHOTOMICROGRAPH, SAW, TOP VIEW

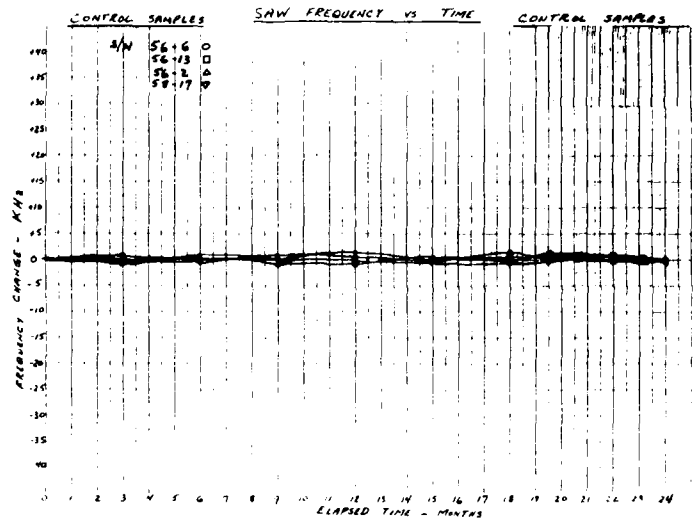


FIGURE 6

SAW STRESS, CONTROL GROUP

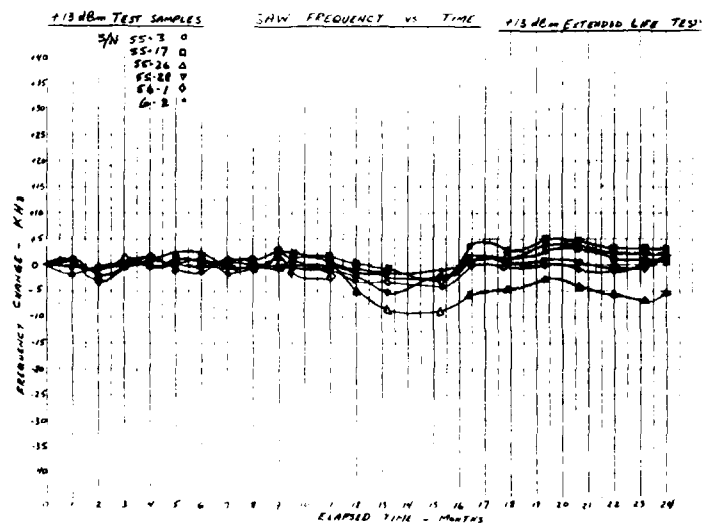


FIGURE 7

SAW STRESS, +13 DBM



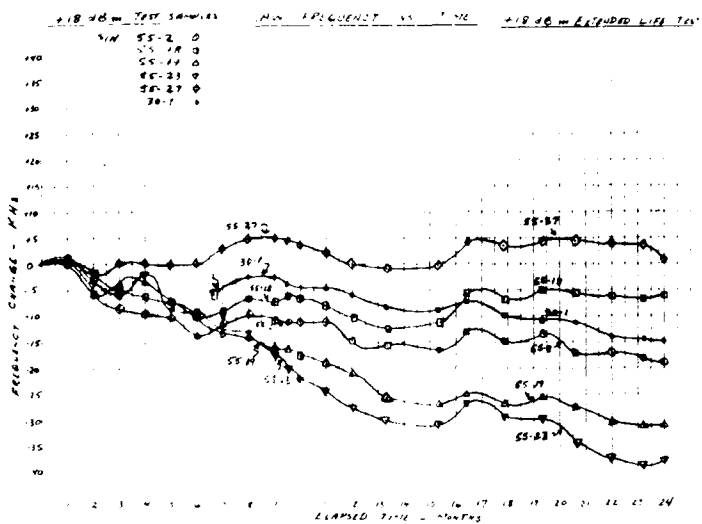
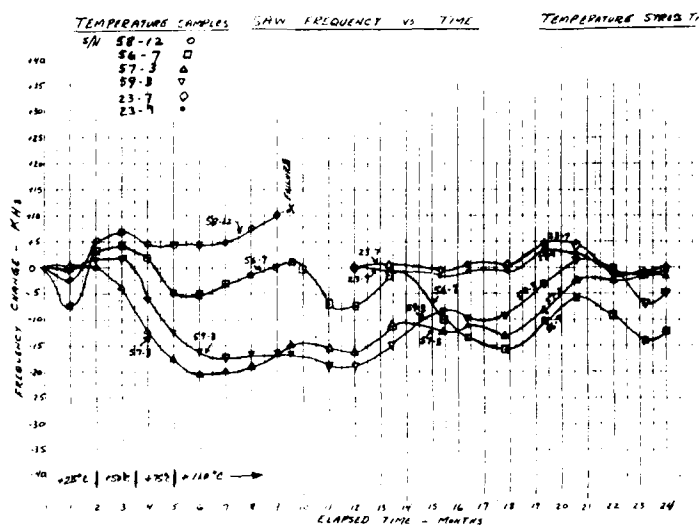


FIGURE 8

SAW STRESS, +18 DBM



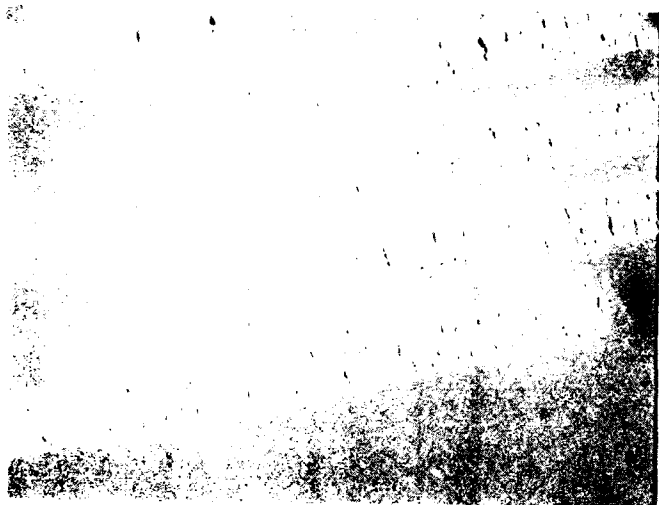


FIGURE 12

SAW RESONATOR SCANNING ELECTRON PHOTOMICROGRAPH #2



FIGURE 13

SAW RESONATOR SCANNING ELECTRON PHOTOMICROGRAPH #3

### Discussion

One advantage of the SAW oscillator implemented in this work, is that the change of the attenuation of the delay line that accompanied the change in the phase velocity was relatively small (less than 0.65 dB). Volluet<sup>6</sup> had implemented a magnetically tunable oscillator using a Gd-Ga YIG film. As a delay line, a relatively large  $\Delta v/v$  was obtained ( $\Delta v/v \sim 5 \times 10^{-3}$ ). However, this phase velocity variation could not be used entirely, owing to the extra attenuation over the same magnetic field range.

Robbins and Simpson<sup>7</sup>, reported a tunable oscillator using a thin film of nickel deposited on YZ-LiNbO<sub>3</sub> delay line. Although for this delay line the maximum relative velocity variation was  $\Delta v/v = 460$  ppm, the maximum change in frequency was only  $\Delta f/f = 254$  ppm. This is because the delay in the magnetic film was only a fraction of the total delay between the SAW transducers in such a configuration where the magnetic film covered only a portion of the acoustic path. In the configuration we used the magnetic film occupied all the acoustic path making our device advantageous in this respect.

### Conclusion

One can conclude that bubble garnet films can be used to offer a means for tuning the SAW oscillators. Our oscillator had the advantages of small attenuation and usage of the whole acoustic path in the delay line.

### Acknowledgements

The authors gratefully acknowledge many stimulating discussions with R. Gunshor and K. Tsubouchi. We thank J. Cassara for lending us the spectrum analyzer.

### References

1. N. A. Howard, "GHz Thick Film Hybrid SAW Oscillators", 1983 Ultrasonics Symposium Proceedings, p.283 (1983).
2. T. E. Parker, "Frequency Stability of Surface Wave Controlled Oscillators", 1978 Ultrasonics Symposium Proceedings, p.558 (1978).
3. M. F. Lewis and T. L. Thorp, "Status of SAW and SSBW Oscillators", 1978 IEEE International Symposium on Circuits and Systems Proceedings, p.553 (1978).
4. M. F. Lewis, "Surface Acoustic Wave Devices and Applications", Ultrasonics, p.115 (1974).
5. A. K. Ganguly, K. L. Davis, D. C. Webb, C. Vittoria and D. W. Forester, "Magnetically Tuned Surface Acoustic Wave Phase Shifter", Elect. Letter, Vol.11, p.610 (1975).
6. G. Volluet, "Surface Acoustic Wave Oscillator Tuned By Magnetoelastic Effect", Elect. Letters, Vol.13, p.588 (1977).
7. W. P. Robbins and E. M. Simpson, "Tunable Surface Acoustic Wave Oscillators Using Magnetostrictive Thin Films", Proc. of the IEEE, Vol.67, p.1572 (1979).
8. S. M. Hanna, F. J. Friedlaender, R. L. Gunshor, and H. Sato, "Propagation of Surface Acoustic Waves in Magnetic Bubble Garnet Films", IEEE Trans. Magnetics, Vol.MAG-19, p.1802 (1983).

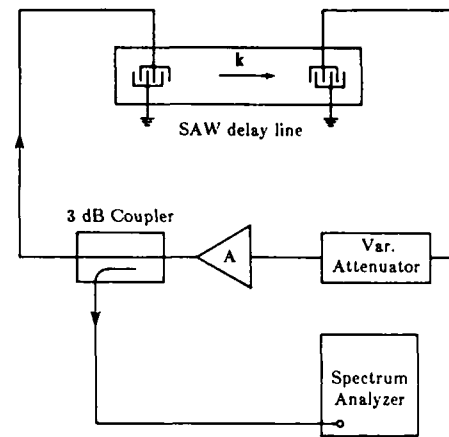


Fig. 1 Schematic diagram of a SAW delay line oscillator.

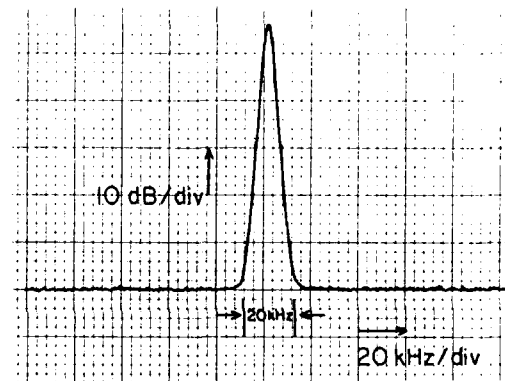


Fig. 2 Output spectrum of the SAW oscillator.

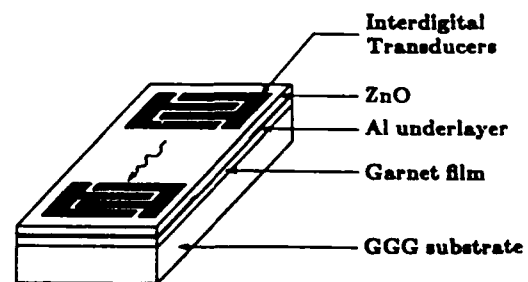


Fig. 3 SAW device configuration for ZnO/garnet layered structure.

### Discussion

One advantage of the SAW oscillator implemented in this work, is that the change of the attenuation of the delay line that accompanied the change in the phase velocity was relatively small (less than 0.65 dB). Volluet<sup>6</sup> had implemented a magnetically tunable oscillator using a Gd-Ga YIG film. As a delay line, a relatively large  $\Delta v/v$  was obtained ( $\Delta v/v \sim 5 \times 10^{-3}$ ). However, this phase velocity variation could not be used entirely, owing to the extra attenuation over the same magnetic field range.

Robbins and Simpson<sup>7</sup>, reported a tunable oscillator using a thin film of nickel deposited on YZ-LiNbO<sub>3</sub> delay line. Although for this delay line the maximum relative velocity variation was  $\Delta v/v = 460$  ppm, the maximum change in frequency was only  $\Delta f/f = 254$  ppm. This is because the delay in the magnetic film was only a fraction of the total delay between the SAW transducers in such a configuration where the magnetic film covered only a portion of the acoustic path. In the configuration we used the magnetic film occupied all the acoustic path making our device advantageous in this respect.

### Conclusion

One can conclude that bubble garnet films can be used to offer a means for tuning the SAW oscillators. Our oscillator had the advantages of small attenuation and usage of the whole acoustic path in the delay line.

### Acknowledgements

The authors gratefully acknowledge many stimulating discussions with R. Gunshor and K. Tsubouchi. We thank F. Cassara for lending us the spectrum analyzer.

### References

1. N. A. Howard, "GHz Thick Film Hybrid SAW Oscillators", 1983 Ultrasonics Symposium Proceedings, p.283 (1983).
2. T. E. Parker, "Frequency Stability of Surface Wave Controlled Oscillators", 1978 Ultrasonics Symposium Proceedings, p.558 (1978).
3. M. F. Lewis and T. L. Thorp, "Status of SAW and SSBW Oscillators", 1978 IEEE International Symposium on Circuits and Systems Proceedings, p.553 (1978).
4. M. F. Lewis, "Surface Acoustic Wave Devices and Applications", Ultrasonics, p.115 (1974).
5. A. K. Ganguly, K. L. Davis, D. C. Webb, C. Vittoria and D. W. Forester, "Magnetically Tuned Surface Acoustic Wave Phase Shifter", Elect. Letter, Vol.11, p.610 (1975).
6. G. Volluet, "Surface Acoustic Wave Oscillator Tuned By Magnetoelastic Effect", Elect. Letters, Vol.13, p.588 (1977).
7. W. P. Robbins and E. M. Simpson, "Tunable Surface Acoustic Wave Oscillators Using Magnetostrictive Thin Films", Proc. of the IEEE, Vol.67, p.1572 (1979).
8. S. M. Hanna, F. J. Friedlaender, R. L. Gunshor, and H. Sato, "Propagation of Surface Acoustic Waves in Magnetic Bubble Garnet Films", IEEE Trans. Magnetics, Vol.MAG-19, p.1802 (1983).

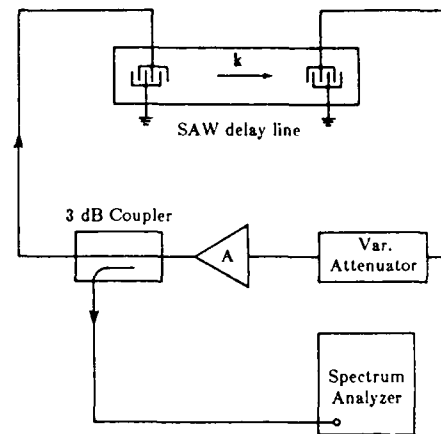


Fig. 1 Schematic diagram of a SAW delay line oscillator.

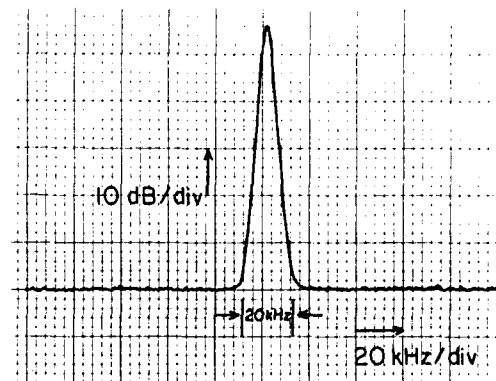


Fig. 2 Output spectrum of the SAW oscillator.

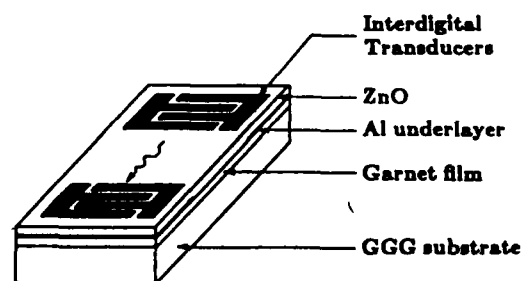


Fig. 3 SAW device configuration for ZnO/garnet layered structure.

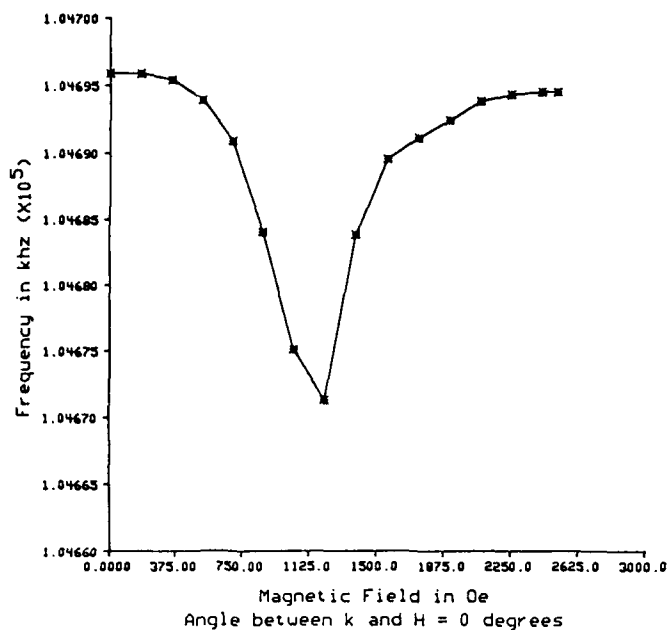


Fig. 4 Variation of the SAW oscillator frequency with a dc magnetic field applied parallel to the SAW propagation direction.

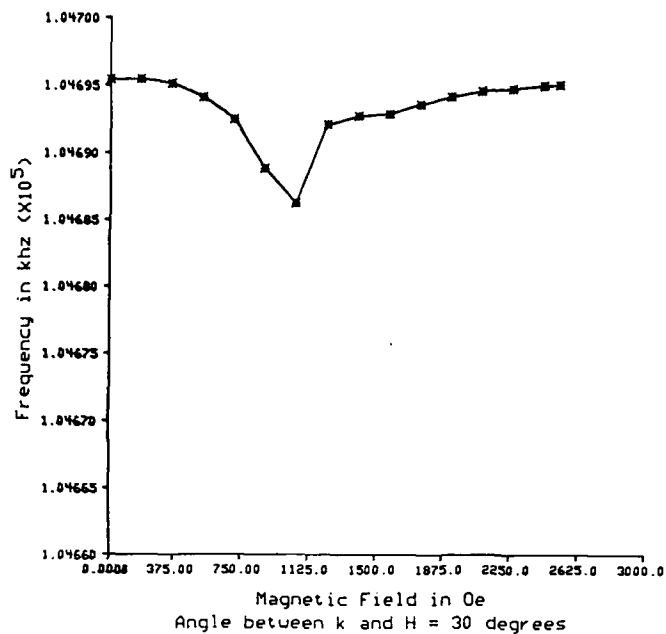


Fig. 5 Variation of the SAW oscillator frequency with the magnetic field for  $\phi = 30^\circ$ .

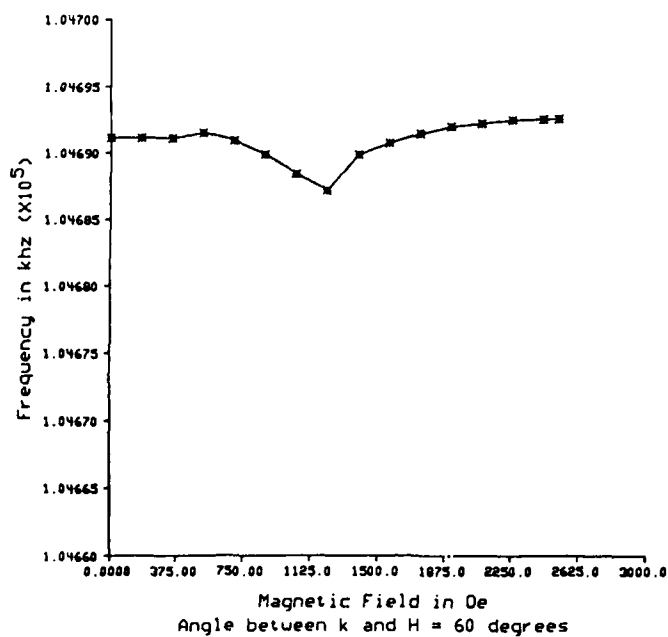


Fig. 6 Variation of the SAW oscillator frequency with the magnetic field for  $\phi = 60^\circ$ .

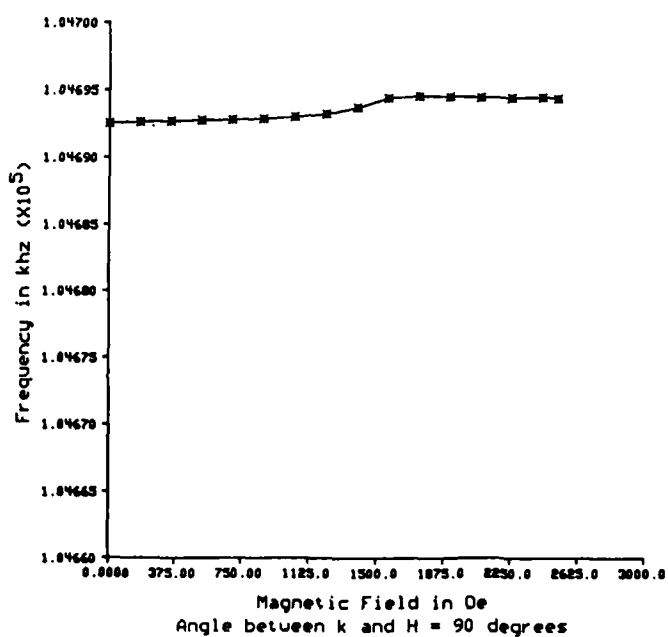


Fig. 7 Variation of the SAW oscillator frequency with the magnetic field for  $\phi = 90^\circ$ .

## SBAW VERSUS SAW OSCILLATOR AGING\*

R. B. Stokes, K. H. Yen, and K. F. Lau

TRW Electronic Systems Group  
One Space Park, Redondo Beach, CA 90278Abstract

The frequency aging of Shallow Bulk Acoustic Wave (SBAW) oscillators operating directly at frequencies from 2 to 3 GHz has been measured. SBAW devices have long been expected to age better than SAW devices because the wave is not confined so closely to the surface. All the oscillators reported here aged upward in frequency, but at widely varying rates. One 2 GHz SBAW oscillator, built on near-BT quartz, has aged only 2.5 ppm in the first eight months. This data compares favorably with data reported in the literature for high frequency (> 1 GHz) SAW oscillators. Other oscillators, built on near-AT quartz and operating at 3 GHz, did not age as well. However, most of the AT device aging is probably due to excessive power levels in the extremely small transducers.

This paper describes the designs of these SBAW oscillators and presents the aging data. This aging data is compared with published aging data for SAW oscillators. The causes of aging in the SBAW oscillators are then analyzed and compared with those which cause SAW aging.

Introduction

In their simplest form, shallow bulk acoustic waves (SBAW), also known as surface skimming bulk waves (SSBW), are bulk shear waves beamed just below the surface of a crystal. Since the presence of the surface is not directly involved in the SBAW wave propagation mechanism, it has been hoped that oscillators based on this wave may have inherently low aging. In the past few years, considerable aging data have been recorded for oscillators stabilized by vacuum-packaged SAW (on ST quartz) and SBAW (on AT and BT quartz) devices. This paper first analyzes how aging mechanisms affect the two types of waves over frequency. Then, SAW aging data from the literature is summarized. Next, new data on high frequency SBAW oscillators is presented. Finally, the SAW and SBAW data are compared in light of the understanding of the aging mechanisms.

SAW and SBAW Aging Mechanisms

The mechanisms for SAW delay line aging have recently been studied. The most important mechanisms for a SAW-stabilized oscillator aging at low power and at constant temperature appear to be adsorption and desorption of surface contaminants, and relaxation of stresses initially present in the crystal and metallization. This assumes that electronics aging and mounting stress relaxation are made negligible by proper design. Since SAW and SBAW devices are very similar and are fabricated and packaged by exactly the same processes, the dominant aging mechanisms should be the same. They will, however, differ in magnitude according to the differences between the two waves.

Surface Acoustic Waves

Table 1 shows how adsorption and desorption, static stress, and overdriving should affect SAW devices as a function of frequency. Adsorption of small amounts of surface contamination causes a fractional change in frequency which is proportional to the adsorbed layer thickness  $t$  divided by the SAW wavelength  $\lambda$ .<sup>2</sup> For a given amount of adsorption, the change in ppm should therefore be proportional to frequency. The proportionality constant depends on the substrate, orientation, and adsorbed material.

Table 1. Sensitivity of SAW Devices to Aging Mechanisms Versus Frequency

Mechanism	Frequency Dependence	Comment
Adsorption of surface contamination	f	Fractional frequency change is proportional to $(t/\lambda)$ with sensitivity determined by contaminant
Relaxation of static stress	Frequency independent	Fractional frequency change is directly proportional to stress
Overdriving damage	Threshold decreases 6 dB/octave	Assuming fixed aperture (in wavelengths) and constant insertion loss

Fractional frequency changes due to locally uniform static stresses, such as those induced by crystal polishing, are frequency independent for a given substrate. For example, for ST quartz SAW devices, the frequency will change about -16 ppm for a tensile stress in the direction of propagation of  $10^6$  N/m<sup>2</sup>. Stresses due to pattern-dependent features, such as the metal film, should scale in a frequency-independent way if the fractional coverage of the wave propagation path is constant. Of course, the effects of adsorption and static stress will be modified somewhat at very high frequencies when transducer mass loading significantly modifies the wave.

When the input power to the SAW device is high, other aging mechanisms are also involved. The effect of overdriving a SAW device has been summarized by Shreve.<sup>3</sup> For a given substrate and metal film, there is an acoustic threshold above which acoustomigration will take place. At stresses somewhat below this threshold, the frequency is seen to age upward at a power-dependent rate. At stresses above threshold, the frequency ages rapidly downward. Shreve summarizes how acoustic stresses are calculated according to the Microwave Acoustics Handbook.<sup>4</sup> It is important to note that for a fixed device geometry which is simply scaled down in size to increase the frequency, the acoustic stress for a given drive level is proportional to frequency (assuming constant transducer losses). Similarly, the drive power threshold for overdriving damage decreases as  $1/f^2$ , or - 6 dB per octave.

\*This work was partially supported by ERADCOM Contract DAAK20-81-C-0415.

## Shallow Bulk Acoustic Waves

The effects of adsorption, static stress, and overdriving which are expected for shallow bulk (SBAW) devices are summarized in Table 2. Static stress effects and overdriving effects should have the same frequency dependence as in SAW devices, since the acoustic stress scales with dimensions the same way as in SAW devices. In fact, the magnitudes of these effects are on the same order as those for ST quartz. For instance, the longitudinal stress sensitivity of AT SBAW devices is  $-13 \text{ ppm per } 10^6 \text{ N/m}^2$ . The overdriving damage threshold for quartz SBAW devices should be similar to that for quartz SAW devices of about the same insertion loss since the materials are the same and the dimensions are similar.

Table 2. Sensitivity of SBAW Devices to Aging Mechanisms Versus Frequency

Mechanism	Frequency Dependence	Comment
Adsorption of surface contamination	f	Fractional velocity change proportional to $(t/\lambda)$ with sensitivity depending on initial mass loading
Relaxation of static stress	Frequency independent	Fractional frequency change is directly proportional to stress
Overdriving damage	Threshold decreases 6 dB/octave	Assuming fixed aperture (in wavelengths) and constant insertion loss

The significant difference between SBAW and SAW devices is in adsorption sensitivity. Lee<sup>5</sup> has shown that an SBAW propagating below a free surface will have a fractional velocity change proportional to  $(t/\lambda)^2$  as a mass loading adsorption layer is applied. This is because the SBAW is slowly converted to a surface wave, becoming increasingly dependent on the surface as the mass loading is increased. When no mass loading is present, this relation shows that the wave is completely insensitive to infinitesimal amounts of mass loading. However, as the loading increases, the slope of the quadratic relation also increases, and the sensitivity to additional mass loading increases along with the loading itself. For small amounts of adsorption of additional mass loading material, the SBAW sensitivity can therefore be modeled with a linear proportionality to  $t/\lambda$  with a proportionality constant which depends on the starting condition. For AT SBAW delay lines, in which the velocity is very high (5100 m/s), transducer aluminum films cause significant mass loading, so sensitivity to additional loading is often similar to that of a SAW device. In BT SBAW delay lines, however, aluminum films cause much less of a mass loading effect because the acoustic velocities and densities of the substrate and metal film are similar. BT SBAW delay lines may therefore be less adsorption-sensitive than equivalent SAW devices.

### Review of SAW Aging

Table 3 summarizes some of the best SAW delay line aging that has been reported in the literature. Unfortunately, recent SAW aging data covering a wide range of frequencies is not available from a single source. However, all the SAW delay lines listed in the table were vacuum packaged, with mountings

Table 3. Summary of SAW Aging Reported in the Literature.\*

Reference	Frequency	Linear Fit to First Year Aging
Parker <sup>6</sup>	400 MHz	+ 1.2 ppm/year average
Lukaszek and Ballato <sup>7</sup>	310 MHz	+ 1 ppm/year
Gilden, et al. <sup>8</sup>	1.4 GHz	+ 5 ppm/year

\*All devices are vacuum-packaged SAW delay lines in which steps have been taken to minimize mounting stress.

designed for minimum stress. Parker<sup>6</sup> recently reported a group of 27 SAW oscillators at 400 MHz, which were vacuum-sealed by cold welding in TO-8 packages. Straight-line fits to this data gave average aging of 1.2 ppm in the first year. Lukaszek and Ballato<sup>7</sup> described a similar delay line at 310 MHz. A straight line fit to the first year of data gives a rate no more than 1 ppm/year. Gilden, et al.<sup>8</sup> reported aging of 1.4 GHz SAW delay lines vacuum sealed in all-quartz packages. The aging data of the best device described shows low total aging (2 ppm in the first year), but this includes fairly rapid upward aging followed by fairly rapid downward aging. A straight-line fit to this data would give about 5 ppm in the first year.

Since the packaging of these two delay lines is different, the cleanliness of the device and the residual mounting stress are probably not the same. However, in both cases, minimizing the stress and achieving maximum cleanliness were major goals. It is interesting to note that if desorption of contamination from the surface was the dominant aging mechanism and equal in both cases, Table 1 would predict that the 1.4 GHz oscillator would age 3.5 times worse than the 400 MHz oscillator, and this ratio is close to what was observed. Similarly, the 310 MHz oscillator should age slightly better than the 400 MHz oscillator, which is also the case.

### SBAW Aging Data

The aging of three SBAW delay line oscillators is shown in Figures 1 through 3. In each case, the delay line was fabricated by direct electron beam writing on a quartz wafer, which was subsequently diced. The transducer fingers were not "buried." All devices were mounted onto TO-8 headers with stainless steel spring clips. The mounted devices were then baked in vacuum overnight at 200°C, and the packages were sealed under vacuum by cold welding. The SBAW delay lines were then assembled into oscillator circuits with commercial amplifiers. These oscillators were aged in an oven stable to 0.1°C after July, 1983. Surprisingly, the aging continues to exhibit rapid fluctuations over several ppm.

The delay lines shown in Figures 1 and 2 are 3.0 GHz fundamental devices built on near-AT quartz. Figure 1 shows aging of a device operating in a circuit providing +11 dBm available power to the

\*\*A straight-line fit to the first year of data in Ref. 7 makes it look worse than it was. In fact, the total aging was only 0.5 ppm at 12 months, and 0.2 ppm at 19 months.

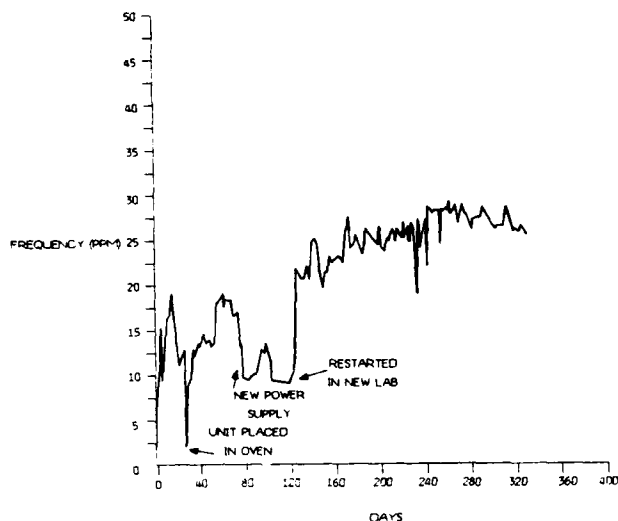


Figure 1. Frequency Aging of 3.0 GHz Near-AT Quartz Fundamental Mode Oscillator #1

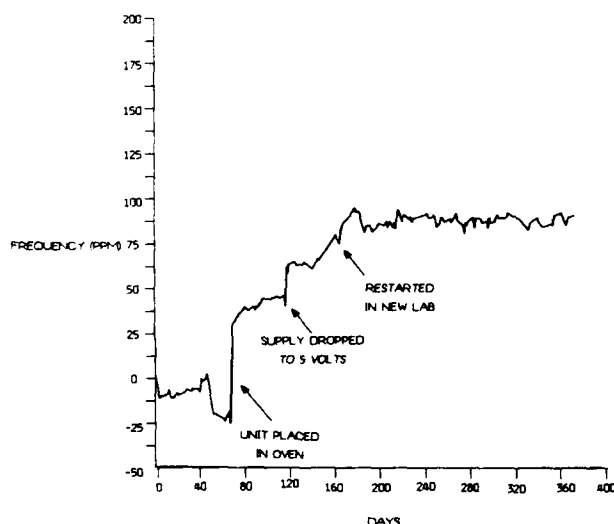


Figure 2. Frequency Aging of 3.0 GHz Near-AT Quartz Fundamental Mode Delay Line Oscillator #2

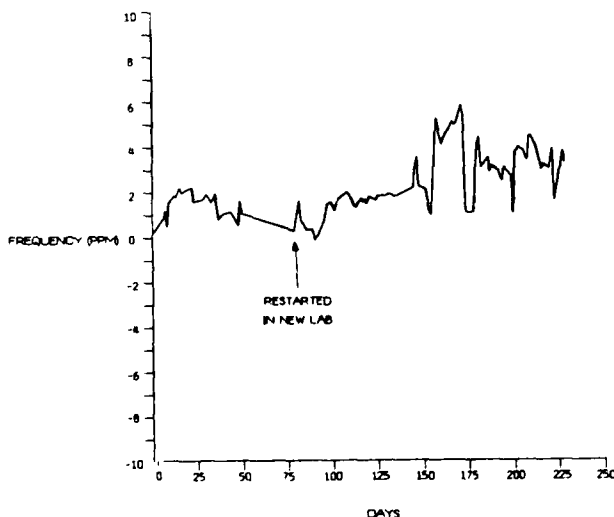


Figure 3. Frequency Aging of 2.1 GHz Near-BT Quartz Third Harmonic SBAW Delay Line Oscillator

input transducer. The aging is seen to be about 25 ppm/year over the first year. Figure 2 shows the aging of a nominally identical device. In this case, initial aging was poor, although this could be partly due to the initially uncontrolled temperature environment. However, at the end of August 1983, overdriving damage was suspected as the cause of the rapid upward aging since this had been seen for SAW devices at high drive levels.<sup>1</sup> To reduce the drive level, the power supply voltage for the oscillator of Figure 2 was reduced from 12 to 5 volts, dropping the device drive power from +10 dBm to 0 dBm. An initial jump in frequency was seen, which is probably a circuit or temperature effect caused by the large power supply change. Aging then slowed, increased, and then slowed again over a period of two months. Finally, the systematic aging rate stabilized to only a few ppm/year, 6 months after aging began. At present, the device of Figure 2 is aging much better than that in Figure 1, implying that the original drive level was damaging these devices.

The delay line in Figure 3 is a third-harmonic device, fabricated on near-BT quartz, and operates at 2.1 GHz. The drive level for this delay line was -6 dBm. As stated before, the lower velocity of the SBAW on near-BT quartz may make transducer mass loading less severe, reducing the effect of additional mass loading from adsorption of contamination. This oscillator ages quite well, only a total of 2.5 ppm in the first 8 months. A straight-line fit, however, shows an aging rate of about 5 ppm/year. This aging is quite good for such a high frequency device.

### Conclusions

A survey of SAW and SBAW aging mechanisms shows few differences. For both waves, aging (measured in ppm) due to relaxation of static stress is independent of frequency. Also, the stress sensitivities are similar. Adsorption and desorption of contamination, however, should cause aging (in ppm) which is proportional to the operating frequency. The sensitivity to adsorption depends only on the contaminant in SAW devices, while it also depends on the amount of initial mass loading in SBAW devices, including that of the transducers. If the initial mass loading is light, as is probably the case in near-BT SBAW delay lines, the sensitivity to adsorption could be significantly less than for SAWs. Finally, the drive threshold at which the power causes aging should drop 6 dB per octave for both types of device.

A sampling of two sources of SAW delay line aging in the literature shows that the aging appears to scale with frequency as expected if the dominant aging mechanism is adsorption or desorption. Similar scaling predicts that low-aging 2 GHz SAW delay lines might age 6 ppm/year (based on Parker's 400 MHz data), while 3 GHz SAW delay lines might age 9 ppm/year.

Several SBAW delay line oscillators were built and aged for nearly a year. Near-AT devices at 3 GHz aged 20 ppm/year or more at drive levels of +10 dBm, but a reduction in power to 0 dBm reduced the aging to only a few ppm/year. Following the 6 dB per octave rule, the overdriving threshold at 3 GHz might be expected to be only -5 dBm if it is +10 dBm at 500 MHz (where overdriving damage has been observed).<sup>1</sup> Overdriving is therefore expected to be responsible for the rapid initial aging of these 3 GHz oscillators. The near-BT SBAW oscillator at 2 GHz, however, aged only about 2.5 ppm over 8 months, considerably better than expected for a SAW oscillator at that frequency if adsorption or desorption is the dominant aging mechanism. This is also consistent with the expectation that BT SBAW oscillators are expected to age



less than AT SBAW oscillators because of less sensitivity to transducer mass loading.

In conclusion, SBAW oscillators in the 2 to 3 GHz range are capable of good long-term aging. Aging of only 2.5 ppm has been observed for 2 GHz near-BT SBAW delay line oscillators in the first 8 months. A near-AT, 3 GHz SBAW oscillator was also observed to age well (a few ppm per year) when the drive power was lowered sufficiently. This data indicates that low-aging SBAW oscillators are possible even when the frequency is pushed far beyond the normal working range for SAWs.

#### References

1. R. B. Stokes and M. J. Delaney, "Aging Mechanisms in SAW Oscillators," Proc. 1983 IEEE Ultrasonics Symposium, p. 247.
2. R. B. Hemphill, "A Surface Wave Thickness Monitor for Thin Evaporated Films," Proc. 1973 IEEE Ultrasonics Symposium, p. 525.
3. W. R. Shreve, R. C. Bray, S. Elliott and Y. C. Chu, "Power Dependence of Aging in SAW Resonators," Proc. 1981 Ultrasonics Symposium, p. 94.
4. A. J. Slobodnik, Jr., E. D. Conway, and R. T. Delmonico, "Microwave Acoustics Handbook," Vol. 1A, Air Force Cambridge Research Laboratories, Hanscom Field, MA (1973).
5. D. L. Lee, "S-Band SSBW Delay Lines for Oscillator Applications," Proc. 1980 IEEE Ultrasonics Symposium, p. 245.
6. T. E. Parker, "Random and Systematic Contributions to Long Term Frequency Stability in SAW Oscillators," Proc. 1983 IEEE Ultrasonics Symposium, p. 257.
7. T. Lukaszek and A. Ballato, "What SAW Can Learn from BAW: Implications for Future Frequency Control, Selection, and Signal Processing," Proc. 1980 Ultrasonics Symposium, p. 173.
8. M. Gilden, G. K. Montress, and R. A. Wagner, "Long-term Aging and Mechanical Stability of 1.4 GHz SAW Oscillators," Proc. 1980 IEEE Ultrasonics Symposium, p. 184.

# NARROW BANDPASS FILTER USING DOUBLE-MODE SAW RESONATORS ON QUARTZ

M. Tanaka, T. Morita, K. Ono and Y. Nakazawa

Toyo Communication Equipment Co., Ltd.  
Kawasaki, Japan

## Summary

Acoustic coupling occurs when two surface acoustic wave (SAW) resonators are arranged in a close, parallel configuration on a single quartz plate, resulting in two distinct resonance modes. This type of SAW resonator has been analyzed using a waveguide model to describe the close, parallel configuration and experiments were performed. The difference in frequency between these two resonance modes was found to depend primarily on the electrode overlap width in the interdigital transducer (IDT) of the two resonators and on the space between the resonators.

Experiments were made on 2-pole and 4-pole narrow bandpass filters constructed using double-mode SAW resonators. The characteristics of the 4-pole filter include a center frequency of 280MHz, a 3dB bandwidth of 220kHz, a minimum insertion loss of 1.6dB, and an out-of-band rejection of 55dB. The spurious response was investigated through study of the energy trapping modes.

## Introduction

In recent years, transversal SAW filters have been widely used in telecommunication equipment for the VHF and UHF range. While these filters have been suitable for medium- and wide-band applications, their bi-directional loss has generally prohibited applications where narrow-band, low-loss filter characteristics are required.

Until recently VHF and UHF range receivers have employed a double conversion system with two intermediate frequencies--the first at 21.4MHz or 10.7MHz and the second at 455kHz. The need to reduce equipment size and complexity, however, has necessitated a single conversion system for direct conversion from the receiver frequency to 455kHz, which requires a filter with both narrow bandwidth and low loss.

Several types of narrow-band, resonator filters in this frequency range have already been reported.<sup>1-3</sup> This paper describes the analysis and experiment of a double-mode SAW resonator filter utilizing waveguide coupling.<sup>4</sup>

With SAW resonators, the propagation velocity through the interdigital electrode section is lower than that on either side. For theoretical analysis, we employed the surface acoustic waveguide model.<sup>5</sup> Depending on the waveguide width, there are displacement distribution modes of different frequencies (fundamental, second, third, etc.) Once a SAW resonator is developed that can excite from the fundamental to the  $n$ th mode, it should be possible to use the frequencies of the  $n$  modes to construct an  $n$ -pole bandpass filter, in the same manner as a monolithic crystal filter (MCF). In this paper, we discuss a double-mode SAW resonator and bandpass filter configured using the basic first and second modes.

## The Double-Mode SAW Resonator

### Resonance Modes of the SAW Resonator

The structure of the SAW resonator is shown in Fig. 1. Periodic gratings in the IDT electrode overlap section (marked A) cause periodic reflections and perturbations, reducing the SAW propagation velocity compared to the regions on either side. These characteristics can be described using the surface acoustic waveguide model.

The propagation velocity in the slow region  $V_s$  depends on the free-surface propagation velocity  $V_0$  and the number of IDT pairs  $N$  as shown below:<sup>6</sup>

$$\frac{V_s}{V_0} = 1 - K_1 - K_2 - \frac{K_2}{0.7q^2 + 0.56q + 0.43} \quad (1)$$

$$q = \pi K_2 N \quad (2)$$

where  $K_1$  and  $K_2$  are constants depending on the substrate material, the electrode material and the electrode thickness. When aluminum electrodes are used on a substrate of ST-cut quartz, the electrode film thickness is  $H$  and the IDT period is  $L$ , these constants have the following values:<sup>7</sup>

$$K_1 = 4.33 \times 10^{-4} + 4.23 \times 10^{-2} \left(\frac{H}{L}\right) + 7.9 \left(\frac{H}{L}\right)^2 \quad (3)$$

$$K_2 = 6.25 \times 10^{-4} + 0.121 \left(\frac{H}{L}\right) \quad (4)$$

The propagation velocity in the fast region  $V_f$  depends on the electromechanical coupling constant of the substrate  $k^2$ :

$$\frac{V_f}{V_0} = 1 - \frac{1}{2}k^2 \quad (5)$$

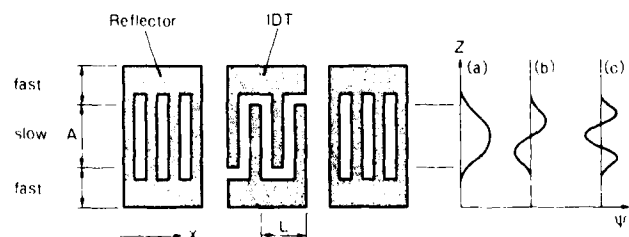


Fig. 1 Electrode configuration and displacement distributions of SAW resonators

- (a) 1st (fundamental) mode
- (b) 2nd mode
- (c) 3rd mode

Fig. 2 shows examples of dispersion curves for SAW resonators calculated by applying the scalar potential theory<sup>5</sup> to the surface acoustic waveguide model.  $f_r$  is the resonance frequency of the individual modes and  $f_0$  is resonant frequency when the IDT electrodes have a sufficient overlap width.  $A$  is the IDT electrode overlap width;  $L$  is the IDT period; the substrate is ST-cut quartz ( $\lambda^2 = 0.0017$ ); the electrodes are aluminum; the number of IDT pairs is 300; and the normalized electrode thickness  $H/L$  is 0.02. Using these parameters,  $V_s$  and  $V_f$  were calculated in equations (1) and (5).

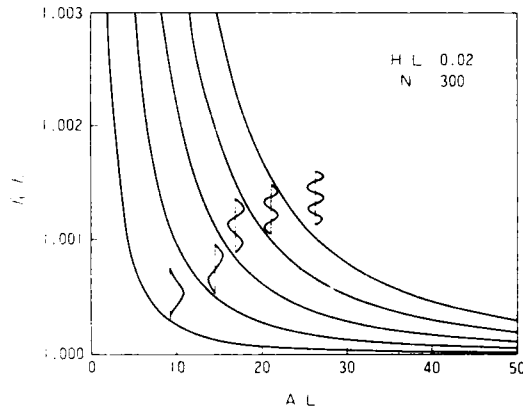


Fig. 2 Theoretical dispersion curves of SAW resonators. ST-cut ( $37^\circ$  rot. Y-cut) quartz substrate; aluminum electrode thickness  $H/L = 0.02$ ; number of IDT pairs  $N = 300$ .

#### Dual SAW Resonators in a Close, Parallel Configuration

If two identical SAW resonators are arranged in a close, parallel configuration, as shown in Fig. 3, and the space between them is small enough, acoustic coupling occurs and two resonance modes are excited. One of these corresponds to the first (fundamental) mode shown in Fig. 1 (a), which has a symmetrical displacement distribution with respect to the center between the two resonators. Another corresponds to the second mode, shown in Fig. 1 (b), which has a displacement distribution with point symmetry around the center. In this paper, the former is referred to as the symmetric mode; the latter as the antisymmetric mode. The two close, parallel resonators could also be thought of as a single resonator with a double-width IDT electrode overlap that has been divided into two parts. The symmetric and antisymmetric modes of this resonator would correspond to the distinct first and second resonance modes with the frequencies shown in Fig. 2.

If we explain this phenomenon by the coupling theory, the frequency difference between the symmetric and antisymmetric modes can be shown to depend on the distance between the two resonators and their vibration energy trapping levels.

As shown in Fig. 3 (a), the configuration consists of two SAW resonator elements with an IDT electrode overlap of  $W$ , arranged in parallel with a spacing (termed coupling gap) of  $G$ . On either side, there are busbars of width  $B$ , for a total of five

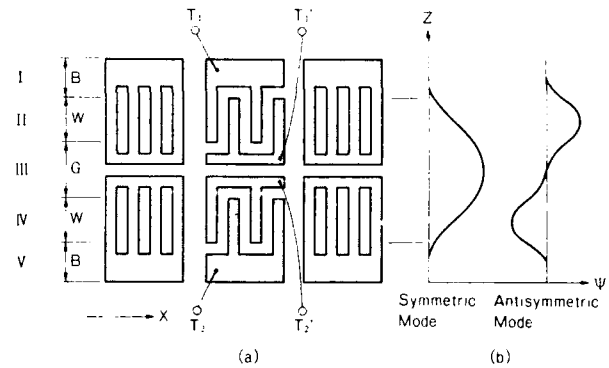


Fig. 3 Schematic diagram of double-mode SAW resonator.

- (a) Two SAW resonators in a close, parallel configuration.
- (b) Displacement distributions of symmetric and antisymmetric modes.

regions (numbered from I ~ V). In this paper, we analyze the double-mode SAW resonator using the waveguide model to consider the effect of the coupling gap.

If, in Fig. 3 (a), we define the SAW propagation direction to be the X-axis and its perpendicular to be the Z-axis, and we assume the isotropic substrate, the SAW propagation can be expressed as the scalar potentials  $\psi_s$  (slow region) and  $\psi_f$  (fast region) as follows:

$$\frac{\partial^2 \psi_s}{\partial X^2} + \frac{\partial^2 \psi_s}{\partial Z^2} + \frac{\omega^2}{V_s^2} \psi_s = 0 \quad (6)$$

$$\frac{\partial^2 \psi_f}{\partial X^2} + \frac{\partial^2 \psi_f}{\partial Z^2} + \frac{\omega^2}{V_f^2} \psi_f = 0 \quad (7)$$

where  $V_s$  and  $V_f$  are the SAW propagation velocities in the slow and fast regions, respectively. The solutions to Eqs. (6) and (7) are given below, with  $D_1 - D_{10}$  representing constants. For clarity, the term  $\exp[-j(Bx - \omega t)]$  has been omitted.

$$\psi_I = D_1 \sinh(k_f' Z) + D_2 \cosh(k_f' Z) \quad (8)$$

$$\psi_{II} = D_3 \sin(k_s' Z) + D_4 \cos(k_s' Z) \quad (9)$$

$$\psi_{III} = D_5 \sinh(k_f' Z) + D_6 \cosh(k_f' Z) \quad (10)$$

$$\psi_{IV} = D_7 \sin(k_s' Z) + D_8 \cos(k_s' Z) \quad (11)$$

$$\psi_V = D_9 \sinh(k_f' Z) + D_{10} \cosh(k_f' Z) \quad (12)$$

$$k_f'^2 = \beta^2 - k_s'^2, \quad k_s'^2 = k_s^2 - \beta^2 \quad (13)$$

$$k_s = \frac{\omega}{V_s}, \quad k_f = \frac{\omega}{V_f}, \quad \beta = \frac{\omega}{V} \quad (14)$$

where  $V$  is the SAW propagation velocity in each mode and  $\omega$  is the angular resonance frequency.

The boundary conditions are assumed to be continuous displacement and stress at each boundary with no force applied at the outermost edges, Eqs. (8) ~ (14) result in the following:

$$k'_S W = \tan^{-1} \left\{ \frac{k'_f}{k'_S} \tanh(k'_f B) \right\} + \tan^{-1} \left\{ \frac{k'_f}{k'_S} \tanh(k'_f \frac{G}{2}) \right\} \quad (15)$$

This equation assumes that the displacement in regions II and IV are in the same direction, i.e. the symmetric resonance mode. If it is assumed that the displacement in regions II and IV are in opposite directions, i.e. the antisymmetric resonance mode, we arrive at the following:

$$k'_S W = \tan^{-1} \left\{ \frac{k'_f}{k'_S} \tanh(k'_f B) \right\} + \tan^{-1} \left\{ \frac{k'_f}{k'_S} \coth(k'_f \frac{G}{2}) \right\} \quad (16)$$

When the width  $B$  of the fast outside regions is large enough,  $\tanh(k'_f B) \approx 1$ , allowing Eqs. (15) and (16) to be approximated as follows:

$$k'_S W = \tan^{-1} \left( \frac{k'_f}{k'_S} \right) + \tan^{-1} \left\{ \frac{k'_f}{k'_S} \tanh(k'_f \frac{G}{2}) \right\} \quad (17)$$

$$k'_S W = \tan^{-1} \left( \frac{k'_f}{k'_S} \right) + \tan^{-1} \left\{ \frac{k'_f}{k'_S} \coth(k'_f \frac{G}{2}) \right\} \quad (18)$$

Substituting (13) and (14) into (17) and (18), and using the relation  $\omega = 2\pi V/L$ , we can express these equations in terms of the normalized IDT electrode overlap width  $W/L$  and the normalized coupling gap  $G/L$  as follows:

$$2\pi \frac{W}{L} P (b_s^{-2} - p^{-2})^{\frac{1}{2}} = \tan^{-1} \left( \frac{p^{-2} - b_f^{-2}}{b_s^{-2} - p^{-2}} \right)^{\frac{1}{2}} + \tan^{-1} \left\{ \left( \frac{p^{-2} - b_f^{-2}}{b_s^{-2} - p^{-2}} \right)^{\frac{1}{2}} \tanh \left( \left( p^{-2} - b_f^{-2} \right)^{\frac{1}{2}} p \pi \frac{G}{L} \right) \right\} \quad (19)$$

$$2\pi \frac{W}{L} P (b_s^{-2} - p^{-2})^{\frac{1}{2}} = \tan^{-1} \left( \frac{p^{-2} - b_f^{-2}}{b_s^{-2} - p^{-2}} \right)^{\frac{1}{2}} + \tan^{-1} \left\{ \left( \frac{p^{-2} - b_f^{-2}}{b_s^{-2} - p^{-2}} \right)^{\frac{1}{2}} \coth \left( \left( p^{-2} - b_f^{-2} \right)^{\frac{1}{2}} p \pi \frac{G}{L} \right) \right\} \quad (20)$$

$$P = \frac{V}{V_0}, \quad b_s = \frac{V_s}{V_0}, \quad b_f = \frac{V_f}{V_0} \quad (21)$$

If, in (19) and (20) we solve for  $P$ , and  $b_s < P < b_f$ , we can term the values  $P_s$  and  $P_a$  corresponding to the symmetric and antisymmetric modes. The frequency of symmetric resonance mode  $f_s$  and of antisymmetric resonance mode  $f_a$ , can then be expressed as  $f_s = V_0 P_s / L$  and  $f_a = V_0 P_a / L$ , allowing us to express the difference  $\Delta f$  as follows:

$$\frac{\Delta f}{f_a} = \frac{f_a - f_s}{f_a} = \frac{P_a - P_s}{P_a} \quad (22)$$

As we have seen, when two SAW resonators are arranged in a close, parallel configuration, the acoustic coupling results in two distinct resonance modes, symmetric and antisymmetric. This configuration is termed a double-mode SAW resonator.

In this same way, if  $n$  SAW resonators are arranged in the close parallel configuration, a multi-mode SAW resonator capable of being excited in  $n$  modes can be obtained.

#### A Narrow Bandpass Filter Using the Double-Mode SAW Resonator

##### An Equivalent Circuit for the Double-Mode SAW Resonator

The operating principles and configuration of the double-mode SAW resonator resemble those of an MCF, allowing the equivalent circuit to be expressed in the same way. If we consider a double-mode SAW resonator with the IDT electrode finger relationships shown in Fig. 3 (a), and the terminal pairs  $T_1/T'_1$  and  $T_2/T'_2$  are driven in phase, the anti-symmetric mode results. If they are driven in reverse phase, the symmetric mode results. From this, the double-mode SAW resonator with the electrode finger relationships shown in Fig. 3 (a) can be expressed as the equivalent circuit shown in Fig. 4 (a).  $f$ ,  $L$ ,  $C$ , and  $R$  indicate the resonance frequency, equivalent inductance, equivalent capacitance and equivalent resistance. The subscript  $s$  indicates the symmetric mode; the subscript  $a$  indicates the antisymmetric mode;  $L_s = L_a$  and  $R_s = R_a$ ;  $C_0$  is the parallel capacitance of the individual resonators. In this paper, double-mode SAW resonators with this kind of electrode finger relationship will be termed the finger-in-phase type.

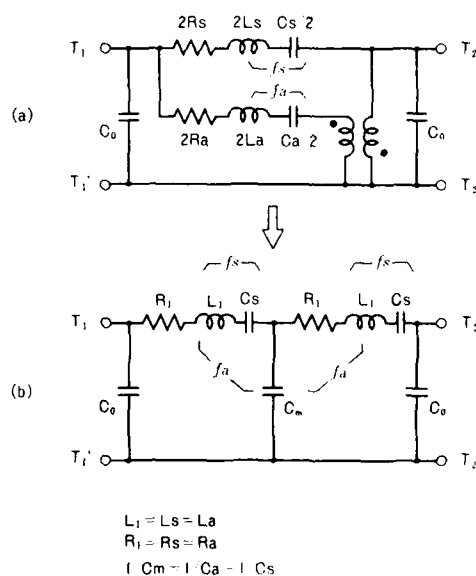


Fig. 4 (a) Equivalent circuit of finger-in-phase type double-mode SAW resonator.  $f_s$ ,  $L_s$ ,  $C_s$ ,  $R_s$ : circuit parameters for symmetric mode.  $f_a$ ,  $L_a$ ,  $C_a$ ,  $R_a$ : circuit parameters for antisymmetric mode.

(b) Ladder circuit transformed from (a)  
 $L_1 = L_a = L_s$ ,  $R_1 = R_s = R_a$ ,  
 $1/C_m = 1/C_a - 1/C_s$

When the two IDT sections are offset by  $L/2$  producing an electrode phase relationship of  $180^\circ$  in the propagation direction (see Fig. 5), the phase relationship between the terminal drive voltages is inverted, resulting in inversion of the excited mode relationships as well. The equivalent circuit would be as in Fig. 4 with the  $f_s$  and  $f_a$  resonance arms exchanged. In this paper, double-mode SAW resonators with this kind of electrode finger relationships will be termed the finger-out-of-phase type.

#### A Narrow Bandpass Filter Using the Double-Mode SAW Resonator

The double-mode SAW resonator equivalent circuit shown in Fig. 4 (a) can be transformed to the ladder circuit structure shown in Fig. 4 (b). Here  $L_1 = L_s = L_a$  and  $R_1 = R_s = R_a$ .  $C_m$  is the equivalent coupling capacitance. In the finger-in-phase type,  $1/C_m = 1/C_a - 1/C_s$ ; in the finger-out-of-phase type,  $C_s$  and  $C_a$  in the figures are exchanged and  $1/C_m = 1/C_s - 1/C_a$ . Both are expressed by the same ladder circuit.

Appropriate termination of the ladder circuit shown in Fig. 4 (b) results in a 2-pole bandpass filter configuration. Connection of  $m$  double-mode SAW resonators in tandem would produce a filter with  $2m$  poles.

When a filter is constructed by finger-in-phase and finger-out-of-phase resonators, both have a bridge capacitance between the input and output terminals ( $T_1$  and  $T_2$ ). In the finger-in-phase type, the resonance arm between  $T_1$  and  $T_2$  has a lower frequency and because there is a parallel bridge capacitance present, an attenuation pole is not produced at the real frequency, resulting in degradation of the filter shape factor. But because the finger-out-of-phase type has the bridge capacitance on the higher frequency resonance arm, the attenuation pole is generated.

#### Experiments

##### The Frequency Difference between Modes in the Double-Mode SAW Resonator

The frequency difference between the two modes of the double-mode SAW resonator  $\Delta f = f_a - f_s$  depends primarily on the IDT electrode overlap width

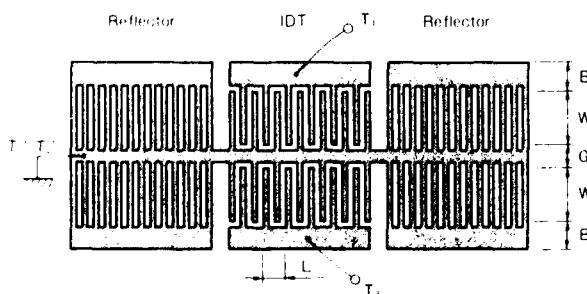


Fig. 5 Schematic illustration of actual SAW resonator (finger-out-of-phase type).  
W : IDT finger overlap width  
G : Coupling gap  
B : Busbar width ( $B \gg L$ )

W and the coupling gap G, as shown in Eqs. (19) and (20). This difference determines the passband width of the filter.

The relationship of W, G and  $\Delta f$  were experimentally determined using the finger-out-of-phase type double-mode resonator configuration shown in Fig. 5. For the experiment, aluminum electrodes were fabricated on a ST-cut ( $37^\circ$  rot. Y-cut) quartz substrate with the following parameters: frequency  $f = 280\text{MHz}$ , IDT period  $L = 11.12\mu\text{m}$ , IDT pair number  $N = 300$ , reflector grating number (per side)  $M = 300$ , and normalized film thickness  $H/L = 0.02$ .

The test results are shown in Fig. 6. The broken lines show the experimental values; the solid lines show the theoretical values calculated from Eqs. (1), (5) and (22). The graph clearly shows that as  $W/L$  and  $G/L$  decrease, the coupling grows stronger and  $\Delta f/f_a$  increases. There was some discrepancy between the experimental and theoretical values, but the trend proved to be a uniform one. This discrepancy is thought to stem from assumption of uniform displacement without considering energy trapping in the SAW propagation direction and also from the approximation in propagation velocity within the individual regions.

#### Narrow Bandpass Filter

**Design and Fabrication.** 2- and 4-pole narrow bandpass filters were fabricated using double-mode SAW resonators. Filter design began with a low-pass prototype filter with Tchebyscheff characteristics. Bandpass transformation and imaginary gyrator transformation were performed and a ladder circuit was configured using the double-mode resonator as the basic element.

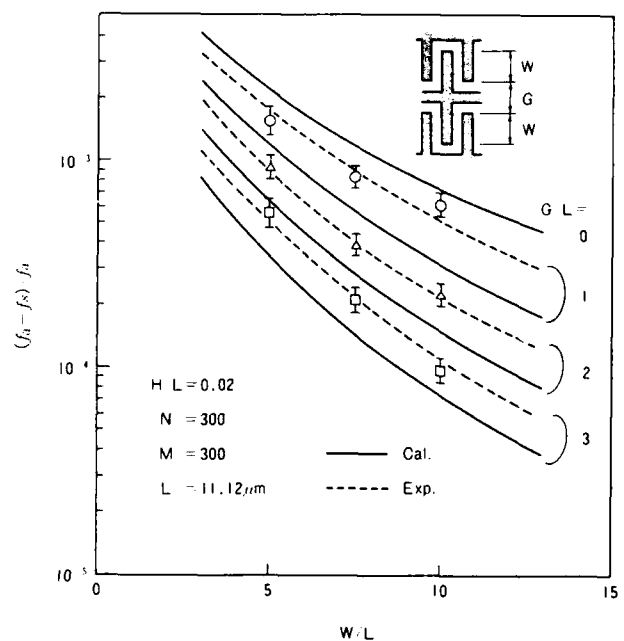


Fig. 6 Frequency difference of double-mode SAW resonators with normalized coupling gap  $G/L$  and normalized finger overlap length  $W/L$ .  
 $H/L$  : Normalized electrode thickness  
 $N$  : Number of IDT pairs  
 $M$  : Number of reflecting gratings  
 $L$  : IDT period

Figs. 7 and 8 show the design parameters of 2- and 4-pole filters with a center frequency of 280MHz. In these figures  $C_1$  equals  $C_a$ . The 2-pole filter consists of one double-mode resonator, while the 4-pole filter consists of two resonators connected in tandem. The 4-pole filter was constructed by fabricating two resonators in tandem on a single chip, as shown in Fig. 9. When the resonator is to be employed as a narrow bandpass filter, the Q must be made as large as possible to minimize filter loss. To maximize reflector efficiency, the design included a slight difference between the IDT period  $L_T$  and the reflector period  $L_R$ . In addition, a  $W/L_T$  of about 10 and a  $G/L_T$  of 1 were selected to raise the Q and widen the passband. A quartz substrate with a  $37^\circ$  rotated Y-cut was selected so that the turnover temperature  $T_p$  in the parabolic temperature-frequency curve would be matched to room temperature. These design parameters are listed in Table I.

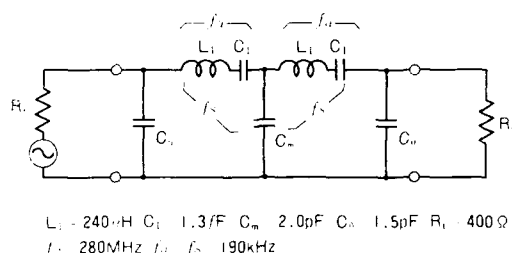


Fig. 7 Ladder circuit of 280MHz 2-pole filter.

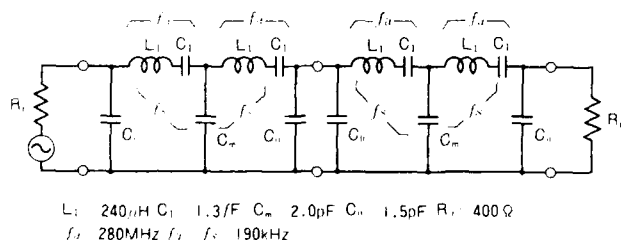


Fig. 8 Ladder circuit of 280MHz 4-pole filter.

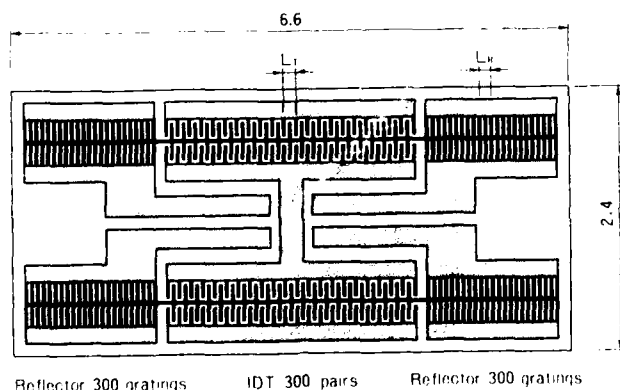


Fig. 9 Electrode configuration and chip size of 280MHz 4-pole filter (dimensions: mm).

TABLE I Design of double-mode SAW resonators

	280MHz	470MHz
Substrate	37° rot. Y quartz	
Electrodes	Aluminum	
Film thickness (H/L <sub>T</sub> )	0.02	0.02
IDT period (L <sub>T</sub> )	11.12μm	6.68μm
Reflector period (L <sub>R</sub> )	11.15μm	6.70μm
IDT overlap (W/L <sub>T</sub> )	10	11
Coupling gap (G/L <sub>T</sub> )	1	1
IDT	300 pairs	400 pairs
Reflector (per side)	300 gratings	400 gratings

The measured circuit values of the resonators shown in Table I are listed in Table II.

TABLE II Measured circuit values of double-mode SAW resonators

	280MHz	470MHz
$f_a$	281.4MHz	467.3MHz
$\Delta f (\Delta f/f_a)$	190kHz ( $6.8 \times 10^{-4}$ )	180kHz ( $3.8 \times 10^{-4}$ )
Q	18,000	12,000
$L_1$	240μH	80μH
$\gamma$	1200	1200

**Frequency-Loss Characteristics.** Figs. 10 ~ 12 show the measured values of the frequency-loss characteristics. Measurements were made using the test circuits shown. The tuning coils were used to neutralize the stray capacitance of the hermetic terminals and the measuring system. As with conventional crystal filters, the performance of these filters is strongly affected by the termination, necessitating accurate control of termination conditions.

Out-of-band rejection is affected by feed-through signals. In the 2-pole filter, out-of-band rejection is 25dB, in the 4-pole filter it is 55dB.

The characteristics of the prototype narrow bandpass filters are shown in Table III.

TABLE III Characteristics of the prototype narrow passband filters

	280MHz	280MHz	470MHz
Center frequency	281.4MHz	281.4MHz	467.3MHz
Construction	2-pole	4-pole	4-pole
3dB bandwidth	260kHz	220kHz	260kHz
Ripple	0.2dB	0.2dB	0.2dB
Min. insertion loss	0.8dB	1.6dB	5dB
Out-of-band rejection	25dB	55dB	60dB
Temp.-freq. chara. (2nd order coeff.)	Parabolic $-3.4 \times 10^{-8}/^\circ\text{C}^2$		
Terminating impedance	400Ω//tuning		200Ω//tuning

In the measured values of the filters, spurious response exists only in the vicinity of the pass-band. Peaks exist on both the low and high sides of the pass-band. These are caused by the inharmonic modes of the resonator.

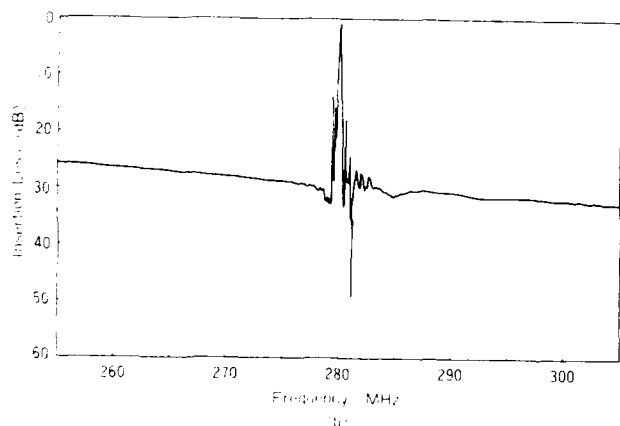
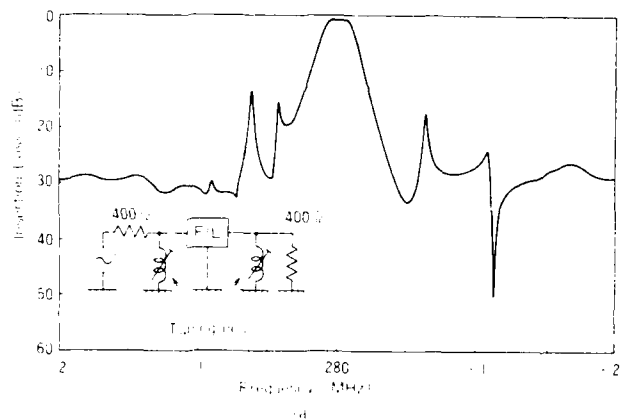


Fig. 10 Narrowband (a) and wideband (b) views of the frequency response of 280MHz 2-pole filter.

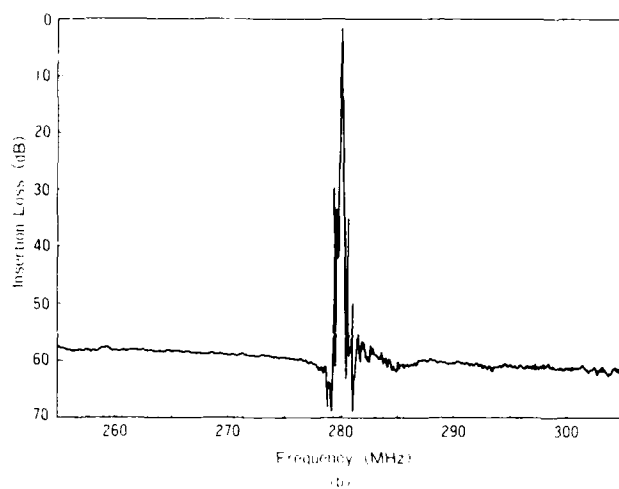
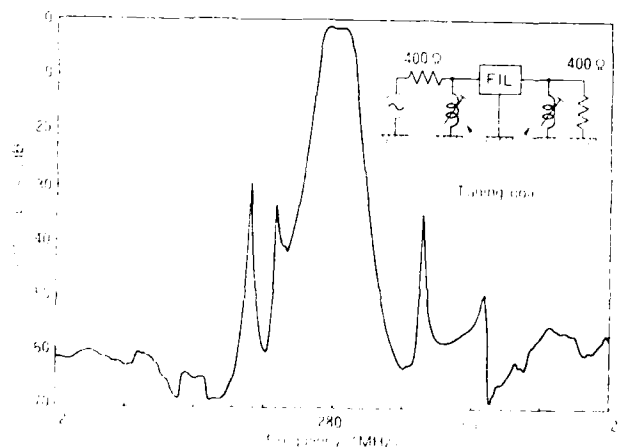


Fig. 11 Narrowband (a) and wideband (b) views of the frequency response of 280MHz 4-pole filter.

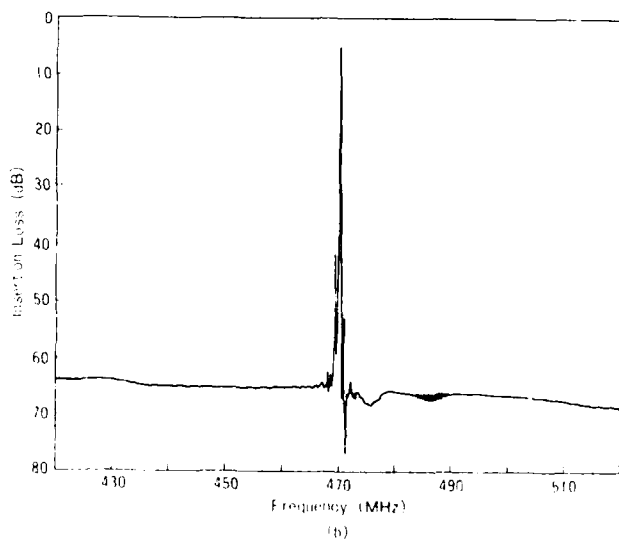
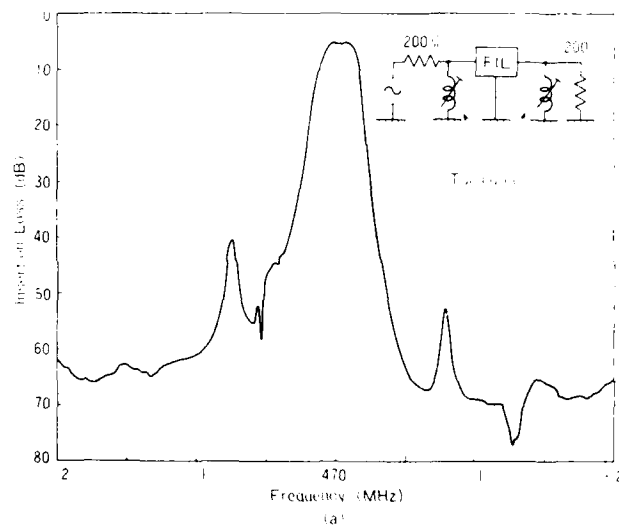


Fig. 12 Narrowband (a) and wideband (b) views of the frequency response of 470MHz 4-pole filter.

Fig. 13 shows a photograph of the 280MHz 4-pole filter. The device is packaged in a flat pack (10.4 x 4.2 x 2.7mm).

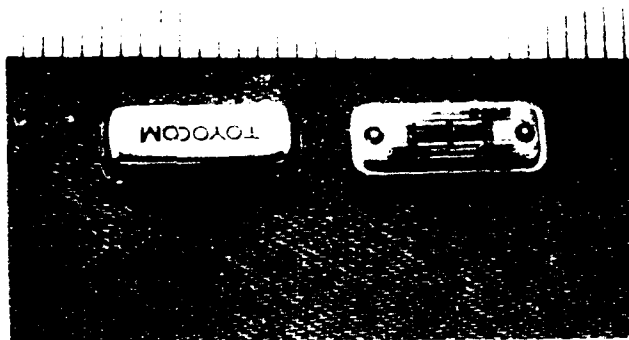


Fig. 13 Photograph of 280MHz 4-pole filter.

**Spurious Response.** We investigated the spurious response on either side of the passband shown in Figs. 10 ~ 12. If the order of the energy trapping mode in the X-direction (propagation direction) and Z-direction are termed X and Z, the mode of the resonator can be expressed as mode [X,Z]. The symmetric mode would be expressed as mode [1,1], while the antisymmetric mode would be expressed as mode [1,2]. Mode [1,1] and [1,2] are the principal modes corresponding to the passband. The other modes correspond to spurious responses. However, all the even modes except for the second order mode in the Z-direction are suppressed by the charge cancelling that occurs within the electrodes. In the inharmonic modes in the Z-direction, the resonance frequency rises as the order of the energy trapping mode increases.<sup>8</sup> However, in the X-direction, the resonance frequency drops as the order of the inharmonic mode rises. Consequently, the resonator has response at the following frequencies, expressed in terms of the resonance mode [X,Z]: . . . , f[5,1], f[5,2], f[3,1], f[3,2], f[1,1], f[1,2], f[1,3], f[1,5], . . . Fig. 14 shows the modes corresponding to the spurious response peaks.

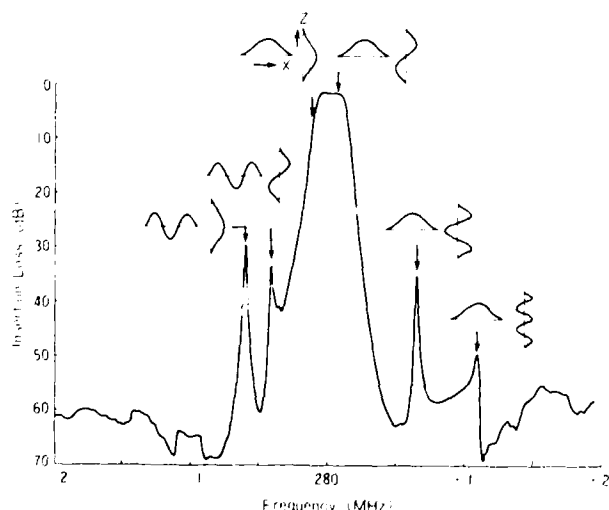


Fig. 14 Spurious responses and their displacement distribution modes of 280MHz 4-pole filter.

The following three methods have been suggested to suppress spurious response. The first is to make the electrodes thinner, in order to reduce the energy trapping of the higher order inharmonic mode. Fig. 15 shows the measured values with an electrode thickness  $H$  that is 1.5% of the IDT period  $L_T$ . Application of this method reduced the spurious response in modes [3,2], [1,3] and [1,5], but showed little effect on mode [3,1]. In addition, the main modes were also affected. The loss increased to somewhat above its minimum value and the coupling between the resonators increased, widening the passband slightly.

The second method can be employed when multiple double-mode resonators are used. The spurious response frequencies of each resonator are made to differ and the group is connected in tandem. Fig. 16 shows the result of this method. In this example, the ratios of the IDT and reflector period  $L_T/L_R$  were made to differ slightly, staggering the spurious response frequencies.

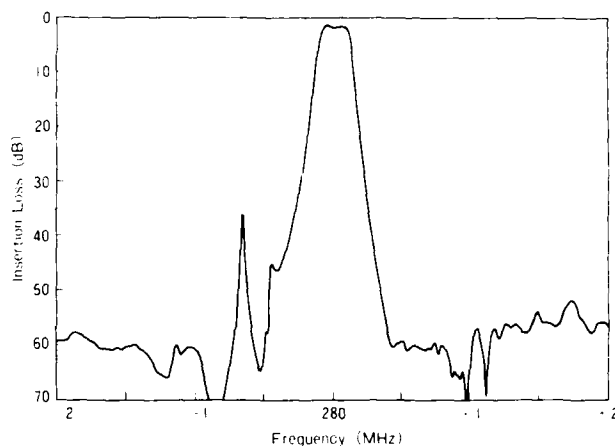


Fig. 15 Measured frequency response of 280MHz 4-pole filter with thin electrodes. (Energy is not trapped in high order modes.)

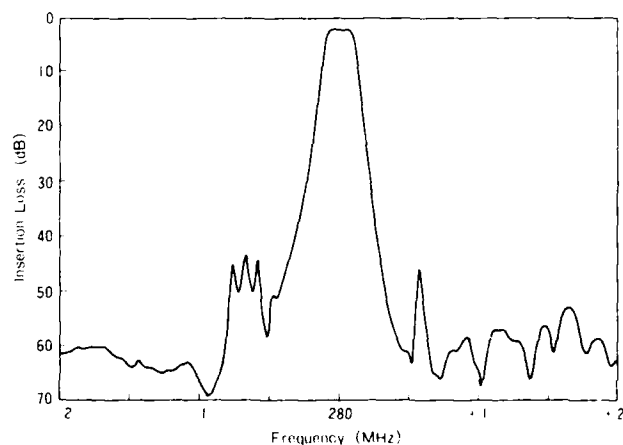


Fig. 16 Measured frequency response of 280MHz 4-pole filter. (two double-mode SAW resonators with different spurious frequencies connected in tandem.)



The third method is the apodization of the IDT. This method suppresses the higher inharmonic modes in the X- and Z-directions, improving the spurious response.

Temperature Characteristics. The temperature-frequency characteristics of these filters were identical to those of the SAW resonators. The characteristic is parabolic, with turnover temperature  $T_p = 25^\circ\text{C}$  and a 2nd order coefficient of  $-3.4 \times 10^{-8}/^\circ\text{C}^2$ .  $T_p$  depends on the cut angle of the substrate and the electrode thickness.

#### Discussion

The range of possible bandwidths and center frequencies was investigated. As in conventional crystal filters, the maximum bandwidth of these filters is limited by the capacitance ratio  $\gamma = C_o/C_i$ , to the rather high maximum value of  $1/\gamma$ . The capacitance ratio of the SAW resonator has a minimum value of about 1000 (in the case of ST quartz), limiting the bandwidth to a maximum of about  $1 \times 10^{-3}$ . To achieve wider bandwidths than this, an elongation coil is required, but it is difficult to realize coils with high  $Q$  and stability. Therefore, to construct a filter with a wider bandwidth, a material with a high coupling constant  $k^2$  (and consequently a small  $\gamma$ ) such as  $\text{LiTaO}_3$  or  $\text{LiNbO}_3$  should be selected. The minimum bandwidth is restricted by temperature-induced frequency variation, the rise in minimum loss caused by a narrow bandwidth, and the precision of the frequency adjustment. When ST quartz is used, the value ranges from  $1 \times 10^{-4} \sim 1 \times 10^{-5}$ . Technical limitations on pattern resolution restrict the center frequency to a maximum of somewhat higher than 1 GHz, while device size limits the minimum value to several tens of MHz.

#### Conclusion

We have discussed double-mode SAW resonators constructed using two SAW resonators in a close, parallel configuration and their applications for narrow bandpass filters. From our experiments, three principal conclusions can be drawn:

- (1) The frequency difference of the two resonance modes of the double-mode SAW resonator constructed using two SAW resonators in a close, parallel configuration is determined by the IDT electrode overlap width  $W$  and the coupling gap  $G$ .
- (2) Double-mode SAW resonators can be used to construct narrow bandpass filters with both compact size and low loss. This type of filter permits center frequencies from several tens of MHz to somewhat above 1 GHz, with a bandwidth of  $1 \times 10^{-4} \sim 1 \times 10^{-3}$ .
- (3) When bandpass filters are constructed using double-mode SAW resonators, the spurious response on the low side of the passband is due to energy trapping of higher order inharmonic modes in the SAW propagation direction, while spurious response on the high side is due to the same phenomenon perpendicular to the propagation direction.

#### References

- 1) W.J. Tanski, "GHz SAW Resonators", IEEE Ultrasonics Symp. Proc., p.815 (1979).
- 2) J. Wise, J. Schoenwald and E. Staples, "Impedance Characterization and Design of 2-pole Hybrid SAW Resonator Filters", IEEE Ultrasonics Symp. Proc., p.200 (1980).
- 3) R.L. Rosenberg and L.A. Coldren, "Broader-band Transducer-coupled SAW Resonator Filters with a Single Critical Masking Step", IEEE Ultrasonics Symp. Proc., p.164 (1980).
- 4) A. Yamada and H. Shimizu, "Double Mode Filter by Elastically Coupled SAW Resonators", Paper of the Technical Group on Ultrasonics, IECE, Japan, US77-33, p.29 (1977).
- 5) R.V. Schmidt and L.A. Coldren, "Thin Film Acoustic Surface Waveguides on Anisotropic Media", IEEE Trans., Vol. SU-22, No.2, p.115 (1975).
- 6) T. Uno and H. Jumonji, "Optimization of Quartz SAW Resonator Structure with Groove Gratings", IEEE Trans., Vol. SU-29, No.6, p.299 (1982).
- 7) S. Urabe, Y. Koyamada and S. Yoshikawa, "Experiments on Metallic-Strip-Grating for SAW Reflector", Trans. IECE Japan, Vol. J60-A, p.875 (1977).
- 8) E.J. Staples and R.C. Smythe, "SAW Resonators and Coupled Resonator Filters", 30th Frequency Control Symp. Proc., p.322 (1976).

## THEORETICAL ANALYSIS OF DYNAMIC THERMAL EFFECTS IN SAW DEVICES

G. Théobald, D. Hauden

Laboratoire de Physique et Métrologie des Oscillateurs du C.N.R.S.  
associé à l'Université de Franche-Comté - Besançon  
32 avenue de l'Observatoire - 25000 Besançon - France

Summary

It has been shown that frequency stability of quartz oscillators is limited by temperature fluctuations and specially by their time dependent parts. In order to evaluate dynamic thermal sensitivities of SAW devices, it needs to develop a theoretical analysis in three steps.

First, the temperature repartition is calculated in a one dimensional model corresponding to an infinite width plate of quartz and in a two dimensional model taking into account lateral boundary conditions. Temperature charts are presented. Secondly, thermal stresses are obtained in the case of a free plate as plane-stress for the one-dimensional model and plane-strain for the two dimensional one. Finally, theoretical sensitivities for several quartz-cuts are determined from a perturbation method. Calculated values are about  $1 \times 10^{-7}$  s/K.

Introduction

The frequency stability of quartz crystal resonators is still mainly due to temperature fluctuations. The static thermal behavior coming from a uniform heating has been studied leading to temperature compensated singly and doubly rotated cuts<sup>1,2,3</sup>.

When heating is nonuniform, the temperature in the crystal has a spatial distribution; moreover temperature can present time variations. Internal stresses and strains take place in the crystal which induce frequency shifts by nonlinear coupling with the high frequency wave. The effect of thermal gradients was quite well studied in the case of bulk wave resonators<sup>4,5,6</sup> but not so much with SAW devices.

In this paper we present a theoretical approach of the dynamic thermal effect in SAW devices. Two cases will be examined: the one dimensional model in which heat is diffusing along the plate thickness and the two dimensional one in which heat is transferred both along the thickness and along the main faces of the plate.

The first step in the analysis of thermal response of SAW resonators consists to obtain the temperature distribution in the quartz plate from the heat conduction equation in respect to appropriate boundary and initial conditions. The time dependent thermally induced biasing state is then obtained from the equations of the static linear thermoelasticity. A perturbation analysis of the equilibrium equation for small vibrations superposed on the thermal bias is performed leading to the determination of the dynamic temperature coefficient for SAW devices.

Numerical calculations reveal that the influence of the dynamic SAW behavior remains of the same order of magnitude as the bulk SC-cut.

Temperature distribution

A long prismatic plate of length in the  $x_3$  direction large compared with the cross sectional dimensions ( $2h \times 2l$ ) is considered (Fig. 1). As a consequence the temperature  $\theta$  inside the crystal depends only on  $x_1$  and  $x_2$  coordinates and obeys to the diffusion equation

$$\frac{\partial^2 \theta}{\partial x_2^2} + \frac{\partial^2 \theta}{k^2 \partial x_1^2} - \frac{1}{\kappa} \frac{\partial \theta}{\partial t} = 0 \quad (1)$$

$k^2 = \lambda_2/\lambda_1$  is the ratio of the thermal conductivities in the  $x_2$  and  $x_1$  direction and  $\kappa$  is the thermal diffusion in the  $x_2$  direction.

The problem of the determination of the temperature distribution in the plate is formulated in various types of heating process where the choice of the appropriate boundary conditions is presented.

One-dimensional model

When the lateral size  $2l$  along  $Ox_1$  direction is considered as infinite, the  $x_1$  dependence of  $\theta$  in (1) can be neglected. The bottom of the plate is submitted to temperature variations  $\Phi(t)$ . Linear heat exchanges with the surrounding medium at  $T_0$  occur on the upper face of the device (Fig. 2). This one-dimensional model can be solved with the aid of the Duhamel's theorem<sup>7</sup> and the solution is obtained in the form of a series

$$\theta(x_2, t) = \sum_{n=1}^{\infty} \frac{2(\beta_n^2 + 4h^2H^2)}{(2hH + 4h^2H^2 + \beta_n^2)} \sin \frac{\beta_n}{2h} (x_2 + 2h) \left\{ \Phi(t) - \frac{\dot{\Phi}(t)}{\kappa \beta_n^2 / 4h^2} \right\} \quad (2)$$

The  $H$  term is proportional to the linear transfer  $H'$  by  $H = H'/\lambda_2$ .  $\Phi(t)$  is considered as a slowly varying function of time.  $\beta_n$  is the  $n$ th root of the equation<sup>7</sup>

$$\beta \cot \beta + 2hH = 0 \quad (3)$$

Two-dimensional model

Two ways of heat exchanges with the surrounding medium are examined.

## a) lower face heating

As shown in figure 3, the temperature  $\Phi(t)$  is prescribed on the face  $x_2 = -h$  and heat is transferred to the external medium at  $T_0$  by a linear transfer on the three remaining faces; consequently the boundary conditions are

$$\pm \lambda_1 \frac{\partial \theta}{\partial x_1} + H'(\theta - T_0) = 0 \quad x_1 = \pm l \quad -h < x_2 < h \quad (4)$$

$$+ \lambda_2 \frac{\partial \theta}{\partial x_2} + H'(\theta - T_0) = 0 \quad x_2 = +h \quad -l < x_1 < l \quad (5)$$

$$\Phi = \Phi(t) \quad x_2 = -h \quad -l < x_1 < l \quad (6)$$

Solving (1) with equations (4-6) leads to the temperature distribution

$$\theta(x_1, x_2, t) = \sum_{n=1}^{\infty} \sum_{l=1}^{\infty} 2Hl \frac{\cos \alpha_n x_1}{\cos \alpha_n l} \frac{1}{(\alpha_n^2 + H^2)l^2 + Hl} \frac{u_1}{2h^2} \cdot \quad (7)$$

$$\sin \frac{u_1}{2h} (x_2 + h) / (1 - \sin 2u_1 / 2u_1) \cdot \left( \frac{\Phi(t)}{\beta^2} - \frac{1}{\kappa \beta^4} \dot{\Phi}(t) \right)$$

with

$$\beta^2 = \kappa^2 \alpha_n^2 + (u_1 / 2h)^2 \quad (8)$$

$\alpha_n$  and  $u_1$  are solutions of the transcendental equations

$$\alpha_n l \tan \alpha_n l = Hl \quad (9)$$

$$-u_1 \cotan u_1 + 2hH = 0 \quad (10)$$

According to relation (7), the temperature  $\theta$  can be written as the sum of two terms proportional respectively to  $\Phi(t)$  and  $\dot{\Phi}(t)$

$$\theta(x_1, x_2, t) = \theta_{\Phi} \Phi(t) + \theta_{\dot{\Phi}} \dot{\Phi}(t) \quad (11)$$

Charts have been prepared giving numerical values of the temperature for quartz plates 2 mm thick and 2 cm long.  $\theta_{\Phi}$  and  $\theta_{\dot{\Phi}}$  are shown in figure 4 as a function of the position along the length of the plate for some values of the depth. These curves indicate temperature  $\theta_{\Phi}$  and  $\theta_{\dot{\Phi}}$  are practically constant in the main range  $-x_f < x_1 < x_f$  ( $x_f \sim 8$  mm) that is, the entire length except for a short region near ends. The same conclusions can be made on figure 5 where  $\theta_{\Phi}$  and  $\theta_{\dot{\Phi}}$  are presented as a function of the depth for some values of the position along the plate length.

#### b) lateral heating

As shown in figure 6, prescribed temperatures  $\Phi_1(t)$  and  $\Phi_2(t)$  are at the end faces. A linear heat transfer occurs at the major faces  $x_2 = \pm h$ . The analytical solutions are obtained as

$$\begin{aligned} \theta(x_1, x_2, t) = & \sum_n 2Hl \frac{\cos \alpha_n x_2}{\cos \alpha_n h} \frac{1}{(\alpha_n^2 + H^2)h^2 + Hh} \\ & + (\Phi_1(t) \frac{\sinh \alpha_n (x_1 + l)}{\sinh \alpha_n 2l} + \Phi_2(t) \frac{\sinh \alpha_n (l - x_1)}{\sinh \alpha_n 2l}) \quad (12) \\ & - \sum_{i=1}^{\infty} (-1)^{i+1} \frac{1\pi}{2l^2} \frac{1}{\kappa \beta^2} \left[ \Phi_1(t) \sin \frac{1\pi}{2l} (x_1 + l) \right. \\ & \left. + \Phi_2(t) \sin \frac{1\pi}{2l} (l - x_1) \right] \end{aligned}$$

with

$$\beta^2 = \kappa^2 \alpha_n^2 + (1\pi / 2l)^2 \quad (13)$$

and  $\alpha_n$  is the  $n$ th root of the equation

$$\alpha h \tan \alpha h = Hh \quad (14)$$

With the values of  $H$ ,  $h$  and  $l$  mentioned previously, the temperature decreases very rapidly near to the plate ends, so that the temperature variation is negligible inside the plate.

### Thermal stresses

Thermal stresses arise in a heated body because of either a nonuniform temperature distribution or external constraints. We consider in this chapter only the effect of a nonuniform temperature and subsequently the case of a plate free to expand.

As a consequence of the form taken by the temperature distribution, two types of thermoelastic problem will be considered. For the one dimensional model, a state of plane stress in which the stresses  $T_{12}$  perpendicular to the plane are zero may be used. For the two dimensional model, a state of plane strain where the displacement components  $u_1$  are given by

$$u_1 = u_1(x_1, x_2, t) \quad u_2 = u_2(x_1, x_2, t) \quad u_3 = 0 \quad (15)$$

will be used.

#### One-dimensional formulation

As the temperature varies through the thickness only, only stress components  $T_{11}$ ,  $T_{13}$  and  $T_{33}$  are non zero.

Their form is obtained from the equilibrium equation and the boundary conditions of zero traction on the edges of the plate according to the method for thin plates used by Boley<sup>8</sup> and Holland<sup>9</sup>.

#### Two-dimensional formulation

A system of approximate plate equations for the determination of thermal stresses in thin piezoelectric plates is performed by the thin plate approximation due to Mindlin<sup>10</sup>. Referred to the  $Ox_1x_2x_3$  coordinate system, displacements  $u_i$  are developed with respect to  $x_2$  powers

$$\begin{aligned} u_1 = & \sum_{n=0}^3 x_2^n u_1^{(n)} \\ u_2 = & \sum_{n=0}^3 x_2^n u_2^{(n)} \\ u_3 = & 0 \end{aligned} \quad (16)$$

The  $n$ -th order plate strains take the following form

$$S_{ij}^{(n)} = \frac{1}{2} (u_{i,j}^{(n)} + u_{j,i}^{(n)} + (n+1)(\delta_{2j} u_i^{(n+1)} + \delta_{2i} u_j^{(n+1)})) \quad (17)$$

and the linear thermoelastic constitutive equations are written

$$T_{ij} = C_{ijkl} S_{kl} - v_{ij} [\theta(x_1, x_2, t) - T_0] \quad (18)$$

The thermoelastic constants  $v_{ij}$  are related to the coefficients of linear expansion  $\alpha_{kl}$  and the elastic constants  $C_{ijkl}$  by the usual relation

$$v_{ij} = C_{ijkl} \alpha_{kl} \quad (19)$$

The static form of Mindlin's equations in which the dependence along  $x_3$  has been disregarded may be written

$$T_{1j,1}^{(n)} - n T_{2j}^{(n-1)} + F_j^{(n)} = 0 \quad n = 0, 1, 2 \quad (20)$$

where 1 takes the value 1 and skips 2 and

$$T_{1j}^{(n)} = \int_{-h}^{+h} x_2^n T_{1j} dx_2 \quad (21)$$

$$F_j^{(n)} = x_2^n T_{2j} \Big|_{-h}^{+h} \quad (22)$$

With the notation

$$\theta^{(m)} = \int_{-h}^{+h} x_2^m \theta(x_1, x_2, t) dx_2 \quad (23)$$

and with (17) and (18) the m-th order stress resultants take the form

$$T_{1j}^{(m)} = C_{1jkl} \sum_{n=0}^2 H_{mn} S_{kl}^{(n)} - \nu_{1j} \theta^{(m)} \quad (24)$$

$$H_{mn} = 2h^{m+n+1} / (m+n+1) \quad \begin{matrix} m+n \text{ even} \\ m+n \text{ odd} \end{matrix} \quad (25)$$

The boundary conditions on the main surfaces

$$T_{22}(\pm h) = 0 \quad T_{12}(\pm h) = 0 \quad (26)$$

and on the end faces

$$T_{1j}^{(n)}(\pm l) = 0 \quad (27)$$

are that of a free stress plate.

Introducing (26) in (20) yields

$$F_j^{(n)} = 0 \quad (28)$$

The equilibrium equations (20) may be expressed in terms of displacements  $u_1^{(n)}$  (16) by means of relations (24) and (17).

Doubly-rotated cuts have elastic constants which introduce coupling between extension and flexure. Then, first calculations are made in the case of singly-rotated cuts, and elastic constants which couple extension and flexure are taken to vanish in the constitutive equations.

Furthermore, in order to allow for free strain  $S_{22}^{(0)}$ ,  $S_{22}^{(2)}$  and  $S_{22}^{(1)}$ , we take<sup>10</sup>

$$T_{22}^{(0)} = 0 \quad T_{22}^{(2)} = 0 \quad (29)$$

and

$$T_{22}^{(1)} = 0. \quad (30)$$

From (29), (28), (27) and (20) the extension components are given by

$$u_{1,1}^{(0)} = \nu_1^* / C_{11}^* \frac{\theta^{(0)} h^2 / 5 - \theta^{(2)} / 3}{8/45 h^3} \quad (31)$$

$$u_{1,1}^{(2)} = \nu_1^* / C_{11}^* \frac{\theta^{(2)} - \theta^{(0)} h^2 / 3}{8/45 h^5} \quad (32)$$

$$u_2^{(1)} = \nu_2^* / C_{22}^* \frac{\theta^{(0)} 3h^2 / 5 - \theta^{(2)}}{8/15 h^3} \quad (33)$$

$$u_2^{(3)} = \nu_2^* / C_{22}^* \frac{\theta^{(2)} - \theta^{(0)} h^2 / 3}{8/15 h^5} \quad (34)$$

and then from (30), (28), (27) and (20) the flexural components

$$u_2^{(2)} = \frac{\theta^{(1)}}{4/3 h^3} \frac{\nu_2^*}{C_{22}^*} \quad (35)$$

$$u_1^{(3)} = -u_{2,1}^{(2)} / 3 \quad (36)$$

$$u_{1,1}^{(1)} = \frac{-3}{5} h^2 u_{1,1}^{(3)} + \frac{3}{2} \frac{\theta^{(1)}}{h^3} \frac{\nu_1^*}{C_{11}^*} \quad (37)$$

$$u_{2,1}^{(0)} = -u_1^{(1)} \quad (38)$$

where

$$C_{11}^* = C_{11} - C_{12}^2 / C_{22} \quad ; \quad C_{22}^* = C_{22} - C_{12}^2 / C_{11} \quad (39)$$

$$\nu_1^* = \nu_1 - \nu_2 C_{12} / C_{22} \quad ; \quad \nu_2^* = \nu_2 - \nu_1 C_{12} / C_{11} \quad (40)$$

When integration with respect to  $x_1$  is performed in the above expressions, integration constants are introduced in  $u_1^{(0)}$  and  $u_2^{(0)}$  representing uniform translation of the plate along the  $x_1$  axis. We can set this to zero without loss of generality. Moreover, integration constants appearing in  $u_1^{(1)}$  and  $u_2^{(1)}$  vanish as a consequence of conditions (27)  $T_{11}^{(0)}(\pm l) = 0$  and  $T_{12}^{(1)}(\pm l) = 0$ .

From these results, displacements, strains and displacement gradients are obtained as function of zero-th, first and second moments of the temperature. According to the form taken by the temperature, moments  $\theta^{(m)}$  are obtained in an series of trigonometric functions which is not suitable for numerical calculation.

A good approximation for the temperature in the main range of the plate length is given by a polynomial in two dimensions, the coefficients of which are obtained from the complete temperature representation by a polynomial regression.

So, m-th order moments of  $\theta$  are readily performed and we can substitute  $\theta^{(m)}$  into eq. (31-38).

#### Sensitivity of SAW to temperature gradients

When a quartz resonator undergoes heating, two kinds of effects affect the natural frequency: a direct thermal effect by means of dilatation and material temperature coefficients like  $\alpha C_{ijkl}$ , and an indirect thermoelastic effect induced by nonlinearities of the quartz crystal.

Both effects can be considered as a bias applied on the crystal substrate which modifies the second order elastic constants. In a natural state coordinate system<sup>11</sup> the nonlinear propagation equation is written

$$\rho_0 u_{1,tt} = \overline{(A_{1kjm} u_{j,m})}_{,k} \quad (41)$$

where  $\rho_0$  is the specific mass and  $u_1$  the displacement due to the high frequency vibrations.

The boundary conditions corresponding to a stress free surface are

$$\overline{A_{1kjm}} u_{j,m} = 0 \quad \text{for} \quad a_2 = 0 \quad (42)$$

$\overline{A_{1kjm}}$  are the modified elastic constants,

$$\overline{A_{1kjm}} = \overline{C_{1kjm}} + \overline{H_{1kjm}} \quad (43)$$

and

$$\begin{aligned} \overline{H_{1kjm}} = & \delta_{1j} \overline{t_{km}} + \overline{U_{1,p}} C_{kpmj} + \overline{U_{j,q}} C_{k1mq} + \overline{S_{uv}} C_{1kjmuv} \\ & + \alpha C_{1kjm} \theta(x_2, t) \end{aligned} \quad (44)$$

$\overline{t_{km}}$ ,  $\overline{S_{uv}}$  and  $\overline{U_{1,p}}$  are respectively the thermodynamic tensions, the deformations and the displacement gradients induced by the temperature.  $\alpha C_{1kjm}$  are the fundamental temperature elastic coefficients.

Since the temperature distribution is proportional partly to  $\Phi(t)$  and partly to the time derivative  $\dot{\Phi}(t)$  (see Eq.(11)) the perturbation terms  $\overline{H_{1kjm}}$  have two parts

$$\overline{H_{1kjm}} = \overline{a_{1kjm}} \Phi(t) + \overline{b_{1kjm}} \dot{\Phi}(t) \quad (45)$$

Relative frequency shifts  $\Delta\omega/\omega_0$  are calculated respectively for  $\Phi(t)$  and  $\dot{\Phi}(t)$  contributions ; therefore, coefficients  $\overline{a}$  and  $\overline{b}$  are introduced as

$$\frac{1}{\Phi(t)} \frac{\Delta\omega}{\omega_0} = \overline{a} \quad \text{and} \quad \frac{1}{\dot{\Phi}(t)} \frac{\Delta\omega}{\omega_0} = \overline{b} \quad (46)$$

Then, when a SAW oscillator is submitted to temperature variations, such as fast fluctuations of temperature  $\Phi(t)$  superimposed on slow temperature changes  $T$ , relative frequency shifts are written

$$\frac{\Delta\omega}{\omega_0} = a_0 (T - T_0) + b_0 (T - T_0)^2 + c_0 (T - T_0)^3 + \overline{a} \Phi(t) + \overline{b} \dot{\Phi}(t) \quad (47)$$

where  $a_0$ ,  $b_0$  and  $c_0$  are respectively the first, second and third order temperature coefficients of the frequency calculated (or measured) in the case of static thermal behavior and  $T_0$  is the reference temperature.

Some comments about the meaning of the coefficients appearing in Eq. (47) may be given :

- coefficients  $a_0$ ,  $b_0$ ,  $c_0$  describe the thermal behavior of the quartz when it experiences a homogeneous temperature variation  $T$ .

- $\overline{a}$ -coefficient determines the frequency change resulting from a local temperature perturbation  $\Phi$  which could be time-dependent or time-independent. This local temperature perturbation induces an inhomogeneous temperature repartition followed by stresses and strains. This leads to modifications in the static frequency temperature characteristics. For instance, there will be a shift of the turnover point.

- $\overline{b}$ -coefficient is related to the time rate of change of the perturbation and its effect vanishes when afore mentioned rates become negligible. It is called dynamic thermal coefficient.

Coefficients  $\overline{a}$  and  $\overline{b}$  have been evaluated in the one-dimensional model and in the two-dimensional model with lower face heating. The results are shown in Table I and II when the normalized transfer coefficient  $Hh$  is equal to 50.

The comparison between the results of the two models allows to the following remarks.

The two-dimensional model gives values of a coefficient weak compared with the ones obtained from the one-dimensional model. The shifts of the turnover point which would be induced by  $\overline{a}$  values obtained in the one-dimensional model are not in accordance with the experimental temperature-frequency curves in which any detectable shift was observed.

For this reason the two-dimensional model seems more realistic. Note that dynamic coefficient  $\overline{b}$  is generally lower in the two-dimensional model. This is due to the thermoelastic problem which is of different type in the two cases : plane stress in one hand and strains non zero only in the cross section in other hand.

Theoretical cyclings of the temperature have been performed for some time rates of changes of the temperature.

Fig. 7 shows a simulation around the turnover point for several temperature variation velocities. The thermal behavior of ST cut, X propagation is governed by the following relation taking into account both static and dynamic effects

$$\begin{aligned} \frac{\Delta f}{f} = & -39.6 \times 10^{-9} (T - T_0)^2 + 58.3 \times 10^{12} (T - T_0)^3 \\ & + 0.067 \cdot 10^{-6} \dot{\Phi}(t) - 0.09 \times 10^{-6} \Phi(t) \end{aligned}$$

Although the previous two-dimensional stress calculations are not adequate for doubly-rotated cuts, we still assume that coupling between extension and flexure is negligible and that calculations hold for the FST cut ( $\Phi = 6^\circ 20'$ ,  $\theta = -41^\circ 30'$ ,  $\Psi = 26^\circ$ ). Corresponding results of sensitivities are presented in Table III. Values obtained are comparable to the singly-rotated ones.

On an experimental point of view, few experimental results on dynamic thermal effects have been made. An experiment performed on AT cut indicates that  $\overline{a}$  is lower than  $1 \mu\text{s/K}$ , ST and FST are respectively  $4 \mu\text{s/K}$  and  $.1 \mu\text{s/K}$ . Therefore the experimental dynamic temperature coefficients are larger than the calculations. In fact, in the experiments, there is in addition the influence of the mountings of the plate which induce constraints on the plate ; these forces will be responsible also of frequency variations. This effect was not taken into account in this model since it corresponds to a free extension plate. The mounting effects will be strongly dependent on the mountings, as it was previously observed with the g-sensitivity of SAW devices. Thus, it is desirable to study the influence of the support on the dynamic thermal behavior.

#### Acknowledgement

This work was supported by the Air Force Office of Scientific Research under grant AFOSR-82-0318.

#### References

- [1] W.G. Cady, Piezoelectricity, Mc Graw Hill Book, N.Y. 1946.
- [2] E.P. Eernisse, Quartz resonator frequency shifts arising from electrode stress. Proc. 29th Ann. Symp. on Freq. Cont., 1975.

- [3] D. Hauden, Etude des propriétés non linéaires des ondes élastiques de surface : applications aux oscillateurs et capteurs à quartz. Thèse, Besançon, 1979.
- [4] A. Ballato, J.R. Vig, Static and dynamic frequency-temperature behavior of singly and doubly rotated oven-controlled quartz resonators. Proc. of 32nd Ann. Freq. Cont. Symp., 180, 1978.
- [5] B.K. Sinha, H.F. Tiersten, Transient thermally induced frequency excursions in doubly rotated quartz thickness mode resonators. Proc. of 34th Ann. Freq. Cont. Symp., 393, 1980.
- [6] G. Théobald, G. Marianneau, R. Prétot, J.J. Cagnepain, Dynamic thermal behavior of quartz resonators. Proc. of 33rd Ann. Freq. Cont. Symp., 239, 1979.
- [7] H. Carslaw, J. Jaeger, Conduction of heat in solids. Oxford University Press, London, 1959.
- [8] B.A. Boley, J.H. Weiner, Theory of thermal stresses. John Wiley and Sons, 1960.
- [9] R. Holland, IEEE Trans. SU-21, n°3, 171, 1974.
- [10] R.D. Mindlin, An introduction to the mathematical theory of vibrations of elastic plates. Monograph USASCEL, Fort Monmouth, N.J., 1955.
- [11] H.F. Tiersten, Perturbation theory for linear electroelastic equations for small fields superposed on a bias. J. Acoust. Soc. Am., 64, 832, 1978.
- [12] M. Planat, D. Hauden, Nonlinear properties of bulk and surface acoustic waves in piezoelectric crystals. Ferroelectrics, vol. 42, 117-136, 1982.

cut	Y,X	AT,X	ST,X
$\bar{a}$ (ppm/K)	1.7	1.6	0.20
$\tilde{a}$ ( $\mu$ s/K)	-0.52	$<10^{-2}$	0.48

Table I  
Sensitivities in the one-dimensional model  
Hh = 50

cut	Y,X	AT,X	ST,X
$\bar{a}$ (ppm/K)	0.09	0.06	0.067
$\tilde{a}$ ( $\mu$ s/K)	-0.11	-0.10	-0.09

Table II  
Sensitivities in the two-dimensional model  
Hh = 50

cut	FST
$\bar{a}$ (ppm/K)	0.17
$\tilde{a}$ ( $\mu$ s/K)	0.06

Table III  
Sensitivities in the two-dimensional model for FST-cut  
Hh = 50

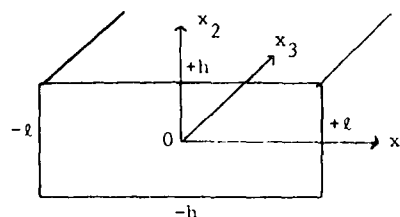


Fig. 1 : Schematic diagram of the crystal plate

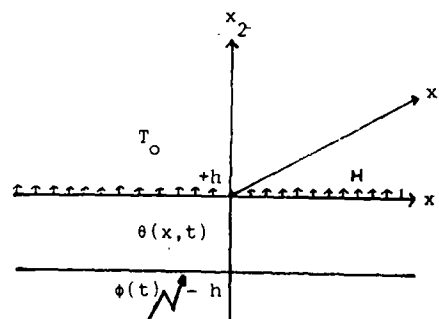


Fig. 2 : One-dimensional diagram of the plate heating at  $x_2 = -h$ . Heat transfer occurs at  $x_2 = +h$

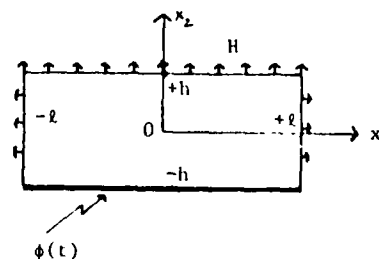


Fig. 3 : Two-dimensional diagram of the plate heating on the lower face. Heat transfer occurs at the three other faces

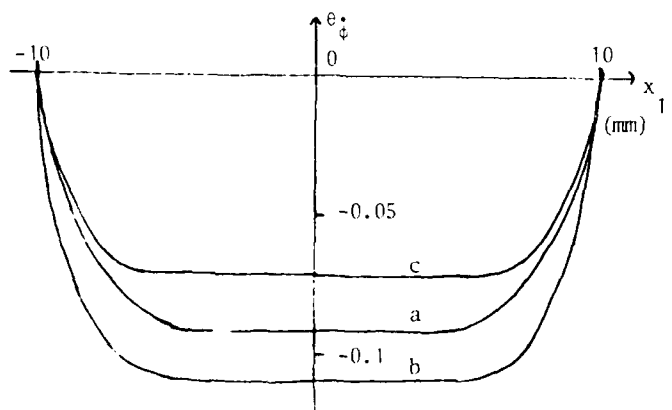
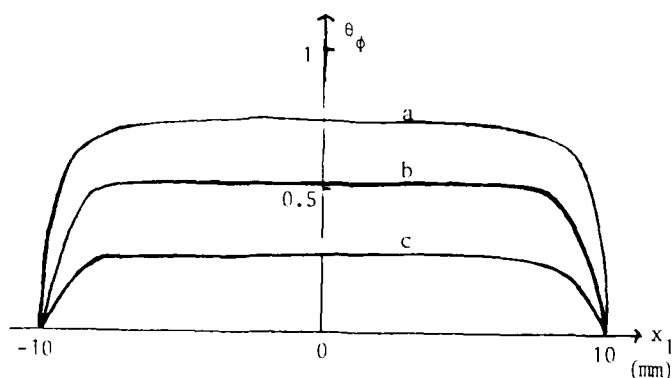


Fig. 4 : Temperature variations of  $\theta_\phi$  and  $\theta_\delta$  along the plate length for some values of the depth  
(a)  $x_2 = -0.5$  mm, (b)  $x_2 = 0$  mm, (c)  $x_2 = 0.5$  mm  
Transfer  $Hh = 500$  Y-cut

$l = 1$  cm  
 $h = 1$  mm

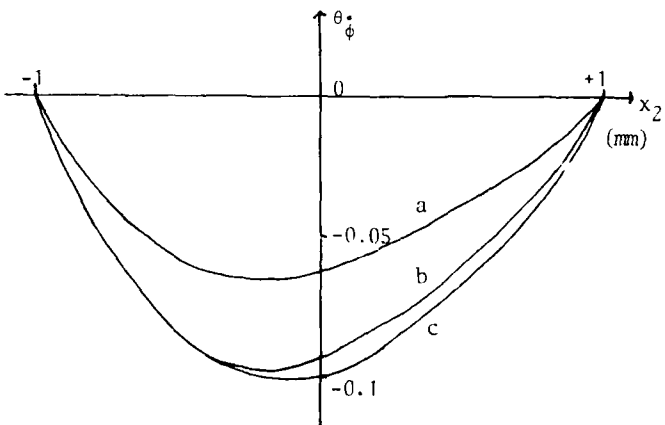
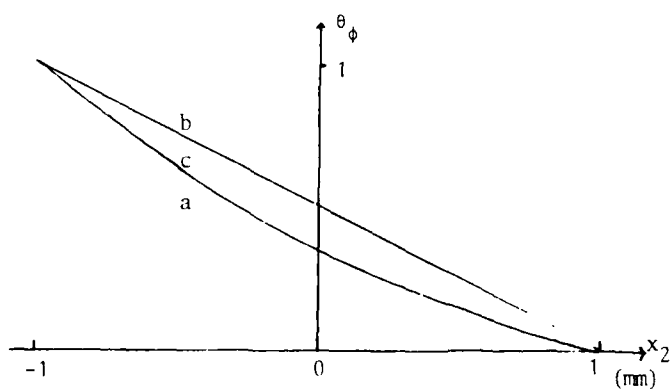


Fig. 5 : Temperature variations of  $\theta_\phi$  and  $\theta_\delta$  along the plate depth for some values along the length  
(a)  $x_1 = 9$  mm, (b)  $x_1 = 8$  mm, (c)  $x_1 = 7$  mm  
Transfer  $Hh = 500$  Y-cut

$l = 1$  cm  
 $h = 1$  mm

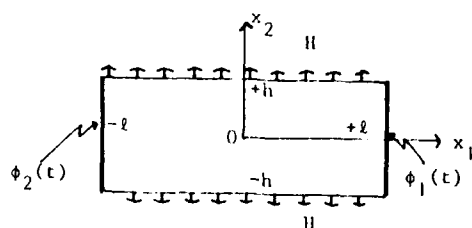


Fig. 6 : two-dimensional diagram of the plate heating on the lateral faces.  
Heat transfer occurs at the main faces.

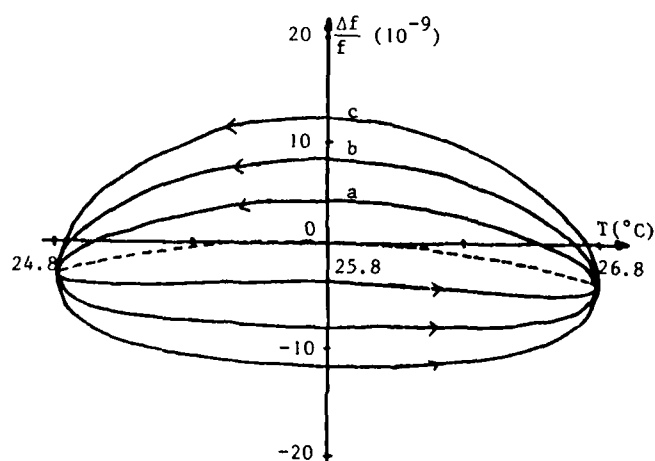


Fig. 7 : Thermal cyclings for different time rates  $v$  of change of the temperature for SI-cut  
(a)  $v = 1.8$  K/mn, (b)  $v = 3.6$  K/mn, (c)  $v = 5.4$  K/mn  
Reference temperature  $T_0 = 25^\circ\text{C}$   
Thermal variation  $\Delta T = 1^\circ\text{C}$  SI-cut

## TRANSIENT THERMAL RESPONSE OF SURFACE ACOUSTIC WAVE RESONATORS

Bikash K. Sinha

Schlumberger-Doll Research  
P. O. Box 307  
Ridgefield, CT 06877

### ABSTRACT

The transient thermal response of quartz resonators is an important contributing factor to the medium term frequency stability of these devices. Even when the quartz resonator is ovenized to operate near its turnover temperature in order to achieve maximum frequency stability, small thermal transients, temperature excursions and cyclings are not completely avoided. The resulting temporal temperature gradients in the quartz resonator plate produce frequency excursions which limit the performance of such high precision devices. The surface acoustic wave (SAW) resonators are generally fabricated on rectangular or circular plates. The devices are packaged and vacuum sealed in various types of enclosures which significantly affect the heat transfer characteristics of the device. In any event, the interaction of straight-crested surface waves with temperature gradients parallel as well as normal to the propagation direction are the two major causes of transient frequency excursions in SAW resonators.

Various steps in the analysis of transient thermal response of SAW resonators consist of first obtaining the temperature distribution in the quartz plate from the uncoupled heat conduction equation subject to appropriate initial and boundary conditions. This information is employed in the equations of static linear thermoelasticity which provides the time-dependent thermally induced biasing state. The temporal frequency excursions in SAW resonators are then obtained from a previously reported equation for the perturbation of the eigenfrequency due to a bias. Computational results have been obtained for several orientations of quartz plates subject to various temperature inputs. In particular, the dynamic temperature coefficient of frequency for SAW resonators have been obtained from the results for unit temperature ramps applied to the exposed surfaces. Good agreement has been obtained between the theoretical and experimental data on transient thermal tests on a SAW device subjected to an exponential rise in the external surface temperature.

### I. INTRODUCTION

When a Surface Acoustic Wave (SAW) device is subject to a temporal temperature disturbance, the interaction of surface waves with temperature gradients in the propagating medium results in a time-dependent perturbation of the *natural* velocity of surface waves. Such a fractional change in the velocity of surface waves is manifested in a fractional change in the time delay between two observation points or frequency of the SAW resonator. Thus transient temperature distributions in the propagating medium cause the frequency of the quartz resonator to drift in time until the new thermal equilibrium state is reached.

A knowledge of transient thermal response of quartz

resonators plays an important role in the design of high precision quartz oscillators. Recent studies have shown [1-3] that the medium term frequency stability of quartz crystal stabilized oscillators for measurement times ranging from  $Q/f$  ( $Q$  and  $f$  being the loaded quality factor and frequency, respectively) to several hours depends largely on two factors. The first factor is described by the flicker noise whose origin is not very well understood, but the level is generally related to the quality factor  $Q$ . The other factor is characterized by the transient thermal response of the resonator due to temperature fluctuations of the environment. Even when the quartz resonator is ovenized to operate near its turnover temperature in order to achieve maximum frequency stability, thermal transients, temperature cyclings and fluctuations are not completely avoided [2]. Some work on the response of SAW devices to thermal radiation [5,6] and sinusoidal thermal disturbance has been reported for a few specialized cases [7].

In this paper we describe the analysis of transient thermal response of SAW devices subject to various temperature inputs to the bounding surfaces. Various steps in the analysis of transient thermal response of SAW devices consist of first obtaining the temperature distribution in the quartz plate from the uncoupled heat conduction equation subject to appropriate initial and boundary conditions. Since the heat conduction is sufficiently slow compared to the velocity of elastic waves, the mechanical inertia term can be neglected in the stress equations of motion, thereby reducing them to quasi-static stress equations of equilibrium. Consequently, the time dependent thermally induced biasing state is determined from the equations of static, linear thermoelasticity for the unplated SAW substrate. The time-dependent change in resonant frequency resulting from the thermally induced biasing state is determined from an equation for the perturbation of the eigenfrequency due to a bias [8-11]. We have considered temperature gradients both along as well as normal to the direction of propagation of surface waves. The former situation arises when the sides of the plate are subjected to a temperature input and one-dimensional heat conduction along the length of the plate is considered. When the sides are subject to identical temperature inputs, we obtain a symmetrical temperature distribution about the center of plate. Under these circumstances, a SAW device placed symmetrically at the center, will exhibit minimal dispersion than a device placed asymmetrically for the same temperature inputs. However, when the outer surface of the substrate (plate) is subject to various temperature inputs and the inner surface is in vacuum, the normal temperature gradient at the inner surface is always zero. Under these circumstances, surface waves propagating on the inner surface is generally nondispersive unless the wavelength is large enough to allow the interaction of surface waves with the normal



temperature gradients.

Since a dominant mode of heat transfer from the external environment to the SAW device is through heat conduction along the thickness of the plate, we have considered various temperature inputs to the external plate surface and studied the interaction of resulting temperature gradients with the surface waves propagating on the internal surface. Computational results for the fractional change in the time delay of surface waves between two observation points have been obtained as a function of time. It has been observed that dynamic frequency transients (or spikes) in SAW resonators are observed only at and around turnover temperatures where the first order, static temperature coefficient of delay is zero. Generally, the magnitude of frequency undershoot or overshoot is on the order of 1 to 100 parts per billion (ppb) per degree C for sharp temperature inputs. Away from the turnover temperatures, the dynamic frequency response of SAW resonators exhibits a monotonic characteristic from the initial equilibrium state to the final equilibrium state. The stabilization time is governed by the thermal time constant of the plate. We have also modeled a thermal transient experiment on a flat plate SAW resonator [12]. It consists of a SAW resonator fabricated on a flat plate of thickness 1mm which has a flat-pack quartz enclosure, hermetically sealed in vacuum. The SAW device was taken from the room temperature to an oil bath at a temperature of about 12 degrees C higher than the room temperature. The outside surface temperature of the SAW device was measured with a thermistor as a function of time along with the frequency output from the SAW oscillator. The outside surface temperature exhibited approximately an exponential rise which provided the temperature input to the heat conduction equation. Good agreement has been obtained between the computational results and measured SAW oscillator frequency response. Some of the discrepancy between the theoretical and experimental results may be due to an uncertainty in the temperature values as measured by the thermistor which has claimed accuracy of plus or minus 0.1 degree C and the assumed exponential rise in the external surface temperature.

## II. TEMPERATURE INDUCED TRANSIENT FREQUENCY SHIFTS IN SAW RESONATORS

When a surface acoustic wave delay line or resonator is subject to a rapid change in the temperature, the substrate (plate) undergoes a time dependent, inhomogeneous temperature distribution which causes the resonant frequency to drift in time until the new thermal equilibrium state is reached. Since the fractional change in the resonant frequency is simply given by the negative of the fractional change in the time delay, and it has been shown [9,10] that when the equations of motion for small dynamic fields superposed on a bias are referred to the reference (or deformed) coordinates and *natural* velocity is employed in the description, the fractional change in the time delay is given by

$$\frac{\Delta \tau}{\tau} = -\frac{\Delta V}{V_m} \quad (2.1)$$

Therefore, the time-dependent change in the resonant frequency can be obtained from a perturbation equation [9,10] which has the form

$$\frac{\Delta f}{f} = -\frac{\Delta \tau}{\tau} = -\frac{H_m}{2\xi^2 V_m^2}, \quad \Delta V = V - V_m, \quad (2.2)$$

where  $H_m$  is the perturbation integral,  $\xi$  is the wavenumber in the unperturbed state,  $V_m$  and  $V$  are the natural velocities of surface waves in the unperturbed and perturbed states, respectively.

A general form of the perturbation integral for the calculation of a fractional change in the time delay for surface waves due to a biasing state may be given by

$$H_m = \int_{S_0} N_L \left[ K_{L\gamma}^l g_\gamma^m - K_{L\gamma}^n g_\gamma^m \right] ds + \int_{V_0} K_{L\gamma,L}^n g_\gamma^m dV_0, \quad (2.3)$$

where  $K_{L\gamma}^l$  and  $K_{L\gamma}^n$ , respectively, are the linear and nonlinear portions of the Piola-Kirchhoff stress tensor and are defined by

$$K_{L\gamma}^l = c_{L\gamma M\alpha} \epsilon_{\alpha,M}, \quad (2.4)$$

$$K_{L\gamma}^n = (\hat{c}_{L\gamma M\alpha} + \Delta c_{L\gamma M\alpha}) \epsilon_{\alpha,M}. \quad (2.5)$$

In Eq. (2.3),  $N_L$  is the outward drawn unit normal to the bounding surface  $S_0$  of the volume  $V_0$ . The normalized eigensolution of surface waves has the form

$$g_\gamma^m = \frac{u_\gamma^m}{N_m}, \quad N_m^2 = \int_{V_0} \rho_0 u_\gamma^m u_\gamma^m dV_0. \quad (2.6)$$

The boundary conditions at a traction free surface under a bias are given by

$$N_L K_{L\gamma} = N_L (K_{L\gamma}^l + K_{L\gamma}^n) = 0. \quad (2.7)$$

Moreover, the normalized eigensolution in the unperturbed state satisfies the boundary conditions

$$N_L K_{L\gamma}^m = 0. \quad (2.8)$$

Substitution of Eqs. (2.7) and (2.8) into (2.3) yields

$$H_m = - \int_{S_0} N_L K_{L\gamma,L}^n g_\gamma^m ds_0 + \int_{V_0} K_{L\gamma,L}^n g_\gamma^m dV_0. \quad (2.9)$$

When referred to the coordinate system shown in Fig. 1, the perturbation integral for inhomogeneous biasing field in the sagittal ( $X_1-X_2$ ) plane of surface waves takes the form

$$\begin{aligned} H_m = & \int_{-M\lambda}^{N\lambda} (K_{21}^n g_1^m + K_{22}^n g_2^m \\ & + K_{23}^n g_3^m) |_{x_2=0} dx_1 \\ & + \int_{-M\lambda}^{N\lambda} dx_1 \int_0^\infty dx_2 \left[ (K_{11,1}^n + K_{21,1}^n) g_1^m \right. \\ & \left. + (K_{12,1}^n + K_{22,2}^n) g_2^m + (K_{13,1}^n + K_{23,2}^n) g_3^m \right], \quad (2.10) \end{aligned}$$

where  $M\lambda$  and  $N\lambda$  define the path length in multiples of the wavelength  $\lambda$  and the nonlinear components of the Piola-Kirchhoff stress tensor  $K_{L\gamma}^n$  are defined in Eq. (2.5). The quantities  $\hat{c}_{L\gamma M\alpha}$  and  $\Delta c_{L\gamma M\alpha}$  respectively, in Eq. (2.5) are defined by

$$\begin{aligned} \hat{c}_{L\gamma M\alpha} = & T_{LM}^1 \delta_{\gamma\alpha} + c_{L\gamma M\alpha B} E_{AB} \\ & + c_{L\gamma PM} w_{\alpha,P} + c_{LPM\alpha} w_{\gamma,P}, \end{aligned} \quad (2.11)$$

and

$$\Delta c_{LYM\alpha} = \frac{dc_{LYM\alpha}}{dT} [T(X_1, X_2, t) - T_0] \quad (2.12)$$

In Eq. (2.11),  $T_{LM}^1$ ,  $E_{AB}^1$  and  $w_{\alpha,p}$  are the biasing stress, strain and displacement gradient components, respectively. The quantities  $c_{LPM\alpha}$  and  $c_{LYM\alpha AB}$  are the second and third order elastic constants, respectively,  $\frac{dc_{LYM\alpha}}{dT}$  are the temperature derivatives of the second order elastic constant [13], and  $T(X_1, t)$  is the temperature distribution at the current time  $t$ . As stated in the Introduction, the biasing deformation state is obtained from the static equations of linear thermoelasticity. The thermal stress-strain and strain-displacement gradient relations, respectively, are given by

$$T_{LM}^1 = c_{LMKN} E_{KN}^1 - \nu_{LM} [T(X_1, X_2, t) - T_0] \quad (2.13)$$

and

$$E_{KN}^1 = \frac{1}{2} (w_{KN} + w_{N,K}) \quad (2.14)$$

where  $\nu_{LM}$  are thermoelastic constants,  $T$  and  $T_0$  are temperature distributions in the propagating medium in the current and reference configurations, respectively. Since we are dealing with the perturbation equations for small dynamic fields superimposed on a bias, the deformation of a material body is given by

$$\mathbf{y}(\mathbf{X}_L, t) = \mathbf{X} + \mathbf{w}(\mathbf{X}_L) + \mathbf{u}(\mathbf{X}_L, t) \quad (2.15)$$

where  $\mathbf{y}$  is the position vector of a material point in the present position at time  $t$  which occupied the position  $\mathbf{X}$  in the reference state. The quantities  $\mathbf{w}$  and  $\mathbf{u}$  are the temperature induced biasing displacement and surface wave displacement vectors, respectively.

Substitution of Eqs. (2.11) and (2.12) into (2.4) and (2.5), and finally into (2.10) yields the following expression for the perturbation integral

$$\begin{aligned} H_m = & \int_{-M\lambda}^{N\lambda} [(\hat{c}_{21Q\alpha} + \Delta c_{21Q\alpha}) g_{\alpha,Q}^m g_1^m \\ & + (\hat{c}_{22Q\alpha} + \Delta c_{22Q\alpha}) g_{\alpha,Q}^m g_2^m \\ & + (\hat{c}_{23Q\alpha} + \Delta c_{23Q\alpha}) g_{\alpha,Q}^m g_3^m]_{x_3=0} dx_1 \\ & + \int_{-M\lambda}^{N\lambda} dx_1 \int_0^\infty dx_2 [(\hat{c}_{11Q\alpha} g_{\alpha,Q}^m)_{,1} + \Delta c_{11Q\alpha} g_{\alpha,Q}^m \\ & + (\hat{c}_{21Q\alpha} g_{\alpha,Q}^m)_{,2} + \Delta c_{21Q\alpha} g_{\alpha,Q}^m] g_1^m \\ & + \{(\hat{c}_{12Q\alpha} g_{\alpha,Q}^m)_{,1} + \Delta c_{12Q\alpha} g_{\alpha,Q}^m \\ & + (\hat{c}_{22Q\alpha} g_{\alpha,Q}^m)_{,2} + \Delta c_{22Q\alpha} g_{\alpha,Q}^m\} g_2^m \\ & + \{(\hat{c}_{13Q\alpha} g_{\alpha,Q}^m)_{,1} + \Delta c_{13Q\alpha} g_{\alpha,Q}^m \\ & + (\hat{c}_{23Q\alpha} g_{\alpha,Q}^m)_{,2} + \Delta c_{23Q\alpha} g_{\alpha,Q}^m\} g_3^m] \quad (2.15) \end{aligned}$$

Thus the temperature dependence of the resonant frequency of SAW devices can be computed from the aforementioned perturbation Eq. (2.2) provided the thermal deformation field in the quartz substrate, the surface wave mode shape and the first temperature derivatives of the fundamental elastic constants of quartz are known.

### III. HEAT CONDUCTION

A one-dimensional heat conduction equation along the

thickness direction is given by

$$\frac{\partial T}{\partial t} = \kappa_{22} \frac{\partial^2 T}{\partial X_2^2} \quad (3.1)$$

where  $\kappa_{22}$  is the thermal diffusivity along the thickness direction  $X_2$ ,  $T$  is the temperature and  $t$  is time.

The boundary conditions are

$$\frac{\partial T}{\partial X_2} = 0 \quad (3.2)$$

for no flow of heat at  $X_2 = 0$ , and the other surface  $X_2 = h$ , can be subjected to various temperature inputs.

#### Case I: Step Rise in the External Surface Temperature

When a plate is subject to a step change in temperature at the face  $X_2 = h$ , with the other face  $X_2 = 0$  exposed to vacuum, the temperature distribution across the plate is given by [14]

$$\begin{aligned} T = & \bar{T} + 4 \sum_{n=0}^{\infty} \exp[-\kappa_{22} (2n+1)^2 \pi^2 t / 4h^2] \\ & \cdot \frac{(-1)^{n+1}}{(2n+1)\pi} (\bar{T} - T_0) \cos[(2n+1)\pi X_2 / 2h] \quad (3.3) \end{aligned}$$

where  $T_0$  and  $\bar{T}$  are the initial and final temperatures, respectively.

#### Case II: Exponential Rise in the External Surface Temperature

For the case when the surface  $X_2 = h$ , is exposed to an exponential rise in temperature given by

$$T = \bar{T}(1 - e^{-\beta t}) \quad (3.4)$$

the temperature distribution across the plate takes the form [14]

$$\begin{aligned} \frac{T(X_2, t) - T_0}{\bar{T} - T_0} = & 1 - e^{-\beta t} \frac{\cos(\beta / \kappa_{22})^{1/2} X_2}{\cos(\beta / \kappa_{22})^{1/2} h} \\ & + \frac{4\beta}{\pi} \sum_{n=0}^{\infty} \frac{(-1)^{n+1}}{(2n+1)} \\ & \frac{\exp[-\kappa_{22} \tau_n^2 t] \cos \tau_n X_2}{(\beta - \kappa_{22} \tau_n^2)} \quad (3.5) \end{aligned}$$

where

$$\tau_n = \frac{(2n+1)\pi}{2h} \quad (3.6)$$

#### Case III: Linear Rise in the External Surface Temperature.

When a plate is subject to a linear rise in temperature at the face  $X_2 = h$ , given by

$$\Delta T_s = (\Delta \bar{T})t, \text{ for } t > 0 \quad (3.7)$$

where  $\Delta \bar{T}$  is the time rate of increase in the surface temperature, the temperature distribution across the substrate (or plate) thickness takes the form [14]

$$\Delta T(X_2, t) = \Delta \bar{T}[(t - h^2/2\kappa_{22}) + X_2^2/2\kappa_{22}]$$

$$+ \frac{2}{\kappa_{22}h} \sum_{n=0}^{\infty} \frac{(-1)^n}{\tau_n^3} \exp[-\kappa_{22}\tau_n^2 t] \cos \tau_n X_2] , \quad (3.8)$$

where  $\tau_n$  is defined by Eq. (3.6). In Eq. (3.8),  $\kappa_{22}$  and  $h$  are the thermal diffusivity along the thickness direction and plate (substrate) thickness, respectively.

When one-dimensional heat conduction along the length of the plate ( $X_1$ -direction) is considered, the resulting temperature distribution is parallel to the surface wave propagation direction. Assuming that the plate is subject to a linear rise in temperature at the faces  $X_1 = \pm l$ , as given by Eq. (3.7), the temperature distribution along the plate is symmetric about  $X_1 = 0$ , and has the form shown in Eq. (3.8) provided we replace  $X_2, h$  and  $\kappa_{22}$  by  $X_1, l$  and  $\kappa_{11}$ , respectively.

#### IV. TEMPERATURE INDUCED BIASING STATE

The thermal biasing state of the substrate is governed by the stress equations of equilibrium which may be written in the form

$$T_{LM,L}^1 = 0 . \quad (4.1)$$

The constitutive relations for a thermoelastic solid is reproduced here from Eq. (2.13) and has the form

$$T_{LM}^1 = c_{LMKN} E_{KN}^1 - \nu_{LM} \Delta T(X_j, t) , \quad (4.2)$$

where  $c_{LMKN}$  are the second-order elastic constants,  $T_{LM}^1$  and  $E_{KN}^1$  are the biasing stresses and strains, respectively. The thermoelastic constants  $\nu_{LM}$  are defined by

$$\nu_{LM} = c_{LMPQ} \alpha_{PQ} , \quad (4.3)$$

where  $\alpha_{PQ}$  are the coefficients of thermal expansion, and  $\Delta T$  is the spatial and temporal change in temperature. Since the outside edges as well as major surfaces of the plate are traction free we have

$$N_L T_{LM}^1 = 0 , \quad (4.4)$$

where  $N_L$  denotes the unit normal to all surfaces of the plate at the reference temperature  $T_0$ .

For a stress-free state resulting from a temperature change we have from Eqs. (4.1) and (4.4),

$$T_{LM}^1 = 0 , \quad (4.5)$$

which satisfies the stress equations of equilibrium trivially and the biasing strains are thus given by

$$E_{KN}^1 = \alpha_{KN} \Delta T , \quad \Delta T = T - T_0 . \quad (4.6)$$

Since the temporal temperature distribution is known from Sec. II, we can solve for the corresponding biasing strains from Eq. (4.5). It should now be carefully noted that in the case of the unelectroded plate, the temperature induced deformation results in time-dependent inhomogeneous strains  $E_{KN}^1$  along with associated rotations  $\Omega_{KN}^1$ , which are given by

$$\Omega_{KN}^1 = \frac{1}{2} (w_{N,K} - w_{K,N}) , \quad (4.7)$$

where  $w_{K,N}$  are the displacement gradient components. However, all variables are functions of the  $X_2$ -coordinate only, and it has been shown that the change in frequency due to a homogeneous infinitesimal rigid rotation vanishes, we can therefore, obtain the three-dimensional rotation field by requiring that the three-dimensional rotation

gradient-strain gradient relations [15-17]

$$\Omega_{KL,M}^1 = E_{ML,K}^1 - E_{MK,L}^1 , \quad (4.8)$$

be satisfied. Thus we have from Eq. (4.8)

$$\Omega_{13}^1 = 0, \quad \Omega_{21}^1 = E_{21}^1, \quad \Omega_{23}^1 = E_{23}^1 , \quad (4.9)$$

and the displacement gradient components take the form

$$w_{A,B} = E_{AB}^1, \quad w_{A,2} = 2E_{2A}^1, \quad (4.10)$$

$$w_{2,A} = 0, \quad w_{2,2} = E_{22}^1 .$$

The substitution of Eq. (4.6) with (4.10) and (4.5) yields  $\hat{c}_{L\gamma M\beta}$  in Eq. (2.11) as a known linear function of  $(T-T_0)$  for the unelectroded plate. Thus, the temperature distribution in the substrate (plate) can be employed in the static equations of thermoelasticity to obtain temporal deformation state of the propagating medium.

#### V. COMPUTATIONAL AND EXPERIMENTAL RESULTS FOR SURFACE ACOUSTIC WAVE (SAW) DEVICES

Before the transient temperature induced frequency shifts in SAW devices can be computed, one needs to determine the eigensolution for surface waves in a piezoelectric substrate of a given orientation and propagation direction. The solution for surface waves propagating in arbitrarily anisotropic, piezoelectric substrates satisfies the differential equations of motion and boundary conditions of linear piezoelectricity and may be written in the form [18,19]

$$(u_j, \phi) = \sum_{m=1}^4 C^{(m)} (A_j^{(m)}, \bar{A}_4^{(m)}) \exp(i\beta_m \xi X_2) \exp[i\xi(X_1 - Vt)] , \quad (5.1)$$

where  $u_j$  and  $\phi$  are the complex representation of the real mechanical displacement and electric potential, respectively, for propagation in the direction  $X_1$  with  $X_2$  normal to the surface as shown in Fig. 1. The quantities  $C^{(m)}$ ,  $A_j^{(m)}$ ,  $\bar{A}_4^{(m)}$  and  $\beta_m$  are determined numerically for traction-free mechanical and open-circuit electrical boundary conditions. The normalized unperturbed surface wave eigensolution for the perturbation equation is obtained from Eqs. (2.6) and (5.1). The normalization integral in Eq. (2.6) takes the form

$$N^2 = \rho \int_0^\infty dX_2 \int_{-\pi/\xi}^{\pi/\xi} u_j u_j dX_1 ,$$

$$= \rho \frac{\pi i}{\xi^2} \sum_{m=1}^4 \sum_{n=1}^4 \frac{C^{(m)} A_j^{(m)} C^{(n)*} A_j^{(n)*}}{(\beta_m - \beta_n^*)} , \quad (5.2)$$

where the  $*$  denotes complex conjugate and  $N^2$  is, of course, real.

Calculations have been performed using the known values of the second order elastic, piezoelectric and dielectric constants of quartz [20], the third order elastic [21], and thermoelastic constants of quartz [22,23], thermal conductivity constants [24], and the recently obtained temperature derivatives of the fundamental elastic constants of quartz [13]. Computational results have been obtained for the time dependent, fractional change in the time delay of surface waves due to its interactions with the temporal temperature gradients in the propagating medium.

We have considered two cases of temperature gradients: normal as well as parallel to the propagation direction. In particular, results have been obtained for a step rise, exponential rise and linear rise in temperature of the external surface of the plate (substrate) while the internal surface is encapsulated in vacuum. Figures 2 and 3 illustrate the transient response to a step change in the external surface temperature of SAW devices with orientations which possess turnover temperatures slightly above and at the reference (room) temperature, respectively. It is interesting to note that the dynamic response of the device with the turnover temperature away from the reference temperature exhibits a monotonic behavior from the initial to final equilibrium states, and the stabilization time is governed by the thermal time constant of the device. However, for orientations whose turnover temperatures coincide with the reference temperature, the transient response of such devices exhibits "undershoots" or "overshoots" in the frequency output before relaxing to the final equilibrium state.

When the external surface of a SAW device substrate is subject to an exponential rise in temperature, the dynamic frequency output of the device qualitatively follows the temperature profile of the external surface. Computational results for this case have been compared with experimental data for a device whose static frequency-temperature characteristic is shown in Figure 4. A schematic diagram of the device is shown in Figure 5. It consists of a "sandwich-type" of structure formed by two thin plates of thickness approximately 1 mm each and width and length of approximately 13 and 15 mm, respectively. Experimental data have been obtained from this device on immersing it into an oil bath which was approximately 12° C higher than the room temperature. The temperature of the external surface was measured with a thermistor as a function of time. The measured external surface temperature rise curve is shown in Figure 6 along with a theoretical curve which is described by Eq. (3.5) with  $\beta$  approximately equal to 0.07 sec<sup>-1</sup>. This theoretical curve for the external surface temperature rise serves as the input to the theoretical model as described in Sec III. The time-dependent, fractional change in the harmonic frequency can be computed from Eq. (5.3) shown below.

$$\frac{\Delta f}{f} = H_1 \cdot \Delta T(t) / 2\xi^2 V_m^2 + A_2 [\Delta T(t)]^2, \quad (5.3)$$

where

$$H_1 = -H_m / \Delta T(t), \quad (5.4)$$

and  $\Delta T(t)$  is the time-dependent change in the internal surface temperature obtained from the solution of the heat conduction equation. It should be noted that as the elapsed time  $t$  becomes large, the fractional change in the harmonic frequency takes the familiar form

$$\frac{\Delta f}{f} = A_1 \Delta T + A_2 (\Delta T)^2, \quad (5.5)$$

where  $A_1$  and  $A_2$  are the first and second order static temperature coefficients of frequency. A comparison of the experimental and theoretical dynamic thermal response of this device is shown in Figure 7. Good agreement has been obtained between the predicted and measured values of the SAW oscillator frequency output.

Next we describe the results for the fractional change in the time delay of surface waves due to time-dependent longitudinal temperature gradients along the direction of propagation of waves. Figure 8 shows temperature distributions along the length of a substrate of length 20 mm subjected to temperature inputs of unit ramps at the two ends. Results for the fractional change in time delay of surface waves between two observation points symmetrically placed on the substrate and subjected to unit ramps are shown in Figure 9 for various lengths of the plate (substrate). These curves are for a harmonic frequency of 100 MHz and they do not show any sharp excursions (or spikes) for this orientation of the plate. It is known that an inhomogeneous biasing state of the propagating medium can produce dispersion in the surface wave propagation. We have thus performed calculations for the fractional change in the time delay of surface waves of different harmonic frequencies. Specifically, computational results shown in Figure 10 are for a path length of 200 wavelengths in an asymmetrically placed delay line on an a rotated Y-cut substrate with the rotation angle  $\theta$  of 35.25°. Curves 1 through 4 are results for harmonic frequencies of 50, 100, 2000 and 4000 MHz, respectively. Clearly, the separation of these curves are due to dispersion. However, for large times the slopes of these curves coincide with each other indicating that the propagation has become nondispersive after steady state has been established. The slope of the curves in Figure 10 is plotted as a function of time in Figure 11, which includes the behavior under steady state conditions.

Figure 12 shows temperatures of the external and internal surfaces of a rotated Y-cut plate ( $\theta=41.3401^\circ$ ) of thickness 2 mm. Curve 1 represents a unit ramp applied to the external surface and curve 2 is the temperature of the internal surface which is encapsulated in vacuum. Curve 2 is obtained from the solution of the one-dimensional heat conduction equation along the thickness direction. The fractional change in time delay of surface waves on a substrate of this temperature compensated orientation exhibits an interesting behavior as shown in Figure 13. This is in contrast with the results shown in Figure 14 obtained for a neighboring orientation ( $\theta=42.75^\circ$ ) which is not temperature compensated to the same degree.

In conclusion, computational results indicate that thermal transients or dynamic frequency spikes are observed only at and around turnover temperatures. Generally, the magnitude of dynamic frequency undershoot or overshoot is on the order of ( $\Delta f/f \Delta T =$ ) 1 to 100 ppb for 1° C step change in the external surface temperature. Away from turnover temperatures, the dynamic response exhibits a monotonic behavior from the initial to final

equilibrium states and the stabilization time is governed by the thermal time constant of the device. Generally, temperature gradients can produce dispersion in surface wave propagation. However, a SAW device with large thickness/wavelength ratio and placed symmetrically in a longitudinal temperature gradient will exhibit minimal amount of dispersion in the transient state. Since a dispersive propagation of surface waves leads to a degradation of the resonator stability, it must be avoided for increased stability of the device.

### ACKNOWLEDGEMENTS

The author would like to thank Dr. M. P. Ekstrom for support and encouragement; Mr. T. Muricchio for help with the calculations; Prof. H. F. Tiersten of Rensselaer Polytechnic Institute for a valuable comment on the analytical procedure; Drs. T. Parker, H. Lin Chao and J. Callerame of Raytheon Research Division for providing experimental data on transient thermal tests on a SAW device.

### REFERENCES

1. R. J. Besson, J. M. Gros Lambert, and F. L. Walls, "Quartz Crystal Resonators and Oscillators, Recent Developments and Future Trends," *Ferroelectrics*, **43** pp. 57-65 (1982).
2. A. Ballato, T. J. Lukaszek, and G. J. Iafrate, "Subtle Effects in High-Stability Quartz Resonators," *Ferroelectrics*, **43** pp. 25-41 (1982).
3. T. E. Parker, "Precision Surface Acoustic Wave (SAW) Oscillators," 1982 *Ultrasonics Symposium Proceedings*, IEEE Catalog No. 82CH1823-4, pp. 268-274 (1982).
4. J. A. Kusters, "Transient Thermal Compensation for Quartz Resonators," *IEEE Trans. SU-23*, pp. 273-276 (1976).
5. D. A. Rockwell and J. H. Parks, "Theory of Acoustic Surface Wave Detection of Radiative Absorption," *J. Appl. Phys.*, **47**, pp. 2889-2897 (1976).
6. K. H. Dinh, "Response of Surface Acoustic Wave Devices to High-Speed Thermal Radiation," *IEEE Trans. SU-26*, pp. 112-119 (1979).
7. D. Hauden and G. Theobald, "Dynamic Thermal Sensitivity of SAW Quartz Oscillators," 1980 *Ultrasonics Symposium Proceedings*, IEEE Catalog No. 80CH1602-2, pp. 264-267 (1980).
8. H. F. Tiersten, "Perturbation Theory for Linear Electroelastic Equations for Small Fields Superposed on a Bias," *J. Acoust. Soc. Am.*, **64**, pp. 832-837 (1978).
9. B. K. Sinha and H. F. Tiersten, "On the Influence of a Flexural Biasing State on the Velocity of Piezoelectric Surface Waves," *Wave Motion*, **1**, pp. 37-51 (1979).
10. B. K. Sinha and H. F. Tiersten, "On the Temperature Dependence of the Velocity of Surface Waves in Quartz," *J. Appl. Phys.*, **51** pp. 4659-4665 (1980).
11. B. K. Sinha, "Elastic Waves in Crystals Under a Bias," *Ferroelectrics*, **41** pp. 61-73 (1982).
12. T. Parker, C. Lin Chao, and J. Callerame, Private Communication, (1984).
13. B. K. Sinha and H. F. Tiersten, "First Temperature Derivatives of the Fundamental Elastic Constants of Quartz," *J. Appl. Phys.*, **50** pp. 2732-2739 (1979).
14. H. S. Carslaw and J. C. Jaeger, "Conduction of Heat in Solids (Oxford University, London, 1959), Sec. 3.
15. H. F. Tiersten and B. K. Sinha, "Temperature Dependence of the Resonant Frequency of Electroded Doubly-Rotated Quartz Thickness-Mode Resonators," *J. Appl. Phys.*, **50** pp. 8038-8051 (1979).
16. D. S. Stevens, H. F. Tiersten, and B. K. Sinha, "Temperature Dependence of the Resonant Frequency of Electroded Contoured AT-Cut Quartz Crystal Resonators," *J. Appl. Phys.*, **54**, pp. 1704-1716 (1983).
17. B. K. Sinha and H. F. Tiersten, "Thermally Generated Transient Frequency Excursions in Doubly Rotated Quartz Thickness-Mode Resonators," *J. Appl. Phys.*, **55**, pp. 3337-3347 (1984).
18. J. J. Campbell and W. R. Jones, "A Method for Estimating Optimal Crystals Cuts and Propagation Directions for Excitation of Piezoelectric Surface Waves," *IEEE Trans. SU-15* pp. 209 (1968).
19. B. K. Sinha, H. F. Tiersten, and "Elastic and Piezoelectric Surface Waves Guided by Thin Films," *J. Appl. Phys.*, **44** pp. 4831-4854 (1973).
20. R. Bechmann, "Elastic and Piezoelectric Constant of Alpha-Quartz," *Phys. Rev.*, **110**, pp. 1060 (1958).
21. R. N. Thurston, H. J. McSkimin, P. Andreatch, Jr., "Third Order Elastic Constant of Quartz," *J. Appl. Phys.*, **37**, pp. 267 (1966).
22. F. Kohlrausch, *Lehrbuch der prakt., Phys.*, **16** Aufl. 5, 158 (1930) Constant employed in Ref. 23.
23. R. Bechmann, A. D. Ballato, and T. N. Lukaszek, "Higher Order Temperature Coefficients of the Elastic Stiffnesses and Compliances of Alpha-Quartz" *Proc. IRE*, **50** pp. 1812-1822 (1962).
24. J. Tasi and G. Herrmann, "Thermoelastic Dissipation in High Frequency Vibrations of Crystal Plates," *J. Acoust. Soc. Am.*, **36** pp. 100 (1964).

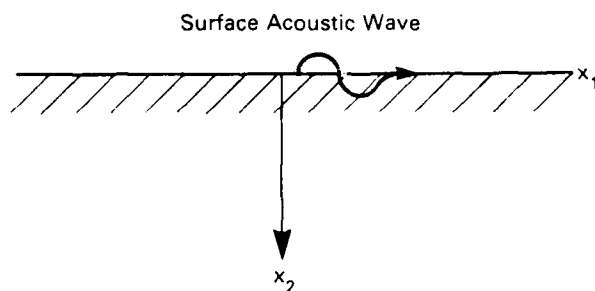


**Figure 1:** Schematic diagram showing the free surface of a semi-infinite solid.

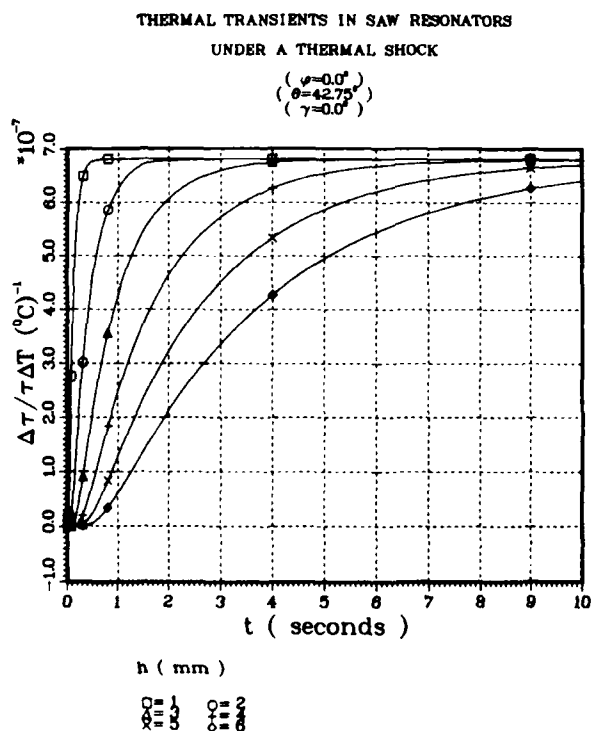


**Figure 2:** Time-dependent fractional change in the time delay of surface waves on a rotated Y-cut ( $\theta=42.75^\circ$ ) plate whose external surface is subject to a  $1^\circ\text{C}$  step rise in temperature. Curves 1 through 6 are for plate thicknesses of 1 through 6 mm, respectively.

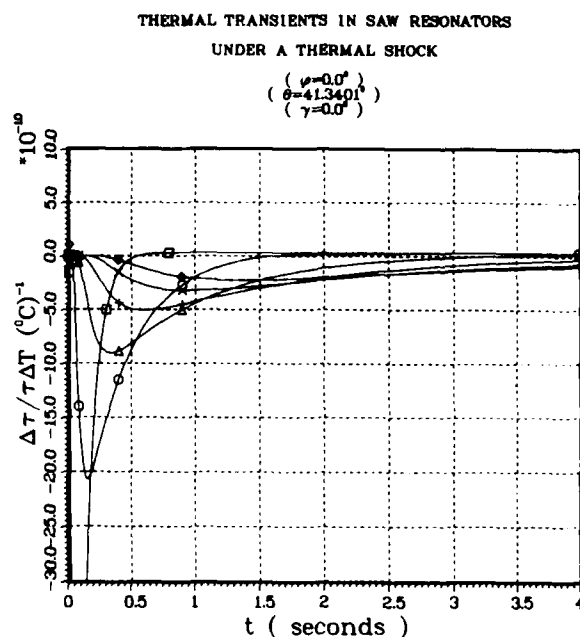


**Figure 3:** Time-dependent fractional change in the time delay of surface waves on a rotated Y-cut ( $\theta=41.3401^\circ$ ) plate whose external surface is subject to a  $1^\circ\text{C}$  step rise in temperature. This nominal orientation exhibits a turnover temperature coincident with the reference temperature. The first order temperature coefficient of delay is 0.1 ppb/degreeC. The notation is same as in Fig. 2.

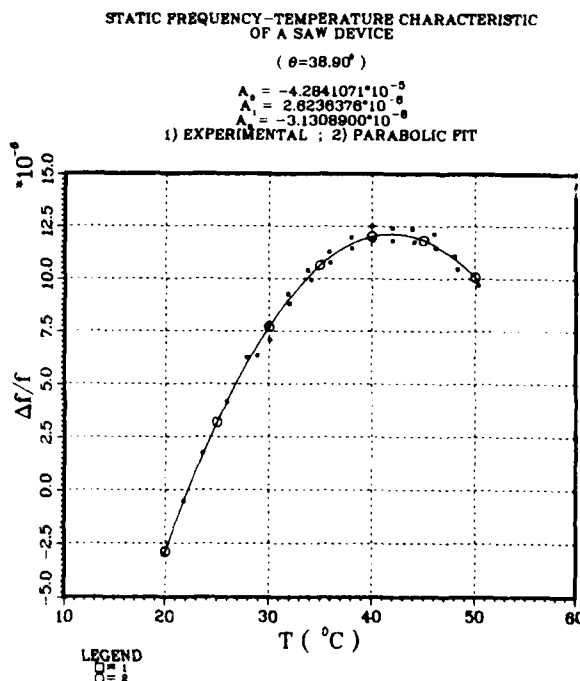


**Figure 4:** Static frequency-temperature characteristic of a SAW device around its turnover temperature of approximately  $42^\circ\text{C}$ . The small squares represent the experimental points and the solid curve is the parabolic fit. The rotation angle  $\theta$  of this device has been estimated from the first order temperature coefficient of frequency at the room temperature and the value of  $\theta$  is  $38.9^\circ$ .

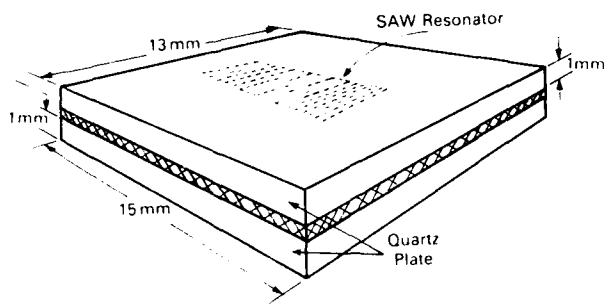


**Figure 5:** Schematic diagram of the SAW device used in the transient thermal test.

#### TOTAL DYNAMIC THERMAL RESPONSE OF A SAW DEVICE

$$(\theta = 38.90^\circ)$$

$$h = 1 \text{ mm}$$

$$\beta = 0.069896914; A2 = -0.1308900 \cdot 10^{-8}$$

1) EXPERIMENTAL ; 2) THEORETICAL

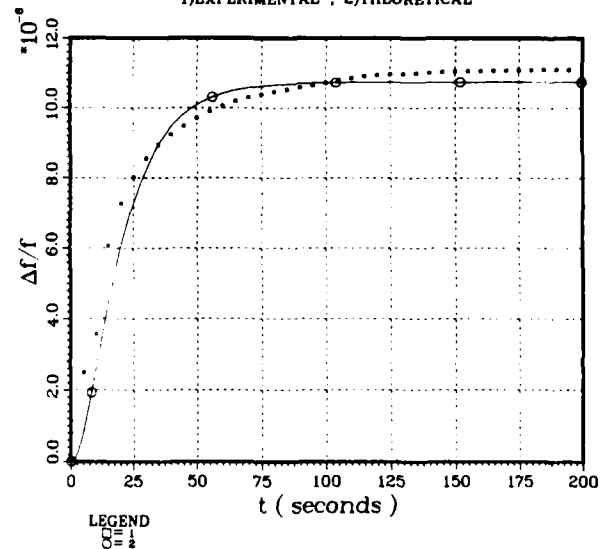


**Figure 7:** Measured and Predicted Values of the Dynamic Thermal Response of the SAW device. The dots denote the experimental data and the solid curve represents the theoretical result.

#### EXTERNAL SURFACE TEMPERATURE RISE FOR A SAW RESONATOR

1) EXPERIMENTAL  
2) THEORETICAL FIT

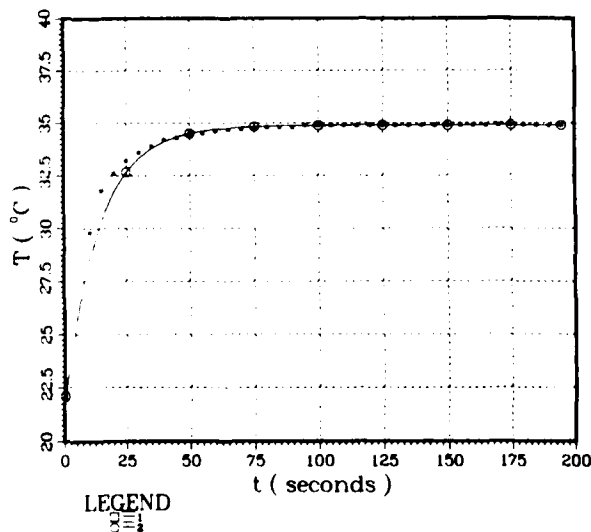


**Figure 6:** External surface temperature rise for the SAW device on immersing it into an oil bath at a temperature of about  $12^\circ \text{C}$  higher than the room temperature. The dots are the measured values and the solid curve is an exponential fit to the data ( $\beta = 0.07 \text{ sec}^{-1}$ ).

#### TEMPERATURE DISTRIBUTION ALONG THE SUBSTRATE

$$(\theta = 42.75^\circ)$$

$$l = 10 \text{ mm}$$

$$t = (2, 4, 6, 8, 10) \text{ sec}$$

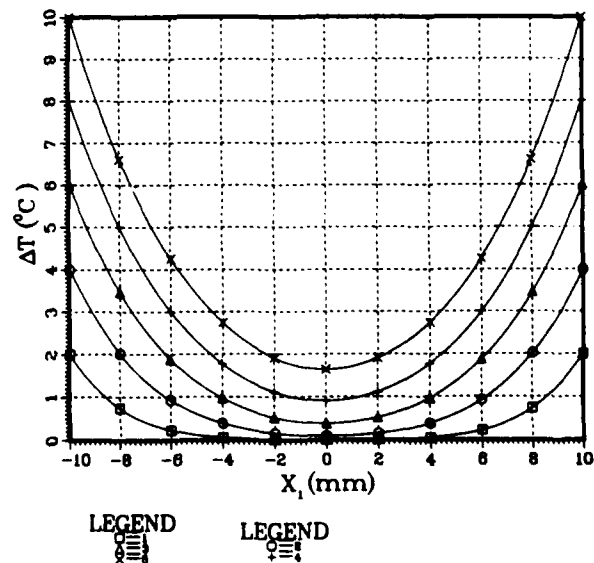


**Figure 8:** Temperature distribution along the substrate of length  $2l = 20 \text{ mm}$  subject to unit temperature ramps at the two ends. Curves 1 through 5 represent temperature distributions along the plate at time intervals of 2, 4, 6, 8 and 10 sec, respectively, after the ends are subjected to a linear temperature rise.

FRACTIONAL CHANGE IN TIME DELAY OF SURFACE WAVES  
FOR RAMP INPUT, NORMAL TO ENDS OF SUBSTRATE

$l = (5, 10, 15, 20, 25) \text{ mm}$   
 $N = 100\lambda$

$(\theta = 42.75^\circ)$   
 $(\gamma = 0^\circ)$

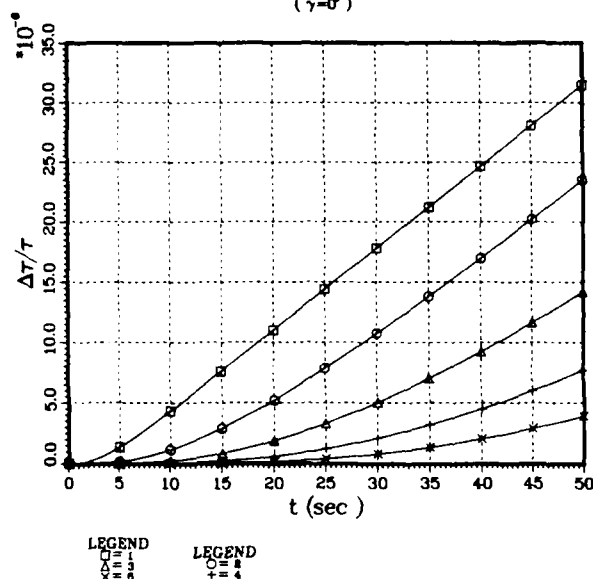


**Figure 9:** Time-dependent fractional change in time delay of surface waves on a rotated Y-cut ( $\theta = 42.75^\circ$ ) plate subject to unit ramps at its ends. Curves 1 through 5 are for lengths 10, 20, 30, 40 and 50 mm, respectively. The path length is 100 wavelengths.

FRACTIONAL CHANGE IN TIME DELAY OF SURFACE WAVES  
FOR RAMP INPUT, NORMAL TO ENDS OF SUBSTRATE

$l = 12.7 \text{ mm}$   
 $(0, +200\lambda)$   
 $(\theta = 35.25^\circ)$   
 $f_1 = (50-100-2000-4000) \text{ MHz}$

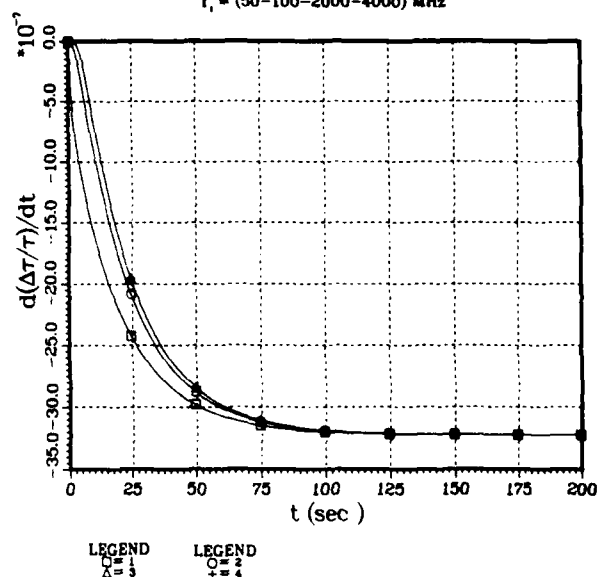


**Figure 11:** The slope of the curves shown in Fig. 10 is plotted as a function of time. The steady state condition is attained when the slope of the curves becomes zero.

FRACTIONAL CHANGE IN TIME DELAY OF SURFACE WAVES  
FOR RAMP INPUT, NORMAL TO ENDS OF SUBSTRATE

$l = 12.7 \text{ mm}$   
 $(0, +200\lambda)$   
 $(\theta = 35.25^\circ)$   
 $f_1 = (50-100-2000-4000) \text{ MHz}$

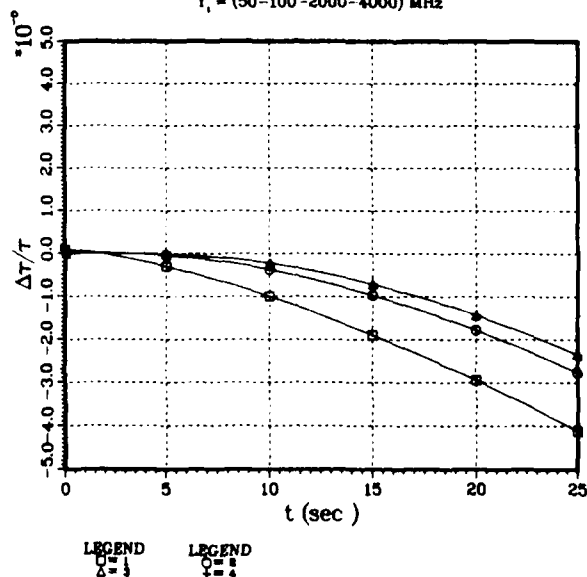


**Figure 10:** Time-dependent fractional change in time delay of surface waves on a rotated Y-cut ( $\theta = 35.25^\circ$ ) plate subject to unit ramps at its ends. The path length is 200 wavelengths, asymmetrically measured from the center. Curves 1 and 2 are for harmonic frequencies of 50 and 100 MHz, respectively. Curves 3 and 4 are for frequencies of 2 and 4 GHz, respectively, and are indistinguishable in this plot.

TEMPERATURE OF SAW DEVICE

$1) X_e = h$   
 $2) X_e = 0$   
 $(\theta = 41.3401^\circ)$   
 $h = 2.00 \text{ mm}$

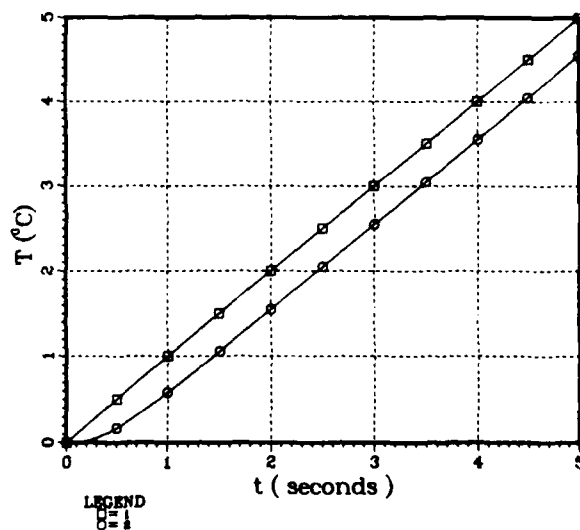


**Figure 12:** Curves 1 and 2 indicate the temperature input to the external surface and the computed temperature of the internal surface of a plate ( $\theta = 41.3401^\circ$ ) of thickness 2 mm.



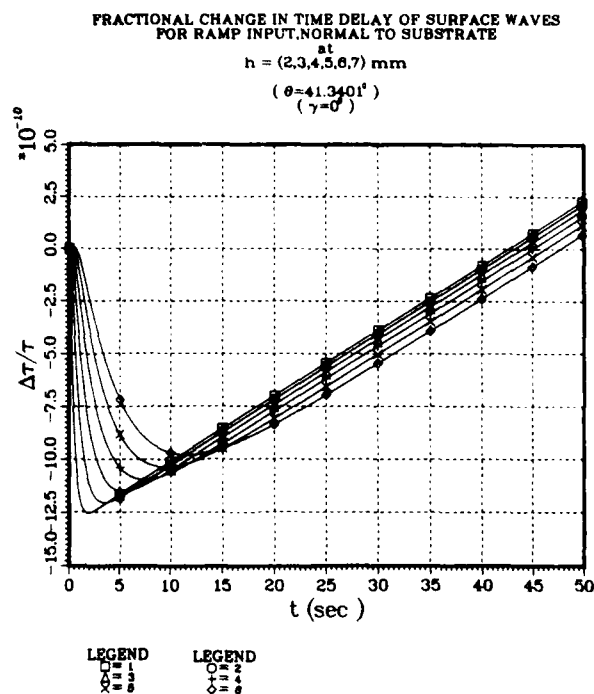


**Figure 13:** Fractional change in time delay of surface waves on a rotated Y-cut ( $\theta=41.3401^\circ$ ) plate of various thicknesses subjected to a unit ramp temperature input to the external surface. Curves 1 through 6 are for thicknesses 2 through 7 mm, respectively.

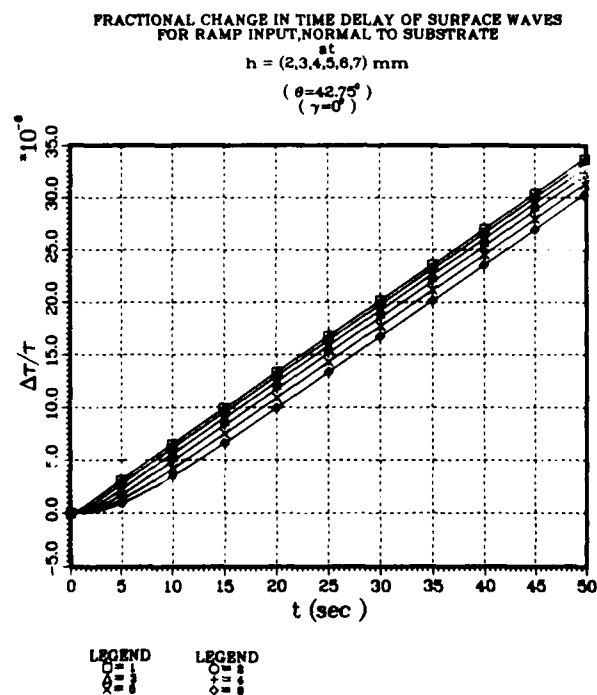


**Figure 14:** Fractional change in time delay of surface waves on a rotated Y-cut ( $\theta=42.75^\circ$ ) plate of various thicknesses. The notation is same as in Fig. 13.

BIAS CONTROLLED FREQUENCY TRIMMING OF SAW DEVICES IN A DC O<sub>2</sub> PLASMA

John Day

Raytheon Research Division, Lexington, MA 02173

Gordon Jackson

Massachusetts Institute of Technology, Cambridge, MA 02139

Thomas E. Parker

Raytheon Research Division, Lexington, MA 02173

Summary

A process is described which allows for tuning SAW devices in oscillator up in frequency. This tuning is accomplished by voltage-controlled anodization of an aluminum film in a dc O<sub>2</sub> plasma. Theoretical and experimental results are presented. A discussion of the effects of the trim pad on device flicker noise is also included.

Introduction

The number of applications for surface acoustic wave (SAW) devices in stable UHF oscillators is growing, and in most cases an accurate frequency setting is required. A typical requirement is a frequency window of  $\pm 10$  PPM which holds for all possible causes of frequency variations, including aging, temperature and settability. In such a case it is desirable to keep the settability error as small as possible so as to give the maximum range for temperature and aging. Generally, a settability on the order of  $\pm 1$  PPM is a reasonable goal.

The initial fabrication of SAW devices is accurate in the range of  $\pm 500$  PPM to  $\pm 50$  PPM depending on how much care is exercised in the fabrication process. More accurate frequency setting requires either an electronic adjustment of the oscillator frequency or a frequency trimming step on the SAW device. The smaller the required electronic adjustment is, the easier it is to implement. Therefore, several techniques for frequency trimming of SAW devices have been developed. The commonly used reactive ion etching (RIE) technique<sup>1</sup>, or the addition of a gold trim pad<sup>2</sup> both lower the frequency of the SAW device. In order to assure a reasonable yield the frequency of an untrimmed device must be designed a little high. This reduces the number of devices that initially are below the desired frequency and hence unuseable. However, this also means that virtually all useable devices must be trimmed and therefore suffer whatever undesirable side effects that invariably accompany the particular trimming technique being used.

To minimize this problem it would be very useful to have a complementary trimming process that increased the SAW frequency. This would mean that an untrimmed device could be designed directly at the desired frequency and that a substantial number of devices would require little or no trimming at all. Furthermore, all of the other devices would be useable since they could be trimmed either up or down. For this reason a trimming technique using the dc plasma anodization of an aluminum pad has been developed. This paper will present a theoretical discussion of how this process acts to increase the SAW frequency and also a discussion of how the anodization was carried out. Experimental results on the trimming of a number

of 425 MHz SAW resonators will be presented and data showing the effect of trimming on flicker noise will also be discussed.

Theory

The theory describing the effect of thin film overlays, particularly waveguides, is well developed<sup>3</sup>. A prediction of the effects of the aluminum oxide overlay on the surface wave velocity is obtained from theoretical analysis. An exact numerical solution for the wave in the overlaid area involves solving the equations of motion for each layer:

$$e_{ikl}u_{k,li} - e_{il}\phi_{,li} = 0 \quad (1)$$

$$c_{ijkl}u_{k,li} + e_{lij}\phi_{,li} = \rho\ddot{u}_j \quad (2)$$

and using a linear superposition of these solutions to satisfy the interface boundary conditions. A computer program developed by Jones, Smith, and Perry at Hughes Aircraft Company<sup>4</sup> was used for the calculations. This method requires several parameters -- elastic stiffness constants  $c_{ijkl}$ , piezoelectric constants  $e_{ijk}$ , dielectric constants  $\epsilon_{ij}$ , and density  $\rho$  -- for each layer. These constants are listed in Table 1. The values for quartz and aluminum are found in reference 5. The constants for polycrystalline aluminum oxide are found in reference 6.

The results of the computer analysis are presented in Figure 1. The analysis is valid for oxide thickness up to about one micron. Above this thickness the method lacks enough partial wave solutions in the various layers to specify the Rayleigh mode of the entire structure. The fractional velocity shift is a monotonically increasing function of the oxide thickness.

The computer also predicts that the mass loading effect of the aluminum is insignificant when compared to the mechanical perturbation caused by the alumina layer. By eliminating the aluminum layer from the theoretical model a linear closed form solution derived using perturbation analysis can be developed and this solution provides a physical insight not obtained from the numerical calculations. Following the treatment developed by Auld<sup>7</sup> assuming a mechanical surface perturbation by a thin, lossless isotropic layer the expression:

$$\frac{-\Delta V}{V_R} = \frac{V_R^h}{4P_R} [(\rho' - \mu'/V_R^2)|v_{Rx}|^2 + \rho'|v_{Ry}|^2 + \{\rho' - \frac{4\mu'}{V_R^2}(\frac{\lambda'}{\lambda'} + \frac{\mu'}{2\mu'})\}|v_{Rz}|^2] \quad (3)$$

is derived. In this expression the subscript R denotes the Rayleigh mode in the substrate, and primed quantities refer to parameters characterizing the oxide overlay. The particle velocities are  $V_{Rx}$ ,  $V_{Ry}$  and  $V_{Rz}$ ,  $V_R$  is the Rayleigh wave velocity, and  $P_R$  is the average power flow of the wave.

The Lamé constants  $\lambda'$  and  $\mu'$ , and the density  $\rho'$  characterize the isotropic oxide layer. For an increase in the SAW velocity the dominant parameter is  $\mu'$ .  $\lambda'$  has little influence, appearing in the ratio  $(\lambda' + \mu')/(\lambda' + 2\mu')$  which is always less than 1 for positive definite quantities  $\lambda'$  and  $\mu'$ . For values of  $\mu'$  large enough to cause the right side of equation (3) to be negative, the SAW velocity will increase. The mass density always acts to decrease velocity as can be seen from equation (3) which monotonically increases with increasing  $\rho'$ .

Using the same values for the oxide parameters given in Table 1, where  $\lambda = c_{12}$  and  $\mu = c_{44}$ , and values for the Rayleigh mode of the substrate equation (3) simplifies to

$$\frac{\Delta V}{V_R} = h (5.84 \times 10^{-5}) \quad (4)$$

where  $h$ , the oxide thickness, is measured in Angstroms. The values obtained for the Rayleigh mode assume an infinitely thin conducting layer at the substrate surface. This allows inclusion of the electrical effect of the unanodized aluminum, but excludes the mechanical perturbation which is predicted to be small.

A plot of (4) is presented in Figure 2. The linear result agrees closely with the numerical result for oxide layers up to 100Å. For thicker oxide layers the lack of agreement arises because the oxide creates a strong perturbation at the surface. The elastic constant of the oxide is 4 times that of the quartz; therefore, the validity of a perturbation solution for increasing oxide thicknesses is questionable. At an oxide thickness of 500Å the computer model calculates only fifty percent of the velocity shift predicted by the perturbation analysis.

#### Experiment Description

To obtain the aluminum oxide layer, anodization of an aluminum trim pad located in the propagation path of a SAW device is accomplished in a dc  $O_2$  plasma discharge. The aluminum pad is deposited to a thickness of 1 kÅ by e-beam evaporation at  $10^{-6}$  to  $10^{-7}$  torr. The device is mounted onto a cold-weld TO-8 header and placed into a vacuum chamber for anodization. RF connections are made to the SAW transducers to allow in situ monitoring and a dc connection is made to the trim pad allowing application of a bias voltage for the anodization process. The anodization geometry is shown in Figure 3.

After all the connections to the device are completed the vacuum chamber is evacuated to  $10^{-5}$  torr to remove most possible contaminants. The chamber is then backfilled with oxygen to a pressure of 50 millitorr. The oxygen is subjected to a 550 Volt dc bias which excites the plasma and which is applied between an aluminum cathode and the vacuum chamber base plate. Aluminum was chosen as the cathode material to reduce any sputtering off the cathode and contamination of the device<sup>8</sup>.

Ionization of the oxygen is easily detectable by the optical emission of the plasma, and a current of 3 mA is drawn through the plasma.

Once the plasma has been established, a bias voltage is applied to the trim pad. A current source which is used to establish the potential draws a constant current density of 1.5 mA/cm<sup>2</sup> through the oxide until a specified voltage limit is reached. Then the voltage is clamped and the current is allowed to drop. All anodization runs are carried out until the current through the oxide has decayed to a steady state.

The frequency of the device is measured after the anodization is complete. To avoid the effects of charge buildup on the substrate which alter the frequency measurements up to 10 kHz, the plasma is turned off during frequency measurements. The oxygen pressure is maintained at 50 millitorr to avoid any effects of pressure variation on frequency.

The primary technique which was used to evaluate oxide thickness was ellipsometry. This consists of measuring the difference in phase shift between two laser beams (which are originally orthogonally polarized) reflected from the oxide film. Assuming an index of refraction for  $Al_2O_3$  of 1.766 and using the Airy analysis<sup>9</sup> for the reflection of the light from the interface, the phase shift as a function of thickness can be predicted. The thickness of the oxide layer can then be found by fitting the data to the synthesized curves. Determinations of the thickness were made over a range of the angle of incidence from 20 to 60 degrees in order to verify the results. Figure 4 shows an example of typical synthesized curves of 20Å and 360Å oxide thickness and the actual ellipsometer data.

Capacitance measurements of the sample films were also used to evaluate the thickness of the grown oxide. Using the simple expression:

$$C = K\epsilon_0 A/t \quad (5)$$

and a value for the dielectric constant  $k$  of  $Al_2O_3$  of 7.5 the thickness of the film was easily found. Although this technique was not as accurate as the ellipsometer measurement it did allow better spatial resolution. This was important in evaluating edge effects which will be discussed later. Figure 5 shows the expected linear relationship between capacitance and inverse thickness (as measured by ellipsometry).

The oxide thickness as a function of bias voltage is shown in Figure 6. Data for two configurations is shown to demonstrate the fact that the geometry of the experimental configuration can substantially affect the growth rate of the oxide. The lower rate was achieved when the RF connections were in place for real time monitoring of the process. The reduction of the rate is the result of the RF ground which connected the device package to the base plate of the vacuum chamber which was the anode of the oxidation apparatus. For the tuning of SAW devices the configuration with the RF connections, placing the TO-8 header at the anode potential, was used. This arrangement influenced the plasma at the trim pad-plasma interface and resulted in a growth rate of about 11Å/Volt of bias applied to the trim pad.

## Results

The trimming experiments were carried out on 425 MHz two port SAW resonators (SAWR) on 40° rotated Y cut quartz. The acoustic aperture was 130 wavelengths and the effective cavity length was approximately 340 wavelengths. The space between the two transducers was approximately 1600 microns and it was in this region that the aluminum trim pad was placed. The trim pads were long enough to cover the entire acoustic aperture, but varied in width depending on how large of a frequency shift was desired. The widths used were 1575 microns, and 890 microns.

The data for the frequency shift as a function of anodizing voltage is shown in Figure 7. Data is shown for three SAWRs with a 1575 micron trim pad and three SAWRs with an 890 micron trim pad. The accompanying table lists the tuning rate for each resonator that was obtained by fitting the data to a straight line. The Root Mean Square (RMS) deviation for the fitted data is also listed. From the RMS deviations it is clear that the resonator can be tuned to within 15 kHz of the desired frequency by presetting the anodizing voltage, and the remainder of the tuning can be accomplished by increasing the voltage by small amounts and monitoring the frequency shift in real time. As expected the tuning rate scales very nearly with the width of the trim pad.

By using the experimentally determined oxide growth rate of 11Å/Volt the frequency shift as a function of oxide thickness may be derived. Further the experimental fractional velocity shift can be obtained by using the expression  $\Delta f/f = A \Delta V/V_R$  where A is the fractional area of the cavity that is covered with the trim pad. We can then compare (see Figure 2) the theoretical and experimental results for fractional velocity shifts as a function of oxide thickness.

The discrepancy between the theoretical and experimental results in Figure 2 is most probably due to the fact that bulk values for the elastic properties of the thin film overlay were used to derive theoretical results. Correction for the differences between the bulk and thin film overlay structures results in a reduction of the values of the elastic constants<sup>10</sup>. The numerical analysis of the fractional velocity shift shows that a reduction in the elastic constants would improve the agreement between the theory and experiment. For example, the theory using bulk film properties predicts a fractional velocity change that is four times greater than the experimentally observed changes. By reducing  $c_{44}$ , the shear elastic stiffness constant, by a factor of two this discrepancy is reduced as shown in Figure 2.

Attempts to eliminate the trim pad and tune the device by anodizing the SAW transducers were unsuccessful. Theory predicts that anodizing the transducer fingers should increase the wave velocity by about the same amount the anodized aluminum pad does<sup>11</sup>, when corrected for geometric coverage. However the resonator fingers, which are 2 microns wide, could not be anodized in a dc plasma. During attempts to trim resonators by anodizing the transducers no frequency shifts were observed. Capacitance measurements verified that no oxide growth occurred on the transducer fingers. It is believed that charging of the insulating substrate interferes with adsorption of oxygen ions near the edges of the metallized areas. Figure 8 shows the

oxide thickness versus distance from the pad's edge. The thickness is inferred from capacitance measurements. The resolution of the measurement is approximately 40 microns due to the finite size of the capacitors. Since the oxide becomes thinner as the pad edge is approached the 2 micron fingers cannot be anodized in a dc plasma discharge. Also a minimum trim pad width will be reached where the edge effects will preclude any velocity increase due to anodization.

The effect of the overlay on the flicker noise of SAWRs is of considerable importance for system applications. In Figure 9 the noise measurement for 20 different resonators is shown as a function of trim pad widths. The noise depends only on the width of the aluminum pad that was deposited and was independent of the amount of  $Al_2O_3$  that was grown. The incremental amount of the noise (relative to the free surface) scales with the width at the rate of about .0088 dB/micron of trim pad width. The maximum amount of oxide that can be grown using this technique is about 500Å which (if limitations of oxide growth due to edge effects are ignored) gives a maximum tuning range of .313 kHz/micron of pad width. Thus there is an increase of .028 dB of noise for each additional kHz of tuning range. For a typical requirement of 100 kHz (240 PPM) tuning range, this results in an increase of the noise by 2.8 dB.

## Conclusion

An experimental demonstration of a tuning process which allows for increasing the frequency of SAWR has been described. This technique is clean, easily controlled by in situ monitoring, and complements other tuning processes which decrease a device's frequency. Existing theory on layered medium can explain the velocity change implemented if a reduced value for the shear elastic constant is used. The side effects of this tuning process includes an increase in flicker noise which must be balanced with the frequency shift desired.

## Acknowledgement

The authors are indebted to E. Sabatino for fabricating the SAWRs and to E. Barsack for the ellipsometry measurements, and would like to thank T. Dorschner for helpful technical discussions.

## References

1. W.J. Tanski, "Surface acoustic wave frequency trimming of resonant and traveling-wave devices on quartz," *Appl. Phys. Lett.* 39 (1), pp.40-42 (July 1981). Also P.S. Cross and W.R. Shreve, "Frequency trimming of SAW Resonators," *IEEE Trans. Sonics Ultrason.* Su-29 (4), pp. 231-234 (July 1982).
2. T.E. Parker, "Precision Surface Acoustic Wave (SAW) Oscillators", *Proc. 1982 IEEE Ultrasonics Symposium*, p. 268-274 (1982).
3. Tiersten, "Elastic Surface Waves Guided by Thin Films," *Journal of Applied Physics*, Vol. 40, No. 2, p. 770, 1969.
4. Jones, Smith and Perry, *Numerical Computation of Acoustic Surface Waves in Layered Piezo-electric Media-Computer Program Description*, FR 71-14-102, Air Force Cambridge Research Laboratories Office of Aerospace Research, Bedford, MA, 1971.

5. Slobodnik and Conway, Microwave Acoustic Handbook; Vol. 1, Surface Wave Velocities, Physical Research Papers No. 414, Air Force Cambridge Research Research Laboratories, Bedford, MA, 1970.
6. Lynch, Ruderer and Duckworth, Engineering Properties of Ceramics; Databook to Guide Material Selection for Structural Application, AFML-TR-66-52, Air Force Materials Lab., Wright-Patterson Air Force Base, Ohio, 1966.
7. Auld, Acoustic Fields and Waves in Solids, Vol. II, John Wiley and Sons, Inc., New York, 1973.
8. O'Hanlon, "Plasma Anodization of Metals and Semiconductor," Journal of Vac. Science and Tech., Vol. 7, No. 2, p. 330, 1970.
9. Born and Wolf, Principles of Optics, Pergamon Press, Oxford, p. 325, 1975.
10. Jelks and Wagers, "Elastic Constants of Electron-Beam-Deposited Thin Films of Molybdenum and Aluminum on LiNbO<sub>3</sub>", Proceedings of the 1983 Ultrasonics Symp., IEEE, New York, p.319, 1983.
11. Hunsinger, Research to Provide a Theoretical Determination of Surface Acoustic Wave Velocity and Impedance Differences Between Metal Strips and Free Surface Regions of Metallic Gratings, RADC-TR-81-173, Rome Air Development Center, Griffiss Air Force Base, New York, 1981.

PBN-84-530

ELASTIC STIFFNESS CONSTANTS ( $10^{10}$  N/m<sup>2</sup>)

	$c_{11}$	$c_{33}$	$c_{44}$	$c_{12}$	$c_{13}$	$c_{14}$
QUARTZ	8.67	10.7	5.79	0.70	1.19	-1.79
AL	11.13	0	2.61	5.19	0	0
AL <sub>2</sub> O <sub>3</sub>	46.91	0	16.33	14.25	0	0

	Dielectric Constants ( $10^{-3}$ F/m)			Density (kg/m <sup>3</sup> )
	$\epsilon_{xx}$	$\epsilon_{yy}$	$\epsilon_{zz}$	
QUARTZ	3.92	3.92	4.10	2650.0
AL	1.0	1.0	1.0	2650.0
AL <sub>2</sub> O <sub>3</sub>	8.8	8.8	8.8	3986.0

Table 1. Material parameters used in theoretical models.

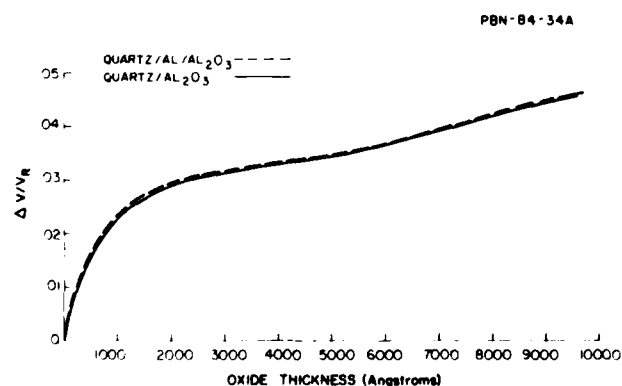


Figure 1. Fractional velocity shift of 2 multi-layered structures obtained by numerical solution. The predicted effect of the aluminum layer is very small.

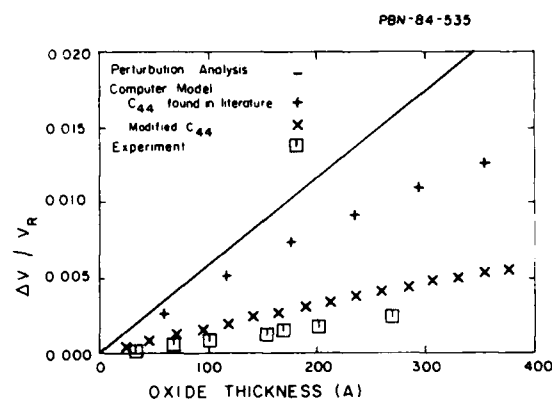


Figure 2. Comparison of experiment and theory, including perturbation analysis and results with a reduced elastic shear constant  $c_{44}$  for better agreement to experiment.

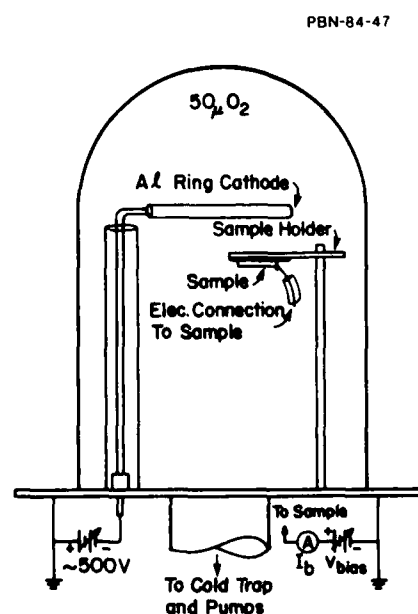


Figure 3. The anodization set-up showing the dc biases for the cathode and the trim pad. The rf connection to the SAW transducers are not shown.

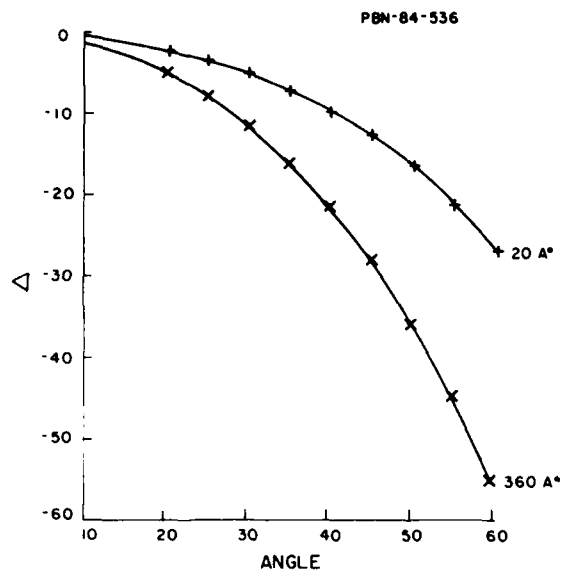


Figure 4. Comparison of theory and experiments for  $\Delta$ , the relative phase shift of reflected laser beams, vs. incident angle in thin film ellipsometry on  $\text{Al}_2\text{O}_3$  films.

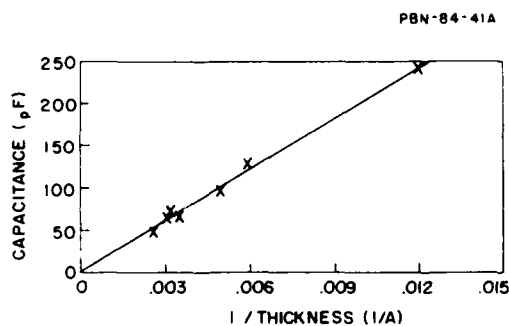


Figure 5. A demonstration of the inverse linear relationship between capacitance and  $\text{Al}_2\text{O}_3$  film thickness. From this curve a value of 7.5 for the relative dielectric constant of  $\text{Al}_2\text{O}_3$  is derived.

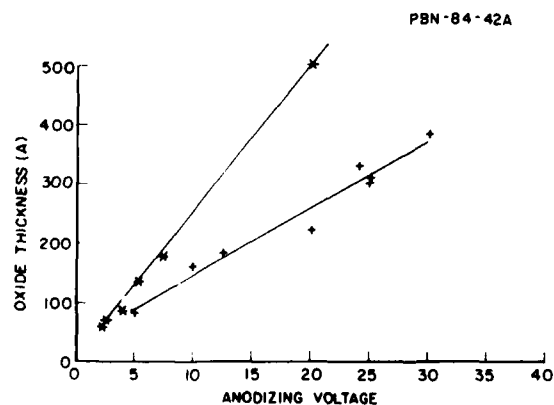
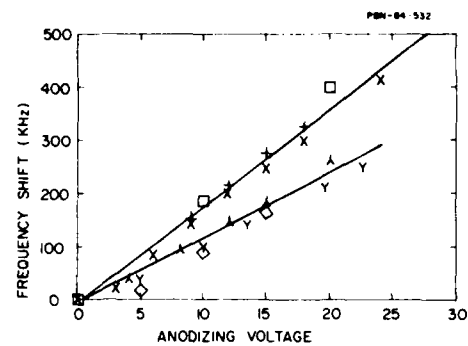


Figure 6. Plasma voltage-controlled oxide growth (a) + with RF connections for in situ monitoring (b) \* without RF connections.



PBN-84-532

DEVICE ID	TUNING RATE kHz/VLT	RMS DEVIATION kHz
+ Q1580B	18.2	12.4
x Q1580C	17.8	8.3
□ Q1580D	18.8	12.5
◇ Q1581A	11.5	15.7
Y Q1585C	11.2	6.1
A Q1586B	13.4	5.6

Figure 7. The tuning curves of 6 SAWR. Q1580 B, C, and D had trim pads 1575 microns wide. The rest had 890 microns wide trim pads.

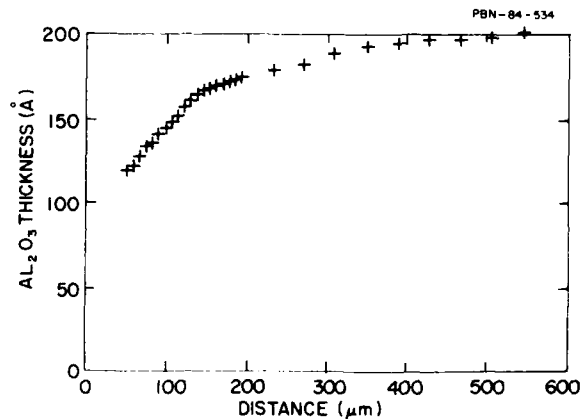


Figure 8. Plot illustrating the effects on oxide growth at the trim pad edge due to charge buildup on the quartz substrate.

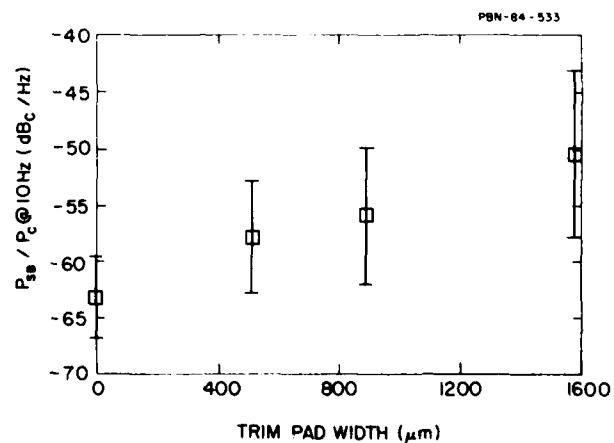


Figure 9. Flicker noise at 10 Hz from carrier as a function of trim pad width.

## DEVELOPMENT OF A LOW "G" SENSITIVITY MISSILE CLOCK

Alfred Vulcan

Frequency Electronics, Inc.  
Mitchel Field, New York 11553Abstract

The development of a very low phase noise missile Frequency Reference Oscillator for use in a powered free flight configuration required the utilization of low vibration sensitivity SC cut crystals and custom designed hybrids. Three separate frequencies in the VHF range are synthesized from a crystal controlled Butler oscillator operating at approximately 60 MHz. Tight mechanical packaging constraints require the use of special vibration isolators to minimize phase noise during the mission.

Three hybrids were developed for the application. Two of them are VHF frequency multipliers and the third provides a voltage regulation/ECL driver function. Incorporation of these hybrids in the final design results in a package volume of approximately five cubic inches. To insure low phase jitter during vibration, all of the crystals undergo vibration screening. The screening applies a sinewave to the three orthogonal axes while the sideband level is monitored. Two crystal resonators are used in each synthesizer; one in the oscillator and another in a narrowband crystal filter which reduces phase noise to a level of  $-161$  dBc/Hz, 8 kHz from the carrier. The two crystals are matched in temperature turning point to insure proper system performance.

Introduction

A missile clock was developed to provide reference frequency signals meeting stringent phase noise requirements at offset frequencies of 1 kHz to 10 MHz from the carrier. Three sinewave output frequencies are generated by direct synthesis: 60 MHz, 120 MHz and 240 MHz. In addition, a differential ECL timing signal at 60 MHz is produced. To achieve a noise floor of  $-161$  dBc/Hz at a Fourier frequency of 8 kHz, a 3 kHz wide crystal filter is employed at the oscillator output. The filter crystal is selected to match the oscillator crystal in temperature turnover point and center frequency to insure that the output level remains constant from  $-55^{\circ}\text{C}$  to  $+85^{\circ}\text{C}$ . The crystals are specially designed SC cut devices and the oscillator/filter subassembly is vibration isolated using resilient mounts.

System Design

Figure 1 is a block diagram of the missile clock system. The Butler oscillator 60 MHz output is amplified, fed to a  $1 \times 2$  power splitter and crystal filtered prior to multiplication. An unfiltered output feeds an ECL differential line driver to supply system squarewave timing signals. The filtered oscillator output drives a multiplier hybrid consisting of an input amplifier and X2 transistor multiplier. The frequency comb output from this hybrid feeds a three-pole helical filter having a bandwidth of 10 MHz and insertion loss of 2 dB. This filter reduces the unwanted multiplier sidebands to a level of  $-65$  dBc. The filter output feeds a power splitter, one of whose outputs is attenuated to a level of +6 dBm to provide the 120 MHz sinewave system output. The other X2 output at a level of +5 dBm is multiplied to 240 MHz, amplified to a level of +25 dBm, and filtered with a three-pole helical resonator device. The filter bandwidth in this case is 25 MHz at the 3 dB points.

This wideband response is required in order to provide a reasonably good source impedance to the output power splitter which must maintain high isolation over a 15 MHz band centered at 240 MHz. The filter reduces the spurious multiplication sidebands to a level of  $-65$  dBc. The filter output is power split and attenuated by 6 dB to present dual outputs at +12 dBm each. The illustrated approach was chosen in order to simplify the circuitry and provide broadband 240 MHz isolation of 30 dB.

Oscillator/Filter Design

The 60 MHz oscillator uses a Butler configuration to provide low phase noise. Since oscillator aging is not critical for this missile application, a relatively high crystal current of 3 milliamps is maintained for maximum signal-to-noise ratio. The oscillator uses a mode trap to insure that the output remains at the desired frequency over the broad temperature range. The 60 MHz SC overtone crystal is packaged in a "C" holder. The oscillator output feeds a common emitter amplifier stage which delivers +16 dBm to a 10 dB directional coupler. The amplifier is designed to provide a 50 ohm impedance at the input to the coupler to insure that the isolation exceeds 20 dB. One port of the coupler provides the +6 dBm 60 MHz system output and the other feeds the one-pole half lattice crystal filter. The RF power levels at the input to the filter is +7 dBm and the insertion loss is 2.5 dB.

All of the oscillator and filter crystals manufactured for the missile clock are swept over the temperature range of  $-55^{\circ}\text{C}$  to  $+85^{\circ}\text{C}$  and the frequency and series resistance recorded. Based upon this data, matched pairs of crystals are selected such that the turnover points lie within  $\pm 2^{\circ}\text{C}$  and the maximum frequency difference at any temperature does not exceed 1 kHz. In addition, all resonators are subjected to a sine vibration sweep while sideband generation is monitored. The "g" sensitivity of each crystal is then calculated for each orthogonal axis at frequencies from 100 Hz to 3 kHz. Any devices exhibiting unusual resonances in this band or having "g"-sensitivities that exceed  $3 \times 10^{-10}/\text{g}$  are not used in the missile clock application.

Multiplier Design

In order to maintain output power levels which vary less than  $\pm 1$  dB over the full operating temperature range, the multipliers are designed with input limiting circuits. A saturating amplifier at the

input frequency maintains constant RF drive level to the multiplier. Figure 2 is a schematic of the 240 MHz multiplier which accepts 120 MHz at the input and produces 240 MHz at a level of +25 dBm. The 120 MHz multiplier is schematically identical to this device except that the third stage of amplification is not required. Transistor Q1 amplifies the input signal from +5 dBm to +10 dBm and maintains a constant output by virtue of the current limiting mechanism inherent in the biasing circuit. The output of this stage feeds Q2 whose collector is tuned to 240 MHz. The single pole collector circuit provides approximately 12 dB of attenuation to fundamental and third harmonic signals. The level of the 240 MHz signal at this point is +15 dBm and transistor Q3 is a Class B amplifier which

raises the level to +25 dBm. The overall hybrid consisting of the three stages consumes approximately 700 milliwatts of dc power to produce 250 milliwatts of RF signal at 240 MHz. Temperature compensated biasing is used in stage three to keep the operating point of the transistor relatively independent of temperature. The multiplier is packaged in a 0.625 inch square flatpack hybrid. The output feeds a three pole capacitively coupled helical resonator which is packaged in a 0.75 inch square by 0.25 inch thick housing. The extremely small size of this filter results in an inductor Q of approximately 120 and insertion loss of 2.5 dB. Sufficient RF power is available from the hybrid so that the overall system output RF level requirements are met. The RF filters are totally encapsulated to eliminate vibratory phase modulation. Figure 3 illustrates the packaging technique employed for the multiplier hybrid/filter combination.

#### Regulator/ECL Driver

This subassembly consists of a 12 volt linear regulator which accepts the +15 volt missile bus input and effectively removes noise and ripple components. The regulator is included in a 0.625 inch square hybrid package along with a differential ECL driver and its associated source terminating resistors. The ECL signals are used to drive various data and telemetry subsystems within the missile. The input to the ECL line driver is a 60 MHz sinewave derived from the unfiltered oscillator output with a directional coupler.

#### Mechanical Design

To meet the stringent phase noise requirement during free flight with a random vibration input of 8.7 G RMS, the oscillator/filter subassembly is packaged in a suspended steel enclosure which is foam encapsulated. This 2" x 1" x 1" subassembly is mounted in a separate compartment with resilient rubber mounts at each of the eight corners. The cutoff frequency of the mounting structure is approximately 70 Hz and since the random noise spectrum covers a range of 20 Hz to 2 kHz, sufficient mechanical isolation exists at 1 kHz, the lower phase noise operational limit, to minimize vibration induced phase jitter in the assembly. The additional subassemblies comprising the missile clock are hard-mounted within the housing and all components are staked to the pc boards with a structural adhesive. Figures 4 and 5 show the top and bottom view of the clock, respectively. The center compartment in Figure 5 contains the oscillator/filter assembly with the multipliers in the right-hand compartments and regulator/ECL driver in the left-hand compartment.

#### Phase Noise Performance

Single sideband phase noise is related to frequency deviation  $\Delta f$  and the modulation frequency by the equation:

$$L(f) = 20 \log (\Delta f / 2f_m) \text{ dBc/Hz.}$$

In the presence of vibration,  $\Delta f = S f_o G$ ,  
where  $f_m$  is Fourier frequency in Hz,  
 $S$  is vibration sensitivity in parts per G  
 $G$  is vibration level  
 $f_o$  is oscillator frequency

For random vibration level of  $\gamma \text{ G}^2/\text{Hz}$ ,  $G = \sqrt{2\gamma}$ .

Thus,  $\Delta f = S f_o \sqrt{2\gamma} \text{ Hz}$   
and  $L(f) = 30 \log (S f_o \sqrt{2\gamma} / 2f_m) \text{ dBc/Hz}$

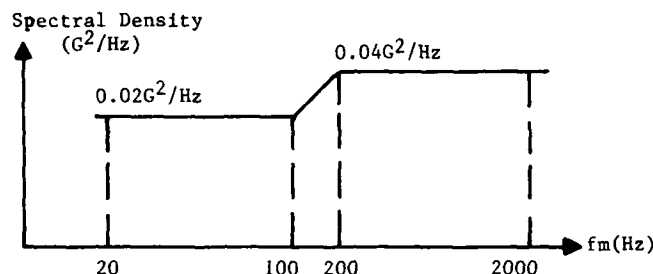
(1)

As an example, the phase noise at a Fourier frequency of 20 Hz is calculated for the following conditions:

$$\begin{aligned} S &= 1 \times 10^{-9} / \text{G} \\ \gamma &= 0.02 \text{ G}^2 / \text{Hz} \\ f_m &= 20 \text{ Hz} \\ f_o &= 60 \text{ MHz} \end{aligned}$$

$$\begin{aligned} L(f) &= 20 \log (1 \times 10^{-9} \times 60 \times 10^6 \sqrt{2 \times 0.02 / 2 \times 20}) \\ L(f) &= 20 \log (3 \times 10^{-4}) = -70.5 \text{ dBc/Hz} \end{aligned}$$

The random vibration profile at the missile clock is plotted below.



Equation (1) is plotted in Figure 6 for three values of crystal "g" sensitivity  $S$ . Curves 1, 2 and 3 are plots of the random vibration spectral density converted to single sideband phase noise for values of oscillator vibration sensitivity of  $1 \times 10^{-9} / \text{G}$ ,  $5 \times 10^{-10} / \text{G}$ , and  $3 \times 10^{-10} / \text{G}$  respectively. Curve 4 is the measured  $f_o$  phase noise of an actual oscillator/filter and curve 5 is the mission specified limit. For the measured oscillator,  $S$  equals  $5 \times 10^{-10} / \text{G}$ . It is seen that 25 dB of vibration isolation at 1 kHz is required to meet the specification. Since the isolation increases at 6 dB per octave, the isolation structure must thus have a 3 dB point of approximately 100 Hz. At 2 kHz 29 dB of isolation is required. Thus 6 dB per octave of rolloff is sufficient to meet the requirements.

Figure 7 shows the measured phase noise of a packaged oscillator/filter which is hard and soft-mounted in a structure using resilient vibration isolators as described above. The hard-mounted response shows a distinct random noise spectrum imposed upon the induced phase noise while the soft-mounted oscillator shows a gradual rolloff occurring between the region of 500 Hz and 2 kHz. The increased phase noise of the soft-mounted oscillator below 500 Hz is due to internal structural resonances in the mounts which were used for this test. The level of noise below 500 Hz was considerably reduced in the production units by increasing the mass of the oscillator housing. This was accomplished by doubling the wall thickness and using a steel enclosure for this subassembly. This technique reduced the oscillator mechanical resonant frequency to about 45 Hz.

The phase noise performance of the overall missile clock assembly is shown in Figure 8 for the worst case axis which is perpendicular to the plane of the crystals. The curve is plotted for the 60 Hz, 120 MHz and 240 MHz outputs (designated  $f_o$ ,  $2f_o$  and  $4f_o$  in the figure). It is seen that the phase noise between 1 kHz and 2 kHz is only slightly perturbed by the incident random vibration due to the resilient mounting of the oscillator/filter and the encapsulation techniques employed.

A distinct departure from the unvibrated reference run is seen below 500 Hz. A 6 dB difference between the three vibration curves is visible at low Fourier frequencies due to the X2 multipliers phase noise enhancement.



### Summary

This paper describes the design and development of a VHF Missile Clock which produces highly stable signals at three VHF frequencies while encountering a high level of random noise. It is seen that by properly selecting doubly rotated SC crystals and using packaging techniques which move structural resonances

out of the operating frequency range, a physically small, light weight assembly can be manufactured which meets the performance requirements. The Missile Clock described in this Paper has been produced in quantities of several hundred which proves the feasibility of advancing the state-of-the-art of high stability oscillators operating under extreme vibratory stresses.

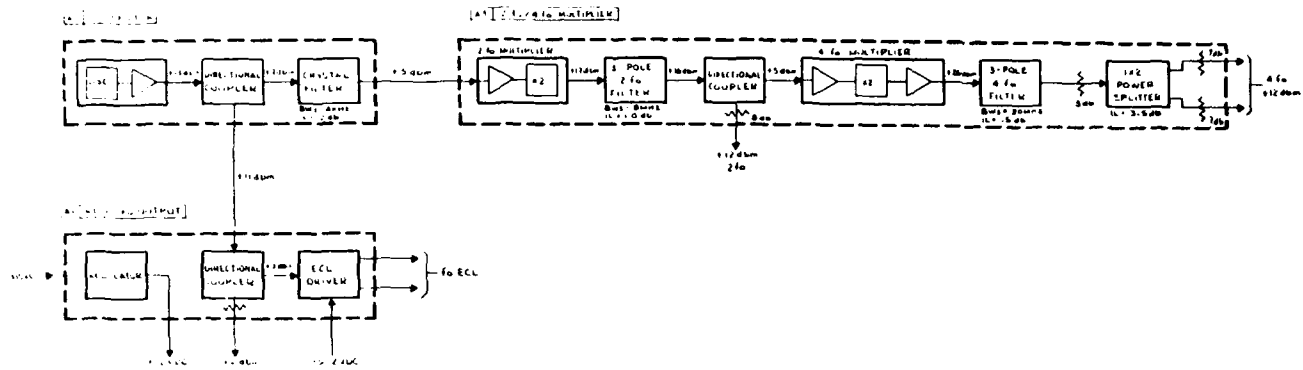


FIGURE 1  
BLOCK DIAGRAM

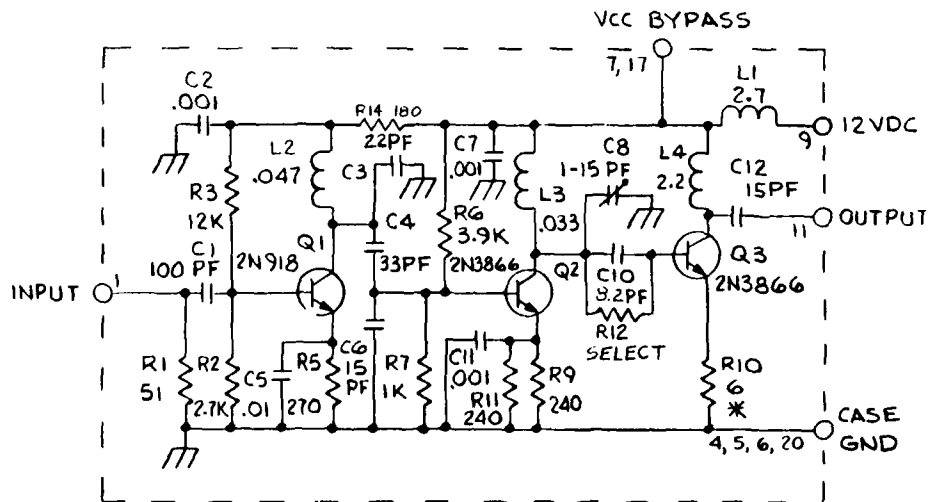


FIGURE 2  
4 Fo MULTIPLIER, SCHEMATIC DIAGRAM

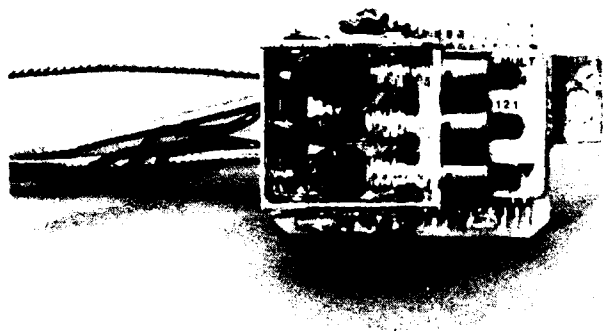


FIGURE 3

2 Fo HYBRID/FILTER ASSEMBLY

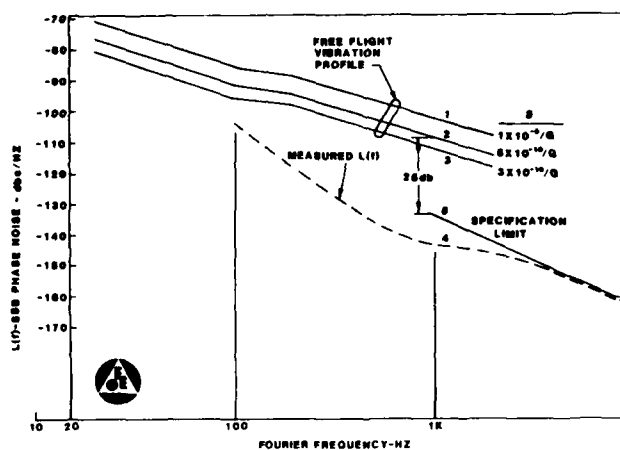


FIGURE 6

PHASE NOISE VS. FOURIER FREQUENCY



FIGURE 4

OVERALL OSCILLATOR/MULTIPLIER ASSEMBLY (TOP VIEW)

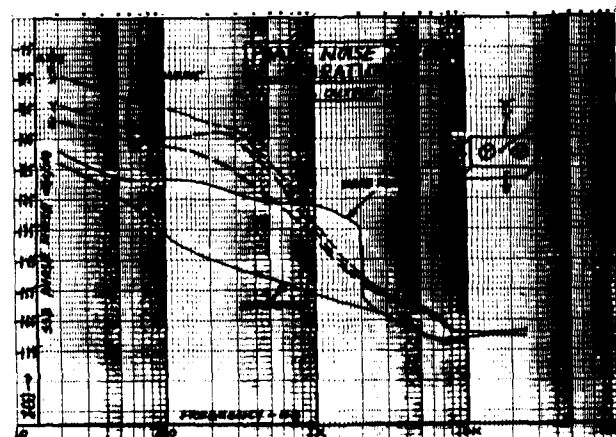


FIGURE 7

SOFT AND HARD MOUNTED OSCILLATOR PHASE NOISE



FIGURE 5

OVERALL OSCILLATOR/MULTIPLIER ASSEMBLY (BOTTOM VIEW)

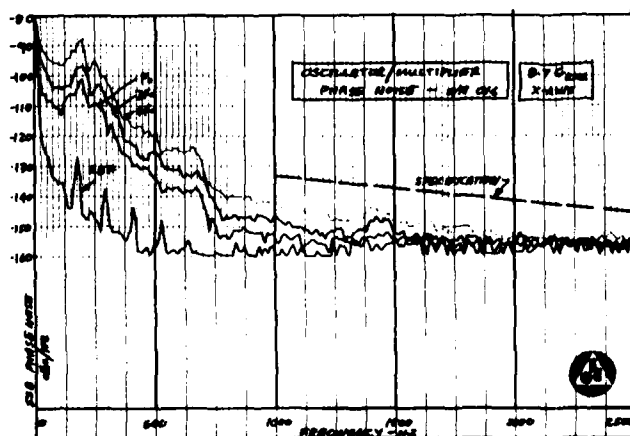


FIGURE 8

ACTUAL NOISE UNDER VIBRATION OF FINAL UNIT AT  $F_o$ ,  
2  $F_o$ , and 4  $F_o$

## SIMULATION OF OSCILLATOR NOISE

by

James A. Barnes

Austron, Inc., P.O. Box 14766

Austin TX 78761

## ABSTRACT

The paper presents methods for simulating the time errors,  $X_n$ , of a clock perturbed by any of several random processes, a linear frequency drift, and diurnals. The random processes include (1) white noise PM, (2) flicker noise PM, (3) white noise FM, (4) flicker noise FM, and (5) random walk noise FM. One first selects a subset of the five noises, and possible diurnals, and linear frequency drift which will adequately model the oscillator in question. One generates each noise separately and then adds them together, point by point, and finally truncates each point to simulate the real data acquisition system.

For each noise type, one obtains the noise level from a plot of the conventional Allan variance. A specific point,  $\tau_u$  and  $\sigma_y^2(\tau_u)$  allows one to estimate the variance of the random "shocks" taken as inputs to digital (recursive) filters. The paper gives the specific recursive functions to produce any of the five random processes listed above, as well as the linear frequency drift. A specific example is included in the paper.

## 1. THE VALUE OF NOISE SIMULATION ROUTINES

Stochastic models of precision clocks and oscillators have existed for some time. Typical models include superpositions of various noises and deterministic (non-random) trends. More specifically, the random model elements include:

- (1) White noise phase modulation (PM);
- (2) Flicker noise PM;
- (3) White noise frequency modulation (FM);  
(same as random walk noise PM);
- (4) Flicker noise FM;
- (5) Random walk noise FM.

A subset of these five random components is usually adequate to describe the random behavior of typical clocks and oscillators.

The five noise types above are called "power-law" spectra since the power spectral densities have a power law dependence on frequency. That is,

$$S_y(f) = h_\alpha f^\alpha \quad \text{for } \alpha = -2, -1, 0, 1, 2 \quad (1)$$

It is conceivable that non-integer values of  $\alpha$  could exist, but as yet there seems little need of them for oscillator modeling.

Clocks and oscillators often display deterministic trends such as:

- (6) Time (phase) offset;
- (7) Frequency offset;
- (8) Linear frequency drift. and
- (9) Periodic (e.g., diurnal) terms.

Two or three of the nine elements, above, suffice for the modeling of most clocks and oscillators. Jones and Tryon<sup>1</sup> have documented a two or three element model for commercial cesium beam frequency standards for periods longer than two hours. The Jones/Tryon model elements are white noise FM, random walk noise FM, and possibly linear frequency drift. The time and frequency offsets (6 and 7 above) are not considered fundamental since all clocks naturally accumulate these errors in the course of operation. That is, time and frequency offsets are the normal consequences of the other model elements. Most clocks require references to external standards routinely. Linear frequency drift, on the other hand, provides the limiting errors for long-term measurements even for the best clocks. In fact, one could devote an appreciable fraction of a clock's life expectancy just to establish a reasonable precision for the drift rate.

The above model elements seem to describe almost every clock currently available. Indeed, these model elements have been in use for the last 15 to 20 years. The point is that the above list of model elements is thought to be practically exhaustive. If one found it to be inadequate, that, in itself, would be noteworthy.

The value of having a reliable model is quite significant. One can design and "test" complex systems at computer speeds before committing the system to a hardware realization. Simulation is especially valuable when a system design forces non-linear constraints. Another use of simulation is to test computer analysis routines when the input "data" is known in advance.

Specifically, this paper develops computer routines to simulate evenly spaced values of clock time errors resulting from the superposition of various noises and deterministic functions. I wish to emphasize that the simulation process simulates TIME errors, not frequency errors. Of course, it is a relatively simple procedure to obtain average frequency by taking the first differences of the time data and dividing by the time interval between points.

In accord with the notation of other work in the field<sup>2,3</sup>, this paper makes use of the following notation:

- A. The voltage output from an oscillator conforms to the relation:

$$V(t) = V_0 \sin [2\pi \nu_0 t + \phi(t)]$$

where  $\nu_0$  is the nominal oscillator frequency (in Hz),  $V_0$  is the constant amplitude of the carrier, and  $\phi(t)$  contains any of the nine random and deterministic elements listed above.

- B. The instantaneous frequency of the oscillator is given by,

$$\begin{aligned} \nu(t) &= \frac{1}{2\pi} \frac{d}{dt} [2\pi \nu_0 t + \phi(t)] \\ &= \nu_0 + \frac{1}{2\pi} \frac{d\phi(t)}{dt} \end{aligned}$$

- C. The time error of a clock run from the oscillator is given by,

$$X(t) = \phi(t) / (2\pi \nu_0)$$

D. The instantaneous fractional frequency is given by,

$$Y(t) = \frac{1}{2\pi \nu_0} \frac{d\phi(t)}{dt} \\ = dX(t) / dt$$

E. The average fractional frequency is given by,

$$\bar{Y}(t) = \frac{1}{\tau} \int_t^{t+\tau} Y(t) dt \\ = [X(t + \tau) - X(t)] / \tau$$

## II. THE WHITE NOISE FAMILY

An important noise is random, uncorrelated, white noise, which is normally distributed, unit variance, and with a zero mean. The noise is considered to have a constant power spectral density (hence, the name "white"). Some people have objected to this noise model on the basis that it has infinite power if the spectrum is everywhere constant. Of course, real electronics do not have an infinite bandwidth<sup>4</sup> and no real problem exists<sup>5</sup>.

Most digital computers have (pseudo) random number generators which produce uncorrelated numbers, uniformly distributed over the range zero to one. Not all of the computer random number generators are adequate for simulation purposes. Some random number generators repeat after fairly few numbers have been called. For non-critical work, one can use a rather simple generation scheme:

```
1000 P = FRC (P * 997)
```

where the next random number is the fractional part of 997 times the previous number. The initial (or "seed") number can be something like  $\pi$  or  $e$ . In spite of its simplicity, it is often quite useful; however, it is beyond the scope of this paper to review the literature on random number generation.

For clock modeling, one needs numbers which have a normal (Gaussian) distribution, not a uniform distribution. I present here two methods of converting uniformly distributed numbers to a Gaussian distribution. The first method<sup>6</sup> generates normally distributed numbers from uniformly distributed numbers using the following algorithm:

```
1010 IF FLAG 1 = 1 THEN 1080
1020 R = RND
1030 Q = SQR(-2*LOG(R))
1040 R = RND
1050 FLAG 1 = 1
1060 P = Q*COS(2*PI*R)
1070 GOTO 1100
1080 FLAG 1 = 0
1090 P = Q*SIN(2*PI*R)
1100 RETURN
```

where each reference to "RND" returns a number from a uniformly distributed population,  $\pi = 3.1415926...$ , and the  $P$  are normally distributed (Gaussian), random numbers with zero mean and unit variance. (The arguments of the trigonometric functions are in radians.)

A second method is as follows<sup>7</sup>:

```
1000 P = 0
1010 FOR J=1 TO 6
1020 P=P+RND-RND
1030 NEXT J
1040 RETURN
```

this routine depends on the fact that the variance of the uniformly distributed numbers ("RND" in the program) is exactly  $1/12$ , and, hence,  $P$  (the sum of twelve RND's) will have unit variance. Since  $P$  is the sum of twelve uncorrelated numbers, the resulting numbers,  $P$ , are very nearly Gaussian (The Central Limit Theorem), and since the program adds as many RND's as it subtracts, the population mean is zero.

### A. White Noise Phase Modulation

There are six aspects which must be known to model any of the random noises:

- (1) Noise type (e.g., white noise PM).
- (2) Noise level (e.g., the Allan variance at a specified  $\tau$ ).
- (3) The units of the data (e.g., microseconds).
- (4) The time interval between data points (e.g., 10 seconds).
- (5) The truncation (or resolution or rounding) of the data (e.g., one nanosecond).
- (6) The number of data points (e.g., 350).

We have already selected the noise type (i.e., white PM), and the next issue is to obtain an estimate of the noise level. I will use estimates obtained from the Allan variance exclusively in this paper. If one desires other estimates, reference<sup>2</sup> provides some translations among the Allan variance; the power spectral density, PSD, of frequency; the PSD of phase; and the PSD of time error. Also, the purpose of this paper is to simulate a known noise, not to analyze a particular oscillator.

Allan<sup>8</sup> has shown that each of the power law spectral densities displays an Allan variance which is also a power-law (although not necessarily unique) in the sample time,  $\tau$ . Specifically, he has shown that:

$$\sigma_y^2(\tau) = A(\mu) \cdot \tau^\mu \quad (1)$$

We determine the level of one specific noise type at a time. I assume that we have a plot of the Allan variance of the noise to be simulated over a suitable range of time intervals to allow adequate models. We select a point on the Allan variance plot which appears typical of the noise type to be simulated (white PM, for this example), and compute the quantity

$$A(-2) = \tau_{-2}^{-2} \cdot \sigma_y^2(\tau_{-2}) \quad (2)$$

where  $\tau_{-2}$  is the tau-value (in seconds) of the chosen point on the Allan variance plot, and  $\sigma_y^2(\tau_{-2})$  is the corresponding Allan variance. Equation (3), below, gives the total variance of the needed random numbers to simulate the desired white phase modulation<sup>2</sup>:

$$\sigma^2 = \frac{1}{3} \cdot [\tau_{-2}^2 \cdot \sigma_y^2(\tau_{-2})] \quad (3)$$

Different noise types than the white PM considered here require different relations than that given in Eq. (3). We must now scale the variance obtained from Eq. (3) to account for the simulated phase units and any sample time effects (not necessary for white PM). Define U as the units of the desired data set (e.g., microseconds) and  $\tau_m$  as the desired time interval between successive data points in seconds. The variance of the needed numbers, then, is given by (see appendix):

$$S_{-2}^2 = \frac{1}{3 U^2} \cdot [\tau_{-2}^2 \cdot \sigma_y^2(\tau_{-2})] \quad (4)$$

In practice, the white phase noise data are computed by multiplying the Gaussian, random numbers,  $P_n$ , by the square root of  $S_{-2}^2$  in Eq. (4), above; that is:

$$X_n = S_{-2} \cdot P_n \quad (5)$$

That is, the numbers intended to simulate the time error of a real oscillator are given by the data,  $X_n$ . The numerical values of  $X_n$  should appear to have comparable values and variations to the recorded values of an actual measurement (except for rounding or truncation discussed below) and the Allan variances are comparable to the white PM part of the Allan variances of the real data.

The next step in the simulation process is to simulate the remaining model elements, both random and deterministic, and add the new elements to the existing simulated data. Obviously, each component added must use the same units, time interval between data points, and the same number of points. After all model elements are added, the truncation program drops unneeded digits corresponding to the resolution of the actual data. The implicit model here is that all the elements are independent and can be added together. The measurement operation then truncates each data point to a specific number of significant digits. The final step in the simulation is to verify the results using the Allan variance and compare it to the Allan variance of the real data, processed as identically as possible.

#### B. White Noise FM

The previous section described the simulation of phase variations which were taken to be white. This section considers white noise modulating the frequency, which makes the phase fluctuations appear to be a random walk. White noise FM corresponds to  $\mu = -1$  in Eq. (2). As in the white PM case, above, we need the variance of the random "shocks" upon which the model is built. For white FM, the desired variance is given by:

$$S_{-1}^2 = \frac{\tau_m}{U^2} \cdot [\tau_{-1} \cdot \sigma_y^2(\tau_{-1})] \quad (6)$$

where  $\tau_{-1}$  is that tau-value on the sigma-Y of tau plot (Allan variance) which corresponds to an Allan variance in the white FM region, and  $\sigma_y^2(\tau_{-1})$  is the Allan variance at that tau-value. In contrast to the white PM model, for white FM, the variance of the random shocks depends on the time interval between data points,  $\tau_m$ . Since we are modeling time errors, variations in frequency affect the rate of change of time (phase) variations. The resulting program to compute the white FM includes:

$$X_n = X_{n-1} + S_{-1} \cdot P_n \quad (7)$$

where, as before, the  $P_n$  are pseudo random, uncorrelated numbers with zero mean, unit variance, and normally distributed.

We now have a new option: The initial value,  $X_0$ , is unspecified. The model specifies only how the numbers develop from some arbitrary beginning, and not where it began. Clearly, this problem corresponds to the needs to provide an initial time calibration of a clock. The user is free to develop his own method for setting the initial value for  $X_n$ , although, one could choose a value near that of the specific data to be simulated.

#### C. Random Walk FM

For the random walk FM case ( $\mu = +1$ ), we proceed as before. We obtain the variance of the random shocks,  $S_1^2$ , from the following equation:

$$S_1^2 = \frac{3\tau_m^3}{U^2} \cdot [\tau_1^{-1} \cdot \sigma_y^2(\tau_1)] \quad (8)$$

We can accomplish the simulation by using the equation:

$$X_n = 2X_{n-1} - X_{n-2} + S_1 \cdot P_n \quad (9)$$

but now we have two arbitrary parameters,  $X_0$  and  $X_{-1}$ , which relate to initial values of  $X_n$  and initial frequency,  $(X_n - X_{n-1}) / \tau_m$ .

At this point, we encounter an interesting problem. We have implicitly assumed that the real data are samples taken from a continuous process, and that these real data points can be simulated with a discrete process,  $X_n$ . While this is true for the processes considered in this paper, random walk FM has a special problem.

For the discrete model described in Eqs. (8) and (9), above, one can show that the Allan variance is given exactly by the relation:

$$\sigma_y^2(\tau) = S_1^2 \cdot \frac{2N^2 + 1}{6N\tau_m^2} \quad (10)$$

where  $\tau = N \cdot \tau_m$ , and  $\tau_m$  is the time interval between data points. Asymptotically for large N, the Eq. (10) approaches:

$$\sigma_y^2(\tau) = S_1^2 \cdot \frac{\tau}{3\tau_m^3} \quad (11)$$

It is interesting that Eq. (11) is the exact result for data samples taken from a continuous random walk (Wiener Process), FM. Dr. Charles Greenhall at JPL<sup>9</sup> pointed out that there is an exact model for the random walk FM, in the discrete sampling of a continuous process which is correct for all N. The exact representation is an "IMA(2,1)" model<sup>10</sup>. Specifically, the exact relation to replace Eq. (9) is:

$$X_n = 2X_{n-1} - X_{n-2} + a_n - \theta a_{n-1} \quad (12)$$

where  $n = 1, 2, \dots, N$ ,  $a_n = S_1 \cdot P_n$  and  $\theta$  is a constant with value

$$\theta = \sqrt{3} - 2 = -0.268 \quad (13)$$

Often, the high frequency (or small tau region of the Allan variance) is predominantly covered with white PM and/or white FM, and the difference between Eq. (9) and (12) is not observable. Still, Eq. (12) is sufficiently simple that one should probably use it in preference to Eq. (9). The addition of the  $\theta$ -term changes the expression for  $S_1^2$  to the following:

$$S_1^2 = \frac{3\tau_m^3}{U^2(1-\theta)^2} \cdot [\tau_1^{-1} \cdot \sigma_y^2(\tau_1)] \quad (14)$$

to replace Eq. (8).

### III. THE FLICKER FAMILY

Barnes and Jarvis<sup>11</sup> developed an empirical ARIMA model<sup>10</sup> which can simulate flicker noise over a large but bounded region. The model can be written in the form:

$$X_n - \sum_{i=1}^4 \phi_i X_{n-i} = a_n - \sum_{j=1}^2 \theta_j a_{n-j} \quad (15)$$

Where the  $\phi_i$ 's and  $\theta_j$ 's can take on the values given in Table (1).

#### A. Flicker Noise PM

The discussion of flicker noise models here follows the same form as for the white noise models, above. There is a potential noise identification problem, however, in that both white noise PM and flicker noise PM have the same  $\mu$ -value, of  $-2$ . This emphasizes the need to have a well identified model prior to the simulation process discussed here. (It is beyond the scope of this paper to discuss the noise identification problem. See Reference [3].)

As before, we obtain the variance of the random shocks driving the system;

$$S_{-2}^2 = \frac{1}{5U^2} \cdot [\tau_{-2}^2 \cdot \sigma_y^2(\tau_{-2})] \quad (16)$$

where  $\tau_{-2}$  is that tau-value on the sigma-Y of tau plot which corresponds to an Allan variance in the flicker PM region. The ARIMA coefficients ( $\phi_i$ 's and  $\theta_j$ 's) should be selected from Table 1, and the inputs to the ARIMA filter,  $a_n$ , come from the Gaussian noise generator,  $P_n$ :

$$a_n = S_{-2} \cdot P_n \quad (17)$$

Equation (18), then generates the flicker phase,  $X_n$ , using the  $a_n$  from Eq. (17):

$$X_n = \sum_{i=1}^3 \phi_i X_{n-i} + a_n - \sum_{j=1}^2 \theta_j a_{n-j} \quad (18)$$

#### B. Flicker Noise FM

Equation (19) gives an estimate of the variance of the random shocks delivered to the flicker filter. As before, the  $P$  are random, normal deviates with zero mean and unit variance:

$$S_0^2 = \frac{1.8 \tau_m^2}{U^2} \cdot [\sigma_y^2(\tau_0)] \quad (19)$$

(Note: For flicker FM, the Allan variance is constant.) The input to the flicker FM filter is:

$$a_n = S_0 \cdot P_n \quad (20)$$

where  $S_0$  comes from Eq. (19). The flicker filter is just:

$$X_n = \sum_{i=1}^4 \phi_i X_{n-i} + a_n - \sum_{j=1}^2 \theta_j a_{n-j} \quad (21)$$

and the  $\phi_i$ 's and  $\theta_j$ 's come from Table 1.

### C. Initial Conditions

In a recent paper, Dr. C. Greenhall<sup>12</sup> points out that starting the flicker filters with all initial variables set to zero is an extreme assumption which affects some statistics but leaves others alone (see also<sup>13</sup>). At the present time, the "zero-infinite past" assumption seems to be acceptable for most simulation studies.

### IV. DETERMINISTIC TRENDS

#### A. Linear Frequency Drift

It is often very difficult to quantify the linear frequency drift term in an oscillator<sup>14</sup>. The primary reason is that the random parts (just modeled above) obscure the drift in "short-term"; where short-term might be for times less than a day or even longer for atomic frequency standards. Of course, to obtain reasonable confidence in the drift rate, the data length must be long compared to the short-term region dominated by the random components.

Linear frequency drift often manifests itself in an Allan variance for long-term. That is, the Allan variance for long-term varies as  $\tau^2$ . Specifically, the drift term contributes the following to the Allan variance:

$$\sigma_y^2(\tau) = \frac{1}{2} D^2 \tau^2 \quad (22)$$

(Note: The sign of the drift term is lost in the Allan variances, and other means must be found to estimate  $D$ .)

Given a drift rate,  $D$ , and the time interval,  $\tau_m$ , the (quadratic) change in time error,  $X_n$ , is generated by:

$$X_n = 2 X_{n-1} - X_{n-2} + D \tau_m^2 / U \quad (23)$$

There are two arbitrary values to be supplied: (1) the initial time error at  $n = 0$ , and (2) the time error at  $n = -1$ . These two constants determine the initial error and the initial rate (i.e., frequency) error. One should select the values to emulate an actual data sample.

The dimensions of  $D$  are (sec.)/(sec.)<sup>2</sup>. Conversion to parts in ten to the  $N$ -th power per day is accomplished by multiplying  $D$  by the constant 86,400 (sec.)/(day).

Other systematic trends (e.g., periodic terms) can be added at this point. The Allan variance can respond to periodic terms in a characteristic way, but, like drift, methods other than the Allan variance are better for parameter estimation.

### V. TRUNCATION

To this point, all appropriate random and systematic "errors" should be added together and exist as a single, one-dimensional array in the computer. We can now truncate the data to correspond to the real data. This is the last operation before testing the model validity with the Allan variance applied to the simulated data. An algorithm which truncates the data to  $N$ -significant digits is:

$$200 \quad X_n = \text{INT}(X_n \cdot 10^N) / (10^N) \quad (24)$$

where INT(Z) is the "integer part of" the argument, Z. One must be aware that some computers treat INT(Z) differently than others. Some computers take INT(Z) as the largest integer less than or equal to Z, while others simply drop the digits following the decimal point. The difference between these two methods occurs when Z has a negative value. For example, if  $Z = -4.221$ , the "largest integer" method returns -5, while the other method returns -4. The assumption for Eq. (24) is the former method (i.e., -5).

## VI. SUMMARY

Computer generated random numbers can simulate the various noises common to clocks and oscillators. An Allan variance can indicate the levels and types of noises present in a given oscillator and we can simulate each of the noises one at a time. Also linear frequency drift and periodic terms complete the model elements studied. The point by point sum of these noises and deterministic terms can be truncated to make the data emulate in detail the underlying processes and the measurement system's finite resolution.

Beginning with an Allan variance of an actual oscillator, we make estimates of the noise types and noise levels. For a given noise type, we select a point on the Allan variance (or sigma-Y of tau) plot which seems to be the most reliable indication of the Allan variance for a given noise type. The tau-value and its corresponding value for sigma-Y of tau allow us to use Table 2 for the formula to estimate the driving noise level (i.e., the amplitude of the random "shocks") for the given noise type. Table 3 contains the recursive formulas needed to calculate an actual noise sample. We follow the same procedure for each noise type and ultimately, along with the deterministic components, add the noises point by point. Truncation of each point to correspond to the actual data resolution completes the simulation. The entire process can end with a comparison of Allan variances for both the actual data and the simulated data.

An example is valuable:

Figure 1a is the time error plot of the time difference between a quartz crystal oscillator and Loran-C as obtained in Boulder, Co. Figure 2a is the Allan variance of this actual data. This data has a total of 311 points separated in time by 900 sec. and has a resolution of 10 nanoseconds. The data units recorded were in microseconds, which means  $U = 1 \times 10^{-6}$ . The model chosen to emulate this data was white noise FM (based on the short-term performance), a linear frequency drift, and a diurnal component.

In short-term, Figure 2a indicates the "best" estimate of the white noise comes from the value at  $\tau_1 = 900$  sec. The corresponding value of the Allan variance is:

$$\sigma_y^2(\tau = 900 \text{ s}) = (2.75 \times 10^{-11})^2 \quad (25)$$

Table 2 provides us with the means to calculate the level of the random shocks needed for the simulation:

$$S_{-1}^2 = \frac{900}{10^{-12}} \cdot [900 \cdot (2.75 \times 10^{-11})^2] \quad (26)$$

or, finally,

$$S_{-1} = 0.0248 \quad (27)$$

Table 3 gives the recursion formula to generate the

time error of a clock displaying white frequency modulation.

Using regression analysis on the actual clock data, I obtained the values for the linear frequency drift term and the diurnal. The three time series modeling the phase which arose from white FM, frequency drift, and diurnals are summarized in Figures 1 through 3. Each Figure contains the results obtained from the actual data (the "a" part of the Figure), and its counterpart from the simulated data (the "b" part). One last comment, about simulation. Given enough trials almost any time series might come from almost any model. The simulated data here was the first and only run made. While it may or may not be representative of the model, it is not an artifact of the author's biases.

Flicker PM or FM	Parameter	(OK Fit) N < 300	(Good Fit) N < 1000	(OK Fit) N < 3000
PM	$\phi_1$	1.549	2.462618155	2.51297305
PM	$\phi_2$	-0.56	-1.94749411	-2.0378810
PM	$\phi_3$	0	0.48481984	0.52489646
PM	$\theta_1$	0.88	1.83075548	1.87697024
PM	$\theta_2$	0	-0.83245797	-0.87756196
FM	$\phi_1$	2.549	3.462618155	3.51297305
FM	$\phi_2$	-2.109	-4.410112265	-4.55085407
FM	$\phi_3$	0.56	2.432313950	2.56277748
FM	$\phi_4$	0	-0.48481984	-0.52489649
FM	$\theta_1$	0.88	1.83075548	1.87697024
FM	$\theta_2$	0	-0.83245797	-0.8775619

Table 1., ARIMA Coefficients for Flicker PM and FM

(Note: The number of significant digits in Table 1 is very large relative to the standard errors. However, dropping digits can materially alter the model beyond what one might expect, because roots of the "operator" equation may change significantly. This is often an annoying feature of digital filters and does not imply exactness in the overall model. Indeed, the model may require more significant digits than are available on some computers.)

TABLE 2. Variances of input white noise to realize a given Allan variance.

NOISE TYPE	$\mu$	$\alpha$	VARIANCES FOR INPUT NOISE
WHITE NOISE PM	-2	+2	$S_{-2}^2 = \frac{1}{3U^2} \cdot [\tau_{-2}^2 \cdot \sigma_y^2(\tau_{-2})]$
FLICKER NOISE PM	-2	+1	$S_{-2}^2 = \frac{1}{2U^2} \cdot [\tau_{-2}^2 \cdot \sigma_y^2(\tau_{-2})]$
WHITE NOISE FM	-1	0	$S_{-1}^2 = \frac{\tau_m}{U^2} \cdot [\tau_{-1}^1 \cdot \sigma_y^2(\tau_{-1})]$
FLICKER NOISE FM	0	-1	$S_0^2 = \frac{1.8 \tau_m^2}{U^2} \cdot [\sigma_y^2(\tau_0)]$
RANDOM WALK NOISE FM	+1	-2	$S_1^2 = \frac{3 \tau_m^3}{U^2 (1-\theta)^2} \cdot [\tau_1^{-1} \cdot \sigma_y^2(\tau_1)]$ (WHERE $\theta = \sqrt{3} - 2 = -0.268$ )

Where:

$\tau_m$  is the time interval between data points.  
(e.g., 10 sec.)

$U$  is the units of the data (e.g., microseconds).

$\tau_\mu$  } are the coordinates of a point on a sigma-y  
of tau plot through which the square root  
of the Allan variance of the simulated  
 $\sigma_y(\tau_\mu)$  data should pass.

TABLE 3. Recursive Formulas to Generate Noise Type

NOISE TYPE	$\mu$	$\alpha$	RECURSIVE FORMULAS
WHITE NOISE PM	-2	+2	$X_n = a_n$
FLICKER NOISE* PM	-2	+1	$X_n = \phi_1 X_{n-1} + \phi_2 X_{n-2} + \phi_3 X_{n-3}$ $+ a_n - \theta_1 a_{n-1} - \theta_2 a_{n-2}$
WHITE NOISE FM	-1	0	$X_n = X_{n-1} + a_n$
FLICKER NOISE* FM	0	-1	$X_n = \phi_1 X_{n-1} + \phi_2 X_{n-2} + \phi_3 X_{n-3} +$ $\phi_4 X_{n-4} + a_n - \theta_1 a_{n-1} - \theta_2 a_{n-2}$
RANDOM WALK NOISE FM	+1	-2	$X_n = 2 X_{n-1} - X_{n-2} + a_n - \theta a_{n-1}$ where $\theta = \sqrt{3} - 2 = -0.268$

Where:

The  $a_n$  are random, normal deviates with zero mean and standard deviation  $S_\mu$ , obtained from Table 2. The individual values for the  $a_n$  are given by:

$$a_n = S_\mu \cdot P_n$$

where the  $P_n$  are random normal deviates with zero mean and UNIT variance.

\*For the flicker noises, empirical values for the phi's and the theta's can be found in Table 1.

The time error,  $X_n$ , arising from a linear frequency drift can be computed from the relation:

$$X_n = 2 X_{n-1} - X_{n-2} + D\tau_m^2/U$$



6.48

## RAW TIME ERROR DATA

 $X(t)$   
( $\mu S$ )

6.0

FIG 1a ACTUAL DATA FROM A COMPARISON OF  
A QUARTZ CRYSTAL OSCILLATOR AND LORAN-C

4.452

 $X(t)$   
( $\mu S$ )

.228

FIG 1b SIMULATED DATA BASED ON THREE ELEMENT MODEL

## AVERAGE FREQUENCY OF DATA OF FIG. 1

(NOTE DISCRETE VERTICAL LEVELS DUE TO TRUNCATION IN BOTH PLOTS)

 $1.2 \times 10^{-10}$  $Y(t)$  $-10^{-10}$   
0

FIG 3a ACTUAL DATA

 $1.3 \times 10^{-10}$  $Y(t)$  $-10^{-10}$   
0

FIG 3b SIMULATED DATA

## ALLAN VARIANCE OF DATA IN FIG. 1

 $10^{-10}$  $10^{-11}$  $\sigma_y(T)$  $10^{-12}$  $10^{-13}$  $10^{-3}$  $10^4$   
T (Sec) $10^5$  $10^6$ 

FIG 2a ACTUAL DATA

 $10^{-14}$  $10^{-15}$  $\sigma_f(T)$  $10^{-16}$  $10^{-2}$  $10^{-3}$  $10^4$   
T (Sec) $10^5$  $10^6$ 

FIG 2b SIMULATED DATA

PARTIAL LISTING OF DATA  
(GIVEN IN MICROSECONDS)

FIG 4a ACTUAL DATA

FIG 4b SIMULATED DATA

# APPENDIX

Noise level for simulations of white PM, white FM, and random walk FM.

The Allan varian can be expressed in the form:

$$\sigma_y^2(\tau) = \frac{1}{2\tau^2} \cdot E[(X_n - 2X_{n+N} + X_{n+2N})^2] \quad (A.1)$$

where  $X_n$  is the clock time error at the  $n$ -th step,  $\tau = N\tau_m$ , and  $\tau_m$  is the time interval between points. We will evaluate the expression for the second time difference with lag- $N$  for each of the three models noted above. The  $a_n$  are normal, random numbers with zero mean and variance  $\sigma_a^2$ .

## A. White phase noise;

This is the simplest case and one need only recognize that:

$$X_n = a_n \quad (A.2)$$

Substitution into (A.1) yields:

$$\sigma_y^2(\tau) = \frac{1}{2\tau^2} \cdot (6\sigma_a^2) \quad (A.3)$$

recognizing that we wish to separate out the units of the data, (A.3) yields:

$$S_{-2}^2 = \frac{1}{3U^2} \cdot [\tau^2 \sigma_y^2(\tau)] \quad (A.4)$$

where  $S_{-2}^2$  is the quantity sought for Eq. (4) in the text and Table 2.

## B. White noise FM:

As noted in the text, white FM is the equivalent of random walk phase modulation. We can simulate a random walk with:

$$X_n = \sum_{i=1}^n a_i \quad (A.5)$$

We must now combine (A.5) with (A.1) to obtain

$$\sigma_y^2(\tau) = \frac{1}{2\tau^2} E \left[ \left( \sum_{i=1}^n a_i - 2 \sum_{i=1}^{n+N} a_i + \sum_{i=1}^{n+2N} a_i \right)^2 \right] \quad (A.6)$$

which can be reduced to

$$\sigma_y^2(\tau) = \frac{1}{2\tau^2} E \left[ \sum_{i=1}^N (a_{n+N+i} - a_{n+i})^2 \right] \quad (A.7)$$

or, finally we get:

$$S_{-1}^2 = \frac{\tau_m}{U^2} \cdot [\tau \cdot \sigma_y^2(\tau)] \quad (A.8)$$

corresponding to Eq. (6) in the text.

## C. Random walk FM:

This case can be evaluated with only slightly more difficulty than white FM if one notes that the double sum of the random shocks,  $a_n$ , can be expressed in the form:

$$X_n = \sum_{i=1}^n (n-i+1)a_i \quad (A.9)$$

Following the above, one obtains:

$$\sigma_y^2(\tau) = \sigma_a^2 \frac{2N^2+1}{6N\tau_m^2} \quad (A.10)$$

which corresponds to Eq. (10) in the text. Asymptotically for large  $N$ , this approaches:

$$\sigma_y^2(\tau) = \sigma_a^2 \frac{\tau}{3\tau_m^3} \quad (A.11)$$

which is the same as Eq. (8).

## REFERENCES

- (1) P.V. Tryon, and R.H. Jones, "Estimation of Parameters in Models for Cesium Beam Atomic clocks," NBS Journal of Research, Vol. 88, No. 1, Jan-Feb. 1983.
- (2) J.A. Barnes, et al., "Characterization of Frequency Stability," IEEE Trans on Inst and Meas., IM-20, p105 (1971).
- (3) J. Rutman, "Characterization of Phase and Frequency Instabilities in Precision Frequency Sources: Fifteen Years of Progress." Proc IEEE, Vol. 66, pp. 1048-1075, Sept. 1978.
- (4) D. Slepian, "On Bandwidth," Proc IEEE, Vol. 64, No. 3, pp. 292-300, March 1976.
- (5) J.A. Barnes, "Models for the Interpretation of Frequency Stability Measurements," NBS Technical Note 683, August 1976.
- (6) G. Box & M.E. Muller, "A Note on the Generation of Random Normal Deviates," Annual. Math. Stat., Vol. 29, pp. 610-1, 1958.
- (7) P.V. Tryon, Private communication.
- (8) D.W. Allan, "Statistics of Atomic Frequency Standards," Proc IEEE, February 1966.
- (9) C. Greenhall, Private communication.
- (10) G.E.P. Box and G.M. Jenkins, "Time Series Analysis," Holden-Day, San Francisco, Calif. 1970.
- (11) J. A. Barnes and S. Jarvis, "Efficient Numerical and Analog Modeling of Flicker Noise Processes," NBS Technical Note 604, June 1971.
- (12) C. Greenhall, Private communication.
- (13) S.M. Kay, "Efficient Generation of Colored Noise," Proc IEEE Vol. 69, No. 4, April 1981.
- (14) J.A. Barnes, "The Measurement of Linear Frequency Drift in Oscillators," PTI Transactions, Nov. 1983.

## BALANCED FEEDBACK OSCILLATORS

Albert Benjaminson

S.T. Research Corporation, Newington, VA

Introduction

A balanced configuration for crystal oscillators, that extends the concept introduced by the Meacham Bridge,<sup>1</sup> is examined in this paper. Through the use of dual feedback paths, the analysis shows the benefits of this approach by defining a Q-multiplication factor. This factor permits the designer to numerically evaluate the improvement in rate of change of phase at the resonant frequency, and its impact on short-term stability.

Several new designs are offered using both integrated and discrete circuits. A new approach to level control that maintains the high performance of the dual feedback approach, is discussed and illustrated. The analysis is also shown to be applicable to the Butler and similar series-type oscillators, and evaluates the benefits of negative feedback in crystal oscillators.

The Differential Crystal Oscillator

Let us consider the characteristics of an oscillator using the bridge configuration as a dual feedback network driving a differential amplifier, whose output in turn, excites the bridge. The basic scheme is shown in Figure 1.

The two feedback paths can be considered separately, one providing positive feedback through the  $Z_1$ ,  $Z_2$  voltage divider, and one negative feedback through the  $Z_3$ ,  $Z_4$  divider. The analysis that follows will show that it is desirable that both feedback ratios, designated as  $\beta_p$  and  $\beta_n$ , be as high as possible and that the sustaining amplifier have high gain also. Since the objective is to produce oscillation at one frequency only, a resonator can replace any one of the four impedances and provide a net positive feedback at its resonant frequency. A series resonant circuit in place of  $Z_2$ , or  $Z_3$ , or an anti-resonant circuit at  $Z_1$ , or  $Z_4$  will accomplish the desired result. This configuration produces a very rapid transfer from positive to negative feedback off resonance and a very high value of  $d\phi/df$  around resonance. The result is a multiplication of the resonator's Q value and a rapid reduction of amplifier induced phase noise at the close-in side band frequencies.

This can be demonstrated by re-examining Figure 1.

The basic equation for feedback amplifiers is

$$A = \frac{A_o}{1 - A_o \beta} \quad (1)$$

where A is the closed loop gain in the presence of a feedback ratio  $\beta$ , and an amplifier gain of  $A_o$ .

In the balanced configuration shown,  $\beta$  is divided between the two arms,  $\beta_n$  and  $\beta_p$ , where

$$\beta_n = \frac{Z_3}{Z_3 + Z_4}, \quad \beta_p = \frac{Z_1}{Z_1 + Z_2} \quad (2)(3)$$

Substituting these for  $\beta$  in equation (1), yields

$$A = \frac{A_o}{1 - A_o (\beta_p - \beta_n)} \quad (4)$$

For oscillation to occur:  $A_o$  must be real and positive,  $\beta_p - \beta_n$  must be real and positive, and the denominator must be equal to zero. That is

$$\beta_p - \beta_n = \frac{1}{A_o} \quad (5)$$

The arrangement can be used as a crystal oscillator if the crystal is used in its series resonant mode, and substituted for  $Z_3$ . The crystal could also be used in its anti-resonant mode at  $Z_1$ , or  $Z_4$ , but this requires impractically high impedance values for  $Z_2$  or  $Z_3$ , to avoid excessive damping of the crystal's Q and does not result in the same benefits that placing the crystal in the  $Z_3$  position provides. Placing the crystal in the  $Z_3$  position also produces a high loaded Q, plus the Q-multiplication factor.

Q Multiplication

Healy<sup>2</sup> has shown that negative feedback in the sustaining amplifier reduces the single sideband phase noise component of a crystal oscillator's output, and that the spectral density  $S\phi(f)$  is a function of oscillator Q as shown by

$$S\phi(f) = (f)(1 + (\frac{f_o}{2Qf})^2) \quad (6)$$

The rate at which phase changes in an oscillator circuit is dependent on the loaded Q of the crystal. In most oscillator circuits this is less than the Q of the resonator alone, varying from 50% to 90%. By considering the impedance of the crystal in the vicinity of series resonance, we can derive the  $d\phi/df$  of the crystal alone, since

$$Z = R + j \frac{\omega^2 LC - 1}{\omega C} \quad (7)$$

$$\phi = \arctan \frac{\omega^2 LC - 1}{\omega C} \quad (8)$$

Since Q is defined as

$$Q = \frac{1}{\omega CR} \quad (9)$$

$$\text{then } \phi = \arctan Q (\omega^2 LC - 1) \quad (10)$$

$$\text{and } \frac{d\phi}{d\omega} = \frac{2Q\omega LC}{(1 + (\omega^2 LC - 1)Q)} \quad (11)$$

At the resonant frequency

$$\omega_o^2 LC = 1 \quad (12)$$

$$\text{and } \frac{d\phi}{d\omega} = 2Q\omega_o LC \quad (13)$$

$$\text{or } \frac{d\phi}{d\omega} = \frac{2Q}{\omega_o} \quad (14)$$

$$\text{or } \frac{d\phi}{df} = \frac{2Q}{f_o} \left( \frac{\text{rad}}{\text{Hz}} \right) \quad (15)$$

Thus the Q of the resonator determines the rate of change of phase and in turn, the sideband phase noise decay rate.

In calculating the  $d\phi/d\omega$  rate for the differential oscillator, assume that  $\beta_p$  is a constant, while  $\beta_n$  is proportional to the crystal impedance, so that

$$A_o = \frac{1}{\beta_p - K(R + j(\omega^2 LC - 1))} \quad (16)$$

(where K is the negative feedback factor.)

Then

$$\phi = \arctan \frac{K(\omega^2 LC - 1)}{\omega C (\beta_p - KR)} \quad (17)$$

Differentiating, and setting  $\omega^2 LC = 1$  at  $\omega = \omega_o$

$$\frac{d\phi}{d\omega} = \frac{2K}{\omega_o^2 C (\beta_p - KR)} \quad (18)$$

substituting  $Q = \frac{1}{\omega_o CR}$ ,

$$\frac{d\phi}{d\omega} = \frac{2Q}{\omega_o} \cdot \frac{\beta_n}{\beta_p - \beta_n} \quad (19)$$

$$\frac{d\phi}{d\omega} = \frac{2Q}{\omega_o} \cdot \beta_n A_o \quad (20)$$

Since  $A_o = \frac{1}{\beta_p - \beta_n}$ , then

$$\frac{d\phi}{d\omega} = \frac{2Q}{\omega_o} \times \beta_n A_o = \frac{2Q}{\omega_o} \times M_Q \quad (20)$$

Thus the Q is multiplied by the factor  $\beta_n A_o$ . Obviously, we cannot change the crystal's Q but we can multiply its effect on  $d\phi/d\omega$  with combined positive and negative feedback in which the negative loop includes the crystal.

Figure 3 shows the results of a computer analysis of the negative feedback loop alone. It shows that the resultant phase and gain performance is similar to that produced by a crystal and amplifier operating in the anti-resonant mode. There are two differences however. Even if the gain,  $A_o$  is changed in magnitude and phase, the effect on closed-loop gain and amplitude performance is minimal. This is due to the relationship between overall gain A, and amplifier gain  $A_o$ , from Equation (1)

$$A = \frac{A_o}{1 - A_o \beta_n} \approx \frac{1}{\beta_n} \quad (21)$$

So that as  $A_o$  increases in magnitude, the value of A approaches the reciprocal of  $\beta_n$ , and becomes increasingly independent of changes in  $A_o$ .

The second computer analysis was run on the complete bridge circuit plus sustaining amplifier  $A_o$ , but with neither loop closed. This is shown in Figure 4, and illustrates the apparent Q-multiplication that results from the nearly balanced condition of the crystal bridge.

## Q Multiplication in the Butler, and Series Cascode Oscillators

It is interesting to analyze the Butler Oscillator, using the dual feedback approach. As shown in Figure 2, this oscillator class can be considered as a dual feedback design since the crystal is in series with the emitter of the sustaining amplifier, providing negative feedback, while the capacitive voltage divider across the output tank, provides positive feedback.

The factors,  $A_o$ ,  $\beta_p$  and  $\beta_n$  can be determined as follows:

$$A_o = \frac{R_L}{r_e} \quad (22)$$

where  $r_e = \frac{.026}{I_E}$

$$\beta_p \approx \frac{C_2}{C_1} \text{ (neglecting gic)} \quad (23)$$

$$\beta_n \approx \frac{R_X}{R_L} \quad (24)$$

The Q multiplication factor is, as before,

$$M_Q = \frac{\beta_n}{\beta_p - \beta_n} = \beta_n A_o \quad (20)$$

The Q-factor is not realized in practice unless  $A_o$  is maintained at a high value. This does not occur when  $\beta_p$  is made much larger than  $\beta_n$ , as is the usual practice, since limiting, or ALC, will reduce  $A_o$  until

$$A_o = \frac{1}{\beta_p - \beta_n} \quad (5)$$

If  $\beta_p \gg \beta_n$ , then  $A_o$  drops to a low value, greatly reducing the Q-factor.

The benefits of Q multiplication cannot be realized then, unless  $\beta_p - \beta_n$  is maintained at a low value commensurate with the available value of  $\frac{1}{\beta_n}$ . Applied to Figure 2

$$A_o M_Q = \frac{R_X}{R_e} \quad (25)$$

This is the factor through which the gain is reduced by the presence of the crystal's resistance in the emitter circuit.

As an example of the magnitude of  $M_Q$ , assume  $r_e = 15$ ,  $R_X = 50$ ,  $R_L = 1500$  then  $A_o = 100$ ,  $\beta_n = .033$  and  $\beta_p = \frac{1}{100} + .033$ , resulting in  $M_Q = \beta_n A_o = .033 \times 100 = 3.3$ . This represents the effective increase in  $\frac{d\phi}{d\omega}$  over that produced in a conventional single-feedback oscillator, such as the Pierce, or Colpitts types, and helps to explain the reduction in phase-noise sidebands previously reported by Driscoll<sup>3</sup> and Healy.

## The Differential Crystal Oscillator

The basic principles of the DXO can also be implemented, as suggested earlier, by using a differential integrated circuit R.F. amplifier such as the CA3001, CA3040, or the MC1733. These amplifiers exhibit voltage gain values from 10 to 400 and bandwidths up to 50 MHz without L-C circuits, so that an essentially aperiodic oscillator can be built

with them. The basic circuit is shown in Figure 5.

Mos I.C. differential amplifiers have very low output impedances and can drive load resistances as low as 500 ohms. This allows the use of resistors in the feedback networks, as shown, and when combined with a dual voltage supply the circuit is very simple. The only adjustment, once  $\beta_p$  and  $A_o$  are selected, is to pick a resistor for feeding the crystal so that the proper value for  $\beta_n$  can be obtained.

It is a simple matter to adjust this value to compensate for the variation in the crystal's series resistance, so that a large amount of excess gain is not produced.

A more flexible design is illustrated in Figure 6. This uses a differential amplifier with a resonant circuit in one collector lead and an output load in the other. The tuned circuit provides positive feedback through a capacitive divider to one base, and negative feedback through a divider comprising a resistor and a crystal resonator to the other base. The two bases are tied together for biasing by an R.F. choke to ensure an equal division of d.c. current.

The result can also be viewed as an L/C oscillator, constrained by the crystal circuit to oscillate only at the series resonant frequency of the crystal.

The L/C ratio can be selected to provide a wide range of bandwidths. A low L/C ratio will produce a narrow bandwidth suitable for use with SC-cut and/or overtone mode crystal operation. Higher L/C ratios can be used for the less critical fundamental modes. It is worth noting that the tuned circuit is loaded by the  $\beta_n$  resistance at  $\omega_o$ , and is loaded only by  $R_n$  plus the input impedance of the transistor, at frequencies immediately off resonance.

A better method of obtaining an output signal is to connect the input of a common-base amplifier in series with the lower terminal of the crystal. Since current only flows through the crystal within its narrow pass-band, the output will contain less noise than the collector resistor connection, and will be sinusoidal in shape.

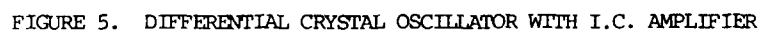
### Conclusions

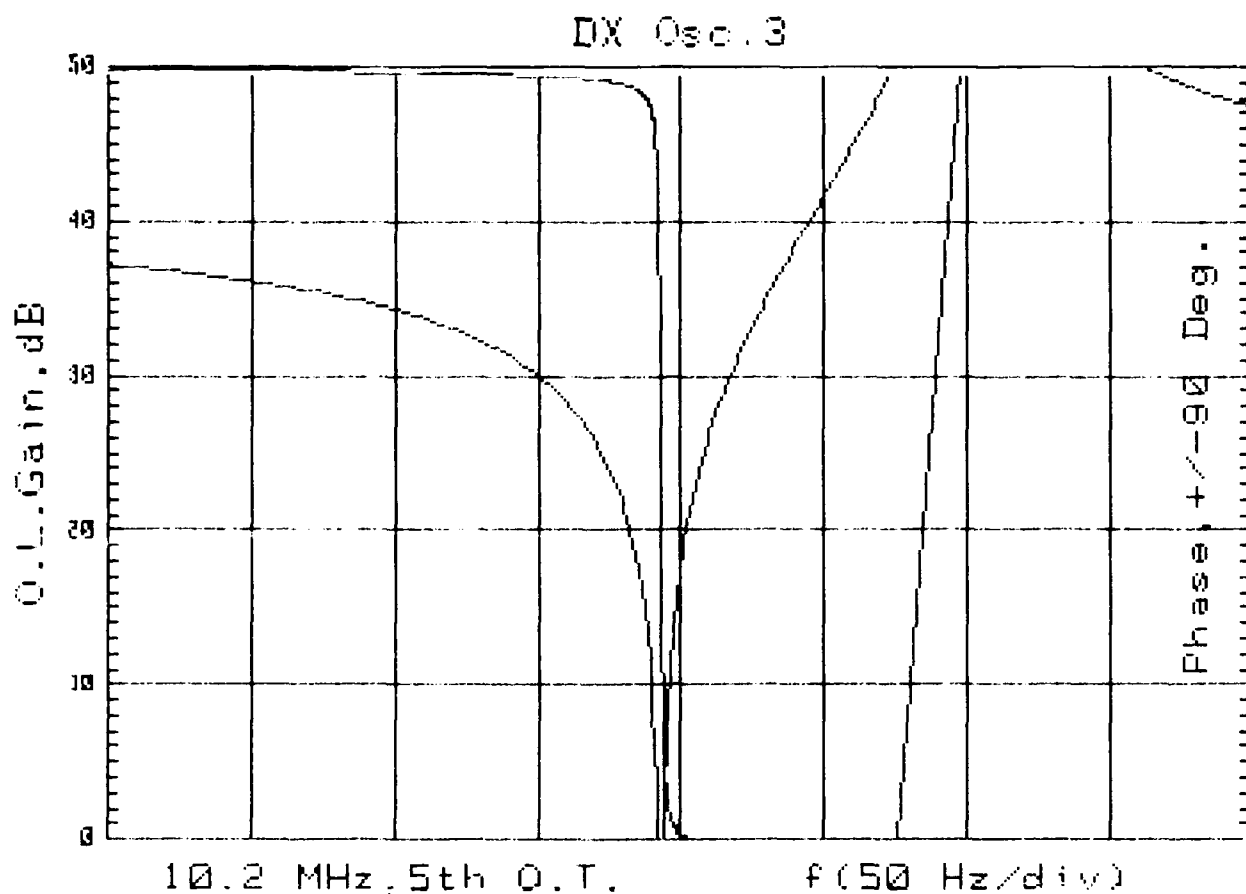
The dual-feedback analysis shows how the benefits of negative feedback can be applied to crystal oscillators, namely, to provide increased immunity to sustaining amplifier noise and parameter changes, by including the crystal in the negative feedback path. This, combined with overall positive feedback, produces an increase in short-term stability, and reduced phase noise.

Full realization of this technique requires the application of limiting, or level control, to the positive feedback path, instead of the sustaining amplifier's gain control.

### References

- <sup>1</sup>L.A. Mescham, "Bridge-Stabilized Oscillator," Proceedings of the IRE 26(10) pp. 1278-1294 (1938).
- <sup>2</sup>D.J. Healy III, "Flicker of Frequency and Phase and White Frequency and Phase Fluctuations in Frequency Sources," Proceedings of the 26th Annual Symposium on Frequency Control, June 1972, pp. 29-42.
- <sup>3</sup>M.M. Driscoll, "Two-Stage Self-Limiting Series Mode Type Quartz Crystal Oscillator Exhibiting Improved Short-Term Stability," Proceedings of the 26th Annual Symposium on Frequency Control, June 1972, pp. 43-49.





INPUT= NODE 1;      OUTPUT= NODE 7;      GROUND= NODE 0

COMPONENT	VALUE	PERCENT TOLERANCE	NODE FROM,	CONNECTIONS TO, (+), (-)
RESISTOR 1	300 ohm	0.00	5	0
RESISTOR 2	1.00 ohm	0.00	7	0
RESISTOR 3	3.00 kohm	0.00	2	3
CAPACITOR 1	2.34 pF	0.00	3	0
CAPACITOR 2	45.0 aF	0.00	4	5
CAPACITOR 3	100 pF	0.00	6	0
CAPACITOR 4	235 pF	0.00	2	0
CAPACITOR 5	11.1 pF	0.00	2	6
INDUCTOR 1	5.45 Hy	0.00	3	4
INDUCTOR 2	1.00 uHy	0.00	2	0
SOURCE 1	16.7 mmho	0.00	0	2 1 0
SOURCE 2	1.00 mho	0.00	0	7 6 3

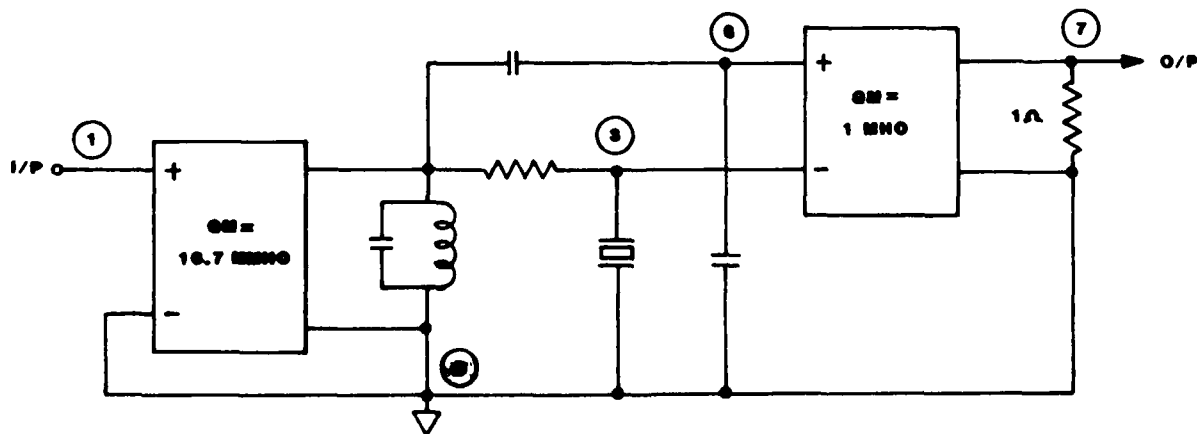


FIGURE 4. COMPUTER ANALYSIS OF CRYSTAL RESONATOR IN DIFFERENTIAL AMPLIFIER CONFIGURATION

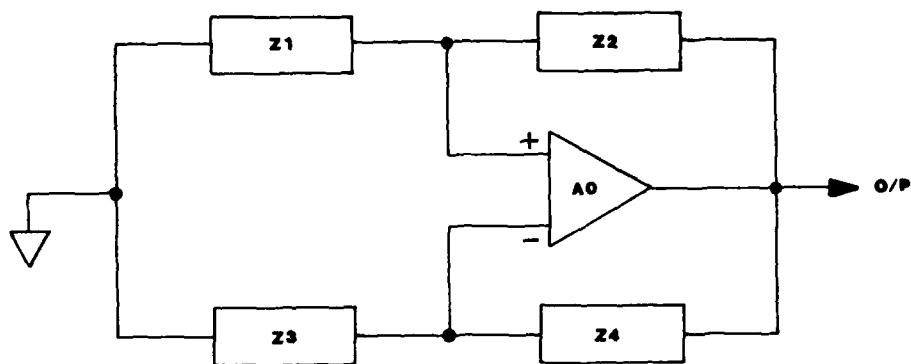


FIGURE 1. BASIC DIFFERENTIAL AMPLIFIER

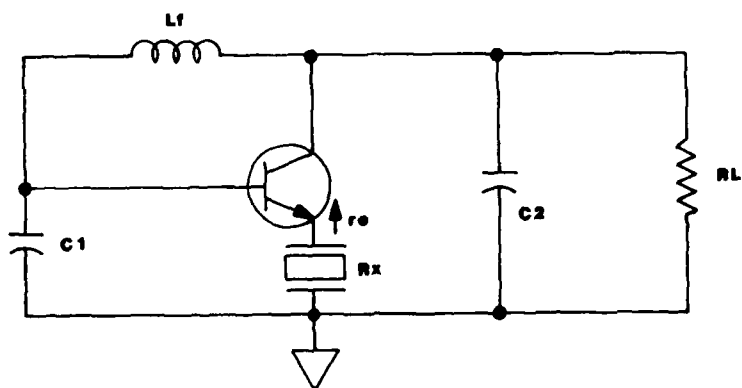
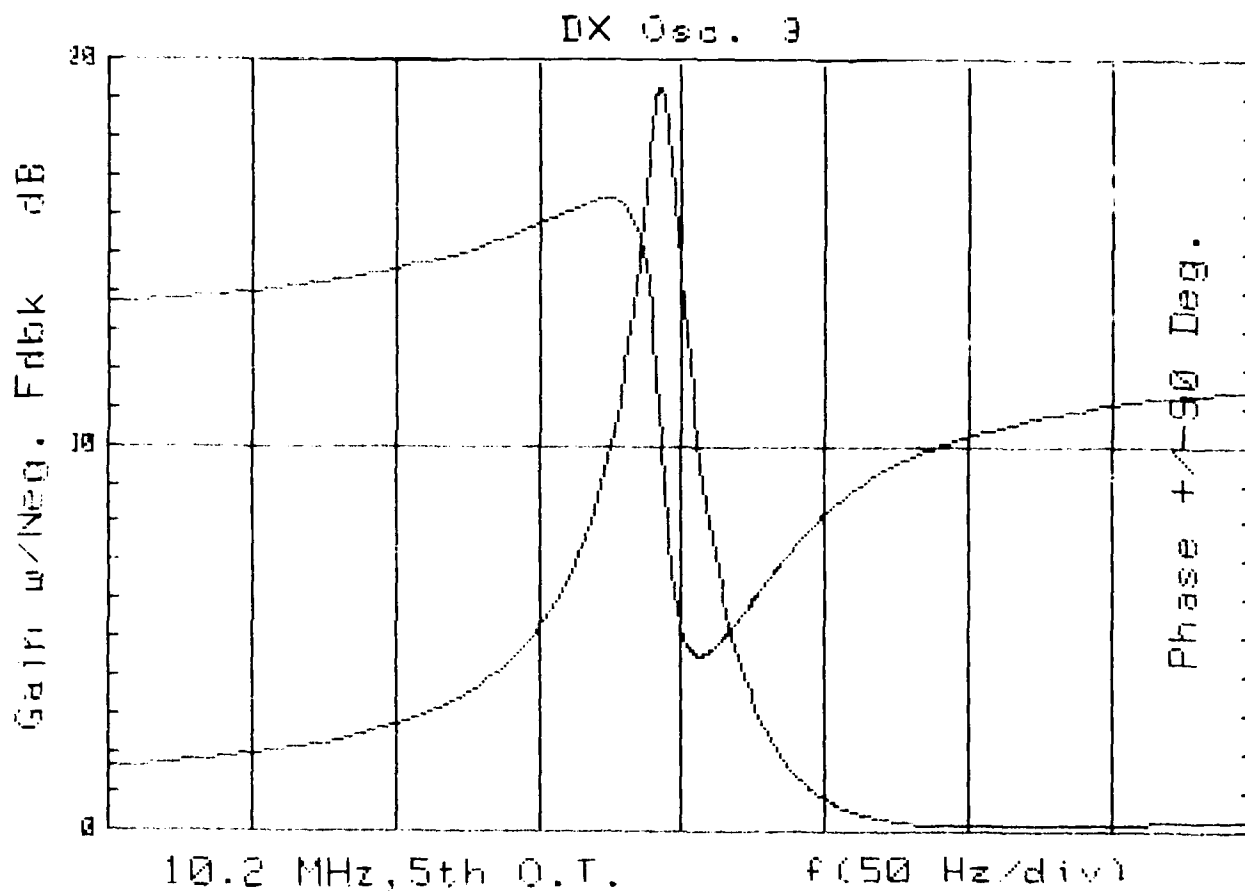


FIGURE 2. BUTLER-TYPE OSCILLATOR





INPUT= NODE 1;		OUTPUT= NODE 2;		GROUND= NODE 0	
COMPONENT	VALUE	PERCENT TOLERANCE	NODE FROM,	CONNECTIONS TO, (+), (-)	
RESISTOR 1	300 ohm	0.00	5	0	
RESISTOR 2	3.00 kohm	0.00	2	3	
CAPACITOR 1	2.34 pF	0.00	3	0	
CAPACITOR 2	45.0 aF	0.00	4	5	
CAPACITOR 3	100 pF	0.00	6	0	
CAPACITOR 4	235 pF	10.0	2	0	
CAPACITOR 5	11.1 pF	0.00	2	6	
INDUCTOR 1	5.45 Hy	0.00	3	4	
INDUCTOR 2	1.00 uHy	0.00	2	0	
SOURCE 1	16.7 mmho	0.00	0	2	1 3

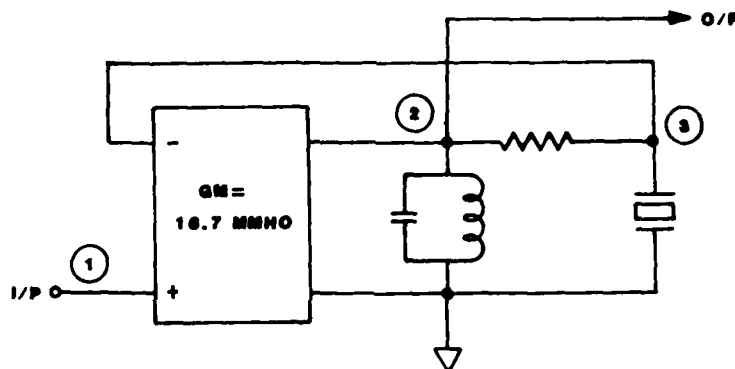


FIGURE 3. COMPUTER ANALYSIS OF CRYSTAL RESONATOR IN NEGATIVE FEEDBACK AMPLIFIER

## ANALYSIS AND DESIGN OF THE RELAXATION QUARTZ CRYSTAL OSCILLATORS

Dragan M. Vasiljević

Faculty of Electrical Engineering, University of Belgrade  
Bulevar Revolucije 73, 11000 Belgrade, YugoslaviaSummary

Recently, many realisations of relaxation quartz crystal oscillators have appeared. They are simply designed and are insensitive to load and temperature variations. Also, they have a small number of components and their short-term frequency stability is good. Operating principle of quartz multivibrator is known in the literature, but this knowledge is insufficient for analysis of oscillating condition, oscillation building up and period. These calculations are performed using topological methods of general theory of relaxation oscillations, that is by phase plane analysis.

First, general electrical and mathematical models of quartz relaxation oscillators are established. Then, phase portrait of crystal multivibrator is constructed. From these results, oscillating condition and period are calculated. Also, oscillation building up and relationship between flicker frequency noise level and oscillator parameters, are studied. Optimal characteristic of active part of oscillator circuit providing highest frequency stability has been discovered. Explained results are sufficient for successful design of relaxation quartz crystal oscillators.

Introduction

The relaxation oscillator is defined as an oscillating system developing rapid and slow changes of its state during the same period of oscillations. Recently, many realisations of relaxation quartz oscillators have appeared<sup>1-8</sup>. They are simply designed and are insensitive to load and temperature variations. Also, they have a small number of components. Their short-term frequency stability is good<sup>9</sup>. A quartz multivibrator operating principle is known in the literature<sup>4</sup>. The quartz crystal unit is excited by a voltage step-function generated by some current-controlled switch. As a response the current through the crystal is generated in the form of a "harmonic oscillation". In the steady-state, the amplitude of the quartz current is stabilized on the value necessary for switching on and off of the current-controlled switch. Such an approach provides a possibility for an intuitive construction of various quartz

multivibrator circuits, but does not enable investigation of the oscillation starting, the oscillating frequency and its stability. All these results may be obtained by the use of the general oscillation theory of relaxation oscillations. This method is used in the present paper for the quartz multivibrator analysis.

Our present discussion will be organised as follows. In first section, the general electrical and mathematical model of the quartz-controlled multivibrators is developed. In second section, the typical phase portrait of the quartz crystal multivibrators is constructed. This phase portrait is subsequently used in next section to determine the oscillation building up and oscillation frequency. In fourth section we consider the relationship between the level of the flicker frequency noise, and the crystal multivibrator parameters.

The Crystal Multivibrators Model

Generally, there are three types of quartz-controlled relaxation oscillators. These are collector coupled<sup>1-3</sup>, emitter-coupled<sup>6</sup>, and complementary switch<sup>4,5</sup> crystal multivibrators. Topologically, all these circuits may be divided into two classes: circuits with quartz crystal outside the feedback loop (Fig.1) and circuits with quartz inserted in feedback loop (Fig.2).

In the theory of oscillations each active element in oscillator active circuit is often modelled by its static characteristic<sup>10</sup>. This approach is complicated and, to our knowledge, it is more simple to represent the whole oscillator active circuit by its input characteristic  $v = \phi(i)$  (Fig.1) or by input and transfer-characteristics  $u = \phi(i)$ ,  $v = \theta(i)$  (Fig.2). These characteristics may be obtained experimentally. It is the first step in the analysis of quartz multivibrators. The resistor  $R$  (Figs.1,2) determines the singular point of the oscillator.

The quartz crystal unit is modelled by a resonant equivalent circuit.

In the theory of relaxation oscillations<sup>10</sup>, it is

well-known that the dynamical behaviour of the relaxation oscillators is determined by small (parasitic) circuit parameters  $Z_{pi}$ ,  $i=0,1,2,\dots$  (Figs.1,2). They enable a rapid change of the multivibrator state. An important problem is how to select the minimal number of parasitic parameters to describe adequately the behaviour of analyzed relaxation oscillator. The general criterion for the validity of the multivibrator electrical model is the agreement between the calculated phase portrait based on this electrical model and the projections of the phase portrait obtained experimentally by means of oscilloscope on the realised circuit. The problem of a parasitic parameter selection must be solved by the trial and error method. In our experience the observing of voltage and current time diagrams in the oscillator by means of an oscilloscope may provide sufficient information for the selection of parasitic parameters. Thus, the trial and error procedure is considerably shortened. Namely, each pair of points in oscillator circuits, where the step voltage change exists, has to contain a parasitic capacitor with a small capacitance. This small capacitance enables the appearance of a voltage step on the capacitor with finite capacitor current. Similarly, each contour of the oscillator circuit where the current has a step change must contain the parasitic inductor with a small inductance. Upon this preliminary selection of small parasitic parameters, the electrical oscillator model is established. Using Kirchhoff's laws and this electrical model, the mathematical model of relaxation crystal oscillator is obtained in the form of a system of nonlinear differential equations. In the theory of oscillations<sup>10</sup> there is a criterion for determining whether parasitic parameters present in the mathematical model are really important or negligible for a multivibrator operation. If a parameter is unimportant, the assumed multivibrator electrical model has to be corrected. Parasitic parameters are often stray capacitances and/or inductances. Sometimes they are equivalent models representing some physical processes in the active part of the oscillator (for example, the input impedance of a common base transistor amplifier is inductive in character due to the cut-off frequency of transistor current gain).

For further analysis we shall suppose that the static characteristic of an active part of the oscillator on Fig.1 has a piece-wise linear form shown on Fig.3 and described by equations:

$$\begin{aligned} v = \phi(i) &= ai & (I) \text{ for } |i| < i_1 \\ &= b(i - i_1) + B' & (II) \text{ for } i > i_1 \\ &= b(i + i_1) - B' & (III) \text{ for } i < -i_1. \end{aligned}$$

By adopting this assumption the general character of the analysis is not diminished because any static characteristic can be represented by its piece-wise linear approximation. We shall later explain why this shape of characteristic was adopted.

The above described electrical model of the relaxation crystal oscillator is shown on Fig.4. The small capacitance  $C_p$  is the sum of a parallel crystal capacitance and input capacitance of the active part of oscillator circuit. The inductor  $L_p$  represents a parasitic input inductance of the active part of multivibrator whose static characteristic is given on Fig.3 (see reference 11). The mathematical model of the circuit from Fig.4 has the form:

$$L \frac{di}{dt} = \phi(i) - u$$

$$RC \frac{du}{dt} = Ri - u - Ri_Q \quad (1)$$

$$L \frac{di_Q}{dt} = u - Ri_Q - u_c$$

$$C \frac{du_c}{dt} = i$$

The singular point(s) of this system ( $i=i_0, u=U_0, u_c=U_{c0}, i_Q=0$ ) is (are) determined by eqns.:

$$Ri_0 - \phi(i_0) = 0$$

$$U_0 = U_{c0} = \phi(i_0)$$

$$i_Q = 0$$

It means that the number and the location of singular points can be selected by a resistor  $R$  value (Fig.1).

For easier manipulation by eqns.(1), we shall normalise the variables:

$$i = I_1 x$$

$$u = V y$$

$$i_Q = I_1 z$$

$$u_c = V w$$

$$t' = (L/R)t$$

$$\phi(i) = RI_1 \psi(x),$$

where current  $I_1$  is defined on Fig.3 and  $V$  is the power supply voltage. The normalised form of the static characteristic is given on Fig.5, and its mathematical expression is:

$$\begin{aligned} \psi(x) &= \frac{a}{R} x & (I) \text{ for } |x| < 1 \\ &= \frac{b}{R}(x-1) + B & (II) \text{ for } x > 1 \\ &= \frac{b}{R}(x+1) - B & (III) \text{ for } x < -1, \end{aligned} \quad (1a)$$

where  $B = B'/(RI_1)$ . After normalisation equations (1) become:

$$\begin{aligned} \mu_1 \frac{dx}{dt} &= \psi(x) - \epsilon y = F_1(x, y) \\ \mu_2 \frac{dy}{dt} &= \frac{1}{\epsilon} x - y - \frac{1}{\epsilon} z = F_2(x, y, z) \\ \frac{dz}{dt} &= \epsilon y - \frac{r}{R} z - \epsilon w \\ \frac{dw}{dt} &= \frac{L}{CR^2} \frac{1}{\epsilon} z, \end{aligned} \quad (2)$$

where  $\mu_1 = L_p/L$  and  $\mu_2 = (RC_p)/(L/R)$  are small parasitic parameters and  $\epsilon = V/(RI_1)$ . The singular point is determined as a solution of equations:

$$x - \psi(x) = 0$$

$$y = w = \frac{1}{\epsilon} \psi(x)$$

$$z = 0.$$

Various crystal multivibrators can be described by such a mathematical model consisting of nonlinear differential equations.

#### Phase Portrait of the Relaxation Quartz Oscillator

It is well known that the location and the nature of singular points determine the shape of the phase portrait. It is shown experimentally that the oscillator starts reliably only if the singular point is unique and unstable, that is if the singular point lies in segment I and if R is larger than  $B'/I_1$  (Fig.5). This statement will be confirmed by further analysis.

The phase portrait of the relaxation oscillator may be calculated analytically dividing the entire phase space into subspace L, where slow motions of the system are possible, and the rest of the phase space, with rapid motions. Subspace L is defined by equations:

$$F_1(x, y) = \psi(x) - \epsilon x = 0$$

$$F_2(x, y, z) = \frac{1}{\epsilon} x - y - \frac{1}{\epsilon} z,$$

obtained from eqns.(2) for  $\mu_1 \rightarrow 0^+$  and  $\mu_2 \rightarrow 0^+$ . The motions in subspace L are actually "slow only" in its part L<sup>+</sup> where conditions:

$$\frac{\partial F_1}{\partial x} + \frac{\partial F_2}{\partial y} = \psi'_x(x) - 1 < 0,$$

and:

$$\frac{\partial(F_1 F_2)}{\partial(x, y)} = \begin{vmatrix} \frac{\partial F_1}{\partial x} & \frac{\partial F_1}{\partial y} \\ \frac{\partial F_2}{\partial x} & \frac{\partial F_2}{\partial y} \end{vmatrix} = -\psi'_x(x) + 1 > 0, \quad (2a)$$

are fulfilled. Both these conditions reduce to the inequality:

$$\psi'_x(x) < 1.$$

It means that the system moves slowly in subspace L for all x except for  $x=-1$  and  $x=1$ . A part of subspace L where motions are rapid is labelled by L<sup>-</sup>.

#### Slow Motion of Crystal Multivibrator State

The slow motion equations:

$$F_1(x, y) = 0$$

$$F_2(x, y, z) = 0$$

$$\frac{dz}{dt} = \epsilon y - \frac{r}{R} z - \epsilon w$$

$$\frac{dw}{dt} = \frac{L}{CR^2} \frac{1}{\epsilon} z$$

are obtained from eqns.(2) when  $\mu_1$  and  $\mu_2$  are very small. It is the second order system. The choice of variables made here, that is the selection of the plane where the phase subspace L<sup>+</sup> is projected, is limited by the characteristics of function  $\psi(x)$ . If  $\psi(x)$  does not have an inverse function, the selected plane has to contain variable x. The choice of another coordinate is determined by functions  $F_1(x, y)=0$  and  $F_2(x, y, z)=0$ . In our case the choice of variables (x, y) gives projection of the phase subspace L<sup>+</sup> providing small information about the phase portrait, because  $F_1(x, y)=0$  gives the obvious result:  $y = \psi(x)/\epsilon$ . The same result is provided by the choice (x, z). The projection of subspace L<sup>+</sup> on plane (x, w) is described by eqns.:

$$\begin{aligned} (1 - \psi'_x(x)) \frac{dx}{dt} &= (1 + \frac{r}{R}) \psi(x) - \frac{r}{R} x - \epsilon w = P(x, w) \\ \frac{dw}{dt} &= \frac{L}{CR^2} \frac{1}{\epsilon} (x - \psi(x)) = Q(x, w). \end{aligned} \quad (3)$$

Since function  $\psi(x)$  is described by a piecewise-linear model, the equations of slow motions phase trajectories must be calculated for each segment separately.

In segment I (Fig.5) we have  $\psi(x) = \frac{a}{R}x$  and the unique singular point at origin. The characteristic equation of system (3) is:

$$\lambda^2 - \frac{L}{R} \frac{\frac{a}{r} + \frac{a}{R} - 1}{Q(1 - \frac{a}{R})} \omega_r \lambda + \frac{L^2}{R^2} \omega_r^2 = 0 \quad (4)$$

and its roots are:

$$\lambda_{1,2} = \frac{L}{R} \left( \frac{\frac{a}{r} + \frac{a}{R} - 1}{2Q(1 - \frac{a}{R})} \omega_r \pm j \omega_r \sqrt{1 - \frac{(\frac{a}{r} + \frac{a}{R} - 1)^2}{4Q^2(1 - \frac{a}{R})^2}} \right), \quad (5)$$

where  $\omega^2 = 1/(LC)$  and  $Q = (\omega_r L)/r$ . For  $a > (Rr)/(R+r)$ , the singular point is the unstable focus, and each phase trajectory is a part of an increasing logarithmic spiral. The spiral is right hand side and its isoclinic line of vertical tangents is:

$$w = \frac{1}{\epsilon} \left( \frac{a}{R} (1 + \frac{r}{R}) - \frac{r}{R} \right) x.$$

The isoclinic line of horizontal tangents is the y-axis.

Function  $\psi(x)$  on segment II has the value  $\psi(x) = (b/R)(x-1)+B$ . In this segment the system under consideration behaves as a system with a singular point at  $x_{sp} = (B - (b/R))/(1 - (b/R)) = B$ ,  $w_{sp} = x_{sp}/\epsilon = B/\epsilon$  (for  $b < R$ ). Its characteristic equation is:

$$\lambda^2 + \frac{L}{R} \frac{1 - \frac{b}{R}(1 + \frac{r}{R})}{Q(1 - \frac{b}{R})} \omega_r \lambda + \frac{L^2}{R^2} \omega_r^2 = 0 \quad (6)$$

and the roots are:

$$\lambda_{1,2} = \frac{L}{R} \left( - \frac{1 - \frac{b}{R}(1 + \frac{r}{R})}{2Q(1 - \frac{b}{R})} \omega_r \pm j \omega_r \sqrt{1 - \frac{(1 - \frac{b}{R}(1 + \frac{r}{R}))^2}{4Q^2(1 - \frac{b}{R})^2}} \right). \quad (7)$$

For  $b < (rR)/(r+R)$ , the singular point is a stable focus, and phase trajectories in segment II are parts

of a decreasing right hand logarithmic spiral. The isoclinic line of vertical tangents of this spiral is  $w = -(r/R)x + B(1+r/R)/\epsilon$  and the isoclinic line of horizontal tangents is the line  $x = B$  (for  $b < R$ ).

In segment III the relaxation crystal oscillator behaves as a system with a singular point at  $x_{sp} = -(B-b/R)/(1-b/R) \approx -B$ ,  $w_{sp} = x_{sp}/\epsilon \approx -B/\epsilon$ . The characteristic equation is the same as that on segment II, and the singular point is a stable focus. Phase trajectories are parts of a right hand decreasing logarithmic spiral with an isoclinic line of its vertical and horizontal tangents:

$$w = \frac{1}{\epsilon} \left( -\frac{r}{R}x - B\left(1 + \frac{r}{R}\right) \right)$$

and  $x = -B$ , respectively.

#### Rapid Motion of the Crystal Multivibrator State

Outside phase subspace  $L^+$ , defined by conditions (2a), the oscillating system changes its state instantaneously. For small values of parasitic parameters  $\mu_1, \mu_2$ , the equations of rapid motion of the crystal multivibrator state<sup>10</sup> are obtained from eqns.(2) in the form:

$$\begin{aligned} \mu_1 \frac{dx}{dt} &= F_1(x, y) \\ \mu_2 \frac{dy}{dt} &= F_2(x, y, z_0) \\ z &= z_0 = \text{const.} \\ w &= w_0 = \text{const.} \end{aligned} \quad (8)$$

where variables  $z$  and  $w$  remain unchanged during rapid motion. In the analysis of oscillating systems in which rapid motions are instantaneously transformed into slow motions (e.g. for crystal relaxation oscillators with small  $\mu_i$ ) it is unnecessary to solve equations (8) for determining rapid phase trajectories<sup>10</sup>. Namely, in this case the so-called jump condition:

$$\begin{aligned} F_1(x^-, y^-) &= F_1(x^+, y^+) = 0 \\ F_2(x^-, y^-, z_0) &= F_2(x^+, y^+, z_0) = 0 \\ z^- &= z^+ = z_0 \\ y^- &= y^+ = y_0, \end{aligned} \quad (9)$$

is fulfilled. It means that the jump initiates at points  $(x^-, y^-, z^-, w^-)$  where slow motion of the system is impossible (That is on boundary of subspaces  $L^+$  and  $L^-$ ) and it finishes at points  $(x^+, y^+, z^+, w^+)$  within subspace  $L^+$ .

For a projection of the phase space on plane  $(x, w)$ , the jump starts either at point  $x^- = +1$  or  $x^- = -1$  and finishes at the point determined by equation:

$$x^+ - x^- = \psi(x^+) - \psi(x^-).$$

Variable  $w$  remains constant. For function  $\psi(x)$  shown

on Fig.5. in our example the jump occurs from  $x = +1$  into the vicinity of  $x = -1$  and inversely.

#### Limit Cycle of the Crystal Multivibrator

The limit cycle is a closed trajectory in the phase space representing the sustained oscillations. The limit cycle is stable if all phase trajectories, starting within some subspace containing a limit cycle, approach this cycle. It means that oscillations are sustained for small variations of oscillator parameters.

Using Bendixson's criterion<sup>10</sup> it may be shown that there is no closed trajectory in the subspace of slow motions, because expression:

$$BX = \frac{\partial P}{\partial x} + \frac{\partial Q}{\partial y}$$

has a constant sign on each segment on Fig.5 (see eqns. (3)). It means that harmonic oscillations are impossible in quartz multivibrators. Therefore, only relaxation oscillations may exist, that is, only the limit cycle consisting of parts of slow and fast phase trajectories may exist. The proof of the existence of the stable limit cycle may be obtained using the point transformation technique<sup>10</sup>. A simple intuitive proof can be easily derived by noting that the spirals in segments II and III are decreasing and right hand and that singular points are located on the line  $w = x/\epsilon$ .

Based on the foregoing results, the phase portrait of quartz relaxation oscillator having nonlinearity  $\psi(x)$  as on Fig.5 with  $b=0$  (see eqns.(1a)) is constructed and shown on Fig.6. The experimentally obtained shape of the limit cycle of a complementary switch crystal multivibrator<sup>4</sup> is shown on Fig.7 to certify the validity of this analysis.

#### The Analysis of Oscillations

The phase portrait of a relaxation quartz oscillator contains sufficient data for calculating the oscillation condition, building up and period of oscillations.

#### Oscillation Condition

For reliable starting of oscillations the quartz multivibrator must have unstable singular points only. It means that the singular point has to lie in segment I on Fig.3, that is that inequality  $R_1 > B'$  must be fulfilled. Then the singular point is unique. The character of this singular point is determined by the real part sign of roots (eqns.(5)) which must be positive for the starting of oscillations. This condition is illustrated on Figs.8(a),(b). We see that for each value of active circuit parameter  $a$ , there is a wide range of values of resistor  $R$  providing starting of oscillations (Fig.8(a)). From Fig.8(b), follows that oscillator controlled by crystal whose series resonant resistance is  $r_0$ , will operate without modifications with any crystal whose resistance is either equal or smaller than  $r_0$ .

#### Building up of Oscillations

The oscillations start from the singular point with exponentially rising amplitude. They are represented by the increasing logarithmic spiral on segment I in the phase portrait (Fig.6). Since the spiral step is proportional to the reciprocal value of the crystal Q factor, the oscillations build up with very large time constant. From imaginary parts of roots given by eqns. (5), (7), we see that frequencies in building up and in the steady state of oscillations are different.

### Period of Oscillations

The first approximation in calculating the relaxation oscillator period is that rapid motions are instantaneous. If parasitic parameters are small the oscillating period may be calculated by integrating slow motion equations (3) onto those parts of the limit cycle where slow motions occur<sup>10</sup>.

To omit further calculations we are demonstrating the case when slow motions in all parts of limit cycle have the same velocity (see imaginary part of eqn.(7) and Figs.6,7). At the same time this case, when oscillation frequencies on each slow motion segment of the limit cycle are the same, gives the highest frequency stability of relaxation oscillations. Namely when operating conditions of a circuit active part are changed, the relationship between the slow motion parts of the limit cycle is transformed. This leads to the change of frequency in all cases where the oscillating frequencies on various limit cycle parts differ.

From the above discussion and eqn.(7) the oscillating period for circuit under consideration is:

$$T \approx \frac{1}{\omega_r} \sqrt{1 - \frac{(1 - \frac{b}{R}(1 + \frac{r}{R}))^2}{4Q^2(1 - \frac{b}{R})^2}} = 2\pi, \quad (10)$$

that is, in real time:

$$T' = \frac{2\pi}{\omega_r} \sqrt{\frac{4Q^2(1 - \frac{b}{R})^2}{4Q^2(1 - \frac{b}{R})^2 - (1 - \frac{b}{R}(1 + \frac{r}{R}))^2}}. \quad (10a)$$

Two very interesting conclusions stem from the last expression. First, that the high Q factor of the quartz crystal unit decreases influence of circuit parameter (b,r,R) variations on frequency stability, and second, that the optimal nonlinear static characteristic of oscillator active circuit must contain slow motion parts of the limit cycle in segments whose slope (that is resistance) is zero. For the circuit under consideration it means that b (Fig.5) has to be small.

### Crystal Multivibrator Flicker Frequency Noise

An empirical law relating the spectral density  $S_Y(f)$  of the fractional frequency fluctuations  $y = \delta\omega_r/\omega_r$  of a quartz crystal resonator to the quality factor Q is known:

$$S_Y(f) = \frac{62}{(Q^{4.3})f}. \quad (11)$$

Recently, a simple derivation of this law and explanation of the nature of flicker frequency fluctuations in quartz crystal oscillators were given in reference 12. The entire free oscillating system of the quartz crystal oscillator is modelled by equation:

$$\ddot{x} + 2\gamma\dot{x} + \omega_0^2 x = 0. \quad (12)$$

If the natural frequency and Q factor are defined as:

$$\omega_n^2 = \omega_0^2 - \gamma^2, \quad (13)$$

$$Q = \frac{\omega_n}{2\gamma},$$

respectively, then the power spectral density of fractional frequency fluctuations is calculated as<sup>12</sup>:

$$S_Y(f) = \frac{\langle(\delta\omega_n)^2\rangle}{\langle\omega_n\rangle^2} = \frac{1}{16Q^4} \frac{\langle(\delta\gamma)^2\rangle}{\langle\gamma\rangle^2}. \quad (14)$$

According to the quantum theory of 1/f noise, it is shown<sup>12</sup> that the variance of fluctuations of the dissipative constant is:

$$\langle(\delta\gamma)^2\rangle / \langle\gamma\rangle^2 = \alpha A / f,$$

where  $\alpha$  and A are constants of the resonator material.

Consequently, the flicker frequency noise is caused by fluctuations of the total dissipative constant  $\gamma$ . Using eqns.(6), (12), (13) and assumption that rapid motions are instantaneous, we calculate the value of the entire oscillator Q factor:

$$Q_{\text{eff}} = Q \sqrt{\frac{(1 - \frac{b}{R})^2}{(1 - b(\frac{1}{r} + \frac{1}{R}))^2} - \frac{1}{4Q^2}} = Q \frac{1 - \frac{b}{R}}{1 - b\frac{r+R}{rR}}.$$

Consequently the power spectral density of fractional frequency fluctuations is(14):

$$S_Y(f) = \frac{\text{const.} (1 - b\frac{r+R}{rR})^4}{Q^4 (1 - \frac{b}{R})^4} \frac{1}{f}.$$

Quartz crystal unit Q factor is labelled by Q. From the last expression it follows that oscillators with optimal active part circuit characteristic (that is with  $b=0$  Fig.3), have the smallest level of the flicker frequency noise. This result is confirmed experimentally on a crystal multivibrator with complementary switch<sup>4</sup>. Optimal operating conditions are provided by  $R=2k\Omega$ ,  $r=128\Omega$ ,  $b=5\Omega$  and  $Q=2 \cdot 10^5$ . The measured level of flicker frequency noise is:  $S_Y(f)=5 \cdot 10^{-21}/f$ , and the value calculated using eqn.(11)<sup>11</sup> is:  $S_Y(f)=10^{-21}/f$ . It confirms that 1/f noise of relaxation crystal oscillator with optimal nonlinear characteristic is determined only by quartz crystal unit Q factor.

### Conclusions

The relaxation crystal oscillators were analysed by phase plane method. This approach is not familiar to most engineers but it gives a complete insight into circuit operation. In this paper, general electrical and mathematical models of a crystal multivibrator and its phase portrait were established. Based on these results, oscillating condition, oscillation building up and period, and level of flicker frequency noise of power spectral density  $S_Y(f)$  were studied. It was shown that relaxation crystal oscillators have the highest frequency stability if the active part of the oscillator circuit has small resistance between control inputs during slow exchange of multivibrator state.

Design conclusions may be easily drawn from the foregoing analysis.

# References

1. H.R.Newhoff, "Crystal-controlled multivibrator", Electronics, Vol. 36, pp. 60-62, April 12, 1963.
2. J.H.Kolataj, "Linearise your TTL gates-then build useful circuits with them", Electronic Design, Vol. 17, pp. 640-641, March 1., 1969.
3. D.D.Damljanović, "New quartz multivibrator", Proc. IEEE, Vol. 62, pp. 640-641, May 1974.
4. S.Tesic, D.Vasiljević, "A quartz complementary multivibrator", Proc. IEE, Vol. 123, pp. 851-854, Sept. 1976.
5. S.Tesic, D.Vasiljević, "A quartz multivibrator using two regenerative switches", Proc. IEEE, Vol. 65, pp. 166-167, Jan. 1977.
6. D.Vasiljević, S.Tesic, "An emitter-coupled quartz multivibrator", Int. J. Electronics, Vol. 42, pp. 551-558, June 1977.
7. W.I.Fletcher, "An engineering approach to digital design", Englewood Cliffs, N.J.: Prentice hall, Inc., 1980, Ch. 5.
8. J.Freeman, "Crystal Controlled Multivibrator", in "Circuit design idea handbook, Edited by B.Furlow, Boston, Massachusetts, 1980, p. 138.
9. D.M.Vasiljević, "Short-term frequency stability of relaxation crystal oscillators", IEEE Trans. Instr. Meas. (to be published).
10. A.A.Andronov, A.A.Witt, S.E.Chaikin, "Theory of Oscillations", Moscow: Fizmatgiz, 1959, Ch. 10 (in Russian).
11. B.D.Rakovich, S.L.Tesic, "A 5-MHz Switching Multivibrator Using a Complementary Pair of Transistors", The Radio and Electronic Engineer, Vol. 35, pp. 297-305, May 1968.
12. P.H.Handel, "Nature of 1/f frequency fluctuations in quartz crystal resonators", Solid-state Electronics, Vol. 22, pp. 875-876, Oct. 1979.

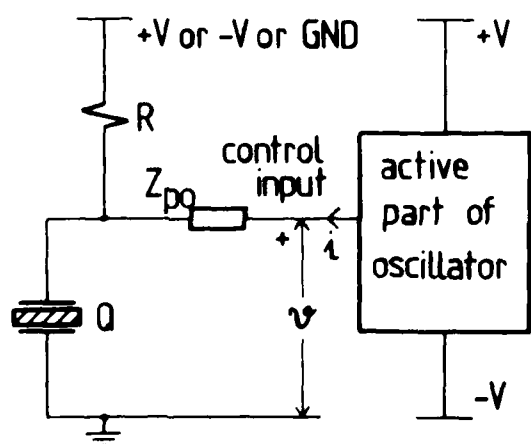


Figure 1. Model of crystal multivibrators with quartz crystal outside the feedback loop.

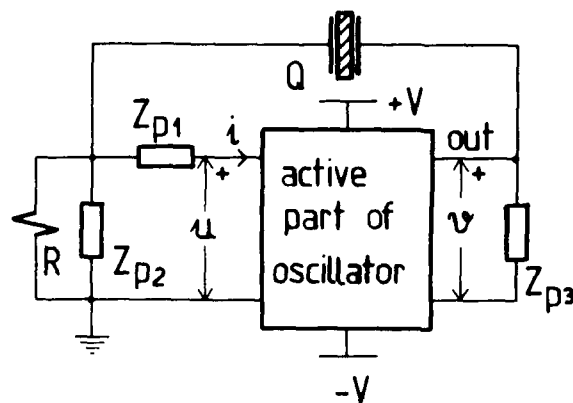


Figure 2. Model of crystal multivibrators with quartz crystal unit inserted in the feedback loop.

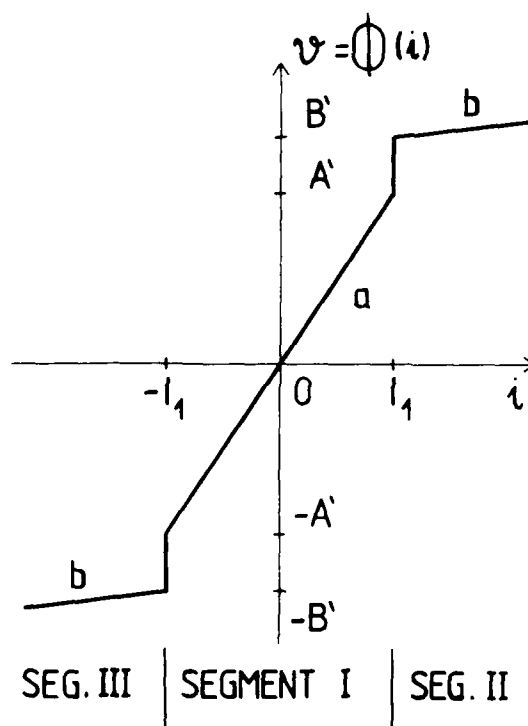


Figure 3. Supposed static characteristic of active part of oscillator from Fig. 1, piecewise-linear approximation.

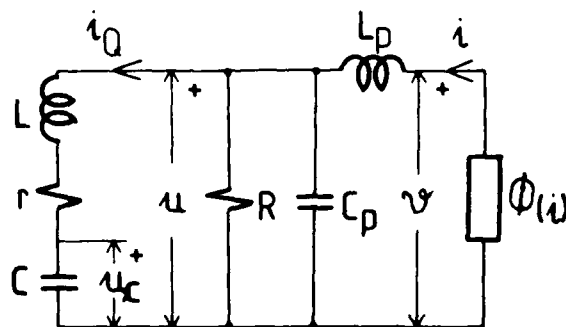


Figure 4. General electrical model of crystal multivibrator from Fig. 1.

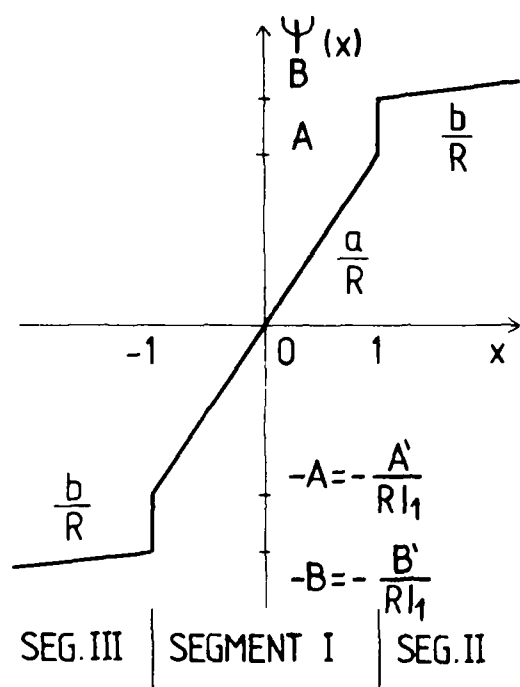


Figure 5. Normalised form of the static characteristic from Fig.3.

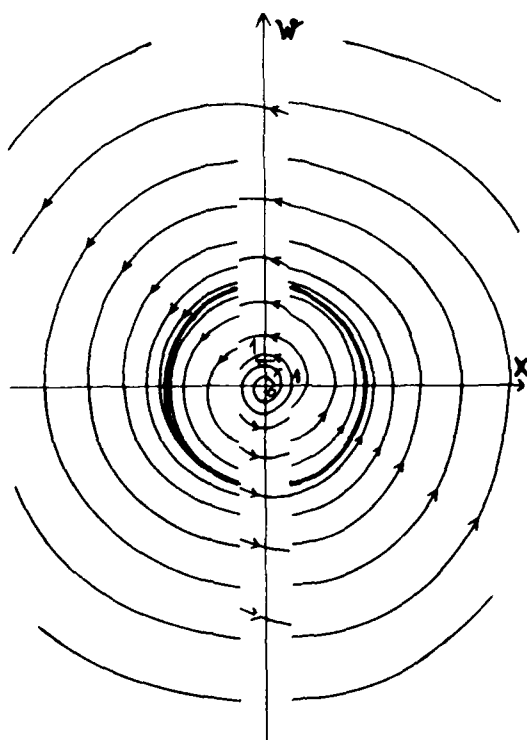


Figure 6. Phase portrait in \$(x, w)\$ plane of crystal relaxation oscillator from Fig.1 with \$b=0\$, \$\epsilon = B \approx 1\$ and \$r \ll R\$.

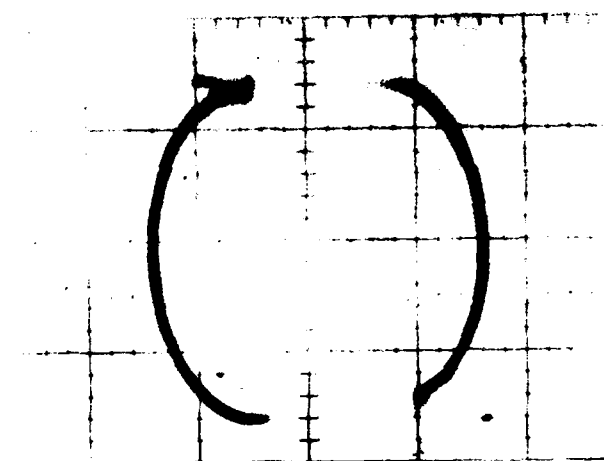


Figure 7. Experimentally obtained limit cycle \$(x, w)\$ plane) for circuit from Fig.1 with characteristic as on Figs.3,5.

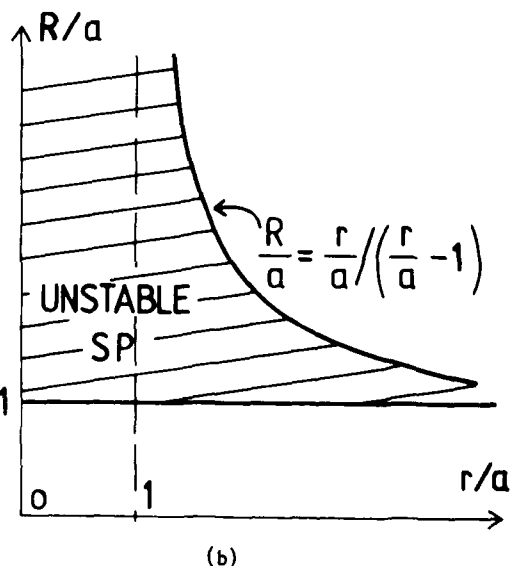
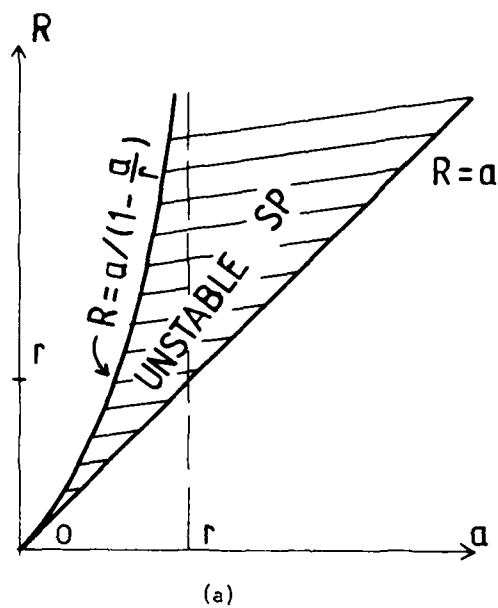


Figure 8. Illustration of dependence of oscillating condition from circuit parameters (see Fig.1)



## GPS USER RECEIVERS AND OSCILLATORS

David L. Hessick and William C. Euler  
 Magnavox Advanced Products and Systems Company  
 Torrance, California

## ABSTRACT

The Navstar Global Positioning System (GPS) is a satellite-based radio navigation and positioning system being developed by the U.S. Government. GPS will provide extremely accurate three-dimensional position, velocity, and timing information on a world-wide and continuous basis to an unlimited number of suitably equipped users. This paper reviews the status of the overall GPS program and the Magnavox User Equipment Full Scale Engineering Development (FSED) Program. The current schedule for the Space and Control segments are presented through the courtesy of the GPS Joint Program Office. Technical difficulties initially experienced by Magnavox have been largely resolved and the various host vehicle user equipment sets are rapidly being made available for support of the ongoing field test program. A substantial amount of informal testing and some formal testing have been accomplished. These initial test results are discussed. The oscillator is a key item in the GPS receivers. Its performance directly affects the navigation solution accuracies desired. This paper presents new information and test results of receiver performance in the laboratory and installed on military ships, aircraft, and land vehicles, of the latest production GPS Phase II equipment from Magnavox, including environmental effects on the oscillator. Test results of the oscillator alone in the laboratory are shown. Also discussed are the present baseline GPS Phase II and Phase III oscillator performance requirements and the requirements for other future GPS oscillators, as the GPS program nears the Phase III production award. Discussed are key performance

parameters, part screening levels, size, cost drivers, and quantities required.

## INTRODUCTION

GPS is a satellite-based, L-band radio navigation system designed to provide global, all-weather, 24-hour, accurate navigation to an unlimited number of authorized users. The three GPS segments; space, ground control, and user equipment are under development by the U.S. Department of Defense (DoD) and are scheduled to become fully operational in 1989. In the interim, 4 or 5 GPS satellites provide several hours of concurrent signal coverage each day on a world-wide basis, depending on user location and receiver-to-satellite geometry. The current satellite constellation can be used for test and development purposes, and for missions scheduled around the availability of the satellite signals. GPS provides highly accurate three-dimensional position and velocity information along with Coordinated Universal Time (UTC) to suitably equipped users. The "real time" navigation/position determinations are based on measuring the satellite-to-user transit times of modulated L-band signals broadcast by the GPS satellites. For navigation, an absolute accuracy of 100 meters is planned to be made available to general systems users. Higher accuracy, specified as position within 16 meters, velocity within 0.1 meters/second, and time within 100 nanoseconds will be available to the U.S. and NATO military and other users.

Referring to Figure 1, the GPS concept validation program (Phase I) was completed in mid 1979. Full scale

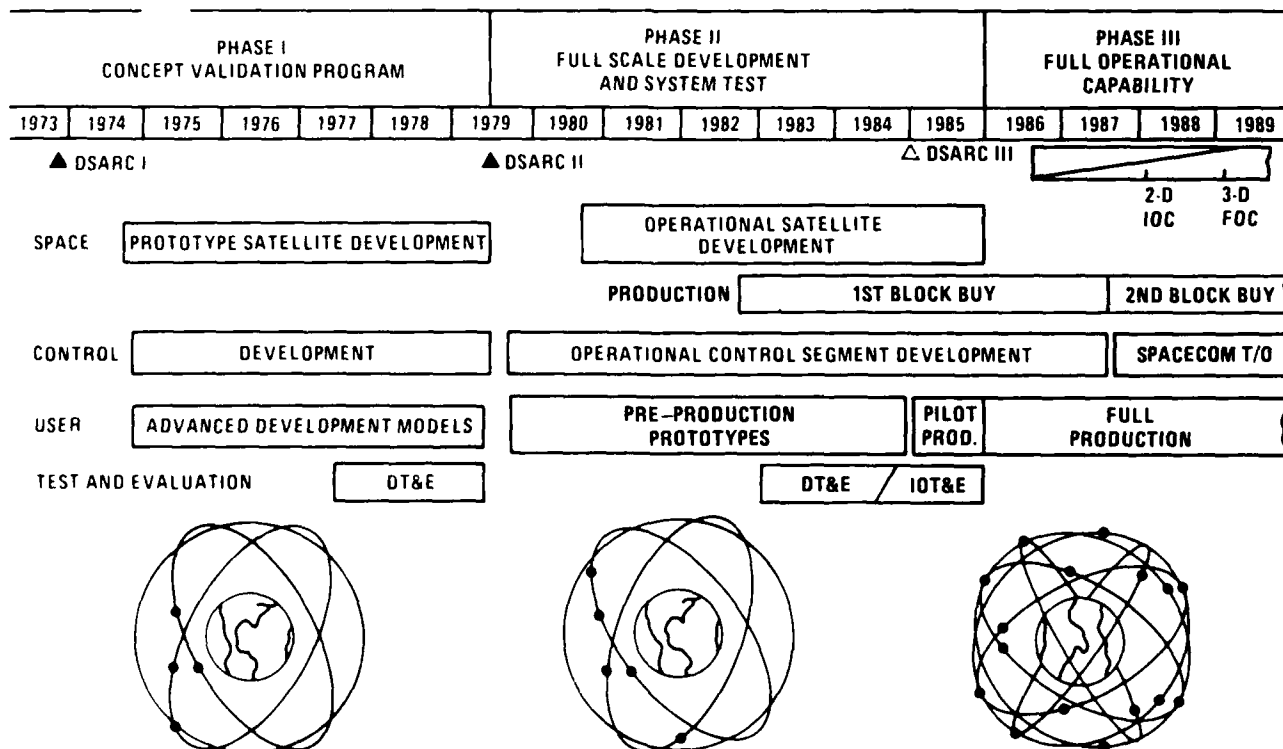


Figure 1. GPS Program Schedule

development and system test (Phase II) is scheduled for completion in January 1985, after which production of user equipment (Phase III) will begin. Initial Operational Capability (IOC) will be reached in 1988 when 10 to 12 of the production satellites are in orbit and two-dimensional navigation is achievable in most areas of the world. Full Operational Capability (FOC) is scheduled for 1989, when it will be possible to achieve continuous, three-dimensional navigation, on a world-wide basis, as the number of GPS satellites in orbit is increased to the full constellation of eighteen.

Magnavox is one of two contractors working on the Phase II User Equipment Full Scale Engineering Development (FSED) Program. Parallel contracts were awarded in July 1979 and are resulting in a quantity of user equipment sets from each contractor for testing on various military host vehicles by the Government. These tests will be conducted under formal Development Test and Evaluation (DT&E) and Initial Operational Test and Evaluation (IOT&E) ground rules. The User Equipment development program has encountered substantial difficulties which have caused schedule delays. Both contractors are now in the process of delivering various configurations of host vehicle sets for the DT&E phase of the Government's test program.

Magnavox is currently supporting informal and formal field testing with one-channel, two-channel and five-channel sets on various military host vehicles. Preliminary test results indicate excellent accuracy, resistance to jamming, and quickness of signal acquisition and reacquisition. Test personnel have expressed favorable reactions to the "user friendliness" of the equipment.

The equipment has been designed to have minimum installation impact on host vehicles and to be amenable to natural product upgrading, without major redesign, as new technology becomes available. This is the result of Pre-Planned Product Improvement (P<sup>2</sup>I) as well as specific product design features that reduce initial acquisition, installation, and total life cycle cost.

Magnavox has built a GPS System Simulator - Multiple Channel Signal Generator (MCSG), which has been used to support the development and evaluation of the GPS User Equipment. Intermediate Maintenance and Test Sets (IMTS) have been built for use in check out and maintenance of the Phase II User Equipment.

## SYSTEM DESCRIPTION

GPS consists of three segments: the space segment, the ground control segment and the user segment (Figure 2). When the operational space segment is completed in 1989, a constellation of 18 satellites will circle the earth in nominal 10,900 nautical mile orbits with a period of 12 sidereal hours. The constellation will be configured in six 55° inclined orbital planes of three satellites each. The configuration of the constellation has as its objective, direct line-of-sight navigation signals from at least four satellites to any point on or near the surface of the earth on a continuous basis.

Each operational GPS satellite will have a mean mission duration of 6 years and a design life of 7.5 years. Electrical power is supplied by two solar energy converting panels that continually track the sun and charge on-board batteries for use when the earth blocks the sun. Each GPS satellite has an on-board propulsion system for maintaining orbit position and for stability control.

Each satellite transmits navigation signals on two L-band frequencies; L1 (1575.42 MHz or 19 cm wavelength) and L2 (1227.6 MHz or 24 cm wavelength). Both L1 and L2 signals are quadriphase modulated by pseudo-random digital sequences consisting of a Precision (P) code and a Coarse Acquisition (C/A) code. These pseudorandom digital sequences are used for ranging. The signals also contain a navigation message which provides satellite position, time (from an on-board atomic frequency standard), and atmospheric propagation correction data generated by the ground control segment. The P-code is transmitted on two frequencies to permit users to correct for frequency sensitive propagation delay anomalies.

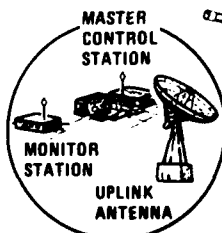
The current ground control segment has four monitor stations located at Guam, Hawaii, Alaska, and Vandenberg AFB in California. The Master Control Station and Data Up-load Station are located at Vandenberg. The monitor sites track the satellites via their broadcast signals as they come into view. The Master Control Station collects the tracking data and generates a navigation message which is uploaded to each satellite memory by way of an S-band telemetry link on a daily basis. In this way, each satellite is able to broadcast an accurate description of its position as a function of time. System time can also be derived from these broadcasts.

### SATELLITE SEGMENT

- 18 SATELLITES IN SIX ORBITAL PLANES
- 12 HOUR ORBITS OF 10,900 MILES



- ### CONTROL SEGMENT
- PASSIVE MONITORS
  - UPLOAD CONTROL



### USER SEGMENT

- LAND BASED
- SHIPBOARD
- AIRBORNE
- MISSILES
- SPACECRAFT

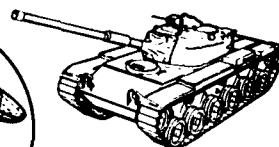


Figure 2. The Three Segments of the Navstar GPS

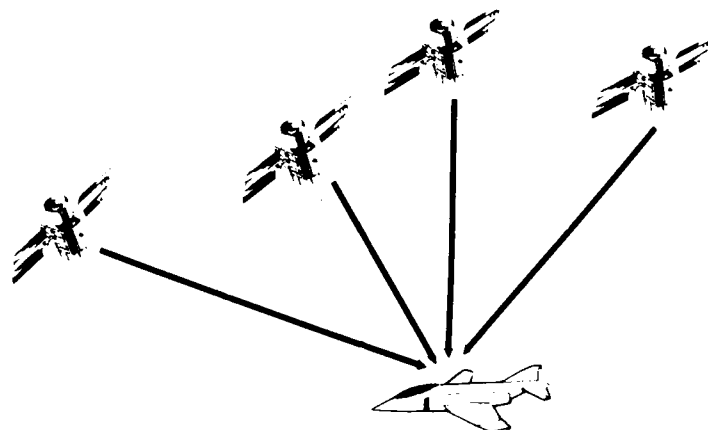
The user segment may consist of ground-based, marine, airborne, or spaceborne platforms, equipped with GPS receiver/processors capable of tracking four satellite signals either simultaneously or sequentially. The receiver/processor selects the optimum four satellites to track that provide the best geometry for accurate position/navigation solution. As the satellites continue their orbits, the receiver/processor drops each satellite with marginal geometry as a different satellite with better geometry becomes available. Position is computed by making time of arrival (TOA) measurements on the P or C/A code transmitted from discrete satellite positions as defined by the navigation message. Each set of four TOA measurements permits calculation of the four independent variables of latitude, longitude, altitude, and user clock offset (Figure 3).

Velocity is computed by making doppler measurements on the transmitted carrier frequency. Each set of four doppler measurements is processed to calculate the

four independent variables of 3-D velocity and user oscillator clock drift.

Navigation is accomplished via a Kalman Filter, which propagates a continuous navigation solution based on the TOA and doppler measurements. Use of the filter's propagation capability permits temporary operation on fewer than four satellites.

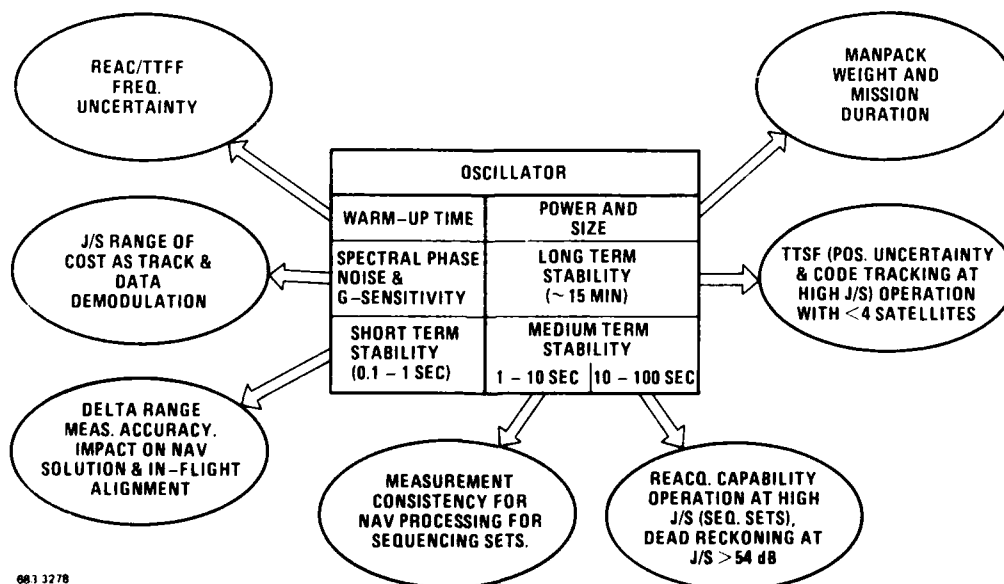
The oscillator is a critical item in the GPS receiver, especially for military use. The requirements demand state-of-the-art oscillator performance in stability, phase noise, warm up, temperature, low power, and vibration (g) sensitivity. Its performance has direct influence on the GPS system performance as shown in Figure 4. Unfortunately, all parameters must be met simultaneously during some missions. The GPS Phase II and Phase III requirement demands the best available in each category. As can be seen from Figure 4 and Figure 5, the oscillator's characteristics have multiple complex effects upon the GPS receivers.



- RECEIVE SYNCHRONIZED SIGNALS FROM SATELLITES
- MEASURE RANGE AND DOPPLER TO EACH SATELLITE
- COMPUTE THREE COORDINATES OF USER POSITION AND USER CLOCK BIAS, AND DETERMINE VELOCITY

494 2163

Figure 3. User Equipment Solves Four Simultaneous Equations to Determine Position and Time



681 3278

Figure 4. GPS Performance Drives Oscillator Requirements

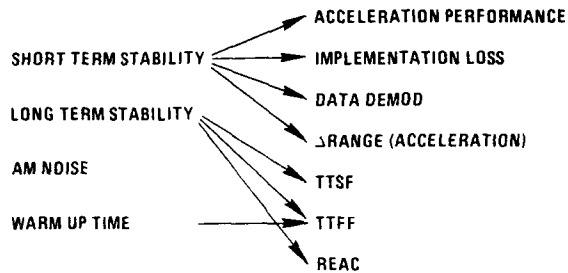


Figure 5. GPS Sensitivity to Oscillator Characteristics

Depending on the GPS user, these parameters can be traded. The military use requires full performance oscillators, while the commercial receivers can use much lower performance and lower cost oscillators. There is also a possibility of using different performance level oscillators for different platforms. However, this complicates the logistics plan and is not compliant with the goal of commonality of modules and parts across users and platforms that has been achieved in the Magnavox design.

#### PROGRAM STATUS

##### Space and Control Segments

The current schedules for the Space and Control segments have been provided through the courtesy of the GPS Joint Program Office and are shown in Figures 6A and 6B. The GPS test constellation consists of a limited number of developmental satellites configured in two planes, inclined at 63° with respect to the equator. This configuration allows for approximately two to four hours of testing each day in selected areas of the globe and is optimized to support government

testing within the continental United States. This test configuration is currently made up of five operating satellites. Two of the seven operational satellites have been turned off due to malfunction. The current plan is to maintain a minimum constellation of five satellites for the completion of the test and evaluation period for the system (Figure 6C).

In 1983 the DoD completed the award of a contract for production of twenty-eight operational satellites. Present launch plans, by way of the Space Shuttle, provide for a constellation of 10 to 12 operational satellites by early 1988. At that time, a continuous, worldwide, two-dimensional, Interim Operational Capability (IOC), with partial three-dimensional capability, will be achieved. Full three-dimensional Final Operational Capability (FOC) will be achieved in early 1989.

With the introduction of these second generation GPS satellites, the U.S. Government will have the ability to implement the selective availability of signals for military and civilian users.

##### User Equipment Segment - Phase II

The User Equipment Full Scale Engineering Development Program provides for design, development and manufacture of a quantity of user equipment sets. These sets are allocated between various host vehicles. A C-141 aircraft and an M-35 truck are used to support the DT&E activities exclusively. The aircraft carrier, UH-60 helicopter, manpack, M-60 tank, SSN submarine, F-16 fighter aircraft, B-52 bomber and A-6E attack aircraft are host vehicles for both DT&E and IOT&E activities. Test activities are divided into four basic phases; System Integration Laboratory (SIL), Modification Center, Development Test and Evaluation (DT&E) and Initial Operational Test and Evaluation (IOT&E).

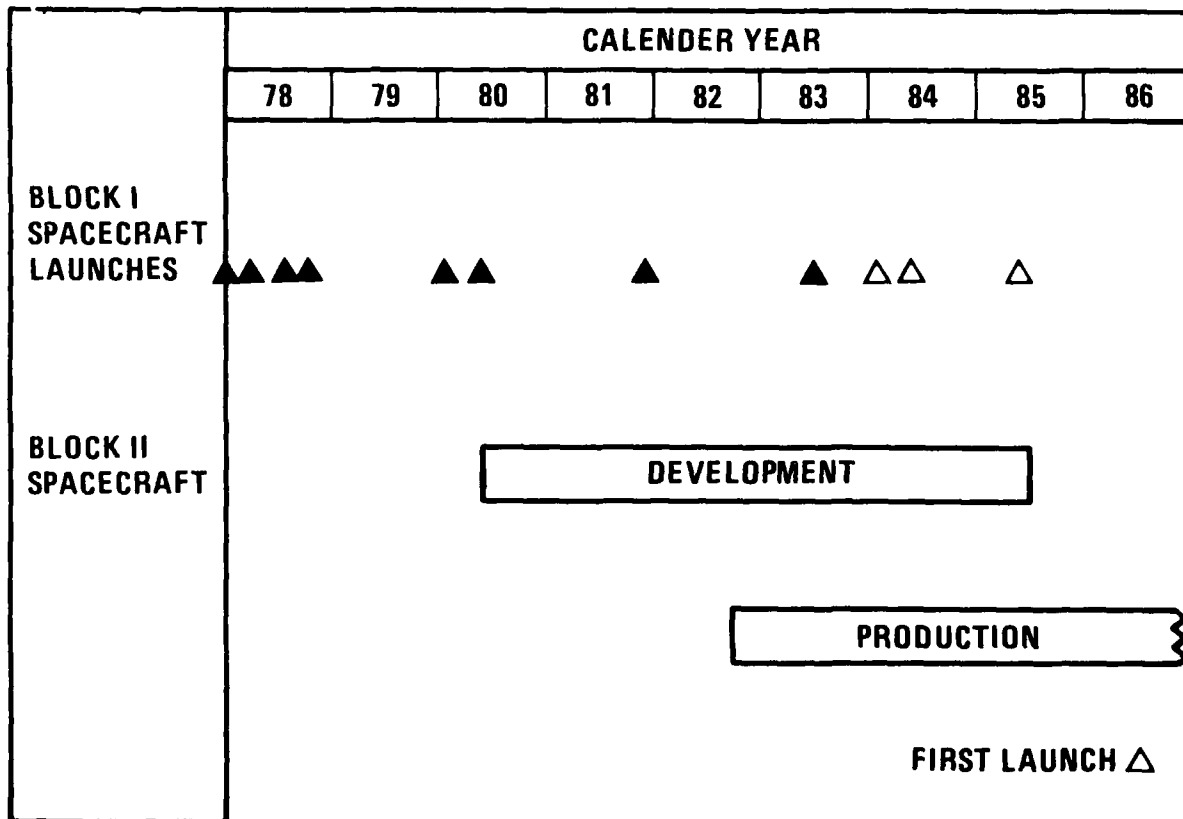
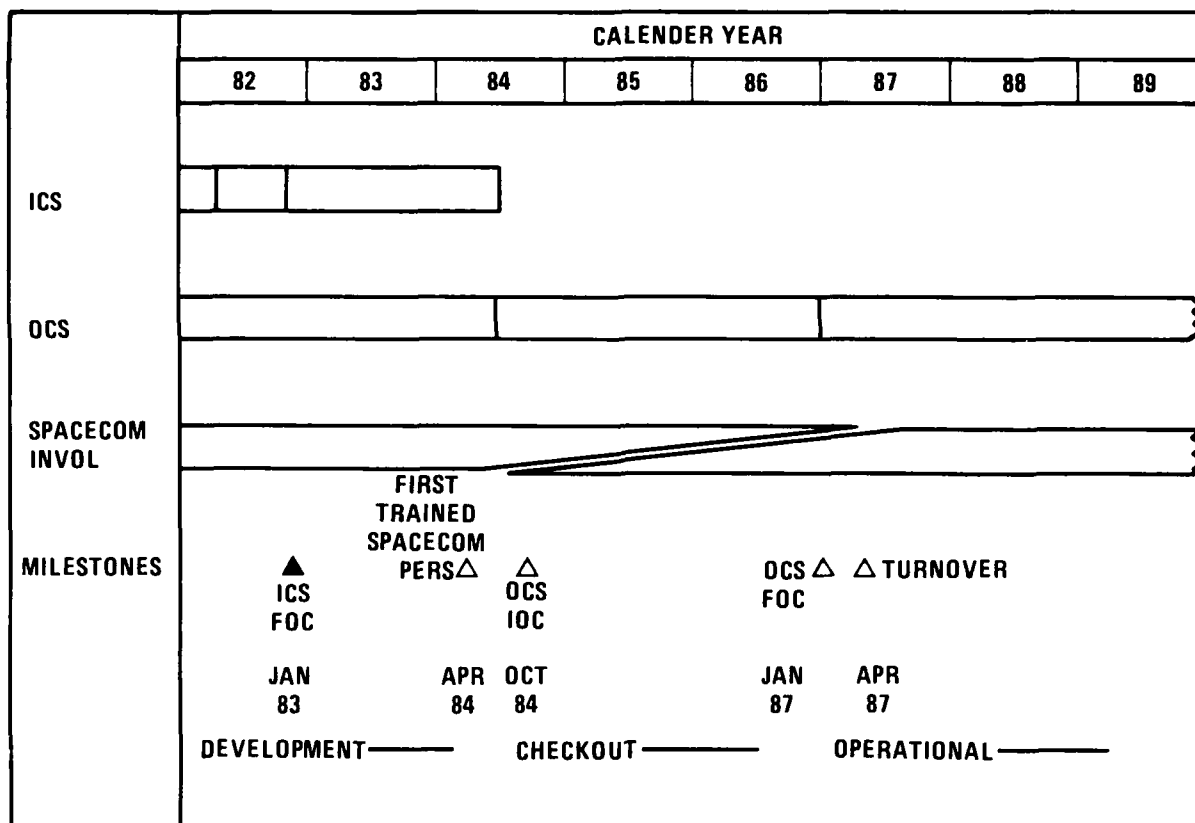


Figure 6A. GPS Space Segment Schedule



484-2170

Figure 6B. GPS Control Segment Schedule

**BLOCK I SATELLITES**

NAVSTAR NUMBER	POSITION NUMBER	PRN NUMBER	ACTIVE	COMMENTS
1	4	4	●	CRYSTAL OSC-DRIFT PROBLEM-HEALTHY
2	-	7		NO LONGER IN SERVICE
3	6	6	●	HEALTHY
4	3	8	●	HEALTHY
5	1	5		TURNED OFF - MAY REACTIVATE
6	5	9	●	HEALTHY
7	-	1		DESTROYED ON LAUNCH PAD
8	2	11	●	HEALTHY
9		13		LAUNCH DELAYED - AS REQD.
10		12		DUE FOR LAUNCH - AS REQD.
11		3		DUE FOR LAUNCH - AS REQD.

**BLOCK II SATELLITES TO BE LAUNCHED BEGINNING OCT 1986 BY SPACE SHUTTLE**

484 2166

Figure 6C. GPS Test Constellation Status

Magnavox user equipment sets are currently being supplied for the various test host vehicles. Some of these sets are still being integrated into their host vehicle System Integration Laboratories (SILs). Others are already installed in the operational host vehicles and are being prepared for DT&E. Figure 7 shows the general arrangement of the palletized GPS installation in the C-141 aircraft for DT&E. Figure 8 shows the sequence from SIL to a typical operational vehicle (F-16) for Operational Readiness (OR) testing. At this time, hardware units for the eight host vehicles are nearly completed and in various stages of final systems integration and test.

NATO

Phase IIB equipment is also being manufactured at Magnavox in response to contracts with German and France Government customers. We are completing the final assembly and check-out of a 5-channel set for use on a German submarine and a 2-channel set for installation on a German Minehunter. For France, we are building a 5-channel set for submarine use, a 2-channel set for the Hydrographic Service and an Air Force transport aircraft, and a 1-channel set to be utilized for manpack and helicopter use.

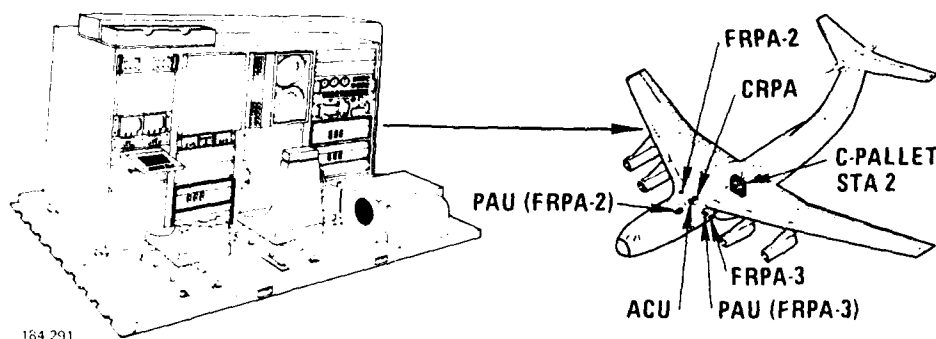


Figure 7. Initial Flight Testing Began in a C-141 Pallet Installation

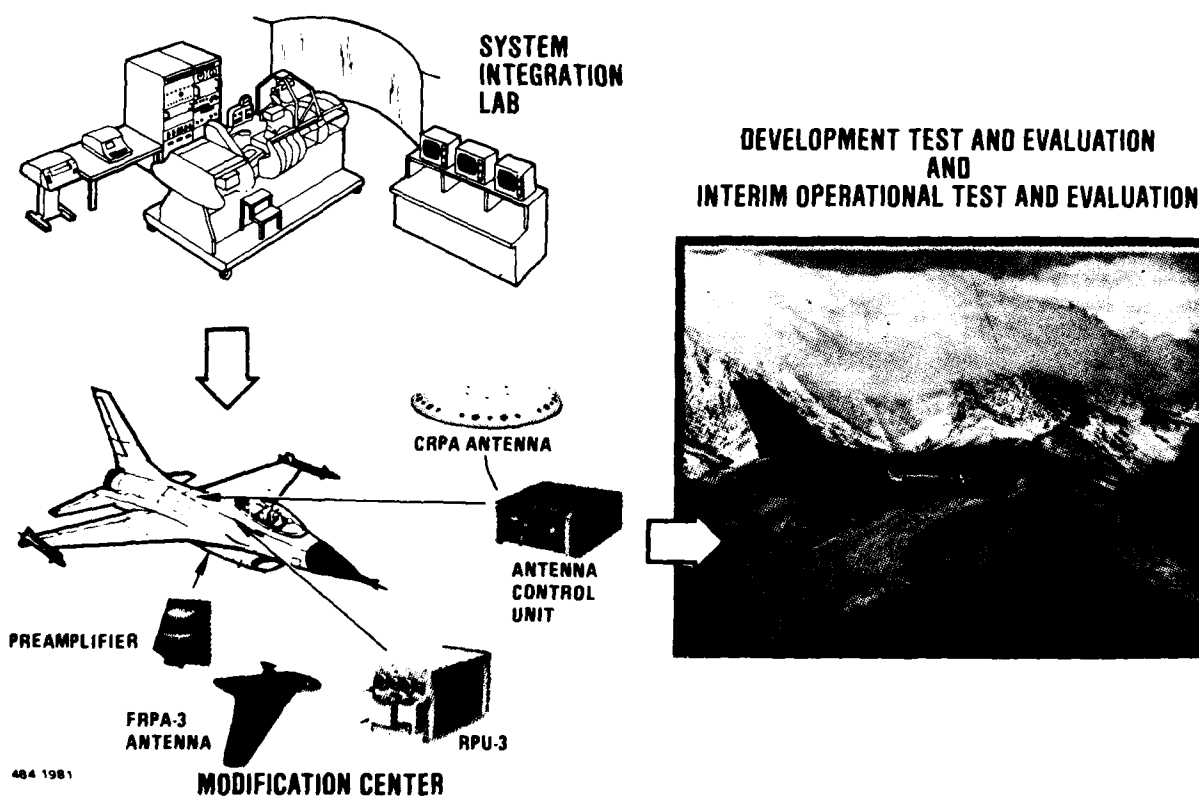


Figure 8. User Equipment From the Factory is Checked Out in a System Integration Lab, then Installed on the Host Vehicle and Tested Again, before Proceeding to DT&E, and/or IOT&E.

Magnavox currently has an approved manufacturing license with Plessey of the United Kingdom, TRT in France, Elmer of Italy, and Japanese Aerospace Electronics (JAE) of Japan are working with Magnavox under individual Memorandum of Understandings which in time will lead to manufacturing licenses for GPS User Equipment in each of these countries.

#### OSCILLATORS

Magnavox has been testing and evaluating oscillators for GPS since 1968 on the 621B, Timation, MX-450, GPS Phase I, GPSPAC, and GPS Phase II programs. A previous Magnavox paper on the GPS oscillator requirements outlined the requirements for the Phase I Manpack Set. Figure 9 shows the Phase II and Phase III oscillator key parameters for User Receivers, and some

of the actual test results of the present HP oscillator used in GPS Phase II. It is an excellent high performance unit. The oscillator is tested in the laboratory during qualification and in the field on the vehicles at oscillator temperatures up to 81°C and sine vibration levels up to 15 g's and random vibration levels up to 0.3 g's/Hz at the oscillator. Oscillators are also used in the GPS transmitter simulators (WFGs) and the IMTS. These are not discussed here.

At present, the key performance parameters that limit the GPS receiver's performance are the warm up at cold temperatures and the vibration g-sensitivity. The slower warm up time means that a user has to wait longer for navigation solution. The g-sensitivity is more important and critical, in that the excellent oscillator static short term stability and phase noise

PARAMETER	$\phi 3$ REQUIREMENT	$\phi 2$ CAPABILITY	MAIN DRIVER(S)
WARM-UP TIME	$1 \times 10^{-7}$ IN 5 MIN/ -40°C/+81°C	2.5 M @ 25°C 6.5 M @ -40°C (17W)	TTFF & REAC
STABILITY			
SHORT TERM 0.1 - 100 SEC	$5 \times 10^{-12}$	$< 2 \times 10^{-12}$	NAVIGATION AND DELTA RANGE ACCURACY (2 CM)
LONG TERM 15 MIN	$< 5 \times 10^{-11}$	$< 3 \times 10^{-12}$	M/V SUBSEQUENT FIX, OPERATIONS WITH 4 SATELLITES
ACCELERATION SENSITIVITY	$< 5 \times 10^{-10}$ /G, 4 - 100 Hz	$< 3 \times 10^{-10}$ Y, Z $2 - 9 \times 10^{-10}$ X	LOW FREQ VIBRATION ON ARMY VEHICLES AND FIGHTER/ ATTACK AIRCRAFT
SPECTRAL PHASE NOISE	$< -115$ dB/Hz @ 10 $-125$ dB/Hz @ 100	$-136$ dBc/Hz @ 10 Hz $-150$ dBc/Hz @ 100 Hz	$< 5^\circ$ TRACKING ERROR DUE TO OSC. JITTER
POWER DC	LESS THAN 20 WATTS WARMUP: LESS THAN 5 WATTS OPERATING	17W PK 4.5W SS @ -40°C	MANPACK BATTERY LIFE
SIZE AND WEIGHT	LESS THAN 0.7 LB ONE DIMENSION LESS THAN 2.8"	9 OZ 2.8 x 2.4 x 2"	MANPACK WEIGHT

Figure 9. GPS Phase III Oscillator Requirements Vs Capabilities

are degraded when a GPS receiver is used on a user (military) with very high vibration (dynamic) levels. Consequently, the GPS receiver navigation solution, jamming resistance, and threshold sensitivity are degraded from the static performance solutions at high vibration levels (10-15  $g_s$  at oscillator). Note that the oscillator at 10.23 MHz is multiplied to L-band (1575 MHz). This adds 44 dB to the phase noise plus the synthesizer contribution.

Figure 10 shows the static vibration short term stability test results of various candidate oscillators, for Phase III and future handheld and commercial sets, ranging in stability from  $10^{-8}$  to  $10^{-12}$  and with prices from \$10 to over \$1000. The HP oscillator used for GPS Phase II is at the bottom. Its short term stability is actually much lower than various cesium standards used on GPS for averaging times ( $\tau$ ) from 0.01 to 1000 seconds. Most of the oven type SC-cut and AT-cut oscillators exhibited worst axis vibration  $g$ -sensitivities of  $3 \times 10^{-9}$ /per one  $g$ . The average HP unit for GPS Phase II exhibited a worst axis vibration  $g$ -sensitivity of  $5 \times 10^{-10}$ /per one  $g$ . Most of the TCXO

types oscillators exhibited  $g$ -sensitivity of  $10^{-8}$  to  $10^{-9}$ /per one  $g$ . This study was done to compare the GPS Phase II oscillator to various quality non-Phase II type available oscillators that are possible candidates for future GPS handheld military and commercial units.

Because of the associated  $g$ -sensitivities, the short term stabilities degrade under random and sine vibration. This causes a navigation error. Similarly, the phase noise degrades under random and sine vibrations (simultaneous for military users). This causes an increase in phase noise or jitter to the demodulator costas loop, and degrades system RF sensitivity, and anti-jamming ability. A carrier and code offset also occurs due to the same vibration induced oscillator error.

The stabilities of the oven oscillators are, in general, not influenced by small temperature changes (say  $10^\circ F$ ) over short times (1-10 minutes) for  $\tau$ 's ( $\tau$ ) from .1 - 10 seconds. However, the TCXO types degrade over 10 to 1 with slight air currents or even smaller temperature changes.

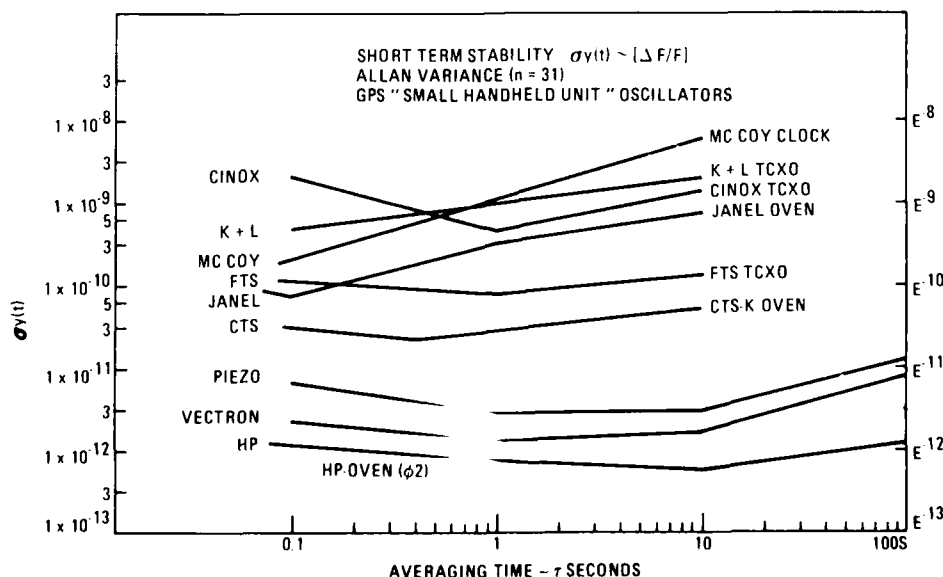


Figure 10. Static Vibration Short-Term Stability Test Results

Figure 11 shows the warm up frequency characteristics of the Phase II HP SC-crystal oscillator for the required temperatures. The main features of the SC-cut crystal over the AT-cut is the fast monotonic smooth frequency pulling. The overshoot and frequency reversal of the AT-cut oscillator during warm up is a slight problem to the GPS receiver. Note from the previous figures that GPS is a short term stability driven system (.1 - 10 seconds are key), and average or long term stability frequency offsets are not especially critical. This is in contrast to the Navy Transit Satellite System where long term, especially 15 minutes, is critical.

Future GPS user receiver requirements for portable and handheld type units will require even faster warm up with less power and size, while maintaining good short term stability. This is quite a challenge for the future.

Figure 12 shows the static short term stability requirements for four different classes of GPS users:

Dash Number	Class of Service
-4	Space
-3	Military
-2	Military/Industrial
-1	Commercial

These are intended to go into the present Phase II/Phase III product, but offering four grades of performance.

Short term stability largely limits navigation performance, pseudorange and delta range. The flicker frequency floor is the key performance area with part of the white FM, white PM and flicker PM regions important for navigation and part of the random walk

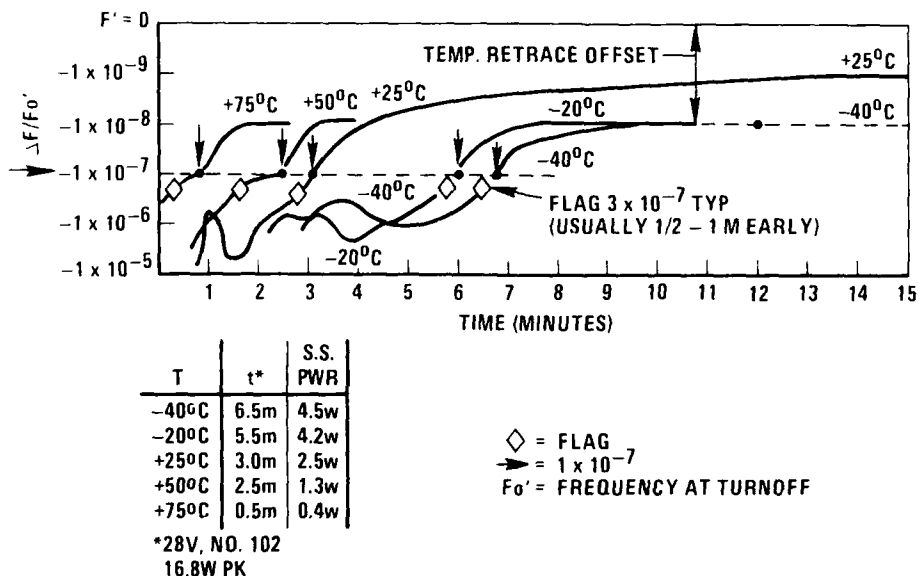
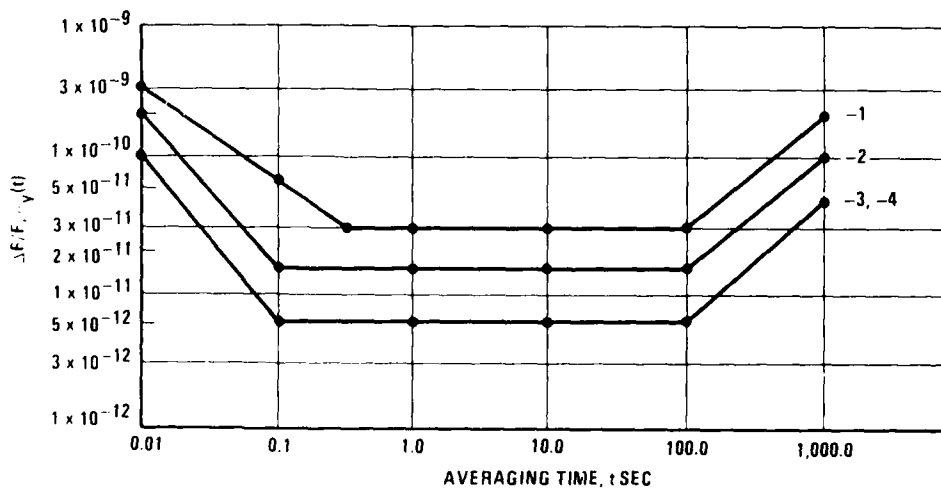


Figure 11. Oscillator Warmup, Accuracy Flag, Power Vs Temp HP 10811B



1. MINIMUM SAMPLE SIZE  $n \geq 30$  FOR  $t = 0.01 - 100S$ .  $n \geq 10$  FOR  $t = > 100S$ .
2. INDICATED REFERENCE POINT (●) AT WHICH ALLAN VARIANCE IS TO BE MEASURED TO DETERMINE COMPLIANCE: 0.1, 1.0, 10.0, 100.0, AND 1,000.0 SECONDS.

Figure 12. Oscillator Short Term Stability



FM region important for acquiring signals when a GPS fix has not been done recently by the GPS user.

Figure 13 shows the allowed g-sensitivity assuming .1 radians or  $5.7^\circ$  of loop jitter error for four different grades of oscillators. The allowed coefficient is a function of sine vibration frequency and amplitude. As can be seen, the low frequency region is the most critical. The use of shock isolators is not practical at the low frequency (4 Hz), and with the space available to mount the GPS receivers, especially in aircraft.

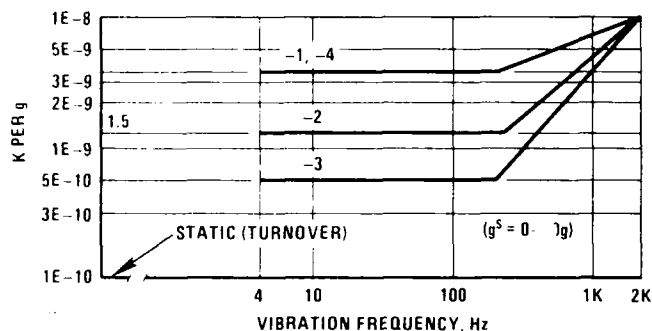


Figure 13. Maximum Allowed Oscillator g-Sensitivity, Each Axis (x,y,z)

The use of a "BVA" type crystal or of an accelerometer corrected oscillator offers some hope to a system solution, however, these types of oscillators are still in the Research Laboratory or are not economically practical for production, i.e., a rubidium type offers the good g-sensitivity and fast warm up, but the cost, size and power approaches that of an entire GPS Manpack Set.

Figure 14 shows dynamic test results of an early prototype HP Phase II oscillator at  $10g$  vibration level. The worst coefficient was  $7 \times 10^{-10}/g$  for the x axis. The y and z axes were less than  $2 \times 10^{-10}/g$ . Later production units were better and had an average K of  $5 \times 10^{-10}/g$  with a  $1\sigma$  of  $1.1 \times 10^{-10}/g$  in the worst axis. Vibration to 30-50 g's was done.

The allowed phase noise for 0.1 radians ( $5.7^\circ$ ) of jitter at L-band for four grades of oscillators, as described before, for static conditions, including the synthesizer error, is shown in Figure 15. The receive

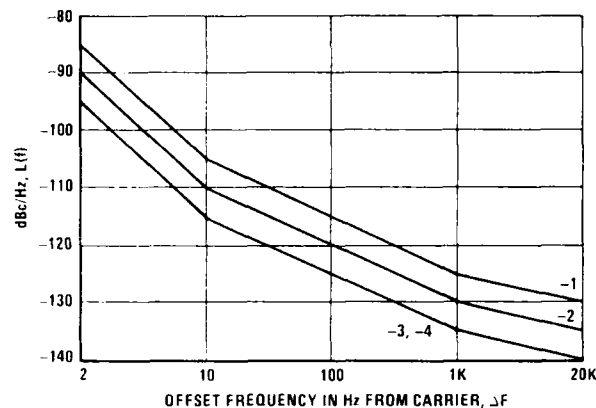


Figure 15. Oscillator Phase Noise and Spectral Density

The receive has a loop bandwidth of 20 Hz, effectively at L-band (1575 MHz), thus the important zone for phase noise into the second order costas loop is 2-10 Hz. This is due to random walk PM and flicker FM and is equivalent to short term stability flicker of frequency noise. Reasonable rolloff beyond 10 Hz to at least 20 KHz is also required. The receiver error budget is set for 0.1 radians of jitter maximum at the costas loop due to the oscillator and synthesizer.

Note that the GPS receiver requires a different value of phase noise performance (costas threshold) than the equivalent Fourier transform value of short term stability performance (navigation pseudorange and delta-range) due to the different system requirements of GPS in the receiver. Note the L-band synthesizer degrades the phase noise and short term stability of the oscillator into the receiver.

Figure 16 shows how important the oscillator static short term stability is to navigation accuracy (P code) during large dynamics. The reference stabilities do not account for synthesizer degradation, and thus the oscillator must be better to achieve this. Also oscillator g-sensitivity is also not factored here. As a result, the oscillator must approach  $3 \times 10^{-12}$  stability and have a g-sensitivity below  $5 \times 10^{-10}$  for a receiver with minimum errors due to the oscillator. For some users, this may not be cost

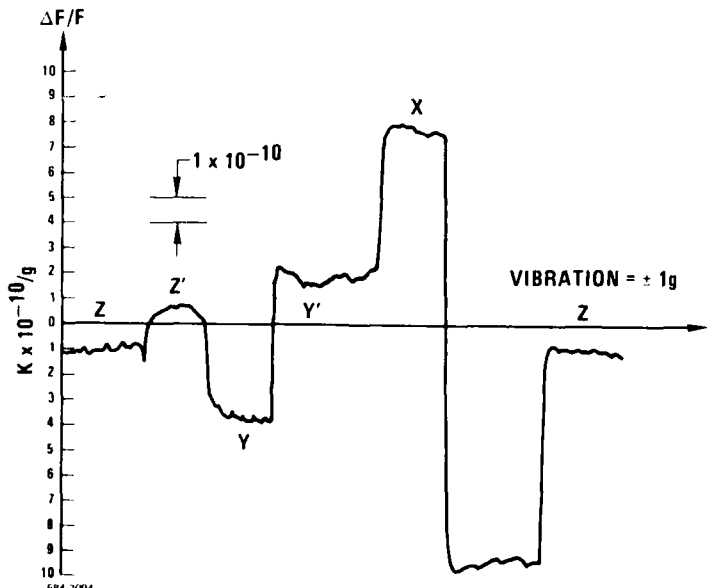


Figure 14. Phase II HP Oscillator g-Sensitivity Test Results (Prototype Unit)

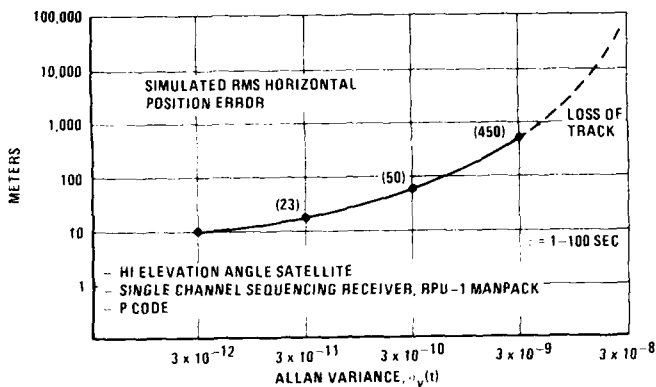


Figure 16. Impact of Oscillator and Synthesizer Stability on Navigation Performance During Flight Dynamics

effective, and a small performance backoff may yield significant dollar savings.

Without dynamics and vibration, the accuracies are much better (10:1+). A static GPS Manpack receiver can resolve a range of 2 meters and a change of position of 0.02 meters (2 cm) on a 10,000 mile orbit satellite.

Figure 17 shows how various quality oscillators would affect a commercial GPS receiver with L1 and C/A code only. The C/A code and a commercial GPS receiver in a relatively benign vibration environment can give respectable results with lower quality performance oscillator than required for the military Phase II P-code type receivers.

Figure 18 shows the product family of oscillators and some key specifications using various grades for

different GPS users. This philosophy allows the oscillator/component vendor to fill different needs and improve his yield by using a lesser performance/quality level part in lower performance/cost user receivers. Also refer to -1, -2, -3, -4 from previous figures. Frequencies of 10 and 10.23 MHz are candidates for now with higher frequencies (86, 347 MHz), a possibility for the future. A -5 and -6 unit will be added for missile and range applications.

CLASS	QUALITY LEVEL	TEMPERATURE	WARMUP	G-SENS.
IV	SPACE	-30°C TO +61°C	30 MIN	$3 \times 10^{-9}/G$
III	MILITARY	-54°C TO +81°C	5 MIN	$<5 \times 10^{-10}/G$
IIIA	SPECIAL MILITARY	-40°C TO +71°C	5 MIN	$3 \times 10^{-9}/G$
II	INDUSTRIAL/MILITARY	-30°C TO +71°C	7.5 MIN	$1.5 \times 10^{-9}/G$
I	COMMERCIAL	-20°C TO +61°C	10 MIN	$3 \times 10^{-9}/G$

Figure 18. MIL-Parts With Large Commercial Base

The future of GPS receivers not only lies in the Phase II, Phase III U.S. Military product but in the foreign military, industrial-military, handheld, missile, space and commercial markets (civil, land, sea, air) as shown in Figure 19. The projected quantities are in the 1000s to 10,000's for each of these for the next 20 years.

Figure 20 shows a wish list of oscillator specs that appear to be required for future new GPS system applications over the next 5-15 years. Magnavox plans to

CLOCK TYPE	APPROX. \$ COST	1 TO 10 SECOND STABILITY AND EQUIVALENT POSITION ERROR (METERS)	FREQUENCY OFFSET AND EQUIVALENT TIMING ERROR	20 MINUTE DRIFT AND EQUIVALENT TIMING ERROR	C/A CODE POSITION ERROR* WITH GDOP = 6, 4 SATELLITES	C/A CODE POSITION ERROR WITH SIGNAL LOSS I.E., 3 SATELLITES
XO	75	$1 \times 10^{-8} \sim 30 \text{ M}$	$1 \times 10^{-6} \sim 300 \mu\text{SEC}$	$1 \times 10^{-7} \sim 1 \mu\text{SEC}$	80 M	500 M
TCXO	300	$1 \times 10^{-9} \sim 3 \text{ M}$	$1 \times 10^{-7} \sim 120 \mu\text{SEC}$	$5 \times 10^{-9} \sim 0.1 \mu\text{SEC}$	50 M	300 M
HIGH QUALITY OVENIZED XO	1,000	$5 \times 10^{-12} \sim 1 \text{ M}$	$1 \times 10^{-8} \sim 15 \mu\text{SEC}$	$1 \times 10^{-10} \sim 0.001 \mu\text{SEC}$	30 M	50 M
HIGH QUALITY OVENIZED XO + CESIUM STD. + LOCK LOOP	1,000 40,000 2,000 43,000	$5 \times 10^{-12} \sim 1 \text{ M}$	0	0	30 M	30 M

\*THIS ERROR IS PRIMARILY DUE TO NATURE OF C/A CODE  
 $\sigma_{C/A} = (10 \text{ M} \times \text{GDOP})/\text{MEASUREMENT FILTERING FACTOR}$

584 2566

Figure 17. Performance and Product Implications of Using C/A Code User Equipment Clock During Poor GDOP or Loss of Signal

PRODUCT	MAIN DRIVERS	TIME
GPS o3/MIL	HI PERF., LOW G-SENS., COST	1985 - 1995
GPS o3/ SEMI-MIL	MED PERF., COST	1985 - 1995
MILITARY HANDHELD	SMALL SIZE, POWER, MED-HI PERF.	1985-1995
MISSILE	MED PERF., COST, SIZE, POWER	1987 - 2000
SPACE	HI PERF, COST	1986 - 2000
COMMERCIAL	MED-LO PERF., COST	1988 - 2XXX

Figure 19. Future Oscillator Requirements

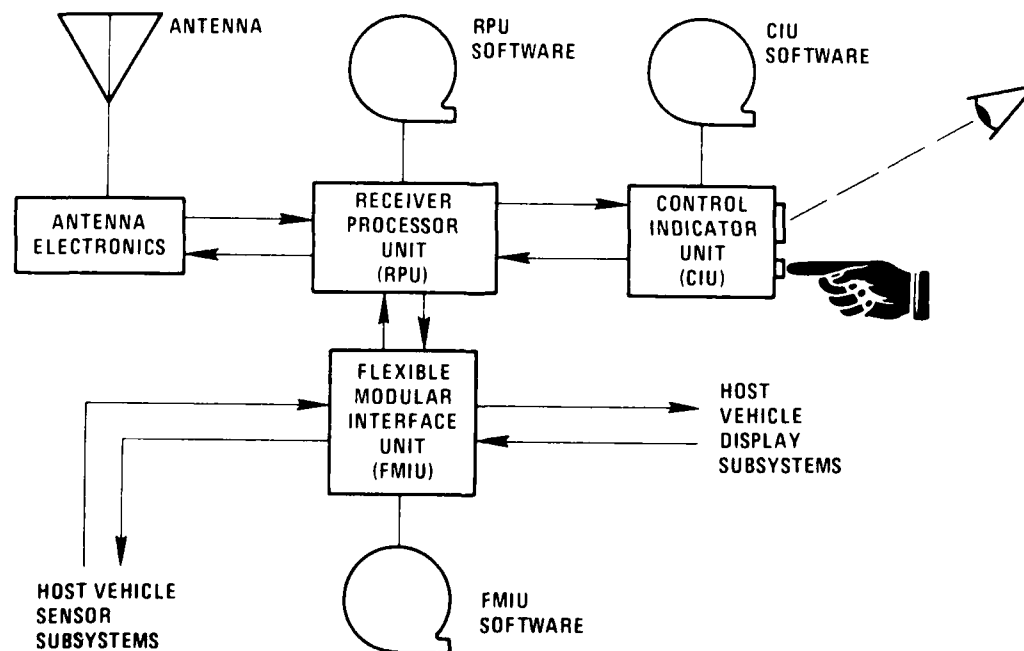
insert new technology into GPS receivers, such as a smaller oscillator, to lower user cost and size of the receiver, whenever practical.

The detailed oscillator requirements are called out in the Magnavox Oscillator Specification.

<b>WARM UP TIME</b>	<b>30 SEC</b>
<b>VIBRATION SENSITIVITY</b>	<b><math>1 \times 10^{-10}/g</math></b>
<b>SHORT TERM (1 S)</b>	<b><math>5 \times 10^{-12}</math></b>
<b>LONG TERM (24 H)</b>	<b><math>5 \times 10^{-10}</math></b>
<b>POWER</b>	<b>&lt; 0.5 W</b>
<b>WEIGHT</b>	<b>4 OZ.</b>
<b>SIZE</b>	<b><math>0.5 - 2 \text{ IN}^3</math></b>

684 3095

Figure 20. Requirements (Wish List)



194 252

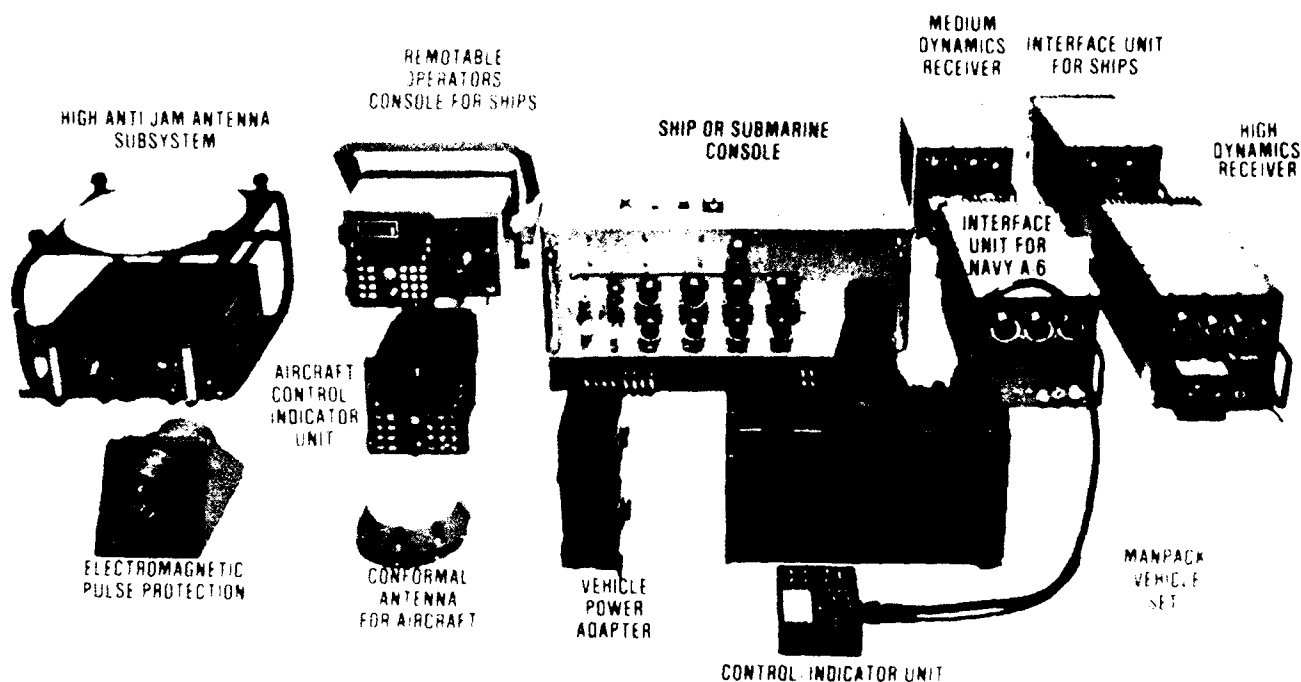
Figure 21. Generalized Block Diagram of a GPS User Equipment Set

#### PRODUCT DESIGN

Figure 21 shows the general user equipment set concept. The configuration is revised, as required, for specific users. For example, most users do not require the Flexible Modular Interface (FMI) unit or its associated software because the basic host vehicle interface circuits are incorporated inside the Receiver Processor Unit (RPU). Therefore, host vehicle sensors and displays, if any, interface directly with the RPU in most vehicles. Also, some vehicles use their existing control/display units in lieu of the GPS Control/Indicator Unit (CIU) shown. Figure 22 shows the family of Line Replaceable Units (LRUs) that satisfy this set concept for the current field test vehicles. Other set configurations of these same LRUs will address the hundreds of host vehicles to be fitted with GPS during Phase III.

#### Receiver/Processor Units (RPU)

By choosing between the three RPUs shown in Figure 23, the user can select a unit that has performance adequate for his needs without the cost burden of



1283 7022  
101182 31

Figure 22. GPS User Equipment Family of LRUs.

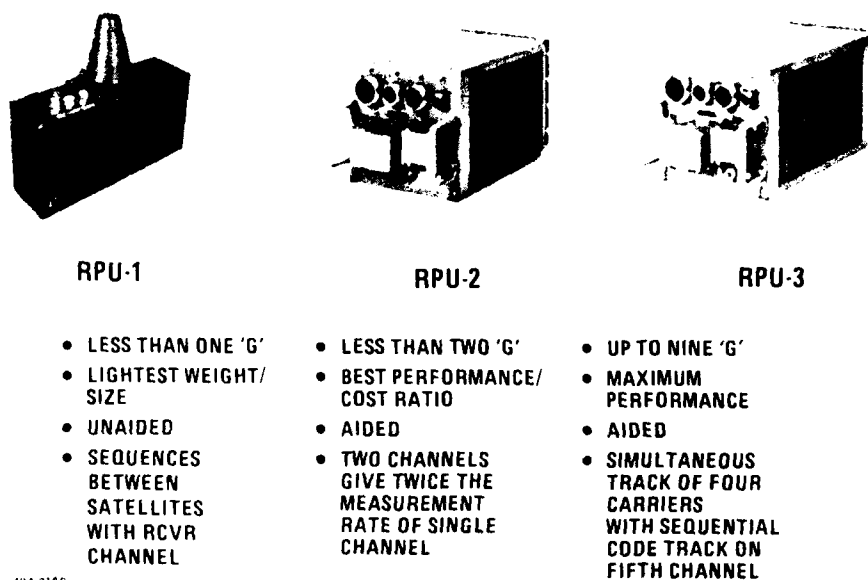


Figure 23. Dynamics, Reaction Time, Weight/Size, and Performance/Cost Establish Three Receiver Types

excessive performance. Thus, the manpack and land vehicle user has a single-channel, low-cost, light-weight set, while high dynamics fighter, attack or strategic aircraft have a five-channel set with attendant moderate increases in cost and weight. The submarine user also requires a five-channel set, even though it is a low dynamic situation. The five-channel set in the case of the SSN provides very fast acquisition and fix times as required to minimize exposure of the antenna above the ocean's surface.

#### Common Modules

Figure 24 shows the modular architecture of the RPUs. One of the attributes of Magnavox user equipment that has delighted service personnel involved in the field tests is the easy interchangeability of circuit boards between units and between card slots within each unit. During field tests, RF and baseband printed circuit boards (there are five baseband modules in a 5-channel set) have been lifted out of their slots and swapped

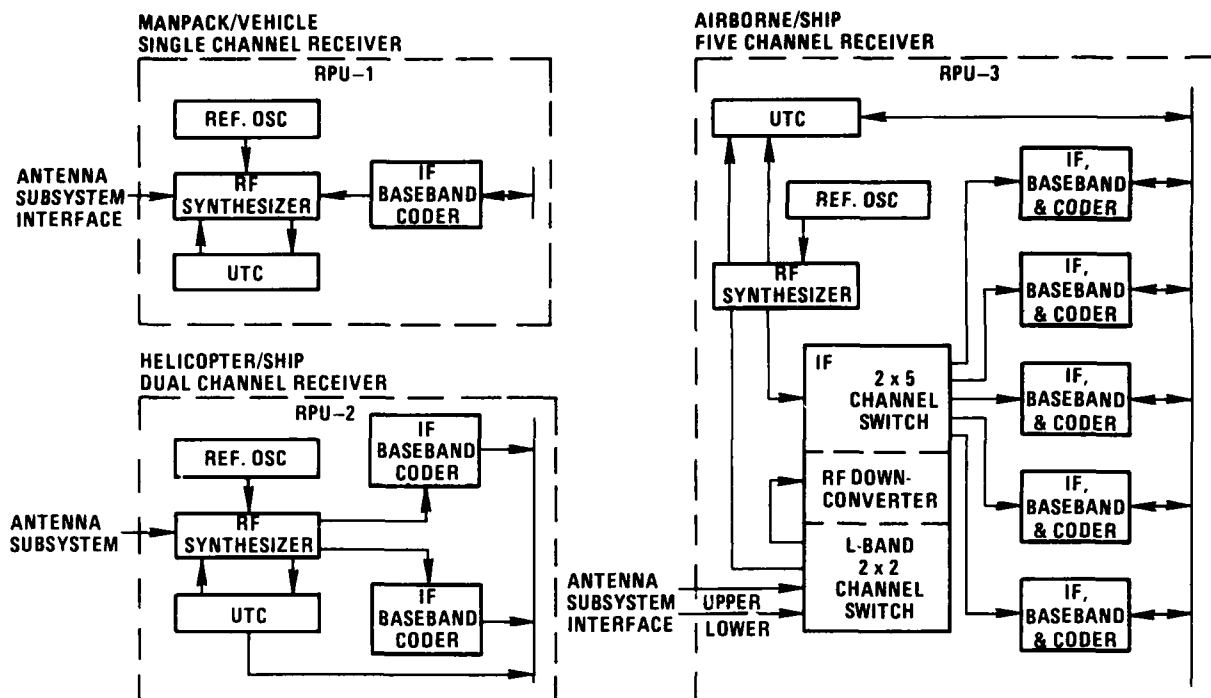


Figure 24. Modules are Interchangeable Between the Three Receivers

with similar boards from other slots in the same receiver/processor, or from a different receiver/processor, and the unit has continued to operate without adjustment after the interchange. Once a circuit board leaves the factory, it can be used in any of the 3 receiver/processor units regardless of number of channels, and without any "tweaking" between installations. The same oscillator is used for all three RPUs. The Phase II oscillator is at 10.23 MHz, but 10 MHz will also be considered for Phase III. This commonality among all RPUs has been designed with the user's reliability, maintainability, and logistics concerns in mind.

#### Host Vehicle Interfaces

The electrical signal interfaces of thirty host vehicles, from manpack to aircraft carrier, were analyzed to establish an equipment architecture that would readily adapt to each vehicle with the least number of "black boxes." Thirty-eight unique signals were identified of which 17 were analog and 21 were digital. By allocating the circuitry necessary for these interfaces across ten plug-in circuit boards, the interface requirements for all thirty vehicles were met. More significantly, 70% of all five-channel requirements were met with only one of these circuit boards and 55% of all two-channel requirements were met with another one of these circuit boards. As shown in Figure 25, these two interface boards are built into their respective GPS receiver/processor units, thus eliminating the need, in the case of most host vehicles, for any extra black boxes or add-on modules for electrical interfacing. Currently, the only vehicles that have required additional interface units are those with special data processing added to their normal interface requirements. These include the Grumman A-6E attack aircraft with its unique requirement for GPS controlled weapon delivery, and surface ships and submarines which require special 60 Hertz synchro signals and processing for fault isolation to the Shop-Replaceable-Unit (SRU). Figure 25

shows the location of the oscillator for RPU-1, 2, and 3. This location was selected for low temperature rise and low vibration amplification.

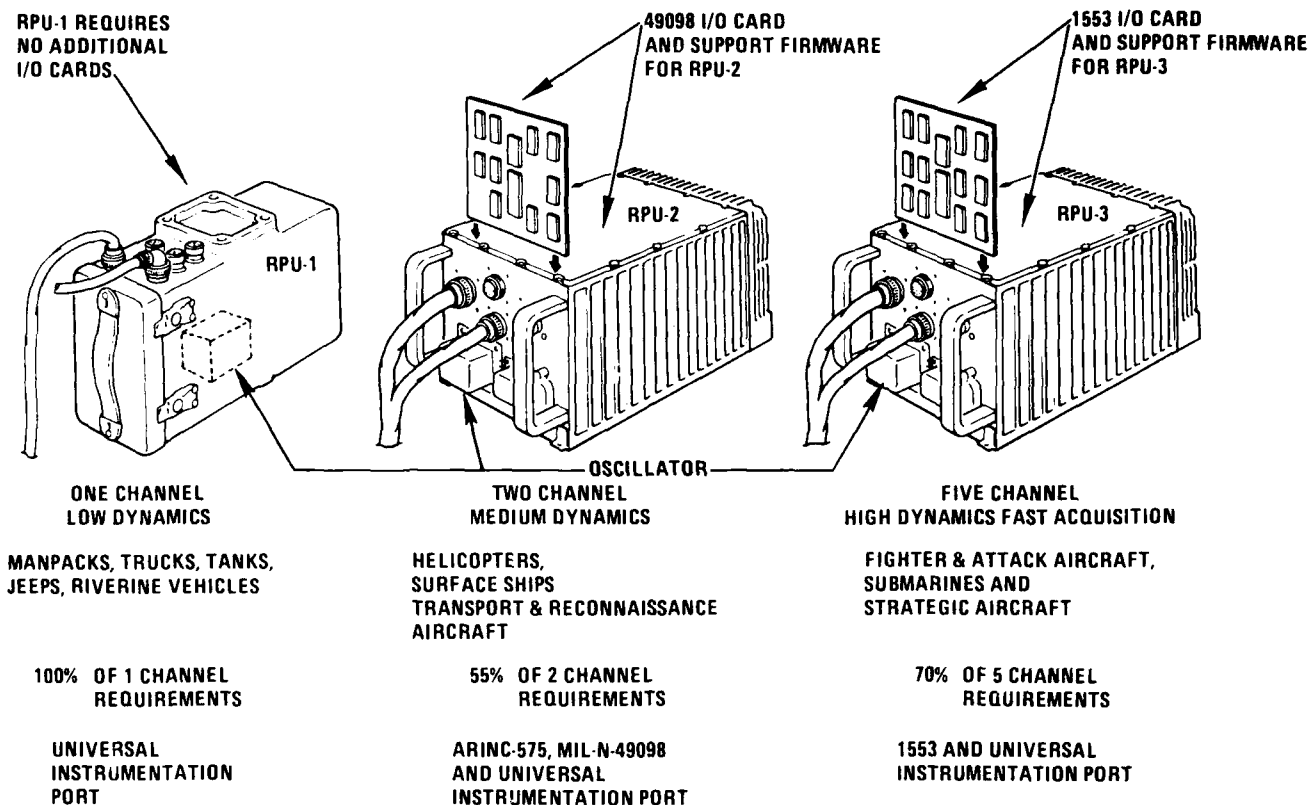
#### Software Adaptation

The software for all vehicles that use a given class of receiver processor unit (1, 2 or 5 channel) resides in that unit along with a table that defines the proper software and signal interface configuration for each vehicle. This table is triggered to the appropriate configuration for any given vehicle by jumper wires in one of the vehicle's interface plugs. Thus units can be swapped between different vehicles and between vehicles and maintenance centers without special stocking or adjustments to match them to the unique host vehicle.

#### Integration With Other Sensors

Three distinct navigation modes were developed to fully exploit the multitude and types of sensor data available within the interfacing constraints imposed by each host vehicle specified for GPS. The mode selection is microprocessor controlled by the host vehicle identification code. Vehicles which have their sensors fully integrated with GPS allow calculation of a more accurate navigation solution. However, in the absence or failure of host sensors, sensor-aided operation (loose coupling) is automatically selected. The three modes are as follows:

1. **Acceleration Coupled:** In this mode, which provides the most accurate navigation performance, the GPS set is fully integrated with an INS, such that the IMU-provided acceleration data are used directly to propagate the navigation states.
2. **Velocity Coupled:** In this mode, the set is integrated with an INS, doppler, or speed-and-heading sensor, and the host vehicle



684-3124

Figure 25. The Majority of Host Vehicle Interfaces are Accommodated Without any Extra Interface Units

sensor velocity data is used directly to propagate the navigation states. When an I.S. is available, the best performance is achieved by the previously mentioned acceleration-coupled mode. However, since outputs for acceleration data are not always available in certain host vehicles, it is sometimes necessary to employ the velocity coupled mode.

3. Loose coupling (unaided): In this mode, host vehicle sensor data are not used for state propagation. The filter estimated velocity (and acceleration for high-dynamics vehicles) is/are used to propagate the navigation states in a self-contained manner. Host vehicle sensor data, if available, are used as level-of-dynamics indicators and as alternate measurements by the Kalman Filter. Furthermore, host vehicle sensor data are calibrated during "good" GPS tracking to facilitate rapid reacquisition in case of signal loss.

Figure 26 shows the use of these three modes across the spectrum of IOT&E vehicles.

#### Antennas

The same omnidirectional antenna that is used in man-pack GPS sets is used for land vehicles, aircraft carrier and helicopter installations and, indeed, in any installation where aerodynamic drag is not a serious factor. This same antenna with a pressure-proof radome is being delivered for submarine installations of certain NATO forces. It has the attribute of an excellent hemispherical reception pattern with relative independence from the type of ground plane upon

USER TYPE	ACCELERATION COUPLING	VELOCITY COUPLING	LOOSE COUPLING
MANPACK & LAND VEHICLE			✓
HELICOPTER (UH-60)		✓	
ATTACK AIRCRAFT (A-6E)	✓		
FIGHTER AIRCRAFT (F-16)	✓		
STRATEGIC BOMBER (B-52)		✓	
SURFACE SHIP (CV)			✓
SUBMARINE			✓

Figure 26. Acceleration Coupling Provides the Most Accurate Performance of the Three Sensor Coupling Modes and is used in the High-Dynamic Vehicles

which it is mounted. A low-profile omnidirectional antenna is available for moderate to high speed aircraft.

A single, seven element, low-profile, null steering antenna is used for those applications from manpack to supersonic fighters, where severe jamming is expected to be encountered. This use of common antenna designs across many different vehicles (see Figure 27) is one of several system design features that contribute toward reduced life-cycle cost.

#### Adaptation To Shipboard Environment

The GPS LRUs are fundamentally aircraft units designed to MIL-E-5400 environmental requirements. However,

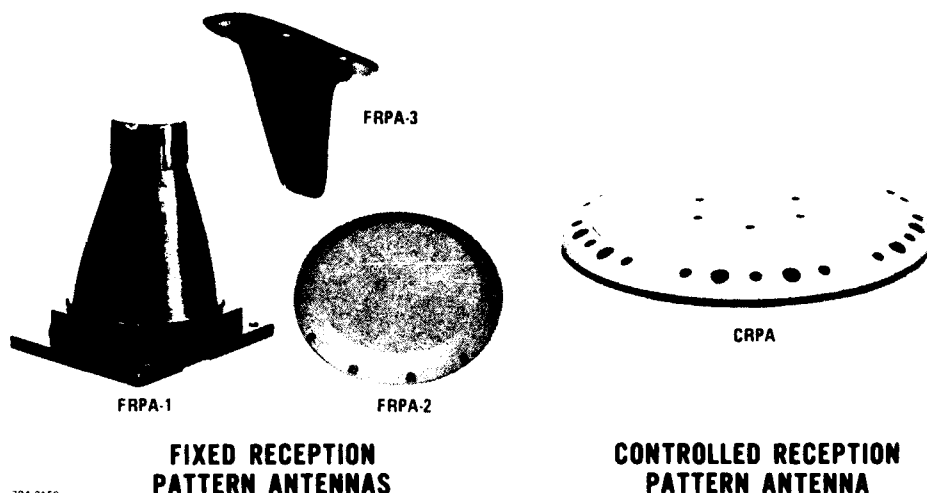


Figure 27. Four GPS Antennas Satisfy all Operational Requirements

they are adapted to the severe shipboard environmental requirements of MIL-E-16400, such as shipboard shock, vibration and hammer blow, by mounting within protective console units as shown in Figure 28. These consoles also provide intra-system wiring harnesses and accommodate additional Navy requirements, such as 60 Hz power, thermal protection, battle-short switches, and master/slave controls and indicators. The master/slave modes allow operation of a single set from two remotely located Control/Indicator Units (CIUs).

The previously mentioned automatic software reconfiguration includes lockout of airborne displays and functions, such as true airspeed and vertical navigation, and substitutes shipboard functions with appropriate nomenclature such as speed-thru-the-water and sea and set drift.

#### GPS System Simulator

Magnavox has designed and constructed several sets of GPS system simulators called the Multiple Channel Signal Generator (MCSG). The MCSG generates six independent GPS RF signals from a GPS Waveform Generator (WFG) and host vehicle data link signals which simulate anticipated operational missions scenarios

involving the GPS user equipment. The MCSG models the combined effects of control segment functions, space segment functions, host vehicle characteristics, mission dynamics and environments. The MCSG also provides the repeatability necessary for effective testing and training. From data recorded during a simulation, the MCSG is capable of producing system performance and mission evaluation data. The MCSG is currently being used in the design and evaluation of the GPS user equipment being built as a part of Phase IIB (see Figure 29). Each of the six WFG transmitters simulates the GPS satellite and can be driven from its own oscillator or each can be phase-locked together and driven from a GPS cesium standard at 5.115 or 10.23 MHz for improved long term stability.

#### Set Maintenance

Magnavox has designed and built a field support test set which detects and isolates faults to a Shop Replaceable Unit (SRU) for all line replaceable units (LRUs) including RPU-1, RPU-2, RPU-3, CIU and FMIU's. This equipment was designed to meet the military intermediate maintenance requirements during the Phase II testing of the user equipment and is known as the Intermediate Maintenance and Test Set (IMTS). Its

- SHIPBOARD SHOCK, VIBRATION
- HAMMERBLOW TEST
- OVERHEAD MOUNTING OR BENCH MOUNTING
- 60 HERTZ POWER
- NO EXTERNAL NIGHT ILLUMINATION SOURCE
- MIL-E-16400 TEMPERATURE AND CIRCUIT PROTECTIVE DEVICES
- SHIPBOARD NOMENCLATURE
- DUAL CIU OPERATION
  - MASTER/SLAVE OPERATION
  - SEPARATE WAYPOINTS FOR EACH CIU

684-3102

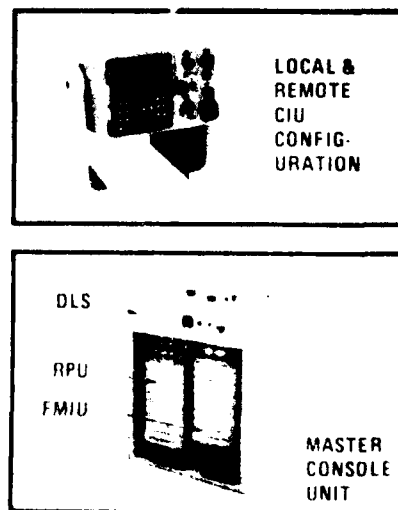


Figure 28. LRUs Adapt to Sea Environment Through Use of Shipboard Housings

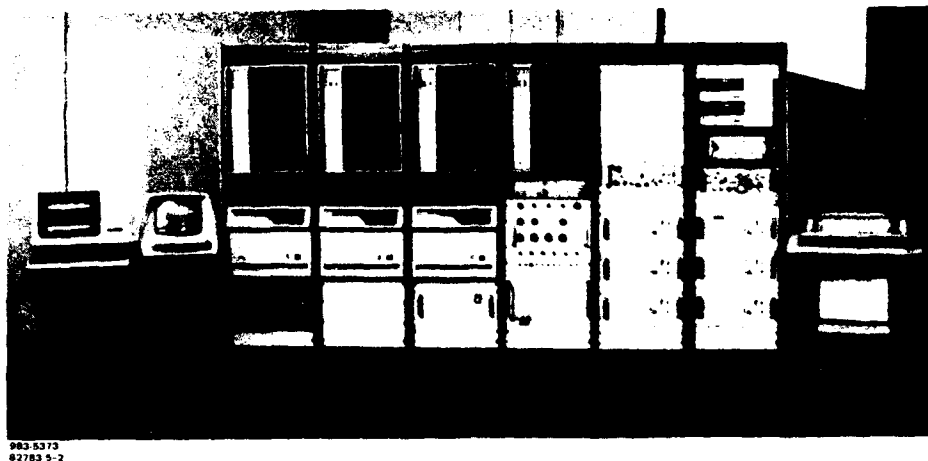


Figure 29. GPS Multi Channel Signal Generator (MCSG)

ruggedized construction, portability, ease of operation and functional capabilities will enable its use in a variety of circumstance, from routine flight line check-out to maintenance support for remote base operations. The IMTS can be operated from a 115 VAC power source, or from an internal battery. This equipment is currently in use at Magnavox Torrance, California and at several of the field test sites (see Figure 30). The oscillator in the IMTS can be used to test the oscillator in the GPS Phase III user equipment or to transfer frequency from a cesium to the user receiver via the IMTS.

#### Pre-Planned Product Improvement (P<sup>3</sup>I)

The Magnavox GPS user equipment was designed from the outset for insertion of new hardware technology as it evolves, without the need for major redesign with each insertion.

An aggressive but disciplined P<sup>3</sup>I program, with progressive technology insertions, will reverse the normal trend of increasing cost of subsequent production buys of military electronic equipment. This decreasing cost will come in spite of factors that tend to add cost, such as inflation, or component obsolescence. Furthermore, if the pre-planning is properly carried out, past and future deliveries can be improved in

overall capability at modest cost without affecting existing or future host vehicle installations. The Magnavox GPS user equipment is pre-planned for future improvements and is configured to capture the inevitable benefits of the improving technology inherent to LSI, VLSI and beyond (see example in Figure 31). Product reliability and overall performance will improve with each technology insertion and lower overall life-cycle cost will prevail as older sets are upgraded through P<sup>3</sup>I (see example in Figure 32).

The P<sup>3</sup>I ground rules which will be applied to GPS Phase III are quite simple:

1. Freeze the basic hardware and software architecture at the beginning of Phase III.
2. Rigidly maintain two-way interchangeability at the SRU or Shop-Replaceable-Unit (e.g., Printed Circuit Board), and the LRU or Line-Replaceable-Unit, (e.g., Black Box).
3. Test new, technology inserted, SRUs for two-way transparency before delivery into any existing or new LRUs.
4. Control Form/Fit/Function at the LRU/SRU level to ensure that the last product delivered is compatible with the first product delivered.

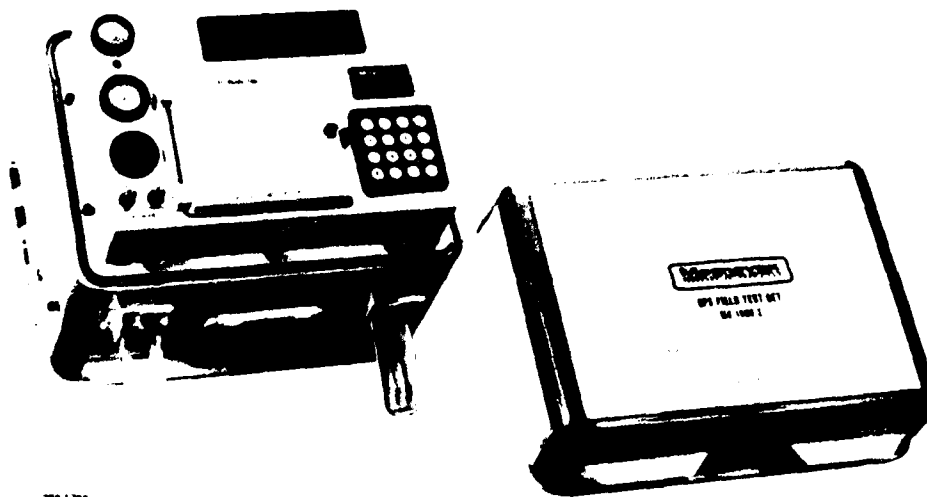
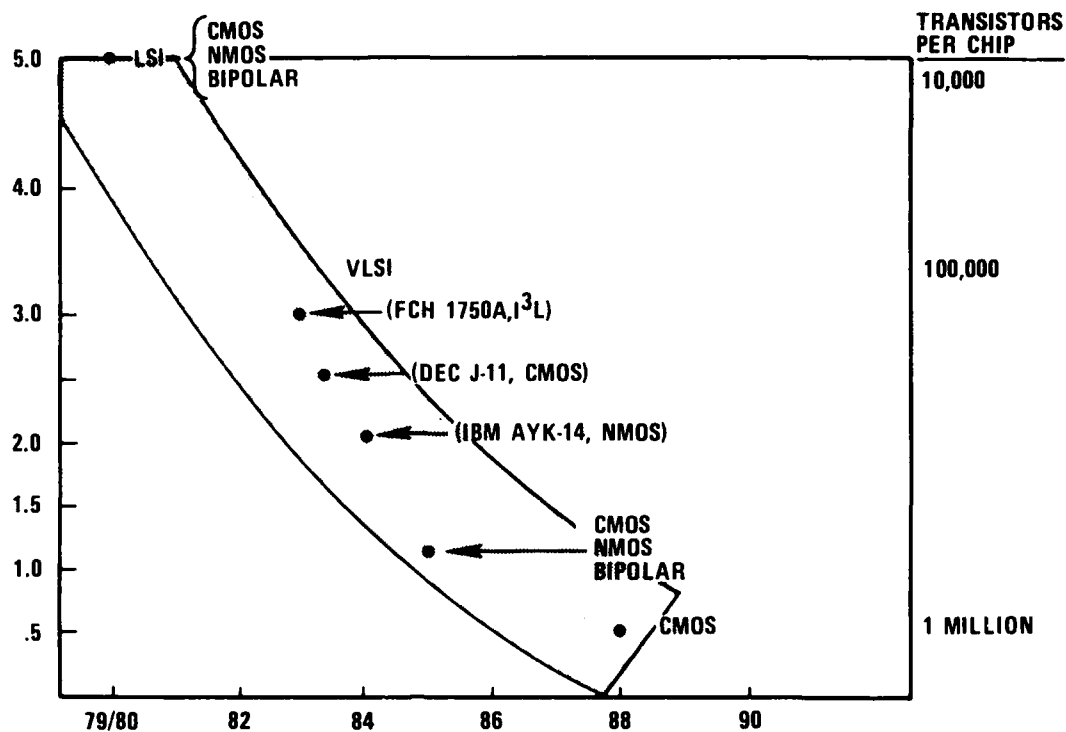


Figure 30. Intermediate Maintenance and Test Set (IMTS)

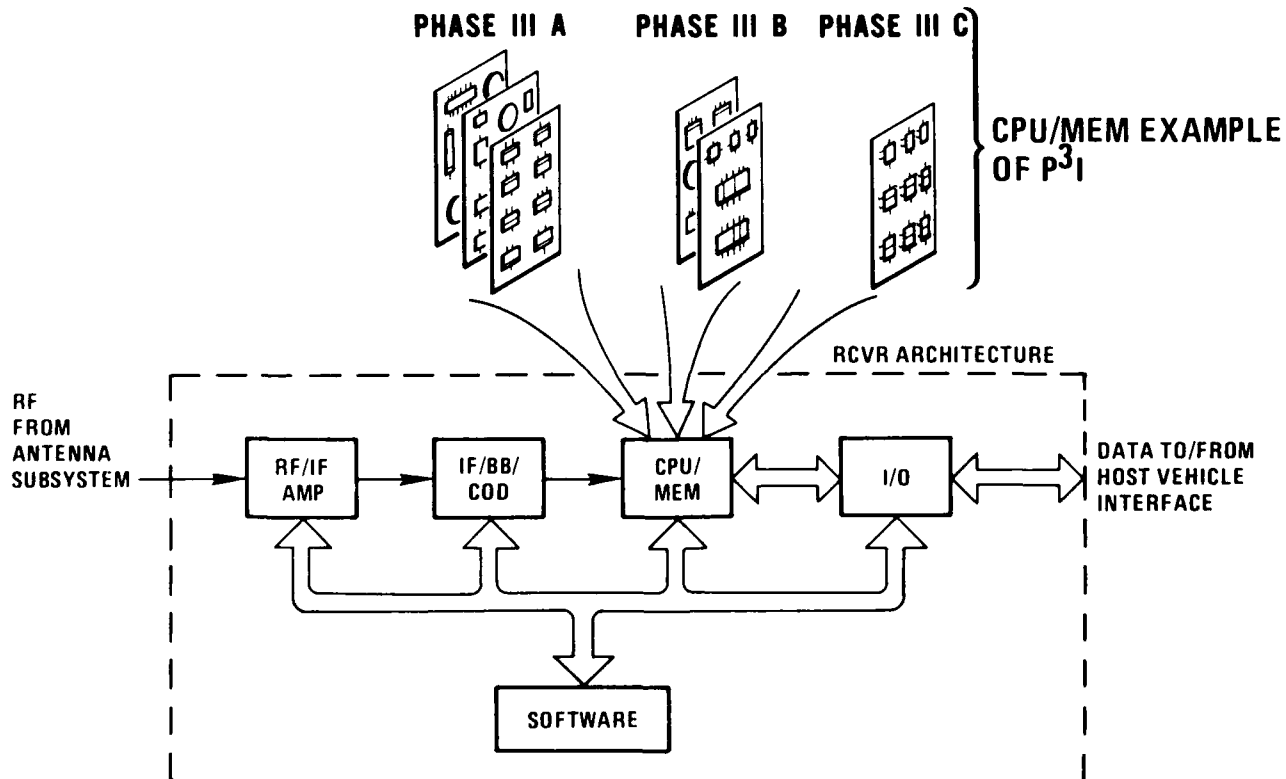


**DESIGN RULES**  
(MINIMUM FEATURE  
SIZE OF GATE  
CHANNEL LENGTH  
IN MICROMETERS)



584 2351

Figure 31. Technology Trends



284 990

Figure 32. System Architecture & Software Remain Constant While Unit Production Cost Comes Down Through Technology Insertion

5. Insert new technology only when economically justified.

#### Transparency Verification

P<sup>3</sup>I implementation can be self-defeating without a rigorous test program to verify the forward and backward compatibility of technology insertion. Under P<sup>3</sup>I ground rules technology insertion should be implemented only if it proves totally transparent to the various platform and user applications.

Progressive tests for transparency are performed starting with parts quality and environmental tests at the module level. Such tests are followed by functional verification tests in a laboratory simulation of full environment requirements to include SRU acceptance tests, regression tests compared to the pre-established baseline, and maintainability tests to ensure the integrity of test sets and IMTS, and the integrity of operational maintenance procedures. Finally, testing is done in the field with in-place resources as well as with user platforms to verify that the new modules do not affect equipment performance in the actual environment and that operator interaction and equipment interfaces have not changed.

#### FIELD TEST RESULTS

The field test program is being conducted using the C-141 and M-35 platforms exclusively for DT&E testing, while the remaining host vehicles (manpack, M-60 tank, CV aircraft carrier, UH-60 helicopter, F-16 fighter aircraft, B-52 bomber, A-6E fighter/attack aircraft and SSN submarine) are used for both DT&E and IOT&E activities. Thus far, tests on Magnavox GPS sets have been conducted in the C-141, M-35, manpack, M-60, UH-60, and CV-63.

Testing to date has concentrated on host vehicle integration confirmation and on set performance verification in such areas as static/dynamic navigation accuracy, acquisition/reacquisition scenarios, jamming performance, antenna pattern verification, and human factors. Magnavox sets have demonstrated compatibility with the host vehicle interfaces to the extent that testing on the UH-60, CV-63, and M-60 have been carried out on the actual platforms. The preliminary test results are reported in the following paragraphs.

#### Accuracy

Initial testing in the C-141 during February 1983 revealed both random and bias errors in the Magnavox equipment. By June, the random errors had been reduced within the specified limit for the system, and by November 1983, the bias error was successfully isolated and eliminated. Figure 33 shows one of the early tests of a two-channel set at Yuma Proving Grounds before the bias error had been eliminated and also before ionospheric correction of the satellite signals had been incorporated. At the start of this plot, all four satellites are acquired while the host vehicle (M-35 truck) is moving at approximately 15 MPH. At 0244 hours, the truck comes to rest and the remainder of the plot shows static performance. Figure 34 shows the "ground truth" errors that prevailed during this test. Ground truth is that part of the position bias error due to the space segment. Ground truth information is obtained from a calibrated GPS receiver located on a surveyed bench mark in the immediate vicinity of the test range.

Figure 35 shows a recent test (January 1984) of the two-channel set in a UH-60 helicopter. Figure 36 shows the ground truth plot for this test. As the test begins, the set is reinitialized and commanded to

collect new ephemerides while the helicopter is stationary near a surveyed bench mark. At 1330, the helicopter takes off and proceeds to the first of two waypoints that are 15 kilometers apart. Four minutes are lost from the plot (1330 to 1334) between take-off and laser-tracker acquisition. The remainder of the plot shows the accuracy performance as the helicopter flies back and forth between the two waypoints. The error peaks on the plots coincide with the turns at the waypoints. The GPS set under test has software improvements incorporated to eliminate the previously mentioned bias error and to perform ionospheric correction. In Figures 35 and 36, it can be seen that it was a good day for the GPS set, but not one of the space segment's better days. In any case, this unaided set demonstrated errors which were typically less than 5 meters from ground truth. In a later test that day, the set was flown with doppler aiding (not shown). The set performance was essentially the same as shown in Figure 35 except that the error peaks in turns were eliminated. These tests include the effects of the oscillator stability during vibration.

Test results in other vehicles are still anecdotal in nature. For example, the aircraft carrier navigator began to use the GPS derived position data in his hourly log instead of the multi-sensor data he normally used. This happened after it was discovered through crosssensor checking and radar measurements that the GPS accuracy was better than that of the system planned for measuring GPS accuracy performance. Army helicopter pilots for a period of time, routinely flew IFR cross-country missions in the New Jersey area using a Magnavox two-channel set to drive the pilot's flight director indicators. The GPS equipment has typically guided the aircraft to within a few meters of enroute checkpoints, including nap-of-the-earth flights where VOR signals drop out, and during flights through very heavy rain and low visibility.

#### Acquisition Time

As shown in Figure 37, initial acquisition times under dynamic conditions are consistently below the 5.5 minute specification limit. Field tests of a single channel set in the M-35 truck resulted in a mean time of 4 minutes 26 seconds with standard deviation of 36 seconds. The minimum acquisition time from a cold start was 3 minutes 27 seconds with a maximum of 5 minutes 31 seconds. Ninety percent of initial acquisitions occurred within 5 minutes 15 seconds of start. Similar results have been obtained, but not yet formally documented, in two-channel helicopter and aircraft carrier sets.

#### Jamming Performance

Tests were conducted on the C-141 aircraft, alternately using a Controlled Reception Pattern Antenna (CRPA) and a Fixed Reception Pattern Antenna (FRPA). The aircraft was flown on a descending path directly over a field of jamming transmitters, while making banking maneuvers to expose the GPS antenna to direct jammer radiation.

Closest encounter was approximately 1500 feet. While the measured performance data are classified, we can state that the Magnavox equipment exceeded the specification requirements for maintaining signal lock by several dB of jammer-to-signal ratio. The null-steering antenna (CRPA) with its Antenna Control Unit (ACU) successfully nulled several jammers simultaneously. When jammers were able to cause break of lock on the CRPA or FRPA equipped sets, the satellite signals were reacquired within seconds after the aircraft banked away from the successful jammer's antenna beam.

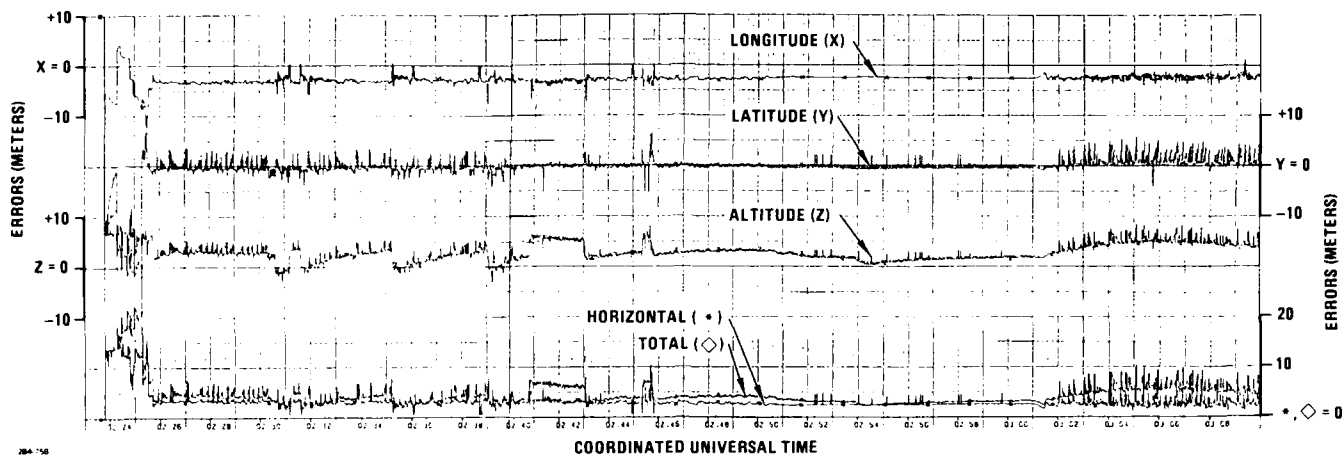


Figure 33. Position Error Plots, 2-Channel GPS Set on M-35 Truck.  
No Ionospheric Correction in Set. Satellite Induced Errors Included.

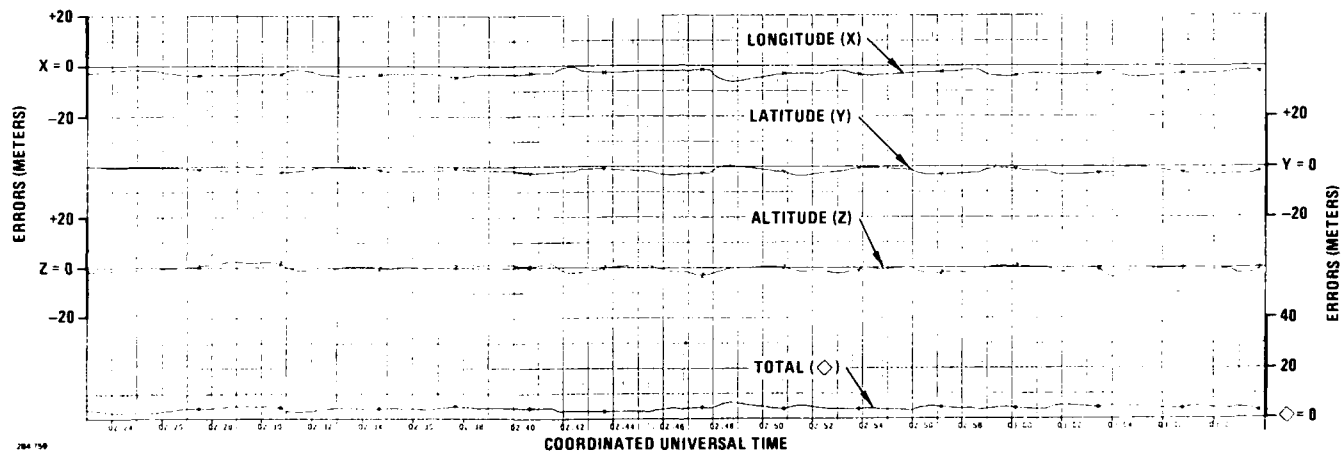


Figure 34. Ground Truth (Satellite Induced Error) Plot During Test  
of 2-Channel GPS Set on M-35 Truck

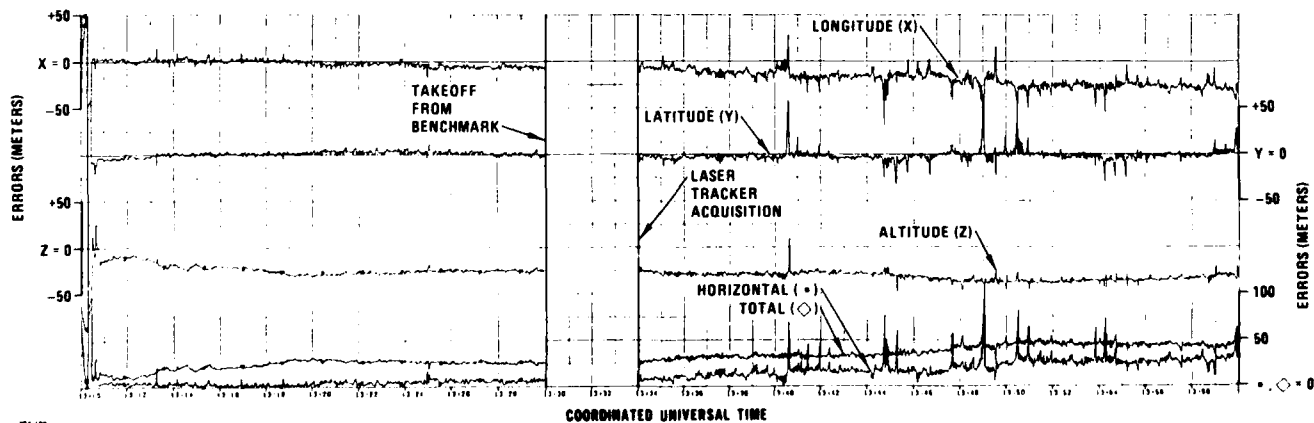


Figure 35. Position Error Plots, Unaided, 2-Channel GPS Set with Ionospheric  
Correction in UH-60 Helicopter, Satellite Induced Errors Included.

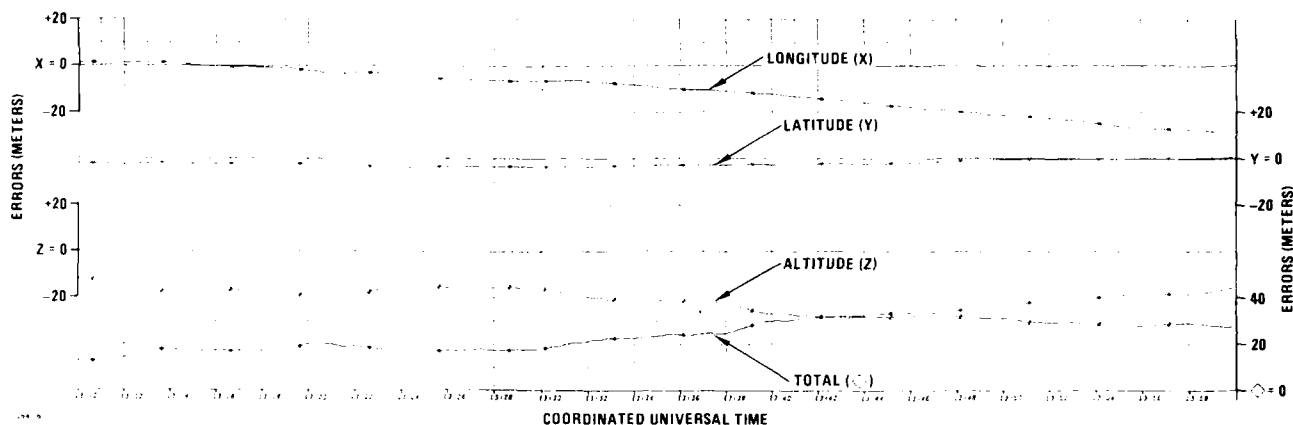


Figure 36. Ground Truth (Satellite Induced Error) Plot During Test of 2-Channel GPS Set in UH-60 Helicopter

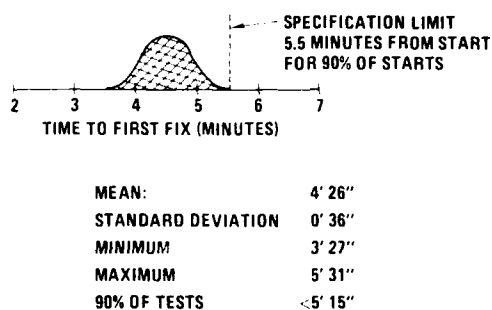


Figure 37. Time to First Fix, Distribution of Field Test Results, Single Channel Set

#### Environmental Performance

Vibration conditions on board the UH-60 helicopter and M-60 tank caused initial problems of a non-structural nature which were quickly resolved. For the most part these problems have not reoccurred. However, an Instrumentation Buffer Box (IBB) and a Digital Tape Recorder (DTR), located on the floor of the M-60 tank turret, encountered a particularly severe shock and vibration problem. While both the IBB and the DTR are for instrumentation purposes during the DT&E and IOT&E phases of the program and are not intended for actual operational use, it is imperative that they be able to survive and adequately perform within the environmental conditions which will be experienced throughout the test program. Combining minor internal modifications with a substantial improvement to the shock and vibration isolation design resolved these problems. Successful testing in the M-60 tank is now underway. The GPS test facilities on-board CV-63 (the Kitty Hawk) are being transferred to CV-64 (the Constellation). As a part of this move, the Controlled Reception Pattern Antenna (CRPA) and Antenna Control Unit (ACU) were removed from the mast. Detailed examination of the removed units revealed that sea air corrosion had advanced more rapidly than expected. Analysis of each unit is underway and resolution of this problem is expected before the next sea air exposed installation is carried out.

#### Human Engineering

Reports from the field have been generally favorable. Soldiers, shipboard personnel and Army helicopter

pilots exhibit an overwhelming preference for the new GPS equipment over the older on-board navigation systems. Military personnel have demonstrated rapid learning times after first exposure to the equipment. Soldiers have become proficient in the use of Magnavox Manpack/Vehicular equipment with one or two hours of coaching by field engineers.

Army helicopter pilots, already trained and accustomed to the control/display unit of their AN/ASN-128 Doppler Radar, have little difficulty transitioning to the GPS control/display, which fits in the same location and uses the same sunlight-readable incandescent displays as the doppler's original control/display unit. In addition to physical compatibility, the GPS equipment expands the helicopters' navigation capability from a 10-waypoint, 2-dimensional, dead-reckoning area navigator, to a 200-waypoint, 3-dimensional, position fixing area navigation system. All of the original capability of the doppler is retained, including the doppler itself as an aiding and back-up navigation sensor.

Similarly, shipboard personnel already trained and accustomed to Transit, Loran and Omega/VLF systems, find the Magnavox GPS equipment easier to use and prefer its large incandescent displays over the CRT displays of some of the older equipment, for across-the-room viewing in the chart room and for viewing in sunlight conditions on the bridge.

The Magnavox approach to human engineering for the military user is based on the assumption that his mind is occupied by more important duties than supervising the operation of a navigation system. Accordingly, a simple command approach to control and data access is used in lieu of the more complex teaching machine, interactive, menu-driven, double-function-keyboard approaches. Using the Control/Indicator Unit (CIU) shown in Figure 38, soldiers simply turn a rotary switch to one of twelve positions to select logical pairs of data, such as latitude/longitude, range/bearing, etc. Sailors and airmen have no difficulty in accessing over fifty different parameters for display by simply pressing one of seven data category buttons until they see the data they want. For example, all three vectors of the classical navigator's wind triangle are available with three presses of the VELOCITY button.

Similarly, data in the categories of POSITION, TIME, MISSION, VERTICAL NAVIGATION, AREA NAVIGATION and STATUS are rapidly accessed. Off-nominal conditions,

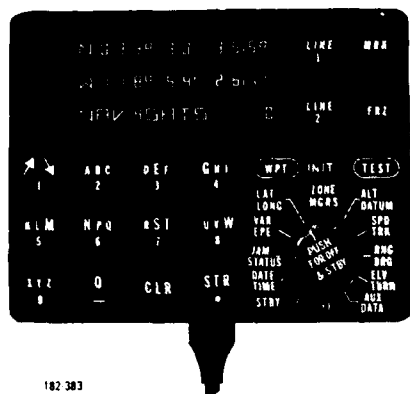


Figure 38. Manpack Control/Indicator in the Size of a Hand Calculator, Fits inside the RPU Case, Has Simple Rotary Switch Data Selection

such as intense jamming, are instantly flashed in an area of the control panel dedicated to alerts and warnings (see Figure 39).

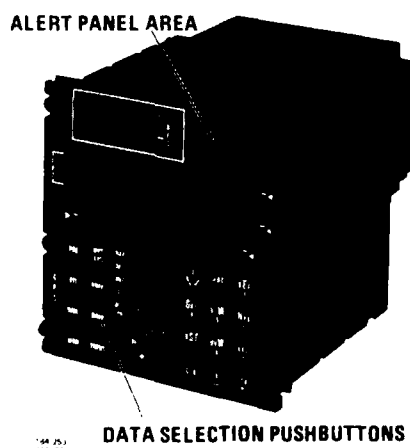


Figure 39. Control/Indicator Unit for Ships and Aircraft has Sunlight Readable Displays, Pushbutton Data Access, No Menus

#### SUMMARY

Results of initial and mostly informal testing have met or exceeded specification requirements for accuracy, acquisition/reacquisition time, anti-jamming performance and human factors. The oscillator is shown to be a key part of the system performance. Within the present limitations of satellite signal availability, soldiers, sailors and airmen exhibit an overwhelming preference for the new GPS equipment over their pre-existing on-board navigation systems. The equipment is designed to capture the performance/cost benefits of advancing technology without major retrofit or redesign implications. New installations may be planned without risk of subsequent retrofit or early obsolescence. The last product delivered will be compatible with the first product delivered.

#### ACKNOWLEDGMENT

The GPS program effort described in this paper is being performed under contract to the Navstar Joint Program Office of the U.S. Air Force Space Division, El Segundo, California.

#### BIOGRAPHIES

David L. Hessick attended the California Polytechnic State University at San Luis Obispo graduating with a Bachelor of Science degree in Electronic Engineering in 1966. He did graduate studies in solid state physics, and communications systems at the University of California at Los Angeles (UCLA) from 1969 to 1971. He further pursued his education and graduated with an MBA from Pepperdine University in Malibu, California, in 1979. He spent the first 2 years of his career as a design engineer at Advanced Communications, Inc. in Chatsworth, California on wideband frequency hopping HF, UHF, and S-band receivers and transmitters. The next 2 years he was at the Magnavox Research Laboratory as a senior RF engineer where he did design and development of wideband PN spread spectrum UHF receivers and transmitters and anti-jam modems for X-band satellite communication terminals.

In 1971 he joined TRW as a senior communications engineer designing, developing, and marketing hybrid microelectronic broadband VHF/UHF RF power modules. He also was program manager for a high power UHF ultra-linear solid state power amplifier.

In 1972 he returned to Magnavox where his first task was to do the RF design for the Navy Timation III receiver. He then worked on the USC-28 satellite spread spectrum transmitter and receiver and the TDRSS S-band transmitter and receiver. Later he was program manager for the research and development prototype model of the Marisat satellite ship terminal and various studies for X, Ku, and Ka band wideband spread spectrum modems. In 1974 he became the cognizant RF engineer for design and development of all GPS Phase I receiver and transmitter products. These included the X, Y, Z, Manpack Sets and the GPSPAC satellite based receiver. For GPS Phase II he has been the Section Manager, Engineering Manager and is currently the Department Manager for Receiver Engineering, responsible for technical management of all GPS receiver and transmitter product designs. He has been actively involved with oscillators on GPS.

William C. Euler attended the University of Buffalo, New York, graduating with a Bachelor of Science degree in Electrical Engineering in 1956. He spent the first two years of his career with Sylvania in Buffalo, involved in circuit design for the B-58 Hustler Electronic Countermeasures System. A tour of duty with the Air Force followed Sylvania. While with the Air Force, he was assigned to the National Security Agency at Ft. Meade, Maryland.

Mr. Euler first joined the Magnavox Company in June 1959. During this first "tour" with Magnavox, he served as a Design Engineer, Project Engineer and Program Manager. He was awarded two patents, one for a digital pattern generator and the second for an RF Multicoupler.

In 1963, Mr. Euler left Magnavox to join Geo Space Systems Inc., in Florida. While at Geo Space, he served first as Director of Engineering and then as Vice President of Marketing. In 1967, he left Geo Space to return to Magnavox in Torrance, California. At Magnavox his assignments have included Product Manager for Space Communications, Director of Engineering, and Director of the Marine Systems Operation. He

<sup>1</sup>J. Moses, et al., Navstar Global Positioning System  
Oscillator Requirements for the GPS Manpack, June  
1976, 30th Annual Symposium on Frequency Control.

was eventually appointed Vice President for that operation. In 1978, he was appointed Vice President of Marketing for the Magnavox Advanced Products and Systems Company and then Vice President of Programs for the Communications and Navigation Division (CND). In 1982, he was selected to form the Navigation Systems Operation (NSO), and serves as Vice President of that operation at the present time. Throughout the 1982/1983 time frame he also served as the Program Director for the Magnavox GPS Phase II User Equipment Program. Mr. Euler is a member of the IEEE, the Association of the U.S. Army, the Navy League, the Air Force Association and Institute of Navigation. He currently serves as the Chairman of the Satellite Navigation Division of the ION.

## A TIME AND FREQUENCY REFERENCE SYSTEM FOR THE TACAMO AIRCRAFT

T.C. Jewell and J. D. Geist  
Frequency and Time Systems, Inc.  
Beverly, MA

### Summary

The Navy's Tacamo program employs a time and frequency reference system consisting of two identical crystal standards -- each capable of fifty hours of battery operation -- and a satellite time reference capable of receiving UTC from the Navy Navigational Satellite System (NNSS). The latter instrument contains an integral rubidium frequency standard for calibration purposes. In use, such a system allows a triple redundancy in the timing signals necessary for the operation of the Tacamo System, and additionally allows the crystal standards to be battery operated (which gives protection against nuclear electromagnetic pulse damage). In case of loss of the NNSS signal the system not only remains functional using the crystal clocks but in addition, one of the crystal clocks can be used to obtain time at a ground facility through its use as a portable clock with fifty hour battery operation. This paper describes the design and function of the Tacamo Survivable Time System.

The Satellite Time Reference is a multiple function rack mountable instrument that provides UTC through reception of the fiducial time mark broadcast by the NNSS satellite constellation. The STR displays time of day and provides a serial time code output, both derived from an internal 1 pps which is derived in turn from the 5 MHz provided by the STR's rubidium standard. A number of other functions are available. These include the capacity to compare external time and frequency sources to each other and to the internal oscillator. The major functions of the instrument are performed using a 6802 microprocessor. UTC can be acquired and maintained to within approximately 30 microseconds.

The Frequency Standard is also a multiple function rack mounted instrument; it employs as its internal reference a version of the FTS 9000 oscillator which features stability in the  $10^{-13}$  range and aging of parts in  $10^{-11}$  per day. The instrument displays time of day and is capable both of synchronizing its clock output to an external signal and of advancing its 1 pps output using front panel controls. Internally, the instrument contains clock buffers and time circuitry as well as automatic switch over capability to protect against loss of its internal or external frequency reference signals. In addition, it contains batteries and a multifunction power supply capable of operation from various power sources.

### Introduction

There exist various methods which have been proposed to satisfy the Navy's need to communicate with its submarines when they are underwater. Among these are the ELF system, whose major drawback is that it cannot be implemented as a hardened system without the possibility of major environmental impact; a system involving the use of laser in the blue-green range mounted on a satellite; and the method to be discussed in this paper -- the VLF TACAMO survivable system..

TACAMO -- an acronym for "take charge and move out" -- consists of a squadron of C-130's and associated communications equipment. One aircraft can be airborne at all times, ready to relay the emergency action message (EAM) to the submarine fleet. The Tacamo aircraft is a communications center whose function is to receive the EAM via UHF, HF, or VLF from a ground, airborne, or satellite source and retransmit it via VLF to the submarine fleet. Transmission of the EAM requires an accurate time and frequency reference. This requirement has been met by Frequency and Time Systems (FTS) through its development of a time and frequency reference system for the Tacamo program.

### Tacamo Message Transmission

Efficient wide-area radiation from a VLF antenna of course requires an antenna whose dimensions are large compared with aircraft dimensions. This is accomplished in the C-130 by trailing a wire of about six miles in length and continuously flying the aircraft in a small circle so as to form the antenna into a rough helix. Because of the short depth of penetration of VLF as compared to ELF, the receiving submarine is required to trail an antenna of its own, some two thousand feet in length. The submarine can stay submerged at some depth, but the trailing end of the antenna must be within about thirty feet of the surface for reception.

### Time System Configuration

The time and frequency reference system on board the aircraft is configured to be triply redundant. The system consists of three instruments -- two identical Frequency Standards (FS) and one Satellite Time Reference (STR). Each FS contains a quartz oscillator -- the FTS 9105 -- whose aging is better than five parts in  $10^{11}$  per day. The STR is a satellite receiver whose function is to receive data from the Transit satellite system, adjust it for range, and correct the instrument's internal clock. Both devices -- the FS and the STR -- make available a variety of digital and sinusoidal signals for use by aircraft systems.

Aircraft use occurs in the Tacamo system according to a specific deployment cycle, and the time system has been designed to fit within the constraints of that cycle. One cycle consists of seven missions of ten hours each, with a fifty hour layover between missions. The frequency standards are required to be portable and to operate on battery power when necessary. The STR remains fixed on the aircraft. During each layover period, One FS is housed in a ground facility; at the beginning of a mission, it is updated with UTC and brought to the aircraft. With aircraft engines on, primary power is now available for the STR which now has time transferred to it from the FS that has just been carried on board. The remaining FS may also receive a time update.

During a mission, satellite time updates are from time to time available through the STR. When this occurs,

the operator has the option to transfer time from the STR to the two frequency standards. At the end of a mission, aircraft power is shut down, one FS is removed from the aircraft; the remaining FS runs on battery power for the length of the layover period.

### Transit

Transit - more formally, the Navy Navigation Satellite System (NNSS) - is a constellation of five satellites arranged in polar orbits of a radius of about 4700 miles. Each satellite continuously transmits time and ephemeris data. Navigational use of the system involves message reception from one satellite and computation of position based on the time and satellite position data the satellite has itself transmitted. Ephemeris data gives satellite position to within five meters; time data gives time to within approximately 30  $\mu$ s. In navigational use, two or more transmissions from the same satellite are used to compute a change in satellite slant range. Using an assumed-position method, several range changes are used to determine a fix.

Time information is transmitted by the satellite in the form of a "fiducial time mark" which occurs every two minutes in the course of a satellite pass. A slant range calculation can be used to compute propagation delay between the satellite and the receiver, and this is in fact the principle of operation of the STR. Calculation of position is not necessary as the system is presently realized; position information can be entered automatically via a link with the aircraft inertial navigation system (INS), or it can be entered manually from the front panel of the STR.

### The Satellite Time Reference

The primary purpose of the STR (block diagram: Figure 1) is to deliver NNSS-derived UTC to the user via a serial time code output and a 1 pps output. There is a front panel time-of-day display, various supplementary outputs, and a variety of additional functions controlled through front panel switches. Digital outputs include 1 pps, 1 ppm, and the time code. There is also a 5 MHz sinusoid output. The STR's frequency reference is an internal rubidium standard, although it is possible to switch to an external 5 MHz reference. Automatic reference switchover is provided to prevent loss of time due to loss of reference.

In use, time is kept by a microsecond clock driven by the 5 MHz reference. The microsecond clock produces the 1 pps and is read when necessary by the STR's microprocessor, a 6802. After satellite message reception and averaging of several satellite corrections, the microprocessor makes a decision about data validity based on the statistical distribution of received corrections. The operator is then alerted that a correction has been calculated, and can at his option allow the microprocessor to correct the microsecond clock.

Additional functions of the STR include measurement of time and frequency difference. Time difference between the instrument's internal 1 pps and an external 1 pps can be measured to within 1  $\mu$ s. Frequency difference between the internal rubidium standard and an external 5 MHz source can be measured to 1 part in  $10^{10}$ .

The STR needs positional information to calculate slant range; this is provided by the aircraft INS in standard ARINC data format. Front panel indicators provide information about this and other functions; additional indicators show fault status of various monitored internal assemblies and functions.

### The Frequency Standard

The FS (block diagram: Figure 2) is a multiple function, multiple output instrument using the FTS 9105 oscillator as its internal reference. The instrument displays time-of-day derived from its 1 pps output, and is capable both of synchronizing its 1 pps output to an external 1 pps and of advancing its 1 pps output using front panel controls.

Provided are a total of six sinusoidal outputs. Four are 5 MHz; the other two are 1 MHz and 100 kHz. Six pulse outputs are provided; there are three 1 ppm outputs, two 1 pps outputs, and a time code output. The time code is a 24 bit serial BCD word.

The internal 5 MHz crystal oscillator normally provides the reference for the instrument, but an external 5 MHz source can be switched in from the front panel. Upon the loss of this source, the instrument automatically switches back to the internal reference.

The front panel time-of-day display is settable via pushbuttons and a thumbwheel switch. The time code output provides the time shown by the time of day display. A set of thumbwheel switches allows the 1 pps to be advanced, in 1  $\mu$ s increments, from 0 to 999,999  $\mu$ s. Additionally, a front panel jack is provided to allow synchronization of the internal 1 pps to an external 1 pps. The time of day display and time code output both move forward to agree with the 1 pps output after it has been advanced or synchronized.

The FS is capable of operation from a variety of power sources, and the instrument automatically varies its use of power, dropping or adding non-essential functions, depending on the power source. Power source selection is automatic - upon loss of AC power, external DC power will be switched on; if neither external DC or AC are available, the internal battery will take over. Battery capacity exceeds 75 hours at 25°C. The internal battery is recharged automatically if external AC or DC power is available.

### Conclusion

The Tacamo time reference system makes available 5 MHz, 1 pps, and time code from each of the three instruments for use by aircraft systems. Because of the strategy of powering one frequency standard on batteries while on ground, the system is rendered resistant to power-line EMP transients. The system has been designed to allow time to be transferred back and forth between all instruments; failure of as many as two instruments will destroy its time-keeping effectiveness. It can be seen, then, that the Tacamo time and frequency reference system has been designed for flexibility and reliability, and will find applications outside of its original purpose as a timekeeper for the Tacamo aircraft.



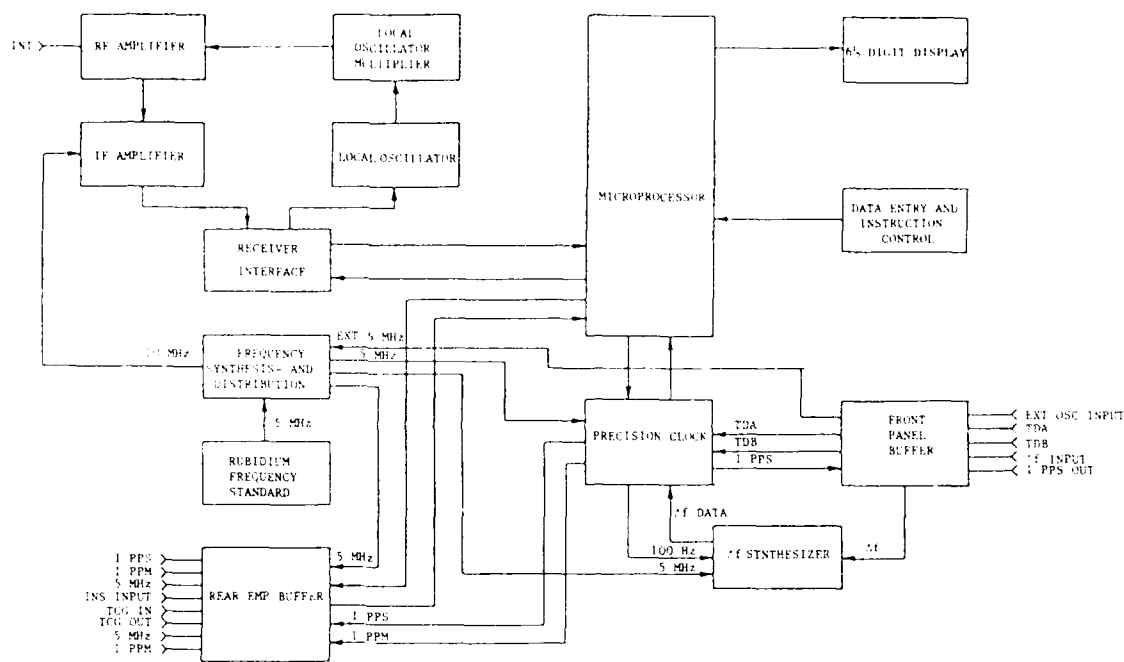


FIGURE 1. SATELLITE TIME REFERENCE BLOCK DIAGRAM

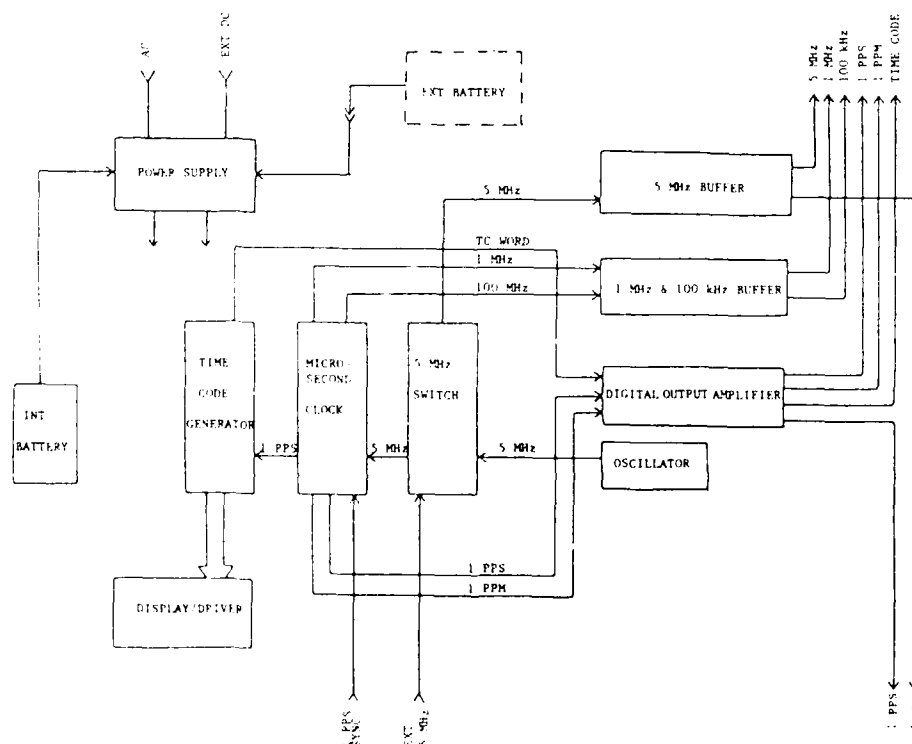


FIGURE 2. FREQUENCY STANDARD BLOCK DIAGRAM

## NEW APPROACH OF FAST WARM UP FOR CRYSTAL RESONATORS AND OSCILLATORS

J.P. Valentin, M.D. Décailliot and R.J. Besson

Ecole Nationale Supérieure de Mécanique et des Microtechniques

La Bouloie, Route de Gray, 25030 Besançon Cédex, France.

Summary

In this paper thermal exchanges in resonators are first considered from a general point of view.

Internal heating of B.V.A. type quartz resonators can be used in conjunction with regular heating inside an oven. Internal heating takes advantage of high vibration levels (typically 1 to 60 mw) and happens inside the very bulk material : as a result thermal gradients are fairly low. In addition warm-up time can be reduced and the oven design can be somewhat simplified. It turns out that the frequency overshoot, usually observed during warm-up, disappears. Warm-up time finally depends almost only on the oven characteristics. Internal heating is also very interesting if a resonator highly isolated thermally is used. Then the resonator allows the use of very poor ovens, leading to size and cost reduction.

Heating caused by dielectric losses, in every microscopic volume of the bulk material, under effect of microwave electric field, can also be used for fast warm up applications.

A new type of crystal has been designed which includes a B.V.A. type regular crystal installed in a quartz reentrant high Q cavity. The high Q of the cavity acts like a multiplier of electric field. In the paper, the total device is described (basic type is a 5 MHz miniature unit using a 3.6 GHz microwave field) and different possible solutions are reviewed. Electrical characteristics are given for the microwave oven and source. This new type of crystal unit allows very fast warm-up characteristics and, at the same time, drastically minimizes thermal gradients. Under certain conditions, the variation of temperature with time can be made very similar for quartz and electrodes materials. As a result an excellent thermal balance is obtained for the unit.

Experimental results on laboratory fast warm-up units are given, yielding warm-up times versus microwave power and various characteristics including frequency behaviour and overshoot reduction. Warm-up times in the order of 100 s can be achieved with microwave powers in the order of 200 mw. Two modes of operation are described.

As a conclusion, potential advantages obtained with internally heated units or microwave fast warm-up crystals are discussed.

INTRODUCTION

An important advance has been accomplished in understanding of dynamic thermal phenomena with introduction of a phenomenological dynamic coefficient by Ballato and Vig. This coefficient is evaluated separately for each crystal design and accounts

for crystal behaviour when the resonator is submitted to temperature variation (this includes warm-up). In fact, for proper use of this advance, a model for temperature and temperature gradient repartition in the very crystal material is needed. Until now, the model used was the model introduced by R. Holland<sup>2,3</sup> in 1974. This model consists in an infinite plane plate exchanging thermal energy with outside world through the two limiting planes. Acoustic energy is considered as uniform throughout the plate. The only thermal gradient supposed to appear is parallel to the plate thickness. A new model taking into account energy trapping and radial dimensions of resonator has recently been proposed<sup>4,5</sup>. This model shows evidence of a radial thermal gradient which turns out to be important since the thickness thermal gradient can be usually ignored in a first order approximation. Using this new model a theoretical understanding of crystal dynamical behaviour is proposed elsewhere in these proceedings<sup>6</sup>.

In this paper, the main results leading to a radial thermal gradient model are presented and discussed. As a consequence, thermal conduction through electrodes can usually be ignored. Thermal energy location is taken into account, the resonator being considered as a Fabry-Perot acoustical interferometer. Thermal energy provided by acoustical energy degeneration inside the very vibrating crystal is calculated (it is very close to electrical energy applied to electrodes). This energy<sup>7,8</sup> can be used for internal heating of crystal<sup>9</sup> and consequently can be used to reduce warm-up time. Only this last aspect is considered here. Then a new type of crystal including a B.V.A. type regular crystal installed in a quartz reentrant high Q cavity will be presented.

Calculation of various thermal conductancesTraditional resonators

Heat transfer occurs by conduction through residual gas and solid material. It also occurs via radiation. Gaseous conduction can always be ignored in ordinary resonators<sup>8</sup>.

\* Solid conduction. It occurs through electrodes and fixations and through the quartz material itself. The first conduction usually corresponds to less than 0.5 % of the conduction through quartz itself<sup>1</sup> (see Fig. 1).

\* Conduction due to radiation processes. Ref 8 shows that, provided temperature difference between quartz and crystal enclosure is small, thermal conductance is given by :

$$\gamma = \frac{4 \epsilon_f \sigma S_f T^3}{1 - (1 - \epsilon_e)(1 - \epsilon_q) \frac{\epsilon_q}{\epsilon_e}} \quad (1)$$

where  $\epsilon_e$  and  $\epsilon_q$  are the emissive factors of crystal enclosure and quartz body,  $\sigma$  is the STEFAN's constant,  $S_e$  and  $S_q$  the surfaces of enclosure and crystal, and  $T$  the temperature of the crystal.

For example, let us consider a glass or ceramic enclosure surrounding a resonator 15 mm in diameter, electrodes beeing 10 mm in diameter and temperature beeing 350 K. We obtain :

- between electrodes and enclosure :  $Y_r = 5.8 \cdot 10^{-5} \text{ WK}^{-1}$
- between crystal and enclosure :  $Y_r = 1.7 \cdot 10^{-3} \text{ WK}^{-1}$

It turns out that radiation exchanges through electrodes are relatively very small.

\* Comparison of exchanges through different processes. Fixations conductance of a 5 MHz AT or SC crystal is usually close to  $2.2 \cdot 10^{-3} \text{ WK}^{-1}$ . In that case, exchanges occur roughly for 50% through fixations and for 50 % via radiation processes (see Fig. 3).

In the particular case of golden enclosures radiation conductances are divided by 10. Radiation exchanges only represent 5 % of total thermal exchanges.

#### B.V.A.<sub>2</sub> Resonators

B.V.A.<sub>2</sub> is the most usual B.V.A. design<sup>10</sup>. Electrodes<sup>2</sup> are deposited onto quartz disks on each side of the vibrating crystal. Distance between electrode and crystal is in the order of 10  $\mu\text{m}$ .

\* Solid conduction. It goes through<sup>3</sup> quartz bridges and typical conduction is  $4.2 \cdot 10^{-3} \text{ WK}^{-1}$ .

\* Conduction by radiation processes. Due to the symmetry of Eq (1) the result is identical to the result obtained for a classical design.

\* Comparison of various exchanges. On Fig. 4 the various contributions to thermal exchanges are summarized.

#### Energy location

##### \* Vibrationnal energy

A plano-convex quartz resonator can be compared to a spherical Fabry-Perot optical interferometer<sup>4</sup>. When an overtone (n, o, o) operation is considered, acoustical energy is located in the central area according to a gaussian law :

$$q(r) = \mu e^{-\frac{r^2}{r_o^2}}$$

Fig. 5 shows a vibration equivalent in energy but exhibiting a constant energy  $\mu$  on a circle of radius  $r_o$ . Usually  $r_o$  is one third of the radius of the total resonator.

In fact vibrations in the crystal cause thermal sources to appear inside the bulk material. Those heat sources correspond to vibration modes (Fig. 6 shows - third overtone repartition). Since thickness of resonator is small compared to other dimensions,

energy density may be considered as constant along thickness (at least as a first approximation).

##### \* Thermal energy

The electrical power  $P_o$  applied via crystal electrodes is dissipated :

- by Joule effect in crystal and connections ( $P_1$ )
- by dielectric losses in piezoelectric medium ( $P_2$ )
- by electromagnetic radiation ( $P_3$ )
- by internal viscosity ( $P_4$ )

Obviously,  $P_2$  and  $P_4$  are dissipated inside the bulk crystal<sup>2</sup> medium. Orders of magnitude can readily be obtained :

- Joule effect can be ignored in crystal but not in connecting wires. Hence  $\frac{P_1}{P_4} \approx 10^{-3}$ .

-  $\frac{P_2}{P_4}$  depends on the quantity  $R_1 C_o \text{ tg } \delta$  where  $R_1$  is the motionnal resistance and  $C_o$  the static capacitance of crystal. For regular units  $\frac{P_2}{P_4}$  ranges from  $10^{-6}$  at 5 MHz to  $10^{-3}$  at 500 MHz.

-  $\frac{P_3}{P_4}$  turns out to practically equal  $\frac{P_2}{P_4}$  (from 5 MHz to 500 MHz).

$10^{-3} - P_4$  turns out to almost equal  $P_o$  (with a approximation) in usual frequency ranges.

Finally, thermal power dissipated in crystal is extremely close to electrical applied power  $P_o$ .

In conclusion, an internal heat source of radius  $r_o$  (Fig. 5) located under electrodes delivering the thermal power  $P_o$  can be considered as a first approximation. Heat flux flows to fixations (Fig. 7). In the electrode zone thermal gradient is radial and does not include a component along thickness. In the area external to electrodes, due to radiation processes, thermal gradient does include a thickness component. Hence the main vibrating zone (radius  $r_o \sqrt{2}$ ) only shows a radial thermal gradient.

#### Internal Heating

Electrodeless B.V.A. type resonators stand very high vibration levels without important degradation of aging (exemple a 5 MHz fifth overtone crystal driven at 2.8 mw yields typical aging of  $3.5 \cdot 10^{-10}$ /day). Traditionnal WARNER'S technique electroded resonators are always driven much lower (in the microwatt range) : as a consequence, internal thermal energy available is negligible. This is no more the case with B.V.A. electrodeless resonators driven at power levels more than  $10^3$  larger. Then, thermal energy internally available can be used for warm-up purposes<sup>7,8</sup>. Two different types of application are now discussed.

##### A - Obtaining turn-over point via Internal heating

In 1979, we discussed a highly isolated electrodeless resonator and showed that the drive level needed to keep it at turn over was reasonable.

But, these highly isolated resonators are laboratory units, quite expensive that do not stand high vibration levels.

So, new resonators of the classical B.V.A. electrodeless design (with only a few changes in supporting structure material) were built. The resonators were 5 MHz, third overtone, SC cut crystals with a thermal conductance of  $2.6 \cdot 10^{-3}$  W/K and a 30 minutes time constant. The crystal was simply placed in a dewar. Turn over ( $-77.5^\circ\text{C}$ ) could be obtained after 1 hour, only by internal heating, without classical oven. The oven was in fact replaced by an external oscillator delivering 60 mw on the crystal<sup>12</sup> during warm-up time. This experience directly leads to low consumption oscillator design.

#### B - Reduction of warm-up time via internal heating

Reduction of warm-up time is an extremely difficult challenge. We experienced several steps in this reduction always using SC cut electrodeless B.V.A. resonators. As a first step ordinary (large) B.V.A. crystals were used, then internal heating was added, finally, important reduction in size of B.V.A. units was used. Much work is still to be done but yet interesting indications can already be given. The warm-up time necessary to reach the frequency with an accuracy of  $10^{-9}$  will be considered.

#### Using ordinary B.V.A. SC cut electrodeless crystals

Ultrastable quartz crystal oscillators usually need 90 minutes to reach the frequency within a  $10^{-9}$  accuracy. Using B.V.A. units do not significantly changes this result. However, using a B.V.A. 5 MHz SC cut third overtone crystal, inside a modified commercial unit allowed a warm-up time of 37 minutes (see Fig. 8). Modifications of the unit basically concerned electrical features of the oven. The crystal was driven at a 210  $\mu\text{W}$  level.

#### Adding internal heating

Preliminary experiments were performed using the type of crystal described in section A inside a commercial ultrastable oscillator. The crystal was driven at a 180  $\mu\text{W}$  level. The warm-up time necessary was 102 minutes, and small overshoot was recorded (see Fig. 9). Then internal heating was added using an external oscillator delivering 60 mw during 20, 30 or 40 minutes. Fig. 9 shows the results obtained with internal heating over 40 minutes. As it can be seen warm up time is reduced to 55 minutes. Moreover frequency overshoot disappears. This last important result is due to compensation, inside the bulk material, of the thermal gradient caused by the oven. Then, it is possible to get rid of dynamical temperature coefficient effects.

Another experiment was also carried out with the same crystal but the oven wiring was wired directly on the crystal enclosure in contact with the temperature sensor. The warm-up time turned out to be 70 minutes. Adding internal heating yielded a warm-up time reduction down to 35 minutes.

Experiments have been recently undertaken using the unit and an ordinary BVA SC cut

crystal in conjunction with internal heating. Experiments are still carried on but preliminary results show warm-up time reduction from 37 minutes down to 25 minutes.

#### Reduction in size of B.V.A. electrodeless units

New 5 MHz B.V.A. crystals have been designed. The total diameter of crystal (external ring included) is 13.2 mm. Then, ordinary 5 MHz resonator enclosures can be used. This reduction in size proved to be extremely helpful.

First, using AT cuts crystal, it was possible to reach the frequency within  $3 \cdot 10^{-9}$  after 9 minutes starting from ambient temperature and after 11 minutes starting from  $-40^\circ\text{C}$ . A simplified oven was used for this preliminary experiment and the oven wiring was directly in contact with the crystal can.

Since the former result is interesting small SC cut electrodeless crystals have also been designed. It is planned to use them in conjunction with internal heating. Warm-up times in the order of 3 minutes are expected (starting from ambient).

In conclusion, we believe the preliminary results to be encouraging. However further improvements can be of interest. Especially the power used for internal heating should be an adequate function of time. For best results, several heating sources will probably have to be used together (power applied on resonator, power on classical oven and/or power used for internal heating ...).

#### Heating quartz material via dielectric losses

Dielectric losses occur in every microscopic volume of the bulk material. Hence, this process is homogeneous and independant from thermal conductivity of the crystal. The power  $P_c$  delivered per unit volume  $U$  is given by :

$$\frac{P_c}{U} = \pi F \epsilon \operatorname{tg} \delta E^2$$

where  $E$  is the electric field,  $F$  the frequency,  $\epsilon$  the permittivity and  $\delta$  the loss angle.

In the microwave frequency range choosen (from 2 GHz to 4 GHz) we measured (by classical perturbation methods) :

$$\operatorname{tg} \delta = 2.5 \cdot 10^{-4}$$

Hence, at  $F \approx 4$  GHz :

$$\frac{P_c}{U} \approx 10^{-3} E^2$$

But, if we wish a temperature increase of  $1^\circ\text{C}$

per second  $\frac{P_c}{U}$  has to be :

$$\frac{P_c}{U} = 1.04 \cdot 10^6 \text{ W/m}^3$$

From which we derive that the power needed to obtain a temperature increase of  $1^\circ\text{C/s}$  in a small B.V.A. perfectly isolated unit ( $0.1 \text{ cm}^3$  in volume) is 200 mw and corresponds to an electric field of  $45 \cdot 10^3 \text{ V/m}$ .

A new type of crystal has been designed<sup>14</sup> which includes a B.V.A. electrodeless crystal installed in a reentrant high Q cavity. The B.V.A. resonator is 13.2 mm in diameter (external ring included) and electrodes deliver at the same time the microwave frequency and the metrological 5 MHz. Since the reentrant cavity can usually be made with a loaded Q of 500 or larger the generator power necessary to obtain a temperature increase of 1°C/s is reasonable. In the case of the previous crystal (1.1 mm in thickness),  $P_c$  is close to 200 mw and only needs a generator<sup>c</sup> of 1.5 W. In fact it is easy to show that the high Q of the cavity acts like a multiplier of electric field.

Fig. 10 shows an experimental reentrant cavity that was used to check the possibility of fast warm-up applications.

The various important dimensions are :

$$\begin{aligned} r_o &= 6.6 \text{ mm} & r_i &= 1.4 \text{ mm} & h &= 13.5 \text{ mm} \\ \text{gap} &= 1.1 \text{ mm} & \ell &= 6.1 \text{ mm} \end{aligned}$$

The cylindrical body ① of cavity is thin (0.3 mm) golden brass and acts also as the usual crystal enclosure. The vibrating quartz wafer is placed inside central gap ②. Electrodes slightly press on the external ring of B.V.A. crystal. Electrodes are metallic hollow cylinders whose faces are recessed from vibrating crystal surface by approximately 20  $\mu$  m. Two gaflon rings isolate and maintain electrodes. Microwave are introduced in cavity by capacitive coupling ⑤. Two tiny wires ⑥ connect electrodes to 5 MHz crystal oscillator. So as to prevent microwave losses those two wires are placed inside small cylinders electrically connected to cavity body in areas where electric field is null.

#### Electrical characteristics for microwave oven and source

Reentrant cavities with one gap are used each time that intense microwave field is needed in a narrow space. Those cavities have been studied in particular by FUJISAWA<sup>15</sup> and JAWORSKI<sup>16</sup> leading to equivalent electrical circuits. However we were needing a cavity with two isolated electrodes so as to allow a B.V.A. type mount. Then a cavity with 3 gaps (hence equivalent to 4 identical cavities with one gap) was chosen (see Fig. 11). In that case the central gap (without crystal) is twice thicker than the two other gaps. The section planes at  $\frac{h}{4}$  and  $\frac{3h}{4}$  are planes of null electric field.

The equivalent electrical circuit of the 3 gaps cavity is shown on Fig. 11. Measured values of various parameters are listed below :

$$\begin{aligned} F &= 3.246 \text{ GHz} & C_{02} &= 4.9 \pm 0.2 \text{ pF} & C_{01} &= C_{03} = 9.8 \pm 0.3 \text{ pF} \\ L &= 0.8 \text{ nH} & Q &= 650 & R_s &= 10.6 \text{ k}\Omega & r &= 0.025 \Omega \end{aligned}$$

It is easy to see that  $\frac{5}{12}$  of total energy stored is located in central gap.

Uniformity of electric field has been carefully determined by a method already used by CARR<sup>17</sup>.

\* Calculations valid for  $Q = 500$ .

From central part to edge the field variation is only 4 %. It is necessary to point out that the external ring of the B.V.A. resonator sits also in the microwave field so as to cancel out thermal gradients in the B.V.A. quartz structure. Using the parameters listed previously (in particular Q is now 650), and since a 3 gaps cavity is considered, it can be seen that an electric field of 5010 V/m is obtained for a microwave source of 1w corresponding to  $P_c = 100$  mw on the crystal.

FUJISAWA calculations are only valid under given assumptions. So we used a method developed by JAWORSKI and extended by RAULIN<sup>18</sup> to the 3 gaps cavity. In particular it could be seen that power appearing by Joule effect in cavity was approximately equally shared between electrodes and cavity envelope.

Finally, the resonator is heated up by dielectric losses and the electrodes and external envelope by Joule effect due to induced currents. Moreover, if the electrodes and external cavity envelope are properly designed, the variation of temperature with time can be made very similar for quartz and electrodes materials.

Preliminary calculations<sup>18</sup> showed that 45 % of power is dissipated in the external envelope of cavity, 46 % in electrodes and 9 % in quartz. Since thermal capacity of resonator is 0.224 J/K thermal capacity of one electrode has to be 0.560 J/K which, for brass, means a mass of 1.5 g. In the same manner the mass of the external envelope of cavity was optimized to 3 g.

Experimental verifications showed that temperature difference between quartz and electrodes was actually less than 0.1°C. As a result an excellent thermal balance is obtained for the unit and thermal gradients are drastically minimized.

#### Experimental set-up

The microwave operation is shown on Fig. (12). A V.C.O. type generator working between 2 and 4 GHz is used together with an amplifier (22 dB) delivering a maximum power of 2W. A circulator separates incident wave from wave reflected by cavity. Control is obtained by detection of reflected wave.

The crystal used is of course a 5 MHz third overtone SC cut small B.V.A. electrodeless crystal. B mode is used as temperature sensor with a linear slope of -161 Hz/°C. Several experiments were performed to obtain :

- temperature of quartz and electrodes versus time
- warm-up time necessary to obtain the resonator frequency
- evidence of dielectric warm-up.

#### Experimental results

Fig. 13 represents the quartz wafer temperature increase versus time for different values of the output power P of generator. B mode of SC cut resonator is used for temperature measurement. The cavity is thermally insulated and placed in vacuum. When P = 2W, turn-over is obtained

after 100 s. The microwave power applied on crystal is 240 mw. Temperature increase at the origin is 1.2°K/s.

Fig. 14 represents a typical variation of the 5 Mhz frequency versus time in the following experimental conditions. The cavity is placed inside a regular oven. Microwave field and regular oven are started at the same time. A thermistor placed inside an electrode suppresses the microwave field when turn-over is reached. As it can be seen, a small frequency oscillation is recorded. Warm up time necessary to reach the frequency within  $10^{-9}$  is 3 minutes. Overshoot reduction is possible by modulation of the microwave field intensity. However optimization of the system has not been tried because frequency oscillation might be caused by some mechanical imperfection in the crystal supporting structure.

Fig. 15 shows temperature increase of quartz and electrodes. In the case of the thick curve each electrode has a mass of 1.5 g ; as a consequence quartz temperature and electrode temperature are almost identical (difference less than 0.1°K).

If the mass of each electrode is 6 g, quartz and electrodes exhibit a temperature difference that can reach 6°K, thus showing evidence of dielectric warm-up in the bulk material.

Finally, heating caused by dielectric losses turns out to be fast enough with reasonable powers. Moreover, the heating process is very homogeneous and able to cancel out temperature differences between the quartz wafer and his immediate environment. This means that almost perfect thermal insulation of the vibrating crystal is possible.

#### Conclusion

Internal heating is possible with B.V.A. units already commercially available. It can reduce warm-up time roughly by a factor of 2. It also proved to be very helpful in overshoot reduction. Reaching frequency within  $10^{-9}$  is possible in 25 minutes. Preliminary results show that this warm-up time could be reduced down to less than 5 minutes by proper design of small crystal B.V.A. electrodeless units.

Microwave ovenized resonators have been achieved as laboratory prototypes only. The crystal can be heated to turn over within 100s with a microwave power of 240 mw. Frequency reaching within  $10^{-9}$  is possible in 9 minutes. This warm-up time can probably be much reduced. Of interest is the fact that temperature difference between quartz resonator and his environnement can be cancelled out. So, microwave ovenized resonators are excellent candidates for very fast warm-up applications. Nevertheless, much work is still to be done especially to obtain industrial production.

#### References

1. A. Ballato and J.R. Vig, 32<sup>nd</sup> Annual Frequency Control Symposium, pp. 180-188 (1978).
2. R. Holland, I.E.E.E. Trans. Sonics and Ultrasonics 21, n°3 (1974).
3. R. Holland, Ultrasonics Symp. CHO 886-ISU-1974.

4. J.P. Valentin, Doctoral Thesis, n° 178, Besançon France (1983).
5. J.P. Valentin, "Thermal gradient distributions in trapped energy quartz resonators". To appear in Journal of Applied Physics.
6. J.P. Valentin, G. Theobald, J.J. Gagnepain, 38th Annual Frequency Control Symposium (1984).
7. R. Besson, J.P. Valentin, French Patent n° 79 18553 (1979).
8. J.P. Valentin, 34<sup>th</sup> Annual Frequency Control Symposium pp. 194-201 (1980).
9. M.D. Decailliot, R.J. Besson, French Patent n° 811006 (1981).
10. R.J. Besson, 31<sup>st</sup> Annual Frequency Control Symposium, pp. 147-152 (1977).
11. A. Berthaut, R.J. Besson, C.R. Acad. Sc. Paris, 289 série B (1979).
12. S. Galliou, These Docteur-Ingénieur, Ecole Nationale Supérieure de Mécanique et des Microtechniques. Besançon 1980.
13. S. Galliou, A. Berthaut and J.P. Valentin, Nuevo Cimento, Vol. 2D, n°4 (1983).
14. M.D. Decailliot and R.J. Besson, European Patent 8110006 (1981).
15. K. Fujisawa, I.E.E.E. transactions on microwave theory and techniques, vol MTT 6, pp 344-350 Oct. 1958.
16. Jaworski, I.E.E.E. transactions on microwave theory and techniques, vol. MTT 26, n°4, April 1978.
17. P.H. Carr, The journal of the Acoustical Society of America, vol. 41, n°1, pp 76-83, (1967).
18. Ph. Raulin, "Chauffage microonde des résonateurs à quartz". These de Docteur-Ingénieur. Ecole Nationale Supérieure de Mécanique et des Microtechniques. Besançon, Mars 1984.

CONDUCTION

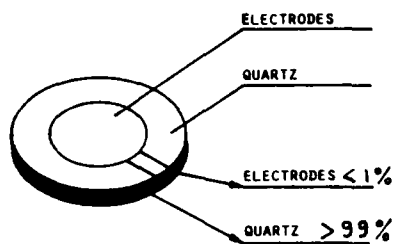


FIGURE 1

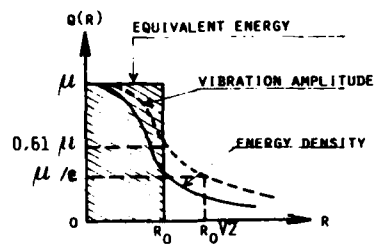


FIGURE 5

RADIATION

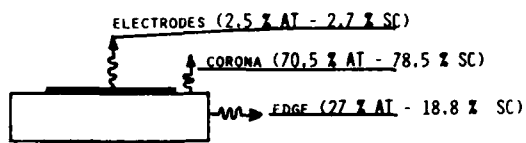


FIGURE 2

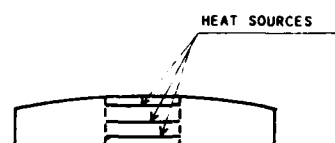


FIGURE 6 : THIRD OVERTONE

COMPARISON

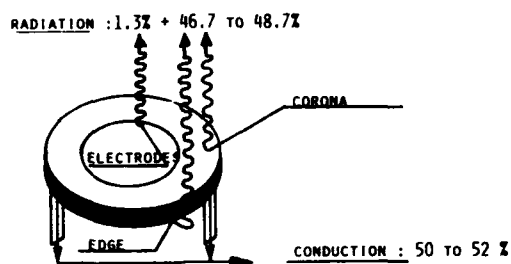


FIGURE 3

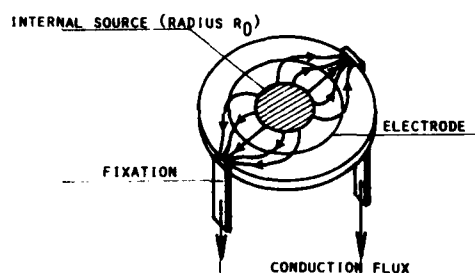


FIGURE 7

COMPARISON

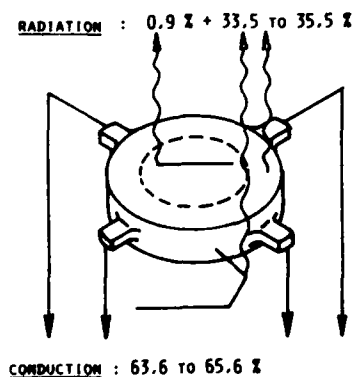


FIGURE 4

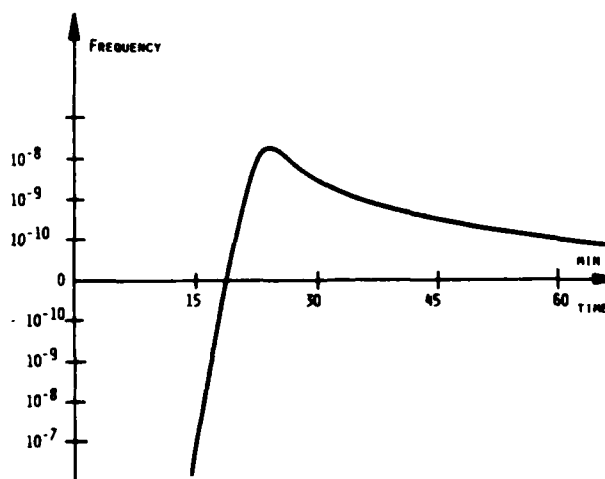


FIGURE 8

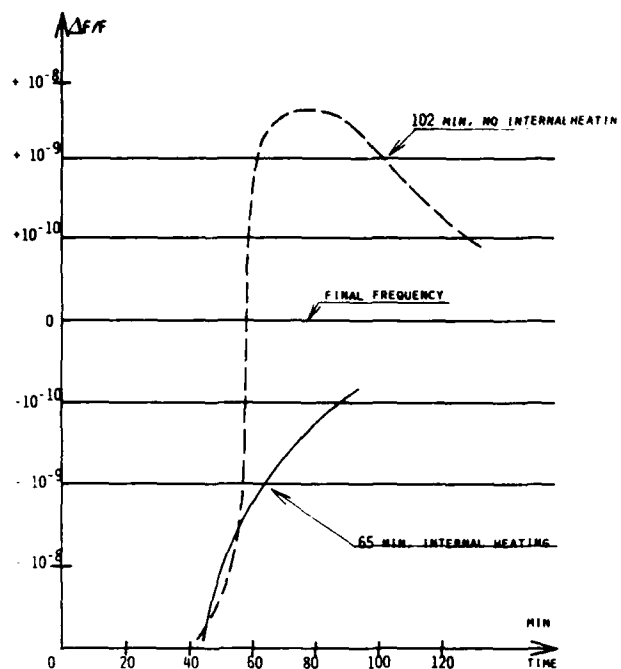


FIGURE 9

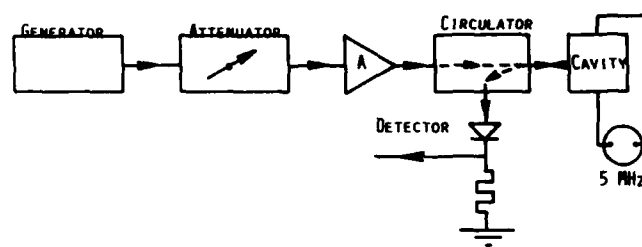


FIGURE 12

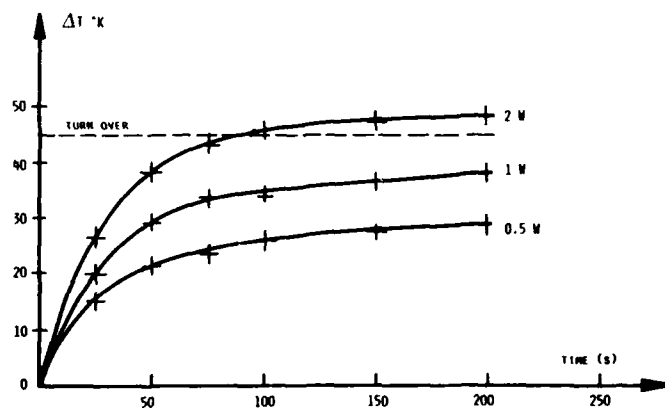


FIGURE 13

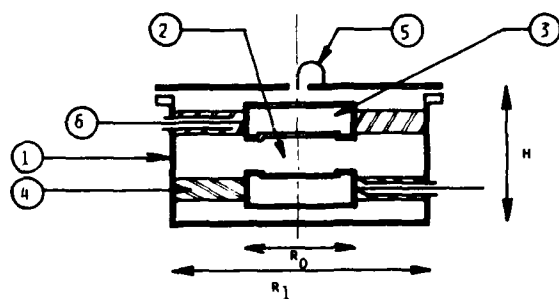


FIGURE 10

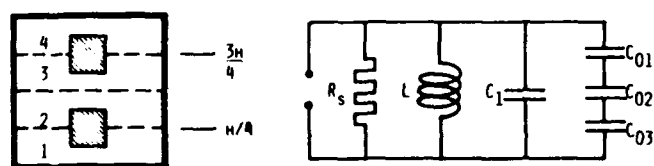


FIGURE 11

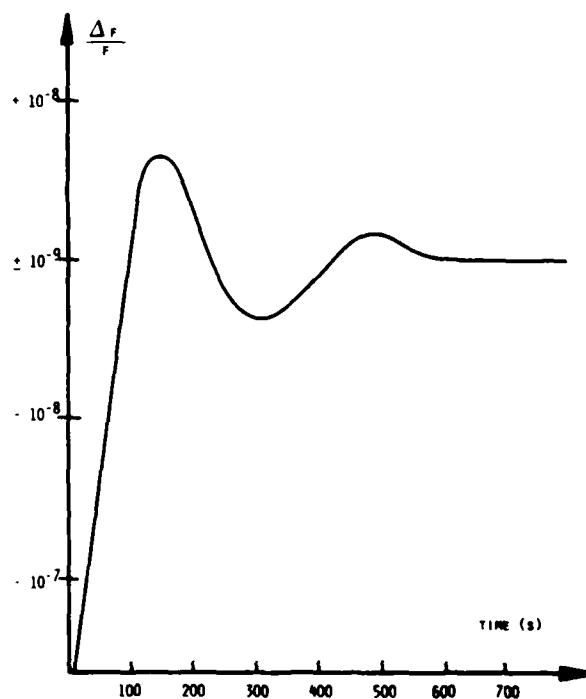


FIGURE 14



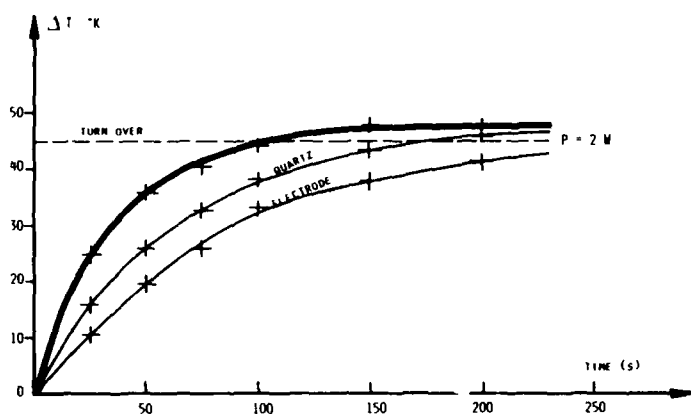


FIGURE 15

# SPACE QUALIFIED HIGH PERFORMANCE DIGITALLY TUNED QUARTZ CRYSTAL OSCILLATORS

R.M. Garvey, D.A. Emmons and A.F. Beaubien  
Frequency and Time Systems, Inc.  
Beverly, MA

## Summary

Two new oscillators for space qualified application have been designed, fabricated and tested. These devices incorporate digital tuning interfaces, allowing the frequency to be controlled by telemetry. Provision for radiation immunity via shielding and component parts selection are additional design features.

The composite requirements for high resolution ( $1 \times 10^{-11}$ /bit) digital tuning coupled with extended device operation ( $> 10$  years) in a spacecraft radiation environment place stringent restrictions upon both oscillator and tuning circuitry designs. The oscillators employ a 12 or 14 bit digital tuning network comprised of either two overlapping resistor networks with parallel latching data or an integrated DAC and associated circuitry to receive and latch a serial data stream.

The crystal resonator is an SC cut fabricated from swept quartz. Additional radiation shielding for the resonator has been incorporated. A crystal filter in the output circuitry provides enhanced phase noise performance.

The design employs a parts complement which provides immunity to radiation effects as well as high reliability. Reductions in power consumption and weight while preserving high performance in terms of thermal sensitivity have been incorporated.

## Introduction

Quartz crystal oscillators for spacecraft application require high reliability in parts selection and in design, as well as high performance in terms of stability and aging behavior. The FTS 9100 oscillator, which was developed for and is used in the Global Positioning System satellites, has demonstrated aging of less than  $10^{-11}$ /day. A calculated mean time between failure for this design is approximately 2 million hours in a space flight environment.

Two new oscillators have been designed for space flight application. They are derivatives from the 9100 design and employ provision for integral digital tuning. The oscillator electronics are contained within a glass dewar which provides a high degree of thermal isolation resulting in low environment sensitivity. The dewar and oscillator electronics have been qualified to vibration levels in excess of 20 g rms and to pyrotechnic shock levels of 2300 g.

The oscillator is comprised of a low-noise sustaining stage with its associated AGC circuitry. A low-noise buffer and the oven control circuitry complete the ovenized portion of the oscillator. A tuned cascode amplifier followed by a double emitter-follower provides load isolation and a well defined 50 ohm sinusoidal output for the instrument. An integral voltage regulator provides immunity from power supply fluctuations.

## Model 9120

The Model 9120 employs a third overtone SC-Cut swept quartz resonator operating at 5 MHz. Tuning is provided by a 14 bit R-2R network which is driven from a latched parallel data word. A crystal filter in the output circuitry provides reduced phase noise at frequencies greater than 100 Hz from the carrier. The oscillator design incorporates hardening for both natural orbital radiation levels as well as for enhanced artificial levels. Magnetic shielding is also provided.

## Performance

Pertinent performance characteristics for the 9120 are shown in Table 1. Note that the magnetic field response is a result of the residual sensitivity of inductors in the oscillator circuitry. Phase noise performance is shown in Figure 1. Resonator drive levels in the 9120 are maintained at a reasonably low level to provide low aging behavior and low phase noise close to the carrier. These design considerations typically result in phase noise levels of -140 dB for frequencies greater than 100 Hz from the carrier. In order to provide enhanced phase noise performance far from the carrier (1 kHz) a crystal filter has been incorporated into the oscillator output amplifier circuitry. This filter, a two-pole monolithic swept quartz filter, provides approximately 30 dB of attenuation 5 kHz from the carrier. This yields the required -168 dBc phase noise performance at 10 kHz.

The 500 ohm characteristic impedance filter, is placed in the tuned output of the cascode isolation stage in the final buffer amplifier. It is followed by the double-emitter follower which in turn drives an output transformer. The source impedance of the final output is 50 ohms.

Stability in the time domain is shown in Figure 2; the Allan variance approaches  $3 \times 10^{-13}$  for averaging times of 3 to 100 seconds.

## Digital Tuning - 9120

Frequency tuning of the 9120 is accomplished through latching magnetic relays which switch a precision R/2R resistive ladder network for digital-to-analog conversion. The relays are MIL approved style and provide upset immunity as well as a non-volatile storage of the tuning command. The relays are driven in parallel by commands through the interface connector.

The extended mission lifetime requirement of 17 years combined with a tuning resolution of  $\pm 5 \times 10^{-12}$  place severe requirements upon the oscillator digital tuning network. In order to satisfy the lifetime and resolution requirements a 14 bit DAC was implemented using two R/2R resistor arrays. A 12 bit array was employed for all but the two most-significant bits. These two MSB were implemented by means of a separately packaged R/2R network having additional

### Conclusions

Digitally tuned oscillators with state-of-the-art performance in noise and aging are available as signal sources for sophisticated satellite applications. The packages are rugged mechanically and can withstand harsh nuclear environments. Reliability in design and in parts selection provide the assurance of extended mission operation.

### Acknowledgements

This work was supported in part by Hughes Aircraft Company and by MIT Lincoln Laboratories.

### Conclusions

Digitally tuned oscillators with state-of-the-art performance in noise and aging are available as signal sources for sophisticated satellite applications. The packages are rugged mechanically and can withstand harsh nuclear environments. Reliability in design and in parts selection provide the assurance of extended mission operation.

### Acknowledgements

This work was supported in part by Hughes Aircraft Company and by MIT Lincoln Laboratories.

TABLE 1.

## 9120 PERFORMANCE

FREQUENCY	5 MHz
AGING	$5 \times 10^{-11}$ /DAY
THERMAL	$1 \times 10^{-12}/^{\circ}\text{C}$ ( $-20^{\circ}\text{C}$ to $+50^{\circ}\text{C}$ )
POWER ( $25^{\circ}\text{C}$ )	2.2 WATTS
SUPPLY VOLTAGE SENSITIVITY	$3.4 \times 10^{-12}$ /VOLT
MAGNETIC FIELD SENSITIVITY	$4.0 \times 10^{-12}$ /GAUSS
LOAD SENSITIVITY	$1.2 \times 10^{-12}/\pm 1\%$
SIZE	7.6x7.6x19.3 cm (3x3x7.6 in)
WEIGHT	1.4 kg (3.0 lbs)

TABLE 2.

## 9125 PERFORMANCE

FREQUENCY	5 MHz
AGING	$1 \times 10^{-10}$ /DAY (10 DAYS)
THERMAL	$< 1 \times 10^{-11}/^{\circ}\text{C}$ ( $-20^{\circ}\text{C}$ TO $+40^{\circ}\text{C}$ )
POWER ( $25^{\circ}\text{C}$ )	1.6 WATTS
SUPPLY VOLTAGE SENSITIVITY	$< 2 \times 10^{-11}$ /VOLT
SUPPLY RIPPLE SENSITIVITY	-110 dBc/100 mV ptp
LOAD SENSITIVITY	$5 \times 10^{-11}/\pm 10\%$
SIZE	10.2x10.2x19.3 cm (4x4x7.6 in)
WEIGHT	1.09 kg (2.4 lbs)

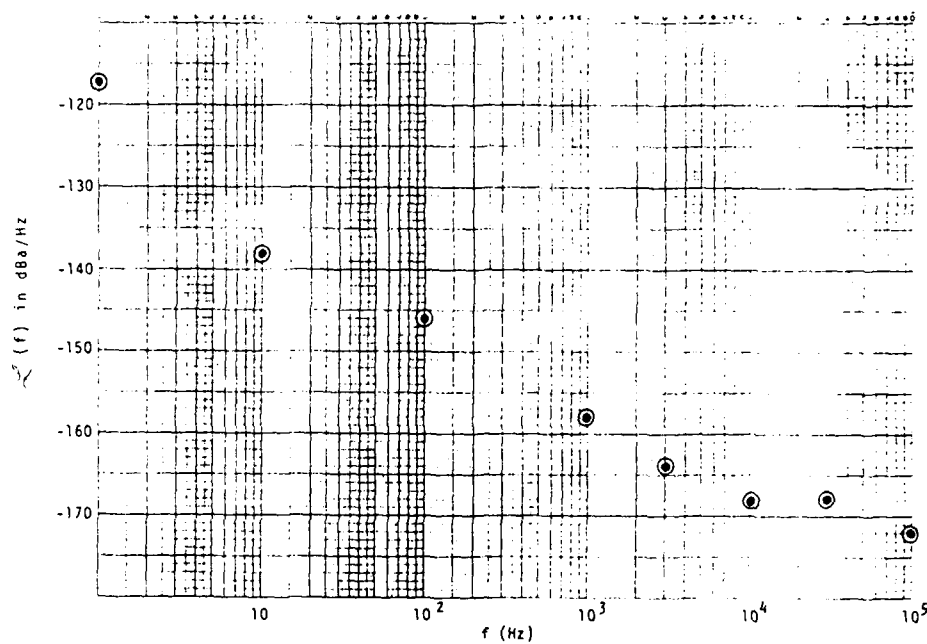


FIGURE 1. FTS 9120 PHASE NOISE  $L(f)$

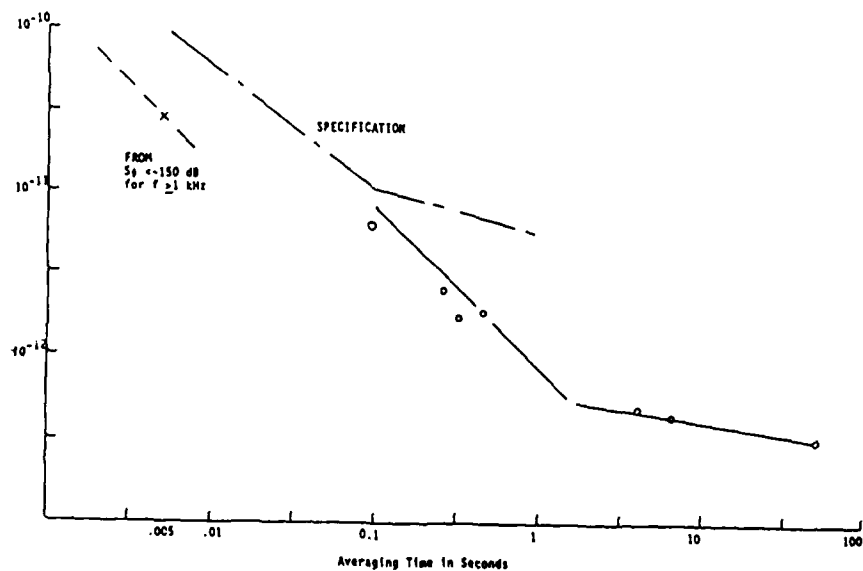


FIGURE 2. FTS 9120 TIME DOMAIN STABILITY

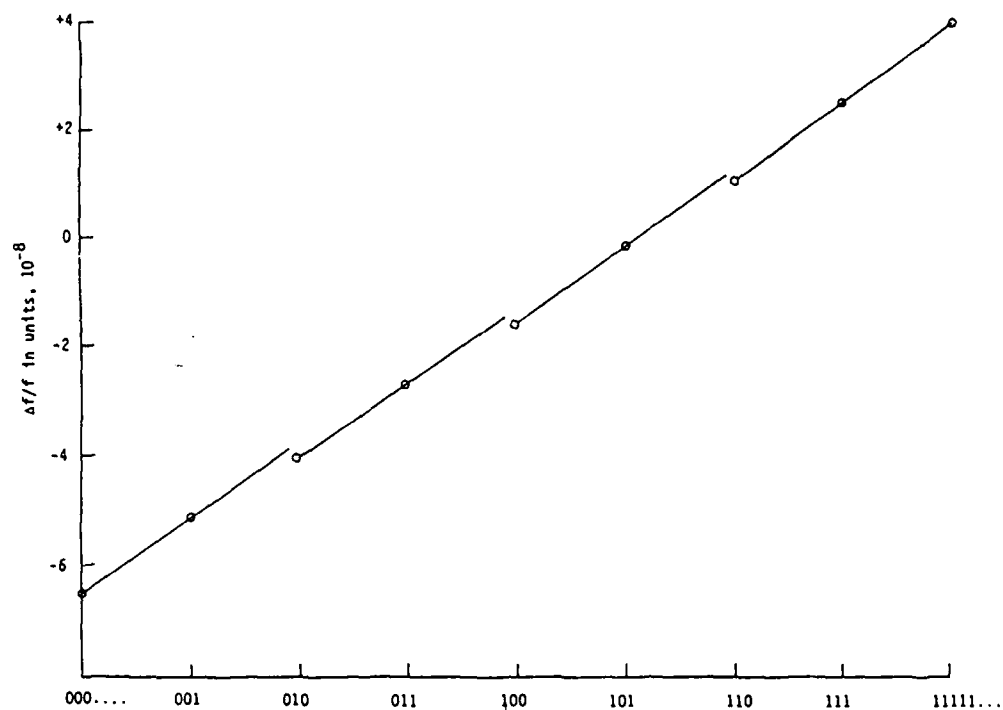


FIGURE 3. 9120 FREQUENCY TUNING

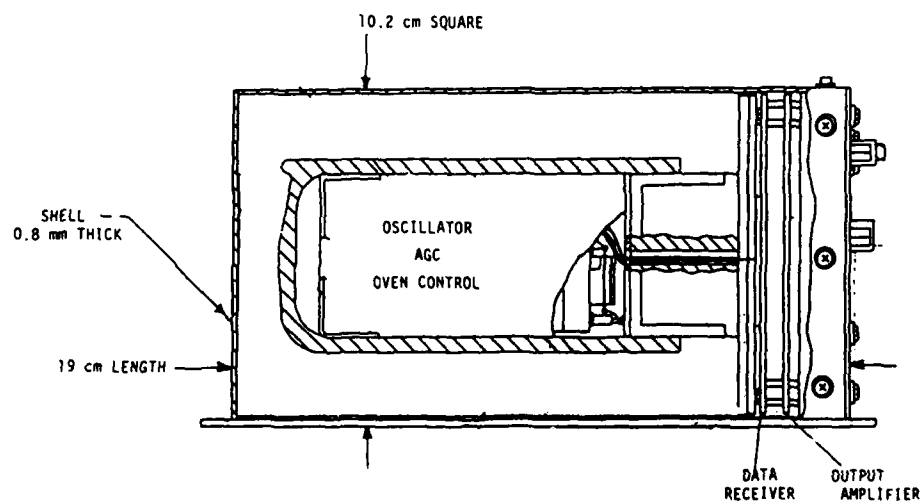


FIGURE 4. FTS 9125 MECHANICAL CONFIGURATION

## MANUFACTURING METHODS AND TECHNOLOGY FOR TACTICAL MINIATURE CRYSTAL OSCILLATOR

D. Brown, E. Laszlo, R. McGill, P. Stoermer

Allied-Bendix Aerospace

Bendix Communications Division

Baltimore, Maryland 21204

The Tactical Miniature Crystal Oscillator, TMXO, features small size, fast warmup, low power dissipation and excellent frequency stability. It is intended for use in tactical communication, navigation, and position location applications where a precision frequency or time source is required. Earlier papers have described the TMXO characteristics and various improvements made in the design to optimize performance.<sup>1,2</sup>

It is the intent of this paper to describe the present Manufacturing Methods and Technology, MM&T, program and its impact on TMXO design, manufacturability and performance. Primary objectives of the MM&T program are enhanced performance and reliability of the oscillator while achieving reasonable cost in manufacturing. To date, fifteen Engineering Models incorporating new processing techniques have been fabricated and evaluated. Their performance will be reviewed.

Improvements in the TMXO design and generation of production tooling and processes on the MM&T program promise availability of TMXO in the near future.

## Key Words (for information retrieval)

TMXO, Oscillator, Crystal  
Temperature Control, Frequency  
Stability, Vacuum, Hybrid

Introduction

Bendix' involvement with TMXO development programs began more than ten years ago as a result of Bendix' independent research with temperature controlled microcircuits. Since that time major technical problems associated with TMXO have been resolved. The purpose of the present program is to develop manufacturing methods and techniques (MM&T) for the production of TMXO (figure 1). At the completion of the program, a demonstration of production capability will be conducted and the TMXO will be incorporated in MIL-O-55310.

Development models of the TMXO were expensive, requiring painstaking individual construction, assembly, and test. It was therefore decided early in the MM&T program that major mechanical and electrical design improvements were necessary to achieve the objectives of the program.

Basic to the resultant improved design was the incorporation of the crystal oscillator circuit and the temperature control circuit in a sealed hybrid, assembled, screened, and tested to the requirements of MIL-M-38510 level B. In addition, the hybrid must be capable of fast uniform heating of the crystal, and must be sealed to prevent leaks in excess of  $1 \times 10^{-10}$  std atm cc./sec. To that end, a custom ceramic hybrid package was developed. Several prototype hybrids, incorporating an improved electrical design, were then assembled and evaluated in engineering. The new circuit and hybrid package proved successful, and twenty five engineering samples were manufactured by Bendix' hybrid manufacturing facility.

The mechanical design of TMXO was also significantly changed. The revised design is simpler and more repairable. Assembly time has been significantly reduced to make the TMXO producible at a lower cost. Materials research has resulted in modifications to the mechanical structure which improve both thermal and vibration performance.

To date, fifteen engineering samples of TMXO have been assembled and are presently under evaluation.

Mechanical Configuration

Thermal analysis of various TMXO designs indicated that optimum frequency stability could be achieved by thermally controlling a crystal resonator at its upper turn temperature in vacuum. By minimizing the amount of heat lost from the crystal, the temperature gradients could be reduced and improved frequency stability with changing ambient temperature would result. With this in mind, a hybrid microcircuit was designed which would provide electrical interface to the crystal and accurately control the crystal set temperature.

Figure 2 is a simplified illustration of the TMXO construction. The crystal-hybrid assembly is supported by six wires within an evacuated enclosure. In order to minimize the thermal radiation losses of the electronics assembly a radiation shield encircles the electronics. Further reduction in radiation losses is accomplished by gold plating the metal parts in the assembly (figure 3). This includes the hybrid cover, the electronics radiation shield, the header radiation shield, and the vacuum case. Spectral reflectance of the gold plated parts between the wavelengths of 0.7 microns and 2.5 microns in the infrared region is 97-99%.

Inconel Alloy 625 was chosen for the support wires because of its low thermal conductivity, high stiffness, and good weldability to Kovar. Four polyimide rods which press fit into tubes on the hybrid package are used for providing lateral support to the electronics assembly. The Vespel rods act to rigidize the assembly so that mechanical resonances are minimized or eliminated in a vibratory environment. Vespel material was chosen because of its very low thermal conductivity, good structural resistance, and compatibility with high vacuum.

The six support wires are welded to tubes brazed in the ceramic vacuum header. A radiation shield is used to cover the exposed ceramic of the vacuum header. A zirconium-graphite getter is welded to two pins which extend through the header (figure 4). After vacuum enclosure welding and vacuum baking the getter is activated providing vacuum maintenance after pinch-off. This non-evaporable getter is capable of sorbing H<sub>2</sub>, N<sub>2</sub>, O<sub>2</sub>, H<sub>2</sub>O, CO, and CO<sub>2</sub> in appreciable quantities. The output buffer circuitry, is located on the exterior surface of the vacuum header. Leadless chip components, including a CMOS buffer are vapor phase reflow soldered to header metallization.

Acknowledgement: This work was done under Contract with the U.S. Army ERADCOM, Contract DAA807-82-CJ277



An important consideration in the design of the TMXO was material and process compatibility with high vacuum. This included leak rates of the packages, vapor pressures of the various materials, and outgassing of the material surfaces. The vacuum enclosure must have a leak rate of  $1 \times 10^{-11}$  std atm cc. per second or less for a ten year life. Any nailing caused by an air leak larger than this amount would cause vacuum degradation since noble gases are not gettered. A similar problem could exist with the hybrid package. To achieve low leak rates in the TMXO enclosure, the vacuum header was fabricated by dry pressing aluminum powder, firing, metalizing and brazing of the Kovar seal ring. The enclosure consists of an Alloy 42 case with an oxygen free high conductivity copper evacuation tube.

The hybrid package was constructed using cofired alumina with fired sidewall and pins. This process provides a homogeneous hermetic ceramic body with integral feedthroughs for electrical connections.

#### Hybrid Microcircuit Configuration

Figure 5 illustrates the internal construction of the hybrid microcircuit. Both the oscillator and thermal control networks are assembled on a thick film external substrate the size of the crystal package cover. A relatively large power transistor located in the center of the substrate serves as the heating element. It is eutectically bonded to gold metalization on a beryllia substrate which is located between the microcircuit and package floor. Figure 6 shows the construction of the substrates and package. Attachment of the substrates to the package floor is made with epoxy preforms. A thermistor is located in a hole in the substrate and epoxied to the beryllia heat spreader.

All semi-conductors, thin film resistors and capacitors are attached to the substrate with epoxies and then wire bonded into the circuit. Thick film resistors are laser trimmed to value.

At the present time each crystal has a somewhat different upper turn temperature requiring a hybrid with a matching thermistor. In order to maintain the identity of the hybrid through processing, serialization is accomplished by laser marking the hybrid as shown in figure 7. The laser provides a permanent and very clean method of marking.

A binary ordered capacitor array used for tuning the oscillator to frequency is wirebonded to hybrid package feedthroughs which are accessible from the package exterior (figure 8). Gold ribbons are welded from capacitor pads to ground pads to facilitate final tuning before packaging. Package hermetic sealing is accomplished by resistance seam welding a Kovar step lid to the hybrid package sidewall. Metalization provides a solderable surface for crystal attachment. An attractive feature of this construction is that the hybrid or crystal can be salvaged if one or the other should fail.

#### Circuit Configuration

In the TMXO MMT program, an effort to simplify circuitry was undertaken, both to enhance manufacturability, as well as to support a mechanical configuration wherein circuitry was confined within a hybrid package of size comparable to the ceramic flat pack crystal. The following paragraphs describe circuit details.

The oscillator circuit shown in figure 9 uses the crystal selectivity to provide a reduction in gain and noise at frequencies removed from the carrier. A single inductance pi circuit provides selectivity to excite the SC-cut crystal C mode while rejecting the B mode appearing about 10 percent higher. A diode limiter establishes the oscillation amplitude. The output RF signal with an amplitude of approximately 0.25 ma RMS, drives a CMOS buffer device, located external to the TMXO package in its base.

Tuning of the oscillator to accommodate individual crystals is accomplished by selection of appropriate units of a binary-ordered capacitor bank, Cy, by connection of feed thru terminals external to the hybrid package. This facility allows future hybrids to be manufactured, tested and sealed prior to assembly to a particular crystal.

Varactor Cy allows electronic tuning of approximately  $\pm 1 \times 10^{-7}$  as well as correction of long term aging.

Remaining circuitry includes the thermal control and voltage regulator functions. Some of the simplifications incorporated to reduce the physical size of this circuitry are shown schematically in figure 10.

In the warm up mode, the heater current in transistor Q6 is sensed across R10, in addition to a component of heater voltage across R21, and used to control the thermal bridge voltage via clamp transistor Q7. The circuit maintains approximately 2°C per second temperature slew rate independent of heater supply over a voltage range of 10 to 18 volts. When thermistor R<sub>T</sub> reaches the set temperature, heater current is controlled by thermal feedback from heater transistor Q6 to thermistor R<sub>T</sub>, and maintains crystal temperature within  $\pm 50$  m°K of the set temperature over a range of -55°C to +75°C ambient temperature.

The National Semiconductor LM10 device performs the functions of voltage reference and comparator for the oscillator supply voltage, as well as high gain amplifier for the thermal control circuit.

#### Hybrid Fabrication

In general, the processes used in fabricating the TMXO hybrid have proven to be very reliable on other Bendix programs. The use of epoxy for component attachment, 100% wire bond pull testing, resistance seam welding and hybrid burn-in insure reliable hybrid fabrication. Two unique hybrid processes developed in this program are pulsed heat bonding of the thermistor and inductor leads and the use of a laser for serialization. The thermistor leads are 0.0254 mm diameter platinum wires and the inductor leads are comprised of insulated .127 mm diameter copper wire. Both leads are welded directly to gold metalization on the circuit substrate. Welding of the copper wires is accomplished directly through the insulation, that is, the wires are not stripped before welding.

#### Soldering

The metalized crystal package is directly soldered to the bottom of the hybrid package. After both the hybrid and crystal are presolder coated with pure tin-lead eutectic preforms and cleaned, they are attached together using vacuum reflow soldering. The hybrid and crystal are loaded into a fixture on a hot plate in a vacuum oven capable of 28 inches Hg vacuum. The oven is evacuated while the parts are heated to approximately 200°C. When the solder melts the vacuum is released and the components are allowed to cool at atmospheric pressure resulting in a solder bond with minimal void formation. Not only is a very good mechanical and

thermal bond achieved but also the risk of the solder interface being a virtual leak is greatly reduced. X-ray pictures taken of various assemblies confirm the void reduction as compared with conventional solder assembly.

Vapor-phase reflow soldering is used for mounting the leadless components of the buffer circuit (figure 11). The metalization on the vacuum header as well as the components are pretinned. Solder paste is then dispensed on the appropriate pads of the vacuum header metalization. Components are placed on the solder paste and baked for 30 minutes at 80°C. After baking the headers are immersed into 210°C vapor of a conventional vapor phase reflow system for approximately 15 seconds. What results is a fully soldered circuit in minimal time.

#### Welding

Resistance spot welding is used for assembly of the radiation shields, support wires, and getter in the TMXO. Figure 12 shows the welding of the getter and support wires to the vacuum header. Spot welding is a quick and clean method of attaching similar and dissimilar metals.

Micro-plasma welding is used to seal the vacuum enclosure to the vacuum header. Once the vacuum enclosure has been mated to the header, the assembly is inserted into copper fixturing in a miniature lathe as shown in figure 13. A microplasma welding torch is placed in close proximity of the weld zone and the lathe turned on. Pure argon plasma gas is introduced at a flow rate of 0.2 liters/minute and is ionized by a continuous pilot arc within the torch. The resulting thermal plasma established allows a pulsed arc to transfer from the cathode to the workpiece and create a uniform weld as the part is turned. A 93% Argon - 7% Hydrogen shield gas is used to constrict the arc, improving wettability of the metals and minimizing contamination. Figures 14 and 15 show the lowering of the torch assembly into the weld zone and the pulsed microplasma welding of the TMXO vacuum enclosure respectively.

#### Cleaning and Vacuum Processing

All assembly processes for the TMXO with the exception of soldering and vacuum baking are done in a Class 100,000 clean room facility. Gross contamination such as finger oils, salts and particulates are removed from TMXO components by chemically cleaning in TMS Freon, deionized water, and methanol. All components except the Vespel rods are then cleaned in an argon plasma before final assembly. Finger cots or clean gloves are used for all handling. Subassemblies are stored in dry nitrogen boxes. Once the final assembly has been completed, the TMXOs are attached to an ion pumped vacuum system using the copper evacuation tube. Heaters are clamped to the enclosures to facilitate 150°C baking for a minimum of 60 hours. The final step before pinch-off is activation of the getter. This is accomplished by forcing a high electrical current through the getter's internal heater. The getter heats up to approximately 500°C and liberates hydrogen. After activation the getter surface absorbs gases liberated within the TMXO vacuum enclosure. The getter can be reactivated to extend the ten year life of the oscillator provided the pressure within the TMXO is less than 10 microns. Following getter activation, the copper evacuation tube is "pinched off" using special tooling. The cold weld is subsequently protected from mechanical change by a small cover which is epoxied over it. The "pinch off" process is shown in figure 16.

#### Leak Testing

In order to guarantee ten year reliable operation measurements of leak rates in the vicinity of  $1 \times 10^{-12}$  atm. cc/sec. are required. Present commercially available equipment is capable of detecting helium leaks as small as  $2 \times 10^{-11}$  atm. cc/sec. It is anticipated that in the near future detectors with better sensitivity will become available. Figure 17 shows a TMXO mounted to a leak detector with a helium gas source and probe.

#### Performance

Performance of the Engineering models, reflecting the design status, is described in the following figures.

Figure 18 shows frequency variation during warm-up, with a worst-case initial temperature of -54°C. During the first 1.5 minutes, the temperature is being slewed at 20°C per second toward the crystal upper turn temperature. About one kilo joule of thermal energy is required to drive the crystal and hybrid assembly to operating temperature. Once this point is reached, the heater current decays toward a steady-state value, and the frequency overshoot resulting from the rapid slew subsides. The performance goal is  $1 \times 10^{-8}$  of final frequency within 3 minutes.

Figure 19 depicts the power dissipated within the vacuum enclosure, to maintain the crystal at set temperature over the range of ambient temperature. The data for several units are clustered on a locus representing approximately 600°C/watt thermal leakage resistance. Variation between units can be associated with the differences in turn temperatures of the specific crystals used.

Figure 20 shows typical frequency stability versus ambient temperature attained by the current models. The specification requires frequency stability better than  $\pm 1/10^{-8}$  over the ambient temperature range.

Figure 21 and 22 show typical short-term and phase noise spectral density performance. For these measurements, the oscillators are compared with reference oscillators having superior stability.

Several engineering model oscillators are presently undergoing frequency aging evaluation, and appear to meet the specification limit of  $\pm 2 \times 10^{-10}$  per day.

#### Crystal Test Facility

The purpose of the crystal test facility is to ensure suitability of crystals for use in the TMXO. It consists of a temperature controlled holder providing intimate thermal contact to the crystal, and circuitry to cause oscillation at series resonance. The holder temperature is slewed through a range that includes the lower and upper turn temperatures. The frequency/temperature characteristic of the crystal is then measured to determine the values of the upper turn temperature (UTP) and corresponding frequency offset ( $\Delta F$ ). A typical representation of this data is given in figure 23.

The UTP value allows selection of a hybrid thermistor of approximate value, while the frequency offset value  $\Delta F$  is used in the final oscillator tuning routine.

#### Hybrid Testing

This test is used to evaluate the performance of a newly constructed hybrid. The crystal is represented by a resistor of value in excess of maximum crystal tolerance. Current consumption, internal voltage reg-

ulator voltage, output frequency and amplitude are noted prior to energizing the heater circuitry. The heater voltage is then applied, and inrush current, and stabilized current are noted, as well as output frequency and amplitude stability with temperature.

With acceptable operating parameters, the hybrid is qualified for lid installation and hybrid burn in testing.

#### Crystal Hybrid Tuning

The required tuning capacitance of the oscillator is determined by this process in which the sealed hybrid, mated to an appropriate crystal, is operated in a fixture having high thermal resistance to the environment. An external temperature trim resistor is adjusted to bring the crystal to the upper turn temperature.

At this stage all internal tuning capacitors have previously been activated using temporary jumpers connected via hybrid package feed through terminals. Based upon the measured frequency and anticipated load capacitance requirement from the crystal evaluation facility, tuning proceeds by removing appropriate jumpers, in order of descending capacity increments, until the measured frequency is close to nominal value.

The range of varactor tuning is checked, and the unit forwarded to the next assembly station.

#### Group A Test Facility

This test facility provides for evaluation of oscillator frequency stability under a variety of input conditions, including variation of applied supply voltages, load capacitance, ambient temperature, and orientation with respect to the gravitational field. Other performance aspects evaluated include stabilization time and retrace accuracy following power interruption, range and linearity of frequency control, output waveform characteristics and absence of spurious emissions and power consumption versus ambient temperature.

#### Conclusions

With the improvements in design and the development of production processes and tooling, which have taken place in the last year, the TMXO offers small size, fast warmup, low power consumption and high stability, and is able to be produced consistently and reliably with simple procedures and facilities.

#### References

1. H. W. Jackson, "Tactical Miniature Crystal Oscillator," Proc. 34th AFCS, May 1980, pp. 449-456.
2. H. W. Jackson, "Update on the Tactical Miniature Crystal Oscillator Program", Proc. 36th AFCS, May 1982.

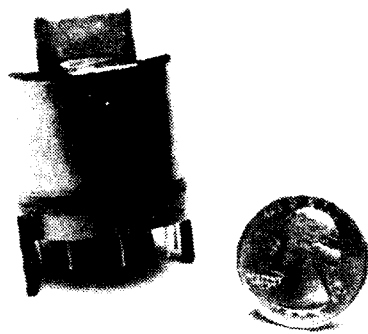


Figure 1. Tactical Miniature Crystal Oscillator

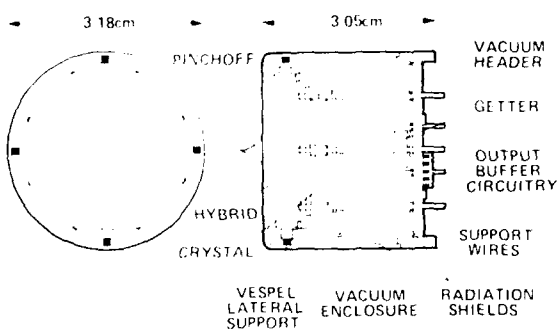


Figure 2. Simplified TMXO Construction

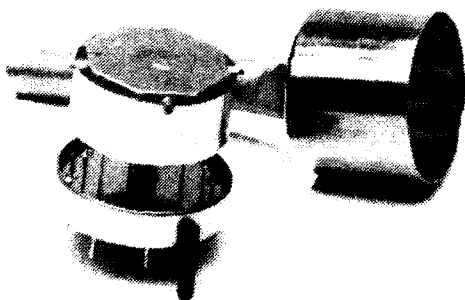


Figure 3. Internal Construction

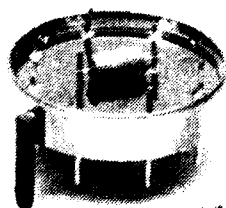


Figure 4. Vacuum Header, Header Shield, and Getter

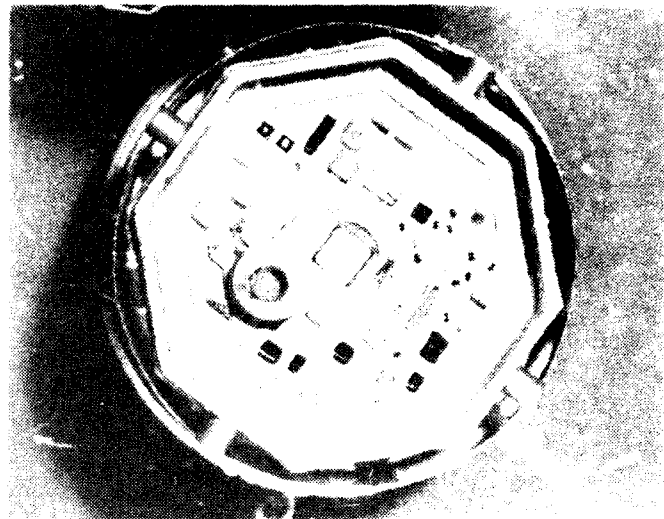


Figure 5. Hybrid Microcircuit



Figure 6. Hybrid Construction



Figure 7. Hybrid Laser Marking

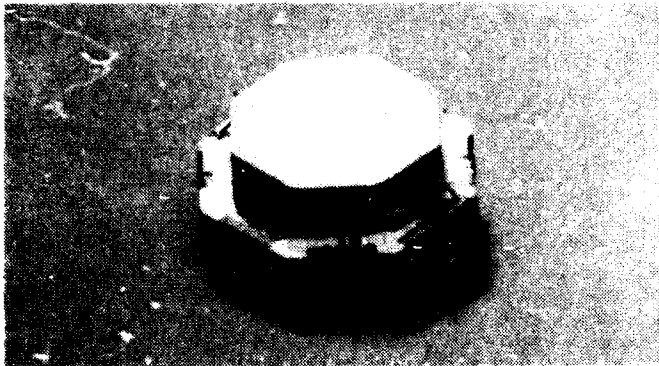


Figure 8. Hybrid and Crystal

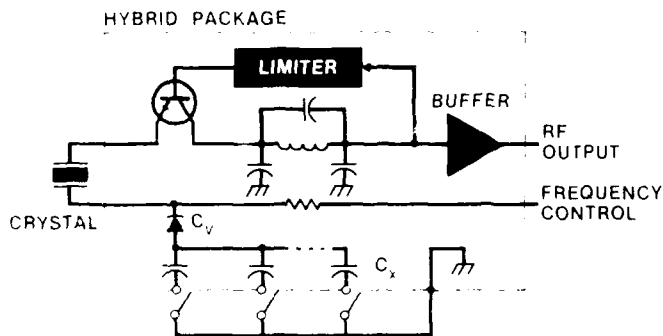


Figure 9. Oscillator Configuration

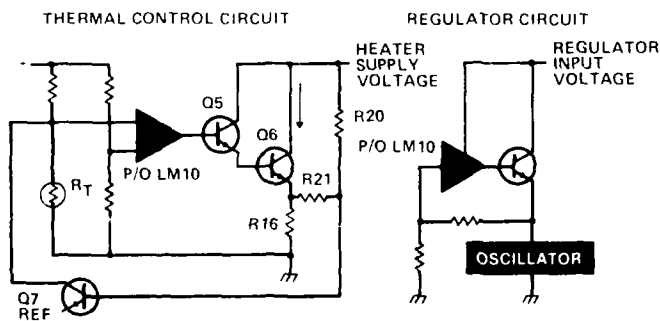


Figure 10. Thermal Control/Voltage Regulator Circuitry



Figure 11. External Buffer Circuit

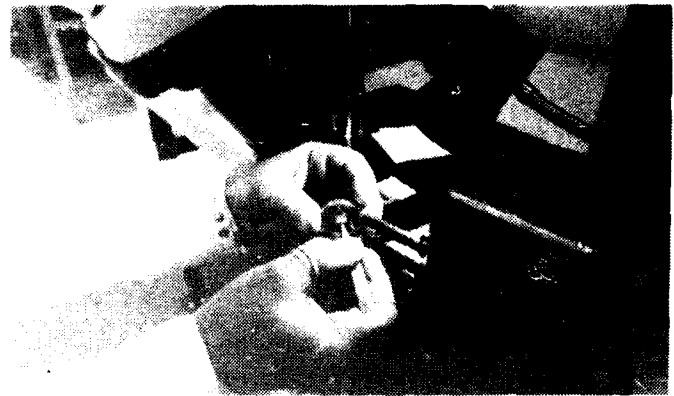


Figure 12. Spot Welding



Figure 13. Plasma Weld Equipment



Figure 14. Plasma Welding

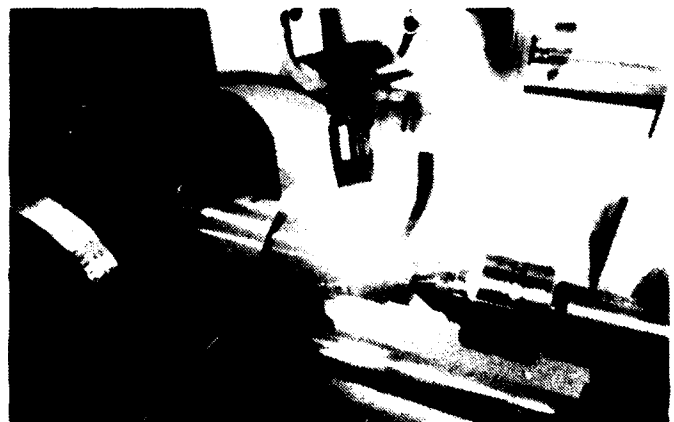


Figure 15. Plasma Welding

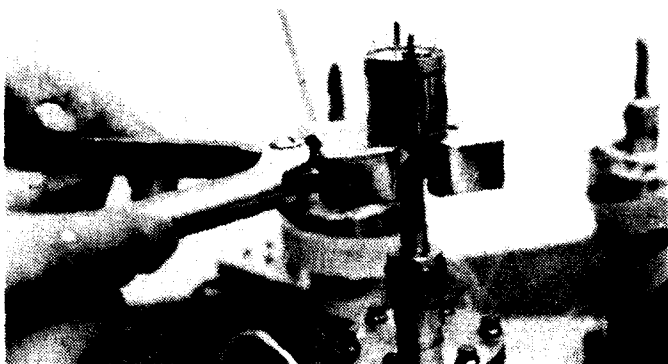


Figure 16. Pinch Off Operation

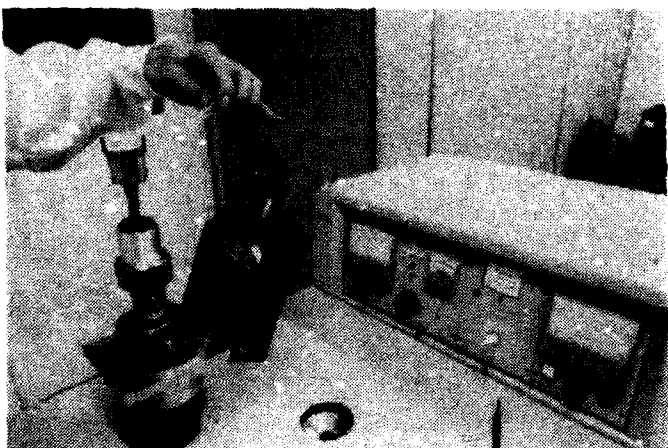


Figure 17. Leak Testing

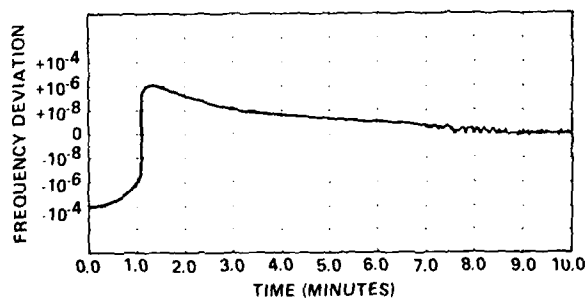


Figure 18. Warmup of TMXO at  $-54^{\circ}\text{C}$

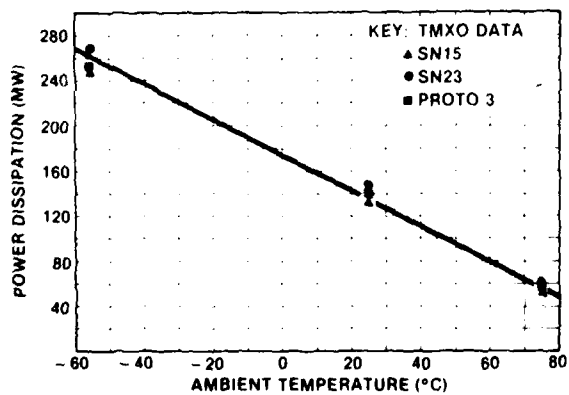


Figure 19. Power Dissipation vs. Ambient Temperature

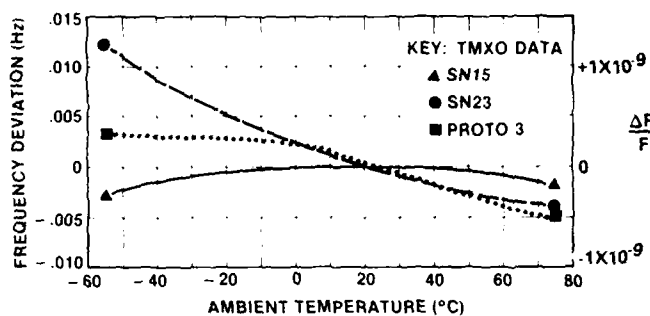


Figure 20. Frequency Stability vs. Ambient Temperature

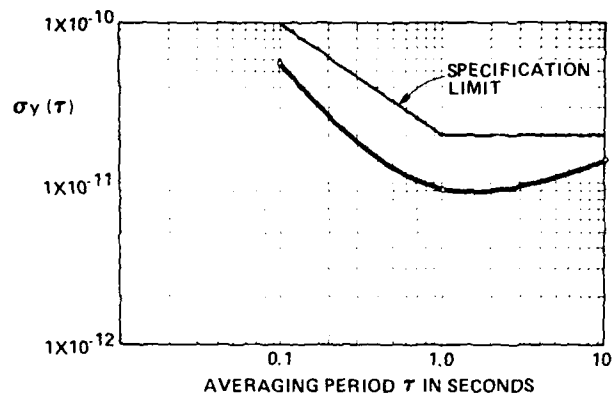


Figure 21. Short Term Stability

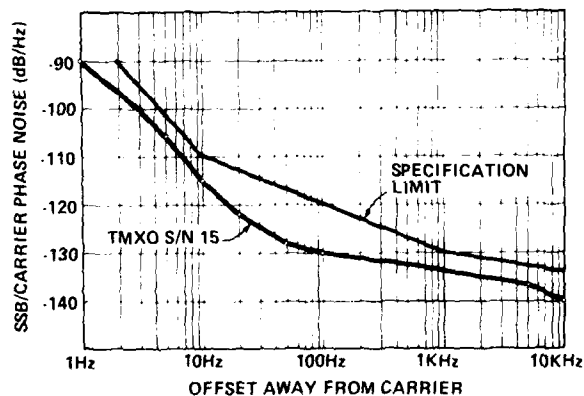


Figure 22. Phase Noise Spectral Density

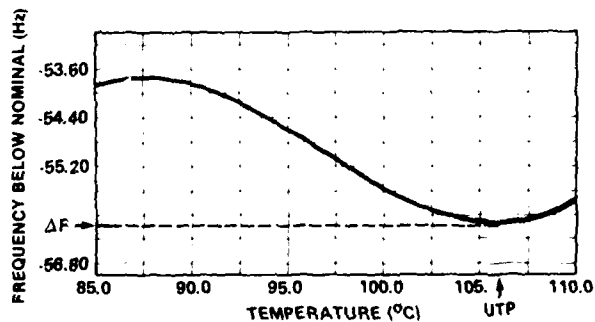


Figure 23. Crystal Frequency vs. Temperature

LIFETIME AND RELIABILITY OF RUBIDIUM DISCHARGE LAMPS  
FOR USE IN ATOMIC FREQUENCY STANDARDS

C. H. Volk and R. P. Frueholz  
 Chemistry and Physics Laboratory  
 The Aerospace Corporation, P. O. Box 92957, Los Angeles, CA 90009

T. C. English  
 Efratom, A Division of Ball Corporation  
 18851 Bardeen Ave, Irvine, CA 92715

and

T. J. Lynch and W. J. Riley  
 EG&G Inc., Electronic Components Division  
 35 Congress St, Salem, MA 01970

#### ABSTRACT

The results of various studies concerning the lifetime and reliability of the rubidium discharge lamps used in rubidium atomic frequency standard are reported. The primary life limiting process in these lamps involves diffusion of the rubidium atoms into the glass envelope of the lamp making them unavailable to the discharge. The rate at which rubidium atoms diffuse into the glass is dependent on lamp conditions including: lamp size, type of glass, lamp temperature and rf drive power. The calorimetric technique to measure the elemental rubidium content in a lamp and its use for quality control in the lamp manufacturing process are discussed.

#### I. INTRODUCTION

The discharge lamp is a critical component of the rubidium (Rb) gas cell atomic frequency standard (clock) and other optically pumped devices. The conventional lamp used in devices such as the gas cell atomic clock is of the type described by Bell, Bloom and Lynch<sup>1</sup> and Brewer<sup>2</sup> consisting of a glass envelope containing a charge of the appropriate metal, e.g. Rb, and a buffer gas under a pressure of a few Torr. The lamp is usually ignited by an rf coil that surrounds the glass envelope. The spectral emission properties of the lamp have long been recognized as extremely important in the operation of the optically pumped devices, and have been thoroughly studied.<sup>3-7</sup> On the other hand, with one notable exception,<sup>8</sup> almost no consideration appears to have been given to the life-limiting factors and hence the reliability of this type of lamp. This situation changed drastically in early 1979, however, due to lamp failures in some of the Rb clocks aboard the satellites<sup>9</sup> of the NAVSTAR Global Positioning System (GPS). As a result of these lamp failures, an effort was begun to develop a long-lived sapphire Rb lamp.<sup>9</sup> Additionally, at about the same time, an extensive investigation<sup>10</sup> of the failure mechanisms of glass lamps was initiated. This latter investigation identified the primary failure mechanism of the low-power, electrodeless Rb discharge lamp to be the diffusion of Rb atoms into the glass envelope of the lamp. The rate at which the atoms diffuse into the glass then controls the life of the lamp. We report here studies that have been concerned with Rb consumption in discharge lamps aimed at quantifying various aspects of lamp life and lamp reliability. Based on these studies, estimates have been made of the dependence of lamp life on parameters such as: initial Rb content, lamp size, lamp operating temperature, rf drive power and the glass type used to construct the envelope. The parametrization of lamp life that we present can be used to estimate lamp and hence device reliability.

In Section II of this paper we review the effort to identify the primary failure mechanism of the low power Rb discharge lamp. The development of the calorimetric technique to measure the elemental Rb content in a lamp is discussed in Section III, while the analyses of Rb consumption measurements and Rb lamp life tests are discussed in Section IV. The prospects for having an accelerated lamp life test or quality control test are presented in Section V. Although this report concerns only the Rb discharge lamp, it should be pointed out that the results presented here apply also, in varying degrees, to other electrodeless discharge lamps containing such elements as sodium (Na), potassium, cesium, mercury, and the like.

#### II. LAMP FAILURE MECHANISM IDENTIFICATION

A typical electrodeless discharge lamp<sup>1,2</sup> is displayed in Fig. 1.<sup>9</sup> The lamp consists of a glass envelope whose front we designate as the lamp face and the opposite end as the tip-off region. Glasses that have been used for the lamp envelope include: Corning 7740 (Pyrex), Corning 1720, Schott 8436 and Schott 8437. The glass envelope contains the metal charge along with a buffer gas. The buffer gas provides a source of electrons to sustain the rf induced plasma and is required to limit the mean free path of the electrons. Typical buffers presently used are either krypton or xenon at a pressure of a few Torr. The excess metal charge is constrained by thermal gradients in the tip-off region. The tip-off is formed when the glass lamp is "pulled" off the vacuum manifold. The lamp envelope is mounted in a metal base with a thermal potting material. The thermal potting material facilitates the transfer of heat from the base, which is the point of temperature control, to the glass envelope. The metal atoms in the vapor are due to the saturated vapor pressure above the metal charge, which is determined by the temperature of the metal, and thus good temperature control is essential for stable lamp operation. A plasma is sustained in the lamp by means of an rf field. Typically the rf frequency is around 100 MHz at powers ranging from tenths to tens of watts.

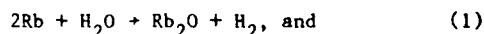
Several possible lamp failure mechanisms were investigated in response to the failures of the Rb atomic clocks on board the GPS satellites.<sup>10</sup> These mechanisms included: quenching of the excited Rb atoms; Rb reaction with impurities; and the interaction of Rb with the glass. We briefly summarize the results of that investigation.

### A. Quenching of Excited Rb Atoms

The possible role of quenching in the failure of discharge lamps was investigated by studying the spectral emission from both normal and failed lamps. In the failed lamps only emission lines present in normal lamps were observed. No emission lines from possibly outgassed materials that could quench excited Rb atoms, such as hydrogen ( $H_2$ ), nitrogen ( $N_2$ ) or oxygen ( $O_2$ ) were detected. These results are consistent with the absence of quenching species.

### B. Rb Reaction with Impurities

Another postulated mechanism for the failure of the Rb lamp was the loss of Rb by reaction with species outgassed from the envelope to form non-volatile rubidium oxide ( $Rb_2O$ ). The most likely reactions are:



Experiments which tested for the presence of  $H_2$  in failed lamps proved that reaction with  $H_2O$  is not significant. Rf-induced emission spectra from a series of standard lamps containing  $H_2$  and Xe were analyzed to obtain a detection limit of  $H_2$  in the presence of Xe buffer. Comparisons of these spectra with those of failed lamps indicated that the pressure of  $H_2$  in the failed lamps was less than 1 Torr. Removal of  $H_2$  from the vapor by either the formation of  $RbH$  or through permeation through the glass was also ruled out. The loss of Rb through this mechanism was set at about 10  $\mu g$  or less, which is small compared to the normal charge in a lamp of between a hundred and a few hundred micrograms. Based on the fact that reaction with  $H_2O$  was not significant, together with literature sources indicating that  $H_2O$  should evolve from the glass envelope much more readily than  $O_2$ , it was argued that the second reaction was also not important in the failure of the Rb lamp. However, as will be discussed in Section III, there does seem to be a reaction of the Rb with some impurity in the lamp consuming between 10 and 20  $\mu g$ . Although this amount of consumption is not significant in terms of the total charge of Rb, we show that it must be taken into account to properly predict the Rb consumption rate and hence the life of the lamp.

### C. Interaction of Rb with Glass

To determine the disposition of Rb in lamps that had been in operation for some period of time, various surface analysis techniques were used. Previous studies that considered the reaction of Na with glass employed techniques such as absorption spectroscopy, magnified examination of the glass cross section or wet chemical etching. These techniques were suitable for studies concerned with Na-glass interactions because of the rate at which Na and glass react. In contrast, the reaction of Rb with glass under conditions similar to that found in discharge lamps is orders of magnitude slower than of Na. To extract physical information concerning the Rb-glass interaction, it was necessary to study the functional form of the Rb penetration profile in the glass. Because of the extremely small amount of Rb that is consumed, simply studying the bulk penetration depth, as is typically done with Na, was found not to be adequate. To study the Rb penetration profile the following surface analysis techniques were used.

### 1. Secondary Ion Mass Spectrometry (SIMS) Studies

To obtain the highly accurate penetration profiles needed to analyze Rb permeation of glass the technique of SIMS was applied to cross-sectional pieces of Rb-exposed lamp walls. In the SIMS technique a 1.5  $\mu m$  diameter beam of oxygen ions is aimed at the sample. Secondary ions sputtered from the surface are mass spectrometrically analyzed allowing determination of elemental compositions. Lamp envelopes were broken and analysis performed along the fracture so that profiles of the Rb penetration into the glass could be obtained without the necessity of having to sputter away large quantities of glass. Our tests were performed on Rb lamps with envelopes constructed out of various glasses and operated under various conditions including heating with no lamp ignition. Varying the lamp conditions allowed the sensitivity of particular parameters of lamp life to be tested.

Figure 2 shows raw SIMS profiles of silicon (Si) and Rb for a lamp that had been operated. Zero micrometers is the inner surface of the lamp wall. The gradual increase of Si and Rb concentrations near zero is due to the finite width of the SIMS beam. Treating these data as simple one-dimensional diffusion allows fitting them to the form<sup>11</sup>

$$\frac{C(X,t)}{C_0} = \operatorname{erfc} \frac{X}{\sqrt{4Dt}}, \quad (3)$$

where  $X$  is the penetration depth,  $t$  is the exposure time,  $C_0$  is the Rb concentration at the wall, and  $D$  is the diffusion coefficient.

Experimental Rb data along with fit curves for lamps made of Pyrex glass are shown in Fig. 3. The data displayed in Fig. 3a were obtained from a sample run under typical lamp conditions while the data in Fig. 3b were obtained from a sample run under similar conditions as that for Fig. 3a but in the absence of an rf plasma. In both cases displayed in Fig. 3 the diffusion coefficient is found to be approximately  $3 \times 10^{-14} \text{ cm}^2/\text{s}$ . This is in good agreement with high temperature diffusion coefficient data<sup>12</sup> extrapolated into the low temperature regime (about 140°C).

The SIMS Rb penetration profiles indicate that Rb has penetrated many micrometers into the glass. This is particularly clear in Fig. 3b, whose sample was exposed to Rb vapor for a longer period of time than that of Fig. 3a. The depth of Rb penetration cannot be attributed to a smearing of the true profile resulting from the finite width of the SIMS ion beam. This beam, which is only approximately 1.5  $\mu m$  in diameter, would smear a surface layer to a depth of at most 2  $\mu m$ . In fact, in Fig. 3b the amount of Rb that has diffused beyond 2  $\mu m$  is greater than the amount found in the surface region.

### 2. Electron Spectroscopy for Chemical Analysis (ESCA) Experiments

The chemical form of the Rb within the glass was investigated using ESCA. In this method the surface of the sample is exposed to monochromatic X-rays and the photoejected electrons are energy analyzed. The resulting core electron binding (ionization) energies are characteristic of both a given element and its chemical form.

Rb-exposed lamp walls were analyzed along with pure samples of rubidium-hydroxide ( $RbOH$ ) and  $Rb_2O$  as reference standards. The glass samples typically had a yellow-brown discoloration as long as they were kept in dry atmospheres. However, upon



exposure to moist air they became colorless in a matter of seconds. The rapidity of this change in discoloration indicates that Rb exists in a colored form on a thin surface layer, probably less than 0.1  $\mu\text{m}$  thick. The results of our ESCA studies suggest that this colored form is  $\text{Rb}_2\text{O}$ . From the SIMS data it was seen that most of the Rb had diffused into the glass many micrometers. While the surface layer is colored, our studies found that the majority of the Rb is in the bulk glass in a colorless form, most likely as Rb-silicate. The disappearance of the colored layer when the glass samples were exposed to the ambient environment is believed to be due to the conversion of  $\text{Rb}_2\text{O}$  to  $\text{RbOH}$  in the presence of water vapor.

Figure 4 is a diagram summarizing the results of our investigations into the Rb-glass interaction. Near the inside surface of the lamp, Rb is found in the form of  $\text{Rb}_2\text{O}$ , which gives the lamp its yellow-brown color after some period of use. The amount of  $\text{Rb}_2\text{O}$  is found to decrease with increasing distance into the glass. The total amount of Rb in this surface layer has been determined to be small in terms of the total Rb consumed in a lamp over many years of operation. In the bulk glass Rb is found in a colorless form, most likely as a Rb-silicate. The penetration profiles of the Rb in the bulk glass have been found to fit quite well to a diffusion form. Based on these results we have concluded that the primary failure mechanism for low power, Rb discharge lamps is a diffusion of Rb into the glass walls. The amount of Rb that is consumed over many years of operation is very small compared with the amount of glass in the lamp envelope, thus there is no saturation effect and the Rb consumption continues, for all practical considerations, forever.

### III. CALORIMETRIC DETERMINATION OF Rb CONSUMPTION

Simple diffusion in glass has been extensively studied.<sup>13</sup> In principle one should be able to use the diffusion law to predict the amount of Rb consumed in a specified length of time or conversely determine the lamp fill requirement for a desired lamp life. In simple diffusion the total mass of the material consumed,  $M$ , penetrating the glass as a function of time, is given by Eq. (4)

$$M = 2AC_0 \left(\frac{\pi}{D}\right)^{1/2} \sqrt{t}, \quad (4)$$

where  $A$  is the surface area,  $C_0$  is the density of the penetrating species at the glass surface and  $D$  is the diffusion coefficient of the penetrating species for the particular glass. The difficulty with Eq. (4) is in obtaining precise knowledge of both  $C_0$  and  $D$  in the lamp application. The density of Rb at the glass surface certainly depends on the temperature of the Rb reservoir that controls the Rb vapor pressure in the lamp. However, based on a mathematical model of the discharge lamp<sup>14</sup> the density of Rb at the lamp wall is also predicted to be a strong function of the rf drive power applied to the lamp. Unfortunately, at present it is not possible to model the exact functional dependence of Rb density on lamp drive power. Additionally, the diffusion coefficients for Rb in the glasses of interest are not well known. The SIMS analyses that we have performed on various lamps have not provided detailed enough information concerning the diffusion coefficients. The best way, to date, to determine the rate of Rb diffusion into the glass envelope of a lamp is by performing Rb consumption measurements under the lamp conditions of interest.

One way to evaluate the rate of Rb consumption in a discharge lamp is to operate numerous lamps to

failure and then post analyze, typically with either atomic absorption (AA) or neutron activation analysis (NAA), to determine the initial Rb fill in a lamp. In this manner a Rb consumption rate for a particular set of lamp operating conditions can be derived. There are many disadvantages to this procedure, including the enormous amount of time that it takes to generate any information. During the course of work performed in support of the GPS program, it was suggested that a differential scanning calorimeter (DSC)<sup>15</sup> could be used to measure the amount of Rb in a lamp. Because this technique has proven to be so successful and has significant implications for future lamp work, the following description is given.

In DSC, sample and reference objects are both heated such that their temperatures increase at the same rate. Heating rates are measured in degrees Celsius/minute. The instrument measures the heat flow, in calories/minute, required to maintain this heating rate for both sample and reference. The difference between these two heat flows is the instrument output, which is typically plotted versus time.

If the sample and reference are identical there will be no differential signal. Typically, though, the reference is an inert material (e.g. sand) and the sample is the material of interest. If the sample does not undergo a phase transition while being heated, the difference signal will be proportional to the difference in heat capacities of the sample and reference. This signal may be electronically nulled out. When the sample undergoes a phase transition, for example melting as is the case for Rb, additional heat is required to maintain its heating rate due to the heat of the phase change. This increase in the differential signal will appear as a peak on the differential signal versus time/temperature plot. The area under the peak will equal the additional calories required to melt the sample. After the phase transition the differential signal will return to a nearly constant value again reflecting the difference in heat capacities of the sample and reference objects. This differential signal may be slightly different from the signal prior to the phase transition as a result of a change in the sample's heat capacity.

In the present Rb consumption studies DSC was used to measure the heat required to melt the Rb contained within a discharge lamp. This heat, when divided by Rb's heat of fusion, 6.14 cal/g, yields the amount of elemental Rb. A typical DSC curve is shown in Fig. 5 for a lamp containing approximately 300  $\mu\text{g}$  of useable, elemental Rb. Depending on the quality of the calorimeter, sensitivities in the microgram range can easily be realized.

The advantages of the DSC technique for lamp measurements are easily seen. The DSC measures only elemental Rb, i.e., useable Rb in the lamp. Once Rb has reacted with the glass or other material, it no longer melts at the same temperature as metallic Rb, and thus does not contribute to the DSC signal. DSC can thus be used to monitor the rate of disappearance of the elemental Rb from the lamp reservoir. The fact that a consumption rate can be determined for an individual lamp implies that the DSC techniques can potentially be used to monitor quality control in the lamp manufacturing process. The DSC technique is also non-destructive, unlike AA, and can be accomplished in considerably less time than NAA; 3 to 5 DSC scans of a lamp can be accomplished in about an hour, whereas the turn-around time for a single NAA measurement is about 3 to 5 months.

At EG&G, Rb lamp fill measurements are made using a standard Perkin-Elmer Model DSC-2C Differential Scanning Calorimeter and a Hewlett-Packard Model 3390A Reporting Integrator. The latter instrument gives a numerical reading of the amount of Rb in a lamp. After an initial calibration, the measurement process is very straightforward. The most critical aspect is "chasing" the Rb to a spot on the face of the lamp (see Fig. 6) so that it all makes good thermal contact with the calorimeter pan. A dummy (empty) lamp is placed on the other pan. A small amount of thermally conductive grease is used between the faces of the lamps and the pans. Typical repeatability between measurements is  $\pm 0.5 \mu\text{g}$ , both for the same "chase" and when the Rb is redistributed and recharged into a new spot. Absolute accuracy is dependent on the calibration procedure and is believed to be about  $\pm 10\%$ . It is the repeatability that is of most concern for the Rb consumption measurements.

#### IV. Rb LAMP LIFE INVESTIGATIONS

Over the past several years there have been a number of efforts undertaken to specify the requirements to ensure reliable operation of the Rb discharge lamp. These studies have included three types of glass; Corning 1720, Schott 8437 and Schott 8436. With the Corning 1720 glass lamps, two different lamp operating conditions have been studied, which correspond to those used in the Efratom and EG&G Rb frequency standards, respectively. These lamp conditions are shown in Table I. Circumstantial evidence<sup>1,16</sup> indicates that it is possible to "overfill" a lamp, thereby generating excessive lamp noise. A possible physical mechanism for such a phenomenon is the displacement of excess Rb in a lamp by thermal and/or mechanical forces which produces changes in light intensity with concomitant frequency instability when the lamp is used in a Rb clock. A quantitative understanding of Rb consumption allows the lamp fill to be chosen so as to minimize noise while providing adequate life for the intended application. The results of the various lamp studies follow.

##### A. Corning 1720 Glass

##### 1. Efratom Operating Conditions

An extensive effort was undertaken at The Aerospace Corporation to measure the Rb consumption rates in Efratom-type, Corning 1720 glass lamps using the calorimetric technique. Lamps of the Efratom design, manufactured both at Efratom and at Aerospace, were studied. All the lamps were operated in oscillators built by Efratom to ensure that each lamp was subjected to the same rf drive power. Figure 7 shows typical results of Rb consumption in this kind of lamp. In Fig. 7 the log of the Rb consumed is plotted versus the log of the lamp operating time. Rb consumption is measured in units of micrograms while the lamp operating time is given in hours. Fitting to a linear function on the log scale yields the power law relation for Rb consumption in time. For this particular lamp, the fitting process yielded

$$M_{\text{Rb}}(t) = 10 t^{0.26} \quad (5)$$

with  $M_{\text{Rb}}(t)$  the mass of Rb consumed in micrograms in a time  $t$ , in hours. This fit is shown as the dashed line in Fig. 7.

Eq. (5) is clearly not of the diffusion form given by Eq. (4). Measurements on other lamps yielded other power law relationships for the amount of Rb consumed in a specified lamp operating time. Two

difficulties with these results were: 1) the power laws that were derived did not have a simple physical explanation, and 2) each lamp seemed to exhibit its own consumption law. It was found, however, that all the Rb consumption data could be fit quite well and quite consistently if one assumed that in addition to simple diffusion of the Rb into the glass, there was also a mechanism by which a small amount of Rb was consumed almost instantaneously at the outset of lamp operation. In this model one predicts the Rb consumption to obey a law of the form

$$M_{\text{Rb}}(t) = R \sqrt{t} + B. \quad (6)$$

The first term on the right hand side of Eq. (6) corresponds to simple diffusion, see Eq. (4), and the second term represents some immediate consumption of Rb. Fitting the data shown in Fig. 7 to the form of Eq. (6) yields

$$M_{\text{Rb}}(t) = 1.09 \sqrt{t} + 24 \mu\text{g}, \quad (7)$$

which is represented by the solid line in Fig. 7. It is not unreasonable to consider that the Rb could get some small amount of impurity in the lamp, see Section II. As long as the amount of the impurity is small and more impurity does not evolve from the lamp walls as a function of time, this initial clean-up process in the lamp could take place almost instantaneously. One feature of this model is that each lamp could have a different quantity of Rb consumed in the clean-up process. The amount of Rb consumed should depend on the impurity level in the particular lamp, which in turn should depend to some extent on the particular processing to which a lamp was subjected during its manufacture.

Averaging the results from ten lamps, where some individual lamps had operating times over 10,000 h, the following Rb consumption law for Corning 1720 glass lamps of the Efratom design operated under the normal Efratom conditions, see Table I, was obtained

$$M_{\text{Rb}}(t) \approx (1.4 \pm 0.4) \sqrt{t} + (18 \pm 6) \mu\text{g}. \quad (8)$$

The factor of approximately  $18 \mu\text{g}$  reflects both the proposed instantaneous consumption of Rb and the error in the calorimetric measurement. The measurement errors should tend to cancel on the average over ten lamps. Thus the  $18 \mu\text{g}$  is the quantity of Rb that one would expect to see consumed on the average upon the initial turn-on of this type of lamp.

Previously a life test of Rb lamps constructed out of Corning 1720 glass was conducted at Efratom. The test involved lamps that were operated to failure and then analyzed using NAA to determine the initial Rb fills. The results of that study are displayed in Fig. 8. A fit of the data shown in Fig. 8 to the form of Eq (6) yields the relation

$$M_{\text{Rb}}(t) = (1.45 \pm 0.1) \sqrt{t}, \quad (9)$$

which is shown in Fig. (8) as the solid line through the data points. Because in this test only one consumption point in time per lamp could be acquired, i.e. total lamp life and initial Rb fill, the second term in Eq. (6) could not be evaluated for the individual lamps. Since the amount of Rb that may be instantaneously consumed could be different for each lamp, fitting lamp data from life tests to the form of Eq. (6) can not, a priori, be justified. However, if all the lamps had been processed in a sufficiently identical manner then one could claim that life test data would yield the same information as the consumption measurements. In this particular case,

the instantaneous consumption factor seems to have been vanishingly small, implying that the processing of these lamps was quite good. The fit to these particular life test data then is sensitive only to the diffusion process. Comparing Eq. (8) with Eq. (9) shows that there is excellent agreement for the factor describing the rate of diffusion of the Rb into the glass.

## 2. EG&G Operating Conditions

Studies of Rb consumption, using DSC, in lamps of the EG&G design and operated under the EG&G normal conditions (see Table I) have been conducted at both EG&G and Aerospace. The consumption data exhibited features similar to that found in the studies conducted with Efratom-type lamps in that power law fits to the data yielded time dependencies much slower than that of simple diffusion. Typical consumption data yielded  $M_{Rb}(t) = 3.7t^{0.25}$ . Assuming that the Rb consumption results from two processes, simple diffusion and rapid, initial clean-up, provides consistent fits to almost all the data for the EG&G lamps. The EG&G and Aerospace studies gave essentially the same results, with the uncertainties in the Aerospace data being somewhat larger due to the poorer quality of the DSC used for that work.<sup>17</sup> Rb consumption in the EG&G lamp, operated under EG&G normal conditions, can be described by the relation

$$M_{Rb}(t) = (0.2 \pm .05) \sqrt{t} + (14 \pm 3) \mu g. \quad (10)$$

In Fig. 9 we show a composite plot of all the Rb consumption data measured at EG&G. For the sake of clarity, the factor representing the instantaneous Rb consumption, the factor B in Eq. (6), was determined for each lamp represented in Fig. 9 and subtracted from the consumption data for each lamp before plotting. The data in Fig. 9 represent Rb consumption through diffusion only. Each symbol in the figure represents a different lamp. From Eq. (10) it is seen that the term representing the rapid consumption of Rb in the lamp appears to be about the same size as that found in the Efratom lamp. This fact seems to indicate that the phenomenon is inherent in the lamp manufacturing process. The fact that the term describing the diffusion of the Rb into the glass is smaller for the EG&G case compared to that of the Efratom case can be readily understood by referring to Eq. (4) and Table I. From Eq. (4) it is seen that the diffusion term depends on the inner surface area of the lamp, the density of the Rb at the walls and the diffusion coefficient for the glass. Since both types of lamps were made of Corning 1720 glass we expect the diffusion coefficients to be nearly identical.<sup>18</sup> The inner surface area for the EG&G lamp is seen from Table I to be about a factor of two less than that for the Efratom lamp. Additionally, the rf drive power of the EG&G lamp is about a factor of 2 or 3 smaller than that for the Efratom lamp. Eckert's lamp model<sup>14</sup> would predict the Rb concentration at the walls to be smaller for the EG&G lamp, because the rf drive power is smaller, than for the Efratom lamp. Thus both factors, the surface area and the rf power, are such that one would predict a slower Rb consumption rate due to diffusion in the EG&G lamp than for the Efratom lamp. Unfortunately, Eckert's model<sup>14</sup> is not sufficiently developed for a quantitative comparison to be made between the results of the consumption/life tests and the model predictions. We believe that it is clear, however, that the Rb consumption in Corning 1720 glass lamps is well described by an initial rapid consumption followed by long term simple diffusion.

## B. Schott 8436 Glass

Rb consumption measurements have been performed for a small sample of Schott 8436 glass, Efratom-type lamps operated under the Efratom normal conditions. The consumption measurements to date are shown in Fig. 10. The solid line in Fig. 10 is a fit of the consumption data to the form of Eq. (6). The resulting Rb consumption law was found to be

$$M_{Rb}(t) = (0.9 \pm 0.15) \sqrt{t} \pm 7 \mu g. \quad (11)$$

The fit shown in Fig. 8 is noteworthy, in that it indicates that the model used to describe Rb consumption in Corning 1720 glass lamps is valid also for the Schott 8436 glass lamps. The seemingly lower diffusion rate for the Schott 8436 glass lamps tends to indicate that this glass is more alkali resistant in the lamp application than the Corning 1720 glass.

## C. Schott 8437 Glass

Schott 8437 glass was used for the lamp envelopes of the early GPS Rb clocks. The failures of lamps on the early GPS satellites prompted a change from Schott 8437 glass to Corning 1720 glass for the lamp envelope. However, it was felt that it would still be important to understand the Rb consumption phenomenon in the Schott 8437 glass lamps to insure that the optimal glass choice had been made.

All the envelopes for lamps involved in this particular study were manufactured by Efratom Elektronik, GmbH in Munich, Germany. The low-filled, short lived lamps were filled by Efratom California, Inc. for special purpose testing at the time of the GPS failures; the other lamps exhibiting long life were filled in Munich as part of Efratom's regular lamp production and testing. These particular lamps were manufactured and put into tests before the technique of calorimetry had been developed to measure initial Rb lamp fill. Efratom California, Inc. had analyzed lamp life versus lamp fill for the sample of short-filled lamps by operating the lamps to failure and then using either NAA or AA to determine the initial Rb fill. Some of the normal production lamps, i.e. those filled in Munich, however, are still operating after eight years of almost continuous non-accelerated life-testing and thus it was necessary to determine the amount of Rb that had been consumed during the operating life to date. For these lamps both the total Rb, i.e. the initial Rb fill, and the amount of Rb remaining in the reservoir had to be determined. NAA was used to determine the initial Rb fill and DSC was used to measure the Rb mass still in the reservoir.

Owing to the nature of the glass envelope, only the  $^{85}\text{Rb}$  content in the lamp can be determined using NAA. Because a non-natural isotopic fill is used in the Efratom lamps,<sup>19</sup> a precise determination of the isotopic ratio had to be made before the total Rb could be determined from the NAA results. A laser excitation fluorescence technique<sup>20</sup> for this measurement was employed which provided an accuracy of about 4% on the  $^{87}\text{Rb}/^{85}\text{Rb}$  ratio. This ratio then allowed computation of the total Rb fill from the NAA determination of the  $^{85}\text{Rb}$  content. Error bars were assigned to the  $^{85}\text{Rb}$  determination based on the results of a previous study of the accuracy of NAA.<sup>21,22</sup> The errors quoted for the total Rb fill in Table II, incorporate both the uncertainties in the isotopic ratio measurement and the assumed inaccuracies in the NAA evaluation. To ensure that there were no systematic effects in the NAA results, other lamps, not shown in Table II, were included as a

check. The Rb fills in these lamps were known with high accuracies through previous NAA and DSC measurements. No evidence for any systematic errors in the NAA results was found.

The DSC results are affected by two major error sources; the uncertainty in the "glass correction" factor<sup>23</sup> and the repeatability of a lamp measurement. A glass correction factor is applied to the DSC measurement to account for perturbations in observed DSC signals due to the lamp's glass envelope. Lamp Nos. 604 and 613 had failed during their operation and thus we identically assigned zero to their Rb reservoir contents. For completeness we verified that the DSC yielded no detectable Rb signal.

We display in Fig. 11 a plot of lamp operating times versus Rb consumed for all Schott 8437 lamps involved in life testing. In Fig. 11 each point represents an individual lamp; points represented by an 'o' with no error bars are lamps that were life tested at Efratom. These lamps were operated until failure and then were analyzed by either NAA or AA to determine the initial Rb fill. No error bars are indicated because of insufficient information on their analyses. Points for which error bars are displayed represent those lamps that were analyzed for consumed Rb. There are five points in Fig. 11 that correspond to lamps that have not failed and thus those points represent Rb consumed over the operating time of the lamp. One of these lamps has operated for 25,000 h and the remainder have operated for about 70,000 h each.

Rb consumption in lamps with Corning 1720 glass and Schott 8436 glass envelopes was found to be well understood in terms of diffusion of the Rb into the glass plus an initial rapid consumption. The life test data from lamps with Schott 8437 glass envelopes, however, does not definitely support that model. Although the Schott 8437 life test data do not allow a definite description based on a single model, they do provide us insight into the following Rb consumption models.

### 1. Alkali Interdiffusion

In some studies of the alkali attack on glass, in particular with Na, it has been shown that the process of alkali atoms or ions diffusing into the glass structure is accompanied by a reverse migration of the alkali atoms already present in the glass.<sup>24</sup> Schott 8437 glass has a Na content of about 2% by weight. Under this model, we would expect a one-for-one exchange of Rb for Na during the operation of the lamp. As Na diffused out of the glass envelope, a Rb-Na amalgam would form. The amalgam would then affect the quality of the DSC scan since a pure Rb melt would no longer be seen. No effect like this was observed, which would have been quite pronounced in lamps Nos. 397, 400, 633, 718 and 881-3; consequently, we believe that this process does not significantly contribute to Rb consumption in these lamps.

### 2. Rubidium Diffusion

Because the data presented in Fig. 11 do not definitely support the model that we used to describe Rb consumption in Corning 1720 glass and Schott 8436 glass lamps, we propose two alternative explanations to describe these data.

#### a. The "Two-Glass" Model

Assume that the Rb diffusion into the Schott 8437 glass is described by two different

diffusion processes: one that controls the Rb diffusion through a thin surface layer, and a second process in the bulk of the glass. Under this model, the thin surface layer controls the rate of Rb consumption in the short term and the bulk glass controls the consumption process in the long term, i.e., after the thin layer has been saturated. In Fig. 12 we re-plot the Schott 8437 lamp data together with a prediction of Rb consumption under this "two-glass" model, assuming a diffusion coefficient in the first layer, with thickness 2.5  $\mu\text{m}$ , of  $\sim 1 \times 10^{-14} \text{ cm}^2/\text{s}$  and for the bulk glass of  $\sim 5 \times 10^{-16} \text{ cm}^2/\text{s}$ . The model is seen to fit the data fairly well with diffusion coefficients that are of the correct order of magnitude. However, there are no data in the critical transition region, i.e., between  $10^2$  and  $10^4$  h, and thus the experimental support for this model is weak.

The origin of a two-glass condition in these lamps can be physically understood in a number of ways. A cleaning process in the manufacture of the lamp, e.g., an HF or some other rinse, might alter the characteristics of the glass in a narrow region at the inner surface. Additionally, the plasma could possibly change the glass properties to some depth. This may be similar to the brown surface layer that occurs during lamp operation. On the other hand, we have not seen an analogous phenomenon for the Corning 1720 or Schott 8436 glasses. It may be that a similar effect occurs for these lamps, but takes place after a much longer time and thus simply has not been observed yet. Because we have no information concerning the manufacture of the Schott 8437 lamps, we must present the two-glass model as speculation.

#### b. Simple Diffusion

In Fig. 13 we display fits of the Schott 8437 lamp data to simple diffusion forms. Because the data naturally break into two groups; short-lived lamps, with operating times less than  $10^3$  h; and long-lived lamps, with operating times greater than  $10^4$  h, we show two diffusion fits. A possible explanation is that the data below  $10^3$  h result from subjecting the lamp to some anomalous procedure during manufacture which resulted in a high rate of Rb consumption. Fitting the long-term data to a simple diffusion form yields

$$M_{\text{Rb}}(t) \sim (0.8 \pm 0.2) \sqrt{t} \quad (12)$$

In this fit, the initial rapid consumption term given in Eq. (6) was found to be insignificant and hence was neglected.

The fact that the Rb consumption in both Corning 1720 glass lamps and Schott 8436 glass lamps is well described by essentially simple diffusion, makes the short-term lamp life data for the Schott 8437 glass lamps and hence the two-glass models somewhat suspect. Additionally, lamps for both Schott glasses exhibited about the same Rb consumption rate in the long term which is what one would expect based on the presumed similarities between the two glasses. More experimental work would be needed to determine whether the Schott 8437 glass lamps are exhibiting either a different consumption process or simply a manufacturing anomaly. Finally, whether the two-glass model or simple diffusion is the correct picture is not critical to long term lamp life prediction. In the long term, greater than  $10^3$  h, the lamp life predictions, derived from the consumption data fits to each model, converge.

#### D. Summary of Empirically Derived Consumption Laws

Rb lamp tests have yielded the following consumption laws for various lamp conditions:

1. Efratom, Corning 1720 Glass Lamps:  
 $M_{Rb}(t) = (1.4 \pm 0.4) \sqrt{t} + B$
2. EG&G, Corning 1720 Glass Lamps:  
 $M_{Rb}(t) = (0.2 \pm 0.05) \sqrt{t} + B$
3. Efratom, Schott 8437 Glass Lamps (consumption law based on the long-lived lamps only):  
 $M_{Rb}(t) = (0.8 \pm 0.2) \sqrt{t} + B$
4. Efratom, Schott 8436 Glass Lamps:  
 $M(t) = (0.9 \pm 0.15) \sqrt{t} + B$

The factor B represents the small amount of initial Rb consumption that we believe occurs in these lamps. This initial Rb clean-up typically involves up to 20  $\mu$ g of Rb. We have at the present time no way to predict, a priori, how much Rb will be initially consumed in a particular lamp; however, we think that any initial consumption much greater than 20  $\mu$ g most likely indicates an anomaly in the lamp processing.

The various empirically derived consumption laws show the effects of the different parameters in Eq. (6). Comparing the Corning 1720 results from Efratom and EG&G lamps demonstrates the effects of both lamp size and rf drive power on Rb consumption. Efratom uses a larger lamp, with greater rf power than does EG&G. The consumption rate of Rb in the Efratom lamp is consequently higher. The results from the Efratom Schott glass lamps compared with those from the Corning 1720 glass lamps seem to indicate that both of the Schott glasses, at least in the long term, have lower diffusion coefficients for Rb than does Corning 1720 glass.

Although the empirically derived consumption laws give strong support for the validity of Eq. (4), it is not possible at the present time to use Eq. (4) to derive the Rb consumption rate for an arbitrary set of lamp conditions. The biggest single problem concerns the exact dependence of the Rb concentration at the lamp walls on the rf drive power. The analytical model of the rf discharge is not sufficiently developed to allow more than a qualitative description of the lamp. Additionally, there are no good measurements of the Rb diffusion coefficients for the glasses of interest. The consumption measurements thus provide us with the best characterization of lamp life and reliability.

#### V. ACCELERATED LAMP LIFE PROCEDURE/QUALITY CONTROL TESTING<sup>25</sup>

Accelerated life testing is an extremely useful technique for determining device reliability. In an accelerated test, the operating life of a device is compressed by some means into a time much shorter than the normal lifetime. Performance characteristics can then be monitored for a statistical sampling of devices and estimates for the normal reliability of the device can be made. Equally important is quality control testing to ensure that particular components have been manufactured properly and will perform according to the prediction of the statistical sampling. To investigate possible means of accelerating the life of a discharge lamp, Rb lamps, all of the Efratom design and constructed out of Corning 1720 glass, were operated under various temperature and rf drive power conditions. Rb

consumption rates in these lamps were determined using DSC. Lamp lifetimes for a "standard" initial Rb fill, for this analysis we arbitrarily considered an initial fill of 400  $\mu$ g of Rb, were then extrapolated for the specific operating conditions.

The lifetime of Rb discharge lamps is limited by the reaction of Rb vapor with the glass envelope of the lamp. In this section we show that there is a good analogy between this type of reaction and the reaction of a gas with a quiescent liquid. The kinetic theory of the latter type of reaction has been well developed by P. V. Danckwerts, and the same mathematical description may be applied to the lamps. The theory has some adjustable parameters which may be used to fit lamp lifetime data and, therefore, the theory may be used to predict the effect of temperature on lifetime and the time dependence of Rb consumption. While this description of the lamp behavior is simplified and incomplete, it provides a useful conceptual framework for the further understanding of lamp behavior, and shows the limitations of accelerated lifetime testing.

The traditional picture of glass is that it is simply a liquid of very high viscosity. While this view is now regarded as oversimplified (and we shall show one way in which it fails), it is very useful as an analogy for reaction kinetics across a phase boundary. The theory of gas-liquid reactions has been well developed for certain simplified cases, and we shall apply the version given by P. V. Danckwerts<sup>26</sup> to the reaction of Rb vapor with Corning 1720 glass. The theory gives a physical picture of the nature of the reaction, and permits the prediction of consumption-versus-time curves as a function of temperature from a limited set of data.

The theory incorporates just two phenomena: diffusion and reaction. In the version employed here, the diffusion problem is simplified to include only diffusion in the condensed phase. This is justified because gas both phase diffusion and the sticking probability of the gas on the surface are sufficiently rapid that the rate of the overall process is not limited by gas processes. Thus, in this theory, it is assumed that an arbitrarily thin surface layer of the condensed phase is in Henry's law equilibrium with the partial pressure of the gas phase reactant, and that the overall transfer of gas across the phase boundary is governed by diffusion into and reaction with the condensed phase. The diffusivity of the gas in the condensed phase, the solubility of the gas, and the reaction rate constant are the parameters required by the theory, although these parameters have different temperature dependencies that must also be included.

The theory predicts that the consumption of gas will vary as the square root of time if diffusion is the dominant process in the condensed phase, and that the consumption will vary linearly with time when chemical reaction dominates. In the region where both processes are competing, the theory predicts an initial square-root-of-time behavior, followed at long times by a linear behavior. It must be pointed out that the validity of this theory rests on the assumption that there are no glass saturation effects. While this is a very good approximation for Rb, it would not be as good for more rapidly reacting species such as Na. Once the reaction between the Na and glass has saturated, consumption will change from linear to square root, implying a diffusion-limited process.

In the case of the Rb-plus-glass reaction, we have shown experimentally the consumption of Rb to

have a square-root-of-time dependence at low temperatures and a linear time dependence at high temperatures. This implies that chemical reaction does not set in until high temperatures are reached, and therefore, the chemical reaction has a low pre-exponential factor and a high activation energy. The pattern of diffusion at low temperatures and reaction at high temperatures has been seen for other alkali-metal-plus-glass reactions.<sup>27,28</sup>

We will follow the nomenclature used by Danckwerts<sup>26</sup> with some minor simplifications. The equation for diffusion and reaction in a condensed phase is:

$$D \frac{d^2 a}{dx^2} = \frac{da}{dt} + ka \quad (13)$$

where  $D$  is the diffusivity of the gas in the condensed phase,  $a$  is the concentration of gas in the condensed phase,  $x$  is the distance from the surface, and  $k$  is the first-order chemical reaction rate constant. The boundary conditions are:

$$a = A^*, x = 0, t > 0, \quad (14a)$$

$$a = 0, x > 0, t = 0, \text{ and} \quad (14b)$$

$$a = 0, x = \infty, t > 0, \quad (14c)$$

where  $A^*$  is the concentration of the gas right at the surface, given by Henry's law and assuming equilibrium with the partial pressure of gas present in the bulk gas phase. The solution to this equation with these boundary conditions is:

$$Q = A^* \left(\frac{D}{k}\right)^{1/2} \left[ \left(kt + \frac{1}{2}\right) \operatorname{erf} \left( \frac{kt}{\pi} \right)^{1/2} + \left(\frac{kt}{\pi}\right)^{1/2} e^{-kt} \right] \quad (15)$$

where  $Q$  is the integrated consumption of gas, in moles per square centimeter of surface,  $t$  is the time, and  $\operatorname{erf}$  is the error function. The exact solution is plotted in dimensionless form in Fig. 14. For times shorter than those shown in the figure, the consumption is a function of the square root of time:

$$Q = 2A^* \left(\frac{Dt}{\pi}\right)^{1/2} \quad kt \ll 1 \quad (16)$$

for times longer than those shown in the figure, the consumption has a linear relation with time:

$$Q = A^* (Dk)^{1/2} t \quad kt \gg 1 \quad (17)$$

All intermediate values must be read off the dimensionless figure. The two approximate solutions may be used for fitting experimental data, with the short time form approximating little chemical reaction and the long time form approximating rapid chemical reaction.

Three parameters are required by the theory:  $A^*$ , the concentration of dissolved gas at the surface;  $D$ , the diffusivity of gas in the condensed phase; and  $k$ , the first-order reaction rate constant.

For the value of  $A^*$ , we have found no direct measurements for Rb in the glass of interest, Corning 1720. In these experiments, the Rb vapor pressure is held more or less constant at  $2 \times 10^{-3}$  Torr, which is the equilibrium vapor pressure at 135°C. Our estimate for  $A^*$  is made by analogy with the solubility of Na vapor in glass, which is typically 2 weight percent for glasses at 300 to 400°C in equilibrium with Na at that temperature.<sup>29,30</sup> For a glass of density of 2.6 g/cm<sup>3</sup>, this corresponds to two moles of Na metal per liter of glass. We have arbitrarily assigned the same molar concentration to Rb in our glass. Two moles per liter gives:

$$A^* = 2 \times 10^{-3} \text{ moles/cm}^3 \quad (18)$$

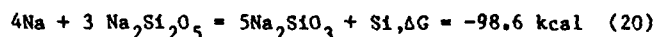
Clearly, the two systems are not the same. The only justification for this choice of  $A^*$  is that the 2 M figure seems to be constant for a wide range of conditions.

For the diffusivity, we use values obtained experimentally from the surface analyses, as described Section II. For a liquid there is an inverse relationship between viscosity and diffusivity,<sup>26</sup> however, that relationship was empirically found not to hold for this glass over the entire temperature range of interest. The failure of the empirically determined diffusivity to follow the viscosity shows that the glass-liquid analogy fails in at least this aspect, but this failure need not invalidate the model.

The chemical reaction rate is the most arbitrary of the three parameters. We have treated the rate constant and its temperature dependence as adjustable, and fit them to two points on the high temperature end of the lamp lifetime data. High temperature lamp lifetime data were obtained by operating lamps both at high temperature but with no rf discharge, and at high rf discharge powers. Lamps operated under high rf power were found to achieve high envelope temperatures as a result of rf heating effects. Lamp drive powers of 5 to 10 Watts resulted in lamp temperatures of 200 and 300°C, respectively. Because there was no way to separate rf and temperature effects in this model, we simply lumped all the data together, characterizing each lamp by some temperature. Although not entirely correct, it is not totally unreasonable to think that each lamp might have a characteristic temperature that would allow Rb consumption to be appropriately described by the combined effects on diffusion and reaction. The constant so obtained is:

$$k = 1.6 \times 10^{13} e^{-\frac{26,000}{T}} \text{ s}^{-1} \quad (19)$$

Alkali metals are not thermodynamically capable of reducing pure silica to give Si plus a metal oxide, but they are able to produce more alkaline glasses and Si.<sup>28</sup>



Rb is very likely to exhibit this same kind of reaction, although the free energy change will probably be different. This kind of reaction may continue until 2.0 weight % metal has been absorbed. Thus, the reactivity exceeds the solubility - a feature required by the solutions to the theory. The exact nature of the reaction and its thermodynamics are not required by the theory, however.

In Fig. 15 the actual lamp lifetimes as a function of temperature are given. The solid curve is the exact solution to the theory when employing the parameters chosen in the previous section. A lamp lifetime is defined for this analysis as the time required for a lamp to consume 400 µg of Rb, and in many cases, this was determined by extrapolation. Using the internal surface area of an Efratom lamp we find that this lifetime corresponds to:

$$Q = 1.18 \times 10^{-16} \text{ moles/cm}^2. \quad (21)$$

Although the data shown in Fig. 15 have a good deal of scatter about the fit line, we believe that the qualitative agreement between the data and the model is quite good. The scatter is due at least in part to the uncertainties in the temperature measurements and a possible inhomogeneity of the lamp

envelope temperature. Figure 15 indicates that the reaction process between the Rb and the glass starts to become important above 200°C. To properly accelerate the life of the discharge lamp, i.e. increase the rate of Rb consumption without changing the primary consumption mechanism, lamp temperatures must remain below 200°C. Referring to Fig. 15 one can see that the model predicts a maximum lamp life compression of about a factor of 2 for a temperature limit of 200°C. A factor of 2 is certainly not adequate, especially when lamp lifetimes of many years are desired. It is doubtful that even with an improved model the conclusion that lamp life acceleration is severely restricted would be altered.

Despite the fact that a lamp life acceleration technique does not appear to be feasible, it should be possible using the DSC technique to verify the quality of a lamp and ensure its reliability. In all cases, with the possible exception of the Schott 8477 glass lamps, Rb consumption was found to obey the relation

$$M_{Rb}(t) = R/t + B \quad (6)$$

The factor R is dependent on the particular lamp conditions. Once this factor is established it can be used as a guide to judge the quality of all subsequently manufactured lamps. Specifically, one can measure Rb consumption in a lamp over its first 1000 h (~ one month) and uniquely determine its consumption law, i.e., the factors R and B can be found for a particular lamp. Comparing the consumption law obtained for a specific lamp with the general consumption law obtained in a more extensive study of lamps under the particular operating conditions will allow one to determine whether that particular lamp is behaving normally or had been subject to any processing anomalies. Because lamp failure is due primarily to the deterministic, predictable phenomenon of diffusion of Rb into the glass walls of the lamp and is not statistical in nature, it is sufficient to know that a particular lamp has been properly manufactured to predict its lifetime, once the general law for Rb consumption for that type of lamp has been determined. The screening of a rubidium lamp therefore involves (1) visual inspection for dimensional tolerances and processing defects, (2) measurement of Rb fill for compliance with limits set with regard to life and noise, and (3) burn-in with calorimetric determination of Rb consumption. Experience has shown that defective lamps have either (1) obvious defects, (2) improper fill or (3) rapid Rb consumption (not necessarily obeying the  $1/t$  law). An accelerated life test would be useful to establish lamp consumption laws under different conditions in a minimum amount of time, but an accelerated test is not required to ensure reliable lamp operation under previously tested conditions.

## VI. SUMMARY

Extensive studies have been conducted on the reliability of the Rb discharge lamp under a limited set of different operating conditions. Under conditions in which this lamp is typically used, the primary life-limiting process was identified to be the diffusion of the Rb atoms into the glass envelope. Because the diffusion of Rb into the glass is completely deterministic, the lamp lifetime can be specified in principle by knowing the initial Rb content and the lamp operating conditions. The reliability of a particular lamp can be ensured by using the DSC technique to identify the presence of any anomalies in the rate of Rb consumption for a particular lamp. With adequate manufacturing procedure and careful initial lamp testing, lamp

lifetimes in excess of ten years can easily be guaranteed. This type of reliability makes these lamps well suited for use in Rb atomic frequency standards designed for use in satellite applications.

## VII. ACKNOWLEDGEMENT

We acknowledge the various contributions of many people, including R. A. Angel, P. A. Bertrand, R. A. Brose, R. A. Cook, H. U. Eckert, S. A. Jackson, P. F. Jones, C. M. Kahla, C. M. Klimcak, W. A. McDermid, L. R. Martin, G. A. To, L. U. Tolentino, and M. Wun-Fogle, all of The Aerospace Corporation; W. Weidemann, H. Fruehauf and J. Hayner of Efratom, a Division of Ball Corporation; E. Jechart, formerly of Efratom; and S. Goldberg and J. McDonald of EG&G, Electronic Components Division and F. Chang formerly of EG&G.

This work was supported in part by the United States Air Force Space Division Contract No. F04701-83-C-0083, in part by internal funds at Efratom, a Division of Ball Corporation and in part by EG&G, Electronic Components Division, under contract to Rockwell International Space Operations/Integration and Satellite Systems Division, Purchase Order No. MOJ3BGR-484107E.

## REFERENCES

1. W. E. Bell, A. L. Bloom and J. Lynch, "Alkali Metal Discharge Lamps," *Rev. Sci. Instrum.* **32**, 688 (1961).
2. R. G. Brewer, "High Intensity Low Noise Rubidium Light Source," *Rev. Sci. Instrum.* **32**, 1356 (1961).
3. H. Fukuyo, K. Iga, N. Kuramochi and H. Tanigawa, "Temperature Dependence of Hyperfine Spectrum of Rb D<sub>1</sub> Line," *Jpn. J. Appl. Phys.* **9**, 729 (1970).
4. H. Fukuyo, K. Iga and N. Kuramochi, "Spectral Characteristics of Rb<sup>87</sup> Lamps Containing Different Carrier Gases," *Bull. Tokyo Inst. Technol.* **113**, 67 (1972).
5. H. Oyamada, K. Takahashi, Y. Sato and H. Uchida, "A Consideration of Rubidium Lamp Stability for Rubidium Frequency Standard," *Proceedings, 28th Annual Symposium on Frequency Control, US Army Electronics Command, Fort Monmouth, NJ*, pp. 340-343 (1974). Copies available from Electronic Industries Association, 2001 Eye Street, NW, Washington, DC 20006.
6. T. Tako, Y. Koga and I. Hirano, "Spectral Profiles of Rb-D Lines," *Jpn. J. Appl. Phys.* **14**, 591 (1975).
7. N. Kuramochi, H. Fukuyo, I. Matsuda and N. Shiomi, "Spectral Profiles of the Rb Light Source," *Jpn. J. Appl. Phys.* **15**, 949 (1976).
8. D. M. Tennant, "NAVSTAR Global Positioning System (GPS) Clock Program: Present and Future," *Proceeding of the 12th Annual Precise Time and Time Interval (PTTI) Applications and Planning Meeting, Dec. 2-4, 1980, Greenbelt MD; NASA Conference Publication 2175*, pp. 703-718.
9. T. C. English and E. Jechart, "Development of A Sapphire Lamp for Use in Satellite-Borne Atomic Rubidium Clocks," *Proceedings, 35th Annual Symposium on Frequency Control, US Army Electronics Command, Ft. Monmouth, NJ*, pp. 637-645 (1981). Copies available from Electronic



Industries Association, 2001 Eye Street, NW, Washington, DC 20006.

10. R. P. Frueholz, M. Wun-Fogle, H. U. Eckert, C. H. Volk and P. F. Jones, "Lamp Reliability Studies for Improved Satellite Rubidium Frequency Standard," Proceedings of the 13th Annual Precise Time and Time Interval (PTTI) Applications and Planning Meeting, Dec. 1-3, 1981, Washington, DC, NASA Conference Publication 2220, pp. 767-788.
11. J. Crank, The Mathematics of Diffusion, Oxford University Press, London (1957), Chapter 8.
12. Kirk-Othmer Encyclopedia of Chemical Technology, V. II, M. Grayson, ed., John Wiley and Sons, Inc. New York (1980), p. 826.
13. R. H. Doremus, "Diffusion in Non-Crystalline Silicates," in Modern Aspects of the Vitreous States, J. D. MacKenzie, ed., Butterworth Inc., Washington, DC, Vol. 2, pp. 1-77, 1962.
14. H. U. Eckert, An Analytical Model for RF Inductive Glow Discharge Columns in Metal-Gas Mixtures and Application to the Rb-Xe System, No. TR-0082(2472-06)-1, The Aerospace Corporation, El Segundo, CA (12 July 1982).
15. T. Lynch of EG&G, Electronic Components Division conceived the original idea that calorimetry might be applied to measuring Rb in discharge lamps and made the first such measurements.
16. T. J. Lynch and W. J. Riley, "Test Results for Prototype GPS Rubidium Clock," Proceedings of the 15th Annual Precise Time and Time Interval (PTTI) Applications and Planning Meeting, Dec. 6-8, 1983, Washington, DC.
17. The consumption measurements at Aerospace were performed with a Perkin-Elmer DSC-1b; those at EG&G were done with a Perkin-Elmer DSC-2c.
18. It is possible that a change in the diffusion coefficient of a glass could occur during the lamp processing. We think that this is unlikely, but must be considered since it can not be disproven at the present time.
19. E. Jechart, Gas Cell Atomic Frequency Standard Having Selected Alkali Vapor Isotopes, U. S. Patent No. 3903481, September 2, 1975.
20. P. J. Elving, J. D. Winefordner and I. M. Kolthoff, ed., Analytical Laser Spectroscopy, John Wiley and Sons, New York (1979), pp. 518-520.
21. Private communication from R. P. Frueholz, M. Wun-Fogle and C. H. Volk, The Aerospace Corporation, 1982.
22. Private communication from L. E. Kovar, Technical Director, General Activation Analysis, Inc. to R. P. Frueholz, 1982.
23. Private communication M. Wun-Fogle and R. A. Cook, The Aerospace Corporation, 1982.
24. G. H. Frischat, U. Eichhorn, R. Kirchmeyer and H. Salge, "Alkaliionenaustausch an Silicatglasern Glastech. Ber. 47, 107 (1974).
25. This Section is based primarily on the work of Dr. L. R. Martin of The Aerospace Corporation.
26. P. V. Danckwerts, Gas-Liquid Reactions, McGraw-Hill, New York (1970).
27. J. Lau and P. W. McMillan, "Interaction of sodium with simple glasses," J. Mater. Sci. 17, 2715 (1982).
28. C. A. Elyard and H. Rawson, "The resistance of glasses of simple composition to attack by sodium vapor at elevated temperatures," Advances in Glass Technology, Plenum Press, New York (1962), pp. 270-286.
29. C. J. Brinker and L. C. Klein, "Behavior of silicate and borosilicate glasses in contact with metallic sodium. Part 1. Sodium silicate glasses," Phys. and Chem. Glasses 21, 141 (1980).
30. C. J. Brinker and L. C. Klein, "Behavior of silicate and borosilicate glasses in contact with metallic sodium. Part 2. Borosilicate glasses," Phys. and Chem. of Glasses 22, 23 (1981).

Table I. Comparison of Lamp Operating Conditions

User/Glass	Efratom/ Corning 1720 <sup>a</sup>	EG&G/ Corning 1720 <sup>b</sup>	Efratom/ Schott <sup>a</sup>
outside dia- meter (cm)	0.9	0.8	1.0
length (cm)	~ 1.5	~ 0.7	1.5
interiorce surface area (cm <sup>2</sup> )	~ 4	~ 2.3	5.1
operating temperature <sup>c</sup> (°C)	120	115	120
rf frequency (MHz)	~ 100	110	~ 100
rf drive power (W)	< 2	0.45	< 2

- a. T. C. English and E. Jechart, "Development of A Sapphire Lamp for Use in Satellite-Borne Atomic Rubidium Clocks," Proceedings, 35th Annual Symposium on Frequency Control, US Army Electronics Command, Ft. Monmouth, NJ (1981), pp. 637-645. Copies available from Electronic Industries Association, 2001 Eye Street, NW, Washington, DC 20006.
- b. W. J. Riley, "A Rubidium Clock for GPS," Proceedings of the 13th Annual Precise Time and Time Interval Applications and Planning Meeting, Naval Research Laboratory, Dec. 1-3, 1981, NASA Conference Publication No. 2220, pp. 609-630.
- c. Lamp operating temperature is controlled at the base of the lamp. The rest of the lamp envelope is hotter depending on the rf drive power and the particular thermal paths associated with the lamp structure. Thermal gradients along the glass envelope can typically be 30°C or more.



Table II. Lamp Measurement Results  
For Efratom 8437 Lamps

Lamp #	Total Rubidium from NAA (ug)	Rubidium Reservoir from DSC (ug)	Rubidium Consumed (ug)	Operating Time $\pm$ 700 (h)
881-3	397 $\pm$ 40	300 $\pm$ 20	97 $\pm$ 45	25 $\times$ 10 <sup>3</sup>
604	184 $\pm$ 20	0	184 $\pm$ 20	50.6 $\times$ 10 <sup>3</sup>
613	220 $\pm$ 22	0	220 $\pm$ 22	57.8 $\times$ 10 <sup>3</sup>
397	221 $\pm$ 21	53 $\pm$ 5	169 $\pm$ 22	69.4 $\times$ 10 <sup>3</sup>
400	233 $\pm$ 23	39 $\pm$ 4	203 $\pm$ 23	69.4 $\times$ 10 <sup>3</sup>
633	229 $\pm$ 22	64 $\pm$ 5	165 $\pm$ 23	69.4 $\times$ 10 <sup>3</sup>
718	266 $\pm$ 26	28 $\pm$ 2	238 $\pm$ 26	69.4 $\times$ 10 <sup>3</sup>

TYPICAL RUBIDIUM LAMP

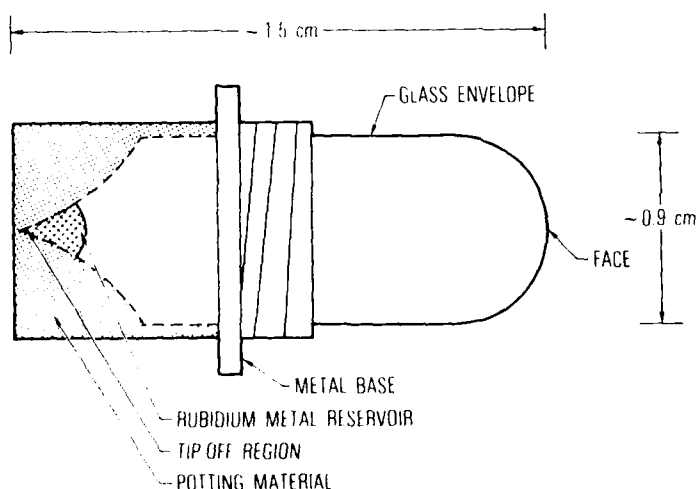


Figure 1. Typical Rb discharge lamp. Lamp consists of a glass envelope which contains excess Rb metal and a buffer gas. An rf coil, not shown, surrounds the exposed portion of the glass envelope and sustains a plasma in the lamp. Figure after Ref. (9).

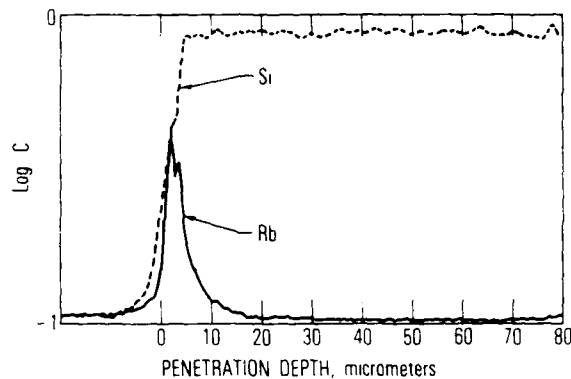


Figure 2. Rb penetration into a Pyrex glass surface from SIMS analysis. The surface occurs at 0  $\mu$ m. The sharp decrease and increase in Rb concentration near 4  $\mu$ m is believed to be due to inhomogeneities in the glass and not related to the penetration mechanism. The vertical axis is relative elemental concentration. Because of differing SIMS elemental sensitivities the relative concentrations between Rb and Si can not be directly compared.

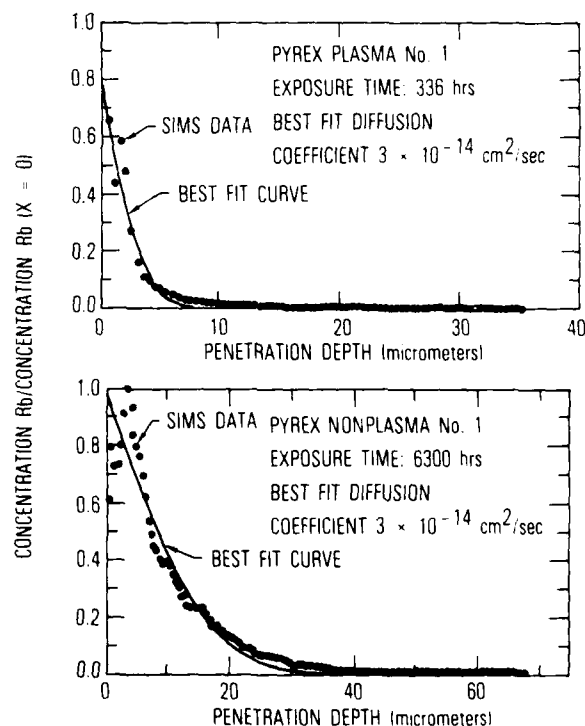


Figure 3. Experimental Rb penetration from SIMS analysis data (●) and fit curve (----) for Pyrex glass samples (a) with discharge present and (b) without discharge.

## ANALYSES OF Rb CONCENTRATION IN LAMP ENVELOPE

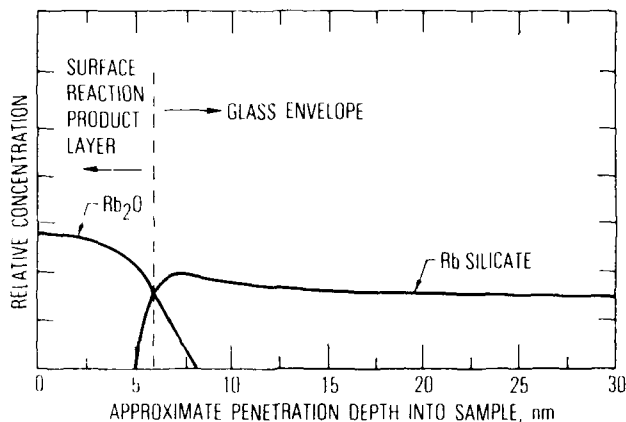


Figure 4. Rb-glass interaction. Rb atoms are found to react with oxygen atoms near the glass surface and then diffuse into the glass as  $\text{Rb}_2\text{O}$ . Unreacted Rb atoms also diffuse into the glass and react to form Rb-silicate.

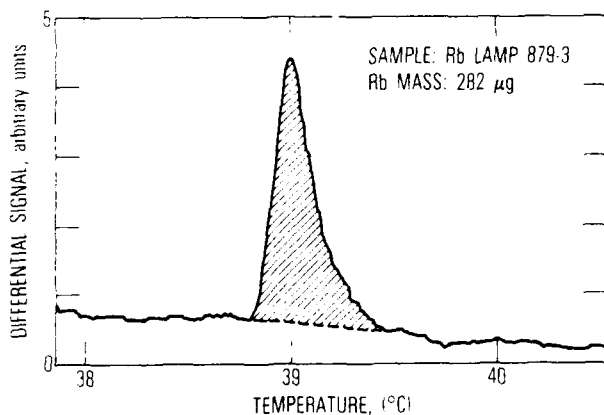


Figure 5. Calorimetric measurement of the Rb content of a Rb lamp. The differential heat pulse is displayed versus temperature for a typical Rb lamp measurement. The area under the pulse can be integrated to determine the total energy that was required to melt the Rb sample and thus determine the elemental Rb content of the lamp.



Rb METAL CONDENSED ON FRONT FACE OF LAMP

Figure 6. Photograph of EG&G lamp showing Rb metal driven to front face in preparation for calorimetric measurement. The Rb metal must form a tight, compact sample to achieve best measurement with calorimeter.

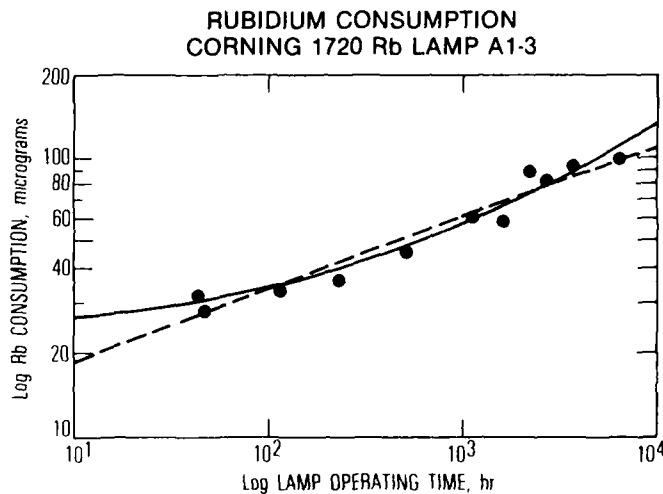
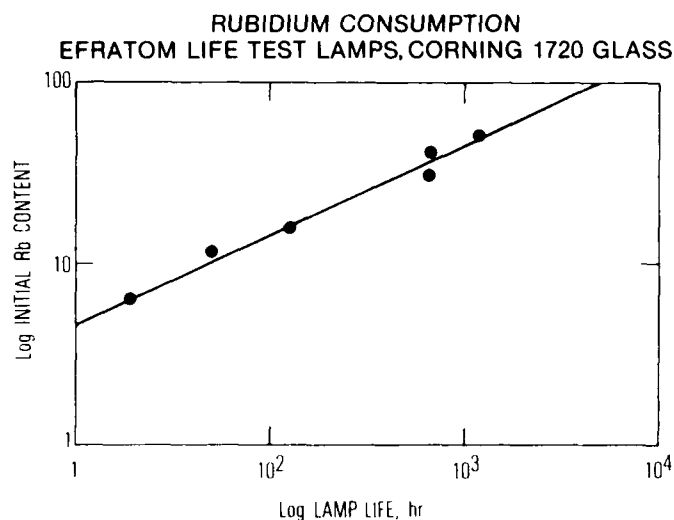
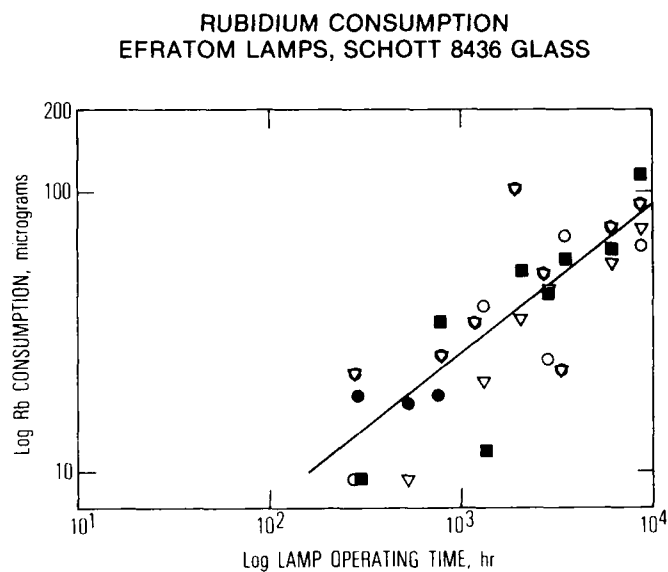


Figure 7. Typical Rb consumption data for Efratom lamp operated under the Efratom normal conditions. Measurements are denoted by the symbol, "e". The dashed line is a power law fit to the data while the solid line represents a fit to the diffusion law, see Eq. (6) in the text.



**Figure 8.** Results of the lamp life test conducted by Efratom for Corning 1720 glass lamps. Each symbol "•" represents a lamp that was operated to failure. Total operating life is plotted on the horizontal axis versus the initial Rb fill of the lamp on the vertical axis.



**Figure 10.** Composite plot of Rb consumption in Schott 8436 lamps of the Efratom design operated under Efratom normal conditions. Each symbol represents a different lamp. Solid line is a diffusion law fit to the data, see Eq. (6) in the text.

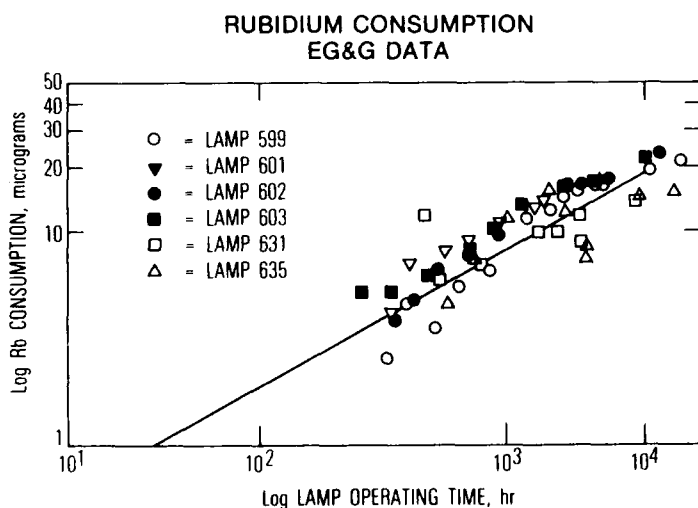


**Figure 9.** Composite plot of Rb consumption data for EG&G lamps measured at EG&G. Solid line represents a diffusion law fit to the data; see Eq. (6) in the text. The initial Rb consumption factor has been subtracted from the data for each lamp before plotting.

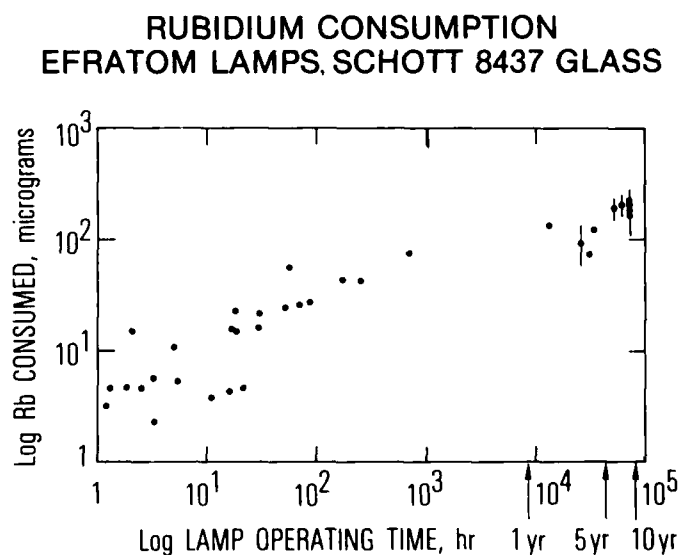


**Figure 11.** Rb life/consumption data for Schott 8437 glass lamps. Total operating times versus either total Rb fills, if lamp has failed, or consumed Rb, if lamp is still operating, are plotted for a number of lamps with Schott 8437 glass envelopes.

# DANCKWERTS SOLUTION

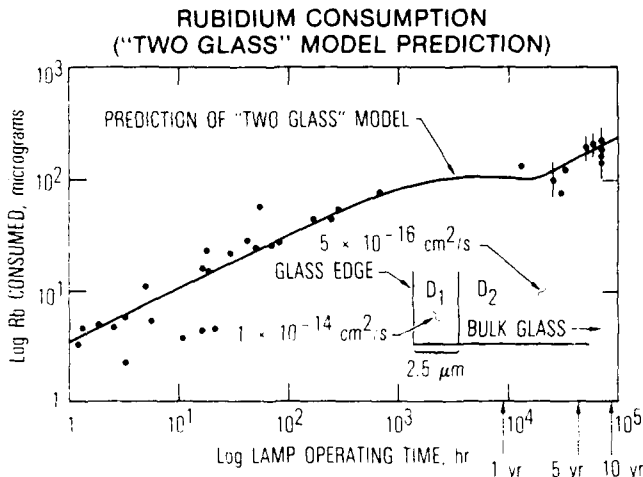


Figure 12. Schott 8437 glass lamp data with a fit, solid line, to the two glass model of Rb consumption. Inset shows the two different diffusion regions in the glass; a narrow region characterized by a relatively large diffusion coefficient for the Rb and the bulk glass which has a lower diffusion coefficient.

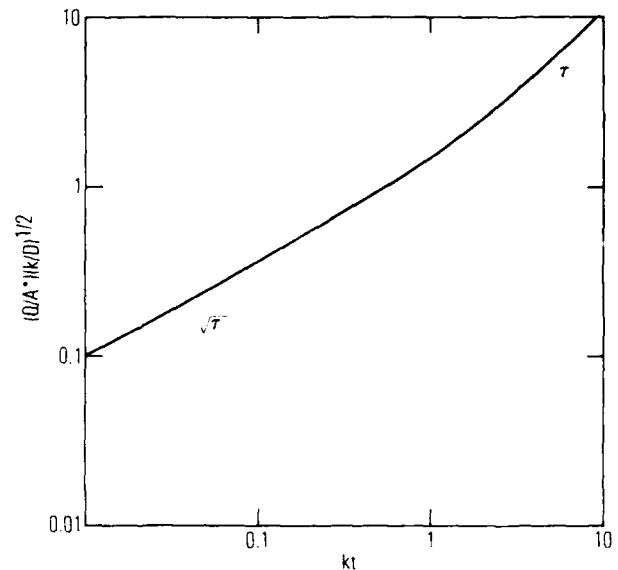


Figure 14. Solution of Eq. (13) is shown as a function of the dimensionless parameter  $kt$ . The time at which Rb consumption begins to be proportional to time depends on the strength of the reaction. This is not seen to occur for the Rb lamps studied under the normal operating conditions out to times approaching 10 yr.

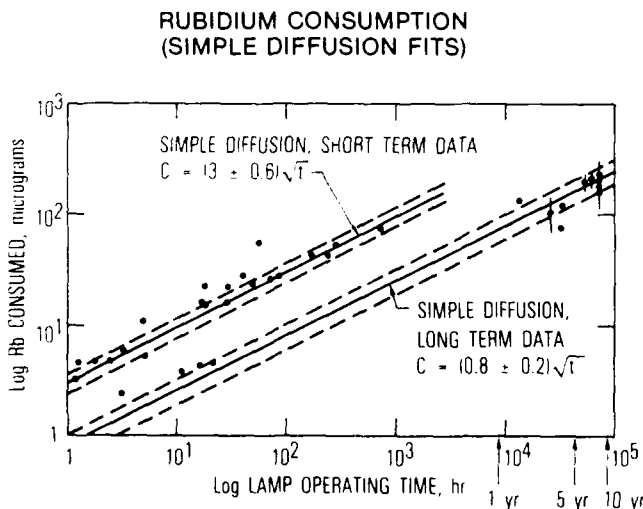


Figure 13. Schott 8437 glass lamp data fit to diffusion model. Because the data seemed to break up into two distinct groups, two fits were performed. Compared with the longer-lived lamps, the short-lived lamps show a much increased diffusion rate.

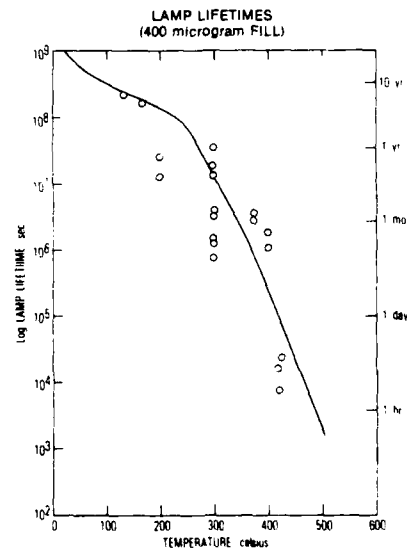


Figure 15. Extrapolated Rb lamp lifetime versus lamp temperature for lamps of the Efratom design constructed out of Corning 1720 glass. Rb lamp lifetime here is arbitrarily defined to be the time it takes a lamp to consume 400  $\mu$ g. Solid line is model prediction based on some adjustable parameters. Above 200°C the Rb consumption process is seen to change from diffusion to reaction. This change severely limits the degree to which lamp failure may be accelerated.

ANALYSIS OF DICKE NARROWING IN WALL COATED AND BUFFER GAS FILLED CELLS  
WITH APPLICATION TO GAS CELL ATOMIC CLOCKS

R. P. Frueholz and C. H. Volk  
Chemistry and Physics Laboratory  
The Aerospace Corporation, P. O. Box 92957, Los Angeles CA 90009

## ABSTRACT

Spectral lineshape narrowing of atomic vapor emission in a bufferless, wall-coated absorption cell has been analyzed using the same formalism developed to describe sub-Doppler linewidths, Dicke-narrowing, in a buffered cell. Dramatic linewidth reductions in the bufferless cell, compared to the buffered cell, occur because of the high probability that Doppler shifts before and after a particular wall collision will cancel each other. The formalism described allows more physical insight than the classic one-dimensional box model previously invoked to explain spectral narrowing in bufferless, wall coated cells. Additionally, this formalism reveals a correlation between post-collision velocities and intercollision times in the buffered cell resulting in modifications of the standard Dicke analysis of these cells. Finally, the computational power of the technique is demonstrated. The effects of varying cell size on Rb and Cs hyperfine lineshapes and the results of the presence of an inhomogeneous magnetic field within the cell are analyzed.

## I. INTRODUCTION

The phenomenon of producing sub-Doppler spectral linewidths in atomic emissions by confining atoms with a buffer gas is well known. This line-narrowing effect was first analyzed by R. H. Dicke and is typically termed Dicke-narrowing.<sup>1</sup> Dicke considered atoms confined by a non-perturbing buffer gas of sufficiently high pressure that the mean free path of the emitting atom was much less than the wavelength of the emitted radiation. Subsequent analyses<sup>2-6</sup> have relieved this constraint and have produced a formalism that predicts a Doppler broadened Gaussian lineshape in the limit of low buffer gas pressure and reproduces Dicke's result, a narrowed Lorentzian lineshape in the limit of high buffer gas pressure. One of the most dramatic realizations of Dicke-narrowing is observed in the magnetic dipole transitions of the hyperfine levels of alkali atoms. The ground state hyperfine transitions of <sup>87</sup>Rb and <sup>133</sup>Cs, at frequencies 6.8 GHz and 9.2 GHz, respectively, have been extensively studied because of their applications in atomic frequency standards.<sup>7-10</sup> In Fig. 1 we compare a typical lineshape that might be observed for the ground state hyperfine transition in <sup>87</sup>Rb in the presence of a few Torr of buffer, with a calculation of the full Doppler profile. Typically observed linewidths are about 300 Hz with only a small fraction of that due to the residual Doppler contribution, while the full Doppler width is computed to be around 10 kHz.

The lineshape derived by Dicke is given by:<sup>1</sup>

$$\frac{I(\omega)}{I_0} = \frac{2\pi D/\lambda^2}{(\omega - \omega_0)^2 + (2\pi D/\lambda^2)^2} \quad (1)$$

where D is the diffusion constant of the atom through the particular buffer gas, and  $\lambda$  is the wavelength of the transition,  $\lambda = c/2\pi\omega$ . The full width at half intensity of the line is  $4\pi D/\lambda^2$  (rad/s). For <sup>87</sup>Rb in a typical noble gas buffer, e.g. Kr, one computes the residual Doppler width, i.e. the Dicke-narrowed

contribution, to be approximately 40 Hz/p, where p is the pressure of the buffer in Torr. In a few Torr of buffer gas then the Dicke narrowed contribution is only a very small fraction of the total linewidth. In the usual experiments the major contributions to the linewidth arise from the effects of the optical pumping radiation, the microwave field, magnetic field gradients and the like.

It is also well known that sub-Doppler linewidths can be obtained in absorption cells containing no buffer gases, rather having wall coatings, such as paraffin, to minimize the relaxation effects of wall collisions on the atomic spin orientation.<sup>11-18</sup> Microwave linewidths as narrow as 11 Hz have been observed in some of these experiments.<sup>18</sup> The spectral narrowing of the rf or microwave lines in these bufferless, wall coated cells have been explained by appealing to the example of an emitting atom confined to a one-dimensional box. In this model with an atom confined to a box of dimension, a, travelling at constant velocity V, and being allowed only to rebound elastically, reversing direction upon a wall collision, it can be easily shown that for non-integral values of  $a/\lambda$  the atom emits at the normal unshifted frequency plus at sideband frequencies determined by its velocity. For an ensemble of atoms with a Maxwell-Boltzmann velocity distribution confined to a one-dimensional box, one finds the lineshape to be composed of a central spike at the normal unshifted frequency, and a broad pedestal built up from the velocity dependent sideband frequencies.

In reality, however, atoms confined to bufferless, wall coated cells are not well described by the one-dimensional box model. All real cells are three dimensional. Simply generalizing the one-dimensional model to two dimensions changes the physical problem significantly. First, the distance that the atom may travel between collisions is no longer fixed, rather it is distributed from zero to the diameter of the cell. Additionally even if the atom is assumed to be emitted from the cell surface with a fixed speed, S, from the observer's point of view a range of velocity components is possible as the atom rebounds randomly within the cell. In two dimensions the well defined sideband emission frequencies disappear. Due to the range of velocities, sideband frequency power is spread over all frequencies between  $\pm S\omega/2\pi c$ . Averaging these lineshapes over a Maxwell-Boltzmann distribution results in a center peak resting on a non-Doppler pedestal. Furthermore, purely elastic collisions with cell walls, allowing atoms to bounce with no change in speed, are not truly realistic. In fact, coated cell walls tend to be somewhat sticky. Atoms that collide with the coated wall stick for some period of time, between  $10^{-11}$  and  $10^{-10}$  s,<sup>13,14</sup> and then are re-emitted at some random angle and random velocity governed by the respective angle and velocity distribution functions. Relaxing the condition of elastic collisions at the wall in the one-dimensional model also results in a sharp central spike resting on a clearly non-Doppler pedestal because once again each atom experiences a number of different velocities over its lifetime and thus would emit at numerous sideband frequencies so that the spectral power is spread out leaving the greatest intensity at the normal unshifted

frequency. Finally, upon close inspection it seems strange that one should need two distinct formalisms to describe spectral line narrowing under collisional confining. Dicke's criterion<sup>1</sup> is that the emitting atom suffer collisions that do not perturb the atom's internal state. As pointed out by Vanier<sup>16</sup>, the mechanism of a wall collision is identical to that of a gas collision, and thus an atom should not really know if it is confined by a buffer gas or a wall. However, a naive application of the line-narrowing formalism to the bufferless, wall coated cell completely fails. In Fig. 2 we plot the full width at half intensity of the residual Doppler contribution to the <sup>87</sup>Rb microwave lineshape at 6.8 GHz, as predicted by the complete line-narrowing formalisms,<sup>2,6</sup> versus the dimensionless parameter,  $a/\lambda$ , where  $a$  is the mean free path of the atoms. The area to the left of the dashed line in the figure indicates the region of applicability of Dicke's result. To the right of the dashed line, the linewidth is seen to smoothly go to the full Doppler width, as expected. In addition, we have also plotted in Fig. 2 the estimate of the residual Doppler contribution to the linewidth observed in Ref. (18), denoted by the symbol, "+". In this particular case we took the mean free path of the Rb atoms to be the radius of the absorption cell. It is quite apparent that the standard formulations of line-narrowing fail dramatically in this situation.

We have investigated the line-narrowing phenomenon in a bufferless, wall coated absorption cell following the same formalisms developed for the buffered cell. We have found that although the trajectories that the atom has over its hyperfine state lifetime have a statistical nature, because atoms striking the coated wall are adsorbed for a finite time onto the coating<sup>12,13</sup> and then re-emitted randomly with a cosine angle distribution, there still is a very high probability that the Doppler shifts before and after a particular wall collision are of opposite sign leading to an effective cancellation of their effects. Additionally, analysis of the atomic trajectories in a wall coated cell demonstrates a correlation between post-collision velocities and intercollision times. While not of great significance in these cells, a similar correlation, albeit much weaker, exists in the buffered cell. This correlation, which has been completely neglected in previous analyses of the line-narrowing phenomenon<sup>1-6</sup> will lead to additional narrowing of the residual Doppler contribution beyond that given in the standard analyses. A major value of our new analysis is that spectral line-narrowing due to confining collisions can be explained by a single formalism despite the origin of the confining collisions. Finally, the analytical value of the technique is demonstrated in Section C where the effects changing cell size and magnetic field inhomogeneities are quantitatively analyzed.

## II. ANALYSIS AND RESULTS

An effective method of analyzing certain aspects of radiation problems, as pointed out by Weisskopf,<sup>19</sup> is to treat each radiating atom as a classical oscillator. This technique has been exploited in previous analyses of line narrowing for an atom surrounded by a buffer gas.<sup>2,4</sup> The displacement of the oscillator,  $x(t)$  is given by,

$$x(t) = A \cos[\omega_0 t + \frac{\omega}{c} \int_0^t V_x(\tau) d\tau], \quad (2)$$

with  $\omega$  the atomic transition frequency,  $V_x$  the velocity component leading to the Doppler shift,  $c$  the

speed of light, and  $A$  a constant. For the time between the  $(i-1)$ th and  $i$ th collisions with the buffer gas atoms,  $T(i)$ , the radiating atom has a fixed velocity,  $V_x(i)$ . This allows rewriting Eq. 2 as

$$x(t) = A \cos[\omega_0 t + \frac{\omega}{c} \sum_{i=1}^N V_x(i) T(i)], \quad (3)$$

with  $N$  being the number of collisions in time  $t$ .

Typically the post-collision velocities and intercollision times are treated as independent, stationary, random variables. The autocorrelation function of the oscillator,  $F(\tau)$  is given by<sup>20</sup>

$$F(\tau) = \langle x(0) \cdot x(\tau) \rangle, \quad (4)$$

where the brackets indicate stochastic averaging over the random variables,  $V_x$  and  $T$ . To perform the averaging the probability density functions for the random variables are required. For the radiating atom surrounded by a buffer gas the post-collision velocities are distributed according to the Maxwell-Boltzmann distribution while the intercollision times are assumed to be distributed according to a simple Poisson distribution.<sup>4</sup> In this model the velocity and hence the Doppler shift after a collision is assumed to be completely independent of those prior to the collision. The Fourier transform of the autocorrelation function is the oscillator's power spectral density or in this case more appropriately termed the transition lineshape. Linewidths obtained using this procedure yield the solid curve plotted on Fig. 2.

### A. Analysis of Motional Narrowing in the Wall Coated Cell

It has been shown that the naive application of the results of the standard buffer gas analysis to motional narrowing in the wall coated cell does not yield the correct linewidth. Carrying out a more detailed analysis of the wall coated cell case within the stochastic averaging framework is not straightforward. First, while the post-collision velocities will undoubtedly be distributed in a Maxwell-Boltzmann form it is not obvious that the intercollision times are still distributed according to a Poisson distribution. Additionally, the assumption that there is no relation between the velocity and Doppler shift before and after a collision is no longer even approximately correct. In a coated cell there is a high probability that the velocities before and after a collision will have opposite signs and their Doppler shifts will tend to cancel. In effect a Markoffian relation exists between the velocities before and after a collision. Aspects of the effects of similar relationships have been discussed by Anderson<sup>21</sup> and Kubo<sup>22</sup> with regard to motional narrowing in NMR spectra. However, attempting to apply their analyses to this problem is quite difficult.

An alternative to these standard stochastic analyses is to explicitly obtain  $x(t)$  as a function of time and then perform its Fourier analysis. To carry this out it is necessary to generate a series of  $V_x(i)$ 's and  $T(i)$ 's as would be observed in a wall coated cell. This has been done by calculating the classical trajectories of a particle in the wall coated cell. For computational simplicity a two dimensional circular cell was used to approximate the actual spherical cell. We do not feel this is a particularly restrictive approximation for this initial analysis as the agreement between our computational results and prior experimental studies will be shown to be very good.

Starting with a particle at a random location on the cell wall two random variables are used to specify the particle's path until its next collision with the wall.  $\theta$  is the angle of particle emission from the cell wall while  $S$  is its speed upon emission.  $\theta$  ranges from  $-\pi/2$  to  $\pi/2$  with respect to the direction normal to the cell wall at the point the particle has impacted. It is well known that in collisions between alkali atoms and cell walls coated with materials like paraffin the colliding atoms are physically adsorbed and then re-emitted.<sup>13,14</sup> The angle,  $\theta$ , has been found to be cosine distributed.<sup>23,24</sup> The emission speeds were assumed to satisfy the Maxwell-Boltzmann speed distribution. Generation of random variables satisfying these distributions were performed using standard techniques.<sup>25,26</sup> Once a particular  $S$  and  $\theta$  are selected it is possible to determine the next impact point, the intercollision time, and the component of velocity in the direction of the detector,  $V_x(1)$ , that leads to the Doppler shift. Repeating this procedure allows generation of a full particle trajectory.

To account for the finite coherence lifetime,  $t_0$ , of the radiating atom, Eq. 3 assumes the form,

$$A \cos \left[ \omega_0 t + \frac{\omega_0}{c} \sum_{i=1}^N V_x(i) T(i) \right] : t < t_0$$

$$x(t) = \quad (5)$$

$$0 : t > t_0$$

with the  $V_x(i)$ 's and  $T(i)$ 's from the trajectory calculation. Rather than calculating the autocorrelation function of  $x(t)$  and then obtaining the lineshape from its Fourier transform, the direct Fourier analysis of  $x(t)$  was performed. The lineshape  $G(\omega)$  is related directly to  $x(t)$  in Eq. 6:<sup>27</sup>

$$G(\omega) = \left| \int_{-\infty}^{+\infty} e^{-i\omega t} x(t) dt \right|^2. \quad (6)$$

The Fourier transform of  $x(t)$  was computed numerically. This is facilitated by noting that between each collision the radiation from the atom appears to have a fixed frequency and that the frequency changes discretely upon each collision. Eq. 6 can then be broken into a sum of integrals one for each intercollision period.

Strictly speaking one should explicitly take into account the fact that  $t_0$  represents an average lifetime of the atom, and weight the collisional effects over the atom's lifetime using an exponential function. Because the average lifetime is so much larger than the average intercollision time in the systems of interest, only a very few atoms do not participate in the collisional averaging. As will be shown, collisional narrowing in these systems is extremely effective and thus we decided for the sake of clarity to consider only an average atomic state lifetime knowing that under the specified conditions the error will be negligible. However in a more general situation in which a substantial fraction of the atoms have relatively few collisions over their lifetimes a properly weighted lifetime function would have to be incorporated into Eq. (5) and appropriate averaging performed. One further computational aspect should also be discussed.  $x(t)$  is specified by a trajectory lasting a period  $t_0$ . In principle an infinite number of different trajectories each lasting  $t_0$  can be generated. Each trajectory will yield a different  $x(t)$  with a slightly different  $G(\omega)$ .

Typically the lineshapes presented were the result of averaging lineshapes from several different trajectories. This eliminates the possibility of an artificial  $G(\omega)$  resulting from a single peculiar trajectory. Additionally, this averaging results in a much smoother more accurate lineshape.

Application of this procedure to <sup>87</sup>Rb at 25°C in a wall coated cell with radius 3.63 cm matching the experimental conditions of Robinson and Johnson yields the lineshape shown in Fig. 3. The linewidth is approximately 10 Hz indicating that in the wall coated cell Dicke narrowing effectively removes all Doppler broadening yielding the linewidth specified by the radiating atom's coherence lifetime in the cell, approximately 0.1 s. This result is in excellent agreement with the measurements in Ref. (18) in which no residual Doppler broadening was observed. Additionally the central peak is found to be resting on a broad Gaussian pedestal with a width of approximately 7.8 kHz. Experimentally, the pedestal was observed to have the full Doppler width of 9 kHz. We do not feel that the origin of the pedestal is fully explained by the present calculations. Further broadening mechanisms not included in our analysis are most likely in action. As our primary concern is the mechanisms leading to the narrow central spike, analysis of the pedestal will be left to subsequent investigations.

The extremely efficient Dicke narrowing found in the wall coated, bufferless cell is due primarily to the high probability that the velocity after a collision will have the opposite sign to that prior to the collision resulting in a cancellation of the Doppler shifts. The significance of this relationship between the pre- and post-collision velocities may be readily demonstrated. To do this, the trajectory calculation is repeated. However, this time upon each collision, the position of the particles is randomized over cell surface. While each trajectory is still subject to the spatial constraints of the cell and the cosine emission distribution, any "memory" of a prior velocity is removed.

In Fig. 4a the lineshape for a particle in a 0.363 cm radius wall coated, bufferless cell obtained from the standard trajectory calculation is shown. Beneath it in Fig. 4b the lineshape resulting from the modified trajectory calculation just described. The 0.363 cm radius is one tenth that used in the experiments of Robinson and Johnson and was chosen for clarity of example such that the uncorrelated linewidth would still be well below the full Doppler width. The linewidth in Fig. 4b is approximately 1400 Hz, over two orders of magnitude larger than the 10 Hz linewidth of Fig. 4a. The linewidth displayed in Fig. 4b is essentially the same as predicted by the standard statistical analyses. Subtle differences between the lineshape displayed in Fig. 4b and that given by the standard analyses are due to the non-Poisson intercollision time distribution found in the wall coated cell and thus an exact comparison with Fig. 2 is not appropriate. This calculation clearly verifies that it is the relationship between the pre-collision and post-collision velocities that leads to the extremely effective narrowing in a wall coated, bufferless cell.

## B. Analysis of Motional Narrowing in the Buffer Gas Case

Study of the trajectories of atoms in the wall coated, bufferless cell shows that there is a correlation between the post-collision velocity of an atom and the intercollision time. Faster moving atoms typically have shorter intercollision times. For the

bufferless cell the trajectory analysis includes these effects. Any similar correlation in the buffer gas cell has typically not been taken into account in the standard Dicke calculations. The standard statistical analysis of motional narrowing for a particle surrounded by a buffer gas assumes that the post-collision velocities and intercollision times are completely independent. While this is a fairly good assumption it is not rigorously correct. Some correlation exists even in the buffer gas case albeit not nearly as strong as found in the wall coated cell. Clearly the velocity of the radiating atom will affect to some extent the intercollision time.

Typically, intercollision times are assumed to obey the simple Poisson distribution with the most probable intercollision time being the inverse of the average collision frequency.<sup>28</sup> This most probable intercollision time does not depend on the precise speed of the radiating atom after each collision. In reality the most probable intercollision time,  $\tau_p$ , is a function of the speed of the radiating atom. The relation between the most probable collision time of a radiating atom with a precise speed,  $S$ , surrounded by a buffer gas of mass  $m$ , at temperature  $T$  and with a number density  $N$  is given by<sup>29</sup>

$$(\tau_p)^{-1} = N \pi \sigma^2 (\pi \beta)^{-1/2} (\beta^{1/2} S)^{-1} \psi(\beta^{1/2} S) \quad (7)$$

with

$$\psi(x) = x e^{-x^2} + (2x^2 + 1) \int_0^x e^{-y^2} dy, \quad (8)$$

$$\beta = \frac{m}{2kT}, \quad (9)$$

and  $k$  is the Boltzmann constant.

To analyze the effects of correlation in the buffer gas case,  $x(t)$ , as specified in Eq. 5, is generated. After each collision a random speed  $S(i)$  is generated by taking the magnitude of a velocity vector whose three components were randomly selected from independent Maxwell-Boltzmann velocity distributions.  $V_x(i)$  generates the Doppler shift after the  $i^{\text{th}}$  collision. The intercollision times are chosen in the following manner. Given the post-collision speed a most probable intercollision time,  $\tau_p(i)$ , is calculated using Eqs. 7-9. This time is then used as the most probable intercollision time, for the Poisson distribution from which a particular intercollision time,  $T(i)$ , is chosen. Since the post-collision speed changes after each collision, the most probable intercollision time, a function of that speed, also changes after each collision. Consequently after each collision the intercollision time  $T(i)$ , is chosen from a different Poisson distribution. In this way the mild correlation between intercollision times and post-collision speeds found even in the buffer gas case is rigorously taken into account. Once the post-collision speeds, velocities and the intercollision times are specified,  $x(t)$  is defined and may be Fourier analyzed as was done for the bufferless, wall coated cell to yield the lineshape.

The calculation was performed for a system in which the correlation should be enhanced. Hydrogen was chosen as the emitting species with a hyperfine frequency of 1.42 GHz, while Kr was used as the buffer species. Due to its large mass compared to H the Kr buffer atoms appear almost motionless to the rapidly moving H atoms. A system temperature of 25°C was used and the radiative lifetime of the H atom was taken to be 0.025 s. The ratio of the mean free path to the emitted wavelength was set at 0.01 placing the

calculation within the standard Dicke regime. The calculated lineshape is Lorentzian with a linewidth of approximately 220 Hz. Since the linewidth is well above that specified by the atom's radiative lifetime there is no need to increase the radiative lifetime employed in the calculation.

The buffer gas calculation was repeated but instead of the velocity dependent intercollision times based on Eqs. 7 through 9, speed independent intercollision times were used. These intercollision times were chosen randomly from a Poisson distribution whose most probable collision time,  $\tau'_p$ , was given by<sup>28</sup>

$$(\tau'_p)^{-1} = \pi \sigma^2 N v_m \quad (10)$$

with

$$v_m = \left( \frac{2 k T}{M^*} \right)^{1/2} \quad (11)$$

and  $M^*$  the H-Kr reduced mass. This calculation also resulted in a Lorentzian lineshape. However the linewidth was found to be nearly 370 Hz. The inclusion of the correlation effects is seen to yield a linewidth reduced by 40% from the uncorrelated linewidth. We find that even in the buffer gas case the effects of the correlation between intercollision times and post-collision velocities must be taken into account.

### C. Applications of the Trajectory Formalism

The trajectory formalism developed in Section A has been found to accurately and quantitatively describe the narrowing processes occurring in a wall coated cell. In this section, the technique is applied to analyze two different aspects of wall coated cell performance. First, it is known that the fraction of the transition lineshape found in the narrowed spike compared to that in the broad pedestal depends on the cell radius. This dependence has been investigated for Rb and Cs in wall coated cells. As a second application the ability of particles within coated cells to average inhomogeneous magnetic fields has also been studied.

In the one dimensional box the criteria ensuring that the major portion of the transition lineshape be located in the central spike is that the box length be less than one-half the transition wavelength. For Rb this corresponds to a box length of less than 2.2 cm. For a spherical cell, though, this is a somewhat ambiguous criteria as all trajectory lengths less than or equal to the cell diameter are possible. In fact, Robinson and Johnson<sup>18</sup> have demonstrated, for Rb, a high relative spike intensity in a cell whose diameter is approximately 7.3 cm.

Analysis of the effects of cell radii on the transition lineshape follows directly from Section A. The cell diameter, a simple calculation parameter, is varied and the resulting lineshapes may be analyzed. For Rb atoms, with coherence lifetimes of approximately 0.1 s, we find that if the cell diameter is less than 4.4 cm, the pedestal intensity is insignificant, with its amplitude less than 1% of the spike amplitude. As the cell diameter increases, the relative size of the pedestal increases. The spike has virtually disappeared for cell radii greater than 7.6 cm. The rate of pedestal growth is largest as the diameter comes within a few millimeters of 7.6 cm. For Cs with a half wavelength equal to 1.6 cm, diameters smaller than approximately 3.2 cm reduce the



pedestal amplitude to less than 1% of the spike amplitude. The central spike is found to disappear for diameters greater than approximately 5.6 cm. Our results indicate that in spherical cells the spike to pedestal amplitude ratio is optimized when the cell diameter is less than the transition wavelength. This is somewhat less restrictive than the  $\lambda/2$  criteria of the one dimensional box.

A second area where trajectory techniques may be employed to analyze performance of wall coated cells involves the ability of particles within these cells to average inhomogeneities throughout the cell. White et al.<sup>13</sup> and Risely et al.<sup>31</sup> have demonstrated experimentally that indeed the motion of the atoms in the wall coated cells can average inhomogeneities resulting from effects such as magnetic fields, optical pumping intensity, and microwave power distributions. In the present studies we consider the effects of an inhomogeneous magnetic field across a spherical cell on the lineshape of the Rb O-O hyperfine transition. The field is assumed to vary linearly across the cell yielding a position dependent atomic resonance. For the O-O transition, the resonance frequency depends quadratically upon the applied field with the change in resonance frequency,  $\Delta\nu$ , given by,

$$\Delta\nu = 575 \text{ (Hz/G}^2\text{)} B^2 \text{ (Gauss)}. \quad (12)$$

To perform the calculation Eq. (2) is modified to include a magnetic field dependent term. The position dependent resonance frequency is converted to a temporally varying frequency using the speed and trajectory of the particle between collisions. The results of a sample calculation are shown in Fig. 5. The magnetic field varies linearly across cell from 0 to 0.296 G corresponding to a resonance frequency variation of 50 Hz across the 5 cm diameter cell. The lower curve shows the hyperfine lineshape resulting if the atoms were held "frozen" in place by a buffer gas. A broad non-lorentzian lineshape is observed. The upper portion of Fig. 5 is the result of the trajectory calculation. The resonance has been shifted due to the magnetic field but its lineshape remains homogeneous. The linewidth is still specified by the coherence time, in this case 0.5 s. These results are consistent with expectations based on the NMR motional narrowing analyses of Anderson<sup>21</sup> and Kubo.<sup>22</sup> The trajectory analysis provides a quantitative method of calculating transition lineshapes in the presence of a variety of inhomogeneities.

### III. SUMMARY

It has been shown that a single formalism can be used to describe collisionally induced motional narrowing, Dicke-narrowing. The extreme narrowing observed in the wall coated, bufferless cell is seen to result from the high probability that the pre-collision and post-collision velocities will be of opposite sign resulting in a cancellation of Doppler shifts. For atoms confined in a buffer gas the effect of the mild correlation between the post-collision velocities and intercollision times have been analyzed. Finally, the computational power of the trajectory method has been demonstrated. This approach proved to be quite efficient in analyzing the effects of cell size and magnetic field inhomogeneities on hyperfine lineshape.

### ACKNOWLEDGMENT

This work was sponsored by the United States Air Force Space Division under Contract No. F04701-82-C-0083.

### REFERENCES

1. R. H. Dicke, Phys. Rev. **89**, 472 (1953).
2. L. Galatry, Phys. Rev. **122**, 1218 (1960).
3. S. G. Rautian and I. I. Sobel'man, Soviet Phys. Usp. **9**, 701 (1967).
4. J. I. Gersten and H. M. Foley, J. Opt. Soc. Am. **58**, 933 (1968).
5. D. R. A. McMahon, Aust. J. Phys. **8**, 1 (1981).
6. M. N. Neuman and G. C. Tabisz, J. Quant. Spectrosc. Transfer **29**, 267 (1983).
7. M. Arditi and T. R. Carver, Phys. Rev. **124**, 800 (1961).
8. M. Arditi and T. R. Carver, Phys. Rev. **126**, A643 (1964).
9. C. W. Beer and R. A. Bernheim, Phys. Rev. A **13**, 1052 (1974).
10. J. Vanier, D. H. Nguyen, G. Busca and M. Tetu, Can. J. of Phys. **57**, 1380 (1979).
11. H. M. Goldenberg, D. Kleppner and N. F. Ramsey, Phys. Rev. **123**, 530 (1961).
12. M. A. Bouchiat, J. de Phys. **24**, 379 (1963).
13. R. G. Brewer, J. Chem. Phys. **38**, 3015 (1963).
14. M. A. Bouchiat and J. Brosset, Phys. Rev. **147**, 41 (1966).
15. C. W. White, W. M. Hughes, G. S. Haynes and H. G. Robinson, Phys. Rev. **174**, 23 (1968).
16. J. Vanier, J. F. Simard, and J-S. Boulanger, Phys. Rev. A **9**, 1031 (1974).
17. A. Risely, S. Jarvis and J. Vanier, J. Appl. Phys. **51**, 4571 (1980).
18. H. G. Robinson and C. E. Johnson, Appl. Phys. Lett. **40**, 771 (1982).
19. V. F. Weisskopf, Rev. Mod. Phys. **21**, 305 (1949).
20. W. B. Davenport, Jr. and W. L. Root, An Introduction to the Theory of Random Signals and Noise (McGraw-Hill, New York, 1958).
21. P. W. Anderson, J. Phys. Soc. Jpn. **9**, 316 (1954).
22. R. Kubo, in Fluctuation, Relaxation and Resonance in Magnetic Systems, Edited by D. ter Haar (Oliver and Boyd, Edinburgh, 1962).
23. E. D. Cashwell and C. J. Everett, A Practical Manual on the Monte Carlo Method for Random Walk Problems (Pergamon Press, New York, 1959), p. 19.
24. Recent experimental measurements performed by L. R. Martin and C. M. Kahla of The Aerospace Corporation show that Cs particles recoiling from a paraffin surface satisfy a  $\cos(\theta)$  distribution. A similar emission distribution should be satisfied by Rb atoms recoiling from a paraffin coating in the standard wall coated cell.
25. J. M. Hammersley and D. C. Handscomb, Monte Carlo Methods (Methuen and Co., London, 1964), p. 39.
26. H. Kahn, Applications of Monte Carlo (Rand Corp., Santa Monica, CA, 1956).
27. R. B. Blackman and J. W. Tukey, The Measurement of Power Spectra (Dover Publications, Inc., New York 1958).
28. R. D. Present, Kinetic Theory of Gases, (McGraw-Hill, New York, 1958), p. 30.
29. R. J. C. Brown, Can. J. Chem. **44**, 1421 (1966).
30. F. Hartmann and F. Hartmann-Boutron Phys. Rev. A **2**, 1885 (1970).
31. A. Risley, S. Jarvis, and J. Vanier, J. Appl. Phys. **51**, 4571 (1980).

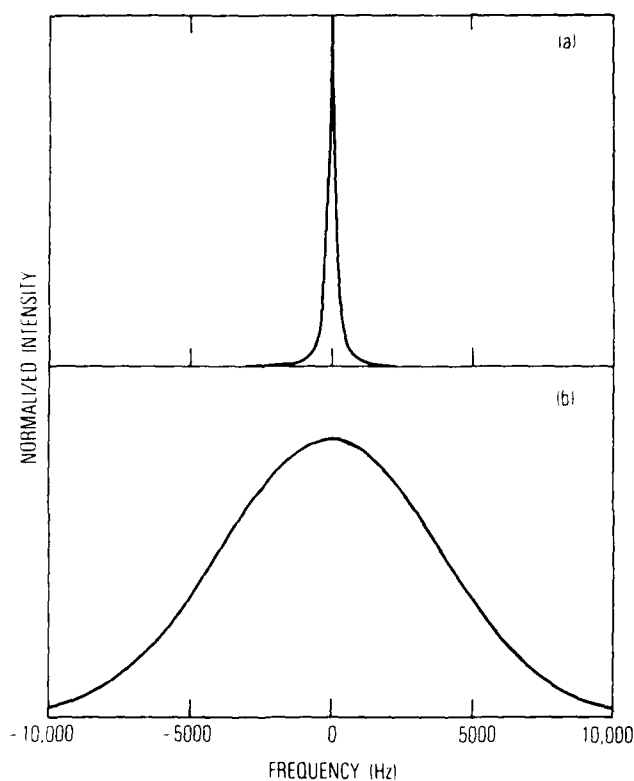


Figure 1. (a) Typical alkali ground state hyperfine transition lineshape in the presence of a few Torr of buffer gas. (b) Full Doppler profile of the alkali ground state hyperfine transition, observed in the absence of buffer gas.

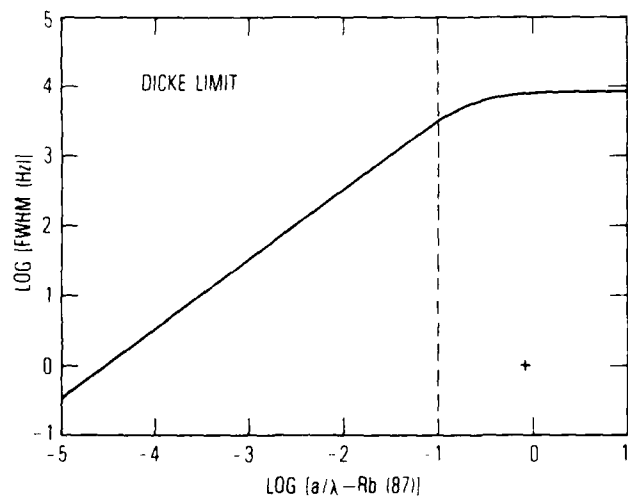


Figure 2. Linewidth of  $^{87}\text{Rb}$  ground state hyperfine transition as a function of the ratio of  $a$ , the atom's mean free path, to  $\lambda$ , the transition wavelength. Linewidths were calculated according to Ref. 2. The dashed line represents the limit of validity of Dicke's original analysis (see Ref. 1). The "+" symbol corresponds to the estimate of the residual Doppler contribution to the measured linewidth in Ref. (12).

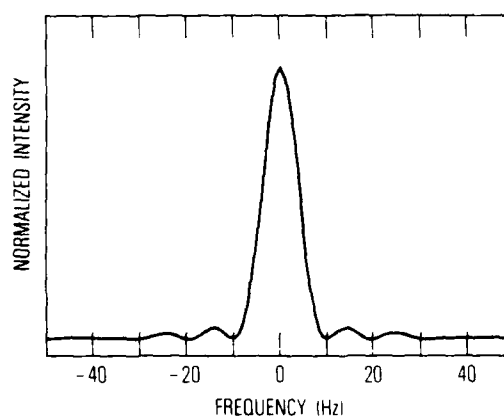


Figure 3. Hyperfine transition lineshape, resulting from trajectory analysis of a  $^{87}\text{Rb}$  atom in a wall coated, bufferless cell. The cell radius is 3.63 cm and the temperature is  $25^\circ\text{C}$ .

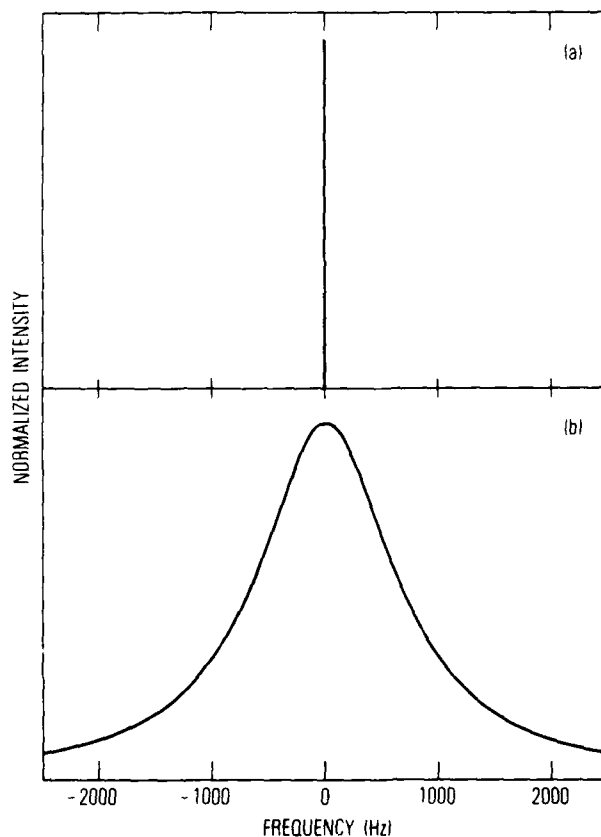


Figure 4. (a) Hyperfine lineshape for a  $^{87}\text{Rb}$  atom in a 0.363 cm radius wall coated, bufferless cell obtained from the trajectory calculation. The linewidth is 10 Hz. (b)  $^{87}\text{Rb}$  hyperfine lineshape after relationship between pre-collision velocities and post-collision velocities, found in the wall coated, bufferless cell, has been ignored. The linewidth is approximately 1400 Hz.

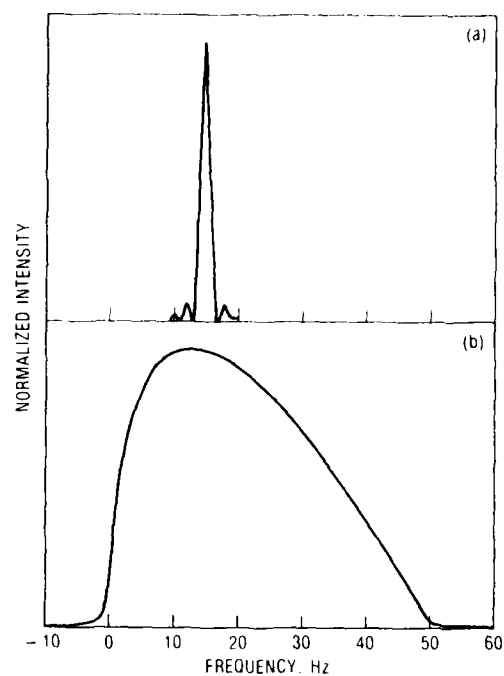


Figure 5. (a) Hyperfine lineshape for a  $^{87}\text{Rb}$  atom in a 5 cm diameter cell in presence of an inhomogeneous magnetic field varying linearly from 0.0 G to 0.296 G across the cell. (b)  $^{87}\text{Rb}$  hyperfine lineshape assuming atoms are frozen in place in the same inhomogeneous magnetic field.

**EVALUATION OF THE PERFORMANCE OF PASSIVE  
RUBIDIUM FREQUENCY STANDARDS USING  
CAVITY OPERATED IN MODE  $TE_{011}$ ,  $TE_{111}$  AND  $TE_{101}$**  \*

by

Pierre Tremblay, Normand Cyr and Michel Têtu  
Laboratoire de Recherche sur les Oscillateurs et Systèmes  
Département de génie électrique  
Université Laval, Québec, G1K 7P4, Canada

Summary

This paper presents a theoretical evaluation of the performance of passive Rb frequency standard operated under various modes of microwave excitation such as  $TE_{011}$ ,  $TE_{111}$  or  $TE_{101}$ . Assuming that the pumping light is generated by an electrodeless lamp and taking into account the inhomogeneity of the atomic system the spatial distribution of the light transmitted through the absorption cell is found. The resonance curve, given by the integral of the light intensity over the photodetector surface as function of microwave excitation frequency, is then calculated. It is shown that the resonance curve pattern depends not only on the light intensity and the microwave power when the atomic system parameters are held constant but also on the area and the location of the photodetector.

The ultimate short term frequency stability of a passive rubidium frequency standard is evaluated through its white frequency noise. This noise contribution can be estimated from the resonance curve and the system parameters. It is presented as function of light intensity and microwave power for various photodetectors and for the three modes of microwave excitation considered. These curves show that optimization of the short term frequency stability could be achieved and give insight toward its realization.

Introduction

Many recent works have been devoted to passive rubidium frequency standard development. The long term frequency stability has been improved (adjustment of the filter cell temperature for zero light shift, compensation of temperature coefficients between the filter and the absorption cell, etc...)(for example, see Riley<sup>1</sup>) and much efforts have been made in order to reduce its volume<sup>2,3,4</sup>. The object of the present work is the evaluation and the comparison of the short term frequency stability of this standard for various approaches.

The spatial distribution of the light transmitted through the absorption cell for different operating conditions and the resonance curves are first calculated. Then the short term frequency stability is evaluated. We show that the performance of the standard depends on the incident light intensity, the injected power, the geometry of the photodetector and the cavity mode ( $TE_{011}$ ,  $TE_{111}$  and  $TE_{101}$ ).

A schematic diagram of the optical package of a passive rubidium frequency standard is shown on Fig. 1. The absorption cell, containing  $^{87}\text{Rb}$  and a buffer gas, is placed in a microwave cavity which is excited by the interrogation signal. A photodetector is located at the end of the microwave cavity to detect the transmitted light intensity and to generate the resonance signal. Optical pumping is done with the light from an electrodeless lamp containing  $^{87}\text{Rb}$  filtered by an hyperfine filter, containing  $^{85}\text{Rb}$ .

Theoretical Approach

Since the pumping light intensity vary through the cavity and the axial microwave magnetic field is not uniform, the atomic system has an inhomogeneously broadened line. The optical transitions involved in the optical pumping process are the A- and B-components of the  $D_1$  and  $D_2$  lines of  $^{87}\text{Rb}$  (see Fig. 2).

We evaluate the transmitted light intensity through the use of the density matrix formalism<sup>5</sup>. The usual hypothesis are made<sup>6</sup>. In order to find this light intensity, we must first evaluate the time evolution of the local density matrix elements taking into account the relaxation processes, the optical pumping and the stimulated emission by the microwave magnetic field. The second step is to consider the only five independent variables which are the real and imaginary parts of the amplitude of the coherence between the first-order field independent sublevels,  $\delta_r(\vec{r})$  and  $\delta_i(\vec{r})$ , the population difference between these two sublevels,  $\Delta(\vec{r})$ , the population of the upper first-order field independent sublevel,  $\rho_{33}(\vec{r})$ , and the total population of the lower hyperfine level,  $n(\vec{r})$ . The following equations show the time evolution of these five variables<sup>6</sup>:

$$\dot{\delta}_r(\vec{r}) = -\left[\frac{1}{2}\Gamma_A(\vec{r}) + \frac{1}{2}\Gamma_B(\vec{r}) + \gamma_2\right]\delta_r(\vec{r}) - [\omega_L(\vec{r}) - \omega]\delta_i(\vec{r}), \quad (1)$$

$$\dot{\delta}_i(\vec{r}) = -\left[\frac{1}{2}\Gamma_A(\vec{r}) + \frac{1}{2}\Gamma_B(\vec{r}) + \gamma_2\right]\delta_i(\vec{r}) + [\omega_L(\vec{r}) - \omega]\delta_r(\vec{r}) - \beta(\vec{r})\Delta(\vec{r}), \quad (2)$$

$$\dot{\Delta}(\vec{r}) = -[\Gamma_A(\vec{r}) + \gamma_1]\Delta(\vec{r}) + [\Gamma_A(\vec{r}) - \Gamma_B(\vec{r})]\rho_{33}(\vec{r}) + 4\beta(\vec{r})\delta_i(\vec{r}), \quad (3)$$

$$\dot{\rho}_{33}(\vec{r}) = -[\Gamma_B(\vec{r}) + \gamma_1][\rho_{33}(\vec{r}) - \frac{1}{8}] + \frac{1}{8}[\Gamma_A(\vec{r}) - \Gamma_B(\vec{r})]\frac{n(\vec{r})}{n_0} + 2\beta(\vec{r})\delta_i(\vec{r}) \quad (4)$$

and

$$\dot{n}(\vec{r}) = -\left[\frac{5}{8}\Gamma_A(\vec{r}) + \frac{3}{8}\Gamma_B(\vec{r}) + \gamma_1\right]n(\vec{r}) + \frac{3}{8}n_0[\Gamma_B(\vec{r}) + \gamma_1] - 2n_0\beta(\vec{r})\delta_i(\vec{r}). \quad (5)$$

They are expressed in terms of the local optical pumping rates,  $\Gamma_A(\vec{r})$  and  $\Gamma_B(\vec{r})$ , the relaxation rates,  $\gamma_1$  and  $\gamma_2$ , the local resonant angular frequency of the atoms,  $\omega_L(\vec{r})$ , the angular frequency of the microwave excitation,  $\omega$ , the local reduced magnetic induction,  $\beta(\vec{r})$ , and the number of  $^{87}\text{Rb}$  atoms per unit volume,  $n_0$ . Steady-state solutions of these equations allow us to find the local density of atoms that can absorb the A-components of the pumping light,  $n(\vec{r})$ ; we obtain the following expression:

\* Part of this work has been submitted for publication in the Canadian Journal of Physics.

$$n_s(\vec{r}) = \frac{3n_0[\Gamma_B(\vec{r}) + \gamma_1]}{5\Gamma_A(\vec{r}) + 3\Gamma_B(\vec{r}) + 8\gamma_1} \left\{ 1 + \frac{16}{3} \frac{[\Gamma_A(\vec{r}) + \gamma_1] \left[ \frac{1}{2}\Gamma_A(\vec{r}) + \frac{1}{2}\Gamma_B(\vec{r}) + \gamma_2 \right] [\Gamma_A(\vec{r}) - \Gamma_B(\vec{r})] \beta^2(\vec{r})}{D(\vec{r})} \right\}, \quad (6)$$

where

$$D(\vec{r}) = \{\Gamma_A(\vec{r}) + \gamma_1\}[\Gamma_B(\vec{r}) + \gamma_1][5\Gamma_A(\vec{r}) + 3\Gamma_B(\vec{r}) + 8\gamma_1] \left\{ \left[ \frac{1}{2}\Gamma_A(\vec{r}) + \frac{1}{2}\Gamma_B(\vec{r}) + \gamma_2 \right]^2 + [\omega_k(\vec{r}) - \omega]^2 + 4\beta^2(\vec{r}) \left[ \frac{1}{2}\Gamma_A(\vec{r}) + \frac{1}{2}\Gamma_B(\vec{r}) + \gamma_2 \right] [2\Gamma_A^2(\vec{r}) + 5\Gamma_A(\vec{r})\Gamma_B(\vec{r}) + \Gamma_B^2(\vec{r}) + 9\gamma_1\Gamma_A(\vec{r}) + 7\gamma_1\Gamma_B(\vec{r}) + 8\gamma_1^2] \right\}.$$

The transmitted light intensity is calculated by means of the absorption of the light at a given frequency when it pass through an infinitesimal slice. By integrating over all frequencies and over the length covered by the light, we get this equation:

$$I(\vec{r}) = I(\vec{r}_0) - \int_0^z \{\Gamma_A(\vec{r}')n(\vec{r}') - \Gamma_B(\vec{r}')[n_0 - n(\vec{r}')]\} dz'. \quad (7)$$

$I(\vec{r})$  is given by the incident light intensity minus the absorption of the A- and B-components of the  $D_1$  and  $D_2$  lines. This absorption is proportional to the optical pumping rates due to the associated components, which are:

$$\Gamma_A(\vec{r}) = \Gamma_{1A}(\vec{r}) + \Gamma_{2A}(\vec{r}) \quad \text{and} \quad \Gamma_B(\vec{r}) = \Gamma_{1B}(\vec{r}) + \Gamma_{2B}(\vec{r}), \quad (8)$$

times the number of  $^{87}\text{Rb}$  atoms per unit volume which can absorb these components.

The previous equations show that the transmitted light intensity at the end of the cavity depends on the spatial distribution of the magnetic field. In order to calculate the transmitted light intensity, we must evaluate the optical pumping rates and the reduced magnetic induction, this is done in Ref. 6.

#### Numerical Calculations

Fig. 3 shows the three microwave cavities considered in the numerical calculations. They are two cylindrical cavities operated respectively in mode  $TE_{011}$  and  $TE_{111}$ , and one rectangular cavity operated in mode  $TE_{101}$ . The case of the rectangular cavity is slightly different since a dielectric slab is inserted along one of its side in order to decrease the dimensions and to almost eliminate the variation of the stimulating field along the X-axis. The particular case considered was described in Ref. 4. This figure shows the relative size of each cavity and the direction of the magnetic field is indicated by the arrows. From these distributions, we see the points where the axial magnetic field vanishes. They are located where the magnetic field is parallel to the end faces of the cavities.

#### A- Spatial Distribution of the Transmitted Light Intensity at the End of the Cavity

We will now calculate the transmitted light intensity through each system when operated at a nominal temperature of 65 °C and when the intensity of the B-components is half the intensity of the A-components. The other parameters are given in Table 1.

Table 1

Difference between the resonant frequency of the corresponding lines in the emission and absorption spectra, $\nu_{ei} - \nu_{ai}$	0
Ratio of the optical linewidths, $\Delta\nu_{ai}/\Delta\nu_{ei}$	0,5
Absorption cross-section (maximum value of), $\sigma_{oi}$	$2 \times 10^{-15} \text{ m}^2$
Resonance frequency of the atoms without pumping light	6,835 GHz
Number of rubidium 87 atoms per unit volume, $n_0$ (at 65 °C)	$4,4 \times 10^{17} \text{ at/m}^3$
Population relaxation rate without light, $\gamma_1$	280 $\text{s}^{-1}$
Coherence relaxation rate without light, $\gamma_2$	230 $\text{s}^{-1}$
Quantum efficiency of the photodetector, $\eta_p$	1
Relative precision used in the numerical calculations	0,001
Cylindrical cavity operated in mode $TE_{011}$	
$x_{lm}$	3,8317
cavity quality factor, $Q_c$	15 000
# of subdivisions, $r, \phi, z$	16,1,18
Cylindrical cavity operated in mode $TE_{111}$	
$x_{lm}$	1,8412
cavity quality factor, $Q_c$	1 000
# of subdivisions, $r, \phi, z$	4,16,8
Rectangular cavity operated in mode $TE_{101}(4)$	
relative permittivity of the dielectric, $\epsilon_d$	6
cavity quality factor, $Q_c$	100
# of subdivisions, $x, y, z$ (for $x$ , it is from 0 to $a'$ )	2,1,8

Fig. 4 shows the spatial distribution of the light intensity along the radial position for some values of the injected microwave power in a cavity operated in the  $TE_{011}$  mode. The absorption is maximum at the center of the cavity and a weak power is needed to saturate this part of the atomic system. The transmitted light intensity does not change with power for positions where the stimulating field vanishes. The transmitted light intensity is then a function of the radial position and is minimum where the stimulating field is maximum.

The same kind of curves, but for a cylindrical cavity operated in the  $TE_{111}$  mode, is given on Fig. 5. The absorption is independent of the injected power at the center of the cavity but increases and becomes maximum close to the walls. For this excitation mode, both the field magnitude and the transmitted light intensity depend on the azimuthal angle because the axial magnetic field vanishes for azimuthal angles of  $\pm 90^\circ$ , then the transmitted light intensity is power independent for these angles.

The curves illustrated on Fig. 6 give the spatial distribution of the transmitted light intensity along the X-axis for some values of the injected power in a rectangular cavity operated in the  $TE_{101}$  mode. Since the stimulating magnetic field is almost uniform on a cross-section of the cavity, the transmitted light intensity has only small variations along the X-axis, as shown on this figure, and no variations along the Y-axis.

The spatial distribution of the transmitted light intensity is closely related to the distribution of the stimulating magnetic field because the  $^{87}\text{Rb}$  atoms are relatively fixed in the buffer gas.

#### B- Calculated Resonance Curves

The resonance signal is generated as the integral over the photodetector surface of the transmitted light intensity through the cell. Since the spatial distribution of the transmitted light intensity is not uniform, we have to consider various photodetector shapes. These are illustrated on Fig. 7. For the  $TE_{011}$  mode, we consider two shapes of photodetector, one which covers one quarter of the cavity area at its center and the other which covers all the surface. In the case of the  $TE_{111}$  mode, the same shapes as for the precedent mode are used plus a special one, made in order to exclude the areas where the stimulating field vanishes. For the  $TE_{101}$  mode, only the photodetector covering all the free surface is considered.

The resonance curve is obtained by plotting the current delivered by the photodetector against the frequency of the stimulating field. Fig. 8 shows a typical resonance curve. We define practical parameters related to this curve:  $\omega_0$ , the resonant angular frequency,  $l_L$ , the linedepth and  $W$ , the fullwidth at half maximum depth.

Resonance curves have been calculated for each cavity modes and photodetector shapes, but we will present only a few related to the  $TE_{111}$  mode of excitation.

Fig. 9 shows the variation of the resonance curves with the injected power for the photodetector which covers all the surface. Only half of the resonance curves is presented since they are symmetrical around the center frequency (we assumed coincidence of the absorption and emission lines of the  $^{87}\text{Rb}$  atoms). The value of the off-resonance current is related to the area of the photodetector. These curves show that both linedepth and linewidth increase with the injected power, although the linedepth reaches a saturation value.

The variation of the resonance curves with the various photodetector shapes at a given injected power is given in Fig. 10. We see from these calculated resonance curves that the relative linedepth and linewidth depend on the photodetector shape. This result is explained by the variation of the mean quadratic value of the stimulating field in the volume over the photodetector surface. These calculations show clearly that a linewidth measurement through this method is function of the shape and location of the photodetector used.

The resonance curves allow us to evaluate the expected short term frequency stability.

#### C- Short Term Frequency Stability

We use the power spectral density of the relative frequency fluctuations to characterize the short term frequency stability of the passive rubidium frequency standard<sup>9</sup>. Its ultimate short term frequency stability is depicted by a white frequency noise type of fluctuations and is expressed by the following equation<sup>10</sup>:

$$S_y(f) = h_o = \frac{4e f(\omega_0)}{(\omega_0/2\pi)^2 m^2(\omega_0)}, \quad (9)$$

where  $m(\omega_0)$  is the slope of the discriminator pattern at resonance which is function of the shape of the resonance line, the type of modulation, its amplitude and its frequency<sup>11</sup>.

We consider the particular case where we have a slow sinewave frequency modulation with an optimum frequency deviation. To simplify the calculation of the white frequency noise contribution, we assume a Lorentzian resonance curve with the same linewidth and linedepth than the calculated resonance curve. The minimum contribution of the white frequency noise then becomes:

$$h_{om} = \frac{27\pi^2}{4\omega_0^2} \cdot \frac{W^2}{l_L^2} e f(\omega_0). \quad (10)$$

which is function of the squared value of the ratio of the linewidth to the linedepth.

Figs 11a, b and c show the variation of the minimum contribution of the white frequency noise as a function of the incident light intensity for the various photodetector shapes respectively for  $TE_{011}$ ,  $TE_{111}$  and  $TE_{101}$  cavity modes. There exists an optimum value for the incident light intensity which is slightly dependent on the photodetector shapes. We see that if the incident light intensity is slightly lower than its optimum value, the frequency stability is greatly reduced.

Figs 12a, b and c represent the variation of the minimum contribution of the white frequency noise as a function of the injected power for the various photodetector shapes respectively for  $TE_{011}$ ,  $TE_{111}$  and  $TE_{101}$  cavity modes. There is an optimum value for the injected power which varies with the photodetector shape. Again, if an injected microwave power different from the optimum is used, we see that the frequency stability is greatly reduced.

#### Conclusions

This study allows us to evaluate the performance of various systems according to their operating parameters. We have shown that there exists an optimum value for the short term frequency stability as a function of incident light intensity and microwave injected power and that this frequency stability could be reduced by a missetting of these variables. We have also shown that the photodetector surface must be chosen in order to exclude the areas where the microwave axial magnetic field vanishes and to cover the remaining surface.

#### References

- 1 W.J. Riley, "A Rubidium Clock for GPS", Proceedings of the 13th Annual Precise Time and Time Interval Applications and Planning Meeting, Washington, D.C., December 1-3, 1981, 609-630.
- 2 H. Fruehauf, W. Weidemann and E. Jeckart, "Development of a Sub-Miniature Rubidium Oscillator for

SEETALK Application", Proceedings of the 12th Annual Precise Time and Time Interval Applications and Planning Meeting, Washington\*, D.C., December 2-4, 1980, 719-742.

- 3 W.J. Riley, "A Rubidium Clock for SEEK-TALK", Proceedings of the 14th Annual Precise Time and Time Interval Applications and Planning Meeting, Washington\*, D.C., November 30-December 2, 1982, 141-154.
- 4 H.E. Williams, T.M. Kwon and T. McClelland, "Compact Rectangular Cavity for Rubidium Vapor Cell Frequency Standard", Proceedings of the 37th Annual Symposium on Frequency Control, Philadelphia (Systematics General Corporation, Brinley Plaza, Route 38, Wall Tornship, N.J. 07719), June 1-3, 1983, 12-17.
- 5 J. Vanier, "Basic Theory of Lasers and Masers: A Density Matrix Approach", Gordon and Breach Science Publishers, New-York, 1971.
- 6 P. Tremblay, N. Cyr, M. Têtu, "Pumping Light Intensity Transmitted Through an Inhomogeneously Broadened Line System: Application to Passive Rubidium Frequency Standards", submitted to Canadian Journal of Physics, January 1984.
- 7 J.P. Gourber, "Horloges atomiques à vapeur de rubidium", Annales de Radioélectricité, Vol. 20, 1965, 191-211.
- 8 E. Jeckart, "A New Miniature Rubidium Gas Cell Frequency Standard", Proceedings of the 27th Annual Symposium on Frequency Control, Cherry Hill, N.J., (National Technical Information Service, Sills Building, 5285, Port Royal Road, Springfield, VA 22161), June 12-14, 1973, 387-389.
- 9 J.A. Barnes, A.R. Chi, L.S. Cutler, P.J. Healey, D.B. Leeson, T.E. McGunigal, J.A. Mullen Jr., W.L. Smith, R.L. Sydnor, R.F.C. Vessot and G.M.R. Winkler, "Characterization of Frequency Stability", IEEE Transactions on Instrumentation and Measurement, Vol. IM-20, N° 2 (May 1971): 105-120.
- 10 J. Vanier and L.-G. Bernier, "On the Signal-to-Noise Ratio and Short Term Stability of Passive Rubidium Frequency Standards", IEEE Transactions on Instrumentation and Measurement, Vol. IM-30, N° 4, (December 1981): 277-282.
- 11 C. Audoin, J. Viennet, N. Cyr and J. Vanier, "Influence of Modulation Frequency in Rubidium Cell Frequency Standards", Proceedings of the 14th Annual Precise Time and Time Interval Applications Meeting, Washington\*, D.C., November 30-December 2, 1982, 87-111.

\* Goddard Space Flight Center, Greenbelt, Maryland 20771, U.S.A.

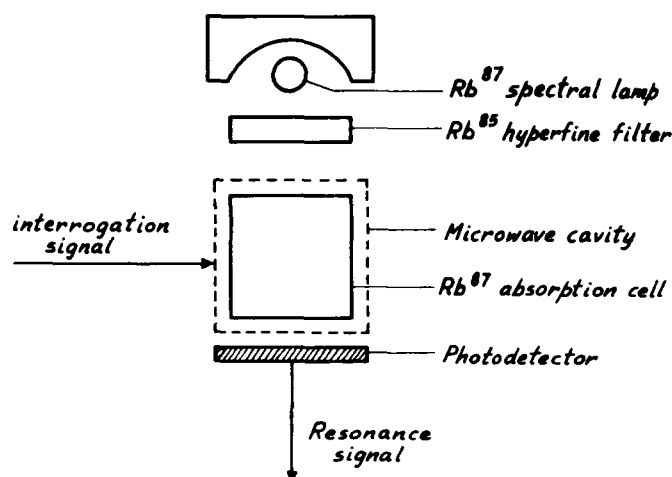


Fig. 1 Schematic diagram of the optical package of a passive rubidium frequency standard.

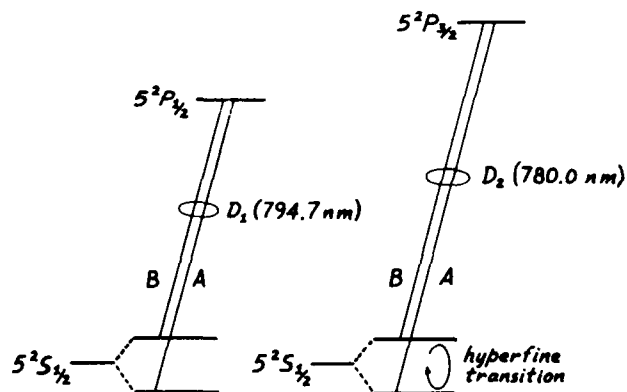


Fig. 2 Transitions involved in the optical pumping process.

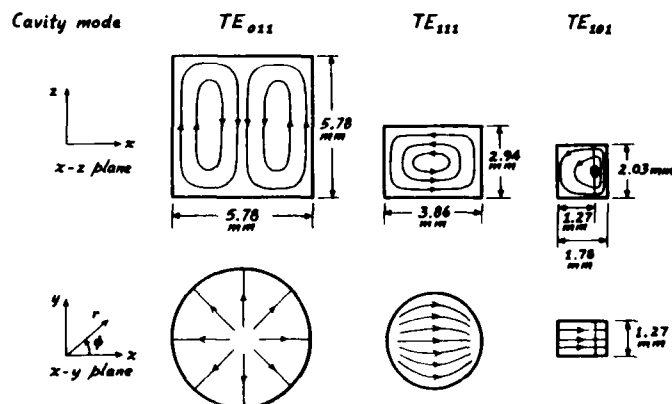


Fig. 3 Description of the three microwave cavities considered.

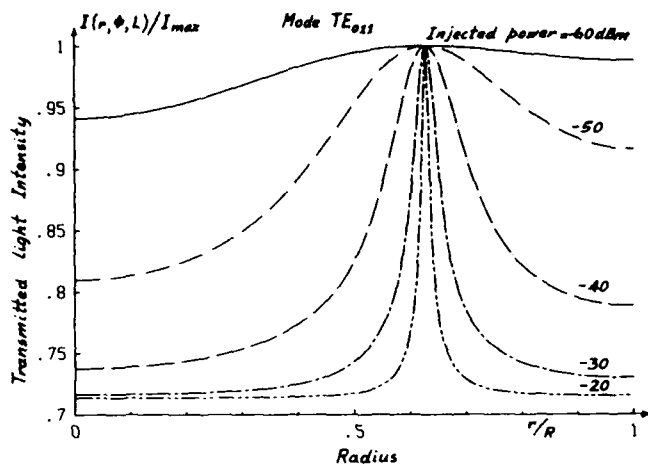


Fig. 4 Spatial distribution of the transmitted light intensity through a cell filling a cylindrical cavity excited in the  $TE_{011}$  mode for various injected microwave powers. The normalization factor,  $I_{\max}$ , is  $4.5 \times 10^{18}$  ph/s $\cdot$ m $^2$ . The total incident light intensity for the two A-components is set to  $1.2 \times 10^{19}$  ph/s $\cdot$ m $^2$ .

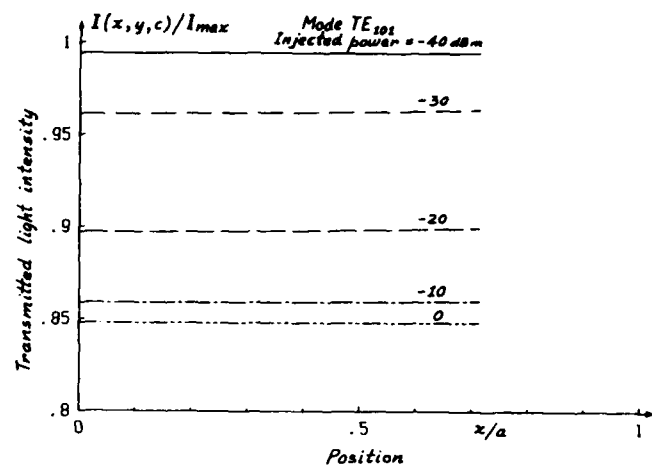


Fig. 6 Spatial distribution of the transmitted light intensity through a cell filling a cylindrical cavity excited in the  $TE_{011}$  mode for various injected microwave powers. The normalization factor,  $I_{\max}$ , is  $3.2 \times 10^{18}$  ph/s $\cdot$ m $^2$ . The total incident light intensity for the two A-components is set to  $5 \times 10^{18}$  ph/s $\cdot$ m $^2$ .

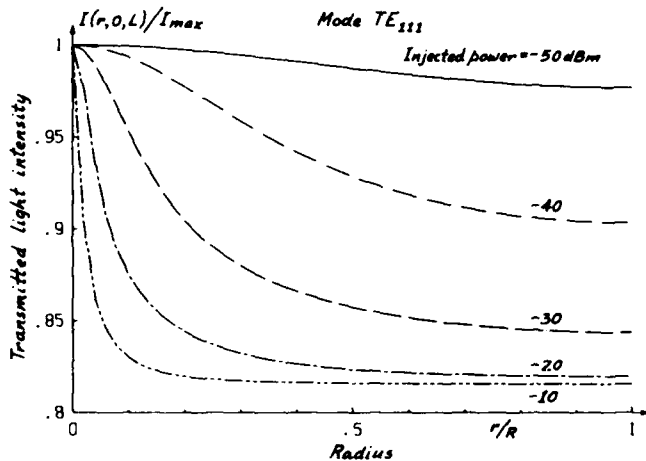


Fig. 5 Spatial distribution of the transmitted light intensity through a cell filling a cylindrical cavity excited in the  $TE_{111}$  mode for various injected microwave powers at  $\phi = 0$ . The normalization factor,  $I_{\max}$ , is  $3.4 \times 10^{18}$  ph/s $\cdot$ m $^2$ . The total incident light intensity for the two A-components is set to  $6 \times 10^{18}$  ph/s $\cdot$ m $^2$ .

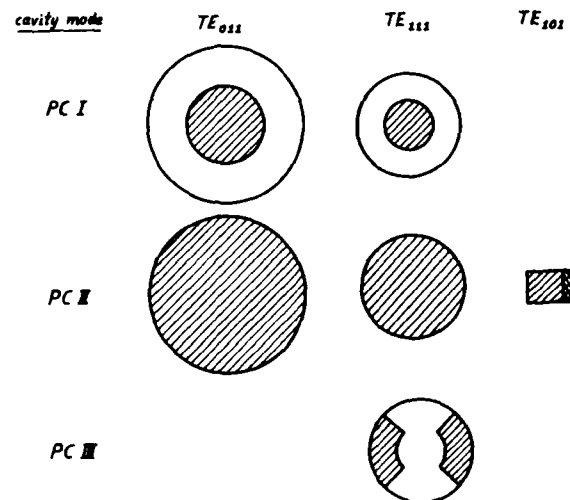


Fig. 7 Shape and location of the photodetectors considered for each cavity mode.



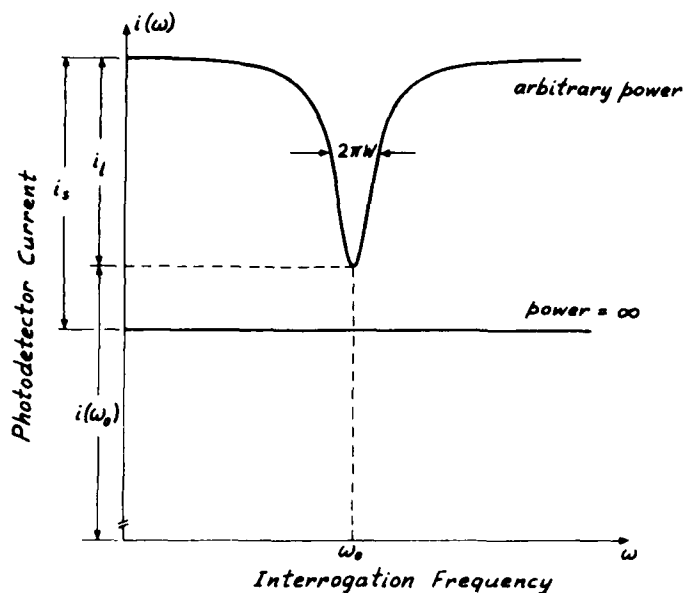


Fig. 8 Typical Lorentzian resonance curve.

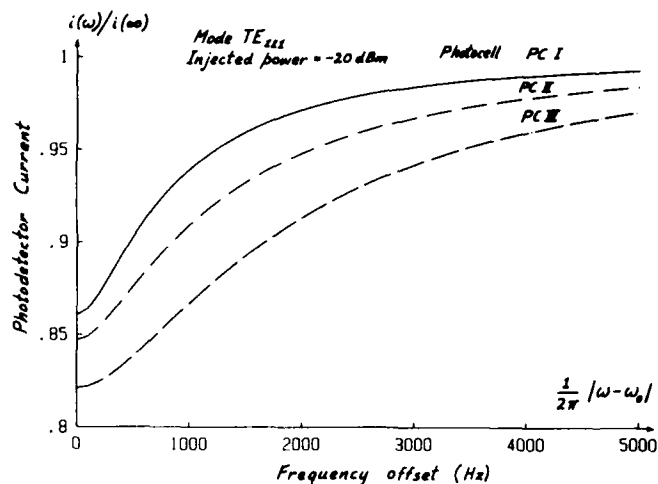


Fig. 10 Resonance curves obtained with a cell filling a rectangular cavity excited in  $TE_{111}$  mode for various photodetector shapes with an injected microwave power of  $-20$  dBm. The normalization factor,  $i_{\max}$ , is  $160 \mu A$  for the curves obtained with PCI,  $620 \mu A$  for those obtained with PCII and  $240 \mu A$  for those obtained with PCIII.

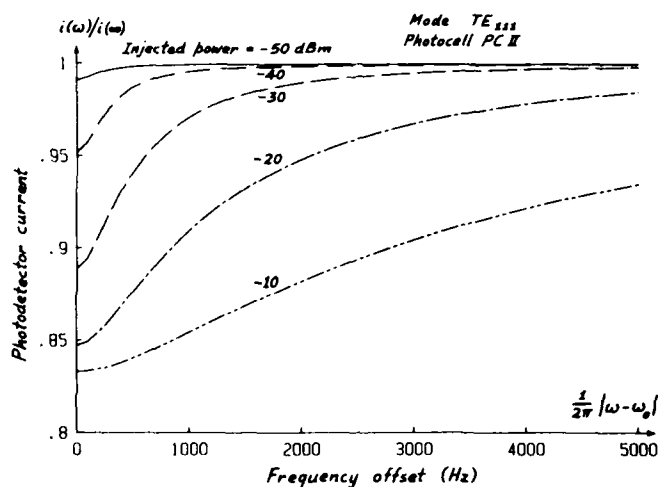


Fig. 9 Resonance curves obtained with a cell filling a cylindrical cavity excited in  $TE_{111}$  mode for various microwave powers with photodetector PCII. The normalization factor,  $i_{\max}$ , is  $620 \mu A$ . The total incident light intensity for the two A-components is set to  $6 \times 10^{18} \text{ ph/s} \cdot \text{m}^2$ .

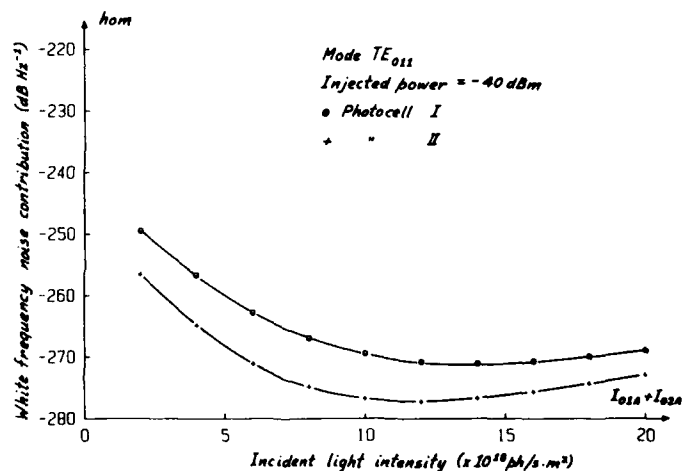


Fig. 11a White frequency noise contribution as a function of the total incident light intensity of the A-components for various photodetector shapes. The cylindrical cavity operated in  $TE_{011}$  mode is considered with an injected microwave power of  $-40$  dBm.

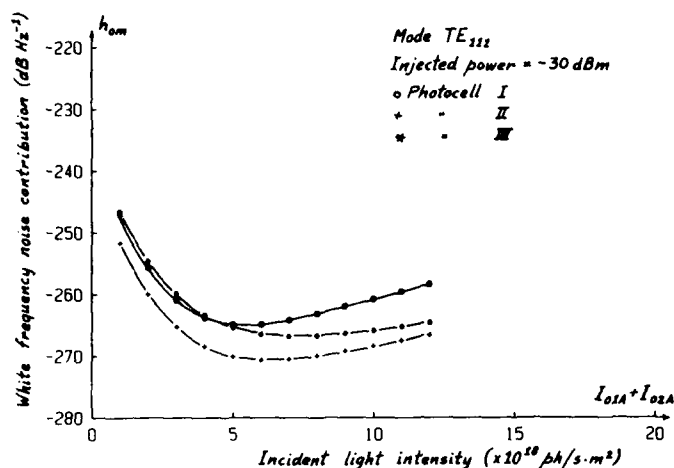


Fig. 11b White frequency noise contribution as a function of the total incident light intensity of the A-components for various photodetector shapes. The cylindrical cavity operated in  $TE_{111}$  mode is considered with an injected microwave power of -30 dBm.

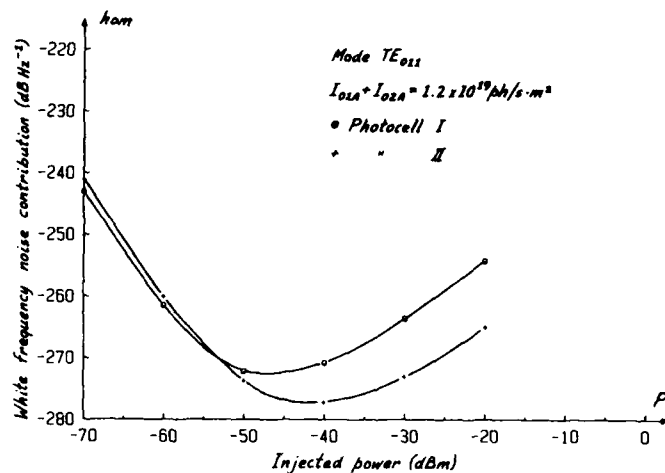


Fig. 12a White frequency noise contribution as a function of the injected microwave power for various photodetector shapes. The cylindrical cavity operated in  $TE_{011}$  mode is considered with a total incident light intensity for the two A-components of  $1.2 \times 10^{19} \text{ ph/s} \cdot \text{m}^2$ .

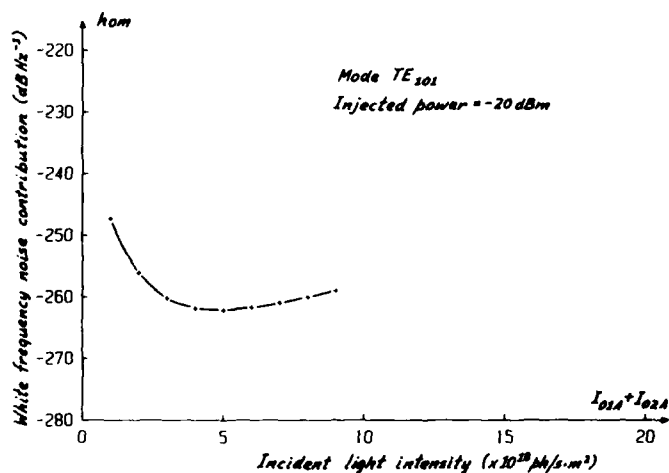


Fig. 11c White frequency noise contribution as a function of the total incident light intensity of the A-components for various photodetector shapes. The rectangular cavity containing a dielectric slab and operated in  $TE_{101}$  mode is considered with an injected microwave power of -20 dBm.

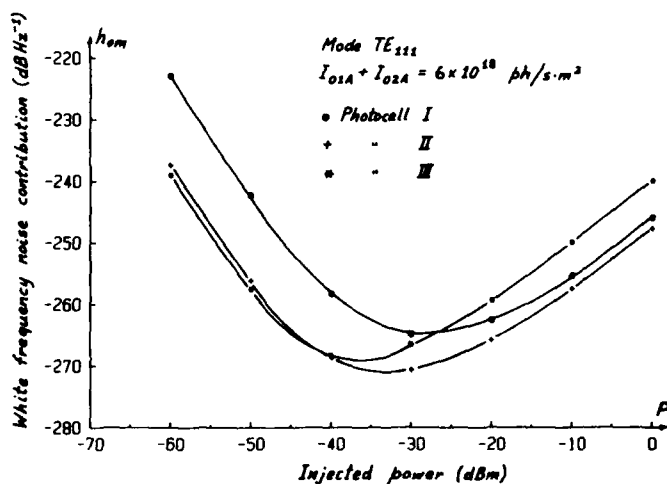


Fig. 12b White frequency noise contribution as a function of the injected microwave power for various photodetector shapes. The cylindrical cavity operated in  $TE_{111}$  mode is considered with a total incident light intensity for the two A-components of  $6 \times 10^{18} \text{ ph/s} \cdot \text{m}^2$ .

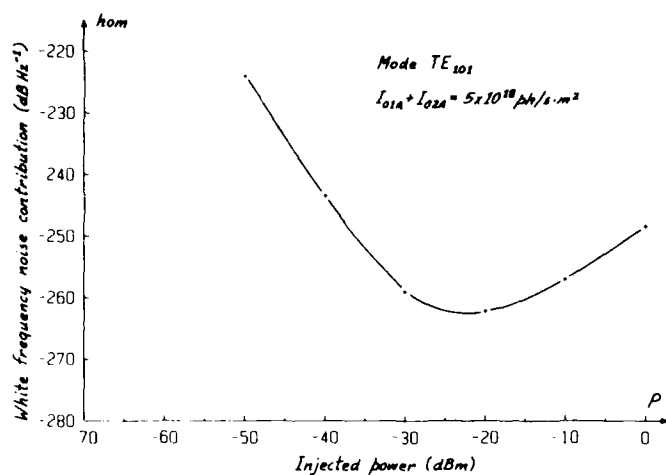


Fig. 12c White frequency noise contribution as a function of the injected microwave power for various photo-detector shapes. The rectangular cavity containing a dielectric slab and operated in  $TE_{101}$  mode is considered with a total incident light intensity for the two A-components of  $5 \times 10^{18} \text{ ph/s} \cdot \text{m}^2$ .

## A New Miniaturized Passive Hydrogen Maser

F. L. Walls and K. B. Persson  
National Bureau of Standards  
Time and Frequency Division  
Boulder, Colorado 80303

## ABSTRACT

The small passive hydrogen maser design developed at NBS has been further refined to produce a much smaller device with enhanced performance. This new miniaturized passive hydrogen maser is rack mounted, measuring 26 1/2 cm high exclusive of its external power supply. The weight is ~ 30 kg with a steady state power consumption of about 54 W at 25°C. The reduction in the size and power has been achieved primarily by major changes in the beam optics, offset frequency synthesizer, and hydrogen supply. The present size is small enough to fit in the NBS environmental chamber used to house commercial cesium frequency standards.

Long-term measurements against the NBS time scale indicate that the new miniature passive maser (MPH) design has a timekeeping ability over at least a few weeks which is better than our entire ensemble of 14 commercial cesium clocks. Frequency measurements vs the time scale (TA NBS) over the last 50 days yield a joint frequency stability of  $4.7^{+1.3}_{-3.6} \times 10^{-15}$  at 10 days. Preliminary analysis indicates that the cesium ensemble is the major contributor to this value. Extrapolation of the 1 day frequency stability sets a lower limit of  $1.5 \times 10^{-15}$  at 10 days for maser MPH 14 at its present flux level. Using a linear least squared fit to frequency drift between MPH 14 and the cesium ensemble yields a value of  $2 \pm 5 \times 10^{-16}$ /day averaged over 50 days. The net result is that this new generation of miniature hydrogen clocks can keep time to a few nanoseconds per week.

## INTRODUCTION

For many years precision timekeeping has relied nearly exclusively on commercially available cesium beam standards with a nominal fractional frequency stability of order  $3 \times 10^{-14}$  at one day and a timekeeping performance of order 20 ns per week. In this paper we describe a new generation of miniature passive hydrogen masers (MPH) developed at NBS, which are comparable in size, weight, and power to the commercially available cesium standards. The new MPH standards, however, have a frequency stability and timekeeping ability which is far superior to any presently available commercial cesium device.

The small hydrogen maser design (SPHM) previously developed at NBS [1-3] demonstrated excellent frequency stability, however it wasn't very portable. Typical fractional frequency stability was  $2 \times 10^{-12} t^{-1/2}$  out to about one week. Frequency drift vs the NBS cesium ensemble was not significant compared to the measurement noise of  $\pm 5 \times 10^{-16}$ /day. The design of this early passive maser was nearly 1.5 m (5 feet) tall and weighed about 90 kg (200 pounds).

The new generation of miniature passive hydrogen maser (MPH) just being completed at NBS exhibits excellent frequency stability and is much, much, smaller than the SPHM design. The current MPH design is 26.7 cm tall, 66 cm deep, and 49.5 cm wide (standard relay rack width). This rack mounted device weighs 30 kg (65 pounds) exclusive of its ac

power supply and uses 54 watts of power at 25°C.

Fractional frequency stability at one day is about  $7 \times 10^{-15}$  and the timekeeping ability exceeds 4 ns a week.

## PASSIVE HYDROGEN MASER BEAM ADVANCES

Several years ago NBS embarked on a program to develop a frequency standard based on the hydrogen magnetic hyperfine resonance shown in Figure 1. The basic technique for state preparation was virtually unchanged from earlier active hydrogen maser work utilizing hexapole magnets [4]. The length of the beam path from the source to the storage bottle in the previous design was 43 cm (17 inches), largely dictated by the focusing/defocusing characteristics of the hexapole magnet. By going to a quadrupole magnet with an inlet bore of 0.05 cm (0.020 inches), it was possible to reduce the beam length to slightly over 10 cm. This is due solely to the large deflection angles of the unwanted atoms achieved with quadrupole magnets [5]. This greatly shortened beam optics then made it possible to make the beam horizontal and still fit in a standard rack mount.

Measurements on the sensitivity of the output frequency of the earlier SPHM series on applied external magnetic field showed a quadratic dependence of order  $1 \times 10^{-13}$  for  $\pm 3 \times 10^{-5}$  T ( $\pm 0.3$  G) change. The quadratic behavior and the fact that the value was much larger than that expected from measurements on the Zeeman shifts, indicated that there was a significant magnetic field inhomogeneity shift (Crampton Effect [6]). Both the SPHM and MPH series use four magnetic shields separated by about 1.2 cm with an overall Zeeman shielding coefficient of about 200,000 along the beam axis. With the greatly shortened beam optics of the MPH series, it was relatively easy to extend the outer magnetic cover in order to partially shield the discharge bulb and the entire beam optics from changes in the external magnetic field. Figure 2 shows the measured shifts in output frequency of the maser due to changes of the external magnetic field. The shifts are still quadratic in nature but of much lower level, indicating that further shielding in this area would probably help reduce this effect even more. Nevertheless, the present performance of  $2 \times 10^{-15}$  for  $\pm 1.5 \times 10^{-5}$  T ( $\pm 0.15$  G) is more than adequate for operation in benign laboratory environments.

The storage cavity for both the older SPHM and the new MPH series uses a right circular cylinder of low-loss  $\text{Al}_2\text{O}_3$  ceramic with a bore down the central axis and a silver coating on the outside. The ends are capped with  $\text{Al}_2\text{O}_3$  plates. The closed central bore is coated with FEP 120 teflon\*. Thus, this dielectrically coated cavity serves as the microwave cavity, the vacuum chamber, and the storage volume. The integral nature of this design makes it very rugged. An additional feature is that the  $\text{Al}_2\text{O}_3$  is a very good thermal conductor thereby greatly reducing temperature gradients along the storage volume. This feature has made it possible to use only a single oven for control

\*Certain commercial materials are identified in this paper in order to adequately specify the experimental procedure. Such identification does not imply recommendation or endorsement by the National Bureau of Standards, nor does it imply that the materials or equipment identified are necessarily the best available for the purpose.

of the cavity frequency for applications with a benign thermal environment. Two ovens will probably be required for use under field conditions. Long term temperature coefficients are less than  $3 \times 10^{-14}/K$ . Additional analysis of this effect is planned over the next several months.

#### SERVO SYSTEMS

In the approach developed at NBS, both the output oscillator and the microwave cavity are locked to the hydrogen resonance using the scheme illustrated in Figure 3 [1-3]. Briefly, a local probe signal ultimately derived from 5 MHz is phase modulated at two frequencies,  $f_1$  and  $f_2$ , and introduced into the microwave cavity containing the state-selected hydrogen atoms. The transmitter signal is envelope-detected and processed in two synchronous detectors, one referenced to the modulation frequency,  $f_1$ , and the other to  $f_2$ .  $f_1$  corresponds to approximately the half-linewidth of the microwave cavity and  $f_2$  corresponds to the half-linewidth of the hydrogen resonance. The output of the  $f_1$  synchronous detector is used to actively correct the microwave cavity frequency with a time constant of about 10 seconds. The output of the  $f_2$  synchronous detector is used to steer the probe frequency to the center of the hydrogen line with a time constant of several seconds. The unique feature of the passive hydrogen masers, as compared to the active hydrogen masers, is the ability to lock the microwave cavity frequency to the hydrogen resonance frequency without the need for an external high-stability reference. Lesage et al., have theoretically examined the expected characteristics of such a system [7]. Their results agree rather well with the experimentally observed characteristics. Recent work by Peters in these proceedings show first results of a cavity switching servo.

#### SYSTEMATIC EFFECTS

Systematic effects which can perturb the output frequency are listed in Table 1 with the expected effect on stability. The temperature coefficient shown is an upper bound as the thermal response hasn't been carefully analyzed over the long times necessary to obtain a precision of parts in  $10^{15}$ .

Several masers of the SPHM series which were let up to air for servicing and repumped, recovered frequency to  $2 \times 10^{-13}$  or better. Adjustments on the electronics of MPH 14 showed shifts of order  $1 \times 10^{-13}$ . The results

Table 1. Summary of Systematic Effects for the Miniature Passive Hydrogen Maser.

EFFECT	OFFSET	INSTABILITY
1. Second-order Doppler Changes	$-4.3 \times 10^{-11}$	$3 \times 10^{-15}$
2. Cavity Pulling and Temperature Coefficient		$\leq 3 \times 10^{-14}/K$
3. Wall Shift	$-2 \times 10^{-11}$	$\leq 10^{-13}/\text{year}$
4. Spin Exchange	$2 \times 10^{-13}$	$5 \times 10^{-15}$
5. Magnetic Field Changes	$+2 \times 10^{-15}$ for $\pm 1.5 \times 10^{-5} \text{ T } (\pm 0.15 \text{ G})$	$10^{-15}$
6. Power Dependence	$< 10^{-13}/\text{dB}$	$10^{-15}$
7. Phase Modulator Drive	$< 10^{-13}/\text{dB}$	$10^{-15}$

on both the SPHM and the first of the MPH masers indicate that the drift is extremely small (less than  $5 \times 10^{-16}/\text{day}$ ) therefore changes in the wall shift are probably negligible. Therefore it is expected that the reproducibility after servicing of virtually any component, save replacing the cavity, will be better than  $3 \times 10^{-13}$ .

#### FREQUENCY STABILITY AND TIMEKEEPING RESULTS

The frequency stability and timekeeping capability of the first of the new series of miniature passive masers, MPH 14, has been analyzed over the past 50 days vs the NBS ensemble of cesium clocks. Figure 4 shows the measured fractional frequency stability vs TA NBS. This time scale is post analyzed monthly and defective clocks are removed. Three corner hat analysis (comparisons between three clocks) out to 1 day shows that a major portion of the instability in the data is attributable to the cesium ensemble. MPH 14 is a part of the ensemble and carries a weight of approximately 24%. The actual weight varies as various clocks are added or removed from the ensemble.

Figure 5 shows the timekeeping performance of MPH 14 vs TA NBS over the past 50 days. This data is particularly remarkable because the power to the maser was off for a short time on MJD 45801 (day 6) and 45814 (day 19). The time scale computer reset the phase after each power outage but didn't adjust frequency. MPH 14 recovered frequency to within several parts in  $10^{15}$  after each outage. Figure 6a shows the timing between MPH 14 and AT1 NBS over a two week period. For comparison the timing performance of a "very good" high performance commercial cesium beam standard over the same time is shown in Figure 6b. The on-line time scale AT1 is slightly smoother than TA NBS in short-term.

Based on the above data, the time dispersion between MPH 14 and NBS time scale varies from 0.9 ns for a prediction interval of one day, to 4 ns at a prediction interval of 7 days.

Most of the time dispersion appears to be due to the noise in the ensemble of cesium standards comprising TA NBS. Nevertheless, we can determine that the performance of MPH 14 is more than a factor of 3 times better than the best commercially available cesium standard for measurement times out to at least several weeks. (Three corner hat data suggests that MPH 14 is 5 times better than the best commercial cesium at 1 day.)

The data of Figure 5 was analyzed for frequency drift. The computed drift of  $2 \times 10^{-16}/\text{day}$  is much less than the uncertainty of  $\pm 5 \times 10^{-16}$  due to noise in the cesium ensemble.

#### CONCLUSION

It has been experimentally demonstrated that the MPH design yields a relatively small clock quite comparable in size, weight, and power to commercial cesium devices but capable of much better performance. The timekeeping of this new design of passive hydrogen maser exceeds 4 ns/week and may be as good as 1.5 ns/week (measurements are limited by instabilities in the cesium clocks used for the reference). Frequency drift is so small as to be hidden within the noise of the cesium ensemble even when averaged over 50 days.

## ACKNOWLEDGEMENTS

This work has been supported by the Naval Research Laboratory. We wish to thank D. W. Allan and J. Levine for assistance in data analysis and our many colleagues, especially D. A. Howe at NBS, for fruitful discussion.

## REFERENCES

- [1] F.L. Walls and H. Hellwig, "A new kind of passively operating hydrogen frequency standard," in Proc. 30th Ann. Symp. on Frequency Control. 443-479, 1976.
- [2] D. A. Howe and F. L. Walls, "A Compact Hydrogen Maser with Exceptional Long-Term Stability". IEEE IM-32, 218-223, 1983
- [3] F. L. Walls and D. A. Howe, "Timekeeping Potentials using Passive Hydrogen Masers", Journal De Physique, Colloque C8, supplement au n°12, Tome 42, C8-151-158, 1981.
- [4] Kleppner, D., Goldenberg, H.M., and Ramsey, N.F., "Properties of the Hydrogen Maser", Appl. Opt. 1 (1962) 55-60, 1962.
- [5] H. E. Peters, "Magnetic State Selection in Atomic Frequency and Time Standards," Proceedings, 13th Annual Precise Time and Time Interval Applications and Planning Meeting, 645-666, 1981.
- [6] S. Crampton and H. Wang, "Density-Dependent Shifts of Hydrogen Maser Standards," 28th Frequency Control Symposium, 355-361, 1974.
- [7] Lesage, P., Audoin, C., and Tetu, M., Proc. 33rd Annual Symposium on Frequency Control (1979) see also C. Audoin, J. Viennet and P. Lesage, "Hydrogen Maser : Active or Passive?", Journal De Physique, Colloque C8, supplement au n°12, Tome 42, C8-159-170, 1981.

## Figure Captions

Figure 1. Upper portion shows the magnetic hyperfine separation of atomic hydrogen vs magnetic field. The lower portion shows the traditional method of state selection using a hexapole magnet.

Figure 2. Change in output frequency of MPH-14 vs externally applied magnetic field. The broken lines are only to help guide the eye.

Figure 3. Block Diagram of the electronic servo concept used in the SPHM and MPH passive masers.

Figure 4. Fractional frequency stability  $\sigma_y(\tau)$  of MPH-14 vs TA NBS as a function of measurement time. MPH-14 has a weight of ~ 24% in TA NBS. No correction has been applied due to the self inclusion of the clock in the time scale or due to possible frequency drift.

Figure 5. Time comparison of MPH-14 vs TA NBS over 50 days starting at MJD 45795. The average frequency difference has been subtracted from the raw data. No correction has been applied due to the self inclusion of the clock in the time scale or due to possible frequency drift. MPH-14 has a weight of 24% in TA NBS.

Figure 6a. Time comparison of MPH-14 vs AT1 NBS starting at MJD 45798. The average frequency difference has been subtracted from the data. No correction has been applied to the self inclusion of the clock in time scale or due to possible drift. MPH-14 has a weight of 18% in AT1 at the time of this data.

Figure 6b. Time dispersion of clock 12, a high performance commercial cesium beam frequency standard, vs AT1 NBS starting at MJD 45798. The average frequency difference has been subtracted from the raw data. No correction has been applied due to the self inclusion of the clock in the time scale or due to possible frequency drift. Clock 12 has a weight of 23% in AT1 at the time of this data.

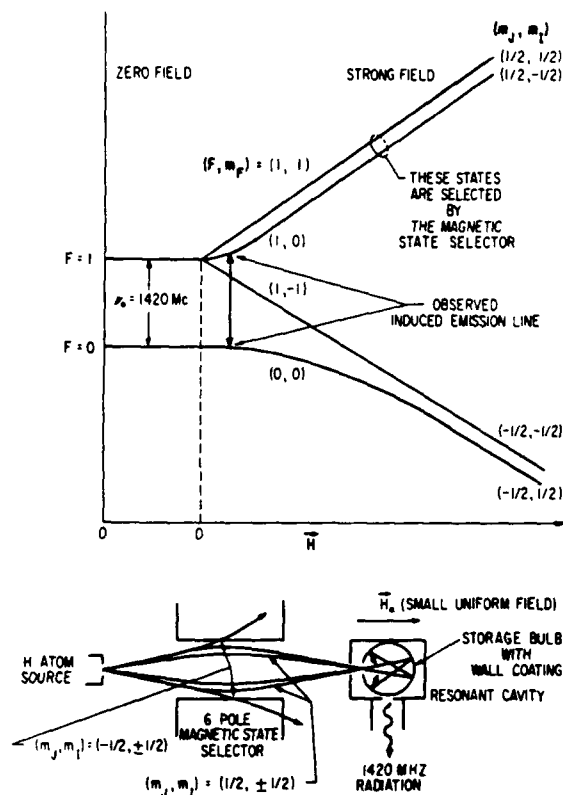


Fig. 1

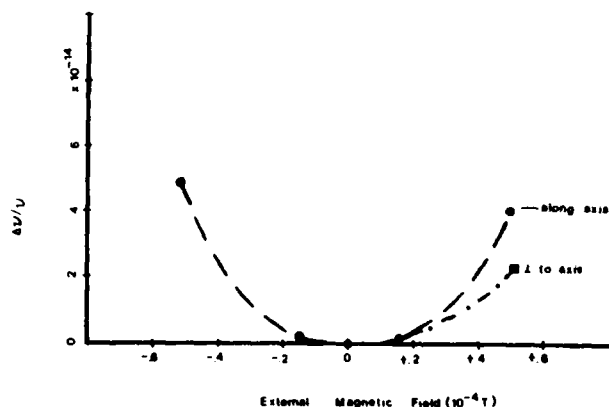


Fig. 2

# PASSIVE HYDROGEN MAGER

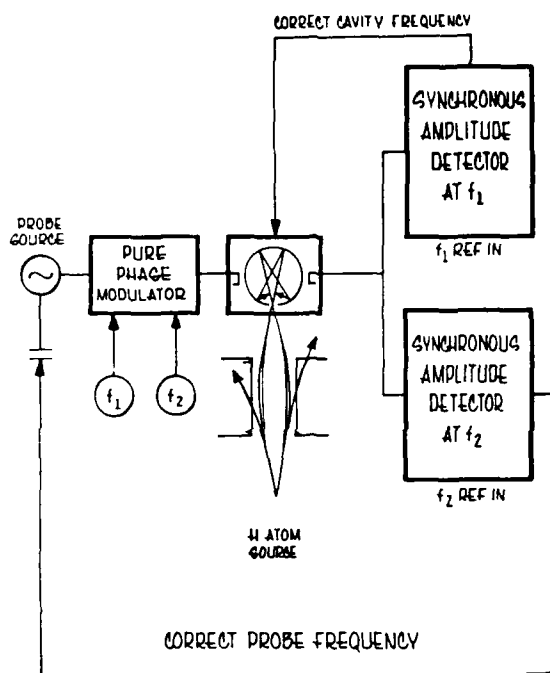


Fig. 3

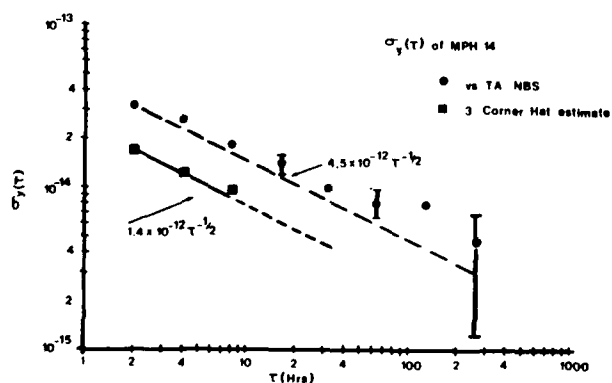


Fig. 4

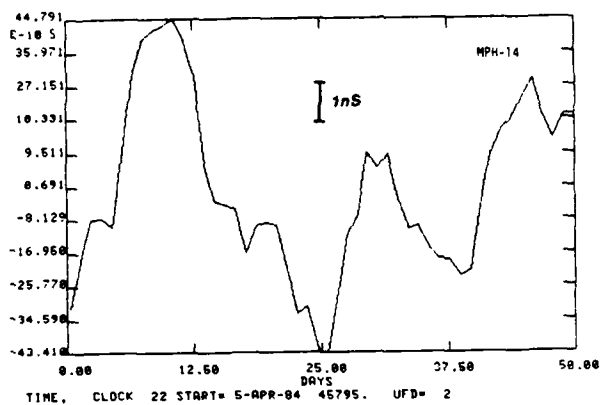


Fig. 5

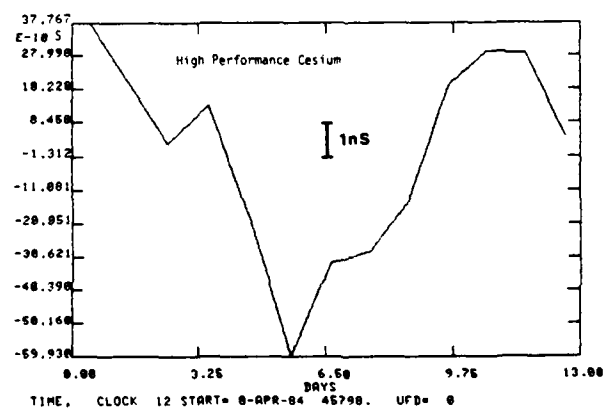
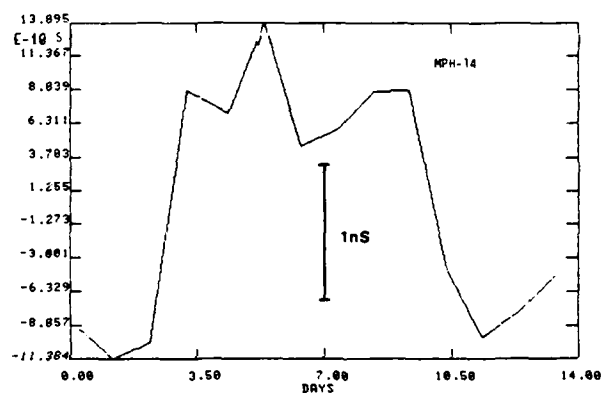


Fig. 6

# DESIGN AND PERFORMANCE OF NEW HYDROGEN MASERS USING CAVITY FREQUENCY SWITCHING SERVOS

H. E. PETERS  
SIGMA TAU STANDARDS CORPORATION  
TUSCALOOSA, ALABAMA

## Summary

Design concepts and performance data are given for two newly designed hydrogen maser frequency standards which incorporate a novel cavity frequency switching servo system to remove cavity related drift. Order of magnitude improvement in stability, hydrogen economy, environmental isolation, and other characteristics has been obtained.

## Introduction

Two new hydrogen maser frequency standards incorporating significant departures from conventional practice have been designed and constructed, and their performance is presently being evaluated. One of the masers was constructed under contract with the Applied Physics Laboratory with support from NASA, Goddard Space Flight Center,<sup>1</sup> and the other was funded by the Naval Research Laboratory.<sup>2</sup> The two masers differ only in the dimensions of the outer magnetic shield and the size of the vacuum pumps; this was done to experimentally determine the relative effectiveness of the shields and the improvement to be realized by the additional space for thermal insulation.

The work reported in this paper is largely an outgrowth of earlier efforts to achieve a compact hydrogen maser under the "Light-Weight Hydrogen Maser Program." That work was supported by the United States Air Force, RADC, Electronics Systems Division.<sup>3</sup> Some further results of experimentation with the "Small Hydrogen Maser" constructed in that program is discussed herein, however the main effort in this paper will be to present a brief introduction to the design concepts and their implementation in the new masers, and to present the experimental results obtained to date.

The new masers have been operating for over five months at this writing. Preliminary results have been obtained for the relative stability, thermal coefficients, magnetic effects and other aspects of performance. Long term frequency measurements have also been made with respect to a high performance cesium standard.

The most important aspect of the new design is the use of a cavity frequency switching servo system to remove cavity related drift. This is the first publication of results using such a servo with hydrogen masers.<sup>4</sup> The system is designed so that the cavity is continuously maintained at the spin exchange offset frequency without the use of a secondary reference oscillator. Therefore each maser is a stand-alone standard essentially free of cavity pulling or hydrogen beam intensity perturbations. While cavity frequency switching introduces a phase modulation of the maser output signal, the effect is negated by a compensating phase modulation designed into the maser synthesizer circuit. This, and the fact that the

modulation frequency is much higher than the receiver phase lock loop bandwidth, results in short term stability essentially unaffected by servo operation.

## Overall Hydrogen Maser Design

Figure 1 illustrates the size and the external arrangement of controls for the two new masers. The larger unit, the APL maser, is 38 inches in height, 18 inches wide and 22 inches deep; it weighs approximately 300 pounds, not including batteries. The smaller NRL maser is only 32 inches high, 15 inches wide, 19 inches deep and weighs approximately 250 pounds. In the figure the masers are mounted on top of a back-up auxiliary battery pack which provides 15 hours of uninterrupted operation in case of line power failure. On batteries, the masers use approximately 65 watts of power, while in normal service the AC line power required is less than 100 watts.

An eleven digit synthesizer provides phase coherent settability of  $\pm 2.5$  parts in  $10^{17}$  and a range which is limited by the range of the maser receiver voltage controlled crystal oscillator to 2 parts in  $10^6$ .

Hydrogen is supplied to the maser source from a small, low pressure, replenishable metal hydride storage bottle containing 2 moles of molecular hydrogen. At the maximum use rate of .01 moles per year, replenishment of hydrogen is not often required.

The maser operational data is displayed on a 4 1/2 digit panel meter and 32 multiplexed channels are selected by binary coded switches. A buffered output voltage allows external monitoring of the selected parameter.

The physical arrangement of cavity, magnetic shields, vacuum enclosure, and vacuum pumps is illustrated in Figure 2. The maser has two separately pumped regions in the vacuum system, each pumped by a field replaceable ion pump. The "upper" pump maintains the vacuum outside the maser bulb and inside the outer vacuum enclosure so as to getter gas diffusing through O-rings or outgassing from other structures. A "lower" pump maintains a much lower background pressure in the source and storage bulb region and getters all the hydrogen entering the system. At the present observed pump currents the 11 liter per second pumps used on the NRL maser are anticipated to have on the order of ten years of life while the 20 liter per second pumps on the APL unit should last over twice as long. Ultec "Differential Ion Pumps" are used on both masers.

The effectiveness of magnetic shields is primarily a function of the shield material, the metal thickness, the annealing treatment, and the number and spacing of the shields. Assuming equal success in obtaining the best of the first three items, the only way to improve



the shielding effectiveness in a maser is to make the outer shield as large as possible, the inner shield as small as possible, and to space the intermediate shields properly to maximize the magnetic impedance of the interspaces. To minimize the size of the inner shield a smaller than usual cavity and bulb assembly is used, and the first two of four shields are placed within the vacuum enclosure. This arrangement provides a factor of 10 or more theoretical improvement over the arrangements traditionally used where all the shields are placed outside the vacuum enclosure and are necessarily more closely spaced.

The spacing of the inner magnetic shields close to the cavity also allows the state selector and source to be placed relatively close to the storage bulb entrance. These masers use tapered quadrupole state selectors<sup>5</sup> which have unusually large capture solid angles for atoms emerging from the source collimator, and a large fraction of the atoms in the upper quantum states which are "captured" enter the storage bulb collimator. The anticipated improvement in hydrogen utilization has experimentally been confirmed. Typical hydrogen pump currents under 50 microamperes indicate an order of magnitude improvement over the most efficient previous designs.

An unusual approach to the maser cavity and bulb assembly construction is used in the new masers; the design is illustrated in Figure 3. A copper cylinder and copper end plates form the cavity walls. A relatively thick circular cylinder of quartz is held by spring tension between the end plates, and the quartz atom storage bulb is secured to the quartz cylinder using quartz shims and hard epoxie. The quartz cylinder provides dielectric loading to reduce the outer diameter of the cavity, and at the same time provides rigid support for the bulb and for the cavity end plates. The cavity quality factor realized with this structure is surprisingly high, and the structure is smaller than usual for an active oscillator maser without electronic cavity gain. The storage bulb in the two present designs is 4.25 inches in diameter and 9 inches long with a 2.5 mm wall thickness, and the quartz cylinders also have a 2.5 mm wall. The cavity is 12 inches long inside, has a diameter of only 9.6 inches, and the loaded  $Q$  is 45,000 with a coupling coefficient of .25.

It should be mentioned that several laboratory experiments were performed with cavity and bulb assembly test structures to arrive at the present design. We have under construction a third maser which uses a cavity with a 6 mm wall quartz cylinder surrounding the same size bulb and it has a loaded  $Q$  of over 40,000; the cavity diameter is only 8.6 inches. From our experiments it is clear that active maser oscillators could be constructed with greater loading and smaller size, however the high  $Q$  obtained in the present masers is very desirable in order to achieve good oscillation parameters, high beam power, and adequate signal to noise ratio for the cavity frequency switching servo.

#### Cavity Frequency Switching Servo System

To describe all the theoretical ramifications of operation of the hydrogen maser under the condition of periodically switched cavity frequency is well beyond the scope of the present paper. Only an adequate basis for explaining the first order effects on maser stability and understanding the results of the present experiments using the new technique will be presented herein. Figure 4 illustrates a maser cavity assembly with the storage bulb containing a population of atoms

oscillating at the hydrogen frequency. Coupling of energy from the ensemble of atoms to the output coupling loop is only through the medium of the cavity electromagnetic field. If the cavity parameters are held constant, the cavity field amplitude and the coupled output power level follow the amplitude of the oscillating atomic moments. If, on the other hand, the cavity frequency or other parameters change, the oscillating magnetic moment of the ensemble of atoms will change, but only slowly, with a time constant of approximately .4 seconds in the present case. However, the amplitude of the cavity fields, as well as the phase relation between atoms and coupling loop, will change rapidly. The time constant for the cavity field to come to a new equilibrium level is only about 10 microseconds.

Thus, if the cavity resonance frequency is switched rapidly between two different frequencies, the phase and amplitude of the oscillating atoms will remain essentially constant at a certain long term equilibrium level, but there will, in general, be an amplitude and phase modulation of the signal coupled out of the cavity. The ensemble of atoms in the bulb may be thought of as a current generator of constant amplitude and phase coupled through a resonant circuit, the cavity, to the output coupling loop.

A good analogy for first order analysis of the cavity response is shown in Figure 5. The abscissa for the resonance curve is the ratio of frequency difference from the cavity resonance frequency,  $(f - f_r)$ , to the cavity bandwidth,  $f_{cw}$ . The equations given in the figure are the basis for calculation of the maser output voltage difference when the cavity resonance,  $f_r$ , is switched between different frequencies with the maser frequency held constant.

Figure 6 illustrates the condition described above. In the present configuration of the servo system, a diode detector circuit detects the signal amplitude, so it is the difference in voltage magnitude at the two cavity resonance frequencies which is obtained. The offset in maser frequency is related to the offset in cavity frequency by

$$(f_m - f_c) = (Q_c/Q_1)(f_c - f_m) \quad (1)$$

where  $Q_c$  is the loaded quality factor of the cavity, and  $Q_1$  is the atomic resonance line  $Q$ .  $Q_c/Q_1$  is approximately  $2.6 \times 10^{-5}$  in the present case, so for the purpose of correcting the cavity frequency the maser frequency may be considered a constant.

A block diagram of the overall servo system is shown in Figure 7. The maser signal amplitude is detected at the 405 KHz IF frequency where the bandwidth of the preceding amplifiers is wide enough not to cause significant reactive amplitude transients. A modulation period generator produces a voltage square wave to modulate the cavity frequency and provides a signal to a synchronous detector circuit where an "UP" or "DOWN" signal is generated and sent to the circuit which controls the average cavity frequency. Two methods of controlling the average cavity frequency have been successfully used. In one method the temperature of the cavity is controlled through the thermal control circuit, in the other a voltage bias is used to vary the average voltage applied to the cavity varactor. The results presented in this paper were obtained while the temperature control method was being used.

An important feature of the present designs is a digital circuit in the period generator by which the relative period duration of the two cavity frequencies

may be set with a resolution of one part in  $10^5$ . Thus, while the servo circuit automatically centers the cavity to the point where the two resonance curves cross, the average cavity frequency actually seen by the atoms may be adjusted so that there is no change in output frequency when the beam intensity is changed. When the maser is first operated it is compared in frequency with another hydrogen maser, and by the technique of a conventional spin exchange tuning method<sup>6</sup> the proper cavity average offset frequency is established and set in the modulation period generator control switches. Since the spin exchange offset is only about 100 Hz, a small fraction of the modulation, (9.5 KHz in the present case), which is also only a small fraction of the maser frequency, subsequent drift in offset is not a serious problem.

#### Cavity Servo Random Thermal Noise

One of the notable features of a maser is the low noise character of the phase or amplitude when used as either a signal source or as an amplifier. The primary source of non-systematic noise affecting the cavity servo in the present case is thermal "KT" noise coupled from the cavity along with the maser signal. Letting N be the noise factor of the receiver input stage and B the bandwidth, the voltage noise to signal ratio is given by

$$V_n/V_s = \sqrt{KTNB/2P} \quad (2)$$

where P is the signal power, K is the Boltzman constant and T is the absolute temperature. The servo system uses a synchronous switched filter after IF detection followed by a synchronous phase detector and digital integrator. The bandwidth for this system is  $B = 1/(2\tau)$  where  $\tau$  is the servo time constant. Using the circuit given in Figure 5 as a model for the cavity resonance, the impedance is given by

$$Z = \frac{R}{1 + jR(\omega C - 1/\omega L)} \quad (3)$$

The cavity Q is given by  $Q_c = R/\omega L = f/f_{cw}$  where  $f_{cw}$  is the cavity width at the half power points. The frequency is given by  $f = \omega/2\pi$  and the frequency deviation from the cavity average is  $\Delta f = f - \bar{f}$ . The following relation is then obtained between the average cavity offset frequency and the modulation voltage  $V_m = \Delta V$ :

$$\frac{V_m}{\Delta f} = \frac{\Delta}{f_{cw}} \left( \frac{\Delta}{1 + \frac{\Delta^2}{2}} \right) V_s \quad (4)$$

Here  $V_s$  is the maser signal voltage output which occurs when the maser frequency equals the average cavity frequency, and  $\Delta$  is defined as  $(f_2 - f_1)/f_{cw}$ .

From equations (1), (2), (3), and (4) and the expression for the servo bandwidth, the maser fractional frequency offset for unity signal to noise ratio is found to be

$$\left( \frac{\Delta f}{f} \right) = \frac{(1 + \frac{\Delta^2}{2})}{8Q_1 \Delta} \sqrt{\frac{KT N}{\pi P \tau}} \quad (5)$$

Inserting typical values for the new masers:

$$\left( \frac{\Delta f}{f} \right) = 1.55 \times 10^{-14} \tau^{-\frac{1}{2}} \quad (6)$$

From the above result it is clear that this cavity servo, as limited by input thermal noise, has the potential for reducing the effect of cavity pulling on the hydrogen maser frequency to extremely low levels. There are, of course, several potential sources of systematic error, offset, or noise in this servo system. Inequality of the cavity Q's at the two modulation frequencies, pickup of coherent modulation noise in the IF strip, amplifier noise or drift in the demodulator circuit, offsets in the hydrogen maser frequency due to variable field inhomogeneity effects, misalignment in the cavity bulb assembly, and several other potential systematic problems could occur which do not lend themselves to ready analysis. The real test for the presence of such effects must therefore rely upon experiment and measurement. Present bench tests of the cavity and bulb assembly, test of the separate servo electronics components, and closed loop signal measurements and analysis indicate that there are no apparent barriers to achieving the cavity related stability level implied by Equation 6.

#### Experimental Results

A block diagram of the frequency comparison system is shown in Figure 8. For measurement intervals less than 10,000 seconds, period measurements were made with a digital counter using a one Hz frequency difference between the masers at a frequency of 120 MHz. This was obtained by frequency multiplication of the 5 MHz standard frequency output of each maser. A one Hz bandwidth was used, and a one second dead time between period counts was not corrected for. For intervals greater than 10,000 seconds, a multiplied offset beat frequency with a period of typically 8 Hours was recorded on a 10 inch width chart recorder at a rate of 1 cm/Hr. For cesium comparisons a similar system was used but the 5 MHz was only multiplied to 100 MHz. The actual oscillation frequency of each maser was offset a small amount from the other by operating at different magnetic field settings, and there were no frequencies exactly common to either maser system, or to the cesium standard. Thus no phase locking of standards was possible, nor have any phase locking or frequency locking noise phenomena been observed.

One of the best ways to test the servo system is to observe the correction rate and time constant for return to the tuned position from a step offset. Another is to observe the cavity correction voltage noise along with measurement of the frequency with regard to another hydrogen maser. Figure 9 shows the result of such measurements on the NRL maser using the APL maser as a reference. The phase plot period was initially 8.6 Hrs. corresponding to a frequency offset of  $2.69 \times 10^{-13}$ . The maser cavity register was then offset by an amount equivalent to  $+3 \times 10^{-12}$  in maser frequency. The servo response shows a linear correction rate of  $1.5 \times 10^{-12}$  per hour and a smooth return to the previous level until the noise floor is reached. The maser also returns to the previous frequency with no measurable error. A similar offset in the opposite direction has the same result. The short term excursions of the register voltage correspond to either noise or corrections of the order of parts in  $10^{14}$ , but this is effectively filtered by the long time constant of the cavity thermal capacitance and thermal impedance. Similar experiments, with the APL maser offset, give similar results. The servo correction rate may be set either faster or slower, but the maser does not have significant cavity related instability in the short term, and the present rate is adequate to effectively remove longer term thermal perturbations.

The relative stability of the two masers is illustrated in Figure 10. The plot gives the sigma tau "Allan Variance" as a function of measuring interval for intervals from 1 second to 60,000 seconds. The long term data was obtained over a 13 day period. No linear drift between the tuned masers has yet been observed within the statistical uncertainty of measurement. (The calculated drift for this 13 day period was  $6 \times 10^{-16}/\text{Day}$ .)

Figure 11 is a picture of the original chart recorder data used in the longer term sigma tau calculations. The relative frequency invariance and low phase noise of the masers are illustrated by comparison to the phase plot of a Hewlett Packard high performance (option 004) cesium standard which was made simultaneously with respect to the NRL hydrogen maser. The cesium standard frequency stability and flicker level measured against the maser is the same as specified by the manufacturer.

The maser beat frequency difference from the sample average during the phase comparison is shown in Figure 12. This figure shows very graphically the real time frequency invariance and the great potential for improved long term timekeeping possible by use of the new cavity switching servo technique.

Magnetic field sensitivity measurements were made on both the NRL and APL hydrogen masers. The applied field was produced by two coils surrounding the maser, one near the top and one near the bottom and the external field was measured with a Hall probe at the top center of the maser. Calibration field measurements were also made on the isolated field coils, and the calculated shielding factor refers to the impressed external field variation referred to the empty field coil divided by the internal field change inferred from measurement of the change in frequency of the maser. For the APL maser, with an external field change of 1.6 to -1.5 Gauss, the shielding factor was  $1.05 \times 10^5$ . For an external field change of +.6 Gauss to -.6 Gauss the shielding factor was  $3.7 \times 10^4$ . For changes from +.06 Gauss to -.06 Gauss the effect was not measurable.

For the NRL maser, which has an external shield 3 inches smaller in width and depth, and which is 5 inches shorter, the shielding factors were not as good. The worst case condition was an axial external change from +1 to -1 Gauss for which the shielding factor was 21,000. Similar measurements with the external coils placed horizontally did not result in a measurable effect.

Sensitivity to ambient temperature was tested by placing the NRL and APL masers in separate rooms and using air conditioning controls and electric heaters to establish different temperatures in the two rooms. The relative frequencies were measured over a period of a day or more at each temperature after approximate equilibrium conditions were achieved. For the NRL maser there was no statistically significant temperature coefficient within a resolution of  $\pm 1 \times 10^{-15}$  per °C. For the APL maser the temperature coefficient was  $6.4 \times 10^{-15} \pm 1 \times 10^{-15}$  per °C. The APL maser is at present operating at a factor of about 4 lower beam intensity than the NRL maser and this may be the cause of its higher temperature coefficient. We plan to increase the beam intensity of the APL unit and to look for other systematic causes in the near future. However the present results for temperature perturbations are very good.

## Experiments With the "Small Hydrogen Maser"

The Small Hydrogen Maser (SHM) is a novel design of a very compact maser which was built in the course of a research and development effort which was funded by the United States Air Force.<sup>3</sup> The maser used a small storage bulb with attached copper electrodes configured such that the overall cavity was only 6" diameter by 9" long.<sup>4</sup> Contrary to original expectations, it was not possible to attain oscillation conditions with this maser at first due to the low cavity Q realized: to overcome the problem a transistor circuit was placed within the cavity to provide active feed-back and reduce cavity losses. External control of the cavity Q and frequency was accomplished by changing the DC bias on the transistor. It was also possible to control the cavity frequency by changing the temperature. With the active cavity gain circuit maser oscillation was easily attained. To improve the maser stability the first experimental cavity frequency switching servo was also installed, and tests of the servo system response gave promise of good control of the cavity frequency. Actual stability measurements awaited the construction of the APL and NRL hydrogen masers.

In the period since the new masers were constructed several tests have been performed on the SHM. First, the stability without use of the cavity servo was examined. For one and ten second intervals the Allan Variance was  $2.5 \pm 1 \times 10^{-12}$ . For longer periods, up to a day, the stability was erratic, with rather large random excursions in frequency. Over a four day measuring interval there was an approximately monotonic drift of  $2.3 \times 10^{-13}$  per Hour.

Tests were then made using the cavity servo with the cavity frequency controlled through the temperature control circuit. This was not successful for the apparent reason that the cavity frequency versus temperature characteristic of the SHM was not monotonic and had a wide hysteresis loop. The servo control voltage as well as the maser frequency varied between rather large extremes. Tests using the servo output to control the frequency through the cavity gain circuit were also very disappointing. Changes in the gain transistor bias not only changed the cavity frequency and modulation width, but it appeared to affect the cavity noise spectra amplified by the transistor circuit, and the variable noise amplitude modulation interfered with the maser signal modulation.

To correct the problems with the SHM it would be necessary to have a mechanism independent of the temperature controls or the gain circuit to vary the frequency. This could be accomplished by use of a varactor as in the APL and NRL masers. Another and better approach would be to use a cavity and bulb design similar to that shown in Figure 3, but with the maximum quartz loading consistent with adequate passive cavity Q.

Work on the SHM at Sigma Tau Standards Corporation has been completed at this time. However, the scientific knowledge and technical fallout have been very valuable in laying a foundation for the conception and realization of the new designs embodied in the APL and NRL masers. We have learned of the difficulties and complexities involved in the cavity and bulb configuration used in the SHM, and arrived at a new design which, though not quite as compact, has more than met the stability goals of the "Light-Weight Hydrogen Maser Development Program."

## Conclusion

Present work with the new masers and use of the new technique for stabilizing the cavity have resulted in extremely good stability. The masers have been operational for only five months at this writing, and a great deal of experimentation and analysis remains to be done to establish the real stability limits which may be attained. Future work will involve operation at different cavity frequency modulation rates and amplitudes; we must examine more closely the fundamental accuracy or reproducibility effects of cavity frequency switching and we should experiment with different configurations of bulb, cavity, and means to modulate the cavity frequency. The present results reported in this paper give a basis for very optimistic projection of the performance levels which may be ultimately achieved.

## Acknowledgements

1. The APL maser work was supported by the Applied Physics Laboratory, The Johns Hopkins University and NASA, Goddard Space Flight Center, under APL Contract Number 601748-S.
2. The NRL maser work was supported by the Naval Research Laboratory under Contract Number N00014-83-C-2015.
3. The Light-Weight Hydrogen Maser effort was sponsored by the Deputy for Electronic Technology (RADCE/T), Air Force Systems Command under Contract Number F19628-79-C-0104.

## References

4. H.E. Peters, "Experimental Results of the Light-Weight Hydrogen Maser Development Program," Proceedings, 36th Annual Symposium on Frequency Control (1982), copies available from Electronic Industries Association, 2001 Eye Street, Washington, DC 20006.
5. H.E. Peters, "Magnetic State Selection in Atomic Frequency and Time Standards," Proceedings, 13th Annual PTTI Meeting (1981), Naval Research Laboratory, Washington, DC.
6. H.E. Peters, T.E. McGunigal, and E.H. Johnson, "Hydrogen Standard Work at Goddard Space Flight Center," Proceedings, 22nd Annual Symposium on Frequency Control (1968), copies available from National Technical Information Service, Stills Building, 5285 Port Royal Road, Springfield, VA 22161.

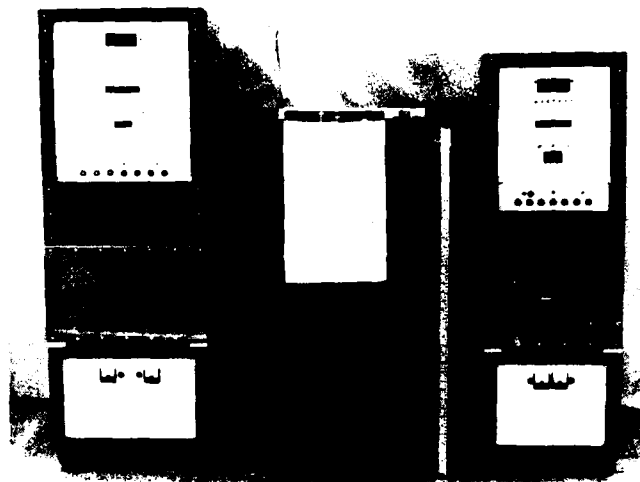


Figure 1. APL and NRL hydrogen masers

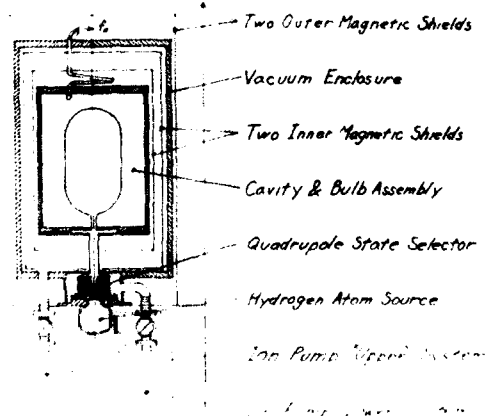


Figure 2. New hydrogen maser physical design

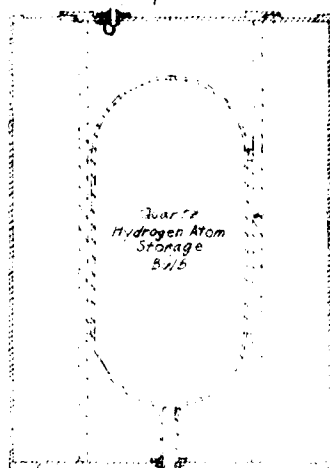


Figure 3. Maser cavity and bulb assembly

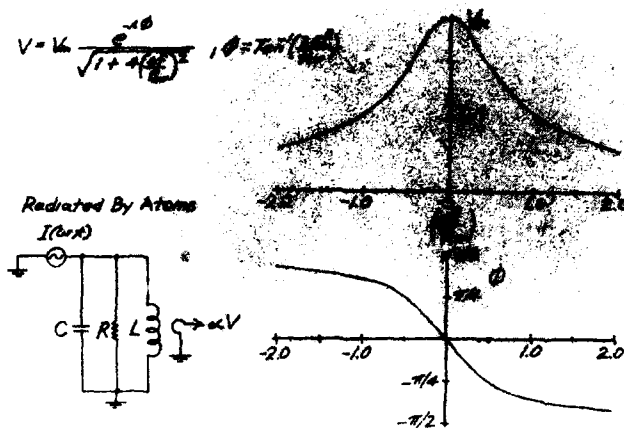


Figure 5. Circuit model for analysis of cavity output voltage change as a function of change in frequency of excitation

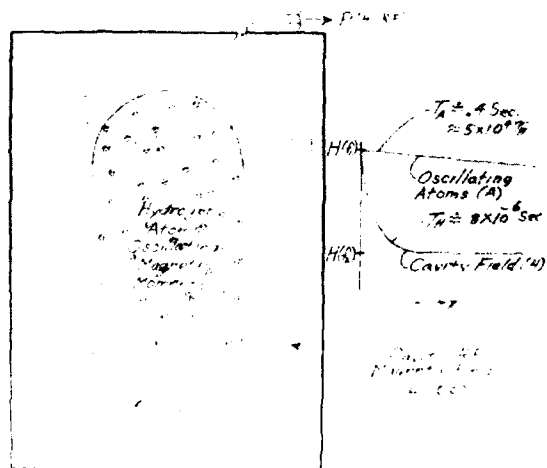


Figure 4. Oscillating atoms and RF field diagram

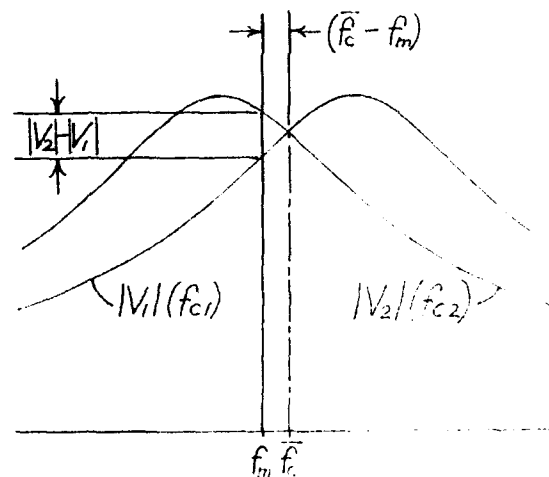


Figure 6. Illustration of output voltage change for a step change in cavity frequency

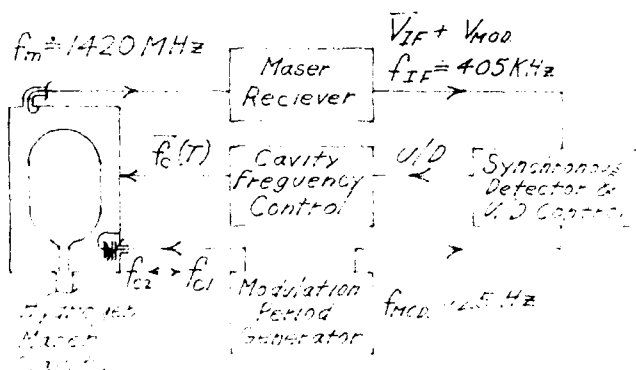


Figure 7. Cavity frequency switching servo system diagram

# CAVITY CONTROL SERVO CORRECTION VOLTAGE

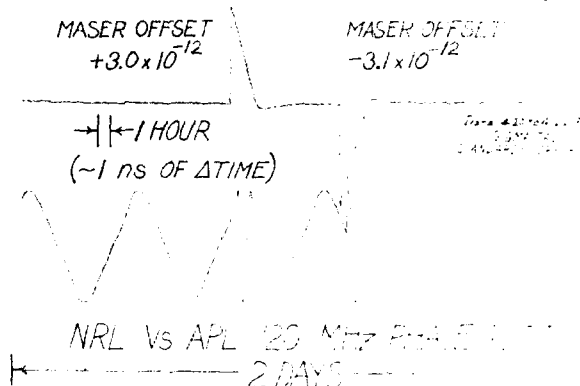


Figure 9. Response of the servo cavity control voltage and the maser output frequency for step offsets in cavity frequency

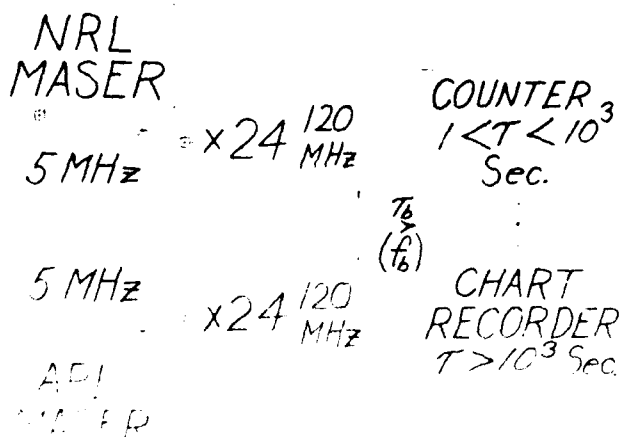


Figure 8. Comparison system

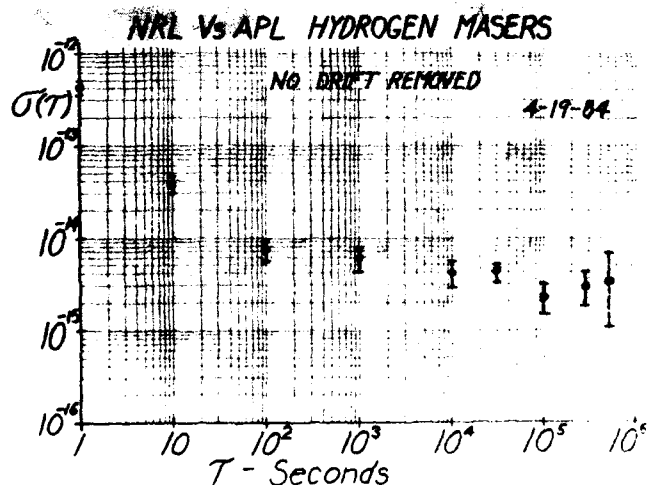


Figure 10. Hydrogen maser relative stability - Allan Variance

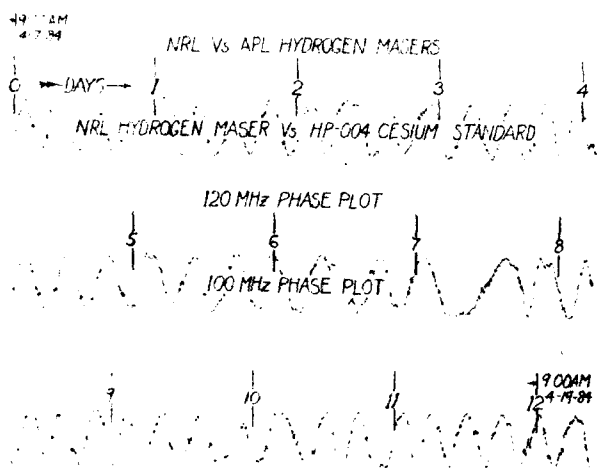


Figure 11. Phase plots: NRL vs APL hydrogen masers and NRL vs HP-004 cesium

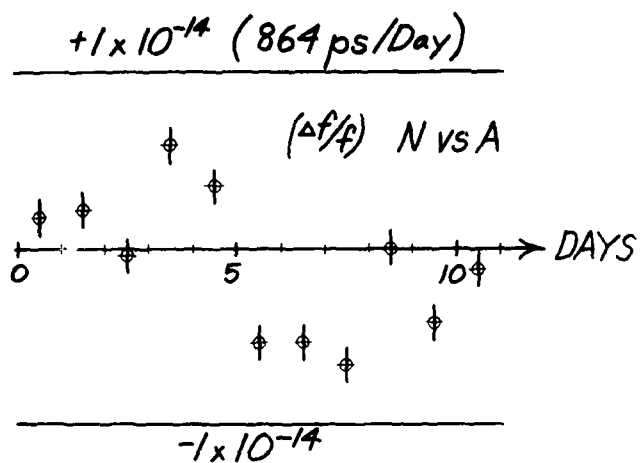


Figure 12. Fractional frequency difference from the average frequency between hydrogen masers over a 12 day period

## OPERATION AND PERFORMANCE OF A HYDROGEN MASER WITH A NEW STATE SELECTOR

Shinji Urabe, Yasusada Ohta, Takao Morikawa and Yoshikazu Saburi

Radio Research Laboratories, Ministry of Posts and Telecommunications  
4-2-1, Nukui-Kitamachi Koganeishi, Tokyo 184, JapanSummary

The results of the operation of the hydrogen maser with a new state selector are described. In the first part of this report, the measurement results of the magnetic inhomogeneity shift of the maser frequency by the use of a new state selector are described. In the next part, the results of the long-term continuous operation of the masers by the automatic cavity tuning method are described.

Maser structure and Electronics

The structure of the maser, H3 or H4, is shown in Fig.1. It is of the laboratory type. This apparatus consists of the two ion pumps, the atomic source system, the double focusing state selector, the four-layer magnetic shields, the microwave cavity and the storage bulb. The shielding factor is about 15000. The loaded  $Q$  of the cavity is about 45000 and the cavity temperature is controlled within the limits of  $\pm 0.01$  C.

The system of the maser electronics and that of the cavity autotuning electronics are shown in Fig.2. The system shown in the upper part of the figure is the phase-locking loop for controlling a 5 MHz quartz crystal oscillator. The system shown in the lower part is the electronics for the automatic cavity tuning<sup>1</sup>. The beat period of the two maser frequencies is measured to detect the cavity offset by varying the atomic flux between the two levels. The detected signal is used to correct the cavity frequency. The frequency stability of the free running maser is about  $3 \times 10^{-15}$  at the averaging time of 500 seconds and that of the autotuned maser is about  $1 \times 10^{-14}$  at the averaging time from 100 seconds to 1 day.

State Selector<sup>2,3</sup>

The structure of the state selector is shown in Fig.3. This selector is designed for eliminating the undesirable atoms in the ( $F=1$ ,  $m_F=1$ ) state. Some attempts have been made for this elimination by the AFP method<sup>4,5</sup>. In our apparatus, the Majorana transition is used<sup>6</sup>. The state selector consists of two hexapole magnet and two solenoid coils. The solenoid coils are placed in series inside the magnetic shields which are placed between the magnets. When the atoms in the  $m_F=1$  state pass through the reverse magnetic field, these atoms make transitions to the  $m_F=-1$  state. Since these atoms are defocused by the next magnet, only desirable atoms in the  $m_F=0$  state can enter the storage bulb. For the purpose of designing the state selector successfully, the beam optics analysis and the transition probability calculation of an atomic spin in the reverse magnetic field are made. The appropriate beam optics configuration is obtained<sup>3</sup>.

When the magnetic fields of the two coils are set in an opposite direction (Majorana method), the undesirable atoms can be eliminated by about 90%. This elimination is confirmed by measuring the line width and the Zeeman response of the maser amplitude. On the other

hand, when the fields are set in the same direction, the conventional state selection (conventional method) can be realized.

Magnetic inhomogeneity shift

The advantage of this state selector is that the dependence of the magnetic inhomogeneity shift (Crampton effect) on the population distribution of the  $F=1$  state can be easily examined. This shift is proportional to the population difference between the ( $F=1$ ,  $m_F=1$ ) state and the ( $F=1$ ,  $m_F=-1$ ) state<sup>6</sup>. Therefore, when the undesirable atoms are eliminated, it is expected that this shift can be reduced sufficiently. The dependence of the tuned frequency on the state selection method is measured<sup>7</sup>. Fig.4 shows one of the measurement results of the tuned frequencies for three operation modes. The state selection is changed at the points A and B. In the selection exchange method, the flux change induced by exchanging the two state selections is used to vary the atomic flux for cavity tuning. It is considered that the change in the tuned frequency is due to the magnetic inhomogeneity shift. The dependence of the tuned frequencies on the static field is also measured. The results are shown in Fig.5. The tuned frequencies of the conventional method and the selection exchange method depend strongly on the static field. This dependence on the static field is due to the magnetic inhomogeneity shift. On the other hand, the tuned frequencies of the Majorana method do not depend on the static field. Therefore, the magnetic inhomogeneity shift is reduced sufficiently in the Majorana method.

Long-term continuous operation

The hydrogen masers are operated continuously by the automatic cavity tuning method, in which mechanical flux controllers or selection exchange controllers are used to vary the atomic flux. The 5 MHz output of the masers are compared with that of the commercial cesium beam frequency standard. The magnetic field is examined by measuring the Zeeman frequency at the beginning and the end of the operation. Fig.6 and Fig.7 show the two typical results obtained for about 200 days from March 1979 and from August 1982 respectively. The operation conditions of the autotuned masers are shown in the lower table, such as the static field, the storage bulb, flux change method for autotuning. Cs5 and Cs7 are the commercial frequency standards and used for time keeping to generate the UTC(RRL). It is confirmed that they do not have large linear frequency drift by comparing them with other Cs frequency standards and a portable clock. According to these results, it is considered that the frequency of H4 in Fig.6 and that of H3 in Fig.7 have the linear drift rate. On the other hand, the frequency of H3 in Fig.6 has no linear drift clearly. The different behaviors of these maser frequencies for the long-term operation are probably due to the change in the wall shift of the maser frequency.



The aging of the storage bulb was reported previously and some causes of it were pointed out<sup>8</sup>. Among these causes, we now consider that the coating procedure is one important problem. Therefore, the coating procedure is now under investigation carefully.

In the selection exchange method for the cavity autotuning, the maser frequency is influenced by the magnetic inhomogeneity shift. However, the influence of this shift on the long-term operation can not be detected clearly at present. It is considered that such influence on the long-term operation will be probably detected after removing the aging of the storage bulb and will be examined clearly by comparing the result of the long-term operation by the selection exchange method with that of the long-term operation by the Majorana method and the mechanical flux controller for cavity autotuning.

#### Acknowledgement

The authors wish to thank Mr. M. Kobayashi for his interest and continuous encouragement, and all o wish to thank Messrs. K. Nakagiri, J. Umezu and M. Shibuki for their useful discussions and advises.

#### References

1. Y. Ohta, K. Yoshimura, M. Shibuki, K. Nakagiri, T. Morikawa and Y. Saburi : Rev. Radio Res. Labs., 20, p.39, 1974. (in Japanese)
2. S. Urabe, K. Nakagiri, Y. Ohta, M. Kobayashi and Y. Saburi : IEEE Trans. Instrum. & Meas., IM-29, p. 304, 1980.
3. S. Urabe and Y. Ohta : Jpn. J. Appl. Phys., 22, p. 1009, 1983.
4. C. Audoin, M. Desaintfuscien, P. Petit and J. P. Scherman : IEEE Trans. Instrum. & Meas., IM-17, p.351, 1968.
5. R. F. Lacey and R. F. Vessot : Proc. 23rd Annual Symp. on Frequency Control, p. 279, 1969.
6. S. B. Crampton, E. C. Fleri and H. T. M. Wang : Metrologia, 13, p. 131, 1977
7. S. Urabe, Y. Ohta and Y. Saburi : to be published in IEEE Trans. Instrum. Meas., IM-33, no.2, 1984.
8. D. Morris : IEEE Trans. Instrum. & Meas., IM-27, p. 339, 1978.

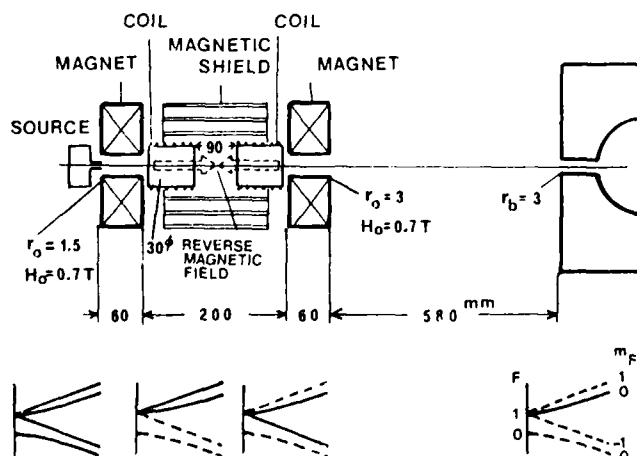


Fig. 3 Structure of the state selector

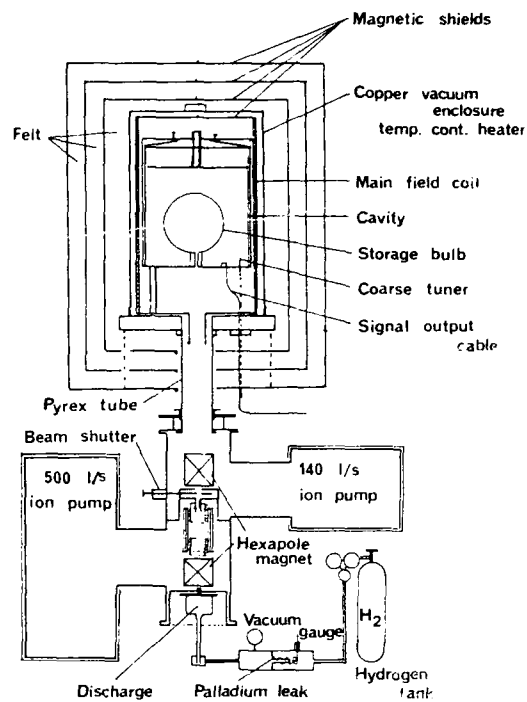


Fig. 1 Structure of RRL hydrogen masers (H3 and H4)

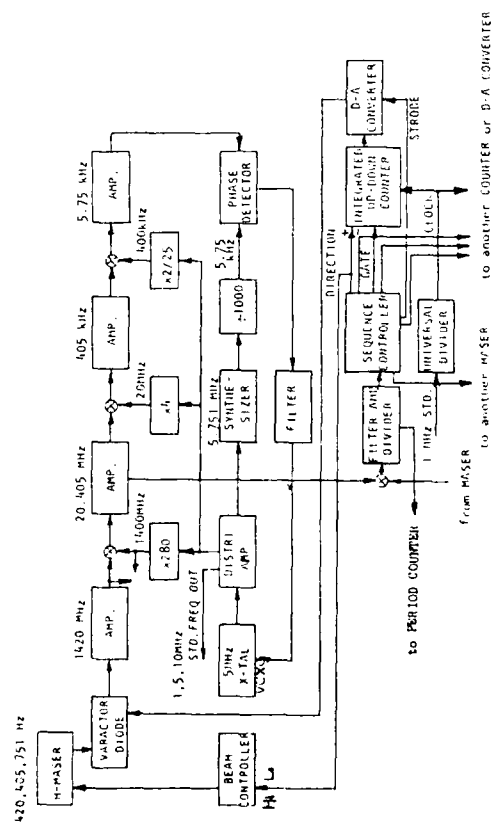


Fig. 2 Block diagram of phase locking and automatic cavity tuning loop

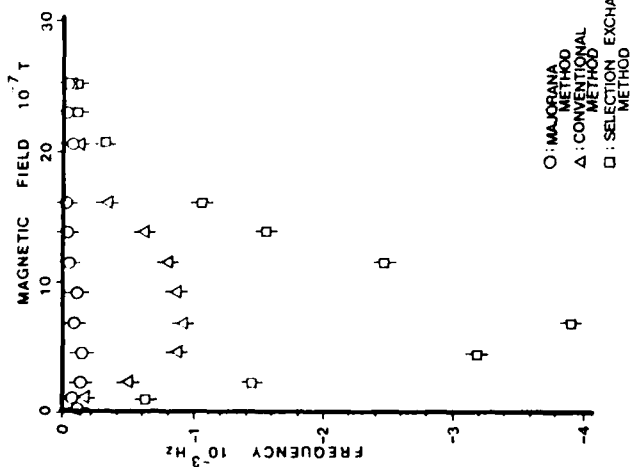


Fig. 5 Dependence of the tuned frequencies on the static field

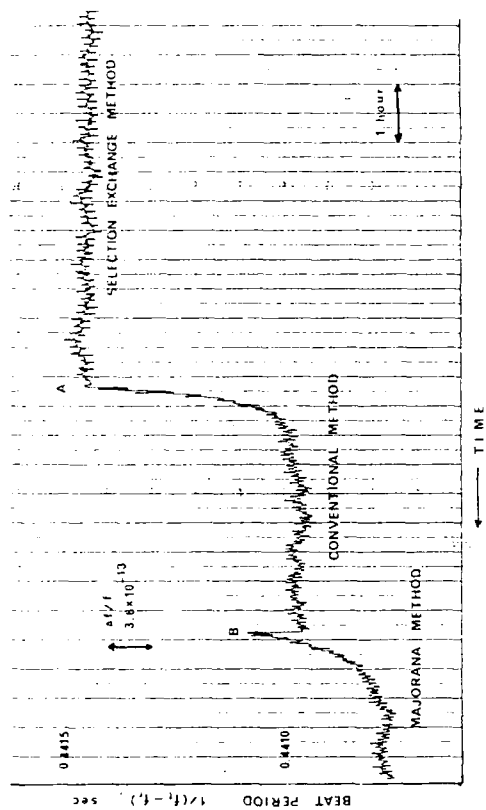
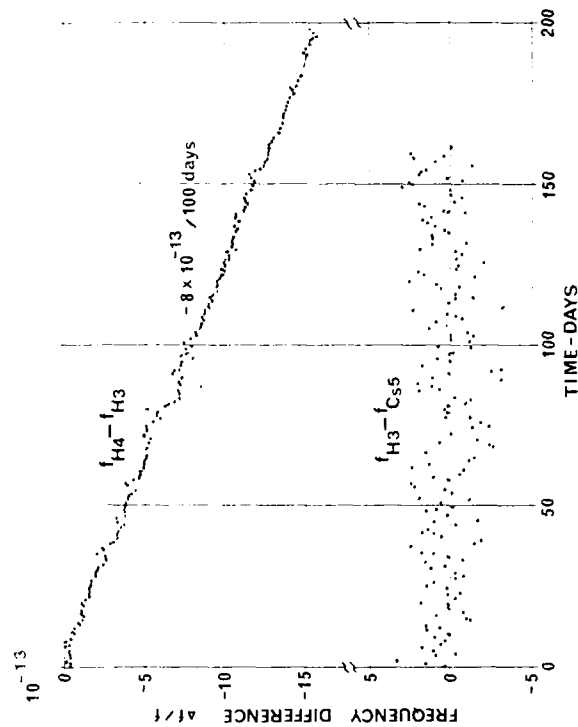
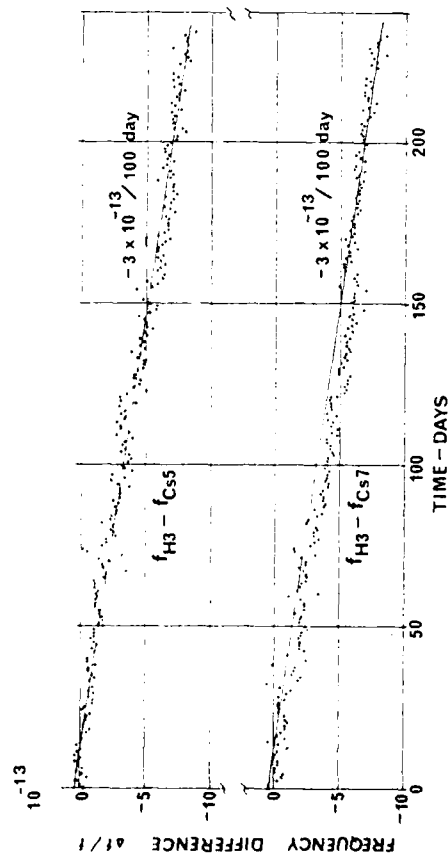


Fig. 4 Tuned frequencies for the three operation modes.



MASER	C FIELD	STORAGE BULB	FLUX CHANGE METHOD
H 3	1.1 mG	diameter 120 mm	MECHANICAL SHUTTER
H 4	21.4 mG	diameter 150 mm	MECHANICAL SHUTTER

Fig. 7 Results of the frequency comparison between H3 and Cs5, H3 and Cs7



MASER	C-FIELD	STORAGE BULB	FLUX CHANGE METHOD
H 3	1.1 mG	diameter 150 mm	SELECTION EXCHANGE

Fig. 6 Results of the frequency comparisons between H3 and H4, H3 and Cs5

EXPERIMENTAL DETERMINATION OF THE ENERGY OF STORED IONS  
FROM THE SIDE-BANDS IN THEIR MICROWAVE SPECTRUM

M. JARDINO, F. PLUMELLE, M. DESAINTEFUSCIEN and J.L. DUCHENE

Laboratoire de l'Horloge Atomique  
Equipe de Recherche du CNRS,  
associée à l'Université Paris-Sud  
Bât. 221 - Université Paris-Sud  
91405 - Orsay - FranceSummary

The measured stability of an oscillator locked on an ion mercury transition has shown its possibilities as a frequency standard <sup>1</sup>.

The main physical limitation of this standard is the 2<sup>nd</sup> order Doppler effect which produces a relative frequency shift of  $5 \cdot 10^{-12}$  for an energy of the ions of 1 eV.

From the experimental results describes here and from some calculations including space charge effect, we are able to deduce the energy of the ions and then the frequency shift due to the 2<sup>nd</sup> order Doppler effect.

Introduction

Ions are stored in a radiofrequency trap in which they undergo an harmonic oscillation at the secular frequency  $\nu_m$ . Then any absorption spectrum of the ions is modulated by this motion (1<sup>st</sup> order Doppler effect).

The wavelength of the atomic transition used in this experiment is 7,4 mm (40,5 GHz). It is of the same order than our trap radius  $r_0$  which is 19 mm. In this case, the absorption spectrum is composed of well separated lines spaced by  $\nu_m$  if coherence time is long enough.

This spectrum has been observed in a few experiments <sup>4,5,6</sup> and Major and Duchêne <sup>7</sup> have shown that the ion energy can be deduce from the intensity of these lines in the case where the microwave excitation is a standing wave. Our calculations assume that the ions are excited by a running wave and include space charge effect which shifts the secular frequency <sup>8</sup>.

Experimental set-up

This experiment has been described in detail elsewhere <sup>1</sup>. Briefly we measure the frequency of the transition between the hyperfine levels  $F = 0$  and  $F = 1$  of the  $^{199}\text{Hg}^+$  ground state at 40,5 GHz. Ions are selectively pumped from the  $^2S_{1/2}$  ( $F = 1$ ) level to the  $^2S_{1/2}$  ( $F = 0$ ) level by optical pumping from a  $202 \text{ Hg}^+$  lamp until the  $^2S_{1/2}$  ( $F = 1$ ) level is depleted. Then a microwave sweeps the hyperfine transition and the absorption spectrum can be seen from the intensity of the fluorescence emitted by the ions due to the mixing of the  $^2S_{1/2}$  levels.

Ions are confined in a cylindrical trap, in a pseudo-potential well which can be varied from 4 eV to 24 eV. The frequency of the microwave electric field being 265 kHz the ion corresponding secular frequencies are between 13 kHz and 40 kHz. The lifetime of the ions is about 1 s.

The maximal microwave power gives a saturation factor of 600 for the central line. In these conditions the saturation factor of the first lateral line is about 1. The microwave is introduced in the trap with a horn and we will assume that it is a running wave in the direction of propagation.

Experimental results

Figure 1 is a typical absorption spectrum which gives the central line and the right part of the Doppler spectrum. We observe mainly two lateral lines whose width gives the coherence time.

The frequency of the oscillating motion of the ions in our cylindrical trap is obtained from the experimental confining parameters according to the computed solution of the equations of the ion motions <sup>9</sup>.

As can be seen on figure 2, the measured frequencies are lower than the theoretical ones for a large set of potential wells. This can be due to space charge effect as pointed out by André <sup>8</sup>.

Interpretation

A mathematical model has been built according to our experimental conditions and assuming a spherical potential well.

An ion with position  $r$  at time  $t$  sees an electromagnetic field:  $-i(2\pi\nu_0 t - kr)$

$$H(t) = H_0 e^{i(2\pi\nu_0 t - kr)} \quad (1)$$

where  $\nu_0$  is the microwave excitation frequency and  $k = 2\pi/\lambda$  is its wave vector.

The spectral density of this excitation  $G(\nu)$  in the ion frame is the Fourier transform of the correlation function  $\Gamma(\tau)$ :

$$\Gamma(\tau) = H_0^2 e^{-2\pi\nu_0 \tau} \langle e^{ik[r(t) - r(t+\tau)]} \rangle \quad (2)$$

where the average is taken over all the ions. Then  $G(\nu)$  is given by:

$$G(\nu) = \int_{-\infty}^{+\infty} \Gamma(\tau) e^{-2i\pi\nu\tau} d\tau \quad (3)$$

i) we calculate the spatial distribution of the ions in the trap taking into account the space charge in the same way as Knight <sup>10</sup>. In this pattern, ion velocity obeys a Maxwellian distribution at the temperature  $T$  and we calculate the density of the ions in the trap modified by the space charge potential  $\phi_{sc}$  from the Poisson's equation

$$\Delta\phi_{sc} = \frac{e n_0}{\epsilon_0} \exp - \left( \frac{m \omega^2 r^2 / 2 + \phi_{sc}}{KT} \right) \quad (4)$$

$n_0$  is the density at the center of the trap

$\omega_0 = 2\pi\nu_m$ ,  $m$  is the mass of the ion

$K^m$  is the Boltzmann constant.

This equation is numerically solved.

Figure 3 shows the density and potential curves versus the ion position for different values of  $n_0$  and for a given value of  $\omega_m$  and  $T$ . As the density increases, the potential becomes less and less harmonic and the ions spread in the trap. For large ion densities we get a quasi uniform distribution of the ions. The deviation from the gaussian distribution can be seen on figure 4. The widths given on figure 4 are defined by the value of  $r$  for which the density is  $e^{-1/2} n_0$ .

ii) In order to calculate  $r(t)$  we assume an initial random position of the ion in the trap and an initial random velocity obeying a Maxwellian distribution at temperature  $T$ . We solve the differential equation giving its motion in the potential well calculated before.  $r(t)$  is calculated over 512 points with a sampling interval of  $1/25 \mu$ . This calculation is repeated 1000 times and averaged to give the correlation function  $\langle r(t) r(t + \tau) \rangle$ .

As an example, figure 5 shows the correlation function with a temperature of 858 K and a central density of  $10^7 \text{ cm}^{-3}$  and a potential well of 13 eV. The value of  $\langle r(t) \rangle$  is calculated to (2) and the Fourier transform of this correlation function gives the relative intensities of the lines and their frequencies (Fig. 6).

In order to show the space charge effect these calculations have been made in a large range of  $n_0$  and  $T$  for a given potential well. Some interesting features can be deduced from these results.

first, we observe the reduction of the secular frequencies as the ion density increase (Fig. 7),

second, this reduction is independent of the temperature.

It is consequently possible to deduce the central density of the ions  $n_0$  from the measured secular frequency, compared to the frequency without space charge effect. Then the temperature is obtained from the relative intensity of the two first lateral lines using figure 8 which gives these value versus  $T$ , for several ion densities.

For example, in our experiment a spherical potential well of 24 eV which corresponds to a frequency  $\omega_p = 40 \text{ kHz}$  gives a variation of the secular frequency of 14 kHz. This value corresponds to a central density of  $1,8 \cdot 10^7 \text{ ions cm}^{-3}$ . Then, from the measured intensities of the two first lines corrected from saturation, we obtain a temperature  $T = 3000 \pm 200 \text{ K}$ . For this temperature, the second order Doppler relative shift is  $1,5 \cdot 10^{-12}$ .

### Conclusion

This model explains what happens when a buffer gas is introduced into the trap. We have observed like Cutler <sup>5</sup> a reduction of the secular frequency. Knowing that this frequency doesn't vary for a given potential well with the temperature but only with the central density, the observed reduction isn't directly due to the reduction of the ion temperature but to the increase of the central densities as the ion cloud contracts <sup>11</sup>.

### References

1. M. Jardino, M. Desaintfusien, R. Barillet, J. Viennet, P. Petit and C. Audoin, Appl. Phys. **24**, 197 (1981)
2. H.G. Dehmelt in "Advances in Atomic and Molecular Physics", vol. 3, 53, Academic Press, New York (1967)
3. R.H. Dicke, Phys. Rev. **89**, n° 2, 472 (1953)
4. H.S. Lakkaraju and H.A. Schuessler, J. Appl. Phys. **53**, n° 6, 3967 (1982)
5. L.S. Cutler, R.P. Giffard and M.D. McGuire, Frequency Control Symposium (1983)
6. M. Jardino, F. Plumelle and M. Desaintfusien, Proceedings of the Sixth International Conference on Laser Spectroscopy, P.173, Interlaken (Springer Verlag)
7. F.G. Major and J.L. Duchêne, J. de Physique **36**, 953 (1975)
8. F. Vedel, J. André et M. Vedel, J. de Physique **42**, 1611 (1981)
9. M.N. Benilan and C. Audoin, Int. J. of Mass Spectrometry and Ion Phys., **11**, 421 (1973)

10. R.D. Knight, Ph. D. Thesis, U. of California, Bekerley (1979), Lawrence Berkeley Lab. Publication LBL 9082
11. M. Schaaf, U. Schmeling and G. Werth, Appl. Phys. **25**, 249 (1981)

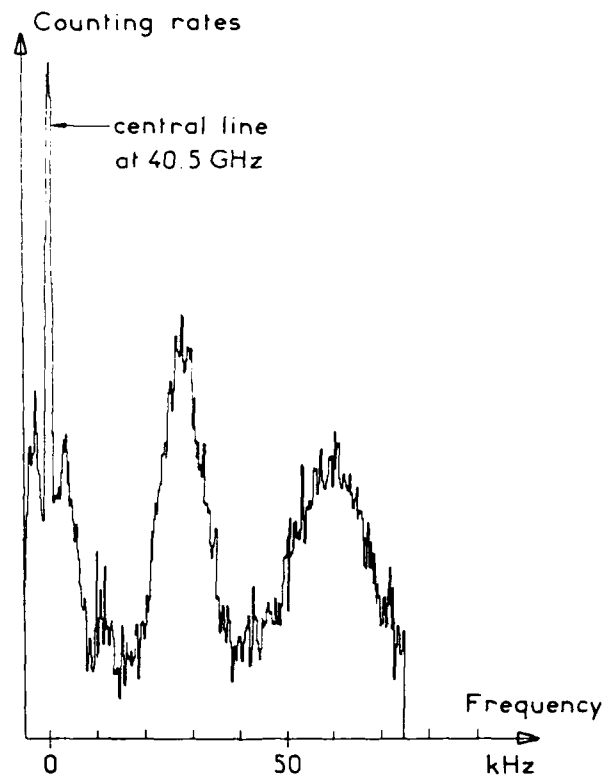


Fig. 1 Experimental absorption spectrum for the hyperfine transition of  $^{199}\text{Hg}^+$ , showing the upper lateral lines due to first order Doppler effect.

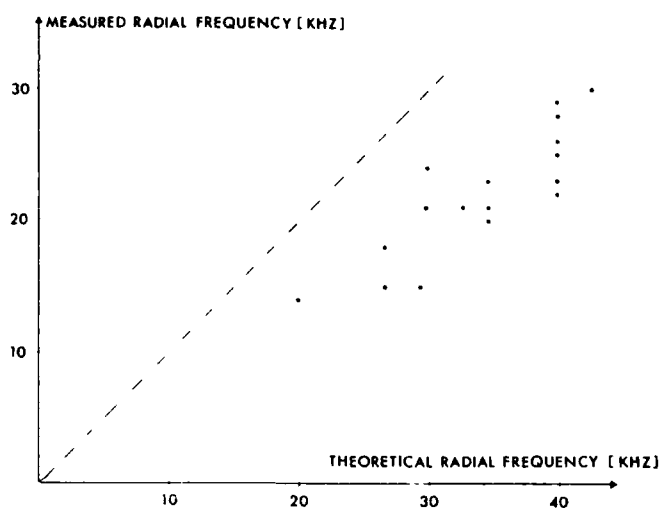


Fig. 2 Experimental values of the secular motion frequency, as a function of the theoretical ones. Experimental values are lower than the theoretical ones, calculated from the potential well and neglecting space charge effect.

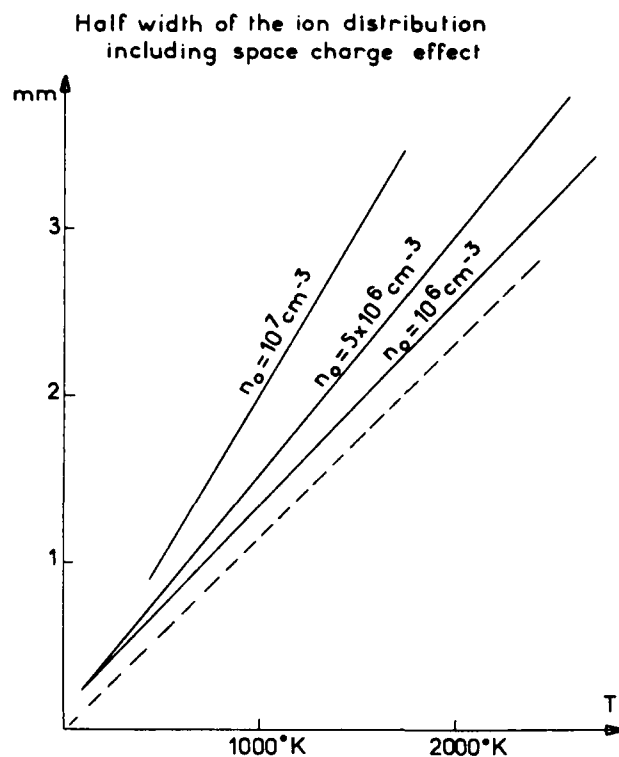


Fig. 4 Half width of the ion distribution as a function of  $n_0$  and for a given value of the temperature and of the potential well. The width is defined as the value of  $r$  for which the density equals  $n_0 e^{-1/2}$

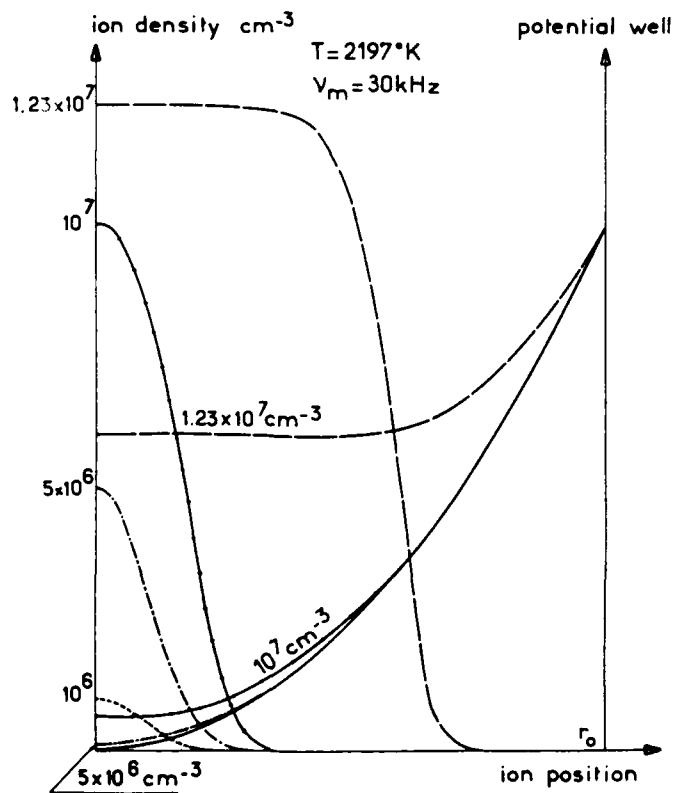


Fig. 3 Ion density and confining potential in the trap, including space charge effect, for various values of  $n_0$ , the density at the center of the trap.  
For these curves we have  $\nu = 3 \cdot 10^4$  Hz  
 $T^m = 2197$  °K

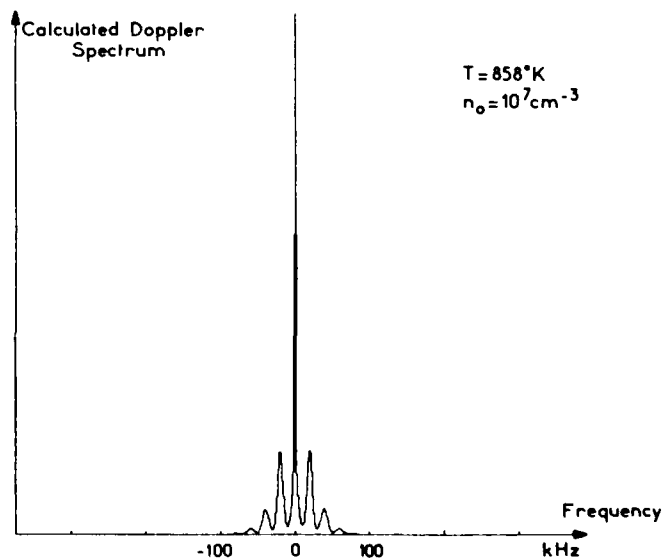


Fig. 5 Correlation function of the ion position calculated for  $T = 858$  °K  
 $n_0 = 10^7$  cm<sup>-3</sup>  
 $\nu_m = 30$  kHz

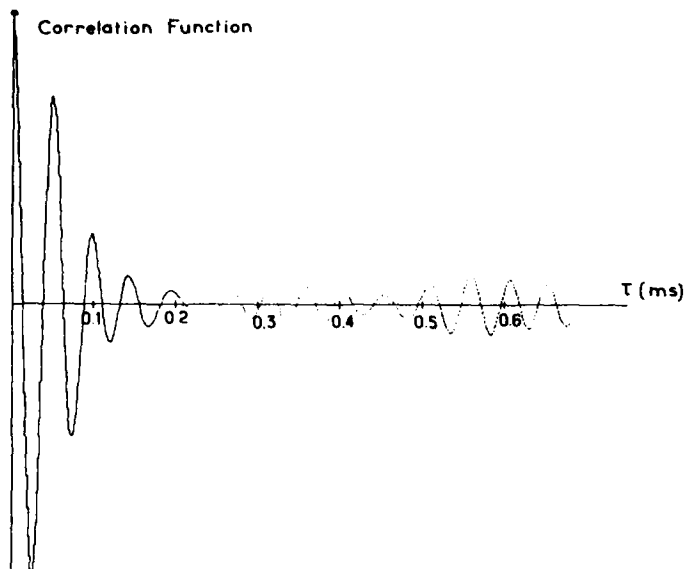


Fig. 6 Calculated absorption spectrum deduced from the correlation function of Fig. 5.

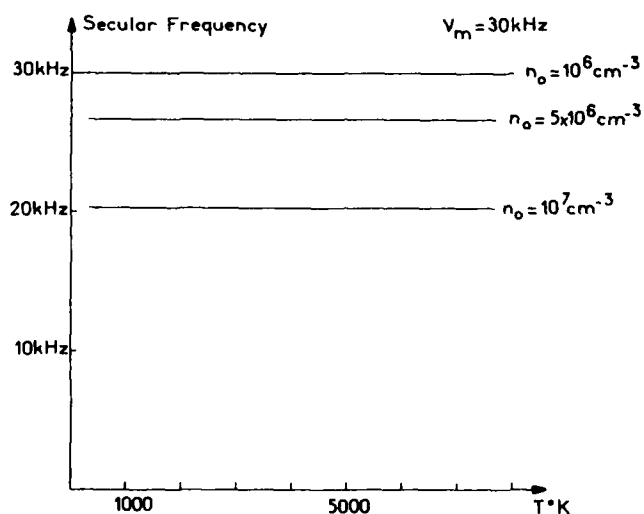


Fig. 7 Variation of the calculated secular frequency of the ions as a function of the temperature  $T$  and of the ion density at the center of the trap  $n_0$ . It is seen that for a given value of  $n_0$ , the secular frequency is independent from the temperature.

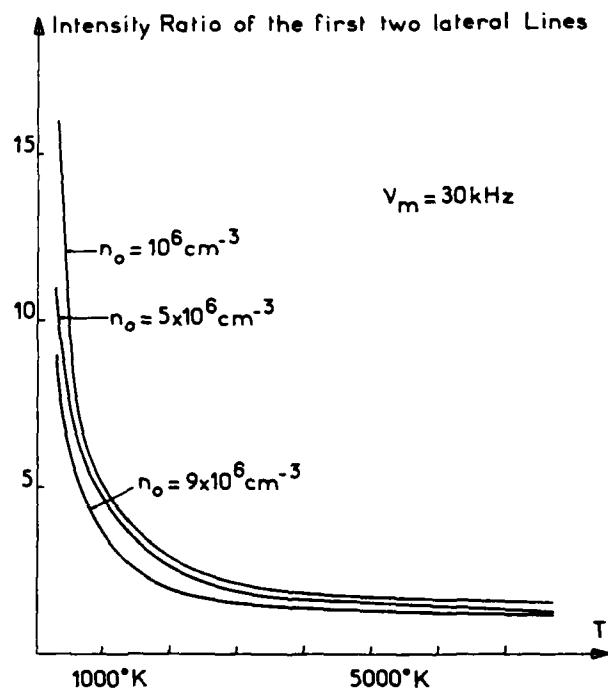


Fig. 8 Variation of the relative intensity of the two first lateral lines as a function of the temperature, for several values of the ion density at the center of the trap.

# DEVELOPMENT OF THE SUPERCONDUCTING CAVITY MASER AS A STABLE FREQUENCY SOURCE

G. J. Dick

Low Temperature Physics  
California Institute of Technology  
Pasadena, California

D. M. Strayer

Jet Propulsion Laboratory  
California Institute of Technology  
Pasadena, California

## Summary

While the high quality factor  $Q$  and the low thermal expansion coefficient attainable in superconducting cavities provide an excellent starting point for stable oscillator design, a practical alternative to atomic frequency standards has not yet emerged from this technology. Many schemes have been proposed combining superconducting cavities with either room temperature or cooled electronics, with varying levels of frequency stability having been achieved. Limitations to stability have been attributed to either the electronic noise of amplifying elements or to disturbing influences of the environment. In this paper we report the design and development progress of a ruby maser oscillator stabilized with a sapphire-filled superconducting cavity. This combination of elements is expected to greatly reduce the effects of amplifier noise and of environmental disturbances and so will allow the potential of a superconducting cavity stabilized oscillator to be more fully realized.

Use of a ruby maser amplifier has been previously proposed to allow an all-cryogenic superconducting cavity oscillator.<sup>1</sup> Such an application of the ruby maser seems optimal since the maser requires cryogenic temperatures for operation, dissipates little power, and allows very low noise temperatures at microwave frequencies. We have developed an oscillator design using the ruby instead as a negative resistance element in a three-cavity oscillator that allows the superconducting cavity to be isolated from the  $Q$ -reducing magnetic field of the maser. To analyze our design, we develop a formalism for describing the arrangement of coupling factors, cavity  $Q$ 's and resonant frequencies that best sets forth the design considerations. This discussion also serves to remove any mystique concerning the use of three cavities in a high-stability oscillator.

To minimize effects of thermal, acoustic, and gravitational disturbances, we form our cavity by placing a superconducting film on a sapphire substrate. Recent results on performance of such cavities will be reported. We also report on tests of the maser in low- $Q$  oscillator operation. Frequency pulling effects and power limitations have been measured, allowing extrapolation of ruby electronic effects to high  $Q$  conditions.

## 1. General Features

Frequency variation in the output of a stabilized oscillator is induced by three different types of sources: variations in the frequency of the stabilizing element itself; variations of the oscillator operating frequency within the bandwidth of the stabilizing element; and fluctuation of the output phase due to receiver noise.

The ability of superconducting cavities to handle rela-

tively high power reduces the output phase fluctuation to allow unparalleled stability for short measuring times where receiver noise dominates. This aspect has been well documented previously<sup>2,3</sup> and will not be discussed further here.

Variation of the natural frequency of the cavity occurs due to mechanical and electrical mechanisms mainly in response to temperature change, gravity forces, and radiation pressure. A cavity constructed of sapphire gives a significant reduction in response to these three sources. Of particular note is a predicted reduction in sensitivity to temperature fluctuations by two orders of magnitude compared to a solid niobium cavity. These considerations and the results of  $Q$  measurements on sapphire-filled cavities are discussed in section 4.

The evaluation of variations of the operating frequency of the ruby maser oscillator within the bandwidth of the cavity form the basis for most of the present work. Such variations appear to limit the long-time stability achievable both in cavity stabilized oscillators and in hydrogen masers, the two sources which presently allow the best frequency stability.

We have developed a design for an all-cryogenic oscillator for which the entire oscillator shows the structural integrity resulting from the "freezing out" of thermal expansion coefficients at low temperatures. This oscillator is a superconducting cavity maser (SCM) which uses a ruby maser as the negative resistance element in a three-cavity self-excited oscillator. The difficulty of combining a ruby maser, with its attendant magnetic field, and a superconducting cavity is circumvented by separating these two elements by a third cavity of some length. A novel formalism for analysis of the multiple-cavity oscillator is given in section 2, along with examples that demonstrate how to select cavity frequencies and coupling strengths to achieve a specific design goal.

The response of the oscillator frequency to fluctuations in environmental parameters relates principally to the response of the dimensions of the superconducting cavity to these fluctuations. While this statement seems reasonable, it actually holds only when the energy of oscillation is concentrated to a sufficient degree in the stabilizing cavity. The formalism presented derives the response of the frequency of the eigenmode of oscillation in a multiple-cavity oscillator to the several elements that can influence this frequency; these elements would include the individual cavity frequencies and intercavity coupling strengths. Using knowledge of the response of the constituent elements to environmental fluctuations, we can then predict the response of the oscillator frequency and thereby establish the relation asserted above between the oscillator frequency stability and the superconducting cavity frequency stability.

Although ruby masers have seen considerable use as low-noise microwave amplifiers, their performance as oscillators has not been well characterized. We report in section 3 measurements that determine the maser's oscillator performance and its dependence on the operating parameters of the maser. From these measurements we derive magni-

tudes of frequency perturbing effects, values that are used in our design procedure to predict the stability of the oscillator.

Maintaining all of the basic elements of the oscillator at low temperatures benefits the performance in several ways: both the superconducting cavity and the ruby maser improve their performance as the temperature is lowered; thermal expansion coefficients of the structural materials are reduced considerably from their room temperature values, decreasing the change of dimensions with temperature; additionally, placing the entire oscillator in the very temperature-stable cryogenic surroundings eliminates all effects associated with temperature gradients and varying temperature profiles common to previous superconducting cavity stabilized oscillators. The magnitudes of these benefits will be presented in the sections that follow.

### 1.1. Application of the Ruby Maser

Ruby maser amplifiers are the quietest amplifiers presently available in the microwave frequency range, with device noise temperatures as low as 1.5K reported.<sup>4</sup> They operate naturally at temperatures below 4K, and can provide output power of a fraction of a microwatt, a value sufficient for excellent short term measurements and far above the  $10^{-11}$  watts available from the H-maser. Furthermore, the pump power required is related only to the signal power, allowing very low power dissipation and consequently lower temperature operation, if desired. By contrast the available transistor amplifiers must dissipate several milliwatts of power in order to maintain their operating point.<sup>5</sup> Operation well below 1K seems feasible, with important consequent reductions in thermally generated frequency shifts in the superconducting cavity itself.

In contrast to the H-maser with its fractional linewidth of  $10^{-9}$ , ruby has a fractional bandwidth of about  $10^{-2}$ , making it unsuitable for determining the frequency itself. However, this wide bandwidth (low Q) is a distinct advantage when used in conjunction with a superconducting cavity, since it results in a reduction of frequency pulling effects. Frequency pulling of the actual operating frequency  $\Delta f_0$  due to frequency change  $\Delta f_c$  in a lower Q circuit element is proportional to the ratio of its Q to that of the frequency stabilizing element.

A comparison between frequency pulling effects in the two devices is instructive. While the H-maser's output closely follows the frequency of the masing transition, the sensitivity to its cavity frequency is given by

$$\frac{\Delta f_0}{\Delta f_c} = \frac{Q_c}{Q_m} = \frac{10^4}{10^9} = 10^{-5} \quad 1)$$

for a cavity  $Q_c = 10^4$  and masing linewidth characterized by  $Q_m = 10^9$ . In a similar manner, the frequency of the output of the SCM closely follows that of the high Q superconducting cavity, while its sensitivity to the ruby resonant frequency  $f_m$  is

$$\frac{\Delta f_0}{\Delta f_m} = \frac{Q_m}{Q_c} = \frac{10^9}{10^4} = 10^{-5} \quad 2)$$

for masing linewidth characterized by  $Q_m = 10^2$  and a cavity  $Q_c = 10^9$ . It is apparent that the roles of the masing and cavity Q's are reversed.

We expect that this source of frequency pulling will be much less significant in the design of the SCM than in the H-maser because of the reduction implied by equations 1) and 2), but more importantly because superconducting magnets allow great stability to be achieved in the applied magnetic field which determines the ruby resonant frequency. Long term stability of better than  $10^{-12}$  has been reported at the relative low magnetic fields ( $\approx 500$  gauss) required for masing action, which would imply, from equation 2), frequency drifts less than  $10^{-19}$  from this source.

The bandwidth of the negative resistance of the ruby is very convenient from the point of view of mode selection. Losses in the containing cavity are sufficient to prevent oscillation at frequencies more than a few percent from its natural operating frequency. We have used this feature in the design that follows.

### 1.2. Magnetic Field Isolation

The magnetic field necessary for the operation of the maser must be shielded very effectively from the superconducting film which forms the high-Q cavity to prevent Q-degradation by penetrating flux lines. A reduction to approximately 0.1 G is sufficient to allow Q's well above  $10^9$  and a further reduction to 0.01 G is desirable.<sup>6</sup> The 500 G field applied to the ruby must therefore be reduced by more than 5000 times at the cavity.

The ruby material is very strongly amplifying in comparison to what is needed to induce oscillation at a Q of  $10^9$ , being able to excite into oscillation a ruby-filled cavity with a Q of only 100. Thus, it is possible to physically separate regions of high Q and high magnetic field. Conceptually, the ruby need only probe the fringe fields of the stabilizing cavity; the coupled system would oscillate with only  $100/10^9 = 10^{-7}$  of the system energy in the ruby. Since the energy is proportional to the second power of the field, this energy drop corresponds to a reduction of  $\approx 3000$  times in the microwave field. However, the ruby is also much smaller than the stabilizing cavity. With a volume approximately 1 cc in the ruby and 100 cc in the cavity, the reduction in field allowed is only 300. Thus, the microwave fields must somehow couple more strongly from the region of the stabilizing cavity to the ruby than the magnet field at the ruby couples to the cavity.

We have chosen to use a coupling cavity between the ruby and superconducting cavities as the means to provide the necessary coupling. The advantage of such a device is that the length is not constrained, greatly relieving the design pressure on the magnetic field reduction problem. A disadvantage is that another dissipative and detuning element has been added, with possible consequential degradation of oscillator performance. Moreover, another mode of oscillation has been added to the system, increasing the problems of mode selection. We shall discuss these aspects in the section that follows.

## 2. The Multiple Cavity Negative Resistance Oscillator

### 2.1. Introduction

The design approach that follows contains two separate aspects which are considered more or less independently. First, we consider the energy balance between the various parts of the oscillator and the effects on the performance that can be attributed solely to that source. Secondly, we present a method of mode construction that allows the frequencies of the constituent cavities and the coupling constants between them to be determined to achieve this energy balance.

A considerable mystique has grown around the subject of multiple-cavity oscillator design and performance and, in particular, the three-cavity oscillator has been proposed<sup>7</sup> and studied<sup>8</sup> as a means to dramatically lower frequency variations due to electronic noise in the feedback element. The reduced effect of electronic noise would be an important step toward a successful cryogenic oscillator since the semiconducting devices available to amplify microwaves at low temperatures (tunnel diode and GaAsFET devices) both show poor performance in oscillator service.<sup>9</sup> This previous work is based on the demonstration that certain combinations of Q's, frequencies and coupling constants result in a condition where the chosen eigenfrequency of a system is insensitive to the frequency of the cavity containing the negative resistance element.

While the frequencies are accurately calculated by the algebraic approach used by these authors, other properties of the system, including the energy balance between the three resonators, are largely ignored. However, it can be shown, both in the framework developed by those authors and more generally as in the following section, that this condition of insensitivity coincides with a proportionate reduction of energy in the exciting cavity.

We shall discuss a more general approach in which it is shown that many of the important properties of such an oscillator depend only on the energy balance between the various resonant elements. In particular, these properties



include frequency pulling effects (eigenmode shifts due to perturbations in the various cavities) and power balance in the oscillator. Thus design trade-offs can be made within this framework without reference to more detailed calculations.

Mode construction for multiple-cavity systems is conventionally done by solving the differential equations for the classical variables (fields) for eigenmode frequencies in terms of the other frequencies and the coupling constants. These calculations are done, either approximately in three dimensions<sup>10</sup> or exactly using lumped-constant models,<sup>11</sup> with an appropriate combination of parameters chosen by inspection of these solutions. Our method uses instead the quantum-mechanical variables of energy and phase to describe the interaction of the various cavities. Families of cavity parameters are generated which are constrained to require that only one mode of the system has the necessary energy balance. The families can then be inspected to choose a solution for which the frequencies and Q's of the other eigenmodes are most appropriate for oscillator operation. Given the nature of the negative resistance element, operation in undesired modes can be suppressed by this choice of solution.

## 2.2. Energy Balance Considerations

### 2.2.1. The Oscillation Condition

In the discussion that follows, the superscripts  $\alpha, \beta$ , and  $\gamma$  identify eigenmodes of a multiple-cavity system, and the subscripts 1, 2, and 3 identify the individual cavities of the system. Thus,  $E_i^\alpha$  is the energy contained in cavity 1 due to excitation of mode  $\alpha$ . Furthermore,  $i$  and  $j$  are used as counters for cavities, and  $\eta$  is used to count modes.

In this section we shall demonstrate that the influence of the properties of any individual cavity on the properties of a mode of a coupled-cavity resonator depends on the fraction of the energy of the mode contained in that cavity. More specifically, the effect of losses in the cavity on overall quality factor and detuning effects on the mode frequency scales linearly with the cavity energy. We begin by considering the contributions of the several elements to the power dissipation in the system.

The quality factor  $Q$  of any mode or component is defined in terms of the dissipated power  $P$ , stored energy  $E$ , and frequency  $\omega$  by

$$P = \frac{E\omega}{Q} \quad (3)$$

Applying this to an eigenmode  $\eta$  gives

$$P^\eta = \frac{E^\eta \omega^\eta}{Q^\eta} \quad (4)$$

which may also be written as the sum of its constituent parts

$$P^\eta = \sum_i P_i^\eta + \sum_{i,j} P_{ij}^\eta \quad (5)$$

where  $P_i^\eta$  are dissipations in the cavities and  $P_{ij}^\eta$  are losses associated with the coupling elements. From (3),

$$P^\eta = \sum_i \frac{E_i^\eta \omega^\eta}{Q_i} + \sum_{i,j} \frac{E_{ij}^\eta \omega^\eta}{Q_{ij}} \quad (6)$$

where  $E_i^\eta$  and  $E_{ij}^\eta$  are the energies associated with the cavities and with the coupling regions between them, respectively, in the mode  $\eta$ . Under many circumstances the coupling losses can be ignored since the coupling energies  $E_{ij}^\eta$  are small (see appendix). In particular this will be true if

$$Q_{ij} \gg k_{ij} \sqrt{Q_i Q_j} \quad (7)$$

where  $k_{ij} = k_{ji}$  is a dimensionless coupling constant<sup>11</sup> such that

$$E_{ij}^\eta = k_{ij} \sqrt{E_i^\eta E_j^\eta} \quad (8)$$

We can then combine (4) and (8) to obtain

$$Q^\eta = \left[ \frac{\sum_i E_i^\eta Q_i^{-1}}{\sum_i E_i^\eta} \right]^{-1} \quad (9)$$

where  $Q^\eta$  is the quality factor of the eigenmode  $\eta$  of the combined system,  $E_i^\eta$  is the energy of the cavity  $i$  in that mode, and  $Q_i$  is the quality factor of that (isolated) cavity. Introducing the fractional energy in cavity  $i$  for mode  $\eta$  as

$$\epsilon_i^\eta = \frac{E_i^\eta}{\sum_j E_j^\eta} \quad (10)$$

9) becomes

$$Q^\eta = \left[ \sum_i \epsilon_i^\eta Q_i^{-1} \right]^{-1} \quad (11)$$

Equation (11) shows that the cavities each contribute to the  $Q$  of the eigenmode in proportion to the fraction of the energy that the cavity contains. (More precisely, the cavity contributes to the loss of the eigenmode,  $(Q^\eta)^{-1}$ , in proportion to its fractional energy content.)

If  $\alpha, \beta$ , and  $\gamma$  are the three eigenmodes of a three coupled-cavity resonator, an oscillation will grow if the  $Q$  of one of the modes, say  $\gamma$ , is negative. In practice, a steady state condition is achieved as the negative resistance saturates, given by  $Q^\gamma = \infty$ . Thus from (11), the steady state is described by

$$0 = \sum_i \epsilon_i^\gamma Q_i^{-1} \quad (12)$$

### 2.2.2. Frequency Pulling

The Boltzman-Ehrenfest theorem<sup>12</sup> describes the change in the frequency of a resonant mode due to any perturbation as due to the work done by the perturbation on the fields of the mode. More specifically, the frequency and energy in any mode  $\eta$  are related by

$$\frac{\Delta \omega^\eta}{\omega^\eta} = \frac{\Delta E^\eta}{E^\eta} \quad (13)$$

Since this theorem is valid for any resonant system, it can be applied to the individual cavities separately as well as to a combined mode of coupled cavities. Under the condition of weak coupling, the fields in each cavity can be supposed to be isolated from those in the others, being characterized only by the energy, phase, and shape of that resonator. Under these circumstances, the work done by any given perturbation in cavity  $i$  will be proportional only to  $E_i^\eta$ , the energy in that cavity in the mode  $\eta$ . Considering, then, the effect of the perturbation on the cavity itself,

$$\frac{\Delta \omega_i}{\omega_i} = \frac{\Delta E_i^\eta}{E_i} \quad (14)$$

which, by equating the work in the two cases,  $\Delta E_i^\eta$  and  $\Delta E^\eta$ , can be combined with (13) to give

$$\frac{\Delta \omega^\eta}{\Delta \omega_i} = \frac{\omega^\eta E_i}{\omega_i E^\eta} = \epsilon_i^\eta \frac{\omega^\eta}{\omega_i} \quad (15)$$

Assuming  $\omega^\eta = \omega_i$ , which is approximately valid for the cases of interest, this becomes

$$\frac{\Delta \omega^\eta}{\Delta \omega_i} = \epsilon_i^\eta \quad (16)$$

Here we have the second result that will be used in the design of an oscillator: the pulling of an eigenmode frequency by a cavity is proportional to the fractional energy it contains.

### 2.2.3. Oscillator Design

Applying equations (12) and (16) to the design of a negative-resistance oscillator consisting of two or more cavities, the roles of the high- $Q$  stabilizing cavity and of the (negative  $Q$ ) exciting cavity can be stated as follows: Suppose cavity 1 is the exciting cavity, number 2 is the stabilizing cavity, and  $\beta$  is a mode with most of the energy in cavity 2. The fraction of energy in cavity 1 which is necessary for oscillation, can be written using (12) as

$$\epsilon_1^\beta = \epsilon_2^\beta \frac{-Q_1}{Q_2} = [1 - \epsilon_1^\beta] \frac{-Q_1}{Q_2} \quad (17)$$

From (16), and solving (17) for  $\epsilon_1^\beta$ , this implies a necessary sensitivity to the frequency of the exciting cavity of

$$\frac{\Delta\omega_p}{\Delta\omega_1} = \epsilon^p = \left[ \frac{Q_2}{-Q_1} + 1 \right]^{-1} \quad (18)$$

$$\approx \frac{-Q_1}{Q_2}$$

for large  $Q_2/Q_1$ . Thus, the high  $Q$  of the stabilizing cavity allows a large fractional energy content, which causes the mode frequency to follow it very closely, and reduces frequency sensitivity to the exciting cavity. The low negative  $Q$  in the exciting cavity also determines the fractional energy which it must contain. For a given negative-resistance mechanism, stronger coupling to the exciting cavity to achieve lower  $-Q_1$  will not generally reduce the effects of noise due to the element itself, because the sensitivity of the frequency of cavity 1 to the element will also proportionately increase. Thus an increase in  $\Delta\omega_1$  will cancel the reduction in  $\Delta\omega_p$  which would otherwise be inferred from (18).

These results are easily generalized to include the effects of losses in an additional coupling cavity. It is clear that the energy in that cavity should be as low as possible to minimize power loss and frequency variation contributions by the coupling cavity.

### 2.3. Mode Construction

In this section we first show that a redefinition of the cavity parameters facilitates the discussion of coupled cavity eigenmodes. We then apply these newly defined parameters along with the results obtained in the last section to the well-understood case of two weakly coupled cavities of equal  $Q$ . Illustrating the design technique again with a second example, we then apply the formalism to the design of a three-cavity oscillator.

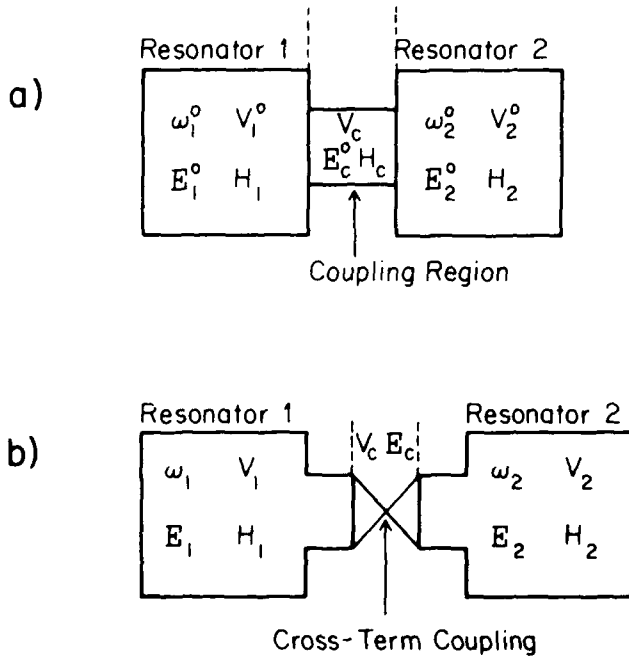


Figure 1. Two models for microwave cavity coupling

- a) Coupling by shared volume  
b) Cross-term coupling

#### 2.3.1. Procedure

Microwave cavities are joined to form multiple-cavity resonators by coupling them through regions of shared fields. A two-cavity resonator can be thought of as containing three regions: the first unperturbed cavity; a coupling volume where the cavity fields superpose; and the second unperturbed cavity. While it may seem apparent that this division is the appropriate starting point for mode calculations, a slightly different starting point provides substantial

benefits. Fig. 1) illustrates a comparison between the two models. In the discussion that follows we shall assume "effective" volumes  $V$  such that the energy  $E$  and field amplitude  $H$  are related by

$$E = V \frac{\mu_0}{2} H^2. \quad (19)$$

The effect of the coupling region in Fig. 1a) is determined by the extent that the fields in the cavities contribute to the coupling field  $H_c$ . We define field coupling constants  $h_{12}$  and  $h_{21}$  such that the effective coupling field is given by:

$$H_c = h_{12}H_1 + h_{21}H_2 \quad (20)$$

The two frequencies, three volumes, and two field coefficients are the geometrically determined constants that determine the properties of the coupled two-cavity system.

The total energy in the system can be written

$$E_{tot} = E_1^0 + E_2^0 + E_c^0 \quad (21A)$$

where the energies in the constituent parts shown in Fig. 1a) are given by

$$E_1^0 = V_1 \frac{\mu_0}{2} H_1^2 \quad E_2^0 = V_2 \frac{\mu_0}{2} H_2^2 \quad (21B)$$

for the cavity energies, and

$$E_c^0 = V_c \frac{\mu_0}{2} [h_{12}H_1 + h_{21}H_2]^2 \quad (21C)$$

$$= V_c \frac{\mu_0}{2} [(h_{12}H_1)^2 + (h_{21}H_2)^2 + 2h_{12}h_{21}H_1H_2]$$

for the coupling energy, which can be written

$$= E_{12}^0 + E_{21}^0 + E_c \quad (21D)$$

where  $E_{12}^0$  and  $E_{21}^0$  are the terms quadratic in  $H_1$  and  $H_2$  respectively, and  $E_c$  is a redefined coupling energy containing only the cross term in  $H_1$  and  $H_2$ .

Identifying the two quadratic terms with the individual resonators, rather than with the coupling, results in the model shown in Fig. 1b). This identification also results in redefined frequencies for the two resonators which are perhaps more difficult to calculate, but the new identification gives an effective coupling containing only a single, symmetric term. In practice, the frequencies of the various resonators need only to be measured in the presence of the coupling holes in order to make the proper identification. The energies for the case of Fig. 1b) can then be written:

$$E_{tot} = E_1 + E_2 + E_c \quad (22A)$$

where cavity energies are given by

$$E_1 = E_1^0 + E_{12}^0 = [V_1^0 + h_{12}^2 V_c] \frac{\mu_0}{2} H_1^2 = V_1 \frac{\mu_0}{2} H_1^2 \quad (22B)$$

$$E_2 = E_2^0 + E_{21}^0 = [V_2^0 + h_{21}^2 V_c] \frac{\mu_0}{2} H_2^2 = V_2 \frac{\mu_0}{2} H_2^2$$

with redefined volumes  $V_1$  and  $V_2$ , and a coupling energy of

$$E_c = V_c \mu_0 h_{12} h_{21} H_1 H_2 \quad (22C)$$

or

$$= 2k_{12} \sqrt{E_1 E_2} \quad (22D)$$

with  $k_{12}$  defined to be

$$k_{12} = \frac{V_c}{\sqrt{V_1 V_2}} h_{12} h_{21}. \quad (23)$$

In effect, this rearrangement of terms allows us to use the mathematical procedures worked out for the case of coupling by mutual inductance (to use a lumped circuit analogy) rather than those for shared inductance. Bethe<sup>10</sup> was the first to point out that the apparent asymmetry in the coupling between two resonators sharing a common wall could be transformed away by a frequency shift.

For the more general case of any number of coupled cavities, the work done on the coupling by each resonator can now be shown to be given by

$$\delta E_i = V_i h_{ij} H_i \cdot \delta(\mu_0 h_{ji} H_j) \quad (24)$$

which gives with 23), assuming a sinusoidal excited mode,

$$\frac{dE_i}{dt} = 2k_{ij}\omega\sqrt{E_i E_j} \sin(\omega t) \cos(\omega t + \varphi_{ij}) \quad (25)$$

where  $\varphi_{ij}$  is the phase difference between the fields in the two cavities. The effect of this energy exchange with the coupling has qualitatively different effects depending on the value assumed by  $\varphi_{ij}$ , itself a result of the initial conditions. If  $\varphi_{ij}$  is an odd multiple of  $\pi/2$ , 25) gives a sine-squared time dependence for the work on the cavity with a sign that reverses between the cavities, since  $\varphi_{ij} = -\varphi_{ji}$ . Thus, if the fields in the cavities are out of phase by an odd multiple of  $\pi/2$ , real power flows between them, because the sine-squared time dependence inferred from 25) has an average value of 1/2. The average power flow becomes

$$P_{ij} = -P_{ji} = \pm k_{ij}\omega\sqrt{E_i E_j} \quad (26)$$

for the transfer of energy between the cavities. These "sloshing" modes of coupled cavities are a familiar result of mixed mode excitation.

A similar, but more surprising, result follows when the cavities are operated exactly in or out of phase, i.e., when  $\varphi_{ij}$  is a multiple of  $\pi$ . In these cases, only reactive power flows at twice the operating frequency, the product of sine and cosine in 25) having an average value of 0. However, the phase of the power flow causes the cavities to be detuned from their natural operating frequencies by an amount

$$\omega_{ij} = \pm \frac{k_{ij}\omega}{2} \sqrt{\frac{E_j}{E_i}} \quad (27)$$

with the sign determined by the symmetry and nature of the coupling (whether magnetic, as our examples, or electric). The sign is the same for each cavity, since for these values of  $\varphi_{ij}$  the cosine term in 25) is unchanged by the sign reversal implied by interchanging  $i$  and  $j$ . Detuning occurs, in the language of the lumped-constant analogue, because the exchange of energy with the coupling element derived from 25) is exactly the same as for a reactive tuning element. The detuning is either capacitive or inductive for both cavities, tuning each of them to the same side of their natural frequency.

Exchanging  $i$  and  $j$  in 27) and dividing,

$$\frac{\omega_{ij}}{\omega_{ji}} = \frac{E_j}{E_i} \quad (28)$$

gives the relative detuning of any two cavities, a relation fundamental to our design procedure.

Equations 26) and 27) predict the time evolution of the fields in coupled cavities. Given only the energy and phases in the cavities, energy will transfer between them at a rate given by 26) for odd phases, and the phase in each one will precess at a rate given by 27) for even phases. In this context, an eigenmode, being a stationary state, must have an even phase between the cavities (or their energy would vary) and the energy ratio between them must be such that they tune one another to the same frequency, the frequency of the eigenmode.

This powerful result can be used to construct, almost by inspection, a mode with any given energy distribution in a multiple cavity system. The eigenfrequency is defined by:

$$\omega^* = \omega_1 + \sum_{j \neq 1} \omega_{1j} = \omega_2 + \sum_{j \neq 2} \omega_{2j} = \dots \quad (29)$$

where the various  $\omega_{ij}$  terms are calculated with  $\omega = \omega^*$  in equation 27), given the various energy ratios of the cavities to which any specified cavity is coupled.

### 2.3.2. A Two-Cavity Example

While the eigenfrequencies calculated by this procedure are the same, for two cavities, as those given in standard reference works,<sup>11</sup> we present this simple example as an illustration of the procedures we shall use to design the more complicated three-cavity system. Fig. 2a) shows the frequency response of a two-cavity resonator with equal Q's together with an identification of the various frequencies characteristic of the system. In this and the other examples which follow, we assume that the coupling is weak ( $k_{ij} = k_{ji} \ll 1$ ) and that all frequency differences are small compared to the frequency itself. Eigenfrequencies  $\omega^*$  and

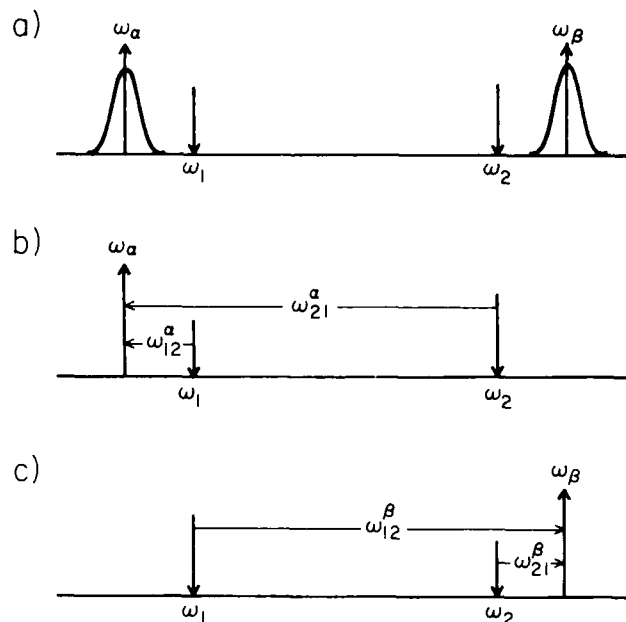


Figure 2. a) Frequency response of two coupled cavities

b), c) Eigenfrequency diagrams

$\omega^*$  result from the detuning of the resonators from their natural frequencies as illustrated in 1b) and 1c). The energy distribution characteristic of this mode is at once apparent by applying equation 28) to the various frequency differences.

Defining the energy ratio between two cavities in any mode  $\eta$  by

$$\epsilon_{ij}^\eta = \frac{E_i^\eta}{E_j^\eta} \quad (30)$$

equations 27) and 29) become, setting  $k_{12} = k_{21} = k$ ,  $\omega = \omega^\eta$ ,

$$\omega^\eta - \omega_2 = \pm \frac{k\omega^\eta}{2} \sqrt{\epsilon_{21}^\eta} \quad (31)$$

$$\omega^\eta - \omega_1 = \pm \frac{k\omega^\eta}{2} \sqrt{\epsilon_{12}^\eta} = \pm \frac{k\omega^\eta}{2} \frac{1}{\sqrt{\epsilon_{21}^\eta}}$$

taking the negative sign for the mode given by  $\eta = \alpha$  and the positive sign for mode  $\beta$ . These differences can be combined to form

$$(\omega^\eta - \omega_2)(\omega^\eta - \omega_1) = \frac{k^2 \omega^{\eta 2}}{4} \quad (32)$$

as expected for two resonators coupled by a mutual inductance. This quadratic equation can be solved for its two roots, giving

$$\omega^\alpha + \omega^\beta = \omega_1 + \omega_2 \quad (33A)$$

and

$$[\omega^\alpha - \omega^\beta]^2 = [\omega_1 - \omega_2]^2 + \frac{k^2}{2} [\omega_1^2 + \omega_2^2] \quad (33B)$$

for the sum and difference of the eigenmode frequencies for  $k$  small. These relations can be combined with 28) to give

$$\epsilon_{21}^\eta = \frac{1}{\epsilon_{12}^\eta} = \frac{(\omega^\beta - \omega^\alpha) \pm (\omega_1 - \omega_2)}{(\omega^\beta - \omega^\alpha) \pm (\omega_2 - \omega_1)} \quad (34)$$

for the energy ratios between cavities, where the + terms refer to the mode given by  $\eta = \alpha$  and the - terms to mode  $\beta$ . Fig. 3 shows a plot of this function: the example illustrated in Fig. 2 corresponds to inductive coupling and  $k\omega^\beta = \omega_2 - \omega_1$  (1 on the abscissa of Fig. 3), yielding an energy ratio of about 5.8.

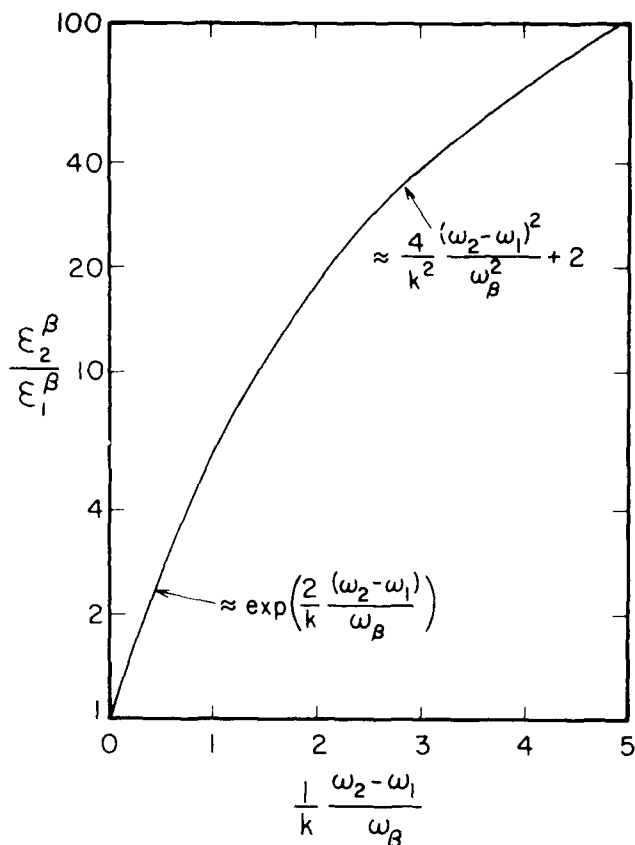


Figure 3. Cavity energy ratios for two coupled cavities

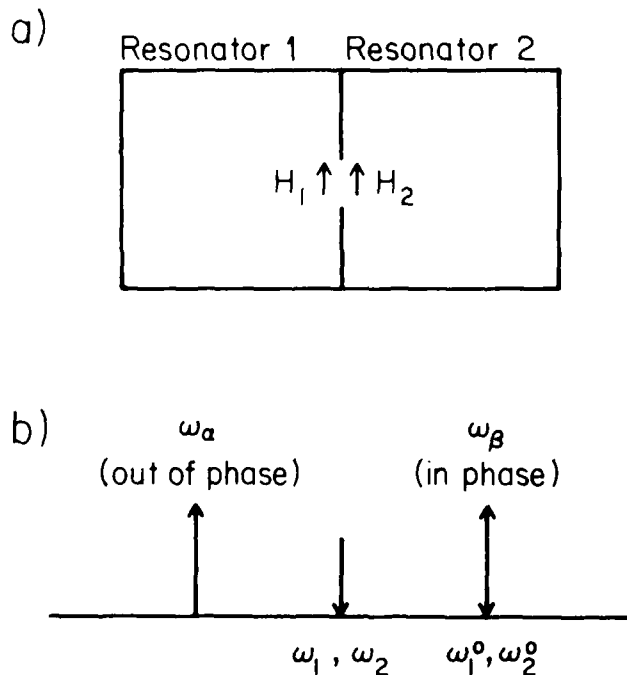


Figure 4. Two identical cavities coupled by an orifice in a thin shared wall

- Configuration
- Identification of eigenfrequencies, cavity frequencies, and original cavity frequencies

A further example is shown in Fig. 4. If two identical cavities are coupled by a thin orifice as shown, one of the modes of the system is seen by inspection to have the same frequency as that of the uncoupled cavities. From symmetry, both cavities are detuned the same amount by the presence of the orifice, and from 33A), the mode picture is symmetric about the detuned cavity frequencies and the eigenmode splitting is just  $k\omega_1$ . The result apparent from Fig. 4,  $k\omega_1 = 2(\omega_1^0 - \omega_1)$  can be generalized to give

$$k_{ij}(\omega_i + \omega_j) = 4\sqrt{(\omega_i^0 - \omega_i)(\omega_j^0 - \omega_j)} \quad (35)$$

for the coupling between any two cavities coupled by a thin orifice and aligned fields. Thus the coupling through a thin orifice of any shape can be related in a simple manner to the frequency shifts induced in the coupled cavities by the orifice.

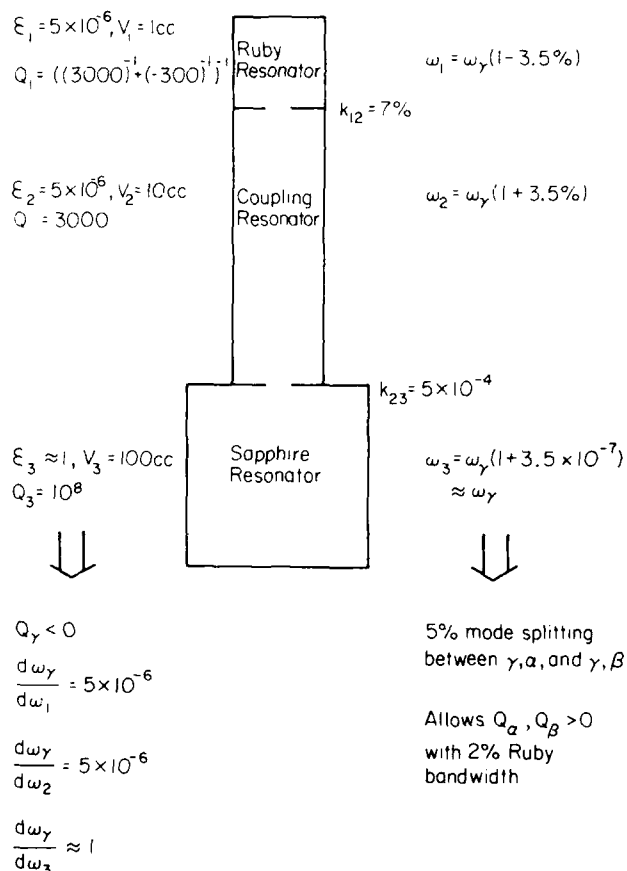


Figure 5. Model for three-cavity maser, showing design parameters on left, calculated constants on right. Consequences of various design features shown below

### 2.3.3. Design of a Three Cavity Oscillator

Fig. 5 illustrates the design parameters for the three-cavity ruby maser oscillator presently under construction. We identify the three modes of the system as  $\alpha$ ,  $\beta$ , and  $\gamma$  having their largest energy in resonators 1, 2, and 3 respectively, with mode  $\gamma$  the desired stabilized mode. On the left are shown the parameters for this mode pertaining to energy balance considerations, and on the right are the frequencies and couplings which we calculate to allow the energy balance required, while maintaining a 5% mode splitting. The values for the various quality factors are conservative estimates of values we expect to be able to attain in a first experiment. The (negative)  $Q$  for the pumped ruby is representative of values that we have obtained using similar one- and two-cavity maser oscillators, as are the  $Q$ 's of the

normal resonators. Superconducting Q's are discussed elsewhere in this paper. The fractional energy in the coupling cavity  $\epsilon_2$  was set equal to that in the ruby cavity to constrain the configuration parameters within the region of validity of the approximations we have made. With this constraint, the energy fractions  $\epsilon_1$  and  $\epsilon_2$  were chosen nearly as small as possible to allow oscillation in mode  $\gamma$ , using the requirement that  $Q'$  be negative in equation 11). Under the conditions shown in Fig. 5, the break-even condition given by 12) would allow a value for the ruby cavity Q of

$$Q_1 = \left[ (3000)^{-1} + (-375)^{-1} \right]^{-1} \quad (36)$$

that is, a cavity Q of 3000 and a Q for the ruby itself of -375. The resulting unavoidable sensitivity of the mode frequency to the various parts is shown at the bottom, as calculated from 18).

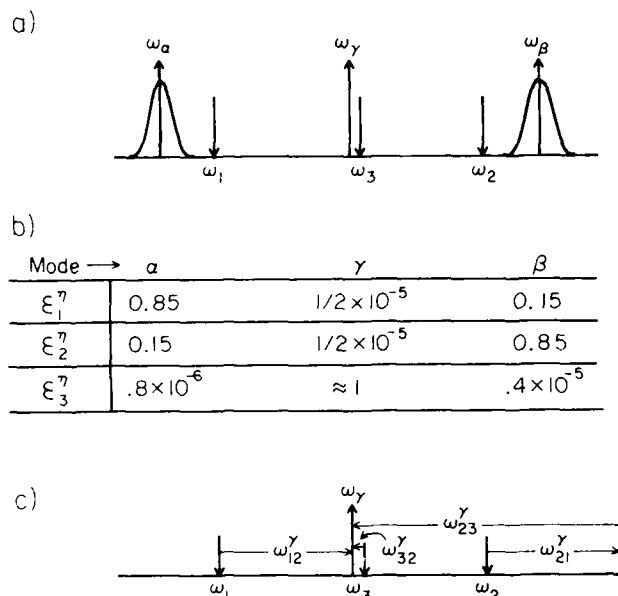


Figure 6. a) Frequency response of three-cavity resonator. Response bandwidth of high Q mode not shown. Cavity frequencies and eigenfrequencies identified  
b) Table of fractional energy in each cavity for the three modes  
c) Eigenfrequency diagram for high-Q mode

The mode structure for this system is shown in Fig. 6 a) and the energy distribution for the modes in 6 b). These results were obtained by a successive application of equations 29) and 27), together with the requirement of equal 5% spacing between  $\omega_a$ ,  $\omega_\gamma$ , and  $\omega_\beta$ , as illustrated by Fig. 6 a). Fig. 6 c) illustrates the terms in equation 29) as applied to the mode  $\gamma$ . These become

$$\omega^\gamma = \omega_1 + \omega_{12}^\gamma = \omega_2 + \omega_{23}^\gamma + \omega_{32}^\gamma = \omega_3 + \omega_{31}^\gamma \quad (37)$$

and the frequencies can be found by application of equation 28);

$$\begin{aligned} \frac{\omega_{12}^\gamma}{\omega_{12}^\gamma} &= \frac{\epsilon_1^\gamma}{\epsilon_2^\gamma} = 1 \\ \frac{\omega_{23}^\gamma}{\omega_{32}^\gamma} &= \frac{\epsilon_2^\gamma}{\epsilon_3^\gamma} = \frac{1}{5 \cdot 10^{-6}} = 2 \cdot 10^5 \end{aligned} \quad (38)$$

given the energy balance shown in Fig 5. Thus it is seen that in the operating eigenmode  $\gamma$ , cavity 1 is tuned 3.5% high by its coupling with cavity 2; cavity 2, being already 3.5% higher than the operating frequency is tuned 3.5% higher yet by its coupling to cavity 1, and must be tuned down approximately

7% by cavity 3. Finally, cavity 3 is tuned down  $7\% \times 5 \cdot 10^{-6}$  by the action of cavity 2. The coupling constants that accomplish this tuning are found by application of equation 27). Given these coupling constants, the frequencies of modes  $a$  and  $\beta$  are found using diagrams similar to Fig. 6 c).

### 3. Measurements of frequency pulling and stability

Contributions to the frequency error in a high-Q oscillator system fall into two categories: Those due to variations in the natural resonant frequency of the stabilizing cavity, and those due to variations within the bandwidth of the cavity caused by elements other than the cavity. The preceding analysis of the multicavity oscillator shows that a proper arrangement of frequencies in the cavities and of the coupling between the cavities will distribute the energy of the mode excited in a way that will reduce sensitivity to frequency pulling effects while still allowing oscillation. Of course, the disturbance of the oscillator frequency by the instability in the pulling element is similarly reduced. The problem remains to characterize the magnitudes of the frequency pulling effects so that oscillation stability resulting from the design can be predicted. These magnitudes would be very small in an oscillator utilizing a high-Q stabilizing cavity, small enough to demand highly stable and expensive comparison oscillators to measure the frequency shifts. To allow us to measure these effects with a modest arrangement of test equipment, we constructed a ruby maser oscillator with cavities of low Q. Because the frequency error caused by these frequency pulling effects will be reduced as  $Q^{-1}$  for higher Q systems, measurements of a stability of  $10^{-10}$  with a Q of 100 allows extrapolation of these effects to a stability of  $10^{-17}$  at a Q of  $10^9$ .

Disturbing effects that can be studied in this way include those due to output voltage standing wave ratio (VSWR) and a number of effects due to the ruby itself. The ruby properties that are of concern are possible 1/f noise, possible pulling effects of the pump signal amplitude and frequency, the previously discussed magnetic field pulling, and fluctuations in the ruby characterized by its effective noise temperature (white noise). Of particular interest and concern in this regard was the possibility of substantial 1/f type modulation noise in the ruby, because no experiments have been previously conducted that place significant limits on such noise. An excessive amount of such noise would place a Q-dependent limit to the stability allowed by the oscillator, and might indicate that a very high Q ( $10^{10}$  or above) was necessary, ruling out the use of a sapphire-filled resonator.

An apparatus was set up to allow measurements of the frequency stability in a ruby maser oscillator, and a two-cavity coupled oscillator system was also constructed to study the performance of coupled systems and to test the Q-dependence of the pulling effects. The various aspects of the oscillator were treated with differing degrees of care. The superconducting magnet was carefully constructed as a first attempt at what might be used in the final system. The ruby itself has been previously used in amplifier service, and can be expected to be a good example of what is available. The signal coupling line, however, was not constructed for stablest VSWR, but was designed to allow a wide range of coupling strengths. Similarly, the pump signal source has poor amplitude and frequency stability. The results to be described serve to place an upper limit on the frequency stability and pulling, but do not represent the best that can be obtained with this technique. Preliminary results were reported at a previous conference.<sup>2</sup>

#### 3.1. Description of the low-Q oscillator

Figure 7 is a drawing of the cavity region of the low-Q oscillator apparatus. The configuration shown has two coupled coaxial cavities with the ruby material located in the upper cavity. An arrangement with only the ruby-filled upper cavity that has also been used to make frequency pulling and stability measurements will be described in a later section of this paper.

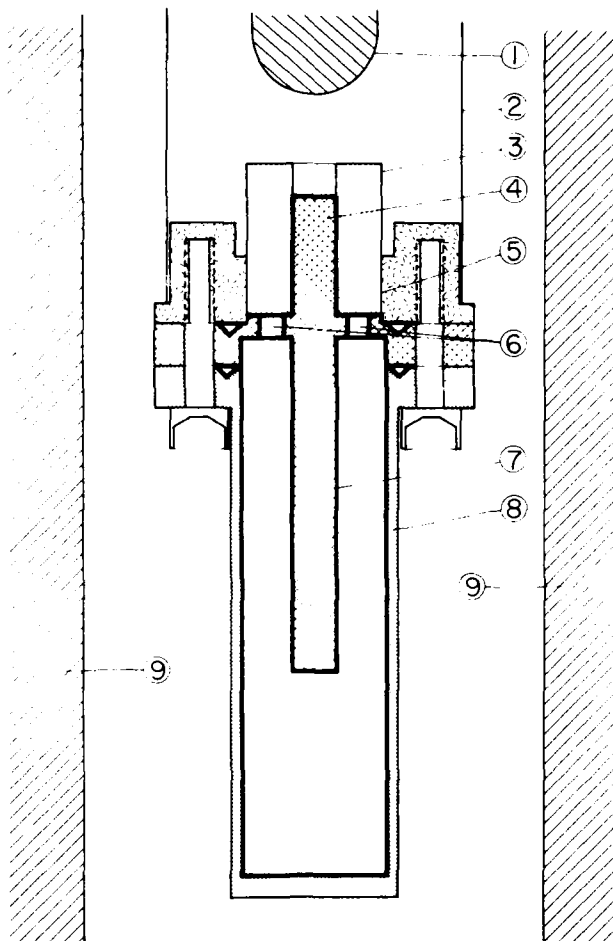


Figure 7. Two-cavity maser

The outer wall (2) of the oscillator probe serves both as the waveguide for the pump signal ( $\sim 13\text{GHz}$ ) and as the outer conductor of a coaxial transmission line for the oscillation signal ( $\sim 2.7\text{GHz}$ ); the inner conductor (1) of the coaxial transmission line can be adjusted vertically at the top of the probe to allow the coupling strength to the upper cavity to be varied. The ruby crystal (3) has dimensions 1.0 cm outer diameter and 1.15 cm length. The height of the outer cavity wall (5), the lengths of the center posts (4) and (7), and the size of the coupling holes (6) were adjusted to provide the energy distribution and the frequency splitting desired. A superconducting magnet (9) supplies the magnetic field to split the chromium ions' energy levels to the frequency of the resonant mode that we wish to excite.

When the magnet is not on, a signal applied to the coax can be used to find the resonant frequencies of the cavity system, and adjusting the coupling strength to obtain critical coupling allows the  $Q$ 's of the modes to be measured. When the magnet is turned on and tuned so the level splitting equals the frequency of one of the cavity modes, strong absorption occurs and the mode  $Q$  is greatly reduced. With the magnetic field set near the peak of the absorption-field curve, applying a pump signal of  $\sim 13\text{GHz}$  causes an inversion of the spin populations, giving the negative resistance that stimulates oscillation. When the stability of the oscillations is being measured, the coupling probe (1) is backed off to provide rather weak coupling to the cavity signal.

In the earlier measurements, the pump signal was supplied by a Hewlett-Packard 8690A sweep oscillator. In later work, this source was replaced by a klystron whose frequency could be stabilized; comparisons of the results will be made. After amplification the oscillator signal is mixed in a Hewlett-Packard 934A harmonic mixer with a signal

from an Ailtech 360D11 frequency synthesizer. The low frequency output is further amplified and then is continuously sampled both by a Hewlett-Packard 5245M counter and by a Digital Equipment Corporation PDP 11/34 computer. A chart recording of the counter output provides a quick check of the oscillator's stability and drift, while statistical stability analysis is carried out on the computer system.

By measuring the lowest resonant frequencies of each cavity alone and of the two coupled modes, the energy splitting between the modes and the coupling strength between the cavities can be determined. The two coupled cavity arrangement had a coupling strength of 2.5%. The stabilized mode had 85% of the energy in the stabilizing cavity and 15% in the ruby-filled cavity, while the other mode had the opposite ratio.

## 3.2. Results of Frequency Stability Measurements

### 3.2.1. Measurements in the Two-cavity Configuration

To allow a range of  $Q$  values to be studied, and to facilitate stimulation of oscillation, the areas of the two-cavity system that are drawn with heavy lines in Fig. 7 were plated with superconductor (lead). Even though the superconductor was placed in a rather high magnetic field, the film reduced the losses on the plated surfaces and allowed higher  $Q$  values to be obtained. With this lower loss condition, the stabilized mode oscillated at  $2.71\text{GHz}$  when cooled to temperatures below  $4.2\text{K}$ . The upper cavity had its outer wall not plated with superconductor, so the mode at  $2.87\text{GHz}$  with most of the energy in the upper cavity displayed lower  $Q$  than the stabilized mode.

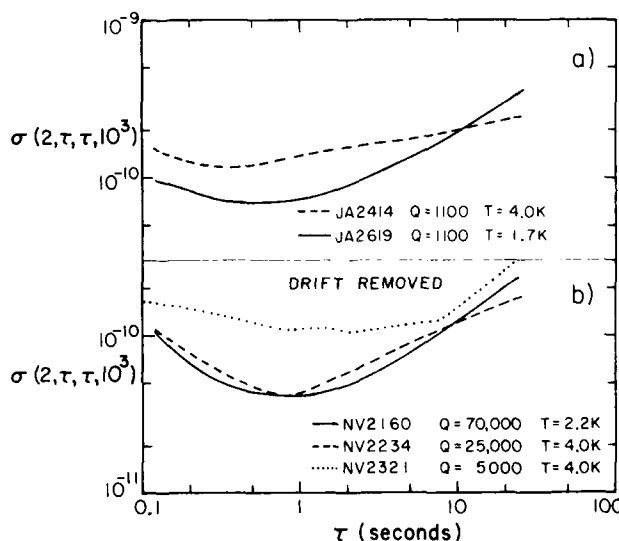


Figure 8. Allen variance of frequency noise measured for cavity masers

- a) Low- $Q$  single-cavity maser with locked pump frequency
- b) Two-cavity maser with unlocked pump frequency

Part (b) of Fig. 8 shows examples of Allan variances of  $\Delta f/f$  calculated from the data obtained with the two-cavity configuration under various conditions. Note that cooling the ruby to  $2.2\text{K}$  and improving the cavity  $Q$  from 25,000 to 70,000 do not yield improvement in the lowest observed  $\sigma$  values. We conclude that the limiting stabilities observed are not characteristic of the ruby maser, but rather are caused by some other device in the measuring system. In fact, subsequent measurements of the stability of the measuring system showed that the frequency synthesizer exhibited stability at the levels shown in Fig. 8(b). If the data for the curve labelled NV2321 are extrapolated to  $Q = 10^5$ , the  $\Delta f/f \approx 10^{-10}$  shown in Fig. 8 would be reduced to  $\Delta f/f \approx 5 \times 10^{-10}$ .

Obviously we cannot attain such extrapolated frequency stabilities in the present apparatus, although the principle obstacles are not so apparent. Distortions of the copper cavities, caused by changes in the pressure above the liquid helium, by changing height of the helium bath, and by thermal expansion due to temperature instability, result in frequency instabilities near the  $10^{-11}$  level at  $\tau = 1$  s. These effects point to the requirement to place the cavities in an evacuated space and to use the thermally and mechanically stable sapphire as the support material for the high-Q cavity. A further deficiency of this test apparatus is the instability of the adjustable coupling probe ((1) in Fig. 7). A considerable reduction in response to vibrational disturbances was obtained by placing damping material around the room temperature portion of this probe. Additionally, a frequency drift was observed to follow the change in liquid nitrogen level surrounding the helium dewar of the cryostat. Almost all the instability shown in Fig. 8 beyond  $\tau = 10$  s can be attributed to this source of frequency drift. A major benefit of employing an all-cryogenic oscillator design is to avoid such response of the oscillator frequency to the temperature profile on transmission paths to room temperature electronics. The oscillator design to be described below will have fixed, stable output signal coupling, with 40 dB of isolation from VSWR changes on the output coax provided by cryogenic isolators<sup>13</sup> placed inside the vacuum can at 4.2K.

The Hewlett-Packard 8690A sweep oscillator used as a pump source for these measurements was found to have great effect on the measured values of frequency and on frequency stability. The best data were acquired by carefully tuning this pump source to minimize the frequency pulling effects. The response of the oscillator frequency to changes in pump signal frequency and pump signal amplitude were measured to determine the required stabilization of the pump signal source for a high-stability system. The measured response to pump signal frequency changes, for  $Q = 5000$ , is

$$\left. \frac{\Delta f}{f} \right|_{\text{osc}} = 5 \times 10^{-4} \left. \frac{\Delta f}{f} \right|_{\text{pump}} \quad (39)$$

while the response to pump signal amplitude (power  $P$ ) changes at  $Q = 5000$  is

$$\left. \frac{\Delta f}{f} \right|_{\text{osc}} = 2 \times 10^{-7} \left. \frac{\Delta P}{P} \right|_{\text{pump}} \quad (40)$$

Both of these responses were observed to scale with  $Q^{-1}$  over the range of  $Q$ -values examined (5,000 to 70,000), a point of some importance to our extrapolations. These results imply that, to achieve a stability of  $10^{-17}$  at a  $Q$  of  $10^9$ , the pump frequency must be stable to four parts in  $10^9$  and the pump amplitude must be stable to one part in  $10^6$  over the measuring time  $\tau$ . The pump frequency stability is readily attainable with stabilizers that lock the microwave source to a quartz frequency standard, or could be managed by synthesizing a pump signal from the oscillator output. The pump signal amplitude stability required for  $10^{-17}$  stability is more challenging, and will not be attained in the design to be described below, which is intended to reach a  $10^{-16}$  oscillator stability level. The cause of this response to pump amplitude is probably inhomogeneity of the magnetic field at the ruby. It is expected that the high-stability oscillator being built will demonstrate improved stability against pump amplitude changes beyond that dictated by higher  $Q$ .

Careful tests of the change of oscillator frequency with change in the magnetic field were conducted to check our understanding of frequency pulling effects and their dependence on  $Q$ . For the unstabilized mode with  $Q = 5,000$ , the fractional frequency pulling was found to be

$$\left. \frac{\Delta f}{f} \right|_{\text{osc}} = 2.5 \times 10^{-3} \frac{\Delta H}{H} \quad (41)$$

and this value also scaled as  $Q^{-1}$  for the other oscillation conditions measured. This value implies that, in order to achieve  $10^{-17}$  stability with a cavity  $Q$  of  $10^9$ , the magnetic field must not have a fractional variation larger than  $10^{-9}$  over the measuring time  $\tau$ . This field stability can be achieved using a superconducting magnet operating in persistent mode, and having superconducting shields to attenu-

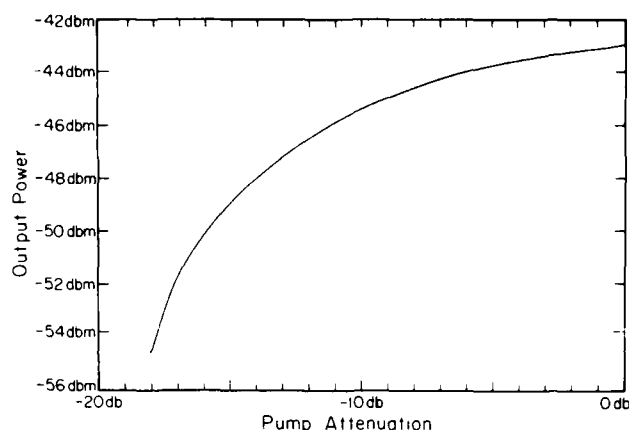


Figure 9. Maser output power vs uncalibrated pump signal

ate ambient field variations.

The output power of the oscillator is shown in Fig. 9 for a range of applied pump power, with the magnetic field tuned to optimum. Zero attenuation of the pump signal corresponds to  $\sim 100$  milliwatts of pump power at the top of the oscillator probe. The maximum output power in the region of saturation is  $0.5 \times 10^{-7}$  watt, a level well within our design requirements. Therefore, the ruby volume will not need to be changed substantially in the final configuration of the oscillator.

### 3.2.2. Measurements in the One-cavity Configuration

The results discussed above for the two-cavity oscillator indicate that distortion of the magnetic field uniformity at the ruby could be causing the rather large response of the oscillation frequency to pump amplitude changes. One source of field distortion is the superconductor on the center-post and base of the ruby-filled cavity. As well, the modest stability of the measuring system indicates the need to use a cavity of lower  $Q$  so the measured stability level will not be limited by the measuring system rather than by the oscillator. The stability and frequency pulling measurements were repeated with an oscillator system having a cavity of lower  $Q$ . Since the previous tests established the performance of a coupled-cavity oscillator system, a single-cavity oscillator was built.

Use was made of the same oscillator probe employed for the two-cavity measurements by merely replacing the base and center post of the ruby-filled cavity by one made of brass, with no coupling holes in the base and no second cavity. While a  $Q$  of several hundred had been expected, the measured value was  $Q = 1100$ , which was found to be independent of temperature over the range of 4.2K to 1.5K.

The only other modification made to the oscillator system was to use a klystron<sup>14</sup> oscillator for the pump signal source, and to stabilize the frequency of the klystron with a quartz crystal frequency stabilizer<sup>15</sup>. Without the stabilizer the klystron's frequency output at  $\sim 13$ GHz fluctuates by several kilohertz. When the stabilizer is applied to lock the microwave frequency to the quartz crystal's frequency, the measured fluctuations are  $\sim 10$ Hz at  $\tau = 1$  s and  $\sim 50$ Hz at  $\tau = 10^3$  s. This improved pump signal frequency stability was a significant benefit to the measured oscillator stability levels. Note also that this pump signal frequency stability satisfies the requirement of 4 parts in  $10^9$  cited above to allow the oscillator to reach  $10^{-17}$  stability with a cavity  $Q$  of  $10^9$ .

Part of Fig. 8 shows the results of measurements of oscillator frequency stability made with this system. The improvement shown upon reducing the temperature indicates that the measured instabilities are characteristic of properties of the maser oscillator system to some extent. Again extrapolating the low-temperature data (the curve

labelled JA2619 in the figure) to a cavity  $Q$  of  $10^9$  would imply that a stability level of  $8 \times 10^{-17}$  could be achieved at  $\tau = 1$  s.

While this high stability is indicated without any need for improved pump signal stability, the averaging time at which high stability is desired is in the range  $\tau \geq 10^3$  s. The data show that the long-term stability values in these measurements suffer from drift, caused principally by the changing temperature profile on the transmission lines. We expect that the different arrangement for coupling out the oscillation signal that will be used in the oscillator being built will eliminate this source of drift and will allow the improved stabilities to be obtained at longer measuring times  $\tau$ .

The removal of superconductor from the region near the ruby did not reduce significantly the effect of frequency pulling by changes in pump signal amplitude. Since the pump amplitude was not stabilized in the measurements reported here, we believe that the lowest instability values may have been determined by this source of disturbance. Therefore, we would expect to measure smaller values of  $\Delta f/f$  if an amplitude-stabilized pump source is used. Amplitude stabilization to one part in  $10^5$  is being arranged for the high-stability oscillator being built. Amplitude stabilization to a few parts in  $10^5$  can be managed with considerable effort and expense.

#### 4. The Superconducting Cavity

##### 4.1. Cavity Design

With the promise of much greater electronic stability allowed by an all-cryogenic oscillator design, the relationship of the cavity  $Q$  to the overall design changes somewhat compared to other SCSO designs. In particular, a lower  $Q$  might be advantageous if it allowed substantially higher frequency stability to be attained in the cavity. This trade-off seems to be possible by the use of a superconductor-on-sapphire resonator when operated at temperatures somewhat lower than has previously been employed. While the thermal coefficient of expansion of solids follows a  $T^3$  dependence at low temperatures, the penetration depth of the superconductor, which also determines the effective size of the resonator, shows a much more rapid exponential temperature dependence. Thus, for a solid niobium cavity, the frequency variation with temperature decreases rapidly as the temperature is reduced down to a temperature of approximately 1.25K, below which the relatively slowly varying  $T^3$  dependence of thermal expansion is dominant.<sup>9</sup> When the physical size is determined by the characteristics of sapphire, the value of the contribution from thermal expansion is reduced by more than 100. Assuming the superconducting character of niobium is unchanged in applying a thin film on a sapphire substrate, reduction in operating temperature to 0.9K would still show the rapid exponential decrease in sensitivity to thermal variations, resulting in an overall improvement of thermal sensitivity from  $\sim 10^{-11}/K$  to  $10^{-13}/K$ .

We have measured the highest  $Q$  reported to date in a sapphire-filled superconducting cavity ( $Q > 10^9$ ) and present details in the following section. Such a resonator would additionally be stronger and lighter than a solid niobium cavity, giving a reduction in the shift caused by gravity forces by 10 times. A further advantage of the sapphire based resonator is that its large dielectric constant ( $\epsilon \sim 10$ ) allows operation at a convenient frequency ( $\sim 3$ GHz) with modest dimensions (overall diameter  $< 7.5$  cm).

##### 4.2. Measurements of the Cavity Losses

To obtain the high cavity  $Q$  required by the design, various sapphire materials have been examined for their electromagnetic losses at frequencies near 2.7GHz and at temperatures below 4.2K. Samples with losses below  $10^{-6}$  have previously been described.<sup>10</sup> A recently acquired new sample has shown significantly lower losses than those previously reported, the loss tangent reaching  $\tan \delta = 7.0 \times 10^{-10}$  at the temperature of 1.5K. The actual material that will be used in the cavity of the high-stability oscillator has not yet been delivered by the supplier, so we have not had the opportunity to characterize its losses. Sapphire material of

the same sort and from the same supplier<sup>17</sup> as the lowest-loss material has been ordered.

In measuring the sapphire losses, the samples are placed inside a lead-coated copper cavity and the decay time of the cavity-sapphire system is measured. Since initially lead will also be used to coat the sapphire substrate in forming the stabilizing cavity, the very low loss values reported above are sufficient evidence that losses in the superconducting film will not prevent the cavity from achieving a  $Q$  of  $10^9$ . However, because the electromagnetic field is to be contained *inside* the cavity, the interface region between the lead film and the sapphire will also be exposed to the signal and could degrade the cavity  $Q$ . A measurement was made on a spherical sapphire substrate coated with a lead film to test this loss mechanism. The uncoated sapphire sphere displayed a loss value of  $\tan \delta = 1.17 \times 10^{-8}$ , while the lead-coated sphere's loss was  $\tan \delta = 1.15 \times 10^{-8}$ , both values measured at 1.5K. These results show that the losses in the interface region do not contribute appreciably to the total loss measured at this region near  $Q = 10^9$ .

Actually, these measurements have indicated the possibility of achieving even higher  $Q$  values in the stabilizing cavity. Both the sapphire loss tangent measurements and the measurements in the spherical cavity demonstrated that a  $Q$  of  $10^9$  is feasible for this cavity. A ruby maser oscillator stabilized with a cavity having a  $Q$  of  $10^9$  would be expected to have stability approaching  $\Delta f/f = 10^{-17}$  for some range of sampling times, if the frequency pulling mechanisms are sufficiently limited as discussed above.

#### 5. A Design for the Three-Cavity SCM

##### 5.1. Electromagnetic Features

Fig. 10 shows schematically some of the features for a 3-cavity superconducting maser designed to achieve a frequency stability of  $\sim 10^{-13}$  for time periods of 100 seconds or longer which is presently under construction. It is closely designed around the model discussed earlier (Figs. 5) and 6)). Some of its features are as follows:

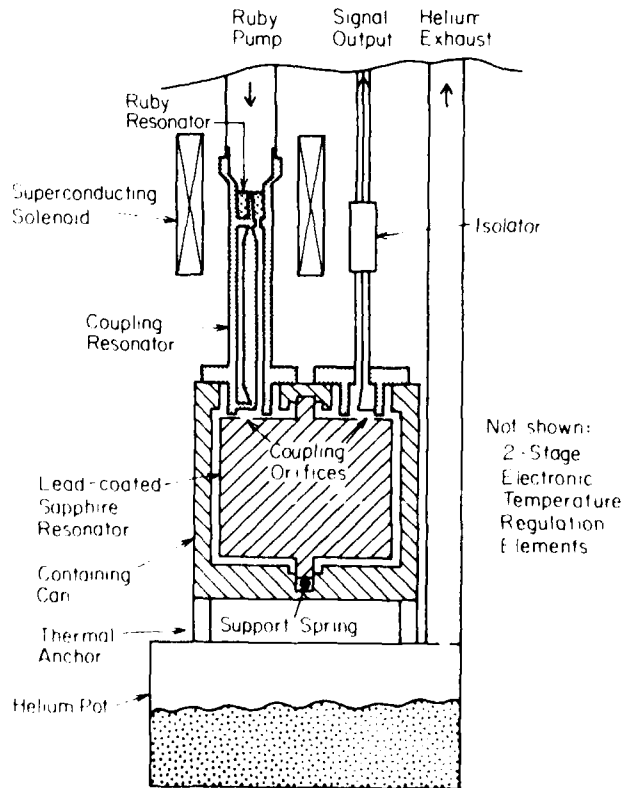


Figure 10. Schematic diagram of three-cavity superconducting maser with sapphire stabilizing resonator



The lead-coated sapphire resonator is supported with small cylindrical ends to allow isolation of the microwave fields from the functions of mounting and thermal anchoring. Orifices in the lead film allow coupling to the signal output and to the coupling cavity. A weak support spring isolates the sapphire from deformations in the copper containing can.

The copper construction technique used for the coupling and ruby cavities has been shown in the one- and two-cavity tests described earlier to have a fractional stability better than  $10^{-10}$  for the time of the measurements. With  $5 \cdot 10^{-6}$  of the system energy in these parts, they should contribute less than  $10^{-15}$  to the frequency variation, even if all of the variation seen in these previous measurements is attributed to this source.

The coupling cavity is a coaxial resonator with a length of  $3\lambda/2$  at the operating frequency of 2.7 GHz. The ruby maser is operated with the magnetic field at  $90^\circ$  to its optic axis in a low-field ( $H \approx 500$  G) mode. Numbering the energy levels of the chromium ion in order of increasing energy, the  $\approx 13$  GHz pump signal excites transitions 1-4 and 2-4, while the signal samples the 3-4 transition. This mode provides less amplification in the ruby than the more conventional one in which the signal samples the 1-2 transition, but the reduction of the magnetic field requirement from  $\approx 3000$  G to  $\approx 500$  G is a substantial advantage.

## 5.2. Cooling and Temperature Stability

The oscillator will be installed in an existing cryostat insert that was originally used as a  $^3\text{He}$ - $^4\text{He}$  dilution refrigerator. The vacuum can is 11.37 cm outside diameter by 63.5 cm long, so ample working volume exists inside the can. The only cooling capability that is being retained inside the vacuum can is a pumped  $^4\text{He}$  pot of 300 cc volume. This pot is filled from the external 4.2 K liquid helium bath through a valve and a capillary. The pot and its pump line will allow cooling the three cavities and the ruby maser to very near 1 OK.

When the oscillator is operating, approximately  $10^{-7}$  watt will be dissipated in the cavities, while  $\sim 10^{-8}$  watt will be absorbed in the ruby from the pump signal. Transport of heat to the  $^4\text{He}$  pot by conduction, radiation and He film flow will be of order  $10^{-4}$  watt. Since all other heat loads on the  $^4\text{He}$  pot are substantially smaller than the pump signal power, the stability of the pump power will be reflected in the temperature stability at the  $^4\text{He}$  pot and, more importantly, at the high-Q cavity. We expect to obtain pump power stability of a part in  $10^3$  to limit frequency pulling effects. This level of pump stability will also provide excellent temperature stability, as a brief description will show.

As shown in Fig. 10, the pumped  $^4\text{He}$  pot will be positioned at the bottom of the vacuum can and will connect directly to the lowest can containing the high-Q cavity. In examining the various resistances to heat flow between the ruby and the  $^4\text{He}$  pot, one finds temperature drops of 4 mK between the ruby and its cavity, 7.5 mK along the coupling cavity, and 10 mK between the lowest can and the  $^4\text{He}$  pot, for each milliwatt of power absorbed in the ruby. Fluctuations of one part in  $10^3$  of the  $\sim 10^{-8}$  watt pump power ( $\pm 10^{-6}$  watt) will therefore cause temperature fluctuations of  $10^{-5}$  K on the high-Q cavity. However, the heater for the temperature controller will be placed on the coupling cavity; a bias power of  $10^{-5}$  watt in this heater will allow the temperature controller to compensate power fluctuations of the magnitude expected. Thermal time constants are all rather short for this system operating at 1.0 K, of order  $10^{-2}$  second or smaller, so response to thermal fluctuations will be limited by the  $\approx 1$  s response time of the temperature control electronics. In addition to the temperature sensor and heater on the cavities, a second level of temperature control will be used to regulate the temperature of the pumped  $^4\text{He}$  pot. A stability of  $10^{-3}$  K for the several days that one fill of the  $^4\text{He}$  pot will last is expected at the high-Q cavity.

## 6. Conclusions

Analysis of an application of the ruby maser to a superconducting cavity stabilized oscillator shows many attractive features. These features derive from the mechanical

stability inherent in an all-cryogenic design and from the properties of the ruby maser itself. A multiple-cavity design has been developed to allow physical separation of the high Q superconducting cavity and the ruby element with its required applied magnetic field. Mode selection is accomplished in this design by tuning the ruby by means of the applied field. We conclude that such an oscillator would perform well, even with cavity Q's as low as  $10^8$ , allowing the use of a superconductor-on-sapphire resonator with its greater rigidity and lower thermal expansion.

A method for the design of multiple-cavity oscillators has been developed which allows a specific energy balance in the oscillating mode to determine requirements for easily measurable frequencies and coupling constants. The design is accomplished without reference to the fields implicit in the measurements. Relationships between power and frequency sensitivity considerations for the various parts are also established in this method. The design of a 3-cavity oscillator system that was evolved using this method is described.

A first test of the superconducting cavity maser confirms the efficacy of the multiple-cavity design and the applicability of the ruby maser. Frequency variation less than  $4 \times 10^{-11}$  was measured and is attributed to the reference oscillator and to instabilities in the pump source. Variation of  $10^{-10}$  was observed in a low Q mode, again attributable to pump fluctuations. Even so, direct scaling to a Q of  $10^8$  predicts a stability better than  $10^{-16}$ . Frequency pulling effects due to amplitude and frequency variations in the pump signal were characterized, and their appropriate scaling with cavity Q was demonstrated. Together with results showing the lowest losses to date in sapphire at microwave frequencies, and preliminary experiments on superconductor-on-sapphire resonators, frequency stability levels as low as  $10^{-17}$  are indicated.

## 7. Acknowledgements

The authors would like to gratefully acknowledge the contributions and support of J. E. Mercereau and R. C. Clauss to this work.

The work described in this paper was carried out at California Institute of Technology with the support of the Jet Propulsion Laboratory under contract with the National Aeronautics and Space Administration.

## 8. Appendix, Coupling Losses

The coupling energy can be related to cavity energies by

$$E_0 = k_{ij} \sqrt{E_i^2 E_j^2}$$

where  $k_{ij} = k_{ji}$  is a dimensionless coupling constant.<sup>11</sup> The relative contribution of losses to the second sum in 5) and 6) can be written:

$$\frac{2P_0}{P_i + P_j} = 2k_{ij} \frac{\frac{\sqrt{E_i^2 E_j^2}}{Q_{ij}}}{\frac{E_i^2}{Q_i} + \frac{E_j^2}{Q_j}}$$

which becomes

$$= 2k_{ij} \frac{\sqrt{Q_i Q_j}}{Q_{ij}} \left[ \left( \frac{E_i^2 Q_j}{E_j^2 Q_i} \right)^{1/2} + \left( \frac{E_i^2 Q_j}{E_j^2 Q_i} \right)^{-1/2} \right]^{-1} \\ \leq k_{ij} \frac{\sqrt{Q_i Q_j}}{Q_{ij}}$$

If the quality factors of the coupling elements are large enough, i.e., if  $Q_{ij} \gg k_{ij} \sqrt{Q_i Q_j}$ , this becomes

$$\frac{2P_0}{P_i + P_j} \ll 1$$

and the second sum in 5) and 6) can be ignored.

## 9. References

- 1 W. H. Higa, Tech. Mem. 33-805, NASA, 1976.
- 2 G. J. Dick and D. M. Strayer, PTTI-15 Conference Report, December, 1983, to be published.
- 3 S. R. Stein and J. P. Turneaure, Proc. Conf. on Future Trends in Superconductive Electronics, AIP Conf. Proc. No. 44, 192 (1978).
- 4 See, for example, J. V. Jelley, Proc. IEEE **51**, 30 (1963). Also R. C. Clauss, private communication.
- 5 S. Weinreb, IEEE Trans. Microwave Theory Tech., **MTT-28**, 1041 (1980).
- 6 J. M. Pierce, J. Appl. Phys., **44**, 1342 (1973).
- 7 V. B. Braginski, I. I. Minakova, and V. I. Panov, Radiotekh. Elektron. **21**, 192 (1976).
- 8 I. E. Campisi and W. O. Hamilton, IEEE Trans. on Microwave Theory Tech., **MTT-31**, 905 (1983).
- 9 C. T. van DeGrift, Rev. Sci. Instr. **46**, 599 (1975). Also, T. Rutton, **Microwaves**, 42 (July, 1972).
- 10 H. A. Bethe, Phys. Rev. **86**, 163 (1944).
- 11 L. Page and N. I. Adams, Jr., **Principles of Electricity**, D. Van Nostrand Co., Inc., Princeton, N. J. (1958).
- 12 J. C. Slater, **Microwave Electronics**, D. Van Nostrand Co., Inc., Princeton, N. J. (1950).
- 13 P. and H. Laboratories, model C1-S13377 isolator.
- 14 Varian Associates, model VA-287P reflex klystron with a Hewlett-Packard model 716A klystron power supply.
- 15 Microwave Associates model MOS/1 frequency stabilizer.
- 16 D. M. Strayer, G. J. Dick and E. Tward, IEEE Magnetics **MAG-19**, 512 (May 1983). Also, V. B. Braginski, V. I. Panov and S. I. Vasiliev, IEEE Trans. Magnetics **MAG-17**, 955, 1981.
- 17 Crystal Systems, Inc., 35 Congress Street, Salem, Mass. 01970

## ACCURACY EVALUATION OF THE RRL PRIMARY CESIUM BEAM FREQUENCY STANDARD

Koji Nakagiri, Masaki Shibuki, Shinji Urabe, Mitsuo Ishizu  
Yasusada Ohta, Takao Morikawa, and Yoshikazu Saburi

Radio Research Laboratories, Ministry of Post and Telecommunications  
4-2-1, Nukui-Kitamachi Koganei, Tokyo 184, JAPAN

Summary

Described is a recent accuracy evaluation of the RRL laboratory type cesium beam standard Cs 1 with some features, including a hexapole magnet beam optics and a Ramsey cavity using a semi-rigid cable and a coaxial line to waveguide transducer.

A number of accuracy evaluation experiments have been made and the total uncertainty of those evaluations gradually lowered because of our various kind of effort at improvement. The measurement often showed large and undesired characteristics in microwave power shift. According to our experiences, the magnitude of this power shift depended mainly upon the condition of the coaxial line to waveguide transducer, the cesium beam trajectory distribution and its power dependence pattern on beam reversal was usually symmetrical. We investigated the root of the cause of the power shift and at the present time we assume that there were spatially distributed phase variations across the cavity and that these variations caused phase modulation because the atoms passed through such variations. On the basis of certain simple calculations, we evaluated these effects.

In the case of magnetic field evaluation, the power shift of the  $(4,1) \rightarrow (3,1)$  transition was compared with the theoretical estimation which is using the frequency difference between the Rabi transition and Ramsey transition. This frequency difference agreed well with the value estimated by the C field distribution measurement.

The total uncertainty ( $1\sigma$ ) was  $1.1 \times 10^{-13}$ . The frequency of Cs 1 (RRL) agreed with that of the International Atomic Time (TAI) within the limits of  $1 \times 10^{-13}$ .

Introduction

Radio Research Laboratories is responsible for determining the national standard of frequency and for maintaining the Japanese Standard Time, based on the Universal Time Co-ordinated (UTC) to be disseminated by JJY (MF and HF) and JG2AS (40 kHz) transmissions. Work on atomic standards of time and frequency at RRL commenced in 1955 with the construction of a microwave resonance absorption cell in the form of ammonia filled waveguide. In recent years, the studies have been made on hydrogen masers, a laboratory type cesium beam standard, an optically pumped cesium beam standard and stored ion standard.

The RRL primary cesium beam frequency standard, Cs 1, has been developed since 1975<sup>1,2,3</sup>. The design features are as follows. Fig. 1 shows the beam tube chamber of 45 cm in diameter and 2 m in length and the electronics. Fig. 2 shows the structure of the beam tube and Fig. 3 shows the beam optics and the structure of the cavity. The hexapole magnet beam optics is similar to that of Cs 1 standard at PTB<sup>4</sup>. However, the C field is produced by passing dc current through four rods inside three molybdenum permalloy magnetic

shields. The exciting microwave signal is fed to the 55 cm cavity through a semi-rigid coaxial cable. The C field distortion caused by a coaxial cable hole of the innermost magnetic shield is small as compared with that caused by other methods using waveguide. The diameter and the length of the innermost cylindrical magnetic shield are 31.1 cm and 100.0 cm, respectively. In order to avoid loss of state identity or Majorana flops in the space between the state selector and the C field region, guiding field coils are placed at each end of the C field structure<sup>5</sup>.

The Ramsey cavity which is of E-plane bends and has an E-plane Tee feed is made by electroforming. The phase adjustment is made after the same method developed<sup>6</sup> by Mungall et al. of NRC<sup>7</sup>.

The block diagram of the electronics which is different from the former one<sup>8</sup> is shown in Fig. 4. Square-wave frequency modulations are performed by changing the output frequency of the synthesizer sequentially, in order to control 5 MHz crystal and C field current source. The C field control signal is obtained by measuring  $(4,1) \rightarrow (3,1)$  transition frequency.

In the following, we report the results of accuracy evaluation for Cs 1 (RRL).

Accuracy evaluation

Figure 5 shows two examples of clock transition microwave power shift. The horizontal scale is proportional to microwave power. Experiment A was conducted during the period from July to August, 1982 by using a Ramsey cavity and a coaxial line to waveguide transducer, both of which being different from those used at present. Experiment B was conducted during the period from December, 1983 to February, 1984 by using the same cavity and transducer as those used at present. However, the lengths of magnets used in Experiment B and the present experiment are 6 cm and 3 cm, respectively. The asymmetry of the power shift on beam reversal in Experiment B is due to the inequality of beam reversal, since the location of the west-side hexapole magnet is found to be slightly deviated from the beam axis of Ramsey cavity. These mean frequencies which were estimated by the zero-power extrapolation agreed with each other within the limits of the experimental errors. The absolute frequencies in Experiment A and B were lower than the present UTC (RRL) by  $2 \times 10^{-13}$  and  $3 \times 10^{-13}$ , respectively.

Figure 6 shows the power shifts on beam reversal in the present experiment. The gradient, magnitude and asymmetry of power shift on beam reversal were clearly improved. However, the mean value at the optimum power was still lower than that given at -3 dB or -6 dB power by  $1 \times 10^{-13}$ .

These power shift behaviors are presumably due to the complex effect caused by interaction between the distributed cavity phase and the atomic trajectory. In order to study and evaluate these power shift, we

used very simple models as follows. There exists a spatial distribution of phase across the cavity and therefore, across the beam<sup>2,3,10,11</sup>. For that reason, this phase variation causes time dependent phase modulation  $\phi_p(t)$  for atom as shown in Reference 12. The phase varies slowly enough in the cavity and does not depend upon the atomic beam trajectory.

According to our calculations for various types of phase distribution in two cavities, the total phase variation  $\Delta\phi_p(t)$  during the time interval  $t$  in a cavity is effective and if the phase distributions in two cavities are asymmetry with respect to the center of Ramsey cavity, the power shift due to these phase distributions is not canceled. If an asymmetry appears in power shift on beam reversal, this magnitude means also the magnitude of asymmetry of the beam trajectory on beam reversal.

Using the experimental data of -3 dB and optimum power in beam direction west to east in Fig. 7, we assigned a phase variation asymmetry of  $1.5 \times 10^{-4}$  rad/cm and a mean phase difference of  $-0.9 \times 10^{-4}$  rad between two cavities. The results of this calculation were applied to Experiment B in Fig. 5. Then the magnitude of the mean value of the power shift gradient in Experiment B was explained well as in the former case. However, the bias of power shift due to the mean phase difference between two cavities cannot be explained. We presumed that the bias depends strongly upon the beam trajectory, which was effectively different from that of the beam optics with 3 cm magnet. As shown in Fig 5, the asymmetry of the power shift on beam reversal in Fig. 5 may also be due to the inequality of beam trajectory on beam reversal. As a result of the above-mentioned calculation, the power shift due to the phase variation asymmetry in two cavities is dominant at optimum power and is about 50 % at -6 dB power. Therefore, we estimated the inequality rate of beam trajectory on beam reversal by the data at optimum power and assigned the same inequality rate to the mean phase difference shift and obtained an uncertainty of  $0.7 \times 10^{-13}$  at -6 dB power.

Table 1 shows the RRL Cs 1 evaluation.

1. The frequency measurement errors in the case of power shift experiments are shown in Fig. 8.
2. Figure 9 shows the beam velocity distributions, which are calculated using the Ramsey pattern<sup>13</sup>. The linewidth and the peak to valley intensity of Ramsey pattern are typically 100 Hz and 3 pa, respectively.
3. Figure 10 shows the C field distribution along the beam axis. We measured the data by using flux-gate gauss meter. Fig. 11 shows the power dependence of (4,1)→(3,1) transition in the case of Experiment A in Fig. 5. Theoretical estimate shown in Fig. 11 is obtained by measuring the frequency difference between Rabi peak and Ramsey peak. This frequency difference agreed well with the value estimated by the C field distribution measurement. In Fig. 11 we made the value of experiment coincide with that of the theoretical calculation at optimum power.
5. The uncertainty of servo system offset was due to the monotonicity of D-A converter which controlled the voltage of crystal oscillator.
6. In Fig. 12 we measured the single sideband spectral density. Fig. 13 shows the theoretical estimation for the effect of sideband spectrum which is 40 dB below the carrier, showing an unbalance of 1 % in Experiment A in Fig. 4.

The total uncertainty ( $1 \sigma_y$ ) was  $1.1 \times 10^{-13}$ . The frequency comparison with UTC (RRL) during the period from April to May, 1984 was carried out. The absolute frequency was found to be higher by  $0.39 \times 10^{-13}$ . Therefore, the frequency of Cs 1 (RRL) agreed with that of the International Atomic Time (TAI) within the limits of  $1 \times 10^{-13}$ .

#### Future work

We intend to improve the frequency stability and determine more precisely the accuracy of the RRL Cs 1. Moreover we plan to improve the coaxial line to waveguide transducer and construct an automatic accuracy evaluation system.

#### Acknowledgment

The authors are much indebted to Mr. M. Kobayashi for his noble and pioneering work on this project, and also wish to express to Dr. T. Igarashi for supporting this work and to Mr. J. Umezaki for his interests and advises.

#### References

1. M. Kobayashi, K. Nakagiri, S. Urabe, M. Shibuki and Y. Saburi, "Design of and Preliminary Results on a Cesium-Beam Standard at the Radio Research Laboratories", IEEE Trans. Instrum. Meas., IM-27, pp. 343-348, 1978.
2. K. Nakagiri, M. Shibuki, S. Urabe, R. Hayashi and Y. Saburi, "Cesium Beam Frequency Standard at the Radio Research Laboratories", Journal de Physique 42 (3rd Sym. on Frequency and Metrology), pp. c8-253-256, 1981.
3. K. Nakagiri, M. Shibuki, S. Urabe, and M. Ishizu, "Cesium Beam Frequency Standard", Review of the Radio Research Laboratories, Vol. 29, pp. 97-115, 1983 (in Japanese).
4. G. Becker, "Recent Progress in Primary Cs Beam Frequency Standards at the PTB", IEEE Trans. Instrum. Meas., IM-25, pp. 458-465, 1976.
5. S. Urabe, K. Nakagiri, Y. Ohta, M. Kobayashi and Y. Saburi, "Majorana Effect on Atomic Frequency Standard", IEEE Trans. IM-29, pp. 304-310, 1980.
6. A. G. Mungall and H. Damm, "Cesium Beam Frequency Standard Cavity Design", Metro., 6, pp. 60-64, 1970.
7. K. Nakagiri, S. Urabe, M. Shibuki, M. Kobayashi and Y. Saburi, "A Squarewave Frequency Modulation Servo System for Cesium Frequency Standard and its influence on Frequency Stability", J. Appl. Phys. Soc. Jap., 50, pp. 122-130, 1981 (in Japanese).
8. N. F. Ramsey, "Shapes of Molecular Beam Resonances", Recent advances in molecular beams, New York: Academic Press, pp. 107-118, 1959.
9. S. Jarvis, Jr., "Molecular Beam Frequency Biases Due To Distributed Cavity Phase Variations", NBS Tech. Note 660, Jan. 1976.
10. D. J. Wineland, D. W. Allan, D. J. Glaze, H. W. Hellwig and S. J. Jarvis, "Results on Limitations in Primary Cesium Standard Operation", IEEE Trans. Instrum. Meas., IM-25, pp. 453-458, 1976.
11. H. W. Hellwig, "Atomic Frequency Standards: A Survey", Proc. IEEE, Vol. 63, No. 2, 1975.

12. C. M. Bell, and D. Babitch, "A System Analysis of the Cesium Beam Atomic Clock," IEEE Trans. Instrum. Meas., IM-17, pp. 155-166, 1968.
13. H. Dams, "Corrections for Second-Order Doppler Shift and Cavity Phase Error in Cesium Atomic Beam Frequency Standards," IEEE Trans. IM-23, pp. 509-514, 1974.
14. C. Audoin, M. Jardino, L. S. Cutler and R. F. Lacey, "Frequency Offsets Due to Spectral Impurities in Cesium-Beam Frequency Standards," IEEE Trans. Instrum. Meas., IM-27, 1978.



Fig. 1 Cesium frequency standard Cs 1

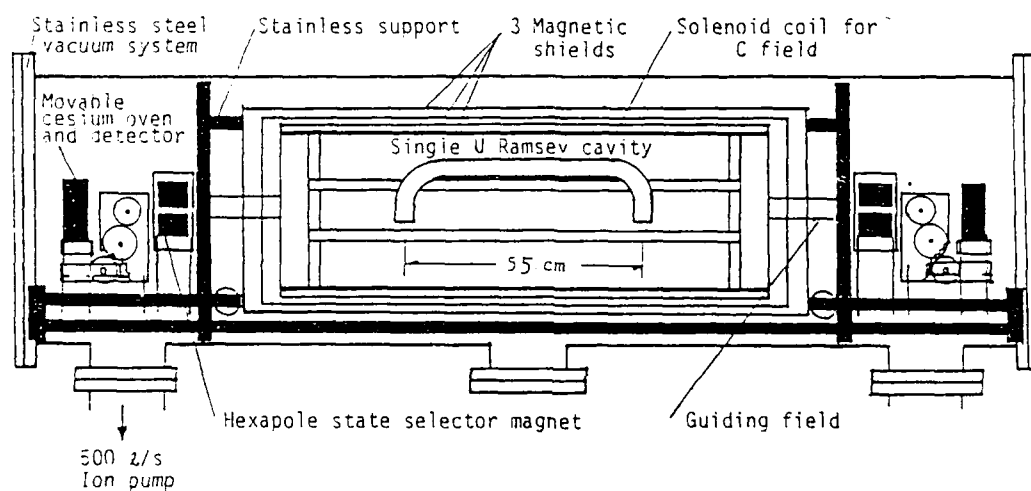


Fig. 2 Structure of RRL Cs Beam Tube

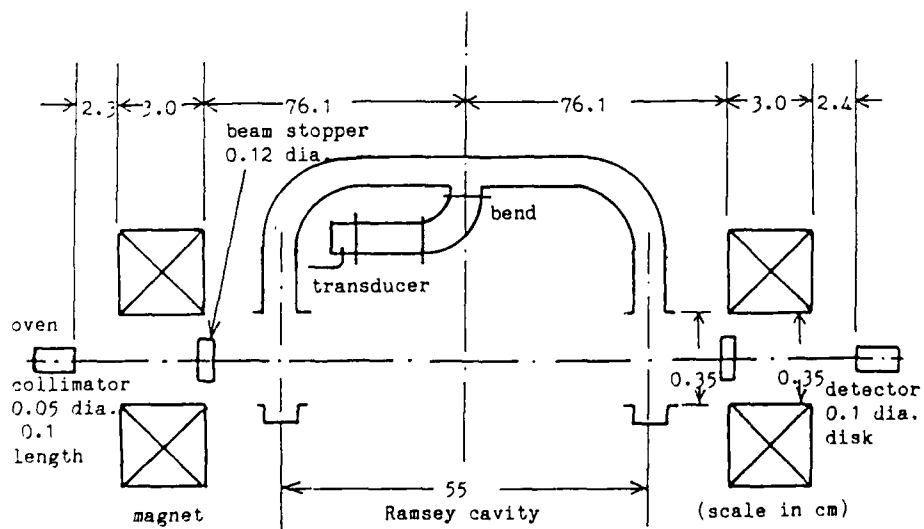


Fig. 3 Beam optics and the structure of Ramsey cavity

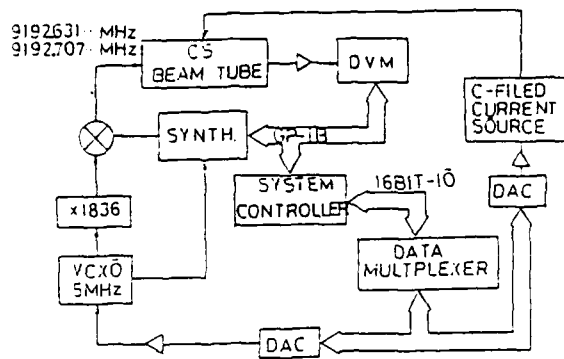


Fig. 4 Block diagram of electronics

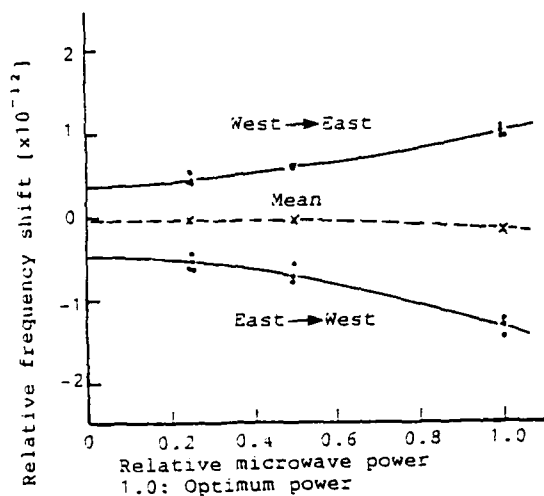


Fig. 6 Clock transition power shift in present experiment

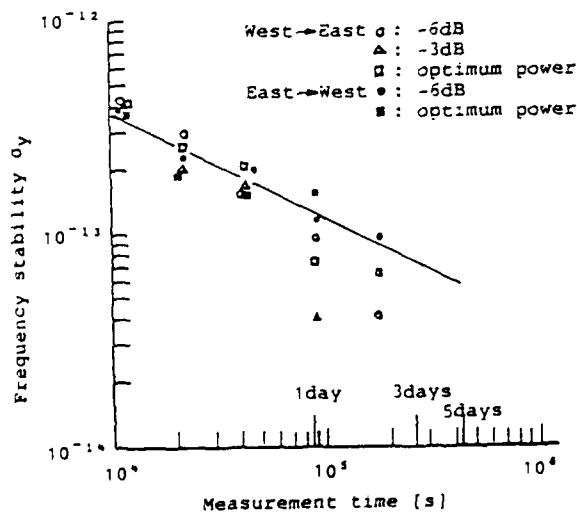


Fig. 8 Frequency stability in power shift experiment

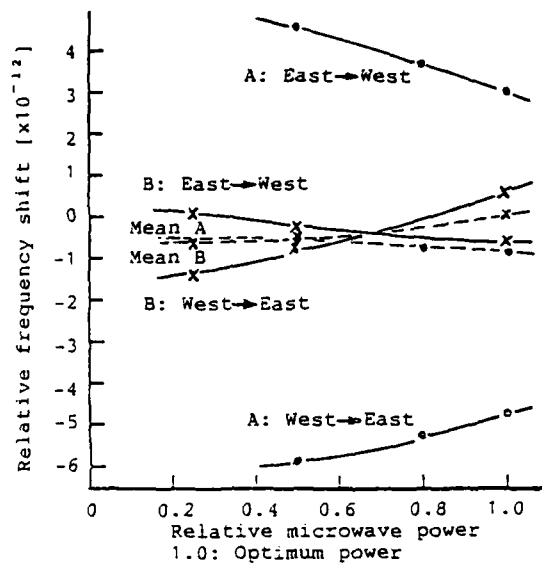


Fig. 5 Two results of clock transition power shift experiment

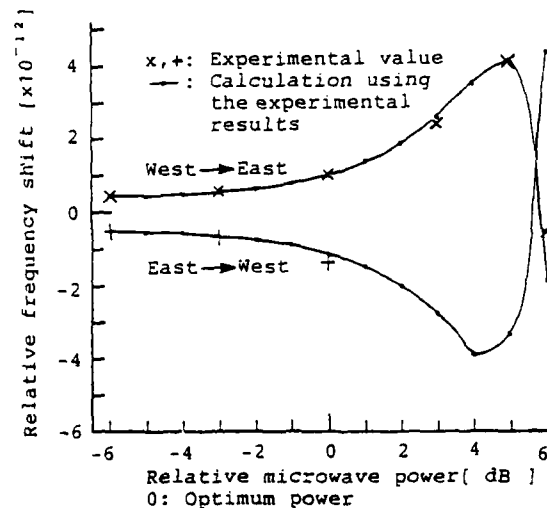


Fig. 7 Theoretical calculation of power shift

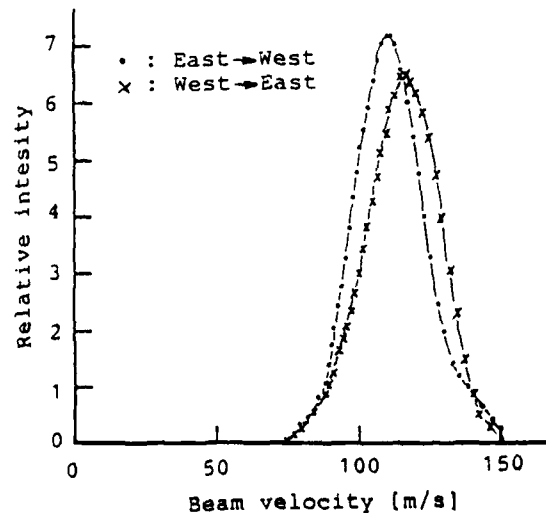


Fig. 9 Beam velocity distribution for different beam direction

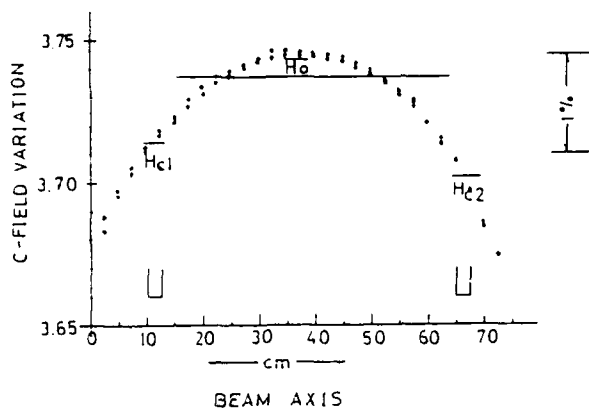


Fig. 10 C field distribution along beam axis

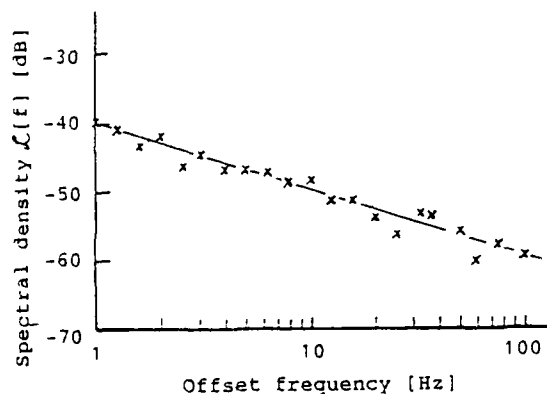


Fig. 12 Single sideband spectral density

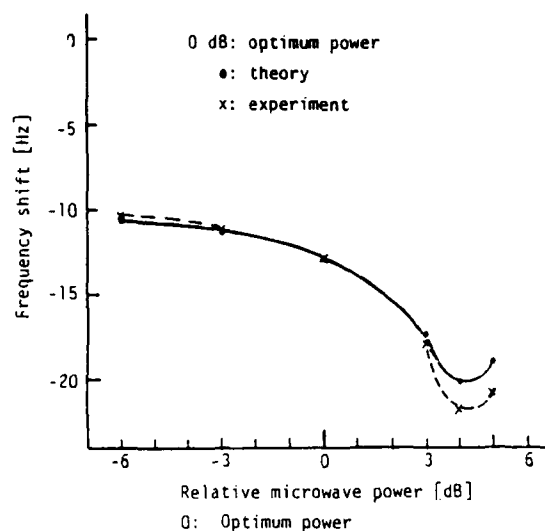


Fig. 17 (4,1)  $\rightarrow$  (3,1) transition power shift

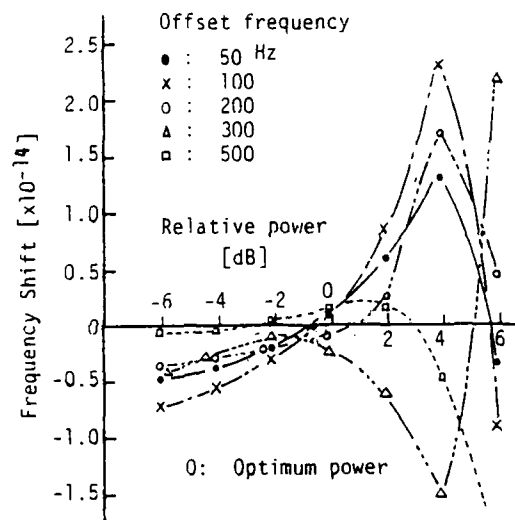


Fig. 13 Theoretical estimation of sideband spurious effect

Table 1. RRL Cs 1 Uncertainty, 1984 April Evaluation

Source of uncertainty	Bias ( $\times 10^{-13}$ )	Uncertainty ( $\sigma_y \times 10^{-13}$ )
1. Cavity phase shift & 1st-order doppler shift	5.08 (typical)	0.9
2. 2nd-order doppler shift	-0.77 (typical)	0.05
3. Magnetic field		
a) Offset due to finite field	5438.91 (typical)	0.23
b) Magnetic field inhomogeneity		0.07
4. Pulling by neighboring transitions	0.23	
5. Servo system offsets		0.50
6. RF spectrum		0.05
7. Black body radiation	-0.17	
8. Gravitational red shift	0.11	
Total uncertainty		1.1

RESULTS ON A LASER DIODE  
OPTICALLY PUMPED CESIUM BEAM

P. CEREZ, G. AVILA, E. de CLERCQ\*, M. de LABACHELERIE, M. TETU\*\*\*

Laboratoire de l'Horloge Atomique  
Equipe de Recherche du CNRS,  
associée à l'Université Paris-Sud  
Bât. 221 - Université Paris-Sud  
91405 - Orsay - France

## I. Introduction

Following Arditi and Picqué<sup>1</sup> pioneering experiments, we have undertaken like several other laboratories researches on a laser diode optically pumped cesium beam. This opens the way for the realization of a new cesium beam frequency standard which should be of higher stability and accuracy than the present conventional one. Basically, the two deflecting magnets used for state selection and detection are replaced by laser light-atomic beam interaction regions. A hyperfine population difference is created in the first (upstream) zone. In the second downstream region the resonance phenomenon, i.e. the Ramsey fringes is detected through fluorescence light variation as a function of the microwave frequency. Optical pumping is expected to improve the frequency stability of cesium frequency standards for several reasons :

i) the signal should be higher than in a classical apparatus. A greater beam intensity can be first used in this straight line highly symmetric device. A complete population inversion can be also achieved when two laser light are used in the pumping region<sup>2</sup>. On the other hand, the detection by fluorescence on a cycling transition produces a large number of photons from each atom of the beam. However, the noise of such a detection might depend not only upon the fluctuations of the number of atoms in the beam, but also to a greater extent, on the fluctuations of the laser frequency and laser intensity. Therefore, the S/N ratio might not increase as strongly as predicts quantum shot noise limitations.

ii) when a cycling transition is used for fluorescence detection, the weight of slower atoms is increased in the velocity averaged 0-0 clock signal. It results in a slight narrowing of the Ramsey pattern. Such increases of S/N and Q factor are obviously suitable for short term frequency stability improvements.

The use of optical pumping should also reduce the size of some systematic frequency offsets and allow a more precise evaluation of their uncertainties. Let us recall that

i) in an optically pumped cesium beam machine (OP Cs BM) the so-called Majorana transitions are highly improbable since the uniform magnetic field of the microwave interaction region can be extended to include both the optical pumping and optical detection regions.

ii) the frequency pulling of the 0-0 central line by the wings of neighbouring field dependent microwave lines should be minimized by using an efficient two laser pumping cycle which removes the populations of the adjacent Zeeman levels.

\* Permanent address : Laboratoire Primaire du Temps et des Fréquences, 61 avenue de l'Observatoire, 75014 Paris, France

\*\*\* On sabbatical leave from Laboratoire de Recherche sur les Oscillateurs et Systèmes, Dept. de Génie Electrique, Université Laval, Ste. Foy, P. Quebec, Canada G1K 7P4.

iii) since nearly all atoms are selected and detected regardless of their spatial position or velocity, the uncertainty in the distributed cavity phase shift determination should be smaller.

In this paper, we shall present our preliminary work on the OP Cs BM. We have made theoretical predictions on the pumping efficiency of a beam with two monochromatic or broadband laser fields.

We have also obtained experimental Ramsey resonance signals when the same laser is used both for the state preparation and detection. Provisional short term frequency stability predictions are then derived from such Ramsey pattern characteristics.

II. Optical pumping with two lasers.  
Theoretical predictions

Figure 1a,b,c, shows the energy level diagram corresponding to the  $D_2$  resonance line of Cs at 852.1 nm. A pumping scheme which tends to concentrate the whole population of the ground state onto the single Zeeman sublevel ( $F = 4$ ,  $m_F = 0$ ) of ( $F = 3$ ,  $m_F = 0$ ) must be realized with two laser light, one of them being necessarily  $\pi$  polarized. For example, if we refer to Fig. 1b and look at Table 1, we can see that the light of laser  $LD_1$ ,  $\pi$  or  $\sigma$  polarized, brings the atoms into the level  $f$  while  $LD_2$ ,  $\pi$  polarized, depopulates the sublevels  $f(M)$  with  $m_F \neq 0$ . Consequently after a sufficient number of pumping cycles, all the atoms should be accumulated in the  $f(0)$  sublevel.

We have done a theoretical analysis of the population difference built up,  $\Delta n(t) = n_f(t) - n_g(t)$ , in this case and compared the results derived with a direct phenomenological approach (rate equations) and a more rigorous treatment (density matrix formalism), the results are the following<sup>3</sup> :

i) if the two lasers are monochromatic, the stationary value of  $\Delta n$  is only 14 % instead of 100 % predicted by the rate equation approach (Fig. 2). This disturbing result is verified over a wide range of pumping power. It is due to the creation of hyperfine coherence when the laser frequency difference equals the hyperfine ground state splitting. This phenomenon is related to coherent population trapping effects<sup>4</sup>. Such effects, cannot be taken into account with the rate equations description.

ii) with the commercially available laser diodes, the spectral width is typically 30 MHz when the output power is around 5 mW. Such a spectral width is wider than the natural width of the  $D_2$  transition which is about 5 MHz. The excitations are then "broad line" provided the intensity remains lower than 50 mW/cm<sup>2</sup>. In this case, the laser fields cannot build up coherences between successive optical transitions. The population difference build up calculated with the density matrix formalism can now reach  $\sim 90$  % when the interaction time is long enough (Fig. 3). A very close result is obtained with the rate equations model in the broadband case<sup>5</sup>.



From the theoretical point of view, a pumping cycle with two commercially available laser diodes which are not too monochromatic, allows achievement of a quite total pumping. However, from the experimental point of view, the preliminary tests performed at NBS<sup>6</sup> have given disappointing results. This point should be clarified.

### III. Experimental set-up

The experimental set-up is shown schematically on figure 4. In our preliminary experiment, we have utilized some vacuum envelope, cesium oven and U-shaped microwave cavity existing in the laboratory. The size of the vacuum envelope is such as we did not had the possibility to design a uniform field region including pumping and Ramsey cavity regions. A vertical magnetic field is created in each "light-atom interaction zone". This gives an orientation for the polarization of the incoming light. A small cylindrical mumetal box insures the magnetic shielding. The C-field in the microwave interaction region is vertical too and it is produced by a U-shaped electromagnet made of conetic metal. The whole assembly cavity and electromagnet is placed inside a cylindrical magnetic shield of mumetal. The orientation field is therefore rather well defined except in the short spacing regions which separate the three shielding boxes. This may cause some trouble by mixing the populations of the hyperfine levels, specially when a two laser excitation is used. In the future, we shall operate a new machine.

The light-atom interaction regions A and B are identical and designed in order to minimize the laser stray light. Laser light beams are tightly focused onto a spot of  $5 \times 3 \text{ mm}^2$ . Large area pin photodiodes collects about 15 % of the whole fluorescence light. The signal in the A region is used for laser frequency locking purposes. The B region signal is an indication of the 0-0 clock transition.

The separation between the two oscillatory field regions is  $L = 21.5 \text{ cm}$ . The light sources are single frequency GaAs laser diodes operating around 852 nm (HLP 140J from Hitachi Company). We have designed and operated circuits which control the laser injection current to  $1 \times 10^{-6}$  and the heat sink temperature to  $2 \times 10^{-3}$  degrees for about one day.

The first derivative of the Cs beam fluorescence as a function of frequency is used to stabilize the laser diode frequency by means of a conventional servo system acting on the current. The servo bandwidth is  $\approx 10 \text{ kHz}$ .

### IV. Experimental results with one laser

The same laser  $\pi$  polarized light is used both for the optical pumping A region and the optical detection B region. In order to check the good efficiency of the pumping cycle, we sweep the laser frequency across the  $3 \rightarrow 2'$ ;  $3 \rightarrow 3'$ ;  $3 \rightarrow 4'$  transitions

Figure 5a-5b shows the fluorescence signal in the B region when the light in the A region is "off" and then "on". This record which has been performed with an intensity  $I_A = 23.4 \text{ mW/cm}^2$  and  $I_B = 0.34 \text{ mW/cm}^2$  shows that the  $3 \rightarrow 4'$  transitions gives a negligible fluorescence signal demonstrating a complete transfer of the population of the  $F = 3$  level onto the  $F = 4$  level without pumping. The whole fluorescence power in the B region is of the order of 1 nW. This value agree with the calculated value  $P_F$ . Assuming  $I_0 = 5 \times 10^{10} \text{ at/s}$ , an average number of photon per atom equals to 0.5, a collection efficiency of 0.15 and  $h\nu = 2.216 \times 10^{-19} \text{ J}$ , one obtain  $P_F = 1.1 \times 10^{-9} \text{ W}$ .

Figure 6a-6b shows the some experimental results when  $I_B \rightarrow I_A$  ( $I_B = 4.5 \text{ mW cm}^{-2}$ ;  $I_A = 0.34 \text{ mW cm}^{-2}$ ).

A hole is burned in the fluorescence signal when a weak pumping light is "on" in the A region. The origin of this dip is not surprising: the laser light is not monochromatic and the pumping efficiency is greater on the top of its power spectrum than on the wings. At low pumping intensity more atoms are removed when the centre frequency of the laser is in coincidence with the centre of the absorption line. The B signal reflects this spectral variation of the pumping efficiency.

Let us mention that the shape of the dip gives an information about the spectral width of the laser while its position on the fluorescence profile probes the orthogonality of the light and atomic beams.

The laser is now tuned onto the centre of the  $3 \rightarrow 4'$  absorption line and the microwave power is fed into the cavity. When the microwave is off we observe a background level composed of stray light, scattered light and fluorescence light. This last one increases when the microwave is on. The contrast of the useful signal is  $0.238 \text{ mW}/4.19 \text{ mW} = 5.7 \%$ . Moreover its S/N ratio can be optimized as a function of the intensity  $I_L$  of the light in the detection region because S increases with  $I_L$  and tends to saturate while N depends strongly on the stray light and scattered light which are strictly proportional to  $I_L$ . We have verified that the scattered light is negligible compared to the stray light ( $1.5 \times 10^{-3}$ ). Figure 7 shows the 0-0 Ramsey pattern obtained at optimum microwave power and optimum laser intensity  $I_L$ . The peak to valley central line exhibits a full width at half intensity  $\Delta\nu = 500 \text{ Hz}$ . The geometrical characteristics of our U-shaped waveguide are  $L = 21.5 \text{ cm}$ ;  $\ell = 1 \text{ cm}$ . The most probable velocity of the atoms in the beam is  $\alpha = 215 \text{ ms}^{-1}$ .

We have then compared the experimental 0-0 Ramsey pattern to the theoretical ones obtained for:

- 1) a Maxwellian distribution of atomic velocities

$$I_3(v)dv = 2 \alpha^{-4} v^3 e^{-v^2/\alpha^2} dv \quad (\text{See Fig. 8a})$$

- 2) a Maxwellian distribution weighted by  $\frac{1}{v}$

$$I_2(v)dv = \frac{4}{\sqrt{\pi}} \alpha^3 v^2 e^{-v^2/\alpha^2} dv \quad (\text{See Fig. 8b})$$

- 3) a Maxwellian distribution weighted by  $\frac{1}{v^2}$

$$I_1(v)dv = 2 \alpha^{-2} v e^{-v^2/\alpha^2} dv \quad (\text{See Fig. 8c})$$

Table II summarizes the main characteristics of the central line obtained in the three cases. Moreover, the best fit between experimental and theoretical results is obtained in the case n° 1 (Fig. 8a). The Maxwellian distribution of velocities is not affected by the optical pumping and optical detection when one uses the same laser. This result agrees with Arditi's conclusion<sup>7</sup>. Let us remember that when one uses a cycling transition for the optical detection of the resonance, the Maxwellian distribution is modified by the  $1/v$  factor leading to a linewidth narrowing factor of  $\sim 1.1$  (Table II). This agrees with Lewis experiments<sup>8</sup>.

If we assume that a square wave modulated microwave interrogating technique is used to lock the frequency of a quartz crystal oscillator to this hyperfine transition, it can be shown that<sup>9</sup>: the one-sided power spectral density  $S_y$  of fractional frequency fluctuation of the controlled quartz oscillator is approximately given by  $S_y \sim 0.30 (\Delta\nu/\nu)^2 S_{11}/I^2$ .  $S_{11}$  is the power spectral density of the mean value  $I'$  of the photo current when the microwave frequency is  $\nu_0 \pm \Delta\nu/2$ ,  $\Delta\nu$  being the depth of the frequency modulation.  $I_0$  is the peak to valley signal. If we assume that  $S_{11}$  has a white spectrum, then the two sample standard deviation of fractional frequency fluctuations of the controlled quartz crystal oscillator is given by:  $\sigma_y^2(\tau) = S_y/2\tau$ . We get from our experimental data:

$$\sigma_y(1\text{ s}) = 5 \times 10^{-11}$$

one may expect to increase this stability by reducing the stray light and by choosing a more sophisticated optical pumping and detection scheme.

### V. Conclusion

Our preliminary results obtained with our one laser diode optically pumped Cs beam machine are promising. Detailed studies have to be done in order to determine the best laser combinations for the optical pumping and detection schemes which would allow to increase as far as possible the S/N ratio. The cycling transition which greatly improves the fluorescence power in the detection zone must be particularly studied in order to know how the laser frequency noise is transformed into fluorescence photon noise via the cycling process. Such investigations are in progress.

### Acknowledgement

The authors would like to thank Dr. C. Audoin for his guidance and encouragement in this project. Strong appreciations are also expressed to P. Petit, J. Viennet, J. Dupont, D. Guitard, J. Cachenauf for contributing technical help. The authors would also acknowledge the Bureau National de M trologie for its financial support.

### References

1. M. Arditi, J.L. Picqu , J. Phys. Let. 41L 379 (1980)
2. H.J. Gerritsen and G. Nieuhuis, Appl. Phys. Let. 26 347 (1975)
3. E. de Clercq, M. de Labachellerie, G. Avila, P. C rez, M. T tu, J. Phys. 45, 239 (1984)
4. G. Alzetta, A. Gozzini, L. Moi, G. Orriols, Nuovo Cimento 36B, 5 (1976)
5. Wu Xinxin, Xu Yueting, Tian Kunyn, Yao Shutong, Xie Linzhen, Wang Yiqiu, "Some aspects in the design of the optically pumped Cs beam tube" presented at the International Conference on Frequency Standards in Hongchow, Sept. 1983
6. L.L. Lewis, Proceedings of the Workshop on Spectroscopic Applications of slow atomic Beams held at NBS Gaithersburg, 14-15 April 1983, ed. by W.D. Phillips, NBS, Spec. pub. 653
7. L. Arditi, Metrologia 18, 59 (1982)
8. L.L. Lewis, private communication, April 1984
9. M. Jardino, M. Desaintfuscien, R. Barillet, J. Viennet, P. Petit, C. Audoin, Applied Phys. 24, 107 (1981)

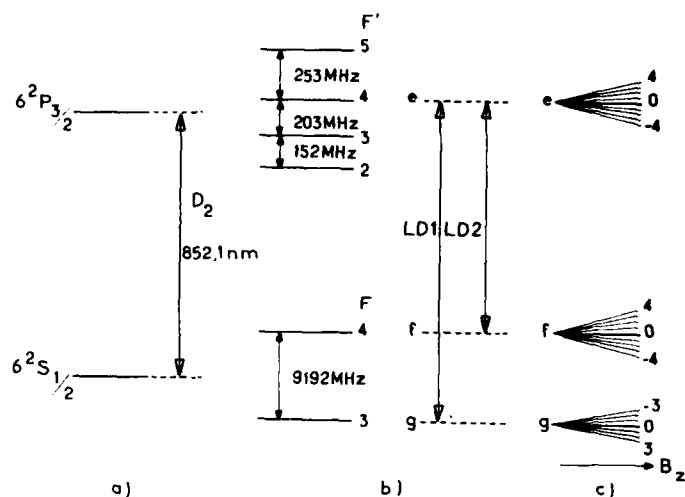


Fig. 1 Energy level diagram of the cesium  $D_2$  resonance line  
a) fine and hyperfine structure  
b) laser excitation: both lasers are  $\pi$  polarized  
c) Zeeman structure of the e, f, g levels.

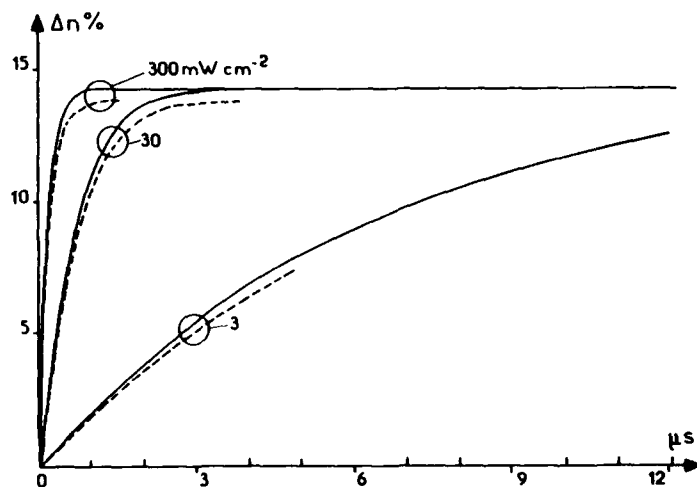


Fig. 2 Time evolution of the population difference between ( $F = 4$ ,  $m_F = 0$ ) and ( $F = 3$ ,  $m_F = 0$ ) levels calculated with the density matrix formalism for monochromatic excitations.  
● full line: two  $\pi$  polarized lasers tuned onto the ( $3 \rightarrow 4'$ ) and ( $4 \rightarrow 4'$ ) transition  
● dotted line: one  $\pi$  polarized laser tuned onto the ( $3 \rightarrow 4'$ ) transition for comparison.

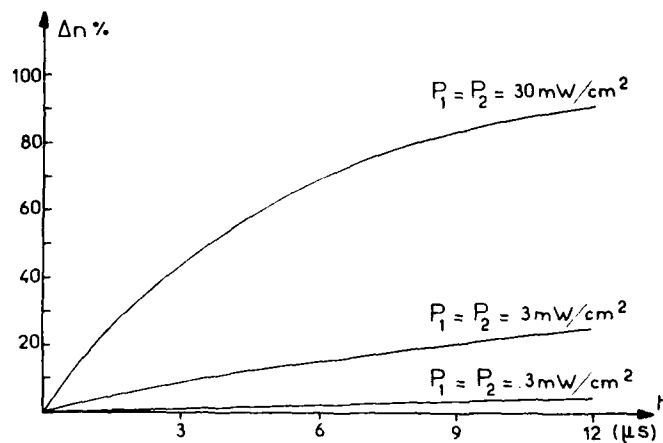


Fig. 3 Time evolution of  $\Delta n(t)$  calculated with the density matrix model for broadband excitation.

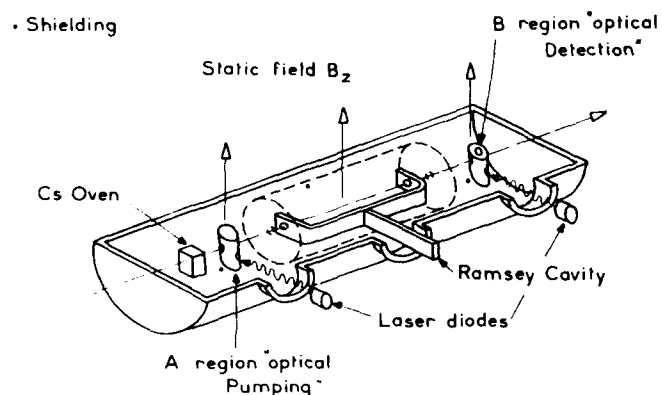


Fig. 4 The experimental set-up.

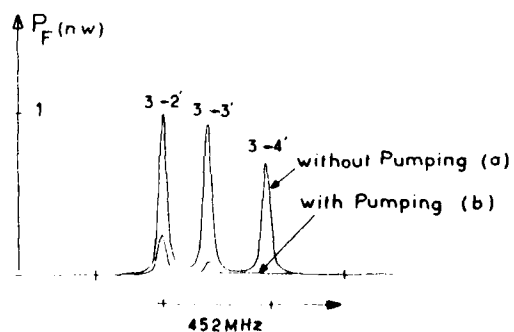


Fig. 5 Fluorescence signal in the detection region:  
a) without upstream pumping  
b) with upstream pumping

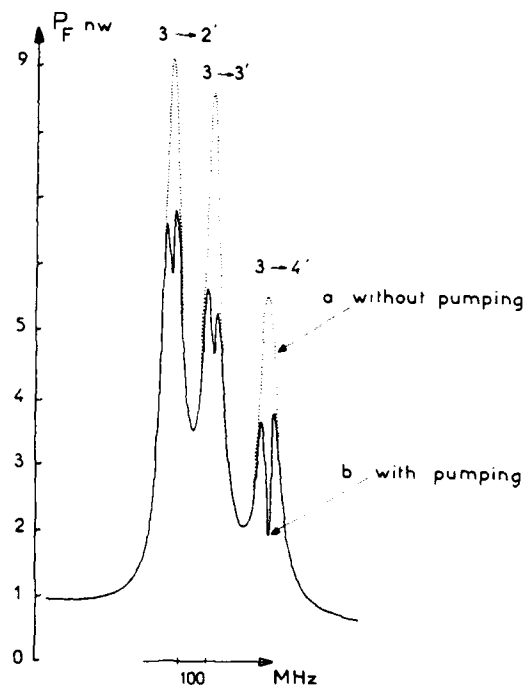


Fig. 6 Same signals as in Fig. 5 except that the laser intensity is greater in the B region than in the pumping region.

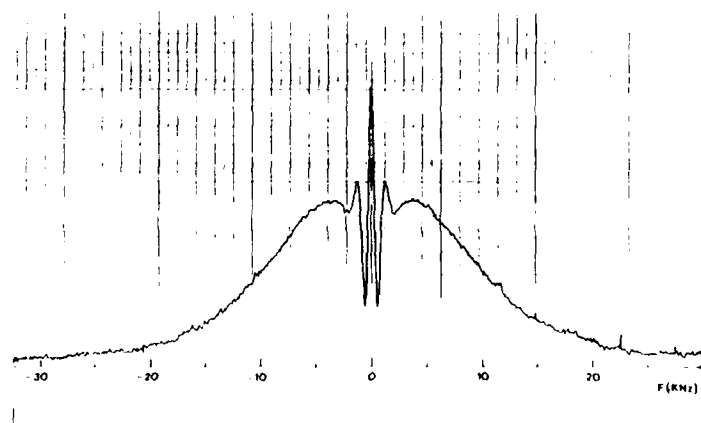


Fig. 7 Ramsey-Rabi 0-0 pattern at optimum microwave field.

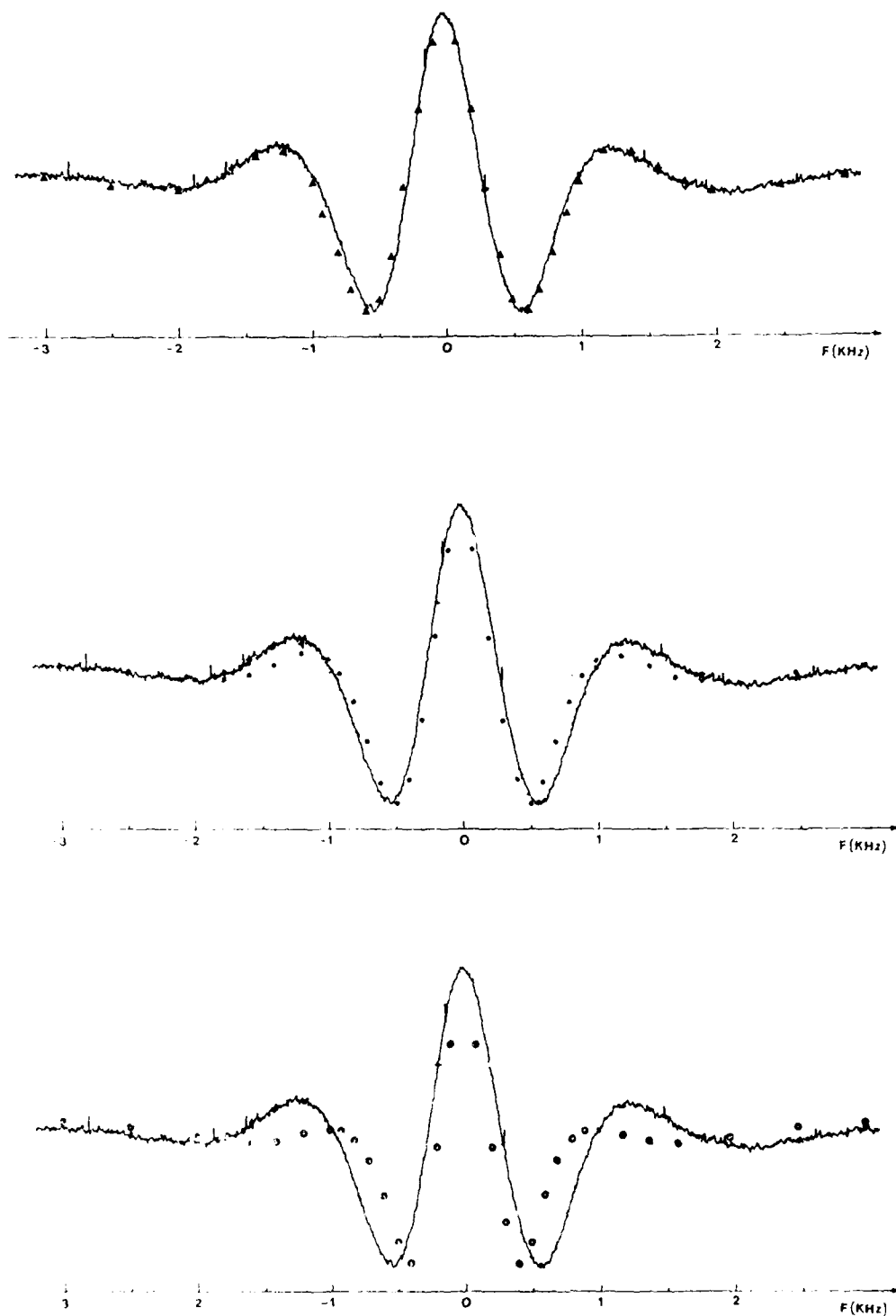


Fig. 8 - Expanded view of the 0-0 Ramsey pattern

- a)  $\blacktriangle$  are computed points using a Maxwellian distribution of atomic velocities
- b)  $\bullet$  are computed points using a modified  $(\frac{1}{v})$  distribution
- c)  $\circ$  are computed points using a modified  $(\frac{1}{v^2})$  distribution

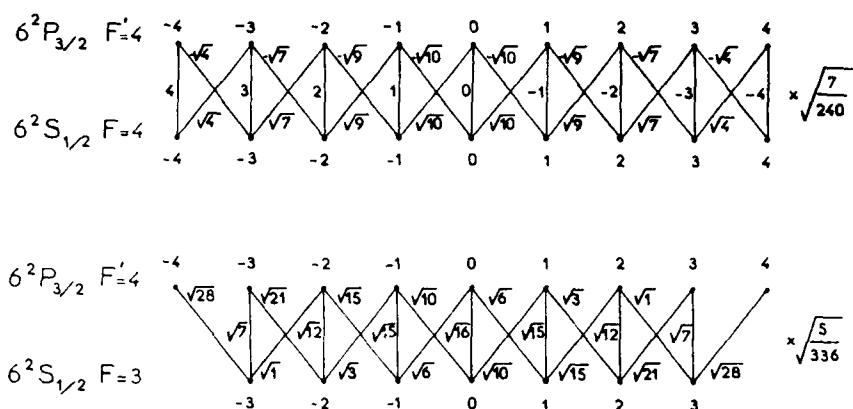


Table I - Probability transfer coefficients for the transitions  $F' = 4 \rightarrow F = 4$  and  $F' = 4 \rightarrow F = 3$ .

WEIGHTING FUNCTION	$(\frac{1}{V})^0$	$\frac{1}{V}$	$\frac{1}{V^2}$
MAXIMUM PROBABILITY $P_{MAX}$	0.755	0.727	0.677
OPTIMUM FIELD $\frac{4b}{\alpha}$	3.8	3.25	2.70
FULL WIDTH AT $P_{MAX}/2$	$0.65 \frac{\alpha}{L}$	$0.56 \frac{\alpha}{L}$	$0.46 \frac{\alpha}{L}$
PEAK TO VALLEY FWHM	$0.52 \frac{\alpha}{L}$	$0.48 \frac{\alpha}{L}$	$0.38 \frac{\alpha}{L}$
NUMERICAL VALUES (Hz) IN OUR CASE : $L = 0.215m$ $\alpha = 215ms^{-1}$	525	480	380

Table II - Theoretical transition probabilities characteristics for a Ramsey type cavity.

# CESIUM CLOCKS DEPLOYED IN THE GLOBAL POSITIONING SYSTEM: DESIGN AND PERFORMANCE DATA

Helmut Hellwig and Martin Levine  
Frequency and Time Systems, Inc.  
Beverly, MA

The first Preproduction Model Cesium Frequency Standard (Model No. FTS 4400) was qualified for spaceflight in 1979. This milestone followed an intense engineering development program dating back to 1973/1974, including the construction of eight flight-candidate and engineering development models, three of which were tested on board of NTS-2 and Navstar 3. Since then, a total of ten fully flight-qualified cesium clocks have been delivered: five Preproduction Models (Model FTS 4400) and five Space Vehicle Clocks (Model FTS 4401). Of these, several are on board Navstar GPS satellites either operating or in operational storage.

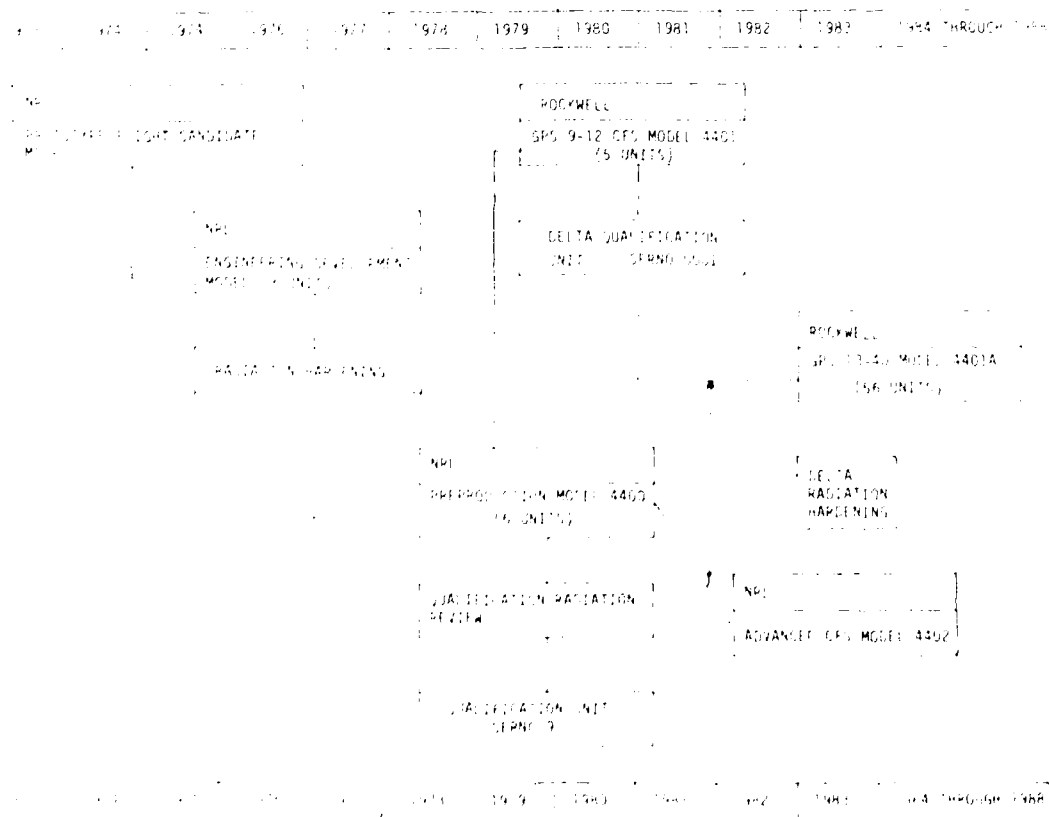
Currently, FTS is constructing five advanced Preproduction Models (Model FTS 4402) as well as manufacturing the full GPS Block II complement of 56 advanced Space Vehicle Clocks (Model FTS 4401A). The design and applications history of these clocks is depicted in Fig. 1 and Tables 1 and 2. The basic design concept of these clocks which include a digital integrator featuring an infinite loop-time constant is depicted in the general block diagram of Fig. 2 and the detailed servo/integrator subsystem in Fig. 3. Table 3 shows the record of failures encountered during qualification and acceptance testing as well as prior to launch of the five units which were produced of the Model 4401 and delivered in 1981. It is interesting to note that none of the failures are related to the specific aspects of cesium clock but are failures related to electronic parts and assembly.

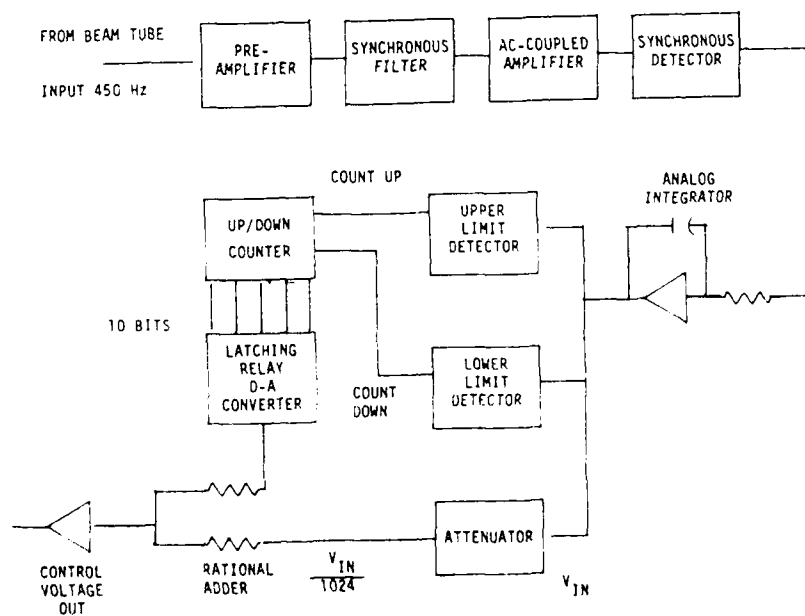
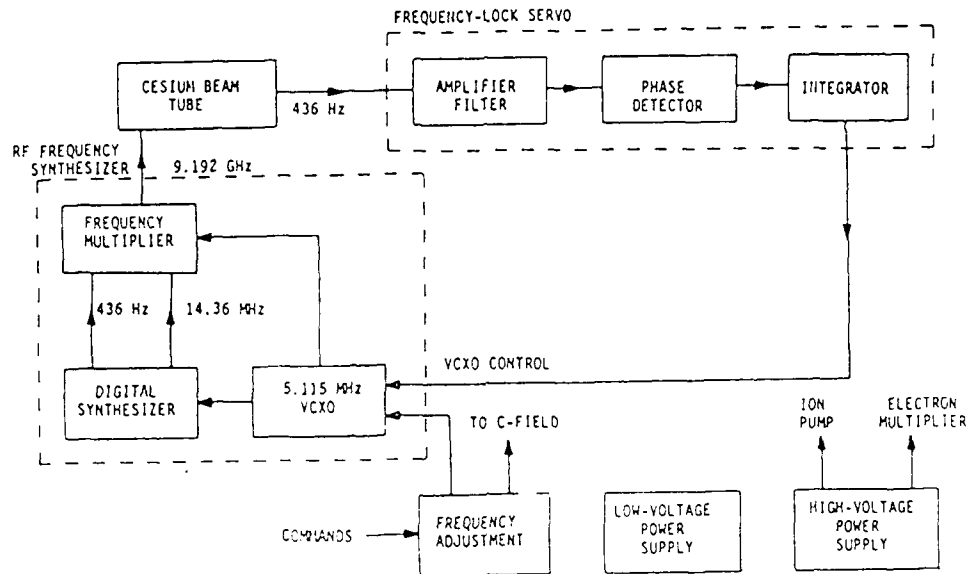
One of the clocks of the earlier Preproduction series, Model 4400, has been taken out of service after about four years of operation as a result of a cesium oven failure. Details are given in Table 4 and Fig. 4. This failure mode has been completely eliminated by FTS through a design change which was implemented in 1980.

The frequency stability results obtained during the acceptance testing of the five clocks of the Model 4401 are summarized in Fig. 5. These results indicate that short-term stabilities of a few parts in  $10^{12}$  and long-term stabilities ( $\geq 1$  day) of nearly  $10^{-13}$  have been consistently achieved and that performance variations between clocks have been unusually small. Data obtained from the clocks on board of Navstar 5 and Navstar 6 demonstrates stabilities in the  $10^{-13}$  region (ref. Fig. 6). The last figure, Fig. 7, depicts the multi-year performance of the quartz crystal oscillators within the cesium clocks on board of Navstar 5 and 6 indicating that the quartz crystal oscillators exhibit a free-running aging of much less than  $1 \times 10^{-11}$  per day.

This work was supported by the U. S. Air Force (through Rockwell International) and the Naval Research Laboratory under the following contracts: FO4701-74-C-0153, FO4701-83-C-0031, N00014-74-C-0061, N00014-81-C-2546, N00014-83-C-2205.

FIG. 1: CESIUM CLOCK DEVELOPMENT HISTORY





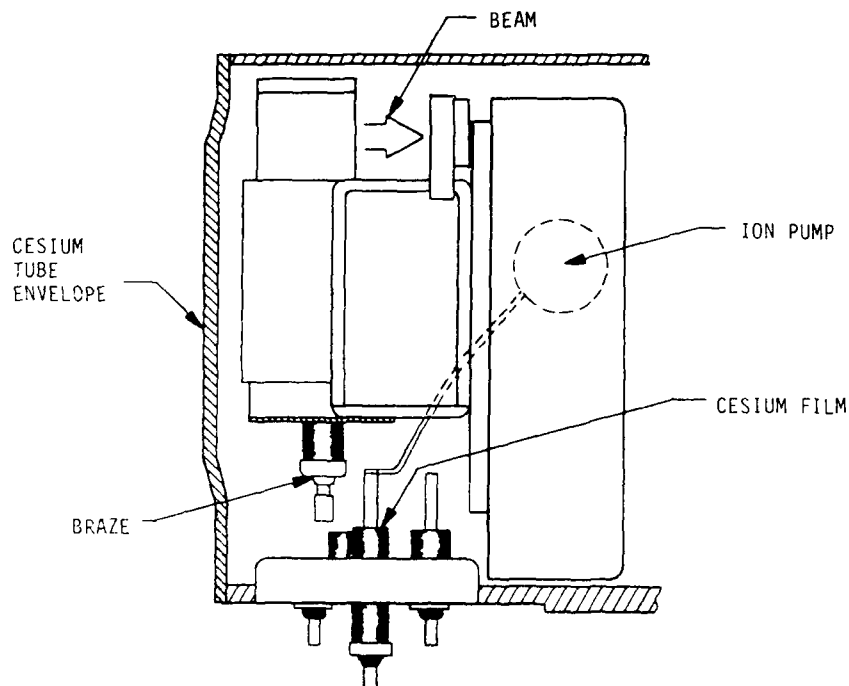


FIG. 4: CROSS-SECTION VIEW OF THE CESIUM OVEN MOUNTING CONFIGURATION INCLUDING THE HIGH-VOLTAGE FEEDTHROUGH FOR THE ION PUMP. THE BRAZE FAILURE OCCURRED AT THE TERMINAL WHICH CARRIES THE ONE-TIME CURRENT USED TO PIERCE THE CESIUM AMPOULE. THIS CAUSED EMISSION OF CESIUM AND ITS DEPOSIT AS A FILM ON THE NEARBY FEEDTHROUGH. THE RESULTING OHMIC CONDUCTIVITY (ABOUT  $10 \text{ M}\Omega$ ) IS DEPENDENT ON THE EQUILIBRIUM BETWEEN CESIUM DEPOSIT RATE AND REEVAPORATION FROM THE FILM. THE OBSERVED ION PUMP CURRENT OF UP TO 200 mA IS DUE TO THIS OHMIC SHUNTING BY THE CESIUM FILM.

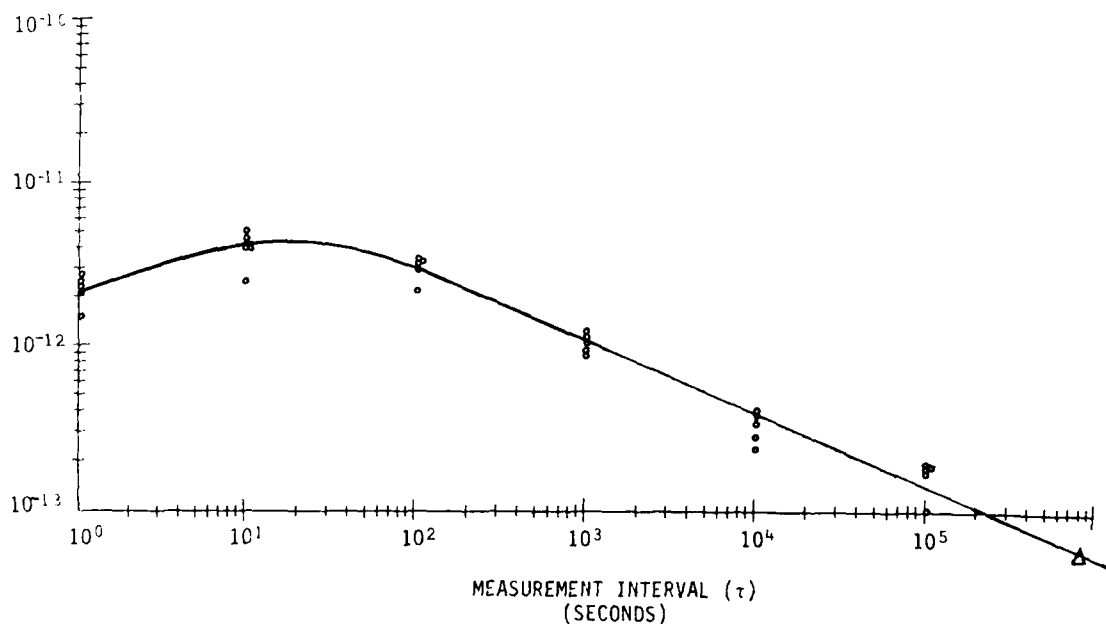


FIG. 5: FTS 4401 CESIUM FREQUENCY STANDARDS FREQUENCY STABILITY SUMMARY FROM THE ACCEPTANCE TESTING OF FIVE DEVICES. ALSO SHOWN IS ONE DATA POINT (TRIANGLE) FROM LONG-TERM, IN-ORBIT OBSERVATIONS OF THE PREPRODUCTION MODEL FTS 4400 SN 11 (ON BOARD OF NAVSTAR 6).



# STABILITY OF SV 9 CS. CLOCK VS. NBS CL. 9

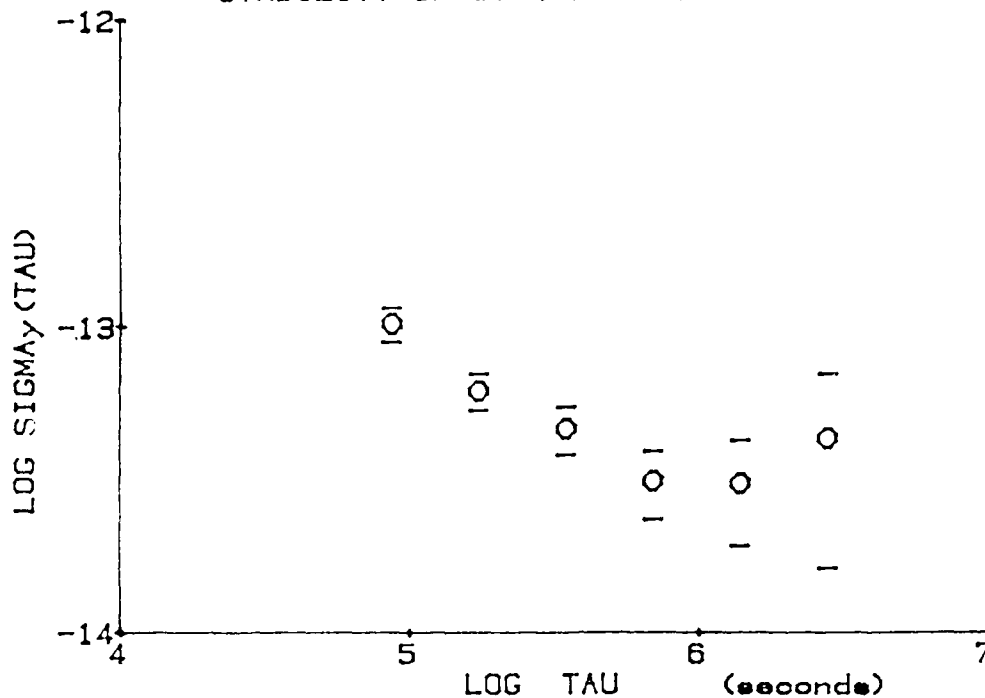


FIG. 6: IN-ORBIT FREQUENCY STABILITY AS MEASURED BY THE NATIONAL BUREAU OF STANDARDS, BOULDER, CO. DATA ARE REPRODUCED FROM THE PAPER, "SEPARATING THE VARIANCES OF NOISE COMPONENTS IN THE GLOBAL POSITIONING SYSTEM" BY DAVID W. ALLAN AND MARC WEISS (PROCEEDINGS OF THE FIFTEENTH ANNUAL PRECISE TIME AND TIME INTERVAL (PTTI) APPLICATIONS AND PLANNING MEETING, DEC. 1983). THE CESIUM CLOCK IS MODEL 4400, SERIAL NO. 11, ON BOARD NAVSTAR 6.

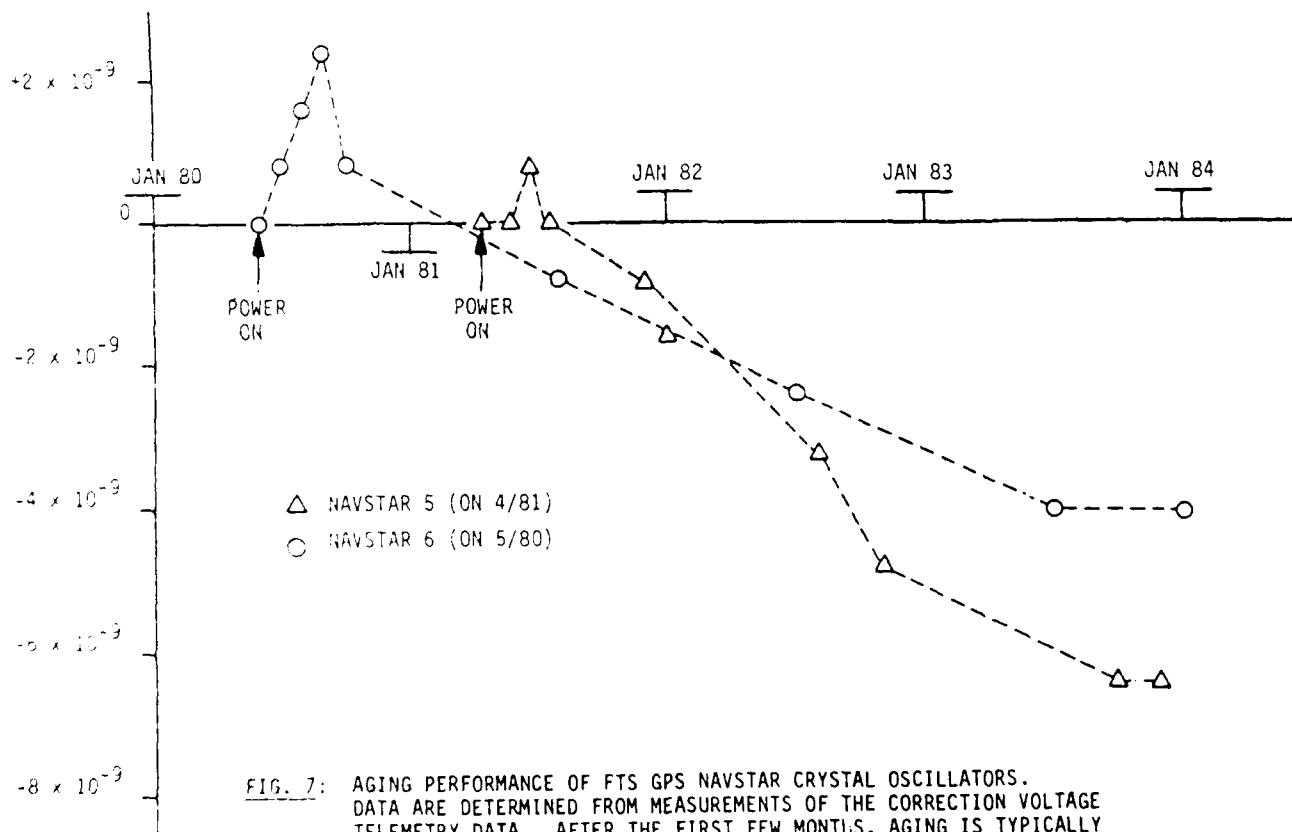


FIG. 7: AGING PERFORMANCE OF FTS GPS NAVSTAR CRYSTAL OSCILLATORS. DATA ARE DETERMINED FROM MEASUREMENTS OF THE CORRECTION VOLTAGE TELEMETRY DATA. AFTER THE FIRST FEW MONTHS, AGING IS TYPICALLY IN THE RANGE OF  $10^{-12}$  PER DAY.

# CESIUM CLOCK APPLICATIONS HISTORY

<u>MODEL</u>	<u>FTS MODEL</u>	<u>APPLICATION</u>
PROTOTYPE	FCM	TWO UNITS FLOWN ON NTS-2, JUNE 1977
ENGINEERING	FTS 4200	INTENDED FOR TEST AND EVALUATION: SN 8 USED AS RADIATION-HARDENING TEST BED.
PREPRODUCTION	FTS 4400	UPGRADED AND QUALIFIED VERSION OF FTS 4200: SN 10 FLOWN ON NAVSTAR 5, SN 11 ON NAVSTAR 6
PRODUCTION	FTS 4401	PRODUCTION VERSION OF FTS 4400: SN 2 FLOWN ON NAVSTAR 8
BLOCK II PRODUCTION	FTS 4401A	BLOCK II IMPROVED VERSION OF FTS 4401: GREATLY ENHANCED NUCLEAR HARDENING.
ADVANCED PREPRODUCTION	FTS 4402	PERFORMANCE UPGRADE OF FTS 4401: ENHANCED NUCLEAR HARDENING.

TABLE 1: APPLICATIONS OF THE VARIOUS MODELS OF THE CESIUM CLOCK FAMILY DEVELOPED AND BUILT BY FTS FOR NAVSTAR/GPS

# CESIUM CLOCK DESIGN HISTORY

<u>MODEL</u>	<u>PARTS PROGRAM</u>	<u>RELIABILITY ANALYSIS</u>	<u>CONTROLS/COMMENTS</u>
PROTOTYPE (FCM)	NONE	NONE	COMMERCIAL PARTS AND PRACTICES
ENGINEERING (FTS 4200)	FLIGHT-QUALIFIED PART TYPES NO SCREENING	NONE	QC INSPECTION
PREPRODUCTION (MODEL FTS 4400)	FLIGHT-QUALIFIED PART TYPES PARTIAL SCREENING	PARTS STRESS ANALYSIS	QC INSPECTION QUALIFICATION TEST
PRODUCTION (MODEL FTS 4401)	FLIGHT-QUALIFIED AND PROGRAM-APPROVED PARTS FULL SCREENING NON-STD PARTS CONTROL	WCCA FMEA PARTS STRESS ANALYSIS RELIABILITY PREDICTION	CONFIGURATION CONTROL PROCESS CONTROLS MATERIALS CONTROLS QC INSPECTION FRACA AUTOMATED SPECIAL TEST EQUIPMENT DELTA-QUALIFICATION TESTING
BLOCK II PRODUCTION (MODEL FTS 4401A)	SAME AS FTS 4401 ADDITIONAL RADIATION SCREENING	SAME AS FTS 4401	SAME AS FTS 4401
ADVANCED PREPRODUCTION (MODEL FTS 4402)	FLIGHT QUALIFIED PARTS FULL SCREENING	SAME AS FTS 4401	SAME AS FTS 4401

TABLE 2: SPACE FLIGHT REQUIREMENTS AS IMPOSED ON THE VARIOUS MODELS OF THE CESIUM CLOCKS DEVELOPED AND BUILT BY FTS FOR NAVSTAR/GPS

# MODEL 4401 HARDWARE FAILURES

<u>SERIAL NO.</u>	<u>DATE OF FAILURE</u>	<u>FAILURE ENVIRONMENT</u>	<u>CAUSE OF FAILURE/ LOCATION OF FAILURE</u>	<u>CORRECTION</u>
0001	8/25/81	QTP (AT 35 °C)	PINCHED CRYSTAL LEAD TO OVEN HEATER ASSEMBLY OSCILLATOR ASSEMBLY OF CFS	UPDATE ASSEMBLY PROCEDURE
	8/28/81	QTP (AT 35 °C)	OPEN TRACE BETWEEN U5-15, AND U14-3 DUE TO CUT D/A CONVERTER	UPDATE ASSEMBLY PROCEDURE
	11/29/82	SPACECRAFT SYSTEM INTEGRATION	U5 (LM109AH) FAILURE ON SERVO BOARD	NONE (PART FAILURE)
0002	4/1/82	SPACECRAFT SYSTEM INTEGRATION	L14 SHORTED TO C46 IN FREQUENCY MULTIPLIER ASSEMBLY	UPDATE ASSEMBLY PROCEDURE
0003	8/18/82	ATP (AT 35 °C)	OPEN CONDITION OF CR35 AND CR36 ON DAC BOARD	NONE (PART FAILURE)
0004	3/16/82	ATP (AT -19 °C)	INSUFFICIENT SOLDER IN SMA CONNECTORS USED ON CABLES	RADIOGRAPHY PERFORMED ON CABLE ASSEMBLIES
0005	--	--	NO FAILURES	

TABLE 3: COMPLETE LISTING OF FAILURES ENCOUNTERED DURING THE QUALIFICATION (QTP) ACCEPTANCE TESTING (ATP) AND AFTER DELIVERY OF THE PRODUCTION SEGMENT OF FIVE CLOCKS (SERIAL NO. 0001 THROUGH 0005) OF THE MODEL 4401. IT IS INTERESTING TO NOTE THAT NONE OF THE FAILURES ARE SPECIFICALLY RELATED TO AN ATOMIC CLOCK BUT ARE FAILURES RELATED TO ELECTRONIC PARTS AND ASSEMBLY.

## NAVSTAR 6 - PRELIMINARY STUDY (FTS 4400, SN 11)

SHIPPED FROM FTS 7 SEPTEMBER 1979

LAUNCHED 26 APRIL 1980

POWER ON IN ORBIT: 6 MAY 1980

POWER OFF: 18 FEBRUARY 1984

- TOTAL HOURS IN ORBIT: 33168

CESIUM BEAM CURRENT DECREASED TO NEGLIGIBLE LEVEL  
BETWEEN 20 JANUARY 1984 AND 4 FEBRUARY 1984

ION PUMP INDICATION

- 40 MICROAMPS IN JANUARY 1981

- ABRUPT RISE TO 140 MICROAMPS IN SEPTEMBER 1982

- SLOW RISE TO 200 MICROAMPS IN NOVEMBER 1983

- ION PUMP CURRENT DECREASE CORRELATED WITH  
END-OF-LIFE BEAM SIGNAL DECREASE

TABLE 4: EVENT HISTORY OF THE CESIUM CLOCK ON BOARD NAVSTAR 6 (SPACE VEHICLE 9). THE DATA SUPPORT THE FOLLOWING FAILURE ANALYSIS: CESIUM OVEN BRAZE FAILURE RESULTING IN ACCELERATED EXPENDITURE OF CESIUM (ALSO CAUSING CESIUM FILM FORMATION ON ION PUMP INSULATOR LEADING TO FALSE CURRENTS) BY A FACTOR OF APPROXIMATELY 2.

FOLLOWING A DESIGN CHANGE IMPLEMENTED IN 1980, FTS-BUILT CESIUM BEAM TUBES HAVE NEVER AGAIN EXHIBITED THIS FAILURE MODE.

MODIFICATION OF AN O-1695A/U  
CESIUM BEAM FREQUENCY STANDARD  
FOR RETROFIT OF REPLACEMENT  
CESIUM BEAM TUBES

J.C. Robb  
Frequency and Time Systems, Inc.  
Beverly, MA

### Summary

Hardware and electronic circuitry has been designed to modify an O-1695A/U Cesium Beam Frequency Standard (Hewlett-Packard 50622 option 010) so that the modified instrument may accept either a FTS-1-100 series cesium beam tube or the original equipment HP-5084 series cesium beam tube. The Navy currently uses O-1695A/U cesium beam frequency standards in the Verdin Program.

The requirement exists for alternate sources of replacement cesium beam tubes for O-1695A/U atomic frequency and time standards deployed in DOD installations. The O-1695A/U Cesium Beam Frequency Standard, developed by Hewlett-Packard originally employs a cesium beam tube 6.5 inches in length and 4 inches in diameter. The design challenge included the achievement of simple electronic interface as well as reconfiguration to accept the larger FTS-1-100 tube featuring a 3 x 3 x 15 inch envelope.

Furthermore, to preserve the alternate source capability, the retrofit design modifications must be compatible with installation of either the original HP-5084 series tube or the FTS-1-100 series tube.

The retrofitting of the FTS-1-100 beam tube into the O-1695A/U improves the performance of the instrument in cesium beam tube related aspects: in particular, the inherently higher line Q results in improved short and long term stability. Other aspects of the instrument's performance including its qualification status that are not cesium beam tube related are preserved by the retrofit design.

Details of the retrofit design are presented with performance data measured in accordance with MIL-F-28811 (Cesium Beam Tube Frequency Standard).

### Introduction

The O-1695A/U is a militarized Cesium Beam Frequency Reference (CBFR). It is a rack mountable 6" x 7" x 20" package with various front and rear panel sinusoidal and pulse outputs as well as a 24 hour digital clock display and BCD time code output. The O-1695A/U was manufactured as option 010 of the Hewlett-Packard (HP) 50622 and is currently deployed in various DOD facilities including both shipboard and airborne applications. The O-1695A/U meets the specifications of MIL-F-28811, the relevant military specification for CBFRs.

### Need For Retrofit Capability

The CBFR depends on the cesium beam tube for proper operation, maintaining the accuracy and long term stability of the instrument. The cesium beam tube is a limited life part and must be replaced periodically during the life of the instrument. HP has discontinued manufacture of the O-1695A/U.

The retrofit design provides a cesium beam tube alternate source capability where one did not previously exist, allowing the retrofitted instrument to accept either the original equipment cesium beam tube or the FTS-1-100 cesium beam tube.

### Design

The threefold design goal of the retrofit effort was achieved:

- (1). After the remodeling process the modified O-1695A/U accepts either cesium beam tube. Furthermore, the replacement of either cesium beam tube does not require special spare parts nor instrumentation or skill levels greater than that required by cesium beam tube replacement in the original equipment.
- (2). The result of remodeling of O-1695A/U has a minimal impact on the electrical subassemblies of the O-1695A/U.
- (3). The remodeled instrument meets or exceeds the specifications of MIL-F-28811.

Figure 1 shows a comparison of the mechanical aspects of the two cesium beam tubes. The dissimilarity in the shapes of the two beam tubes posed the major design challenge. Figure 2 a-f shows the instrument before and after the retrofit. In the retrofitted instrument either tube can be replaced without disturbing any other subassemblies. The mounting hardware for the FTS cesium beam tube remains permanently in the retrofitted instrument and does not interfere with the mounting of the HP tube. A simple electrical harness interface consisting of a 16 pin socket and two high voltage connector junctions both mounted on the instrument center panel accommodate either cesium beam tube. (See Figure 2d).

A comparison of Figures 2a and 2b points out the basic mechanical differences between the original instrument and the retrofitted instrument. The transition from the original equipment to the retrofitted instrument is described, with the aid of Figures 2a and 2b, as follows:

The batteries and the card cage (located in the upper middle section of Figure 2a) have been removed to create a volume to house either the HP or FTS cesium beam tube (see Figures 2b and 2e) as well as part (two thirds) of the new battery supply. An L-shaped shelf has been added in this volume the top side of which supports the battery pack (see Figure 2b) and the bottom side of which provides a mounting surface for the multiplier and harmonic generator (see Figure 2d). The L-shaped shelf also provides a rigid coupling between the side and the center panels and the front and rear sections of the instrument. To accommodate the length of the FTS cesium beam tube, the power supply section (in the upper left hand section of Figure 2a) has been altered by reshaping the power

supply section housing. The volume originally occupied by the HP cesium beam tube, multiplier and harmonic generator (lower middle section of Figure 2a) houses the card cage, removed from the upper section, and the remainder of the new battery supply (lower middle section of 2b).

The major change in mass distribution resulting from the chassis redesign is the change in mounting location of the cesium beam tube from the side panel of the instrument to the center panel. The center panel is rigidly attached to both side panels by support brackets and mechanical subassemblies with the overall effect of making the retrofit chassis as rigid as the original equipment chassis.

The electrical adjustment range of the O-1695A/U is wide enough in all aspects to accommodate proper operation of the FTS cesium beam tube.

#### Performance Considerations

Using the FTS cesium beam tube in the retrofitted O-1695A/U should yield improved performance in cesium beam tube related aspects of stability due to the increased figure of merit. Table 1 below compares performance of the two cesium beam tubes.

	<u>FTS-1-100</u>	<u>HP5084</u>
Figure of Merit	>3	1.5 (estimate)
Linewidth	450 (typical)	1300 (typical)

Table 1.

#### Testing and Results

Two O-1695A/U CBFR's were retrofitted and FTS-1-100 cesium beam tubes were installed. The two units were subjected to first article and environmental tests as specified in MIL-F-28811. Table 2 lists relevant results of the testing. They indicate that the retrofitted O-1695A/U with an FTS cesium beam tube installed meets or exceeds the requirements of MIL-F-28811 in performance related aspects. In particular, the improved stability reflects the better performance parameters of the FTS-1-100 cesium beam tube. No damage or physical upset of any kind resulted from shock and vibration testing. Furthermore, the change in frequency during shock and vibration testing was well within the specification and reflects the mechanical integrity of the retrofit design.

#### Acknowledgements

The author would like to thank Richard Bachler and Gary Alexanian, both of Frequency and Time Systems, Inc. for their time and efforts in all phases of the work described above.

The work described was performed under contract with Naval Research Laboratories (N0014-83-2090).

# TEST RESULTS

<u>PARAMETER</u>	<u>MIL-F-28811 SPECIFICATION</u>	<u>MEASURED (AVERAGE OF 2 UNITS)</u>
ACCURACY	$\pm 3 \times 10^{-11}$	$0.33 \times 10^{-11}$
STABILITY 1 (sec)	$7 \times 10^{-11}$	$2.8 \times 10^{-11}$
10 (sec)	$2.2 \times 10^{-11}$	$0.95 \times 10^{-11}$
100 (sec)	$7 \times 10^{-12}$	$3.5 \times 10^{-12}$
1000 (sec)	$2.2 \times 10^{-12}$	$1.4 \times 10^{-12}$
10000 (sec)	$7 \times 10^{-13}$	$4.5 \times 10^{-13}$
WARM-UP (from $-28^{\circ}\text{C}$ )	$\leq 20$ minutes	15 minutes
SETTABILITY	$\pm 2 \times 10^{-12}$	$0.9 \times 10^{-12}$
REPRODUCIBILITY	$\pm 1 \times 10^{-11}$	$< 0.2 \times 10^{-11}$
SHOCK (accuracy $\Delta f$ ) MIL-S-901-C	$\pm 2 \times 10^{-11}$	$0.1 \times 10^{-11}$
VIBRATION (accuracy $\Delta f$ ) MIL-STD-167-1	$\pm 2 \times 10^{-11}$	$0.15 \times 10^{-11}$
BATTERY LIFE $+25^{\circ}\text{C}$	1.0 hour	1.0 hour
$-28^{\circ}\text{C}$	0.5 hour	0.5 hour
$+65^{\circ}\text{C}$	0.5 hour	0.5 hour

Table 2.

CESIUM BEAM TUBE COMPARISON - MECHANICAL

HP5084

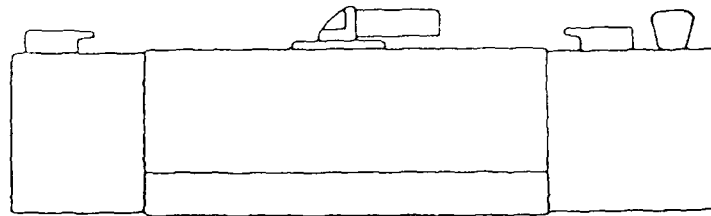
$L \approx 6.5"$

$D \approx 4"$  (cylindrical)

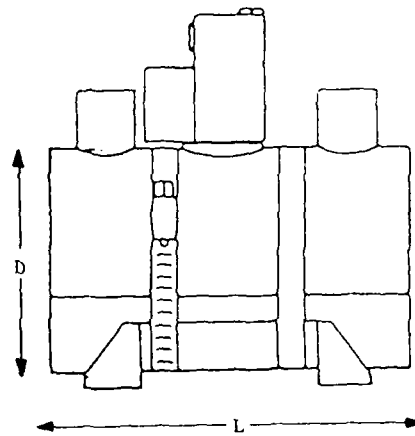
FTS-1-100

$L \approx 13"$

3" x 3" (rectangular)



FTS-1-100



HP5084

Figure 1.

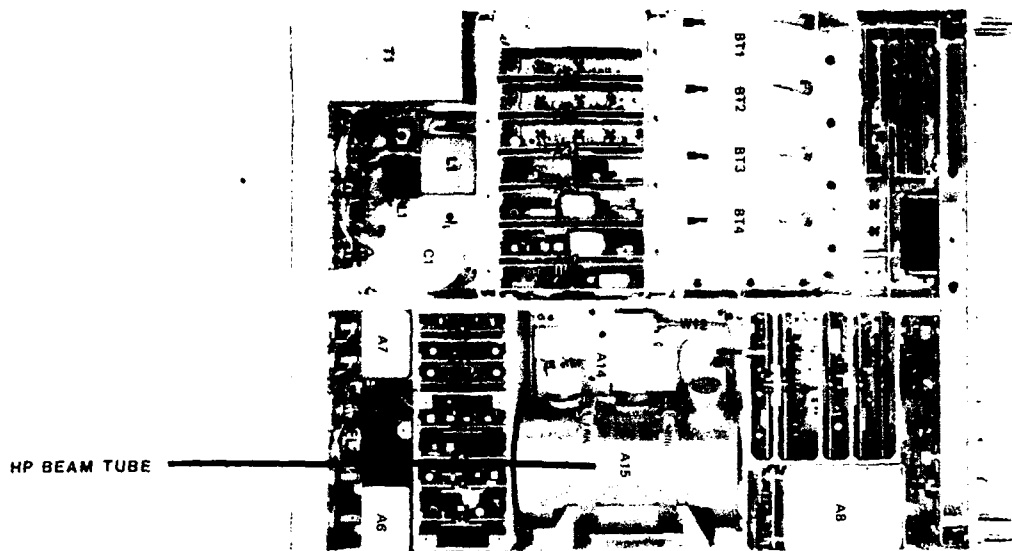


Figure 2a. Top View before Retrofit

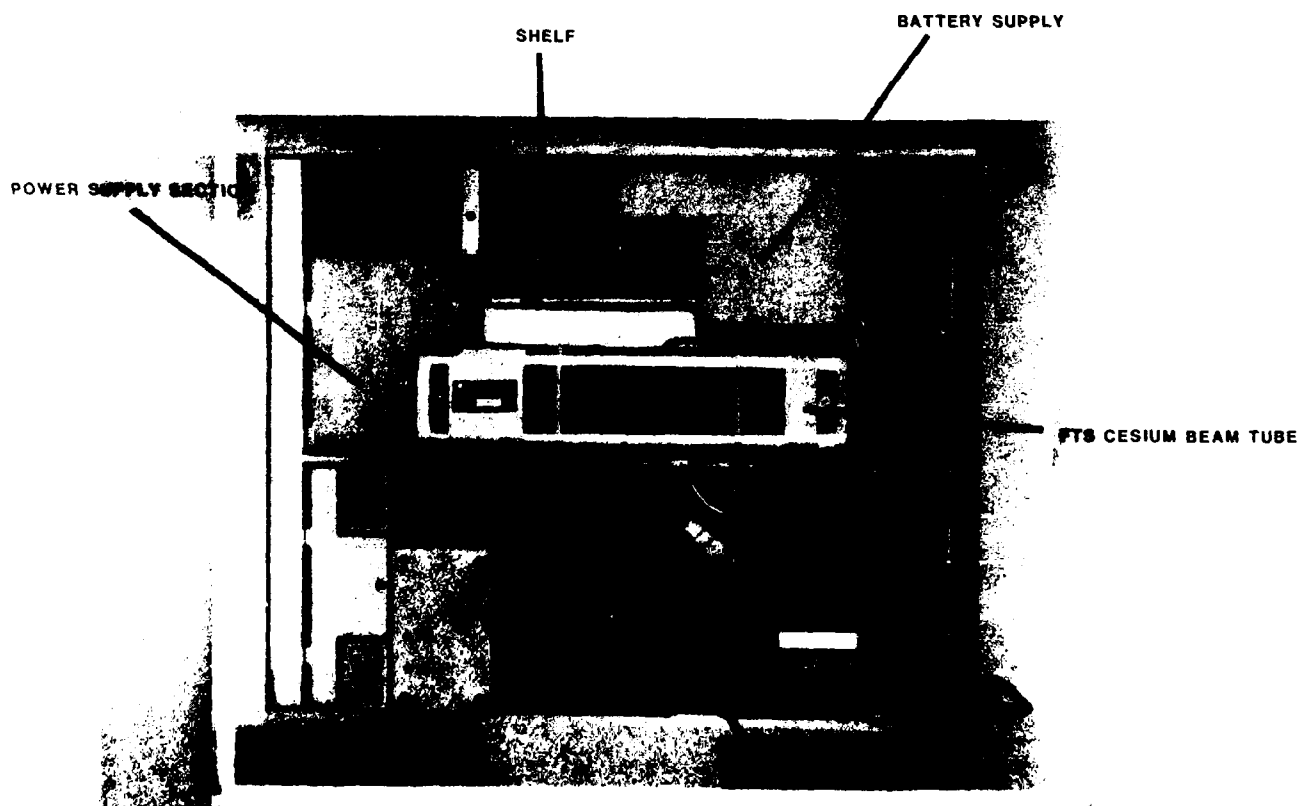


Figure 2b. Top View after Retrofit with FTS Cesium Beam Tube Installed



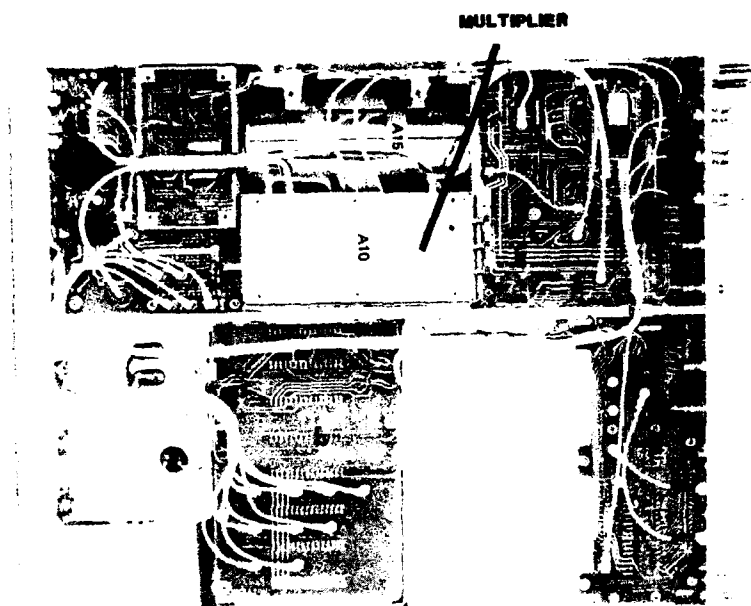


Figure 2c. Bottom View before Retrofit

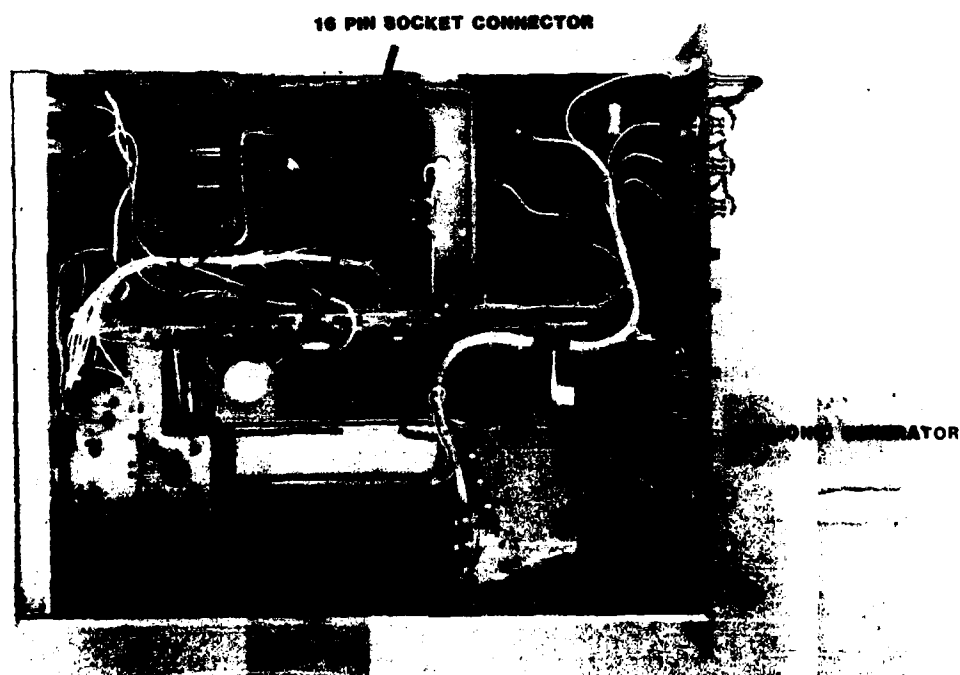


Figure 2d. Bottom View after Retrofit with FTS Cesium Beam Tube Installed

MODIFIED O-1695A/U; HP TUBE INSTALLED

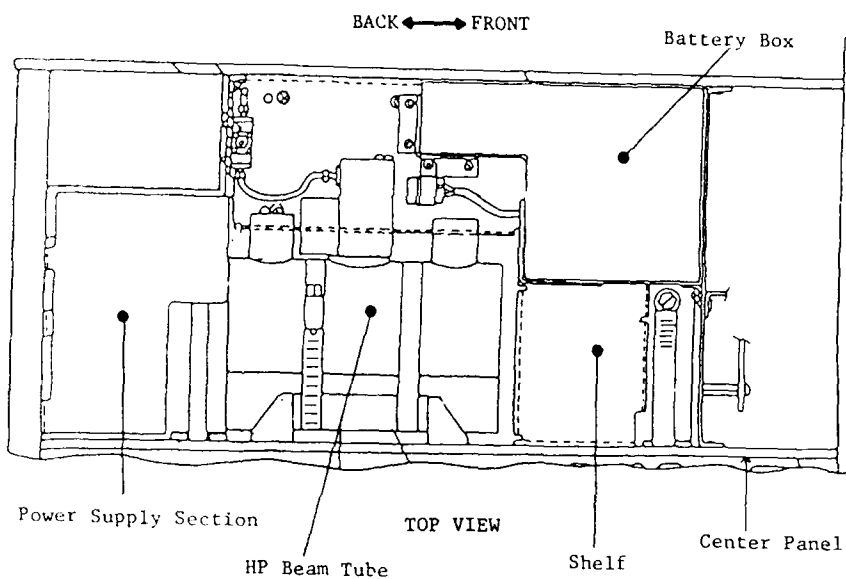


Figure 2e.

MODIFIED O-1695A/U; HP TUBE INSTALLED

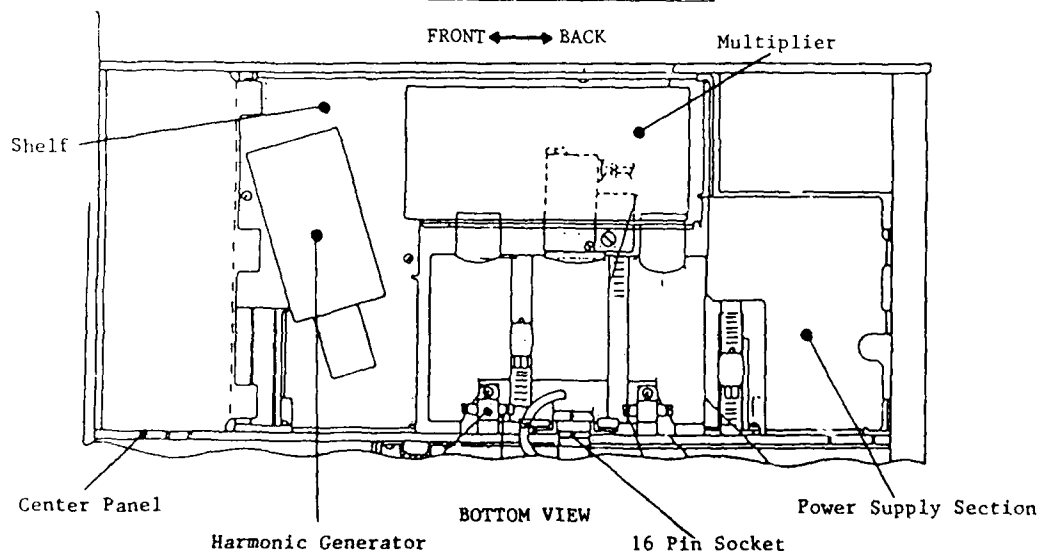


Figure 2f.

## O-1695A/U - RETROFIT OR REPLACE?

Marvin Meirs, Iancu Pascaru, David Silvermetz and Dean Jones

Frequency Electronics, Inc.  
Mitchel Field, New York 11553Summary

In 1983, Frequency Electronics, Inc. (FEI) undertook an NRL contract to retrofit two Model O-1695A/U Cesium Frequency Standards with the FEI cesium beam tube. The project was successful and resulted in a frequency standard which meets or exceeds the requirements of the governing specification, MIL-F-28811(EC), and offers the further advantage of increasing the time between tube replacement.

The retrofit modification included some skillful mechanical changes to the unit in order to accommodate either the present tube or the FEI tube. These changes permitted maximum utilization of existing assemblies and batteries, to minimize modification costs. An environmental test program has been completed on the modified standard.

During the same period, Frequency Electronics developed the O-1824/U Master Regulating Clock. This frequency standard is qualified to MIL-F-28811(EC) and can serve as a high-performance replacement for the O-1695A/U.

Introduction

This paper deals with the results of two Navy contracts which Frequency Electronics received last year. The first was for the development of a form, fit and function replacement of the O-1695A/U Cesium Frequency Standard meeting the requirements of MIL-F-28811(EC), and subsequently given the nomenclature O-1824/U. The second contract resulted from a request by the Navy to retrofit the O-1695A/U with Frequency Electronics' cesium beam tube.

O-1695A/U Retrofit ProgramTechnical Requirements

A photograph of the O-1695A/U Cesium Frequency Standard is shown in Figure 1. Technical requirements of the retrofit contract were to replace the existing HP-5084 series tube with a field-proven cesium beam tube performing the modification in such a manner that the retrofitted O-1695A/U could accept either tube without further modification. The resulting equipment was required to be identical to the existing O-1695A/U in form, fit and performance and meet the requirements of MIL-F-28811(EC) and Amendment 1 with the following allowable deviations:

Warm-up Time	< 30 minutes
Battery Capacity	> 30 minutes at 65°C
	> 15 minutes at -28°C
Weight	< 62 pounds (without battery)

Development Goals

At the outset, Frequency Electronics established three project goals. These were: 1) Incorporate our cesium beam tube assembly with its integral oven control, C-field control and preamplifier; 2) Strive for incorporation of the four original batteries; and 3) Minimize modification costs in production.

The Frequency Electronics Cesium Beam Tube

Frequency Electronics' cesium beam tube has an established field history. Cesium frequency standards shipped by Frequency Electronics over the past 7 years have accumulated over 4 million field hours. The proven accuracy, reproducibility, settability, stability and reliability of these standards are well within the parametric limits of MIL-F-28811(EC). The tube is used in the TD-1251/U Master Regulating Clock and TD-1335/V Portable Real-Time Clock.

The basic cesium beam tube is shown in Figure 2. The detector end and vac-ion pump are to the left, the cesium oven is to the right, and the microwave injection port is in the center. Table I contains several performance characteristics of the Frequency Electronics (FEI) tube.

TABLE I

PERFORMANCE OF FEI CESIUM BEAM TUBE

Line Width	< 800 Hz
Signal-to-Background Ratio	6
Signal-to-Noise Ratio	58 dB (1 Hz Bandwidth)
Figure of Merit	5.5

A mechanical comparison between the FEI tube and the existing O-1695A/U tube is shown in Table II. Note that while the weights and volumes are comparable, the form factors are quite different.

TABLE II

TUBE COMPARISON-MECHANICAL

PARAMETER	FEI TUBE	EXISTING O-1695A/U TUBE
Basic Dimension	14.9" x 3" x 2.5"	6.6" x 4.2" dia.
Weight	12.5 lbs.	11.3 lbs.
Volume	112 cu. in.	91 cu. in.

Retrofit Design

The design approach taken by Frequency Electronics is best seen by studying Figure 3, a top view of the original O-1695A/U, and Figure 4, a top view of the retrofitted O-1695A/U. The existing tube in the top center and the battery section (containing 4 batteries) below to the left were removed. The card cage was moved to the left, replacing the battery section. The Frequency Electronics cesium beam tube was mounted into a unified aluminum channel which spans top to bottom and retains the four original batteries. An interface board containing a normalizing amplifier and ionizer hot-wire power supply was mounted into the spare slot in the relocated card cage.

Bottom views of the O-1695A/U and the retrofitted unit are shown in Figures 5 and 6, respectively. Some of the re-cabling to the relocated card cage can be seen in these views.

The existing O-1695A/U cesium beam tube can be installed into the modified unit with relative ease. The tube remounts at its original position and the original battery section fits easily into a new position next to the card cage.

A significant feature of this retrofit modification by Frequency Electronics is that all of the existing O-1695A/U circuitry is used without redesign.

#### Program Results

The resulting retrofitted cesium frequency standard met all of the established project goals. In addition, the unit passed all contractually required qualification tests, without invoking any allowable specification deviations. Qualification test results are tabulated in Table III.

TABLE III

#### RETROFITTED O-1695A/U QUALIFICATION TESTS

TEST	PASSED
Electrical Parameters	✓
Temperature (Operating and Non-Operating)	✓
Magnetic Environment	✓
Inclination	✓
Vibration	✓
Shock (MIL-S-901C, 400 lb. Hammer Blows)	✓
Electromagnetic Compatibility (CE01, 02, 03, 04; CS01, 02, 06; RE01, 02; RS01, 02)	✓
Production Inspection	✓

#### The O-1824/U Master Regulating Clock

Key to the success of the previously described retrofit program was the use of the Frequency Electronics high-performance, lightweight cesium beam

tube. The same production tube is incorporated into the O-1824/U which was qualified to MIL-F-28811(EC) this past year, and is presently in production.

#### Simplicity of Design

Figures 7, 8 and 9 show the front, top and bottom views of the O-1824/U, respectively. Note the simplicity of design and absence of clutter.

Performance of the O-1824/U exceeds that of the O-1695A/U, yet contains only 12 replaceable subassemblies, compared to 36 for the latter. This design was accomplished by judicious use of thick film hybrid technology in the design of several modules. Figure 10 shows some examples of thick and thin film hybrids fabricated at Frequency Electronics. The O-1824/U Modulator/Multiplier Module, A5, shown in Figure 11 uses four thick film hybrids. Two of the hybrids (with lids removed) are visible in the photograph. The remaining two are on the underside of the module.

#### Comparison Among Standards

In Table IV, significant parameters of the O-1824/U are compared with those of the O-1695A/U as well as with the O-1695A/U retrofitted with the FEI cesium beam tube.

#### Conclusion

Frequency Electronics' successful retrofit of the O-1695A/U Frequency Standard has made available another option to the government: a low-cost modification, using a production cesium beam tube with a guaranteed 3-year tube life. In addition, the O-1824/U Frequency Standard uses the identical tube, is fully qualified to MIL-F-28811(EC), is currently in production, and is a high-performance replacement for the O-1695A/U Frequency Standard.

TABLE IV

#### COMPARISON OF CESIUM FREQUENCY STANDARD

PARAMETER	SYSTEM		
	O-1695A/U	O-1695A/U RETROFITTED WITH FEI TUBE	O-1824/U
$\sigma_y(\tau)$	$7 \times 10^{-11}/\sqrt{\tau}$	$3 \times 10^{-11}/\sqrt{\tau}$	$3 \times 10^{-11}/\sqrt{\tau}$
Battery Capacity (Hrs)	1	1	2-1/2
Vibration Sensitivity	$3 \times 10^{-9}/G$	$3 \times 10^{-9}/G$	$3 \times 10^{-10}/G$
Size (Inches)	19 x 20 x 5-1/4	19 x 20 x 5-1/4	19 x 20 x 5-1/4
Weight (Lbs.)	70	70	62
Module Count	36	36	12
Qualification Status	Complete	Complete	Complete

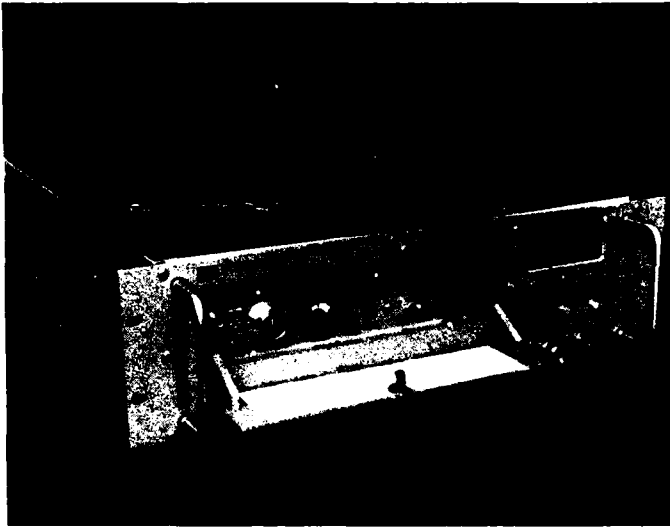


FIGURE 1

O-1695A/U CESIUM FREQUENCY STANDARD

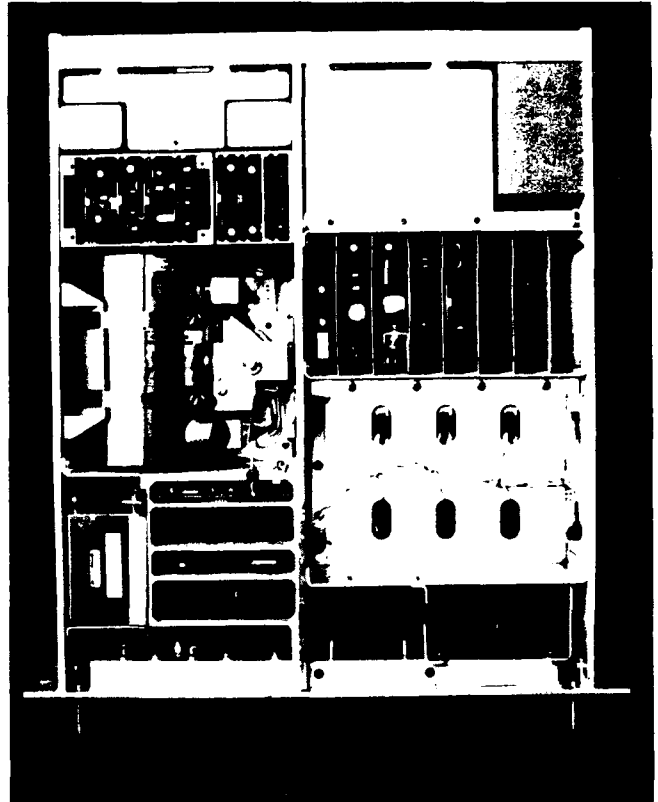


FIGURE 3

O-1695A/U - TOP VIEW (COVER REMOVED)

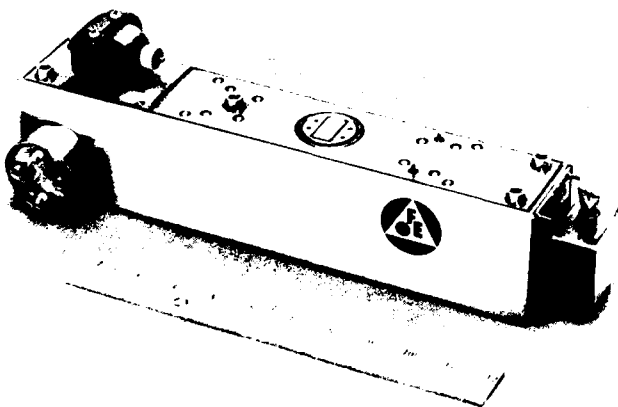


FIGURE 2

FREQUENCY ELECTRONICS CESIUM BEAM TUBE



FIGURE 4

RETROFITTED O-1695A/U - TOP VIEW (COVER REMOVED)



FIGURE 5

O-1695A/U - BOTTOM VIEW (COVER REMOVED)

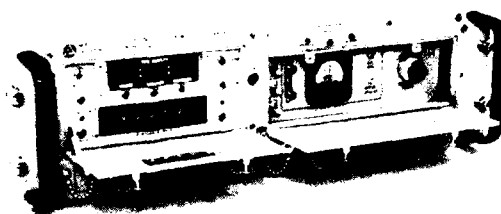


FIGURE 7

MASTER REGULATING CLOCK, O-1824/U

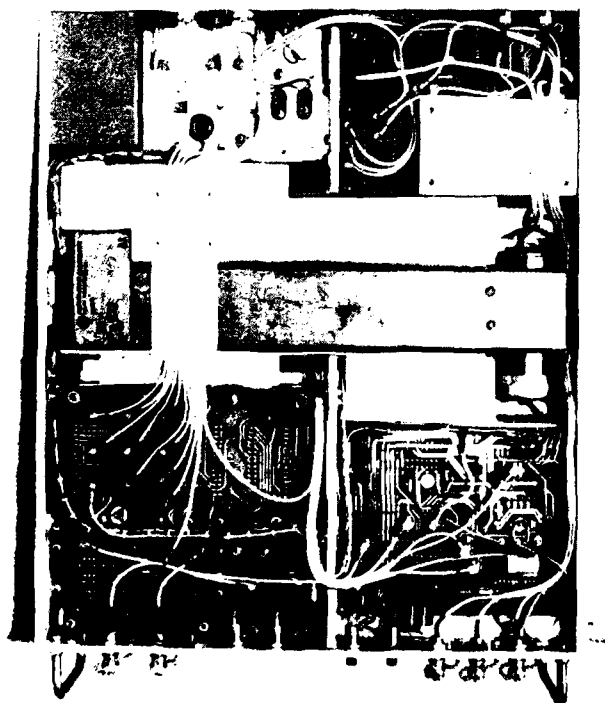


FIGURE 6

RETROFITTED O-1695A/U - BOTTOM VIEW (COVER REMOVED)

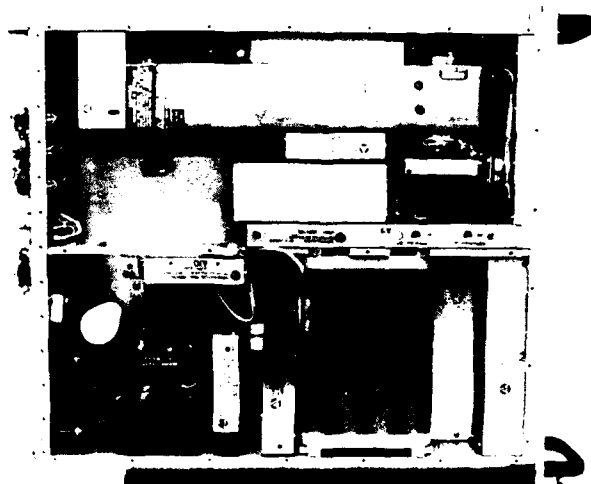
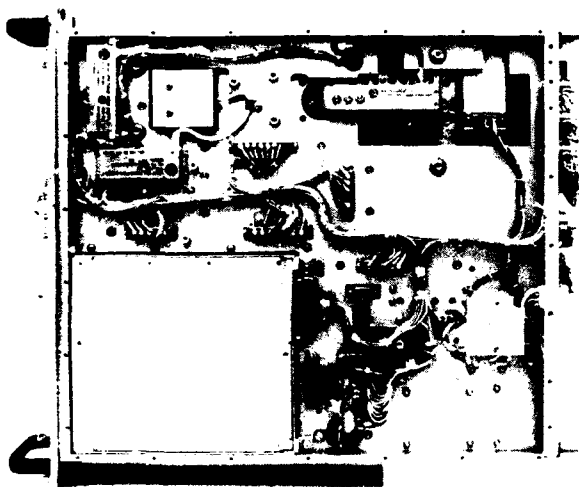


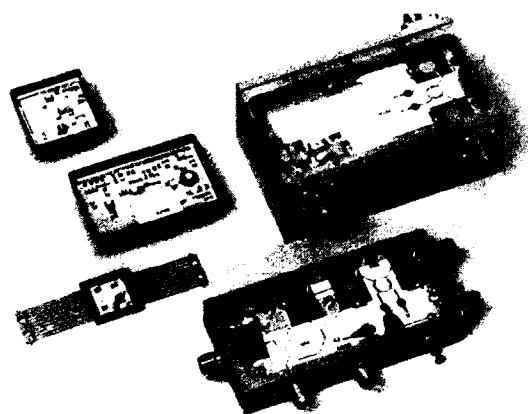
FIGURE 8

O-1824/U - TOP VIEW (COVER REMOVED)



**FIGURE 9**

O-1824/U - BOTTOM VIEW (COVER REMOVED)



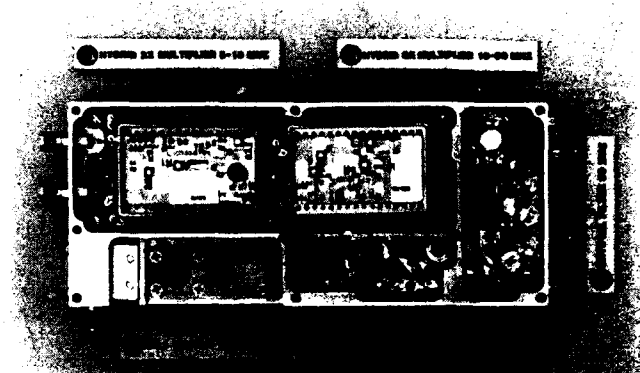
Thick Film Hybrids  
 (a) 90 MHz to 180 MHz Multiplier Driver  
 (b) 5.115 MHz Multiplier Amplifier  
 Thin Film Hybrids  
 (c) 2.1 MHz Crystal Oscillator  
 (d) "X" Band Up Converter  
 (e) "C" Band Mixer-Coupler



FREQUENCY ELECTRONICS, INC.  
 Timekeeper for Outer Space

**FIGURE 10**

THICK AND THIN FILM HYBRIDS FABRICATED AT FREQUENCY ELECTRONICS



Modulator/Multiplier Module, A5  
 FEI Part No D35860-7905



FREQUENCY ELECTRONICS, INC.  
 Timekeeper for Outer Space

**FIGURE 11**

O-1824/U MODULATOR/MULTIPLIER MODULE, A5

A BRIEF INTRODUCTION TO THE ATOMIC TIME  
AND FREQUENCY STANDARDS AT SHANGHAI OBSERVATORY

Zhai Zao-Cheng\*, Zhuang Ji-Xian\*,  
Huang Han-Xiang, Hou Wen-wei,  
and Ju Xiu-Feng

Shanghai Observatory, Academia Sinica

ABSTRACT

This paper introduces briefly the development of atomic time and frequency standards at Shanghai Observatory and describes briefly the main characteristics of the systems and their major performances. In addition, some applications of these standards in astrometry new techniques developing at Shanghai Observatory are also introduced.

In past years, different types of atomic frequency standards such as rubidium gas cell, hydrogen maser and caesium beam tube have been developed in China. These standards are used at Shanghai Observatory to establish atomic time scale and are used in astronomical measurements.

Shanghai Observatory began its atomic frequency standard research with an ammonia maser in 1953. The ammonia maser achieved an accuracy of  $1 \times 10^{-9}$  and had a reproducibility of the order of  $10^{-10}$ . They were no longer used because of the poor performances.

At the beginning of 1970, Shanghai Observatory started development of hydrogen maser and got maser oscillation in 1972. Since 1973, Shanghai Observatory has been involved in research on a laboratory Cs frequency standard to provide a primary standard for atomic time and astronomy. On the other hand, Shanghai Observatory uses several Rb gas cells which were made in China and two HP Cs (from 1982) for keeping atomic time.

HYDROGEN MASERS

Based on the success of the first hydrogen maser of Shanghai Observatory, in 1974 the design was improved and four more hydrogen masers were made. Figure 1 shows two of them. As seen from figure 1, Shanghai Observatory's hydrogen masers are of the typical construction of conventional hydrogen maser. Their design characteristics were described in ref 1,2,3. The current performances of them are shown in figure 2.

Shanghai Observatory is still developing new hydrogen masers. The success of the first flight hydrogen maser<sup>4</sup> in the world, which was developed in Dr. Vessot's maser Lab, was a breakthrough in the state of the art of atomic standard for space and earth based applications. Its success is enormously encouraging to our new maser program. We absorbed many design ideas of the space maser and rebuilt a new hydrogen maser which is shown in figure 3. The new maser achieved a stability of  $2.5 \times 10^{-13}/\text{sec}$ ,  $8 \times 10^{-14}/10\text{sec}$ ,  $5 \times 10^{-14}/100\text{sec}$ , and the order of  $10^{-14}/\text{day}$ . As seen from these data, they are better

\* Learning hydrogen maser at Smithsonian Center for Astrophysics,  
Cambridge, Mass-02138.



than those shown in figure 2, but systematic effects on the maser are still rather severe. Lately, many design ideas from SAO continually go to our maser Lab. A substantial effort for improving the stability of masers is underway in our maser Lab. we expect the new maser will give better performance.

#### LAB Cs BEAM STANDARD

The Cs beam frequency standard which is used at Shanghai Observatory was originally built by National Institute of Metrology of China in Peking in 1965. The length of beam tube is about 3 m, the length of interaction is 160 cm. The beam optics system with single oven and detector is flop-out setting. It has never been used as a standard before. Since 1978, the standard has been moved to Shanghai Observatory and has been modified. The beam optics of double direction and symmetry was designed and assembled. In the modified system, the electrical length of the cavity was readjusted and redetermined. The length differences of both arms of the cavity is less than 0.03 mm. In new electronics, a microwave solid-state source whose phase was locked to the 5 MHz of the quartz crystal oscillator is used as the stimulating signal source for the beam. The frequency synthesizer provides frequency-modulated output, the modulation frequency is changeable from 8 Hz to 0.03 Hz. Since the modulation frequency is decreased, it is possible to use a lower temperature at the detector. The total gain of phase control loop is about  $5 \times 10^4$ , the time constant of the loop is 2 seconds.

The accuracy performance of the improved Cs standard was evaluated again with Shanghai Observatory's hydrogen maser as frequency reference. The preliminary measurement indicates that the frequency stability is better than  $5 \times 10^{-15}$ /hr, while the accuracy is on the order of  $10^{-13}$ . Further improvement of the Cs standard can be expected.

The photograph of the Cs standard is presented in figure 4.

#### ATOMIC TIME SCALE

Using atomic clocks which were made in China, the atomic time scale was established at Shanghai Observatory in 1978 and was denoted by AT(SO). Since 1980, the Lab Cs standard which was mentioned above has been the primary standard of time scale and has been operated intermittently. It is used to provide the basic calibration reference for the second, being defined by the International System of Units. The working standard consists of three hydrogen masers which are operated continuously after cavity tuning. hydrogen clocks are used to provide continuous calibration and to determine the rate change of the Rb clocks. Since 1982, Shanghai Observatory got two HF Cs standards. The HF Cs standards, Rb standards and hydrogen masers together ensure the continuity of the time scale.

AT(SO) is compared with other atomic time scale of laboratories in China and abroad via TV, Loran-C and satellite methods. Among these, TV and Loran-C are routinely made.

Figure 5 shows Shanghai Observatory's atomic time system. The clock room for time service is shown in figure 6.

#### SOME APPLICATIONS

Some subjects of scientific research such as VLBI, Laser ranging, Satellite Doppler observation and tests of the theory of relativity need time and frequency source with extremely high stability. In these experiments and new

techniques, the precision of the results of the observation and the calculation depends on the performance of the time and frequency standards, and is limited by the precision of time and frequency measurements. Time and frequency standards play an important role in these fields.

Shanghai Observatory has begun research in the radio astronomy since 1974, and has built an experimental VLBI system. For these observations, it is necessary to provide precise time synchronization and to keep a high level of frequency and phase stabilization of local oscillators. Shanghai Observatory's hydrogen masers have been used in the experimental VLBI system as independent local oscillators.

Satellite Doppler observation has important applications in astrometry research and geodesy. Shanghai Observatory has built a set of satellite observing system which can be used to determine the geocentric coordinate for astrometry research. The received frequency transmitted from the satellite must be measured precisely and the precise time for performing this measurement is needed in each ground station. Each station must have stable time and frequency standard as well as a common link for time and frequency synchronization. This is the core of Doppler observation system. Shanghai Observatory's atomic time and frequency standards have been used in the Doppler observation and satisfy the requirements.

Satellite Laser Ranging has made great progress in the precision determination of satellite orbits and gravity field research. Shanghai Observatory has built a system of laser ranging that is used in geodynamics research, including determination of distance and orbit of satellite, as well as research of polar motion. Shanghai Observatory's atomic time and frequency standards have been used in this system.

Shanghai Observatory's atomic time and frequency standards are also used in other fields of astronomy research, such as the research of rotation of the earth. In addition, Shanghai Observatory is broadcasting standard frequency and standard time signals in China. The time and frequency signals are emitted based on Shanghai Observatory's atomic time and frequency standards and broadcast as the XSG time service.

#### ACKNOWLEDGEMENT

Authors wish to thank our colleagues for supporting this work and assisting in experiment works.

Recently, several scientists, including Dr. Vessot of JAO, Dr. Allan of NBS, and Dr. Klapczynski of USNO in USA, and Dr. Costain and Dr. Vanier of NRC in CANADA as well as Dr. Saburi of NRL in Japan et al, visited Shanghai Observatory and have given our work a lot of help, we'd like to thank them.

#### REFERENCES

1. Chi-Hsiang Chuang and Zao-Cheng Zhai, IEEE Trans. IM-29, 3, 1980, 158.
2. Zhai Zao-Cheng and Chuang Chi-Hsiang, Journal of the Institution of Electronics and Telecommunication Engineers, Vol 27, No 10 1981, 500.
3. Zhai Zao-Cheng, IETE, Vol 27, No 11, 1981, 510-513.
4. R.F.J. Vessot, M.W. Levine, E.M. Mattison, et al, PIFI of 8th, 1976.
5. A.G. Mungall, H. Daams, J. Morris and J.C. Costain, Metrologia, 12, 1976.

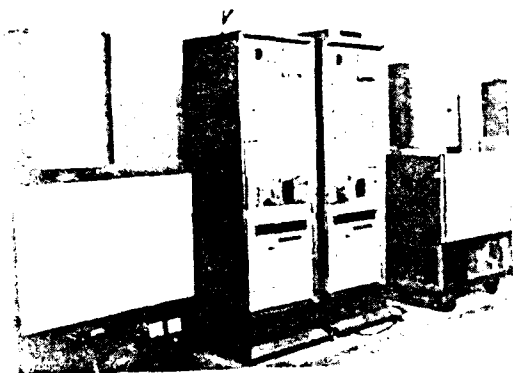


Figure 1  
The hydrogen masers developed by  
Shanghai Observatory



Figure 6  
Shanghai Observatory's time service

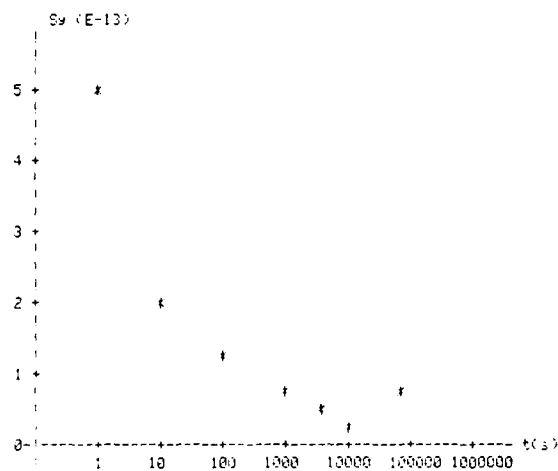


Figure 2

The performance of Shanghai Observatory's H-Maser

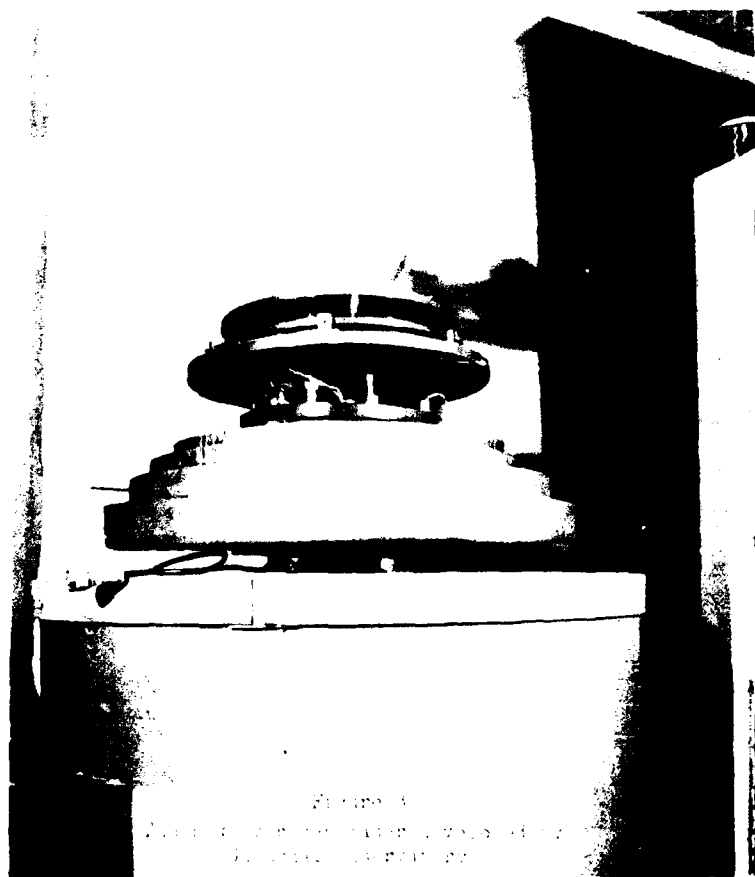


Figure 3

The Shanghai Observatory's H-Maser  
in its protective enclosure

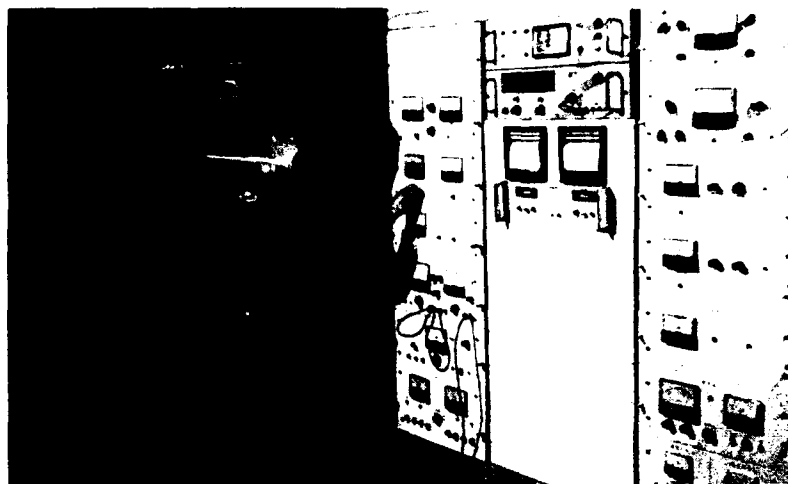


Figure 4  
Shanghai Observatory's Lab Cs standard

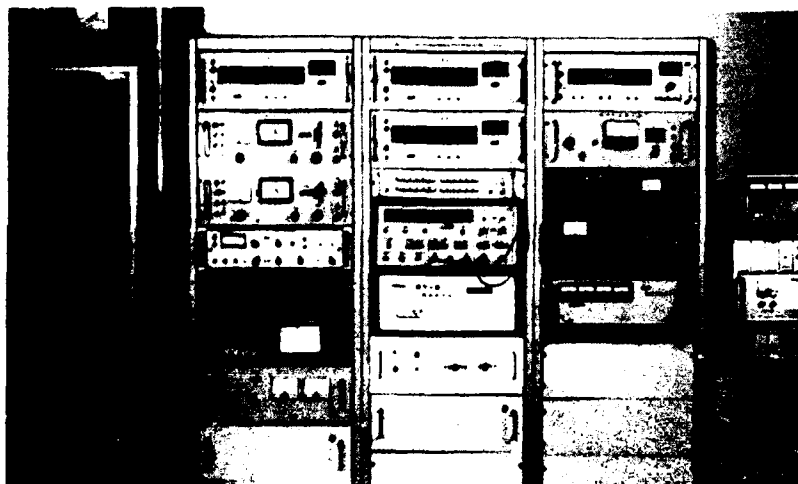


Figure 5  
Shanghai Observatory's atomic time system

## SOFTWARE FOR TWO AUTOMATED TIME MEASUREMENT SYSTEMS

S. R. Stein<sup>†</sup>  
Ball Corporation, Efratom Division  
Westminster, CO

and

G. A. Gifford  
Naval Research Laboratory  
Washington, DC

Summary

The purpose of this paper is to inform the frequency control community of the availability of several computer programs which will assist anyone who needs to make automated time and frequency measurements and analyze the data. The text below summarizes the capabilities of the equipment and the programs. A reader who feels that this approach may be useful for his application can find more details on the equipment in earlier papers.<sup>1, 2</sup> A detailed description of the programs, an operations manual, and source code may be obtained by writing to one of the authors (Gifford) and enclosing a blank data cassette.<sup>3</sup>

Measurement Capabilities

The measurement system was developed by Stein and co-workers at the National Bureau of Standards. It utilizes an enhanced dual mixer technique to achieve picosecond resolution measurements for time intervals of up to 2 seconds. The system was designed to be a cost effective solution to the problem of continuously monitoring a group of atomic clocks. It is suitable for all existing rubidium, cesium and passive hydrogen masers. It is also appropriate for aging or radiation studies of quartz crystal oscillators. Table I summarizes the measurement capabilities.

TABLE I

## MEASUREMENT CAPABILITIES

Noise floor	$3 \times 10^{-12}$ / averaging time
Number of devices under test	unlimited
Measurement dead time	0
Input frequency	1 to 50 MHz nominal, All clocks within $\pm 2 \times 10^{-6}$ of nominal
Ambiguity	none
Sampling rate	up to one per second
Simultaneity of measurements	0.1s

Equipment Requirements

All of the equipment needed for such a measurement system is available as stock commercial components. The dual mixer components adhere to the IEEE-583 interface standard and can be easily integrated into a custom system. Two systems are described in this paper. Their differences are determined by the choice of either the Hewlett-Packard 85 or the Hewlett-Packard 9825 as the instrument controller. Table II lists the required equipment. Entries preceded by asterisks are unique to the extent that any substitution will probably require changes in the computer programs.

TABLE II

## EQUIPMENT LIST

* Pulse distribution module <sup>4</sup>
* Quad clock measurement module <sup>4</sup>
Model 1012 coherent source <sup>5</sup>
Model 1500-PlK CAMAC crate <sup>6</sup>
*Model 3988 CAMAC crate controller <sup>6</sup>
Distribution amplifiers
*HP85A or HP 9825A/T instrument controller <sup>7</sup>
IEEE-488 interface
Advanced programming ROM
Input/Output ROM
Maximum memory
HP 7245B plotter (for 9825 only)
HP 59308A timing generator (for 9825 only)

Analysis Capabilities

The instrument controllers selected for these systems and the programs written for them are best suited for applications requiring successive measurements of limited duration. Screen prompts from the controller assist the operator with the entry of the experimental parameters such as the number of clocks, the number of measurements and the nominal frequency. Both systems must complete all data acquisition before data analysis can be

performed. However, both provide limited monitoring of the measurement while it is taking place. Table III summarizes the data acquisition and analysis abilities for the two systems.

TABLE III

DATA ACQUISITION AND ANALYSIS

	85A	9825 A/T
No. OF OSCILLATORS	2-24	2-8
No. OF MEASUREMENTS	14,000	3,000/10,000
DATA VOLATILITY	None	Duration of measurement
FREQUENCY MONITOR	Plot	Numeric display
POST ANALYSIS		
phase difference plot	Yes	Yes
frequency difference plot	Yes	Yes
Allan variance plot	Yes	Yes
Quadratic fit to phase data	Yes	Yes
Linear fit to frequency data	Yes	Yes
Spectrum analysis	Yes	No

The acquisition and analysis programs have been used for several years at the National Bureau of Standards and the Naval Research Laboratory. Suggestions from many users at these laboratories have been incorporated to make the systems satisfying for a variety of applications. Most of the analysis is straight forward but the spectrum analyzer is unusual. The spectrum of the frequency fluctuations is computed by the Fourier transformation of the autocorrelation function. Thus, no a priori knowledge of the dominant noise process is needed. Furthermore, the resolution of the analyzer is limited only by the length of the measurement making it possible to directly estimate the spectrum at Fourier frequencies on the order of one cycle per hour to one cycle per day! Figures 1 through 5 illustrate program outputs from both systems.

Conclusions

We have reported on the equipment and software for two automated phase measurement systems. Programs on data cassette and an informal but thorough manual are available from the Naval Research Laboratory. The authors believe that these programs can be used as is for some applications and can serve as training and verification aids for those who wish to set up similar customized measurement systems.

Acknowledgements

Some of the source code was written by Trudi Pepler and James A. Barnes. Their contribution is significant. The comments and advice of David Allan and Joe White were extremely helpful. This work was partially supported by the MILSTAR program through Hughes Aircraft Co. and Frequency Electronics, Inc. Additional support was provided by RADC, Hanscom Air Force Base.

References

- † Formerly at the National Bureau of Standards, Time and Frequency Division.
1. S. R. Stein, D. Glaze, J. Levine, J. Gray, D. Hilliard, D. Howe, and L. Erb, "Performance of an automated high accuracy phase measurement system," Proc. 36th Annual Symposium on Frequency Control, 1982. (Available from Electronic Industries Association, 2001 Eye St. NW, Washington, DC 20006).
2. S. Stein, D. Glaze, J. Levine, J. Gray, D. Hilliard, D. Howe, and L. A. Erb, "Automated High Accuracy Phase Measurement System," IEEE Trans. Instrum. Meas., vol. IM-32, No. 1, pp 227-231, March, 1983.
3. Mr. Guy A. Gifford  
Code 7962  
Naval Research Laboratory  
4555 Overlook Avenue, S.W.  
Washington, DC 20375
4. Erbtex Engineering Inc.  
5680 Valmont Road  
Boulder, CO 80301
5. Brightline Corp.  
P. O. Box 1016  
Cedar Park, TX 78613
6. Kinetic Systems Inc.  
39175 Liberty St. Suite 245  
Fremont, CA 94538
7. Hewlett-Packard Co.  
3155 Parker Oaks Dr.  
Palo Alto, CA 94304

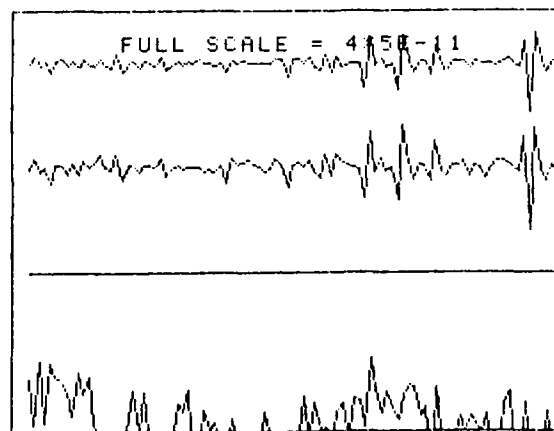


Figure 1. The frequency of every clock under test is plotted on the CRT by the HP85A after each measurement of the experiment. The scale is selected before starting the data acquisition process. In this example 1/4 of the screen is  $5 \times 10^{-11}$ .

Phase Graph  
Channel 2 minus 1

Scale for y axis =  $1.00e-09$  per division  
(20.00 nano seconds full scale)

Scale for x axis = 41 points per division

Tau = 100sec Date 04/19/84

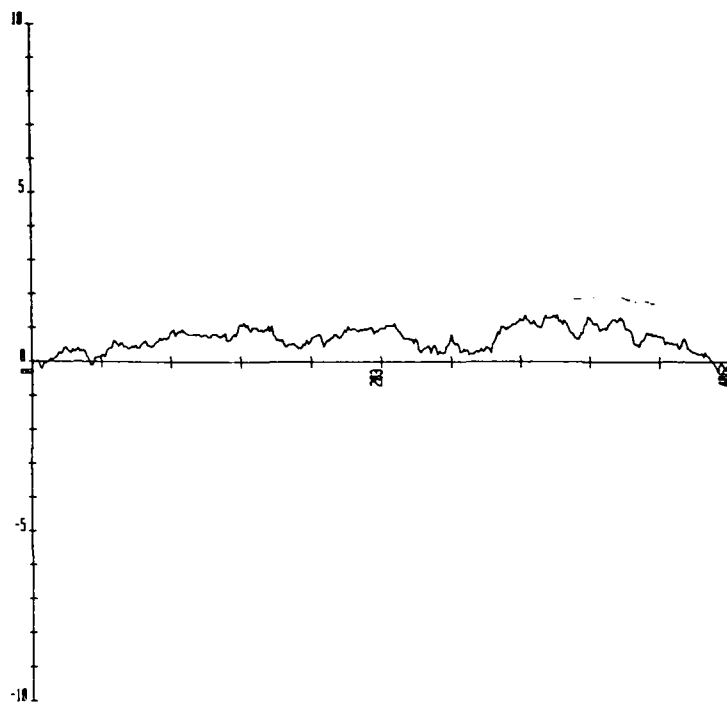


Figure 2. A plot of the phase deviation between two oscillators produced by the HP9825A on the 7245B plotter.

PLOT OF FRACTIONAL FREQUENCIES R  
ESIDUALS AFTER MEAN REMOVED

XMIN=1 TICS=10  
YMIN=-.000000000004 TICS=  
.000000000008  
DEMONSTRATION

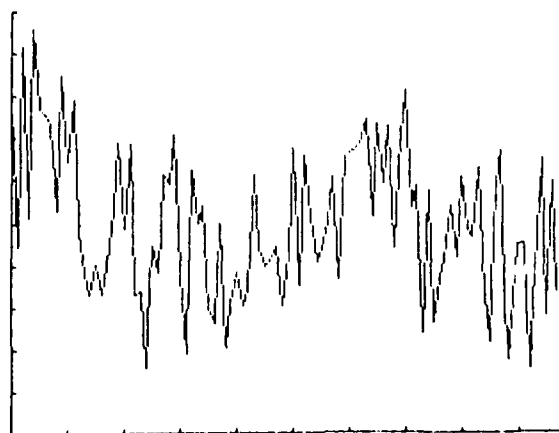


Figure 3. A plot of the fractional frequency deviation between two oscillators produced by the HP85A internal printer.



Allan Variance  
Channel 4 minus 1  
 $\tau_{av} = 16\text{sec}$  Date 85/12/84

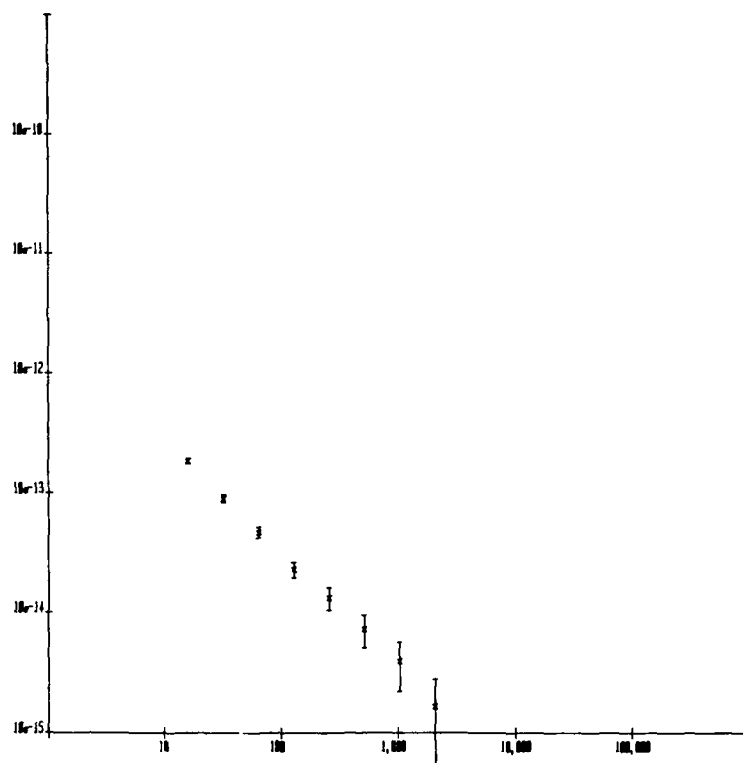


Figure 4. An Allan variance plot produced by the HP9825A on the 7245B plotter.

PLOT OF LOG BASE 10 OF THE SPECT  
RAL DENSITY OF YEAR  
XAXIS UNITS Hz  
YAXIS DIMENSIONLESS  
XMIN=-3 TICS=1  
YMIN=-15 TICS=1

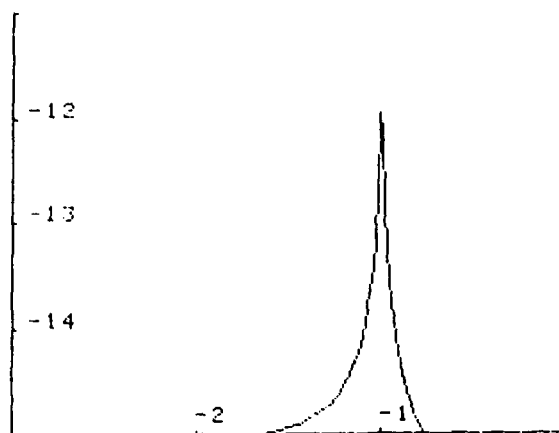


Figure 5. The spectral density of the fractional frequency fluctuations plotted by the HP85A on its internal printer. Model phase data with a single frequency sinusoidal phase modulation was used to illustrate the capability of the spectrum analyzer.

## THE SPECIFICATION OF QUARTZ FOR PIEZOELECTRIC DEVICES

J.C. BRICE

Philips Research Laboratories  
Redhill, Surrey, RH1 5HA, EnglandSummary

This paper discusses the correlations between the densities of various defects (e.g. impurity and dislocation concentrations) and the yields and properties (e.g. equivalent series resistances, temperature coefficients and their spreads) of quartz bulk wave devices. While the details of the correlations depend on the process parameters used in crystal growth and device fabrication, the relations found are sufficiently general to allow a materials specification and acceptance tests to be formulated. For devices made in large numbers the tests required can be simple and cheap: visual inspection and small scale infra-red testing plus 100% thermal shock testing under conditions which destroy only boules which would be unsatisfactory. To obtain high yields of technically superior devices at minimum cost an infra-red Q over about 2 million and a dislocation density below some hundreds per square cm are needed.

1. INTRODUCTION

Improved yields of quartz devices can be obtained by selecting the raw material used. The higher cost of material to a better specification is more than offset by the savings due to higher yields.

This paper describes how we reached one specification which is satisfactory for all the devices (bulk wave resonators, surface wave devices and even some optical components) which we manufacture. Some of the evidence used has been published by my colleagues<sup>1-10</sup> and others<sup>11-24</sup>. This is briefly reviewed. Previously unpublished data representing an update of the information presented in 1978<sup>1</sup> is also summarised. We now have data relating to over 2000 samples drawn from 200 batches of quartz from 15 suppliers. However, 60% of the data are for 5 of these suppliers. In terms of averages and spreads, the differences between this 60% and the residual 40% is small: usually less than 10% and exceptions are noted. Thus we think that our data are a fair representation of what may be expected.

It is important for the statistical approach given here that a batch is defined as the set of boules produced in one autoclave run. We are interested in only a few parameters - infra-red Q, purity and dislocation densities are the main ones. We then need to know how these parameters vary within boules and between boules from one batch, how batches from one supplier vary and how batches from different suppliers vary from each other. To do this we quote averages which are arithmetic means when the spread of data follows a Gaussian (normal) distribution. For these data the spreads quoted are standard deviations i.e. root mean square (rms) deviations from the mean. In the cases of impurity concentrations and dislocation densities, the frequency curves are such that the logarithms of the quantities are normally distributed and for these we quote median values and the spreads are the standard deviations of the logarithms which are often given as a factor e.g. a logarithmic standard deviation of 0.3 is given as factor of 2 variation. In general we are interested in worst values for which we quote the worst decile i.e. 10% of the samples are worse than this

value. The worst decile is 1.28 standard deviations from the average for a Gaussian distribution.

2. INFRA-RED Q

Most of the parameters of interest to us vary with the infra-red Q ( $Q_{IR}$ ). Here we use a scale defined by

$$Q_{IR} = C_v / (\alpha_v + \alpha_v^0) \quad (1)$$

where the parameters take the values given in Table 1 at the three popular values of the measurement wave number  $v$ . The techniques used and the reasons for preferring  $v = 3410 \text{ cm}^{-1}$  have been discussed in detail previously<sup>1-3</sup>. The scale defined by equation (1) can be compared with other scales and Table 2 shows that in the range of interest the (Philips) scale which we use is the average of the others. With the provisos given in the footnote to Table 1, the Philips scale has been tested for  $0.3 < Q_{IR} \times 10^{-6} \lesssim 3$  and for variations between instruments. Because the scale is valid at three wavenumbers (i.e.  $Q_{3585} = Q_{3500} = Q_{3410}$  over the range given), we can look at rms variations of  $Q_{3585} - Q_{3500}$ ,  $Q_{3585} - Q_{3410}$  and  $Q_{3500} - Q_{3410}$  on individual samples. See Figure 1. These quantities are just the appropriate sums of experimental errors i.e.

$$\text{rms}(Q_{3585} - Q_{3500}) = (\sigma_{3585}^2 + \sigma_{3500}^2)^{1/2} \quad (2)$$

where the  $\sigma_v$  are rms measurement errors at the wave number  $v$ . We give these sums in Table 3 and the individual  $\sigma_v$  are given in Table 4. These data are only valid for measurements made exactly as we do but we can use them here to deduce the real variations  $\sigma_{\text{real}}$  by using the relation

$$\sigma_{\text{found}}^2 = \sigma_{\text{real}}^2 + \sigma_{\text{measurement}}^2 \quad (3)$$

where  $\sigma_{\text{found}}$  are the standard deviations of the measured values. (Note that  $\sigma_{\text{measurement}}^2$  can be replaced by the sum of the squares of deviations from individual sources).

3. THE PARAMETERS OF IMPORTANCE

We now look briefly at the evidence linking device performance and yield with the properties of the quartz from which the devices are made. It is important to note in connection with device yields that we are interested in the number of devices which meet a specification. Thus we are interested not only in the mean value of a device property as a function of some material parameter but also in the spread about that value. If, for example, we aim to make devices with a temperature coefficient with a magnitude of say less than  $0.2 \text{ ppm}/^\circ\text{C}$ , it is little use having a batch mean of zero if the batch standard deviation is  $0.3 \text{ ppm}/^\circ\text{C}$  so that 25% of the devices have coefficients  $> 0.2 \text{ ppm}/^\circ\text{C}$  and a further 25% have ones  $< -0.2 \text{ ppm}/^\circ\text{C}$ . Thus we can define good material as that which gives useful average device properties and small spreads of these properties.

In a paper<sup>9</sup> at the 1981 Symposium we showed that drive level effects (changes in the equivalent series resistance and resonant frequency with power level) increased as  $Q_{IR}$  fell below about 1.8 million. Table

5 gives an abstract of the data. We attributed the effect shown to the lower breaking strain of low Q material. Table 6 summarizes the measured variation of breaking strain with  $Q_{IR}$ . Note that we now believe that there is a correlation with dislocation density: doubling the dislocation density from the expected value (discussed later) reduces the breaking strain by about  $0.23 \times 10^{-3}$ . The fragility of the material also accounts for the cutting yield data (Figure 2) and the variation of damage depth with  $Q_{IR}$  for which we find that the damage depth  $d$  is  $K$  times the abrasive size where  $K = 0.8$  for  $Q = 1$  million and  $K = 0.2$  for  $Q = 2$  million. The data available are consistent with

$$K = 0.8/Q_{IR}^2 \quad (4)$$

when  $Q_{IR}$  is in millions.

There are many examples of the correlation of device  $Q(Q_D)$  with  $Q_{IR}$ . It is often assumed<sup>(5)</sup> that

$$\frac{1}{Q_D} = \frac{1}{Q_{IR}} + \sum \frac{1}{Q_i} \quad (5)$$

where the  $Q_i$  account for other device losses (i.e. losses to the electrodes and mounts etc). Table 7 gives some data on devices made by constant processes<sup>3</sup>. (See also reference 22). These strongly suggest that at least one of the  $Q_i$  terms depends on  $Q_{IR}$  or a parameter correlated with  $Q_{IR}$ . There are a number of possibilities (e.g. the failure to remove all the damaged layer at low  $Q_{IR}$  could give increased losses).

An obvious factor to consider is the dislocation density  $N_D$ , which as we shall see correlates inversely with  $Q_{IR}$ . An individual dislocation should not really affect the performance of a device but when the spacing between dislocations ( $\approx N_D^{-1/2}$ ) is comparable to the wavelength  $\lambda$  of the vibrations ( $\lambda \approx 0.3/f$  when  $f$  is the frequency in MHz) we might expect effects. This suggests a maximum  $N_D$  ( $\text{cm}^{-2}$ ) given by

$$N_D < 11 \alpha f^2 \quad (6)$$

where  $\alpha$  is a factor ( $\approx 7.2$ ) which allows for the fact that the dislocations are randomly distributed. (The distribution is assumed to be a Poisson one). Hence we arrive at a maximum density of about  $80 f^2 \text{ cm}^{-2}$ . Bye and Cosier<sup>5</sup> studied 1.4 MHz resonators. Access to their original data allows the classification of the values of the equivalent series resistance  $R_1$  for a number of narrow ranges of  $N_D$  producing the result on Figure 3. It can be seen that  $R_1$  does rise rapidly for  $N_D$  larger than the predicted critical one. Note on Figure 3 that the change in  $R_1$  greatly exceeds that which could occur as the result of the change in  $Q_{IR}$ . Clearly, this effect is important for low frequency devices but is not important once the operating frequency exceeds 5 MHz. There is some evidence that for high frequency devices with a constant  $Q_{IR}$  better yields are obtained with low dislocation densities. This may be the result of the greater breaking strain. However, we have not found sufficient evidence to be able to quantify this. However, at the very highest frequencies using very thin blanks, Vig et al<sup>11</sup> have shown that the strained material around dislocations can etch away to leave a hole through the blank. The yield of devices with no dislocations under an electrode of area  $A$  is  $\exp(-AN_D)$ . To obtain useful yields then requires that  $AN_D$  is small. In a typical case  $A \approx 0.05 \text{ cm}^2$  so that  $N_D$  less than  $10 \text{ cm}^{-2}$  is needed to obtain a 60% yield.

Finally, we should mention impurity concentrations. It is known that small amounts of some impurities can adversely affect the properties of some

devices. Thus for example, the migration of lithium can adversely affect aging<sup>8</sup>, and the presence of aluminium and iron adversely affects devices operating in high radiation fluxes<sup>25</sup>. We have not systematically investigated these effects because, as will be shown, our specification of  $Q_{IR} > 1.8$  million automatically ensures low concentrations of these impurities.

A piece of unexpected experimental data which needs to be considered is the angle of cut to be used. Data<sup>3</sup> has been presented which enables us to plot the deviation of target angle from an arbitrary origin as a function of  $Q_{IR}$ . This is given on Figure 4 which is a plot of angle deviation from ideal against the reciprocal of  $Q_{IR}$ . By current standards these are serious deviations and strongly suggest that we need a large  $Q_{IR}$  and a small spread of  $Q_{IR}$  in a batch.

Finally, Table 8 gives yield data for one of our devices when we deliberately used material with different  $Q_{IR}$  values. The potential blanks are the ones we would have obtained with zero cutting and lapping losses. The surviving blanks are those fed to the device assembly line. It is clear that for  $Q = 1$  million we used nearly twice as much quartz as well as having 30% rejects.

#### 4. THE PARAMETERS OF AVAILABLE QUARTZ AND THEIR CORRELATIONS

##### 4.1 Purity

If we measure impurity concentrations and look at median values as a function of  $Q_{IR}$  we obtain Figure 5. If we look at one value of  $Q_{IR}$  we find that the logarithms of the concentrations are normally distributed with standard deviations of 0.3 to 0.5 corresponding to factors of 2 to 3 in concentrations. If we look at individual suppliers, their data are less spread out but still vary by factors of about 1.5 so that highest decile concentrations can be about 3 times lowest decile values. Differences between supplier median values are such that the upper and lower deciles deviate by a factor of about 2.8 from the median value given on the figure. Thus the worst suppliers worst batch might have levels of 5 times the median value given. (Here "worst" is the least favourable decile value). However in general the worst batch should not be more than about 4 times the median value.

It is important to note that:

- (1) The data apply to the Z-zone: for the X-zones H and L<sub>1</sub> concentrations are typically 3 times higher and the other impurities can have concentrations 10 to 30 times higher. (See reference 26 for a discussion of the reasons for the differences in impurity incorporation in the various zones).
- (2) The data for crystals grown with NaOH mineraliser are not significantly different from those grown with  $\text{Na}_2\text{CO}_3$  except in terms of carbon content which is a factor of 5 to 6 higher than the median for crystals grown from NaOH.
- (3) Alkali metals were determined by flame photometry. Other data are from solid source mass spectrometry. It is possible that there are systematic errors due to incorrect choice of yield constants. These should not exceed a factor of 3. Thus in a randomly selected sample absolute values are unlikely to exceed 15 times the median value given on the figure for impurities other than alkali metals. For the alkali metals likely upper limits are the factor of 5 suggested above.

##### 4.2 $Q_{IR}$ Variations

In 1978 we pointed out that there was a correlation between the spread of  $Q_{IR}$  values in a

batch and the mean  $Q_{IR}$  in the batch. Now we have about about 10 times as much data we believe that the curves for different suppliers differ. Figure 6 gives data for two suppliers. The full lines are for measurements at  $3410 \text{ cm}^{-1}$ . The broken line is for measurements at  $3585 \text{ cm}^{-1}$  (Supplier B). Note that we believe that for a given supplier  $\alpha$  has a Gaussian distribution. For  $Q_{IR} \geq 2$  million,  $Q_{IR}$  is essentially Gaussian. For  $Q_{IR} < 2$  million the distribution of  $Q_{IR}$  is slightly skewed with an excess of high  $Q$  values i.e. the mean exceeds the median by an amount which increases as  $Q_{IR}$  falls but the differences are small. At  $Q_{IR} = 1$  million the difference is about 0.035 million. (We can see these small differences by comparing mean  $Q_{IR}$  calculated from actual  $Q_{IR}$  data and the  $Q$  calculated from mean  $\alpha$ ). For most purposes we can neglect these differences. For  $Q_{IR} < 1.8$  million Suppliers A and B are respectively the best and worst suppliers that we deal with on a regular basis. With a few exceptions data at  $3410 \text{ cm}^{-1}$  for other suppliers lie between the two full lines. The average Supplier's line is just above A at  $Q = 1$  million and just below B at  $Q = 3$  million. The worst expected (i.e. upper decile supplier follows the line for B up to  $Q = 1.8$  million (standard deviation as measured 0.15 million, actual about 0.14 million) and then falls slowly: values at  $Q = 2.5$  million are about 0.11 million (measured) or 0.10 million (actual). For  $Q \leq 1.5$  million, the fractional spread of  $Q$  values is related to the fractional spread of the  $Z$  dimension by

$$\frac{\Delta Q}{Q} = (1.1 \pm 0.3) \frac{\Delta Z}{Z} \quad (7)$$

The standard errors of the data points shown on Figure 6 are about 9% of the plotted standard deviation. However, at any mean batch  $Q$ , the variation of standard deviation between batches is  $21 \pm 9\%$  of the value shown. This order of variation is shown by all suppliers. The broken lines are standard deviations corrected for measurement errors. Note that the data plotted are on the basis of boule averages being the mean of  $Q_{IR}$  at two points halfway between the outside and the seed in the boule. For Supplier B, the corrected data for  $3410$  and  $3585 \text{ cm}^{-1}$  coincide. We have done the obvious experiments of using boule averages based on more points per boule. (Table 9 gives some illustrative data). The corrected values all lie on the same lines. Note that most of our data (all the data on the figure) relate to Y-bar boules. When we look at boules with plate-like instead of bar-like seeds we suspect that the same relations are valid. The corrected lines i.e. the intrinsic variation of  $Q_{IR}$  are given by

$$\sigma_A = 0.333 - 0.133 Q_{IR} \quad (8)$$

$$\sigma_B = 0.375 - 0.125 Q_{IR} \quad (9)$$

for  $Q_{IR} < 2.1$  million. Note that the deviations and  $Q_{IR}$  values are in units of 1 million. For  $Q \leq 2$  million (8) and (9) represent upper and lower decile values. As noted for  $Q \geq 2$  million the upper decile value is larger than  $\sigma_B$  but  $\sigma_A$  remains the lower decile value.

#### 4.3 Gradients With Boules

From the information given in section 3, it is clear that we would like a small gradient of  $Q$  in the boules used. Large gradients of  $Q$  and  $\alpha$  have associated with them large gradients of impurity concentrations which in turn imply large gradients of lattice constants i.e. inhomogeneous boules are strained. It is easier to measure  $d\alpha/dz$ . If we do this, we find that boules with  $d\alpha/dz > 0.1 \text{ cm}^{-2}$  have a high probability of cracking with a  $50^\circ$  thermal shock.

Figure 7 gives some data on gradients in boules from suppliers A and B. Note that we only measure variation in the  $z$  direction. Variations in the  $x$  and  $y$  directions are difficult to measure: with errors of  $\pm 50\%$  values range from  $0.014 \text{ cm}^{-2}$  ( $Q = 1$  million) to  $0.007 \text{ cm}^{-2}$  ( $Q = 2$  million) for gradients in the  $x$  direction while gradients in the  $y$  direction range from  $0.02 \text{ cm}^{-2}$  ( $Q = 1$  million) to  $0.01 \text{ cm}^{-2}$  ( $Q = 2$  million). The figure shows that low  $Q$  crystals are less homogeneous than high  $Q$  ones and that Supplier B's boules are less homogeneous than Supplier A's material. The figure gives data for boules with bar-like seeds. However, when we have measured crystals grown on platelike seeds, the gradients found are scattered about a line midway between the lines for Suppliers A and B. In fact all the data for other suppliers is also scattered about the same line with rms deviations of about  $0.035 \text{ cm}^{-2}$ .

#### 4.4 Dislocation Densities

Previous work showed that at a given infra-red  $Q$ ,  $\log N_D$  is normally distributed and can be described by a relation

$$\log N_D = A \pm B + 2.5 \log \alpha^* \quad (10)$$

where  $\alpha^* = \alpha_U + \alpha_V$ . Previously, we used  $\alpha_U$  at  $\nu = 3500 \text{ cm}^{-1}$  because this quantity is directly proportional to the hydrogen content. We can, of course, convert data from any other wave number. In (10)  $B$  is the spread of  $\log N_D$  at a fixed  $\alpha^*$  (i.e. at a fixed  $Q_{IR}$ ). The majority of our data (perhaps 90%) applies to boules grown on bar-type seeds. Dislocation densities in boules grown on plate-like seeds are less, typically by a factor of two and give an over all distribution with  $A = 4.7$  and  $B = 0.4$  with no size dependence.

For bar type seeds, the dislocations fan out from the seed. Thus the measured value of  $N_D$  falls as the measurement area moves from the seed to the outer surface. We measure  $N_D$  halfway from the seed to the outer surface. Thus if other factors are constant our measured value falls as the  $Z$  dimension of the boule increases. The data in Table 10 are for average  $Z = 30 \text{ mm}$ . (In calculating the residual  $B$ , the size variation in the samples has been included). To deduce  $N_D$  for an arbitrary  $Z$  dimension (in mm) apply the relation

$$N_D = 30 N_{D10}/Z \quad (11)$$

where  $N_{D10}$  is the value given by (10). Other measurement uncertainties contributing to the  $B$  (total) value are 0.18 (errors in measuring  $N_D$  which are equivalent to a factor 1.5) and 0.05 (errors in measuring  $\alpha^*$ ). Subtracting the total measurement errors still leaves a residual  $B$  value which represents the spread of  $N_D$  in one run presumably caused by point to point variations in the growth conditions. The average residual  $B$  represents a range of  $N_D$  values from upper to lower decile equivalent to a factor of 1.9. The tabulated values show quite clearly that different suppliers have very different values of  $A$  i.e. their median  $N_D$  values at a given  $Q_{IR}$  vary very significantly. See Table 11, which also gives the expected upper decile values. Calculating the batch mean  $Q_{IR}$  to give a target upper decile dislocation density then becomes a little difficult but we have had batches meeting upper decile  $N_D < 100 \text{ cm}^{-2}$  from Suppliers A and B. The batch mean  $Q_{IR}$  values were 2.2 and 2.5 million respectively.

#### 5. SPECIFICATION AND TESTING

As  $Q_{IR}$  falls the various parameters which we believe to be significant degrade only slowly. Thus it

is not possible to set a definitely unacceptable level. However, the rate of degradation does seem on average to start to increase when the Q falls below about 1.8 million so somewhat arbitrarily we say that less than 10% of a batch should have  $Q_{IR} < 1.8$  million. At this level we expect:

- (1) All impurities except hydrogen at levels  $< 10$  ppm
- (2) Dislocation densities  $< 500 \text{ cm}^{-2}$
- (3) Cutting losses  $< 10\%$
- (4) Batch  $Q_{IR}$  spreads  $< 0.15$  million (worst case, with errors for measurement at  $3410 \text{ cm}^{-1}$  included)
- (5) Angle of cut variations  $\pm 0.5$  arc minutes.

To meet a 90% greater than 1.8 million specification, the batch mean Q must exceed about 1.97 million (worst case (i.e.  $1.80 + 1.28 \sigma$  actual). If we measure a sample of 6 boules measuring at two points per boule to be 90% confident that the batch mean Q exceeds 1.97 million we need  $t = 1.476$  i.e. our measured mean batch  $Q_{IR}$  must exceed 2.05 million (if we measure at  $3410 \text{ cm}^{-1}$ ). This gives us 90% confidence in the short term. In the long term it implies that 97.7% of the boules have  $Q_{IR} > 1.80$  million. Thus we can afford to relax a little and we set a limit of 2.00 million which gives a worst case long term average of 94.5% of boules with  $Q_{IR} < 1.8$  million. (Note with our best supplier the long term average is 99.8% exceed 1.80 million or 90% exceed 1.91 million). We now need to set a rejection level. By reversing the arguments, we can see that if our measured mean batch Q is less than 1.92 million then we can be 90% confident that the batch does not meet the criterion mean batch  $Q > 2.00$  million. At this level, the batch from our worst supplier contains 20% boules with  $Q < 1.8$  million. (The best supplier's batch at this level should still contain 95.6% of good boules). Thus there appears to be no real problem. Unfortunately, this is not the case. All batches of quartz contain some rogues - crystals which have poor seeds, incorrectly mounted seeds or crystals which have suffered as a result of spurious nucleation etc. Typically, the number of rogues may be 5%. The supplier will see many of these rogues - they are mishaped or contain obvious inclusions. However, even the most conscientious suppliers do not remove all the rogues. If 2% rogues remain, there is a 12% probability that our test batch contains at least one rogue which we may not be able to spot at the infra-red test stage. We would be suspicious of any sample of six with a range (i.e. maximum measured Q - minimum measured Q) which exceeded 3.6 times the expected standard deviation (in a batch of 6 the expected range is 2.53 times the standard deviation and should exceed 3.6 times the standard deviation only once in 10 samples). Thus we become suspicious if the range exceeds 0.5 million. However, there could be a large fraction of rogues in a batch or even in the test sample without any suspicion being aroused we therefore instituted a 100% inspection for deformed boules and boules with very obvious seed veils. Crystals with very obvious seed veils have high dislocation densities and low  $Q_{IR}$  but it is not easy to quantify "very obvious". Typically we may eliminate 1 or 2% of boules at this stage. (We believe that perhaps half of the boules eliminated would not survive cutting or if they did would not make satisfactory devices). With the type of figures quoted in Table 8 it can be seen that this contributes significantly to yields).

For non-obvious rogues we have one further test. We subject all boules to a  $50^\circ\text{C}$  thermal shock. (This test should eliminate most boules with breaking strains less than  $1.2 \times 10^{-3}$  i.e. with  $Q_{IR}$  below about 1.75 million). The fraction of a batch breaking is correlated with the batch mean  $Q_{IR}$ . Typical data are 4 to 5% losses for a batch mean  $Q_{IR}$  of 2.1 million

falling to about 1% at a  $Q_{IR}$  of 2.4 million and perhaps  $< 0.1\%$  at  $Q_{IR} > 2.7$  million. Tests on 21,000 boules and data deduced from a knowledge of the spreads of the thermal shock to break single boules suggest that the probability (p) of breaking a boule with our  $50^\circ\text{C}$  shock test is given by

$$\log p = 4.07 \pm 0.12 - 2.5 Q_{IR} \quad (12)$$

where  $Q_{IR}$  is in millions. In a batch of n the number found to have cracked might be expected to follow a binomial distribution i.e. the average should be np with a standard deviation of  $[np(1-p)]^{1/2}$  and the fraction of batches with no boules cracked should be  $(1-p)^n$ . For  $n = 1000$  and  $Q = 2.75$  million, p is about 0.001 and we expect (and find)  $1 \pm 1$  boules. In a set of 8 batches 3 had no boules cracked. We expect 2.94. However, at lower Q values we find large variations. At  $Q = 2.0$  million we expect  $100 \pm 9.5$  boules in a batch of 1000. The spread found is roughly a factor of 2. The logarithmic standard deviation in the range 2.0 to 2.6 million is about 0.35. Some of this dispersion can be attributed to variations in the spread of Q values in a batch, the uncertainties in batch mean Q values and to variations in dislocation densities.

As far as we are concerned the inspection and thermal shock tests are valuable: using them can decrease losses both during cutting and device fabrication by factors of about two.

## 6. CONCLUSIONS

This paper has attempted to show how measurable parameters of quartz ( $Q_{IR}$ , dislocation density, purity) affect device yields and performance. This leads to a specification in terms of these parameters and while there are different trends for different suppliers, imposing the specification (batch mean  $Q_{IR} > 2.00$  million plus inspection and thermal shock testing) has roughly doubled the yield of useful devices per kilogram of quartz and has significantly reduced fabrication losses when compared with a specification  $Q_{IR} < 1$  million. It is noteworthy that these improvements have occurred over a period in which device specifications have been very significantly tightened with respect to parameters (e.g. drive level effects and aging) which we expect to be related to the properties of the quartz used.

## ACKNOWLEDGEMENTS

Many of my colleagues in the Philips Concern have contributed to the work described here. I have also received a great deal of help in the form of information and samples to unusual specifications from many suppliers of quartz.

## REFERENCES

1. J.C. Brice and A.M. Cole, Proc. Annual Frequency Control Symposium (1978) 1.
2. J.C. Brice and A.M. Cole, J. Phys. D. 12(1979) 459.
3. J.C. Brice, Rev. Mod. Phys. in the press.
4. A. Kats, Philips Res. Repts 17(1962) 133 and 201.
5. K.L. Bye and R.S. Cosier, J. Mater. Sci. 14(1979) 800.
6. J.E. Knowles, Proc. Annual Frequency Control Symposium (1975) 230.
7. J.C. Brice, J. Mater. Sci. 15 (1980) 161.
8. J.C. Brice and W.S. Metcalf, Philips Tech. Rev. 40 (1982) 1.
9. J.C. Brice, J. Dowsett and E.D. Fletcher, Proc. Annual Frequency Control Symposium (1981) 312.
10. J.C. Brice, Physics Educ. 16 (1981) 162.

11. J.R. Vig, J.W. LeBus and R.L. Filler, Research and Development Technical Report: ECOM-4548(1977).
12. D.M. Dodd and D.B. Fraser, J. Phys. Chem. Solids 26 (1965) 673.
13. B. Sawyer, IEEE Trans. SU-19 (1972) 41.
14. N.C. Lias, J. Crystal Growth 18 (1973) 1.
15. D.B. Fraser, Frequency 4 (1966) 18.
16. D.W. Rudd and E.E. Houghton, Western Electric Engineer 10 (1966) 22.
17. Toyo Technical Bulletin B-1 (1975).
18. Toyo Technical Paper 77-03 (1977).
19. Toyo Technical Bulletin C-5 (1975)
20. J. Asahara, E. Yazaki, K. Takazawa and M. Kita, Proc. Annual Frequency Control Symposium (1975) 211.
21. N. Asanuma and J. Asahara, Proc. Annual Frequency Control Symposium (1980) 120.
22. J. Asahara, K. Nagai and S. Harada, Proc. First Int. Symp. Hydrothermal Reactions (S. Somiya (Editor) Gakujutsu Bunken Fukya-kai, Tokyo 1983) 430.
23. B. Sawyer, Proc. Annual Frequency Control Symposium (1983) 151.
24. J.J. Martin, L.E. Halliburton, R.B. Bossoli and A.F. Armington, Proc. Annual Frequency Control Symposium (1982) 77.
24. S.P. Doherty, S.E. Morris, D.C. Andrews and D.F. Croxall, Proc. Annual. Frequency Control Symposium (1982) 66.
26. J.C. Brice, Rep. Prog. Phys. 40 (1977) 567.

TABLE 1

The Constants in Equation (1)

$\nu(\text{cm}^{-1})$	$C_v$	$\alpha_v$
3410	0.169	-0.0190
3500	0.135	+0.0250
3585	0.144	+0.0250

- (1)  $C_v$  gives Q in millions
- (2) For 3585  $\text{cm}^{-1}$ ,  $C_v$  depends on resolving power. For instrument resolutions of < 1.2, 1.4, 1.6, 1.8 and > 2  $\text{cm}^{-1}$ ,  $C_v$  has values of 0.160, 0.156, 0.146, 0.141 and 0.139 respectively.
- (3) For Q3410 > 2.4 million, Q3585 from (1) exceeds Q3410. For Q3410 = 2.5, 2.6, 2.7, 2.8 and 2.9, these excesses are respectively 0.03, 0.06, 0.10, 0.15 and 0.22 million for a resolving power of 1.7  $\text{cm}^{-1}$ .
- (4) The most recent data<sup>17-23</sup> suggest that the values of  $C_v$  may be 3.5 ± 1.5% too large. However, this is less than the uncertainties of about 4.5% in  $C_v$ .
- (5) Note that the scale defined by equation (1) presents average device performance. If we make IEC standard devices from boules from different suppliers, we can expect the measured device Q values to have a real spread due to systematic variations in dislocation densities etc. The six known scales<sup>1,12-14,17-23</sup> suggest spreads of 8 ± 3% at Q = 1 million and 10 ± 4% at Q = 2 million.

TABLE 2

QIR Scales

	Q x 10 <sup>-6</sup>		
Philips 1,2	1.50	1.80	2.00
Toyo <sup>17-19</sup>	1.43	1.73	1.94
Sawyer <sup>13</sup>	1.67	2.08	2.33
Dodd <sup>12</sup>	1.29	1.48	1.65
Lias <sup>14</sup>	1.60	1.91	2.12
Mean	1.50 ± 0.17	1.80 ± 0.26	2.01 ± 0.29

The Philips scale is best defined at 3410  $\text{cm}^{-1}$  but can be defined at 3500 and 3585  $\text{cm}^{-1}$ . The Toyo scale is for 3585  $\text{cm}^{-1}$ . The other scales are defined for 3500  $\text{cm}^{-1}$ . The Sawyer scale has recently been revised<sup>23</sup>. The tabulated value is the old scale. The new scale values are 1.45, 1.77 and 1.95 respectively.

TABLE 3

RMS Differences

Quantity	Difference x 10 <sup>-6</sup>		
Q3585 - Q3410	0.105	0.119	0.127
Q3585 - Q3500	0.101	0.113	0.123
Q3500 - Q3410	0.081	0.094	0.105
Q range (millions)	0.8-1.5	1.5-2.5	2.5-3.2

Standard errors are about 0.007 x 10<sup>6</sup>. Arithmetic average differences in the quantities have average values of about 0.006 million. Hence the ratios of the  $C_v$  values in Table 1 cannot vary much from the ones assumed. Actual ratios are  $C_{3410}/C_{3500} = 1.252 \pm 0.019$ ,  $C_{3410}/C_{3585} = 1.174 \pm 0.018$  and  $C_{3585}/C_{3500} = 1.067 \pm 0.016$ . Similarly the errors in the  $\alpha_v$  values should not exceed ± 0.0009.

TABLE 4

QIR Measurement Errors

Wave number (cm <sup>-1</sup> )	RMS Errors x 10 <sup>-6</sup>		
3585	0.086	0.095	0.101
3500	0.053	0.061	0.071
3410	0.061	0.071	0.077
Q x 10 <sup>-6</sup>	0.8 to 1.5	1.5 to 2.5	2.5 to 3.2

Standard errors are about 0.005 x 10<sup>6</sup>

TABLE 5

Drive Level Dependence (Power Change 5 nW to 100  $\mu$ W)

	QIR = 2 million	QIR = 1 million
$\Delta R_1$ (ohms)	$1.0 \pm 1.0$	$2.5 \pm 3.0$
$R_1$ (ohms)	17	30
$\Delta f$ (Hz)	$8.0 \pm 4.9$	$23.3 \pm 8.7$
f (MHz)	10	10

$R_1$  is equivalent series resistance f is the resonant frequency.  
 $\Delta R_1$  and  $\Delta f$  are average values of the changes seen.

TABLE 6

Breaking Strain as a Function of QIR

QIR (Millions)	Breaking Strain	$N_D^*$ ( $\text{cm}^{-2}$ )
2.3	$2.0 \times 10^{-3}$	80
2.1	$1.5 \times 10^{-3}$	105
1.7	$1.25 \times 10^{-3}$	180
1.0	$1.05 \times 10^{-3}$	670

\*These are the expected dislocation densities.  
 The thermal shock to break a crystal is roughly  
 $T_B = 34 + 5Q^2$  ( $^{\circ}\text{C}$ ) when  $N_D = N_D^*$  and Q is in millions.  
 For each factor of 2 by which  $N_D$  exceeds  $N_D^*$  subtract  
 $8.8^{\circ}\text{C}$ .

TABLE 7

Changes in Device Q Values

QD for QIR = 1 million		Increase when QIR raised to 2 million	
		Expected	Found
Philips	$2.7 \times 10^4$	2%	37%
Toyo	$2.0 \times 10^5$	10%	20%

Expected changes are calculated using equation (5)  
 assuming that the  $Q_L$  are constant.

TABLE 8

Device Yields

QIR (Millions)	Good devices per 100 potential blanks	Good Devices per 100 surviving blanks
1	48	70
2	90	95

Variations in yields at various times give uncertainties  
 of about  $\pm 2$  or  $\pm 3$  in the yield figures. These may  
 reflect the variations in Q values in the batches. For  
 $Q = 1$  million the variations were  $\pm 0.2$  million and for  
 $Q = 2$  the variations were  $\pm 0.1$  million.

TABLE 9

QIR Data on Two Samples of Six Boules From Different Batches

Q3410		Q3585	
2 point	6 point	2 point	6 point
2.66	2.66	2.63	2.69
2.77	2.72	2.76	2.72
2.68	2.73	2.65	2.76
2.79	2.71	2.78	2.63
2.60	2.60	2.50	2.59
2.58	2.69	2.57	2.59
$2.680 \pm 0.086$	$2.682 \pm 0.049$	$2.648 \pm 0.108$	$2.663 \pm 0.071$
2.87	2.79	2.91	2.80
2.79	2.71	2.72	2.70
2.73	2.79	2.78	2.87
2.70	2.74	2.78	2.73
2.56	2.65	2.47	2.54
2.74	2.75	2.77	2.77
$2.732 \pm 0.103$	$2.738 \pm 0.053$	$2.738 \pm 0.146$	$2.735 \pm 0.112$

Data are  $Q_{IR} \times 10^{-6}$ . Columns headed n-point contain Q's measured  
 at n points per boule. Standard deviations are for the sample.  
 To obtain batch values it is necessary to multiply by Yates'  
 correction  $[N/(N-1)]^{1/2}$  where N is the number in the sample.

TABLE 10

The Values of A and B in Equation (10)

	A	B(total)	B(residual)
Over all Distribution	5.00	0.37	0.30
Supplier A	4.75	0.26	0.14
Supplier B	4.94	0.24	0.10
Supplier C	5.36	0.20	0.09
Average Supplier	5.00 $\pm$ 0.31	0.23	0.11

Uncertainties in A, B (total) and B (residual) values are respectively about  $\pm 0.06$ ,  $\pm 0.04$  and  $\pm 0.05$ . Variations between batches from one supplier do not significantly exceed these values. B (total) may depend on  $Q_{IR}$ : B (total) values for  $Q_{IR} > 2.5$  are on average 0.02 less than the tabulated ones and for  $Q_{IR} < 1.5$  the B (total) values are about 0.02 higher. Note that with these values  $N_D$  is in  $\text{cm}^{-2}$ .

TABLE 11

Dislocation Densities ( $\text{cm}^{-2}$ )

Median Values		
	$Q_{IR} = 1$ million	$Q_{IR} =$ million
Over all Distribution	670	120
Supplier A	380	70
Supplier B	580	100
Supplier C	1530	270
Average Supplier	650	110
Upper Decile Values		
Over all Distribution	1700	300
Supplier A	630	100
Supplier B	850	150
Supplier C	1700	300
Average Supplier	1310	230
Worst Supplier	2100	400



Standard deviation

$0.123 \pm 0.007$  from graph

$0.125 \pm 0.007$  from data

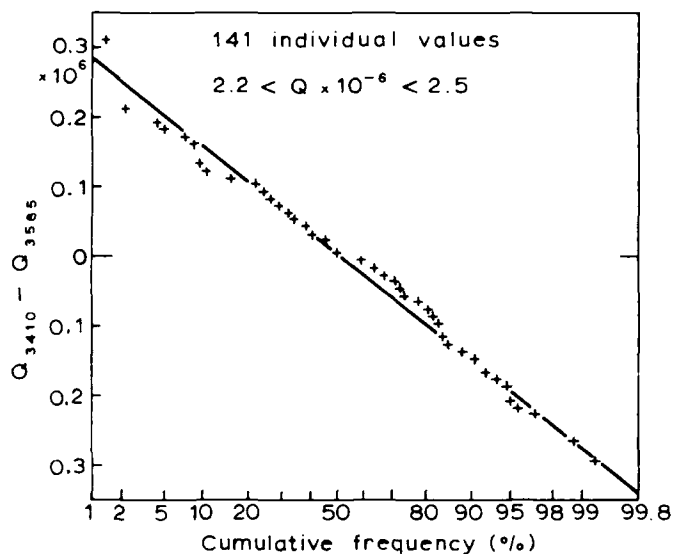


Fig. 1

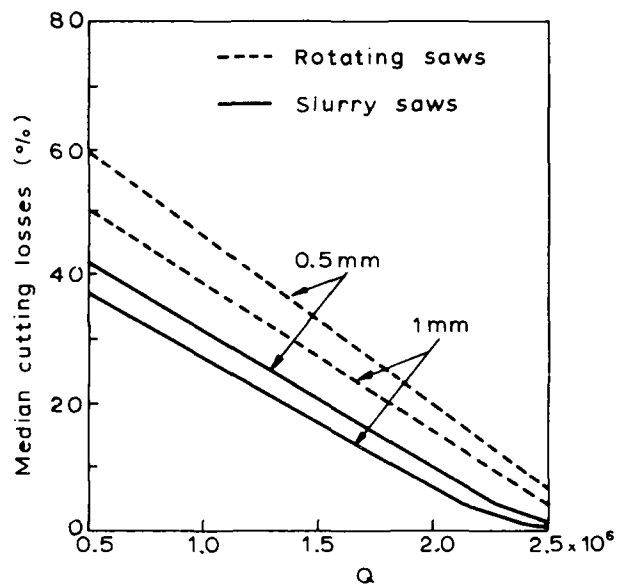


Fig. 2

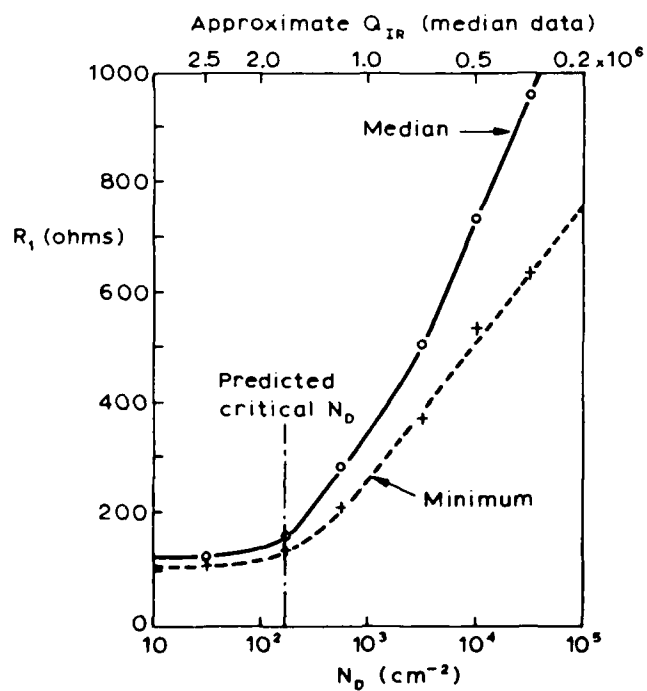


Fig. 3

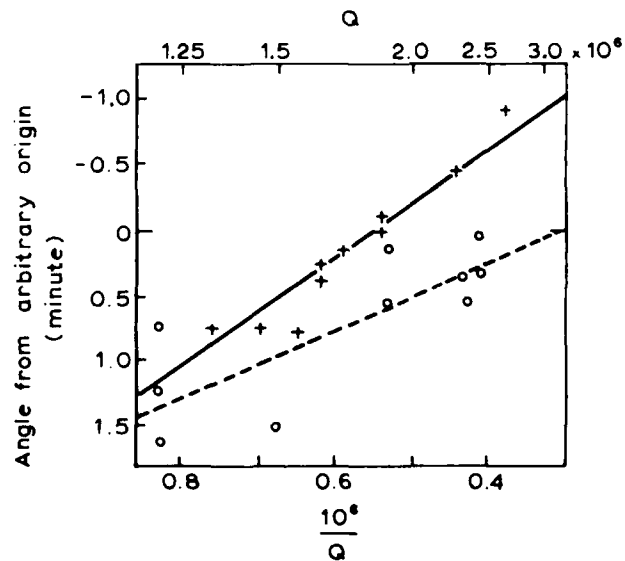


Fig. 4

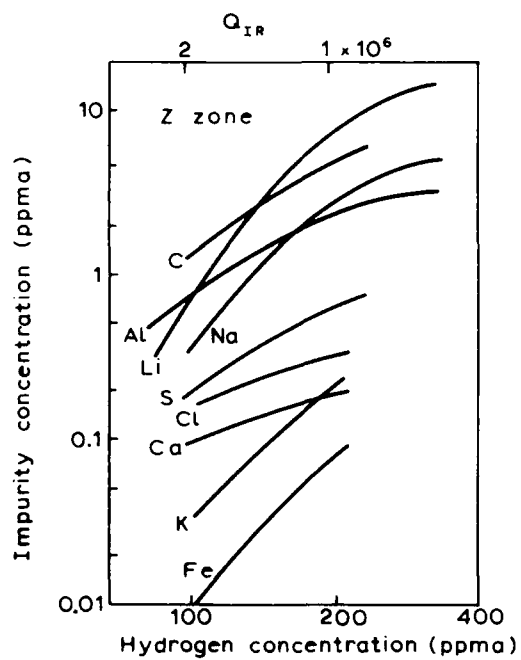


Fig. 5

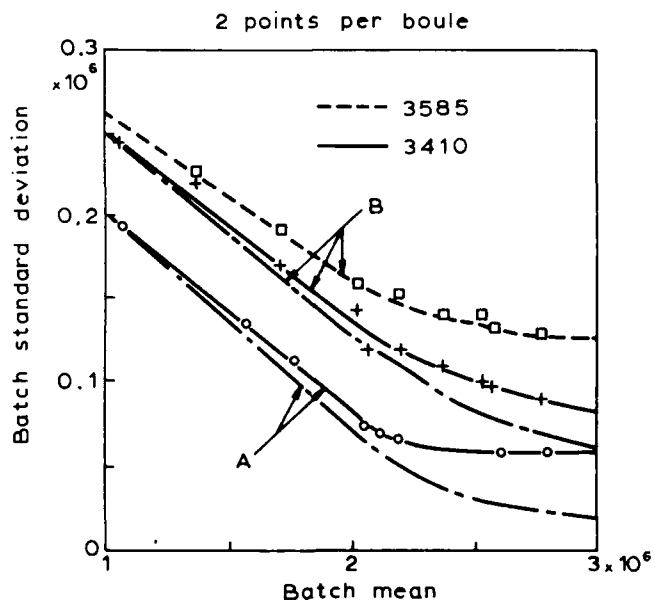


Fig. 6

3410  $\text{cm}^{-1}$  median values.

rms deviations of data  
about the median values  
are  $\pm 0,02$

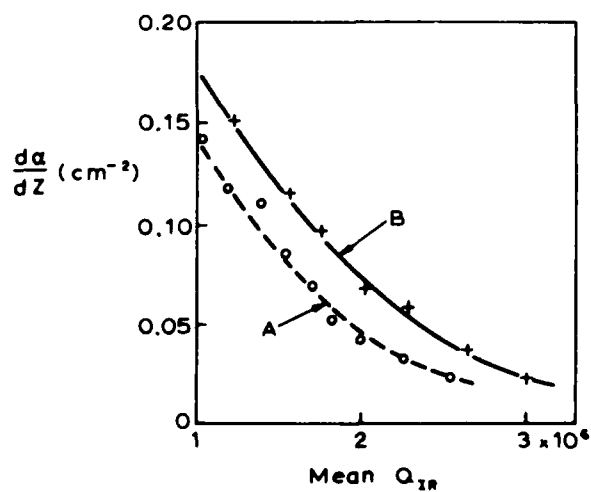


Fig. 7

X-RAY HANDEDNESS DETERMINATION ON FINISHED  
DOUBLY ROTATED QUARTZ PLATES

Henri Mériquoux and Jean-François Darces  
Laboratoire de Cristallographie et Synthèses Minérales  
Faculté des Sciences et des Techniques  
25030 Besançon Cedex - France

Jacques Lamboley  
Q.E. Alcatel  
B.P. 19  
92602 Asnières - France

Summary

A non destructive method using X-ray diffraction provides a fast solution to the determination of crystal handedness on a quartz plate. We observe successively both sides of the blank, measuring the intensity of the reflected beam on some lattice planes. With a chart calculated according to the anomalous scattering for a quartz crystal we can settle the handedness. Before this observation, we only have to know which of the two sides of the plate is the side corresponding to the " $\phi$ " angle value. Results are given for several doubly rotated quartz plates cut in cultured or natural, right or left handed, crystals.

Key words : X-ray diffraction, quartz, handedness, anomalous scattering, absolute orientation.

Introduction

Theoretically when we prepare a quartz resonator we always know the handedness of the crystal. If it is a natural quartz this property has been optically verified on the block at the very beginning of the preparation of the sawing. If it is a cultured quartz the handedness is known either from the observation of natural faces grown in the autoclave at both ends of the quartz bar, or optically verified. This quality is not lost during the process of the manufacturing of the resonator whose handedness is identified by a tag. So it seems useless to try to determine this property on a finished resonator, but sometimes we wish to verify this quality if we match right and left-handed quartz for a resonator. We also may have a set of unlabeled old quartz resonators for which we need absolutely this qualification. In such a case an optical method cannot be undertaken because it works only with plates whose orientation is close to a Z cut. The etching methods are destructive and they cannot be used on a finished resonator.

We propose a non destructive method using X-ray diffraction. On a goniometer we observe successively each side of the plate, measuring the intensity of the reflected beam on some special lattice planes. This method has been checked with slides we have made and with finished resonators, some even coated with their metallic electrodes.

The X-ray goniometer we use has been conceived in our laboratory in Besançon. This device is useful for measuring the orientation of doubly rotated cuts.<sup>1</sup> It is also very convenient for the handedness determination. The crystal is placed on a rotating table. The plate orientation is determined without any reference sample. This procedure avoids error coming from a reference measurement. The size of the quartz is of no importance. We can measure easily a quartz as big as those coming from autoclaves or as small as a watch resonator or a finished 100 MHz resonator.

Before introducing our method we recall a well known property in X-ray diffraction called anomalous scattering which gives a difference between left and right-handed crystals. This property may be also linked to the lack of an inversion center in a crystal.

Effect of the anomalous scattering

Without using the diffraction formalism but only with the reflection model of an X-ray beam upon a lattice plane, we can describe the effects of the anomalous scattering. If we call  $I_{(hkl)}$  the intensity of the X-ray reflected beam on a lattice plane of which  $h, k, l$  are the indexes, this intensity is associated with the positive direction of the perpendicular to the plane. This direction corresponds to the "+" side. Then we call  $I_{(\bar{h}\bar{k}\bar{l})}$  the intensity of the reflected beam on the same plane, but on the other side, now called "-".

The anomalous scattering theory foresees that with a non centrosymmetrical crystal as quartz the ratio  $I_{(hkl)}/I_{(\bar{h}\bar{k}\bar{l})}$  may be different from 1.<sup>2</sup> If for a right-handed quartz this ratio is greater than one :  $I_{(hkl)}/I_{(\bar{h}\bar{k}\bar{l})} > 1$ , then it will be smaller than one for a left-handed quartz :  $I_{(hkl)}/I_{(\bar{h}\bar{k}\bar{l})} < 1$ . With quartz this ratio is very close to one because the crystal is built with only silicium and oxygen atoms, which are light atoms, and because we use here the copper wavelength.

Now, the only task is to distinguish which side of the lattice plane we are observing, because the same side will give, for instance, the great value if the quartz is right-handed and the low value if it is left-handed. But we are in an actual maze because when we turn the blank on the goniometer table, the side formerly placed in front is now behind and all the observations are changed. The same observation conditions give the weak value instead of the strong one given just before. We cannot yet determine the handedness because the observed effect cannot be ascribed to the handedness. We would be able to answer the question if we had known before these observations where the side called "+" of the lattice plane is placed in the blank. This problem is nothing other than knowing the absolute orientation of the blank, i.e. determining the  $\theta$  and  $\phi$  angles with their signs on both sides of the blank.<sup>3</sup> Theoretically, when we observe the front side or the back side of a blank they have the same absolute value for  $\theta$  and  $\phi$ . Only the sign of  $\phi$  is changed. No the problem is to find the value of  $\theta$  and  $\phi$  with their signs.

### Determination of $\Theta$ and $\Phi$ angles

The absolute value of these angles are deduced from the observation of two different reflections. For a doubly rotated cut these two angles are calculated from the observation of three or more reflections. A theoretical point of view requires thus because from the three perpendiculars to the observed lattice planes we have a three axis system. By angular transformations we can express the blank orientation with  $\Theta$  and  $\Phi$ . If it is a routine control, we need only two measurements.

#### Determination of the $\Theta$ angle sign

The sign of  $\Theta$  angle is very easily determined using the symmetry difference between the quartz crystal and its lattice. The quartz symmetry is lower than that of the lattice. Their point groups are respectively 32 and 6/m mm. For that very reason we have a difference between the reflected beam on two lattice planes as (hkl) and (khl). In chart we find the value of the ratio  $I_{(hkl)}/I_{(khl)}$ . For the sign determination it is very helpful to observe planes for which this ratio is very small or very large. So if we can see a reflection on one of them, the reflection on the other is too weak to be noticed. If the chart gives the indexes of the plane and its  $\Theta$  and  $\Phi$  position, with the reflective power we deduce immediately the sign of the  $\Theta$  angle. The absolute value has been determined before. This method can only give the sign of  $\Theta$  because as we have seen that the sign of  $\Phi$  is changed with the side of the observed blank.

#### Determination of the $\Phi$ angle sign

For the determination of the  $\Phi$  angle sign we use a very different method. Given three lattice planes 1, 2, 3 of the quartz crystal and their perpendiculars, respectively  $\vec{n}_1, \vec{n}_2, \vec{n}_3$ , these three directions form an axis system. The blank being placed on the goniometer table, from the front side we can see this axis system as a right-handed system. Turning the blank to the opposite side, the same axis system is now left-handed.

If we project these three directions  $\vec{n}_1, \vec{n}_2, \vec{n}_3$  on the plane of the blank, we have  $\vec{p}_1, \vec{p}_2, \vec{p}_3$ . With the goniometer we use, we are able to measure the angles  $\mu_1, \mu_2, \mu_3$  between  $\vec{p}_1, \vec{p}_2, \vec{p}_3$  and a direction on the blank, for instance the edge of the blank. When the axis system is right-handed we have the following inequality  $\mu_1 < \mu_2 < \mu_3$ . When it is left-handed we have:  $\mu_1 > \mu_2 > \mu_3$ . So we can find a distinction between both sides of the blank. In practice we compute these  $\mu$  angles for three or more reflections on both sides of the blank. It corresponds to the orientations  $\Theta, +\Phi$  and  $\Theta, -\Phi$ . Then we measure the  $\mu_0$  angle on one side of the blank. Comparing the observed values  $\mu_0$  with the calculated values  $\mu_c$  we deduce the "sign" of the front side.

#### Handedness determination

As previously seen, we know which side of the plate is placed in front of us on the goniometer sample holder. We measure the intensity of the reflected beam on the same lattice plane for each side of the plate and, from the difference which appears, we deduce the crystal handedness. This method

has been checked for plates of several origins.

#### First plate

$\Theta = 12,24^\circ \quad  \Phi  = 8,55^\circ$						
Side "+ $\Phi$ "			Side "- $\Phi$ "			Observed side
(hkl)	$\mu_c$	$\mu_c - \mu_0$	(hkl)	$\mu_c$	$\mu_c - \mu_0$	$\mu_0$
(040)	55	290	(0 $\bar{4}$ 0)	305	180	125
(124)	259	338	( $\bar{1}$ 2 $\bar{4}$ )	101	180	281
(120)	131	82	( $\bar{1}$ 20)	229	180	49
The observed side is the side "- $\Phi$ "						

Table 1

On this table we have, on the first line, the plate orientation expressed by  $\Theta$  and  $|\Phi|$ . Then, we have three columns: one for the side corresponding to the  $+\Phi$  angle, one for the side corresponding to the  $-\Phi$  angle and one for the observed side we have called previously the front side. The indexes of the lattice planes and the differences between the calculated and observed values of the  $\mu$  angles are indicated for each sign of the  $\Phi$  angle. As the difference remains constant for one of the two hypotheses on the  $\Phi$  angle sign, the absolute orientation of the front side is  $\Theta = 12,24^\circ$ ,  $\Phi = -8,55^\circ$ .

On the chart we read  $I_{(120)}/I_{(\bar{1}20)} = 1,22$  and  $I_{(124)}/I_{(\bar{1}2\bar{4})} = 0,98$  for a left-handed crystal. The first measured intensity associated with ( $\bar{1}20$ ) is 3350 (arbitrary unit), and the second associated with (120) is 4200. With the same arbitrary unit,  $I_{(124)} = 13100$  and  $I_{(\bar{1}2\bar{4})} = 13400$ . We conclude that the plate has been cut in a left-handed crystal. It is the expected handedness, because it was a natural quartz, with the characteristic left trigonal trapezohedron, in which a very thick Z-cut has been optically checked.

#### Second plate

$\Theta = 34,65^\circ \quad  \Phi  = 22,50^\circ$						
Side "+ $\Phi$ "			Side "- $\Phi$ "			Observed side
(hkl)	$\mu_c$	$\mu_c - \mu_0$	(hkl)	$\mu_c$	$\mu_c - \mu_0$	$\mu_0$
( $\bar{1}$ 16)	280	204	(1 $\bar{1}$ 6)	80	4	76
( $\bar{1}$ 43)	175	354	(14 $\bar{3}$ )	185	4	181
( $\bar{1}$ 21)	52	108	(12 $\bar{1}$ )	308	4	304
The observed side is the side "- $\Phi$ "						

Table 2

For a left-handed crystal :  $I_{(1\bar{2}\bar{1})}/I_{(\bar{1}21)} = 1,18$   
and  $I_{(1\bar{4}\bar{3})}/I_{(\bar{1}43)} = 1,05$

$$I_{(1\bar{2}\bar{1})} = 27400 \quad I_{(\bar{1}21)} = 32400$$

Observation :  $I_{(1\bar{4}\bar{3})} = 8900 \quad I_{(\bar{1}43)} = 9500$

Conclusion : Right-handed quartz.

This plate has been cut in a cultured quartz block.

#### Third plate

$\Theta = 35,11^\circ \quad  \Phi  = 21,50^\circ$						
Side "+ $\Phi$ "			Side "- $\Phi$ "			Observed side
(hkl)	$\mu_c$	$\mu_c - \mu_o$	(hkl)	$\mu_c$	$\mu_c - \mu_o$	$\mu_o$
(052)	143	282	(0 $\bar{5}\bar{2}$ )	217	356	221
( $\bar{1}21$ )	53	282	( $1\bar{2}\bar{1}$ )	307	176	131
( $\bar{2}34$ )	308	282	( $2\bar{3}\bar{4}$ )	52	26	26
The observed side is the side "+ $\Phi$ "						

Table 3

For a left-handed crystal :  $I_{(1\bar{2}\bar{1})}/I_{(\bar{1}21)} = 1,18$   
and  $I_{(\bar{2}34)}/I_{(2\bar{3}\bar{4})} = 1,21$

$$I_{(1\bar{2}\bar{1})} = 29500 \quad I_{(\bar{1}21)} = 24700$$

Observation :  $I_{(\bar{2}34)} = 2450 \quad I_{(2\bar{3}\bar{4})} = 2050$

Conclusion : left-handed quartz

This plate has been cut in a cultured quartz block.

#### Fourth plate

$\Theta = 9,25^\circ \quad  \Phi  = 15,08^\circ$						
Side "+ $\Phi$ "			Side "- $\Phi$ "			Observed side
(hkl)	$\mu_c$	$\mu_c - \mu_o$	(hkl)	$\mu_c$	$\mu_c - \mu_o$	$\mu_o$
(021)	222	4	(0 $\bar{2}\bar{1}$ )	138	280	218
( $\bar{1}41$ )	251	62	( $1\bar{4}\bar{1}$ )	109	280	189
( $\bar{1}30$ )	66	52	( $\bar{1}30$ )	294	280	14
The observed side is the side "- $\Phi$ "						

Table 4

For a left-handed crystal :  $I_{(1\bar{3}0)}/I_{(\bar{1}30)} = 1,22$

Observation :  $I_{(1\bar{3}0)} = 6600 \quad I_{(\bar{1}30)} = 5300$

Conclusion : Left-handed quartz.

This plate is a finished resonator, coated with electrodes.

Note : When measuring the intensities of the reflected X-ray beam, we have to take care that each side of the plate presents the same surface finish.

#### Conclusion

The quartz handedness determination for doubly rotated plates is easily obtained taking in account X-ray diffraction properties, in particular the anomalous scattering effect, and using a special goniometer. This method is suitable for all enantiomorphous crystals.

#### Acknowledgements

We would like to express our thanks to Professor Karl Hruska of the York University Toronto who supplied us with some of his resonators and to the D.R.E.T. (Direction des Recherches Etudes et Techniques) of the Ministry of Defense who sponsored this research.

#### References

- 1) "Final X-ray control of the orientation of round or rectangular quartz slides for industrial purposes", J.F. Darces, H. Mérioux, 32nd Annual Frequency Control Symposium, Atlantic City 1978.
- 2) The crystalline state. Vol. II : The optical principles of the diffraction of X-rays, R.W. James, G. Bell and Sons Ltd, London 1965.
- 3) "Dissymmetry used for  $\Phi$ ,  $\Theta$  angle sign determination of a piezoelectric crystal blank by a non destructive method", J.F. Darces, J. Lamboley, H. Mérioux, Ferroelectrics, vol. 40, pp. 245-248, 1982.

RESISTANCE - MEASUREMENTS OF QUARTZ CRYSTALS AT VERY LOW DRIVE LEVELS

J.S. Yerna

Philips Quartz Crystal Devices  
Doetinchem, HollandSummary

The change in application caused by the introduction of I.C.'s with low power and low noise level has an impact on the starting up behaviour of quartz crystals. This paper discusses various ways of measurement with respect to the behaviour of  $R_R$  in a large drive level spectrum.

1. INTRODUCTION

Since Prof. Cady demonstrated the first quartz stabilized oscillator in the year of 1919, the construction and also the application of quartz crystal units have changed tremendously. When we consider the progress over the past forty years, we see that the frequency stability of quartz crystal oscillators has improved roughly by a factor 10 each decade. The growing demand for quartz crystal units with better stability figures has forced the crystal industry to improve their crystal design techniques and to look for new materials and technologies. (CAD and CAM).

The availability of new active components like transistors and integrated circuits (which are essential low-voltage solid-state devices) has opened the way to oscillators with lower power consumption and with that a neglectable own warming-up which is important for a good stability. The introduction of such oscillators had had an impact on quartz crystal design and specification. It may be of interest to see how the applied drive level changed through the years as a result of new oscillator design. (See fig. 1.)

In 1950 to 1960, drive levels of 10 mW. were normal and even drive levels of 20 mW. were not unusual. Nowadays, drive levels for AT-cut bulkwave resonators are mostly specified at 500  $\mu$ W., but we see a growing number of applications where the level of drive is reduced to a few  $\mu$ W.

The subject we will discuss now is the measurement of the dependency of some quartz crystal parameters to drive level variations. We prefer the use of the term D(rive) L(evel) D(ependency) which is, in our opinion, more universal than S.L.D.

2. NONLINEARITIES OF  $R_R$  AT LOW DRIVE LEVELS

The lowering of the drive levels in crystal oscillators introduced a phenomenon that hardly was known before. Namely the increasing of the resonance resistance of crystal units at low drive levels. Back in the year of 1954 Mr. E.A. Gerber reported this effect for the first time. After that, it became more and more evident, that this effect could have a great influence on the reliability of quartz crystal oscillators, especially when the applied drive level is low. In MIL-C-3098 D appears for the first time a low drive level test, the well known  $\frac{1}{4}$  scale division method. This means a check at a level of drive of approximately 100  $\mu$ W. A more sophisticated version of the MIL-method was proposed by Mr. M. Bernstein in 1967. A diagram of this set up is given in fig. 2. Fig. 3 shows some graphic results obtained with this method. This method was later adopted in MIL-C-3098 E, F and G. One of the most important disadvantages of this measuring method is, that the lowest detectable drive level is somewhat below 1  $\mu$ W. which is much too high to investigate the crystal behaviour at noise levels. Some other attempts were made after that, to measure D.L.D., but no solution was usable for final check of crystal units before shipment.

In order to overcome this lack of adequate measuring equipment for D.L.D. testing PHILIPS has developed its own measuring systems. Before discussing these systems, we have to remember the basic principles of quartz crystal oscillators. (See fig. 4.)

Every crystal oscillator can be considered as an amplifier with a feed back network in which the quartz crystal is incorporated. To make such circuit oscillating, there are 2 important conditions which have to be fulfilled.

1. The loop gain must be  $>1$ .
2. The feed-back signal at the amplifier input must have the correct phase angle.

When a crystal oscillator is switched on, there is only some noise power at the amplifier output which is for modern devices far below 1  $\mu$ W.

A very small part of this noise spectrum can pass the feed back network with the quartz crystal. When this signal arrives at the input with the correct phase angle, oscillation will be build up in accordance with the e-law.

It will be clear, that the presence of some non-linearity of  $R_R$  can cause starting troubles during this critical phase.

### 3. THE PHILIPS APPROACH FOR MEASUREMENT OF D.L.D.

In general one can say that there are basically 2 ways for quartz crystal measurement: active and passive, each having its own advantages and disadvantages.

Measurement of the D.L.D. effect of quartz crystal units can also be done both active and passive. Block diagram 5 shows schematically the measuring systems which have been developed within PHILIPS including the usable frequency and drive level range of each method.

Before discussing in detail the 4 measuring methods, it is good to point out the application field each method was developed for.

**METHOD 1:** This is a fast go-nogo test for screening large quantities of fundamental quartz crystal units which we are producing for consumer and semi-professional applications.

**METHOD 2:** This is an improved version of method 1 which gives more qualitative information about the quartz crystal unit under test. The measuring time is about 4 times method 1.

**METHODS 3 and 4:** These methods are based on the passive transmission method according to the I.E.C.-444 recommendation. The advantages of these methods are, that the D.L.D. of both resonance frequency and resonance resistance can be measured at the same time over wide power ranges in a good, reproducible way. The application field is primarily the manufacture of high professional quartz crystal units.

### 4. D.L.D. OSCILLATOR FOR GO-NOGO TEST OF QUARTZ CRYSTAL UNITS

**PRINCIPLE OF MEASUREMENT:** (See fig. 6). This test set up consists of a carefully designed crystal oscillator which can be considered as a true negative resistance over a wide frequency range, a feed back network which limits the power dissipation in the crystal unit to  $10^{-3}$  Watts and a detector circuit with a LED for visual indication. The negative resistance (and with this the D.L.D. reject level) of the oscillator can be changed by connecting a positive resistor in series with the oscillator. In this manner, each value between 0 and 200  $\Omega$  may be selected. Connecting a quartz crystal unit with a

sufficient low  $R_R$ -value between the test clamps, an oscillation will build up starting from the initial noise level (approximately  $10^{-10}$  to  $10^{-15}$  Watts) to its limitation point of  $10^{-3}$  W. following the e-law. (Fig. 7).

If the crystal under test should show a certain degree of D.L.D., it is possible that the oscillation amplitude cannot reach the  $10^{-3}$  W. limiting point (point B in fig. 8).

In the example of fig. 8, the building up of the oscillation is terminated at a much lower level of drive (point A). Normally, in such cases no oscillation is observed and only with very sensitive equipment, some oscillation can be established.

If a crystal reaches the 1 mW. level (point B), the LED indicator will light up. This means that the quartz crystal's resonance resistance did not exceed the D.L.D. reject level during its starting up from  $10^{-15}$  Watts.

D.L.D. test oscillators of this type are employed on automatic inspection machines used for quantity production. A disadvantage of this method (which had led to the development of method 2) is, that it is not a real D.L.D. measurement rather than a check for  $R_R$ -max. in a certain drive level range.

A crystal unit with a  $R_R$ -curve like curve I in fig. 9 for example, would pass this test as a good one. On the other hand, crystals with curves like curve II would have been rejected although the D.L.D. is much smaller.

The advantages of this measurement are: fast, easy to calibrate, simple set up and inexpensive.

### 5. "AR" MEASUREMENT (METHOD 2)

This is essentially the same negative resistance oscillator of -200 $\Omega$  as described with method 1.

The difference is, that the oscillator's negative resistance is almost 0 $\Omega$  at normal state. This means no oscillation can occur. After triggering the control logic, (manual or automatic, see fig. 10) the negative resistance of the oscillator will grow very slowly.

This is done by a pindiode attenuator. At a certain negative resistance level, the loop gain will exceed 1 and oscillation starts. When the amplitude of oscillation reaches the 1 mW. level, the pindiode attenuator will keep oscillation at this level for approximately 1 second. After that, the oscillator is brought back to its normal state which means -R is almost 0 $\Omega$  and oscillation stops. The oscillator is ready now for the next trigger command.

The principle behind this measuring method is as follows: The control voltage to the pindiode attenuator has a close relation to the crystal's  $R_R$ .

So the maximum control voltage (corresponding with highest  $R_R$ -value) necessary for maintaining oscillation between  $10^{-5}$  and  $10^{-3}$  Watt is stored in an analogue memory. Reaching the  $10^{-3}$  Watt level, this corresponding  $R_R$ -value is subtracted from the stored  $R_R$ -max. value. The result, we call this " $\Delta R$ ", is displayed on a meter, or, in case of automatic repeating measurement, recorded with an X-t recorder. (See fig. 11).

The advantages of this method are:

- relative simple set up, inexpensive;
- method gives qualitative information about D.L.D.;
- relative short measuring time (between 2 and 5 seconds).

Some disadvantages are:

- limited frequency range;
- difficult callibration of  $\Delta R$ ;
- no measurement of  $F_R$ , as a function of drive level changes.

#### 6. D.L.D. MEASUREMENT OF QUARTZ CRYSTAL UNITS, USING THE I.E.C. $\pi$ -NETWORK (METHODS 3 AND 4)

##### PRINCIPLE OF MEASUREMENT

Fig. 13 shows the well known  $\pi$ -network which is adapted with 2 stepping attenuators. With this set up, a drive level range from  $2,5 \times 10^{-5}$  to  $5 \times 10^{-3}$  Watts can be scanned automatically in two ranges, using 1 dB steps.

The great advantage of using 2 attenuators is, that the RF voltage on channel B of the vector volt meter remains constant over the entire 64 dB power range. This means for example, that crystals can be driven over a dynamic power range of 64 dB without changing meter settings or re-callibration of the  $R_R$  measurement.

During the development of this measuring method, it became clear, that for drive levels below 10 nW., the vector volt meter sensitivity was not sufficient and also the S/N ratio was bad. For these reasons, a different  $\pi$ -network has been developed. A simplified diagram of this network is shown in fig. 14. The last part of the  $\pi$ -network was replaced by a low noise transistor in a common base configuration. Using this special network, the drive level range was extended to 0,25 pW. with a reasonable S/N ratio.

##### MEASURING PROCEDURE

- Connect network A or B to the measuring system, depending on the desired drive level range.

- Insert the quartz crystal unit and wait for automatic lock of the PLL.

- Depress the start button. Both attenuators are switched now in an opposite sense at regular intervals by a signal from the control logic. The stepping time (scanning speed) may be selected between 1 dB per 10 seconds to 10 dB per second.

- During one complete measuring cycle, the drive level of the crystal unit under test is varied from -64 dB to max. and than back to -64 dB in 1 dB steps.

- The resonance frequency  $F_R$  and the resonance resistance  $R_R$  of the crystal unit as a function of the level of drive are recorded simultaneously using a 2 pen XY-recorder.

Fig. 15 to 18 are showing some measuring results, obtained with these methods.

##### References

1. E.A. Gerber: "VHF crystal grinding"; Electronics, Vol. 27 No. 3, pp. 161 - 163. March 1954.
2. M. Bernstein: "Increased crystal unit resistance at oscillator noise levels"; Proc. of the 21st Annual Frequency Control Symposium.
3. MIL-C-3098 D through G and MIL-C-3098 H (Draft).
4. A. Verhulst: "D.L.D. measurement using an EBM oscillator"; PRR 54/18-822 (Internal PHILIPS report).
5. H. Dohmen: "Guide to the measurement of quartz crystal unit parameters"; PRR 54/18-811 (Internal PHILIPS report).
6. IEC publication 444.
7. C. Franx: "On precision measurements of frequency and resistance of quartz crystal units"; Proc. of the 23rd Annual Frequency Control Symposium, Atlantic City, May 1969.



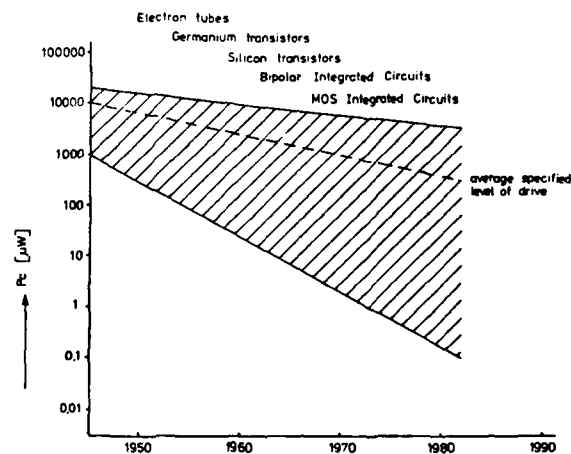
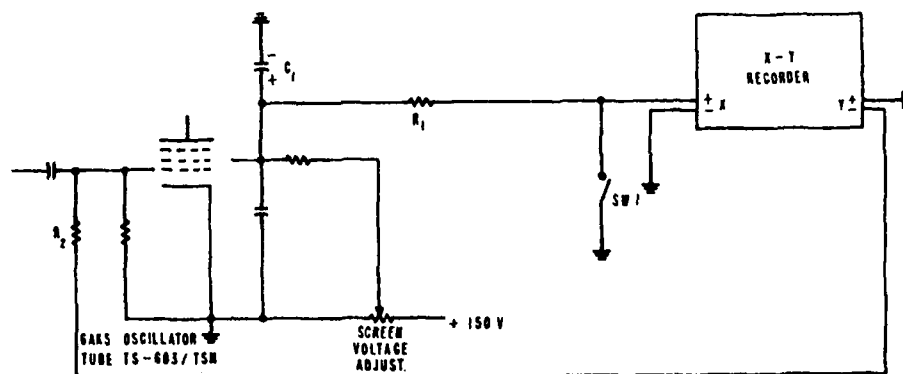


fig. 1



COMPONENTS ADDED TO C.I. METER TS 603/TSN

$C_1$  1000  $\mu F$  / 35 V

$R_1$  1 K  $\Omega$  1/4 W

$R_2$  15 K  $\Omega$  1/4 W

SW 1 NO. PUSH TO CLOSE SWITCH

FIG. 2 MODIFICATION OF CRYSTAL TEST SET

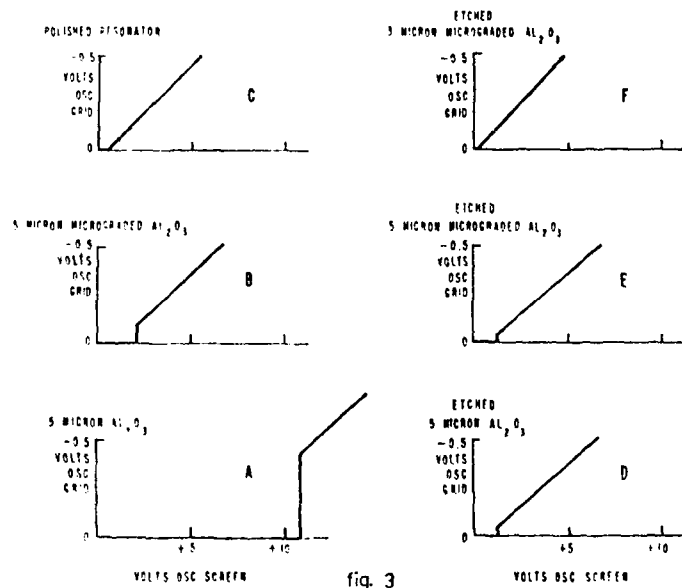
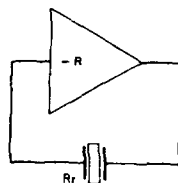


fig. 3

PLOT OF HIGH-STARTING RESISTANCE IN QUARTZ CRYSTAL UNITS



- loop gain  $> 1$ , which means  $-R > R_r$   
 - feed back signal at osc. input must have correct phase

fig. 4

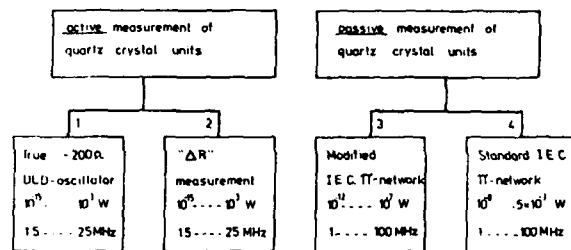


fig. 5

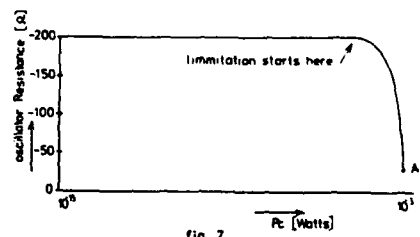


fig. 7

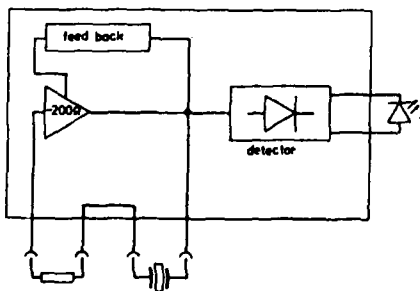


fig. 8

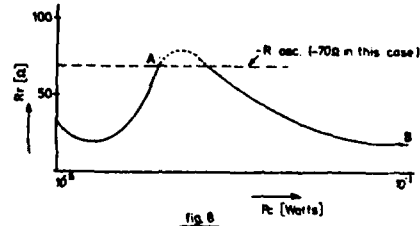
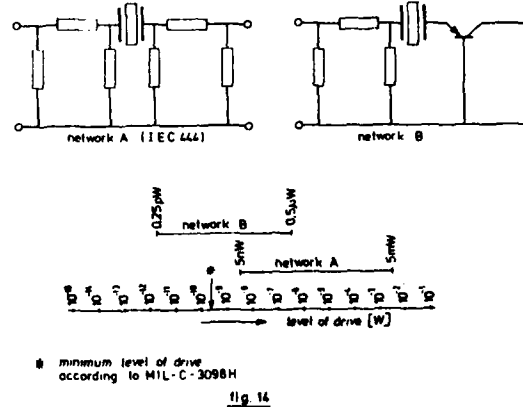
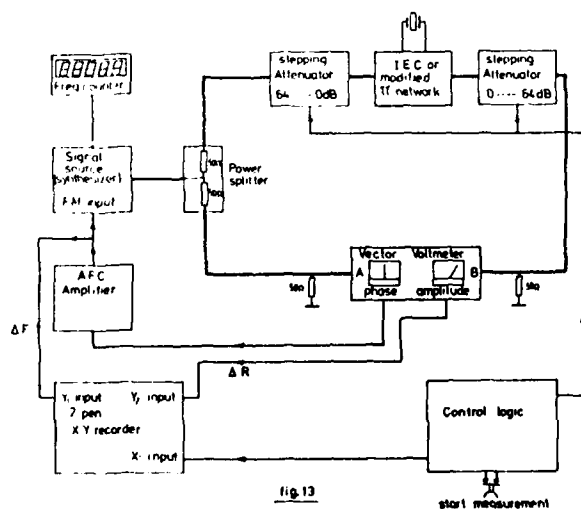
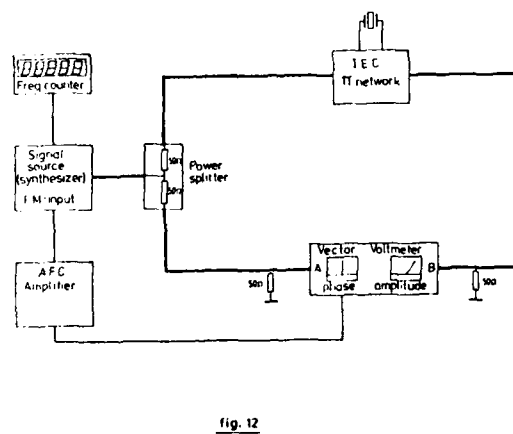
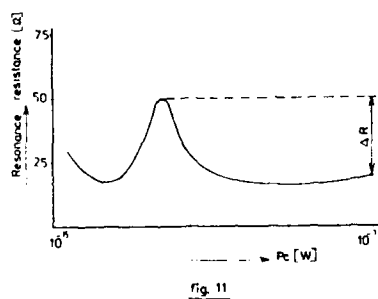
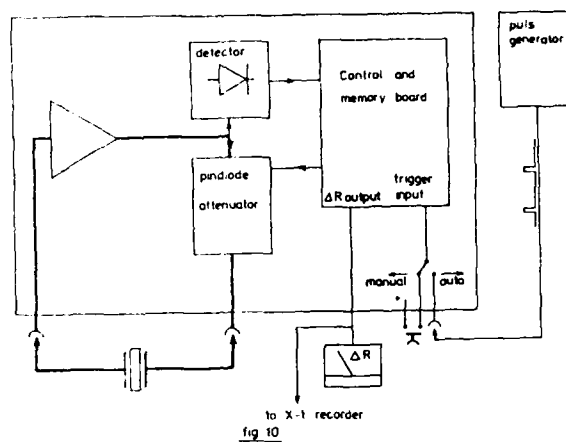
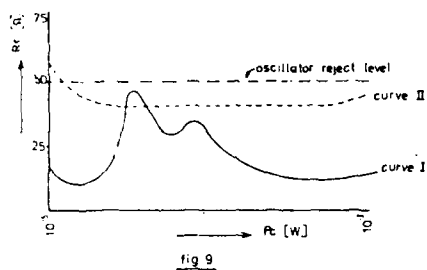


fig. 8



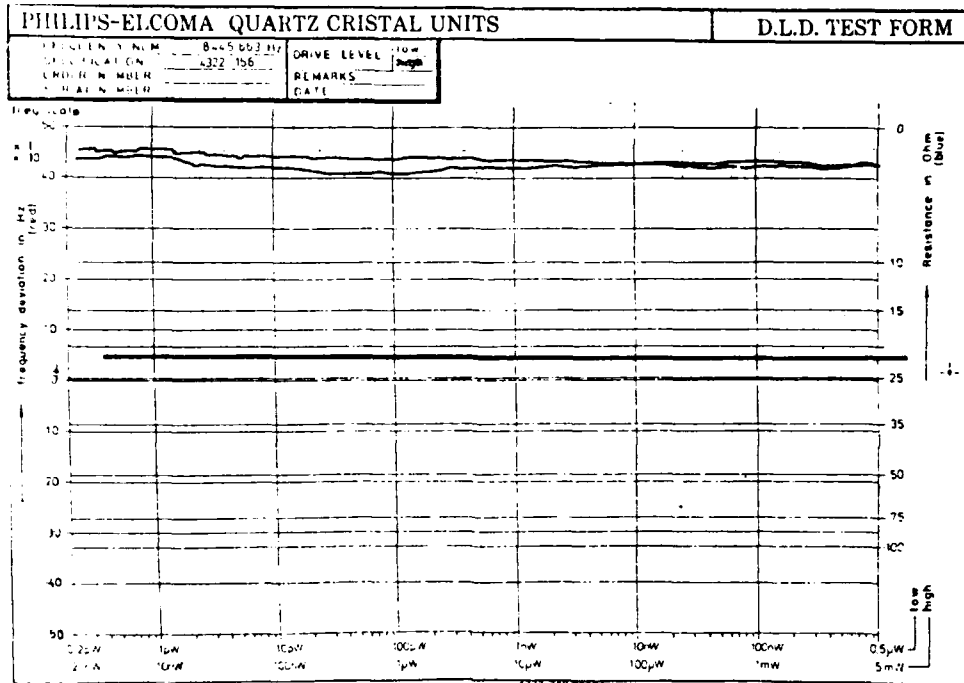


fig. 15

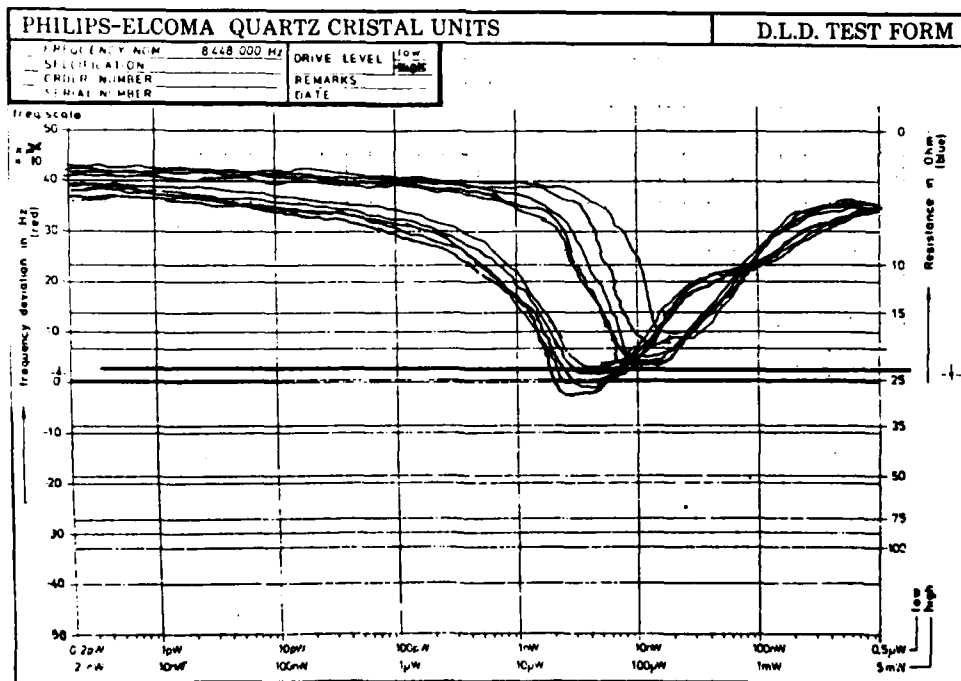


fig. 16

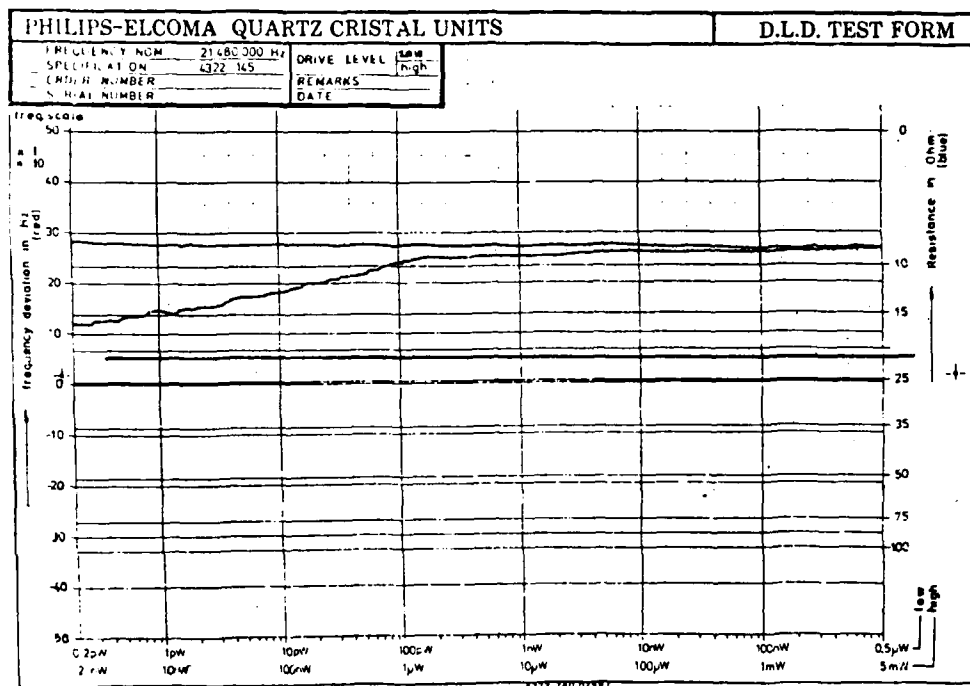


fig. 17

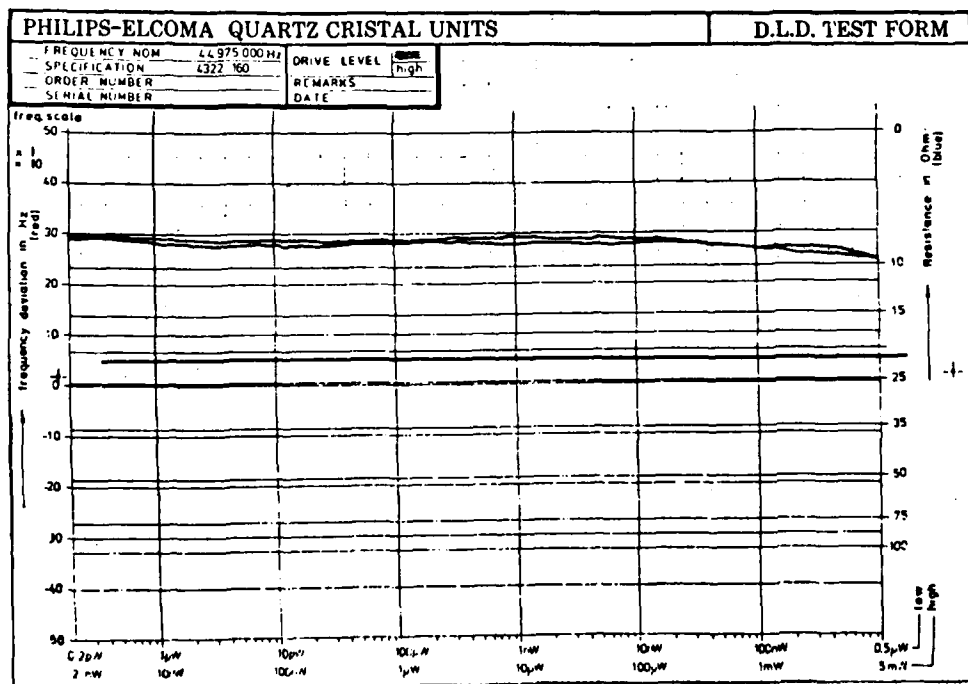


fig. 18

happens normally during its service lifetime. Clearly, an aging measurement made during thermal cycling, as described above, gives a more realistic indication of how an oscillator will age in the field, particularly if the duration of the test is limited to 30 days. The present standard aging test will probably be revised.

It is interesting, and unexplained, that one group showed better aging during thermal cycling than at constant temperature.

#### DC Bias Induced Aging

Elsewhere in these proceedings is a paper entitled "Aging Studies On Quartz Crystal Resonators and Oscillators" in which it is shown that a DC bias on a resonator can have a long term effect on the frequency of the resonator. The effect is independent from the polarization effect observed for SC-cut crystals.

Several of the TCXO that were tested for this paper were opened and tested for the presence of such a DC bias. A voltage was found in all cases, ranging in value from 100 millivolts to more than four volts.

While further investigation of the effects of low voltages on TCXO resonators remains to be done, designers may want to take this phenomenon into account and design new circuits to eliminate any DC bias on the resonator.

#### References

1. Rosati, V., Schodowski, S., Filler, R., "Temperature Compensated Crystal Oscillator and Test Results," Proceedings of the 37th Annual Frequency Control Symposium, Philadelphia, PA, June, 1983
2. Ballato, A., "Frequency-Temperature-Load Capacitance Behavior of Resonators For TCXO Applications," IEEE Transactions on Sonics and Ultrasonics, Vol. SU-25, No. 4, July, 1978

## FURTHER RESULTS OF TEMPERATURE COMPENSATED CRYSTAL OSCILLATOR TESTING

Vincent Rosati and Peter Thompson

US Army Electronics Technology and Devices Laboratory (ERADCOM)  
Fort Monmouth, New Jersey, 07703Summary

The availability of Temperature Compensated Crystal Oscillators (TCXO) in the one part per million (ppm) class remains a problem for military designers.

A continuing evaluation at Fort Monmouth, NJ, is aimed at determining the capabilities of TCXO, particularly the higher stability types.

Since the last (37th) Frequency Control Symposium, at which initial results of the program were reported, additional high stability TCXO have been ordered. Significantly, three of the vendors who had claimed a capability of making 0.6 or better TCXO requested cancellation of orders after more than one year.

This paper will present the results of measurements of frequency-temperature stability, trim effect, aging at constant temperature, and aging during repeated temperature cycling.

The data reinforce our previously stated findings that TCXO in the one ppm stability class are at the edge of the state of the art, and notwithstanding manufacturer's claims to the contrary, 0.6 ppm or better TCXO are not available for use over a wide (e.g., -55 C to +85 C) temperature range.

Key words

Crystal oscillator, aging, stability, trim effect

Introduction

It is often found that the Temperature Compensated Crystal Oscillators (TCXO) that are specified for military systems fail after a relatively short time, sometimes even before a delivered system is released to the field. The failures are chiefly related to out-of-tolerance frequency performance. In some cases the cause has been found to be poor aging and, as a result, the consequent distortion of the frequency-temperature curve due to the trim effect (sometimes referred to as "skew"). In other cases, the oscillators could not provide the required frequency-temperature (f-T) stability even before any long term aging.

To assess the current state of the art of moderate precision TCXO, there has been an ongoing program of testing and evaluation at Fort Monmouth. Initial results of the program

were presented at the 37th Frequency Control symposium and the reader is referred to the Proceedings for a description of the tests and apparatus used.<sup>1</sup>

Since the first presentation of this work, an additional 40 oscillators have been received and tested. The new oscillators were specified to have f-T stability better than 1 part per million (ppm).

Two additional tests have been added to the previous battery, namely, trim effect and aging during thermal cycling. (The trim effect<sup>2</sup> is the rotation of a resonator's f-T characteristic caused by the insertion or adjustment, i.e., trimming, of a series load capacitor to tune the resonator to frequency.) The trim effect test gives an indication of the useful life of a particular TCXO design when coupled to the typical aging performance of that design. The aging during thermal cycling gives a more realistic indication of the performance of an oscillator than aging at constant temperature.

Trim Effect

Oscillator f-T curves were first obtained after setting the frequency to the marked calibration frequency at the marked calibration temperature by adjustment of the trimmer capacitor or potentiometer. The oscillators were then offset +2, +4, -2, and -4 ppm. After each readjustment the f-T curve was again observed. Figure 1 is typical of the results obtained. Note that when this

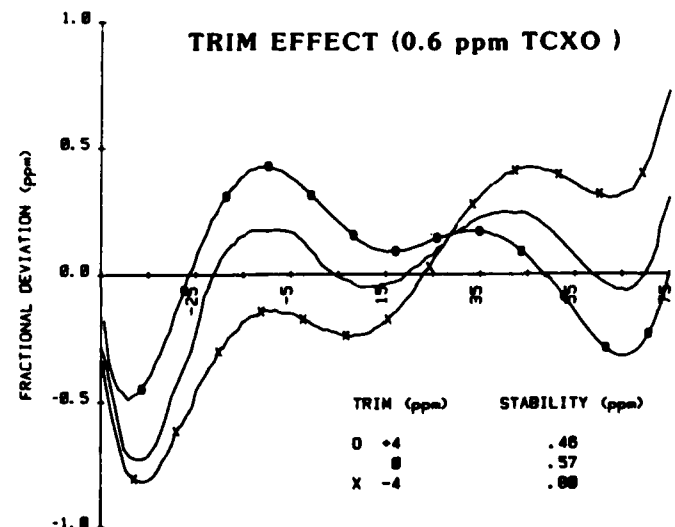


Fig. 1 Frequency-temperature stability of a typical 0.6 ppm TCXO at different trimmed frequency offsets.

oscillator is adjusted for -4 ppm offset (to correct for a hypothetical aging of +4 ppm), the stability falls outside the 0.6 ppm specification limit. The rotation of the f-T curve is obvious.

Table I shows the results of trim effect tests on 56 TCXO. Observe that for oscillators in the classes of one to three ppm the trim effect has no influence on f-T stability. However, for stabilities better than 0.6 ppm a frequency trim of four ppm caused all but one of the models to degrade beyond the f-T specification. Also note that three vendors, who had promised delivery of five TCXO each with 0.2, 0.5, and 0.6 ppm, cancelled the orders at their own request. It is evidently still true that 0.6 ppm (f-T stability) and better TCXO are at the edge of the state of the art.

### FREQUENCY-TEMPERATURE RESULTS

CLAIMED STAB (ppm)	# PASSED F-T (zero trim)	# PASSED F-T (4 ppm trim)
3	4/5	4/5
2	5/5	5/5
1	4/5	4/5
1	5/5	5/5
1	4/5	4/5
1	3/3	3/3
.6	0/3	0/3
.6	3/5	0/5
.6	4/5	0/5
.5	5/5	5/5
.5	3/5	1/5
.5	0/5	0/5
.6	MFG. CANCELLED	
.5	MFG. CANCELLED	
.2	MFG. CANCELLED	

TABLE I Summary of results of trim effect test.

### Aging During Thermal Cycling

Two oscillators from each group of five from seven vendors were subjected to the thermal cycling profile shown in Fig. 2. The other three oscillators from each group were aged at a constant temperature (60 deg. C).

The cycled oscillators were held at 60 C for twenty hours. The frequency was then measured and recorded. Following the frequency measurement, the temperature chamber was set to -60 C for two hours, then to +80 C for two hours, then returned to 60 C. This profile was repeated daily except that once every seven days a f-T curve was generated. The temperature of the constant-temperature chamber was stable to  $\pm 0.05$  C for the duration of the test. The temperature of the cycled-temperature chamber retraced to  $\pm 0.125$  C. The data shown below represent the results of 38 days of testing.

Figure 3 is a representative plot of the aging of a thermally cycled TCXO versus the aging of a TCXO of the same design held at constant temperature. Table II is a summary of the results of aging 35 TCXO (14 cycled and 21 constant temperature). Note here that the usual effect is to worsen the total aging if the TCXO is repeatedly temperature cycled, as

## "CYCLE" CHAMBER TEMPERATURE PROFILE

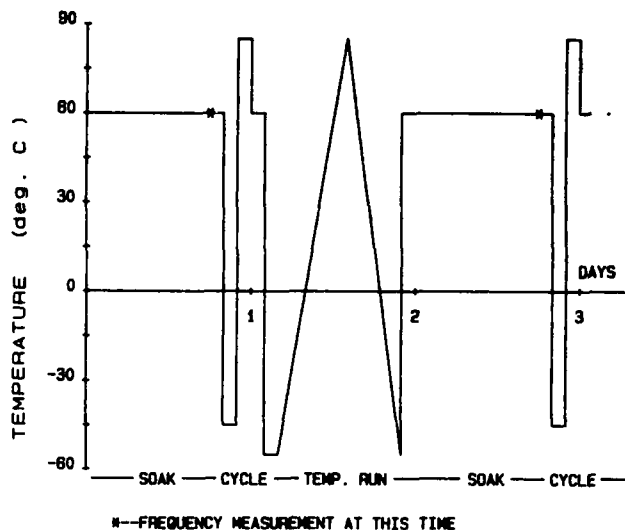


Fig. 2 Thermal profile used for the aging-during-thermal-cycling measurement. Frequency-temperature runs, indicated by the triangular profile, were made once per week.

### AGING VS THERMAL HISTORY

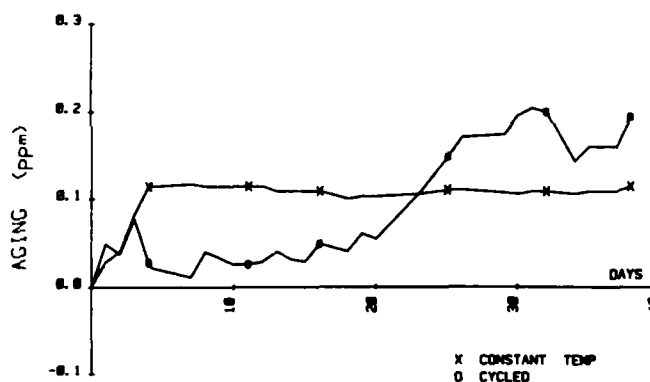


Fig. 3 Representative aging curves comparing TCXO aged at constant temperature and during thermal cycling.

### AGING VS THERMAL HISTORY

LOT NUMBER	AGING + (ppm) CONST TEMP	AGING + (ppm) TEMP CYCLE	RATIO CYC/CONST
1	.06	.13	2.1
2	.11	.30	2.7
3	.12	.44	3.6
4	.14	.19	1.3
5	.15	2.3	15.3
6	.17	1.3	7.6
7	.25	.11	.44

\* TOTAL FREQUENCY CHANGE FOR 38 DAYS OF AGING

TABLE II Summary of results of aging test.



## AUTHOR INDEX

AUTHOR	PAGE	AUTHOR	PAGE	AUTHOR	PAGE
Albert, W.C.	233	Hays, Jr. R.M.	271	Qi-Xiang, Z.	476
Armington, A.F.	3	Hellwig, H.	458	Riley, W.J.	387
Aubry, J.P.	190	Hessick, D.	341	Robb, J.C.	464
Avila, G.	452	Ishizu, M.	447	Robichon, G.	201
Balascio, J.F.	3	Jackson, G.	310	Rosati, V.	225, 507
Ballato, A.	206, 240	Jardino, M.	431	Rosenfeld, R.C.	271
Barnes, J.A.	319	Jewell, T.C.	363	Saburi, Y.	428, 447
Beaubien, A.F.	374	Jones, D.	471	Sawyer, B.	8
Benjaminson, A.	327	Kahan, A.	10, 150	Shibuki, M.	447
Besson, R.J.	366	Kaitz, G.	245	Silvermetz, D.	471
Brice, J.C.	487	Kavolis, P.J.	251	Sinha, B.K.	300
Brown, D.	380	Ketcham, R.S.	266	Stein, S.R.	483
Burns, S.G.	266	Kinloch, D.R.	8	Stevens, D.S.	176
Cerez, P.	452	Kojima, Y.	114	Stoermer, P.	380
Chai, B.	206	Kosinski, J.A.	225	Stokes, R.B.	282
Cloeren, J.M.	63	Krishnaswamy, S.V.	263	Strayer, D.M.	435
Cyr, N.	408	Lambole, J.	496	Suter, J.J.	63
D'Aleget, B.	254	Laszlo, E.	380	Tanaka, M.	286
Darcs, J.F.	496	Lau, K.F.	101, 282	Tellier, C.R.	105
Day, J.	310	Lee, P.C.Y.	164	Tetu, M.	408, 452
Debaisieux, A.	190	Levine, M.	458	Tiersten, H.F.	132, 176
Decailliot, M.D.	366	Lipson, H.G.	10	Tilton, R.	206
deClercq, E.	452	Lukaszek, T.	206, 240	Theobald, G.	157, 294
deLabachellerie, M.	452	Lynch, T.J.	387	Thompson, P.	507
Desaintfusen, M.	431	Manabe, N.	119	Tomase, J.	141
Dick, G.J.	435	Martin, J.J.	16	Toulouse, J.	32
Duchene, J.L.	431	McAvoy, B.R.	263	Tremblay, P.	408
Dworsky, L.	141	McGill, R.	380	Truong, Q.T.	55
EerNisse, E.P.	126	Meirs, M.	471	Urabe, S.	428, 447
Emmons, D.A.	80, 374	Merigoux, H.	496	Valentin, J.P.	157, 366
English, T.C.	387	Merlina, J.	184	Vasiljevic, D.	334
Euler, F.	150	Milliren, B.T.	80	Vig, J.R.	42, 225
Euler, W.	341	Miyazaki, J.	184	Volk, C.H.	387, 401
Filler, R.L.	225	Mizan, M.	206	Vulcan, A.	273, 315
Friedlaender, F.J.	279	Moore, R.A.	263	Wacks, J.	32
Frueholz, R.P.	387, 401	Morikawa, T.	428, 447	Wakatsuki, N.	114
Fujishima, S.	184	Morita, T.	286	Walls, F.L.	416
Fujiwara, Y.	114	Nakagiri, K.	447	Wang, J.S.	101
Gagnepain, J.J.	157, 201	Nakazawa, M.	140	Ward, R.W.	22
Garvey, R.M.	80, 374	Nakazawa, Y.	286	Watson, S.K.	101
Geist, J.D.	363	Norton, J.R.	63	Weglein, R.D.	73
Gifford, G.A.	483	Nowick, A.S.	32	Weidemann, W.	86
Gloeckl, C.	273	Ohta, Y.	428, 447	Wen-Wei, K.	476
Green, E.R.	32	Okazaki, M.	119	Xiu-Feng, D.	476
Gros Lambert, J.	201	Ono, K.	286	Yamada, S.	114
Gualtieri, J.G.	42	Palkuti, L.J.	55	Yamaguchi, H.	240
Hang-Xiang, H.	476	Parker, T.E.	310	Yen, K.H.	282
Hanna, S.M.	279	Pascaru, I.	471	Yerna, J.S.	499
Hanson, W.P.	38, 50, 251	Perdue, E.M.	92	Yong, Y.K.	164
Hatch, E.R.	206	Persson, K.B.	416	Zao-Cheng, Z.	476
Hauden, D.	294	Peters, H.E.	420		
		Plumelle, F.	431		

## SPECIFICATIONS AND STANDARDS GERMANE TO FREQUENCY CONTROL

Institute of Electrical and Electronic Engineers

Order through: IEEE Service Center  
445 Hoes Lane  
Piscataway, NJ 08854  
(201)-981-0060

- 176-1978 Piezoelectricity \$ 9.00
- 177-1966 Piezoelectric Vibrators, Definitions and Methods of Measurements for (ANSI C83.17-1970) \$ 4.00
- 180-1962 Ferroelectric Crystal Terms, Definitions of \$ 3.00
- 319-1971 Piezomagnetic Nomenclature \$ 4.00

Electronic Industries Association

Order through: Electronic Industries Assn.  
2001 Eye Street, N.W.  
Washington, DC 20006  
(202)-457-4900

(a) Holders and Sockets

RS-192-A, Holder Outlines and Pin Connections for Quartz Crystal Units. (Standard Dimensions for older types.) \$ 6.80

RS-367, Dimensional and Electrical Characteristics Defining Receiver Type Sockets. (Including crystal sockets.) \$20.20

RS-417, Crystal Outlines (Standard dimensions and pin connections for current quartz crystal units - 1974.) \$ 7.80

(b) Production Tests

RS-186-E, (All Sections), Standard Test Methods for Electronic Component Parts \$42.00

(c) Application Information

Components Bulletin No. 6, Guide for the Use of Quartz Crystals for Frequency Control \$ 4.90

(d) RS-477, Cultured Quartz (Apr. 81) \$ 5.50International Electrotechnical Commission

Order through: American National Standards Inst.  
1430 Broadway  
New York, New York 10018

\*ANSI can quote prices on specific IEC publication on a day to day basis only. All IEC and ISO standards have been removed from its Standards Catalog. Call ANSI, NYC (212)-354-3300 for prices.

IEC Publication 122-1 (1976)

Quartz crystal units for frequency crystal and selection. Part 1: Standard values and test conditions. (Second edition)

IEC Publication 122-2 (1962) Section 3:

Guide to the use of Quartz Oscillator Crystals, including Amendment 1 (1969).

IEC Publication 122-3 (1977) Part 3: Standard Outlines and Pin Connections. (Second edition)IEC Publication 283 (1968) Methods for the Measurement of Frequency and Equivalent Resistance of Unwanted Resonances of Filter Crystal UnitsIEC Publication 302 (1969) Standard Definitions and Methods of Measurement for Piezoelectric Vibrators Operating Over the Frequency Range up to 30 MHzIEC Publication 314 (1970) Temperature Control Devices for Quartz Crystal Units, including Supplement 314A Contents: General Characteristics & Standards; Test Conditions; Pin ConnectionsIEC Publication 314A (1971) First Supplement to Publication 314 (1970) Contents: Guide to the Use of Temperature Control Devices for Quartz Crystal UnitsIEC Publication 368 (1971) Piezoelectric Filters including Amendment 1, Amendment 2, and Supplement 368A and 368B Contents: General Information & Standards Values; Test ConditionsIEC Publication 368A (1973) First Supplement to Publication 368 (1971) Contents: Guide to the Use of Piezoelectric FiltersIEC Publication 368B (1975) Second Supplement to Publication 368 (1971) Contents: Piezoelectric Ceramic FiltersIEC Publication 444 (1973) Basic Method for the Measurement of Resonance Frequency and Equivalent Series Resistance Quartz Crystal Units by Zero Phase Technique in a  $\pi$  - NetworkIEC Publication 483 (1976) Guide to Dynamic Measurements of Piezoelectric Ceramics with High Electromechanical CouplingDepartment of Defense

Order through: Naval Publication & Form Center  
5801 Tabor Avenue  
Philadelphia, PA 19120

MIL-C-3098 Crystal Unit, Quartz, General Specification ForMIL-H-10056 Holders (Enclosures), Crystal, General Specifications ForMIL-STD-683 Crystal Units, Quartz/And Holders, CrystalMIL-O-55310 Oscillators, Crystal, General Specification ForMIL-F-18327 Filters, High Pass, Low Pass, Band Pass Suppression and Dual Functioning, General Specification ForMIL-O-39021 Oven, Crystal, General Specification ForMIL-O-55240 Oscillators, Audio FrequencyMIL-F-28734 Frequency Standards, Cesium Beam, General Specification ForMIL-F-28811 Frequency Standard, Cesium Beam TubeMIL-C-24523-(SHIPS), Chronometer Quartz Crystal....

PROCEEDINGS  
ANNUAL FREQUENCY CONTROL SYMPOSIA

<u>NO.</u>	<u>YEAR</u>	<u>DOCUMENT NO.</u>	<u>OBTAIN FROM*</u>	<u>COST</u>
10	1956	AD298322	NTIS	\$41.50
11	1957	AD298323	"	44.50
12	1958	AD298324	"	46.00
13	1959	AD298325	"	49.00
14	1960	AD246500	"	32.50
15	1961	AD265455	"	28.00
16	1962	PB162343	"	35.50
17	1963	AD423381	"	43.00
18	1964	AD450341	"	43.00
19	1965	AD471229	"	47.50
20	1966	AD800523	"	47.50
21	1967	AD659792	"	41.50
22	1968	AD844911	"	44.50
23	1969	AD746209	"	25.00
24	1970	AD746210	"	28.00
25	1971	AD746211	"	28.00
26	1972	AD771043	"	26.50
27	1973	AD771042	"	34.00
28	1974	ADA011113	"	31.00
29	1975	ADA017466	"	34.00
30	1976	ADA046089	"	40.00
31	1977	ADA088221	"	44.50
32	1978		EIA	20.00
33	1979		"	20.00
34	1980		"	20.00
35	1981		"	20.00
36	1982	ADA130811	NTIS	41.50
37	1983	83CH1957-0	IEEE	59.00
38	1984	84CH2062-8	"	

\*NTIS-National Technical Information Service  
Sills Building  
5285 Port Royal Road  
Springfield, VA 22161

(All prices are as of June 1984 and are subject to change.)

\* EIA-Annual Frequency Control Symposium  
c/o Electronic Industries Association  
2001 Eye Street  
Washington, DC 20006

\*IEEE-Institute of Electrical & Electronics Engineers  
445 Hoes Lane  
Piscataway, NJ 08854

\* SGC-Systematics General Corporation  
Brinley Plaza Route 38  
Wall Township, NJ 07719

Remittance must be enclosed with all orders.

The Proceedings of the 33rd (1979) and 34th (1980) Symposia contain a bibliography of the world-wide literature on precision frequency control and selection compiled by Dr. E. A. Gerber for the years 1968-1978 with part of 1980, respectively.

A subject and author index for the Proceedings of the 10th through the 38th Symposia appears as a supplement to the 38th Proceedings volume.